UNIVERSITÀ degli STUDI di CATANIA

Dottorato di ricerca in Scienze Geologiche, Biologiche e Ambientali

UNDERSTANDING BLOCK ROTATION ALONG STRIKE-SLIP FAULT ZONES IN YUNNAN (CHINA): PALEOMAGNETIC AND STRUCTURAL APPROACH

Ph.D Thesis

Dott.ssa Alessandra Giovanna Pellegrino

Coordinatore dottorato :

Prof. Agata Di Stefano

Relatore/Correlatore :

Prof. Rosanna Maniscalco

Prof. Fabio Speranza

XXXI CICLO

2015/2018

Introduzione e scopo del Progetto di Ricerca

Durante gli ultimi decenni, sono stati proposti diversi modelli tettonici per spiegare la deformazione e le rotazioni di blocchi crostali, attorno ad assi verticali, in zone di taglio o *strike-slip*. Un metodo per validare questi modelli è l'analisi paleomagnetico - strutturale realizzata proprio lungo le più importanti faglie trascorrenti del mondo.

L'area di studio proposta per il progetto di ricerca di questo dottorato, è stata analizzata da un classico e noto lavoro di *Tapponnier et alii* [1982], che descrive, attraverso un modello analogico con la plastilina, l'indentazione della placca Indiana nel continente Euro-Asiatico. Ciò avrebbe prodotto, a partire da 40-50 Ma, età della collisione tra i continenti India ed Eurasia, ispessimento crostale nell'area a nord e nord-est della catena Himalayana e l'estrusione del blocco Indocinese verso sud-est. Uno dei principali punti d'interesse sulla deformazione continentale e sull'evoluzione tettonica dell'Asia [*Molnar*, 1988], ed ancora oggetto di acceso dibattito, è il ruolo delle grandi faglie strike-slip che, probabilmente, hanno guidato l'estrusione del blocco Indocinese.

Un primo gruppo di studiosi considera la crosta essenzialmente rigida, con la deformazione concentrata lungo i suoi margini: in questo modello, le faglie trascorrenti litosferiche hanno grandi rigetti ed grandi tassi di movimento. Un secondo gruppo lega la deformazione della crosta continentale ispessita, come quella Tibetana, allo scollamento ed alla deformazione omogenea di un sottile settore crostale, a comportamento viscoso, soggetto a rotazioni e raccorciamento. Gran parte di questa controversia è focalizzata proprio sul ruolo e sul rigetto orizzontale della faglia del Red River, lunga circa 1000 km e che si estende con orientazione NW-SE dall'angolo SE del Tibet fino al Mar Cinese Meridionale. Questa faglia, insieme alla Gaoligong e alla Chongshan, dividono strutturalmente la provincia dello Yunnan (Cina sud-occidentale) in tre blocchi crostali più piccoli caratterizzati da un'intensa attività sismica.

In questa tesi, si propone pertanto uno studio paleomagnetico e strutturale lungo queste faglie, al fine di valutare se, e con quale entità, queste siano responsabili della deformazione e delle rotazioni dei blocchi crostali che compongono la regione dello Yunnan.

Riassunto

I dati raccolti durante i tre anni di attività di Dottorato di Ricerca riguardano il paleomagnetismo di rocce sedimentarie e vulcaniche affioranti lungo due importanti zone di taglio che caratterizzano la provincia dello Yunnan (Cina): la faglia Gaoligong e la faglia del Red River. Durante il primo anno, sono stati campionati 50 siti (per un totale di 503 campioni) a distanze variabili (fino a ~25 km) dalle miloniti affioranti lungo la zona di taglio Gaoligong. I *red beds* di età Giurassico-Cretaceo, registrano rotazioni orarie rispetto al blocco Euro-Asiatico, che raggiungono il picco massimo (176°) in prossimità della faglia e diminuiscono progressivamente spostandosi verso est. Ad ovest della faglia Gaoligong invece, i siti di età Pliocene-Olocene, affioranti nel campo vulcanico di Tengchong, non evidenziano significative rotazioni. Pertanto, i dati dimostrano che l'attività della zona di taglio Gaoligong ha prodotto rotazioni orarie significative probabilmente coeve ai principali movimenti tettonici avvenuti nell'Eocene-Miocene. Il modello di rotazione dei blocchi crostali lungo la zona di taglio Gaoligong, risponde ad un modello cinematico crostale "quasi - continuo", con blocchi di dimensioni ≤1 km vicino alla faglia, la cui dimensione aumenta allontanandosi verso est. I valori di rotazione e di dimensione della zona di deformazione, si traducono in un rigetto orizzontale della faglia Gaoligong di circa 230-290 km.

Al fine di investigare ulteriormente il ruolo delle faglie nella cinematica dello Yunnan, durante il secondo anno di dottorato, sono stati campionati altri 44 siti di età Triassico - Cretaceo (per un totale di 425 campioni) su entrambi i lati della zona di taglio del Red River e all'interno dei blocchi Chuandian, Lanping e Simao settentrionale. Quasi tutti i siti hanno prodotto componenti di magnetizzazione misurabili e stabili, ma la cronologia di acquisizione della magnetizzazione appare diversa nei tre blocchi. I dati evidenziano una rotazione variabile e differenziale che, anche in questo caso, non supporta un modello di rotazione rigida dei blocchi come proposto da autori precedenti, ma piuttosto suggerisce che: 1) il blocco Simao è costituito da blocchi minori (pochi km) che ruotano in senso orario, separati

da domini non rotanti di dimensioni simili; 2) una componente di magnetizzazione di alta temperatura (640-680 °C) suggerisce un comportamento rotazionale simile (blocchi secondari con rotazione oraria, antioraria e non-ruotati), anche al centro del “blocco” Lanping; al contrario, una componente di media temperatura (300-640 °C) acquisita successivamente al 28% della fase di piegamento non ha registrato alcuna rotazione. I siti vicini (entro i 25 km) al sistema di faglie della Red River, localizzati nel “blocco” Lanping producono invece grandi rotazioni dell'ordine di 180°. Anche i siti localizzati a 10-15 km di distanza dalla zona di taglio Chongshan mostrano rotazioni antiorarie di circa 90°, in accordo con il movimento sinistro della faglia.

I dati del presente lavoro, per la prima volta mostrano che le tre faglie Gaoligong, Chongshan e Red River influenzano significativamente le rotazioni di piccoli blocchi crostali nelle immediate vicinanze delle grandi faglie trascorrenti. Tuttavia, il verificarsi di ulteriori rotazioni (dell’ordine di 20°) all’interno dei blocchi Baoshan e Lanping - Simao, a distanze di oltre 20 km dalle faglie, lascia ancora aperto il quadro della deformazione e delle rotazioni di blocchi crostali che caratterizzano la provincia dello Yunnan.

Abstract

Data from this study report on the paleomagnetism of sedimentary and volcanic rocks cropping out near the Gaoligong and Ailao-Shan Red River Shear Zones. Fifty paleomagnetic sites were analyzed collecting 503 samples, during the first year of Ph.D., at variable distances (up to ~25 km) from mylonites exposed along the Gaoligong fault. Jurassic-Cretaceous red bed sites yield systematic CW rotations with respect to Eurasia reaching the peak values of 176° close to the fault, and progressively decrease moving eastward, up to be virtually annulled ~20 km E of mylonite contact. West of the Gaoligong fault, Pliocene-Holocene sites from the Tengchong volcanic field do not rotate. Thus, data show that the Gaoligong Shear Zone activity yielded significant CW rotations that were likely coeval to the main Eocene-Miocene episodes of dextral fault shear. The Gaoligong zone rotation pattern conforms to a quasi-continuous crust kinematic model, and shows blocks of ≤1 km size close to the fault, which become bigger moving eastward. Rotation and width values of the rotated-deformed zone translate to a 230-290 km Gaoligong Shear Zone dextral offset, which shows that fault shear plays a significant role in Indochina CW block rotation.

During the second year of Ph.D., forty-four Triassic-Cretaceous sites (425 samples) were collected at both sides of the Ailao-Shan Red River Shear Zone (ARRSZ), within the Chuandian, Lanping and Northern Simao blocks. Nearly all sites yielded measurable and stable magnetization components, but magnetization acquisition timing was different in the three blocks. Sites from the Chuandian block show a normal polarity and were remagnetized after folding. In the northern Simao block the magnetization was acquired before folding (about 33 Ma ago), but the ubiquitous normal polarity in Jurassic-Cretaceous sites suggests a pre-folding magnetic overprint. The data show variable and different rotation that do not display evidence of a rigid block rotation, but suggest that the northern Simao block is made of small (few km size) sub-blocks rotating CW, separated by non-rotating domains of similar

size. Finally, a high-temperature (640-680°C) magnetization component suggests a similar rotational behaviour (CW-rotating and non-rotating sub-blocks) in the centre of the Lanping block. Conversely, a 300-640°C component was later acquired at 28% unfolding and subsequently underwent no rotation. The sites close (less than 25 km) to the ARRSZ yield great rotations of nearly 180°, which confirm past occurrence of significant strike-slip shear along the ARRSZ itself. Conversely, sites located at 10-15 km distance from the Chongshan Shear Zone show ca. 90° CCW rotations that imply a left-lateral shear along the fault zone, consistently with recent geological evidence. Summarizing, data from my Ph.D. study, together with previous evidence of rotations documented both near the fault zones and within the blocks themselves, show that crustal deformation of the Yunnan is extremely complex and still puzzling. The Baoshan and Lanping-Simao blocks underwent strong internal deformation and were likely fragmented in smaller independent sub-blocks whose kinematics and tectonics are still a matter of speculation.

This research is divided into four parts.

Part I contains six chapters. A brief introduction to the aim of the research presented in this thesis. *Chapter 1*, shows the state-of-the-art of the kinematic models of block rotation, fundamental setting to this research. The *second* and *third Chapter* include a brief overview of the matter of Paleomagnetism and the methods used for gathering paleomagnetic directions through *in situ* sampling and paleomagnetic analysis in laboratory. *Chapter 4* and *5* regard the geological setting of the studied area and the description of paleomagnetic data collected by the previous authors in adjacent areas.

Part II, reports the outcomes from the research along the Gaoligong Shear Zone in Yunnan (*Chapter 6*), recently published on Tectonics by *Pellegrino et al.* [2018].

Part III, includes the results of the paleomagnetic analysis of the rotation pattern along the Ailaoshan Red River Shear Zone (*Chapter 7*), and of the deformation inside the Lanping, Simao and Chuandian blocks. The use of anisotropy of magnetic susceptibility (AMS) measurements (*Chapter 8*) and magnetic mineralogy analysis (*Chapter 9*) permit to infer tectonic deformation.

Finally, in **Part IV** there are the concluding remarks of this research (*Chapter 10*), followed by references and supplementary information.

Introduction

Previous paleomagnetic data from Yunnan (China) showed a predominant post-Cretaceous clockwise (CW) rotation pattern, mostly explained invoking huge (hundreds of km wide) blocks, laterally escaping (and/or rotating) due to India-Asia collision, separated by major strike-slip shear zones. However, the matter of crustal blocks rotation pattern inside the deforming zone of strike-slip faults, remains still highly controversial. Two set of models have been proposed to explain the rotation of Indochina block: a first set of models suggests that CW rotations of Yunnan are the result of lateral escape of Tibet that rotated CW around the north-eastern corner of the Indian Plate called "Eastern Himalayan syntaxis" [e.g. *Chen et al.,* 1995*; Funahara et al.,* 1992, 1993*; Kondo et al.,* 2012*; Sato et al.,* 2001, 2007*; Tanaka et al.,* 2008*; Tong et al.,* 2013]. However, this may explain CW rotations of the northern part of Indochina, but can hardly account for the CW rotations documented further south, at 21°-22°N latitudes.

A second set of models [*Gao et al.,* 2015*; Wang et al.,* 2008*; Zhao et al.,* 2015] argues that CW rotations occur along rigid mega-blocks (hundreds of km wide) or slates bounded by strike-slip faults, conforming to the so-called "bookshelf" tectonics [*Cowan et al.,* 1986*; Garfunkel and Ron,* 1985*; Li et al.,* 2017a*; Mandl,* 1987*; Mckenzie and Jackson,* 1986*; Nur et al.,* 1986*; Ron et al.,* 1984]. This model is hard to maintain-at least for the northern Yunnan-as the elongated slates located between the faults are some 1000 km long and only 200-300 km wide, so that their rotations would lay a significant space problem according to *Pellegrino et al*. [2018]. Alternatively, the land stripes between the faults might be broken into several small slates, each rotating independently, of which –however- no field evidence has been found so far. There is a third tectonic mechanism possibly yielding vertical-axis rotations that has not been investigated in Indochina so far: strike-slip fault shear. In fact, it has been observed that strike-slip zones are bounded by damage zones where large (even >90°) vertical-axis rotations may occur in response to the ductile deformation taking place in the lower crust [*Beck,* 1976*; Hernandez-Moreno et al.,* 2014 and references therein*; Kimura et al.,* 2011*; Piper et al.,* 1997*; Randall et al.,* 2011*; Ron et al.,* 1984*; Sonder et al.,* 1994; *Pellegrino et al*., 2018]. Depending upon fault displacement and locking, and crust rheology, such local rotation zone may be even 20-30 km wide on each fault side [*Randall et al.,* 2011*; Sonder et al.,* 1994]. Therefore, paleomagnetism is a powerful tool for documenting and quantifying such tectonic data and this thesis project will aid in the unravelling of the Indochina rotation pattern puzzle.

Therefore, pursued goals of this research are focused on the understanding of: (1) the vertical axis rotation pattern associated to main strike-slip fault systems in Yunnan and (2) the behavior of crustal blocks, during the rotation process in order to (3) evaluate if - and to what extent - the faults can play an important role in the Indochina block extrusion.

To reach these outcomes I investigated the distribution of vertical-axis paleomagnetic rotations inside the deforming zone of the important strike slip fault zones in Yunnan (China), which are interpreted as the extrusion guides of the Indochina block during the collision between India and Eurasia blocks.

Index

Chapter I

1. KINEMATIC MODELS OF BLOCK ROTATION RELATED TO STRIKE-SLIP FAULTING

A primary component of the intraplate deformation of Earth occurs in strike-slip tectonic domains, yielding both strike-slip fault displacement and vertical-axis rotation of crustal blocks [*Freund*, 1974*; Garfunkel*, 1974; *MacDonald*, 1980; *Lamb and Bibby*, 1989; *Jackson and Molnar*, 1990].

In the last decades, several different geometric models have been suggested to explain the pattern of deformation and paleomagnetic rotation along strike-slip fault zones. These models consider geologic parameters, such as crust rheology, length, sense and total slip of the main shear zone, structural arrangement, deformed zone width, and deformation scale. The rotation amount can be quantified using simple mathematic relations, if some of these parameters are known with good approximation [*Hernandez-Moreno*, 2015].

To validate the models, paleomagnetic measurements along first-order strike-slip faults have been conducted in different parts of the world: Dead Sea transform fault [Israel, *Ron et al.*,1984], North and Central Anatolian fault zone [Turkey, *Piper et al.*, 1997; *Lucifora et al.*, 2013], Las Vegas Valley Shear Zone [Western US, *Sonder et al.*, 1994] , Alpine Fault [New Zealand, *Randall et al.*, 2011], Eneko and Tanna fault zones [Japan, *Kimura et al.*, 2004, 2011], fault systems of the Aegean Sea [central Greece, *McKenzie and Jackson*, 1986], Alpine Himalayan Belt [Iran, *Jackson and McKenzie*, 1984], San Andreas Fault System [Central California, *Beck*, 1986; *McKenzie and Jackson*, 1983; *Terres and Luyendyk*, 1985; *Titus et al.*, 2011], and Liquine-Ofqui fault zone [Cile, *Hernandez-Moreno et al.*, 2014, 2016].

Depending on block size and shape, and rotation pattern, crust deformation models can be subdivided into three main groups, called **discontinuous**, **continuous**, or **quasi-continuous models** [*Hernandez-Moreno et al.*, 2014].

The *discontinuous models* consider the bookshelf tectonics [*Ransome et al.*, 1910; *Morton and Black*, 1975; *Cowan et al.*, 1986; *Mandl*, 1987], where sets of strike-slip secondary faults, within a shear zone, bound rigid or undeformed blocks with similar dimensions to the width of the shear zone that rotate as the faults move laterally [*Ron et al.*, 1984; *Garfunkel and Ron*, 1985; *McKenzie and Jackson*, 1986; *Nur et al.*, 1986] (Figure 1).

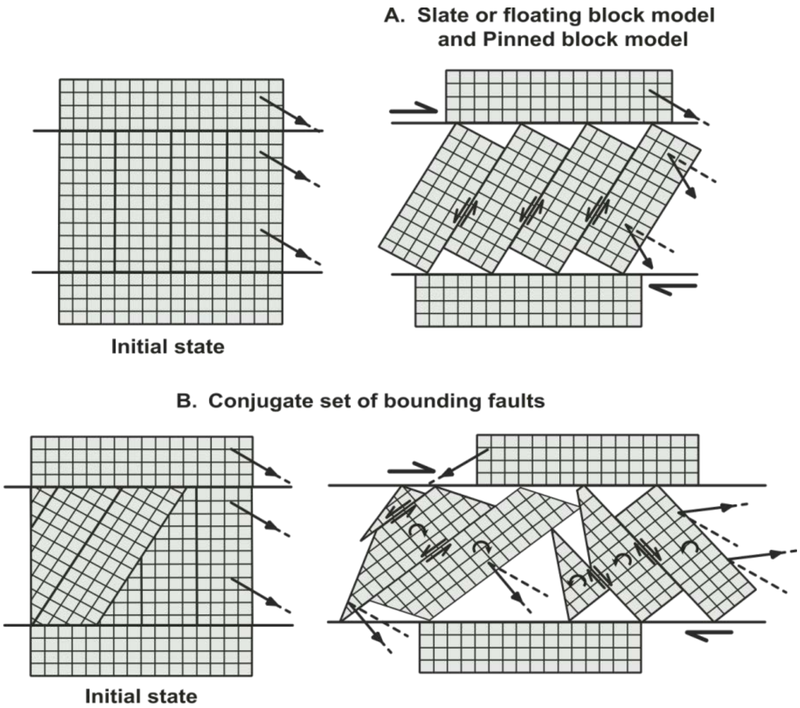

Figure 1. DISCONTINUOUS KINEMATIC MODELS. Modified after *Hernandez-Moreno et al*. [2014]. A) Slate or floating block model and Pinned block model [*Ron et al*., 1984; *Nur et al*., 1986; *Garfunkel and Ron*,. 1985; *McKenzie and Jackson*, 1986]; B) Conjugate set of bounding faults [*Ron et al*., 1984; *Garfunkel and Ron*, 1985].

Within the same domain, rotation is spatially constant in amount and sense, cannot exceed 90º, and decreases to zero when the secondary faults become parallel to the domain boundary. In the case of sets of conjugate faults (Figure 1B), expected rotations should be of both senses: CW (CCW) at blocks bounded by sets of left-lateral (right-lateral) strike-slip faults [*Freund*, 1974; *Garfunkel*, 1974; *Ron et al.*, 1984; *Garfunkel and Ron*, 1985; *McKenzie and Jackson*, 1986; *Beck et al.*, 1993; *Hernandez-Moreno*, 2015 and reference therein].

The second group of models corresponds to the <u>*continuous models*</u>.

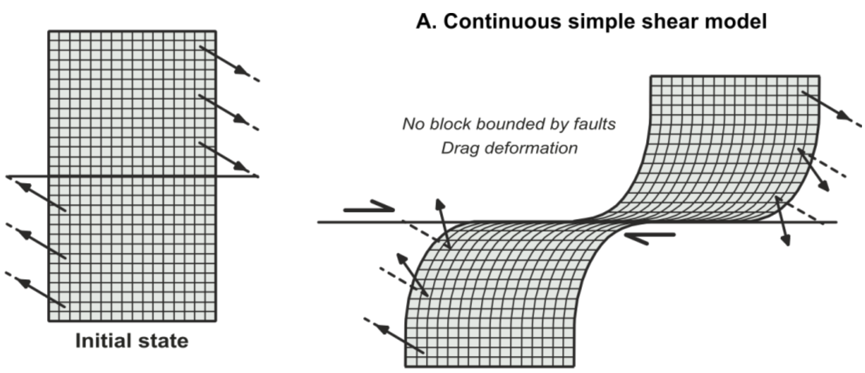

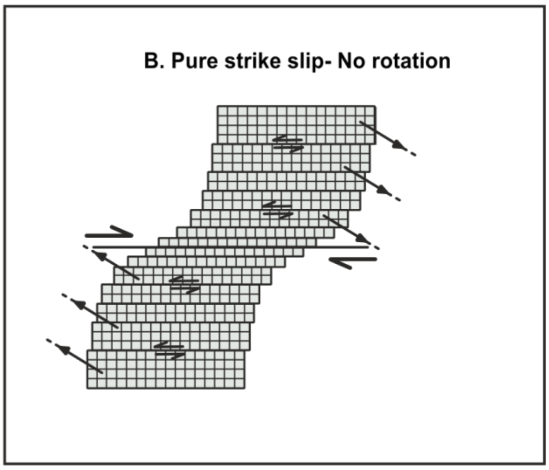

Figure 2. CONTINUOUS KINEMATIC MODELS. Modified by *Hernandez-Moreno et al*. [2014]. A) Continuous simple shear models [*England et al.*, 1985; *Sonder et al.*, 1986; *Mckenzie and Jackson*, 1986; *Kimura et al.*, 2004, 2011]; B) Pure strike slip- No rotation [*Geissman et al.*, 1984; *Platzman and Platt*, 1994; *Bourne et al.*, 1998].

McKenzie and Jackson [1986] postulated that if the scale of deformation has a large wavelength compared to the brittle layer crust thickness, the surface deformation is expected to be continuous. Differently from the discontinuous models, the shear is distributed within the deforming zone with no through-going faults over a wide uniform domain (Figure 2). Rotations are expected to be CW (CCW) in right-lateral (left-lateral) fault systems, to progressively increase towards the fault, and to be up to 90º in magnitude [*Kimura et al.,* 2004, 2011].

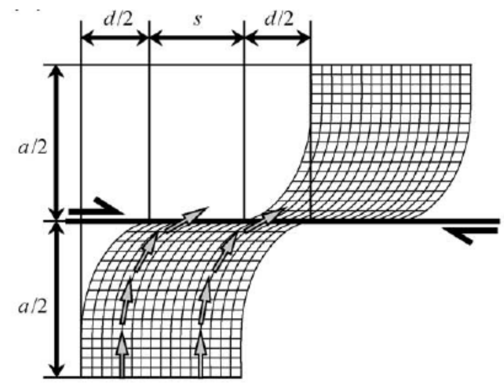

Figure 3. Continuous deformation model. Detail of Figure 5A. The amount of rotation at a point close to the fault trace is larger than at a point far from the fault. *a* width of the Shear Zone; *d* displacement parallel to the fault caused by strike-slip deformations, *s* strike-slip offset on the fault trace. Modified from *Nelson and Jones* [1987].

Based on the assumption that the entire lithosphere behaves as a thin viscous sheet [*Bird and Piper*, 1980; *England and McKenzie*, 1982, 1983; *Sonder and England*, 1986], these models suggest that the rotation occurs in the brittle upper crust that forms a thin rigid plastic veneer upon the rest of the lithosphere. Deforming upper crust presumably follows passively the motion of the deeper parts of the lithosphere, expected to behave like a viscous medium [*England et al.*, 1985; *Sonder et al.*, 1986; *England and Wells*, 1991].

Several methods have been applied to quantify the total displacement of strike-slip faults: the continuous models consider necessary add the drag deformation within the shear zone (*d*, continuous rotational drag) to the offset on the fault trace (*s*, rigid deformation) (Figure 3) [*Nelson and Jones*, 1987]. Ignoring the drag deformation yields to underestimation of both individual faulting events magnitude and fault slip rates [*Salyards et al.*, 1992; *Nagy and Sieh*, 1993; *Kimura et al.*, 2004, 2011].

The continuous drag deformation *d* along a strike-slip fault and the amount of rotation at any point are mathematically expressed by *Kimura et al.* [2004; 2011] equations, but it can also be calculated based on the power law rheology model [*England et al.*, 1985; *McKenzie and Jackson*, 1983; *Sonder and England*, 1986; *Nelson and Jones*, 1987; *Kimura et al.*, 2011].

Finally, the third group (Figure 4), the *quasi-continuous* models, is also based on a viscous model for lithospheric deformation [*England and McKenzie*, 1982; *England et al.*, 1985; *Sonder et al.*, 1986; *Sonder and England*, 1986; *England and Wells*, 1991].

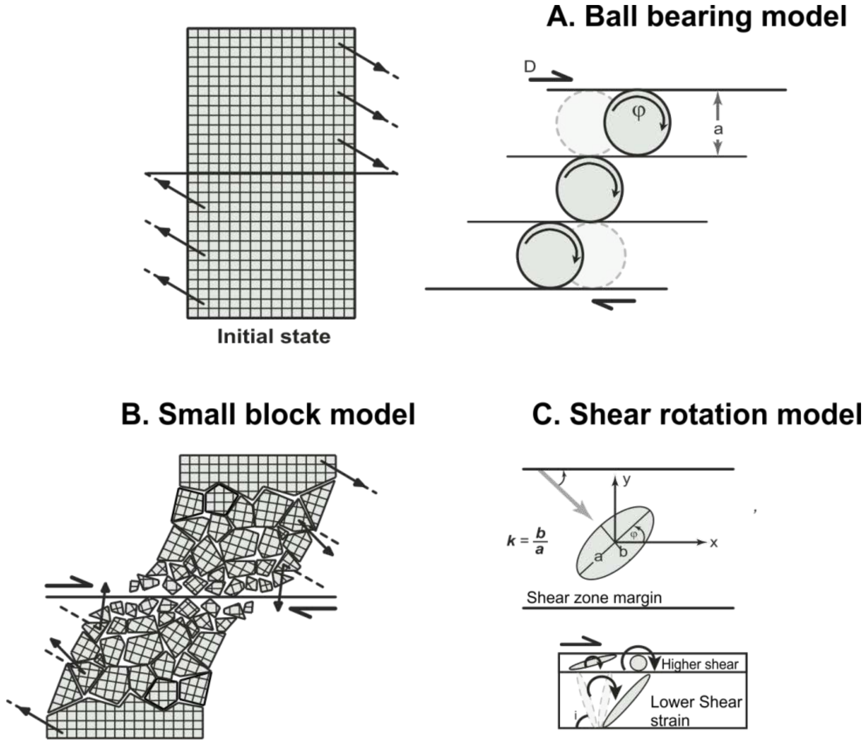

Figure 4. QUASI-CONTINUOUS KINEMATIC MODELS. Modified by *Hernandez-Moreno et al.*, 2014. A) Ball bearing model [*Beck*, 1976; *Piper et al.*, 1997]; B) Small block model [*McKenzie and Jackson*, 1983; *Nelson and Jones*, 1987; *Sonder et al.*, 1994]; C) Shear rotation model [*Lamb*, 1987; *Randall et al.*, 2011].

Here the thin viscous sheet represents the ductile middle and lower crusts under the uppermost brittle seismogenic crust, which unlike in the continuous models, is broken into small rigid blocks with sizes smaller than the shear zone width (Figure 4B-5). Block rotations occur in response to the angular velocity of the ductile deformation, taking place at great depth in the lower crust [*Beck*, 1976; *McKenzie and Jackson*, 1983; *Lamb*, 1987; *Nelson and Jones*, 1987; *Salyards et al.*, 1992; *Sonder et al.*, 1994; *Piper et al.*, 1997; *Randall et al.*, 2011].

The rotation magnitude will depend on fault length, lithosphere rheology, displacement amount, block aspect ratio (short/long axis) and their orientation with respect to the system-bounding fault [*Lamb*, 1987; *Piper et al.*, 1997; *Randall et al.*, 2011]. The rotation is CW (CCW) in regions of dextral (sinistral) shear, and increases gradually getting closer to the fault, reaching values greater than 90º [*Nelson and Jones*, 1987; *Sonder et al.*, 1994; *Piper et al.*, 1997].

Figure 5. Small-block (quasi-continuous model) from *Lamb* [1987].

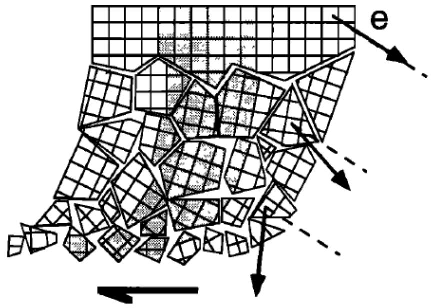

One of the most simple quasi-continuous models is the *ball bearing fashion* [*Beck*, 1976; *Piper et al.*, 1997], where crustal blocks can rotate freely like balls in a bearing into narrow zones bounded by strike-slip faults parallel to the main shear zone (Figure 4A-6). As the rotation is a continue process, brittle destruction at the corners of the blocks tends to produce sub-rounded equidimensional blocks [*Hernandez- Moreno*, 2015].

The relationship between fault displacement D and rotation φ (expressed as a proportion of 360º) of a fault block of width a approximated by a freely moving circular block is:

$$D = \varphi \pi a \qquad (1)$$

But rotating blocks are not usually equidimensional, as might be required to accommodate very large rotations prevented by the friction between them [*Nur et al.*, 1986].

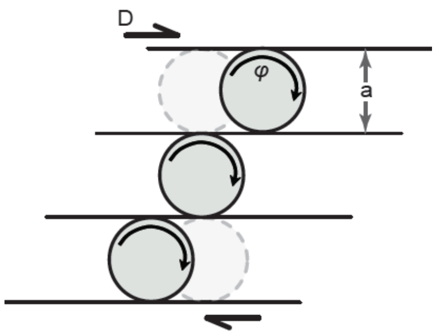

Figure 6. Ball bearing fashion model from *Beck* [1976] and *Piper et al*. [1997].

Since from structural observations, may not be possible to know the block size or size distribution, *Sonder et al.* [1994] present two block geometry models to estimate the maximum characteristic block size associated with a strike-slip fault (Figure 7).

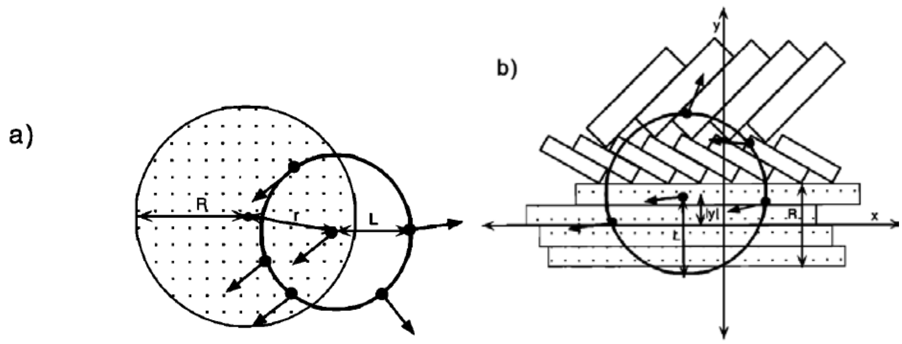

Figure 7. Models proposed by *Sonder et al.* [1994] to estimate block size. Arrows indicate paleomagnetic declinations at hypothetical localities. **a)** Circular block model, *R* is the radius of shaded rigid circular block, *r* the position of a locality relative to the centre of the block, and *L* the inter locality distance, $\bar{p}$ (the average probability that a site a distance *L* from the locality at *r* is indistinguishable from that at *r*) is related to the fraction of the circle of radius *L* inside the rigid block (shaded circle). **b)** Domain block model. In this case *R* is the width of the domain, $|y|$ the distance from the domain axis of a locality, and *L* the distance of other localities from the first.

The first model (equal blocks rotating independently), considers a rigid circular block of radius *R* sampled at a distance *r* from its center (Figure 7a) [*Sonder et al.*, 1994].

The second model concerns to highly elongated blocks rotating together as domains [*McKenzie and Jackson*, 1983, 1986; *Ron et al.*, 1984; *Taymaz et al.*, 1991a,b] (Figure 7b).

Conversely, *Lamb* [1987] and *Randall et al.* [2011] in their *shear rotation model* showed ellipsoidal blocks whose rotation rate and amount are function of both their aspect ratio (*k* = short axis *b*/long axis *a*) and orientation with respect to the system bounding fault through time (Figure 4C). Thus, this model predicts a marked decrease in rotation rate for elongate blocks (*k* <1, constant) when they rotate into a direction more nearly parallel to the Shear Zone margins [*Randall et al.*, 2011]. Conversely, if the aspect ratio k increases by breakup during rotation (*k* ~ 1), the resulting equidimensional block will continue to rotate at a constant rate [*Lamb*, 1987].

For a width shear zone W, and fault displacement D, the total amount of rotation at any particular time, given the initial orientation ϕ_i of the long block axis a, is determined by the ratio D/W and the aspect ratio k [*Lamb*, 1987].

The block rotation for $k > 5$ can be approximated within 10% accuracy to that of a passive marker line, equation 2, while for $k \sim 1$ is defined by the equation 3 [*Lamb*, 1987]:

$$\theta = 90° - \phi_i + \mathrm{atan}(D/W - \tan(90° - \phi_i)) \qquad (2)$$

$$\theta = 0.5\, D/W \qquad (3)$$

If k does not equal to 1, also there is a simplified expression for R, the instantaneous rotation rate ($d\phi/dt$), by *Lamb* [1987]:

$$R = \frac{W}{2}\left[\left(\frac{1-k^2}{1+k^2}\right)(\cos 2\phi + tan\theta \sin 2\phi) - 1\right] \qquad (4)$$

Positive values of R indicate CCW rotations.

When $k = 1$, R is constant and equals $-W/2$ (CW to dextral shear). For $k < 1$, the rotation rate varies with orientation. For sufficiently small values of k, R changes sign for certain orientations and hence the block will rotate in the opposite direction. The overall effect of all this deformation is a "straightening-out" of the major faults, where shear could be taken up by slip on the faults without any rotation of the intervening faults blocks or slow rotation.

The end-member of the quasi-continuous models would be in the case of elongated blocks trending approximately parallel to the relative plate motion across the strike-slip zone. Pure strike-slip is applied to blocks displacing parallel to the deformation zone, implying a lack of rotations [*Geissman et al.*, 1984; *Platzman and Platt*, 1994; *Bourne et al.*, 1998] (Figure 8).

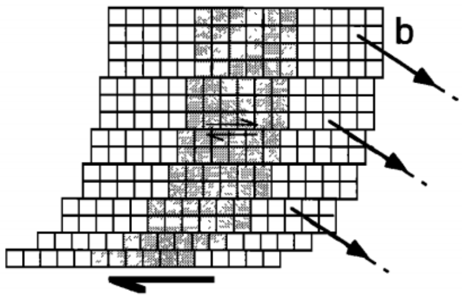

Figure 8. Transcurrent deformation by displacement on parallel faults, with no rotation. Modified from *Sonder et al*. [1994].

If the frictional forces on faults walls are negligible in comparison with basal traction, the block will be in equilibrium when the net drag force on their base is zero [*Bourne et al.*, 1998]. This coincides with one of the stationary states of *Lamb* [1987].

Chapter II

2. FUNDAMENTALS OF PALEOMAGNETISM

Paleomagnetism [*Tarling*, 1983; *Tauxe*, 1998; 2009; *Butler*, 1992] is a branch of Geophysics that studies the geomagnetic field behaviour of the geological past. It has widespread applications for a variety of disciplines: the study of atmosphere and biosphere interactions, the study of the early history of the Earth [e.g., *Tarduno et al*., 2006], the physics of the Earth's interior [e.g., *Christensen and Wicht, 2007*], tectonics [e.g., *Torsvik et al*., 2008, 2012; *Hernandez Moreno et al*., 2014; 2016], geologic applications from magnetostratigraphy, biostratigraphy [e.g., *Opdyke and Channell*, 1996], and archaeomagnetic dating [e.g., *Lanos*, 2004; *Pavòn-Carrasco et al*., 2011].

This subject has been vastly addressed in the last forty years by both research papers and books [e.g, *Irving,* 1964; *McElhinny*, 1973; *Beck* 1976, 1980, 1984; *McElhinny,* 1976; *Jelinek,* 1977, 1978; *Hillhouse*, 1977; *Simpson and Cox*, 1977; *Beck and Burr*, 1979; *Kamerling and Luyendyk,* 1979; *Coney et al*., 1980; *Magill and Cox*, 1980; *Bates et al*., 1981; *Magill et al*., 1981; *Globerman et al*., 1982; *Magill et al*., 1982; *Demarest*, 1983; *Merril and McElhinny*, 1983; *Tarling,* 1983; *Hillhouse and Grommé,* 1984; *Coe et al*., 1985; *Luyendyk et al*., 1985; *Wells and Coe,* 1985; *Beck et al*., 1986; *Grommé et al*., 1986; *May and Butler,* 1986; *Hagstrum et al*., 1987; *Wells and Heller,* 1988; *Butler et al*., 1989; *Butler*, 1992; *Dunlop and Özdemir,* 1997; *Tauxe,* 1998, 2009; *McElhinny and McFadden,* 2000].

The Earth's magnetic field is approximately a dipolar field (95% of the field component), resulting from an internal source (the dynamo in Earth's core mantle and crustal field) and external source (atmospheric field, and crustal induced field; *Merrill et al*., 1996). The non-dipolar field is that part of internal geomagnetic field, remaining after that dipole contribution has been removed.

Assuming the validity of dipolar geocentric field, the geomagnetic field can be represented as a vector framed into a three-dimensional, orthogonal coordinate system usually with origin in a specific point on the earth surface. This vector has an H magnitude and can be broken into two components, H_v vertical and H_h horizontal (Figure 9). The direction of geomagnetic field is describe by **Inclination I** (angle between the horizontal plane and the geomagnetic field vector, ranging from -90° to 90° and positive when downward) and **declination D** (angle from geographic north to horizontal component, ranging from 0º to 360º, positive clockwise).

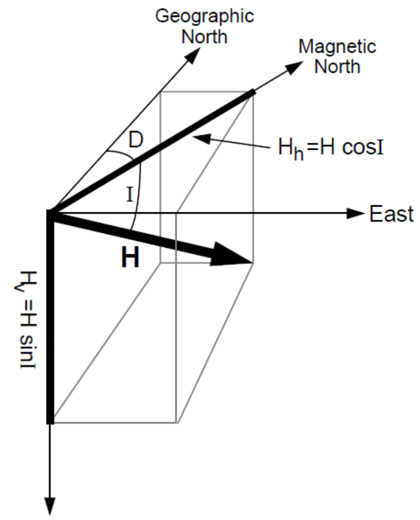

Figure 9. Geomagnetic field *H* components: H_v vertical component, H_h horizontal component, *I* inclination, *D* declination. Modified after *McElhinny* [1973].

The vertical component, H_v, of the surface geomagnetic field, H, is defined as positive downwards and is given by

$$\mathbf{H_v = H}\ \boldsymbol{sin}\ \mathbf{I} \qquad (5)$$

where H is the magnitude of H and I is the inclination of H from horizontal, ranging from –90° to +90° and defined as positive downward. The horizontal component, H_h, is given by

$$\mathbf{H_h = H}\ \boldsymbol{cos}\ \mathrm{I} \qquad (6)$$

and geographic north and east components are respectively,

$$\mathbf{H_N = H}\ \boldsymbol{cos}\ \mathbf{I}\ \boldsymbol{cos}\ \mathbf{D} \quad \mathbf{H_E = H}\ \boldsymbol{cos}\ \mathbf{I}\ \boldsymbol{sin}\ \mathbf{D} \qquad (7)$$

where D is declination, the angle from geographic north to horizontal component, ranging from 0° to 360°, positive clockwise [*Butler et al*, 1998].

Determination of I and D completely describes the direction of the geomagnetic field. If the components are known, the total intensity of the field is given by the equation:

$$\boldsymbol{H} = \sqrt{H_N^2 + H_E^2 + H_V^2} \qquad (\mathbf{8})$$

A central concept to many principles of paleomagnetism is the **Geocentric Axial Dipole (GAD)** model, where the magnetic field produced by a single magnetic dipole at the center of the Earth and aligned with the rotation axis is considered (Figure 10).

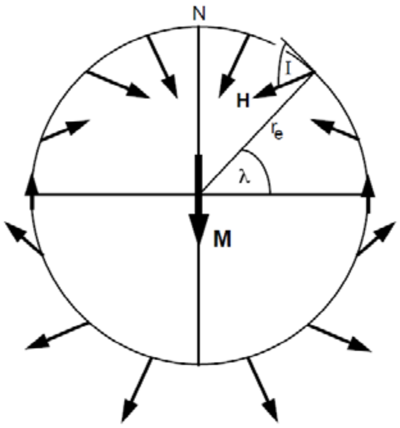

Figure 10. Modified after *Butle*r [1998]. Geocentric axial dipole model. Magnetic dipole M is placed at the center of the Earth and aligned with the rotation axis; the geographic latitude is λ; the mean Earth radius is r_e; the magnetic field directions at the Earth's surface produced by the geocentric axial dipole are schematically shown; inclination, I, is shown for one location; N is the north geographic pole. Redrawn after *McElhinny* [1973].

The geographic latitude λ is ranging from –90° at the south geographic pole to +90° at the north geographic pole. The inclination of the field can be determined by

$$\tan I = \left(\frac{H_v}{H_h}\right) = \left(\frac{2\sin\lambda}{\cos\lambda}\right) = 2\tan\lambda \qquad (\mathbf{9})$$

and I increases from –90° at the geographic south pole to +90° at the geographic north pole. This relationship between I and latitude will be essential for paleogeographic reconstructions and tectonic applications of paleomagnetism. For a GAD, D = 0° everywhere.

The magnetic field in a generic point is described by the equation:

$$B = \mu_0 H + \mu_0 J \qquad (10)$$

where B is magnetic induction (expressed in T), H magnetic field strength (A m^{-1}), J magnetization (Am^{-1}) or magnetic moment per unit of volume.

In vacuum, J is nil, in matter its properties depend on those of the elementary particles, according to which substances are subdivided into three categories: dia-, para- and ferromagnetic.

The ***diamagnetic*** response to application of a magnetic field is acquisition of a small induced magnetization, J_i, opposite to the applied field, H. The magnetization depends linearly on the applied field and reduces to zero on removal of the field. **Magnetic susceptibility values**, χ, for a diamagnetic material is negative ($\chi < -10^{-5}$ SI) and independent of temperature (Figure 11a). An example of a diamagnetic mineral is quartz, calcite and dolomite.

For ***Paramagnetic*** solids, the acquisition of induced magnetization is parallel to the applied field. Magnetic susceptibility values for these materials are positive ($10^{-5} \leq \chi \leq 10^{-3}$ SI) and depend on temperature (Figure 11b). For any geologically relevant conditions, J_i is linearly dependent on H. As with diamagnetic materials, magnetization reduces to zero when the magnetizing field is removed. An example of a paramagnetic mineral are clay minerals, fayalite, Fe_2SiO_4.

Ferromagnetic substances "sensu latu" are magnetite, titanomagnetites, greigyte. The $\chi >> 0$ and varies in a complex way according to the variation of applied field and temperature (Figure 11c-12). The main characteristic of ferromagnetic substances is a magnetic field of their own, also in absence of an external field H.

In this type of substance, very strong interaction exists at atomic level, called exchange interaction, which favour the orderly arrangement of the dipole magnetic moments. Above a certain temperature, characteristic of each ferromagnetic substance, spontaneous magnetization material fades, and the material becomes paramagnetic. This characteristic temperature is called the ***Curie Temperature*** **(T_C)**, instead for anti-ferromagnetic substances (hematite) is known as ***Neel Temperature*** **(T_N)**. Based on the size of a single ferromagnetic granule, it is possible that its internal structure is divided into a series of microscopic volumes each characterized by a preferential direction (and versus) of magnetization J. These regions are called ***magnetic domains*** and are developed to minimize the overall magnetic energy of the ferromagnetic granule.

Depending on the size, granules will be:

- **Single Domain (SD)** (a granule SD of cube-shaped magnetite, has size less than 0.1 μm);
- **Pseudo Single Domain (PSD)** (a PSD granule of cube-shaped magnetite, has dimensions between 0.1 μm and 1 μm) and
- **Multi Domain (MD)**.

There is another category of ferromagnetic substances called ***superparamagnetic*** **(SP)**. A superparamagnetic granule is a ferromagnetic granule of extremely small size (of the order of 0.01-0.03 μm for magnetite). Because of their dimensions, in order to remove an external magnetic field H, these granules are not able to maintain a remaining magnetization for a long time (paramagnetic substances loose the remaining magnetization instantly). Another feature of these substances is that they have a very high magnetic susceptibility (allowing easy identification) [*Butler*, 1992].

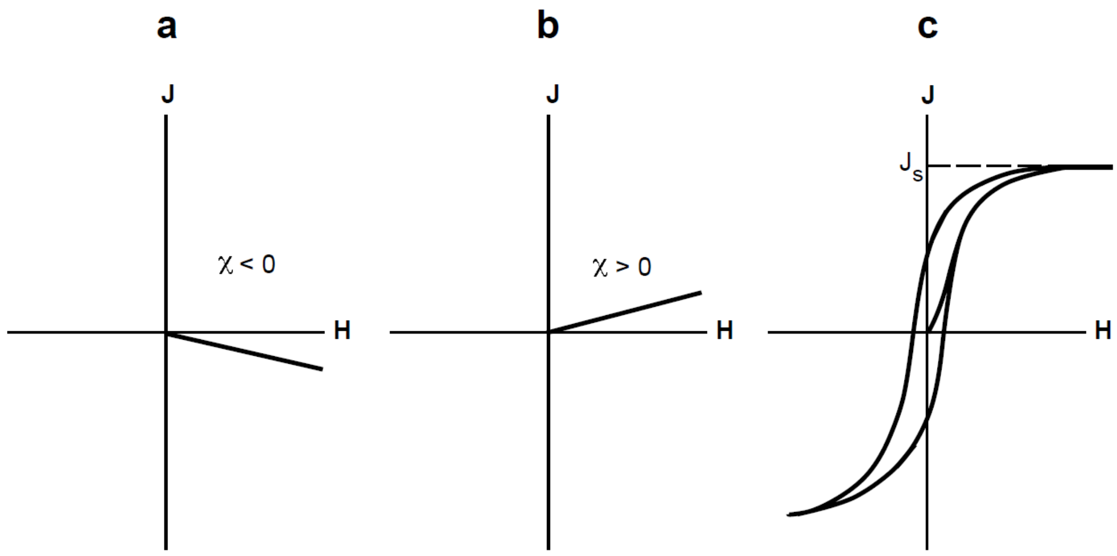

Figure 11. Modified after *Butler* [1998]. **a**) Magnetization, J, versus magnetizing field, H, for a diamagnetic substance. Magnetic susceptibility, c, is a negative constant. (**b**) J versus H for a paramagnetic substance. Magnetic susceptibility, c, is a positive constant. (**c**) J versus H for a ferromagnetic substance. The path of magnetization exhibits hysteresis (is irreversible), and magnetic susceptibility, c, is not a simple constant.

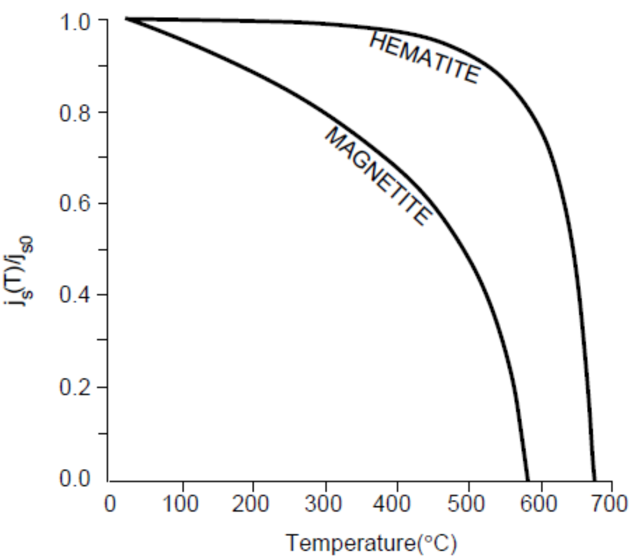

Figure 12.
Modified after *Pullaiah et al.* [1975]. Normalized saturation magnetization versus temperature for magnetite and hematite. js_0 = saturation magnetization at room temperature; for hematite, $js_0 \approx 2$ G; for magnetite, $js_0 = 480$ G.

Paleomagnetism entails the assumption that the "frozen" magnetization (primary) during rock formation (consolidation, diagenesis, cooling, etc), by means of several acquisition mechanisms (detrital, thermal, chemical magnetization), is parallel to the contemporaneous geomagnetic field at the time of the formation.

The essential paleomagnetism theory was presented by the Noble prize winner Louis Néel [1949, 1955], who explained how the ancient magnetic field (B_{anc}) might be preserved in rock's magnetic memory.

The Néel relaxation theory [1949] defines the characteristic **relaxation time** (τ) by the equation, which relates τ to frequency factor (≈ 10^8 s^{-1}), volume of single domain grains (*v)*, the anisotropy constant (k), the absolute temperature (T) (*kT* is the thermal energy), the microscopic coercitive force in single domain grains (h_c) and the saturation magnetization of the ferromagnetic material (j_s):

$$\tau = \frac{1}{C}\, exp\left(\frac{v\, h_c\, j_s}{2kT}\right) \qquad (\mathbf{11})$$

The Nèel theory is valid for the single domain grains (SD, i.e. of ~ 0.03 μm with a single and stable domain). Depending on Temperature, the relaxation time can overcome the geological time or be unstable over minutes (as the T closes in the unblocking temperature of magnetic grains the relaxation time decrease exponentially).

The capability of rocks to record a stable remanent magnetization depends on the relaxation time, as stated by the Néel theory [1949, 1955], depending, in turn, from temperature, and volume of magnetic grains [*Butler*, 1992; *Tauxe*, 2009].

The original magnetization can be stable along geological times, although rocks may be exposed to other magnetic field, and undergo thermal, chemical processes that can overprint or even remove the primary magnetization, then acquiring secondary remagnetization.

Secondary magnetizations can be partial or total, deleting completely the original magnetization. Let's distinguish:

The Natural Remanent Magnetization (NRM) is the remanent magnetization in a rock sample prior to laboratory treatment, and depends on the geomagnetic field and the geological processes occurred during rock formation. NRM is typically composed of different components; a primary component is the component acquired during the rock formation, secondary components are acquired subsequently, altering or even obscuring the primary NRM. The main forms in which the NRM can be recorded are the TRM, DRM and CRM.

The Thermo Remanent Magnetization (TRM) is acquired during cooling from high temperatures to temperatures below Curie Temperatures (temperature below which the magnetic material retains a remanent magnetization (Figure 13); it changes with respect to magnetic minerals).

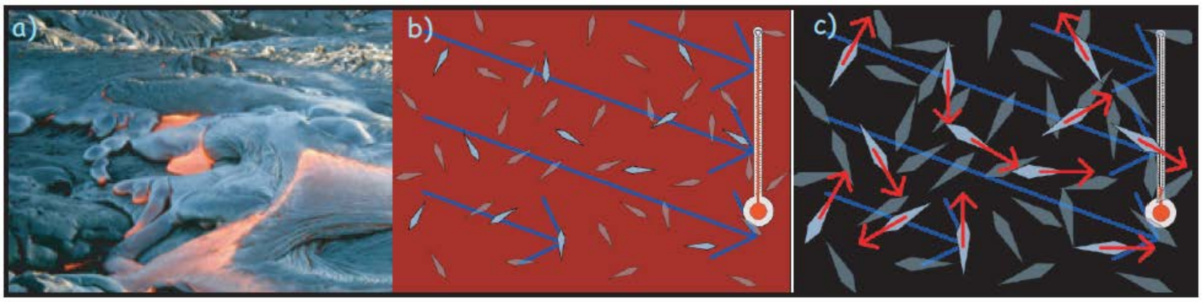

Figure 13. Modified after *Tauxe*, 2005; a) Picture of lava flow courtesy of Daniel Staudigel. b) While the lava is still well above the Curie temperature, crystals start to form, but are non-magnetic. c) Below the *Curie temperature* but above the blocking temperature, certain minerals become magnetic, but their moments continually flip among the easy axes with a statistical preference for the applied magnetic field. As the lava cools down, the moments become fixed, preserving a thermal remanence.

The Detrital Remanent Magnetization (DRM) is acquired during the accumulation of magnetic minerals during sedimentation and diagenesis.

The Chemical Remanent Magnetization (CRM) is acquired during the formation (precipitation of ferromagnetic minerals from a solution) of magnetic minerals within a rock, or the alteration of pre-existent magnetic minerals (Figure 14).

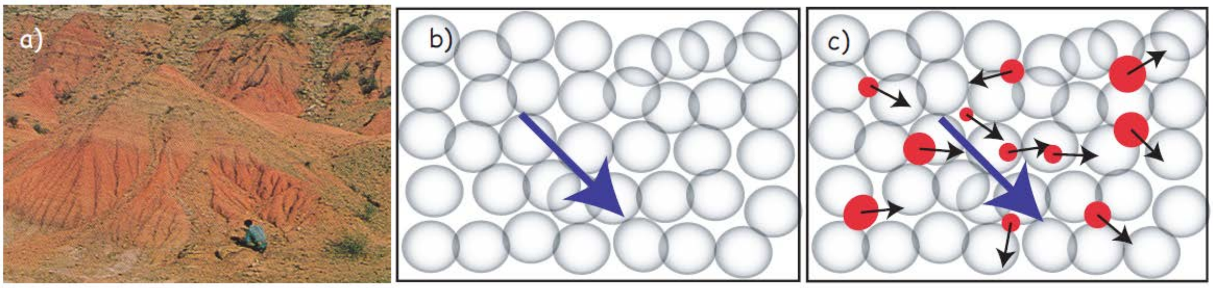

Figure 14. Modified after *Tauxe* [2005]; Grain growth CRM. a) Red beds of the Chinji Formation, Siwaliks, Pakistan. The red soil horizons have a CRM carried by pigmentary hematite. b) Initial state of non-magnetic matrix. c) Formation of superparamagnetic minerals with a statistical alignment with the ambient magnetic field (shown in blue).

Secondary component of remanent magnetization should be detected and rejected (as the Isothermal and **Viscous Remanent Magnetizations - IRM and VRM).**

For the interpretation it is critical to isolate the primary and secondary magnetizations and evaluate rocks post-depositional tilting, or folding and other geological processes overprinting the original component of remanent magnetization.

For further details, see reference books by *Butler* [1998], *Lanza and Meloni* [2006] and *Tauxe* [2009].

2.1. GEOLOGICAL AND TECTONIC APPLICATIONS

Since decades [e.g. *Torsvik et al.,* 2008, 2012*; Hernandez Moreno et al.,* 2014 and reference therein] the paleomagnetism has played a central role in the solution of tectonic problems from lithospheric plates scale (paleogeographic reconstructions, poles migrations, etc.) to small scale, detecting tectonic motions as rotations with respect to a reference paleomagnetic pole.

The paleomagnetism is the only tool that permits to measure the intensity H, inclination I and declination D of the magnetic field, and therefore deduce all the components of a remanent magnetization of rocks, necessary to detect vertical-axis rotation and latitudinal motion of crustal blocks.

To determine the expected paleomagnetic direction for rocks of any age at any point on Earth surface and then the motions of crustal blocks with respect to the rotation axis, we need to know reference poles. If the measured paleomagnetic declination and inclination are different with respect to those expected, in relation to the geographic position and the age of the analyzed rocks, tectonic rotations can be inferred.

There are two basic methods of analyzing vertical-axis rotations and latitudinal motions from paleomagnetic directions, the direction-space and pole-space approaches. These methods have been developed by *Beck* [1976, 1980], *Demarest* [1983], and *Beck et al*. [1986].

In this work, the direction-space approach is considered, where the observed paleomagnetic direction for a particular site (I_o, D_o) is simply compared with the expected direction (I_x, D_x) obtained on rocks of the same age from the stable part of the continent (Figure 15). The inclination flattening or latitudinal motion, F, and the rotation, R, of declination is given by, respectively:

$$F = I_x - I_o$$

$$R = D_o - D_x$$

R is defined as positive when D_o is clockwise with respect to D_x.

Both the expected and observed directions have associated confidence cones (α_{95}), so F and R have 95% confidence limits ΔF and ΔR, respectively. Results of direction-space analyses are usually reported by listings of R ± ΔR and F ± ΔF. A significant positive flattening of inclination, F ± ΔF, indicates motion toward the paleomagnetic pole. To a complete explanation of the confidence limit mathematical development refer to *Demarest* [1983] and *Butler* [1992].

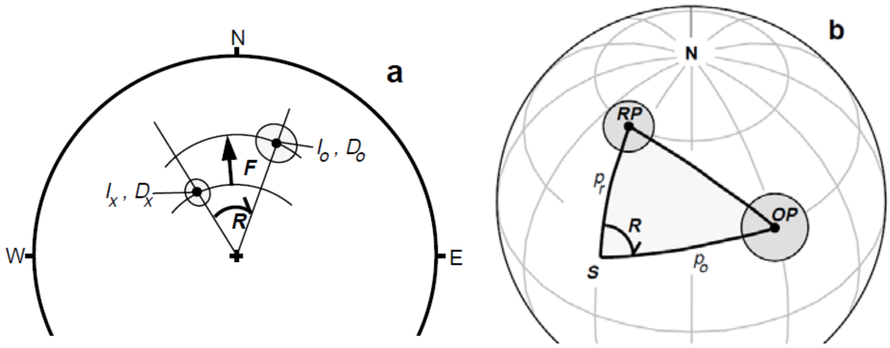

Figure 15. Modified after *Butler* [1992]. a) Equal-areal projection of an observed discordant paleomagnetic direction, inclination Io and declination Do, compared to an expected direction, inclination I_x and declination D_x. The observed direction is shallower than the expected direction by the flattening angle F. Observed declination is clockwise from the expected declination by the rotation angle R. b) Comparison of observed and reference paleomagnetic poles. The discordant paleomagnetic pole OP (observed pole) was determined from paleomagnetic analysis of rocks at the collection location labeled S; RP is the reference paleomagnetic pole; the spherical triangle with apices at S, OP, and RP is shown by the heavy lines; pr = great circle distance from S to RP; po = great circle distance from S to OP; poleward transport p = po – pr; vertical-axis rotation R = angle of spherical triangle at S.

This analytical approximation can be used when the 95% confidence cone of the paleomagnetic direction is less than 10º and the mean inclination is not too close to vertical [*Clark and Morrison,* 1983*; Demarest,* 1983]. For I >80º the paleomagnetic declination is poorly defined.

2.2. MAGNETIC ANISOTROPY

Other important structural information may also come from the **magnetic anisotropy** studies, a field also widely investigated in the last forty years [*Janák,* 1967*; Hrouda and Janák,* 1976*; Jelinek,* 1977*,* 1978*; Borradaile,* 1981, 1987*, 1988; Hrouda,* 1982*; Borradaile and Tarling,* 1984*; MacDonald and Ellwood,* 1987*, Hrouda and Jelinek,* 1990*; Parés et al.,* 1999].

Rocks in which intensity of induced or remanent magnetization depends on direction of the applied magnetic field gain a magnetic anisotropy. One type of magnetic susceptibility (**K**, which represents the ratio between the induced magnetization M and the applied magnetic field **H**) is the Anisotropy of Magnetic Susceptibility (AMS), in which susceptibility is a function of direction of the applied field.

Measurement of the AMS is the technique used to determine the preferred orientation of fine-grained minerals in sediments where no mineral fabric is appreciable to the naked eye ("***magnetic fabric***", eg. *Owens and Barnford,* 1976*; Goldstein*, 1980; *Hrouda,* 1982; *Borradaile,* 1988; *Lowrie,* 1989*; Pearce and Fueten,* 1989; *Jackson and Tauxe,* 1991*; Rochette et al*., 1992; *Sagnotti and Speranza,* 1993; *Tarling and Hrouda*, 1993; *Borradaile and Henry,* 1997; *Bouchez,* 1997; *Mattei et al*., 1997; *Cifelli et al*., 2005; *Pares et a.l*, 2015; *Caricchi et al*., 2016).

The fabric is the result of various forces acting during the formation and eventual geologic history of the rock: mainly gravity, Earth's magnetic field, hydrodynamic forces and tectonic stress.

The AMS can be geometrically defined as a second-rank tensor, commonly expressed in terms of a **triaxial ellipsoid** with its own orientation defined by the directions of the three main axes (Figure 16): $\mathbf{K_1} \geq \mathbf{K_2} \geq \mathbf{K_3}$, maximum, intermediate, and minimum susceptibility.

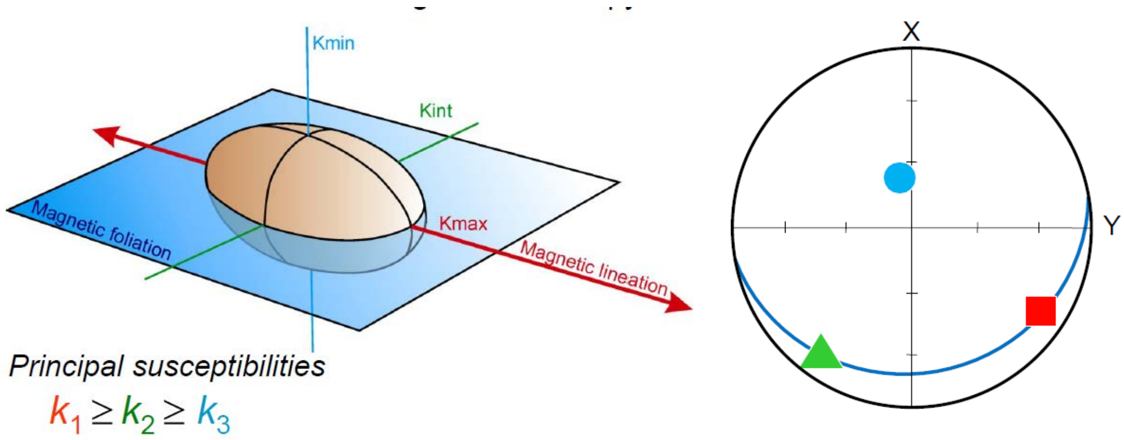

Figure 16. The magnetic susceptibility ellipsoid. M maximum (or **K_1- Magnetic Lineation**), K intermediate (or K_2), K minimum (or **K_3 - Magnetic Foliation**). Modified after *Chadima and Jelinek* [2009].

The AMS ellipsoid principal axes usually correspond to the strain ellipsoid axes, indicating that the magnetic fabric is a strain proxy, and suggesting that magnetic fabric measurements are significant with respect to the strain history of rocks [*e.g. Goldstein and Brown,* 1988].

Several parameters are used for the quantification of the magnitude of anisotropy and for defining the shape of the AMS ellipsoid [Figure 17; *Jelinek*, 1981; *Hrouda*, 1982; *Tarling and Hrouda,* 1993*; Winkler et al.,* 1997].

Parameter name	Parameter symbol	Parameter formula	Author
Anisotropy degree	P	k_1/k_3	Nagata (1961)
Corrected anisotropy degree	P'	$\exp\sqrt{\{2[(\eta_1-\eta)^2+(\eta_2-\eta)^2+(\eta_3-\eta)^2]\}}$	Jelinek (1981)
Magnetic lineation	L	k_1/k_2	Balsley and Buddington (1960)
Magnetic foliation	F	k_2/k_3	Stacey *et al.* (1960) Balsley and Buddington (1960)
Ellipsoid shape	T	$2(\eta_2-\eta_3)/(\eta_1-\eta_3)-1$	Jelinek (1981)
Mean susceptibility	k_m	$(k_1+k_2+k_3)/3$	Nagata (1961)

$\eta_1 = \ln k_1,\ \eta_2 = \ln k_2,\ \eta_3 = \ln k_3,\ \eta = (\eta_1+\eta_2+\eta_3)/3.$

Figure 17. Most commonly used AMS parameters (SI units). Modified after *Winkler et al.,* [1997], see references therein.

The magnetic lineation (L) and foliation (F) describe the shape of ellipsoid with a geometrical meaning: the lineation corresponds to the direction of K1, the foliation to the plane being defined by the directions of K1 and k_2 and hence orthogonal to k_3.

When the ellipsoid is prolate ($k_1>k_2=k_3$) L prevails, and when it is oblate ($k_1=k_2>k_3$) F prevails (Figure 18-19).

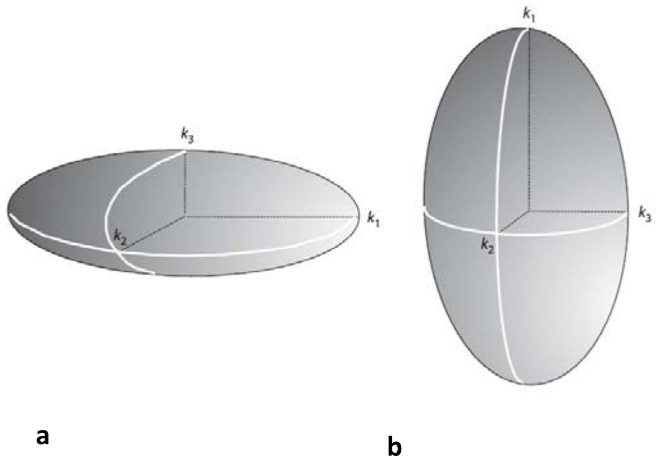

Figure 18. Shape of AMS ellipsoids;
a) oblate (= planar fabric);
b) prolate (= linear fabric).
Modified after *Lanza and Meloni,* [*2006*]

A more detailed evaluation of the shape of the ellipsoid is given by the Jelinek shape parameter, T, for which $-1 \leq T < 0$ corresponds to prolate ellipsoids, and $0 < T \leq 1$ to oblate ellipsoids [*Jelinek,* 1981; Figure 19].

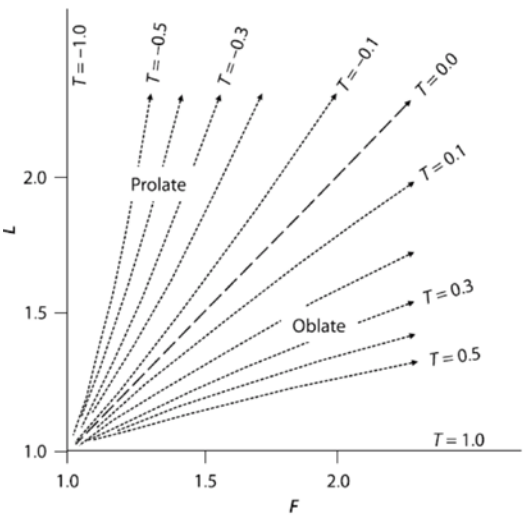

Figure 19. Flinn diagram [*Flinn*,1962] . Shape parameter T as a function of lineation (L) and foliation (F). Arrows point towards increasing degree of anisotropy (P). Modified after *Tarling and Hrouda* [1993].

One of the main breakthroughs in the last decade has been the wide recognition of a **specific magnetic mineralogy related to AMS**. In particular, there are important mineral sources of susceptibility that are not carriers of NRM (ferromagnetic minerals *sensu lato*) such as the diamagnetic, paramagnetic, and anti-ferromagnetic minerals, referred to as matrix minerals because they constitute the main volume fraction of common rocks [see detail in Figure 20; *Owens and Barnford,* 1976*; Borradaile,* 1987*; Rochette,* 1987]. The paramagnetic minerals, often play a major role in the magnetic susceptibility of rocks [*Rochette,* 1987], different from diamagnetic compounds like quartz, calcite or water which do not vary to a great extent, having a mean value of about -14 x 10^{-6} SI.

Mineral	*Symmetry*	*Type*	K_m	*P*	*Reference*
		Diamagnetic			
Quartz	0	···	−14.5	<1.01	1,2,13
Calcite	1c	*N*(*C*)	−13.0	1.13	1,2
		Paramagnetic			
Biotite	1c	*N*(*CS*)	1–3	1.35	2,3,4,5
Other phyllosilicates	1c	*N*(*CS*)	0.05–1	1.2–1.35	2,3,5
Pyroxenes	4	*N*(*S*)?	0.5–5	1.2–1.4	2
Amphiboles	4	*N*(*S*)?	0.5–5	1.08–1.3	2
Riebeckite	1a	?	2.6	1.16	0
Orthoferrosilite	1a	?	5	1.21	14
Staurolite	2b	?	0.8	1.06	0
Garnet	0	···	3	1.001	0
Tourmaline	1c	*I*(*S*)	0.9	1.12	0
Cordierite	1c	*I*(*S*)	0.6	1.15–1.31	0
Siderite	2c	*I*(*C*)	3.8–4.2	1.7	6
Other Fe carbonates	2c	*I*(*C*)	0.05–0.7	1.08–1.45	6
		Ordered			
Goethite	1c	*I*(*S*)	1.3–5	2?	7,8,9
Hematite	3	*N*(*CS*)	2–50	2.5–100	2,9,10
Pyrrhotite	3	*N*(*CS*)	50–300	>100	9,11
Magnetite MD	4	*N*(*S*)	≤3000	<5	2,12
Magnetite SD	3	*I*(*S*)	≤1500	∞?	12
Magnetite SP	4	*N*(*S*)?	≤5000	···	12

K_m is in 10^{-3} SI, except for the diamagnetic minerals (10^{-6}). Symmetry code: 0, isotropic; 1, uniaxial oblate; 2, uniaxial prolate; 3, triaxial oblate; 4, triaxial prolate. For uniaxial, the symmetry is indicated by the crystallographic axis of revolution. Type code: normal *N* or inverse *I* with mechanism of preferred orientation either controlled by shape *S* or by intracrystalline gliding during ductile deformation *C*. References: 0, unpublished or *Rochette* [1988*b*]; 1, *Rochette* [1987]; 2, *Hrouda* [1982]; 3, *Ballet* [1979]; 4, *Zapletal* [1990]; 5, *Borradaile et al.* [1987]; 6, *Rochette* [1988*a*]; 7, *Hedley* [1971]; 8, *Rochette and Fillion* [1989]; 9, *Dekkers* [1988]; 10, *Dunlop* [1971]; 11, *Rochette* [1988*a*]; 12, *Maher* [1988]; 13, *Hrouda* [1986]; 14, *Wiedenmann et al.* [1986].

Figure 20. Modified after *Rochette et al.* [1992], see references therein. Selected AMS Data for rock-Forming Minerals.

The anti-ferromagnetic matrix behaviour exemplified by goethite and hematite, leads to a linear susceptibility smaller than the paramagnetic susceptibility. According to *Neel and Pauthenet* [1952], at this point it is worth mentioning a difficulty arising from the present definition of matrix susceptibility: hematite contributes to both the matrix component, with an isotropic anti-ferromagnetic susceptibility, and the ferromagnetic component which is alone responsible for the anisotropy.

In weakly deformed (non-metamorphic) sedimentary rocks, AMS reflects the pristine fabric produced during incipient deformation at the time of, or shortly after, deposition and diagenesis of the sediment [*Sintubin,* 1994*; Mattei et al.,* 1995, 1997*; Sagnotti et al.,* 1998, 1999*; Parés et al.,* 1999*; Coutand et al.,* 2001*; Cifelli et al.,* 2004, 2005, 2009*; Soto et al,* 2009].

AMS analysis of weakly deformed sediments, have frequently been used in orogenic settings to document the syn-sedimentary tectonic regime [*Kissel et al*., 1986; *Mattei et al*., 1995, 1997, 1999; *Sagnotti and Speranza*, 1993; *Sagnotti et al*., 1998; *Parés et al*., 1999, 2015; *Maffione et al*., 2008, 2012, 2015; *Macrì et al*., 2014; *Cifelli et al*., 2013, 2015; *Caricchi et al*., 2016].

During deposition, sedimentary rocks acquire the so called '***sedimentary fabric***' characterized by the k_{max} and k_{int} axes dispersed within a plane (magnetic foliation, the orthogonal plane to the minimum magnetic susceptibility direction) that is sub-parallel to the stratification plane. This sedimentary fabric can be partially overprinted by a '***tectonic fabric***' during incipient deformation [e.g., *Parés et al.,* 1999; *Alimohammadian et al*., 2013]. The result of this process is the development of a magnetic lineation (the direction of maximum susceptibility in a rock) whereby k_{max} aligns parallel to the maximum axis of stretching (ε_1), hence perpendicular to the maximum axis of compression (σ_1). This mechanism allows a direct correlation between the AMS and strain ellipsoids [e.g., *Parés et al.,* 1999, 2015].

A series investigations of correlation between the AMS fabric and structural observations, confirmed that in **compressional settings** the magnetic lineation is usually sub-horizontal and parallel to fold axes or local thrusts strikes [e.g. *Borradaile and Henry,* 1997*; Mattei et al.,* 1997*; Sagnotti and Speranza,* 1993*; Mattei et al.,* 1997*; Sagnotti et al.,* 1998*; Maffione et al.,* 2008], whereas it coincides with the stretching direction in extensional basins [e.g. *Sagnotti et al.,* 1994*; Cifelli et al.,* 2005*; Oliva-Urcia et al.,* 2009]. In **extensional settings**, the magnetic lineation coincides with the local dip of the bedding, and is therefore perpendicular to the local normal fault planes [*Sagnotti et al.*, 1994; *Mattei et al.*, 1997, 1999; *Cifelli et al.*, 2004, 2005; *Maffione et al.*, 2012; *Porreca and Mattei*, 2012]. Few attempts of using AMS analyses in strike-slip tectonic settings have been done in the past [e.g., *Cifelli et al.*, 2013; *Ferré et al.*, 2002].

Increasing deformation progressively modifies the shape of the AMS ellipsoid from a pure sedimentary fabric (oblate ellipsoid: $k_{max} \approx k_{int} >> k_{min}$), to a sedimentary fabric with a marked tectonic imprint (triaxial ellipsoid: $k_{max} > k_{int} > k_{min}$), to a tectonic fabric (prolate ellipsoid: $k_{max} >> k_{int} \approx k_{min}$), and eventually returning during the highest strain to an oblate ellipsoid with the magnetic foliation parallel to the cleavage/schistosity [e.g., *Parés,* 2004, 2015] (Figure 21).

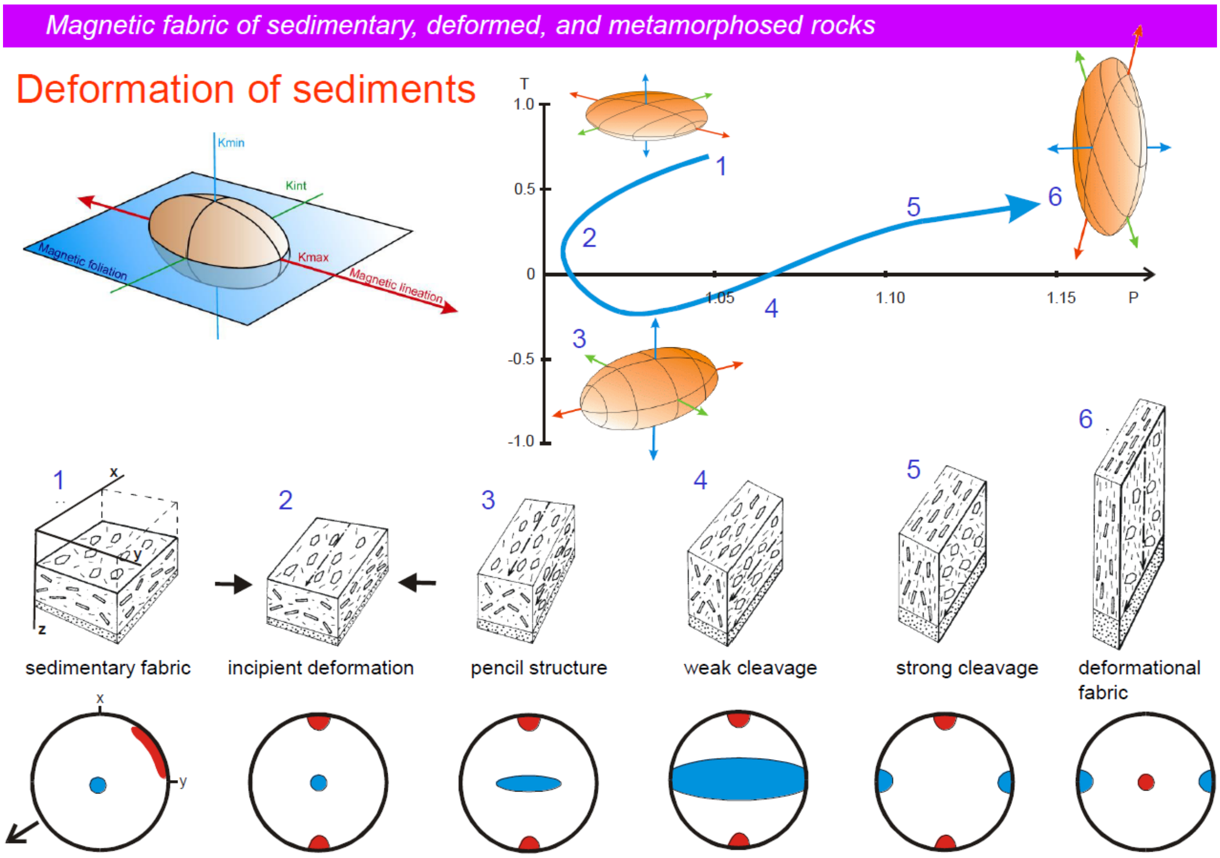

Figure 21. Magnetic fabric evolution during progressive deformation. The ellipsoid is oblate (flattened) when K_1»K_2 but K_2>K_3, and prolate (cigar-shaped) when K_1> K_2, K_2»K_3. Modified after *Graham* [1966] *Pares et al.* [1999].

In the last stage of deformation, which corresponds to incipient metamorphism, the pristine tectonic fabric developed during the initial (syn-sedimentary) phases of deformation is completely obliterated. Conversely, the pristine tectonic fabric is not easily overprinted by small strains at low temperature [e.g., *Borradaile,* 1988*; Sagnotti et al.,* 1994, 1998*; Cifelli et al.,* 2004, 2005*; Parés,* 2004*; Soto et al.,* 2009]. This implies that, compared to classical structural geological analysis, where the definition of the age of deformation requires additional constraints (i.e., crosscutting relationships or unconformities), the finite strain determined from AMS analyses of weakly deformed rocks is a direct and powerful tool that can be used to study the deformation active at the time of sedimentation.

Sometimes, unusual relationships between structural and magnetic axes, consisting in the "exchange" of the maximum and minimum anisotropy axes (Figure 22, so called ***inverse magnetic fabric***) can occur because of the presence of certain magnetic minerals, either SD magnetite, iron-bearing carbonates or various paramagnetic minerals like tourmaline, cordierite, goethite or siderite [*Rochette et al*., 1992]. Rocks with fine-grained magnetite, are particularly prone to anomalous AMS fabric. Therefore it is strongly recommended to investigate the mineralogical source of AMS and to compare AMS with other types of anisotropy or mineralogical investigation. Accordingly, in the past, authors strongly recommended to investigate the mineralogical source of AMS and to compare AMS with other data of different types of anisotropy or mineralogical investigation.

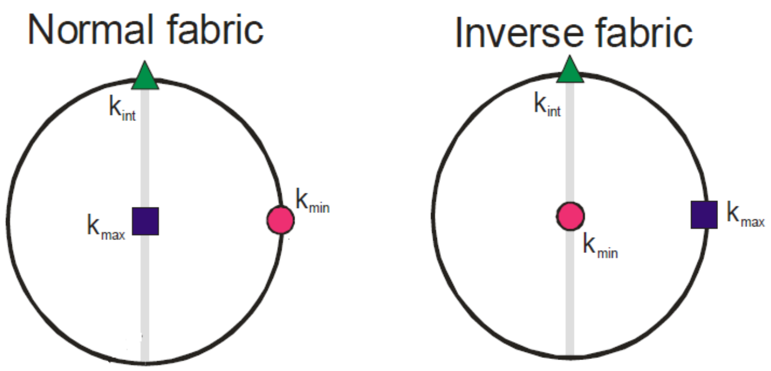

Figure 22.
Example of Inverse Fabric projection.

Chapter III

3. Sampling and laboratory methods

During this research activity, two field campaigns for sample collection were carried out on April 2016 and 2017, providing a total number of 930 core samples. The samples were collected following a classic paleomagnetic sampling method: several sites have been selected in the same rock unit and several samples in the same site (ca. 10 on average). The samples include volcanic rocks (n. 17 basalt sites) and sedimentary rocks (n. 5 whitish siltstones sites and n. 72 continental red beds).

Sampled sites were aligned along transects cutting the main strike-slip faults considering that several studies demonstrated that shear-related rotations virtually end within 10–20 km from the fault trace [*Ron et al.*, 1984; *Sonder et al.*, 1994; *Piper et al.*, 1997; *Randall et al.*, 2011; *Hernandez-Moreno et al.*, 2014, 2016].

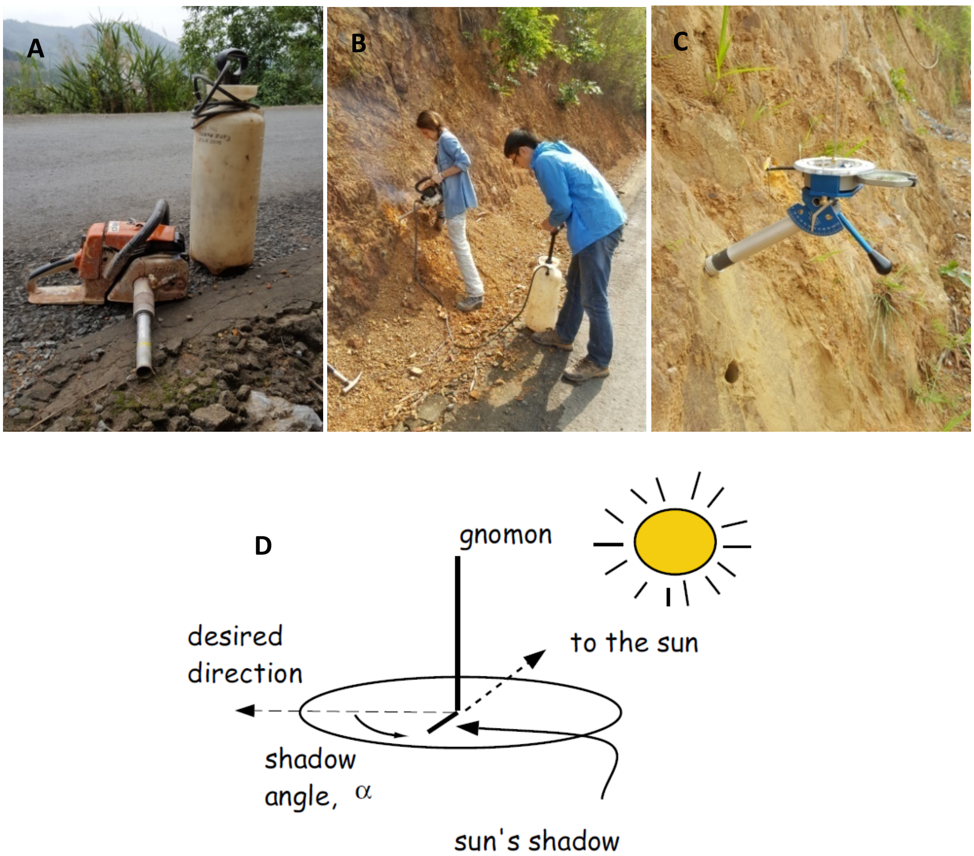

Figure 23. A) Portable petrol-powered drill; B) paleomagnetic sampling; C) Pomeroy orientation device in use as a sun magnetic compass; D) Schematic of the principles of sun compass orientation (by *Tauxe*, 2005).

The samples were drilled using a portable petrol-powered and water-cooled drill (Figure 23). Cores were oriented *in situ* before extraction using a magnetic compass, corrected for the local magnetic declination for year 2016/2017 (between 0° and 0.9° W according to NOAA's National Geophysical Data Center, http://www.ngdc.noaa.gov/geomag/declination.shtml) and, when possible, the sun. Afterward, the cores were cut into standard cylindrical paleomagnetic specimens of 22 mm height.

Paleomagnetic measurements were later carried out in the shielded room of the paleomagnetic laboratory of the Istituto Nazionale di Geofisica e Vulcanologia (Rome), using a 2G Enterprises DC-superconducting quantum interference device cryogenic magnetometer (Figure 24).

Neogene volcanic samples were demagnetized in 10 steps by alternating field (AF) yielded by three orthogonal coils in-line with the magnetometer up-to a maximum AF peak of 100 mT (Figure 24a). Red beds, Jurassic basalts and whitish siltstones samples were thermally demagnetized using a Pyrox shielded oven (Figure 24b) in 12 steps (20°, 200°, 300°, 350°, 400°, 440°, 480°, 520°, 560°, 600°, 640°, 680°C) of temperature up to 680°C. Demagnetization data were plotted on orthogonal vector component diagrams [*Zijderveld*, 1967].

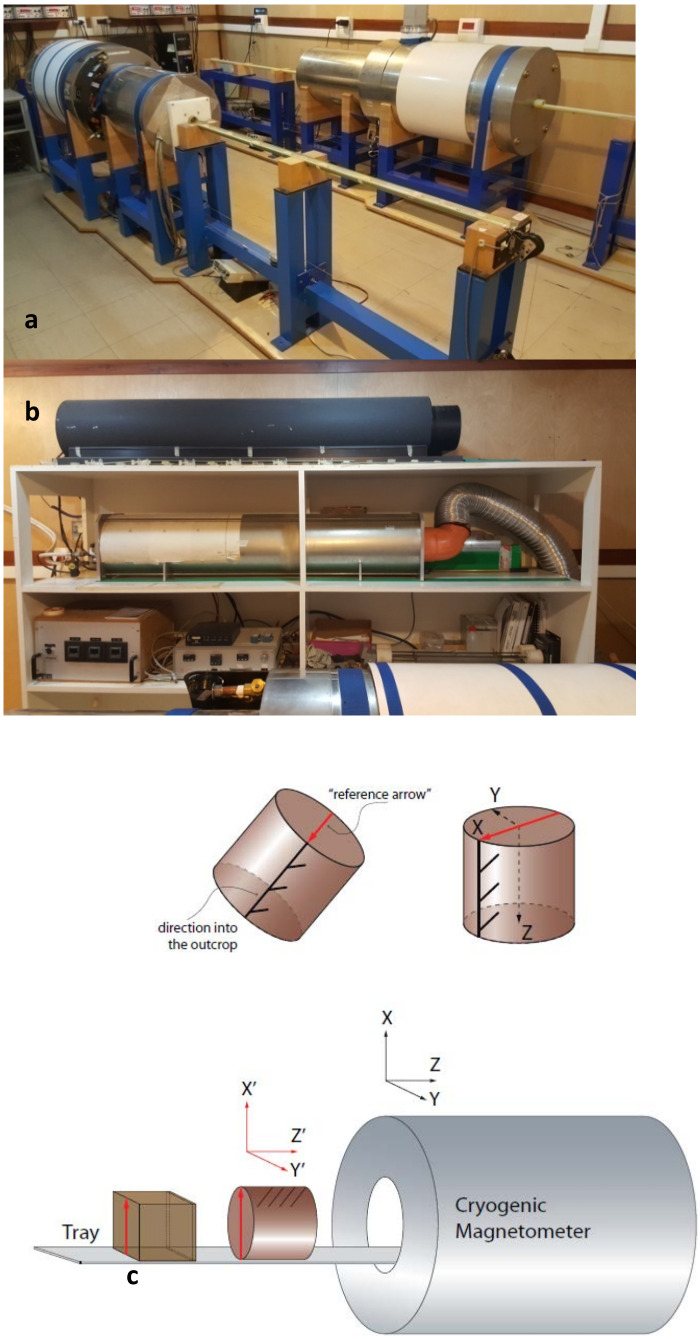

Figure 24. a-c) View of the magnetically shielded room of the paleomagnetic laboratory (INGV, Rome) and schematic description of samples position into cryogenic magnetometer ; **b)** The Pyrox oven and its controller, to demagnetize up to 700 °C.

The magnetization components were identified by principal component analysis (PCA) [*Kirschvink*, 1980] using *Remasoft 3.0*, a freeware distributed by Agico [*Chadima and Hrouda*, 2007]. The site mean paleomagnetic directions were computed using *Fisher* [1953] statistics, and plotted on equal-angle projections. Finally, the rotation and flattening values with respect to Eurasia were evaluated according to *Demarest* [1983], using the reference paleopoles by *Torsvik et al.* [2012] for 170-140 Ma sites (Europe), and the most recent East Asia-focused poles by *Cogné et al.* [2013] for 130 to 10 Ma sites (Figure 25-26).

Age (Ma)		Width	Palaeopole						
Window	Mean	(Myr)	N	N_{rot}	N_{ign}/N_{sed}	Latitude (°N)	Longitude (°E)	k	$A95$(°)
0	1.0	20	5	0	0/5	89.0	76.6	200.7	5.4
10	12.4	20	21	5	13/8	87.5	257.3	154.8	2.6
20	18.2	20	20	7	16/4	84.7	255.9	112.5	3.1
30	23.7	40	25	10	17/8	83.9	259.6	106.7	2.8
40	41.7	40	14	7	8/6	81.9	260.8	94.8	4.2
50	55.0	40	13	2	6/7	81.6	238.8	51.6	5.9
60	65.2	40	22	5	11/11	81.9	247.5	57.4	4.1
70	77.3	40	45	5	17/28	79.7	219.5	42.6	3.3
80	79.7	40	44	4	19/25	79.5	216.9	42.2	3.4
90	87.8	40	53	5	23/30	77.9	212.8	46.2	2.9
100	105.1	20	16	6	8/8	82.2	205.4	118.1	3.5
110	109.8	20	22	6	8/14	80.8	199.5	78.9	3.5
120	121.6	20	41	9	15/26	80.6	192.9	60.4	2.9
130	126.2	20	44	14	16/28	79.9	193.5	70.0	2.6

Notes: Width: temporal window width; N: Number of data in the statistics; Nrot: number of rotated poles in the computations; Nign/Nsed: number of poles from igneous/sedimentary formations; k. A95: Fisher (1953) statistics parameters.

Figure 25. East Asia paleopoles from *Cogné* et al. [2013].

			North America		Europe		India	
Age	N	A95	Plat	Plon	Plat	Plon	Plat	Plon
0	24	1.9	−88.5	353.9	−88.5	353.9	−88.5	353.9
10	49	1.8	−86.4	342.2	−86.7	330.0	−87.2	60.4
20	31	2.6	−83.7	343.2	−84.4	332.1	−83.7	74.7
30	24	2.6	−82.1	338.7	−83.1	326.5	−79.7	101.7
40	24	2.9	−80.1	337.2	−81.1	324.3	−74.7	106.8
50	33	2.8	−76.4	354.5	−78.9	344.7	−65.1	98.4
60	44	2.1	−73.6	7.5	−78.2	352.6	−48.5	100.8
70	32	2.5	−73.5	12.6	−79.2	355.7	−36.4	100.7
80	25	2.9	−74.7	10.5	−79.7	357.9	−29.0	103.5
90	28	2.5	−76.8	4.8	−80.4	347.2	−20.9	111.4
100	14	3.3	−78.7	358.4	−80.8	332.3	−19.7	113.0
110	21	3.3	−75.2	21.7	−81.2	13.1	−11.1	115.9
120	28	2.6	−73.7	15.5	−79.0	10.1	−8.6	116.4
130	18	2.8	−70.9	5.4	−75.0	3.4	1.0	117.1
140	9	6.0	−67.9	5.7	−72.4	7.9	5.3	117.9
150	15	6.4	−72.6	339.4	−72.9	334.2	−2.9	122.3
160	19	5.1	−72.0	325.9	−70.5	323.4	−9.7	126.6
170	18	4.6	−70.1	314.8	−67.3	316.4	−10.7	125.8

Figure 26. Paleopoles from *Torsvik* et al. [2012].

To define the sense and amount of rotation, have been always considered the smaller angle between the observed and expected declinations, thereby calculating rotation values always ≤|180°|. This is a conservative approach, although we are aware that in the past, some authors considered rotation values exceeding 180° [*e.g. Hernandez-Moreno et al., 2014; Nelson and Jones, 1987; Nelson and Piper et al., 1997*].

Moreover, for each sampling site, have been selected specimens for additional magnetic analyses carried out with the aim of characterizing the magnetic mineralogy.
For hysteresis measurements, the samples were crushed into powder and then placed in pharmaceutical gel caps #4 (corresponding to a filled volume of about 0.15 ml), in order to vibrate by means of a carbon fiber probe in the Princeton Measurement Corporation Micromag 3900 Vibrating Sample Magnetometer (VSM) (Figure 27). The software *MicroMagVSM* was used for hystresis data analysis (Figure 28).

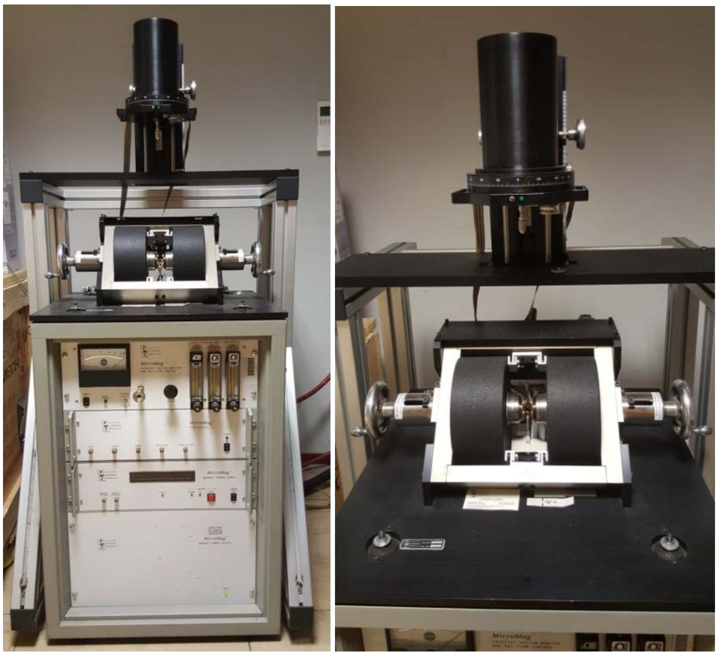

Figure 27. The Micromag magnetometer, for high-sensitivity hysteresis loops.

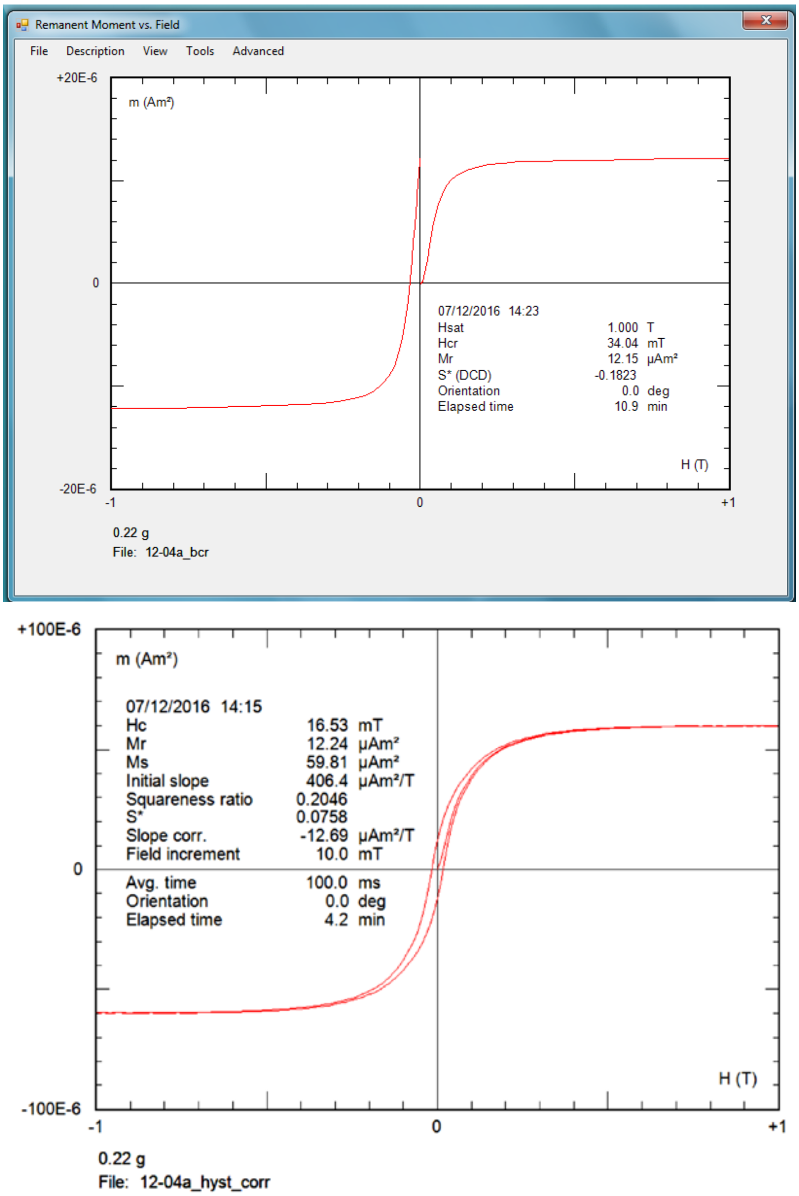

Figure 28. Graphic interface of *MicroMagVSM* program used for data visualization of hysteresis measurements

The coercive force (Bc), the saturation or maximum remanent magnetization (Mrs) and the saturation/maximum magnetization (Ms) were measured using the VSM under cycling in a maximum field of 1.0 T, and determined after subtracting the high field paramagnetic linear trend when saturated samples. The coercivity of remanence (Bcr) values have been extrapolated from the backfield remagnetization curves up to -1 T, following a forward magnetization in +1 T field. Bcr represents the negative field needed to remove the remanent magnetization after applying the maximum positive field. The saturation remanence to saturation magnetization (Mrs/Ms) vs. the ratio of remanent coercive force to coercive force (Bcr/Bc) has been plotted in a Day plot [*Day et al.,* 1977*; Dunlop,* 2002].

First order reversal curves (FORCs) have been measured using the Micromag operating software, and processed, smoothed and drawn with the FORCINEL Igor Pro routine [*Harrison and Feinberg*, 2008]. FORCs are a series of partial hysteresis loops made after the sample magnetization is saturated [*Pike et al*., 1999; *Roberts et al*., 2000]. Selected FORCs have been measured in steps of 2 mT with an averaging time of 100 ms; the maximum applied field was 1.0 T. The optimum smoothing factor was calculated by the FORCINEL software.

For one specimen from each basalt and red bed sites, have been also measured the variation of the low-field magnetic susceptibility (K) during a heating and cooling cycle performed in air, from room temperature up to 700°C, using an AGICO KLY-3 Kappabridge coupled with a CS-3 furnace (Figure 29). The Curie/Néel points have been estimated as the temperature, or range of temperatures, at which the paramagnetic behavior starts to dominate, following the approach outlined by *Petrovsky and Kapicka* [2006]. *Cureval8* software was used for data analysis (Figure 29).

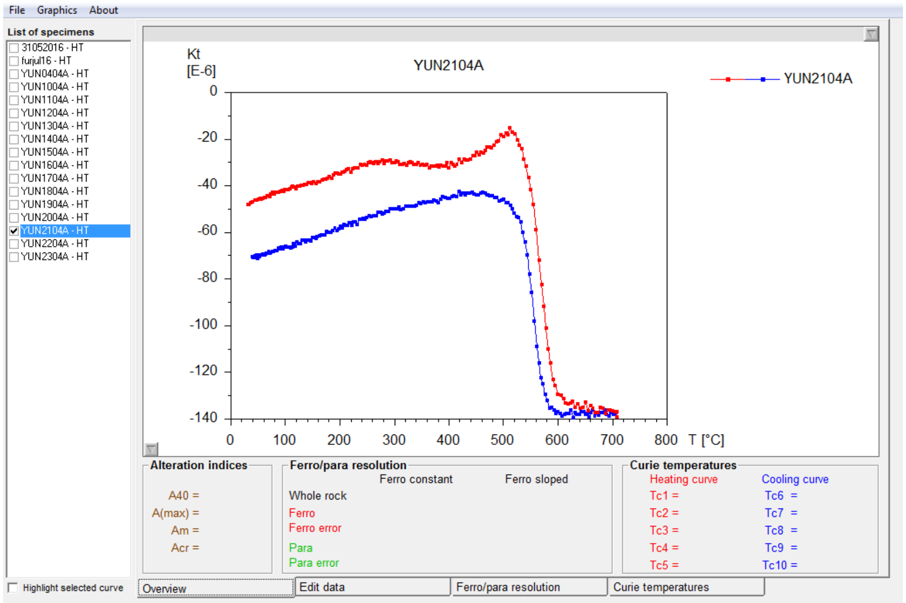

Figure 29. Graphic interface of *Cureval8* program used for data visualization of thermal curves.

Analysis of low-field anisotropy of magnetic susceptibility (AMS) was done using a MFK1 Kappabridge (AGICO) (Figure 30-31). During measurement, the specimen slowly rotates subsequently along three perpendicular axes (total of 64 measurements are made during one spin). The AMS parameters were evaluated using Jelinek statistics [*Jelinek*, 1977, 1978; see details in chapter II]. *Anisoft42* software was used for data analysis [*Chadima and Jelinek*, 2009] (Figure 32).

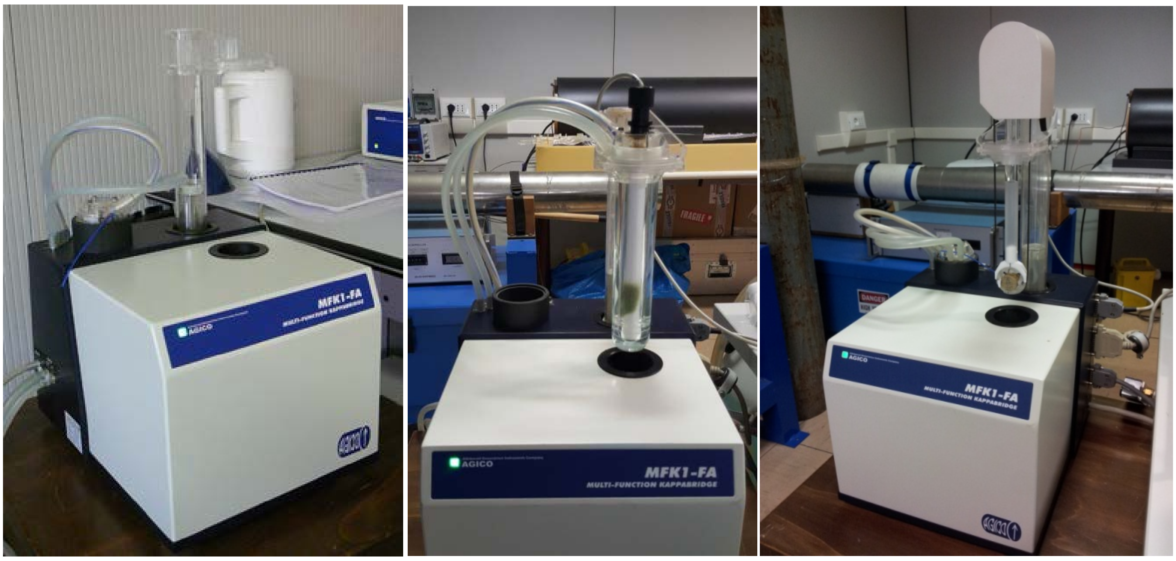

Figure 30. AGICO MFK1-FA susceptibility meter, connected to the furnace for measuring the variation of susceptibility vs. temperature.

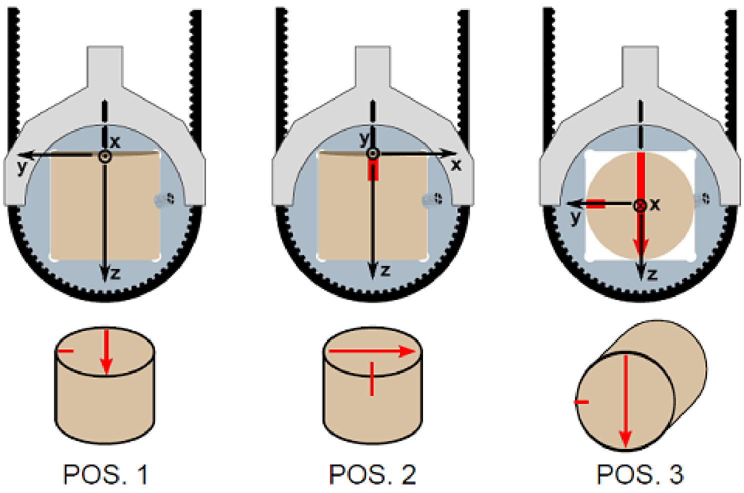

Figure 31. Three specimen positions for the automatic AMS measurements using the rotator.

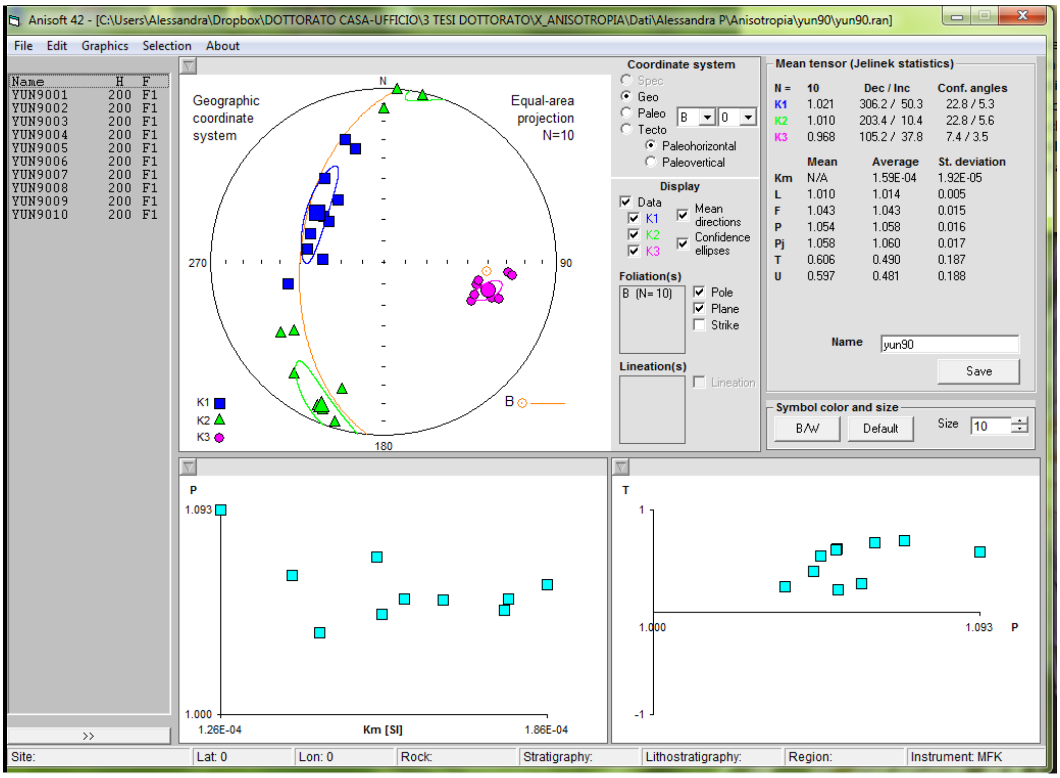

Figure 32. Graphic interface of the program used for data visualization AMS analysis [*Chadima and Jelinek*, 2009].

Finally, have been also used a tool to apply a pulse magnetic field up to 2.7 T, in order to impart an isothermal remanent magnetization. This method, called the "**Three Axis Method**" or the "**Lowrie Method**" [*Lowrie*, 1990], applies to a sample three decreasing fields along three orthogonal directions (2700 mT, 600 mT and 120 mT respectively from z, y and x axes) using a pulse magnetizer (Figure 33). Then the sample is thermally demagnetized by increasing temperature steps. From the analysis of the demagnetization curves along the three x, y and z components, it's possible to discriminate the Curie (or Néel) temperatures of distinct ferromagnetic fractions of analyzed sample and characterized by specific coercivity spectrum.

Figure 33.
The 2G pulse magnetizer, the field can reach up to 2.7 T

3.1 The fold test

With the fold test (or bedding-tilt test) can be evaluated relative timing of acquisition of a component of NRM (usually ChRM) and folding. If a ChRM was acquired prior to folding, directions of ChRM from sites on opposing limbs of a fold are dispersed when plotted in geographic coordinates (*in situ*) but converge when the structural correction is made ("restoring" the beds to horizontal). The ChRM directions are said to "pass the fold test" if clustering increases through application of the structural correction or "fail the fold test" if the ChRM directions become more scattered. The fold test can be applied either to a single fold or to several sites from widely separated localities at which different bedding tilts are observed (Figure 34). The fold test is used to understand when the magnetizations were acquired with respect to the tilting process [*Butler*, 1992].

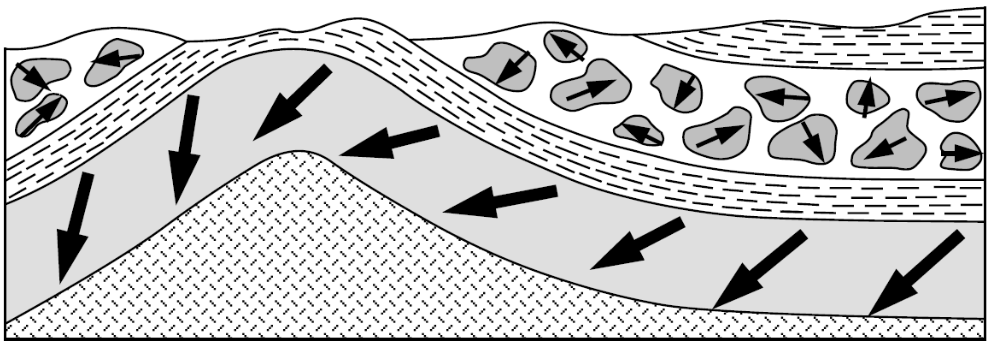

Figure 34. Modified after *Butler* [1992]. Schematic illustration of the fold and conglomerate tests of paleomagnetic stability. Bold arrows are directions of ChRM in limbs of the fold and in cobbles of the conglomerate; random distribution of ChRM directions from cobble to cobble within the conglomerate indicates that ChRM was acquired prior to formation of the conglomerate; improved grouping of ChRM upon restoring the limbs of the fold to horizontal indicates ChRM formation prior to folding. Redrawn from *Cox and Doell* [1960].

3.2 THE REVERSAL TEST

The time-averaged geocentric axial dipolar nature of the geomagnetic field holds during both normal- and reversed-polarity intervals.

At all locations, the time-averaged geomagnetic field directions during a normal-polarity interval and during a reversed-polarity interval differ by 180°. This property of the geomagnetic field is the basis for the reversals test of paleomagnetic stability. If a sets of paleomagnetic sites affords adequate averaging of secular variation during both normal and reversed polarity intervals, the average direction of primary NRM for the normal polarity sites is expected to be antiparallel to the average direction of primary NRM for the reversed-polarity sites [*Butler*, 1992]. However, acquisition of later secondary NRM components will cause resultant NRM vectors to deviate by less than 180°. ChRM directions are said to "**pass the reversals test**" if the mean direction computed from the normal-polarity sites is antiparallel to the mean direction for the reversed-polarity sites. Passage of the reversals test indicates that ChRM directions are free of secondary NRM components and that the time sampling afforded by the set of paleomagnetic data has adequately averaged geomagnetic secular variation. Furthermore, if the sets of normal- and reversed-polarity sites conform to stratigraphic layering, the ChRM is probably a primary NRM.

If a paleomagnetic data set "**fails the reversals test**", the average directions for the normal and reversed polarity sites differ by an angle that is significantly less than 180°. Failure of the reversals test can indicate either: (1) presence of an un-removed secondary NRM component or (2) inadequate sampling of geomagnetic secular variation during either (or both) of the polarity intervals. Because polarity reversals are characteristic of most geologic time intervals, paleomagnetic data sets often contain normal- and reversed-polarity ChRM (Figure 35).

The reversals test of paleomagnetic stability is often applicable and, unlike the conglomerate or fold test, does not require special geologic settings. Quantitative evaluation of the reversals test involves computation of the mean directions (and confidence intervals about those mean directions) for both normal and reversed-polarity groups and comparison of one mean direction with the antipode of the other mean direction [*Butler*, 1992].

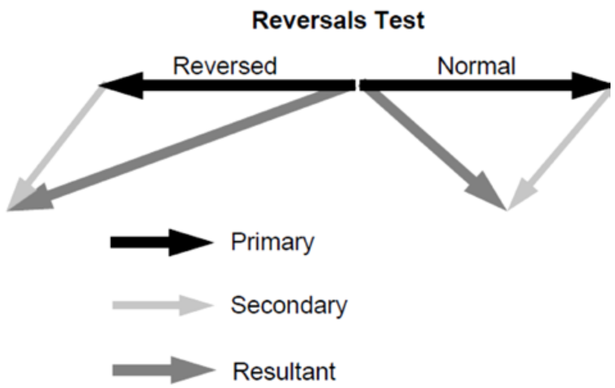

Figure 35. Modified after *Butler* [1992]. Schematic illustration of the reversals test of paleomagnetic stability. Solid arrows indicate the expected anti-parallel configuration of the average direction of primary NRM vectors resulting from magnetization during normal- and reversed- polarity intervals of the geomagnetic field; an unremoved secondary NRM component is shown by the lightly stippled arrows; the resultant NRM directions are shown by the heavily stippled arrows. Redrawn from *McElhinny* [1973].

Chapter

IV

4. Geological Setting

Eastward drift of Tibet and tectonic deformation of East Asia

Asia formed during the Phanerozoic by the welding of several continental blocks including Siberia, Tarim, North China, South China, Indochina, India, and others small-sized micro continents. All published models acknowledge subduction, and accretion of Gondwana derived fragments drifting to the North, but in many cases the timing and nature of collision is poorly defined.

Since early Cenozoic times, the northward drift of Indian plate and its progressive indentation into Asia [Figure 36; *Tapponnier and Molnar*, 1977] is amazingly producing spreading and crustal deformation in SE Asia [*Leloup et al*., 2001; *Morley*, 2007; *Roger et al*., 1995; *Searle*, 2006; *Tapponnier et al*., 1986; *Yin*, 2010; *Zhong et al.,* 1990; *Aitchison et al*., 2007].

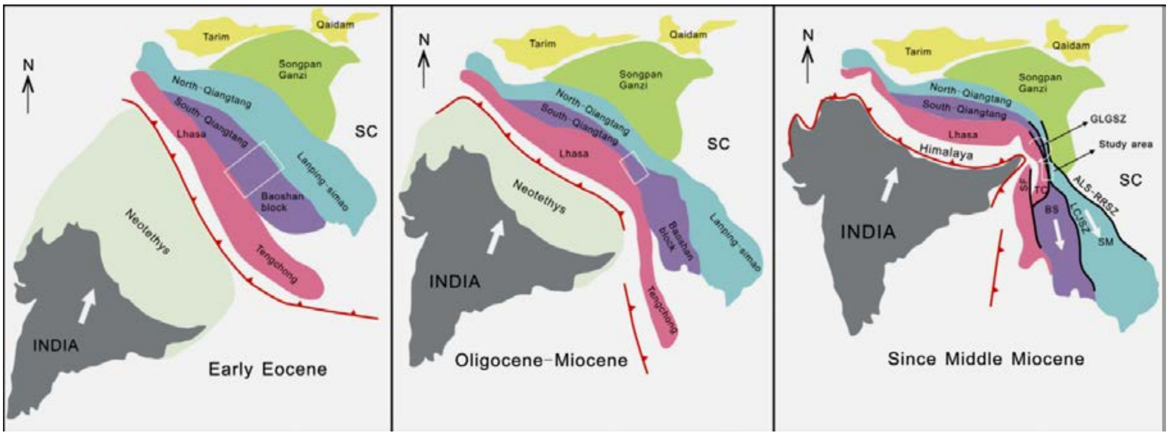

Figure 36. Tectonic reconstructions of the Himalayan–Tibet area since early Eocene. Modified by *Huang et al*. [2015] after *Replumaz and Tapponnier* [2003]; *Royden et al*. [2008]; *Pan et al*. [2012]; *Xu et al*. [2013].

Plate collision yielded the 2000 km wide and 5000 m high Tibet Plateau, the most outstanding high elevation plateau of the Earth [*Besse et al*., 1984; *Najmanet al*., 2010; *Searle et al*., 2007], edged by the Himalayan arc. Since the Oligocene/Miocene, the closure of Neotethys and consequent plate convergence and collision has been partly accommodated by the SE-ward lateral extrusion along major continental-scale-strike-slip shear zones in the South China and Indochina blocks [*Tapponnier et al*., 1990; *Leloup et al*., 1995; *Wang E. et al*., 1998; *Sato et al*., 1999; *Wang and Burchfield*, 2000; *Molnar and Dayem*, 2010]. Geological data suggested about 700±200 km southward displacement of Indochina block during the late Paleogene to early Miocene time span [*Lacassin et al*., 1996; *Leloup et al*., 1995, 2001]. As clearly shown by GPS, seismological and geophysical data [*Maurin et al*., 2010; *Liang et al*., 2013; *Huang et al*., 2017; *Zhu et al*., 2017], Tibet is nowadays squeezed by the surrounding plates and is escaping towards the E-SE, likely floating above hot and ductile lower crust.

The upper brittle crust of SE Tibet is, infact, characterized by a set of curved strike-slip faults, running around the north-eastern edge of the Indian indenter (Eastern Himalayan Syntaxis, EHS; Figure 37, 38), which are inferred to concentrate the deformation between major crustal blocks [*Wang et al*., 1998]. Identifying and determining the role and kinematic variability of the continental-scale strike-slip faults, responsible for accommodating a significant portion of the post-50 Ma India-Eurasia convergence, have great significance to understand the geologic evolution during Tibet Plateau growth [*Hall*, 2002; *Hall et al*., 2008; *Houseman and Englan*d, 1986, 1993; *Molnar and Dayem*, 2010; *Peltzer and Tapponnier*, 1988; *Royden et al*., 2008; *Tapponnier et al*., 1982, 1990; *Vilotte* et al., 1986; *Wang and Burchfiel*, 2000; *Yin and Taylor*, 2011].

In the past, the ductile high temperature deformation of the Shear Zones, addressed by structural geology studies coupled with radiometric dating, traced an activity spanning a wide time window between 35 and 15 Ma (late Eocene to middle Miocene; *Leloup et al*., 1993,1995; *Searle et al*. 2006, 2007 and references therein). However, the apparent lack of post-15 Ma shear zone activity conflicts with both GPS evidence [Figure 37; *Liang et al*., 2013], showing southward drift of Indochina at a ~2 cm/yr rate, and significant seismic activity with mainly strike-slip focal mechanisms [*Socquet and Pubellier*, 2005].

Lower magnitude events are diffuse in the whole region, and focal mechanisms of the main events are available in the Harvard Global CMT catalog (http://www.globalcmt.org/)[*Ekstrom et al.*, 2012].

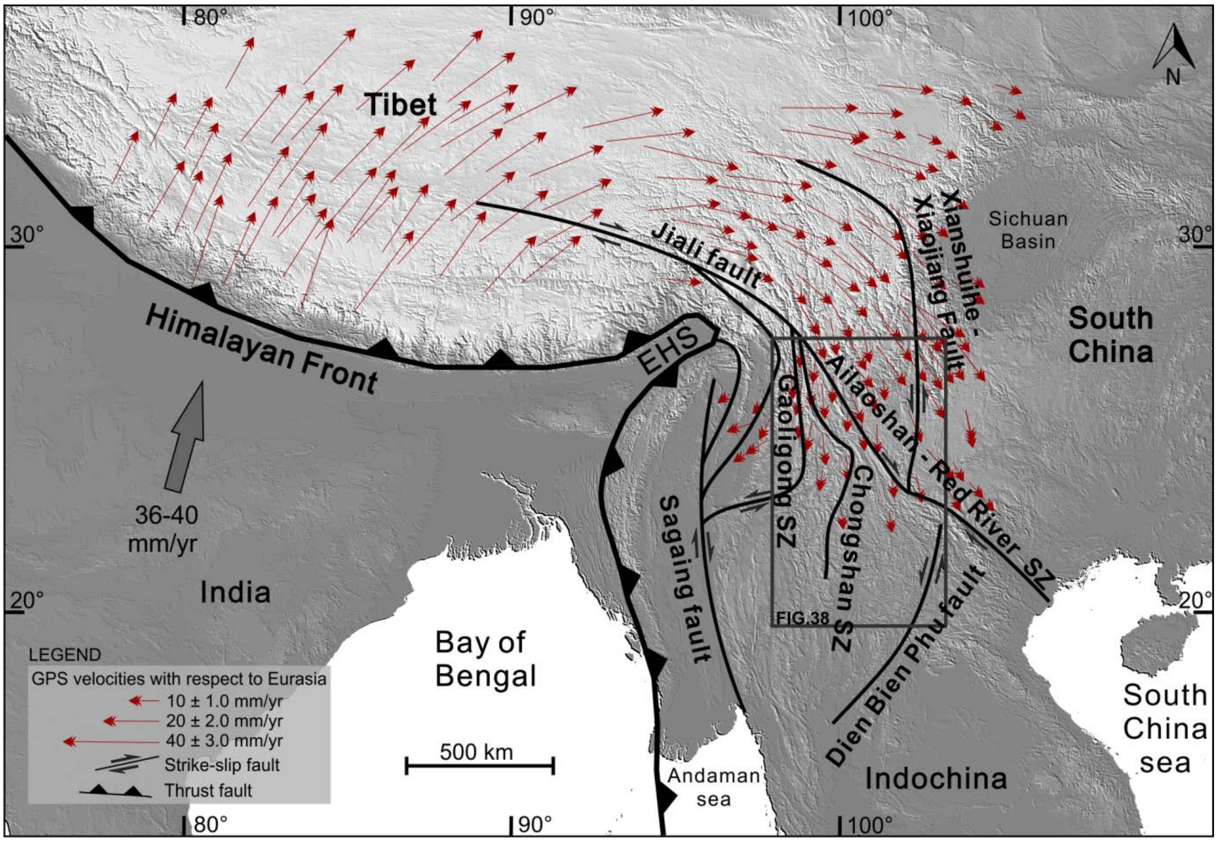

Figure 37. Schematic tectonic map of the South Asia and surrounding areas generated by GIS- Geographic Information System (DEM source: Esri, User Community, Coordinate System & Projection: world geodetic system 1984-Web Mercator Auxiliary Sphere). The grey rectangle represents the study area (see Figure 38). Red thin arrows show present-day global positioning system velocities around the Tibetan Plateau relative to stable Eurasia [*Liang et al.*, 2013]. EHS Eastern Himalayan Syntaxis; SZ shear zone.

There are two end-member models commonly used to interpret the deformation mechanisms of eastern and SE Tibet. The first is the 'tectonic escape' model: strain is localized on a limited number of major faults bounding rigid lithospheric mega-blocks, and is driven solely by stresses exerted at plate boundaries [*Avouac and Tapponnier*, 1993; *Ji et al.*, 2000; *Molnar and Tapponnier*, 1975; *Replumaz and Tapponnier*, 2003; *Tapponnier et al.*, 1982; *Tapponnier* *and Molnar* 1976, 1977]; the second is the 'crustal flow' model: deformation is pervasive and driven, for a significant part, by buoyancy forces resulting from lateral variations of crustal thickness. Deformation of the crust is continuous, and there are no blocks separated by strike-slip faults [*Bird*, 1991; *Clark and Royden*, 2000; *England and Houseman*, 1986; *Houseman and England*, 1993; *Royden et al*., 1997]. Additionally, *Wang and Burchfiel* [1997] were the first to notice that the extrusion was accompanied by strong internal deformation and rotation of smaller crustal fragments. *Clark et al*. [2006] and *Liu-Zheng* et al. [2008] noticed that Mesozoic-Cenozoic red beds in northern Indochina are tightly folded around NNW trending fold axes, and *Hall* [2002] also suggested a major shortening in N-NW Indochina block. Finally, *Li et al*. [2017a] proposed that this shortening is in part accommodated by large-scale block rotations.

A key for evaluating the validity of the two models may lie in the investigation of block motion scale and crustal deformation style and timing, especially in the vicinity of large strike-slip faults [*Wang et al*., 2001; *Zhang et al*., 2004; *Gan et al*., 2007; *Maurin et al*., 2010; *Liang et al*., 2013].

Paleomagnetism may represent a powerful tool for documenting and quantifying such tectonic data and this work will focus on this main goal.

4.1 Tectonics of Yunnan and characteristics of its major Shear Zones

To the SE of Tibet, the Indochina block is thought to have been extruded south-eastward during the initial phases of India-Eurasia collision [*Molnar and Tapponnier*, 1975; *Molnar et al*., 1988; *Patriat and Achache*, 1984; *Replumaz and Tapponnier*, 2003]. This convergence not only formed the Himalaya and the mountain system of the Central Asia, but also induced an intensive internal tectonic deformation within the Eurasia. Around the Eastern Himalayan Syntaxis (Figure 37, 38) and the area to the southeast, the large-scale strike-slip-dominated deformation zones curve from trending WNW-ESE at the eastern extremities of Tibetan plateau to trending NW-SE in northwestern Yunnan, China, and the rocks are strongly metamorphosed and deformed [*Tapponnier et al*., 1990; *Leloup et al*., 1993, 2007; *Searle*, 2006]. Within this area itself, four major ~N-S Shear Zone occur: the Sagaing, Gaoligong, Biluoxueshan-Chongshan (hereinafter referred as to Chongshan) and the Ailaoshan Red River Shear Zones [*Akciz et al*., 2008; *Leloup et al*., 1995; *Lin et al*., 2009]. These faults separate different tectono-metamorphic mega-terranes (Figure 38), focus of this thesis, called Tengchong, Baoshan, Lanping–Simao and Chuandian blocks.

They are characterized by different lithologies, protolith ages, intracontinental deformation, paleogeography, and orogenic history, with additional internal deformation and variable vertical axis rotations [*Kondo et al*., 2012; *Li et al*., 2017; *Sato et al*., 2007; *Sato et al.* 2001; *Tanaka et al*., 2008; *Tong et al*., 2013; *Wang and Burchfiel*, 1997; *Metcalfe*, 2006; BGMRYP, 1990; BGMRXZR, 1993].

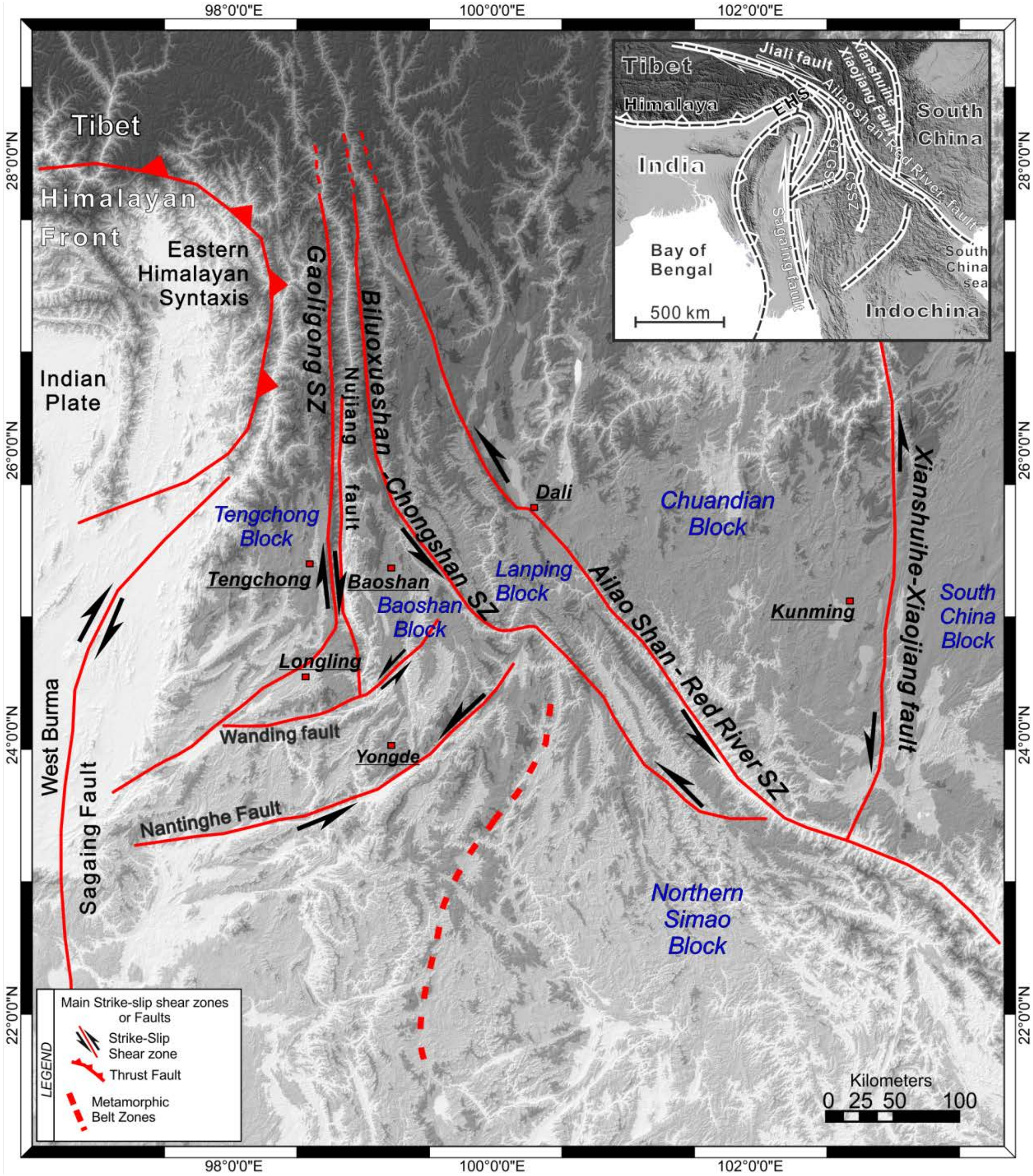

Figure 38. Schematic tectonic map of the Yunnan area (China). Detail of the grey rectangle showed in Figure 37. Here are shown the different blocks (in blue) and the major strike-slip faults (in red).

A brief description of the most important faults that characterize the Yunnan area, two of which are the subject of this study (Gaoligong and Ailaoshan Red River) follows.

4.2 THE SAGAING FAULT

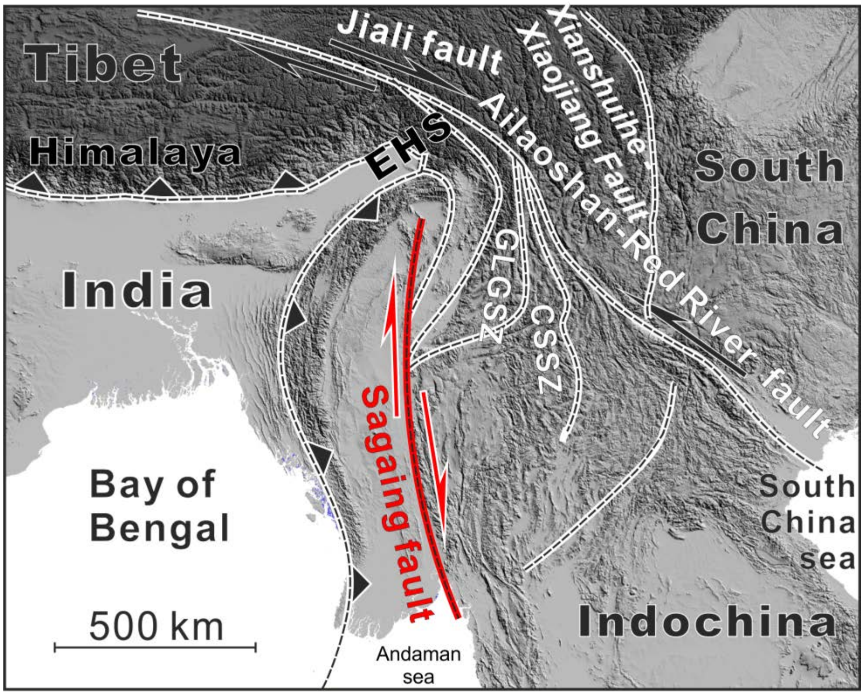

Figure 39. Schematic tectonic map of South Tibet. In red The Sagaing Fault.

The Sagaing fault is interpreted as a recent dextral continental strike-slip fault which has long and straight traces for 1000 km along the entire length of Myanmar and separates the Indochina continental fragment from the Burma block [Figure 38-39; *Akciz et al*., 2008; *Lin et al*., 2009; *Metcalfe*, 2013; *Replumaz and Tapponnier*, 2003; *Wang et al*., 2006]. The Sagaing fault is linked with Central Andaman spreading center to the south [*Curray et al*., 1979]. The Andaman Sea has been formed by seafloor spreading along short ENE-striking spreading center that is offset by NNW striking transform faults [Figure 39, 40; *Curray et al*., 1979]. Extension and rifting in the Central Andaman Basin began around 11 Ma ago and extension and sea floor spreading has been ongoing since 4-5 Ma [*Khan and Chakraborty*, 2005]. Spreading in a 335° (N25°W) direction, relative to present N, is at an average rate of 30 mm/yr the northward component is 27 mm/yr [*Curray*, 2005]. The average trend of the Sagaing Fault is 351°(N9°W) [*Soquet et al*., 2006].

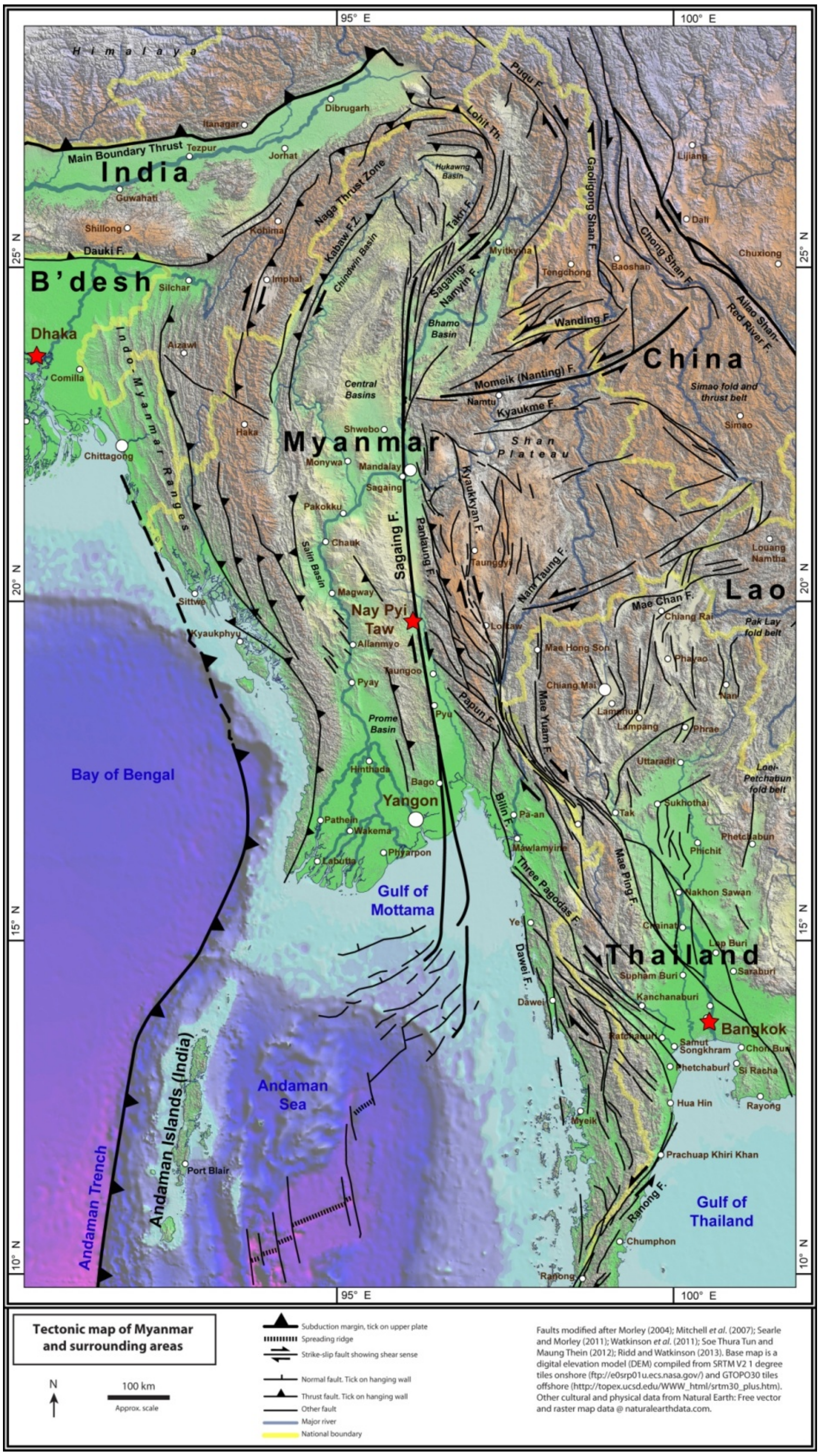

Figure 40. Tectonic features of Myanmar and surrounding areas (http://www.sagaingfault.info/index.html).
Faults modified after *Morley* [2004].

Since its formation about 22 to 15 million years ago, during the Miocene epoch [*Curray*, 2005; *Socquet and Pubellier*, 2005; *Searle et al.*, 2007], the Sagaing Fault has accommodated about 330 km [*Curray*, 2005] to 460 [*Mitchell*, 1993] of dextral displacement between its eastern and western sides. It is characterized at present by several right-lateral focal mechanisms, particularly along its northern end [*Ratschbacher et al., 1996; Wang et al., 1998; Xu et al., 2015*].

4.3 THE GAOLIGONG SHEAR ZONE

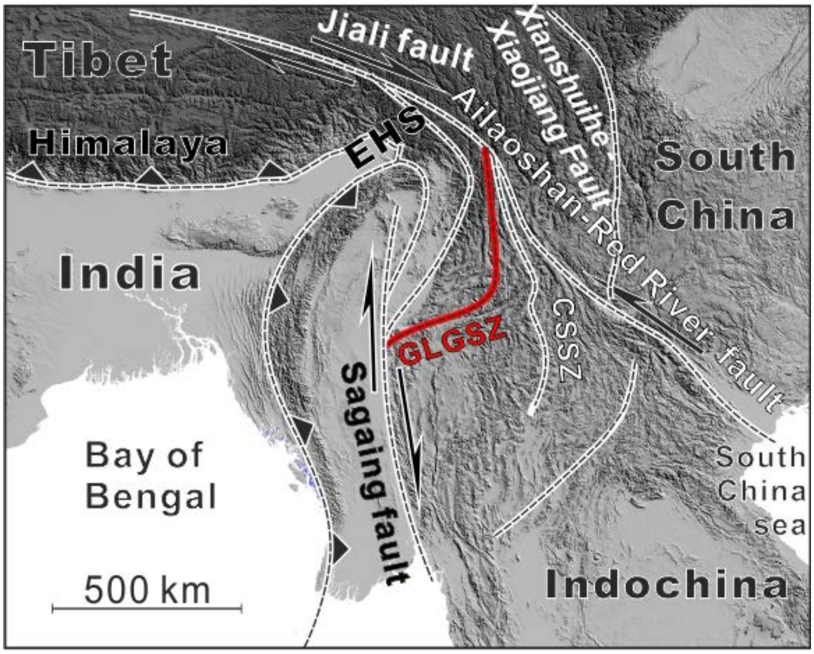

Figure 41. Schematic tectonic map of South Tibet. In red the Gaoligong Shear Zone (GLGSZ).

The Gaoligong Shear Zone extends eastward and southward from the Eastern Himalayan Syntaxis forming the boundary between the Tengchong and Baoshan blocks [Figure 38, 41; *Li et al*., 2004; *Mitchell*, 1992, 1993; *Xu et al*., 2012]. It is exposed completely along the Gaoligong Mountains west of the Nujiang river valley [*Wang and Burchfiel*, 1997; *Wang et al*., 2008], where dextral ductile shear indicators are widely preserved.

Field observations along the Gaoligong Mountains showed that the 500 m to 6 km wide Gaoligong Shear Zone contains mylonitic granites, gneisses, quartz schists and marble lens, and is characterized by steep foliation and nearly N-S trending sub-horizontal stretching lineations [*Wang et al*., 2008]. The banded mylonitic rocks were tightly folded with the hinges parallel to the lineations [*Zhang et al*., 2012a]. The S-C fabrics in shear bands and asymmetric boudins of quartz veins, confirm the dextral movement [*Xu et al*., 2015].

The Shear Zone is truncated by brittle normal faults with dextral shear component along both sides of the mylonitic belt (GEDF and GWDF in Figure 40). Moving southwards, shear zone width increases from 10 to 20 km, and the mountains decrease in elevation from 3500 m to 2500 m. Near Longling, the mylonitic rocks of the Gaoligong Shear Zone curve to the southwest, are exposed at the southwest tip of the mountain range, and finally crop out close to the Zhefang and Ruili basins (Figure 42 from *Pellegrino et al*., 2018).

The age of activity and kinematics along the shear zone was constrained by several Ar/Ar ages and structural studies on ductile deformation, which consistently suggest a dextral shear sense. *Lin et al*. [2009] and *Zhang et al*. [2012b] provided 13-18 and 10-16 Ma activity windows (respectively) relying on Ar/Ar mica ages, whereas an older 27-32 Ma activity age was radiometrically documented by *Wang et al*. [2006]. Ductile right-lateral deformation indicators are widespread all along the shear zone. No younger activity is documented in its central-northern N-S branch.

To the south, the Gaoligong Shear Zone is reactivated and truncated with left-lateral movement by the active NE-trending Longling and Wanding brittle faults [*Wang et al*., 2008; *Xu et al*., 2012; Figures 42] yielding the M 7.4 Longling earthquake in 1976. Apatite fission track data by *Wang et al*. [2008] constrain the onset of left-lateral brittle fault activity between 8.4 and 0.9 Ma. More recent (and possibly on-going) dextral strike-slip activity of the Gaoligong Shear Zone was proposed by *Socquet and Pubellier* [2005] relying on satellite image analysis. In agreement with the latter work, *Morley* [2007] suggested that the shear zone is a late Neogene transpressional deformation zone.

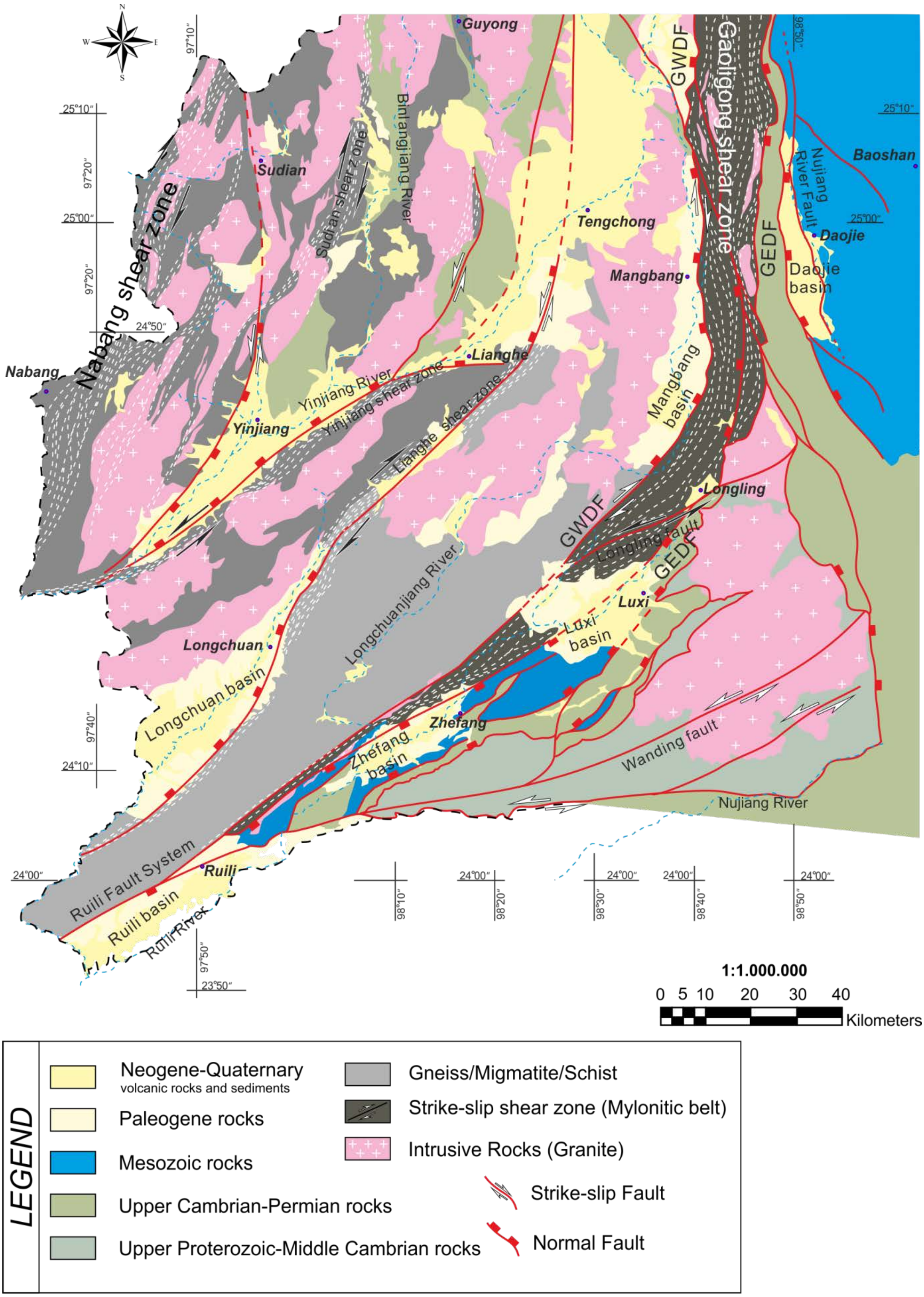

Figure 42. Modified after *Pellegrino et al*. [2018]. Simplified geological and tectonic map of the Gaoligong Shear Zone and adjacent areas. GEDF = Gaoligong east detachment fault; GWDF = Gaoligong west detachment fault.

Seismic activity has been recorded along the southern NE-trending part of the Gaoligong Shear Zone (also called Ruili fault system, Figure 42). On May 29, 1976, two large magnitude earthquakes (Ms>7) occurred in the Longling area south of Tengchong [*Wang et al.*, 2006; *Zhang et al.*, 1994]. The first Ms=7.4 event was located close to the NE-trending Gaoligong Shear Zone branch [*Holt et al.*, 1991]. The second Ms=7.3 event occurred close to the Wanding fault [Figure 42, 43; *Xu et al.*, 2012]. Both of them are strike-slip events with steep fault planes and ~N-S P axes, and have been interpreted as related to the recent left-lateral shear along NE-trending Longling and Wanding faults [Figure 42, 43; *Wang et al.*, 2006; *Xu et al.*, 2012]. It is noteworthy that the present-day sinistral kinematics along NE faults entering and cross-cutting the southern branch of the Gaoligong Shear Zone is opposite to the dextral kinematics reported for Oligo-Miocene times.

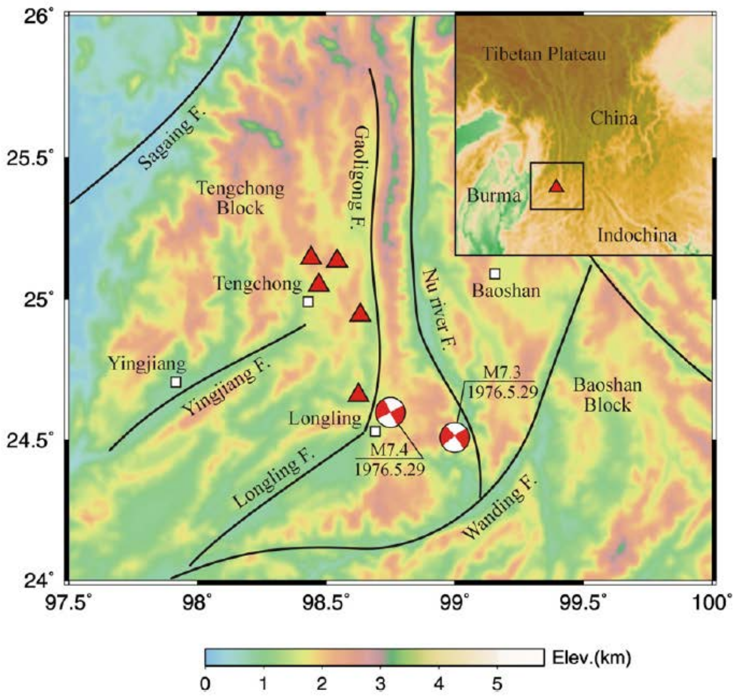

Figure 43. Tectonic outline from [*Xu et al.*, 2012]. Red triangles are main volcanic locations. Focal mechanisms are two M>7.0 earthquakes on May 29, 1976 (derived from the Harvard Global CMT Catalog). Their locations and magnitudes refer to the China National Earthquake Bulletins. Black solid lines are major active faults. The color scale bar denotes topography of the study area. Inset sub-figure is a large scale map showing the location of the study area.

4.4 THE CHONGSHAN SHEAR ZONE

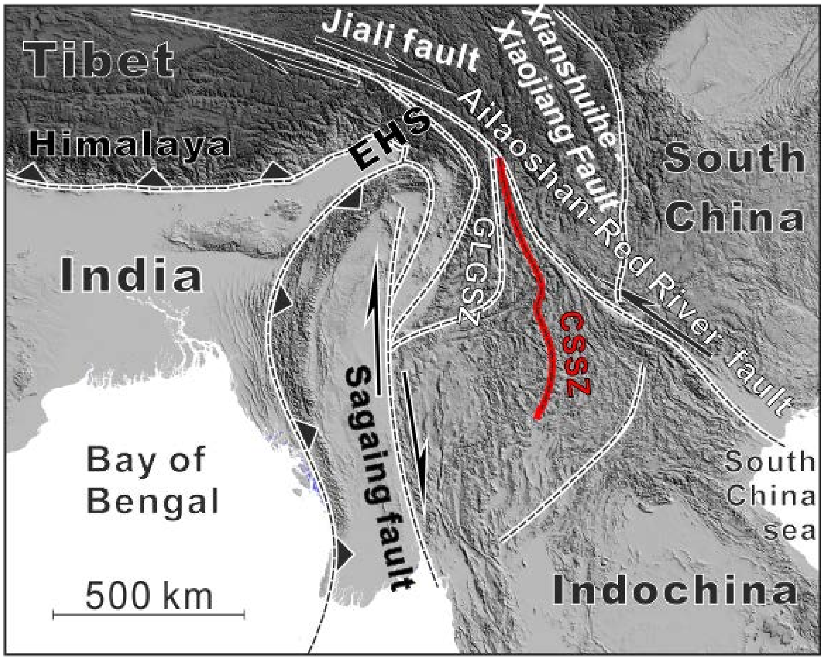

Figure 44. Schematic tectonic map of South Tibet. In red the Chongshan Shear Zone (CSSZ).

The Chongshan Shear Zone extends for hundreds of kilometers along the Biluoxueshan-Chongshan Mountains in western Yunnan with a width of ca. 10 km (Figure 38, 44). The shear zone is inconsistent along its southern and northern branches, in fact is divided into two belts (N-S trending) with contrasting metamorphic facies: an eastern low-grade schist belt and a western high-grade gneiss belt, considered to be a paired-metamorphic zone [*Wang et al*., 2008; *Zhang et al*., 1993; *Zhang et al*., 2010, 2011, 2012b]. The shear zone formed during the Cenozoic, and exhumation (from a depth of approximately 20 km) occurred from late Paleocene (ca. 57 Ma) to Miocene times [*Akciz et al*., 2008].

The northern segment of the Chongshan Shear Zone show a dextral displacement exceeding 100 km, related to the ductile deformation, spanning along 57-16 Ma time window. Subsequently a dextral and sinistral strike-slip displacement reported for the 32-14 Ma time windows, was documented along its northern and southern segment, respectively [*Zhang et al*., 2010; 2012a]. Sediments predominantly older than strike-slip fault activity are widely exposed in the western sector (Lanping block, see description later), and are made almost entirely of a 7.5 km thick succession of continental red beds of Jurassic-early Cenozoic age.

The ductile sinistral Chongshan and dextral Gaoligong Shear Zone were formed in Oligocene and are thought to be conjugate shear zones [*Wang et al.*, 2006; *Akciz et al.*, 2008]. They probably deformed contemporaneously with the Ailaoshan Red River Shear Zone, and all of their motions accommodated the southeastward extrusion of Southeast Asia.

4.5 The Ailaoshan-Red River Shear Zone

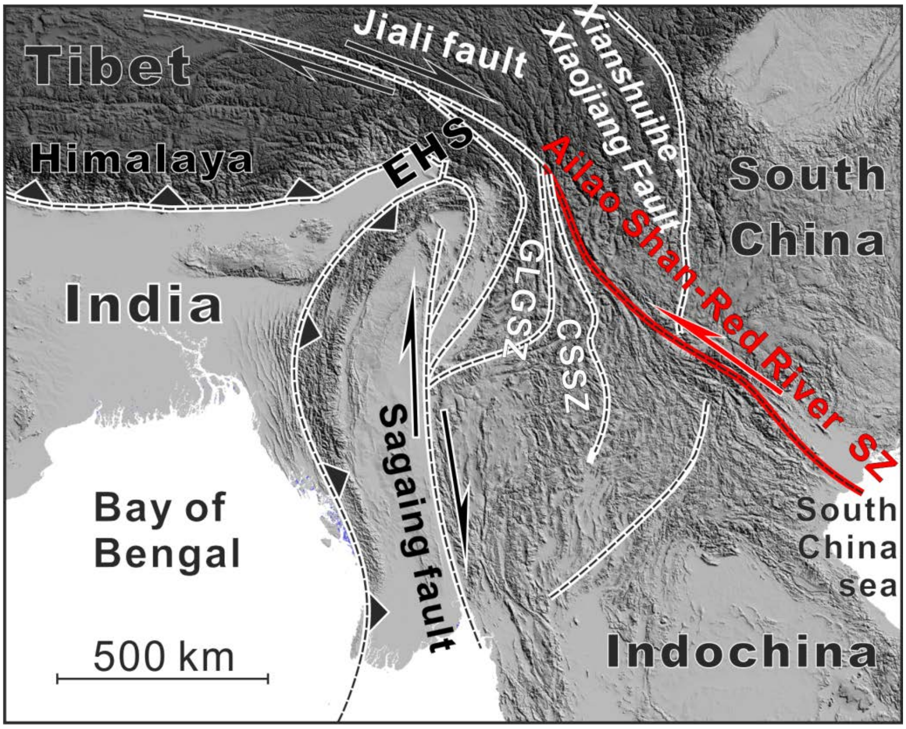

Figure 45. Schematic tectonic map of South Tibet. In red the Ailaoshan-Red River Shear Zone.

The Ailaoshan-Red River Shear Zone (ARRSZ) is a first-order tectonic structure that may be followed from the east margin of the Tibetan Plateau to the South China Sea and plays an important role in the distributed shortening model, with Tibet rotating around the eastern

Himalayan Syntaxis by introduction of a weak crustal layer through lower crustal flow southeastward [Figure 45; *Royden et al*., 1997; *Clark et al*., 2005a,b].

The Ailaoshan Red River Shear Zone is the major geological discontinuity that separates the Chuandian and South China blocks to the north-east from the extruding Indochina block to the south-east [Figure 38; *Leloup et al*., 1995; *Tapponnier et al*., 1990; *Zhang et al*., 2006; *Zhong et al.*, 1990]. The Shear Zone extends over a length of more than 1000 km between the South China Sea to the south and the Tibet Plateau to the north, and stands out as the most striking discontinuity in the morphology and geology of Yunnan. It is regarded as the eastern boundary of the southeastward extruded Indochina block, in agreement with the observed left-lateral ductile shear [*Leloup et al*., 1995; *Tapponnier et al*., 1982]. The onshore segment of the Red River Fault is exposed in four ranges about 10–20 km wide underlain by mylonitic gneiss, metamorphosed to amphibolite grade: Xuelong Shan (XLS), Diancang Shan (DCS), Ailaoshan (ALS) and Day Nui Con VOI (DNCV) [Figure 46; *Leloup et al*., 1995; *Zhang et al*., 2017]. In the central sector, the foliation is usually steep, and the lineation is usually nearly horizontal, both being almost parallel to the trend of the mylonitization in the gneiss massifs [e.g., *Leloup et al*., 1993, 2001; *Jolivet et al*., 2001; *Cao et al*., 2010; *Zhang et al*., 2017].

The timing and the amount of displacement along the shear zone have been strongly debated over the last decades. Its reflects at least two successive deformation phases [*Zhu et al*., 2009], but reversal of slip on the ARRSZ from 17 to 5 Ma is not well documented. Pliocene–Quaternary right-lateral movement of the Red River Fault is documented onshore by sharp geomorphic fault traces, large river offsets, and well-preserved cumulative scarps. Dextral motion on the Red River Fault likely started around 8–5 Ma, and the total slip has been estimated to be ≤40 km [*Allen et al*.,1984; 2016; *Replumaz et al*., 2001; *Burchfield and Wang*, 2002; *Schoenbohm et al*., 2006].

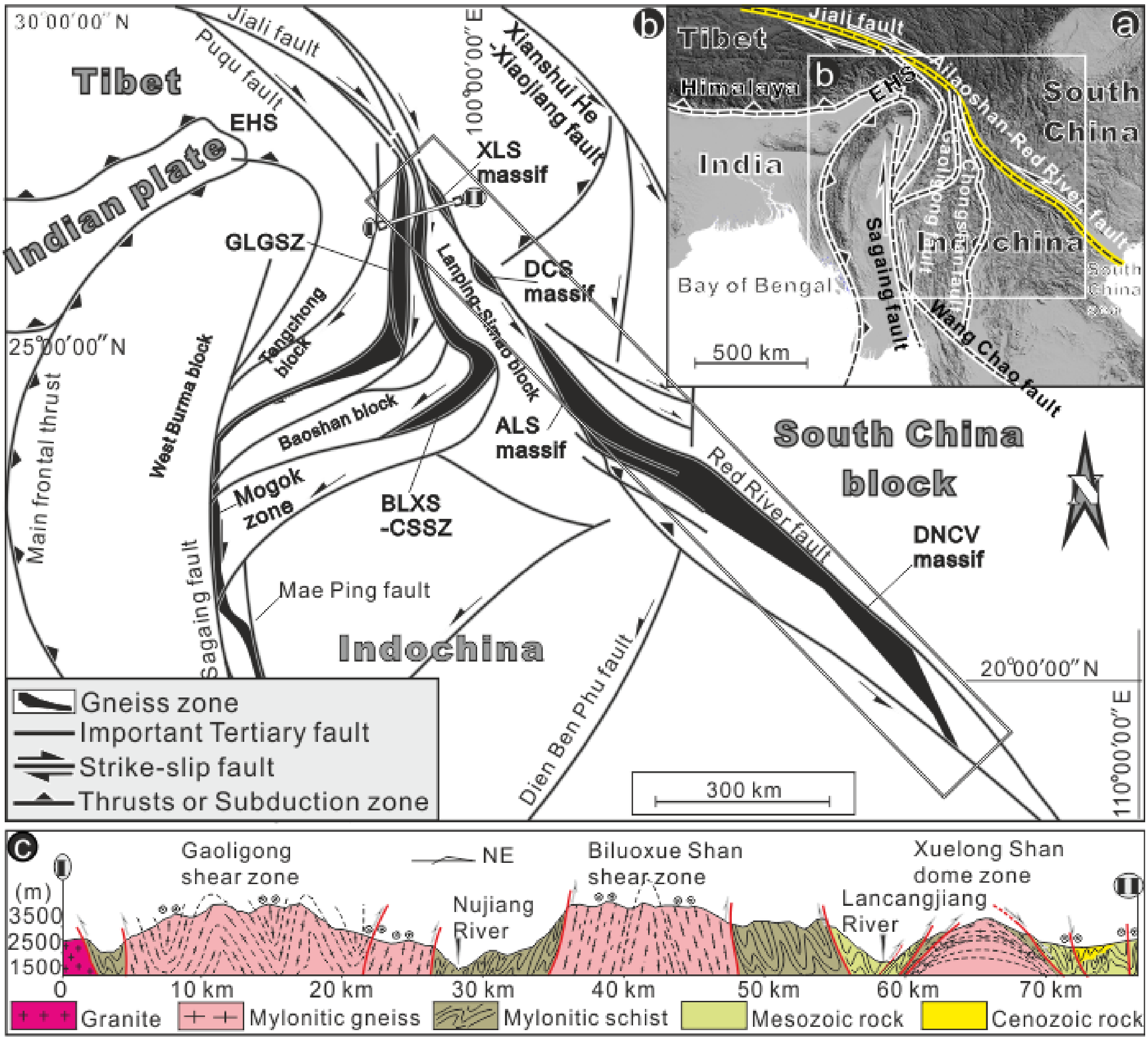

Figure 46. Simplified regional tectonic framework in southeastern Asia (modified after *Zhang et al.*, [2017] after *Tapponnier and Molnar* [1977], *Tapponnier et al.* [2001], *Leloup et al.* [1995, 2001], *Wang and Burchfiel* [1997], *Ding et al.* [2005], *Searle* [2006], *Liu et al.* [2007], and *Xu et al.* [2015]). (**a** and **b**) The Cenozoic major fault systems, the Jiali-Ailaoshan-Red River fault, and the Gaoligong-Sagaing- Wang Chao fault curving around the EHS region extending to southeast. (**c**) A regional profile I–II across the Gaoligong, Biluoxueshan, and Xuelong Shan massifs [*Zhang et al.*, 2010, 2014]. Xuelong Shan (XLS), Diancang Shan (DCS), Ailaoshan (ALS), Gaoligong Shan Shear Zone (GLGSZ), Biluoxueshan-Chong Shan Shear Zone (BLXS-CSSZ), Day Nui Con Voi (DNCV), Eastern Himalaya Syntaxis (EHS).

In addition, the Red River Fault was characterized by left-lateral movement about 34–17 Ma (Oligo-Miocene), with widely varying estimation of total slip of 100–1400 km specifically between 700 ± 200 km in the NW and ~250 km in the SE [*Tapponnier et al.*,1990; *Zhong et al.*, 1990; *Harrison et al.*,1992, 1996; *Leloup and Kienast*, 1993; *Scharer et al.*, 1994; *Leloup et al.*, 1995; *Chung et al.*, 1997; *Wang E. et al.*, 1998; *Zhang and Scharer*, 1999; *Wang et al.*, 2000; *Leloup et al.*, 2001; 2007; *Gilley et al.*, 2003; *Searle*, 2006; *Zhang et al.*, 2017; *Li et al.*, 2017a]. The latter offset of the ARRSZ has been strongly debated.

Following the pioneering work of *Tapponnier et al.* [1990], many geologists have posited- mainly relying on displaced geological markers- that the ductile, left-lateral deformation of the Red River Fault absorbed hundreds of kilometers of slip and a substantial part of Asian shortening during the Cenozoic India–Asia collision, and led to the opening of the South China Sea [e.g. *Scharer et al.*, 1994; *Leloup et al.*, 2001]. However, some evidence is incompatible with the continental extrusion model [*Schoenbohm et al.*, 2006 and reference therein], because this would imply that the ARRSZ was a proper transform fault and that Indochina behaved as a microplate during Oligo-Miocene times. On the other hand, *Searle* [2006; 2007] recognized the ARRSZ as an Oligo-Miocene crustal strike slip fault reactivating an older exhumed metamorphic core complex, and stressed that the left-lateral offset cannot be constrained.

After the description of the major shear zones, below is a brief geological description of the adjacent blocks, known as Tengchong, Baoshan, Lanping-Simao and Chuandian blocks. They are characterized by tectono-metamorphic settings showing different lithologies, intracontinental deformation and orogenic history [*Lee et al.*, 2003; *Leloup et al.*, 1995; *Wang and Burchfiel*, 1997; *Wang et al.*, 2006].

4.6 THE TENGCHONG BLOCK

The Tengchong block, located in southwestern China (Yunnan Province) and part of the SE Himalayan tectonic belt [*Zhu et al.*, 1983], underwent ca. E–W extension in the Late Cenozoic along ca. N-trending fault-bounded grabens [e.g. *Wang et al.*, 2008]. The basement consists of Neoproterozoic to Paleozoic gneisses, migmatites, granites, and small lenses of mafic rocks [e.g. *Chen et al.*, 2002], covered by mostly Late Paleozoic sedimentary rocks and intruded by volcanic rocks of late Miocene to Holocene (sporadic Late Mesozoic to Early Cenozoic granites, locally foliated) age which constitute the well-known "Tengchong Volcanic field" [*Wang et al.*, 2007; *Zhu et al.*, 1983; *Zou et al.*, 2010; *Kornfeld et al.*, 2014; *Xu et al.*, 2015].

The magmatism was active since Mesozoic times [*Dong et al.*, 2006; *Li et al.*, 2011]. Widely exposed Pliocene-Holocene volcanics of the Tengchong field are mainly distributed along NE–NNE trending basins, alternated with Mesozoic granites and sedimentary strata. The distribution of upper Cenozoic volcanic rocks covers an area of 792 km^2. Pliocene-Holocene volcanic activity of the Tengchong field can be grouped into at least three different types [*Jiang*, 1998; *Li et al.*, 1999]: (1) Middle-Upper Pliocene to Upper Pleistocene basalts, (2) Lower Pleistocene silicic pyroclastic rocks and (3) Holocene basaltic andesites [*Li et al.*, 1999; *Mu et al.*, 1987; *Wang et al.*, 1999; *Zou et al.*, 2014]. Further south, the Mangbang basin was interpreted as a half-graben developed along the Gaoligong Shear Zone. It is filled with upper Miocene-Pliocene sandstones and mudstone intercalated with tuffs and basalts [Figure 42; *Wang et al.*, 2008].

Volcanic centers are located within a 90 km long and 50 km wide N-S-trending graben. There are 68 late Neogene–Quaternary volcanic centers, 145 hot springs and 25 preserved volcanic craters and cones [*Jiang*, 1998; *Jiang et al.*, 2003].

The three youngest of the 68 Quaternary volcanoes in Tengchong Volcanic Province [*Jiang*, 1998; *Huangpu and Jiang*, 2000; *Turker et al*., 2013] are thought to be of Holocene age. The centers are named Dayingshan (Shooting Eagle Mountain), Maanshan (Saddle Peak), and Heikongshan (Black Emptied Peak) (Figure 47). These are active volcanoes, identified by their current geothermal activity [*Shangguan*, 2005], geophysical surveys that indicate the presence of magma, and dating of young volcanic rocks [*Li et al*., 1999, 2000; *Wang et al*., 1999]. Dayingshan Volcano (E 98°; N 25°) is the oldest and largest of the three, with a base to the cone of 2 x 1 km and cone height of 120 m and it is made up of lavas erupted in several episodes and a scoria cone.

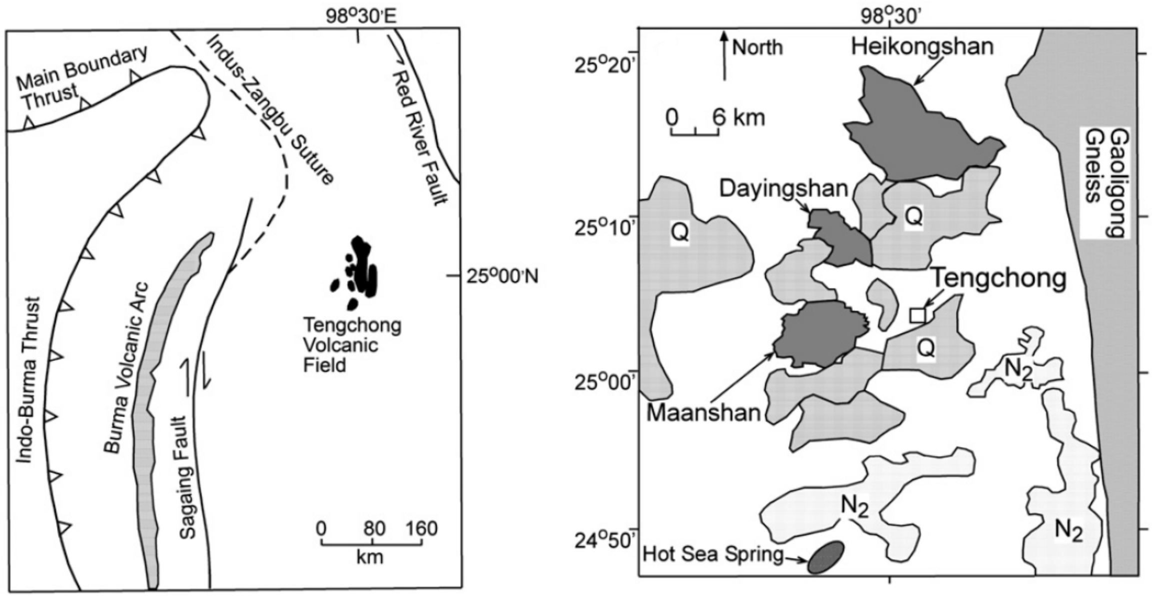

Figure 47. Location map of the Tengchong volcanic field in SE China (left) and distribution and relative ages of the three most recently active volcanoes and surrounding rocks. Modified after *Turker et al.* [2013].

To the west of the Gaoligong strike-slip Shear Zone, new mapping identified widespread mylonitic ortho- and paragneisses with gently dipping foliation and nearly horizontal stretching lineation defined by long axes of amphibole and sillimanite grains and boudinage of felsic veins. Despite the varying attitude of the foliation, the stretching lineation has a consistent NE-azimuth, parallel to the strike of the Gaoligong Shear Zone. These strongly sheared rocks can be traced for more than 100 km from the northern Longling area, the western Mangshi area, to the northern Ruili area, forming a gently folded, low-angle ductile Shear Zone, the Donghe detachment [*Xu et al*., 2015].

4.7 The Baoshan block

The Baoshan Block appears to pinch out where the GSSZ and CSSZ merge [*Akciz,* 2004, 2008]. The Baoshan Block accreted to Asia in the Late Mesozoic shortened internally along N-trending folds and thrusts (present-day orientation) before or during the Eocene–Oligocene, possibly associated with the strike-slip movements along the GSSZ and CSSZ [*Wang and Burchfiel* 1997; *Wang et al.,* 2008]. The Baoshan Block exposes thick Upper Proterozoic to Triassic marine strata consisting of carbonates, sandstones, siltstones and shales deposited in a platform environment, unconformably covered by Middle Jurassic marine sedimentary rocks and continental deposits made of Jurassic-lower Cenozoic red beds [*Huang et al*., 2015; *Wang and Burchfiel*, 1997; *Kornfeld et al*., 2014a].

The Paleozoic strata are mainly carbonatic and clastic and locally intercalated with mainly rift-related tholeiitic basalts and basaltic volcanoclastic rocks that erupted when the Baoshan Block separated from Gondwana [e.g. *Wopfner*, 1996; *Wang et al*., 2008; *Kornfeld et al*., 2014a; *Xu Y. et al*., 2015]. In the central part of the BST, between Baoshan and Yongde city (Figure 38), several approximately N-S trending thrust faults develop, which were offset by a series of E-W trending strike-slip faults. The Eocene-Oligocene formations (conglomerate and sandstone resting unconformably on older rocks) have undergone approximately east-west compression forming folds with approximately N-S trending fold axes [e.g. *Wang and Burchfiel*, 1997; *Tong et al*., 2016 and reference therein]. Pliocene volcanic and sedimentary rocks and Quaternary strata remain mostly undeformed [*Wang and Burchfiel*, 1997; *Kornfeld et al*., 2014a].

Cenozoic rocks were involved in intensive shortening along a number of N-S-trending folds and thrust faults, which narrow and merge with each other at the northern end of the Baoshan block. To the east of the Gaoligong fault, just to the south, the Baoshan block is cut by three sinistral strike-slip shear zone NNE-SSO oriented called Longling, Wanding and Nujiang fault, interrupted by normal faults running parallel to the Gaoligong east detachment fault. Further south, the Baoshan block is bounded by the active left-lateral Nantinghe fault with the same orientation as the three just mentioned faults [Figure 38; *Socquet and Pubellier*, 2005]. Seismicity and stream-offset analysis indicate that the Nantinghe fault may accommodate at present a 1 mm/yr deformation rate [*Lacassin et al*., 1998].

4.8 LANPING SIMAO BLOCK

The Lanping-Simao block contains the Proterozoic basement and the Palaeozoic marine strata [BGMRY, 1990]. The Lanping-Simao Basin in this terrane consists of the Mesozoic (Upper Triassic to Eocene) continental red beds, which unconformably overlie the Pre-Mesozoic strata. These Mesozoic red beds are generally affected by the NNW-SSE trending folds and thrusts, but an arcuate trend is maintained in the Simao Basin [*Leloup*, 1995]. Timing of fold and thrust formation remains controversial. Although, fairly recent fold and trust growth has been claimed by *Leloup* [1995] on the basis of its study on ramp anticlines, other researchers [*Wang and Burchfiel*, 2000; *Socquet and Pubellier*, 2005; *Akciz*, 2008; *Kondo et al*., 2012] have suggested an older age (between the Paleocene and Oligocene) for compressive tectonics.

The Cretaceous sequence of the Simao fold belt is of terrestrial origin and has been subdivided into four different formations, they are: the Lower Cretaceous Jinxing Formation, the Middle Cretaceous Nanxin Formation, the Upper Cretaceous Hutousi Formation and the

Upper Cretaceous Mankuanhe Formation [BGMRY 1990; *Leloup* 1995; *Kondo et al*., 2012]. The Jinxing Formation is mainly composed of greyish sandstone intercalated with purplish-red, greyish and green mudstone. The presence of rich Lamellibranchiate indicates the Early Cretaceous age for this formation. The Middle Cretaceous Nanxin Formation mainly consists of purplish-red sandstone, which conformably overlies the Early Cretaceous Jinxing Formation. This formation is overlain by the Upper Cretaceous Hutousi Formation. The occurrences of Estheria, Cypridea, Gastropods, and Sporopollen indicate an age of Middle Cretaceous for the Nanxin Formation. The Upper Cretaceous Mankuanhe Formation is distributed only in the Pu'er-Mengla area [*Kondo et al*., 2012]. The Nanxin Formation, around Jingdong area, forms an E-W trending anticlinal structure; more southern, in the Zhengyuan area, this formation is separate by several N-S trending anticlines and, to the west others monoclinal stuctural. Also in Mengla locality, a monoclinal structure with N-S trending axis and a dip of 2°-63° always in Nanxin Formation (from northeastward to eastward) has been observed by *Tanaka et al*. [2008].

4.9 CHUANDIAN BLOCK

The Chuandian block in delimited by the Ailaoshan Red River Shear Zone and the Xianshuihe-Xiaojiang fault, which is considered to be a boundary fault to accommodate the different rotations around the eastern Himalayan Syntaxis and the total offset is of 78–100 km [*Wang et al*., 1998]. The Xianshuihe-Xiaojiang fault developed only in the last 10 Ma, with a brittle sinistral offset of ca. 60 km [*Wang et al*., 1998; *Zhang et al*., 2004; *Meade*, 2007; *Wang et al*., 2016a,b]. GPS measurements and geological observations along the Xianshuihe-Xiaojiang fault system suggest a southward displacement of the Chuandian Fragment (CDF) during the last 12 Ma [*Roger et al*., 1995; *Wang et al*., 1998, 2001; *Chen et al*., 2000]. In the Chuxiong basin, Upper Triassic gray sandstones and marls grade upwards into Jurassic and

Cretaceous red sandstones. The lower red sandstones display decametric cross-bedding [*Leloup* , 1995]. The youngest red beds, cropping out to the north of Chuxiong (N25°02', E101°31'), are of Eocene age [BGMRY, 1983]. To the west, the maximum thickness of the Chuxiong Mesozoic-Tertiary continental sequence is about 6 km [*Gao et al.,* 2017].

Previous studies reported from the area suggest that this fragment experienced more than 300 km of southward displacement after Cretaceous times. Neogene southward displacement of this fragment is also supported by geological observation and GPS measurements [*Tamai et al*., 2004 and reference therein]. The indentation of India into Asia brought about some internal deformation to the Chuandian Fragment during its southward translation; this deformation can be seen in significant amount of rotation deduced from Cretaceous paleomagnetic data of this fragment [*Funahara et al*., 1992; *Avouac and Tapponnier*, 1993; *Huang and Opdyke*, 1992; *Lacassin et al*., 1997; *Otofuji et al*., 1998; *Yoshioka et a*l., 2003; *Tamai et al*., 2004; Figure 48]. As suggested by these data, the southward movement of the Chuandian fragment has been continuing since the time of India-Asia collision.

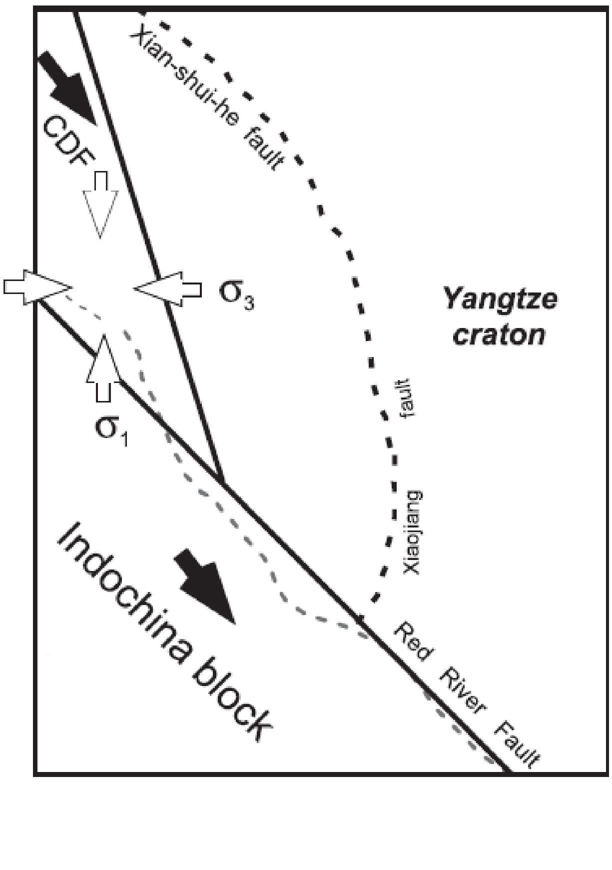

Figure 48. A deformation model for the CDF from *Yoshioka et al*. [2003]. The paleo-shape of the CDF was originally apex. An initially linear Xianshuihe-Xiaojiang fault system (solid line) changed into present curvilinear shape (dashed line) as a result of deformation in the CDF. During its southward displacement (closed arrows) in the Cenozoic era, the CDF tectonically interacted with the Yangtze and Indochina blocks. Roughly, east– west extension (σ1) and north– south compression (σ3) are raised up (open arrows) in the southern part of the CDF. Due to these compressive stresses, an eastward bulge has been formed in the Xianshuihe-Xiaojiang fault system accompanied by a differential tectonic rotation in the Chuxiong basin.

Chapter V

5. PREVIOUS PALEOMAGNETIC DATA

A wealth of paleomagnetic data has been gathered during the last decades in Yunnan area, straddling the northern Indochina block and the southeastern Tibetan Plateau (Figure 49 and Table 1). In the present work, all the previously obtained rotations were recalculated using updated 170-140 Ma Eurasian and 130-10 Ma East Asia reference poles from *Torsvik et al*. [2012] and *Cogné et al*. [2013], respectively (Chapter 3, Figure 25, 26). Data are reported, for each block, moving from west to east.

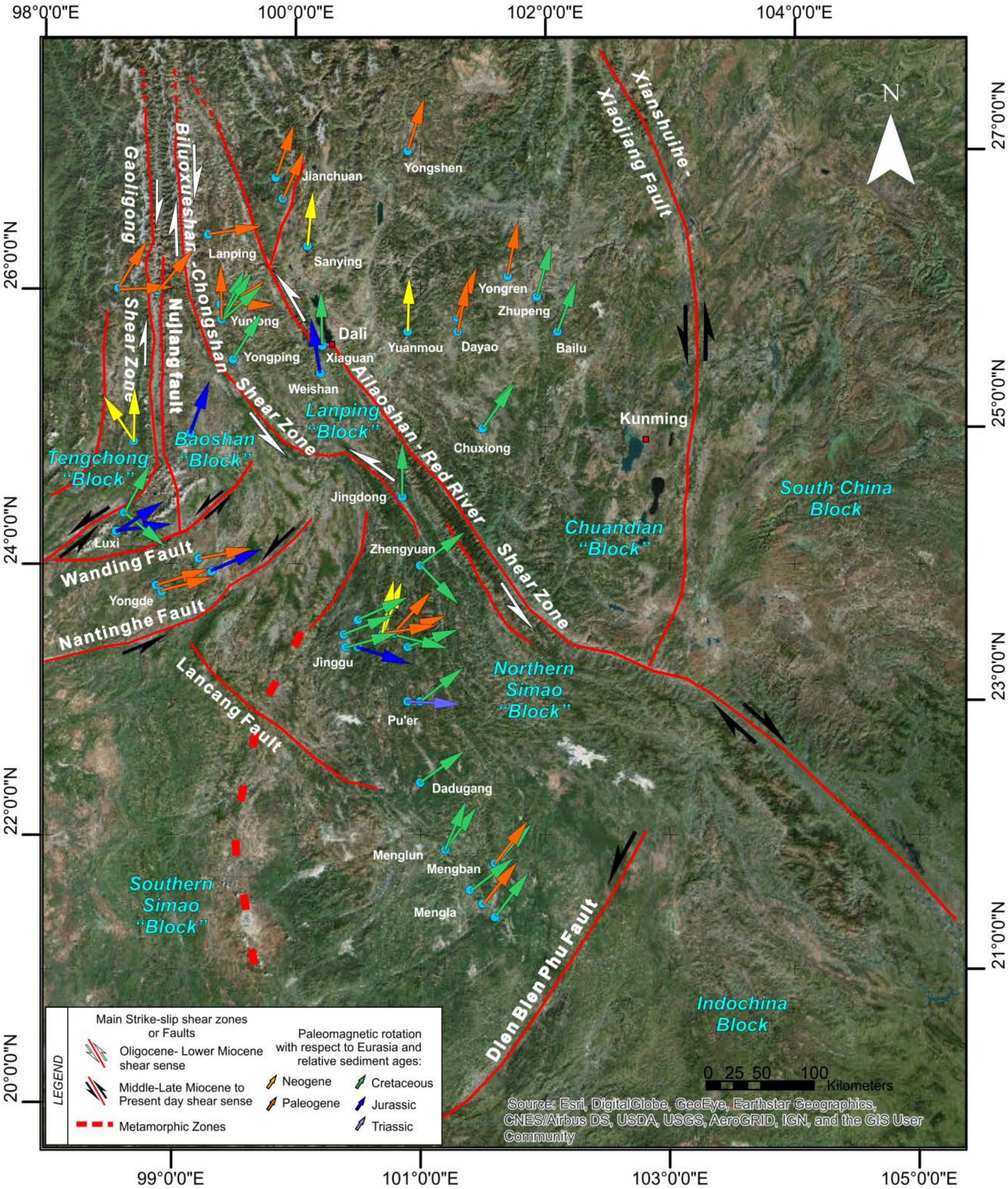

Figure 49. Map of western Yunnan and southeastern Eastern Himalayan Syntaxis, main tectonic features, and synthesis of the main paleomagnetic data. Base map source: GIS (Esri), WGS 1984-Web Mercator Auxiliary Sphere. Colored arrows (see legend) represent paleomagnetic rotations with respect to Eurasia, recalculated from previous paleomagnetic directions (See Table 1), according to *Demarest* [*1983*] and using updated Eurasia (from 170 to 140 Ma) and East Asia (from 130 to 10 Ma) poles by *Torsvik et al*. [2012] and *Cogné et al*. [2013], respectively.

Locality	Geographic Coordinates		Age	Age (Ma)	N	Considered paleopoles Age	Observed direction					Recalculated by Us		Reference
							In Situ		Tilt corrected			Rotation	Flattening	
	Latitude °N	Longitude °E					*D* (deg)	*I* (deg)	*D* (deg)	*I* (deg)	α_{95} (deg)	R ± ΔR	F ± ΔF	
Tengchong Block														
Pianma-Nujiang	26.0	98.7	Oligocene	30	6	30	38.5	20.0	33.3	41.4	24.5	31.2 ± 26.3	-5.0 ± 19.4	Kornfeld et al. [2014b]
	26.0	98.7	Eocene	40	6	40	84.5	14.9	89.8	35.1	11.8	87.2 ± 11.8	-1.6 ± 10.5	Kornfeld et al. [2014b]
Tengchong v.f	25.1	98.4	Pleistocene-Holocene	2.5-0	16	0	352.5	25.4	_	_	44.9	-7.5 ± 40.3	-5.7 ± 14.1	Kornfeld et al. [2014c]
Mangbang b.	24.8	98.6	Upper Miocene-Pliocene	14-2.5	16	10	327.3	48.7	_	_	14.1	-33.7 ± 17.3	-9.1 ± 11.3	Kornfeld et al. [2014c]
Baoshan Block														
Luxi	24.3	98.4	Middle Jurassic	163-174	6	170	110.0	-2.9	99.7	35.2	11.3	81.3 ± 11.8	24.9 ± 9.3	Huang and Opdyke [1993]
Baoshan	26.0	98.8	Oligocene	30	16	30	32.6	51.8	42.2	47.0	7.8	40.0 ± 9.2	-10.6 ± 6.9	Kornfeld et al. [2014a]
Yongde	24.4	99.3	Eocene-Oligocene	56-23	22	20	81.7	35.1	_	_	3.8	79.4 ± 4.4	0.2 ± 4.7	Tong et al. [2016]
	24.2	99.0	Paleocene	66-56	5	60	_	_	76.9	17.8	3.8	72.5 ± 9.1	14.0 ± 9.5	Tong et al. [2016]
Lanping Block														
Yunlong	25.8	99.4	Middle Cretaceous	100	20	100	50.9	29.8	40.2	49.9	3.9	32.0 ± 5.6	-9.0 ± 4.8	Sato et al. [1999]
			Lower Cretaceous	145-100.5	23	120	103.2	61.6	59.7	41.0	11.9	49.3 ± 12.6	1.8 ± 9.7	Yang et al. [2001b]
			Upper Cretaceous	100.5-66	9	80	52.4	62.1	34.0	52.4	7.3	24.0 ± 9.8	-15.4 ± 6.9	Yang et al. [2001b]
			Paleocene	66-56	11	60	49.2	7.6	50.2	31.1	13.2	45.7 ± 12.5	3.2 ± 11.4	Yang et al. [2001b]
Lanping area	26.4	99.3	Eocene	38-29	9	30	274.0	-35.6	263.8	-42.1	14.1	81.6 ± 15.1	-5.1 ± 11.4	Sato et al. [2001]
Yunlong area	25.9	99.4	Eocene	38-29	5	30	271.8	-19.8	273.0	-31.8	11.1	90.8 ± 10.5	4.4 ± 9.2	Sato et al. [2001]
Weishan	25.4	100.2	Upper Jurassic	163-145	5	150	356.5	34.5	7.3	25.3	10.4	-9.5 ± 10.8	28.6 ± 9.6	Huang and Opdyke [1993]
Xiaguan	25.6	100.2	Middle Cretaceous	100	9	100	8.9	59.2	6.9	47.7	8.6	-1.3 ± 10.4	-6.9 ± 7.6	Huang and Opdyke [1993]
Yongping	25.5	99.5	Lower Cretaceous	145-100.5	12	120	48.9	50.8	42.0	51.1	15.7	31.7 ± 20.0	-8.6 ± 12.6	Funahara et al. [1993]
Northern Simao Block														
Jinggu	23.4	100.9	Middle Cretaceous	100	8	100	73.2	67.7	79.4	43.3	9.1	71.3 ± 10.2	-5.4 ± 8.1	Huang and Opdyke [1993]
Jinggu	23.6	100.5	Middle Jurassic	174.1-163.5	10	170	75.5	31.4	83.3	36.8	5.4	65.8 ± 7.1	23.3 ± 5.2	Huang and Opdyke [1993]
Mengla	21.6	101.4	Midddle Cretaceous	100	10	100	288.7	19.3	60.8	37.8	7.6	52.7 ± 8.0	-2.4 ± 7.2	Huang and Opdyke [1993]
Jinggu (Jingxing Fm.)	23.4	100.4	Lower Cretaceous	145-100.5	3	120	78.4	58.0	84.4	39.6	17.8	74.2 ± 18.4	0.3 ± 14.2	Chen et al. [1995]
Jinggu (Mangang Fm.)	23.4	100.5	Lower Cretaceous	145-100.5	3	120	294.2	23.1	297.5	-33.3	7.1	107.3 ± 7.0	6.6 ± 6.4	Chen et al. [1995]
	23.5	100.8	Lower Cretaceous	145-100.5	4	120	309.3	-6.2	294.4	-38.1	12.1	104.2 ± 12.3	2.0 ± 9.9	Chen et al. [1995]
Jinggu (Mengyujing Fm.)	23.5	100.8	Paleocene	66-56	9	10**	42.8	26.1	23.9	51.6	7.9	41.7 ± 7.2	11.7 ± 6.8	Chen et al. [1995]
Jinggu (Mengla Group)	23.5	100.7	Eocene-Oligocene	56-23	7	40	106.4	49.1	84.7	38.9	7.6	81.8 ± 8.3	-9.3 ± 8.0	Chen et al. [1995]
Jinggu (Sanhaogou Fm.)	23.5	100.7	Miocene	23-5.3	6	10	34.6	20.2	21.1	35.5	7.5	20.0 ± 7.5	2.3 ± 6.5	Chen et al. [1995]
Jinggu	23.5	100.8	Eocene	56-33.9	6	40	_	_	73.1	39.9	11.8	70.2 ± 12.5	-10.3 ± 10.6	Yang et al. [2001a]
Jingdong	24.5	100.8	Cretaceous	145-66	15	100	20.7	55.9	8.3	48.8	7.7	0.1 ± 9.6	-9.4 ± 7.1	Tanaka et al. [2008]
Zhengyuan	24.0	101.0	Cretaceous	145-66	14	100	94.7	88.2	61.8	46.1	8.1	53.6 ± 9.6	-7.4 ± 7.4	Tanaka et al. [2008]
West Zhengyuan	24.0	101.0	Cretaceous	145-66	5	100	315.6	-8.2	324.2	-49.4	6.4	136.0 ± 8.2	-10.7 ± 6.3	Tanaka et al. [2008]
South Mengla	21.4	101.6	Cretaceous	145-66	19	100	353.6	50.3	51.2	46.4	5.6	43.2 ± 7.0	-11.3 ± 6.0	Tanaka et al. [2008]
Pu'er	23.0	101.0	Cretaceous	145-66	31	100	82.4	49.5	59.9	45.2	5.1	51.8 ± 6.4	-7.9 ± 5.6	Sato et al. [2007]
Zhengwan	22.8	100.9	Upper Cretaceous	100-66	11	80	267.5	57.4	51.8	47.9	6.9	41.9 ± 8.5	-15.0 ± 6.8	Kondo et al. [2012]
Dadugang	22.4	101.0	Upper Cretaceous	100-66	12	80	78.1	69.0	64.1	48.1	7.3	54.2 ± 9.0	-15.8 ± 7.0	Kondo et al. [2012]
Mengban	21.8	101.6	Paleocene-Eocene	66-33.9	6	50	12.9	45.8	43.5	23.0	13.4	37.6 ± 12.3	6.1 ± 12.9	Tong et al. [2013]
Mengla	21.5	101.5	Eocene-Oligocene	56-23	17	40	32.3	34.0	41.8	23.8	5.8	38.8 ± 6.0	2.5 ± 7.2	Tong et al. [2013]
	21.4	101.6	Lower Cretaceous	145-100.5	14	120	10.7	40.1	46.9	42.2	7.7	36.8 ± 8.5	-4.8 ± 6.8	Tong et al. [2013]
Menglun	21.9	101.2	Upper Cretaceous	100-66	6	80	44.7	58.3	33.2	30.9	8.2	23.3 ± 8.0	0.6 ± 7.7	Tong et al. [2013]
	21.9	101.2	Lower Cretaceous	145-100.5	19	120	66.7	72.6	46.2	45.9	11.0	36.1 ± 12.6	-7.9 ± 9.2	Tong et al. [2013]
Mengban	21.8	101.6	Cretaceous	145-66	4	100	27.5	31.4	50.5	31.0	6.4	42.4 ± 6.5	4.7 ± 6.4	Tong et al. [2013]
Pu'er	23.0	100.9	Middle Triassic	237-247.2	18	30**	95.4	28.4	98.2	22.8	6.2	93.1 ± 5.9	3.5 ± 5.9	Huang and Opdyke [2015]
Jinggu	23.5	100.4	Middle Cretaceous	100	47	100	73.4	42.8	77.0	43.0	2.9	68.9 ± 4.3	-5.1 ± 4.5	Gao et al. [2015]
	23.5	100.7	Miocene	23-5.3	38	10	32.3	26.9	13.7	36.0	3.3	12.6 ± 3.8	1.8 ± 3.9	Gao et al. [2015]
Jinggu	23.5	100.7	Miocene	23-5.3	10	10	16.4	15.4	13.5	32.2	5.8	12.4 ± 5.8	5.6 ± 5.4	Li et al. [2017b]
			Paleocene	66-56	12	20**	43.0	41.7	36.1	31.5	8.4	40.6 ± 9.2	-7.6 ± 7.5	Li et al. [2017b]
			Eocene	56-33.9	12	20**	27.8	32.1	35.2	35.7	6.5	25.4 ± 6.5	1.9 ± 6.3	Li et al. [2017b]
			Eocene	56-33.9	18	20**	37.0	32.8	53.0	33.6	4.3	34.6 ± 4.7	1.2 ± 5.0	Li et al. [2017b]
			Eocene-Oligocene	56-23	11	20**	34.9	33.2	38.4	37.3	9.7	32.5 ± 9.4	0.8 ± 8.4	Li et al. [2017b]
			Eocene-Oligocene	56-23	17	20**	35.2	20.2	38.6	33.0	5.7	32.8 ± 5.4	13.8 ± 5.8	Li et al. [2017b]
			Eocene-Oligocene	56-23	14	20**	45.0	22.8	50.8	31.8	5.8	42.6 ± 5.5	11.2 ± 5.8	Li et al. [2017b]
Chuandian Block														
Chuxiong	25.0	101.5	Lower Cretaceous	145-100.5	11	120	28.9	37.1	43.7	36.2	17.1	33.4 ± 16.8	6.0 ± 13.6	Funahara et al. [1992]
			Upper Cretaceous	100-66	10	80	58.6	31.7	45.6	46.6	14.3	35.5 ± 16.7	-10.3 ± 11.8	Funahara et al. [1992]
Bailu	25.7	102.1	Upper Cretaceous	100-66	6	80	359.9	35.5	30.7	38.9	10.6	20.5 ± 11.0	-1.5 ± 9.1	Otofuji et al. [1998]
Zhupeng	25.9	101.8	Upper Cretaceous	100-66	15	80	30.8	34.4	25.4	34.3	3.4	15.2 ± 4.3	3.3 ± 4.6	Otofuji et al. [1998]
Dayao	25.8	101.3	Paleocene-Eocene	66-33.9	18	50	28.7	27.8	27.8	33.1	4.3	21.8 ± 6.3	2.2 ± 7.7	Wang et al. [2016]
	25.7	101.3	Paleocene-Eocene	66-33.9	10	50	10.7	31.3	16.5	31.1	4.8	10.5 ± 6.5	4.0 ± 7.9	Yoshioka et al. [2003]
Yongren	26.1	101.7	Paleocene-Eocene	66-33.9	16	50	11.5	27.7	17.2	26.6	5.8	11.1 ± 7.0	9.2 ± 8.2	Yoshioka et al. [2003]
Yuanmou	25.7	100.9	Pliocene	~ 3.0	17	0	1.4	27.8	_	_	1.1	1.4 ± 1.2	13.8 ± 1.1	Zhu et al. [2008]
Sanying	26.3	100.1	Upper Miocene-Pliocene	~ 5.0		0	_	_	5.6	27.9	1.5	5.6 ± 1.7	13.8 ± 1.5	Li et al. [2013]
Jianchuan (SJ)	26.6	99.3	Oligocene	33.9-23	8	30	213.6	-46.5	200.9	-31.3	7.7	18.7 ± 7.4	6.0 ± 6.8	Tong et al. [2015]
Jianchuan (JL)	26.5	99.8	Lower/Middle Eocene	~ 56-40	16	50	28.8	35.0	29.7	32.0	5.6	23.8 ± 7.1	4.1 ± 8.0	Tong et al. [2015]
Yongshen	27.0	100.9	Upper Eocene -Lower Oligocene	56-23	20	30	19.0	44.1	19.7	40.0	2.9	17.3 ± 3.7	-2.0 ± 3.9	Gao et al. [2017]

Table 1. Paleomagnetic site-mean directions obtained from previous studies in Triassic-Neogene rocks from Tengchong, Baoshan, Lanping, Northern Simao and Chuandian blocks, and updated rotation and flattening values with respect to Eurasia calculated using paleopoles by *Torsvik et al*. [2012] and *Cognè et al*. [2013]. Age in Ma is from the geologic timescale of *Cohen et al*. [2013]. D and I are site mean declination and inclination calculated before and after tectonic correction; a_{95} is statistical parameter after *Fisher* [1953]; N is number of sites; site mean rotation R and flattening F values, and relative errors ΔR and ΔF (according to *Demarest*, 1983) are relative to coeval D and I values expected at the sampling area from East Asia paleopoles by *Cognè et al*. [2013], except 150 and 170 Ma from European poles by *Torsvik et al*. [2012]. **Post-tilting remagnetized sites, R and F values are calculated using the in-situ D and I values.

In the Tengchong block, *Kornfeld et al*. [2014b] found 87° CW rotation in 40 Ma dykes from the Tengchong block (Table 1). In addition, *Kornfeld et al*. [2014c] reported counterclockwise (CCW) paleomagnetic rotations from lower Pliocene to Holocene volcanics of the Mangbang basin, and interpreted them as apparent rotations due to tilting around horizontal axes along listric normal faults cutting the Tengchong volcanic field.

Data from Upper Carboniferous and Early Permian basalts in the Baoshan block respectively reported by *Huang and Opdyke* [1991] and *Ali et al*. [2013], reveal their former position within the Gondwana supercontinent. However, in this thesis we will only deal with data from Triassic to Neogene age.

In the Baoshan block*, Huang and Opdyke* [1993] documented a strong CW rotation in Jurassic rocks from Luxi area. *Kornfeld et al*. [2014a] showed a 40° CW rotation in 30 Ma basalts from the Baoshan block. Subsequently, *Tong et al.* [2016] studied Paleocene-Oligocene red beds located at the centre of the Baoshan block, NE of Yongde (Figure 49). A primary magnetization was isolated in the Paleocene sediments, while the Eocene-Oligocene red beds were magnetically overprinted during the Miocene. In any case, both localities and sedimentary sequences yield significant CW rotations, ranging from 70° to 80° (Table 1).

In the Lanping block, the rotation pattern from Jurassic and Cretaceous red beds, revealed that the Xiaguan and Weishan areas did not rotate with respect to stable Eurasia since Late Cretaceous times [*Huang and Opdyke*, 1993]. In contrast, in the Yunlong and Lanping area, about 50 km west of the Ailaoshan-Red River Shear Zone, *Sato et al*. [1999, 2001, 2007] and *Yang et al*. [2001a,b], documented strong CW rotations and inferred that Indochina was squeezed out of the Asian continent due to collision of India, accompanied by CW rotations (Figure 50).

Similar evidence was found from Lower Cretaceous sites near the city of Yongping, where data show a CW rotation of 25° ± 16°, associated with rotation of the Yongping area [*Funahara et al*., 1993].

Additionally, a series of works were conducted between 1993 and 2009 on the Jurassic-upper Cretaceous red beds exposed mostly in the Lanping-Simao block, between the Ailaoshan-Red River and Chongshan Shear Zones. The data show variable predominant CW rotations up to 132° with respect to Eurasia.

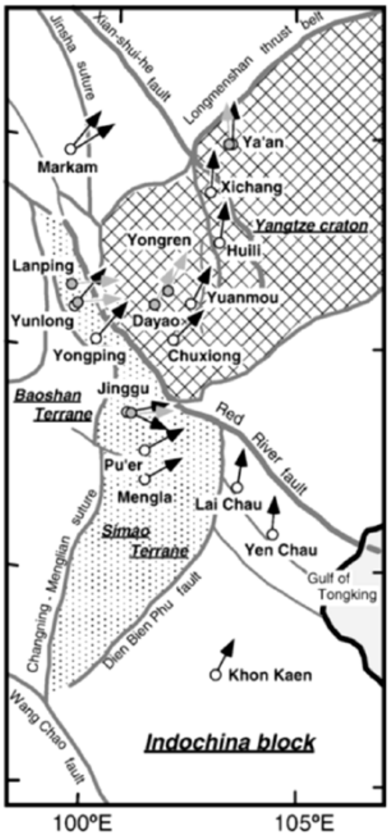

Figure 50. From *Sato et al.* [2007]. Declinations of the Cretaceous (black) and Tertiary (gray) paleomagnetic directions in the Lanping-Simao and Chuxiong blocks and its surrounding regions, are shown by arrows.

In the northern Simao block, Jurassic and Cretaceous red beds have been paleomagnetically studied mostly in the northern sector [*Huang and Opdyke,* 1993] and the rotation pattern revealed that the Jinggu-Mengla area rotated CW by 46°-65°. *Chen et al*. [1995] documented CW rotations >90°, 77°, and 15° respectively in Lower Cretaceous, Eo-Oligocene, and Miocene sediments from the Jinggu area. The available Cretaceous paleomagnetic data from the Jinggu area and neighboring regions demonstrate variable rotations in different sampling localities, possibly bounded by strike-slip faults.

This would imply that the Yunnan region and surrounding areas were not deformed as a coherent block in response to the collision of India with Asia [*Chen et al.,* 1995].

Sato et al. [2007] investigated Cretaceous red sandstones and siltstones in Pu'er, finding a 46° ± 9° CW rotation, which is consistent with the large rotations in the Mengla and Jinggu areas (47° and 66°). The CW rotation of the northern part of the Simao block is larger by more than 20° compared to the Yunlong and Yongping areas belonging to the Lanping block [*Sato et al.,* 2001]. Geological, geochronological and GPS data, obtained from the Lanping-Simao block, seem to demonstrate the close relationship between the Lanping-Simao arcuate structural zone and differential tectonic rotations [*Kondo et al.,* 2012*; Tanaka et al.,* 2008*; Tong et al.,* 2013].

Recently, *Li et al.* [2017b] focused on Paleocene-Oligocene red beds and mid-Miocene silts from the Jinggu Basin, northern Simao block. Although a pre-folding magnetization was proved in red beds, exclusively normal polarity sites were documented (consistently with previous evidence by *Chen et al.,* 1995*; Gao et al.,* 2015*; Huang and Opdyke,* 1993). Thus *Li et al*. [*2017b*] concluded that either the studied strata were deposited during the long normal Cretaceous superchron, or the red beds underwent a widespread pre-folding Tertiary overprint. In any case, red beds yield greatly variable CW rotations (ranging from 0° to >90°) that *Li et al*. [2017b] average to a 30° value, while mid-Miocene sediments do not rotate.

Li et al. [2017a] explained rotation with a model of semi-rigid blocks rotation. Other papers (listed below) observe that there are internal deformation and variable rotations in the Simao block [*Kondo et al.,* 2012; *Tong et al.,* 2013*; Gao et al., 2015* even consider the possibility of internal oroclinal deformation] rising doubts on rigid "microplate" rotations in the Yunnan.

Recently, *Li et al*. [2018], suggest that the northern Sibumasu region (area between Nantinghe fault and Dien Bien Phu fault; Figure 49), cut by a series of NE–SW strike-slip faults, experienced a much larger clockwise rotation than the remaining areas of southeast margin of

Tibetan Plateau. They ascribe this large rotation to a sum of rotations acquired after the middle Miocene andassociated with Indochina extrusion and rotation and the south-eastward extrusion of Tibetan crust along the Xianshuihe-Xiaojiang fault (Figure 49-50). If correct, this indicates that the eastward motion of Tibetan crust crossed the Ailaoshan-Red River fault and was transferred through the southwestern Yunnan toward Myanmar. Furthermore, their paleomagnetic results, together with Jurassic/Cretaceous paleomagnetic data, suggest that the northern Sibumasu changed direction from a pre-collisional strike of ~N 60° W in eastern Tibet to N 10° W in southern Sibumasu.

Regarding the **Chuandian Block** (CDB, also called Chuandian Fragment, CDF), many authors support the hypothesis that it was extruded along the left-lateral Xianshuihe-Xiaojiang fault system under the tectonic influence of India–Asia collision [*Avouac and Tapponnier,* 1993*; Lacassin et al.,* 1997], but its southward movement was eventually obstructed by the rigid Yangtze and Indochina blocks [*Wang et al., 2001; Yoshioka et al., 2003;* Figure 50-51]. GPS measurements and geological observations along the Xianshuihe-Xiaojiang fault system suggest a southward displacement of the Chuandian Fragment during the last 12 Ma [*Roger et al*., 1995; *Wang et al*., 1998, 2001; *Chen et al*., 2000].

Previous paleomagnetic studies reported from the area suggest that this fragment experienced more than 300 km of southward displacement after Cretaceous times [*Tamai et al*., 2004]; the declination values increase in latitude from north to south [*Funahara et al*., 1992; *Huang and Opdyke*, 1992; *Otofuji et al*., 1998; *Tamai et al*., 2004] and the magnitude of rotational motion significantly increases in the southern part of this fragment.

The Chuandian domain yields a clear pattern of ca. 20° CW rotations for Cretaceous-Oligocene red beds [*Funahara et al*., 1992; *Otofuji et al*., 1998; *Yang et al*., 2001a; *Yoshioka et al*., 2003; *Zhu et al*., 2008; *Li et al*., 2013; 2015; *Tong et al*., 2015; *Wang et al*., 2016a; *Gao et al*., 2017].

Paleomagnetic samples of Paleocene–Eocene red sandstones were investigated by *Yoshioka et al*. [2003] around the Yongren (26.1°N, 101.7 °E) and Dayao areas (25.7°N, 101.3°E), located in the Chuxiong basin (Figure 49 and Table 1).

Their data of Easterly deflected declinations are consistent with those reported from other areas of the Chuxiong basin supporting a CW rotation of about 30°, indicating its wide presence in the Cretaceous–Eocene formations of the said basin.

Comparison with declination values expected from the Cretaceous–Eocene Paleopoles of Eurasia indicates that the magnitude of clockwise rotation systematically increases toward the southeast within the Chuxiong basin as well as in the Chuandian Fragment. This trend of the differential tectonic rotation in the Chuandian Fragment is consistent with curvature of the Xianshuihe-Xiaojiang fault system.

They interpret the deformation of the Chuxiong basin connected with the formation of eastward bulge in the southern part of the CDF. During southward displacement, the Chuandian Fragment was probably subjected to tectonic stresses as a result of interaction with the Yangtze and Indochina blocks, which resulted into east–west extension and north–south shortening [Figure 48-51, *Yoshioka et al*., 2003].

Cretaceous red sandstones in Xichang were studied also by *Tamai et al*. [2004].

Combined with earlier reported paleomagnetic data from this block, they estimate a significant southward displacement of 6.7° ± 3.5° in latitude for the whole fragment with respect to the Sichuan Basin since the Late Cretaceous. Extrusion dynamics in the Asian continent due to its collision with India brought about the southward displacement of the CDB. In agreement with previous authors, their declination data indicate that the southern part of the block was subjected to clockwise sense rotation of up to 45° and this probably occurred during extrusion of this fragment from the north.

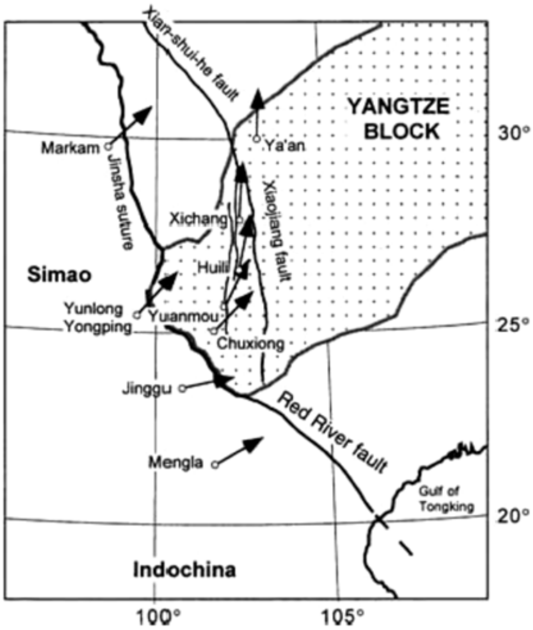

Figure 51. Horizontal projections of paleomagnetic remanent directions synthetized by *Tamai et al*. [2004] for Lanping-Simao block, Chuandian and Yangtze blocks; Ya'an [*Otofuji et al*., 1990; *Enkin et al.,* 1991], Xichang [*Tamai et al*., 2004], Huili [*Huang and Opdyke*, 1992], Yuanmou [*Otofuji et al*., 1998], Chuxiong [*Funahara et al*., 1992], Markam [*Otofuji et al*., 1990; *Huang and Opdyke*, 1993], Yunlong [*Sato et al*., 1999], Yongping [*Funahara et al*., 1993], Jinggu [*Huang and Opdyke*, 1993; *Haihong et al*., 1995] and Mengla [*Huang and Opdyke*, 1993].

More recently, late Eocene-early Oligocene red beds were studied in the Yongsheng area by *Gao et al*. [2017]. In their samples, the higher temperature components (HTC) were isolated by stepwise thermal demagnetization between ~300–680°C and they passed the fold test. However, all the HTCs are of normal polarity, which appears to conflict with the frequent occurrence of reversed polarities during the late Eocene-early Oligocene, and therefore the possibility of remagnetization needs to be considered. Widespread secondary hematite was detected in the red beds that further indicates the remagnetization of samples. From the events analysis of the sampling area, they suggest an early Oligocene (~35 Ma) remagnetization event. Their comparison of the pole calculated from the remagnetized remanent directions with the ~35 Ma paleopole for Eurasia indicate that the degree of clockwise rotation in the Yongsheng area is 17.0 ± 4.1° relative to stable Eurasia. The rotation value is consistent at the 95% confidence level with results obtained from Paleogene and Cretaceous strata in other areas of the CDB. Their paleomagnetic data indicate that a consistent clockwise rotation of 20.6 ± 6.3° occurred in different areas in the CDB: at Yongsheng, Zhupeng, Bailu, Dayao, Chuxiong west and Jianchuan (Figure 49).

That rotation process occurred into two discrete time intervals: approximately 11° of quasi-rigid clockwise rotation occurred between ∼35 and 12.7 Ma compared to stable Eurasia. Subsequently, a clockwise rotation of about 10° of the CDB with respect to stable Eurasia is inferred from the paleomagnetic results since 12.7 Ma, which is consistent with the change in the geometry of the Ailaoshan–Red River Shear Zone around the western Chuxiong Basin. The later CW rotation was related to shearing movement of the Xianshuihe-Xiaojiang fault. They also ascribe that these faults movements and their related block rotation have a close relationship with the northward subduction of the Indian lithosphere beneath the Tibetan Plateau. Thus, according to other authors, the CDB was extruded along the left-lateral Xianshuihe-Xiaojiang fault system under the tectonic influence of India–Asia collision [*Avouac and Tapponnier*, 1993; *Lacassin et al*., 1997], but its southward movement was eventually obstructed by the rigid Yangtze and Indochina blocks [*Wang et al*., 2001; *Gao et al*., 2017].

A compilation of paleomagnetic data set available from 112 localities around the Himalayan Syntaxis is well synthesized by *Otofuji et al*. [2010] and covers a period between the Early Cretaceous and Eocene (Figure 49 and Table 1). Other recent paleomagnetic works from Yunnan, mostly realized from Cretaceous continental red beds, showed a predominant clockwise (CW) rotation pattern determining about 1000 km in the 22°-25°N latitude range [*Li et al.,* 2017a*; Tong et al.,* 2016 and references therein] and indicate that rotation of crustal fragments in this region was not homogeneous, likely due to crustal heterogeneity and spatial and temporal stress field variations [*Li et al.,* 2017*a; Metcalfe,* 2002, 2011*; Yin and Harrison,* 2000].

Although this paleomagnetic data set from Yunnan is undoubtedly robust, the tectonic explanations for such rotational pattern remain is still not completely convincing. This research study will aim at clarifying it.

Chapter VI

6. Paleomagnetic results and magnetic overprint evaluation:

- **The case of Gaoligong Shear Zone**

Part of the following chapter was recently published on Tectonics by myself and my colleagues [Pellegrino et al., 2018].

Tectonics and Paleomagnetic Rotation Pattern of Yunnan (24°N–25°N, China): Gaoligong Fault Shear Versus Megablock Drift

Alessandra G. Pellegrino[1], Bo Zhang[2], Fabio Speranza[3], Rosanna Maniscalco[1], Congyuan Yin[2], Catalina Hernandez-Moreno[3], and Aldo Winkler[3]

[1]Università degli Studi di Catania, Dipartimento di Scienze Biologiche, Geologiche e Ambientali, Catania, Italy, [2]School of Earth and Space Science, Peking University, Beijing, China, [3]Istituto Nazionale di Geofisica e Vulcanologia, Rome, Italy

To assess the validity of models previously exposed and to better understand the structural architecture and crustal deformation processes in this region, field-based paleomagnetic and structural analyses along main strike-slip shear zone were performed. The first field work was conducted on April 2016 along the Gaoligong Shear Zone (99°E, 25°N) in Yunnan province (Figure 52A, B; 53). *Pellegrino et al*. [2018] sampled 50 paleomagnetic sites at variable distances (up to ~25 km) from the contact with mylonites and metamorphic rocks exposed along the shear zone (Figure 52).

Sites were selected from three main areas to the west, east, and south of the Gaoligong Shear Zone, in the Tengchong, Baoshan, and Mangshi areas, respectively (Figures 52A, B, C1 and C2). From west to east, 15 paleomagnetic sites in Pliocene-Holocene lavas from the Tengchong volcanic field (Figure 52a,b,c1), 5 sites in Pliocene whitish lacustrine siltstones in Mangbang basin, 2 sites in Jurassic basalt and 28 sites in Jurassic-Cretaceous continental red beds in the Baoshan block, have been gathered. The continental red beds are typically made of red fine-grained sandstone or siltstone. In the southern transect, the red beds are exposed in the Luxi Basin (Figure 52c2), delimited by two normal faults. As suggested by structural data, the Mesozoic rocks, in the basin outcropped, could be represent the core of a monoclinal folded structure [*Huang and Opdyke*, 1993].

Bedding of Jurassic basalts was inferred considering the attitude of neighbor sediments, forming continuous volcano-sedimentary sequences according to available geological maps. In volcanic sites, several samples were gathered in the same flow, while samples from sedimentary sites were spread as much as possible on a given outcrop to try to average out the paleosecular variation (PSV) of the geomagnetic field. Each volcanic site is expected to record an almost instantaneous geomagnetic direction, so that PSV is surely not averaged out within the 17 sites from Pliocene-Holocene and Jurassic basalts.

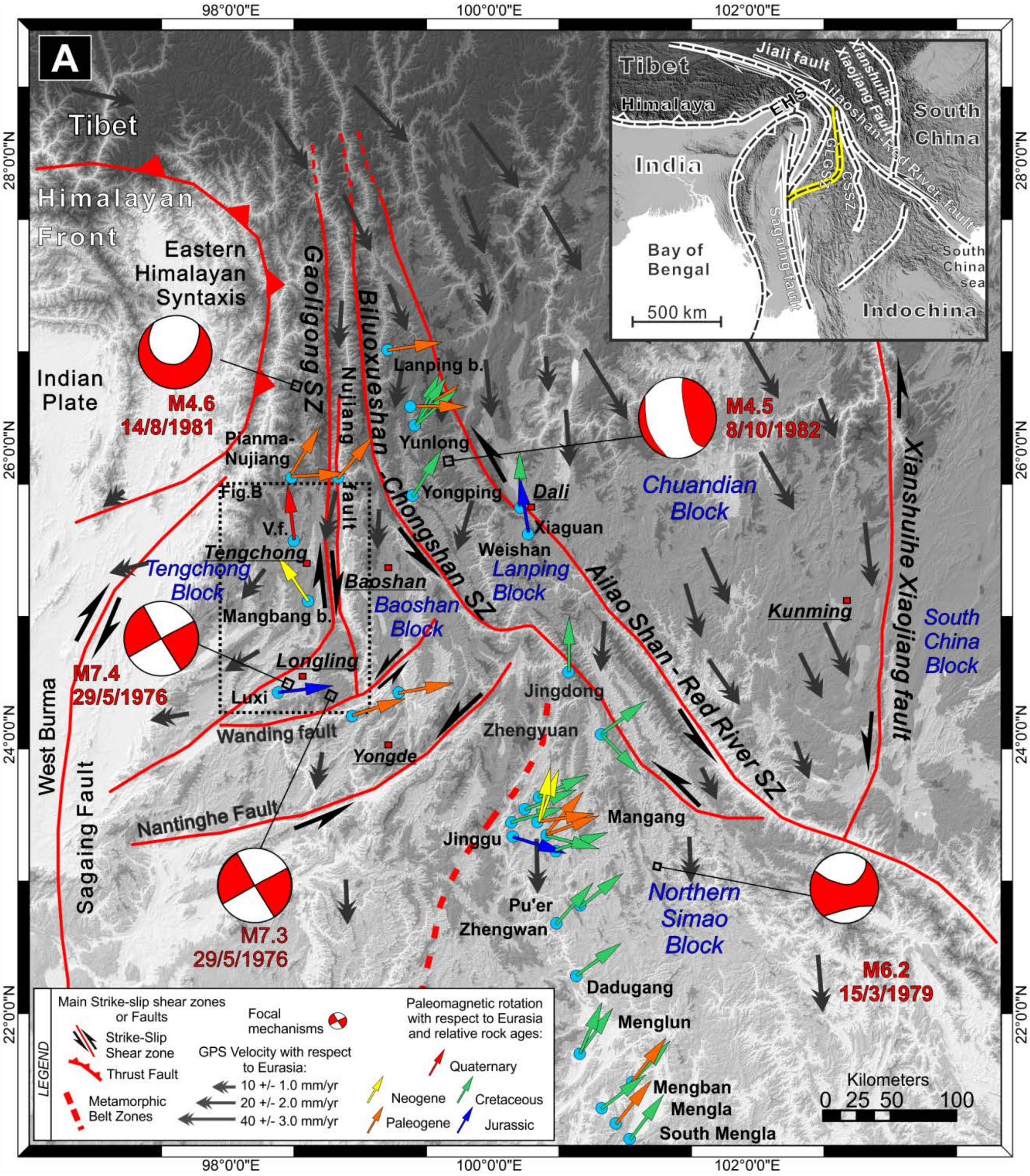

A
98°0'0"E
100°0'0"E
102°0'0"E
28°0'0"N
26°0'0"N
24°0'0"N
22°0'0"N
Tibet
Himalayan Front
Eastern Himalayan Syntaxis
Indian Plate
M4.6
14/8/1981
Gaoligong SZ
Biluoxueshan
Nujiang fault
Pianma-Nujiang
Fig.B
V.f.
Tengchong
Tengchong Block
Mangbang b.
Baoshan
Baoshan Block
Longling
Luxi
M7.4
29/5/1976
West Burma
Sagaing Fault
Wanding fault
Yongde
Nantinghe Fault
M7.3
29/5/1976
Lanping b.
Yunlong
Yongping
Chongshan SZ
Dali
Xiaguan
Weishan
Lanping Block
M4.5
8/10/1982
Chuandian Block
Ailao Shan - Red River SZ
Kunming
South China Block
Xianshuihe Xiaojiang fault
Jingdong
Zhengyuan
Mangang
Jinggu
Pu'er
Zhengwan
Northern Simao Block
M6.2
15/3/1979
Dadugang
Menglun
Mengban
Mengla
South Mengla
Tibet
Himalaya
India
Bay of Bengal
500 km
Jiali fault
Xianshuihe
Xiaojiang Fault
Ailaoshan-Red River fault
EHS
South China
South China sea
Indochina
Sagaing fault
CSSZ
LEGEND
Main Strike-slip shear zones or Faults
Strike-Slip Shear zone
Thrust Fault
Metamorphic Belt Zones
Focal mechanisms
GPS Velocity with respect to Eurasia:
10 +/- 1.0 mm/yr
20 +/- 2.0 mm/yr
40 +/- 3.0 mm/yr
Paleomagnetic rotation with respect to Eurasia and relative rock ages:
Quaternary
Neogene
Cretaceous
Paleogene
Jurassic
Kilometers
0 25 50 100

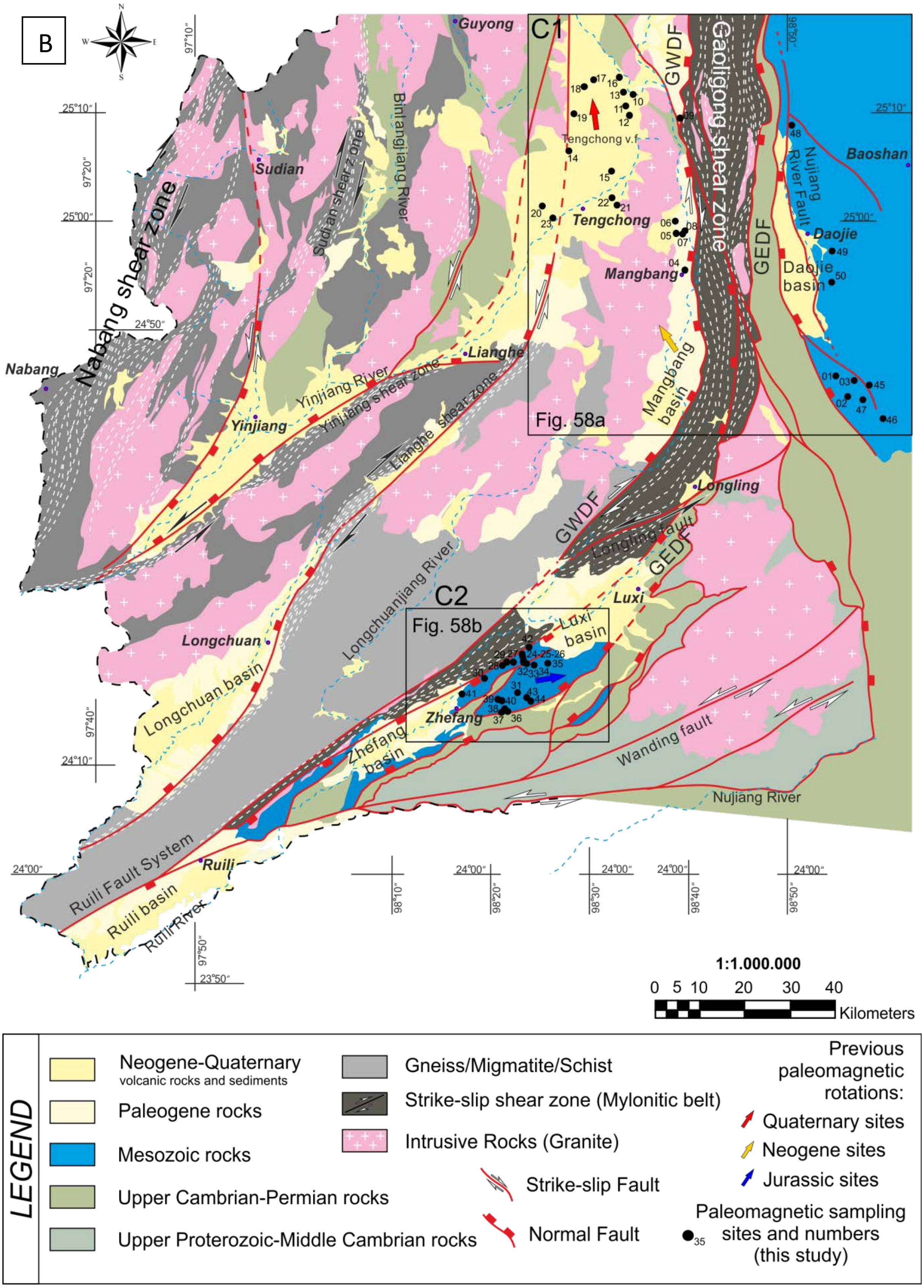
B
C1
C2
Fig. 58a
Fig. 58b
Nabang shear zone
Sudian shear zone
Binlangjiang River
Gaoligong shear zone
GWDF
GEDF
Nujiang River Fault
Yinjiang River
Yinjiang shear zone
Lianghe shear zone
Longchuanjiang River
Longling fault
Wanding fault
Nujiang River
Ruili Fault System
Ruili basin
Ruili River
Longchuan basin
Zhefang basin
Luxi basin
Mangbang basin
Daojie basin
Tengchong v.f.
Guyong
Sudian
Nabang
Yinjiang
Lianghe
Tengchong
Mangbang
Baoshan
Daojie
Longling
Luxi
Longchuan
Zhefang
Ruili
1:1.000.000
0 5 10 20 30 40
Kilometers
LEGEND
Neogene-Quaternary
volcanic rocks and sediments
Paleogene rocks
Mesozoic rocks
Upper Cambrian-Permian rocks
Upper Proterozoic-Middle Cambrian rocks
Gneiss/Migmatite/Schist
Strike-slip shear zone (Mylonitic belt)
Intrusive Rocks (Granite)
Strike-slip Fault
Normal Fault
Previous paleomagnetic rotations:
Quaternary sites
Neogene sites
Jurassic sites
Paleomagnetic sampling sites and numbers (this study)

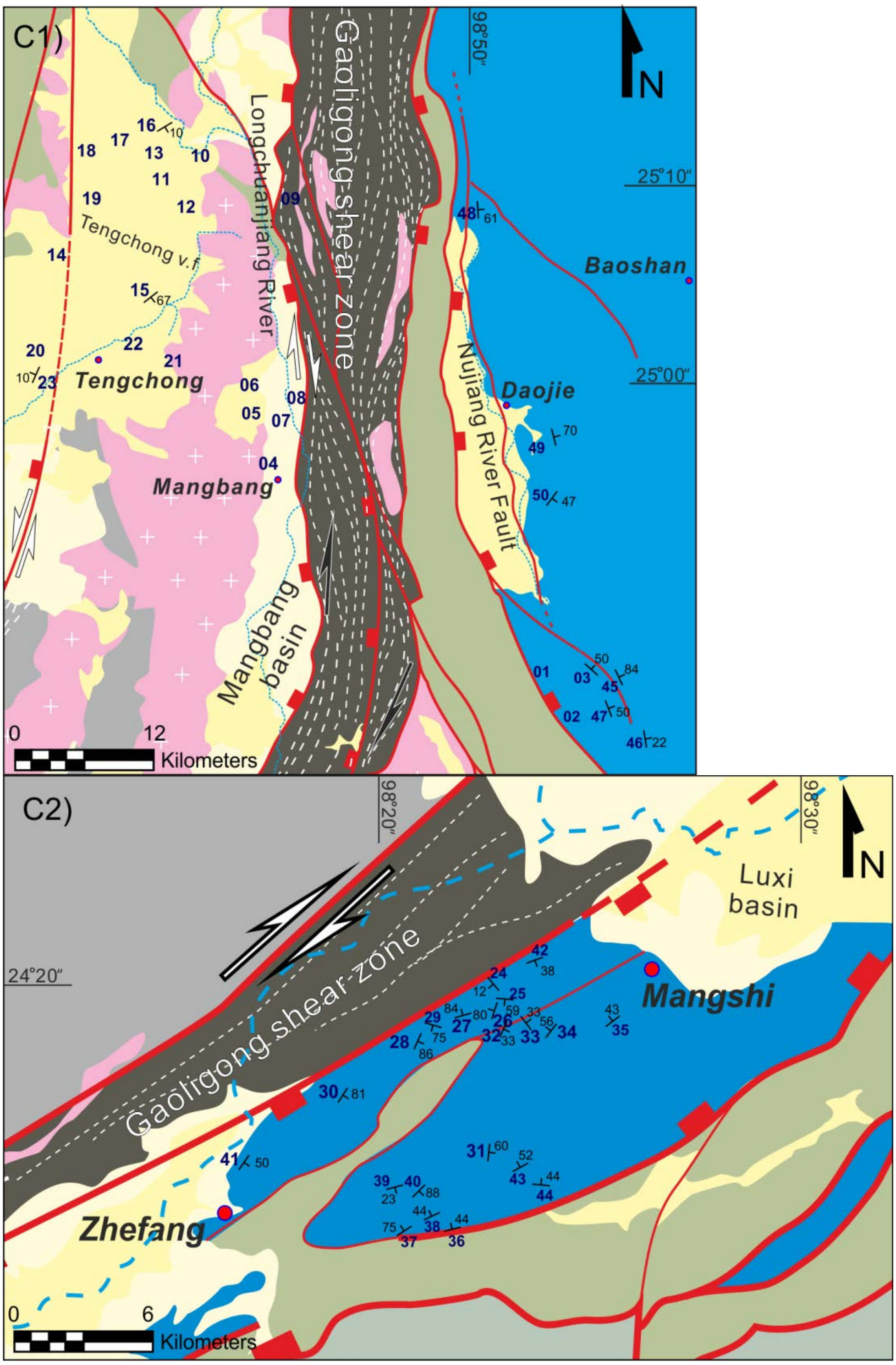

Figure 52. Modified after *Pellegrino et al.* [2018]. **A)** Study area along the Gaoligong Shear Zone. Pink circles indicates the sampling locations. Focal mechanisms from Harvard Global CMT Catalog (see chapter 4.3) **B)** Simplified geological and tectonic map of the Gaoligong Shear Zone and adjacent areas. Boxes indicate the two areas of paleomagnetic investigation (see Figure 58a,b). GEDF = Gaoligong east detachment fault; GWDF = Gaoligong west detachment fault. **C1 and C2)** Structural details of the sites sampled. Sampled sites in blue.

Table 2. From *Pellegrino et al.* [2018]. Paleomagnetic site-mean directions from the Gaoligong Shear Zone (Yunnan, China)

Table 2. Paleomagnetic site-mean directions from the Gaoligong Shear Zone (Yunnan, China)

Site	Geographic Coordinates		Rock Type	Series/ Epoch	Numerical Age (Ma)	Considered palepoles age (Ma)	Bedding (deg)	n/N	ChRM/High-Temperature Component				k	α_{95} (deg)	R (deg)	ΔR (deg)	F (deg)	ΔF (deg)
									In Situ		Tilt Corrected							
	Latitude °N	Longitude °E							*D* (deg)	*I* (deg)	*D* (deg)	*I* (deg)						
YUN01*	24.7760824	98.9282752	Basalts	MJ	163-174	170	80/20	10/10	52.6	-51.0	31.8	-67.1	39.3	7.8	-166.5	16.6	-6.44	6.8
YUN02*	24.7437355	98.9482315	Basalts	MJ	163-174	170	80/20	5/10	27.9	10.6	29.1	-1.9	298.5	4.4	-169.2	5.9	58.7	4.6
YUN03	24.7694685	98.9593802	Red Beds	MJ	163-174	170	42/50	7/10	346.9	81.4	33.5	34.8	40.3	9.6	15.2	10.3	25.8	8.1
YUN04	24.9399358	98.6699462	Basalts	MP	3.6	—	—	8/8	196.3	-37.9	—	—	164.8	4.3	16.3	-6.1	5.1	4.3
YUN05	24.9971886	98.6553678	Whitish Siltstones	LP	3.6-5.3	—	—	—	—	—	—	—	—	—	—	—	—	—
YUN06	25.015892	98.6535897	Whitish Siltstones	LP	3.6-5.3	—	—	—	—	—	—	—	—	—	—	—	—	—
YUN07	24.9967763	98.6658433	Whitish Siltstones	LP	3.6-5.3	—	—	6/10	5.8	31.4	—	—	13.7	18.8	5.8	22.1	11.6	18.8
YUN08	24.9977035	98.6675056	Whitish Siltstones	LP	3.6-5.3	—	—	—	—	—	—	—	—	—	—	—	—	—
YUN09	25.1686698	98.668388	Whitish Siltstones	LP	3.6-5.3	—	—	—	—	—	—	—	—	—	—	—	—	—
YUN10	25.2115518	98.5821019	Basalts	MP	3.6	—	—	10/10	4.6	20.0	—	—	163.3	3.8	4.6	4.1	23.0	3.8
YUN11	25.194456	98.5693205	Basalts	LPS	1.5-2.5	—	—	9/10	343.5	22.5	—	—	53.5	7.1	-16.5	7.7	20.5	7.1
YUN12	25.1795786	98.5758987	Basalts	LPS	1.5-2.5	—	—	10/10	12.2	47.1	—	—	40.3	7.7	12.2	11.3	-4.1	7.7
YUN13	25.213207	98.5749002	Basalts	MP	3.6	—	—	10/10	15.5	35.1	—	—	184.4	3.6	15.5	4.4	7.9	3.6
YUN14	25.1249219	98.4719548	Basalts	H	Present-0.0117	—	—	9/11	2.9	24.4	—	—	261.3	3.2	2.9	3.5	18.6	3.2
YUN15	25.0935656	98.5443339	Basalts	LPS	1.5-2.5	—	142/67	10/10	324.7	20.2	—	—	20.8	10.8	-35.3	11.6	22.8	10.8
YUN16	25.238754	98.5577044	Basalts	H	Present-0.0117	—	149/10	10/10	6.8	34.7	12.0	42.3	176.6	3.6	6.8	4.4	8.3	3.6
YUN17	25.234284	98.5142608	Basalts	H	Present-0.0117	—	—	9/11	11.5	35.0	—	—	89.9	5.5	11.5	6.8	8.0	5.5
YUN18	25.2238856	98.4980389	Basalts	H	Present-0.0117	—	—	10/11	8.3	33.7	—	—	46.9	7.1	8.3	8.6	9.3	7.1
YUN19	25.1826527	98.4799935	Basalts	H	Present-0.0117	—	—	9/10	356.0	16.9	—	—	84.3	5.6	-4.0	5.9	26.1	5.6
YUN20	25.0393686	98.4258614	Basalts	H	Present-0.0117	—	—	9/10	3.7	28.5	—	—	297.0	3.0	3.7	3.4	14.5	3.0
YUN21	25.0406369	98.5537038	Basalts	LPS	1.5-2.5	—	—	10/10	179.1	-42.8	—	—	63.7	6.1	-0.9	8.4	0.2	6.1
YUN22	25.0521541	98.5450541	Basalts	LPS	1.5-2.5	—	—	10/11	230.0	-47.3	—	—	50.5	6.9	50.0	10.3	-4.3	6.9
YUN23	25.0208672	98.4448747	Basalts	H	Present-0.0117	—	294/10	10/10	5.2	29.2	0.3	25.5	92.5	5.1	5.2	5.9	13.8	5.1
YUN24	24.3443875	98.3921232	Red Beds	K	66-145	**100**	230/12	9/12	299.8	-17.2	303.8	-21.0	19.1	12.1	115.8	10.5	17.7	10.2
YUN25	24.3405986	98.3929158	Red Beds	J-K	66-201	160	185/59	7/12	165.5	-72.7	13.4	-47.1	10.1	20.0	176.2	24.0	9.4	16.0
YUN26	24.3347198	98.394079	Red Beds	K	66-145	—	—	—	—	—	—	—	—	—	—	—	—	—
YUN27	24.331493	98.3774904	Red Beds	K	66-145	—	—	—	—	—	—	—	—	—	—	—	—	—
YUN28	24.32577171	98.35766892	Red Beds	K	66-145	—	—	—	—	—	—	—	—	—	—	—	—	—
YUN29	24.33141523	98.36594508	Red Beds	K	66-145	**100**	164/75	9/11	302.9	-21.1	294.8	35.9	10.7	16.5	-73.7	16.3	12.6	13.2
YUN30	24.3064965	98.3273209	Red Beds	K	66-145	—	—	—	—	—	—	—	—	—	—	—	—	—

Site	Geographic Coordinates		Rock Type	Series/ Epoch	Numerical Age (Ma)	Considered palepoles age (Ma)	Bedding (deg)	n/N	ChRM/High-Temperature Component				k	α_{95} (deg)	R (deg)	ΔR (deg)	F (deg)	ΔF (deg)
									In Situ		Tilt Corrected							
	Latitude °N	Longitude °E							*D* (deg)	*I* (deg)	*D* (deg)	*I* (deg)						
YUN31	24.2846044	98.3841427	Red Beds	MJ	163-174	—	—	—	—	—	—	—	—	—	—	—	—	—
YUN32	24.3316463	98.393859	Red Beds	K	66-145	—	—	—	—	—	—	—	—	—	—	—	—	—
YUN33	24.32879722	98.39939239	Red Beds	MJ	163-174	—	—	—	—	—	—	—	—	—	—	—	—	—
YUN34	24.3266414	98.41226722	Red Beds	MJ	163-174	—	—	—	—	—	—	—	—	—	—	—	—	—
YUN35	24.3294147	98.4357429	Red Beds	J-K	66-201	160	323/43	5/10	351.3	18.2	351.6	-20.0	86.8	8.3	154.4	8.5	36.6	7.5
YUN36	24.255107	98.3670267	Red Beds	MJ	163-174	160	346/44	9/10	108.3	25.1	80.0	40.0	70.2	6.2	62.7	8.0	16.6	6.2
YUN37	24.2530733	98.3559025	Red Beds	MJ	163-174	160	327/75	9/10	92.8	7.6	58.6	36.5	106.7	5.0	41.2	6.9	19.8	5.5
YUN38	24.2588832	98.361492	Red Beds	MJ	163-174	160	335/44	6/10	118.6	-4.6	111.9	30.0	14.8	18.0	94.7	17.0	26.5	15.5
YUN39	24.2737808	98.3497701	Red Beds	MJ	163-174	160	165/23	8/8	70.7	32.3	85.1	30.9	17.0	13.8	67.9	13.5	25.6	11.4
YUN40	24.2716601	98.3572075	Red Beds	MJ	163-174	160	135/88	8/10	21.5	25.5	71.8	22.0	14.3	15.1	54.6	13.7	34.5	12.4
YUN41	24.2826614	98.28916	Red Beds	K	66-145	—	—	—	—	—	—	—	—	—	—	—	—	—
YUN42	24.3547169	98.40384259	Red Beds	K	66-145	**100**	160/38	5/5	14.0	38.1	53.1	62.6	51.7	10.7	45.1	18.8	-23.9	9.2
YUN43	24.2767445	98.3995939	Red Beds	MJ	163-174	160	331/52	7/10	87.8	29.0	50.8	37.5	41.1	9.5	33.6	10.6	19.0	8.3
YUN44	24.2710038	98.4064307	Red Beds	MJ	163-174	160	5/44	10/10	110.1	30.2	82.3	31.2	69.3	5.8	65.1	7.3	25.3	5.9
YUN45	24.7620875	98.985785	Red Beds	MJ	163-174	160	65/84	9/10	260.8	52.7	52.3	41.5	15.7	13.4	34.6	14.9	15.0	11.1
YUN46	24.7103859	99.0088921	Red Beds	MJ	163-174	160	81/22	9/10	6.9	44.2	23.8	35.0	19.7	11.9	6.6	12.4	22.0	10.0
YUN47	24.7390466	98.9747164	Red Beds	MJ	163-174	160	69/50	10/10	319.5	70.3	42.9	43.7	45.8	7.2	25.7	9.3	13.4	6.8
YUN48	25.1643668	98.8513117	Red Beds	MJ	163-174	—	—	—	—	—	—	—	—	—	—	—	—	—
YUN49	24.9697763	98.9220494	Red Beds	MJ	163-174	160	76/70	10/10	310.8	58.1	44.2	35.2	29.0	9.1	27.0	10.1	22.0	8.0
YUN50	24.9209456	98.9212281	Red Beds	MJ	163-174	160	127/47	10/10	341.1	63.1	94.3	61.9	32.7	8.6	77.1	15.3	-4.6	7.7

Ages, J= Jurassic, MJ=Middle Jurassic, K=Cretaceous, LP= Lower Pliocene, MP= Middle Pliocene, LPS= Lower Pleistocene, H= Holocene. The geographic coordinates are referred to WGS84 datum. Age in Ma is from the geologic timescale of Choen et al. [2013]. Bedding is expressed in dip azimuth/dip values. D and I are site mean declination and inclination calculated before and after tectonic correction; k and α95 are statistical parameters after Fisher [1953]; n/N is number of samples giving reliable results/number of studied samples at a site. Site mean rotation R and flattening F values, and relative errors ΔR and ΔF (according to Demarest [1983]) are relative to coeval D and I Eurasian values expected at the sampling area considering Eurasian paleopoles from Torsvik et al. [2012] and Cognè et al. [2013] (in bold). R and F for Holocene sites were evaluated comparing the paleomagnetic directions with local geocentric axial dipole field direction. * Discarded site (see text).

Thirty-five (18 Jurassic-Cretaceous red beds, 2 Jurassic basalts, 15 Pliocene-Holocene basalts, 1 Lower Pliocene whitish siltstone) out of 50 sites gave reliable paleomagnetic results, the remaining 14 sites yielded erratic demagnetization diagrams and were discarded from further consideration (Table 2). All Pliocene lacustrine siltstone samples, except site Yun07, gave not-interpretable diagrams.

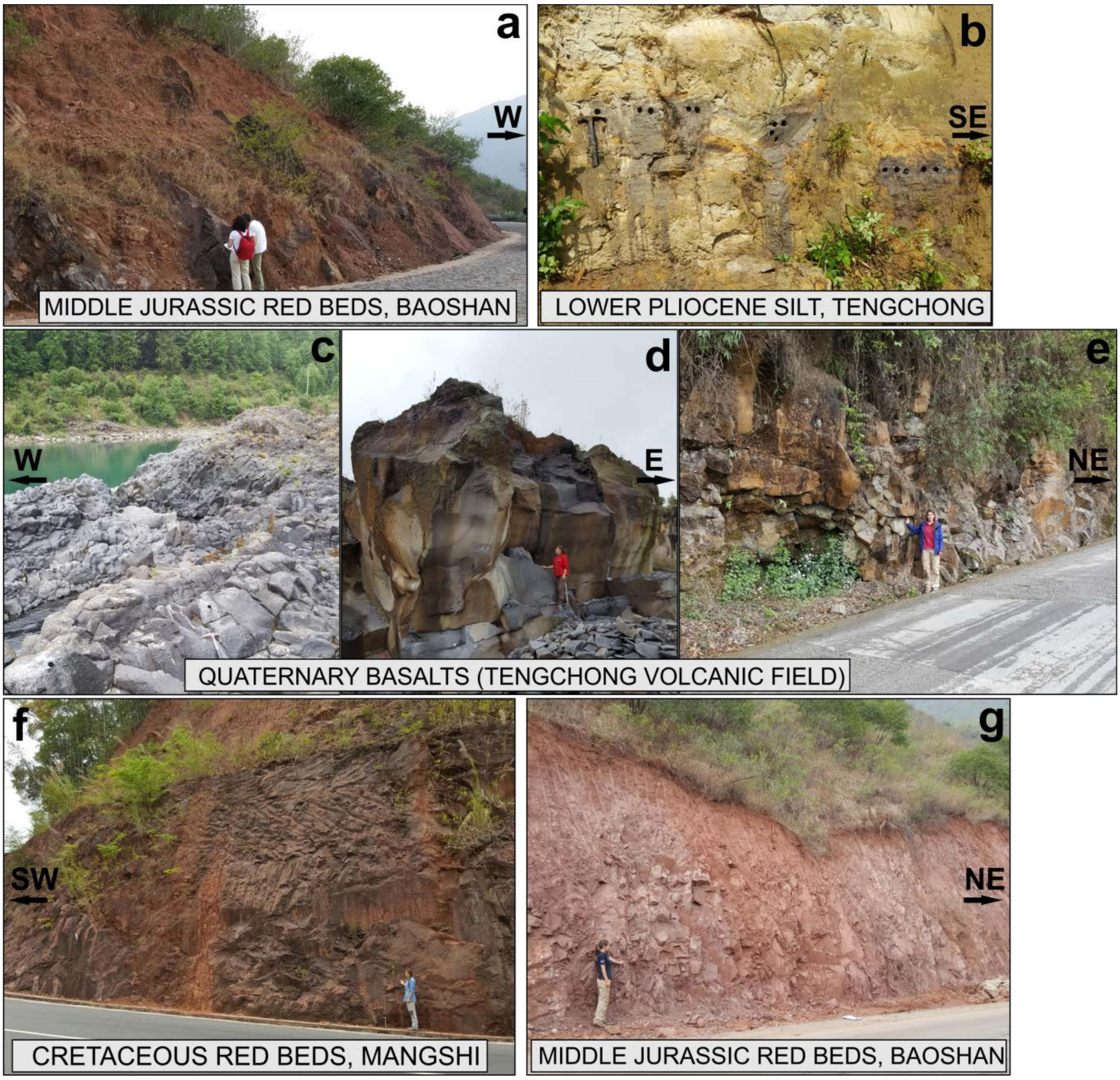

Figure 53. Field pictures of some paleomagnetic sites. a) Yun03; b) Yun08; c) Yun10; d) Yun16; e) Yun13; f) Yun26; g) Yun49. See figure 52 for location and Table 2 for details.

In the AF demagnetized volcanic rocks, a viscous component was removed between 10 and 30 mT, and a characteristic magnetization (ChRM) was isolated between 30 and 120 mT

(Figure 54), confirming the occurrence of magnetite and titanomagnetite. In the thermally demagnetized Jurassic basalts, a ChRM was isolated between 480 and 680 °C.

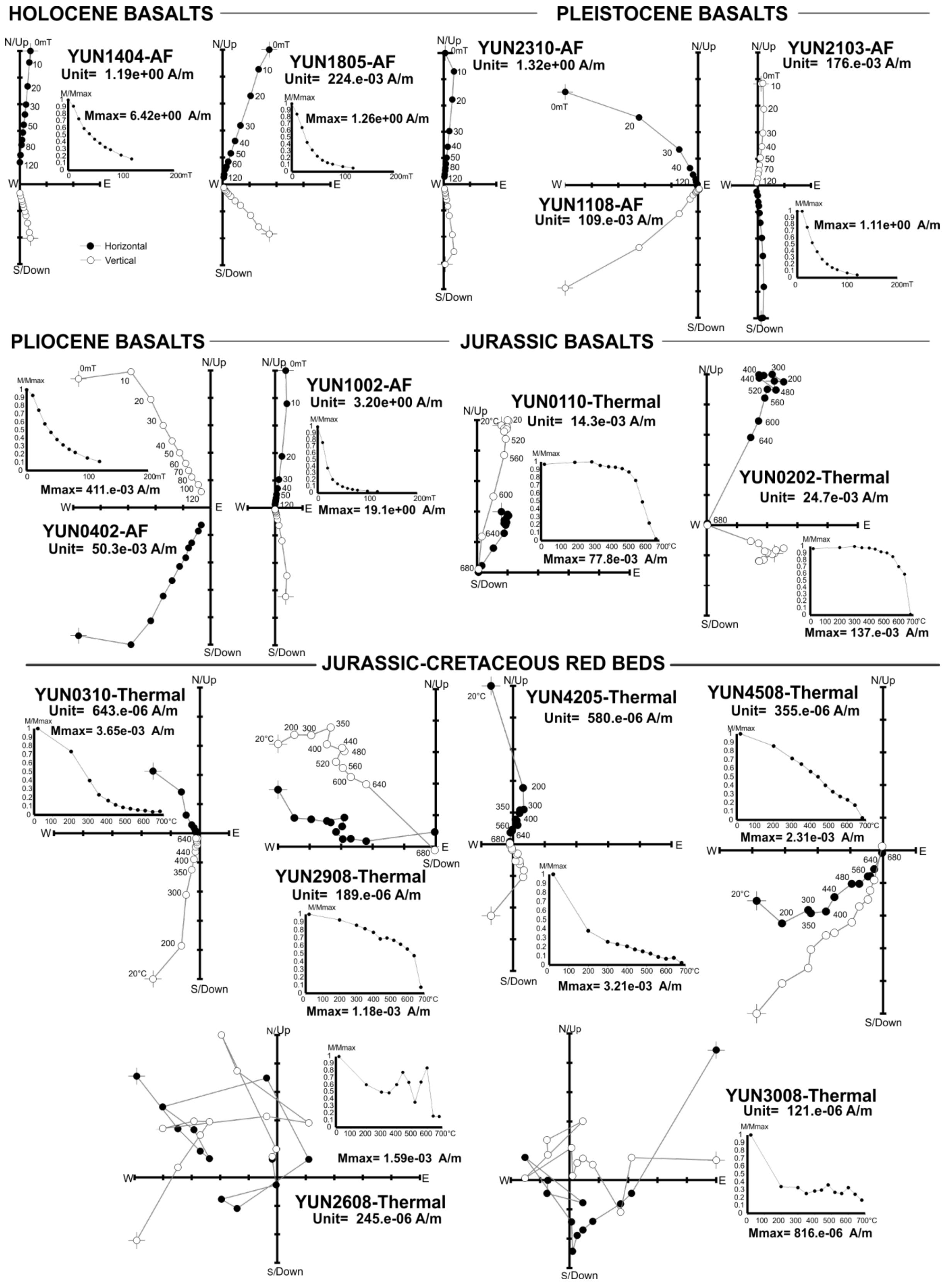

Figure 54. From *Pellegrino et al.* [2018]. Orthogonal vector diagrams of typical demagnetization data (*in situ* coordinates) showing representative samples carrying characteristic magnetization components (ChRMs), low/high temperature components (Yun2908, Yun4508), and scattered magnetization (Yun2608, Yun3008). Solid (open) symbols represent projection onto the horizontal (vertical) plane. Demagnetization step values are in milli Tesla (mT) and °C for the alternating field and thermally demagnetized samples, respectively. (See supplementary information to examine all diagrams).

In the red beds samples, after the elimination of a viscous component up to 200°C, a ChRM was isolated in about half of the samples between 200° and 680°C. In the remaining samples, a low– and high-temperature (HT) components were defined in the 200°-400°C and 400°-680° intervals, respectively (sample Yun2908 in Figure 54). The high unblocking temperature spectra and Curie temperature of 680°C combined with high coercivity spectra show that hematite is the main magnetic carrier in the red beds (confirming evidence from previous paleomagnetic studies from Yunnan, e.g. *Sato et al*., 2007; *Tong et al*., 2013, 2016). Several studies carried out over nearly the last fifty years have showed that hematite in red beds may have both a detrital and a chemical origin (see review by *Jiang et al*., 2015).

By combining ChRMs and HT components, well-defined site-mean directions (3.0°≤α_{95}≤ 20.0°, 9.1° on average) were obtained from 15 Pliocene-Holocene volcanic sites, 1 Pliocene lacustrine site, 18 Jurassic-Cretaceous red bed sites, and 2 Jurassic volcanic sites (Table 2).

In Figure 55, are shown the paleomagnetic site mean directions from Pliocene-Holocene basalts obtained by *Pellegrino et al*. [2018] (Figure 55a) and Eocene-Pliocene volcanics sampled in neighbour regions by *Kornfeld at al*. [2014a; 2014b; 2014c; Figures 55b-55d].

Pellegrino et al. [2018] and *Kornfeld et al*. [2014c] data, come from the same rocks from the Tengchong volcanic field, so that they should compare. The results are effectively the same (considering respective confidence cones), and show mostly northward declinations in the Tengchong volcanic field. Data by *Pellegrino et al.* [2018] reveal higher inclination with respect to data by *Kornfeld et al*. [2014c]. Moreover, three sites (two Pleistocene and one

Pliocene in age) yield reverse polarities and inclinations as high as -37.9° -47.3°. Therefore data by *Pellegrino et al.* [2018] demonstrate that the Tengchong volcanic field is older than 0.78 Ma (age of the Brunhes-Matuyama transition; geomagnetic polarity scale from *Ogg*, 2012), confirming radiometric data by *Wang et al*. [2008, and references therein].

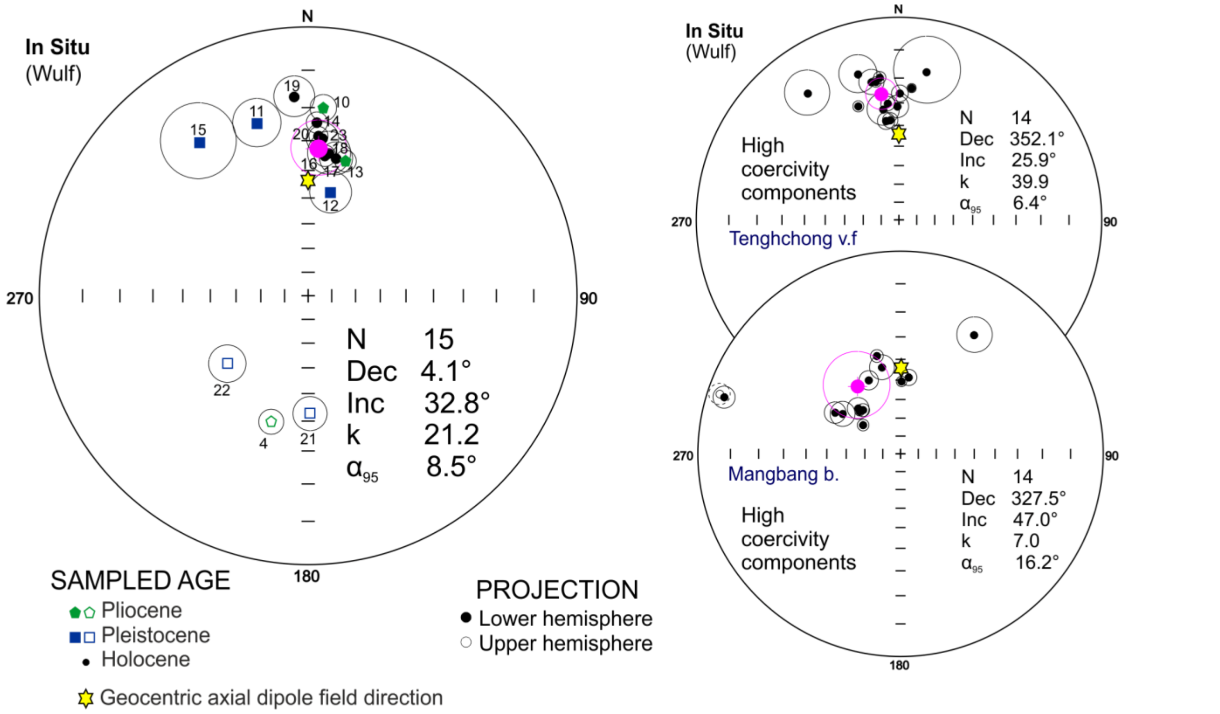

***a.* Data from Pellegrino et al.,(2018). Basalts, Tengchong volcanic field and city;**

***b.* Data from Kornfeld et al. (2014c), volcanic rocks of the Tengchong volcanic field and Mangbang basin (late Miocene-Pliocene);**

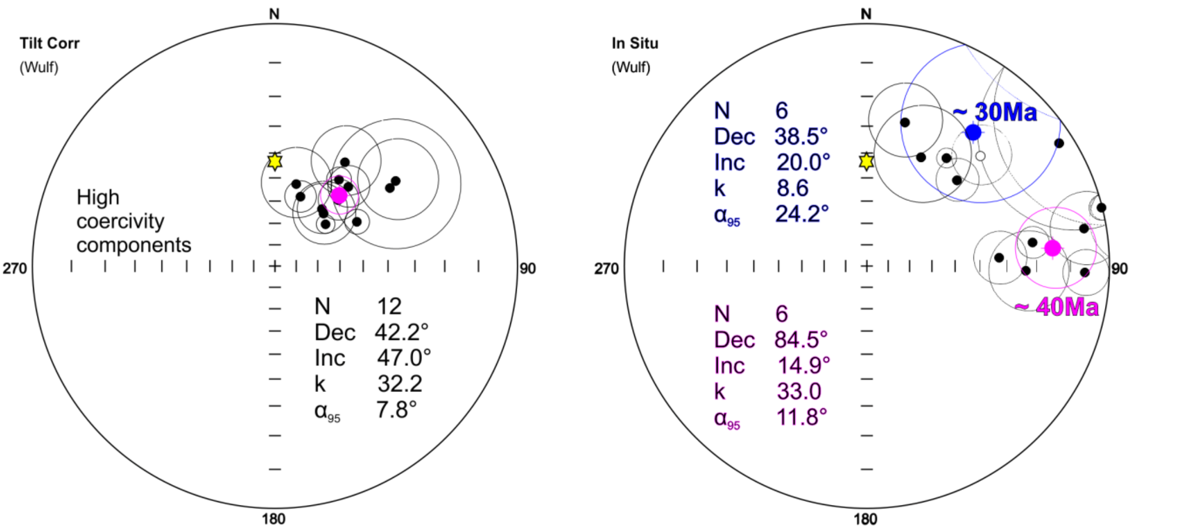

***c.* Data from Kornfeld et al. (2014a), volcanic rocks (~ 30-40 Ma) of the Baoshan block;**

***d.* Data from Kornfeld et al. (2014b), volcanic rocks of the Tengchong block.**

Figure 55. Equal-angle projection of the site-mean paleomagnetic directions gathered by *Pellegrino et al*. [2018] from Pliocene-Holocene basalts exposed west of the Gaoligong Shear Zone (a), and by *Kornfeld et al*. [2014c]; *Kornfeld et al*. [2014a]; *Kornfeld et al*. [2014b] (b–d). N = number of sites; Dec = declination; Inc = inclination; k = precision parameter; a_{95} = 95% confidence angle. The yellow stars represent the normal polarity geocentric axial dipole field direction (D = 0°; I = 43°) expected at the study area. Solid (open) symbols represent projection onto the lower (upper) hemisphere, and open circles represent confidence cones. Pink points and open circles represent the mean paleomagnetic directions and the relative 95% confidence cones, respectively.

The lower inclination with respect to the geocentric axial dipole (GAD) field inclination expected at the study area may be due to the incomplete averaging of the PSV of the geomagnetic field, as they got samples from only fifteen lava flows. Thus, *Pellegrino et al.* [2018] put forward an alternative explanation for the low normal polarity inclinations from the Tengchong volcanic field than the regional tilting proposed by *Kornfeld et al*. [2014c].

In Figure 55b, are also shown data from *Kornfeld et al*. [2014c] obtained from upper Miocene-Pliocene volcanic rocks of the Mangbang Basin. They explained the CCW rotations as apparent rotations due to tilting along the half graben hosting the basin itself. *Kornfeld et al*. [2014a] also documented a 40° CW rotation in 30 Ma basalts from the Baoshan block (Figure 55c) and a CW rotation of 87° in 40 Ma dykes from the Tengchong block (Figure 55d).

Paleomagnetic directions from Jurassic-Cretaceous red beds sampled east of the Gaoligong Shear Zone are shown in Figure 56.

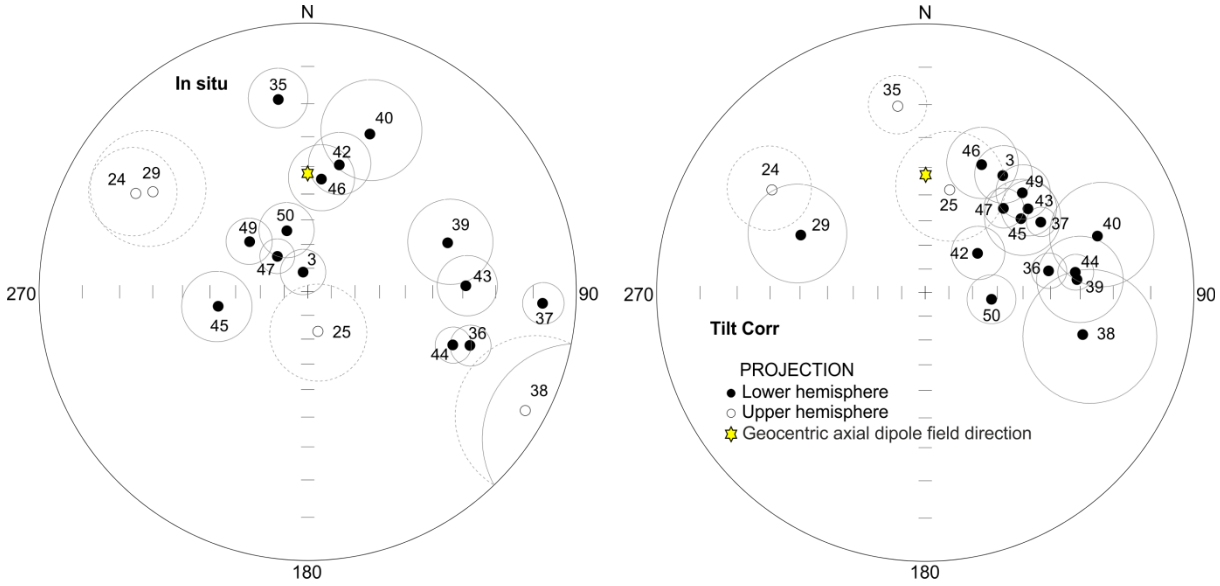

Figure 56. Modified after *Pellegrino et al.* [2018]. Equal-angle projection of the paleomagnetic directions obtained from Jurassic-Cretaceous red beds exposed in the Baoshan and Mangshi areas, east of the Gaoligong Shear Zone (see Figure 52-58a-b).

Site-mean directions were evaluated by averaging out ChRMs and HT components from the individual specimens. Both the in-situ and tilt-corrected directions are far from the GAD field direction expected at the sampling localities. Most of the tilt corrected directions (15 out of 18 sites) are of normal polarity and show variable amounts of westward declinations (exceeding 100° for site Yun38). Directions from Jurassic volcanics (sites Yun01-02) were discarded, as they were completely different from nearby red bed site directions (Figure 58 and Table 2). Moreover, site Yun02 yielded a sub-horizontal tilt-corrected direction that is incompatible with the expected Jurassic inclinations (42°-61°, e.g. *Torsvik et al.*, 2012).

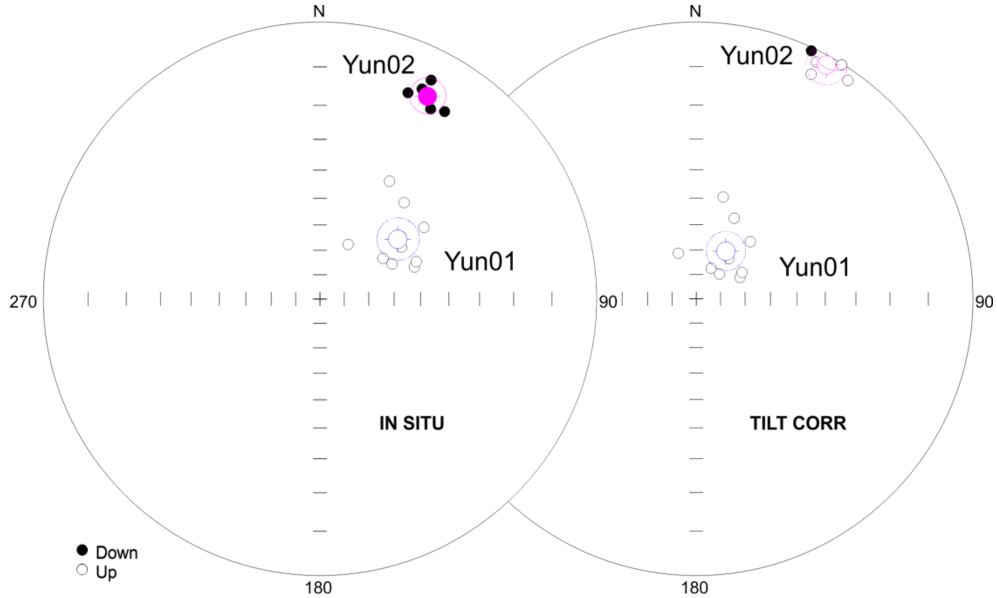

Figure 57. Equal-angle projection of the paleomagnetic directions obtained from Jurassic basalt exposed in the Baoshan areas, east of the Gaoligong Shear Zone. Pink points and open circles represent the mean paleomagnetic directions and the relative 95% confidence cones, respectively (See Table 2 for mean values).

The paleomagnetic data from red beds support a positive fold test at the 99% significance level according to *McFadden* [1990] (N=18; $Scos_{insitu}$=11.9; $Scos_{tilt\ corrected}$=1.1, critical Scos at the 99% significance level =6.9). Maximum k and minimum Scos values are obtained at 93% and 95% of complete unfolding, respectively [*Pellegrino et al*., 2018]. This suggests a pre-folding (i.e. pre-Eo-Oligocene) [*Chen et al*., 1995] magnetization. Furthermore, site Yun38 showed dual polarity samples (and consistent polarities in the same beds), indicating that the sampled strata encompass different polarity chrons (the reversal test on individual ChRMs according to *McFadden and McElhinny*, 1990 is indeterminate). This proves that, at least for site Yun38, the magnetization is of primary origin. The normal and reverse polarity site-mean directions are not antipodal (negative fold test according to *McFadden*, 1990), probably due to local block rotations [*Pellegrino et al*., 2018].

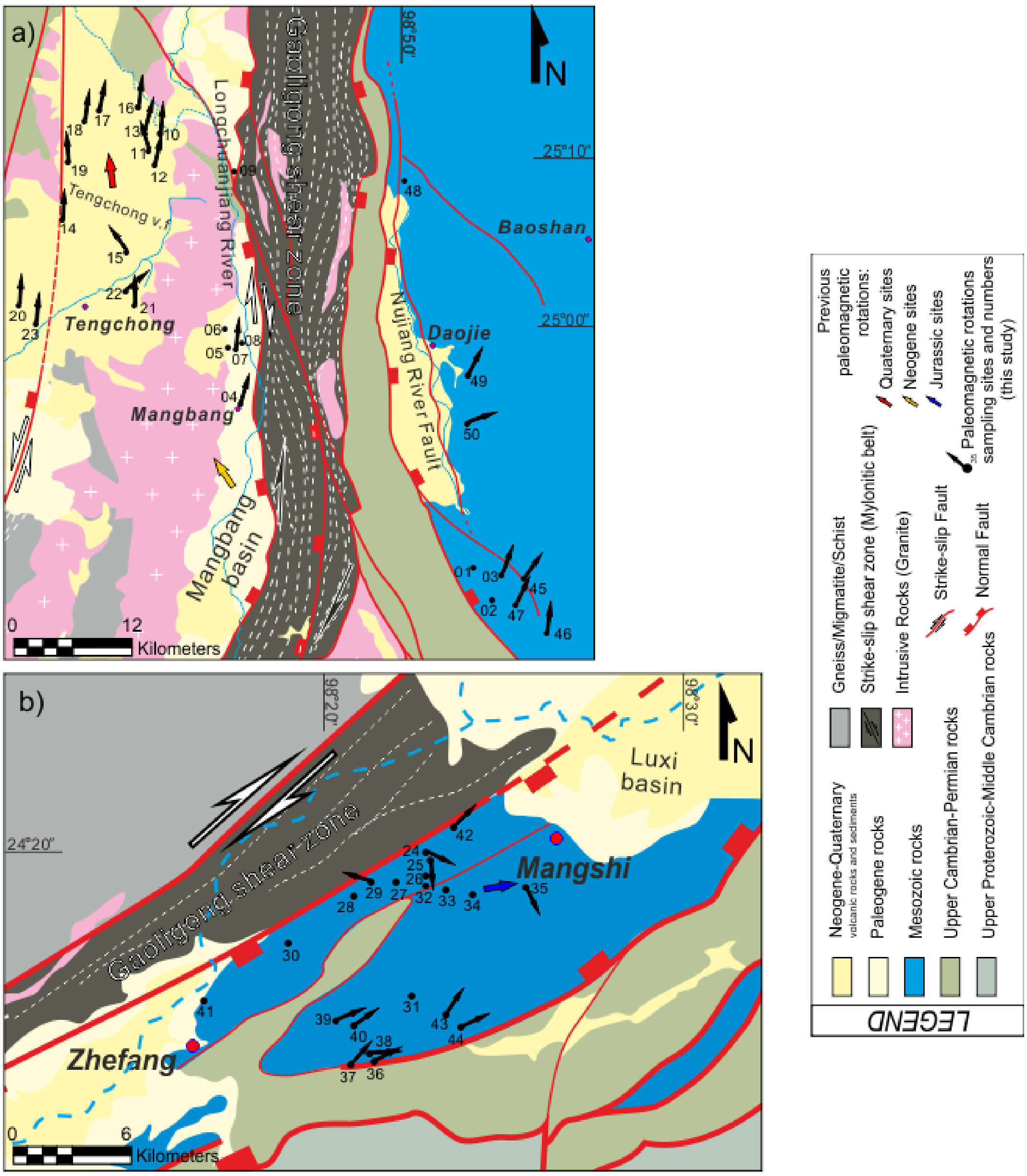

Figure 58. Modified after *Pellegrino et al.* [2018]. Paleomagnetic sampling areas in the northern (a, Baoshan and Tengchong area) and southern (b, Mangshi basin) segment of the Gaoligong Shear Zone. Black arrows indicate paleomagnetic rotations from Jurassic to Holocene sediments and basalts (see Table 2). Rotation values were calculated with the same method and Eurasian poles as in Figure 49 and 52A.

It is noteworthy that three sites (Yun24, 25 and 35) from our red bed data set yield a reverse polarity (and Yun38 dual polarity samples), while previous studies of red beds from the Lanping and Simao blocks systematically reported a normal polarity, for which a magnetic overprint has been suggested [*Chen et al.*, 1995; *Gao et al.*, 2015; *Huang and Opdyke*, 1993; *Li et al.*, 2017b]. Red beds sites Yun24, 25 and 35 support themselves a positive fold test at the 95% significance level according to *McFadden* [1990] ($Scos_{insitu}$= 2.6; $Scos_{tiltcorr}$= 1.8, critical Scos at the 95% significance level = 2.1, maximum K and minimum Scos values arise at 100% of complete unfolding). *Pellegrino et al.* [2018] data support for sure a pre-folding (i.e. pre-Eo-Oligocene) magnetization of the whole data set, and the reverse polarity sites suggest that magnetization is possibly of primary origin. In this case, most of the studied sites would have been deposited during the long normal Cretaceous superchron. Detailed age evaluation is often problematic in continental sediments, so that the issue of age determination and possible lower Tertiary pre-folding remagnetization of most of the sites remains open at present (see also similar conclusions by *Li et al*., 2017b for the Simao block).

Although sites Yun24, 25, 29 and 42 are located at less than 2 km from the contact with the mylonites of the Gaoligong fault, a post-rotation (i.e. post-Oligo-Miocene) magnetic overprint is excluded (with the possible exception of site Yun42) by the evidence that both the *in situ* and tilt-corrected directions are far from the GAD field direction (Figure 56 and Table 2). The apparently puzzling lack of a late Tertiary magnetic overprint for sites adjacent to mylonites is explained considering that the high-grade rocks were exhumed along an extensional detachment that presumably elided the whole upper crust, juxtaposing high-grade metamorphic rocks and unmetamorphosed sediments [*Zhang et al*., 2011].

6.1 Rotation pattern along the Gaoligong Shear Zone

To evaluate tectonic rotations with respect to Eurasia, the paleomagnetic directions were compared to coeval Eurasian paleopoles from *Torsvik et al*. [2012] and *Cogné et al*. [2013] (see details in chapter 3 Figure 25-26). Sites younger than 5 Ma (i.e. Pliocene to Holocene in age) were compared to the local GAD field direction, assuming that no paleomagnetically significant East Asia rotation or drift occurred after 5 Ma. The expected Eurasian declinations and inclinations at Yunnan are shown in Figure 59.

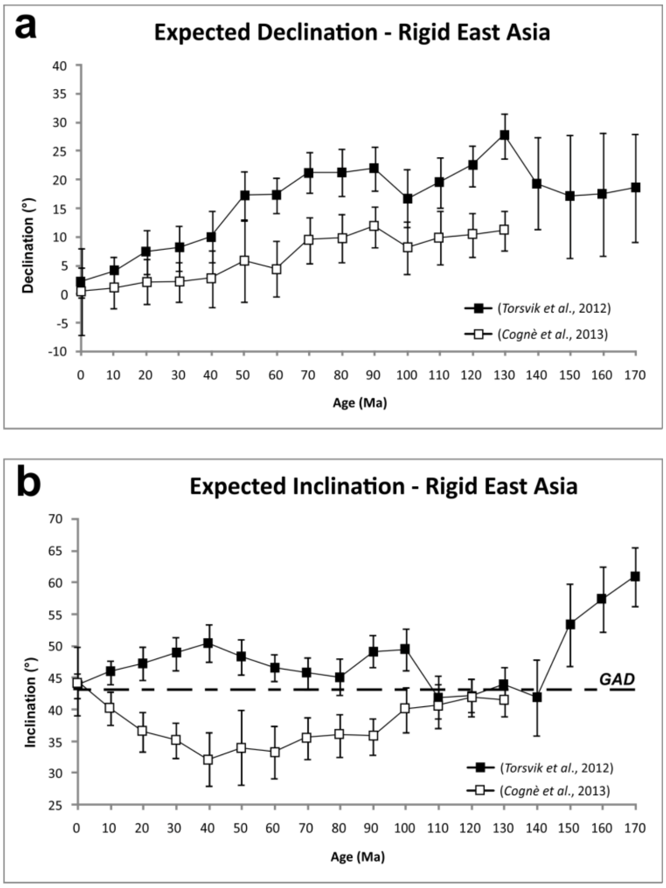

Figure 59. From *Pellegrino et al*. [2018]. Expected declination (a) and inclination (b) values (and relative error bars) in the study area, considering Eurasian (from 170 to 140 Ma) and East Asia (from 130 to 10 Ma) paleopoles by *Torsvik et al*. [2012] and *Cogné et al*. [2013], respectively. Reference point is at 25.21°N, 98.58°E. The black line indicates the geocentric axial dipole field inclination (43°) for the study area.

Inclination data show rapid changes in the 180-150 Ma time window, followed by contrasting paths when the two paleopoles lists are considered. Expected declinations are always positive, although they are significant (around 20°) only at 180-150 Ma, between 140 and 80 Ma they are around 10°-20°, and are progressively annulled afterwards.

Site rotations with respect to their distance to the Gaoligong Shear Zone are shown in Figure 56. Site distances are calculated with respect to both the Shear Zone center (Figure 60a), and the contact with the fault mylonites (Figure 60b).

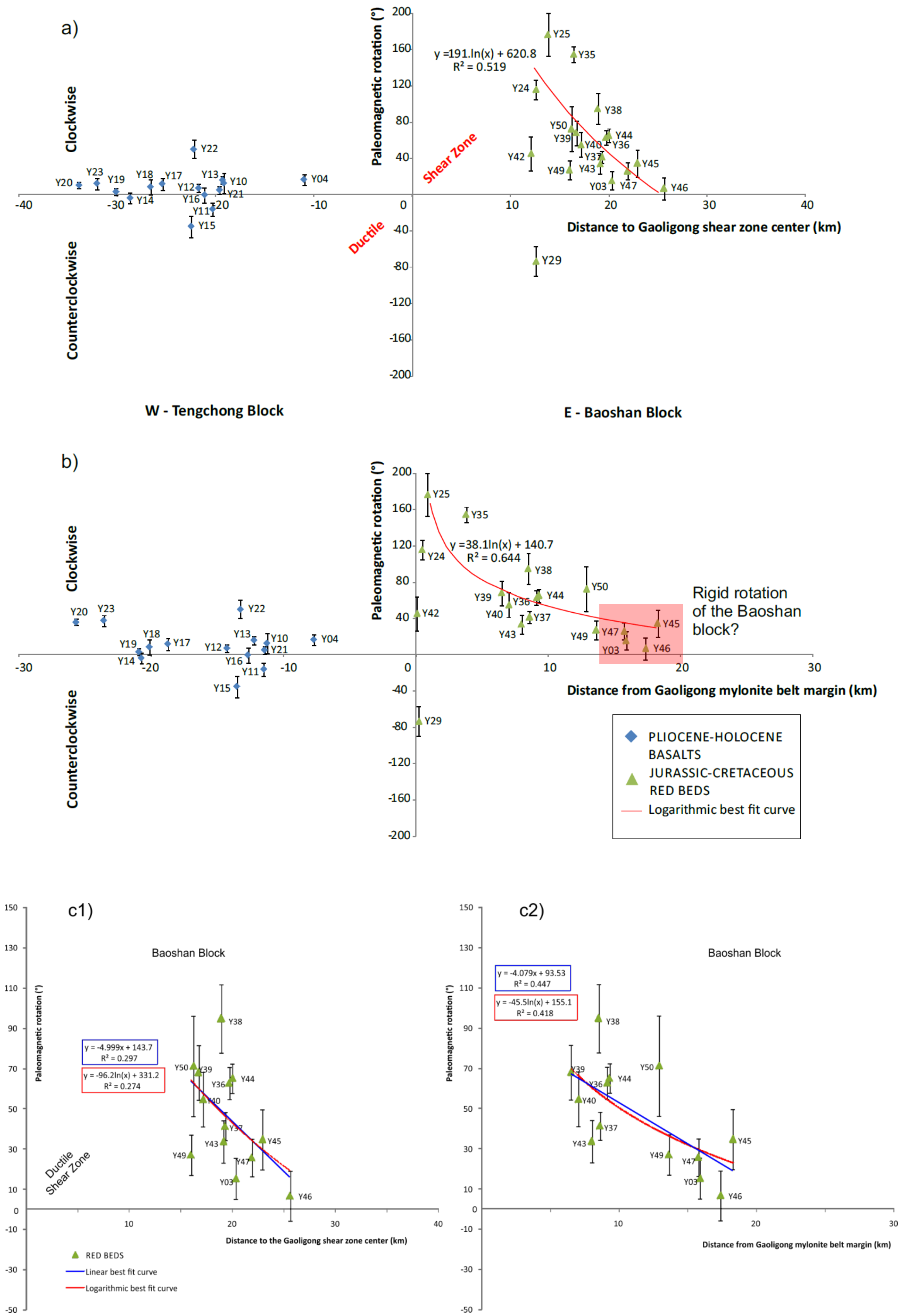

a)
Clockwise
Counterclockwise
Paleomagnetic rotation (°)
y =191.ln(x) + 620.8
R² = 0.519
Shear Zone
Ductile
Distance to Gaoligong shear zone center (km)
W - Tengchong Block
E - Baoshan Block
b)
Clockwise
Counterclockwise
Paleomagnetic rotation (°)
y =38.1ln(x) + 140.7
R² = 0.644
Rigid rotation of the Baoshan block?
Distance from Gaoligong mylonite belt margin (km)
PLIOCENE-HOLOCENE BASALTS
JURASSIC-CRETACEOUS RED BEDS
Logarithmic best fit curve
c1)
Baoshan Block
Paleomagnetic rotation (°)
y = -4.999x + 143.7
R² = 0.297
y = -96.2ln(x) + 331.2
R² = 0.274
Ductile Shear Zone
Distance to the Gaoligong shear zone center (km)
RED BEDS
Linear best fit curve
Logarithmic best fit curve
c2)
Baoshan Block
Paleomagnetic rotation (°)
y = -4.079x + 93.53
R² = 0.447
y = -45.5ln(x) + 155.1
R² = 0.418
Distance from Gaoligong mylonite belt margin (km)

Figure 60. From *Pellegrino et al*. [2018]. Plot of rotations with respect to Eurasia versus site distance to both Gaoligong Shear Zone center (a) and mylonite- sediment contact (b). See Figure 52-58a-b for site location. Red lines are logarithmic best fit curves for the red bed sites located east of the Gaoligong Shear Zone (disregarding sites Yun24, Yun29, and Yun42 located adjacent to fault mylonites). (c) Detail of rotations with respect to Eurasia versus site distance to both Gaoligong Shear Zone center (c1) and mylonite- sediment contact (c2) disregarding site Yun24, 25, 29, 35 and 42. Red and blue lines are logarithmic and linear best fit curves. Sense and amount of rotation are defined by the smaller angle between observed and expected Eurasian declinations, thus rotation values are ≤|180°| by definition.

To the west of the fault, Pliocene-Holocene basalts overall show null rotations, consistently with results from the Pliocene whitish silt site Yun07. As discussed above, PSV from basalt sites is likely not averaged out, and we may expect a geomagnetic declination scatter that mostly ranges within ± 20° at such latitudes [*Hernandez-Moreno et al*., 2016, and discussion therein]. Thus a bias can exist on the average null rotation obtained from volcanic data, but such error is expected to be much smaller than the large CW rotations (up to 176°) observed in Mesozoic red beds. *Pellegrino et al*. [2018] conclude that data from basalts -although probably scattered by PSV effects–do prove that rotations ceased in Yunnan by Early Pliocene (5 Ma) times. Red beds east of the fault yield always CW rotations (apart from site Yun29), reaching values as high as 176° for site Yun25. Apart for scattered rotations adjacent to the fault (sites Yun24, 29, 42), in both plots there is a clear trend of decreasing rotation values moving away from the fault. Rotations are virtually annulled at ca. 20 km from mylonite-sediment contact (Figure 60b). Sites with number of directions less than 8/10 samples (eg. Yun25 and 35; Figure c) have been excluded, however, as clearly shown in figures (c1) and (c2), the rotation pattern is still the same in both cases (distance to the Gaoligong Shear Zone center and from Gaoligong mylonite belt margin). Linear and logarithmic best fit curves fit well and are in agreement with the interpretation proposed by *Pellegrino et al.* [2018]. There is not clear evidence, in the field, of the width of the rotating blocks. By scrutinizing rotations of sites Yun24, 25, 29, and 42, located adjacent to the

Gaoligong Shear Zone contact (Figure 60), rotations change abruptly from close sites, suggesting that the crust along the Gaoligong damage zone is broken into small blocks, width in the order of 1 km, or smaller (see sites Yun24 and Yun25). Obviously, block size seems to increase moving away from the fault, and in fact sites located in the southern boundary of the Mangshi basin (Figure 58b-60) show similar rotations over a distance of 6-7 km.

Rotations of sites with respect to the distance of the Gaoligong Shear Zone center and mylonite belt margin, in northern and southern transect, have been shown in Figure 61. There is a clear trend of decreasing rotation values moving away from the fault. All these tests, which gave consistent results, are useful for further confirming the proposed interpretations (Figures 60 c1,c2 and 61).

Figure 61. Plot of rotations with respect to Eurasia versus site distance to both Gaoligong Shear Zone center and mylonite-sediment contact in Northern (a) and southern (b) transects. See Figure 52-58a-b for site location. Red lines are logarithmic best fit curves for the red bed sites located east of the Gaoligong Shear Zone (disregarding sitesYun24, 29, and 42 located adjacent to fault mylonites).

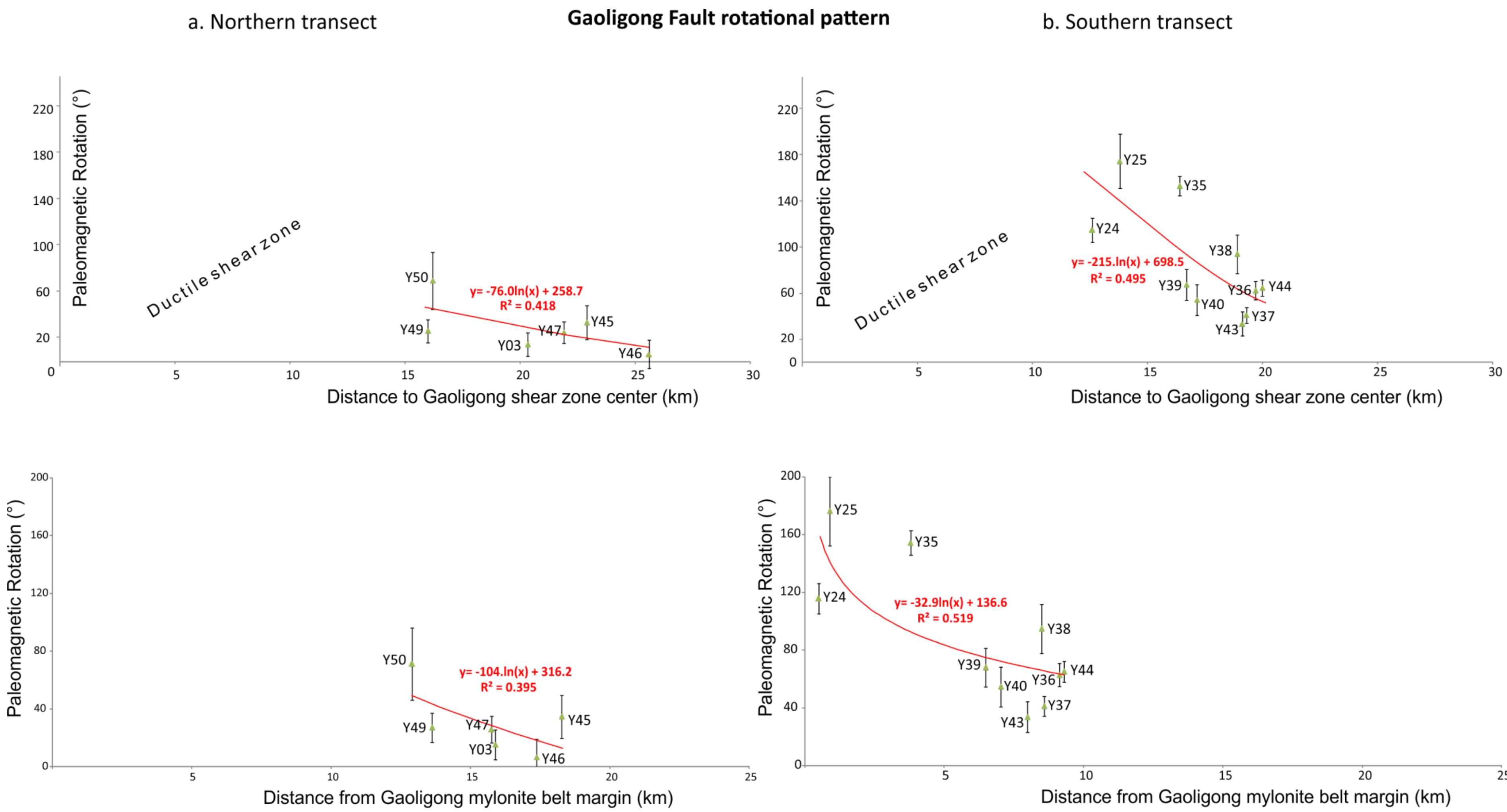

Gaoligong Fault rotational pattern
a. Northern transect
b. Southern transect
Paleomagnetic Rotation (°)
Ductile shear zone
y= -76.0ln(x) + 258.7
R² = 0.418
Y50
Y49
Y03
Y47
Y45
Y46
Distance to Gaoligong shear zone center (km)
y= -215.ln(x) + 698.5
R² = 0.495
Y25
Y35
Y24
Y38
Y39
Y40
Y36
Y44
Y37
Y43
y= -104.ln(x) + 316.2
R² = 0.395
Distance from Gaoligong mylonite belt margin (km)
y= -32.9ln(x) + 136.6
R² = 0.519

The described CW paleomagnetic data seem to support a "*quasi-continuous*" crust deformation model of strike-slip fault zones, where the upper brittle crust is broken into small rigid blocks with sizes smaller than the shear zone width, the rotation is CW (CCW) in regions of dextral (sinistral) shear and gradually increases getting closer to the fault, reaching values > 90° [Figure 62c; *Hernandez-Moreno et al.*, 2014; 2016; *McKenzie and Jackson*, 1983; *Nelson and Jones*, 1987; *Randall et al.*, 2011; *Sonder et al.*, 1994].

According to such model, the rotation is not directly driven by fault shear, but is a consequence of the angular velocity of the ductile deformation, taking place in the ductile lower crust.

Pellegrino et al. [2018] note that this CW rotation pattern is not consistent with 1) the continuous crust deformation models (where even the brittle upper crust behaves as a viscous fluid and rotations are ≤90° [*Bird and Piper*, 1980; *England and McKenzie*, 1982; *England and Wells*, 1991; *England et al*., 1985; *Kimura et al*., 2004, 2011; *Sonder and England*, 1986; *Sonder et al*., 1986], or 2) the discontinuous models, where set of secondary faults inside the deforming zone bound large rigid domains that rotate uniformly CW and CCW ≤90º [*Garfunkel and Ron*, 1985; *McKenzie and Jackson*, 1986; *Nur et al*., 1986; *Ron et al*., 1984].

In quasi-continuous deformation models, the rotation magnitude of the blocks has been assumed to depend upon fault length, displacement amount, fault wall locking, and lithosphere rheology [*Piper et al*., 1997; *Randall et al*., 2011; *Sonder et al*., 1994]. The simpler equation by *Lamb* [1987], which relates fault zone deformation-rotation width (W) and displacement (D) with the maximum rotation value of equidimensional blocks (Θ) was recently successfully used to infer the displacement along the 1000 km-long Liquiñe-Ofqui fault from southern Chile [*Hernandez-Moreno et al*., 2014; 2016]:

$$\Theta = 0.5\ D/W$$

Other formulas by *Lamb* [1987; see previous chapter] consider also the occurrence of elongated blocks, and their aspect ratio. However, *Pellegrino et al.* [2018] have no kind of evidence of the shape of the rotating blocks east of the Gaoligong Shear Zone, so that we assume for simplicity the occurrence of equidimensional blocks.

By considering 165° as maximum CW rotation value (average rotation of sites Yun25 and Yun35, Figure 60, 61), and 50 and 40 km as total deformation zone width W (although we have no red bed data west of the fault) with respect to the shear zone center (Figure 60a) and the contact with mylonites (Figure 60b), respectively, the formula by *Lamb* [1987] gives displacement of 290 and 230 km. Such values would be too large if an intra-continental strike-slip fault is considered [*Cao et al*., 2011a, 2011b; *Otofuji et al*., 2010; *Tanaka et al*., 2008; *Tapponnier et al*., 1990; *Zhong et al*., 1991]. However, by taking in mind that the Gaoligong Shear Zone would have bounded rigid blocks - or "microplates"- escaping laterally from the India-Eurasia collision (thus being a sort of transform fault), the 230-290 km offset values given by paleomagnetism become realistic. *Pellegrino et al.* [2018] remind that an even greater total offset of ca. 700 km was proposed for the Ailaoshan-Red River Shear Zone [*Chung et al*., 1997; *Leloup et al*., 1995, 2001], although such estimate was considered unrealistically high by other authors [*Allen et al*., 1984; *Replumaz et al*., 2001; *Schoenbohm et al*., 2006a; *Wang E. et al*., 1998].

Pellegrino et al. [2018] note that sites Yun24, Yun42 and Yun29 yield smaller CW (116°, 45°) and 74° CCW rotations (respectively), even if they were sampled adjacent to the fault (Figures 58b and 60). Therefore, it is possible that such sites rotated in fact CW more than 180°.

Pellegrino et al. [2018] conclude that small blocks located adjacent to the fault underwent variable and/or very large CW rotations exceeding largely 180°, but their behavior is not representative of deformation occurring in the 20 km-wide crust slices located at both fault edges. Probably a sort of "rotation channel" exists adjacent to the fault where small blocks rotate freely by large amounts reminding the "ball-bearing model" of *Beck* [1976].

Average flattening (F) values for volcanics and red beds are 12.7°±9.4° and 17.4°±14.0°, respectively. This confirms that Pliocene-Holocene volcanics have smaller inclinations than those predicted by a GAD field model, likely due to the incomplete averaging of the paleosecular variation of the geomagnetic field. On the other hand, the positive F for red beds may be due to the so-called "*inclination shallowing*", a phenomenon frequently observed in sediments and related to compaction-diagenetic effects on rock fabric and magnetic grains [e.g. *Arason and Levi*, 1990; *Deamer and Kodama*, 1990; *Tauxe and Kent*, 2004]. By the way, the positive F value would testify that no remagnetization process occurred after sediment diagenesis, thus it may represent an additional proof for the primary nature of the ChRMs and HT components isolated by us in the red beds.

6.2 Discussion

Pellegrino et al. [2018] paleomagnetic transects across the Gaoligong Shear Zone show that the dextral shear of the fault caused in the Baoshan block CW rotations of the Jurassic-Cretaceous red beds, whose magnitude decreases progressively moving away from the fault (Figure 60). Sites located adjacent to the fault underwent scattered rotations, and likely rotated CW by more than 180°. To the west of the fault, Pliocene-Holocene volcanics do not record significant rotations. Rotation of red beds blocks (whose size is likely ≤1 km adjacent to the fault) occurred presumably during the period of main Shear Zone activity, which is Oligo-Miocene [*Lin et al.*, 2009; *Wang et al.*, 2006; 2008; *Zhang et al.*, 2012a,b].

The paleomagnetic data show that the dextral shear along the Gaoligong Shear Zone ended 5 Ma ago (at least) being later reactivated as sinistral, consistently with the focal mechanism of the 1976 M=7.4 event, which yields for the southern part of the Gaoligong zone a sinistral strike-slip fault kinematics (Figure 52a). Moreover, the CW rotation shown today by GPS data in SE Tibet and northern Yunnan [*Liang et al*., 2013; Figure 48a] is certainly not related to the paleomagnetic rotation that ended by 5 Ma.

The paleomagnetism of the Gaoligong Shear Zone thus suggests that in the Yunnan area the extrusion of blocks bounded by strike-slip shear zones occurred in Oligo-Miocene times. Such tectonics ceased around 10 Ma (considering the younger Ar/Ar ages provided by *Zhang et a*l., 2012b), and was followed by an almost continuous southward drift of Yunnan driven by ductile lower crust squeezed out from Tibet. The present-day southern drift of Yunnan and its collision with Indochina is consistent with both GPS data [*Liang et al*., 2013; *Meade*, 2007; *Vergnolle* et al., 2007], and focal mechanisms of the major earthquakes (Figure 52a), yielding ~N-S sub-horizontal P axes, thus ~N-S horizontal shortening.

In the past, the predominantly CW rotation pattern of Yunnan (Figure 62) has been related to (1) the lateral extrusion of Tibet describing CW rotation trajectories (Figure 62; *Allmendinger et al*., 2007; *Copley*, 2008; *Gan et al*., 2007; *Wang et al*., 2001; *Zhang et al*., 2004), and 2) large semi-rigid block rotation driven by strike-slip fault activity following the “broken slate” model (Figure 62a; *Li et al*., 2017a; *Tanaka et al*., 2008; *Yang and Besse*, 1993; *Yang et al*., 2001b).

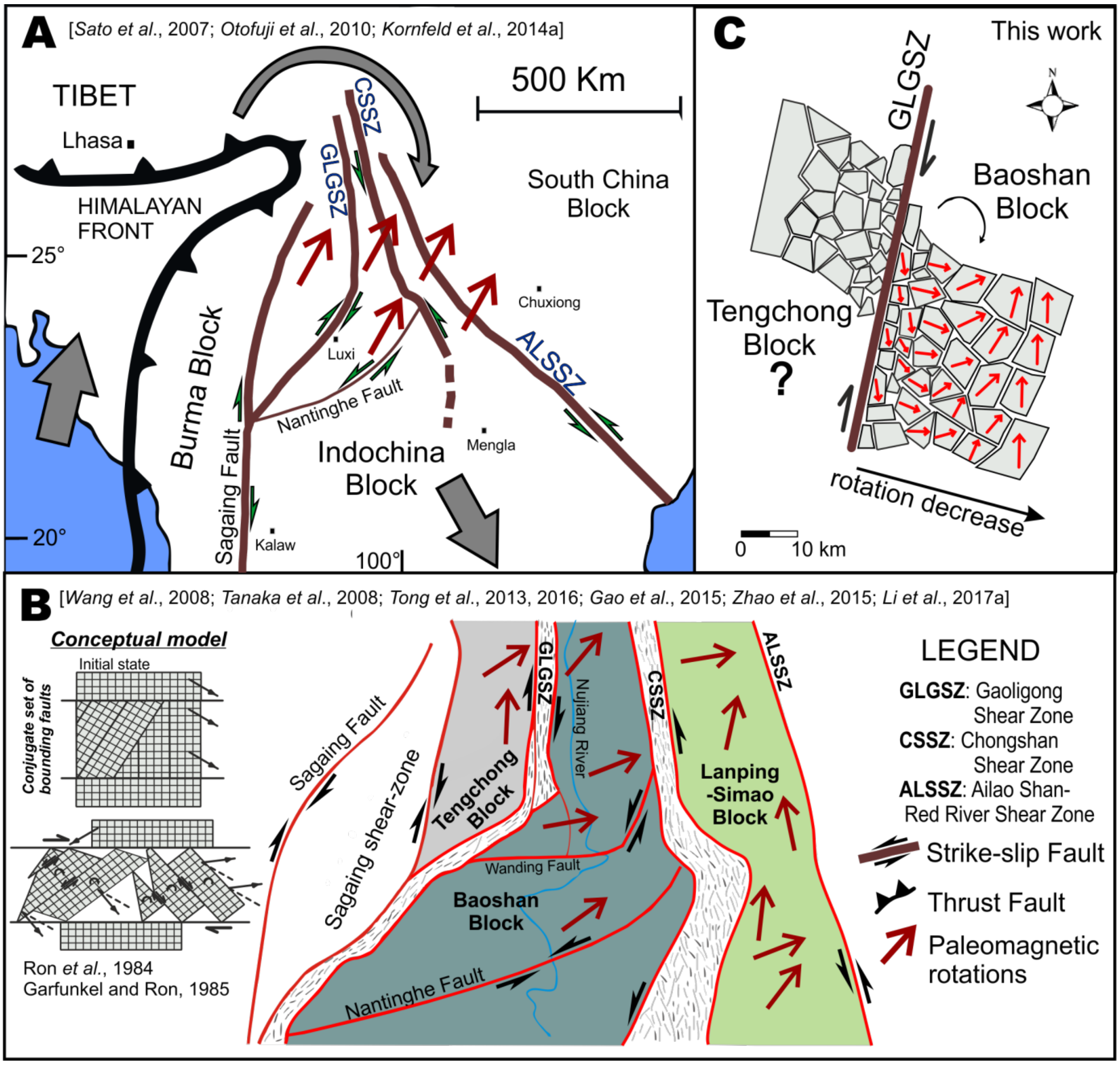

Figure 62. From *Pellegrino et al.* [2018]. Kinematic models of block rotations proposed for the Yunnan region. (a) Eastward extrusion of the Tibet plateau, yielding clockwise crust rotation around the East Himalayan Syntaxis, and inducing constant-magnitude clockwise rotations in Yunnan [*Kornfeld et al.*, 2014a; *Otofuji et al.*, 2010; *Sato et al.*, 2007]; (b) rigid mega-block rotations induced by shear along the Gaoligong and adjacent Shear Zones of Yunnan (similar to "broken slate" model by *Ron et al.*, 1984; *Garfunkel and Ron*, 1985; *Nur et al.*, 1986). Each block rotates rigidly and is bounded by a major Shear Zone [*Gao et al.*, 2015; *Li et al.*, 2017; *Tanaka et al.*, 2008; *Tong et al.*, 2013; *Wang et al.*, 2008; *Zhao et al.*, 2015]; c) *quasi-continuous* block rotation model [e.g., *Lamb*, 1987; *Randall et al.*, 2011; *Sonder et al.*, 1994; see also *Hernandez-Moreno et al.*, 2014, 2016] for the Tengchong and Baoshan blocks at both edges of the Gaoligong Shear Zone, based on paleomagnetic rotations reported by *Pellegrino et al.* [2018]. Rotations of small blocks of Jurassic-Cretaceous red beds east of the Gaoligong Shear Zone (Baoshan block) are caused uniquely by dextral shear along the Gaoligong Shear Zone. Rotations reach maximum values (176°) close to the fault and diminish moving east of it being virtually annulled at ca. 20 km from the Shear Zone contact. The dimension and shape of individual crustal blocks are speculative, although— relying on

rotation value scatter—blocks adjacent to the fault are ≤1 km wide (see Figure 52-58a-b). Pliocene-Holocene sites located west of the Gaoligong Shear Zone (Tengchong block) do not rotate, likely because dextral fault activity and its related rotations are older than Pliocene times.

Pellegrino et al. [2018] data show for the first time that CW rotations in Yunnan are also due to strike-slip fault activity itself, and occurred in small (few km of width) blocks inside the 40-50 km wide damage zone of the Gaoligong Shear Zone (total width at both sides of the fault, although we lack red bed data west of the fault). The rotation pattern and block dimensions are consistent with a quasi-continuous crust deformation model (Figure 62c).

However, it is clear that the rotation kinematics of Yunnan is complex and cannot be solely related to the rotation zones bounding the major strike-slip faults. In fact in *Pellegrino et al.* [2018] working zone, CW rotations of 42°-100° were obtained from 170-30 Ma rocks at distances that are generally greater than 20 km from both the Gaoligong and Chongshan Shear Zones, roughly within the centre of the Baoshan and Tengchong blocks (Table 1, *Huang and Opdyke*, 1993; *Kornfeld et al*., 2014b; *Tong et al*., 2016). Thus, such rotations cannot be definitely caused by Gaoligong or Chongshan lateral shear alone. Further E and S of our study area, the recent overview by *Li et al*. [2017a] similarly suggests a rigid CW rotation for both the Lanping and Simao blocks.

Relying on *Pellegrino et al.* [2018] and literature data, the rotational behavior of the Baoshan block itself is far from being clear. *Tong et al*. [2016] reported 70°-80° CW rotations from two localities (NE of Yongde, Figure 52 and Table 1) that are 60-80 km far from the Gaoligong Shear Zone, thus unquestionably not influenced by fault kinematics. Yet, *Pellegrino et al.* [2018] data suggest that at ~25 km from the contact with fault mylonites, the Baoshan block rotation is virtually annulled (Figure 62b). It is also true –however – that a statistically significant rotation of 20.5° ± 12.2° can be evaluated by considering the four farthest sites from fault contact (Yun03, 45, 46, 47; Figure 60b). A 20° rigid rotation of the

Baoshan block would imply that the maximum rotation value due to fault shear is reduced to 145° (instead of 165°), and this would translate –by using the formula by *Lamb* [1987] – into a smaller 200-250 km paleomagnetically-evaluated Gaoligong fault offset.

These results of *Pellegrino et al*. [2008] study put forward two hypotheses to explain the complexity of the Yunnan rotational pattern:

1) Rotations of the whole Tengchong, Baoshan, and Lanping mega-blocks coexist with rotations of small blocks (few km in size) inside the fault damage zones (Figure 62). Their relative magnitude and kinematic relation –however-have not been clarified yet;

However, it is difficult to imagine that such elongated rock stripes (400 km long and only 20-30 km wide) located between strike-slip faults underwent large rotation, as a big problem of space would arise (Figure 62b). Thus, it is possible that such rotations occurred (at least partly) before that the strike-slip activity of the huge N-S shear zones started in Eocene times.

2) Other unrecognized strike-slip faults exist within the Tengchong and Baoshan blocks, and their activity caused the rotations documented in apparently "undeformed" block centers. Rotating folds and thrust sheets might also contribute to the rotation pattern, as suggested for the Simao block by *Kondo et al*. [2012], *Tong et al*. [2013], and *Gao et al*. [2015].

Therefore, during the second year of Ph.D. project, to try unraveling the complexity of the Yunnan rotational pattern, three transect orthogonal to ARRSZ and within Simao, Lanping and Chuandian blocks have been paleomagnetically sampled.

Chapter VII

7. Paleomagnetic results and magnetic overprint evaluation:

- **THE CASE OF AILAOSHAN RED RIVER SHEAR ZONE**

All sites sampled along the Ailaoshan Red River Shear Zone into the Lanping, Simao and Chuandian "Block" (or Domain), during the second field campaign on April 2017, yielded a measurable magnetization.

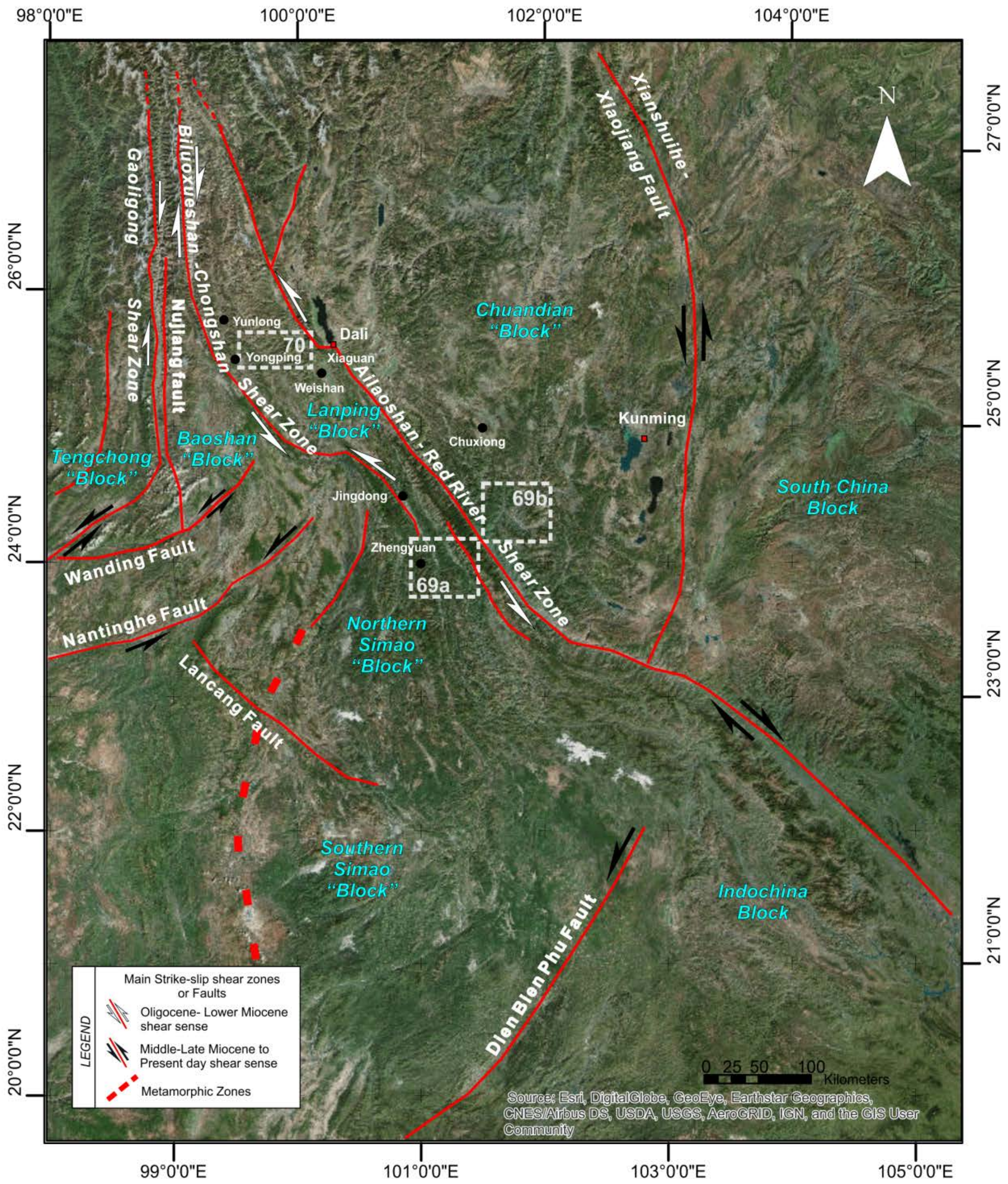

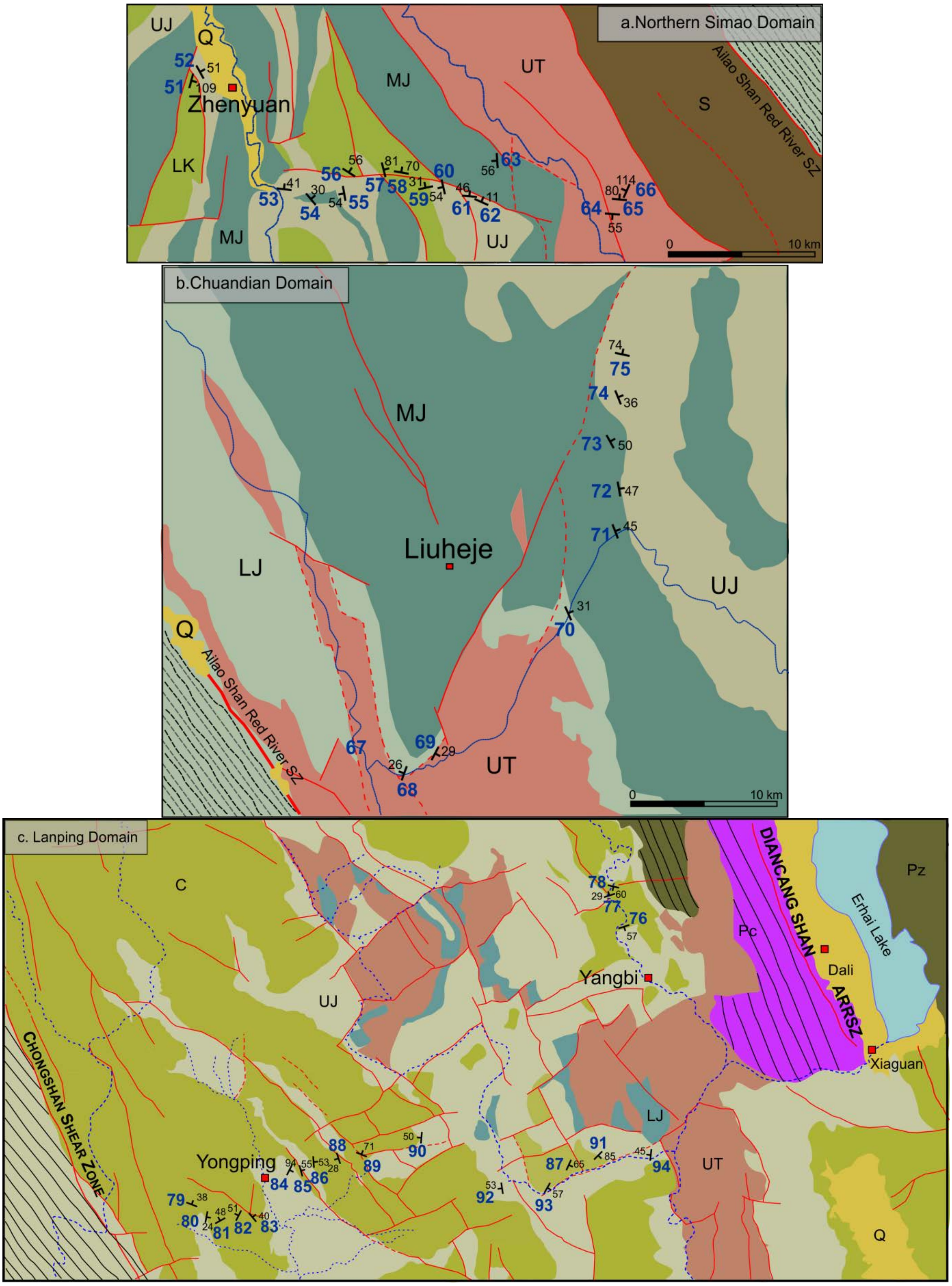

Figure 63. Schematic and structural map of Yunnan region modified after *Bureau of Geology and Mineral Resources of Yunnan Province* [1990]. The white boxes indicate the three areas of paleomagnetic investigation with structural details of the sites sampled [a= Figure 69a, b= Figure 69b and c= Figure 70] in Northern Simao, Chuandian and Lanping Domain. Sampled sites in blue.

Sampled sites are 44 (tot. 425 samples, 6 Upper Triassic, 20 Jurassic and 18 Lower Cretaceous red beds sites), located at both sides of the Ailaoshan Red River Shear Zone moving along transect perpendicular to the fault: 16 sites in the southern area within the northern Simao block (south-west of the fault), 9 sites within the Chuandian block (south-east of the fault) and 19 within Simao block (North-west of the fault) between the Ailaoshan Red River Shear Zone and the Chongshan Shear Zone (Table 3, Figure 63, 69a,b and 70).

Differently from the Gaoligong case, we chose sites within a maximum distance of 40 km from the contact with the shear zone, because the estimated offset of the Red River fault is greater than other faults. Furthermore, investigation took place not only in the area adjacent to the fault but also inside the blocks bounding the main structure. Continental red beds, Triassic to Cretaceous in age, were sampled. Sampling methods and laboratory analysis have been described in previous chapters.

The sampled area in the northern Simao Domain, between Zhengyuan city and the Ailao Shan Red River shear zone (Figure 63a), presents several anticlines N-S trending and, to the westernmost others monoclinal stuctural [*Tanaka et al*., 2008; Bureau of Geology and Mineral Resources of Yunnan Province, 1990]. Sites located into the Chuandian Domain (Figure 63b), have been sampled in the southern part of the so called Chuxiong Basin. In this basin, Upper Triassic gray sandstones and marls grade upwards into Jurassic and Cretaceous red sandstones. The youngest redbeds of this basin are placed in Eocene age [*Yoshioka et al*., 2003; *Gao et al*., 2017 and reference therein]. The Upper Cretaceous–Eocene redbeds in the Chuxiong basin is folded into NW to NNW trending anticlines [*Leloup et al*., 1995]. The folding took place in the Upper Eocene–Oligocene, as evidenced by an unconformity between the Lower Eocene and the Upper Eocene–Oligocene [Bureau of Geology and Mineral Resources of Yunnan Province, 1990; *Yoshioka et al*., 2003]. Finally, the red beds sampled in the Lanping Domain, between Yongping and Dali city (Figure 63c), are folded, often with steep NNW-striking axial clivage. The folding took place in the Paleogene, resulting in north-south trending fold axes in the Mesozoic system of Yunnan Province [*Tapponnier et al*., 1990; *Sharer et al*., 1994; *Funahara et al*., 1993].

Red beds samples were thermally demagnetized using a Pyrox shielded oven in 12 steps of temperature up to 680°C. Demagnetization data were plotted on orthogonal vector component diagrams [*Zijderveld*, 1967]. In most of the sites, after the elimination of a viscous component up to 200°C, a characteristic component (ChRM) was isolated in the 300°-680°C interval or 300°-640°C (called MT component) (Figure 64). Only in 12 samples was isolated also an high-temperature (HT) component defined in the 640°-680°C interval (Figure 64 and Table 3). In agreement with results cropping out from sampled red beds along the Gaoligong fault (see previous chapter), the high unblocking temperature spectra and the Curie temperature of 680°C combined with high coercivity spectra, seem to confirm that hematite is the main magnetic carrier in the red beds (confirming evidence from previous paleomagnetic studies from Yunnan, e.g., *Sato et al*., 2007; *Tong et al*., 2013, 2016). Furthermore, several studies carried out over nearly the last 50 years have showed that hematite in red beds may have both a detrital and a chemical origin (see review by *Jiang et al*., 2015, 2017 and our results of magnetic analysis in next chapter). By combining ChRM-MT and HT components, well-defined site-mean direction ($1.8 \leq \alpha95 \leq 20.5°$, 11.0° on average) were obtained from 6 Upper Triassic sites, 1 Lower Jurassic site, 6 Middle Jurassic sites, 13 Upper Jurassic sites and 18 Lower Cretaceous sites (Table 3). See supplementary information to all diagrams.

Figure 64. Orthogonal vector diagrams of typical demagnetization data (in situ coordinates) showing representative samples carrying characteristic magnetization (ChRM), medium temperature (MT) or high temperature (HT) components (See Table 3 for more details). Solid (open) symbols represent projection onto the horizontal (vertical) plane. Demagnetization step values are in degrees Celsius.

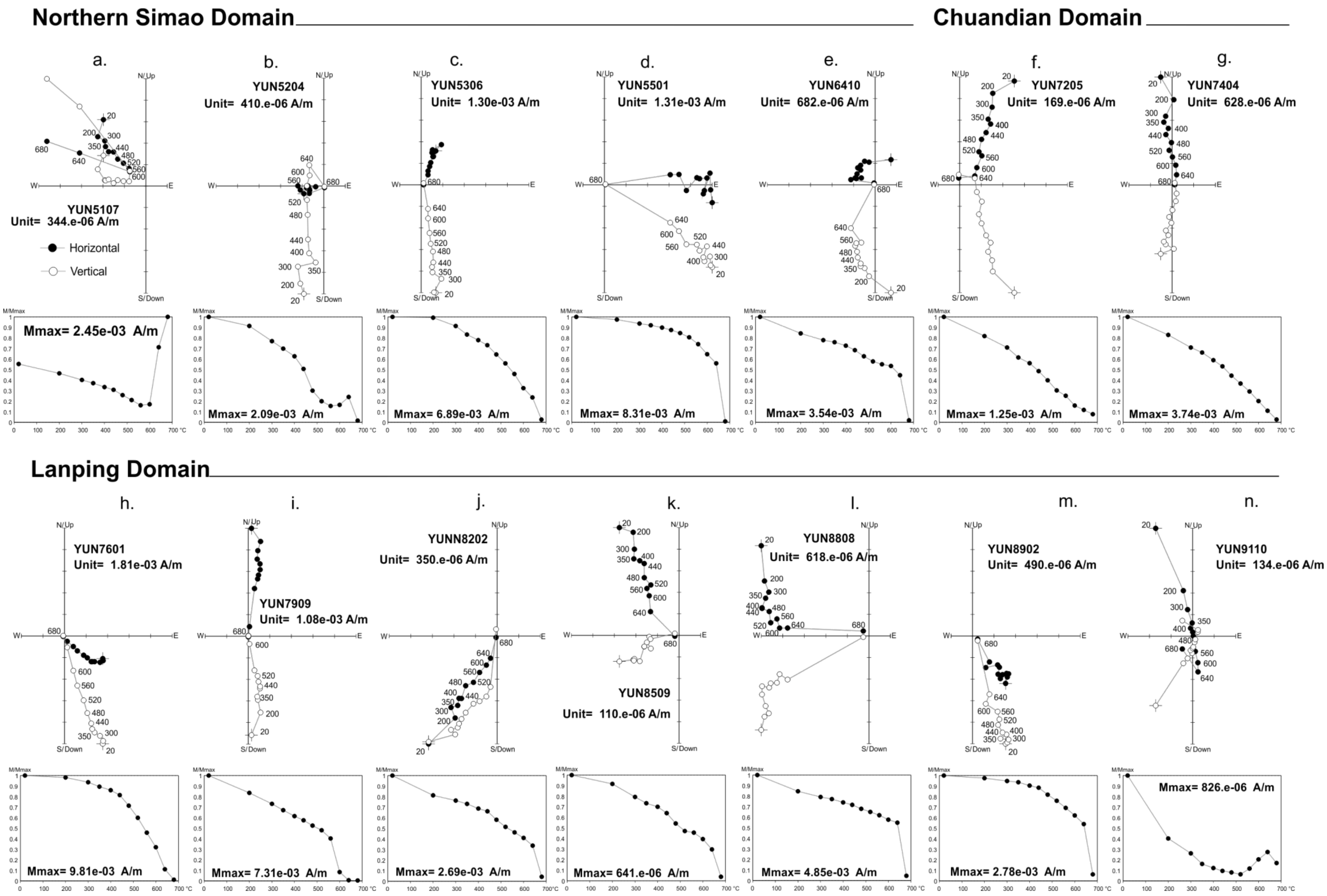

Northern Simao Domain
Chuandian Domain
Lanping Domain
a.
YUN5107
Unit= 344.e-06 A/m
Horizontal
Vertical
Mmax= 2.45e-03 A/m
b.
YUN5204
Unit= 410.e-06 A/m
Mmax= 2.09e-03 A/m
c.
YUN5306
Unit= 1.30e-03 A/m
Mmax= 6.89e-03 A/m
d.
YUN5501
Unit= 1.31e-03 A/m
Mmax= 8.31e-03 A/m
e.
YUN6410
Unit= 682.e-06 A/m
Mmax= 3.54e-03 A/m
f.
YUN7205
Unit= 169.e-06 A/m
Mmax= 1.25e-03 A/m
g.
YUN7404
Unit= 628.e-06 A/m
Mmax= 3.74e-03 A/m
h.
YUN7601
Unit= 1.81e-03 A/m
Mmax= 9.81e-03 A/m
i.
YUN7909
Unit= 1.08e-03 A/m
Mmax= 7.31e-03 A/m
j.
YUNN8202
Unit= 350.e-06 A/m
Mmax= 2.69e-03 A/m
k.
YUN8509
Unit= 110.e-06 A/m
Mmax= 641.e-06 A/m
l.
YUN8808
Unit= 618.e-06 A/m
Mmax= 4.85e-03 A/m
m.
YUN8902
Unit= 490.e-06 A/m
Mmax= 2.78e-03 A/m
n.
YUN9110
Unit= 134.e-06 A/m
Mmax= 826.e-06 A/m
N/Up
S/Down
W
E
M/Mmax
700 °C

Table 3. Paleomagnetic site-mean directions from the northern Simao, Chuandian and Lanping domains (Northern Indochina).

Table 2. Paleomagnetic directions from red beds from the northern Simao, Chuandian, and Lanping blocks (Northern Indochina)

Site	Geographic Coordinates		Age	Age (Ma)	Considered palepoles age (Ma)	Demagnetization component	Bedding (deg)	n/N	In Situ		Tilt Corrected		k	α_{95} (deg)	R (deg)	ΔR (deg)	F (deg)	ΔF (deg)
	Latitude °N	Longitude °E							*D* (deg)	*I* (deg)	*D* (deg)	*I* (deg)						
Northern Simao Block																		
YUN51	24°00'36.8"	101°04'47.8"	LK	100-145	30	ChRM	105/109	7/10	306.2	10.7	68.2	53.7	34.2	10.5	65.9	14.2	-20.2	8.9
YUN52	24°00'39.6"	101°05'12.6"	UJ	145-163	30	MT	61/51	9/10	240.5	71.5	61.3	57.5	58.7	6.8	58.9	10.2	-24.0	6.3
					150	HT		9/10	256.8	-68.1	247.1	-17.8	17.0	12.8	50.7	12.1	35.0	11.3
YUN53	23°56'26.8"	101°08'43.3"	UJ	145-163	30	ChRM	7/41	10/10	9.9	70.3	8.2	29.3	713.2	1.8	5.8	2.8	4.1	3.6
YUN54	23°55'57.0"	101°09'59.6"	MJ	163-174	30	ChRM	50/30	8/10	342.2	46.4	2.6	29.8	40.9	8.8	0.2	8.2	3.6	7.6
YUN55	23°56'22.3"	101°11'17.3"	UJ	145-163	30	ChRM	260/54	9/10	60.2	-0.5	48.8	49.1	46.3	7.6	46.4	9.4	-15.7	6.8
YUN56	23°56'56.3"	101°11'31.9"	LK	100-145	30	ChRM	33/56	10/10	283.7	86.1	28.5	35.2	49.4	6.9	26.1	7.0	-1.8	6.4
YUN57	23°57'06.9"	101°12'41.4"	LK	100-145	30	ChRM	76/81	9/10	252.0	45.0	80.8	53.8	224.6	3.4	78.4	5.0	-20.4	4.3
YUN58	23°56'55.6"	101°13'31.7"	LK	100-145	30	ChRM	10/70	9/10	201.8	77.1	6.9	32.6	52.1	7.2	4.5	7.1	0.8	6.6
YUN59	23°56'23.2"	101°14'34.6	LK	100-145	30	ChRM	348/31	9/10	38.8	64.7	13.4	39.5	66.7	6.4	11.0	6.9	-6.1	6.0
YUN60	23°56'25.8"	101°14'57.7"	UJ	145-163	30	MT	257/54	10/10	74.5	-15.0	73.9	39.0	24.9	9.9	71.5	10.2	-5.6	8.4
YUN61	23°56'00.4"	101°16'22.8"	UJ	145-163	30	ChRM	5/46	10/10	108.3	35.1	75.5	32.4	102.8	4.8	73.1	5.0	1.0	5.0
YUN62	23°55'53.2"	101°16'38.7"	UJ	145-163	30	ChRM	24/11	9/10	41.9	64.3	37.0	53.7	118.3	4.8	34.6	6.7	-20.3	5.0
YUN63	23°57'11.5.0"	101°17'35.5"	MJ	163-174	30	ChRM	266/56	9/10	41.5	7.2	18.8	41.1	75.3	6.0	16.4	6.6	-8.2	5.8
YUN64*	23°55'27.5"	101°22'21.3"	UT	201-237	30	HT	184/55	9/10	357.0	71.2	187.8	53.6	17.3	12.7	-5.4	33.6	-37.8	10.5
YUN65*	23°56'09.7"	101'22'33.8"	UT	201-237	30	HT	5/80	10/10	2.1	49.8	2.9	-30.1	27.7	9.3	-0.3	11.5	-16.4	8.0
YUN66*	23°56'15.9"	101°22'44.1"	UT	201-237	30	ChRM	294/114	6/10	18.7	51.3	336.0	-21.7	30.6	12.3	16.3	15.7	-17.9	10.2
Chuandian Block																		
YUN67*	24°15'08.5"	101°28'44.3"	UT	201-237	20	ChRM	_	10/11	329.6	25.4	_	_	19.8	11.1	-32.8	9.9	9.8	9.4
YUN68*	24°13'33.6"	101°30'47.7"	UT	201-237	20	ChRM	290/26	6/10	2.3	39.3	346.4	27.7	11.7	20.4	-0.1	21.0	-4.1	16.3
YUN69*	24°14'26.2"	101°31'53.9"	UT	201-237	20	ChRM	118/29	6/10	348.7	53.0	34.6	62.1	11.6	20.5	-13.7	27.9	-17.8	16.4
YUN70*	24°19'10.4"	101°37'20.9"	LJ	174-201	20	ChRM	66/31	8/10	16.8	36.3	27.1	13.6	29.8	10.3	14.4	10.3	-1.0	8.8
YUN71*	24°21'59.7"	101°38'47.1"	MJ	163-174	20	ChRM	69/45	7/10	26.3	80.8	61.1	38.0	18.6	14.4	23.9	14.2	-45.4	14.4
YUN72*	24°24'08.8"	101°39'42.9"	MJ	163-174	20	MT	80/47	9/10	29.0	55.7	52.7	17.7	33.1	9.1	26.6	13.0	-20.2	8.0
YUN73*	24°26'12.2"	101°39'24.7"	MJ	163-174	20	MT	61/50	7/10	21.9	71.7	48.3	25.1	11.8	18.3	19.5	70.2	-36.2	14.7
YUN74*	24°27'19.3"	101°39'34.2"	UJ	145-163	20	ChRM	68/36	7/10	355.1	39.7	15.2	22.6	28.7	11.4	-7.3	11.9	-4.2	9.6
YUN75*	24°29'15.0"	101°39'49.1"	UJ	145-163	20	MT	12/74	7/10	154.2	59.1	35.7	38.8	67.0	7.4	151.8	11.6	-23.5	6.8

Site	Geographic Coordinates		Age	Age (Ma)	Considered palepoles age (Ma)	Demagnetization component	Bedding (deg)	n/N	In Situ		Tilt Corrected		k	α_{95} (deg)	R (deg)	ΔR (deg)	F (deg)	ΔF (deg)
	Latitude °N	Longitude °E							*D* (deg)	*I* (deg)	*D* (deg)	*I* (deg)						
Lanping Block																		
YUN76	25°43'20.7"	099°55'31.2"	LK	100-145	120	ChRM	162/57	10/10	123.0	71.4	149.8	18.0	212.3	3.3	139.4	3.7	24.8	3.9
YUN77	25°45'05.9"	099°54'44.2"	LK	100-145	120	ChRM	342/29	9/10	317.7	6.3	316.2	-20.1	13.6	14.5	125.8	12.3	22.8	11.7
YUN78	25°45'43.0"	099°54'41.6"	LK	100-145	120	ChRM	193/60	8/10	322.6	58.9	227.7	45.5	19.8	12.8	-142.6	14.6	-3.1	10.4
YUN79*	25°26'14.1"	099°26'31.1"	LK	100-145	20	ChRM	21/38	8/10	3.7	40.1	7.8	3.3	811.9	1.9	5.5	3.0	33.6	3.8
YUN80	25°25'44.7"	099°27'06.5"	LK	100-145	120	ChRM	101/24	7/10	290.1	34.6	295.3	58.1	19.4	14.0	-75.0	21.4	-15.7	11.3
YUN81	25°25'28.5"	099°28'24.0"	LK	100-145	120	ChRM	331/48	8/10	64.5	76.8	348.6	41.4	69.6	6.7	-21.7	7.4	0.9	6.0
YUN82	25°25'35.9"	099°30'01.3"	LK	100-145	120	MT	297/51	8/10	205.1	30.4	230.5	19.9	15.8	14.4	-139.8	12.2	22.4	11.6
					120	HT		8/10	200.8	64.6	264.6	37.2	17.0	12.7	-105.7	12.7	5.2	10.3
YUN83	25°25'23.1"	099°30'57.6"	LK	100-145	120	HT	50/40	9/10	333.0	-33.5	305.4	-32.9	25.3	10.4	115.1	10.0	9.4	8.6
YUN84**	25°27'56.0"	099°33'17.6"	UJ	145-163	20	MT	117/94	9/10	319.3	12.7	(325.1)	(38.1)	14.9	13.8	-37.2	14.0	-1.2	11.3
					150	HT		8/10	316.5	31.5	90.8	49.9	8.7	19.9	73.9	25.6	3.9	16.3
YUN85**	25°27'49.3"	099°33'41.6"	UJ	145-163	20	MT	75/55	9/10	355.9	51.3	(13.2)	(45.9)	10.1	17.0	10.9	19.5	-9.0	13.7
					150	HT		8/10	320.8	25.4	354.6	33.3	10.1	18.1	-22.3	18.7	20.5	15.5
YUN86	25°28'16.2"	099°34'42.2"	UJ	145-163	150	HT	86/53	9/10	324.3	11.2	345.5	31.9	55.1	7.0	-31.4	8.8	21.9	7.5
YUN87**	25°28'11.2"	099°52'09.6"	LK	100-145	20	MT	115/65	9/10	343.9	27.7	(354.1)	(39.0)	18.4	12.3	-8.2	12.7	-2.1	10.2
YUN88**	25°29'21.7"	099°36'26.9"	LK	100-145	20	MT	252/28	8/10	0.6	29.4	(356.0)	(31.6)	10.4	18.0	-6.3	16.8	5.3	14.5
					120	HT		7/10	283.1	16.2	282.1	-8.0	12.0	18.1	91.8	14.5	34.5	14.4
YUN89	25°29'24.4"	099°38'09.6"	LK	100-145	120	HT	22/71	10/10	143.6	64.6	47.1	30.5	80.3	5.4	36.8	5.5	11.9	5.2
YUN90	25°30'52.2"	099°41'15.1"	UJ	145-163	150	HT	275/50	8/10	284.8	-6.5	292.3	-55.4	12.0	16.5	95.4	24.2	-1.5	13.8
YUN91**	25°28'36.2"	099°54'08.4"	LK	100-145	20	MT	135/85	9/11	8.1	19.9	(18.9)	(33.2)	8.0	19.4	16.6	18.4	3.7	15.5
					120	HT		9/11	170.3	-12.0	238.7	-54.4	17.7	12.6	41.9	18.2	-0.5	11.1
YUN92**	25°27'12.7"	099°47'08.9"	UJ	145-163	20	MT	262/53	9/10	9.2	44.5	(352.8)	(47.1)	40.4	8.2	-9.5	9.8	-10.2	7.3
YUN93**	25°27'09.4"	099°50'24.9"	LK	100-163	20	MT	120/57	8/10	341.9	16.4	(346.9)	(28.6)	35.8	9.4	-15.4	8.8	8.3	8.1
YUN94**	25°29'03.7"	099°57'02.7"	MJ	163-174	20	ChRM	276/45	8/10	354.6	41.1	(344.4)	(37.3)	37.0	9.2	-17.9	9.4	-0.3	8.0

Ages: UT, Upper Triassic; LJ, Lower Jurassic; MJ, Middle Jurassic; UJ, Upper Jurassic; LK, Lower Cretaceous. Demagnetization component: ChRM, characteristic remanent magnetization (300-680°C); MT, medium temperature (300-640°C) component; HT, high temperature component (640-680°C). The geographic coordinates are referred to WGS84 datum. Age in Ma is from the geologic timescale of Choen et al. [2013]. Bedding is expressed in dip azimuth/dip values. D and I are site mean declination and inclination calculated before and after tectonic correction; k and α_{95} are statistical parameters after Fisher [1953]; n/N is number of samples giving reliable results/number of studied samples at a site. Site mean rotation R and flattening F values, and relative errors ΔR and ΔF (according to Demarest [1983]) are relative to coeval D and I Eurasian values expected at the sampling area considering Eurasian paleopoles from Cogné et al. [2013], or Torsvik et al. [2012] for poles older then 150 Ma. * Post-tilting remagnetized sites, R and F values are calculated using the in-situ D and I values. ** syn-tilting remagnetized sites, the R and F values are calculated using the D and I values obtained at 30% unfolding (in parenthesis).

All paleomagnetic direction are shown in Figure 65 for Northern Simao and Chuandian domains and in Figure 68 for Lanping domain. Site-mean directions were evaluated by averaging out ChRMs, MT and HT components from the individual specimens. Data are shown in Table 3, and a fold test was applied separately to the different zones and group sites (see Table 4).

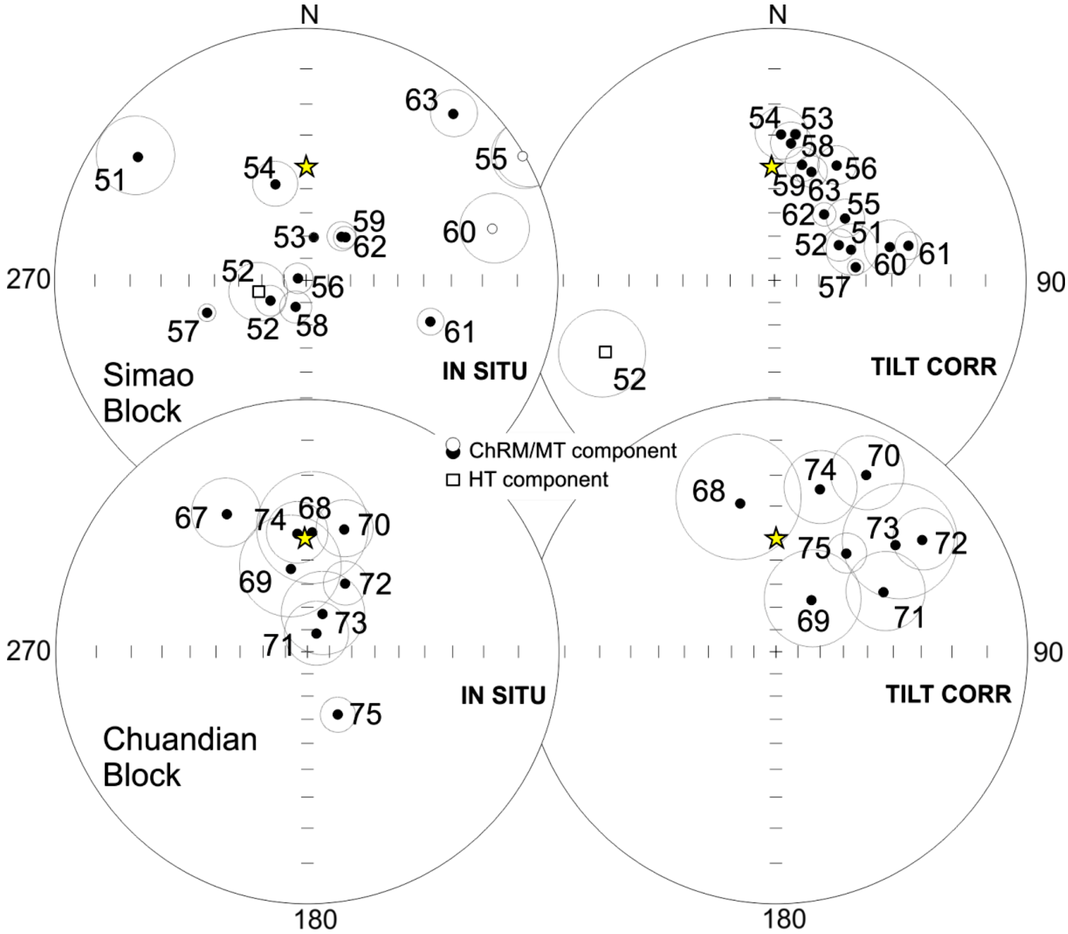

Figure 65. Equal-angle projection of the paleomagnetic directions obtained from Triassic-Cretaceous red beds exposed in the Simao and Chuandian domains. The three Triassic sites (Yun64, 65, 66) from the Simao domain are shown in Figure 67. The yellow stars represent the normal polarity geocentric axial dipole field direction (*D*=0°; *I*=42°) expected at the study area.

As shown in Figure 65, both the *in situ* and tilt-corrected directions, for Simao and Chuandian domains, are far from the GAD field direction expected at the sampling localities (represented by the yellow star). All tilt-corrected directions from Simao domain (sites from Yun51 to

Yun63; Yun64, Yun65, Yun66 are Triassic red beds) are of normal polarity, excepted for site Yun52, where a reverse-polarity HT of possible primary origin was observed. Two different components (of both normal and reverse polarity) was isolated in the 350-600°C (MT) and 640°C (HT) interval, respectively (Figure 66). The mean values are shown in Table 3.

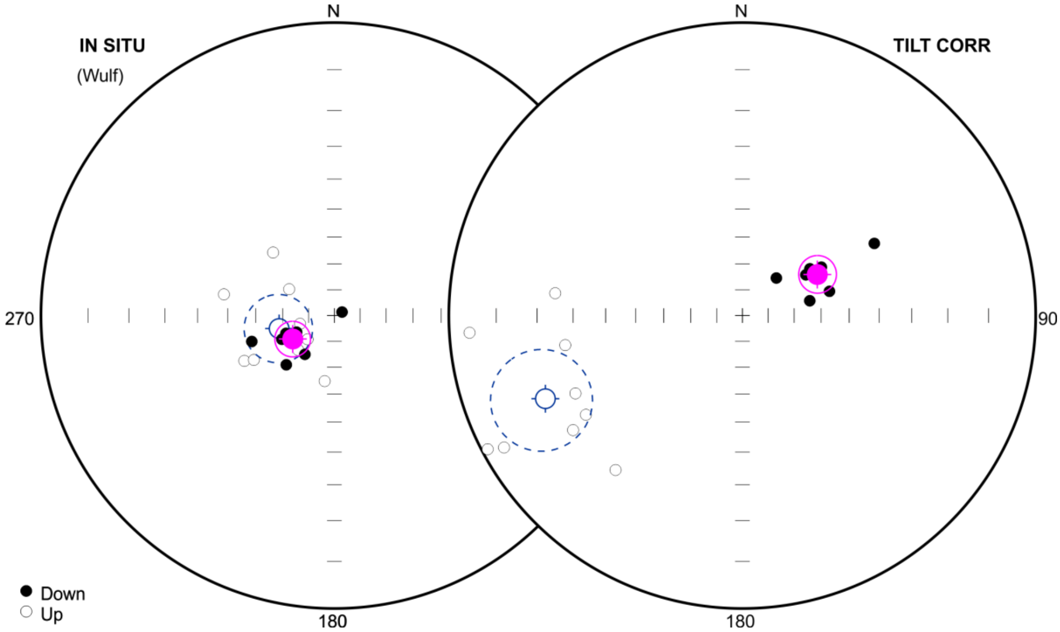

Figure 66. Different components and polarity of the Yun52. Blue (pink) open (solid) circles represent the mean paleomagnetic directions and relative 95% confidence cone of HT and MT components, respectively (see Table 3 for mean values). The yellow stars represent the normal polarity geocentric axial dipole field direction (*D*=0°; *I*=44°) expected at the study area.

The paleomagnetic data from Jurassic-Cretaceous sites from Northern Simao domain (from Yun51 to Yun63) support a positive fold test at 99% significance level according to *McFadden* [1990; N=13; $Scos_{insitu}$= 8.5; $Scos_{tilt\ corrected}$= 1.8; critical Scos at the 95% significance level = 4.2; critical Scos at the 99% significance level = 5.9; see table 4]. Maximum ĸ and minimum Scos values arise at 92% of complete unfolding. This suggest a pre-folding [~ 30 Ma according to *Yang et al*., 2001b; *Sato et al* ., 2001; *Gao et al*., 2017 and reference therein].

In contrast, Upper Triassic red beds sites Yun64, Yun65 and Yun66 support a negative fold test at 99% significance level [N=3; $Scos_{insitu}$= 1.4; $Scos_{tilt\ corrected}$= 2.7; critical Scos at the 95% significance level = 2.1; critical Scos at the 99% significance level = 2.7; see Table 4]. Maximum ҡ and minimum Scos values arise at 0% of complete unfolding. This suggest a post-folding magnetization (post- 30 Ma).

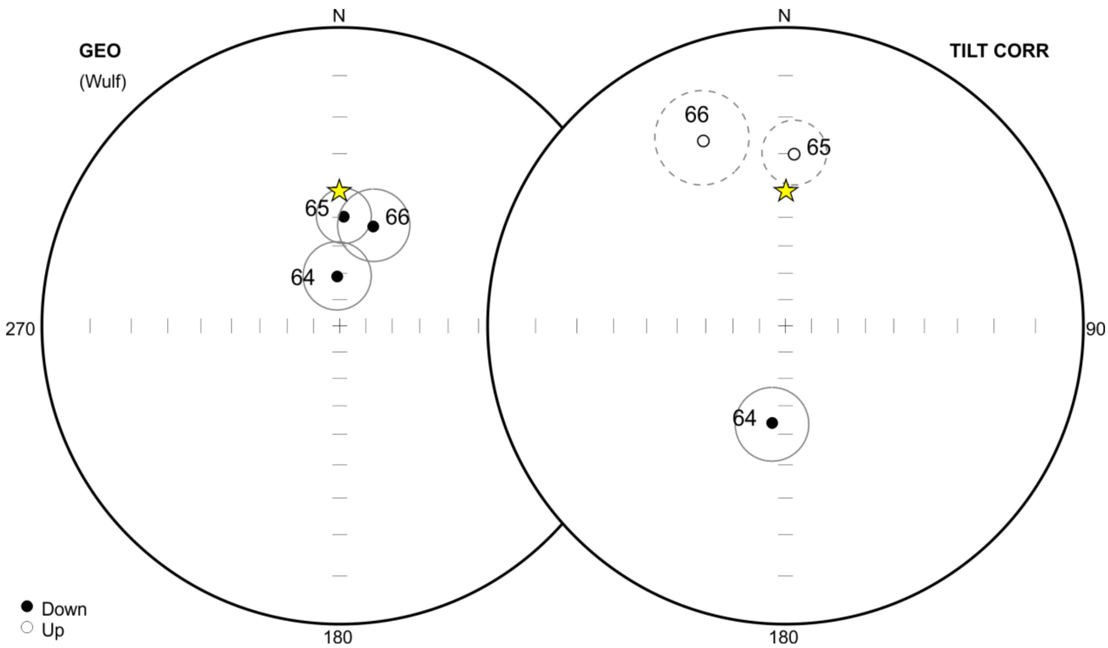

Figure 67. Equal-angle projection of the paleomagnetic direction obtained from three Triassic red beds sites exposed in the Simao block. The yellow stars represent the normal polarity geocentric axial dipole field direction (*D*=0°; *I*=42°) expected at the study area.

All components of Chuandian block sites are also of normal polarity and far from the GAD field direction expected at the sampling localities (Figure 65). The paleomagnetic data from this group of samples (sites from Yun67 to Yun75) support a negative fold test at 99% significance level [N=9; $Scos_{insitu}$= 0.6; $Scos_{tilt\ corrected}$= 3.9; critical Scos at the 95% significance level = 3.5; critical Scos at the 99% significance level = 4.8; see Table 4]. Maximum ҡ values arise at 32% of complete unfolding and minimum Scos values arise at 0% of complete unfolding. Also in this case, these suggest a post-folding magnetization (post-Late Eocene-Early Oligocene).

Different behavior is observed at sites close to the faults ARRSZ and Chongshan fault (CF), and at the centre of the Lanping block. In the Lanping block, our three Lower Cretaceous sites (Yun76, Yun77, Yun78), located just west of the Ailaoshan Red River fault (near Yangby city, Figure 68) support a positive fold test at 99% significance level suggesting a pre-folding magnetization [N=3; $Scos_{insitu}$= 2.5; $Scos_{tilt\ corrected}$= 0.1; critical Scos at the 95% significance level = 2.1; critical Scos at the 99% significance level = 2.7; see Table 4]. Maximum ĸ values arise at 100% of complete unfolding and minimum Scos values arise at 96% of complete unfolding.

Sites located near the Chongshan fault (from site Yun80 to Yun83) support an indeterminate fold test at 99% significance level [N=4; $Scos_{insitu}$= 0.4; $Scos_{tilt\ corrected}$= 0.8; critical Scos at the 95% significance level = 2.3; critical Scos at the 99% significance level = 3.2; see Table 4]. Maximum ĸ values arise at 8% of complete unfolding and minimum Scos values arise at 29% of complete unfolding. No evidence of remagnetization is apparent here.

Figure 68. Equal-angle projection of the paleomagnetic directions obtained from Jurassic-Cretaceous red beds exposed in the Lanping domain. The yellow stars represent the normal polarity geocentric axial dipole field direction (*D*=0°; *I*=44°) expected at the study area.

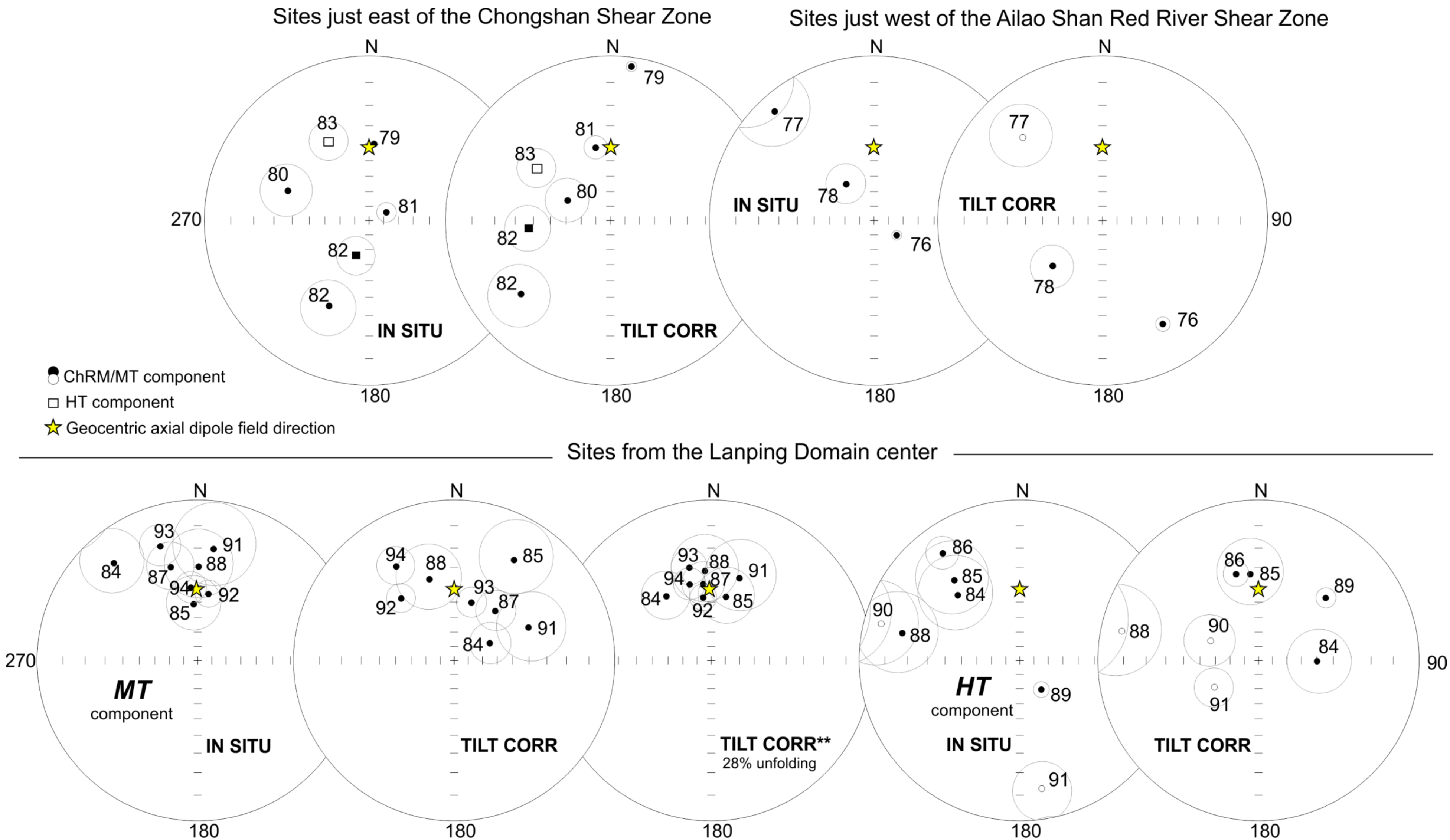
Sites just east of the Chongshan Shear Zone
Sites just west of the Ailao Shan Red River Shear Zone
N
270
90
180
IN SITU
TILT CORR
ChRM/MT component
HT component
Geocentric axial dipole field direction
Sites from the Lanping Domain center
MT
component
HT
component
TILT CORR**
28% unfolding
76
77
78
79
80
81
82
83
84
85
86
87
88
89
90
91
92
93
94

Sites with MT component (Yun84, 85, 86, 88, 89, 90, 91) support a positive fold test at 99% significance level suggesting a syn-folding magnetization [N=8; $Scos_{insitu}$= 5.3; $Scos_{tilt\ corrected}$= 6.9; critical Scos at the 95% significance level = 3.3; critical Scos at the 99% significance level = 4.6; see Table 4]. Maximum κ values arise at 32% of complete unfolding and minimum Scos values arise at 28% of complete unfolding.

At the end, sites with HT component support a positive fold test fold test at 99% significance level suggesting a pre-folding magnetization [N=7; $Scos_{insitu}$= 6.1; $Scos_{tilt\ corrected}$= 0.3; critical Scos at the 95% significance level = 3.1; critical Scos at the 99% significance level = 4.2; see Table 4]. Maximum κ values arise at 100% of complete unfolding and minimum Scos values arise at 98% of complete unfolding.

Table 3. Results of the fold test [according to McFadden , 1990] for sites from different domains.

Sites (Yun)	N	95% cr. va	99% cr. va	In Situ Statistics					Unfolded Statistics					Minimum SCOS Statistics						Test result
				D (deg)	I (deg)	k	α_{95} (deg)	SCOS	D (deg)	I (deg)	k	α_{95} (deg)	SCOS	D (deg)	I (deg)	k	α_{95} (deg)	SCOS	% unfolding	
Northern Simao Domain																				
51,52,53,54,55,56, 57,58,59,60,61,62,63	13	4.200	5.860	31.1	66.3	2.6	32.2	8.494	37.4	45.7	11.9	12.5	1.756	37.3	47.6	12.3	12.3	0.087	92%	P
64,65,66	3	2.076	2.662	7.6	57.7	36.9	20.6	1.355	339.8	-3.2	1.1	180.0	2.701	7.6	57.7	36.9	20.6	1.355	0%	N
Chuandian Domain																				
67,68,69,70,71, 72,73,74, 75	9	3.497	4.849	4.2	58.2	7.2	20.5	0.606	24.4	31.0	6.0	22.8	3.914	4.2	58.2	7.2	20.5	0.606	0%	N
Lanping Domain																				
76,77,78	3	2.076	2.662	128.7	64.8	1.8	180.0	2.479	162.8	33.5	3.8	74.7	0.112	162.4	34.7	3.8	75	0.009	96%	P
80,81,82,83	4	2.335	3.180	205.9	64.0	2.7	69.9	0.435	259.5	74.2	2.0	92.3	0.787	217.2	69.0	2.7	70.7	0.002	29%	I
84,85,87,88,91,92,93,94 (ChRM/MT-HT)	8	3.298	4.562	350.7	31.3	16.3	14.1	5.321	12.8	45.2	5.8	25.2	6.865	353.6	38.3	30.1	10.3	0.502	28%	S
84,85,86,88,89,90,91 (HT)	7	3.086	4.253	6.4	42.6	1.5	79.6	6.095	54.6	48.5	4.0	34.5	0.268	54.0	48.9	4.0	34.5	0.031	98%	P

N, number of sites; D and I are mean declination and inclination, respectively; k and α_{95} are statistical parameters after Fisher [1953]; SCOS, 95% cr.va and 99% cr.va are statistical parameters and 95-99% critical values, respectively [see McFadden, 1990]. Test results: P positive, S Syn-folding, N negative, I indeterminate.

Table 4. Results of the fold test [according to *McFadden*, 1990] for sites from different domains.

7.1 Rotation pattern

To evaluate tectonic rotations with respect to Eurasia, the paleomagnetic directions were compared to coeval Eurasian paleopoles from *Torsvik et al*. [2012] and *Cogné et al*. [2013]. Paleomagnetic rotations (R) and flattening (F) with relative errors, according to *Demarest* [1983], are reported in Table 3.

As discussed above, the paleomagnetic results revealed different structural behavior in the analyzed domains. **In the Northern Simao block** (west to the fault, Figure 69) clockwise rotation between ~30°-70° CW have been recorded. Some sites show a null rotation. At site Yun52, located at ~30 km from the western boundary of the Ailaoshan Red River Shear Zone, rotations from MT and HT components are similar, confirming the reliability of the normal polarity data set.

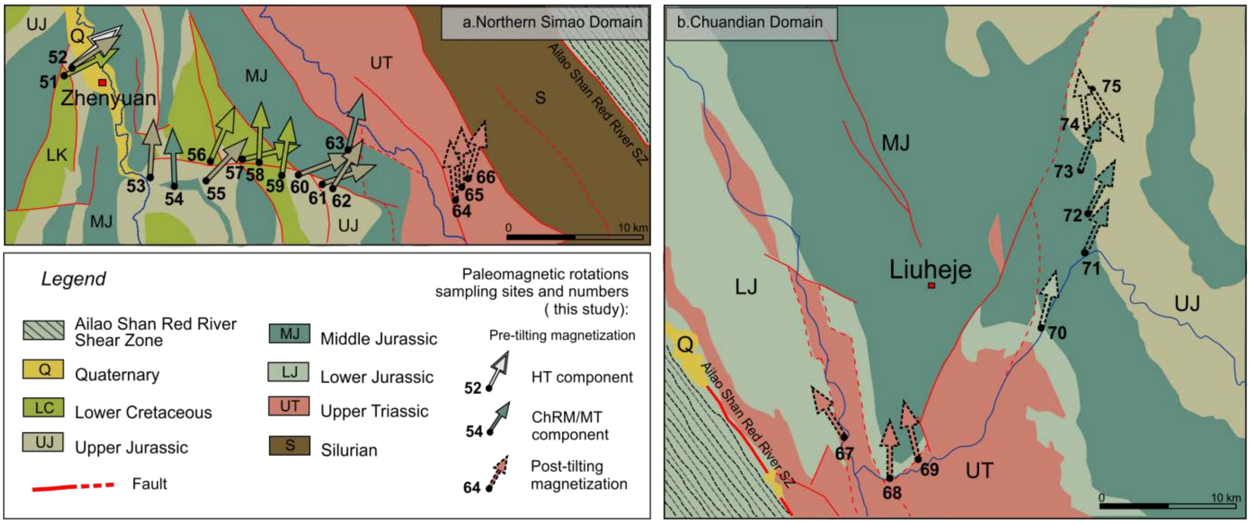

Figure 69. Paleomagnetic rotations with respect to Asia from the (a) Northern Simao and (b) Chuandian domains, along the Ailaoshan Red River Shear Zone (geological map modified after *Bureau of Geology and Mineral Resources of Yunnan Province*, 1990). Rotation values are reported in Table 3. Solid contour arrows show the rotation values with respect to tilt-corrected characteristic/medium temperature (ChRM/MT) paleomagnetic directions and pre-tilting normal-polarity magnetic overprint (30 Ma Asia paleopole, see text). The rotation of reverse-polarity high temperature (HT) component from site Yun52 was also calculated with respect to 150 Ma paleopole, coeval to sediment age. Dashed arrows show rotation values relative to in-situ paleomagnetic directions (post-tilting remagnetization).

From W to E (Figure 69a), we report three blocks undergoing 57° ± 9°, 48° ± 26° and 70° ± 1° CW rotations, separated by two unrotated blocks (sites Yun53-54 and Yun58-59). Finally the two easternmost sites Yun62-63 define a 23° ± 13° CW rotation.

Directions of the three Triassic sites located at about 10 km from the western boundary of the ARRSZ (Yun64, 65, 66) and sites from the **Chuandian domain** (Yun67 to Yun75) post-date tilting, evaluated using the 20 Ma Asia pole and in-situ paleomagnetic directions. Rotation values are small (Figure 69a,b), except for easternmost site Yun75 located at ~35 km from the fault, which is possibly an outlier (CW rotation more than 150° and bedding was completely different that in nearby sites, Table 2). The post-tilting rotations of the three Triassic sites in the Northern Simao domain (4° ± 11° on average), the three sites located just east the ARRSZ (-15° ± 16°) and the five sites located farther east in the Chuandian domain (15° ± 14°) seem to be remagnetized after folding, according to the fold test result. These are not or barely significant, implying an overall null rotation of the ARRSZ and the Chuandian domain occurring after magnetic overprint (in turn post-dating 25-15 Ma folding). Thus our paleomagnetic data from the ARRSZ and the Chuandian domain are not relevant to constrain their rotation history, as we cannot exclude a recent overprint (i.e. within the last 0.78 Ma of the Brunhes polarity chron).

Differently from the Gaoligong case, the distribution of the rotation values with respect to the distance to both sides of the Ailaoshan Red River Shear Zone (km), do not show a significant logarithmic trend. West of the fault, in the Northern Simao block, sites show different crustal portion (size < 5 km) undergoing independent variable rotations (Figure 70a). East of the fault, in the Chuandian domain, the low and post-tilting rotations suggest a recent overprint, probably after 25-15 Ma (Figure 70b).

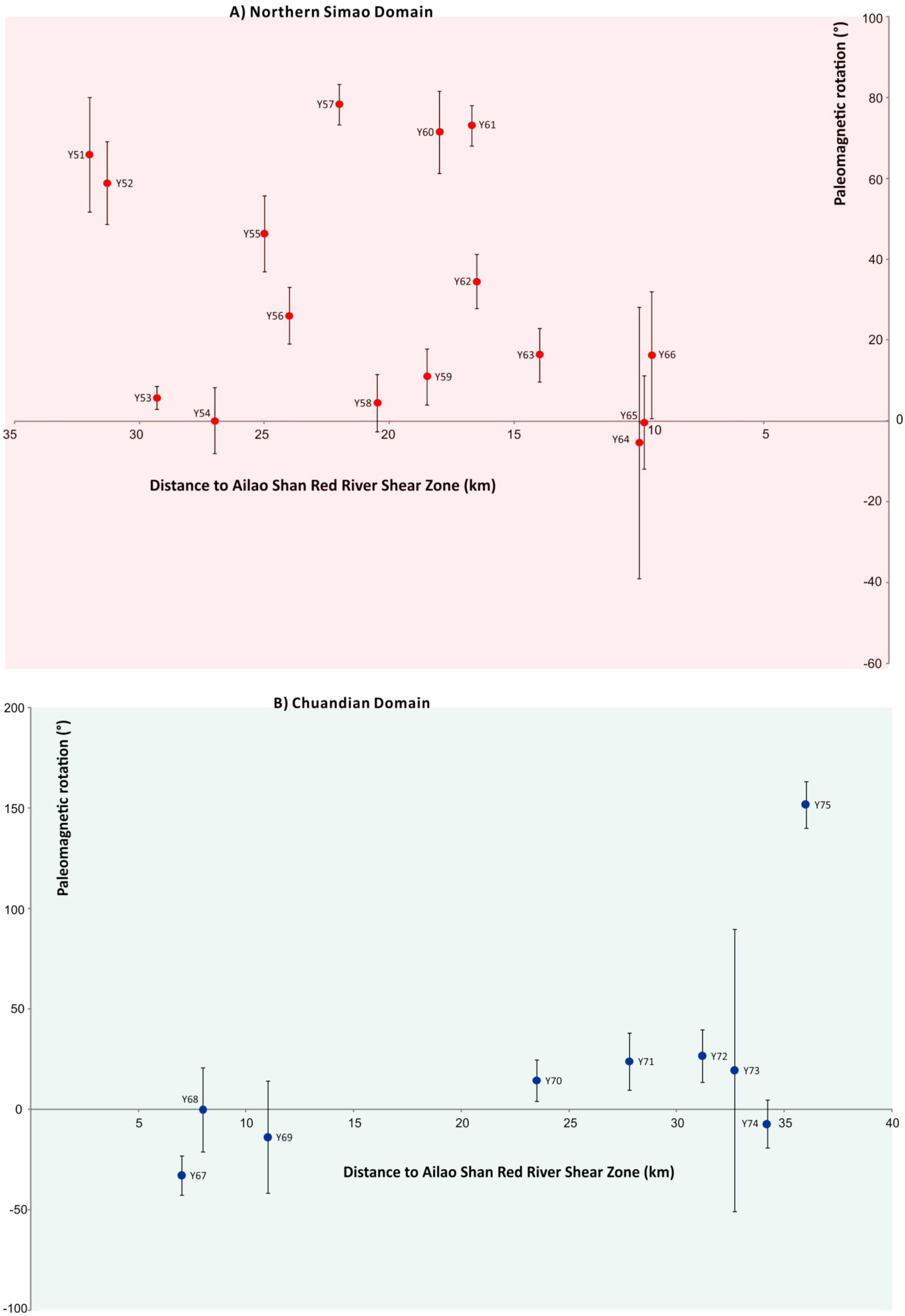

Figure 70. Plot of rotation with respect to Eurasia versus site distance to both Ailaoshan Red River Shear Zone in Northern Simao (a) and Chuandian (b) domains. See figures 69 an 70 for site location. Sense and amount of rotation are defined by the smaller angel between observed and expected Eurasian declinations, thus rotation values are ≤|180°| by definition.

In the northern transect adjacent to Lanping block (Figure 71), we identified three different rotation patterns. Sites sampled close to the Chongshan Shear Zone (Yun80 to Yun83- site Yun79 is remagnetized post-folding) yield a 22°-140° CCW rotation (the MT and HT components from site Yun82 give a 106° ± 13° and 140° ± 12° CCW rotation, respectively). Sites from the block centre (Yun84 to Yun94) showed two different magnetization components: HT component (640-680°C) yield variable 37°-115° CW rotation interrupted by two sites just E of Yongping (Yun85 to Yun86) where a slightly 27° ± 6° CCW rotation is recorded. MT components (300-640°C) from the same sites are yield remagnetization later acquired at 28% unfolding, and a subsequent lack of rotation (Figure 68).

Finally, three sites located adjacent to ARRSZ, yields a strong CW (CCW) rotation between 126° and 143° in Yun76 and Yun77 (Yun78), respectively. The sense is unclear because they approach 180°, so cannot exclude that this site rotated CW more than 180°.

Unfortunately, sites located adjacent to the shear zone are not enough to evaluate the pattern of rotation approaching major structures.

In Figure 72a,b report separately the direction of ChRM/MT and HT component pre-, syn- and post-tilting. The ChRM/MT give a congruous rotation values of 8° ± 16° on average, scenario that could be confirm related magnetic overprint due to fluid migration.

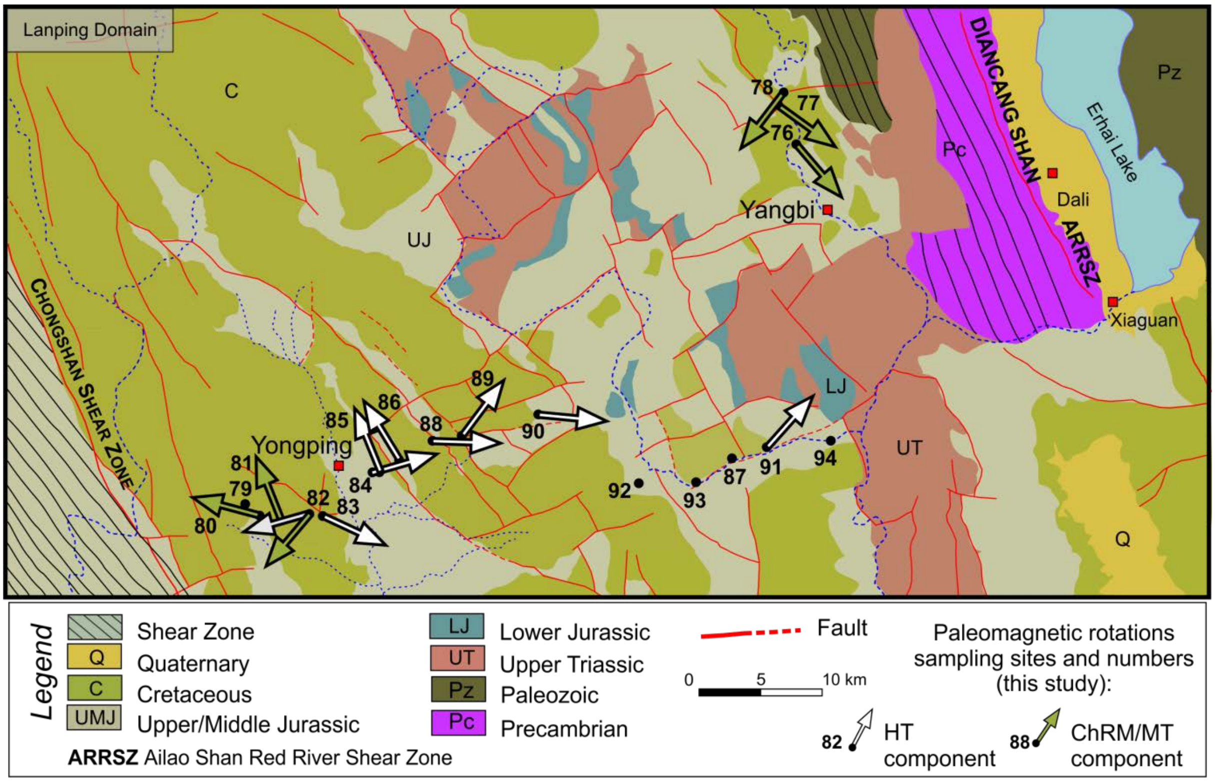

Figure 71. Paleomagnetic rotations with respect to Asia from the Lanping domain (geological map modified after *Bureau of Geology and Mineral Resources of Yunnan Province*, 1990). White and green arrows show the rotations evaluated after high temperature (HT) and characteristic (ChRM) magnetization components, respectively. The medium temperature (MT) components shown to have undergone an overprint at 28% unfolding (see text) are shown in Figure 72a,b.

a)

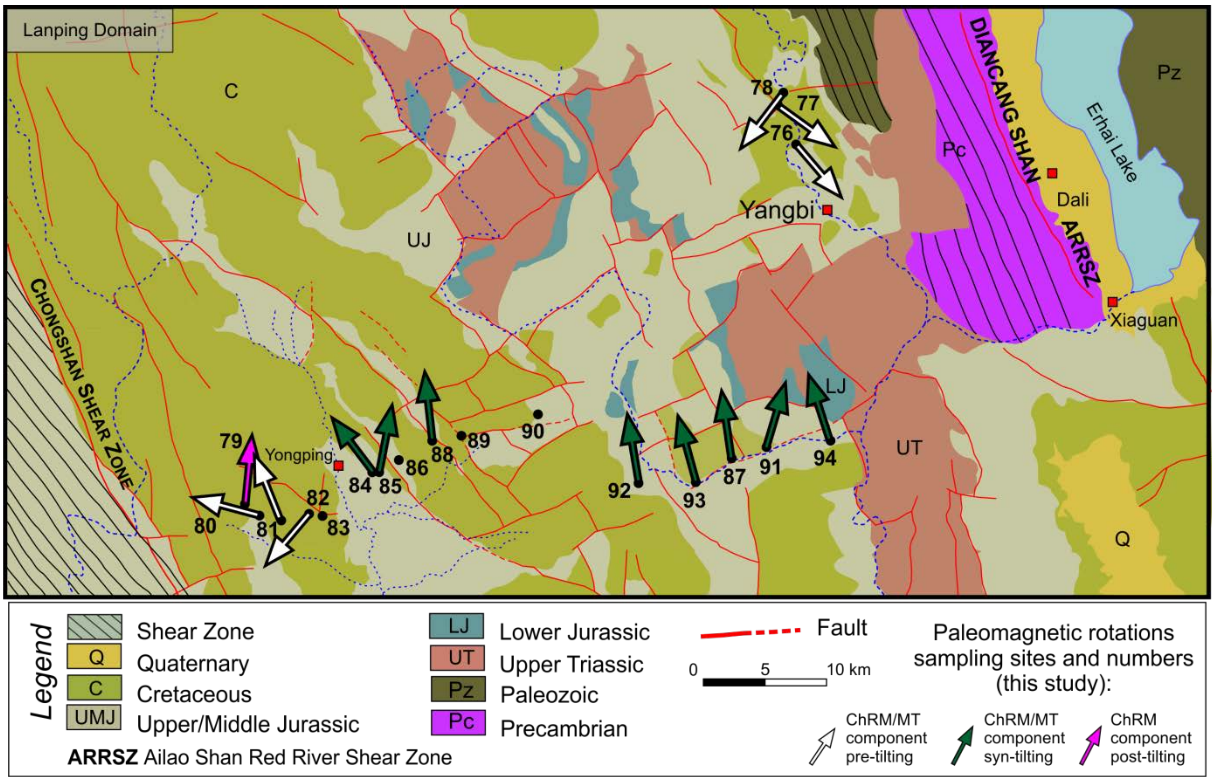

b)

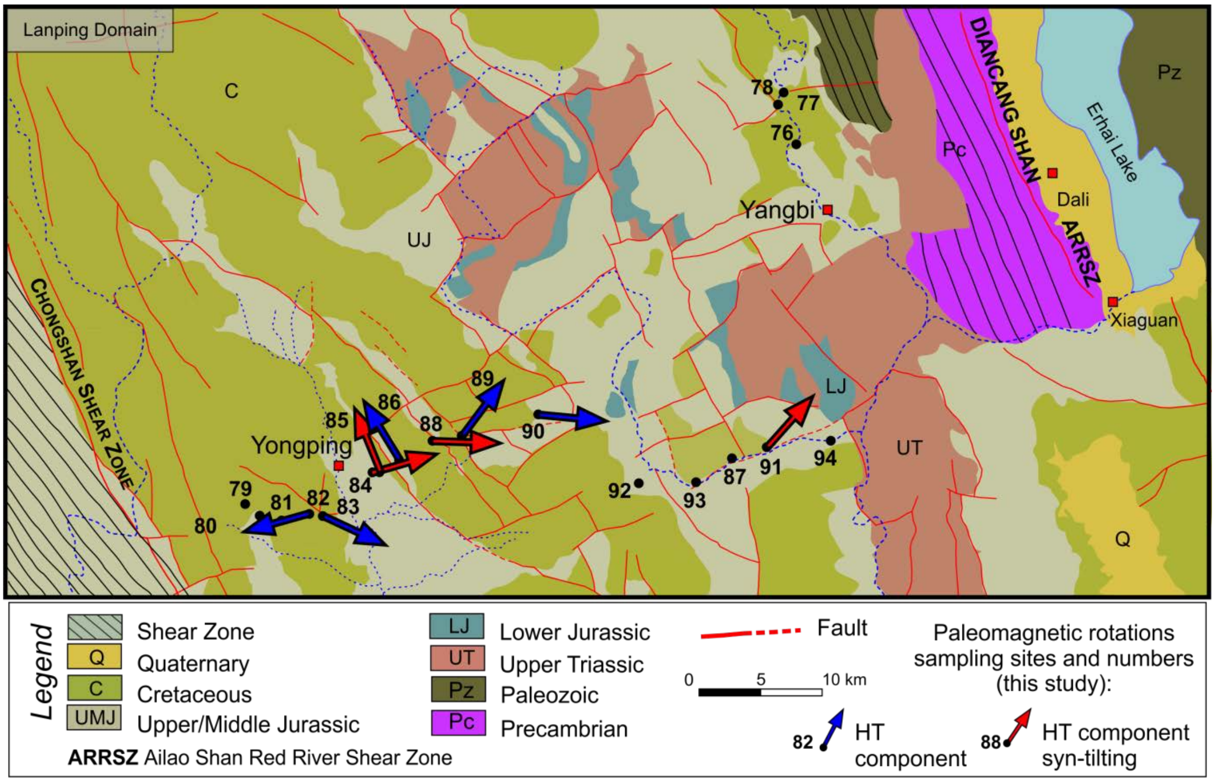

Figure 72. Paleomagnetic sampling areas in the north-western Lanping domain of the Ailaoshan Red River Shear Zone modified after *Bureau of Geology and Mineral Resources of Yunnan Province*, 1990. Rotation values are reported in Table 3. a) White, green and pink arrows indicate ChRM/MT components pre-, syn- and post-tilting**;** b) Blue and red HT components pre- and syn-tilting.

Certainly, our data show that the northern Simao and the Lanping Domain do not rotate rigidly, but are composed of small (few km of size) blocks/domains rotating CW, separated by non-rotating domains, as previously reported by other authors [e.g. *Chen et al.,* 1995; *Tanaka et al.,* 2008; *Tong et al.,* 2013].

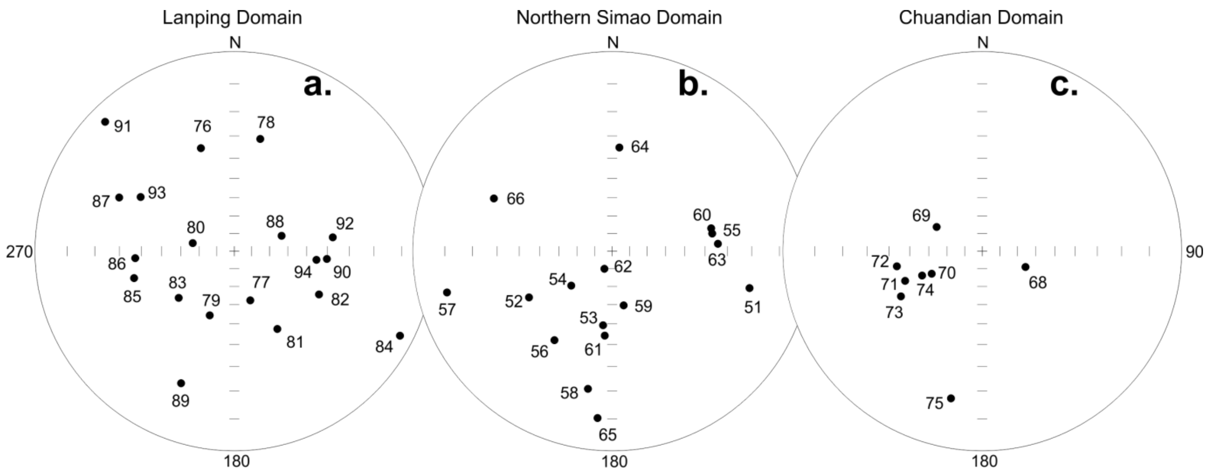

Figure 73. Poles of bedding at sampling sites from a) Lanping, b) Northern Simao, and c) Chuandian domains.

As clearly shown in Figure 73, the dip of strata in the studied sites is differently oriented being scattered in the Lanping domain, confirming the strong and non-coaxial deformation of the block itself as shown on the geological map; in northern Simao, except for some sites, a SE dip orientation is observed; finally, in the Chuandian domain the poles concentration in SW quadrant is much more clustered.

The relation between paleomagnetic rotations and orogenic trends is routinely investigated through the so-called "oroclinal plot", evaluating the correlation between rotations and structural (fold axis) directions (*Schwartz and Van der Voo*, 1983; *Cifelli and Mattei*, 2010; *Weil et al.*, 2010). A positive correlation indicates orogens that are (progressively) bent, normally by rotational thrust sheet emplacement. Conversely, a lack of correlation indicates chains –or primary arcs - that originated with a curved shape without any rotation (typically around a foreland buttress or an hinterland indenter).

Data from both the Simao and the Lanping domains are very scattered, and show a lack of correlation between rotations and bed strikes (that are used as proxies of unavailable fold axes, Figure 74). The data show that highly variable structural trends arise, if local bed strikes are back-rotated according to paleomagnetic data. Such result makes further unlikely a thrust-driven rotation scenario or rotations related to orogenic arc formation, and strengthens the hypothesis of local small-block rotations driven by strike-slip tectonics.

To quantify the relationship between structural trends and rotations the correlation between the paleomagnetic rotation values (R) of sites with ChRM/MT and HT components and the orientation value of the structure (S, strike) was tested [*Mattei et al.*, 1995; *Speranza et al.,* 1997; *Macrì et al.,* 2014] using the method originally proposed by *Schwartz* and *Van der Voo* [1983] and successively applied by *Eldredge* et al. [1985], *Lowie and Hirt* [1986], and *Hirt and Lowie* [1988] (Figure 66). By considering a ~N-S orientation of the structures running parallel to the ARRSZ, as determined from geological maps, we considered a reference value S_0=0. Likewise we chose 0° for the reference rotation R_0=0, indicating with positive (negative) value the clockwise (counterclockwise) rotation degree.

Figure 66 shows that in northern Simao and Lanping domain sites with ChRM/MT and HT components respectively, a lack of correlation (R^2<0.3) between rotations and bed strikes (that are used as proxies of unavailable fold axes, Figure 74). The data show that highly variable structural trends arise, if local bed strikes are back-rotated according to paleomagnetic data. Such result makes further unlikely a thrust-driven rotation scenario or rotations related to orogenic arc formation, and strengthens the hypothesis of local small-block rotations driven by strike-slip tectonics, even if before rotations occurred, there was no constant tectonic trend with sub-parallel strata and/or folds [*Mattei et al*., 1995].

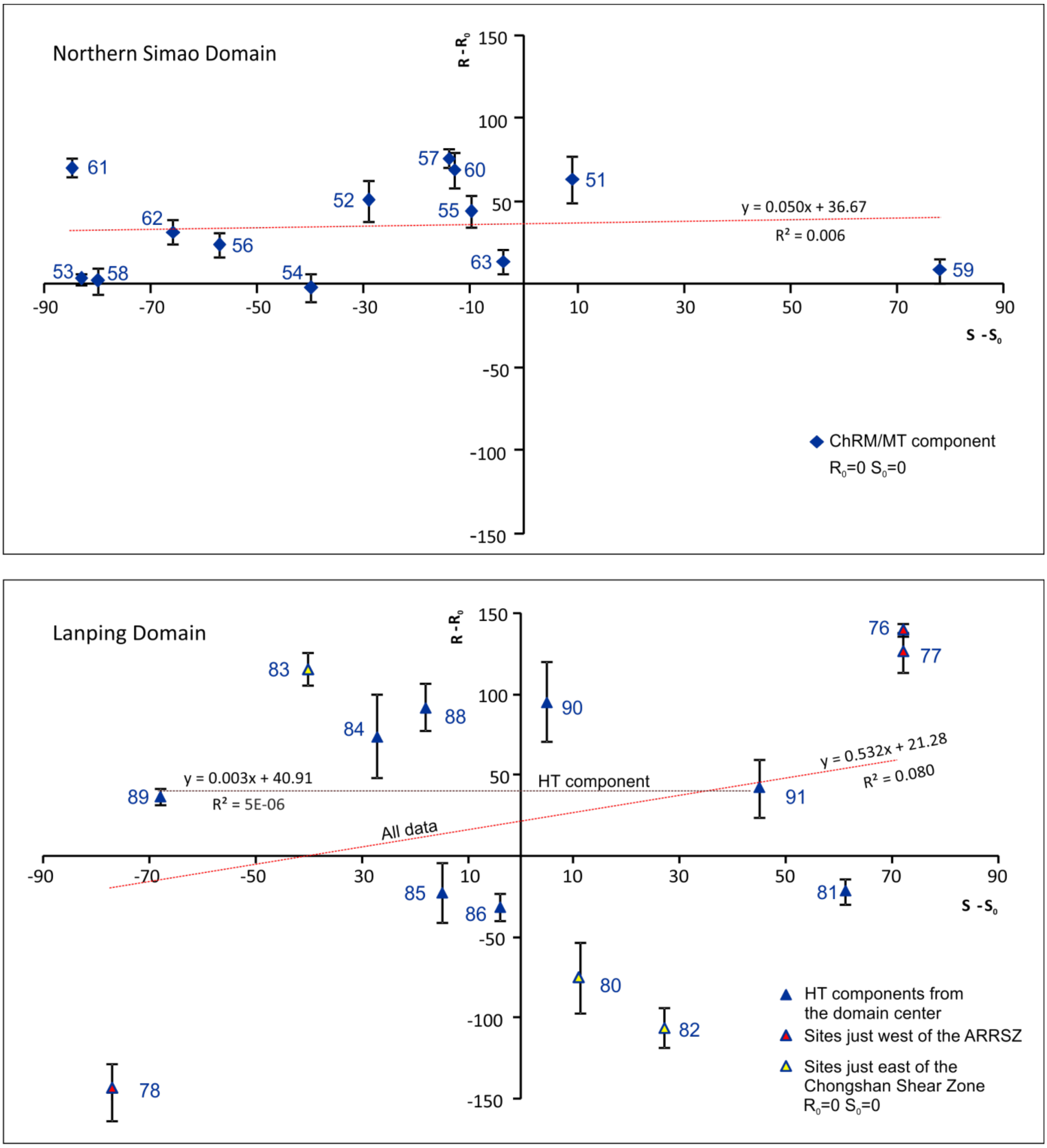

Figure 74. Paleomagnetic rotation deviations relative to structure direction (approximated by bed strike) deviations in the northern Simao and Lanping domains [e.g. *Schwartz and Van der Voo*, 1983]. R_0 and S_0 are respectively reference rotation (R_0=0°) and strike value (S_0=0°, i.e. N-S trend). Error bars for rotation are the $\alpha_{95}/\cos I$ site values. R^2 is the correlation coefficient. Red and brown lines are the best fit lines calculated by linear regression analysis on the whole data set and on the sole HT component directions, respectively. Triassic sites from the Simao domain and MT component directions from the Lanping domain are omitted.

Chapter VIII

8. AMS RESULTS

AMS was measured for the same sites sampled for paleomagnetic analyses.

The AMS parameters were evaluated using Jelinek statistics [see chapter 2.2; *Jelinek*, 1977; 1978] and are reported in Table 5. The results were processed using the software package ANISOFT supplied with the Kappabridge instrument [*Chadima and Jelinek*, 2009].

The available data associated with each specimen are the geographical orientation and the magnitude of the three principal axes of its AMS ellipsoid.

Sites from Gaoligong Shear Zone (Yun03 to Yun50) are characterized by:

- mean values of magnetic susceptibility Km (between 2.93×10^{-5} to 1.90×10^{-4} SI)
- anisotropy degree ($1.007 < P < 1.149$)
- shape of ellipsoid ($-0.339 < T < 0.786$)

Sites from Ailaoshan Red River Shear Zone (Yun 51 to Yun 92) are characterized by:

- mean values of magnetic susceptibility Km (between 4.02×10^{-5} to 1.41×10^{-2} SI)
- anisotropy degree ($1.010 < P < 1.066$)
- shape of ellipsoid ($-0.395 < T < 0.772$)

Table 5. Anisotropy factors computed at each sites. Age: UT Upper Triassic, LJ Lower Jurassic, MJ Middle Jurassic, UJ Upper Jurassic, J Jurassic, LK Lower Cretaceous, K Cretaceous, J-K Jurassic-Cretaceous. D and I are *in situ* site-mean declination and inclination, respectively, of the maximum susceptibility axis; km = (kmax + kint + kmin)/3 is mean susceptibility ; P and T are corrected anisotropy degree and shape factor, respectively, according to *Jelinek* [1981]. Bedding is expressed in dip azimuth/dip values. Fabric: PS pure sedimentary, TS triaxial sedimentary, PR prolate, TT triaxial tectonic, N normal, I Inverse

Table 5. Anisotropy of Magnetic Susceptibility Results of red beds sites from Baoshan, Lanping, Northern Simao and Chuandian blocks

Site	Age	D,deg (K1)	I,deg (K1)	e_{12}, deg	D,deg (K3)	I,deg (K3)	e_{31}, deg	Km Average	Km St. Deviation	P	St. deviation	T	St. deviation	Bedding (deg)
Baoshan block														
YUN03	MJ	124.2	36.1	22.3	4.5	34.3	32.5	4.69E-05	2.74E-05	1.038	0.054	0.026	0.476	42/50
YUN24	K	68.6	7.3	31.0	331.3	44.9	43.2	7.02E-05	1.92E-05	1.016	0.005	0.241	0.25	230/12
YUN25	J-K	–	–	–	–	–	–	–	–	–	–	–	–	–
YUN26	K	63.4	12.9	15.6	155.6	9.5	7	6.68E-05	2.81E-05	1.097	0.028	0.551	0.181	336/72
YUN27	K	66.9	16.1	12.5	336.0	3.2	13.6	7.11E-05	3.59E-05	1.100	0.054	0.321	0.253	344/84
YUN28	K	99.9	11.0	13.2	6.1	18.7	13.8	8.73E-05	2.66E-05	1.119	0.023	0.677	0.057	186/72
YUN29	K	258.8	45.7	32.7	148.7	18.6	58.6	3.86E-05	1.18E-05	1.033	0.034	0.338	0.382	164/75
YUN30	K	86.6	74.2	65.4	310.9	11.5	10.6	6.29E-05	1.50E-05	1.149	0.017	0.786	0.112	123/81
YUN31	MJ	109.2	28.8	44.4	322.2	56.8	14.4	9.10E-05	2.43E-05	1.048	0.016	0.728	0.171	142/33
YUN32	K	236.3	66.5	30.5	141.8	2.0	20.8	8.97E-05	3.73E-05	1.011	0.003	0.378	0.445	314/88
YUN33	MJ	–	–	–	–	–	–	–	–	–	–	–	–	–
YUN34*	MJ	181.2	55.7	16.9	84.6	4.5	62.9	5.99E-05	1.57E-05	1.014	0.005	-0.332	0.357	1/34
YUN35	J-K	29.3	36.5	23.8	151.0	35.4	7.2	1.07E-04	3.31E-05	1.018	0.006	0.46	0.222	323/43
YUN36	MJ	353.2	64.4	23.5	214.1	19.9	35.6	1.13E-04	1.86E-05	1.007	0.003	-0.153	0.365	346/44
YUN37	MJ	253.0	46.1	27.8	147.2	14.7	17.0	1.09E-04	3.02E-05	1.017	0.005	0.251	0.278	327/75
YUN38	MJ	44.2	19.7	34.9	158.4	48.8	19.0	9.51E-05	1.87E-05	1.017	0.005	0.489	0.318	335/44
YUN39	MJ	22.6	62.3	27.8	131.8	9.8	30.7	9.76E-05	2.57E-05	1.043	0.006	0.192	0.247	165/23
YUN40	K	49.5	70.4	28.9	314.6	1.7	18.7	5.57E-05	1.86E-05	1.054	0.018	0.11	0.133	135/88
YUN41	K	37.3	27.1	13.6	128.3	2.0	73.4	2.93E-05	7.14E-06	1.048	0.078	0.157	0.473	125/55
YUN43	MJ	270.8	2.7	20.6	180.7	1.0	22.6	1.90E-04	6.24E-05	1.008	0.002	-0.047	0.357	331/52
YUN44	MJ	312.9	3.6	28.6	183.0	41.5	7.1	1.34E-04	2.83E-05	1.019	0.005	0.417	0.338	5/44
YUN45	MJ	336.1	6.0	15.5	245.5	5.9	8.2	1.11E-04	3.12E-05	1.026	0.006	0.486	0.187	65/84
YUN46	MJ	21.7	21.1	6.5	120.9	22.4	53.8	8.23E-05	8.83E-06	1.023	0.007	-0.155	0.25	81/22
YUN47*	MJ	261.3	30.5	20	11.6	30.5	34.0	1.06E-04	1.84E-05	1.012	0.004	-0.339	0.249	69/50
YUN48	MJ	149.4	14.9	10.6	246.3	24.3	10.2	6.12E-05	3.02E-05	1.096	0.053	0.443	0.203	66/66
YUN49	MJ	184.3	67.3	37.7	77.9	6.7	17.2	1.21E-04	1.49E-05	1.017	0.003	0.534	0.284	76/70
YUN50	MJ	162.8	72.6	16.6	305.5	14.0	15.1	1.55E-04	2.55E-05	1.009	0.004	0.179	0.428	127/47
Northern Simao Block														
YUN51	LK	36.4	15	10.0	272.9	64.1	22.9	1.20E-04	1.81E-05	1.010	0.003	0.190	0.233	105/109
YUN52	UJ	335.3	15.4	72.0	232.8	38.3	8.6	1.12E-04	1.17E-05	1.033	0.007	0.644	0.251	61/51
YUN53	UJ	299.4	26.7	11.6	97.2	61.5	35.1	1.28E-04	2.74E-05	1.017	0.007	-0.160	0.371	7/41
YUN54	MJ	124.8	16.5	39.7	312.2	73.4	10.6	1.34E-04	2.61E-05	1.013	0.005	0.374	0.27	50/30
YUN55	UJ	180.6	23.9	22.7	295.5	43.5	12.8	6.71E-05	3.43E-05	1.029	0.029	0.071	0.564	260/54
YUN56	LK	–	–	–	–	–	–	–	–	–	–	–	–	–
YUN57	LK	–	–	–	–	–	–	–	–	–	–	–	–	–
YUN58	LK	295.6	49.9	26.2	189.5	13.2	12.3	9.03E-05	1.57E-05	1.035	0.015	0.508	0.292	10/70
YUN59	LK	344.9	15.1	7.6	243.1	37.0	43.5	1.13E-04	2.88E-05	1.031	0.013	0.049	0.379	348/31
YUN60*	UJ	84.2	35.1	42.2	309.8	44.9	32.3	4.02E-05	1.35E-05	1.024	0.011	0.334	0.325	257/54
YUN61	UJ	7.0	27.0	14.5	151.9	58.1	18.6	1.05E-04	1.17E-05	1.015	0.003	-0.001	0.316	5/46

Table 5. Anisotropy of Magnetic Susceptibility Results of red beds sites from Baoshan, Lanping, Northern Simao and Chuandian blocks

Site	Age	D,deg (K1)	I,deg (K1)	e_{12}, deg	D,deg (K3)	I,deg (K3)	e_{31}, deg	Km Average	Km St. Deviation	P	St. deviation	T	St. deviation	Bedding (deg)
YUN62	UJ	354.0	7.1	13.1	88.0	29.3	12.5	1.28E-04	1.81E-05	1.019	0.003	-0.13	0.236	24/11
YUN63	MJ	20.5	15.5	7.7	235.5	71.3	18.7	1.22E-04	1.19E-05	1.039	0.013	-0.247	0.262	266/56
YUN64	UT	201.9	67.2	22.3	94.2	7.3	20.8	1.29E-04	1.02E-05	1.04	0.013	0.040	0.323	184/55
YUN65	UT	139.6	60.4	13.7	289.0	26.1	12.0	1.42E-04	2.07E-05	1.034	0.008	0.105	0.236	5/80
YUN66	UT	67.4	59.1	17.7	257.2	30.5	37.4	1.14E-04	1.24E-05	1.027	0.008	0.031	0.434	294/114
Chuandian block														
YUN67	UT	299.8	35.0	21.2	97.2	52.9	8.3	1.36E-04	2.08E-05	1.195	0.016	0.772	0.127	277/27
YUN68	UT	349.7	24.1	40.2	100.2	38.1	14.8	6.16E-05	1.78E-05	1.064	0.035	0.250	0.361	290/26
YUN69	UT	244.0	61.4	21.4	81.9	27.4	20.0	1.47E-04	6.63E-05	1.062	0.030	0.343	0.273	118/29
YUN70	LJ	–	–	–	–	–	–	–	–	–	–	–	–	–
YUN71	MJ	79.2	60.2	41.5	243.2	28.9	42.4	1.21E-04	2.13E-05	1.037	0.033	0.169	0.404	69/45
YUN72	MJ	164.5	7.0	33.0	261.2	43.4	18.9	1.14E-04	1.77E-05	1.023	0.009	0.394	0.322	80/47
YUN73	MJ	24.5	47.6	27.8	246.2	34.3	26.5	9.05E-05	1.44E-05	1.042	0.024	0.656	0.228	61/50
YUN74	UJ	330.8	57.9	5.9	233.2	4.7	6.3	1.57E-04	1.04E-05	1.026	0.001	0.292	0.130	68/36
YUN75	UJ	296.2	27.0	16.9	192.1	25.6	9.1	1.40E-04	5.97E-06	1.029	0.002	0.557	0.069	12/74
Lanping block														
YUN76	LK	203.6	48.7	49.4	342.1	33.3	23.7	7.19E-05	7.60E-06	1.014	0.005	-0.025	0.307	162/57
YUN77	LK	317.8	13.4	25.6	199.6	63.2	21.3	9.93E-05	3.74E-05	1.021	0.007	0.311	0.346	342/29
YUN78	LK	272.4	17.4	28.4	12.7	29.8	22.7	8.11E-05	1.58E-05	1.020	0.006	0.146	0.403	193/60
YUN79	LK	318.1	4.6	17.3	223.5	44.8	13.7	6.63E-05	8.46E-06	1.018	0.005	0.371	0.341	21/38
YUN80*	LK	264.7	20.7	34.5	80.7	69.3	8.1	1.55E-04	1.87E-05	1.066	0.009	0.565	0.227	101/24
YUN81	LK	57.0	4.5	37.1	151.0	41.8	12.9	9.86E-05	1.06E-05	1.013	0.003	0.374	0.289	331/48
YUN82	LK	227.7	22.9	38.1	117.4	39.2	9.3	8.74E-05	3.72E-06	1.046	0.078	0.154	0.291	297/51
YUN83	LK	25.7	24.7	13.5	213.8	65.1	15.8	1.17E-04	1.26E-05	1.053	0.009	0.503	0.192	50/40
YUN84	UJ	213.0	56.8	24.8	117.3	3.7	14.0	1.17E-04	1.08E-05	1.025	0.004	0.468	0.159	117/94
YUN85	UJ	147.6	33.5	18.5	262.1	31.9	28.8	7.45E-05	1.23E-05	1.025	0.012	0.315	0.374	75/55
YUN86	UJ	4.9	11.4	33.0	266.1	37.1	5.0	9.37E-05	9.56E-06	1.032	0.003	0.688	0.168	86/53
YUN87	LK	178.8	28.8	7.2	273.3	8.2	14.5	8.78E-05	7.61E-06	1.037	0.006	-0.395	0.251	115/65
YUN88*	LK	27.1	64.6	16.0	257.0	17.2	9.3	1.49E-04	2.24E-05	1.038	0.007	-0.002	0.256	252/28
YUN89	LK	353.3	68.2	15.6	202.4	19.3	13.7	1.52E-04	2.98E-05	1.053	0.008	0.178	0.518	22/71
YUN90	UJ	306.2	50.3	22.8	105.2	37.8	7.4	1.59E-04	1.92E-05	1.058	0.016	0.490	0.187	275/50
YUN91	LK	222.8	37.6	8.4	324.4	14.6	13.1	8.59E-05	1.90E-05	1.040	0.010	-0.070	0.352	13/85
YUN92	UJ	185.6	17.6	16.0	81.8	36.9	9.5	1.41E-02	1.52E-05	1.014	0.005	0.030	0.272	262/53
YUN93	LK	–	–	–	–	–	–	–	–	–	–	–	–	–
YUN94	MJ	–	–	–	–	–	–	–	–	–	–	–	–	–

Age: UT Upper Triassic, LJ Lower Jurassic, MJ Middle Jurassic, UJ Upper Jurassic, J Jurassic, LK Lower Cretaceous, K Cretaceous, J-K Jurassic-Cretaceous. D and I are in situ site-mean declination and inclination, respectively, of the maximum susceptibility axis; km = (kmax + kint + kmin)/3 is mean susceptibility ; P and T are corrected anisotropy degree and shape factor, respectively, according to Jelinek [1981]. Bedding is expressed in dip azimuth/dip values. Fabric: PS pure sedimentary, TS triaxial sedimentary, PR prolate, TT triaxial tectonic, N normal, I Inverse

The magnetic lineation relative to GLG data is well defined only in 18 sites, where the e_{12} confidence angle of the K_{max} in the K_{max}-K_{int} plane is < 30°. In 5 sites (Yun24, 29, 32, 38, 49) the magnetic lineation is still defined but has a larger confidence angle (30° <e_{12}< 40°), while the remaining 2 sites (Yun30, 31) have a purely scattered results with no virtually lineation (e_{12} >or >> 40°).

Relatively to ARRSZ, magnetic lineation data is well defined in 28 sites, where the e_{12} confidence angle of the K_{max} in the K_{max}-K_{int} plane is <30°. In 6 other sites (Yun54, 72, 80, 81, 82, 86) the magnetic lineation is still defined but has a larger confidence angle (30°<e_{12}< 40°), while the remaining 5 sites (Yun52, 60, 68 71, 76) have a purely scattered results with virtually no lineation (e_{12} > 40°). Sites with poorly defined lineation have been discarded from further analysis but are shown in Figure 77.

Unusual relationships between structural and magnetic axes occurred in two/three sampled sites along the Gaoligong Shear Zone (Yun34 and Yun47) and ARRSZ (Yun60, Yun80, Yun88) transect respectively, showing an inverse, or tendentially inverse magnetic fabric, with well defined lineation (e_{12} < 30) and prolate ellipsoid shape orthogonal to bedding (* in Table 5 and plots in Figure 75). As explained in chapter 2.2, this unusual relationships between structural and magnetic axes, can occur because of the presence of certain magnetic minerals, either SD magnetite, iron-bearing carbonates or various paramagnetic minerals like tourmaline, cordierite, goethite or siderite [*Rochette et al.*, 1992]. In particular, rocks with fine-grained magnetite, are prone to anomalous AMS fabric.

Figure 75. Sites with inverse (or tendentially inverse) magnetic fabric respectively from Gaoligong and Ailaoshan Red River fault areas (equal area Schmidt projection, lower hemisphere). The squares, triangle, and dots represent K_{max} , K_{int} and k_{min} respectively. The ellipses indicate the 95% region around the principal susceptibility axes. The orange line indicates the bedding planes (expressed in dip azimuth/dip values).

Sites with Inverse Magnetic Fabrics from Gaoligong Fault

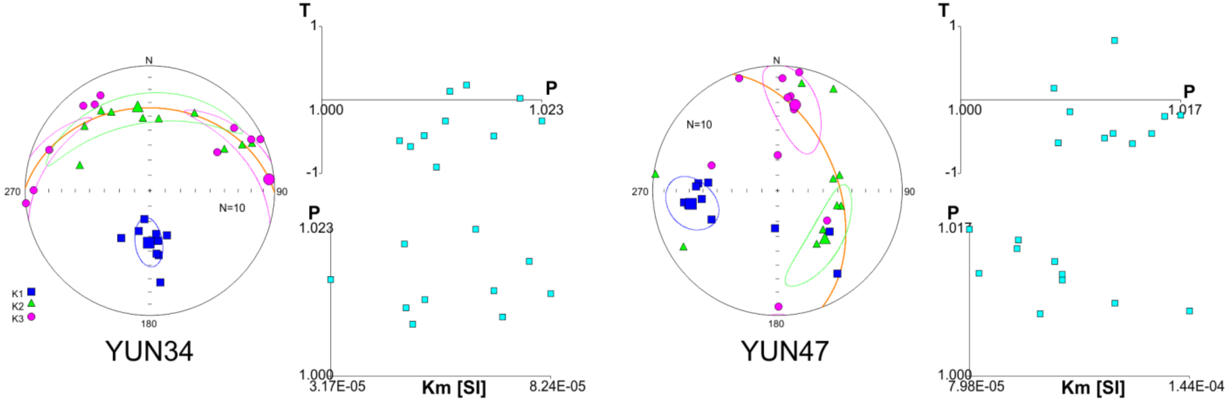

Sites with Inverse Magnetic Fabrics from Ailao Shan Red River Fault

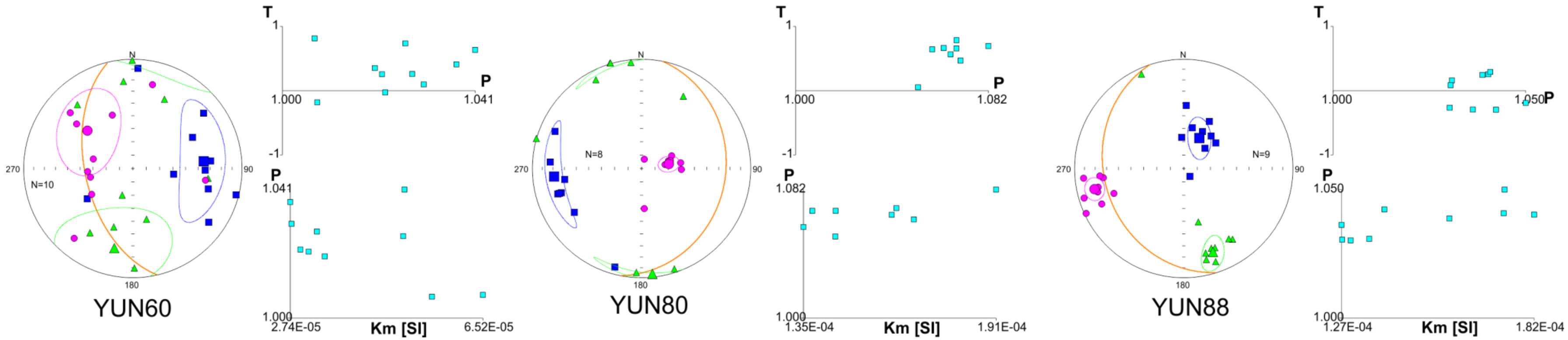

As already described in previous chapters, previous field observations along the Gaoligong Mountains showed that the Gaoligong Shear Zone is characterized by steep foliation and nearly N-S trending sub-horizontal stretching lineations [*Wang et al*., 2008]. The banded mylonitic rocks are tightly folded with the hinges parallel to the lineations [*Zhang et al*., 2012a]. To the west of the Gaoligong strike-slip Shear Zone, *Xu et al*. [2015] identified widespread mylonitic ortho- and paragneisses with gently dipping foliation and nearly horizontal stretching lineation defined by long axes of amphibole and sillimanite grains and boudinage of felsic veins. Despite the varying attitude of the foliation, the stretching lineation has a consistent NE-azimuth, parallel to the strike of the Gaoligong Shear Zone.

In the Lanping-Simao Basin, the red beds are generally affected by the NNW-SSE trending folds and thrusts, but an arcuate trend is maintained in the Simao Basin [*Leloup*, 1995]. Timing of fold and thrust formation remains controversial. In the central sector of the Red River Fault, the foliation is usually steep, and the lineation is usually nearly horizontal, both being almost parallel to the trend of the mylonitization in the gneiss massifs [e.g., *Leloup et al*., 1993, 2001; *Jolivet et al*., 2001; *Cao et al*., 2010; *Zhang et al*., 2017]. In the southern transect of the ARRSZ in the Zhengyuan area, the Nanxin Formation is separate by several anticlines N-S trending and, to the west others monoclinal stuctural. Also in Mengla locality, a monoclinal structure with N-S trending axis and a dip of 2°-63° always in Nanxin Formation (from northeastward to eastward) has been observed by *Tanaka et al*. [2008].

Observing the distribution of the K1 axes on a stereoplot obtained by our data (Figure 76), it is noteworthy that in both cases ~ N-S orientation is predominant, similar to the orientation of primary tectonic structures analysed by us (GLG and ARRSZ) but also with minor secondary structures bordering the shear zones (eg. Nujiang River Fault; see structural and geological maps in previous chapter). The most striking evidence is the frequently sub-vertical trend of the magnetic lineations that is inusual in fold and thrust tectonics, and might reflect the main influence of strike-slip tectonics on the sediments located within the blocks.

In particular, for samples collected along the GLG, the mean distribution of the K1 axis seem to have a roughly subvertical ~NE-SO orientation and therefore a perpendicular K3 orientation ~ NO-SE. Instead, for the ARRSZ, the mean distribution of the K1 axes seem to have a rough orientation ~N-S and therefore a perpendicular K3 axes distribution, ~E-O oriented (Figure 76). In both cases, data suggest a medium structural compressive deformation phase (from oblate to triaxial fabric according to relations between shape factor (T) of AMS ellipsoid and the anisotropy degree parameter (P), discussed below; Figure 77 A-F).

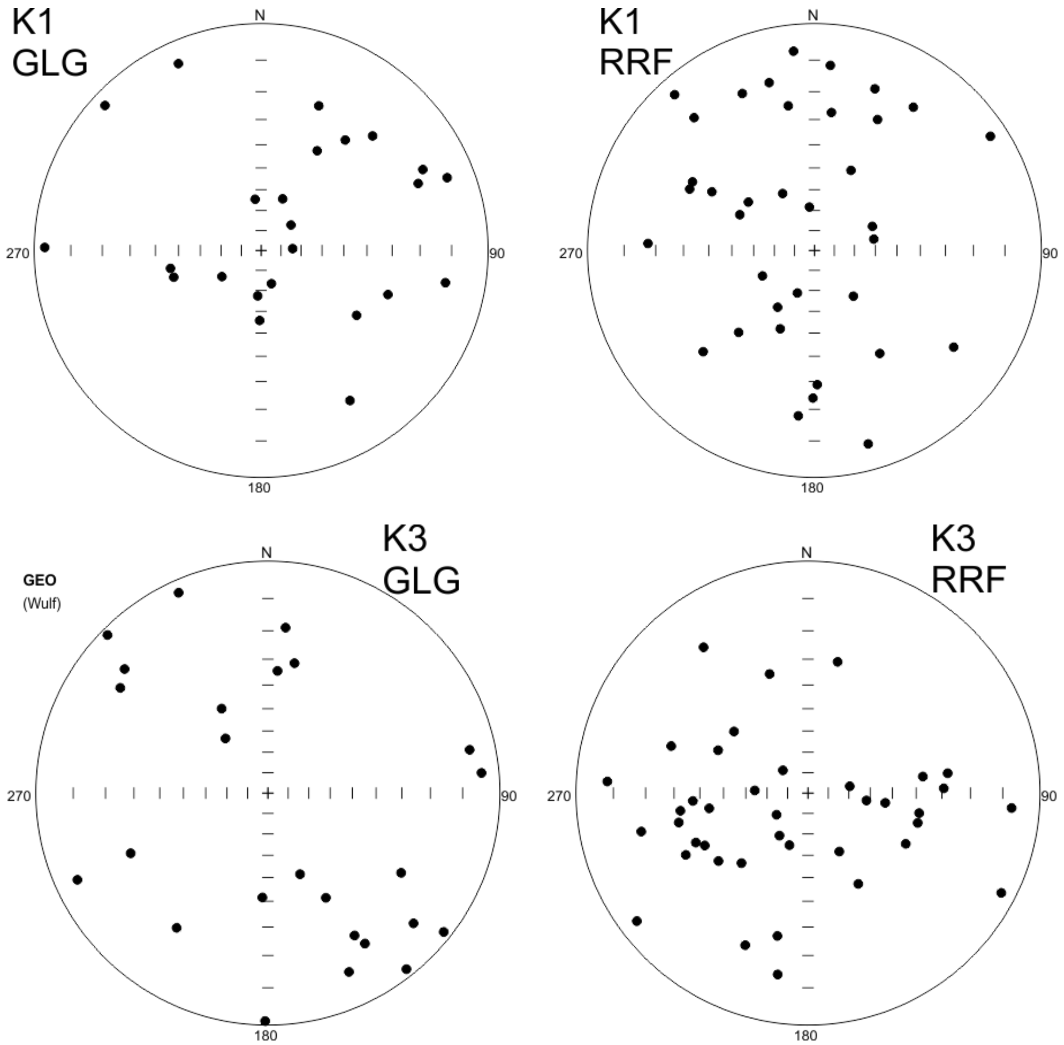

Figure 76. Lower hemisphere equal area projection of magnetic lineations (K1) (A) and foliations poles (K3) (B) respectively, in the sites carried out from Gaoligong fault and from Red River fault. Open circles represent samples from red beds.

Moreover, the shape factor (T) of AMS ellipsoid and the anisotropy degree parameter (P) seem to be broadly constant also moving away from the faults. For all sites (Figure 77 A-F) the shape of the AMS ellipsoid is predominantly oblate, with a shape factor $0 < T < 1$, and the anisotropy degree parameter is $1 < P < 1.080$ indicating a prevalent undeformed state. Only in 5 sites (Yun48; Yun26, 27, 28, 30; Figure 77 A-B) located at a distance of less than 2 km from the Gaoligong Shear Zone, respectively to the north-east and south-east of the structure, show an higher anisotropy degree parameter with respect to the others ($P>1.080$) suggesting a degree of deformation between fracure and slaty cleavage. Indeed, site Yun48 showed an unusual strong macroscopic foliation *in situ* (Figure 77 A, 78), not found in other sites (see supplementary information for each detailed plots). This confirms, once again, which the deformation in areas very close to the major structure, is influenced by tectonic structure and that the structural behaviors also change according to the distance from the faults. The same is true for the Yun67 site, located in the Chuandian domain, which present a P value higher than 1.150 and well defined foliation is visible *in situ* (Figure 77E, 80).

Sites Yun24, 41, 46, 47 have a shape factor $T <0$ and a fabric tendentially inverse, except for Yun24 in which we have no evidence of inverse fabric (Table 5 and Figure 77, 79).

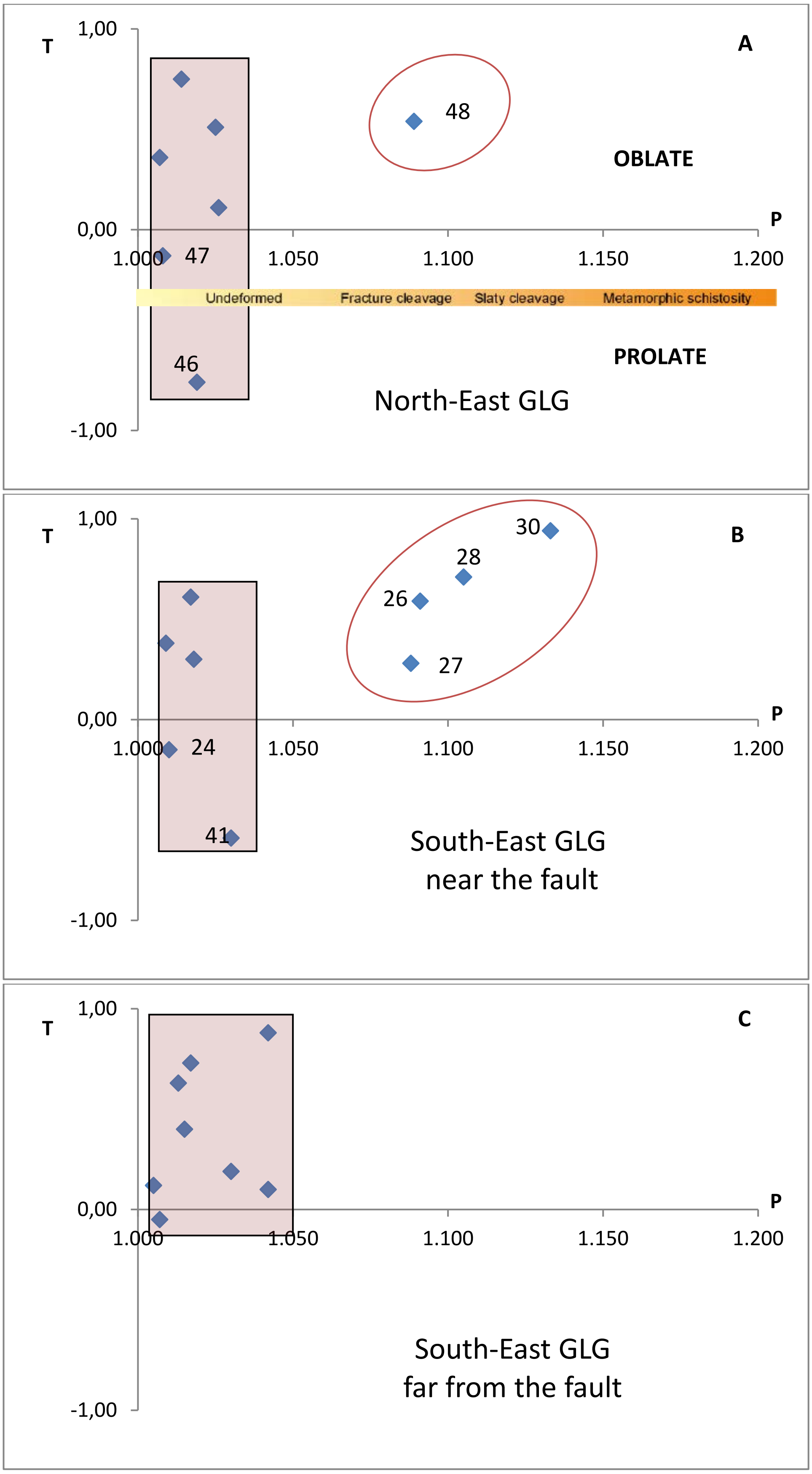

T
1,00
0,00
-1,00
A
48
OBLATE
P
47
1.000
1.050
1.100
1.150
1.200
Undeformed
Fracture cleavage
Slaty cleavage
Metamorphic schistosity
PROLATE
46
North-East GLG
B
30
28
26
27
24
41
South-East GLG
near the fault
C
South-East GLG
far from the fault

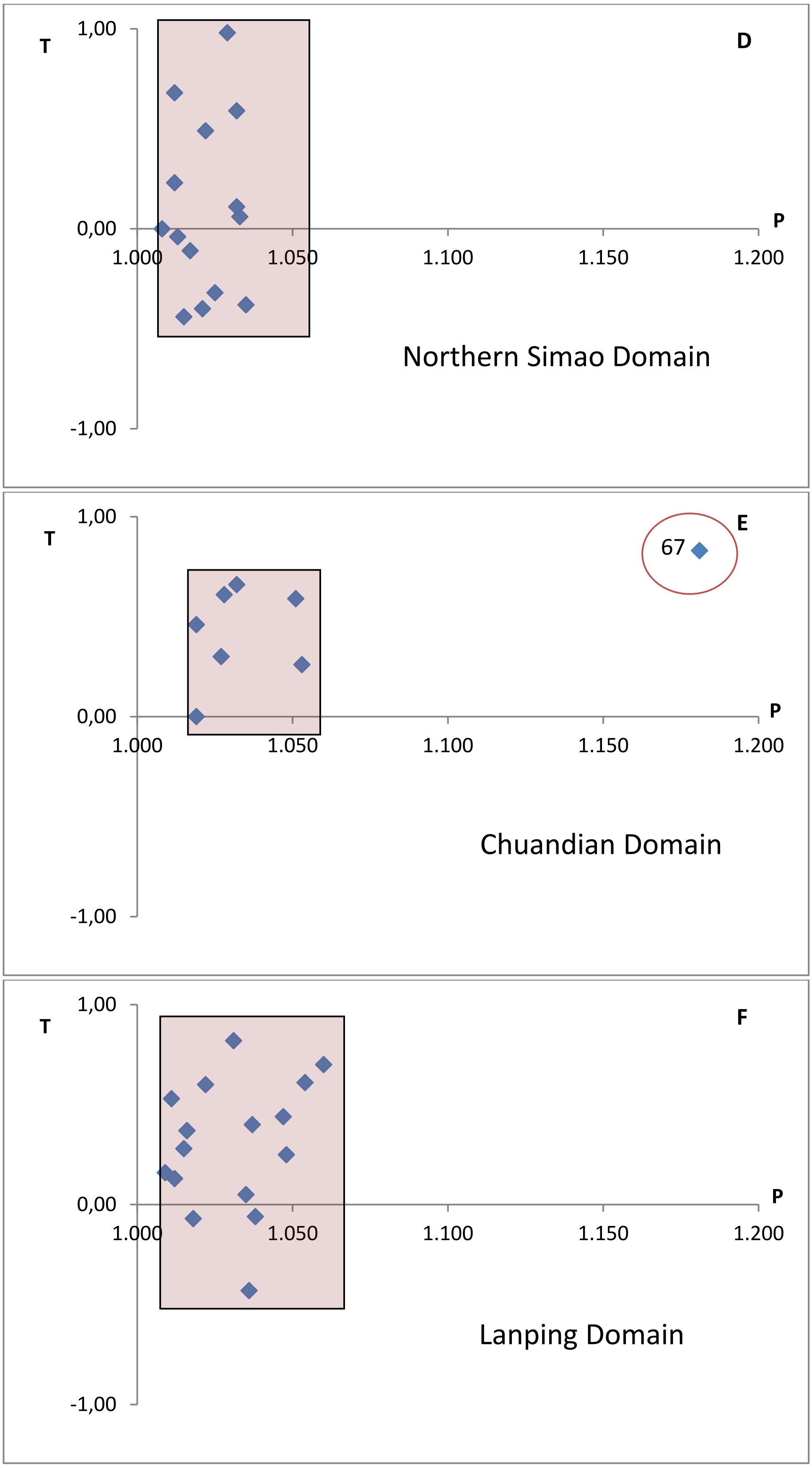

Figure 77. A-F Jelinek plot from different sampling areas. T, shape factor of AMS ellipsoid; P, anisotropy degree parameter. See Table 5 for values. the red rectangle indicates the average distribution area of the analyzed sites. The red circle highlights sites with a value of P> 1.050.

The eccentricity of the susceptibility ellipsoids have been evaluated (Figure 78) by plotting L (lineation) versus F (foliation). The distribution of both the foliation and lineations values, is indicative of predominant triaxial magnetic fabric, except for sites Yun26, 27, 28, 30, 31, 48, cropping out less than 5 km from the Gaoligong Shear Zone (Figure 79), and Yun67 sampled in Chuandian domain (Figure 80).

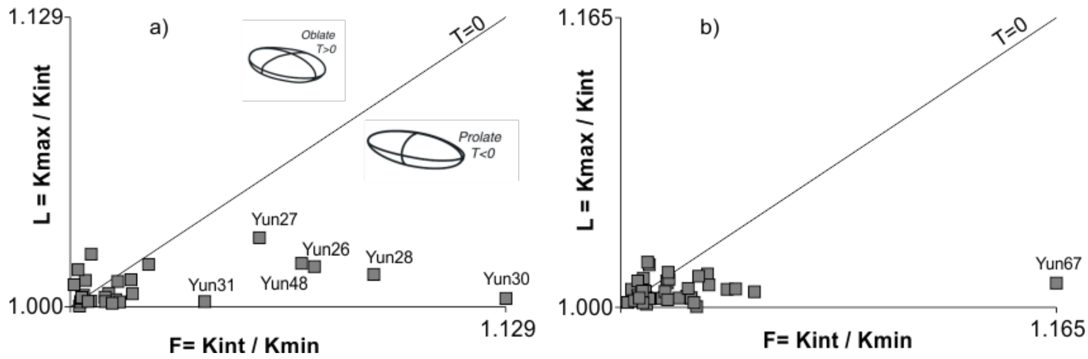

Figure 78. Flinn diagrams [*Flinn*, 1962] of shape parameters (L lineation, F foliation) relative to AMS results from a) Gaoligong Shear Zone and b) Ailaoshan Red River Shear Zone. Lineation/Foliation values are the results of Kmax/Kint and Kint/Kmin, respectively. T, is the shape factor of AMS ellipsoid (oblate, T>0; prolate T<0).

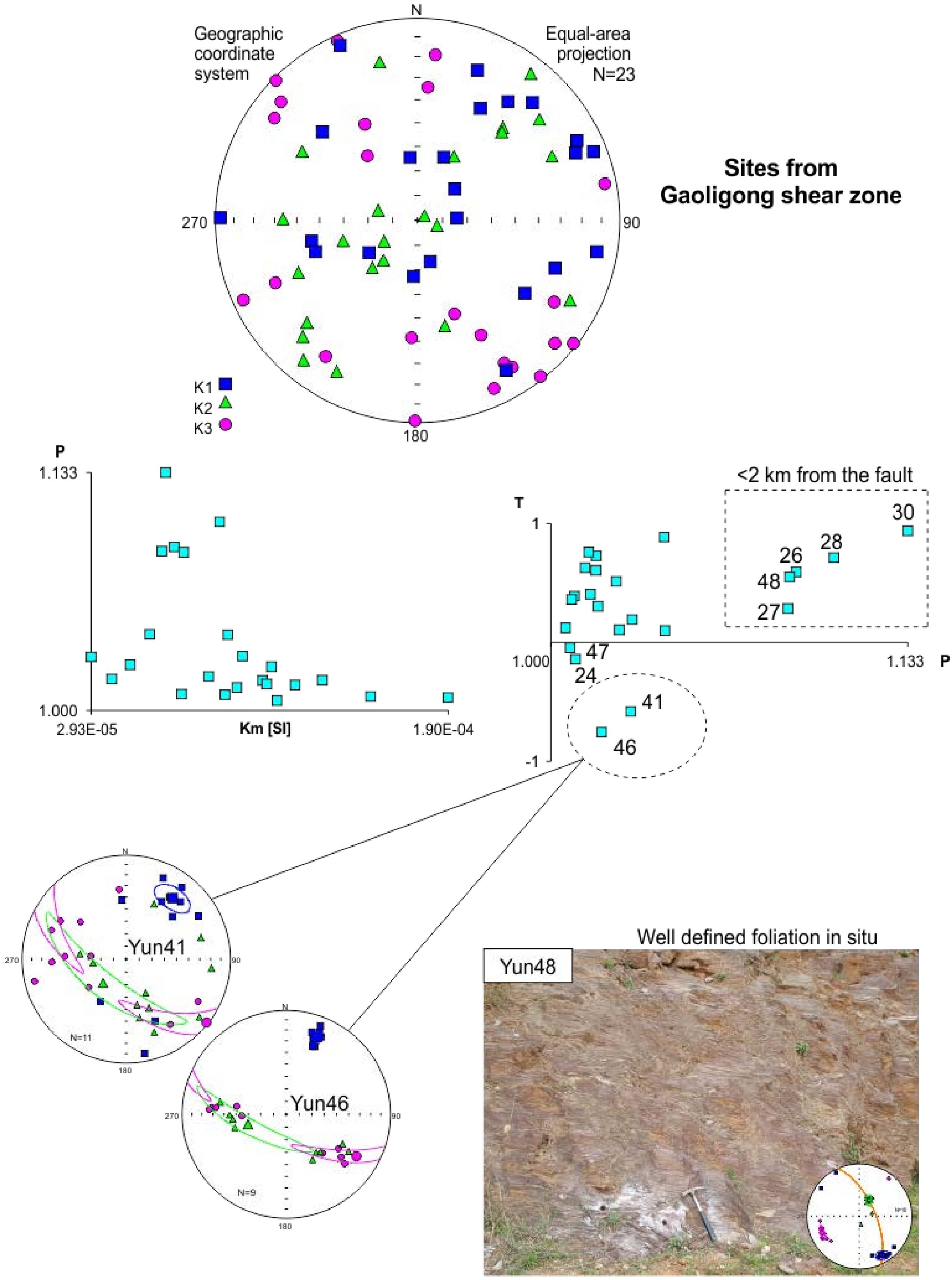

Figure 79. Summary of AMS results obtained from the Gaoligong Shear Zone. The squares, triangle, and dots represent K_{max}, K_{int} and k_{min} respectively. The ellipses indicate the 95% region around the principal susceptibility axes. The orange line indicates the bedding planes (expressed in dip azimuth/dip values).

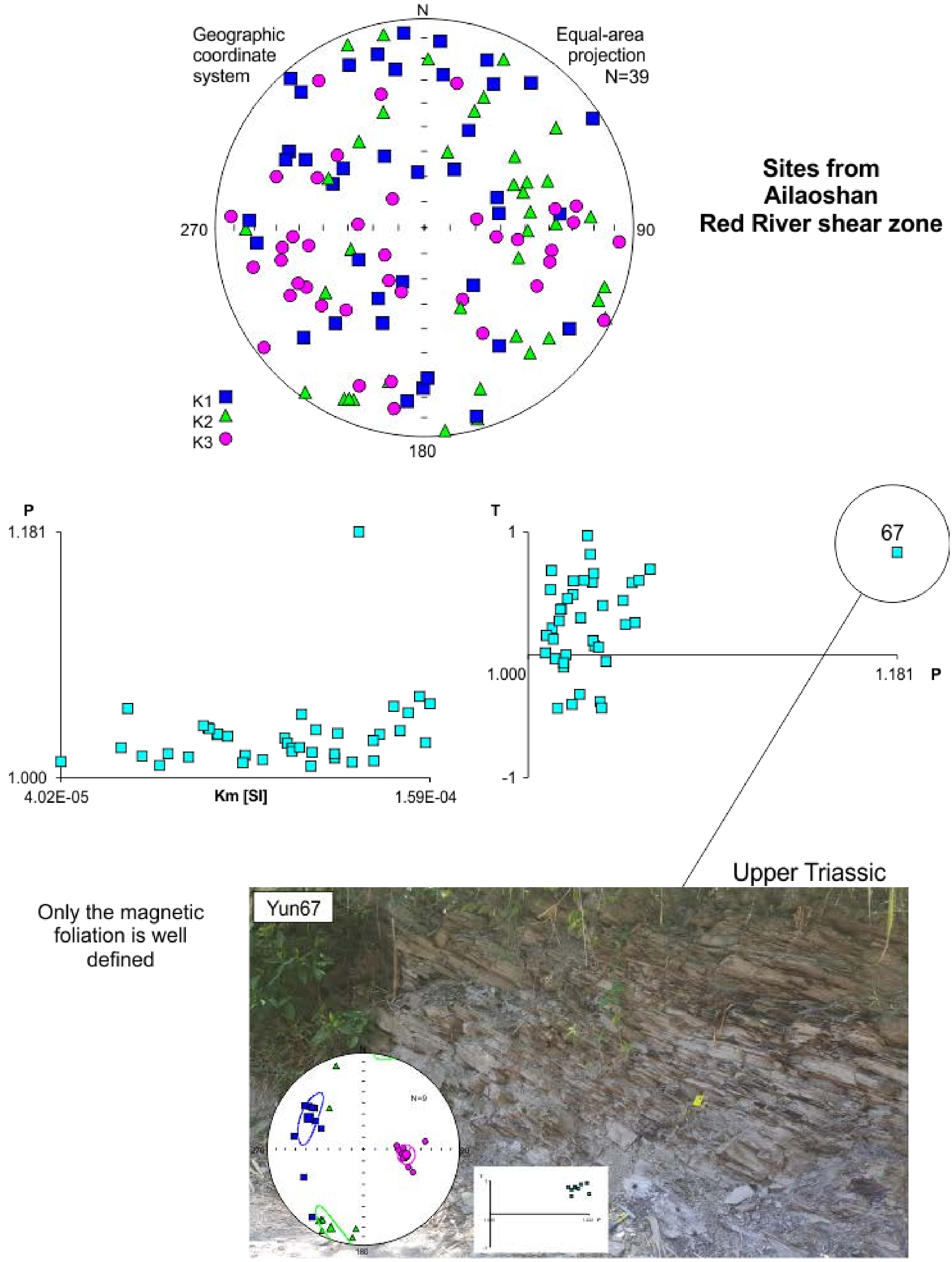

Figure 80. Summary of AMS results obtained from the Ailaoshan Red River Shear Zone. The squares, triangle, and dots represent K_{max}, K_{int} and k_{min} respectively. The ellipses indicate the 95% region around the principal susceptibility axes. The orange line indicates the bedding planes (expressed in dip azimuth/dip values).

Observing plots with projection of the bedding, lineation and the foliation planes, it is possible to summarize that:

(1) along the Gaoligong Shear Zone, in the north-eastern area (Figure 81a), the magnetic foliation (in pink) is predominantly sub-parallel, and sometimes coincident, to the bedding plane (in yellow), exception for sites Yun03 and Yun46 (Middle Jurassic), as is commonly observed in sediments. Furthermore, the magnetic lineation clusters are mostly oriented NW-SE exception for site Yun46 NNE-SSW oriented. Also in the south-eastern transect (Figure 81b), the magnetic foliation is predominantly sub-parallel, and sometimes coincident, to the bedding plane, exception for sites Yun24 and 29 (Cretaceous age), and Yun36, 39, 43 (Middle Jurassic age). But, we note that the axis of maximum elongation, parallel to K1, is sometimes sub-vertical, according to predominantly strike-slip regime, completely different from cases of thrust tectonics, where it appears mainly sub-horizontal [eg. *Speranza et al.*, 1999; *Maffione et al.*, 2015]. The distribution of the magnetic lineations cluster is the southern part, is variable. The sampled sites are located in an area delimited by two normal faults (Figure 81b). *Huang and Opdyke* [1993] describe this area as a monocline with moderate dip. In a group of sites to the north (Yun24, 26, 27, 39, 32, 35) and to the south (Yun37, 38, 39, 40, 41), located near the two main structure, a NE-SW direction seems to prevail, consistent with the orientation of the Gaoligong west detachment fault. An opposite trend respect to two group mentioned above, is shown by sites Yun28, 30, 31, 36, 43, 44;

(2) along the Red River Shear Zone, the situation is more complicated because the results are scattered. In northern Simao block (Figure 81c), from site Yun59 to Yun66, the foliation is perpendicular to the bedding plane, in Yun58 are almost coincident, Yun53, 54, 55 again perpendicular and in Yun51 and Yun52 are respectively perpendicular and parallel. This seems to highlight a different behaviour in different areas but very close to each other. Furthermore, the dispersion of the fabric indicates that it was probably acquired after rotation. Parallelism between K1 and the fold axis direction within the Lanping–Simao Basin, was also

evidenced by *Sato et al.* [2007], confirming the tectonic origin of the observed magnetic lineation, implying that K1 is a passive marker that was rotated during shortening [*Gao et* al., 2015];

(3) different are the results in Chuandian domain (Figure 81d), where bedding and foliation planes are predominantly parallel, exception for Yun69 and Yun74. Also here we have no other evidence to correlate these two results;

(4) finally, in the Lanping domain, the bedding and foliation planes are almost all parallel (Figure 81e). In both cases, the irregular foliations orthogonal to the bedding plane, indicate that there is a strong tectonic activity inside the blocks and these are deformed inside them.

This confirms, once again, which there are no evidence of rigid rotations of the crustal blocks, but the deformation is widely distributed both along the main structures and within the blocks delimited by them. Indeed, according to our paleomagnetic results and previous data, especially for the Gaoligong strike-slip fault area, it seems clear that tectonic deformation was mainly driven by strike-slip fault activity.

Figure 81. Structural sketch maps and plotted AMS results. Pink line represents the foliation planes (k_{min}) and blue square indicate the lineation planes (K_{max}). The ellipses indicate the 95% region around the principal susceptibility axes. The orange line indicates the bedding planes (expressed in dip azimuth/dip values). **a)** and **b)** are relative to the Gaoligong Shear Zone. **c)**, **d)** and **e)** are relative to the Ailaoshan Red River Shear Zone.

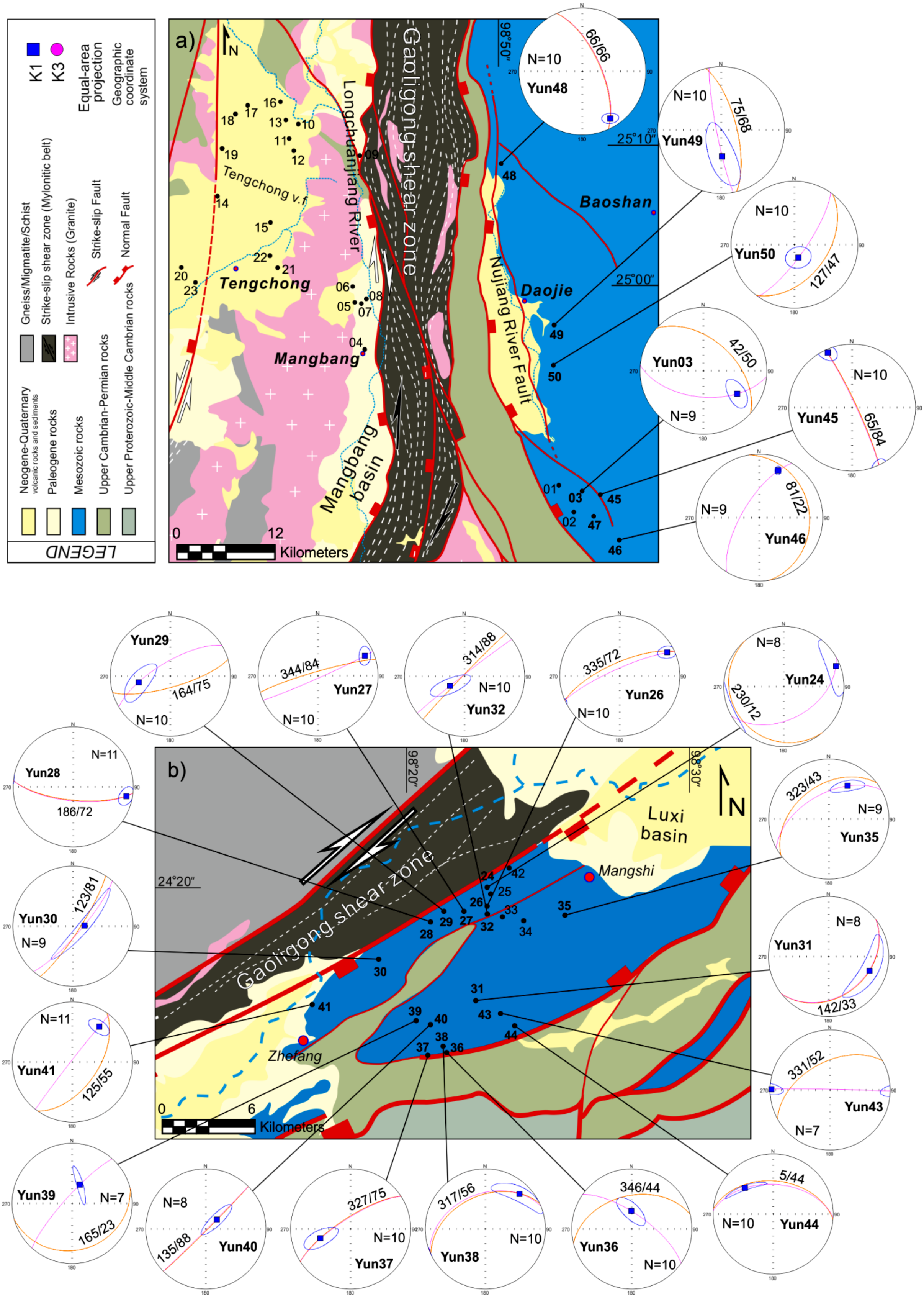
LEGEND
Neogene-Quaternary volcanic rocks and sediments
Paleogene rocks
Mesozoic rocks
Upper Cambrian-Permian rocks
Upper Proterozoic-Middle Cambrian rocks
Gneiss/Migmatite/Schist
Strike-slip shear zone (Mylonitic belt)
Intrusive Rocks (Granite)
Strike-slip Fault
Normal Fault
K1
K3
Equal-area projection
Geographic coordinate system
a)
N
Tengchong v.f
Tengchong
Mangbang
Mangbang basin
Longchuanjiang River
Gaoligong shear zone
Nujiang River Fault
Baoshan
Daojie
98°50'
25°10'
25°00'
0
12
Kilometers
Yun48 N=10 66/66
Yun49 N=10 75/68
Yun50 N=10 127/47
Yun03 N=9 42/50
Yun45 N=10 65/84
Yun46 N=9 81/22
b)
N
Gaoligong shear zone
Luxi basin
Mangshi
Zhefang
98°20'
98°30'
24°20'
0
6
Kilometers
Yun29 N=10 164/75
Yun27 N=10 344/84
Yun32 N=10 314/88
Yun26 N=10 335/72
Yun24 N=8 230/12
Yun28 N=11 186/72
Yun35 N=9 323/43
Yun30 N=9 123/81
Yun31 N=8 142/33
Yun41 N=11 125/55
Yun43 N=7 331/52
Yun39 N=7 165/23
Yun40 N=8 135/88
Yun37 N=10 327/75
Yun38 N=10 317/56
Yun36 N=10 346/44
Yun44 N=10 5/44

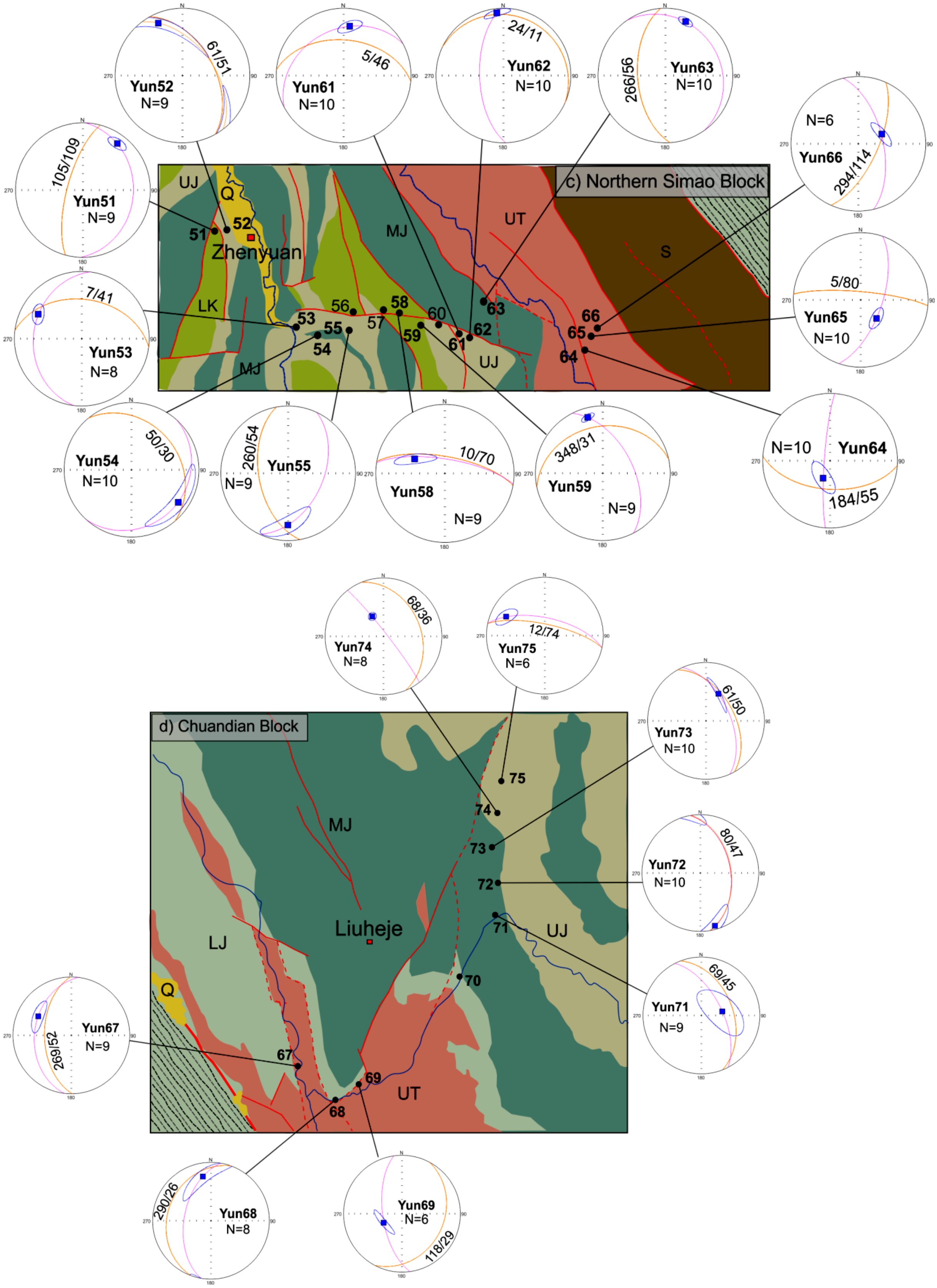
c) Northern Simao Block
Zhenyuan
UJ
Q
MJ
UT
S
LK
51
52
53
54
55
56
57
58
59
60
61
62
63
64
65
66
Yun51
N=9
105/109
Yun52
N=9
61/51
Yun61
N=10
5/46
Yun62
N=10
24/11
Yun63
N=10
266/56
Yun66
N=6
294/114
Yun65
N=10
5/80
Yun64
N=10
184/55
Yun53
N=8
7/41
Yun54
N=10
50/30
Yun55
N=9
260/54
Yun58
N=9
10/70
Yun59
N=9
348/31
d) Chuandian Block
Liuheje
MJ
LJ
UJ
UT
Q
67
68
69
70
71
72
73
74
75
Yun74
N=8
68/36
Yun75
N=6
12/74
Yun73
N=10
61/50
Yun72
N=10
80/47
Yun71
N=9
69/45
Yun67
N=9
269/52
Yun68
N=8
290/26
Yun69
N=6
118/29

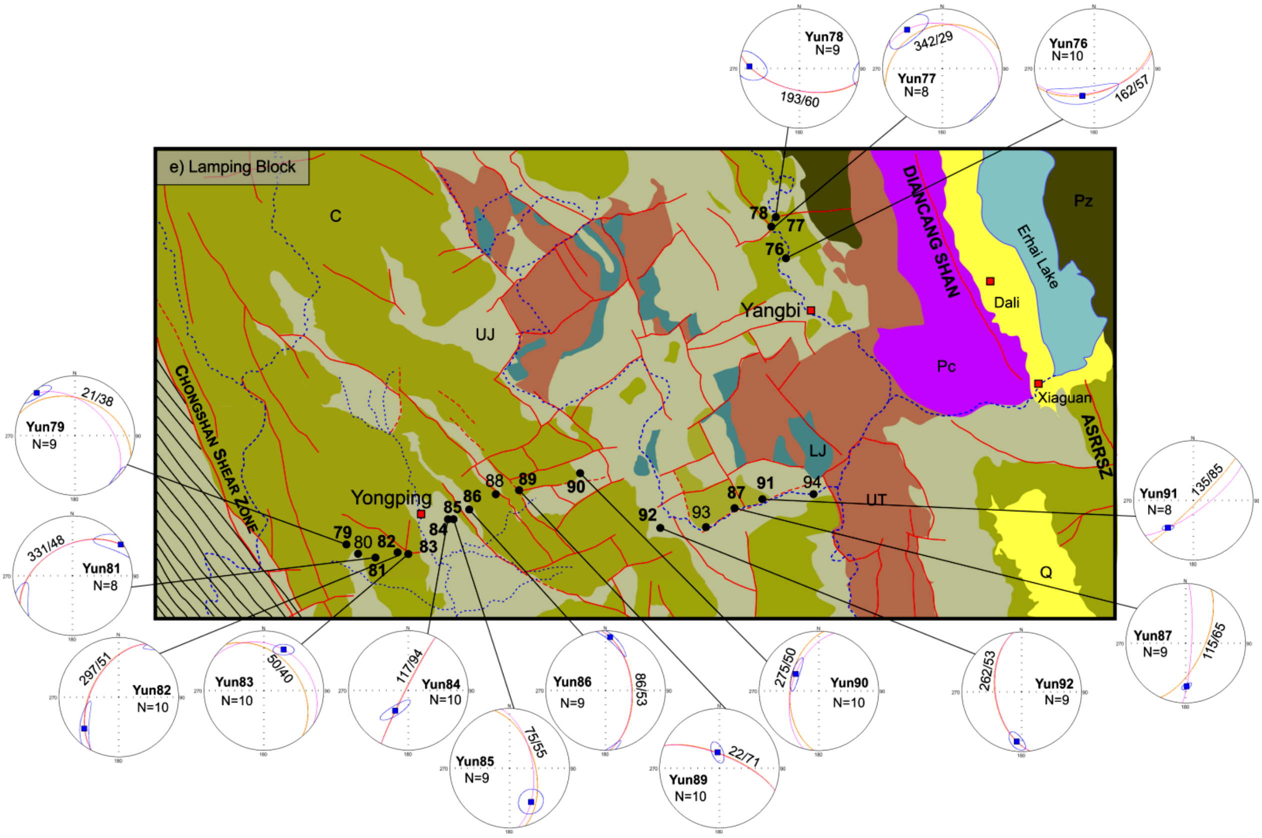
e) Lamping Block
C
UJ
LJ
UT
Pc
Pz
Q
Yangbi
Yongping
Dali
Xiaguan
Erhai Lake
DIANCANG SHAN
CHONGSHAN SHEAR ZONE
ASRRSZ
Yun78 N=9 193/60
Yun77 N=8 342/29
Yun76 N=10 162/57
Yun79 N=9 21/38
Yun81 N=8 331/48
Yun82 N=10 297/51
Yun83 N=10 50/40
Yun84 N=10 117/94
Yun85 N=9 75/55
Yun86 N=9 86/53
Yun89 N=10 22/71
Yun90 N=10 275/50
Yun92 N=9 262/53
Yun91 N=8 135/85
Yun87 N=9 115/65

Chapter IX

9. MAGNETIC MINERALOGY RESULTS

Additional magnetic analyses were carried to characterize the magnetic mineralogy. The measured hysteresis parameters include saturation magnetization (Ms), saturation remanent magnetization (Mrs), and coercive force (Bc) (Table 6 and 7). Acquisition of an isothermal remanent magnetization (IRM) and subsequent back-field DC remagnetization (both in a succession of fields up to 1 T), were also carried out on the same specimens (Figure 86, 87, 88). Data were also used to compute the coercivity of remanence (Bcr). Furthermore, for lavas specimens, we also measured the variation of the low-field magnetic susceptibility during a heating and cooling cycle performed in air, from room temperature up to 700°C. The Curie point of the magnetic minerals present in the samples was determined from the thermomagnetic curves as the temperature, or range of temperatures, at which paramagnetic behavior starts to dominate.

The magnetic mineralogy of the volcanic samples is heterogeneous (Figure 82), ranging from almost paramagnetic (whitish siltstones sites Yun05 to 09 and red beds site Yun32), to prevailing low coercivity and saturated at low field properties (Pliocene-Holocene basalt sites Yun04, 11 to 16, 18 to 23, and red beds sites 33 to 34), up to high coercivity and/or markedly unsaturated features at 1 T (Jurassic basalt sites Yun01 and 02, red beds sites Yun03, 24 to 31, 35 to 50) [*Pellegrino et al.*, 2018].

The main ubiquitous magnetic minerals are magnetite/titanomagnetite in the volcanics and hematite in the red beds; the magnetic susceptibility vs. temperature curves show that hematite is also present in the low coercivity class of samples, considering that k does not completely drop before 680°C (Figure 82). In this case, the presence of hematite in the thermomagnetic curves can also be ascribed to the inversion of ferromagnetic maghemite occurring from T>350°. For most of the samples, cooling curves are below the heating curves, thus excluding the relevant formation of ferrimagnetic minerals while heating in air [*Pellegrino et al.*, 2018].

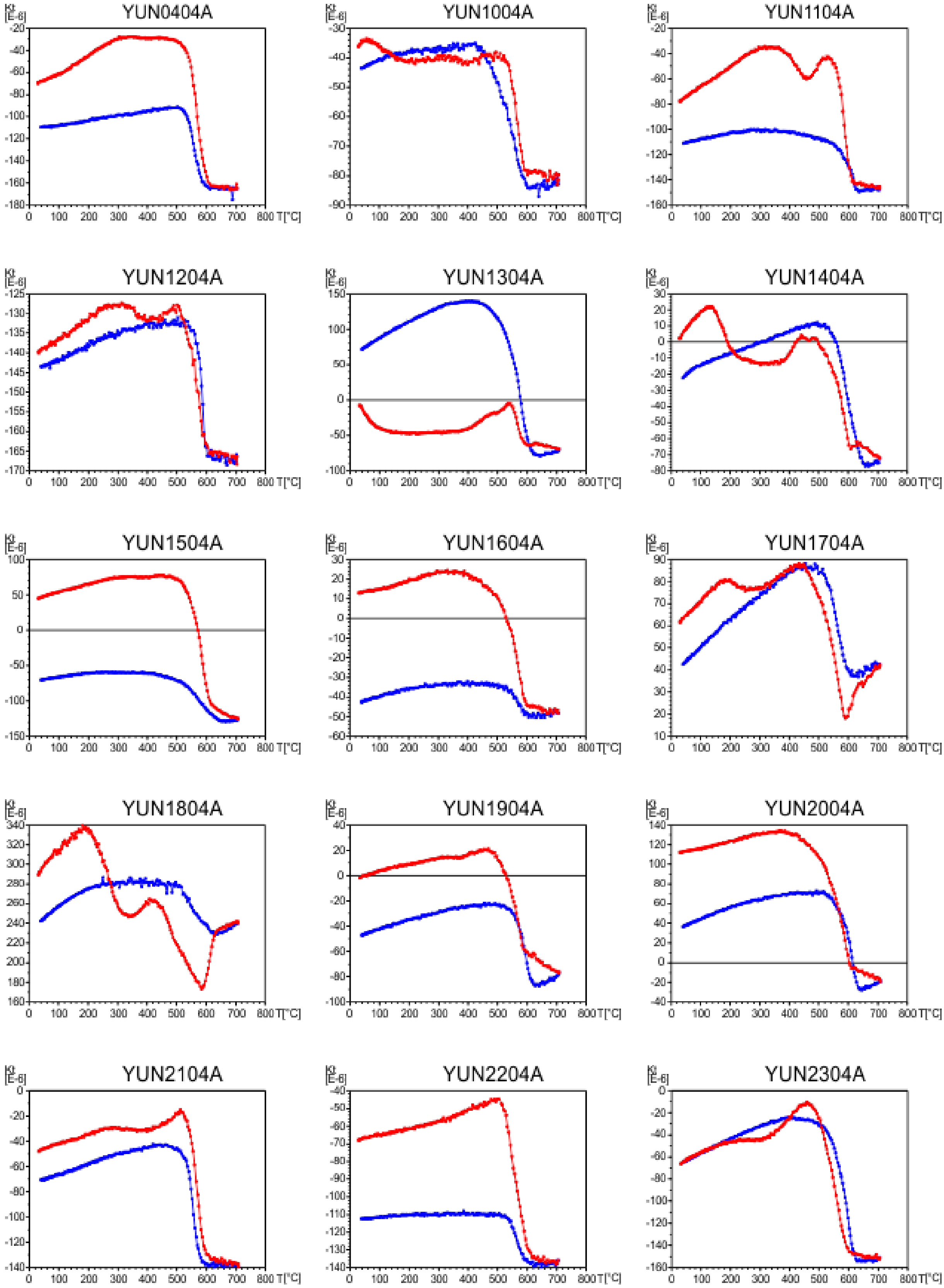

Figure 82. Thermomagnetic curves for basalt specimens; data are raw and not corrected for the empty furnace.

Different situation occurred in red beds samples in which the heating and cooling curves are not well defined but note a trend of decrease of susceptibility with the increasing temperature.

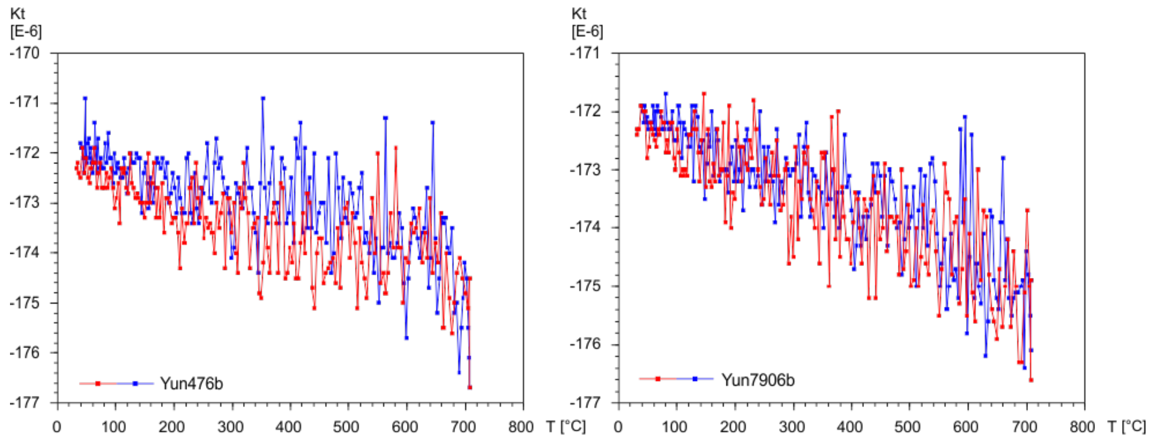

Figure 83. Thermomagnetic curves for representative red beds specimens (Yun47 and Yun79).

The "Day plot" has been drawn only for the low coercivity/saturated samples (Table 6), in order to define the domain state and the consequent magnetic grainsize according to the theoretical hysteresis ratios expected for magnetite and titanomagnetite (Figure 84b).

Table 6. Hysteresis Parameters of samples relative to "Day plot" shown in Figure 84b.

Samples	Mass (g)	Mass (kg) (=[Mass]/1000)	Ms (Am^2)	Mass_Ms (Am^2/kg) (=[Ms]/[Mass])	Mrs (Am^2)	Mass_Mrs (Am^2/kg) (=[Mrs]/[Mass])	Bc (T)	Bcr (T)	Bcr/Bc	Mrs/Ms
04-04a	0.16	0.00016	8.03473E-05	0.502170375	1.15606E-05	0.072253813	0.01230367	0.03086621	2.51	0.14
11-04a	0.26	0.00026	0.000108264	0.416401538	1.81067E-05	0.069641038	0.009290813	0.01977991	2.13	0.17
12-04a	0.22	0.00022	5.98083E-05	0.271855818	1.22364E-05	0.055620045	0.01653307	0.03403819	2.06	0.20
13-04a	0.25	0.00025	0.0000762	0.3048	1.43589E-05	0.05743556	0.006049184	0.01413916	2.34	0.19
15-04a	0.25	0.00025	0.000167472	0.6698868	2.73662E-05	0.1094648	0.01158414	0.02547041	2.20	0.16
16-04a	0.28	0.00028	7.89221E-05	0.281864786	1.74328E-05	0.062260036	0.0192496	0.04005314	2.08	0.22
18-04a	0.19	0.00019	0.000112137	0.590195263	1.21231E-05	0.063806	0.004727123	0.01557542	3.29	0.11
19-04a	0.25	0.00025	5.79663E-05	0.2318652	1.49559E-05	0.05982364	0.01253398	0.01840643	1.47	0.26
20-04a	0.25	0.00025	8.31621E-05	0.33264832	1.81376E-05	0.07255028	0.01471912	0.01878878	1.28	0.22
21-04a	0.21	0.00021	0.000143387	0.682796667	2.10463E-05	0.100220524	0.01352794	0.03143721	2.32	0.15
22-04a	0.24	0.00024	0.000163223	0.680096667	2.03443E-05	0.084767875	0.0116234	0.02649358	2.28	0.12
23-04a	0.26	0.00026	0.000143302	0.551159615	6.38942E-05	0.245746923	0.03123689	0.04238027	1.36	0.45
33-04c	0.21	0.00021	4.44939E-07	0.002118755	1.06661E-07	0.000507911	0.01753115	0.05317518	3.03	0.24
34-03b	0.23	0.00023	3.34486E-07	0.001454289	6.64024E-08	0.000288706	0.02130191	0.06908135	3.24	0.20

Most of these samples fall in the upper-central region of the plot, not far from the upper segment of the theoretical curves calculated for mixtures of single domain (SD) and multidomain (MD) magnetite grains, thus suggesting a significant contribution of stable SD particles to the overall magnetic mineralogy, according to *Zhao et al.* [2015; *Day et al.,* 1977; *Dunlop,* 2002].

Noteworthy, selected samples from volcanic sites Yun10, 14 and 17 show wasp-waisted hysteresis loops, which can be ascribed both to the coexistence of superparamagnetic (SP) and single-domain (SD) particles or to the mixing of hard and soft coercivity magnetic minerals, as magnetite and hematite [Table 7 and Figure 84a; *Roberts et al.,* 1995].

Table 7. Hysteresis Parameters of samples from Gaoligong Shear Zone.

Samples	Mass (g)	Mass (kg) (=[Mass]/1000)	Ms (Am^2)	Mass_Ms (Am^2/kg) (=[Ms]/[Mass])	Mrs (Am^2)	Mass_Mrs (Am^2/kg) (=[Mrs]/[Mass])	Bc (T)	Bcr (T)	Bcr/Bc	Mrs/Ms
01-03b	0.27	0.00027	1.39E-05	5.13E-02	3.29E-06	1.22E-02	1.85E-02	5.07E-02	2.74	0.24
02-08b	0.29	0.00029	4.31E-06	1.49E-02	1.69E-06	5.81E-03	3.07E-02	1.04E-01	3.38	0.39
05-01a	0.21	0.00021	8.50E-08	4.05E-04	1.03E-08	4.93E-05	8.12E-03	4.52E-02	5.57	0.12
10-04a	0.25	0.00025	6.47E-05	2.59E-01	3.10E-05	1.24E-01	1.92E-02	2.60E-02	1.36	0.48
14-04a	0.21	0.00021	6.81E-05	3.24E-01	2.96E-05	1.41E-01	2.15E-02	3.47E-02	1.61	0.43
17-04a	0.25	0.00025	8.02E-05	3.21E-01	4.23E-05	1.69E-01	3.71E-02	4.04E-02	1.09	0.53
24-08b	0.24	0.00024	1.50E-06	6.23E-03	1.06E-06	4.43E-03	3.71E-01	4.98E-01	1.34	0.71
25-04c	0.26	0.00026	5.43E-07	2.09E-03	3.56E-07	1.37E-03	2.62E-01	4.28E-01	1.63	0.66
26-04c	0.25	0.00025	8.47E-07	3.39E-03	4.96E-07	1.98E-03	1.83E-01	3.73E-01	2.04	0.59
27-08b	0.25	0.00025	6.61E-07	2.64E-03	3.38E-07	1.35E-03	1.40E-01	4.33E-01	3.08	0.51
28-05a	0.2	0.0002	7.10E-07	3.55E-03	3.05E-07	1.52E-03	5.66E-02	3.98E-01	7.04	0.43
29-02c	0.27	0.00027	6.48E-07	2.40E-03	3.80E-07	1.41E-03	2.13E-01	3.30E-01	1.55	0.59
30-10b	0.25	0.00025	8.64E-07	3.46E-03	4.44E-07	1.77E-03	1.41E-01	4.06E-01	2.88	0.51
31-06c	0.19	0.00019	1.17E-06	6.17E-03	8.72E-07	4.59E-03	4.28E-01	5.46E-01	1.28	0.74
32-01c	0.22	0.00022	2.11E-07	9.58E-04	1.45E-08	6.60E-05	7.36E-03	3.65E-02	4.95	0.07
35-02b	0.2	0.0002	5.67E-07	2.83E-03	2.91E-07	1.46E-03	1.73E-01	3.28E-01	1.89	0.51
36-07c	0.27	0.00027	1.04E-06	3.86E-03	7.06E-07	2.61E-03	3.39E-01	5.03E-01	1.48	0.68
37-03c	0.29	0.00029	1.01E-06	3.49E-03	6.17E-07	2.13E-03	2.64E-01	5.10E-01	1.93	0.61
38-04c	0.26	0.00026	9.77E-07	3.76E-03	5.13E-07	1.97E-03	2.01E-01	5.12E-01	2.54	0.53
39-04b	0.24	0.00024	1.40E-06	5.82E-03	8.81E-07	3.67E-03	3.02E-01	4.85E-01	1.61	0.63
40-05c	0.22	0.00022	7.10E-07	3.23E-03	4.65E-07	2.11E-03	2.90E-01	4.88E-01	1.68	0.65
41-04c	0.26	0.00026	4.75E-07	1.83E-03	3.17E-07	1.22E-03	2.97E-01	4.53E-01	1.53	0.67
42-03b	0.27	0.00027	3.07E-06	1.14E-02	1.97E-06	7.31E-03	2.42E-01	3.97E-01	1.64	0.64
43-05c	0.24	0.00024	1.16E-06	4.84E-03	6.87E-07	2.86E-03	1.71E-01	2.75E-01	1.61	0.59
44-10c	0.24	0.00024	1.15E-06	4.78E-03	6.28E-07	2.62E-03	2.02E-01	4.46E-01	2.21	0.55
45-03c	0.22	0.00022	8.27E-07	3.76E-03	4.07E-07	1.85E-03	1.94E-01	4.47E-01	2.30	0.49
46-09c	0.25	0.00025	5.59E-07	2.24E-03	2.90E-07	1.16E-03	1.73E-01	4.82E-01	2.78	0.52
47-08b	0.23	0.00023	8.25E-07	3.58E-03	5.39E-07	2.34E-03	3.32E-01	5.03E-01	1.52	0.65
48-05c	0.25	0.00025	5.74E-07	2.29E-03	3.69E-07	1.48E-03	3.30E-01	5.37E-01	1.63	0.64
49-04c	0.28	0.00028	1.02E-06	3.64E-03	6.87E-07	2.46E-03	4.13E-01	5.75E-01	1.39	0.67
50-10c	0.22	0.00022	1.40E-06	6.38E-03	9.16E-07	4.16E-03	2.85E-01	4.35E-01	1.53	0.65

The FORC diagram (Figure 84c) of a selected sample from site Yun10 shows closed contours peaked at about 15-20 mT, with a concurring secondary peak at the origin and asymmetric nearly vertical contours extending into the lower quadrant [*Pike at al.,* 2001], thus indicating that the wasp-waisted shape of the hysteresis loop, in this case, is due to the coexistence of ultrafine SP and fine SD magnetite particles.

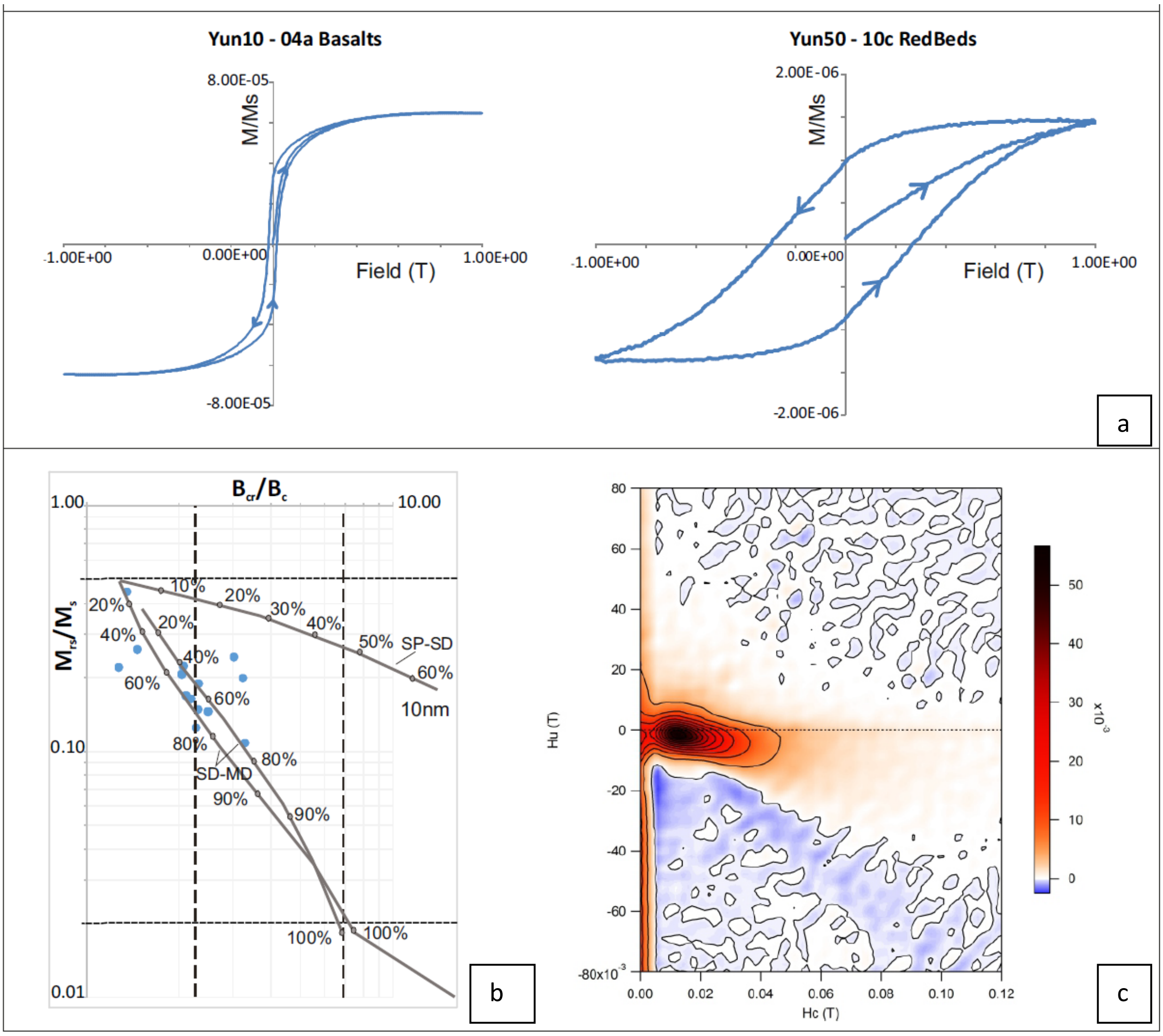

Figure 84. a) Representative wasp-waisted and high-coercivity/unsaturated hysteresis loops; b) "Day plot" for the low coercivity/saturated (up to 1 T applied magnetic field) set of samples; the SD, PSD and MD fields and the theoretical mixing lines for SD-MD and SP-SD grains are from *Dunlop* [2002] and refer to magnetite; c) FORC diagram of a specimen with wasp-waisted hysteresis features; the smoothing factor SF = 3. Modified after *Pellegrino et al.* [2018].

Red beds sediments are widely distributed in tropical and subtropical areas [*Robb,* 1949*; Walker,* 1967*; Van Houten,* 1968, 1973*; Collinson,* 1974] and have been extensively used for paleomagnetic studies [*Kent et al.,* 1986*; Tan et al.,* 2003*; Iosifidi et al., 2010*]. Often, these sediments, are re-magnetized and when it occurs, the interpretation of paleomagnetic, and magnetic mineralogy data becomes complicated [*Collinson, 1965; Kent et al.,* 1987; *McCabe and Elmore,* 1989; *Suk et al*., 1993; *Wang and Vander Voo,* 1993; *Lu et al.*, 1994; *Piper et al.,* 1999; *Kodama and Dekkers,* 2004; *Roberts and Weaver,* 2005; *Elmore et al.,* 2006; *Rowan and Roberts,* 2006; *Deng et al.,* 2007; *Jin and Liu,* 2011; *Liu et al.*, 2011; *Vander Voo and Torsvik,* 2012; *Roberts,* 2015]. Remagnetization may happen with different mechanisms: 1) mineral transformations associated with redox process, i.e. magnetite, greigite, or pyrrhotite formation [*Katz et al.,* 2000; *Weaver et al.,* 2002; *Roberts and Weaver,* 2005], 2) deformation-associated to fluid migration and/or pressure solution [*McCabe and Elmore*, 1989; *Elmore and McCabe,* 1991; *Housen et al.,* 1993], 3) chemical weathering in moist, tropical climates, and soil-forming environments [*Creer,* 1961, 1968; *Jin and Liu,* 2011; *Liu et al.,* 2011], or 4) thermoviscous remanent magnetization acquisition [*Scotese et al.,* 1982; *Kent,* 1985; *Hashimoto et al.,* 2008; *Jiang et al.,* 2017]. The natural remanent magnetization (NRM), infact, in most red beds is a composite of detrital and authigenic hematite [*Collinson,* 1966, 1974*; Tauxe et al.,* 1980].

In South China, several paleomagnetic investigations were conducted on the red beds, especially for regional paleogeographic reconstructions [e.g. *Achache et al.,* 1984; *Zaman and Torii*, 1999; *Steiner and Lucas,* 2000; *Sun et al.,* 2006]. Recently, data reported by *Jiang et al.,* [2017], show that two remanence components carried by secondary and primary hematite are isolated with thermal demagnetization. CRM carried by secondary hematite was interpreted, generated by magnetite oxidation during tectonic activity. Therefore, the secondary magnetization with steep inclination, commonly observed in Triassic samples of the South China Block, was interpreted to have been influenced by a combination of the remanence carried by parent magnetite, the orogenic stress field, and the contemporaneous geomagnetic field direction during deformation [*Jiang et al.,* 2017].

Liu et al., [2011] investigated the remagnetization mechanism in red beds from Lower Triassic sandstones in Yunnan Province. They put forward a remagnetization process summarized as follow: initially, the relatively coarse-grained haematite and magnetite of detrital origin were deposited during the early Triassic. These two minerals carried the primary detrital remanent magnetization (DRM). During the Quaternary–Palaeogene period, the region went through a fluid event that accelerated the neoformation of fine-grained haematite and maghemite with variable unblocking temperature spectra. These newly formed magnetic minerals, particularly the haematite, carry the secondary CRM, which fully or partially contaminated the primary DRM. This region was uplifted at the same time as the Tibetan plateau to the northwest as the result of the India–Eurasia collision during the early Palaeogene [e.g. *Wang et al.,* 1998; *Najman et al.*, 2010]. This uplift of the Tibetan plateau could have been responsible for the fluid migration that instigated the formation of the authigenic maghemite and haematite [*Liu et al.,* 2011].

A progressive acquisition of isothermal remanent magnetization (IRM) up to a maximum field of 2.7 T was performed on my red beds, samples along the Red River faults, using a 2G Enterprises 2G 660 Pulse Magnetizer.

The acquisition of **IRM** curves, through the laboratory application of stepwise-increasing uniaxial fields to a rock-magnetic sample, provides an important non-destructive tool for the investigation of coercivity spectra [*Dunlop and O¨ zdemir,* 1997]. A ferromagnetic substance subject to the action of an external magnetic field retains a remanent magnetization even when the field is removed. The coexistence of different phases can be highlighted with the procedure proposed by *Lowrie* [1990]. The samples are magnetized at three decreasing field values in three orthogonal directions $H_z > H_y > H_x$. The three components of the IRM are thus carried by grains with high (J_z), intermediate (J_y) and low-coercivity (J_x). For a more complete interpretation, IRM acquisition must be combined with subsequent thermal demagnetization of the IRM gradually removes the three components and provides indications on their blocking temperature spectrum and Curie point (Figure 85).

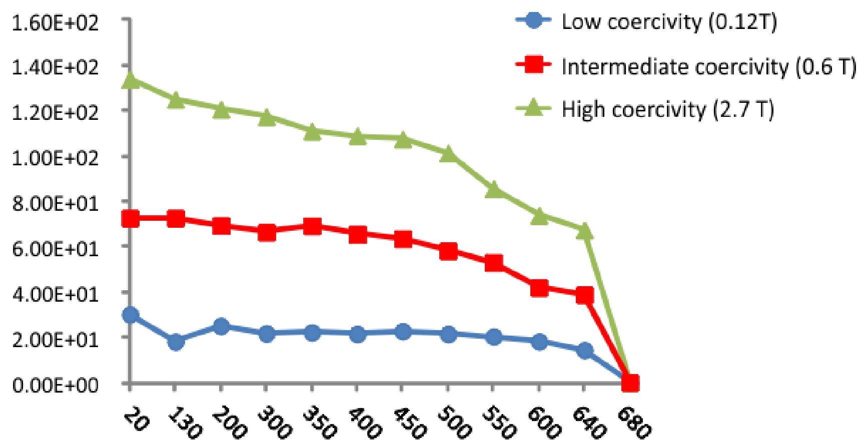

Figure 85. Example of thermal demagnetization of three-component isothermal remanent magnetization (IRM) curves, according to the *Lowrie* [1990] method. T (°C) in x axis from 20° to 680°; Intensity of magnetization in y axis. Green, red and blue lines represents respectively Y, Z and X axis of coercivity.

A thermal demagnetization of the composite IRMs (imparted at 2.7 T, 0.6 T and 0.12 T along z, y and x axes of the specimens, respectively) was conducted for samples outcropping along the Ailaoshan Red River Fault Zone, to identify the unblocking temperature spectra of the representative samples [*Lowrie*, 1990].

Thermal demagnetization curves of the three-component IRM show that the intensity of all the three components decrease quickly above 650°C and unblock up to 680°C, suggesting the dominance of high-coercivity hematite (the Néel temperature for hematite is approximately 685 °C). This is confirmed also by the results of hysteresis loops. All of these results indicate that hematite is the main magnetic remanence carrier in the sediments.

As shown in Figures 86,87,88 in which the data are clustered respectively in pre-, syn- and post-tilting (indicating post, syn and pre-tilting overprint, respectively – see table 3 for more datails), according to our paleomagnetic results (see Table 3), a clear mineralogical fingerprint is evident in almost all analyzed samples. The low coercivity component is mostly absent and the medium and high magnetization components essentially prevail. The shape of prevailing convex decay of high-coercivity component (carried by hematite) is similar for all sediments. Thus such magnetic mineralogy experiments are unfortunately not useful to identify sites undergoing (or not undergoing) magnetic overprint, and sites remagnetized before, during or after strata tilting.

In agreement to *Jiang et al*. [2015], my data suggests that two components of intermediate and high coercivity could be indicate a double magnetization case: ChRM/MT and HT components discriminate, respectively, a first chemical (gradual decay between ~200 and 640°C) and then detritic remagnetization (most decay in the 600–680°C range). *Jiang et al*., [2017] interpreted the CRM to have been generated by magnetite oxidation during tectonic activity. As said, is valid for each step of magnetization respect to tilting events (Figure 86,87,88), and its clearly shown from different sites (Yun80, 85, 88, 65, 70, 75).

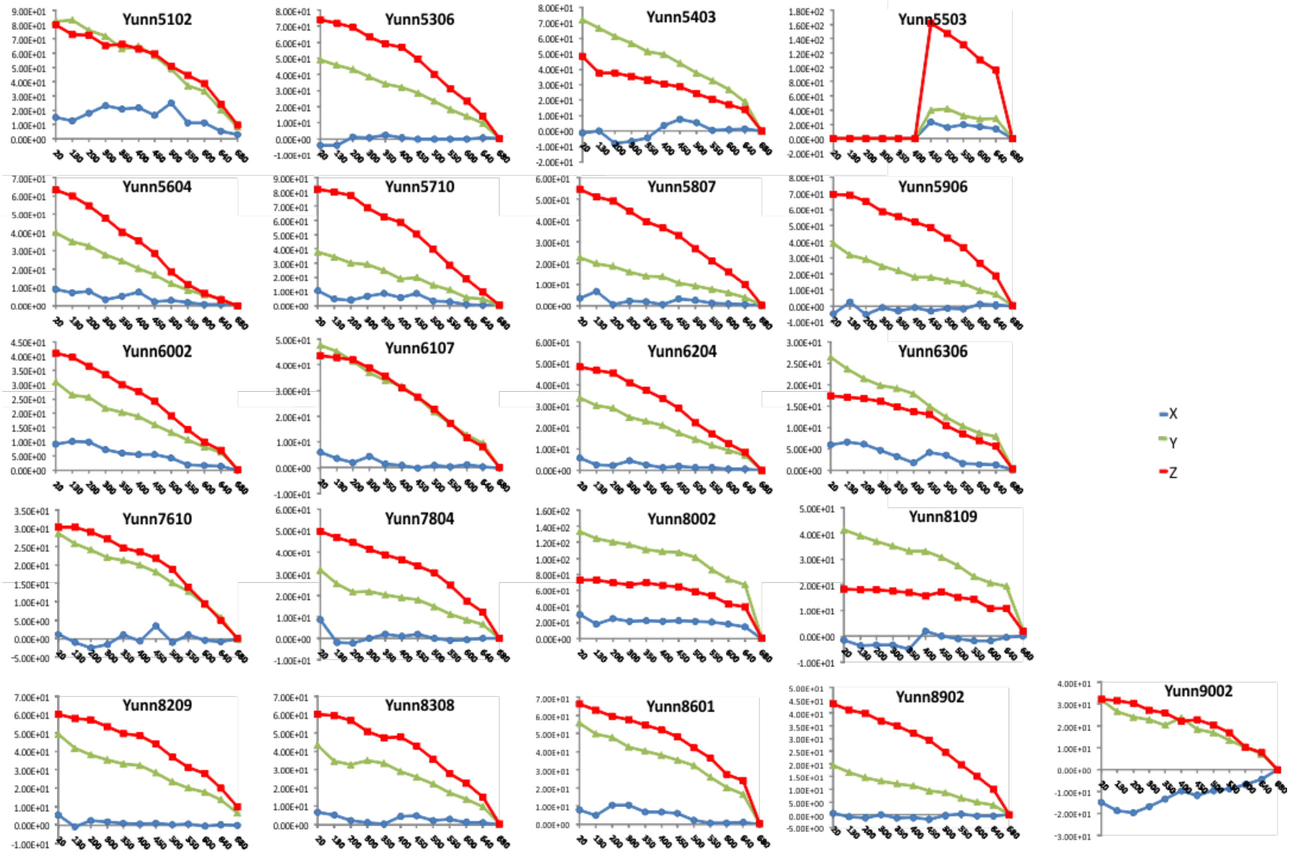

Figure 86. IRM curves relative to sites with pre-tilting magnetization.

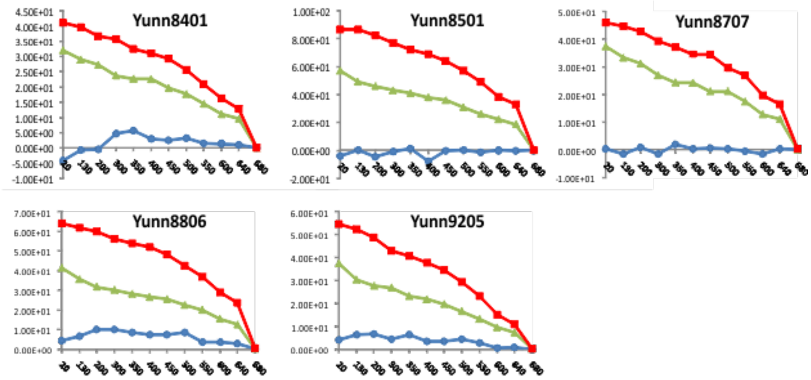

Figure 87. IRM curves relative to sites with syn-tilting magnetization.

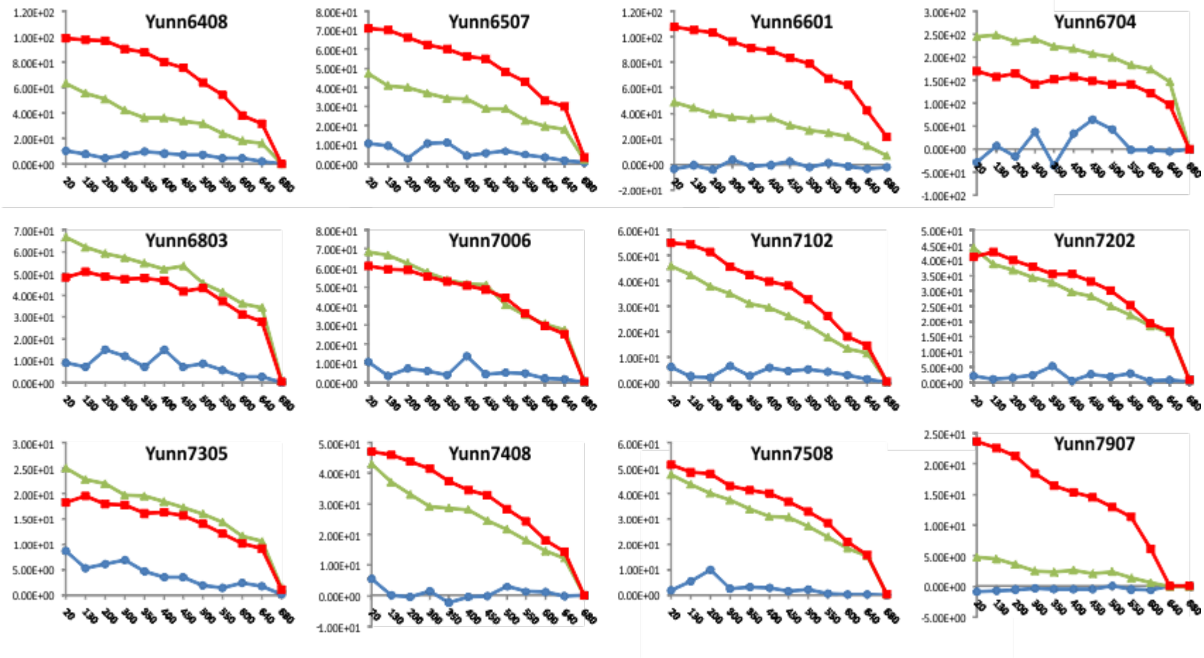

Figure 88. IRM curves relative to sites with post-tilting magnetization.

Chapter X

10. CONCLUSIONS

The conclusions of this thesis can be summarized as follows:

- According to *Pellegrino et al*. [2018], the paleomagnetic study of Pliocene-Holocene volcanics and Mesozoic red beds exposed east and west (respectively) of the Gaoligong Shear Zone show that low Ti-magnetite and hematite dominate the respective magnetic mineralogy. Three bits of evidence suggest that the magnetization in the red beds is here of primary origin (detrital hematite), and/or acquired during early diagenesis by chemical hematite growth: 1) the data support a positive fold test at the 99% significance level, indicating that magnetization acquisition is pre-tilting (i.e. pre-Eo-Oligocene) in age; 2) although the majority of the sites yield a normal polarity, three sites show a reverse polarity, and alternating normal and reverse polarity beds were documented in an additional site; 3) a statistically significant positive inclination flattening of the whole red bed data set proves that magnetization acquisition predate diagenesis. Thus we speculate that – assuming a primary magnetization origin- the majority of our sites were deposited during the long normal Cretaceous superchron. Similar paleomagnetic evidence was previously documented at several other red beds sites from Yunnan (e.g. *Li et al*., 2017b and references therein), and the final resolution of this problem would lie in the accurate site age determination, indeed a problematic issue given the continental nature and the coarse grain size of the studied sediments.

- The clockwise rotations pattern observed in Mesozoic red beds exposed east of the Gaoligong Shear Zone (Baoshan block) points to a quasi-continuous crust kinematics model, characterized by rigid blocks of smaller size (≤1 km close to the fault) than the fault deformation zone itself and by rotation values >90° close to strike-slip faults. CW rotations close to the fault reach 176°, and decrease moving east up to be virtually annulled at ca. 20 km east from the contact with mylonites exposed along the shear zone. As discussed in chapter 1, block rotations adjacent to shear zones occur in response to the angular velocity of the ductile deformation, taking place at great depth in the lower crust [*Beck*, 1976; *McKenzie and Jackson*, 1983; *Lamb*, 1987; *Nelson and Jones*, 1987; *Salyards et al*., 1992; *Sonder et al*., 1994; *Piper et al*., 1997; *Randall et al*., 2011]. We cannot exclude that the same behavior is reflected even at greater depths beyond the crust, but more data (eg. deep sismic data, ect..) would be necessary to prove it. Paleomagnetism is restricted to the examination of the upper crust and does not provide a deep crust/lithospheric depth evaluation.

- By using the equation of *Lamb* [1987], which relates rotations to fault displacement in a quasi-continuous crust deformation model, we find a total Gaoligong fault dextral offset ranging between 230 and 290 km, which is consistent with the 600 km total fault length, if offset is related to mega-block extrusion due to India-Asia collision [*Wang and Burchfiel*, 1997; *Zhang et al*., 2012a]. Three sites sampled adjacent to the fault yielded scattered rotations (from 74° CCW to 116° CW) that may be interpreted as huge CW rotations exceeding 180°. This suggests that a sort of "rotation channel" exists adjacent to the fault, where small block rotate freely by large magnitude, conforming to the "ball bearing" model of *Beck* [1976].

- Four sites sampled at greatest distance (15-20 km) from the contact with Gaoligong Shear Zone mylonites yield a mean CW rotation of 20.5° ± 12.2°. Although the trend of rotation values vs. fault distance is suggestive of a complete rotation cessation at ca. 25 km from mylonite contact, a 20° rigid CW rotation of the Baoshan block cannot be excluded by our data set. A 20° Baoshan block rotation indeed does not compare with the 70°-80° CW rotations gathered by *Tong et al.*

[2016] from two additional localities from the centre of the block itself. A 20° rigid Baoshan block rotation would also reduce to 145° the maximum CW rotation due to Gaoligong fault shear, and this in turn would change to 200-250 km the paleomagnetically-evaluated dextral fault offset. However, the discrepancy between our data and those by *Tong et al*. [2016] strongly suggests that the Baoshan block is broken in additional sub-blocks undergoing independent rotations.

- Pliocene-Holocene volcanic sites (and one Pliocene sedimentary site) located west of the fault (Tengchong block) do not rotate, implying that the Gaoligong dextral Shear Zone yielding CW rotations has been active during the Oligo-Miocene time span (early Oligocene Gaoligong Shear Zone activity onset according to *Wang et al*., 2006), but not over the last 5 Ma. This is in good agreement with the focal mechanism of the 1976 M=7.4 earthquake, showing a sinistral shear sense along the southern end of the Gaoligong Shear Zone, and prove that the present-day CW rotation of SE Tibet and northern Yunnan shown GPS data [*Liang et al*., 2013] has nothing to do with significantly older paleomagnetic rotation. The geomagnetic field PSV is not averaged out in our volcanic paleomagnetic data, thus possibly implying a few degree bias on average null rotation value that is however much smaller than the large (up to 176°) rotations observed in Mesozoic red beds.

- The data collected along the Gaoligong fault, show for the first time, which fault shear may represent a significant tectonics contributing to the CW rotations frequently documented along the Indochina blocks [e.g. *Li et al*., 2017a; *Tong et al*., 2016]. However, CW rotations were also documented far (i.e. >20 km) from the strike-slip faults and within the rough centre of the blocks themselves, so that it is possible that some blocks - at least the south Indochina, Simao and Lanping terranes- underwent also semi-rigid rotations. Yet, the tectonics and dynamics of such block rotations (whether a sort of "ball-bearing" or "domino" model) have not been properly elucidated at presently, and it is unclear why predominantly CW rotations occur. Furthermore, several works [*Chen et al*., 1995; *Sato et al*., 2001, 2007; *Tanaka et al*., 2008; *Otofuji et al*., 2012] seem to support internal deformation (and variable rotations) in the Simao domain, so that no rigid mega-block rotation would exist. *Kondo et al*. [2012], *Tong et al*. [2013, 2017], and *Gao et al*. [2015] even report data suggesting a folding-related oroclinal bending within the Simao domain itself, which again would be at odds with the rigid "microplate" rotation model proposed by *Li et al*. [2017a].

- Trying to solve this question, Triassic-Cretaceous sites were sampled, at both sides of the Ailao-Shan Red River Shear Zone (ARRSZ), within the Chuandian, Lanping and Northern Simao domains. The sites yielded measurable and stable magnetization components, but magnetization acquisition timing was different in the three blocks. Sites from the Chuandian domain show a normal polarity and were remagnetized after folding that probably occurred from Late Eocene to Early Oligocene (about 33 Ma ago) [*Gao et al*., 2017]. The tectonic rotations calculated by us and previous authors within this block, are mostly CW and do not exceed 20°. Thus, we have no evidence of fragmentation of the Chuandian domain.

In the northern Simao domain the magnetization was acquired before folding event, but the ubiquitous normal polarity in Jurassic-Cretaceous sites suggests a pre-folding magnetic overprint. Unlike to the Chuandian block, here data do not support a rigid block rotation, but suggest that the northern Simao domain is made of small (few km of size) sub-blocks rotating CW, separated by non-rotating domains of similar size, according to previous authors [Figure 81, *Chen et al.*, 1995; *Sato et al.*, 2007].

Finally, a high-temperature magnetization component (640-680°C) suggests a similar rotational behaviour (CW-rotating and non-rotating sub-blocks) in the centre of the Lanping domain. Conversely, a 300-640°C component was later acquired at 28% unfolding and subsequently underwent no rotation. The folding events took place in Paleogene, resulting in north-south trending fold axes in Mesozoic system [*Funahara et al.*, 1993]. The sites close to the ARRSZ yield great rotations on the order of 180° that confirm past occurrence of significant left strike-slip shear along the ARRSZ itself. Conversely, sites located at 10-15 km distance from the Chongshan Shear Zone show ca. 90° CCW rotations that imply also a left-lateral shear along the fault zone, consistently with recent geological evidence.

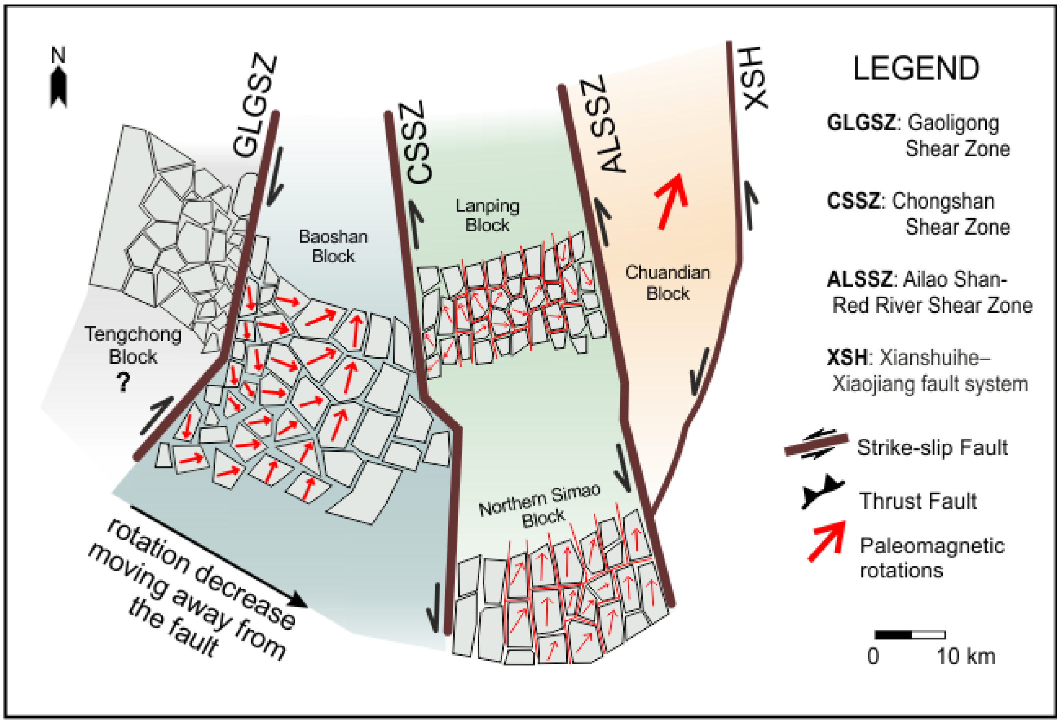

Figure 89. Cartoon explaining the blocks rotational model in Yunnan (China) in Oligocene-Miocene age, along the major strike-slip fault zones and inside the block itself.

- Magnetic anisotropy data confirm the different behaviour of the crustal blocks, in particular, in the investigated areas, we highlight the presence of foliated planes oriented NNE-SSO, approximately parallel to the orientation of the main structures. Along the Gaoligong fault zone the direction of the lineation is often strikingly sub-vertical, a setting uncommon in fold and thrust belts. Instead, along the Red River fault zone, the direction of the foliation planes is predominantly N-S. This implies a compression oriented mainly E-W probably responsible of the strong deformation inside the blocks.
- Hematite is the dominant magnetic carrier in the Jurassic-Cretaceous red beds and it also plays a fundamental role in the magnetic anisotropy fabric setting (typically normal fabric) of these sediments.
- The results of this PhD work along with previous paleomagnetic data, indicate that crust deformation of the Yunnan is extremely complex and still to be completely elucidated. The “blocks” certainly underwent a strong internal deformation and were fragmented in smaller independent sub-blocks whose kinematics and tectonics are still a matter of speculation. Additional structural and paleomagnetic data are necessary to fully constrain the kinematics and tectonics of the small size blocks. In any case, this work shows that no “big” (hundred of km wide) rigid crustal blocks exist between Tibet and Indochina.

References

A

Achache, J., Courtillot, V., & Xiu, Z. Y. (1984). Paleogeographic and tectonic evolution of southern Tibet since middle Cretaceous time: new paleomagnetic data and synthesis. *Journal of Geophysical Research*, 89, 10311-10339. https://doi.org/10.1029/JB089iB12p10311

Aitchison, J. C., Ali, J. R. & Davis, A. M. (2007). When and where did India and Asia collide?. *Journal of Geophysical Research: Solid Earth*, 112(B5). https://doi.org/10.1029/2006JB004706

Akciz, S., Burchfiel, B. C., Crowley, J. L., Yin, J., & Chen, L. (2008). Geometry, kinematics, and regional significance of the Chong Shan shear zone, Eastern Himalayan Syntaxis. *Geosphere*, 4(1), 292-314. https://doi.org/10.1130/GES00111.1

Ali, J. R., Cheung, H. M. C., Aitchison, J. C., & Sun, Y. (2013). Paleomagnetic re-investigations of Early Permian rift basalts from the Baoshan Block, SW China: constraints on the site-of-origin of the Gondwana-derived eastern Cimmerian terranes. *Geophysical Journal International*, 193, 650-663. https://doi.org/10.1093/gji/ggt012

Alimohammadian, H., Hamidi, Z., Aslani, A., Shahidi, A., Cifelli, F., & Mattei M. (2013). A tectonic origin of magnetic fabric in the Shemshak Group from Alborz Mts. (northern Iran). *Journal of Asian Earth Sciences*, 73, 419-428. https://doi.org/10.1016/j.jseaes.2013.05.014

Allen, C. R., Gillespie, A. R., Han, Y., Sieh, K. E., Zhang, B., & Zhu, C. (1984). Red River and associated faults, Yunnan Province, China. Quaternary geology, slip rates, and seismic hazard. *Geological Society of America Bulletin,* 95, 686-700. https://doi.org/10.1130/0016-7606(1984)95<686:RRAAFY>2.0.CO;2

Allmendinger, R. W., Reilinger, R., & Loveless, J. (2007). Strain and rotation rate from GPS in Tibet, Anatolia and the Altiplano. *Tectonics*, 26(3). https://doi.org/10.1029/2006TC002030

Arason, P., & Levi S. (1990). Models of inclination shallowing during sediment compaction, *Journal of Geophysical Research*, 95, 4481-4499. https://doi.org/10.1029/JB095iB04p04481

Avouac, J.-P., & Tapponnier P. (1993). Kinematic model of active deformation in central Asia, *Geophysical Research Letters*, 20, 895– 898. https://doi.org/10.1029/93GL00128

B

Bates R. B., Beck, M. E., & Burmester, R. F. (1981). Tectonic rotations in the Cascade range of southern Washington. *Geology*, 9, 184-189. https://doi.org/10.1130/0091-7613(1981)9<184:TRITCR>2.0.CO;2

Beck, M. E. (1976). Discordant paleomagnetic pole positions as evidence of regional shear in the western Cordillera of North America. *American Journal of Science*, 276, 694–712. https://doi.org/10.2475/ajs.276.6.694

Beck, M. E. (1980). Paleomagnetic record of plate-margin tectonic processes along the western edge of North America. *Journal of Geophysical Research: Solid Earth*, 85(B12), 7115-7131. https://doi.org/10.1029/JB085iB12p07115

Beck M. E. (1984). Has the Washington-Oregon Coast Range moved northward?. *Geology*, 12, 737-740. https://doi.org/10.1130/0091-7613(1984)12<737:HTWCRM>2.0.CO;2

Beck, M. E. (1986). Model for Late Mesozoic-Early Tertiary tectonics of coastal California and western Mexico and speculations on the origin of the San Andreas Fault. *Tectonics*, 5(1), 49-64. https://doi.org/10.1029/TC005i001p00049

Beck, M. E., Burmester, R. F., Craig, D. E., Grommé, C. S., & Wells, R. E. (1986). Paleomagnetism of middle Tertiary volcanic rocks from the Western Cascade series, northern California: Timing and scale of rotation in the southern Cascades and Klamath Mountains. *Journal of Geophysical Research: Solid Earth,* 91, 8219-8230. https://doi.org/10.1029/JB091iB08p08219

Beck, M. E., & Burr, C. D. (1979). Paleomagnetism and tectonic significance of the Goble Volcanic Series, southwestern Washington. *Geology*, *7*, 175-179. https://doi.org/10.1130/0091-7613(1979)7<175:PATSOT>2.0.CO;2

Beck, M., Rojas, C., & Cembrano J. (1993). On the nature of buttressing in margin-parallel strike slip fault systems. *Geology*, 21, 755-758. https://doi.org/10.1130/0091-7613(1993)021<0755:OTNOBI>2.3.CO;2

Besse, J., Courtillot, V., Pozzi, J.P., Westphal, M., & Zhou, Y.X. (1984). Paleomagnetic estimates of crustal shortening in the Himalayan thrusts and Zangbo suture. *Nature*, 311, 621–626. http://doi.org/10.1038/311621a0

Bird, P. (1991). Lateral extrusion of lower crust from under high topography, in the isostatic limit. *Journal of Geophysical Research: Solid Earth*, 96(B6), 10275–10286. https://doi.org/10.1029/91JB00370

Bird, P., & Piper, K. (1980). Plane-stress finite element models of tectonic flow in southern California. *Physics of the Earth and Planetary Interiors*, 21(2-3), 158–175. https://doi.org/10.1016/0031-9201(80)90067-9

Borradaile, G.J. (1981). Particulate flow of rock and the formation of rock cleavage. *Tectonophysics*, 72(3-4), 305-321. https://doi.org/10.1016/0040-1951(81)90243-2

Borradaile, G.J. (1987). Anisotropy of magnetic susceptibility: rock composition versus strain. *Tectonophysic*s, 138(2-4), 327-329. https://doi.org/10.1016/0040-1951(87)90051-5

Borradaile, G.J. (1988). Magnetic susceptibility, petrofabrics and strain. *Tectonophysics*, 156(1-2), 1-20. https://doi.org/10.1016/0040-1951(88)90279-X

Borradaile, G.J., & Henry, B. (1997). Tectonic applications of magnetic susceptibility and its anisotropy. *Earth-Science Reviews*, 42(1-2), 49-93. https://doi.org/10.1016/S0012-8252(96)00044-X

Borradaile G.J., & Tarling, D. (1984). Strain partitioning and magnetic fabrics in particulate flow. *Canadian Journal of Earth Sciences*, 21(6), 694-697. https://doi.org/10.1139/e84-075

Bouchez, J.L. (1997). Granite is never isotropic: an introduction to AMS studies of granitic rocks, In: *Granite: from segregation of melt to emplacement fabrics*, edited by Bochez, J.L., et al., Klumer, Rotterdam, 95-112. https://doi.org/10.1007/978-94-017-1717-5_6

Bourne, S., England, P., & Parsons, B. (1998). The motion of crustal blocks driven by flow of the lower lithosphere and implications for slip rates of continental strike-slip faults. *Nature*, 391, 655–659. https://doi.org/10.1038/35556

Bureau of Geology and Mineral Resources of Xizang Autonomous Region (1993). Regional geology of Xizang (Tibet) with 1/1,500,000 geological map (in Chinese with English abstract). Beijing: Geological Publishing House.

Bureau of Geology and Mineral Resources of Yunnan Province (1990). Regional geology of Yunnan Province (in Chinese with English Abstract). Beijing: Geological Publishing House.

Butler, R. F. (1992). Paleomagnetism: Magnetic Domains to Geological Terranes. *Blackwell Scientific Publications*. https://trove.nla.gov.au/version/42539440

Butler R. F., Gehrels, G. E., McClelland, W. C., May, S. R., & Klepacki, D. (1989). Discordant paleomagnetic poles from the Canadian Coast Plutonic Complex: Regional tilt rather than large-scale displacement?. *Geology*, 17(8), 691-694. https://doi.org/10.1130/0091-7613(1989)017<0691:DPPFTC>2.3.CO;2

C

Cao, S. Y., Liu, J. L., & Leiss, B. (2010). Orientation-related deformation mechanisms of naturally deformed in amphibolite mylonite from the Diancang Shan, SW, Yunnan, China. Journal of Structural Geology, 32, 606–622. https://doi.org/10.1016/j.jsg.2010.03.012

Cao, S.Y., Liu, J.L., Leiss, B., Neubauer, F., Genser, J., & Zhao, C.Q. (2011a). Oligo-Miocene shearing along the Ailaoshan-Red River Shear Zone: constraints from structural analysis and zircon U/Pb geochronology of magmatic rocks in the Diancang Shan massif, SE Tibet, China. *Gondwana Research,* 19(4), 975–993. https://doi.org/10.1016/j.gr.2010.10.006

Cao, S.Y., Neubauer, F., Liu, J.L., Genser, J., & Leiss B. (2011b). Exhumation of the Diancang Shan metamorphic complex along the Ailaoshan-Red River belt, southwestern Yunnan, China: evidence from ^{40}Ar/^{39}Ar thermochronology. *Journal of Asian Earth Sciences* 42(3), 525–550. https://doi.org/10.1016/j.jseaes.2011.04.017

Caricchi, C., Cifelli, F., Kissel, C., Sagnotti, L., & Mattei, M. (2016). Distinct magnetic fabric in weakly deformed sediments from extensional basins and fold-and thrust structures in the Northern Apennine orogenic belt (Italy). *Tectonics*, 35(10). https://doi.org/10.1002/2015TC003940

Chadima, M., & Hrouda, F. (2007). Remasoft 3.0 software. Paleomagnetic data browser and analyzer. — AGICO *Travaux Géophysiques*, XXVII, 20–21. https://www.agico.com

Chadima M., & Jelinek V. (2009). Anisoft 4.2 software. — AGICO, Inc., Brno, Czech Republic. https://www.agico.com

Chen, F., Satir, M., Ji, J., & Zhong, D. (2002). Nd–Sr–Pb isotopes of Tengchong Cenozoic volcanic rocks from western Yunnan, China: evidence from an enriched-mantle source. *Journal of Asian Earth Sciences*, 21(1), 39–45. https://doi.org/10.1016/S1367-9120(02)00007-X

Chen, H., Dobson, J., Heller, F., & Hao, J. (1995). Paleomagnetic evidence for clockwise rotation of the Simao region since the Cretaceous: A consequence of India-Asia collision. *Earth and Planetary Science Letters*, 134(1-2), 203–217. https://doi.org/10.1016/0012-821X(95)00118-V

Chen, Z., Burchfiel, B., Liu, Y., King, R., Royden, L., Tang, W., Wang, E., Zhao, J., & Zhang, X (2000). Global positioning system measurements from eastern Tibet and their implications for India/Eurasia intercontinental deformation. *Journal of Geophysical Research: Solid Earth*, 105(B7), 16 215–16 227. https://doi.org/10.1029/2000JB900092

Christensen, U. R., & Wicht, J. (2007). Numerical dynamo simulations. G. Schubert (Ed.), *Treatise of Geophysics*, 8, Elsevier, Amsterdam, 245–282.

Chung, S.-L., Lee, T.-Y., Lo, C.-H., Wang, P.-L., Chen, C.-Y., Trong Yem, N., Trong Hoa, T., & Genyao, W. (1997). Intraplate extension prior to continental extrusion along the Ailaoshan–Red River Shear Zone. *Geology*, 25(4), 311–314. https://doi.org/10.1130/0091-7613(1997)025<0311:IEPTCE>2.3.CO;2

Cifelli, F., Ballato, P., Alimohammadian, H., Sabouri, J., & Mattei, M. (2015). Tectonic magnetic lineation and oroclinal bending of the Alborz range: Implications on the Iran-Southern Caspian geodynamics. *Tectonics*, 34, 116–132. https://doi.org/10.1002/2014TC003626

Cifelli, F., & Mattei, M. (2010). Curved orogenic systems in the Italian peninsula: A paleomagnetic review. *Journal of the Virtual Explorer*, 36. https://doi.org/10.3809/jvirtex.2010.00239

Cifelli, F., Mattei, M., Chadima, M., Hirt, A.M., & Hansen, A. (2005). The origin of tectonic lineations in extensional basins: Combined neutron texture and magnetic analyses of ‘‘undeformed’’ clays. *Earth and Planetary Science Letters*, 235(1-2), 62-78. https://doi.org/10.1016/j.epsl.2005.02.042

Cifelli, F., Mattei, M., Chadima, M., Lenser, S. & Hirt, A.M. (2009). The magnetic fabric in “undeformed clays”: AMS and neutron texture analyses from the Rif Chain (Morocco). *Tectonophysics*, 466(1-2), 79-88. https://doi.org/10.1016/j.tecto.2008.08.008

Cifelli, F., Mattei, M., Rashid, H., & Ghalamghash, J. (2013). Right-lateral transpressional tectonics along the boundary between Lut and Tabas blocks (Central Iran). *Geophysical Journal International*, 193(3), 1153–1165. https://doi.org/10.1093/gji/ggt070

Cifelli, F., Rossetti, F., Mattei, M., Hirt, A. M., Funicello, R., & Tortorici L. (2004). An AMS, structural and paleomagnetic study of quaternary deformation in Eastern Sicily. *Journal of Structural Geology*, 26, 29-46. https://doi.org/10.1016/S0191-8141(03)00092-0

Clark, R. M., & Morrison, B. J. (1983). A Normal approximations to the Fisher distribution. *Australian Journal of Statistics,* 25(1). https://doi.org/10.1111/j.1467-842X.1983.tb01201.x

Clark, M. K., & Royden, L. H. (2000). Topographic ooze: Building the eastern margin of Tibet by lower crustal flow. *Geology*, 28(8), 703–706. https://doi.org/10.1130/0091-7613(2000)28<703:TOBTEM>2.0.CO;2

Clark, M. K., Bush, J. W. M., & Royden, L. H. (2005a). Dynamic topography produced by lower crustal flow against rheologic strength heterogeneities bordering the Tibetan Plateau. *Geophysical Journal International*, 162(2), 575–590. https://doi.org/10.1111/j.1365-246X.2005.02580.x

Clark, M. K., House, M. A., Royden, L. H., Whipple, K. X., Burchfiel, B. C., Zhang, X., & Tang, W. (2005b). Late Cenozoic uplift of eastern Tibet. *Geology*, 33(6), 525–528. https://doi.org/10.1130/G21265.1

Clark, M.K., Royden, LH., Whipple, K.X., Burchfiel, B.C., Zhang, X., & Tang, W. (2006). Use of a regional, relict landscape to measure vertical deformation of the eastern Tibetan Plateau. *Journal of Geophysical Research: Earth Surface*, 111(F3). https://doi.org/10.1029/2005JF000294

Coe R. S., Globerman, B. R.,. Plumley, P. W, & Thrupp, G. A. (1985). Paleomagnetic results from Alaska and their tectonic implications, In: Tectonostratigraphic Terranes of the Circum-Pacific Region, Earth Science Series, ed. D. G. Howell, Am. Assoc. Petrol. Geol., Houston Circum-Pacific Council for Energy and Mineral Resources Series, 1, pp. 85-108.

Cogné, J. P., Besse, J., Chen, Y., & Hankard, F. (2013). A new Late Cretaceous to Present APWP for Asia and its implications for paleomagnetic shallow inclinations in Central Asia and Cenozoic Eurasian plate deformation. *Geophysical Journal International*, 192(3), 1000–1024. https://doi.org/10.1093/gji/ggs104

Cohen, K. M., Finney, S. C., Gibbard, P. L., & Fan, J.-X. (2013). The ICS international chronostratigraphic chart. Episodes, 36, 199–204. http://www.stratigraphy.org/index.php/ics-chart-timescale

Collinson, D. W. (1965). The remanent magnetization and magnetic properties of red sediments. *Geophysical Journal of the Royal Astronomical Society,* 10, 105–126. https://doi.org/10.1111/j.1365-246X.1965.tb03055.x

Collinson, D. W. (1966). Carrier of remanent magnetization in certain red sandstones. *Nature*, 210, 516–517. https://doi.org/10.1038/210516a0

Collinson, D. W. (1974). The role of pigment and specularite in the remanent magnetism of red sandstones. *Geophysical Journal International*, 38(2), 253–264. https://doi.org/10.1111/j.1365-246X.1974.tb04119.x

Coney, P.J., Jones, D.L., & Monger, J. (1980). Cordilleran suspect terranes. *Nature*, 288, 329-333. https://doi.org/10.1038/288329a0

Copley, A. (2008). Kinematics and dynamics of the southeastern margin of the Tibetan Plateau. *Geophysical Journal International*, 174(3), 1081–1100. https://doi.org/10.1111/j.1365-246X.2008.03853.x

Coutand, I., Cobbold, P. R., de Urreiztita, M., Gautier, P., Chauvin, A., Gapais, D., & E. Rossello (2001). Style and history of Andean deformation, Puna plateau, northwestern Argentina. *Tectonics*, 20, 210-234. https://doi.org/10.1029/2000TC900031

Cowan, D., Botros, M., & Johnson, H. (1986). Bookshelf tectonics: Rotated crustal blocks within the Sovanco Fracture Zone. *Geophysical Research Letters*, 13(10), 995–998. https://doi.org/10.1029/GL013i010p00995

Cox, A., & Doell, R. R. (1960). Review of paleomagnetism. *Bullettin of the Geological Society of America*, 71, 645-768

Creer, K. M. (1961). Superparamagnetism in red sandstones. *Geophysical Journal International*, 5(1), 16–28. https://doi.org/10.1111/j.1365-246X.1961.tb02925.x

Creer, K. M (1968). Palaeozoic palaeomagnetism. *Nature*, 219, 246–250. https://doi.org/10.1038/219246a0

Curray, J.R., Moore, D.G., Lawver, L.A., Emmel, F.J., Raitt, R.W., Henry, M., & Kieckhefer R. (1979). Tectonics of the Andaman Sea and Burma, in *Geological and Geophysical Investigations of Continental Margins*, J.S. Watkins, L. Montadert, and P.W. Dickerson (Editors), *American Association of Petroleum Geologists Memoir*, 29, 189-198.

Curray, J.R. (2005). Tectonics and history of the Andaman Sea region. *Journal of Asian Earth Sciences* 25 (1), 187–232. https://doi.org/10.1016/j.jseaes.2004.09.001

D

Day, R., Fuller, M., & Schmidt, V.A. (1977). Hysteresis properties of titanomagnetite. Grain-size and compositional dependence. *Physics of the Earth and Planetary Interiors*, 13(4), 260-267. https://doi.org/10.1016/0031-9201(77)90108-X

Deamer, G. A., & Kodama, K. P. (1990). Compaction-induced inclination shallowing in synthetic and natural clay-rich sediments. *Journal of Geophysical Research: Solid Earth*, 95(B4), 4511–4529. https://doi.org/10.1029/JB095iB04p04511

Dekkers, M.J. (2012). End-member modelling as an aid to diagnose remagnetization: a brief review. *Geological Society, London, Special Publications*, 371 (1), 253–269. https://doi.org/10.1144/SP371.12

Demarest, H. (1983). Error analysis for the determination of tectonic rotation from paleomagnetic data. *Journal of Geophysical Research: Solid Earth*, 88(B5),4321-4328. https://doi.org/10.1029/JB088iB05p04321

Deng, C., Liu, Q., Wang, W., & Liu, C. (2007). Chemical overprint on the natural remanent magnetization of a subtropical red soil sequence in the Bose Basin, southern China. *Geophysical Research Letters*, 34(22). https://doi.org/10.1029/2007GL031400

Ding, L., Kapp, P., & Wan, X. (2005). Paleocene-Eocene record of ophiolite obduction and initial India-Asia collision, south-central Tibet. *Tectonics*, 24(3), 1–18. https://doi.org/10.1029/2004TC001729

Dong, F., Hou, Z., Gao, Y., Zeng, P., & Jiang, C. (2006). Cenozoic granitoid in Tengchong, western Yunnan: genesis type and implication for tectonics. *Acta Petrologica Sinica*, 22(4), 927–937 (in Chinese with English abstract).

Dunlop, D. J., & O¨ . O¨zdemir (1997). Rock Magnetism: Fundamentals and Frontiers. *Cambridge University Press*, New York, 573. https://doi.org/10.1017/CBO9780511612794

Dunlop, D. J. (2002). Theory and application of the "day plot" (M_{RS}/M_S versus H_{cr}/H_c): Theoretical curves and tests using titanomagnetite data. *Journal of Geophysical Research: Solid Earth*, 107 (B3), 2056. https://doi.org/10.1029/2001JB000486

E__________

Ekström, G., Nettles, M., & Dziewonski, A. M. (2012). The global CMT project 2004-2010: Centroid-moment tensors for 13,017 earthquakes. *Physics of the Earth and Planetary Interiors*, 200-201, 1-9. https://doi.org/10.1016/j.pepi.2012.04.002

Eldredge, S., Bachtadse, V., & Van der Voo, R. (1985). Paleomagnetism and the orocline hypothesis. *Tectonophysics*, 119(1-4), 153-179. https://doi.org/10.1016/0040-1951(85)90037-X

Elmore, R.D., & McCabe, C. (1991). The occurrence and origin of remagnetization in the sedimentary rocks of North America. *Reviews of Geophysics,* 29(S1), 377–383. https://doi.org/10.1002/rog.1991.29.s1.377

Elmore, R. D., Dulin, S., Engel, M. H., & Parnell, J. (2006). Remagnetization and fluid flow in the old red sandstone along the Great Glen Fault, Scotland. *Journal of Geochemical Exploration,* 89(1-3), 96–99. https://doi.org/10.1016/j.gexplo.2005.11.034

England, P., & Mckenzie, D. (1983). Correction: a thin viscous sheet model from continental deformation. *Geophysical Journal International*, 73(2), 523-532. https://doi.org/10.1111/j.1365-246X.1983.tb03328.x

England, P., & McKenzie, D. (1982). A thin viscous sheet model for continental deformation. *Geophysical Journal of the Royal Astronomical Society*, 70(2), 295–321. https://doi.org/10.1111/j.1365-246X.1982.tb04969.x

England, P., & Houseman, G. (1986). Finite strain calculations of continental deformation 2.Comparison with the India-Asia collision zone. *Journal of Geophysical Research: Solid Earth*, 91(B3), 3664–3676. https://doi.org/10.1029/JB091iB03p03664

England, P., & Wells, R. E. (1991). Neogene rotations and quasi-continuous deformation of the Pacific Northwest continental margin. *Geology*, 19(10), 978–981. https://doi.org/10.1130/0091-7613(1991)019<0978:NRAQDO>2.3.CO;2

England, P., Houseman, G., & Sonder, L. (1985). Length scales for continental deformation in convergent, divergent, and strike-slip environments: Analytical and approximate solutions for a thin viscous sheet model. *Journal of Geophysical Research: Solid Earth*, 90(B5), 3551–3557. https://doi.org/10.1029/JB090iB05p03551

Enkin, R. J., Courtillot, V., Xing, L., Zhang, Z., Zhuang, Z. & Zhang, J. (1991). The stationary Cretaceous paleomagnetic pole of Sichuan (South China Block). *Tectonics*, 10(3), 547–559. https://doi.org/10.1029/90TC02554

F

Ferré, E., Gleizes, G., & Caby, R. (2002). Obliquely convergent tectonics and granite emplacement in the Trans-Saharan belt of Eastern Nigeria: A synthesis. *Precambrian Research,* 114(3-4), 199–219. https://doi.org/10.1016/S0301-9268(01)00226-1

Fisher, R. A. (1953). Dispersion on a sphere. *Proceedings of the Royal Society A,* 217(1130), 295–305. https://doi.org/10.1098/rspa.1953.0064

Flinn, D. (1962). On folding during three-dimensional progressive deformation. *Quarterly Journal of the Geological Society*, 118, 385-433. https://doi.org/10.1144/gsjgs.118.1.0385

Freund, R. (1974). Kinematics of transform and transcurrent faults. *Tectonophysics*, 21(1-2), 93-134. https://doi.org/10.1016/0040-1951(74)90064-X

Funahara S., Nishiwaki. N., Miki. M., Murata. F., Otofuji. Y., & Wang, Y. (1992). Paleomagnetic study of Cretaceous rocks from the Yangtze block, central Yunnan, China: implications for the India-Asia collision. *Earth and Planetary Science Letters*, 113(1-2), 77–91. https://doi.org/10.1016/0012-821X(92)90212-E

Funahara, S., Nishiwaki, N., Murata, F., Otofuji, Y., & Wang, Y.Z. (1993). Clockwise rotation of the Red River fault inferred from paleomagnetic study of Cretaceous rocks in the Shan-Thai-Malay Block of western Yunnan, China. *Earth and Planetary Science Letters*, 117(1-2), 29–42. https://doi.org/10.1016/0012-821X(93)90115-P

G

Gan, W., Zhang, P., Shen, Z.-K., Niu, Z., Wang, M., Wan, Y., Zhou, D., & Cheng, J. (2007). Present-day crustal motion within the Tibetan Plateau inferred from GPS measurements. *Journal of Geophysical Research: Solid Earth*, 112(B8). https://doi.org/10.1029/2005JB004120

Gao, L., Yang Z., Tong Y., Wang H., & An C. (2015). New paleomagnetic studies of Cretaceous and Miocene rocks from Jinggu, western Yunnan, China: evidence for internal deformation of the Lanping–Simao Terrane. *Journal of Geodynamics*, 89, 39–59. https://doi.org/10.1016/j.jog.2015.06.004

Gao, L., Yang Z., Tong Y., Wang H., An C., & Zhang H. (2017). Cenozoic clockwise rotation of the Chuan Dian Fragment, southeastern edge of the Tibetan Plateau: Evidence from a new paleomagnetic study. *Journal of Geodynamics*, 112, 46-57. https://doi.org/10.1016/j.jog.2017.10.001

Garfunkel, Z. (1974). Model for the late Cenozoic tectonic history of the Mojave Desert, California, and for its relation to adjacent regions. *Geological Society of America Bulletin*, *85*(12), 1931–1944. https://doi.org/10.1130/0016-7606(1974)85<1931:MFTLCT>2.0.CO;2

Garfunkel, Z., & Ron, H. (1985). Block rotation and deformation by strike-slip faults: 2. The properties of a type of macroscopic discontinuous deformation. *Journal of Geophysical Research: Solid Earth*, 90(B10), 8589. https://doi.org/10.1029/JB090iB10p08589

Geissman, J. W., Callian, J. T, Oldow, J. S., & Humphries, S. E. (1984). Paleomagnetic assessment of oroflexural deformation in west-central Nevada and significance for emplacement of allochthonous assemblages. *Tectonics*, 3(2), 179–200. https://doi.org/10.1029/TC003i002p00179

Gilley, L. D.,. Harrison, T. M, Leloup, P. H., Ryerson, F. J., Lovera, O., & Wang, J.-H. (2003). Direct dating of left-lateral deformation along the Red River Shear Zone, China and Vietnam. *Journal of Geophysical Research: Solid Earth*, 108(B2). https://doi.org/10.1029/2001JB001726

Globerman B. R., Beck, M. E., Jr., & Duncan, R. A. (1982). Paleomagnetism and tectonic significance of Eocene basalts from the Black Hills, Washington Coast Range. *Geological Society of America Bulletin*, 93(11), 1151-1159. https://doi.org/10.1130/0016-7606(1982)93<1151:PATSOE>2.0.CO;2

Goldstein, A.G. (1980). Magnetic susceptibility anisotropy of mylonites from the Lake Char mylonite zone, southeastern New England. *Tectonophysics*, 66(1-3), 197-211. https://doi.org/10.1016/0040-1951(80)90046-3

Goldstein A.G., & Brown, L.L. (1988). Magnetic susceptibility anisotropy of mylonites from the Brevard Zone, North Carolina, USA. *Physics of the Earth and Planetary Interiors*, 51, 290-300. https://doi.org/10.1016/0031-9201(88)90070-2

Graham, J.W. (1966). Significance of magnetic anisotropy in Appalachian sedimentary rocks, In: The Earth Beneath the Continents, edited by J.S. Steinhart and T.J. Smith. *American Geophysical Monograph Series*, 10, 627-648. https://doi.org/10.1029/GM010p0627

Grommé C. S., Beck, M. E., Jr., Wells, R. E., & Engebretson, D. C. (1986). Paleomagnetism of the Tertiary Clarno Hills Formation of central Oregon and its significance for the tectonic history of the Pacific Northwest. *Journal of Geophysical Research: Solid Earth*, 91(B14), 14089-14103. https://doi.org/10.1029/JB091iB14p14089

H

Hagstrum J. T., Sawlan, M. G., Hausback, B. P., Smith, J. G., &. Grommé, C. S. (1987). Miocene paleomagnetism and tectonic setting of the Baja California Peninsula, Mexico.

Journal of Geophysical Research: Solid Earth, 92(B3), 2627-2639. https://doi.org/10.1029/JB092iB03p02627

Haihong, C., Dobson, J., Heller, F. & Jie, H. (1995). Paleomagnetic evidence for clockwise rotation of the Simao region since the Cretaceous: a consequence of India-Asia collision. *Earth and Planetary Science Letters*, 134(1-2), 203–217. https://doi.org/10.1016/0012-821X(95)00118-V

Hall, R. (2002). Cenozoic geological and plate tectonic evolution of SE Asia and the SW Pacific: computer-based reconstructions, model and animations. *Journal of Asian Earth Sciences*, 20(4), 353-431. https://doi.org/10.1016/S1367-9120(01)00069-4

Hall, R., van Hattum, M. W., & Spakman, W. (2008). Impact of India-Asia collision on SE Asia: the record in Borneo. *Tectonophysics*, 451(1), 366-389. https://doi.org/10.1016/j.tecto.2007.11.058

Harrison, T.M., Chan, W., Leloup, P.H., Ryerson, F.J., & Tapponnier P. (1992). An early Miocene transition in deformation regime within the Red River fault zone, Yunnan, and its significance for Indo-Asian tectonics. *Journal of Geophysical Research: Solid Earth*, 97(B5), 7159–7182. https://doi.org/10.1029/92JB00109

Harrison, T.M., Leloup, P.H., Ryerson, F.J., Tapponnier, P., Lacassin, R., & W. Chen (1996). Diachronous initiation of transtension along the Ailaoshan–Red River Shear Zone, Yunnan and Vietnam, In: *Yin, A. and Harrison, T.M. (eds) The Tectonic Evolution of Asia, Cambridge Univ. Press, Cambridge*, 208–225.

Harrison, R. J., & Feinberg, J. M. (2008). FORCinel: An improved algorithm for calculating first-order reversal curve distributions using locally weighted regression smoothing. *Geochemistry, Geophysics, Geosystems*, 9(5). https://doi.org/10.1029/2008GC001987

Hashimoto, T., Hurst, T., Suzuki, A., Mogi, T., Yamaya, Y., & Tamura, M. (2008). The role of thermal viscous remanent magnetisation (TVRM) in magnetic changes associ-ated with volcanic eruptions: insights from the 2000 eruption of Mt Usu, Japan. *Journal of Volcanology and Geothermal Research*, 176(4), 610–616. https://doi.org/10.1016/j.jvolgeores.2008.05.009

Hernandez-Moreno C. (2015). Understanding block rotation of strike-slip fault zones: Paleomagnetic and structural approach. PhD Thesis, Alma Master Studiorum–Università di Bologna.

Hernandez-Moreno, C., Speranza, F., & Di Chiara, A. (2014). Understanding kinematics of intra-arc transcurrent deformation: Paleomagnetic evidence from the Liquiñe-Ofqui fault zone (Chile, 38–41°S). Tectonics, 33, 1964–1988. https://doi.org/10.1002/2014TC003622

Hernandez-Moreno, C., Speranza, F., & Di Chiara, A. (2016). Paleomagnetic rotation pattern of the southern Chile fore-arc sliver (38°S–42°S): A new tool to evaluate plate locking along subduction zones. Journal of Geophysical Research: Solid Earth, 121(2), 469–490. https://doi.org/10.1002/2015JB012382

Hillhouse J. W. (1977). Paleomagnetism of the Triassic Nikolai Greenstone, McCarthy quadrangle, Alaska. *Canadian Journal of Earth Sciences*, *14*, 2578-2592. https://doi.org/10.1139/e77-223

Hillhouse, J. W., & Grommé, C. S. (1984). Northward displacement and accretion of Wrangellia: New paleomagnetic evidence from Alaska. *Journal of Geophysical Research: Solid Earth*, 89(B6), 4461-4477. https://doi.org/10.1029/JB089iB06p04461

Hirt, A. M., & Lowrie, W. (1988). Paleomagnetism of the Umbrian-Marches orogenic belt. *Tectonophysics*, 146(1-4), 91–103. https://doi.org/10.1016/0040-1951(88)90084-4

Holt, W.E., Ni, J.F., Wallace, T.C., & Haines, A. (1991). The active tectonics of the eastern Himalayan Syntaxis and surrounding regions. *Journal of Geophysical Research: Solid Earth*, 96(b9), 14595–14632. https://doi.org/10.1029/91JB01021

Houseman, G., & England, P. (1986). Finite strain calculations of continental deformation 1.Method and general results for convergent ones. Journal of Geophysical Research, 91(B3), 3651–3663. https://doi.org/10.1029/JB091iB03p03651

Houseman, G., & England, P. (1993). Crustal thickening versus lateral expulsion in the Indian-Asian continental collision. Journal of Geophysical Research, 98(B7), 12233–12249, http://dx.doi.org/10.1029/93JB00443

Housen, B.A., Van der Pluijm, B.A., & Van der Voo, R. (1993). Magnetite dissolution and neocrys-tallization during cleavage formation: paleomagnetic study of the Martinsburg Formation, Lehigh Gap, Pennsylvania. *Journal of Geophysical Research: Solid Earth,* 98(B8), 13799–13813. https://doi.org/10.1029/93JB01088

Hrouda, F. (1982). Magnetic anisotropy of rocks and its application in geology and geophysics. *Geophysical Surveys*, 5(1), 37-82. https://doi.org/10.1007/BF01450244

Hrouda, F., & Janák, F. (1976). The changes in shape of the magnetic susceptibility ellipsoid during progressive metamorphism and deformation. *Tectonophysics*, 34(1-2), 135-148. https://doi.org/10.1016/0040-1951(76)90181-5

Hrouda F., & Jelinek, V. (1990). Resolution of ferromagnetic and paramagnetic anisotropies in rocks, using combined low-field and high-field measurements. *Geophysical Journal International*, 103(1), 75-84. https://doi.org/10.1111/j.1365-246X.1990.tb01753.x

Huangpu, G., & Jiang, C.S. (2000). Study on Tengchong Volcanic Activity. Yunnan Technology Press, Kunming, China, pp. 18–76 (in Chinese with English abstract)

Huang, K.N., & Opdyke, N.D. (1991). Paleomagnetic results from the Upper Carboniferous of the Shan-Thai-Malay Block of Western Yunnan, China, *Tectonophysics*, 192(3-4), 333–344. https://doi.org/10.1016/0040-1951(91)90107-4

Huang, K., & Opdyke, N.D. (1992). Paleomagnetism of Cretaceous to lower Tertiary rocks from Southwestern Sichuan: a revisit. *Earth and Planetary Science Letters*, 112(1-4), 29–40. https://doi.org/10.1016/0012-821X(92)90004-F

Huang, K., & Opdyke, N. D. (1993). Paleomagnetic results from Cretaceous and Jurassic rocks of South and Southwest Yunnan: evidence for large clockwise rotations in the Indochina and Shan-Thai-Malay terranes. Earth and Planetary Science Letters, 117(3-4), 507–524. https://doi.org/10.1016/0012-821X(93)90100-N

Huang, K., & Opdyke, N. D. (2015). Post-folding magnetization of the Triassic rocks from western Guizhou and southern Yunnan provinces: new evidence for large clockwise rotations in the Simao Terrane. Earth and Planetary Science Letters, 423, 155–163. https://doi.org/10.1016/j.epsl.2015.05.015

Huang Z., Tilmann, F., Xu, M., Wang, L., Ding, Z., Mi, N., Yu, D., & Li, H. (2017). Insight into NE Tibetan Plateau expansion from crustal and upper mantle anisotropy revealed by shear-wave splitting. *Earth and Planetary Science Letters*, 478, 66-75. https://doi.org/10.1016/j.epsl.2017.08.030

I

Iosifidi, A.G., Mac Niocaill, C., Khramov, A.N., Dekkers, M.J., Popov, V.V. (2010). Palaeogeographic implications of differential inclination shallowing in Permo-Carboniferous sediments from the Donets basin, Ukraine. *Tectonophysics,* 490(3-4), 229–240. https://doi.org/10.1016/j.tecto.2010.05.017

Irving, E. (1964). Paleomagnetism and its application to geological and geophysical problems. *Science*, 147(3657), 494. https://doi.org/10.1126/science.147.3657.494

J

Jackson, J., & McKenzie, D. (1984). Active tectonics of the Alpine-Himalayan Belt between western Turkey and Pakistan. *Geophysical Journal of the Royal Astronomical Society*, 77(1), 185-264. https://doi.org/10.1111/j.1365-246X.1984.tb01931.x

Jackson, J., & Molnar, P. (1990). Active faulting and block rotations in the western Transverse Ranges, California. *Journal of Geophysical Research: Solid Earth*, 95(B13), 22073-22087. https://doi.org/10.1029/JB095iB13p22073

Jackson., M., & Tauxe, L. (1991). Anisotropy of magnetic susceptibility and remanence: development in the characterization of tectonic, sedimentary and igneous fabric. *Reviews of Geophysics*,29 (S1) 371-376. https://doi.org/10.1002/rog.1991.29.s1.371

Janák, F. (1967). The effect of the anisotropy of magnetic susceptibility on the direction of the vector of isothermal remanent magnetic polarization. *Studia Geophysica et Geodaetica*, 11(4), 419-429. https://doi.org/10.1007%2FBF02589593

Jelinek, V. (1977). The statistical theory of measuring anisotropy of magnetic susceptibility of rocks and its application. *Geofyzika, Brno*., pp. 88.

Jelinek, V. (1978). Statistical processing of magnetic susceptibility on groups of specimens. *Studia Geophysica et Geodaetica*, *22*(1), 50-62. https://doi.org/10.1007/BF01613632

Jelinek, V. (1981). Characterization of the magnetic fabrics of rocks. *Tectonophysics*, 79(3-4), T63-T67. https://doi.org/10.1016/0040-1951(81)90110-4

Ji, J., D. Zhong, Sang, H., & L. Zhang (2000). The western boundary of extrusion blocks in southeastern Tibet Plateau. *Chinese Science Bulletin*, 45 (876). https://doi.org/10.1007/BF02886191

Jiang, C. (1998). Distribution characteristics of Tengchong volcano in the Cenozoic era. *Journal of Seismological Research,* 21 (4), 309–319 (in Chinese with English abstract).

Jiang, C., Zhou, R., & Zhao, C. (2003). The relationship between the tectonic geomorphic features and volcano activity in Tengchong Region, *Journal of Seismological Research*, 26 (4), 361–366 (in Chinese with English abstract).

Jiang, Z., Liu, Q., Dekkers, M. J., Tauxe, L., Qin, H., Barrón, V., & Torrent, J. (2015). Acquisition of chemical remanent magnetization during experimental ferrihydrite-hematite conversion in Earth-like magnetic field-implications for paleomagnetic studies of red beds. *Earth and Planetary Science Letters*, 428, 1–10. https://doi.org/10.1016/j.epsl.2015.07.024

Jiang, Z., Liu, Q., Dekkers, M. J., Zhao, X., Roberts, A. P., Yang, Z., Jin, C., & Liu, J. (2017). Remagnetization mechanisms in Triassic red beds from South China. Earth and Planetary Science Letters, 479, 219-230. https://doi.org/10.1016/j.epsl.2017.09.019

Jin, C., & Liu, Q. (2011). Remagnetization mechanism and a new age model for L9 in Chinese loess. *Physics of the Earth and Planetary Interiors*, 187(3-4), 261–275. https://doi.org/10.1016/j.pepi.2011.03.010

Jolivet, L., Beyssac, O., Goffè, B., Avigad, D., Lepvrier, C., Maluski, H., & Thang, T. T. (2001). Oligo-Miocene midcrustal subhorizontal shear zone in Indochina. *Tectonics*, 20(1), 46–57. https://doi.org/10.1029/2000TC900021

K

Kamerling M. J. & Luyendyk, B. P. (1979). Tectonic rotations of the Santa Monica Mountains region, western Transverse Ranges, California, suggested by paleomagnetic vectors. *Geological Society of America Bulletin*, 90(4), 331-337. https://doi.org/10.1130/0016-7606(1979)90<331:TROTSM>2.0.CO;2

Katz, B., Elmore, R.D., Cogoini, M., Engel, M.H., & Ferry, S. (2000). Associations between burial diagenesis of smectite, chemical remagnetization, and magnetite authigenesis in the Vocontian trough, SE France. *Journal of Geophysical Research: Solid Earth*, 105(B1), 851–868. https://doi.org/10.1029/1999JB900309

Khan, P. K., & Chakraborty, P. P. (2005). Two-phase opening of Andaman Sea: a new seismotectonic insight. *Earth and Planetary Science Letters,* 229, 259-271. https://doi.org/10.1016/j.epsl.2004.11.010

Kent, D.V. (1985). Thermoviscous remagnetization in some Appalachian limestones. *Geophysical Research Letters,*12(12), 805–808. https://doi.org/10.1029/GL012i012p00805

Kent, D.V., Xu, G., Huang, K., Zhang, W., & Opdyke, N.D. (1986). Paleomagnetism of upper Cretaceous rocks from South China. *Earth and Planetary Science Letters,* 79 (1), 179–184. https://doi.org/10.1016/0012-821X(86)90051-8

Kent, D.V., Zeng, X., Zhang, W.Y., & Opdyke, N.D. (1987). Widespread late Mesozoic to recent remagnetization of Paleozoic and lower Triassic sedimentary rocks from South China. *Tectonophysics,* 139(1-2), 133–143. https://doi.org/10.1016/0040-1951(87)90202-2

Kimura, H., Itoh, Y., & Tsutsumi, H. (2004). Quaternary strike-slip crustal deformation around an active fault based on paleomagnetic analysis: A case study of the Enako fault in central Japan. Earth and Planetary Science Letters, 226(3–4), 321–334. https://doi.org/10.1016/j.epsl.2004.08.003

Kimura, H., Ishikawa, N., & Sato, H. (2011). Estimation of total lateral displacement including strike-slip offset and broader drag deformation on an active fault: Tectonic geomorphic and paleomagnetic evidence on the Tanna fault zone in central Japan. Tectonophysics, 501(1–4), 87–97. https://doi.org/10.1016/j.tecto.2011.01.016

Kirschvink, J. L. (1980). The least-squares line and plane and the analysis of paleomagnetic data. Geophysics Journal International, 62(3), 699–718. https://doi.org/10.1111/j.1365-246X.1980.tb02601.x

Kissel, C., Barrier, E., Laj, C., & Lee, T. Q. (1986). Magnetic fabric in “undeformed” marine clays from compressional zones. *Tectonics*, 5(5), 769–781. https://doi.org/10.1029/TC005i005p00769

Kodama, K. P., & Dekkers, M.J. (2004). Magnetic anisotropy as an aid to identifying CRM and DRM in red sedimentary rocks. *Studia Geophysica et Geodaetica*, 48(4), 747–766. https://doi.org/10.1023/B:SGEG.0000045481.47203.33

Kondo, K., Mu, C., Yamamoto, T., Zaman, H., Miura, D., Yokoyama, M., Ahn, H. S., & Otofuji, Y. (2012). Oroclinal origin of the Simao Arc in the Shan-Thai Block inferred from the Cretaceous paleomagnetic data. Geophysical Journal International, 190(1), 201–216. https://doi.org/10.1111/j.1365-246X.2012.05467.x

Kornfeld, D., Eckert, S., Appel, E., Ratschbacher, L., Pfänder, J., Liu, D., & Ding, L. (2014a). Clockwise rotation of the Baoshan block due to southeastward tectonic escape of Tibetan crust since the Oligocene. Geophysical Journal International, 197(1), 149–163. https://doi.org/10.1093/gji/ggu009

Kornfeld, D., Eckert, S., Appel, E., Ratschbacher, L., Sonntag, B-L., Pfänder, J.A., Ding, L., & Liu, D. (2014b). Cenozoic clockwise rotation of the Tengchong block, southeastern Tibetan Plateau: A paleomagnetic and geochronologic study. Tectonophysics, 628, 105-122. https://doi.org/10.1016/j.tecto.2014.04.032

Kornfeld, D., Sonntag, B.-L., Gast, S., Matthes, J., Ratschbacher, L., Pfänder, J.A., Eckert, S., Liu, D., Appel E., & Ding L. (2014c). Apparent paleomagnetic rotations reveal Pliocene–Holocene internal deformation of the Tengchong Block, southeastern Tibetan Plateau. *Journal of Asian Earth Sciences*, 96, 1–16. https://doi.org/10.1016/j.jseaes.2014.08.034

L

Lacassin, R., Schärer, U., Leloup, P.H., Arnaud, N., Tapponnier, P., Liu, X., Zhang, L., (1996). Tertiary deformation and metamorphism SE of Tibet: the folded Tigerleap décollement of NW Yunnan, China. *Tectonics,* 15(3), 605–622. https://doi.org/10.1029/95TC03749

Lacassin, R., Maluski, H., Leloup, P.H., Tapponnier, P., Hinthong, C., Siribhakdi, K., Chuaviroj, S., Charoenravat, A., (1997). Tertiary diachronic extrusion and deformation of western Indochina: structural and 40Ar/39Ar evidence from NW Thailand. *Journal of Geophysical Research: Solid Earth*, 102(B5), 10013–10037. https://doi.org/10.1029/96JB03831

Laccassin, R., Replumaz, A. & Leloup, P.H. (1998). Hairpin river loops and slip-sense inversion on southeast Asian strike–slip faults. *Geology*, 26, 703–706. https://doi.org/10.1130/0091-7613(1998)026<0703:HRLASS>2.3.CO;2

Lamb, S. H. (1987). A model for tectonic rotations about a vertical axis, *Earth and Planetary Science Letters*, 84(1), 75–86. https://doi.org/10.1016/0012-821X(87)90178-6

Lamb, S., & H. Bibby (1989). The last 25 Ma of rotational deformation in part of the New Zealand plate-boundary zone. *Journal of Structural Geology*, 11(4), 473-492. https://doi.org/10.1016/0191-8141(89)90024-2

Lanza, R. & Meloni A. (2006). The Earth's Magnetism: An Introduction for Geologist. *Springer*

Lanos, P. (2004). Bayesian inference of calibration curves: application to archaeomagnetism. In: Buck, C., Millard, A. (Eds.), *Tools for Constructing Chronologies*: Crossing Disciplinary Boundaries. Springer-Verlag, London, 177, 43-82. https://doi.org/10.1007/978-1-4471-0231-1_3

Lanza, R. & Meloni, A. (2006). The Earth's Magnetism. An Introduction for Geologists.: xi + 278 pp. Berlin, Heidelberg, New York: Springer-Verlag.. ISBN13 978 3 540 27979 2. Geological Magazine; 144 (6): 1027–1028. https://doi.org/10.1017/S0016756807003238

Lee, H. Y., Chung S. L., Wang J. R., Wen D. J., Lo C. H., Yang T. F., Zhang Y. Q., Xie Y. W., Lee T. Y., Wu G. Y., & Ji J. Q. (2003). Miocene Jiali faulting and its implication for Tibetan tectonic evolution. *Earth and Planetary Science Letters,* 205(3-4), 185–194. https://doi.org/10.1016/S0012-821X(02)01040-3

Leloup, P.H., Harrison, T. M., Ryerson, F.J., Wenji, C., Qi, L., Tapponnier, P., & Lacassin, R. (1993). Structural, petrological and thermal evolution of a Tertiary ductile strike-slip shear zone, Diancang Shan, Yunnan. Journal of Geophysical Research: Solid Earth, 98(B4). https://doi.org/10.1029/92JB02791

Leloup, P.H., Lacassin, R., Tapponnier, P., Scharer, U., Zhong, D., Liu, X., Zhang, L., Ji, S., & PhanTrong, T. (1995). The Ailao Shan-Red River shear zone (Yunnan, China), Tertiary transform boundary of Indochina. *Tectonophysics*, 251(1-4), 3-10, 13-84. https://doi.org/10.1016/0040-1951(95)00070-4

Leloup, P.H., Lacassin, R., Tapponnier, P., & Harrison, T. M. (2001). Comment on "Onset timing of left-lateral movement along the Ailao Shan-Red river shear zone: Ar-40/Ar-39 dating constraint from the Nam Dinh area, northeastern Vietnam" by Wang et al., 2000. Journal of Asian Earth Sciences 18, 281–292. *Journal of Asian Earth Sciences*, 20(1), 95–99. https://doi.org/10.1016/S1367-9120(01)00034-7

Leloup, P. H., Tapponnier, P., & Lacassin, R., (2007). Discussion on the role of the Red River shear zone, Yunnan and Vietnam, in the continental extrusion of SE Asia. *Journal of the Geological Society*, 164, 1253–1260. http://dx.doi.org/10.1144/0016-76492007-065

Li, D. M., Li, Q., & Chen, W. J. (1999). Excess argon in plagioclase phenocryst of Tengchong volcanics and the related volcano erupting stages. *Geological Review*, 45, 892–894 (in Chinese with English abstract).

Li, D., Li, Q., & Chen, W. (2000). Volcanic activities in the Tengchong volcano area since Pliocene. *Acta Petrologica Sinica*, 16, 362–370 (in Chinese with English abstract).

Li, P., Rui, G., Cui, J., & Ye, G. (2004). Paleomagnetic analysis of eastern Tibet: Implications for the collision and amalgamation history of the Three River Region, SW China. *Journal of Asian Earth Sciences*, 24(3), 291–310. https://doi.org/10.1016/j.jseaes.2003.12.003

Li, H., Xu, Z., Cai, Z., Tang, Z., & Yang, M. (2011). Indosinian epoch magmatic event and geological significance in the Tengchong block, western Yunnan Province. *Acta Petrologica Sinica*, 27 (7), 2165–2172 (in Chinese with English abstract).

Li, S., Advokaat, E. L., Van Hinsbergen, D. J. J., Koymans, M., Deng, C., & Zhu, R. (2017a). Paleomagnetic constraints on the Mesozoic-Cenozoic paleolatitudinal and rotational history of Indochina and South China: Review and updated kinematic reconstruction. *Earth-Science Reviews*, 171, 58-77. https://doi.org/10.1016/j.earscirev.2017.05.007

Li, S., Deng, C., Dong, W., Sun, L., Liu, S., Qin, H., Yin, J., Ji, X., & Zhu, R. (2015). Magnetostratigraphy of the Xiaolongtan Formation bearing Lufengpithecus keiyuanensis in Yunnan, southwestern China: Constraint on the initiation time of the southern segment of the Xianshuihe-Xiaojiang fault. *Tectonophysics*, 655, 213–226. https://doi.org/10.1016/j.tecto.2015.06.002

Li, S., Deng, C., Yao, H., Huang, S., Liu, C., He, H., Pan, Y., & Zhu R. (2013). Magnetostratigraphy of the Dali Basin in Yunnan and implications for late Neogene rotation of the southeast margin of the Tibetan Plateau. *Journal of Geophysical Research: Solid Earth*, 118(3), 791–807. https://doi.org/10.1002/jgrb.50129

Li, S., Yang, Z., Deng, C., He, H., Qin, H., Sun, L., Yuan, J., van Hinsbergen, D. J. J., Krijgsman, W., Dekkers, M.J., Pan, Y., & Zhu R. (2017b). Clockwise rotations recorded in redbeds from the Jinggu Basin of northwestern Indochina. *Geological Society of America Bulletin*, 129(9-10), 1100-1122. https://doi.org/10.1130/B31637.1

Liang, S., Gan, W., Shen, C., Xiao, G., Liu, J., Chen, W., Ding, X., & Zhou, D. (2013). Three-dimensional velocity field of present-day crustal motion of the Tibetan Plateau derived from GPS measurements. *Journal of Geophysical Research: Solid Earth*, 118(10), 5722–5732, https://doi.org/10.1002/2013JB010503

Lin, T.H., Lo, C.H., Chung, S.L., Hsu, F.J., Yeh, M.W., Lee, T.Y., Ji, J.Q., Wang, Y.Z., & Liu, D.Y. (2009). ^{40}Ar/^{39}Ar dating of the Jiali and Gaoligong Shear Zones: implications for crustal deformation around the Eastern Himalayan Syntaxis. *Journal of Asian Earth Sciences*, 34(5), 674–685. https://doi.org/10.1016/j.jseaes.2008.10.009

Liu, J. L., Cao, S. Y., Zhai, Y. F., Song, Z. J., Wang, A. J., Xiu, Q. Y., Cao, D. H., Gao, L., & Guan, Y. (2007). Rotation of crustal blocks as an explanation of Oligo-Miocene extension in southeastern Tibet-evidenced by the Diancangshan and nearby metamorphic core complexes, *Earth Science Frontiers*, 14(4), 40–48. https://doi.org/10.1016/S1872-5791(07)60028-1

Liu-Zeng, J., Tapponnier, P., Gaudemer, Y., & Ding, L. (2008). Quantifying landscape differences across the Tibetan plateau: implications for topographic relief evolution. *Journal of Geophysical Research: Earth Surface*,113(F4). https://doi.org/10.1029/2007JF000897

Liu, C., Ge, K., Zhang, C., Liu, Q., Deng, C., & Zhu, R. (2011). Nature of remagnetization of Lower Triassic red beds in southwestern China. Geophysical Journal International, 187(3), 1237–1249. https://doi.org/10.1111/j.1365-246X.2011.05196.x

Lowrie, W., & Hirt, A. (1986). Paleomagnetism in the arcuate mountain belts. *Developments in Geotectonics,* 21*,* 141-158, In: The Origin of Arcs, edited by F. C. Wezel. https://doi.org/10.1016/B978-0-444-42688-8.50012-6

Lowrie, W. (1989). Magnetic analysis of rock fabric. In: The Encyclopedia of Solid Earth *Geophysics* edited by D. E. James, 698- 706, D. Van Nostrand Reinhold, Princeton, N.J. https://doi.org/10.1007/0-387-30752-4_87

Lowrie, W. (1990). Identification of Ferromagnetic minerals in a rock by coercivity and unblocking temperature properties. *Geophysical Research Letters*, 17(2), 159-162. https://doi.org/10.1029/GL017i002p00159

Lu, G., McCabe, C., Henry, D.J., & Schedl, A., (1994). Origin of hematite carrying a Late Paleozoic remagnetization in a quartz sandstone bed from the Silurian Rose Hill Formation, Virginia, USA. *Earth and Planetary Science Letters*, 126(4), 235–246. https://doi.org/10.1016/0012-821X(94)90109-0

Lucifora, S., Cifelli, F., Rojay, F. B. & Mattei, M. (2013). Paleomagnetic rotations in the Late Miocene sequence from the Çankırı Basin (Central Anatolia, Turkey): the role of strike-slip tectonics. *Turkish Journal of Earth Sciences*, 22. https://doi.org/10.3906/yer-1207-2

Luyendyk, B. P., Kamerling, M. J., Terres, R. R., & Hornafius, J. S. (1985). Simple shear of southern California during Neogene time suggested by paleomagnetic declinations. *Journal of Geophysical Research: Solid Earth*, 90(B14). https://doi.org/10.1029/JB090iB14p12454

M

McCabe, C., & Elmore, R.D. (1989). The occurrence and origin of Late Paleozoic re-magnetization in the sedimentary rocks of North America. *Reviews of Geophysics*, 27(4), 471–494. https://doi.org/10.1029/RG027i004p00471

MacDonald, W. D. (1980). Net tectonic rotation, apparent tectonic rotation, and the structural tilt correction in paleomagnetic studies. *Journal of Geophysical Research: Solid Earth*, *85*(B7), 3659. https://doi.org/10.1029/JB085iB07p03659

MacDonald, W. D., & Ellwood, B. B. (1987). Anisotropy of magnetic susceptibility: Sedimentological, igneous and structural-tectonic applications. *Reviews of Geophysics*, 25(5), 905-909. https://doi.org/10.1029/RG025i005p00905

Macrì, P., Speranza, F., & Capraro, L. (2014). Magnetic fabric of Plio-Pleistocene sediments from the Crotone fore-arc basin: Insights on the recent tectonic evolution of the Calabrian Arc (Italy). *Journal of Geodynamics*, 81, 67-79. https://doi.org/10.1016/j.jog.2014.07.002

Maffione, M., Speranza, F., Faccenna, C., Cascella, A., Vignaroli, G., & Sagnotti, L. (2008). A synchronous Alpine and Corsica-Sardinia rotation. *Journal of Geophysical Research: Solid Earth*, 113(B3). https://doi.org/10.1029/2007JB005214

Maffione, M., Pucci, S., Sagnotti, L., & Speranza, F. (2012). Magnetic fabric of Pleistocene continental clays from the hanging-wall of an active low-angle normal fault (Altotiberina Fault, Italy). *International Journal of Earth Sciences*, 101(3), 849-861. https://doi.org/10.1007/s00531-011-0704-9

Maffione, M., Hernandez-Moreno, C., Ghiglione, M. C., Speranza, F., Douwe, J.J. van Hinsbergen, & Lodolo, E. (2015). Constraints on deformation of the Southern Andes since the Cretaceous from anisotropy of magnetic susceptibility. *Tectonophysics*, 665, 236-250. https://doi.org/10.1016/j.tecto.2015.10.008

Magill, J. R., & Cox, A. (1980). Tectonic rotation of the Oregon Western Cascades. Special Paper 10, Oregon Dept. Geol. Min. Ind., Portland, 67 pp. https://digital.osl.state.or.us/islandora/object/osl:27127

Magill J. R., Cox, A., & Duncan, R. (1981). Tillamook volcanic series: Further evidence for tectonic rotation of the Oregon Coast Range. *Journal of Geophysical Research*, 86, 2953-2970. https://doi.org/10.1029/JB086iB04p02953

Magill J. R., Wells, R. E., Simpson, R. W., & Cox, A. V. (1982). Post-12 m.y. rotation of southwest Washington. *Journal of Geophysical Research: Solid Earth*, 87(B5), 3761-3776. https://doi.org/10.1029/JB087iB05p03761

Mandl, G. (1987). Tectonic deformation by rotating parallel faults: The “bookshelf” mechanism. *Tectonophysics*, 141(4), 277–316. https://doi.org/10.1016/0040-1951(87)90205-8

Mattei M., Funiciello, R., & Kissel, C. (1995). Paleomagnetic and structural evidence for Neogene block rotations in the central Apennines, Italy. *Journal of Geophysical Research: Solid Earth*, 100, 17863-17883. https://doi.org/10.1029/95JB00864

Mattei, M., Sagnotti, L., Faccena, C., & Funiciello, R. (1997). Magnetic fabric of weak deformed clay-rich sediments in the Italian peninsula: Relationship with compressional and extensional tectonics. *Tectonophysics*, 271(1-2), 107-122. https://doi.org/10.1016/S0040-1951(96)00244-2

Mattei, M., Speranza, F., Argentieri, A., Rossetti, F., Sagnotti, L., & Funiciello, R. (1999). Extensional tectonics in the Amantea basin (Calabria, Italy): a comparison between structural and magnetic anisotropy data. *Tectonophysics*, 307(1-2), 33-49. https://doi.org/10.1016/S0040-1951(99)00117-1

May, S. R., & Butler, R. F. (1986). North American Jurassic Apparent polar wander: Implications for plate motions, paleogeography and Cordilleran tectonics. *Journal of Geophysical Research: Solid Earth*, 91(B11), 11519-11544. https://doi.org/10.1029/JB091iB11p11519

Maurin, T., Masson, F., Rangin, C., Min, U. Than, & Collard, P. (2010). First global positioning system results in northern Myanmar: Constant and localized slip rate along the Sagaing fault. *Geology*, 38(7), 591–594. https://doi.org/10.1130/G30872.1

McCabe, C., & Elmore, R.D. (1989). The occurrence and origin of Late Paleozoic remagnetization in the sedimentary rocks of North America. *Reviews of Geophysics*, 27, 471–494. https://doi.org/10.1029/RG027i004p00471

McElhinny, M. W. (1973). Paleomagnetism and Plate Tectonics. Cambridge Earth Science Series, Cambridge University Press, Cambridge. https://doi.org/10.1017/S0016756800038036

McElhinny, M. W., & McFadden, P. L. (2000). Paleomagnetism: Continents and Oceans. edited by Dmowska R., J.R. Holton and H.T. Rossby, Academic Press, 386 pp.

McFadden, P. L. (1990). A new fold test for paleomagnetic studies. Geophysical Journal International, 103(1), 163– 169. https://doi.org/10.1111/j.1365-246X.1990.tb01761.x

McFadden, P. L., & McElhinny, M. W. (1990). Classification of the reversal test in paleomagnetism. *Geophysical Journal International*, 130(3), 725–729. https://doi.org/10.1111/j.1365-246X.1990.tb05683.x

McKenzie, D., & Jackson, J. (1983). The relationship between strain rates, crustal thickening, palaeomagnetism, finite strain and fault movements within a deforming zone. *Earth and Planetary Science Letters*, 65(1), 182–202. https://doi.org/10.1016/0012-821X(83)90198-X

McKenzie, D., & Jackson, J. (1986). A block model of distributed deformation by faulting. *Journal of Geological Society*, 143(2), 349–353. https://doi.org/10.1144/gsjgs.143.2.0349

Meade, B.J. (2007). Present-day kinematics at the India-Asia collision zone. *Geology*, 35(1), 81-84, https://doi.org/10.1130/G22924A.1

Merrill R. T. & McElhinny, M. W. (1983). The Earth's Magnetic Field. Academic Press, London, 401 pp. https://doi.org/10.1017/S0022112085212233

Merrill, R.T., McElhinny, M.W., & McFadden, P.L. (1996). The magnetic field of the earth: paleomagnetism, the core, and the deep mantle. Elsevier, New York

Metcalfe, I. (2002). Permian tectonic framework and palaeogeography of SE Asia. *Journal of Asian Earth Sciences*, 20(6), 551–566. https://doi.org/10.1016/S1367-9120(02)00022-6

Metcalfe, I. (2006). Paleozoic and Mesozoic tectonic evolution and palaeogeography of East Asian crustal fragments: The Korean Peninsula in context. *Gondwana Research*, 9(1-2), 24–46. https://doi.org/10.1016/j.gr.2005.04.002

Metcalfe, I. (2011). Palaeozoic–Mesozoic history of SE Asia, In: Hall, R., Cottam, M. Wilson, M. (Eds.), The SE Asian Gateway: History and Tectonics of Australia–Asia Collision. *Geological Society, London, Special Publications*, 355, 7–35. https://doi.org/10.1144/SP355.2

Metcalfe, I. (2013). Gondwana dispersion and Asian accretion: tectonic and palaeogeographic evolution of eastern Tethys. *Journal of Asian Earth Sciences,* 66, 1-33. https://doi.org/10.1016/j.jseaes.2012.12.020

Mitchell, A.H.G. (1992). Late Permian–Mesozoic events and the Mergui Group Nappe in Myanmar and Thailand. *Journal of Southeast Asian Earth Sciences,* 7(2-3), 165– 178. https://doi.org/10.1016/0743-9547(92)90051-C

Mitchell, A.H.G. (1993). Cretaceous-Cenozoic tectonic events in western Myanmar (Burma)-Assam region. *Journal of the Geological Society*, 150, 1089–1102. https://doi.org/10.1144/gsjgs.150.6.1089

Molnar, P., & Tapponnier, P. (1975). Cenozoic tectonics of Asia: effects of a continental collision. *Science*, 189(4201), 419–426. https://doi.org/10.1126/science.189.4201.419

Molnar, P., & Dayem, K. E. (2010). Major intracontinental strike-slip faults and contrasts in lithospheric strength. *Geoshpere*, 6(4), 444–467. https://doi.org/10.1130/GES00519.1

Molnar, P., Parco-Casas, F., & Stock, J. (1988). The Cenozoic and Late Cretaceous evolution of the Indian Ocean Basin: Uncertainties in the reconstructed positions of the Indian, African and Antarctic plates. *Basin Research*, 1(1), 23–40. https://doi.org/10.1111/j.1365-2117.1988.tb00003.x

Morley, C.K. (2004). Nested strike-slip duplexes, and other evidence for Late Cretaceous - Paleogene transpressional tectonics before and during India Eurasia collision, in Thailand, Myanmar and Malaysia. *Journal of the Geological Society of London,* 161, 799-812. https://doi.org/10.1144/0016-764903-124

Morley, C.K. (2007). Variation in Late Cenozoic-recent strike-slip and oblique-extensional geometries, within Indochina: the influence of pre-existing fabrics. *Journal of Structural Geology*, 29(1), 36–58. https://doi.org/10.1016/j.jsg.2006.07.003

Morton, W. H., & Black, R. (1975). Crustal attenuation in Afar, in Afar Depression of Ethiopia, edited by A. Pilger and A. Rösler, pp. 55–65, Schweizerbart, Stuttgart, Germany.

Mu, Z., Tong, W., & Garniss, H. C. (1987). Times of volcanic activity and origin of magma in Tengchong geothermal area, west Yunnan province. *Chinese Journal of Geophysics*, 30 (3), 261–270 (in Chinese with English abstract).

N

Nagy, E. A., & Sieh, K. E. (1993). The use of paleomagnetism analysis to assess nonbrittle deformation within the San Andreas Fault Zone. *Journal of Geophysical Research: Solid earth*, 98(B10), 17965-17979. https://doi.org/10.1029/93JB01329

Najman, Y., Appel, E., Boudagher-Fadel, M., Brown, P., Carter, A., Garzanti, E., Godin, L., Han, J., Liebke, U., Oliver, G., Parrish, R., & Vezzoli, G. (2010). Timing of India–Asia collision: geological, biostratigraphic, and paleomagnetic constraints. *Journal of Geophysical Research Solid Earth*, 115/B12. https://doi.org/10.1029/2010JB007673

Néel, N. (1955). Some theoretical aspects of rock magnetism. *Advances in Physics*, 4, 191-242. https://doi.org/10.1080/00018735500101204

Néel, L. (1949). Théorie du traìnage magnétique des ferromagnéniques en grains fins avec applications aux terres cuites. *Annales Geophysicae*, 5, 99–136.

Néel, L., & Pauthenet, R. (1952). Etude thermomagnetique d' un monocristal de monocristal de Fe203. Comptes Rendus de l'Académie des Sciences, Paris, 234, 2172-2174.

Nelson, M. R., & Jones, C. H. (1987). Paleomagnetism and crustal rotations along a shear zone, Las Vegas Range, southern Nevada. *Tectonics*, 6(1), 13-33. https://doi.org/10.1029/TC006i001p00013

Nur, A., Ron, H., & Scotti, O. (1986). Fault mechanics and the kinematics of block rotations. *Geology*, 14, 746–749. https://doi.org/10.1130/0091-7613(1986)14<746:FMATKO>2.0.CO;2

O

Ogg, J. G. (2012). Chapter 5: Geomagnetic Polarity Time Scale. In: Gradstein, F. M., Ogg, J.G., Schmitz, M., and Ogg, G., The geologic time scale, Elsevier.

Oliva-Urcia, B., Larrasoaña, J.C., Pueyo, E.L., Gil, A., Mata, P., Parés, J.M., Schleicher, A.M., & Pueyo, O. (2009). Disentangling magnetic subfabrics and their link to deformation processes in cleaved sedimentary rocks from the Internal Sierras (west central Pyrenees, Spain). *Journal of Structural Geology*, 31(2), 163-176. https://doi.org/10.1016/j.jsg.2008.11.002

Opdyke, N. D., & Channell, J. E. T. (1996). Magnetic Stratigraphy. *International Geophysics Series*, 64.

Otofuji, Y., Inoue, Y., Funahara, S., Murata, F. & Zheng, X. (1990). Palaeomagnetic study of eastern Tibet—deformation of the Three Rivers region. *Geophysical Journal International*, 103(1), 85–94. https://doi.org/10.1111/j.1365-246X.1990.tb01754.x

Otofuji, Y., Liu, Y., Yokoyama, M., Tamai, M., & Yin, J. (1998). Tectonic deformation of the southwestern part of the Yangtze craton inferred from paleomagnetism. *Earth and Planetary Science Letters*, 156(1-2), 47– 60. https://doi.org/10.1016/S0012-821X(98)00009-0

Otofuji, Y., Yokoyama, M., Kitada, K., & Zaman H. (2010). Paleomagnetic versus GPS determined tectonic rotation around eastern Himalayan Syntaxis in East Asia. *Journal of Asian Earth Sciences*, 37(5-6), 438–451. https://doi.org/10.1016/j.jseaes.2009.11.003

Otofuji, Y., Tung, V. D., Fujihara, M., Tanaka, M., Yokoyama, M., Kitada, K., & Zaman, H. (2012). Tectonic deformation of the southeastern tip of the Indochina Peninsula during its southward displacement in the Cenozoic time. *Gondwana Research*, 22(2), 615–627. https://doi.org/10.1016/j.gr.2011.09.015

Owens, W . H. & D. Barnford, (1976). Magnetic, seismic and other anisotropic properties of rock fabrics. *Philosophical Transactions of the Royal Society of London. Series A, Mathematical and Physical Sciences*, 283(1312), 55-68.

P

Pan, G., Wang, L., Li, R., Yuan, S., Ji, W., Yin, F., Zhang, W., & Wang, B. (2012). Tectonic evolution of the Qinghai-Tibet plateau. *Journal of Asian Earth Sciences*, 53, 3–14. https://doi.org/10.1016/j.jseaes.2011.12.018

Parés, J.M., Van der Pluijm, B.A., & Dinarés-Turell, J. (1999). Evolution of magnetic fabrics during incipient deformation of mudrocks (Pyrenees, Northern Spain). *Tectonophysics*, 307(1-2), 1-14. https://doi.org/10.1016/S0040-1951(99)00115-8

Parés, J.M. (2004). How deformed are weakly deformed mudrocks? Insights from magnetic anisotropy. In: Martin-Hernandez, F, Luneburg, C., Aubourg, C., Jackson, M. (Eds.), Magnetic fabric: methods and applications. *Geological Society, London, Special Publications*, 238, 191–203. https://doi.org/10.1144/GSL.SP.2004.238.01.13

Parés, J. M. (2015). Sixty years of anisotropy of magnetic susceptibility in deformed sedimentary rocks. *Frontiers in Earth Sciences*, 3, 4. https://doi.org/10.3389/feart.2015.00004

Patriat, P., & Achache, J. (1984). India-Eurasia collision chronology has implications for crustal shortening and driving mechanism of plates. *Nature*, 311, 615– 621. https://doi.org/10.1038/311615a0

Pavòn-Carrasco, F. J., Rodríguez-González, J., Osete, M. L., & Torta, M. J. (2011). A Matlab tool for archaeomagnetic dating. *Journal of Archaeological Science*, 38(2), 408-419. https://doi.org/10.1016/j.jas.2010.09.021

Pearce, G. W., & Fueten, F. (1989). An intensive study of magnetic susceptibility anisotropy of amphibolite layers of the Thompson belt, North Manitoba. *Tectonophysics*, 162(3-4), 315-329. https://doi.org/10.1016/0040-1951(89)90252-7

Pellegrino, A. G., Zhang, B., Speranza, F., Maniscalco, R., Yin, C., Hernandez-Moreno, C., & Winkler, A. (2018). Tectonics and paleomagnetic rotation pattern of Yunnan (24°N–25°N, China): Gaoligong fault shear versus megablock drift. *Tectonics*, 37(5), 1524–1551. https://doi.org/10.1029/2017TC004899

Peltzer, G., & Tapponnier, P. (1988). Formation and evolution of strike-slip faults, rifts, and basins during the India-Asia collision: An experimental approach. *Journal of Geophysical Research: Solid Earth*, 93(B12), 15085–15117. https://doi.org/10.1029/JB093iB12p15085

Petrovský, E., & Kapička A. (2006). On determination of the Curie point from thermomagnetic curves. *Journal of Geophysical Research: Solid Earth*, 111(B12). https://doi.org/10.1029/2006JB004507

Pike, C. R., Roberts, A. P., & Verosub, K. L. (1999). Characterizing interactions in fine magnetic particle systems using first order reversal curves. *Journal of Applied Physics*, 85(9), 6660 – 6667. https://doi.org/10.1063/1.370176

Pike, C. R., Roberts, A.P., & Verosub, K.L. (2001). First-order reversal curve diagrams and thermal relaxation effects in magnetic particles. *Geophysical Journal International*, 145(3), 721-730. https://doi.org/10.1046/j.0956-540x.2001.01419.x

Platzman, E., & Platt, J. (1994). Why are there no clockwise rotations along the North Anatolian fault zone?. *Journal of Geophysical Research: Solid Earth*, 99(B11), 21705–21715. https://doi.org/10.1029/94JB01665

Piper, J. D. A., Tatar, O., & Gürsoy, H. (1997). Deformational behavior of continental lithosphere deduced from block rotations across the North Anatolian Fault Zone in Turkey. *Earth and Planetary Science Letters*, 150, (3-4), 191–203. https://doi.org/10.1016/S0012-821X(97)00103-9

Piper, J.D.A., Thomas, D.N., Share, S., & Rui, Z.Q. (1999). The palaeomagnetism of (Meso-proterozoic) Eriksfjord Group red beds, South Greenland: multiphase remagnetization during the Gardar and Grenville episodes. *Geophysical Journal International*,136(3), 739–756. https://doi.org/10.1046/j.1365-246x.1999.00756.x

Porreca, M. & Mattei, M. (2012). AMS fabric and tectonic evolution of Quaternary intramontane extensional basins in the Picentini Mountains (Southern Apennines, Italy). *International Journal of Earth Sciences*, 101(3), 787–802. https://doi.org/10.1007/s00531-011-0670-2

Pullaiah, G., Ivring, E., Buchan, K.L., & Dunlop, D. J. (1975). Magnetization changes caused by burial and uplift. *Earth and Planetary Science Letters*, 28(2), 133-143. https://doi.org/10.1016/0012-821X(75)90221-6

R

Randall, K., Lamb, S., & Mac Niocaill, C. (2011). Large tectonic rotations in a wide zone of Neogene distributed dextral shear, northeastern South Island, New Zealand. *Tectonophysics*, 509(3-4), 165–180. https://doi.org/10.1016/j.tecto.2011.05.006

Ransome, F. L., Emmons, W. H., & Garrey, G. H. (1910). Geology of ore deposits of the Bullfrog district, Nevada. *United States Geological Survey Numbered Series, Bulletin*, 407, 130. https://doi.org/10.3133/b407

Ratschbacher, L., Frisch, W., Chen, C., & Pan, G. (1996). Cenozoic deformation, rotation, and stress patterns in eastern Tibet and western Sichuan, China, In: Yin, A., Harrison, T.M. (Eds.), The tectonic evolution of Asia. *Cambridge University Press*, 227–249.

Replumaz, A., & Tapponnier, P. (2003). Reconstruction of the deformed collision zone between India and Asia by backward motion of lithospheric blocks. *Journal of Geophysical Research: Solid Earth*, 108(B6), 2285. https://doi.org/10.1029/2001JB000661

Replumaz, A., Lacassin, R., Tapponnier, P., & Leloup, P. H. (2001). Large river offsets and Plio-Quaternary dextral slip rate on the Red River fault (Yunnan, China). *Journal of Geophysical Research: Solid Earth*, 106(B1), 819–836. https://doi.org/10.1029/2000JB900135

Robb, G.L. (1949). Red bed coloration. *Journal of Sedimentary Petrology*, 19(3), 99–103.

Roberts, A. P., Cui, Y., & Verosub, K. L. (1995). Wasp-waisted hysteresis loops: Mineral magnetic characteristics and discrimination of components in mixed magnetic systems. *Journal of Geophysical Research: Solid Earth*, 100(B9), 17909–17924. https://doi.org/10.1029/95JB00672

Roberts, A.P., Pike, C.R., & Verosub, K.L. (2000). First order reversal curve diagrams: a new tool for characterizing the magnetic properties of natural samples. *Journal of Geophysical Research: Solid Earth*, 105(B12) 28461-28475. https://doi.org/10.1029/2000JB900326

Roberts, A.P., & Weaver, R. (2005). Multiple mechanisms of remagnetization involving sedimentary greigite (Fe_3S_4). *Earth and Planetary Science Letters,* 231(3-4), 263–277. https://doi.org/10.1016/j.epsl.2004.11.024

Roberts, A.P. (2015). Magnetic mineral diagenesis. *Earth-Science Reviews,* 151, 1–47. https://doi.org/10.1016/j.earscirev.2015.09.010

Rochette P. (1987). Magnetic susceptibility of the rock matrix related to magnetic fabric studies. *Journal of Structural Geology*, 9(8), 1015-1020. https://doi.org/10.1016/0191-8141(87)90009-5

Rochette, P., Jackson, M., & Aubourg, C. (1992). Rock magnetism and the interpretation of anisotropy of magnetic susceptibility. *Reviews of Geophysics*, 30(3), 209-226. https://doi.org/10.1029/92RG00733

Roger, F., Calassou, S., Lancelot, J., Malavieille, J., Mattauer, M., Xu, Z., Hao, Z., & Hou, L. (1995). Miocene emplacement and deformation of the Konga Shan granite (Xianshui He fault zone, west Sichuan, China): geodynamic implications. *Earth and Planetary Science Letters*, 130, 201–216. https://doi.org/10.1016/0012-821X(94)00252-T

Ron, H., Freund, R., Garfunkel, Z., & Nur, A. (1984). Block rotation by strike-slip faulting: Structural and paleomagnetic evidence. *Journal of Geophysical Research: Solid Earth*, 89(B7), 6256–6270. https://doi.org/10.1029/JB089iB07p06256

Royden, L. H., Burchfiel, B. C., King, R., Wang, E., Chen, Z., Shen, F., & Liu, Y. (1997). Surface deformation and lower crustal flow in Eastern Tibet. *Science*, 276(5313),788–790. https://doi.org/10.1126/science.276.5313.788

Royden, L. H., Burchfiel, B. C., & Van der Hilst, R. D. (2008). The Geological Evolution of the Tibetan Plateau. *Science*, 321(5892), 1054-1058. https://doi.org/10.1126/science.1155371

Rowan, C. J., & Roberts, A. P. (2006). Magnetite dissolution, diachronous greigite formation, and secondary magnetizations from pyrite oxidation: unravelling complex magnetizations in Neogene marine sediments from New Zealand. *Earth and Planetary Science Letters*, 241(1-2), 119–137. https://doi.org/10.1016/j.epsl.2005.10.017

S

Sagnotti, L., & Speranza, F. (1993). Magnetic fabric analysis of the Plio-Pleistocene clayey units of the Sant'Arcangelo basin, southern Italy. *Physics of the Earth and Planetary Interiors*, 77(3-4), 165-176. https://doi.org/10.1016/0031-9201(93)90096-R

Sagnotti, L., Faccenna, C., Funiciello, R., & Mattei, M. (1994). Magnetic fabric and structural setting of Plio-Pleistocene clayey units in an extensional regime: the Tyrrhenian margin of central Italy. *Journal of Structural Geology*, 16(9), 1243-1257. https://doi.org/10.1016/0191-8141(94)90067-1

Sagnotti, L., Speranza, F., Winkler, A., Mattei, M., & Funiciello, R. (1998). Magnetic fabric of clay sediments from the external northern Apennines (Italy). *Physics of the Earth and Planetary Interiors*, 105(1-2), 73-93. https://doi.org/10.1016/S0031-9201(97)00071-X

Sagnotti, L., Winkler, A., Montone, P., Di Bella, L., Florindo, F., Mariucci, M. T., Marra, F., Alfonsi, L., & Frepoli, A. (1999). Magnetic anisotropy of Plio-Pleistocene sediments from the Adriatic margin of the northern Apennines (Italy): implications for the time-space evolution of the stress field. *Tectonophysics*, 311(1-4), 139-153. https://doi.org/10.1016/S0040-1951(99)00159-6

Salyards, S. L., Sieh, K. E., & Kirschvink, J. L. (1992). Paleomagnetic measurement of nonbrittle coseismic deformation across the San Andreas fault at Pallett Creek. *Journal of Geophysical Research*, 97(B9), 12457–12470. https://doi.org/10.1029/92JB00194

Sato, K., Liu, Y., Zhu, Z., Yang, Z., & Otofuji, Y. (1999). Paleomagnetic study of middle Cretaceous rocks from Yunlong, western Yunnan, China: evidence of south-ward displacement of Indochina. *Earth and Planetary Science Letters*, 165(1), 1–15. https://doi.org/10.1016/S0012-821X(98)00257-X

Sato, K., Liu, Y., Zhu, Z., Yang, Z., & Otofuji, Y. (2001). Tertiary paleomagnetic data from northwestern Yunnan, China: Further evidence for large clockwise rotation of the Indochina

Block and its tectonic implications. *Earth and Planetary Science Letters*, 185(1-2), 185–198. https://doi.org/10.1016/S0012-821X(00)00377-0

Sato, K., Liu, Y., Wang, Y., Yokoyama, M., Yoshioka, S., Yang, Z., & Otofuji, Y. (2007). Paleomagnetic study of Cretaceous rocks from Pu'er, western Yunnan, China: Evidence of internal deformation of the Indochina Block. *Earth and Planetary Science Letters*, 258(1-2), 1–15. https://doi.org/10.1016/j.epsl.2007.02.043

Scha¨rer, U., Zhang, L.S., & Tapponnier, P. (1994). Duration of strike-slip movements in large Shear Zones: the Red River belt, China. *Earth and Planetary Science Letters*, 126(4), 379–397. https://doi.org/10.1016/0012-821X(94)90119-8

Schoenbohm, L., Burchfiel, B. C., Chen, L., & Yin, J. (2006). Miocene to present activity along the Red River fault, China, in the context of continental extrusion, upper-crustal rotation, and lower-crustal flow. *Geological Society of America Bulletin*, 118(5-6), 672–688. https://doi.org/10.1130/B25816.1

Schwartz, S.Y., & Van der Voo, R. (1983). Paleomagnetic evaluation of the orocline hypothesis in the central and southern Appalachians. *Geophysical Research Letters*, 10(7), 505–508. https://doi.org/10.1029/GL010i007p00505

Scotese, C.R., Van derVoo, R., & McCabe, C. (1982). Paleomagnetism of the Upper Silurian and Lower Devonian carbonates of New York State: evidence for secondary magnetizations residing in magnetite. *Physics of the Earth and Planetary Interiors*, 30, 385–395. http://dx.doi.org/10.1016/0031-9201(82)90048-6

Searle, M. P. (2006). Role of the Red River Shear zone, Yunnan and Vietnam, in the continental extrusion of SE Asia. *Journal of the Geological Society*, 163(6), 1025–1036. https://doi.org/10.1144/0016-76492005-144

Searle, M. P., Noble, S. R., Cottle, J. M., Waters, D. J., Mitchell, A. H. G., Hlaing, T., & Horstwood, M. S. A. (2007). Tectonic evolution of the Mogok metamorphic belt, Burma (Myanmar) constrained by U-Th-Pb dating of metamorphic and magmatic rocks. *Tectonics*, 26(3). https://doi.org/10.1029/2006TC002083

Shangguan, Z., Zhao, C., Li, H., Gao, Q., & Sun, M. (2005). Evolution of hydrothermal explosions at Rehai geothermal field, Tengchong volcanic region, China. *Geothermics,* 34(4), 518–526. https://doi.org/10.1016/j.geothermics.2005.05.002

Simpson, R. W., & Cox, A. (1977). Paleomagnetic evidence for tectonic rotation of the Oregon Coast Range. *Geology*, 5(10), 585-589. https://doi.org/10.1130/0091-7613(1977)5<585:PEFTRO>2.0.CO;2

Sintubin M. (1994). Clay fabrics in relation to the burial history of shales. *Sedimentology*, 41(6), 1161-1169. https://doi.org/10.1111/j.1365-3091.1994.tb01447.x

Socquet, A., & Pubellier, M. (2005). Cenozoic deformation in western Yunnan (China–Myanmar border). *Journal of Asian Earth Sciences*, 24(4), 495–515. https://doi.org/10.1016/j.jseaes.2004.03.006

Sonder, L., & England, P. (1986). Vertical averages of rheology of the continental lithosphere: Relation to thin sheet parameters. *Earth and Planetary Science Letters*, 77(1), 81–90. https://doi.org/10.1016/0012-821X(86)90134-2

Sonder, L. J., England, P. C., & Houseman, G. A. (1986). Continuum calculation of continental deformation in transcurrent environments. *Journal of Geophysical Research: Solid Earth*, 91(B5), 4797–4810. https://doi.org/10.1029/JB091iB05p04797

Sonder, L. J., Jones, C. H., Salyards, S. L., & Murphy, K. M. (1994). Vertical axis rotations in the Las Vegas Valley Shear Zone, southern Nevada: Paleomagnetic constraints on kinematics and dynamics of block rotations. *Tectonics*, 13(4), 769–788. https://doi.org/10.1029/94TC00352

Soquet, A., Vigny, C., Chamot-Rooke, N., Simons, W., Rangin, C., & Ambrosius, B. (2006). India and Sunda plates motion and deformation along their boundary in Myanmar determined by GPS. *Journal of Geophysical Research: Solid Earth*, 111(B5). https://doi.org/10.1029/2005JB003877

Soto, R., Larrasoaña, J. C., Arlegui, L. E., Beamud, E., Oliva-Urcia, B., & Simón, J. L. (2009). Reliability of magnetic fabric of weakly deformed mudrocks as a palaeostress indicator in compressive settings. *Journal of Structural Geology*, 31(5), 512-522. https://doi.org/10.1016/j.jsg.2009.03.006

Speranza, F., Sagnotti, L., & Mattei, M. (1997). Tectonics of the Umbria Marche-Romagna Arc (central northern Apennines, Italy): New paleomagnetic constraints. *Journal of Geophysical Research: Solid Earth*, 102 (B2), 3153-3166. https://doi.org/10.1029/96JB03116

Speranza, F., Maniscalco, R., Mattei, M., Di Stefano, A., Butler, R. W. H., & Funiciello, R. (1999). Timing and magnitude of rotations in the frontal thrust system of southwestern Sicily. *Tectonics*, 18(6), 1178–1197. https://doi.org/10.1029/1999TC900029

Steiner, M.B., & Lucas, S.G., (2000). Paleomagnetism of the Late Triassic Petrified Forest Formation, Chinle Group, western United States: further evidence of “large” rotation of the Colorado Plateau. *Journal of Geophysical Research: Solid Earth*, 105(B11), 25791–25808. https://doi.org/10.1029/2000JB900093

Suk, D., Van Der Voo, R., & Peacor, D.R. (1993). Origin of magnetite responsible for remagnetization of early Paleozoic limestones of New York State. *Journal of Geophysical Research: Solid Earth*, 98, 419–434. https://doi.org/10.1029/92JB01323

Sun, Z., Yang, Z., Pei, J., Yang, T., & Wang, X. (2006). New Early Cretaceous paleomagnetic data from volcanic and red beds of the eastern Qaidam Block and its implications for tectonics of Central Asia. *Earth and Planetary Science Letters*, 243(1-2), 268–281. https://doi.org/10.1016/j.epsl.2005.12.016

T

Taymaz, T., Jackson, J. A. & Mckenzie, D. P. (1991a). Active tectonics of the North and Central Aegean Sea. *Geophysical Journal International*, 106(2), 433–490. https://doi.org/10.1111/j.1365-246X.1991.tb03906.x

Taymaz, T., Eyidogˇ an, H. & Jackson, J. A. (1991b). Source parameters of large earthquakes in the East Anatolian Zone (Turkey). *Geophysical Journal International*, 106(3), 537–550. https://doi.org/10.1111/j.1365-246X.1991.tb06328.x

Tamai, M., Liu, Y.Y., Lu, L.Z., Yokoyama, M., Zaman, H., Otofuji, Y. (2004). Palaeomagnetic evidence for southward displacement of the Chuan Dian Fragment of the Yangtze block. *Geophysical Journal International*, 158(1), 297-309. https://doi.org/10.1111/j.1365-246X.2004.02108.x

Tan, X., Kodama, K.P., Chen, H., Fang, D., Sun, D., Li, Y. (2003). Paleomagnetism and magnetic anisotropy of Cretaceous red beds from the Tarim basin, north-west China: evidence for a rock magnetic cause of anomalously shallow paleomagnetic inclinations from central Asia. *Journal of Geophysical Research: Solid Earth*, 108(B2), 2107. http://dx.doi.org/10.1029/2001JB001608

Tanaka, K., Mu, C., Sato, K., Takemoto, K., Miura, D., Liu, Y., Haider, Z., Yang, Z., Yokoyama, M., Hisanori, I., Uno, K., & Otofuji, Y. (2008). Tectonic deformation around the eastern Himalayan Syntaxis: constraints from the Cretaceous palaeomagnetic data of the Shan-Thai Block. *Geophysical Journal International*, 175(2), 713–728. https://doi.org/10.1111/j.1365-246X.2008.03885.x

Tapponnier, P., & Molnar, P. (1976). Slip line field theory and large-scale continental tectonics. *Nature*, 264, 319–324. https://doi.org/10.1038/264319a0

Tapponnier, P., & Molnar, P. (1977). Active faulting and tectonics in China. *Journal of Geophysical Research*, 82(20), 2905–2930. https://doi.org/10.1029/JB082i020p02905

Tapponnier, P., Peltzer, G., Le Dain, A. Y., Armijo, R., & Cobbold, P. (1982). Propagating extrusion tectonics in Asia: New insights from simple experiments with plasticine. *Geology*, 10(12), 611-616. https://doi.org/10.1130/0091-7613(1982)10<611:PETIAN>2.0.CO;2

Tapponnier, P., Peltzer, G., & Armijo, P. (1986). On the mechanics of the collision between India and Asia. In Coward, M.P., Ries, A.C. (Eds.), *Collision Tectonics, Geological Society London,* Special Publication, 19, 115–157. https://doi.org/10.1144/GSL.SP.1986.019.01.07

Tapponnier P., Lacassin, R., Leloup, P. H., Schärer, U., Zhong, D. L., Wu, H., Liu, X. H., Ji, S.C., Zhang, L. S., & Zhong J. (1990). The Ailaoshan/Red River Metamorphic belt: Tertiary left lateral shear between Indochina and South China. *Nature*, 343, 431–437. https://doi.org/10.1038/343431a0

Tarduno, J. A., Cottrell, R. D., & Smirnov, A. V. (2006). The paleomagnetism of single silicate crystals: recording geomagnetic field strength during mixed polarity intervals, superchrons, and inner core growth. *Reviews of Geophysics*, 44(1). https://doi.org/10.1029/2005RG000189

Tarling, D. H. (1983). Palaeomagnetism: Principles and applications in geology, geophysics, and archaeology. *Springer Netherlands*. https://doi.org/10.1007/978-94-009-5955-2

Tarling, D.H., & Hrouda, F. (1993). The Magnetic Anisotropy of Rocks. Chapman and Hall, London, 217. *Geological Journal*, 30, 1. https://doi.org/10.1002/gj.3350300111

Tauxe, L., Kent, D.V., & Opdyke, N.D. (1980). Magnetic components contributing to the NRM of Middle Siwalik red beds. *Earth and Planetary Science Letters*, 47(2), 279–284. https://doi.org/10.1016/0012-821X(80)90044-8

Tauxe, L. (1998). Paleomagnetic principles and practice. Modern approaches in geophysics, 299, Dordrecht, Boston, Kluwer Academic Publishers

Tauxe, L., & Kent, D. V. (2004). A simplified statistical model for the geomagnetic field and the detection of shallow bias in paleomagnetic inclinations: was the ancient magnetic field dipolar? In: Channell, J.E.T., Kent, D.V., Lowrie, W., Meert, J.G. (Eds.), Timescales of the Paleomagnetic Field. *Geophysical Monographic Series*, 145, American Geophysical Union, Washington, D.C.,101-115. https://doi.org/10.1029/145GM08

Tauxe, L. (2005). Inclination flattening and the geocentric axial dipole hypothesis. *Earth and Planetary Science Letters*, 233(3-4), 247-261. https://doi.org/10.1016/j.epsl.2005.01.027

Tauxe, L. (2009). Essentials of Paleomagnetism, University of California Press, 489, Berkeley.

Terres, R. R., & Luyendyk, B. P. (1985). Neogene tectonic rotation of the San Gabriel region, California, suggested by paleomagnetic vectors. *Journal of Geophysical Research: Solid Earth*, 90(B14). https://doi.org/10.1029/JB090iB14p12467

Titus, S. J., Crump, S., McGuire, Z., Horsman, E., & Housen, B. (2011). Using vertical axis rotations to characterize off-fault deformation across the San Andreas fault system, central California. *Geology*, 39(8), 711-714. https://doi.org/10.1130/G31802.1

Tong, Y.-B., Yang, Z., Wang, H., Gao, L., An, C.-Z., Zhang, X.-D., & Xu, Y.-C.(2015). The Cenozoic rotational extrusion of the Chuan Dian Fragment: New paleomagnetic results from Paleogene red-beds on the southeastern edge of the Tibetan Plateau. *Tectonophysics*, 658, 46-60. https://doi.org/10.1016/j.tecto.2015.07.007

Tong, Y.-B, Yang, Z., Jing, X., Zhao, Y., Li, C., Huang, D., & Zhang, X. (2016). New insights into the Cenozoic lateral extrusion of crustal blocks on the southeastern edge of Tibetan Plateau: Evidence from paleomagnetic results from Paleogene sedimentary strata of the Baoshan Terrane. *Tectonics*, 35(11), 2494–2514. https://doi.org/10.1002/2016TC004221

Tong, Y.-B, Yang, Z., Mao, C., Pei, J., Pu, Z., & Xu, Y. (2017). Paleomagnetism of Eocene red-beds in the eastern part of the Qiangtang Terrane and its implications for uplift and southward crustal extrusion in the southeastern edge of the Tibetan Plateau. *Earth and Planetary Science Letters*, 475, 1-14. https://doi.org/10.1016/j.epsl.2017.07.026

Tong, Y.-B., Yang, Z., Zheng, L. D., Xu, Y. L., Wang, H., Gao, L., & Hu, X. Z. (2013). Internal crustal deformation in the northern part of Shan-Thai Block: New evidence from paleomagnetic results of Cretaceous and Paleogene redbeds. *Tectonophysics*, 608, 1138–1158. https://doi.org/10.1016/j.tecto.2013.06.031

Torsvik, T., Müller, R., Van der Voo, R., Steinberger, B., & Gaina, C. (2008). Global plate motion frames: Toward a unified model. *Reviews of Geophysics*, 46(3). https://doi.org/10.1029/2007RG000227

Torsvik, T. H., Van der Voo, R., Preeden, U., Mac Niocaill, C., Steinberger, B., Doubrovine, P. V., Van Hinsbergen, D. J. J., Domeier, M., Gaina, C., Tohver, E., Meert, J. G., McCausland, P. J. A., &. Cocks, L. R. M (2012). Phanerozoic polar wander, paleogeography and dynamics. *Earth-Science Reviews*, 114(3-4), 325-368. https://doi.org/10.1016/j.earscirev.2012.06.007

Tucker, R. T., Zou, H., Fan, Q., & Schmitt, A. K. (2013). Ion microprobe dating of zircons from active Dayingshan volcano, Tengchong, SE Tibetan Plateau: time scales and nature of magma chamber storage. *Lithos*, 172–173, 214–221. https://doi.org/10.1016/j.lithos.2013.04.017

V

Van der Voo, R., & Torsvik, T.H. (2012). The history of remagnetization of sedimentary rocks: deceptions, developments and discoveries. *Geological Society, London, Special Publications*, 371, 23–53. https://doi.org/10.1144/SP371.2

Van Houten, F.B. (1968). Iron oxides in red beds. *Geological Society of America Bulletin,* 79, 399–416. https://doi.org/10.1130/0016-7606(1968)79[399:IOIRB]2.0.CO;2

Van Houten, F.B. (1973). Origin of red beds: a review—1961–1972. *Annual Review of Earth and Planetary Sciences*, 1, 39–61. https://doi.org/10.1146/annurev.ea.01.050173.000351

Vergnolle, M., Calais, E., & Dong, L. (2007). Dynamics of continental deformation in Asia, *Journal of Geophysical Research: Solid Earth*, 112(B11). https://doi.org/10.1029/2006JB004807

Vilotte, J.P., Madariaga, R., Daignieres, M., & Zienkiewicz, O. (1986). Numerical study of continental collision: influence of buoyancy forces and an initial inclusion. *Geophysical Journal International*, 84(2), 279–310. https://doi.org/10.1111/j.1365-246X.1986.tb04357.x

W

Walker, T.R., (1967). Color of recent sediments in tropical Mexico: a contribution to the origin of red beds. *Geological Society of America Bulletin*, 78, 917–920. https://doi.org/10.1130/0016-7606(1967)78[917:CORSIT]2.0.CO;2

Wang, E., & Burchfiel, B. C. (1997). Interpretation of Cenozoic tectonics in the right-lateral accommodation zone between the Ailao Shan shear zone and the Eastern Himalayan Syntaxis. *International Geology Review*, 39, 191–219. https://doi.org/10.1080/00206819709465267

Wang, E., & Burchfiel, B.C. (2000). Late Cenozoic to Holocene deformation in southwestern Sichuan and adjacent Yunnan, China, and its role in formation of the southeastern part of the Tibetan Plateau. *Geological Society of America Bulletin,* 112(3), 413–423. https://doi.org/10.1130/0016-7606(2000)112<413:LCTHDI>2.0.CO;2

Wang, E., Burchfiel, B. C., Royden, L. H., Chen, L. Z., Chen, J. S., Li, W. X., & Chen, Z. L. (1998). Late Cenozoic Xianshuihe–Xiaojiang, Red River, and Dali Fault Systems of Southwestern Sichuan and Central Yunnan, China. *Geological Society of America Special Papers*, 327, 1–108. https://doi.org/10.1130/0-8137-2327-2.1

Wang, F., Chen, W. J., Pen, Z. C., Zhang, Z. L., & Hu, Y. T. (1999). Chronology of young volcanic rocks of Changbaishan Tianchi and Tengchong, China, by using the Uranium-series TIMS method. *Geological Review*, 45, 914–925 (in Chinese with English abstract).

Wang, G., Wan, J., Wang, E., Zheng, D., & Li, F. (2008). Late Cenozoic to recent transtensional deformation across the Southern part of the Gaoligong shear zone between the Indian plate and SE margin of the Tibetan plateau and its tectonic origin. *Tectonophysics*, 460(1-4), 1–20. https://doi.org/10.1016/j.tecto.2008.04.007

Wang, H., Yang, Z., Tong, Y., Gao, L., Jing, X., & Zhang, H. (2016a). Palaeomagnetic results from Palaeogene red beds of the Chuan-Dian Fragment, southeastern margin of the Tibetan Plateau: implications for the displacement on the Xianshuihe–Xiaojiang fault systems. *International Geology Review*, 58(11), 1363-1381. https://doi.org/10.1080/00206814.2016.1157710

Wang, J. H., Yin, A., Harrison, T. M., Grove, M., Zhang, Y.-Q., & Xie, G.-H. (2001). A tectonic model for Cenozoic igneous activities in the eastern Indo–Asian collision zone. *Earth and Planetary Science Letters*, 188(1-2), 123–133. https://doi.org/10.1016/S0012-821X(01)00315-6

Wang, P.-L., C.-H. Lo, Lee, T.-Y., Chung, S.-L., Lan, C.-Y., & Yem N.T. (1998). Thermochronological evidence for the movement of the Ailaoshan–Red River Shear Zone: A perspective from Vietnam. *Geology*, 26(10), 897–890. https://doi.org/10.1130/0091-7613(1998)026<0887:TEFTMO>2.3.CO;2

Wang, P.-L., Lo, C.-H., Chung, S.-L., Lee, T.-Y., Lan, C.-Y., & Thang, T.V. (2000). Onset timing of left-lateral movement along the Ailaoshan–Red River Shear Zone: $^{40}Ar/^{39}Ar$ dating constraint from Nam Dinh area, northeastern Vietnam. *Journal of Asian Earth Sciences*,18(3), 281–292. https://doi.org/10.1016/S1367-9120(99)00064-4

Wang, Y., Zhang, B., Schoenbohm, L. M, Zhang, J., Zhou, R., Hou, J., & Ai, S. (2016b). Late Cenozoic tectonic evolution of the Ailao Shan-Red River fault (SE Tibet): Implications for kinematic change during plateau growth. *Tectonics*, 35(8), 1969–1988. https://doi.org/10.1002/2016TC004229

Wang, Y., Zhang X., Jiang C., Wei H., & Wan J. (2007). Tectonic controls on the late Miocene– Holocene volcanic eruptions of the Tengchong volcanic field along the southeastern margin of the Tibetan plateau. *Journal of Asian Earth Sciences*, 30 (2), 375–389. https://doi.org/10.1016/j.jseaes.2006.11.005

Wang, Y. J., Fan, W.M., Zhang, Y.H., Peng, T.P., Chen, X.Y., & Xu, Y.G. (2006). Kinematics and $^{40}Ar/^{39}Ar$ geochronology of the Gaoligong and Chongshan shear systems, western Yunnan, China: implications for early Oligocene tectonic extrusion of SE Asia. *Tectonophysics*, 418(3-4), 235–254. https://doi.org/10.1016/j.tecto.2006.02.005

Wang, Z., & Van der Voo, R. (1993). Pervasive remagnetization of Paleozoic rocks acquired at the time of Mesozoic folding in the South China Block. *Journal of Geophysical Research*: *Solid Earth*, 98(B2), 1729–1741. https://doi.org/10.1029/92JB02405

Weaver, R., Roberts, A. P., & Barker, A. J. (2002). A late diagenetic (synfolding) magnetization carried by pyrrhotite: implications for paleomagnetic studies from magnetic iron sulphide-bearing sediments. *Earth and Planetary Science Letters*, 200(3-4), 371–386. https://doi.org/10.1016/S0012-821X(02)00652-0

Weil, A. B., Yonkee, A., & Sussman, A. (2010). Reconstructing the kinematic evolution of curved mountain belts: A paleomagnetic study of Triassic red beds from the Wyoming salient, Sevier thrust belt, U.S.A. *Geological Society of America Bulletin*, 122(1-2), 3–23. https://doi.org/10.1130/B26483.1

Wells, R. E. & Coe, R. S. (1985). Paleomagnetism and geology of Eocene volcanic rocks of southwest Washington: Implications for mechanisms of rotation. *Journal of Geophysical Research: Solid Earth*, 90(B2), 1925-1947. https://doi.org/10.1029/JB090iB02p01925

Wells, R. E. & Heller, P. L. (1988). The relative contribution of accretion, shear, and extension to Cenozoic tectonic rotation in the Pacific Northwest. *Geological Society of America Bulletin*, 100(3), 325-338. https://doi.org/10.1130/0016-7606(1988)100<0325:TRCOAS>2.3.CO;2

Winkler A., Alfonsi, L., Florindo, F., Sagnotti, L. & Speranza, F. (1997). The magnetic anisotropy of rocks: principles, techniques and geodynamic applications in the Italian peninsula. *Annals of Geophysics*, XL, 3, 729-740. https://doi.org/10.4401/ag-3899

Wopfner, H. (1996). Gondwana origin of the Baoshan and Tengchong terranes of West Yunnan. In: Tectonic Evolution of Southeast Asia, eds. Hall, R. and Blundell, D., *Geological Society, London, Special Publications*, 106, 539–547. https://doi.org/10.1144/GSL.SP.1996.106.01.34

X

Xu, Y., Yang, Q., Lan, J., Luo, Z., Huang, X., Shi, Y., & Xie, L. (2012). Temporal-spatial distribution and tectonic implications of the batholiths in the Gaoligong-Tengliang-Yingjiang area, western Yunnan: constraints from zircon U-Pb ages and Hf isotopes. *Journal of Asian Earth Sciences*, 53, 151–175. https://doi.org/10.1016/j.jseaes.2011.06.018

Xu, Z., Yang, J., Li, W., Li, H., Cai, Z., Yan, Z., & Ma, C. (2013). Plaoe-Tethys system and accretionary orogen in the Tibet Plateau. *Acta Petrologica Sinica*, 29 (6), 1847–1860.

Xu, Z., Wang, Q., Cai, Z. H., Dong, H. W., Li, H. Q., Chen, X. J., Duan, X. D., Cao, H., Li, J., & J. Burg, P. (2015). Kinematics of the Tengchong Terrane in SE Tibet from the late Eocene to early Miocene: Insights from coeval mid-crustal detachments and strike-slip Shear Zones. *Tectonophysics*, 665, 127–148. https://doi.org/10.1016/j.tecto.2015.09.033

Y

Yang, Z. Y., & Besse, J. (1993). Paleomagnetic study of Permian and Mesozoic sedimentary rocks from Northern Thailand supports the extrusion model for Indochina. *Earth and Planetary Science Letters*, 117(3-4), 525–552. https://doi.org/10.1016/0012-821X(93)90101-E

Yang, Z. Y., Sun, Z. M., Ma, X. H., Yin, J. Y., & Otofuji, Y. (2001a). Paleomagnetic study of the Early Tertiary on both Sides of the Red River Fault and its geological implications. *Acta Geologica Sinica*, 75, 35–44 (in Chinese with English abstract).

Yang, Z. Y., Yin, J. Y., Sun, Z. M., Otofuji, Y., & Sato, K. (2001b). Discrepant Cretaceous paleomagnetic poles between Eastern China and Indochina: A consequence of the extrusion of Indochina. *Tectonophysics*, 334(2), 101–113. https://doi.org/10.1016/S0040-1951(01)00061-0

Yin, A. (2010). Cenozoic tectonic evolution of Asia: a preliminary synthesis. *Tectonophysics*, 488(1-4), 293–325. https://doi.org/10.1016/j.tecto.2009.06.002

Yin, A., & Harrison, T.M. (2000). Geologic evolution of the Himalaya–Tibetan orogen. *Annual Review of Earth and Planetary Sciences*, 28, 211–280. https://doi.org/10.1146/annurev.earth.28.1.211

Yin, A., & Taylor, M.H. (2011). Mechanics of V-shaped conjugate strike-slip faults and the corresponding continuum mode of continental deformation. *Geological Society of America Bulletin*, 123(9-10), 1798-1821. https://doi.org/10.1130/B30159.1

Yoshioka, S., Liu, Y. Y., Sato, K., Inokuchic, H., Su, L., Zamana, H., & Otofuji, Y. (2003). Paleomagnetism evidence for post–cretaceous internal deformation of the Chuan Dian Fragment in the Yangtze Block: a consequence of indentation of India into Asia. *Tectonophysics*, 376(1-2), 61–74. https://doi.org/10.1016/j.tecto.2003.08.010

Z

Zaman, H., & Torii, M. (1999). Palaeomagnetic study of Cretaceous red beds from the eastern Hindukush ranges, northern Pakistan: palaeoreconstruction of the Kohistan–Karakoram composite unit before the India–Asia collision. *Geophysical Journal International*, 136(3), 719–738. https://doi.org/10.1046/j.1365-246x.1999.00757.x

Zhang, L. S., & Scharer, U. (1999). Age and origin of magmatism along the Cenozoic Red River shear belt, China. *Contributions to Mineralogy and Petrology*,134(1), 67–85.

Zhang, R., Cong, B., Maruyama, S., & Liou, J. G. (1993). Metamorphism and tectonic evolution of the Lancang paired metamorphic belts, southwestern China. *Journal of Metamorphic Geology,* 11(4), 605–619. https://doi.org/10.1111/j.1525-1314.1993.tb00175.x

Zhang, S.C., Diao, G.L., Wang, S.J., & Long, X.F. (1994). Rupture characteristics of the 1976 Longling earthquake sequence. *Earthquake Research in China*, 10(2), 152–159 (in Chinese with English abstract).

Zhang, P. Z., Shen, Z., Wang, M., Gan, W. J., Burgmann, R., Molnar, P., Wang, Q., Niu, Z., Sun, J., Wu, J., Hanrong, S., & Xinshao, Y. (2004). Continuous deformation of the Tibetan Plateau from global positioning system data. *Geology*, 32(9), 809–812. https://doi.org/10.1130/G20554.1

Zhang, J. J., Zhong, D. L., Sang, H. Q., & Zhou, Y. (2006). Structural and geochronological evidence for multiple episodes of Tertiary deformation along the AilaoShan–Red River Shear Zone, Southeastern Asia, since the Paleocene. *Acta Geologica Sinica - English Edition,* 80(1), 79–96. https://doi.org/10.1111/j.1755-6724.2006.tb00798.x

Zhang, B., Zhang, J., & Zhong, D. (2010). Structure, kinematics and ages of transpression during strain partitioning in the Chongshan shear zone, western Yunnan, China. Journal of Structural Geology, 32(4), 445–463. https://doi.org/10.1016/j.jsg.2010.02.001

Zhang, B., Zhang, J.J., Zhong, D.L, Wang, X.X., Qu, J.F., & Guo, L. (2011). Structural feature and its significance of the northernmost segment of the Tertiary Biluoxueshan-Chongshan Shear Zone, east of the Eastern Himalayan Syntaxis. *Science China Earth Sciences*, 54(7), 959–974. https://doi.org/10.1007/s11430-011-4197-y

Zhang, B., Zhang, J., Chang, Z., Wang, X., Cai, F., & Lai, Q. (2012a). The Biluoxueshan transpressive deformation zone monitored by synkinematic plutons, around the Eastern Himalayan Syntaxis. *Tectonophysics*, 574-575, 158–180. https://doi.org/10.1016/j.tecto.2012.08.017

Zhang, B., Zhang, J., Zhong, D., Yang, L., Yue, Y., & Yan, S. (2012b). Polystage deformation of the Gaoligong metamorphic zone: structures, $^{40}Ar/^{39}Ar$ mica ages, and tectonic implications. *Journal of Structural Geology*, 37, 1-18. https://doi.org/10.1016/j.jsg.2012.02.007

Zhang, B., Yin, C. Y., Zhang, J. J., Wang, J. M., Zhong, D. L., Wang, Y., Lai, Q. Z., Yue, Y. H., & Zhou, Q. Y. (2017). Midcrustal shearing and doming in a Cenozoic compressive setting along the Ailao Shan-Red River shear zone. *Geochemistry, Geophysics, Geosystems*, 18(1), 400–433. https://doi.org/10.1002/2016GC006520

Zhang, Y. Q., Chen, W., & Yang, N. (2004). Ar-40/Ar-39 dating of shear deformation of the Xianshuihe fault zone in west Sichuan and its tectonic significance. *Science in China Series D-Earth Sciences*, 47(9), 794–803.

Zhao, J., Huang, B. C., Yang, Y. G., & Zhang, D. H. (2015). Late Triassic paleomagnetic result from the Baoshan Terrane, West Yunnan of China: Implication for orientation of the East Paleotethys suture zone and timing of the Sibumasu-Indochina collision. *Journal of Asian Earth Sciences*, 111, 350–364. https://doi.org/10.1016/j.jseaes.2015.06.033

Zhong, D.-L., Tapponnier, P., Wu, H.-W., Zhang, L.-S., Ji, S.-C., Zhong, J.-Y., Liu, X.-H., Schaerer, U., Lacassiu, R., & Leloup, P. (1990). Large-scale strike-slip-fault—the major structure of intracontinental deformation after collision. *Chinese Science Bulletin*, 35(4), 304–309.

Zhong, D. L., Wang, Y., & Ding, L. (1991). The Tertiary Gaoligong intracontinental strike-slip fault and its associated extensional structure in western Yunnan, China (in Chinese with English abstract), in Annual Report 1989–1990 Lab. *Lithos*. Tectonic Evolution. Inst. Geol, edited by X. Zhang, pp. 18–22, Academia Sinica, Beijing.

Zhu, B.Q., Mao, C.X., Lugmair, G.W., & Macdougall, J.D. (1983). Isotopic and geochemical evidence for the origin of Plio-Pleistocene volcanic rocks near the Indo-Eurasian collisional margin at Tengchong, China. *Earth and Planetary Science Letters*, 65 (2), 263–275. https://doi.org/10.1016/0012-821X(83)90165-6

Zhu, D. C., Zhao, Z. D., Pan, G. T., Lee, H. Y., Kang, Z. Q., Liao, Z. L., Wang, L. Q., Li, G. M., Dong, G. C., Liu, B., (2009). Early Cretaceous subduction-related adakite-like rocks of the Gangdese Belt, southern Tibet: products of slab melting and subsequent melt peridotite interaction?. *Journal of Asian Earth Sciences,* 34(3), 298–309. https://doi.org/10.1016/j.jseaes.2008.05.003

Zhu, R., Potts, R., Pan, Y. X., Lue, L. Q., Yao, H. T., Deng, C. L., & Qin, H. F. (2008). Paleomagnetism of the Yuanmou Basin near the southeastern margin of the Tibetan Plateau and its constraints on late Neogene sedimentation and tectonic rotation. *Earth and Planetary Science Letters*, 272(1-2), 97–104. https://doi.org/10.1016/j.epsl.2008.04.016

Zijderveld, J. D. (1967). A. C. demagnetization of rocks: Analysis of results, in *Methods in Paleomagnetism*, edited by D. W. Collinson, K. M. Creer, and S. K. Runcorn:254-286, Elsevier, New York.

Zou, H.,Q. Fan, A.K. Schmitt, and J. Sui (2010). U–Th dating of zircons from Holocene Potassic andesites (Maanshan volcano, Tengchong, SE Tibetan Plateau) by depth profiling: time scales and nature of magma storage, *Lithos*,118 (1–2), 202–210.

Zou, H., C.-C. Shen, Q. Fan, and K. Lin (2014). U-series disequilibrium in young Tengchong volcanics: recycling of mature clay sediments or mudstones into the SE Tibetan mantle, *Lithos*, 192–195, 132–141.

ACKNOWLEDGEMENTS/ RINGRAZIAMENTI

I'm grateful to Prof. Zhang, Congyuan Yin, Siyu Chen (Peking University) and Mr. Mu for their kindness and for safely driving me in the whole Yunnan during my field campaigns.

Un ringraziamento particolare va alla *Prof.ssa Rosanna Maniscalco*, mia relatrice di tesi di laurea triennale, laurea magistrale e dottorato di ricerca. Un percorso lunghissimo, che ho scelto di percorrere sempre al suo fianco, e che rifarei altre mille volte! Da sempre ha creduto in me, dimostrandomi disponibilità e attenzioni costanti che mi hanno consentito non solo di raggiungere questo traguardo ma anche di fare innumerevoli esperienze formative e umane;

Al *Prof. Fabio Speranza*, mio correlatore, per la pazienza e l'ospitalità dimostratami durante i lunghi soggiorni presso l'INGV di Roma, ma soprattutto per l'incoraggiamento e i preziosi consigli necessari "per diventare un buon Ricercatore";

Entrambi hanno sempre cercato di trasmettermi il loro sapere e questo non può che essere la base per definirli dei bravi Docenti. Se sono cresciuta professionalmente è solo grazie a loro …. a loro va la mia infinita gratitudine ed il mio affetto!

A tutti i componenti del gruppo di paleomagnetismo dell'INGV di Roma, in particolare Aldo Winkler e Patrizia Macrì, per il tempo trascorso insieme al "fresco" in laboratorio e per il supporto tecnico/morale durante i lunghi cicli di misure.

Ai revisori della mia Tesi di Dottorato, Prof. Massimo Mattei e Prof. Rodolfo Carosi, per gli attenti commenti e per i preziosi consigli che hanno contribuito certamente a valorizzare e migliorare il lavoro finale.

Al coordinatore Prof.ssa Agata Di Stefano, per il costante supporto e per essere sempre stata attiva nella formazione e nella crescita di tutti i dottorandi.

Ai miei amici e colleghi (vecchi e nuovi), ed a Catalina Hernandez-Moreno, per aver condiviso con me i momenti più belli e difficili di questi tre anni.

E poi non finirò mai di ringraziare mio padre, mia madre, i miei fratelli e Mirko, mio più grande amore e compagno di vita, che mi hanno sempre sostenuto in tutte le scelto che ho fatto, mi sono sempre stati vicino e mi hanno "sopportato" dandomi ogni giorno un motivo in più per andare avanti.

Università degli Studi di Catania, Catania, Italy

Supporting Information for

UNDERSTANDING BLOCK ROTATION ALONG STRIKE-SLIP FAULT ZONES IN YUNNAN (CHINA): PALEOMAGNETIC AND STRUCTURAL APPROACH

Ph.D. Thesis

Dott.ssa Alessandra Giovanna Pellegrino

Contents of this file : Caption for Data Set

- Equal angle projections (Wulf), both sample mean (ChRM/ High-Temperature Component) and site mean paleomagnetic directions, gathered by us along **a)** Gaoligong shear zone and **b)** Red River shear zone. Geographic or In-situ (GEO) and Tilt correction coordinate system (TILT CORR). The magnetization components were identified by principal component analysis [Kirschvink, 1980], and the site mean paleomagnetic directions were computed using *Fisher* [1953] statistics. Software: Remasoft 3.0 [*Chadima and Hrouda*, 2007].
- Equal area projections on lower hemisphere of the Anisotropy of magnetic susceptibility (AMS) directions for sites gathered by us along **c)** Gaoligong shear zone and **d)** Red River shear zone. The squares, triangle, and dots represent K_{max} , K_{int} and k_{min} respectively. The ellipses indicate the 95% region around the principal susceptibility axes. The orange line (open circle) indicates the bedding planes (poles) (expressed in dip azimuth/dip values). Software: Anisoft 4.2 [*Chadima and Jelinek, 2009*].
- **e)** Wasp-waisted hysteresis loops from basalts and red beds sites sampled along Gaoligong shear zone. The hysteresis parameters for these samples are shown in Table 6 and 7.

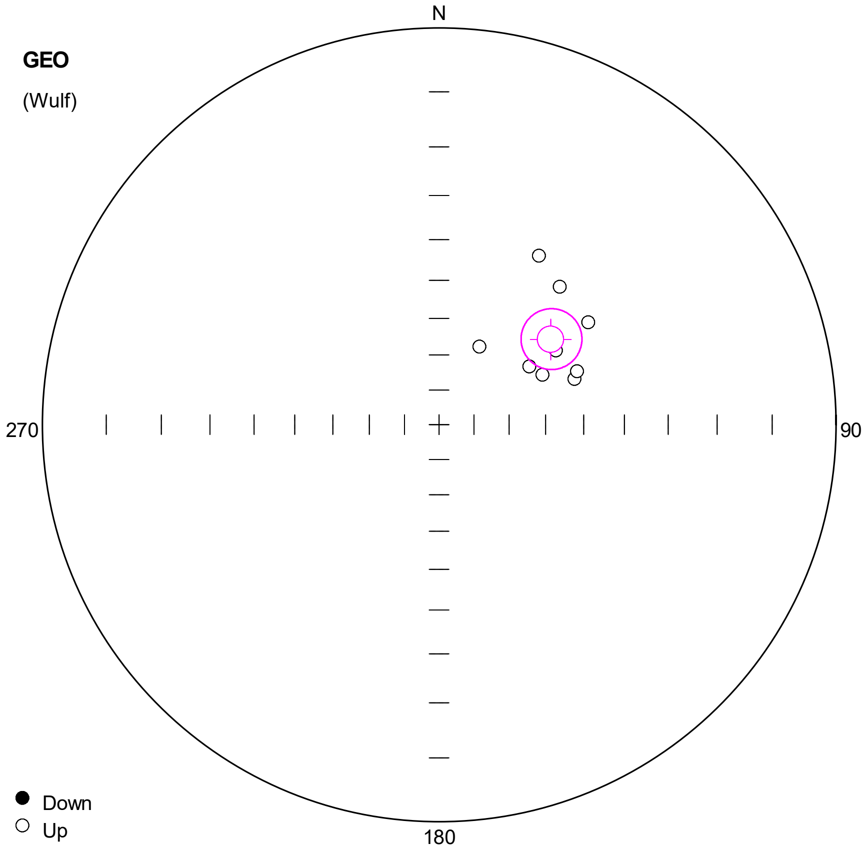

Number of data points: 10

Fisher statistics
Mean vector: 52.59 / -51.02
Resultant vector: 9.77
(X= 3.73, Y= 4.88, Z= -7.6)
Estimated precision, k: 39.4
95% Confidence limit: 7.79
95% Confidence limit, approximation: 7.05

Orientation matrix
1st eigenvalue: 0.96
1st eigenvector: 232.82 / 51.02
2nd eigenvalue: 0.03
2nd eigenvector: 353.26 / 22.29
3rd eigenvalue: 0.02
3rd eigenvector: 97.01 / 30.12

VGP
Site latitude: 65
Site longitude: 14.04
Pole latitude: -14.95 (14.95)
Pole longitude: 149.66 (-30.34)
Paleolatitude: -31.71 (31.71)
dp: 7.13
dm: 10.54

#	Name	State	Dec	Inc	MAD	Limit1	Limit2	
1	YUN0101	CCH	41.2	-40.4	12.1	35	64	
2	YUN0102	CCH	30.6	-37.4	12.5	30	64	
3	YUN0103	CCH	71.4	-50.4	9.0	35	64	
4	YUN0104	CCH	68.9	-49.1	7.5	35	64	
5	YUN0105	CCH	55.5	-41.0	10.8	48	64	O
6	YUN0106	CCH	52.4	-49.5	8.6	40	64	
7	YUN0107	CCH	57.6	-51.5	12.2	35	64	
8	YUN0108	CCH	57.2	-59.7	14.2	35	64	O
9	YUN0109	CCH	64.2	-57.7	17.5	40	64	
10	YUN0110	CCH	27.4	-65.0	3.0	35	64	

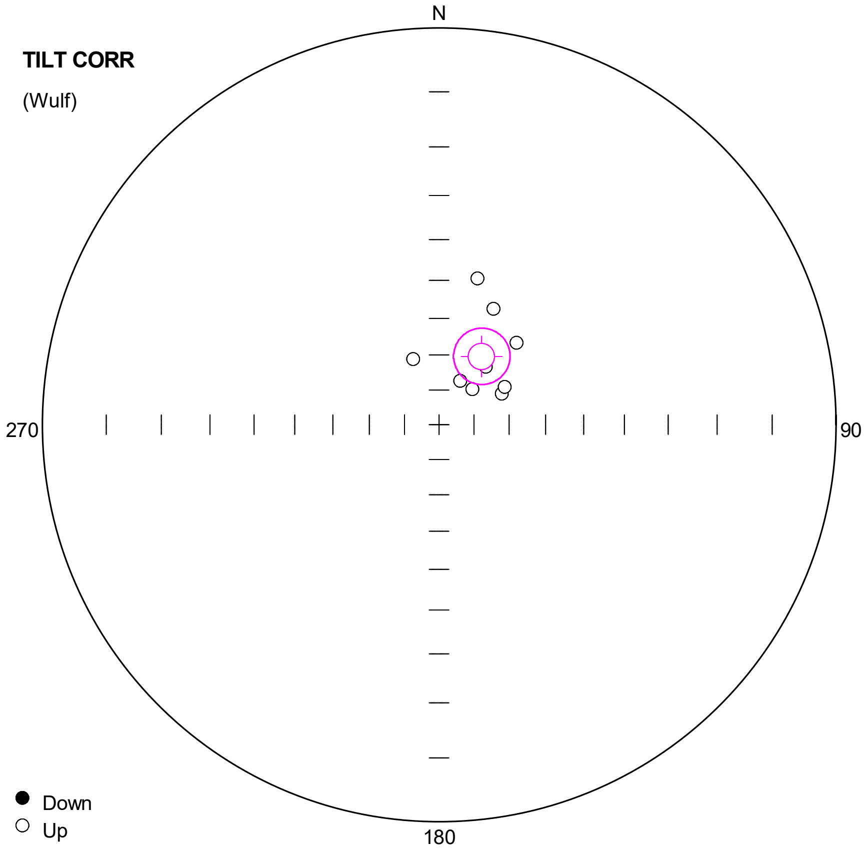

Number of data points: 10

Fisher statistics

Mean vector: 31.81 / -67.12

Resultant vector: 9.77

(X= 3.23, Y= 2, Z= -9)

Estimated precision, k: 39.3

95% Confidence limit: 7.8

95% Confidence limit, approximation: 7.06

Orientation matrix

1st eigenvalue: 0.96

1st eigenvector: 212.14 / 67.19

2nd eigenvalue: 0.03

2nd eigenvector: 1.09 / 19.82

3rd eigenvalue: 0.02

3rd eigenvector: 95.05 / 10.84

VGP

Site latitude: 65

Site longitude: 14.04

Pole latitude: -27.45 (27.45)

Pole longitude: 171.51 (-8.49)

Paleolatitude: -49.84 (49.84)

dp: 10.74

dm: 12.94

#	Name	State	Dec	Inc	MAD	Limit1	Limit2	
1	YUN0101	CCH	25.2	-54.3	12.1	35	64	
2	YUN0102	CCH	14.8	-48.3	12.5	30	64	
3	YUN0103	CCH	63.8	-70.0	9.0	35	64	
4	YUN0104	CCH	60.0	-68.4	7.5	35	64	
5	YUN0105	CCH	43.4	-58.3	10.8	48	64	O
6	YUN0106	CCH	33.1	-65.7	8.6	40	64	
7	YUN0107	CCH	39.0	-68.8	12.2	35	64	
8	YUN0108	CCH	25.9	-76.0	14.2	35	64	O
9	YUN0109	CCH	43.1	-76.0	17.5	40	64	
10	YUN0110	CCH	338.5	-69.9	3.0	35	64	

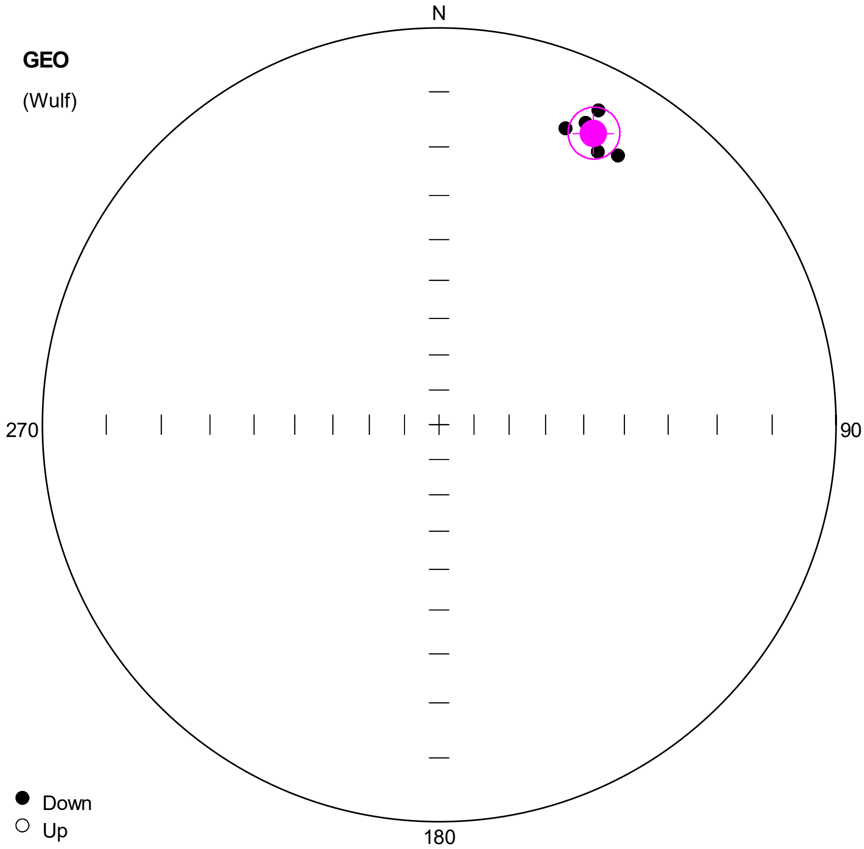

Number of data points: 5

Fisher statistics

Mean vector: 27.93 / 10.62
Resultant vector: 4.99
(X= 4.33, Y= 2.3, Z= 0.92)
Estimated precision, k: 300.49
95% Confidence limit: 4.42
95% Confidence limit, approximation: 3.61

Orientation matrix

1st eigenvalue: 0.99
1st eigenvector: 27.93 / 10.62
2nd eigenvalue: 0
2nd eigenvector: 120.78 / 14.85
3rd eigenvalue: 0
3rd eigenvector: 263.62 / 71.6

VGP

Site latitude: 24.27
Site longitude: 98.39
Pole latitude: 57.17 (-57.17)
Pole longitude: -140.95 (39.05)
Paleolatitude: 5.36 (-5.36)
dp: 2.27
dm: 4.48

#	Name	State	Dec	Inc	MAD	Limit1	Limit2	
1	YUN0201	CCH	26.9	6.8	10.5	40	64	
2	YUN0202	CCH	23.1	11.9	8.4	48	64	
3	YUN0203	CCH	25.9	9.6	4.6	30	64	O
4	YUN0209	CCH	33.6	11.7	7.6	40	64	O
5	YUN0210	CCH	30.2	13.0	8.3	40	64	O

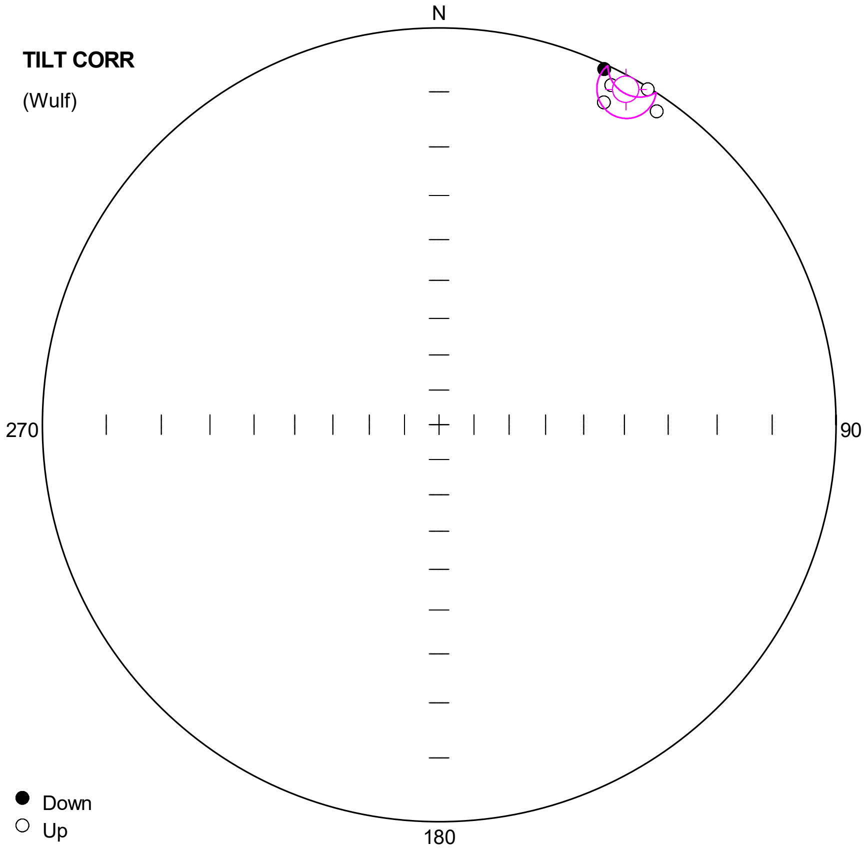

Number of data points: 5

Fisher statistics

Mean vector: 29.12 / -1.92
Resultant vector: 4.99
(X= 4.35, Y= 2.43, Z= -0.17)
Estimated precision, k: 298.55
95% Confidence limit: 4.44
95% Confidence limit, approximation: 3.62

Orientation matrix

1st eigenvalue: 0.99
1st eigenvector: 209.12 / 1.92
2nd eigenvalue: 0
2nd eigenvector: 299.15 / 1.1
3rd eigenvalue: 0
3rd eigenvector: 58.83 / 87.78

VGP

Site latitude: 24.27
Site longitude: 98.39
Pole latitude: 52.13 (-52.13)
Pole longitude: -134.04 (45.96)
Paleolatitude: -0.96 (0.96)
dp: 2.22
dm: 4.44

#	Name	State	Dec	Inc	MAD	Limit1	Limit2	
1	YUN0201	CCH	27.1	-5.3	10.5	40	64	
2	YUN0202	CCH	24.9	0.7	8.4	48	64	
3	YUN0203	CCH	26.9	-2.4	4.6	30	64	O
4	YUN0209	CCH	34.8	-2.3	7.6	40	64	O
5	YUN0210	CCH	31.9	-0.3	8.3	40	64	O

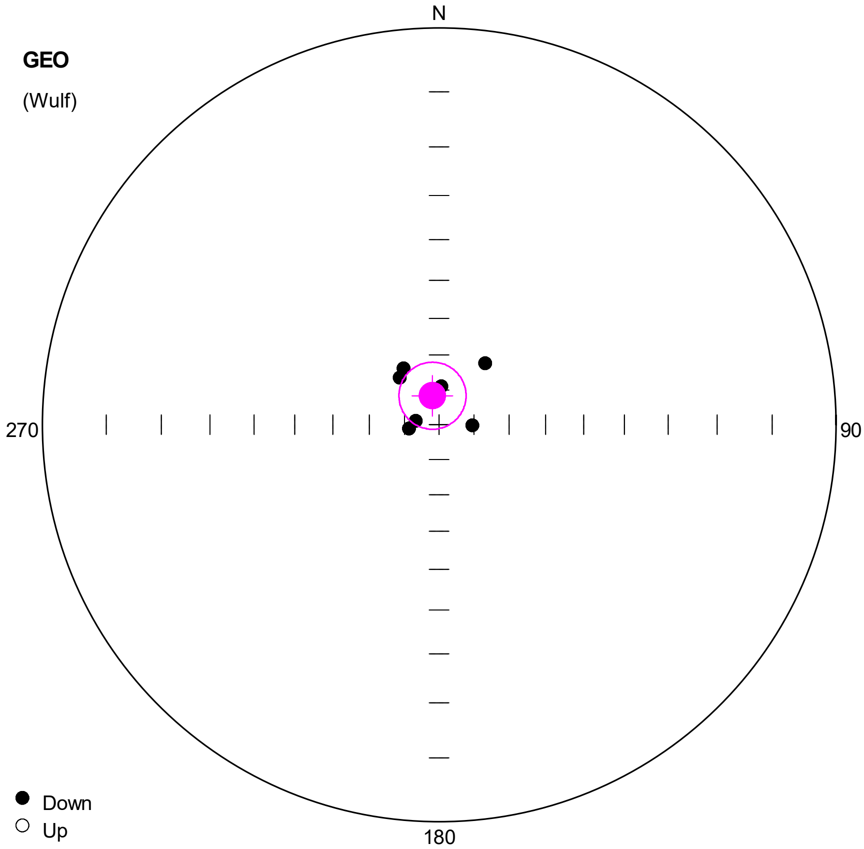

Number of data points: 7

Fisher statistics

Mean vector: 346.89 / 81.44
Resultant vector: 6.85
(X= 0.99, Y= -0.23, Z= 6.78)
Estimated precision, k: 40.43
95% Confidence limit: 9.61
95% Confidence limit, approximation: 8.32

Orientation matrix

1st eigenvalue: 0.96
1st eigenvector: 346.31 / 81.44
2nd eigenvalue: 0.03
2nd eigenvector: 79.88 / 0.54
3rd eigenvalue: 0.02
3rd eigenvector: 169.96 / 8.54

VGP

Site latitude: 24.27
Site longitude: 98.39
Pole latitude: 40.5 (-40.5)
Pole longitude: 93.46 (-86.54)
Paleolatitude: 73.25 (-73.25)
dp: 18.02
dm: 18.61

#	Name	State	Dec	Inc	MAD	Limit1	Limit2
1	YUN0301	CCH	91.0	80.4	12.3	35	64
2	YUN0302	CCH	3.5	78.9	9.1	35	64
3	YUN0303	CCH	37.0	68.1	12.6	35	60
4	YUN0304	CCH	279.1	83.2	7.2	35	64
5	YUN0306	CCH	320.1	72.4	11.6	40	64
6	YUN0307	CCH	262.3	81.3	10.1	35	60
7	YUN0310	CCH	327.8	71.0	3.2	35	64

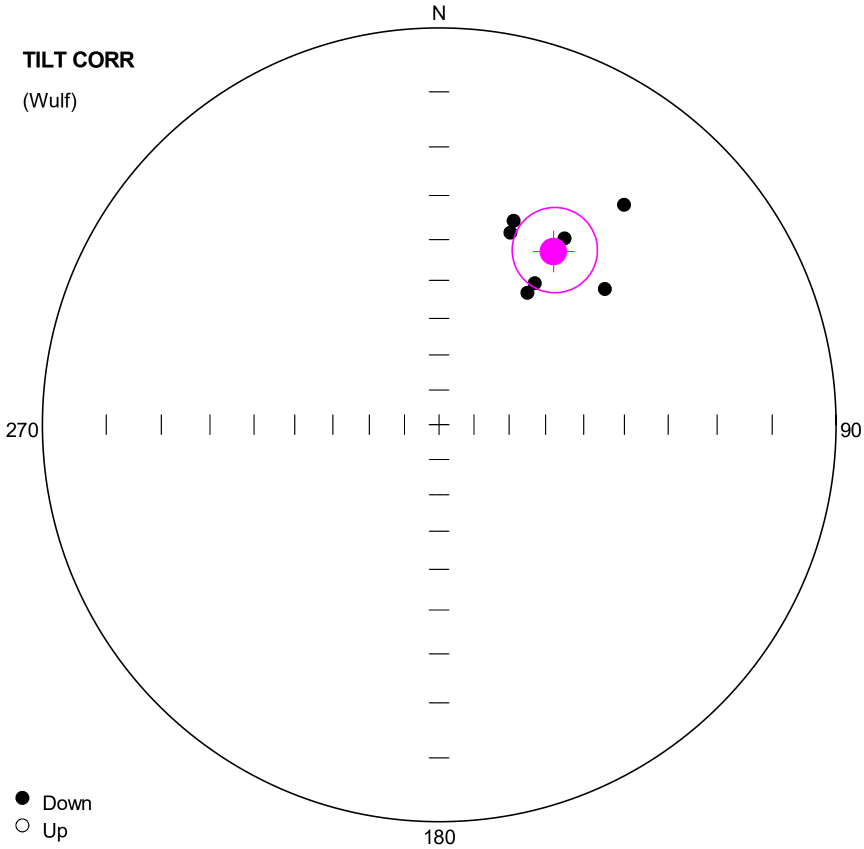

Number of data points: 7

Fisher statistics

Mean vector: 33.45 / 34.77
Resultant vector: 6.85
(X= 4.7, Y= 3.1, Z= 3.91)
Estimated precision, k: 40.33
95% Confidence limit: 9.62
95% Confidence limit, approximation: 8.33

Orientation matrix

1st eigenvalue: 0.96
1st eigenvector: 33.39 / 34.84
2nd eigenvalue: 0.03
2nd eigenvector: 272.64 / 36.3
3rd eigenvalue: 0.02
3rd eigenvector: 152.14 / 34.65

VGP

Site latitude: 24.27
Site longitude: 98.39
Pole latitude: 58.58 (-58.58)
Pole longitude: -168.86 (11.14)
Paleolatitude: 19.14 (-19.14)
dp: 6.36
dm: 11.06

#	Name	State	Dec	Inc	MAD	Limit1	Limit2
1	YUN0301	CCH	50.7	33.3	12.3	35	64
2	YUN0302	CCH	34.0	31.0	9.1	35	64
3	YUN0303	CCH	40.1	18.2	12.6	35	60
4	YUN0304	CCH	34.1	43.4	7.2	35	64
5	YUN0306	CCH	20.4	35.4	11.6	40	64
6	YUN0307	CCH	33.8	46.4	10.1	35	60
7	YUN0310	CCH	20.1	32.7	3.2	35	64

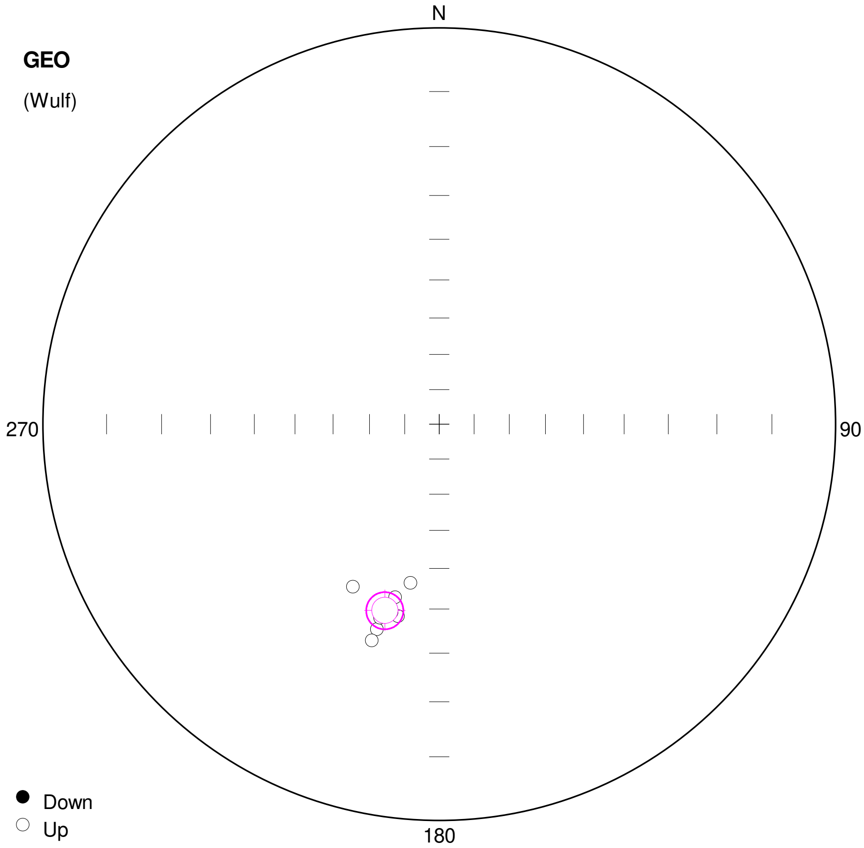

Number of data points: 8

Fisher statistics

Mean vector: 196.3 / -37.86
Resultant vector: 7.96
(X= -6.03, Y= -1.76, Z= -4.88)
Estimated precision, k: 164.83
95% Confidence limit: 4.33
95% Confidence limit, approximation: 3.86

Orientation matrix

1st eigenvalue: 0.99
1st eigenvector: 16.29 / 37.85
2nd eigenvalue: 0.01
2nd eigenvector: 227.28 / 47.8
3rd eigenvalue: 0
3rd eigenvector: 119.03 / 15.85

VGP

Site latitude: 65
Site longitude: 14.04
Pole latitude: -44.95 (44.95)
Pole longitude: -7.65 (172.35)
Paleolatitude: -21.24 (21.24)
dp: 3.02
dm: 5.11

#	Name	State	Dec	Inc	MAD	Limit1	Limit2
1	YUN0401	CPCA	196.9	-33.2	0.4	30	100
2	YUN0402	CPCA	207.9	-40.2	1.5	20	120
3	YUN0403	CPCA	197.0	-35.9	1.3	20	120
4	YUN0404	CPCA	192.1	-37.3	0.9	20	120
5	YUN0405	CPCA	197.3	-30.5	2.2	20	120
6	YUN0406	CPCA	194.2	-37.8	1.5	20	120
7	YUN0407	CPCA	194.3	-41.5	1.6	20	120
8	YUN0408	CPCA	190.2	-45.7	2.0	20	120

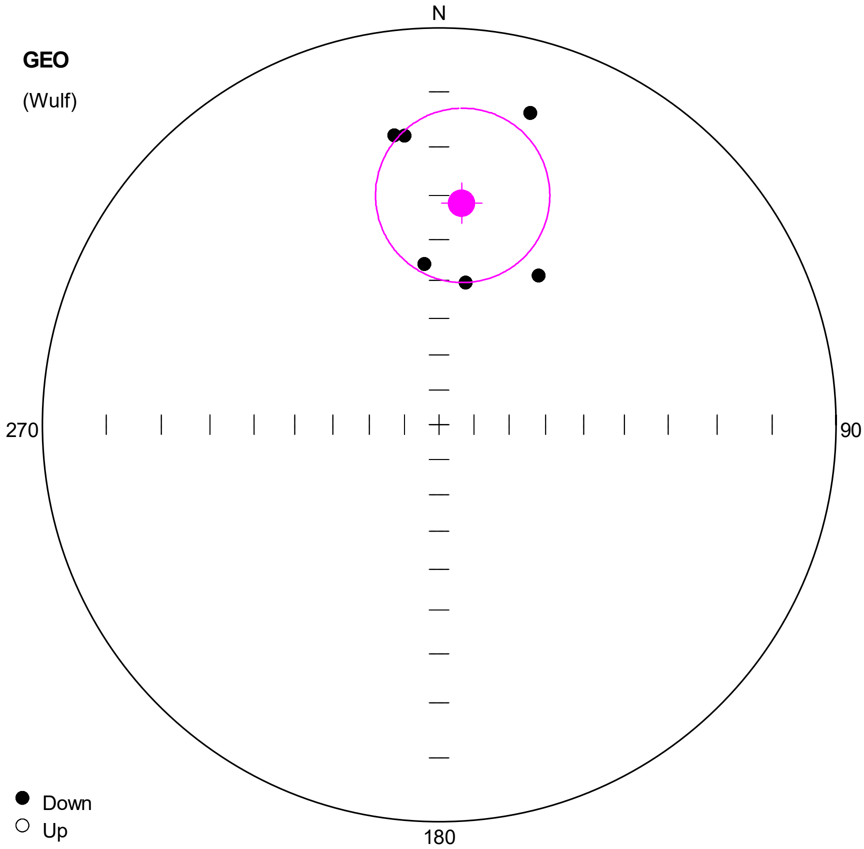

Number of data points: 6

Fisher statistics

Mean vector: 5.82 / 31.44
Resultant vector: 5.63
(X= 4.78, Y= 0.49, Z= 2.94)
Estimated precision, k: 13.65
95% Confidence limit: 18.8
95% Confidence limit, approximation: 15.47

Orientation matrix

1st eigenvalue: 0.88
1st eigenvector: 5.58 / 31.45
2nd eigenvalue: 0.08
2nd eigenvector: 141.91 / 49.78
3rd eigenvalue: 0.04
3rd eigenvector: 261.01 / 22.35

VGP

Site latitude: 24.27
Site longitude: 98.39
Pole latitude: 80.92 (-80.92)
Pole longitude: -119.5 (60.5)
Paleolatitude: 17 (-17)
dp: 11.81
dm: 21.07

#	Name	State	Dec	Inc	MAD	Limit1	Limit2
1	YUN0701	CPCA	33.7	41.4	23.2	25	70
2	YUN0702	CPCA	351.2	17.2	34.3	25	70
3	YUN0703	CPCA	354.8	45.8	19.0	25	70
4	YUN0706	CPCA	10.6	50.0	27.3	25	70
5	YUN0707	CPCA	16.3	11.4	40.9	25	70
6	YUN0708	CPCA	353.2	17.5	30.4	25	70

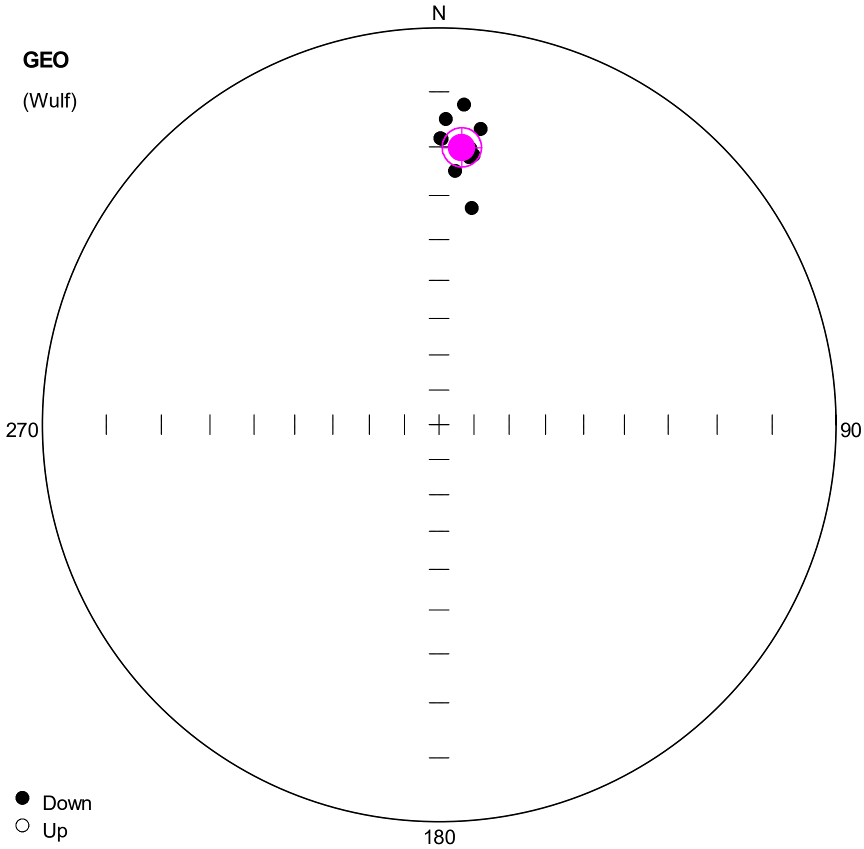

Number of data points: 10

Fisher statistics

Mean vector: 4.65 / 19.99
Resultant vector: 9.94
(X= 9.32, Y= 0.76, Z= 3.4)
Estimated precision, k: 163.34
95% Confidence limit: 3.79
95% Confidence limit, approximation: 3.46

Orientation matrix

1st eigenvalue: 0.99
1st eigenvector: 4.64 / 19.97
2nd eigenvalue: 0.01
2nd eigenvector: 146.43 / 65.18
3rd eigenvalue: 0
3rd eigenvector: 269.4 / 14.12

VGP

Site latitude: 24.27
Site longitude: 98.39
Pole latitude: 75.35 (-75.35)
Pole longitude: -100 (80)
Paleolatitude: 10.31 (-10.31)
dp: 2.08
dm: 3.97

#	Name	State	Dec	Inc	MAD	Limit1	Limit2
1	YUN1001	CPCA	3.6	24.7	0.6	30	120
2	YUN1002	CPCA	8.6	32.2	0.4	30	120
3	YUN1003	CPCA	0.3	18.4	0.5	30	120
4	YUN1004	CPCA	7.3	21.2	0.6	30	120
5	YUN1005	CPCA	6.4	21.7	0.5	30	120
6	YUN1006	CPCA	1.3	14.8	0.9	40	120
7	YUN1007	CPCA	6.5	20.0	1.0	40	120
8	YUN1008	CPCA	8.0	16.1	0.9	30	120
9	YUN1009	CPCA	0.5	18.5	0.5	20	120
10	YUN1010	CPCA	4.5	12.1	0.3	30	120

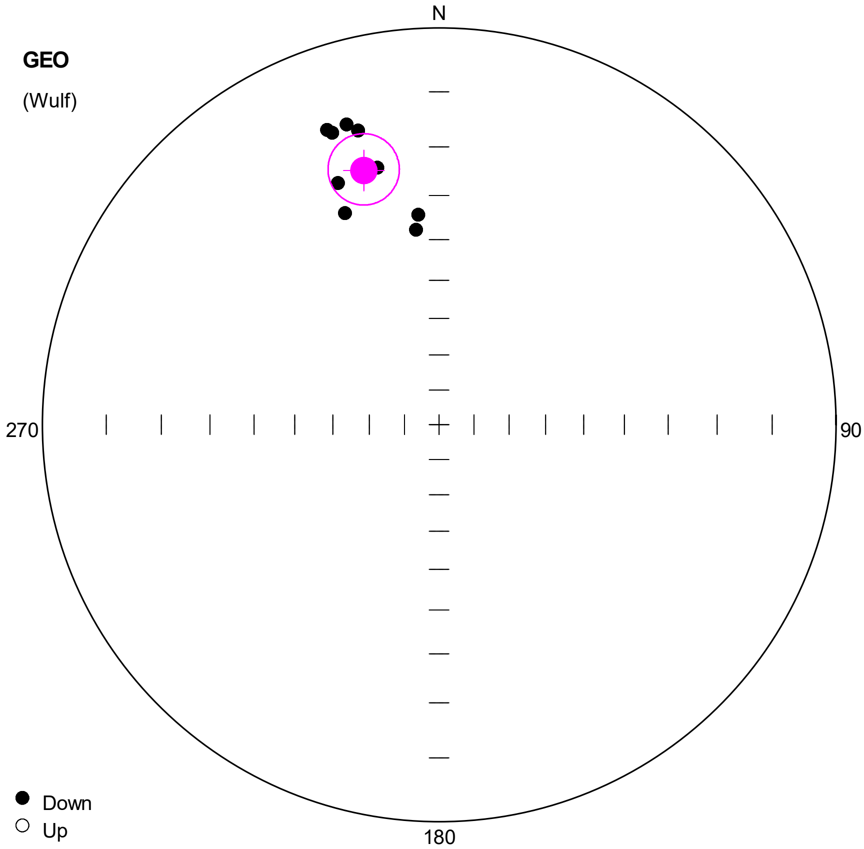

Number of data points: 9

Fisher statistics

Mean vector: 343.51 / 22.54
Resultant vector: 8.85
(X= 7.84, Y= -2.32, Z= 3.39)
Estimated precision, k: 53.47
95% Confidence limit: 7.1
95% Confidence limit, approximation: 6.38

Orientation matrix

1st eigenvalue: 0.97
1st eigenvector: 343.46 / 22.46
2nd eigenvalue: 0.03
2nd eigenvector: 115.58 / 58.36
3rd eigenvalue: 0.01
3rd eigenvector: 244.29 / 21.08

VGP

Site latitude: 24.27
Site longitude: 98.39
Pole latitude: 69.95 (-69.95)
Pole longitude: -27.44 (152.56)
Paleolatitude: 11.72 (-11.72)
dp: 3.99
dm: 7.53

#	Name	State	Dec	Inc	MAD	Limit1	Limit2
1	YUN1101	CPCA	339.9	13.9	3.1	20	120
2	YUN1102	CPCA	339.2	13.1	3.7	30	100
3	YUN1103	CPCA	344.6	14.9	4.3	30	120
4	YUN1104	CPCA	346.5	22.7	3.4	30	120
5	YUN1105	CPCA	342.9	13.3	3.7	30	120
6	YUN1106	CPCA	336.0	29.5	3.3	30	120
7	YUN1107	CPCA	353.3	37.4	2.0	30	120
8	YUN1108	CPCA	337.3	23.2	4.2	30	120
9	YUN1110	CPCA	354.4	34.0	1.7	30	120

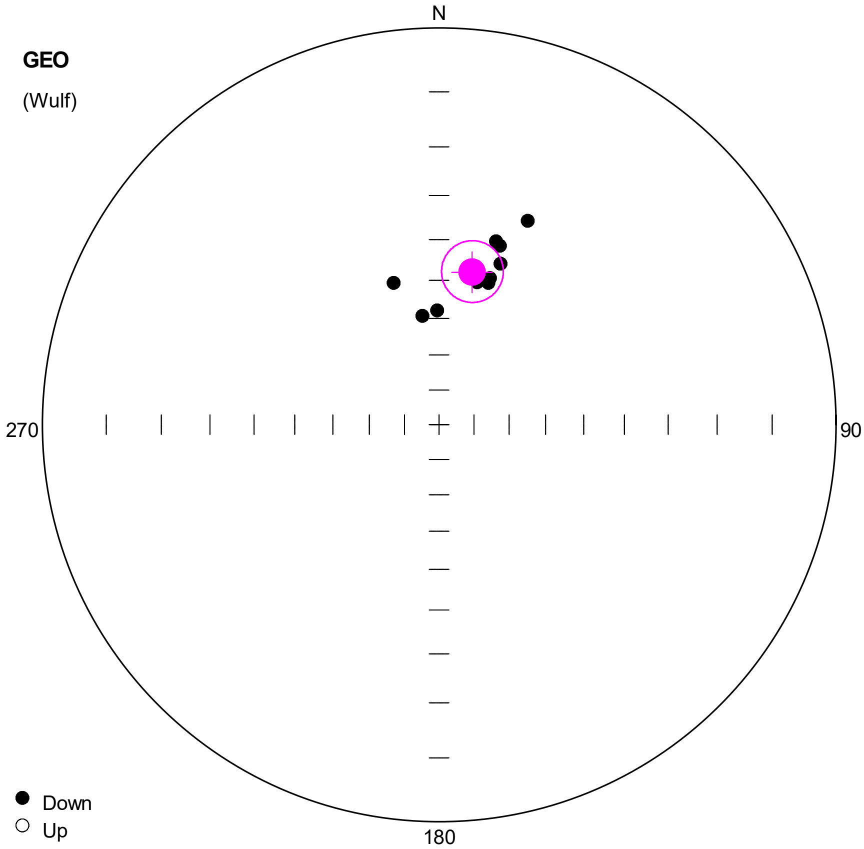

Number of data points: 10

Fisher statistics

Mean vector: 12.19 / 47.07
Resultant vector: 9.78
(X= 6.51, Y= 1.41, Z= 7.16)
Estimated precision, k: 40.26
95% Confidence limit: 7.71
95% Confidence limit, approximation: 6.98

Orientation matrix

1st eigenvalue: 0.96
1st eigenvector: 12.36 / 47.04
2nd eigenvalue: 0.04
2nd eigenvector: 246.78 / 28.45
3rd eigenvalue: 0.01
3rd eigenvector: 139.18 / 29.16

VGP

Site latitude: 24.27
Site longitude: 98.39
Pole latitude: 78.37 (-78.37)
Pole longitude: 165.7 (-14.3)
Paleolatitude: 28.26 (-28.26)
dp: 6.44
dm: 9.97

#	Name	State	Dec	Inc	MAD	Limit1	Limit2
1	YUN1201	CPCA	15.0	49.3	1.4	30	120
2	YUN1202	CPCA	19.2	47.3	1.2	10	120
3	YUN1203	CPCA	18.8	39.1	1.3	20	120
4	YUN1204	CPCA	17.3	38.4	1.1	20	120
5	YUN1205	CPCA	342.2	48.9	0.8	30	120
6	YUN1206	CPCA	20.9	43.1	2.7	30	120
7	YUN1207	CPCA	23.5	31.5	0.6	20	120
8	YUN1208	CPCA	351.4	59.0	1.7	30	120
9	YUN1209	CPCA	359.0	57.9	0.6	30	120
10	YUN1210	CPCA	19.2	48.6	0.7	20	120

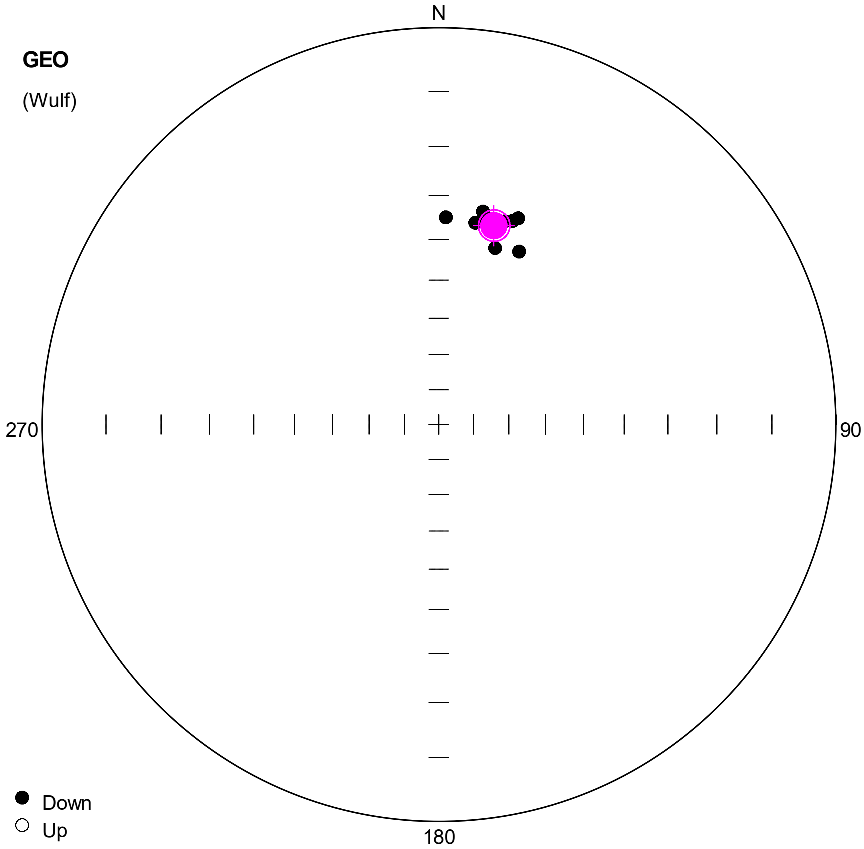

Number of data points: 10

Fisher statistics

Mean vector: 15.48 / 35.08
Resultant vector: 9.95
(X= 7.85, Y= 2.17, Z= 5.72)
Estimated precision, k: 184.35
95% Confidence limit: 3.57
95% Confidence limit, approximation: 3.26

Orientation matrix

1st eigenvalue: 0.99
1st eigenvector: 15.5 / 35.07
2nd eigenvalue: 0.01
2nd eigenvector: 107.65 / 3.06
3rd eigenvalue: 0
3rd eigenvector: 201.98 / 54.75

VGP

Site latitude: 24.27
Site longitude: 98.39
Pole latitude: 74.82 (-74.82)
Pole longitude: -155.71 (24.29)
Paleolatitude: 19.35 (-19.35)
dp: 2.37
dm: 4.11

#	Name	State	Dec	Inc	MAD	Limit1	Limit2
1	YUN1301	CPCA	25.0	38.7	0.7	30	120
2	YUN1302	CPCA	10.3	35.4	1.1	30	120
3	YUN1303	CPCA	20.0	32.8	0.6	30	120
4	YUN1304	CPCA	21.1	31.8	1.4	30	120
5	YUN1305	CPCA	18.0	33.5	1.0	20	120
6	YUN1306	CPCA	16.9	35.1	0.7	20	120
7	YUN1307	CPCA	11.7	32.6	0.7	20	120
8	YUN1308	CPCA	2.0	34.9	0.6	10	120
9	YUN1309	CPCA	12.4	34.4	0.8	10	120
10	YUN1310	CPCA	17.7	40.0	0.5	10	120

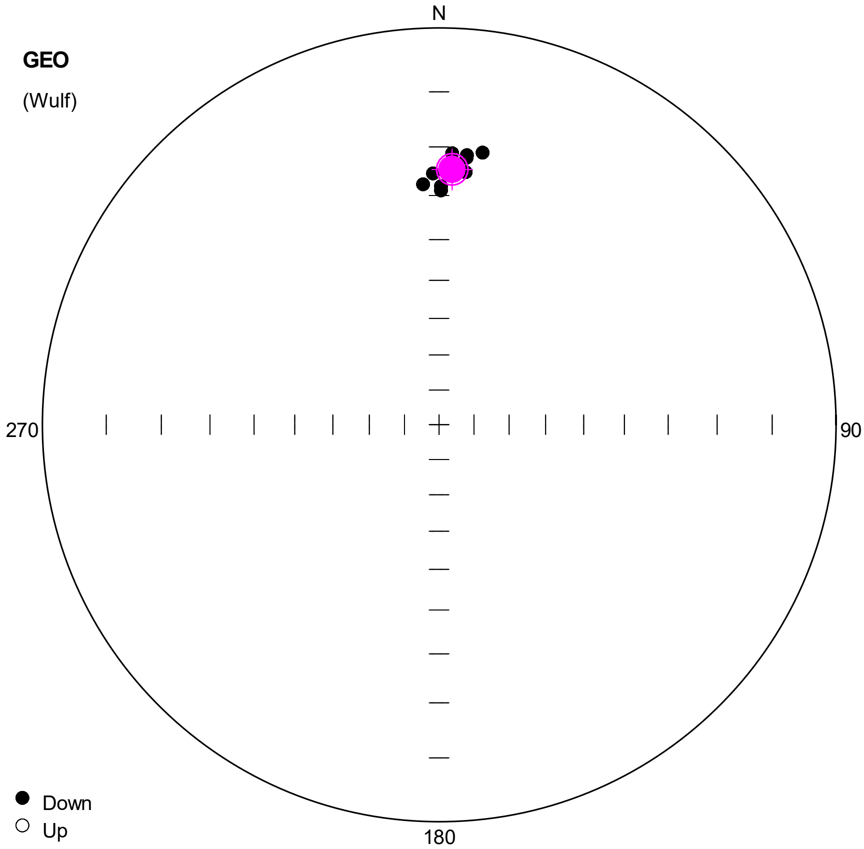

Number of data points: 9

Fisher statistics

Mean vector: 2.91 / 24.44
Resultant vector: 8.97
(X= 8.16, Y= 0.41, Z= 3.71)
Estimated precision, k: 261.25
95% Confidence limit: 3.19
95% Confidence limit, approximation: 2.89

Orientation matrix

1st eigenvalue: 0.99
1st eigenvector: 2.91 / 24.44
2nd eigenvalue: 0.01
2nd eigenvector: 254.35 / 35.01
3rd eigenvalue: 0
3rd eigenvector: 119.92 / 44.98

VGP

Site latitude: 24.27
Site longitude: 98.39
Pole latitude: 78.21 (-78.21)
Pole longitude: -95.61 (84.39)
Paleolatitude: 12.8 (-12.8)
dp: 1.83
dm: 3.42

#	Name	State	Dec	Inc	MAD	Limit1	Limit2
1	YUN1401	CPCA	5.9	21.9	0.6	10	120
2	YUN1402	CPCA	9.1	20.5	0.7	10	120
3	YUN1403	CPCA	6.0	24.8	0.5	10	120
4	YUN1404	CPCA	5.9	21.4	0.4	20	120
5	YUN1405	CPCA	358.6	25.3	0.2	10	120
6	YUN1406	CPCA	2.8	21.2	0.2	30	120
7	YUN1407	CPCA	356.2	27.5	0.5	30	120
8	YUN1409	CPCA	0.5	28.9	0.3	30	120
9	YUN1410	CPCA	0.5	28.0	0.2	30	120

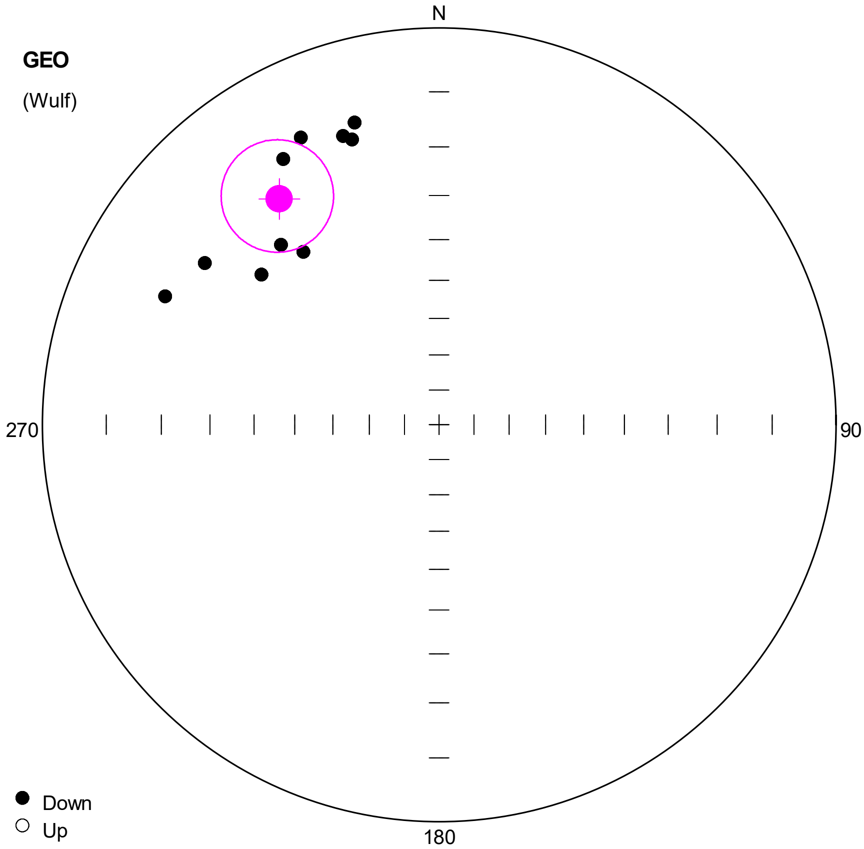

Number of data points: 10

Fisher statistics

Mean vector: 324.71 / 20.24
Resultant vector: 9.57
(X= 7.33, Y= -5.19, Z= 3.31)
Estimated precision, k: 20.82
95% Confidence limit: 10.84
95% Confidence limit, approximation: 9.7

Orientation matrix

1st eigenvalue: 0.92
1st eigenvector: 324.97 / 20.29
2nd eigenvalue: 0.07
2nd eigenvector: 230.45 / 12.04
3rd eigenvalue: 0.01
3rd eigenvector: 111.64 / 66.14

VGP

Site latitude: 24.27
Site longitude: 98.39
Pole latitude: 53.74 (-53.74)
Pole longitude: -7.78 (172.22)
Paleolatitude: 10.44 (-10.44)
dp: 5.96
dm: 11.36

#	Name	State	Dec	Inc	MAD	Limit1	Limit2
1	YUN1501	CPCA	321.9	32.1	5.6	50	120
2	YUN1502	CPCA	318.7	27.8	6.2	40	120
3	YUN1503	CPCA	343.0	16.2	2.5	30	80
4	YUN1504	CPCA	341.6	15.1	4.5	30	80
5	YUN1505	CPCA	344.4	13.4	4.8	40	120
6	YUN1506	CPCA	334.3	12.5	2.6	30	120
7	YUN1507	CPCA	329.6	14.4	2.2	20	50
8	YUN1508	CPCA	310.2	29.3	3.6	30	120
9	YUN1509	CPCA	304.6	18.7	5.9	60	120
10	YUN1510	CPCA	295.1	15.4	11.6	60	120

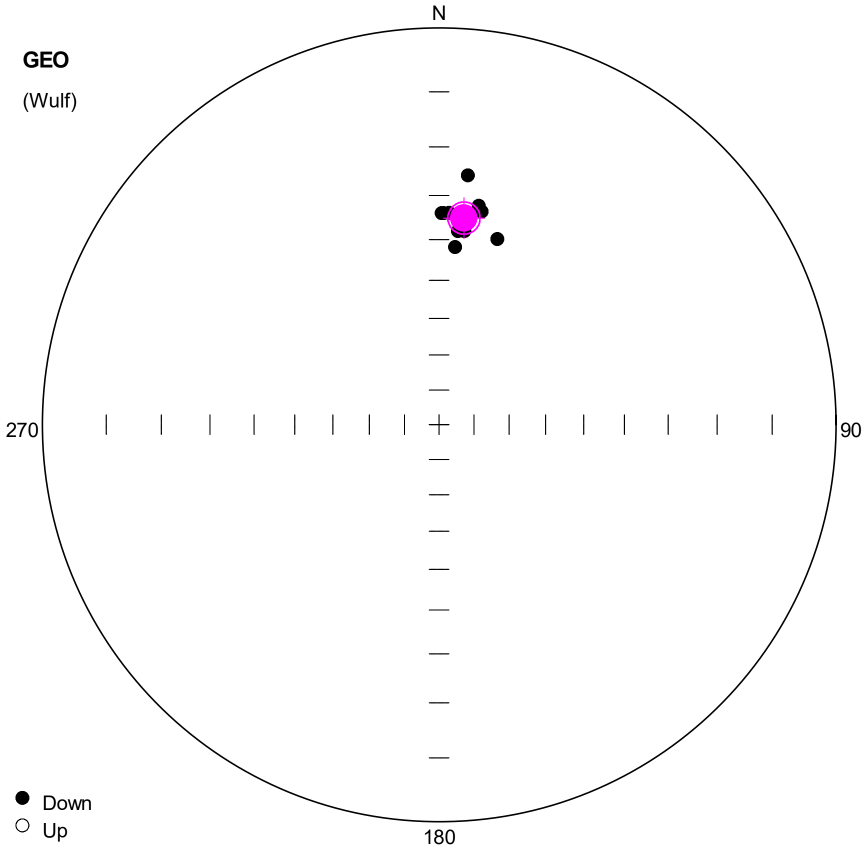

Number of data points: 10

Fisher statistics
Mean vector: 6.83 / 34.69
Resultant vector: 9.95
(X= 8.12, Y= 0.97, Z= 5.66)
Estimated precision, k: 176.56
95% Confidence limit: 3.65
95% Confidence limit, approximation: 3.33

Orientation matrix
1st eigenvalue: 0.99
1st eigenvector: 6.82 / 34.69
2nd eigenvalue: 0.01
2nd eigenvector: 149.24 / 48.87
3rd eigenvalue: 0
3rd eigenvector: 262.82 / 19.26

VGP
Site latitude: 24.27
Site longitude: 98.39
Pole latitude: 81.81 (-81.81)
Pole longitude: -133.68 (46.32)
Paleolatitude: 19.09 (-19.09)
dp: 2.41
dm: 4.19

#	Name	State	Dec	Inc	MAD	Limit1	Limit2
1	YUN1601	CPCA	6.6	25.4	1.0	20	120
2	YUN1602	CPCA	5.6	37.8	1.1	20	120
3	YUN1603	CPCA	0.7	33.9	1.1	20	120
4	YUN1604	CPCA	5.2	41.6	1.0	20	120
5	YUN1605	CPCA	2.7	33.8	0.7	30	120
6	YUN1606	CPCA	1.2	33.9	0.6	30	120
7	YUN1607	CPCA	11.3	32.6	0.5	30	120
8	YUN1608	CPCA	10.3	31.5	0.7	30	120
9	YUN1609	CPCA	7.5	37.6	0.5	30	120
10	YUN1610	CPCA	17.4	37.8	0.4	30	120

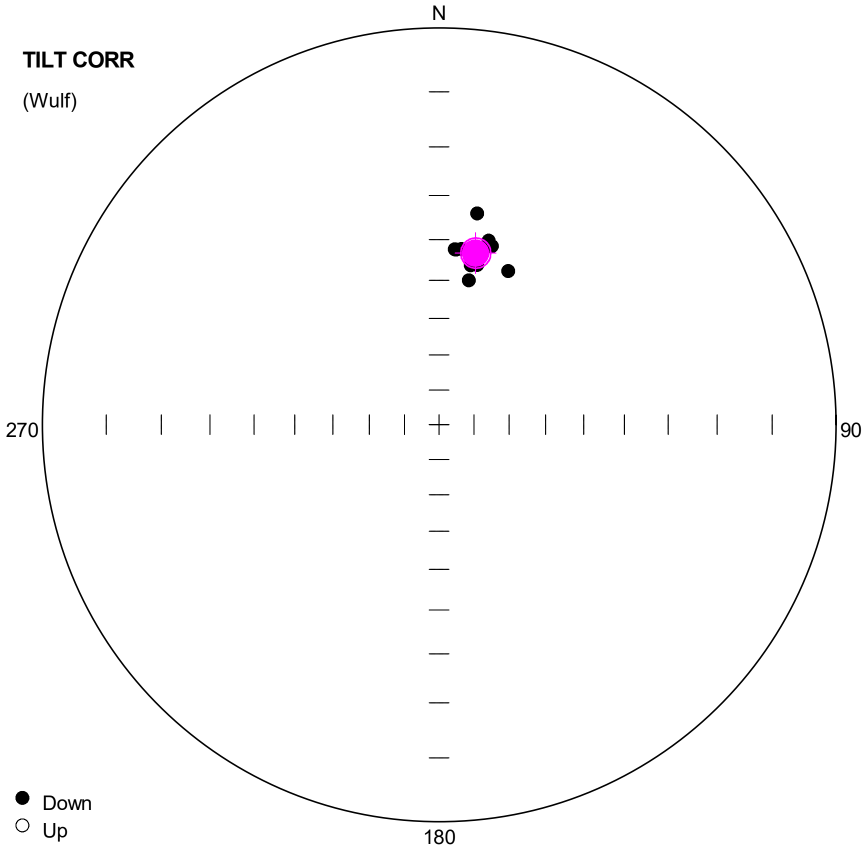

Number of data points: 10

Fisher statistics
Mean vector: 12.02 / 42.31
Resultant vector: 9.95
(X= 7.2, Y= 1.53, Z= 6.7)
Estimated precision, k: 177.11
95% Confidence limit: 3.64
95% Confidence limit, approximation: 3.33

Orientation matrix
1st eigenvalue: 0.99
1st eigenvector: 12.01 / 42.31
2nd eigenvalue: 0.01
2nd eigenvector: 147.38 / 38.02
3rd eigenvalue: 0
3rd eigenvector: 257.91 / 24.16

VGP
Site latitude: 24.27
Site longitude: 98.39
Pole latitude: 79.06 (-79.06)
Pole longitude: -175.15 (4.85)
Paleolatitude: 24.47 (-24.47)
dp: 2.76
dm: 4.48

#	Name	State	Dec	Inc	MAD	Limit1	Limit2
1	YUN1601	CPCA	10.2	33.2	1.0	20	120
2	YUN1602	CPCA	11.3	45.5	1.1	20	120
3	YUN1603	CPCA	5.1	42.2	1.1	20	120
4	YUN1604	CPCA	11.7	49.3	1.0	20	120
5	YUN1605	CPCA	7.3	41.9	0.7	30	120
6	YUN1606	CPCA	5.6	42.2	0.6	30	120
7	YUN1607	CPCA	16.5	39.7	0.5	30	120
8	YUN1608	CPCA	15.1	38.7	0.7	30	120
9	YUN1609	CPCA	13.4	45.1	0.5	30	120
10	YUN1610	CPCA	24.3	44.0	0.4	30	120

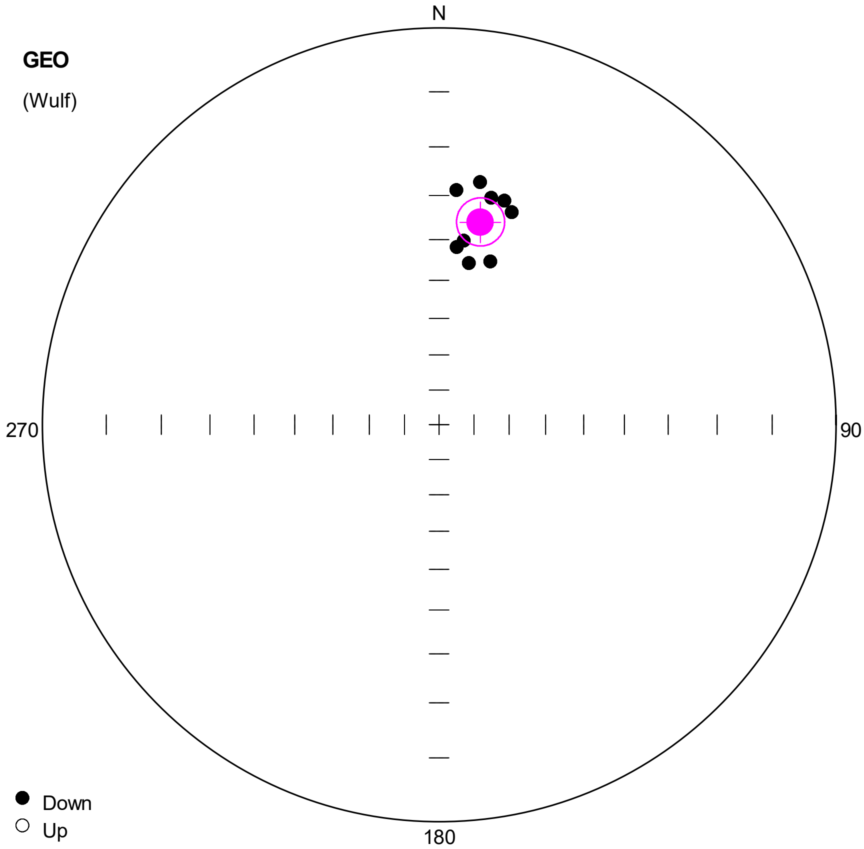

Number of data points: 9

Fisher statistics

Mean vector: 11.5 / 35.02
Resultant vector: 8.91
(X= 7.15, Y= 1.45, Z= 5.11)
Estimated precision, k: 89.94
95% Confidence limit: 5.46
95% Confidence limit, approximation: 4.92

Orientation matrix

1st eigenvalue: 0.98
1st eigenvector: 11.5 / 35.01
2nd eigenvalue: 0.01
2nd eigenvector: 197.56 / 54.84
3rd eigenvalue: 0.01
3rd eigenvector: 103.5 / 2.85

VGP

Site latitude: 24.27
Site longitude: 98.39
Pole latitude: 78.23 (-78.23)
Pole longitude: -148.91 (31.09)
Paleolatitude: 19.31 (-19.31)
dp: 3.62
dm: 6.29

#	Name	State	Dec	Inc	MAD	Limit1	Limit2
1	YUN1701	CPCA	18.9	31.0	0.8	30	120
2	YUN1702	CPCA	17.4	43.4	0.6	20	120
3	YUN1703	CPCA	5.7	41.6	0.3	30	120
4	YUN1704	CPCA	10.4	45.0	0.6	20	120
5	YUN1705	CPCA	4.2	28.7	1.0	20	120
6	YUN1706	CPCA	7.7	39.9	1.0	20	120
7	YUN1708	CPCA	9.6	26.4	0.5	20	120
8	YUN1709	CPCA	13.0	29.2	0.6	20	120
9	YUN1710	CPCA	16.3	29.1	0.4	20	120

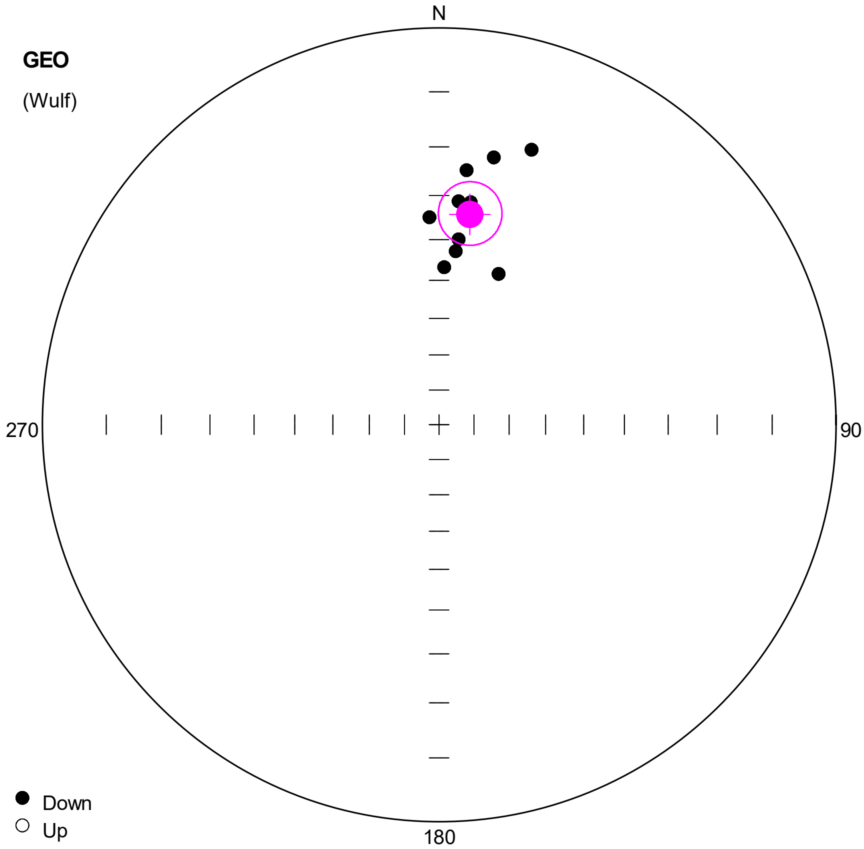

Number of data points: 10

Fisher statistics

Mean vector: 8.31 / 33.66
Resultant vector: 9.81
(X= 8.08, Y= 1.18, Z= 5.44)
Estimated precision, k: 46.92
95% Confidence limit: 7.13
95% Confidence limit, approximation: 6.46

Orientation matrix

1st eigenvalue: 0.96
1st eigenvector: 8.23 / 33.68
2nd eigenvalue: 0.03
2nd eigenvector: 210.38 / 54.26
3rd eigenvalue: 0.01
3rd eigenvector: 105.37 / 10.56

VGP

Site latitude: 24.27
Site longitude: 98.39
Pole latitude: 80.3 (-80.3)
Pole longitude: -136.05 (43.95)
Paleolatitude: 18.41 (-18.41)
dp: 4.63
dm: 8.12

#	Name	State	Dec	Inc	MAD	Limit1	Limit2
1	YUN1801	CPCA	5.0	31.1	0.4	20	120
2	YUN1802	CPCA	8.1	31.0	0.4	30	120
3	YUN1803	CPCA	6.0	39.7	0.3	30	120
4	YUN1804	CPCA	11.6	21.0	2.3	30	120
5	YUN1805	CPCA	18.6	17.7	1.0	20	120
6	YUN1806	CPCA	6.2	24.4	1.4	30	120
7	YUN1807	CPCA	1.9	46.7	1.0	30	120
8	YUN1808	CPCA	357.4	34.8	2.2	40	120
9	YUN1810	CPCA	5.5	42.6	0.2	30	120
10	YUN1811	CPCA	21.6	45.6	0.1	30	120

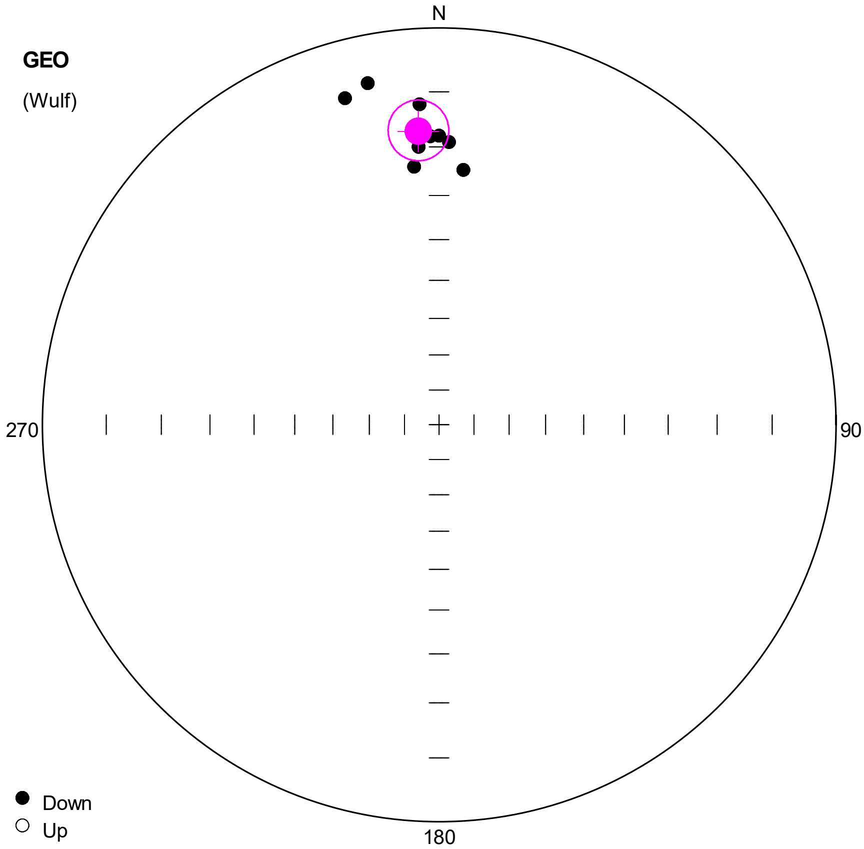

Number of data points: 9

Fisher statistics

Mean vector: 355.95 / 16.92

Resultant vector: 8.91

(X= 8.5, Y= -0.6, Z= 2.59)

Estimated precision, k: 84.25

95% Confidence limit: 5.64

95% Confidence limit, approximation: 5.08

Orientation matrix

1st eigenvalue: 0.98

1st eigenvector: 355.99 / 16.95

2nd eigenvalue: 0.02

2nd eigenvector: 101.03 / 40.4

3rd eigenvalue: 0

3rd eigenvector: 248.43 / 44.71

VGP

Site latitude: 24.27

Site longitude: 98.39

Pole latitude: 73.91 (-73.91)

Pole longitude: -67.03 (112.97)

Paleolatitude: 8.65 (-8.65)

dp: 3.01

dm: 5.83

#	Name	State	Dec	Inc	MAD	Limit1	Limit2
1	YUN1901	CPCA	343.9	8.9	1.0	30	120
2	YUN1902	CPCA	348.2	7.4	1.2	30	120
3	YUN1904	CPCA	358.3	18.0	0.6	30	120
4	YUN1905	CPCA	360.0	17.9	0.4	20	120
5	YUN1906	CPCA	5.5	24.4	0.7	30	120
6	YUN1907	CPCA	2.0	19.1	0.8	30	120
7	YUN1908	CPCA	354.5	23.7	0.4	20	120
8	YUN1909	CPCA	356.5	12.1	0.5	20	120
9	YUN1910	CPCA	355.8	19.9	0.4	20	120

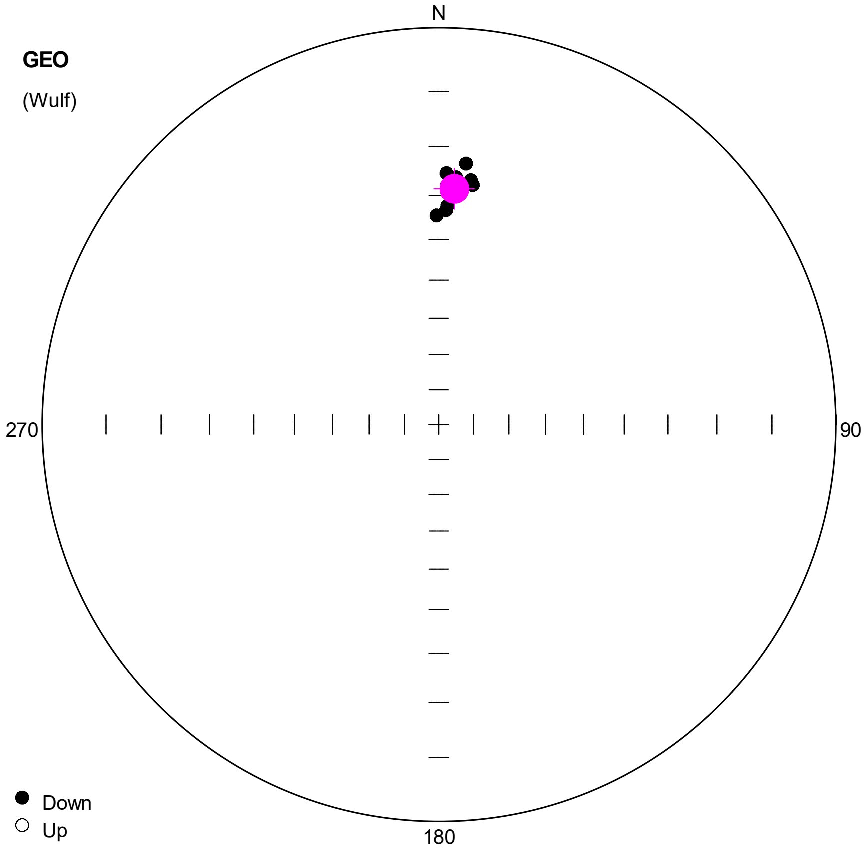

Number of data points: 9

Fisher statistics

Mean vector: 3.73 / 28.49

Resultant vector: 8.97

(X= 7.87, Y= 0.51, Z= 4.28)

Estimated precision, k: 296.96

95% Confidence limit: 2.99

95% Confidence limit, approximation: 2.71

Orientation matrix

1st eigenvalue: 0.99

1st eigenvector: 3.73 / 28.49

2nd eigenvalue: 0.01

2nd eigenvector: 230.93 / 51.39

3rd eigenvalue: 0

3rd eigenvector: 107.53 / 23.73

VGP

Site latitude: 24.27

Site longitude: 98.39

Pole latitude: 80.26 (-80.26)

Pole longitude: -103.4 (76.6)

Paleolatitude: 15.18 (-15.18)

dp: 1.8

dm: 3.29

#	Name	State	Dec	Inc	MAD	Limit1	Limit2
1	YUN2002	CPCA	8.1	27.3	0.2	30	120
2	YUN2003	CPCA	359.4	34.5	0.3	30	120
3	YUN2004	CPCA	6.0	23.1	0.4	30	120
4	YUN2005	CPCA	7.5	26.4	0.3	30	120
5	YUN2006	CPCA	1.9	28.0	0.5	30	120
6	YUN2007	CPCA	2.0	33.2	0.4	30	120
7	YUN2008	CPCA	4.0	26.1	0.6	30	120
8	YUN2009	CPCA	1.8	25.3	0.7	30	120
9	YUN2010	CPCA	2.3	32.3	0.2	30	120

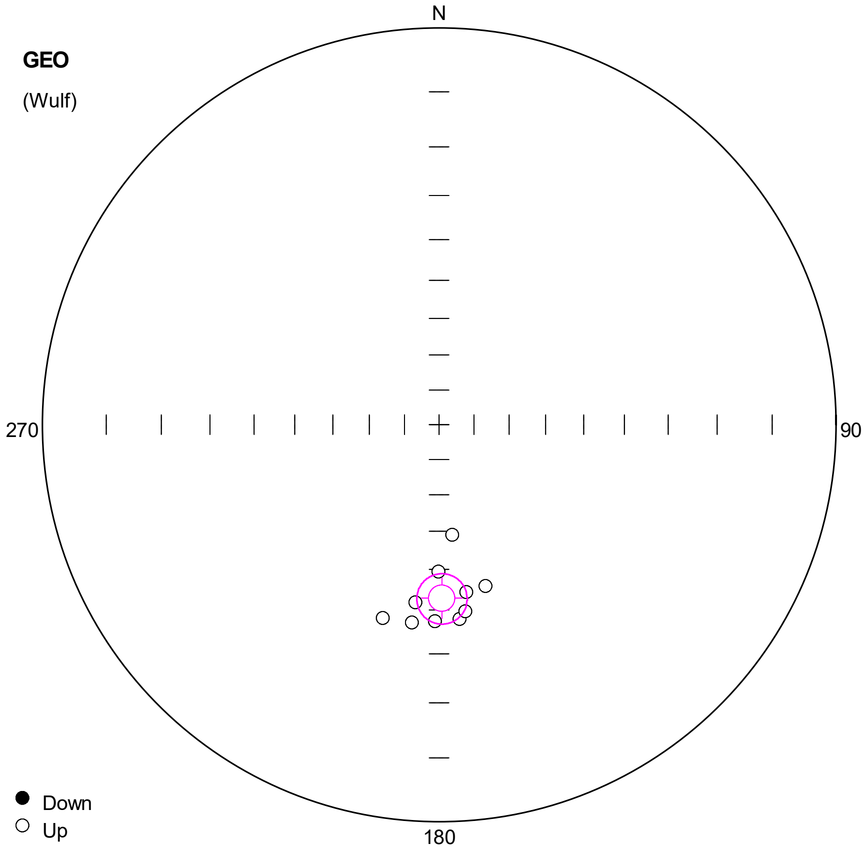

Number of data points: 10

Fisher statistics
Mean vector: 179.09 / -42.79
Resultant vector: 9.86
(X= -7.23, Y= 0.11, Z= -6.7)
Estimated precision, k: 63.67
95% Confidence limit: 6.1
95% Confidence limit, approximation: 5.55

Orientation matrix
1st eigenvalue: 0.97
1st eigenvector: 359.07 / 42.75
2nd eigenvalue: 0.02
2nd eigenvector: 239.05 / 28.42
3rd eigenvalue: 0.01
3rd eigenvector: 127.65 / 34

VGP
Site latitude: 24.27
Site longitude: 98.39
Pole latitude: -89 (89)
Pole longitude: -136.75 (43.25)
Paleolatitude: -24.84 (24.84)
dp: 4.67
dm: 7.54

#	Name	State	Dec	Inc	MAD	Limit1	Limit2
1	YUN2101	CPCA	181.2	-37.3	1.5	30	120
2	YUN2102	CPCA	187.6	-41.4	0.9	30	120
3	YUN2103	CPCA	174.0	-37.6	1.1	40	120
4	YUN2104	CPCA	170.8	-43.7	1.0	30	120
5	YUN2105	CPCA	172.0	-39.2	0.8	30	120
6	YUN2106	CPCA	180.2	-49.4	0.6	30	120
7	YUN2107	CPCA	187.8	-36.6	1.7	30	120
8	YUN2108	CPCA	196.2	-36.2	0.6	30	120
9	YUN2109	CPCA	163.9	-44.1	0.6	30	120
10	YUN2110	CPCA	173.2	-58.8	1.0	30	120

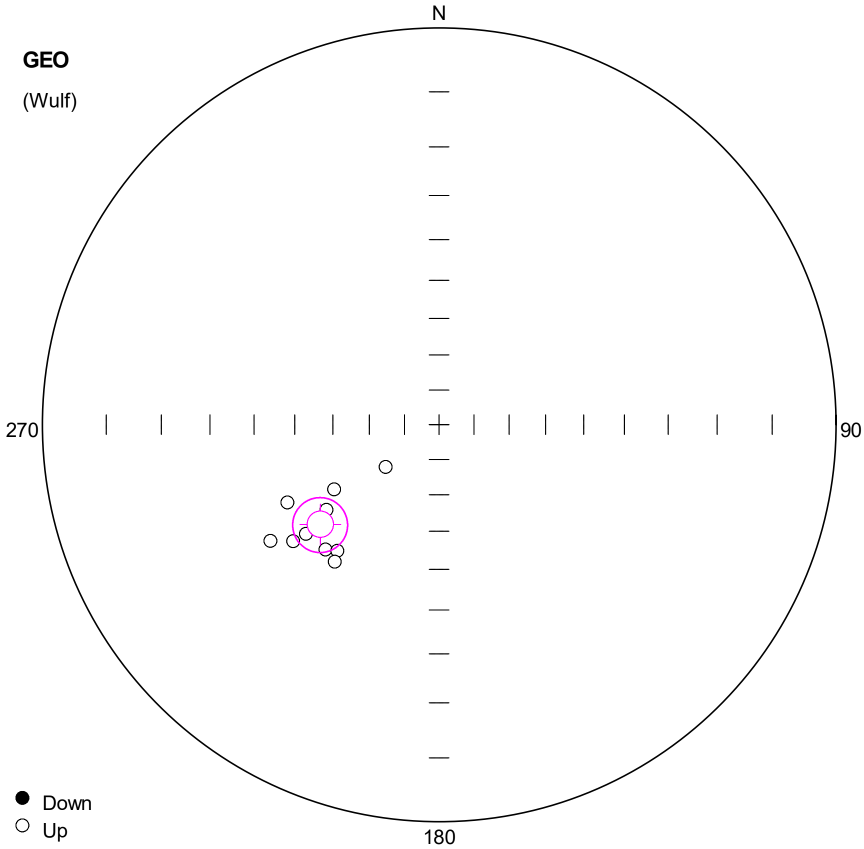

Number of data points: 10

Fisher statistics

Mean vector: 229.96 / -47.33
Resultant vector: 9.82
(X= -4.28, Y= -5.1, Z= -7.22)
Estimated precision, k: 50.5
95% Confidence limit: 6.86
95% Confidence limit, approximation: 6.23

Orientation matrix

1st eigenvalue: 0.97
1st eigenvector: 49.94 / 47.17
2nd eigenvalue: 0.03
2nd eigenvector: 226.17 / 42.77
3rd eigenvalue: 0.01
3rd eigenvector: 317.91 / 1.88

VGP

Site latitude: 24.27
Site longitude: 98.39
Pole latitude: -45.35 (45.35)
Pole longitude: -8.33 (171.67)
Paleolatitude: -28.47 (28.47)
dp: 5.77
dm: 8.9

#	Name	State	Dec	Inc	MAD	Limit1	Limit2
1	YUN2201	CPCA	232.9	-50.8	1.5	30	120
2	YUN2202	CPCA	238.4	-55.5	1.4	30	120
3	YUN2203	CPCA	231.4	-39.6	2.0	30	120
4	YUN2204	CPCA	222.3	-43.9	1.8	30	120
5	YUN2205	CPCA	231.5	-70.5	1.1	30	120
6	YUN2206	CPCA	242.8	-43.5	1.1	30	120
7	YUN2207	CPCA	235.4	-35.4	1.1	30	120
8	YUN2208	CPCA	218.9	-45.6	1.4	30	120
9	YUN2210	CPCA	217.3	-43.1	1.1	30	120
10	YUN2211	CPCA	230.6	-43.1	2.0	30	120

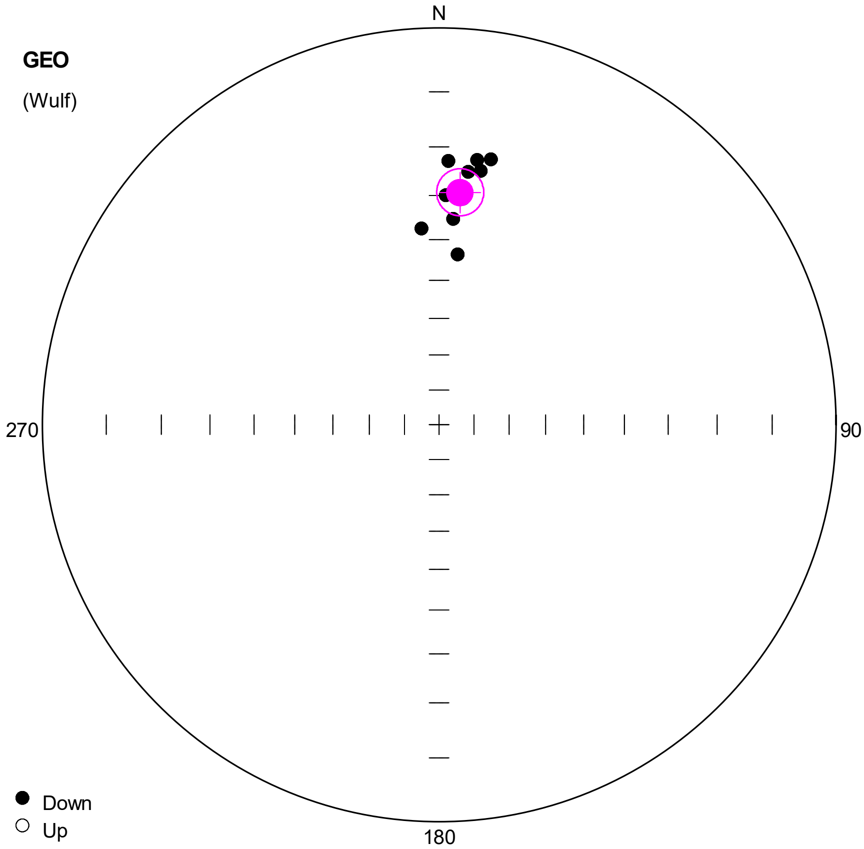

Number of data points: 10

Fisher statistics

Mean vector: 5.15 / 29.17

Resultant vector: 9.9

(X= 8.61, Y= 0.78, Z= 4.83)

Estimated precision, k: 92.46

95% Confidence limit: 5.05

95% Confidence limit, approximation: 4.6

Orientation matrix

1st eigenvalue: 0.98

1st eigenvector: 5.16 / 29.13

2nd eigenvalue: 0.02

2nd eigenvector: 219.54 / 55.97

3rd eigenvalue: 0

3rd eigenvector: 104.37 / 16.03

VGP

Site latitude: 24.27

Site longitude: 98.39

Pole latitude: 80.07 (-80.07)

Pole longitude: -111.69 (68.31)

Paleolatitude: 15.59 (-15.59)

dp: 3.07

dm: 5.57

#	Name	State	Dec	Inc	MAD	Limit1	Limit2
1	YUN2301	CPCA	3.9	35.1	0.2	30	120
2	YUN2302	CPCA	2.0	22.8	0.2	30	120
3	YUN2303	CPCA	1.7	29.9	0.4	30	120
4	YUN2304	CPCA	11.1	21.5	0.2	30	120
5	YUN2305	CPCA	8.2	22.1	0.4	30	120
6	YUN2306	CPCA	6.2	43.3	0.2	30	120
7	YUN2307	CPCA	6.6	24.7	0.1	30	120
8	YUN2308	CPCA	9.3	24.1	0.4	30	120
9	YUN2309	CPCA	354.9	37.2	0.6	30	120
10	YUN2310	CPCA	6.1	30.4	0.2	30	120

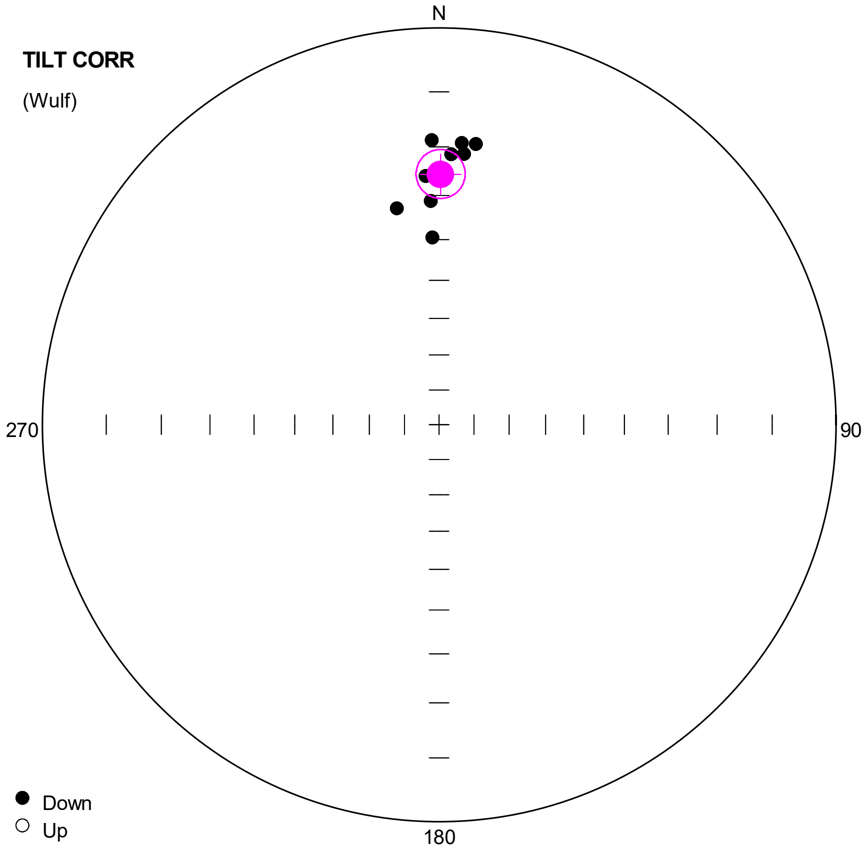

Number of data points: 10

Fisher statistics

Mean vector: 0.32 / 25.53
Resultant vector: 9.9
(X= 8.94, Y= 0.05, Z= 4.27)
Estimated precision, k: 92.56
95% Confidence limit: 5.05
95% Confidence limit, approximation: 4.6

Orientation matrix

1st eigenvalue: 0.98
1st eigenvector: 0.33 / 25.5
2nd eigenvalue: 0.02
2nd eigenvector: 232.47 / 52.15
3rd eigenvalue: 0
3rd eigenvector: 103.74 / 25.93

VGP

Site latitude: 24.27
Site longitude: 98.39
Pole latitude: 79.16 (-79.16)
Pole longitude: -83.25 (96.75)
Paleolatitude: 13.43 (-13.43)
dp: 2.93
dm: 5.44

#	Name	State	Dec	Inc	MAD	Limit1	Limit2
1	YUN2301	CPCA	357.9	31.2	0.2	30	120
2	YUN2302	CPCA	358.5	18.7	0.2	30	120
3	YUN2303	CPCA	356.9	25.8	0.4	30	120
4	YUN2304	CPCA	7.5	19.0	0.2	30	120
5	YUN2305	CPCA	4.6	19.1	0.4	30	120
6	YUN2306	CPCA	358.0	39.5	0.2	30	120
7	YUN2307	CPCA	2.6	21.4	0.1	30	120
8	YUN2308	CPCA	5.3	21.2	0.4	30	120
9	YUN2309	CPCA	349.0	31.9	0.6	30	120
10	YUN2310	CPCA	1.0	26.8	0.2	30	120

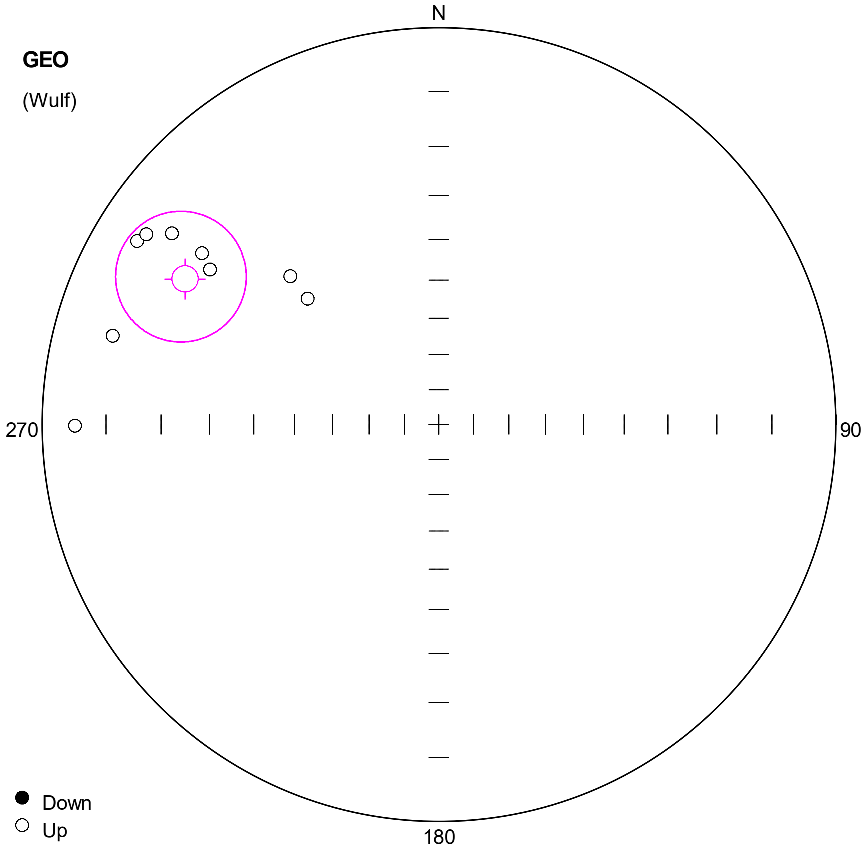

Number of data points: 9

Fisher statistics

Mean vector: 299.83 / -17.23
Resultant vector: 8.58
(X= 4.08, Y= -7.11, Z= -2.54)
Estimated precision, k: 19.04
95% Confidence limit: 12.11
95% Confidence limit, approximation: 10.69

Orientation matrix

1st eigenvalue: 0.91
1st eigenvector: 120.19 / 17.05
2nd eigenvalue: 0.07
2nd eigenvector: 225.27 / 40.33
3rd eigenvalue: 0.02
3rd eigenvector: 12.51 / 44.73

VGP

Site latitude: 24.27
Site longitude: 98.39
Pole latitude: 22.65 (-22.65)
Pole longitude: -13.34 (166.66)
Paleolatitude: -8.81 (8.81)
dp: 6.48
dm: 12.53

#	Name	State	Dec	Inc	MAD	Limit1	Limit2
1	YUN2401	CCH	313.8	-40.8	9.1	44	64
2	YUN2402	CCH	269.8	-5.0	4.7	35	52
3	YUN2403	CCH	304.1	-20.3	7.0	30	52
4	YUN2404	CCH	314.9	-34.3	5.2	44	60
5	YUN2405	CCH	301.3	-6.7	4.8	35	52
6	YUN2408	CCH	305.9	-17.3	16.0	20	48
7	YUN2409	CCH	303.0	-7.4	5.6	20	44
8	YUN2410	CCH	285.2	-9.2	4.0	20	52
9	YUN2412	CCH	305.6	-10.8	14.5	40	56

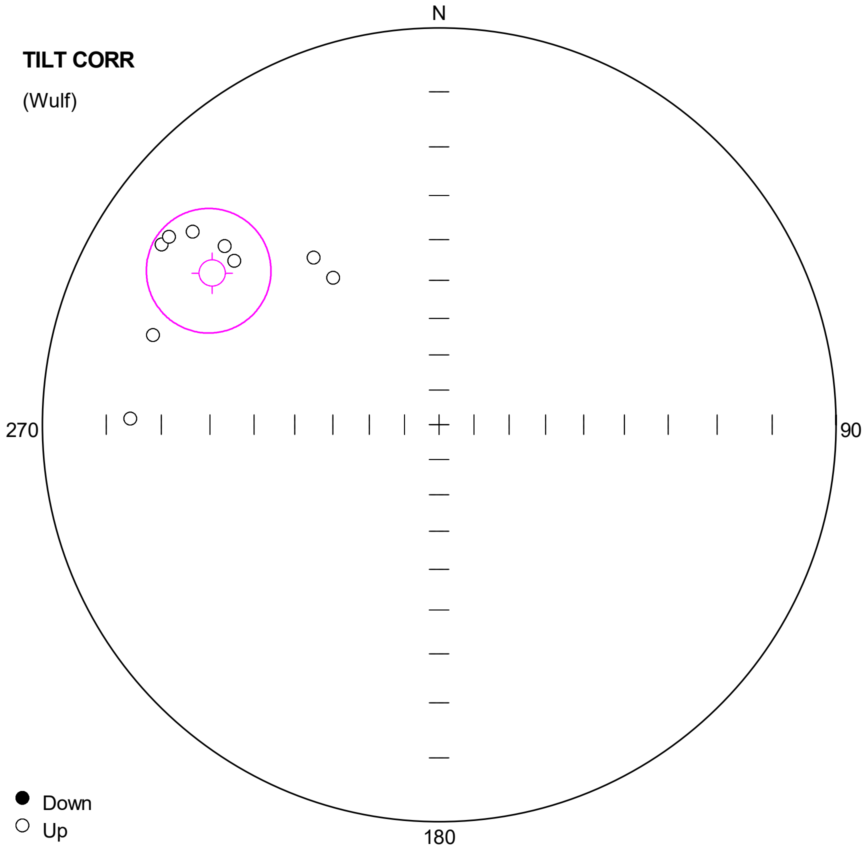

Number of data points: 9

Fisher statistics

Mean vector: 303.75 / -20.98
Resultant vector: 8.58
(X= 4.45, Y= -6.66, Z= -3.07)
Estimated precision, k: 19.06
95% Confidence limit: 12.1
95% Confidence limit, approximation: 10.69

Orientation matrix

1st eigenvalue: 0.91
1st eigenvector: 124.07 / 20.73
2nd eigenvalue: 0.07
2nd eigenvector: 225.86 / 28.35
3rd eigenvalue: 0.02
3rd eigenvector: 3.08 / 53.68

VGP

Site latitude: 24.27
Site longitude: 98.39
Pole latitude: 24.84 (-24.84)
Pole longitude: -17.48 (162.52)
Paleolatitude: -10.85 (10.85)
dp: 6.69
dm: 12.73

#	Name	State	Dec	Inc	MAD	Limit1	Limit2
1	YUN2401	CCH	324.2	-41.0	9.1	44	64
2	YUN2402	CCH	271.1	-14.2	4.7	35	52
3	YUN2403	CCH	308.7	-23.1	7.0	30	52
4	YUN2404	CCH	323.1	-34.5	5.2	44	60
5	YUN2405	CCH	303.0	-10.4	4.8	35	52
6	YUN2408	CCH	309.8	-19.8	16.0	20	48
7	YUN2409	CCH	304.8	-10.7	5.6	20	44
8	YUN2410	CCH	287.4	-15.9	4.0	20	52
9	YUN2412	CCH	308.1	-13.5	14.5	40	56

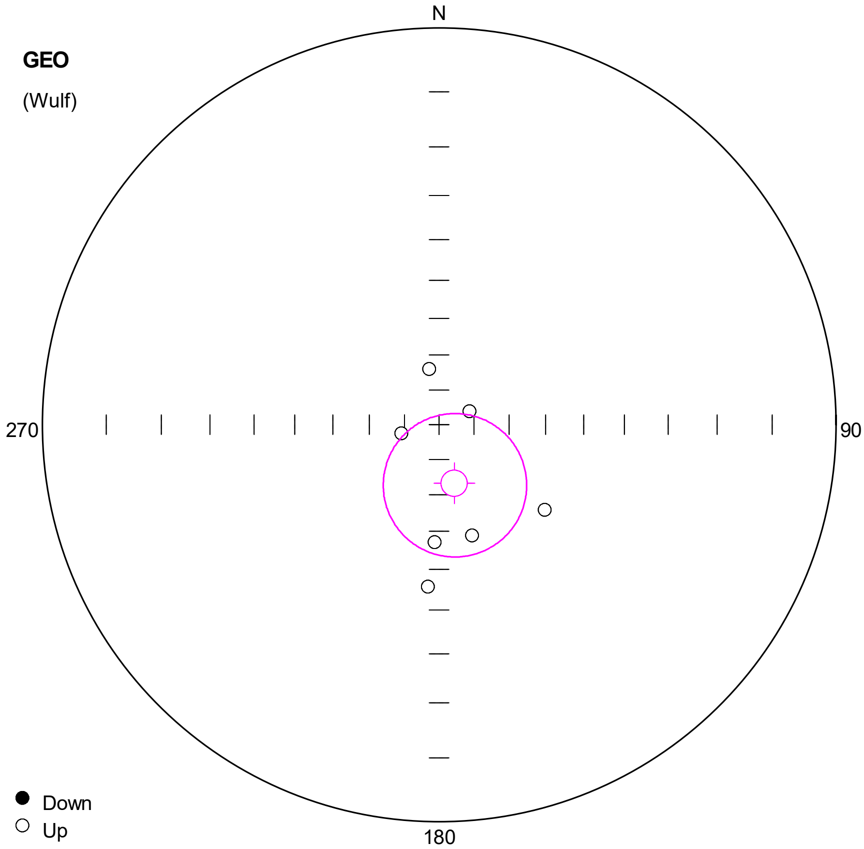

Number of data points: 7

Fisher statistics

Mean vector: 165.46 / -72.68
Resultant vector: 6.4
(X= -1.84, Y= 0.48, Z= -6.11)
Estimated precision, k: 10.06
95% Confidence limit: 20.01
95% Confidence limit, approximation: 16.69

Orientation matrix

1st eigenvalue: 0.84
1st eigenvector: 345.64 / 72.25
2nd eigenvalue: 0.12
2nd eigenvector: 170.4 / 17.69
3rd eigenvalue: 0.04
3rd eigenvector: 79.96 / 1.38

VGP

Site latitude: 24.27
Site longitude: 98.39
Pole latitude: -54.66 (54.66)
Pole longitude: -94.89 (85.11)
Paleolatitude: -58.05 (58.05)
dp: 31.61
dm: 35.56

#	Name	State	Dec	Inc	MAD	Limit1	Limit2	
1	YUN2503	CCH	257.1	-78.9	14.8	35	64	
2	YUN2504	CCH	182.1	-57.0	11.9	30	64	O
3	YUN2505	CCH	66.4	-80.4	6.7	30	64	O
4	YUN2507	CCH	183.9	-45.5	15.3	30	64	O
5	YUN2509	CCH	128.9	-52.2	14.3	30	60	O
6	YUN2510	CCH	163.4	-57.5	15.7	30	60	O
7	YUN2511	CCH	349.8	-73.8	7.2	35	60	O

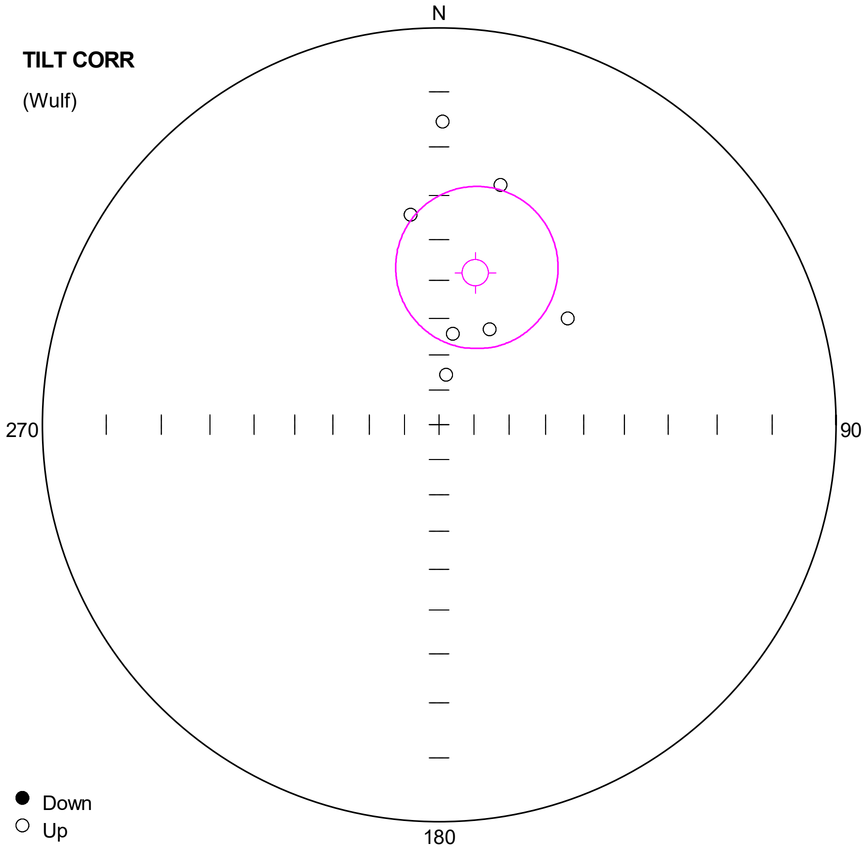

Number of data points: 7

Fisher statistics

Mean vector: 13.43 / -47.06
Resultant vector: 6.4
(X= 4.24, Y= 1.01, Z= -4.69)
Estimated precision, k: 10.07
95% Confidence limit: 19.99
95% Confidence limit, approximation: 16.68

Orientation matrix

1st eigenvalue: 0.84
1st eigenvector: 193.62 / 47.47
2nd eigenvalue: 0.12
2nd eigenvector: 347 / 39.35
3rd eigenvalue: 0.04
3rd eigenvector: 88.39 / 13.55

VGP

Site latitude: 24.27
Site longitude: 98.39
Pole latitude: 35.91 (-35.91)
Pole longitude: -96.24 (83.76)
Paleolatitude: -28.25 (28.25)
dp: 16.72
dm: 25.86

#	Name	State	Dec	Inc	MAD	Limit1	Limit2	
1	YUN2503	CCH	352.3	-33.8	14.8	35	64	
2	YUN2504	CCH	8.7	-63.9	11.9	30	64	O
3	YUN2505	CCH	14.4	-26.1	6.7	30	64	O
4	YUN2507	CCH	8.0	-75.5	15.3	30	64	O
5	YUN2509	CCH	50.4	-44.4	14.3	30	60	O
6	YUN2510	CCH	28.0	-59.6	15.7	30	60	O
7	YUN2511	CCH	0.7	-15.3	7.2	35	60	O

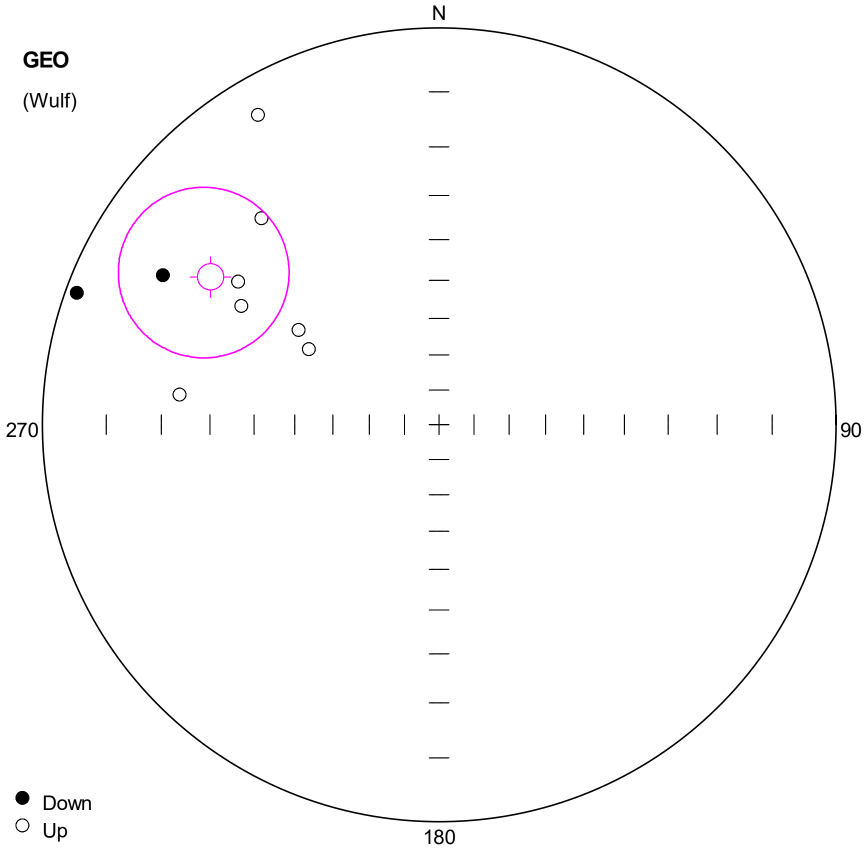

Number of data points: 9

Fisher statistics

Mean vector: 302.88 / -21.14

Resultant vector: 8.25

(X= 4.18, Y= -6.46, Z= -2.98)

Estimated precision, k: 10.72

95% Confidence limit: 16.48

95% Confidence limit, approximation: 14.25

Orientation matrix

1st eigenvalue: 0.84

1st eigenvector: 122.92 / 21.82

2nd eigenvalue: 0.1

2nd eigenvector: 306.59 / 68.14

3rd eigenvalue: 0.06

3rd eigenvector: 213.43 / 1.27

VGP

Site latitude: 65

Site longitude: 14.04

Pole latitude: 3.05 (-3.05)

Pole longitude: -110.3 (69.7)

Paleolatitude: -10.94 (10.94)

dp: 9.13

dm: 17.35

#	Name	State	Dec	Inc	MAD	Limit1	Limit2
1	YUN2901	CCH	298.4	13.3	14.2	30	56
2	YUN2902	CCH	301.0	-29.7	12.0	30	60
3	YUN2903	CCH	319.3	-21.1	20.2	35	60
4	YUN2904	CCH	304.0	-43.8	8.4	35	60
5	YUN2905	CCH	329.7	-5.8	9.5	44	64
6	YUN2906	CCH	290.0	1.7	12.8	30	56
7	YUN2908	CCH	300.1	-48.5	18.7	30	64
8	YUN2909	CCH	276.6	-23.3	18.1	30	52
9	YUN2911	CCH	305.4	-26.3	8.1	40	52

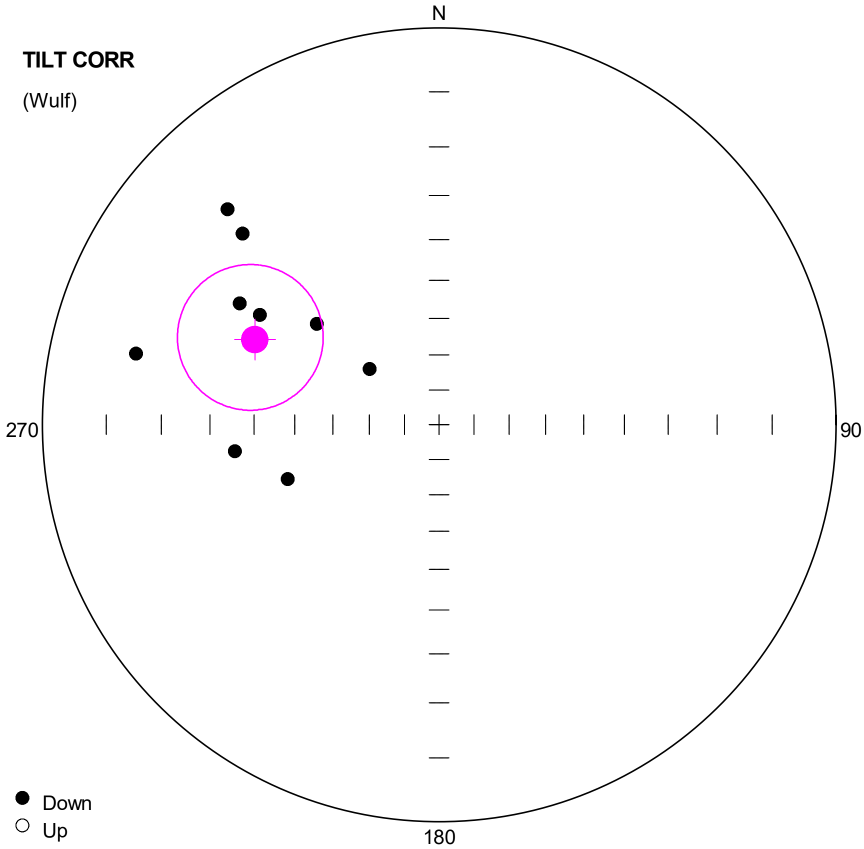

Number of data points: 9

Fisher statistics

Mean vector: 294.84 / 35.85
Resultant vector: 8.25
(X= 2.81, Y= -6.07, Z= 4.83)
Estimated precision, k: 10.72
95% Confidence limit: 16.48
95% Confidence limit, approximation: 14.25

Orientation matrix

1st eigenvalue: 0.84
1st eigenvector: 295.52 / 35.46
2nd eigenvalue: 0.1
2nd eigenvector: 179.32 / 31.79
3rd eigenvalue: 0.05
3rd eigenvector: 59.89 / 38.4

VGP

Site latitude: 65
Site longitude: 14.04
Pole latitude: 28.35 (-28.35)
Pole longitude: -90.06 (89.94)
Paleolatitude: 19.86 (-19.86)
dp: 11.09
dm: 19.12

#	Name	State	Dec	Inc	MAD	Limit1	Limit2
1	YUN2901	CCH	250.2	45.9	14.2	30	56
2	YUN2902	CCH	301.3	29.1	12.0	30	60
3	YUN2903	CCH	309.5	46.5	20.2	35	60
4	YUN2904	CCH	314.2	20.8	8.4	35	60
5	YUN2905	CCH	308.7	64.8	9.5	44	64
6	YUN2906	CCH	262.6	35.2	12.8	30	56
7	YUN2908	CCH	315.5	15.5	18.7	30	64
8	YUN2909	CCH	283.2	13.8	18.1	30	52
9	YUN2911	CCH	301.5	34.2	8.1	40	52

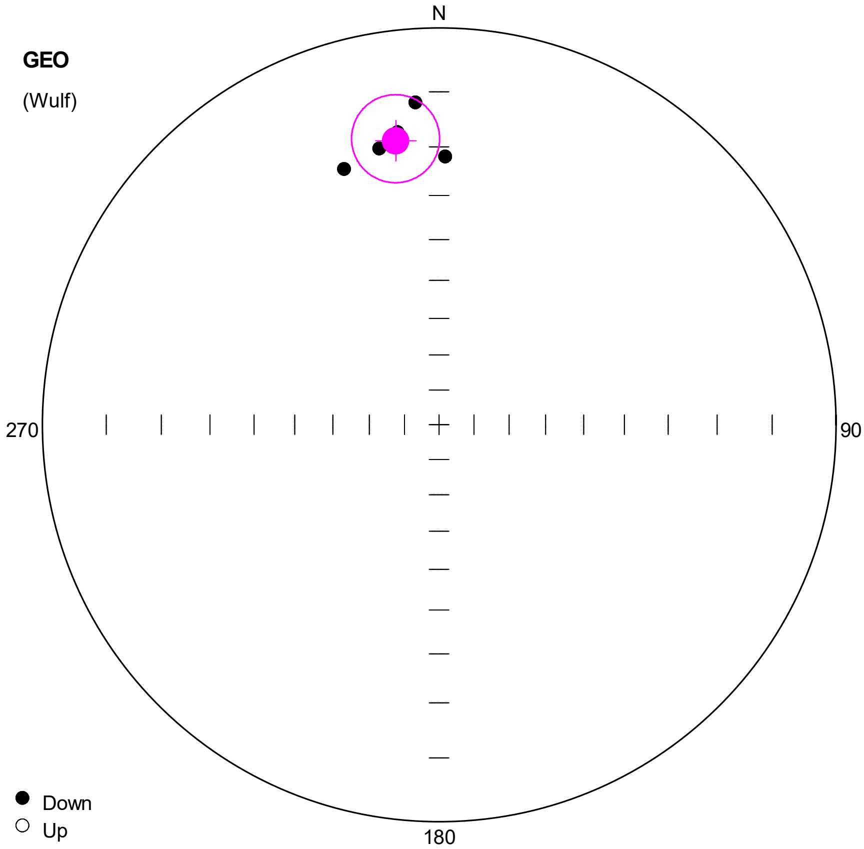

Number of data points: 5

Fisher statistics

Mean vector: 351.31 / 18.22
Resultant vector: 4.95
(X= 4.65, Y= -0.71, Z= 1.55)
Estimated precision, k: 85.87
95% Confidence limit: 8.3
95% Confidence limit, approximation: 6.76

Orientation matrix

1st eigenvalue: 0.98
1st eigenvector: 351.32 / 18.21
2nd eigenvalue: 0.01
2nd eigenvector: 258.15 / 9.55
3rd eigenvalue: 0
3rd eigenvector: 141.74 / 69.28

VGP

Site latitude: 24.27
Site longitude: 98.39
Pole latitude: 72.93 (-72.93)
Pole longitude: -51.09 (128.91)
Paleolatitude: 9.35 (-9.35)
dp: 4.48
dm: 8.63

#	Name	State	Dec	Inc	MAD	Limit1	Limit2
1	YUN3501	CCH	351.9	16.7	4.8	30	68
2	YUN3502	CCH	355.8	11.7	4.4	30	68
3	YUN3503	CCH	1.3	21.9	4.7	30	68
4	YUN3504	CCH	339.6	21.0	5.6	40	68
5	YUN3505	CCH	347.8	19.1	5.7	30	68

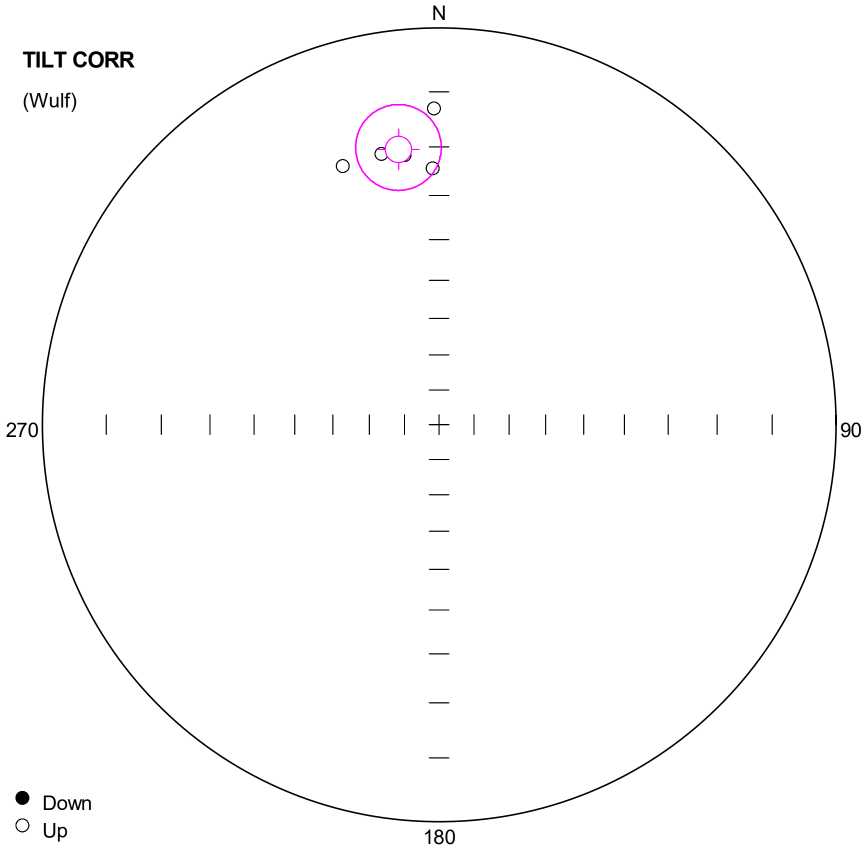

Number of data points: 5

Fisher statistics

Mean vector: 351.63 / -19.95
Resultant vector: 4.95
(X= 4.61, Y= -0.68, Z= -1.69)
Estimated precision, k: 86.77
95% Confidence limit: 8.26
95% Confidence limit, approximation: 6.72

Orientation matrix

1st eigenvalue: 0.98
1st eigenvector: 171.64 / 19.96
2nd eigenvalue: 0.01
2nd eigenvector: 78.04 / 9.83
3rd eigenvalue: 0
3rd eigenvector: 323.24 / 67.57

VGP

Site latitude: 24.27
Site longitude: 98.39
Pole latitude: 54.49 (-54.49)
Pole longitude: -67.33 (112.67)
Paleolatitude: -10.29 (10.29)
dp: 4.53
dm: 8.65

#	Name	State	Dec	Inc	MAD	Limit1	Limit2
1	YUN3501	CCH	352.7	-21.2	4.8	30	68
2	YUN3502	CCH	358.6	-24.3	4.4	30	68
3	YUN3503	CCH	359.1	-12.9	4.7	30	68
4	YUN3504	CCH	339.6	-20.4	5.6	40	68
5	YUN3505	CCH	348.0	-20.2	5.7	30	68

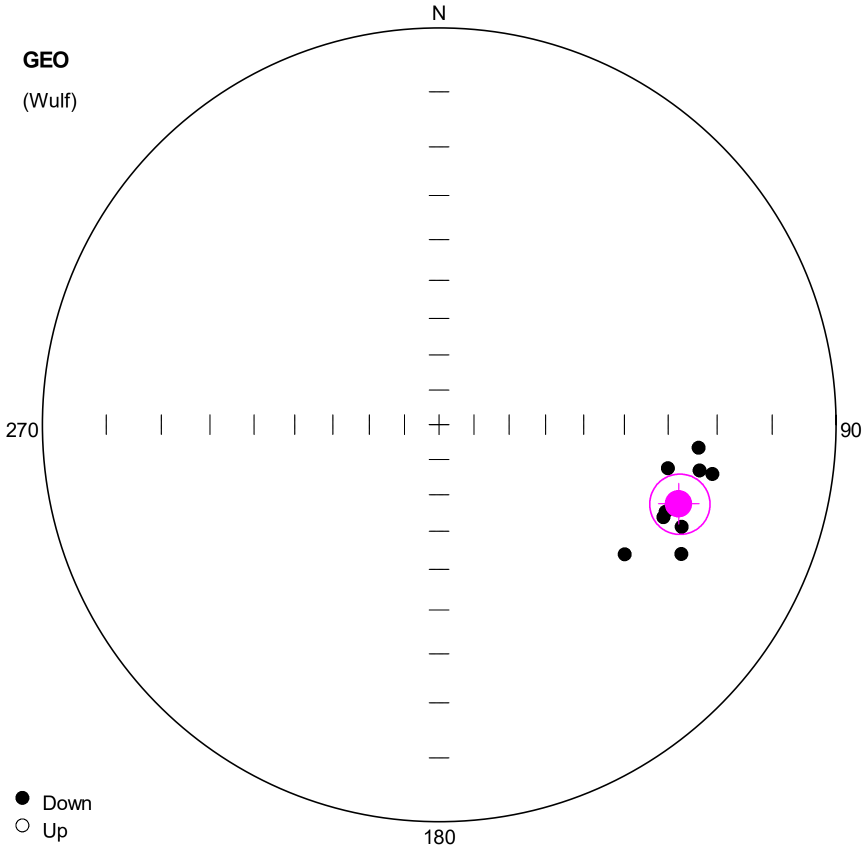

Number of data points: 9

Fisher statistics

Mean vector: 108.26 / 25.12
Resultant vector: 8.89
(X= -2.52, Y= 7.64, Z= 3.77)
Estimated precision, k: 70.24
95% Confidence limit: 6.19
95% Confidence limit, approximation: 5.57

Orientation matrix

1st eigenvalue: 0.97
1st eigenvector: 108.23 / 25.11
2nd eigenvalue: 0.02
2nd eigenvector: 202.68 / 9.39
3rd eigenvalue: 0
3rd eigenvector: 311.58 / 62.96

VGP

Site latitude: 24.27
Site longitude: 98.39
Pole latitude: -10.62 (10.62)
Pole longitude: 168.56 (-11.44)
Paleolatitude: 13.19 (-13.19)
dp: 3.58
dm: 6.65

#	Name	State	Dec	Inc	MAD	Limit1	Limit2	
1	YUN3601	CCH	112.4	27.1	6.4	35	64	
2	YUN3602	CCH	100.8	29.2	4.5	44	64	
3	YUN3603	CCH	112.8	22.9	7.4	35	64	
4	YUN3604	CCH	111.0	27.1	8.2	40	64	
5	YUN3605	CCH	118.1	20.6	5.3	30	64	
6	YUN3606	CCH	95.1	23.4	5.3	35	64	
7	YUN3608	CHT	124.9	30.6	6.8	60	68	OA
8	YUN3609	CCH	100.0	22.6	5.0	40	64	
9	YUN3610	CCH	100.2	20.0	8.2	35	64	

TILT CORR

(Wulf)

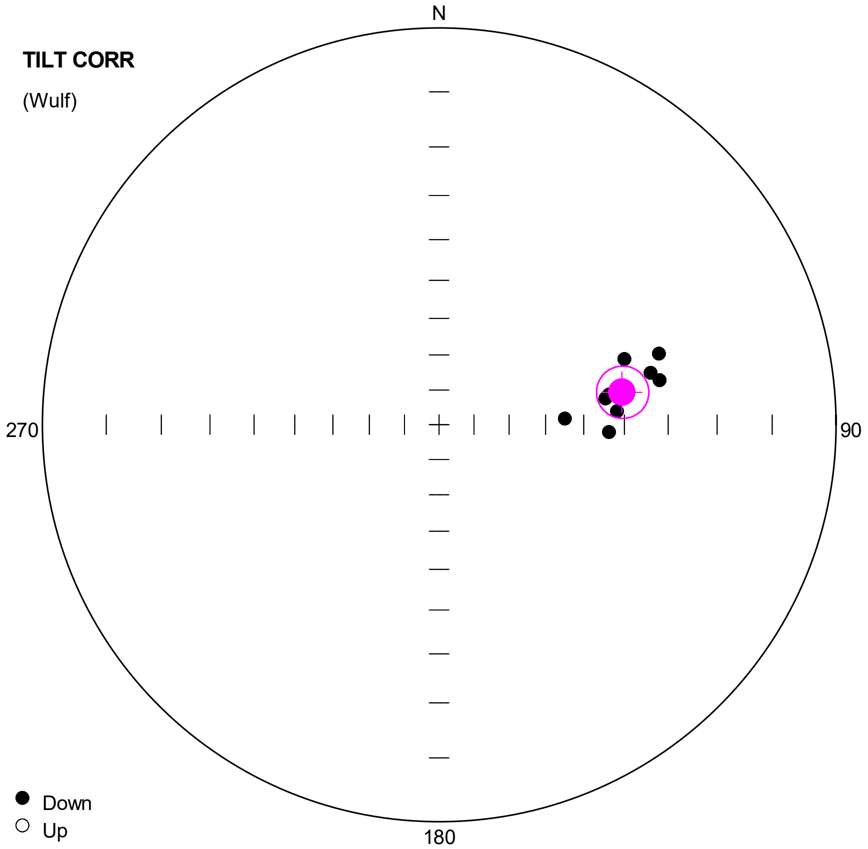

Number of data points: 9

Fisher statistics

Mean vector: 79.92 / 39.88

Resultant vector: 8.89

(X= 1.19, Y= 6.71, Z= 5.7)

Estimated precision, k: 70.2

95% Confidence limit: 6.19

95% Confidence limit, approximation: 5.57

Orientation matrix

1st eigenvalue: 0.97

1st eigenvector: 79.91 / 39.86

2nd eigenvalue: 0.02

2nd eigenvector: 218.43 / 41.9

3rd eigenvalue: 0

3rd eigenvector: 329.95 / 22.24

VGP

Site latitude: 24.27

Site longitude: 98.39

Pole latitude: 17.8 (-17.8)

Pole longitude: 170.97 (-9.03)

Paleolatitude: 22.68 (-22.68)

dp: 4.47

dm: 7.44

#	Name	State	Dec	Inc	MAD	Limit1	Limit2	
1	YUN3601	CCH	81.1	44.0	6.4	35	64	
2	YUN3602	CCH	70.5	37.3	4.5	44	64	
3	YUN3603	CCH	85.7	41.6	7.4	35	64	
4	YUN3604	CCH	80.0	43.0	8.2	40	64	
5	YUN3605	CCH	92.5	43.6	5.3	30	64	
6	YUN3606	CCH	72.1	29.6	5.3	35	64	
7	YUN3608	CHT	87.3	54.8	6.8	60	68	OA
8	YUN3609	CCH	76.2	32.5	5.0	40	64	
9	YUN3610	CCH	78.6	30.9	8.2	35	64	

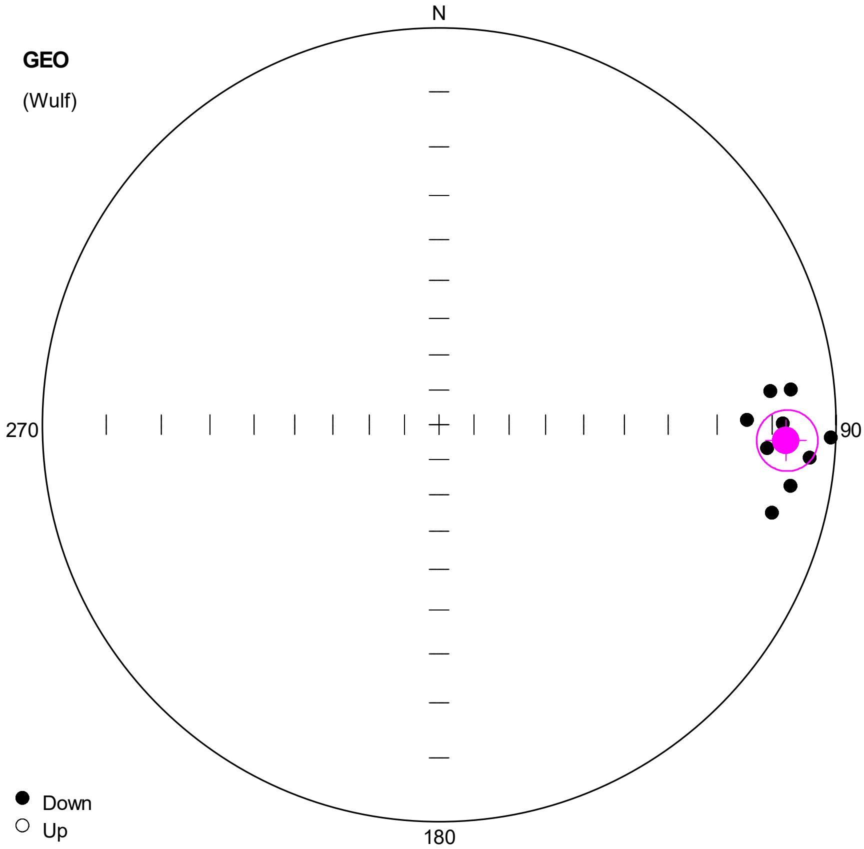

Number of data points: 9

Fisher statistics

Mean vector: 92.59 / 7.66

Resultant vector: 8.93

(X= -0.4, Y= 8.84, Z= 1.19)

Estimated precision, k: 107

95% Confidence limit: 5

95% Confidence limit, approximation: 4.51

Orientation matrix

1st eigenvalue: 0.98

1st eigenvector: 92.57 / 7.66

2nd eigenvalue: 0.01

2nd eigenvector: 1.28 / 9.51

3rd eigenvalue: 0

3rd eigenvector: 220.82 / 77.75

VGP

Site latitude: 65

Site longitude: 14.04

Pole latitude: 2.39 (-2.39)

Pole longitude: 100.07 (-79.93)

Paleolatitude: 3.85 (-3.85)

dp: 2.53

dm: 5.03

#	Name	State	Dec	Inc	MAD	Limit1	Limit2
1	YUN3701	CCH	104.8	8.1	4.8	40	64
2	YUN3702	CCH	84.2	10.0	7.3	40	64
3	YUN3704	CCH	89.1	14.4	5.9	44	64
4	YUN3705	CCH	99.9	6.1	8.9	40	64
5	YUN3706	CCH	94.1	10.7	9.3	40	64
6	YUN3707	CCH	89.8	8.2	6.4	35	60
7	YUN3708	CCH	84.3	6.6	6.1	40	64
8	YUN3709	CCH	95.1	3.7	7.2	35	64
9	YUN3710	CCH	91.9	0.7	5.4	35	64

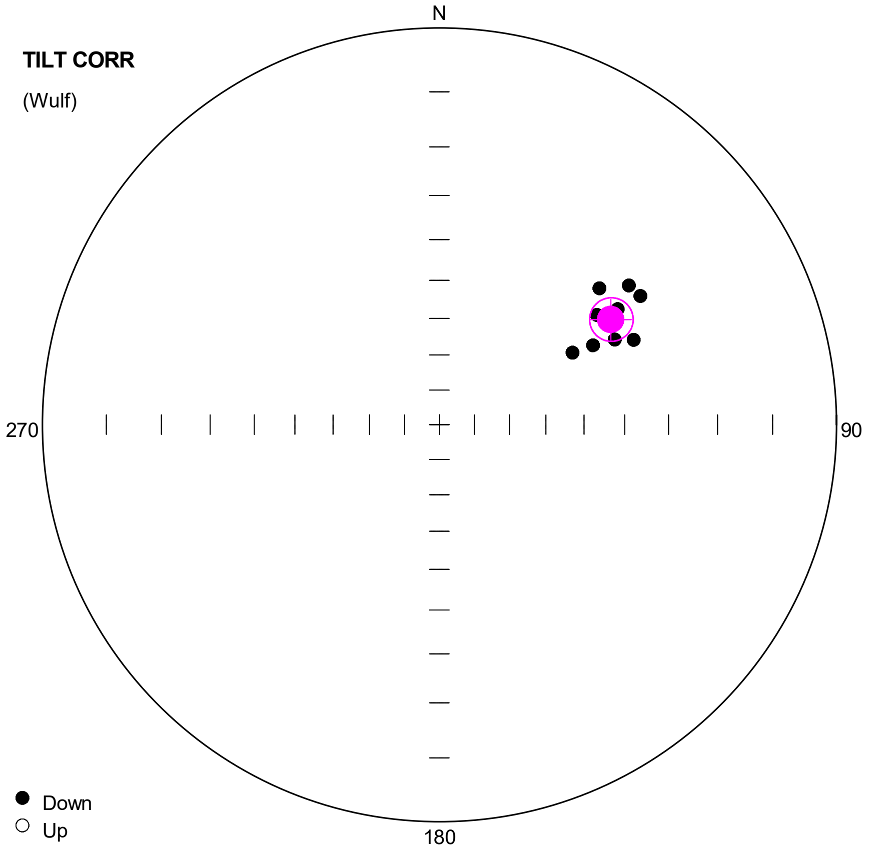

Number of data points: 9

Fisher statistics

Mean vector: 58.47 / 36.28

Resultant vector: 8.93

(X= 3.76, Y= 6.13, Z= 5.28)

Estimated precision, k: 107.07

95% Confidence limit: 5

95% Confidence limit, approximation: 4.51

Orientation matrix

1st eigenvalue: 0.98

1st eigenvector: 58.47 / 36.27

2nd eigenvalue: 0.01

2nd eigenvector: 203.51 / 48.16

3rd eigenvalue: 0

3rd eigenvector: 314.72 / 17.95

VGP

Site latitude: 65

Site longitude: 14.04

Pole latitude: 31.32 (-31.32)

Pole longitude: 124.55 (-55.45)

Paleolatitude: 20.16 (-20.16)

dp: 3.39

dm: 5.82

#	Name	State	Dec	Inc	MAD	Limit1	Limit2
1	YUN3701	CCH	61.6	48.2	4.8	40	64
2	YUN3702	CCH	53.7	28.7	7.3	40	64
3	YUN3704	CCH	49.6	34.2	5.9	44	64
4	YUN3705	CCH	62.7	42.9	8.9	40	64
5	YUN3706	CCH	55.1	38.4	9.3	40	64
6	YUN3707	CCH	57.1	33.7	6.4	35	60
7	YUN3708	CCH	57.4	28.0	6.1	40	64
8	YUN3709	CCH	64.1	37.7	7.2	35	64
9	YUN3710	CCH	66.4	33.8	5.4	35	64

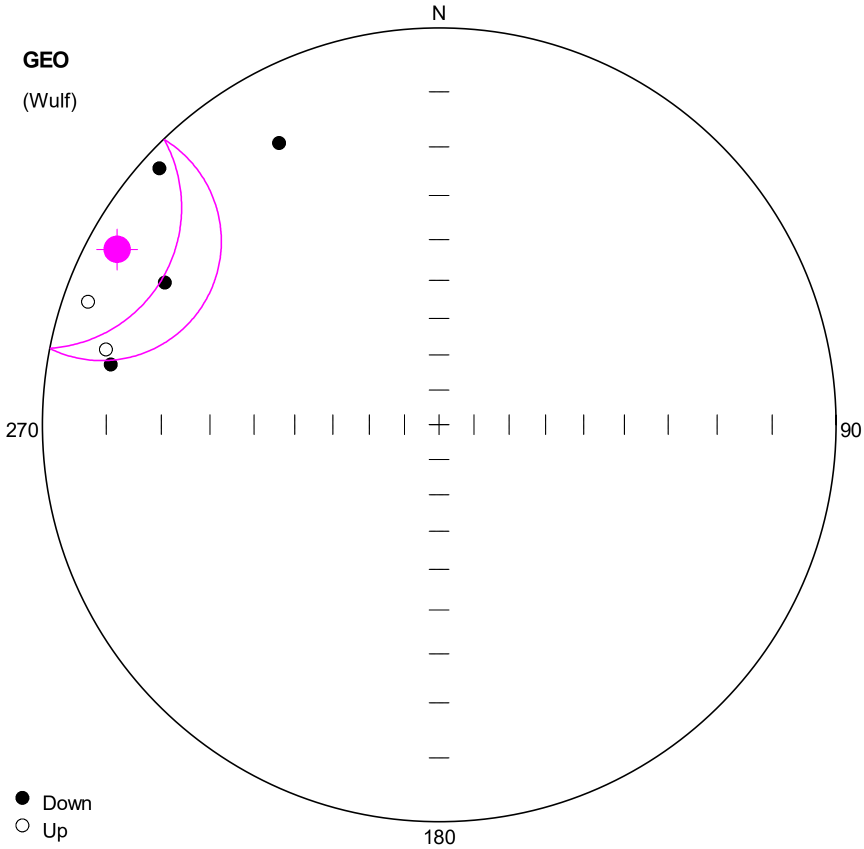

Number of data points: 6

Fisher statistics

Mean vector: 298.56 / 4.56
Resultant vector: 5.66
(X= 2.7, Y= -4.96, Z= 0.45)
Estimated precision, k: 14.75
95% Confidence limit: 18.04
95% Confidence limit, approximation: 14.88

Orientation matrix

1st eigenvalue: 0.89
1st eigenvector: 297.97 / 4.44
2nd eigenvalue: 0.09
2nd eigenvector: 29.16 / 14.94
3rd eigenvalue: 0.02
3rd eigenvector: 191.85 / 74.39

VGP

Site latitude: 65
Site longitude: 14.04
Pole latitude: 13.77 (-13.77)
Pole longitude: -101.33 (78.67)
Paleolatitude: 2.28 (-2.28)
dp: 9.06
dm: 18.08

#	Name	State	Dec	Inc	MAD	Limit1	Limit2
1	YUN3803	CCH	297.4	14.2	5.0	30	64
2	YUN3804	CCH	312.5	2.6	11.2	30	52
3	YUN3805	CCH	289.3	-3.7	19.1	40	56
4	YUN3807	CCH	330.4	11.6	6.9	40	64
5	YUN3808	CCH	282.7	-8.6	2.6	30	56
6	YUN3809	CCH	280.4	9.9	2.3	35	56

TILT CORR

(Wulf)

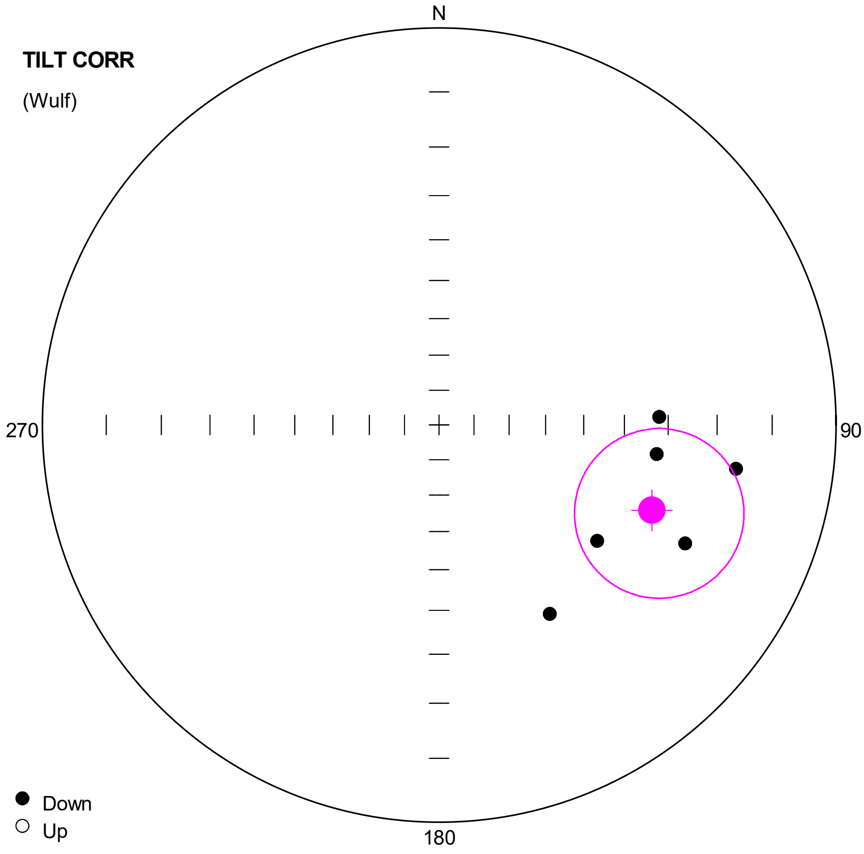

Number of data points: 6

Fisher statistics

Mean vector: 111.86 / 29.98

Resultant vector: 5.66

(X= -1.83, Y= 4.55, Z= 2.83)

Estimated precision, k: 14.76

95% Confidence limit: 18.03

95% Confidence limit, approximation: 14.88

Orientation matrix

1st eigenvalue: 0.89

1st eigenvector: 111.2 / 29.81

2nd eigenvalue: 0.09

2nd eigenvector: 208.11 / 11.86

3rd eigenvalue: 0.02

3rd eigenvector: 317.33 / 57.46

VGP

Site latitude: 65

Site longitude: 14.04

Pole latitude: 5.74 (-5.74)

Pole longitude: 77.71 (-102.29)

Paleolatitude: 16.09 (-16.09)

dp: 11.09

dm: 20

#	Name	State	Dec	Inc	MAD	Limit1	Limit2
1	YUN3803	CCH	115.7	20.9	5.0	30	64
2	YUN3804	CCH	126.2	37.4	11.2	30	52
3	YUN3805	CCH	97.6	32.1	19.1	40	56
4	YUN3807	CCH	149.6	32.2	6.9	40	64
5	YUN3808	CCH	87.9	31.9	2.6	30	56
6	YUN3809	CCH	98.4	15.8	2.3	35	56

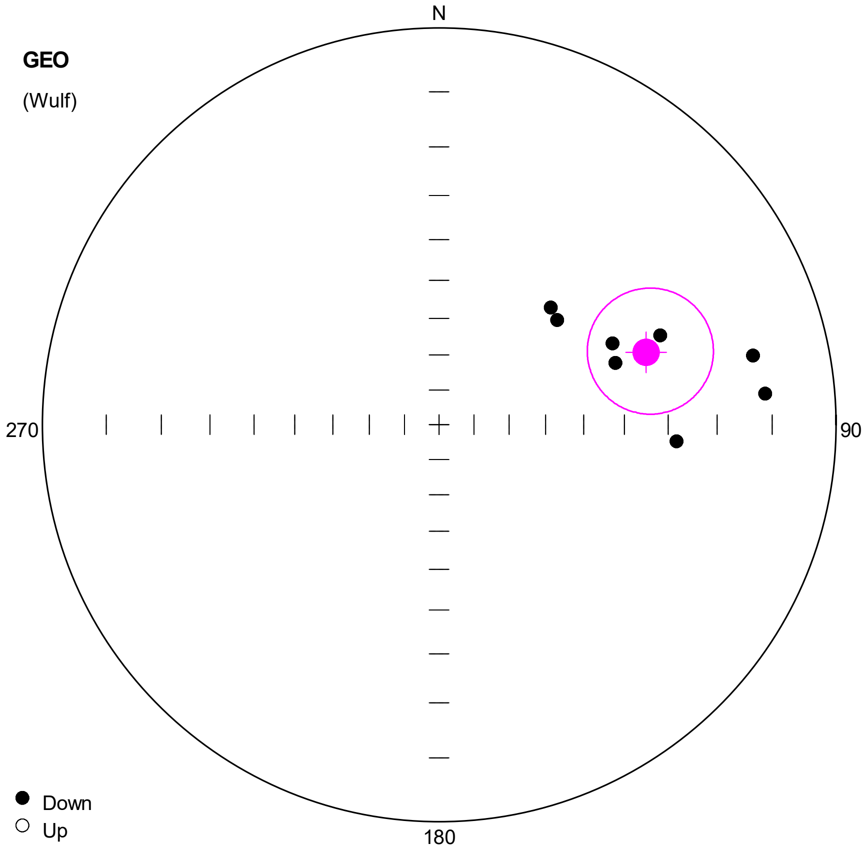

Number of data points: 8

Fisher statistics

Mean vector: 70.74 / 32.15
Resultant vector: 7.59
(X= 2.12, Y= 6.07, Z= 4.04)
Estimated precision, k: 17.03
95% Confidence limit: 13.82
95% Confidence limit, approximation: 12

Orientation matrix

1st eigenvalue: 0.9
1st eigenvector: 70.72 / 32.23
2nd eigenvalue: 0.09
2nd eigenvector: 310.35 / 38.73
3rd eigenvalue: 0.01
3rd eigenvector: 186.61 / 34.71

VGP

Site latitude: 65
Site longitude: 14.04
Pole latitude: 23.87 (-23.87)
Pole longitude: 114.02 (-65.98)
Paleolatitude: 17.45 (-17.45)
dp: 8.77
dm: 15.57

#	Name	State	Dec	Inc	MAD	Limit1	Limit2
1	YUN3901	CCH	43.7	45.6	3.4	48	64
2	YUN3902	CCH	48.5	46.6	3.6	44	64
3	YUN3903	CCH	68.0	28.0	4.4	40	64
4	YUN3904	CCH	84.6	10.9	12.0	30	52
5	YUN3905	CCH	64.9	38.5	13.3	40	64
6	YUN3906	CCH	77.6	12.0	4.4	35	60
7	YUN3907	CCH	70.7	39.6	11.7	48	60
8	YUN3908	CCH	94.0	28.1	7.7	40	56

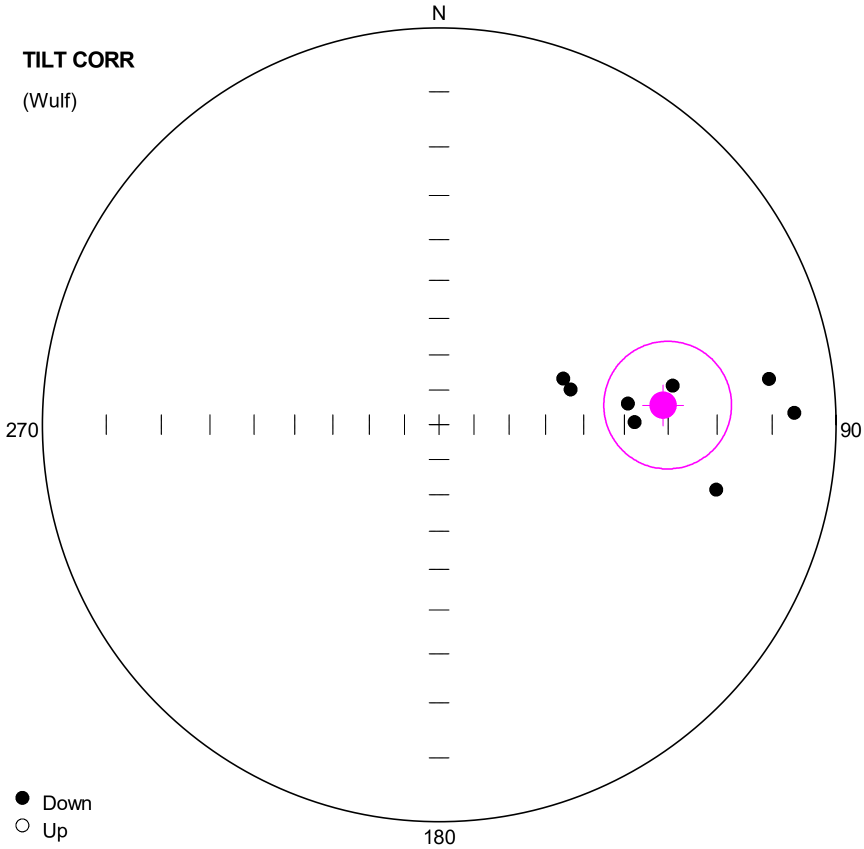

Number of data points: 8

Fisher statistics

Mean vector: 85.06 / 30.95

Resultant vector: 7.59

(X= 0.56, Y= 6.48, Z= 3.9)

Estimated precision, k: 17.01

95% Confidence limit: 13.83

95% Confidence limit, approximation: 12

Orientation matrix

1st eigenvalue: 0.9

1st eigenvector: 85.08 / 31.02

2nd eigenvalue: 0.09

2nd eigenvector: 293.01 / 55.76

3rd eigenvalue: 0.01

3rd eigenvector: 183.1 / 13.05

VGP

Site latitude: 65

Site longitude: 14.04

Pole latitude: 17.16 (-17.16)

Pole longitude: 101.24 (-78.76)

Paleolatitude: 16.69 (-16.69)

dp: 8.62

dm: 15.44

#	Name	State	Dec	Inc	MAD	Limit1	Limit2
1	YUN3901	CCH	69.7	53.1	3.4	48	64
2	YUN3902	CCH	75.1	52.1	3.6	44	64
3	YUN3903	CCH	80.5	28.3	4.4	40	64
4	YUN3904	CCH	88.1	6.3	12.0	30	52
5	YUN3905	CCH	83.6	38.8	13.3	40	64
6	YUN3906	CCH	82.1	10.0	4.4	35	60
7	YUN3907	CCH	89.3	37.5	11.7	48	60
8	YUN3908	CCH	103.2	18.7	7.7	40	56

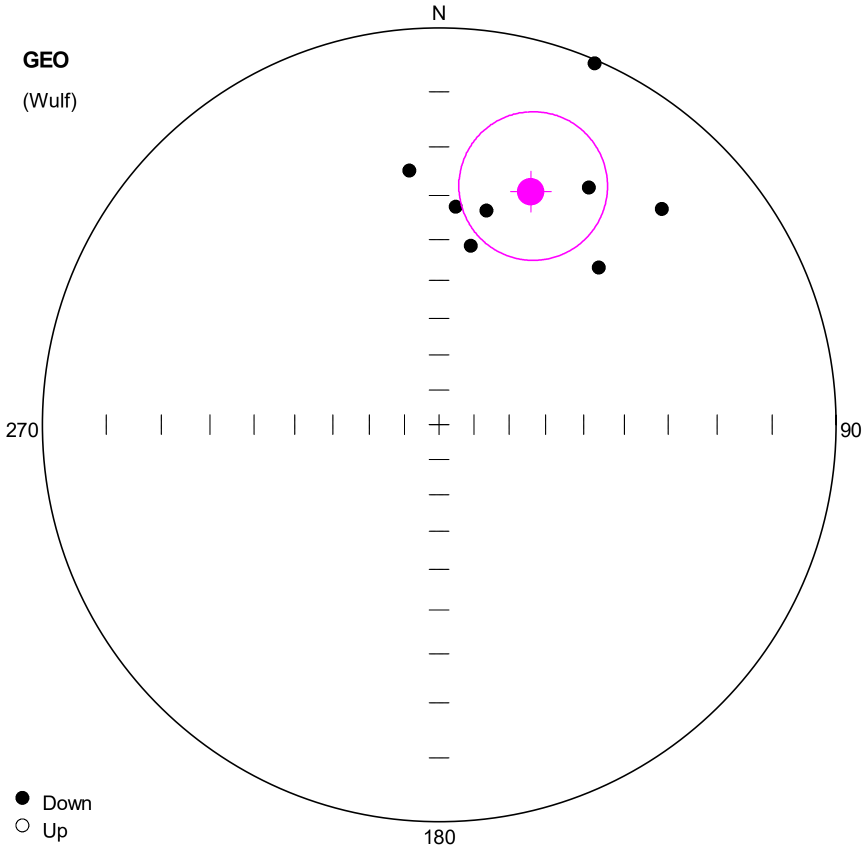

Number of data points: 8

Fisher statistics

Mean vector: 21.47 / 25.51
Resultant vector: 7.51
(X= 6.31, Y= 2.48, Z= 3.23)
Estimated precision, k: 14.34
95% Confidence limit: 15.14
95% Confidence limit, approximation: 13.07

Orientation matrix

1st eigenvalue: 0.88
1st eigenvector: 21.37 / 25.72
2nd eigenvalue: 0.08
2nd eigenvector: 280.19 / 21.91
3rd eigenvalue: 0.03
3rd eigenvector: 155.01 / 55.08

VGP

Site latitude: 65
Site longitude: 14.04
Pole latitude: 36.36 (-36.36)
Pole longitude: 167.8 (-12.2)
Paleolatitude: 13.42 (-13.42)
dp: 8.79
dm: 16.32

#	Name	State	Dec	Inc	MAD	Limit1	Limit2
1	YUN4001	CCH	23.3	0.5	12.9	30	64
2	YUN4003	CCH	4.4	32.3	9.8	40	60
3	YUN4004	CCH	10.1	40.8	15.0	40	60
4	YUN4005	CCH	32.3	19.5	16.4	30	60
5	YUN4006	CCH	353.3	24.4	8.6	30	64
6	YUN4007	CCH	12.5	32.2	8.6	30	64
7	YUN4009	CCH	45.5	31.1	7.7	30	60
8	YUN4010	CCH	45.9	14.0	15.0	35	64

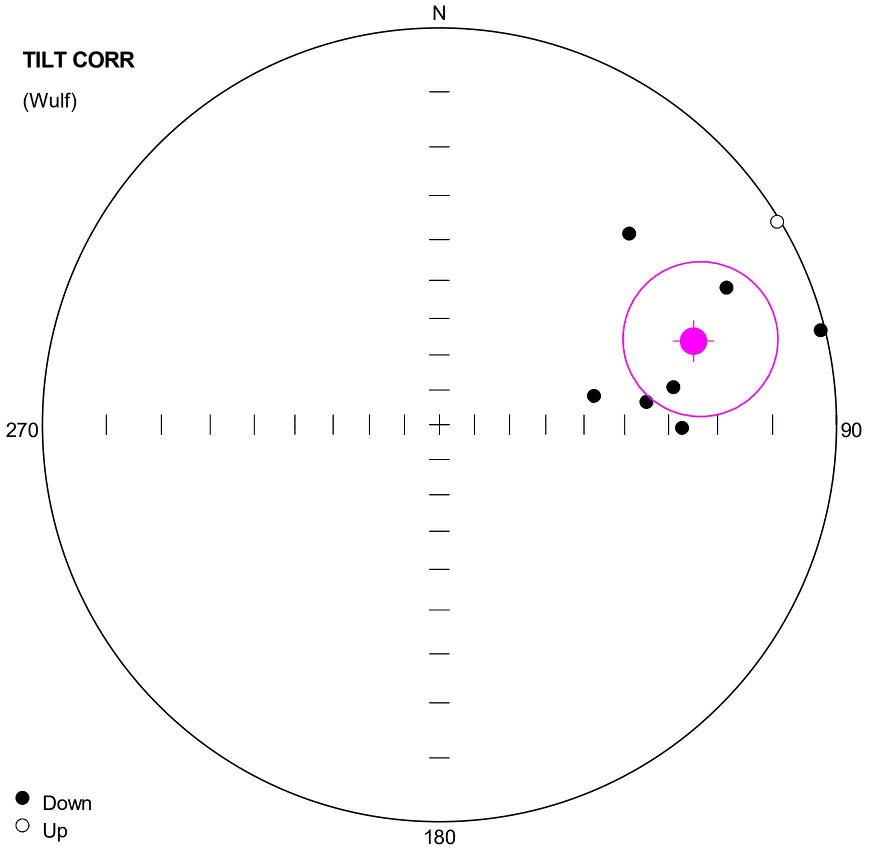

Number of data points: 8

Fisher statistics

Mean vector: 71.8 / 22.03

Resultant vector: 7.51

(X= 2.18, Y= 6.61, Z= 2.82)

Estimated precision, k: 14.32

95% Confidence limit: 15.15

95% Confidence limit, approximation: 13.08

Orientation matrix

1st eigenvalue: 0.88

1st eigenvector: 72.04 / 22.09

2nd eigenvalue: 0.08

2nd eigenvector: 191.81 / 50.73

3rd eigenvalue: 0.03

3rd eigenvector: 328.15 / 30.6

VGP

Site latitude: 65

Site longitude: 14.04

Pole latitude: 18.01 (-18.01)

Pole longitude: 115.79 (-64.21)

Paleolatitude: 11.44 (-11.44)

dp: 8.47

dm: 16.02

#	Name	State	Dec	Inc	MAD	Limit1	Limit2
1	YUN4001	CCH	44.8	21.7	12.9	30	64
2	YUN4003	CCH	83.8	34.6	9.8	40	60
3	YUN4004	CCH	90.8	27.1	15.0	40	60
4	YUN4005	CCH	64.5	12.6	16.4	30	60
5	YUN4006	CCH	79.5	46.8	8.6	30	64
6	YUN4007	CCH	80.9	28.3	8.6	30	64
7	YUN4009	CCH	76.1	0.6	7.7	30	60
8	YUN4010	CCH	59.0	-0.4	15.0	35	64

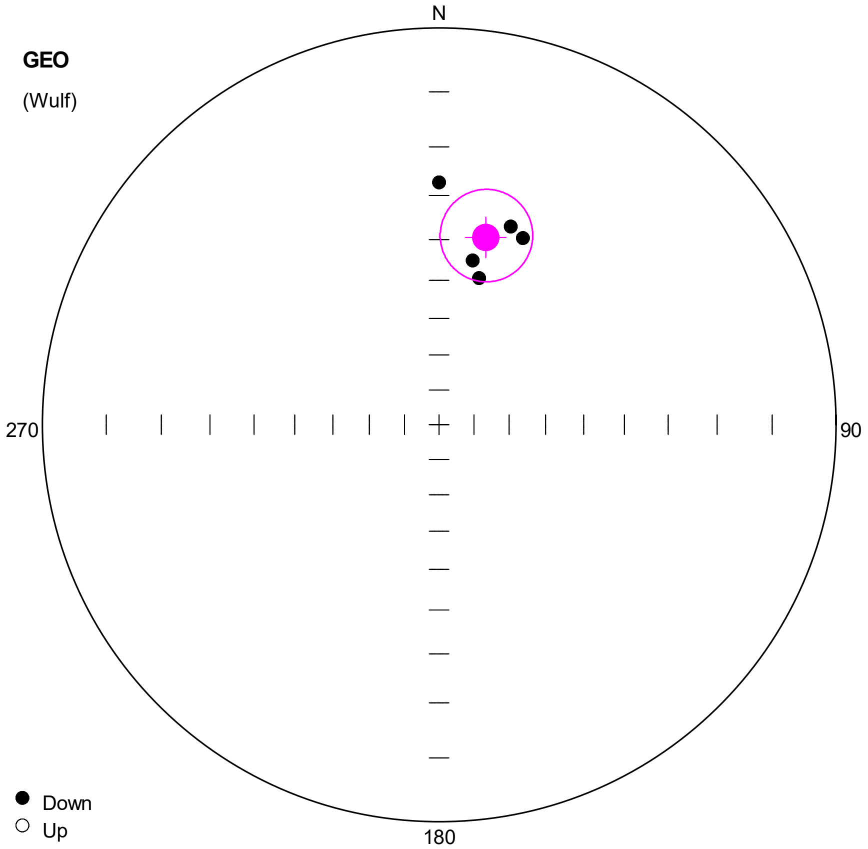

Number of data points: 5

Fisher statistics

Mean vector: 13.99 / 38.14

Resultant vector: 4.92

(X= 3.76, Y= 0.94, Z= 3.04)

Estimated precision, k: 51.71

95% Confidence limit: 10.74

95% Confidence limit, approximation: 8.71

Orientation matrix

1st eigenvalue: 0.97

1st eigenvector: 14.08 / 38.19

2nd eigenvalue: 0.02

2nd eigenvector: 136.7 / 34.42

3rd eigenvalue: 0.01

3rd eigenvector: 253.24 / 33.1

VGP

Site latitude: 65

Site longitude: 14.04

Pole latitude: 45.47 (-45.47)

Pole longitude: 175.32 (-4.68)

Paleolatitude: 21.43 (-21.43)

dp: 7.52

dm: 12.71

#	Name	State	Dec	Inc	MAD	Limit1	Limit2	
1	YUN4201	Cch	15.3	48.1	9.0	40	68	OA
2	YUN4202	Cch	0.0	27.2	8.3	35	64	OA
3	YUN4203	Cch	11.6	44.2	4.8	40	64	OA
4	YUN4204	Cch	24.2	35.5	13.5	40	60	
5	YUN4205	Cch	19.9	34.1	8.8	35	68	

TILT CORR

(Wulf)

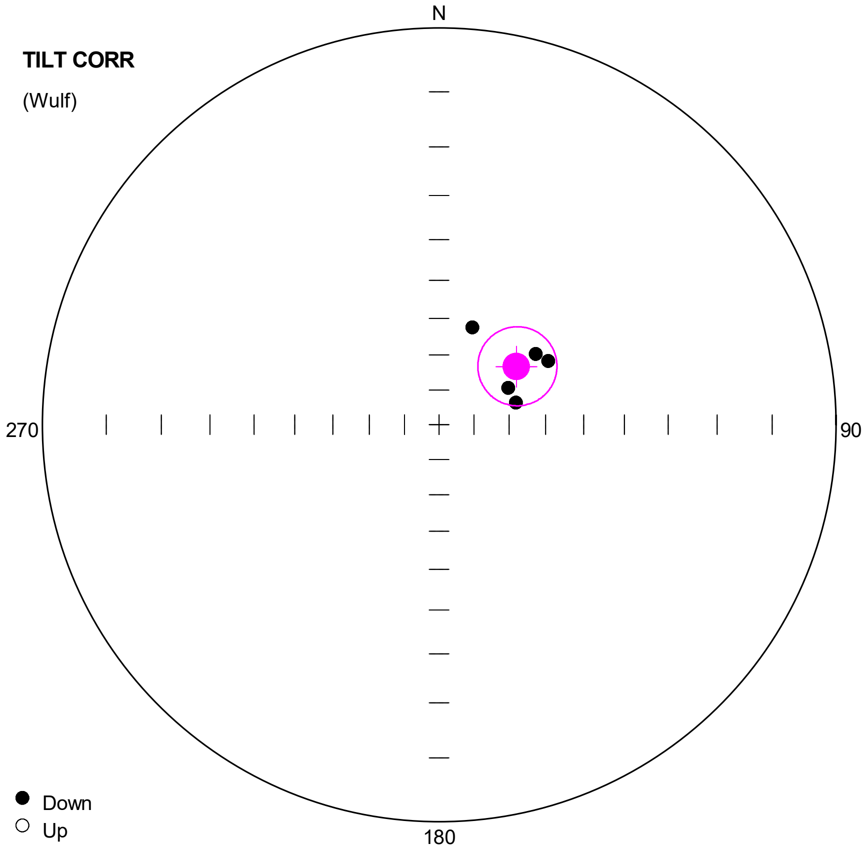

Number of data points: 5

Fisher statistics

Mean vector: 53.1 / 62.61
Resultant vector: 4.92
(X= 1.36, Y= 1.81, Z= 4.37)
Estimated precision, k: 51.73
95% Confidence limit: 10.74
95% Confidence limit, approximation: 8.7

Orientation matrix

1st eigenvalue: 0.97
1st eigenvector: 53.29 / 62.59
2nd eigenvalue: 0.02
2nd eigenvector: 320.54 / 1.43
3rd eigenvalue: 0.01
3rd eigenvector: 229.8 / 27.37

VGP

Site latitude: 65
Site longitude: 14.04
Pole latitude: 54.28 (-54.28)
Pole longitude: 113.72 (-66.28)
Paleolatitude: 43.98 (-43.98)
dp: 13.13
dm: 16.79

#	Name	State	Dec	Inc	MAD	Limit1	Limit2	
1	YUN4201	Cch	74.1	67.2	9.0	40	68	OA
2	YUN4202	Cch	18.9	61.0	8.3	35	64	OA
3	YUN4203	Cch	62.1	67.7	4.8	40	64	OA
4	YUN4204	Cch	59.8	54.7	13.5	40	60	
5	YUN4205	Cch	53.8	56.4	8.8	35	68	

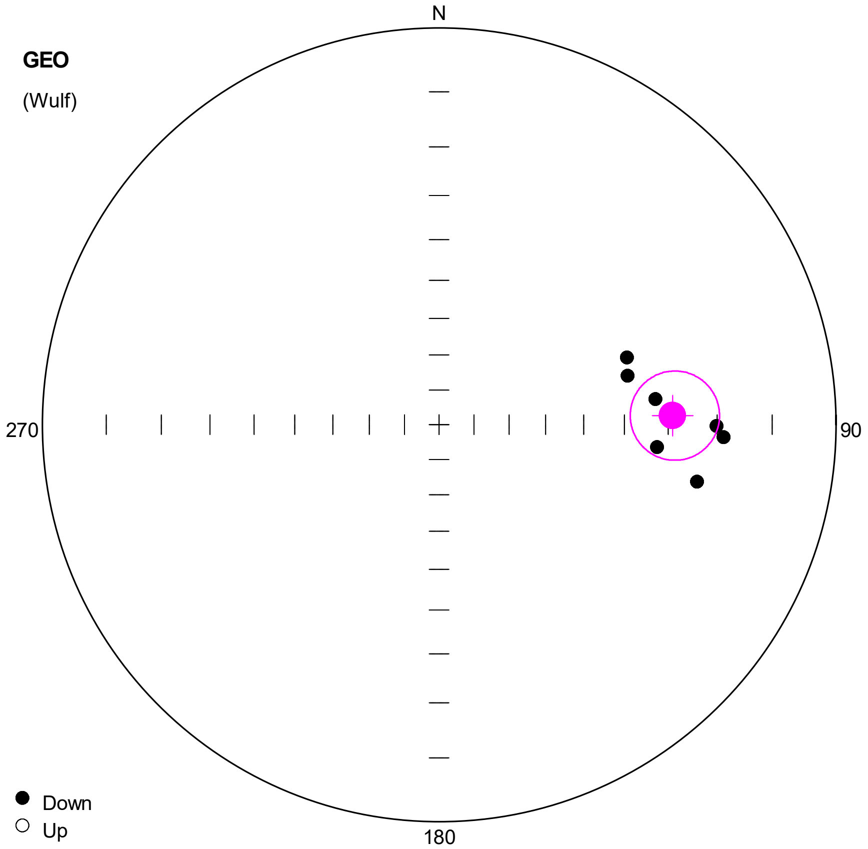

Number of data points: 7

Fisher statistics

Mean vector: 87.76 / 29.05

Resultant vector: 6.85

(X= 0.23, Y= 5.99, Z= 3.33)

Estimated precision, k: 41.12

95% Confidence limit: 9.52

95% Confidence limit, approximation: 8.25

Orientation matrix

1st eigenvalue: 0.96

1st eigenvector: 87.8 / 29.03

2nd eigenvalue: 0.04

2nd eigenvector: 336.74 / 32.93

3rd eigenvalue: 0.01

3rd eigenvector: 209.24 / 43.23

VGP

Site latitude: 65

Site longitude: 14.04

Pole latitude: 14.98 (-14.98)

Pole longitude: 99.35 (-80.65)

Paleolatitude: 15.52 (-15.52)

dp: 5.79

dm: 10.5

#	Name	State	Dec	Inc	MAD	Limit1	Limit2
1	YUN4301	CCH	70.3	36.6	2.3	40	68
2	YUN4302	CCH	83.3	32.5	2.9	44	68
3	YUN4303	CCH	90.3	20.1	4.2	40	68
4	YUN4304	CCH	75.5	37.7	6.0	40	68
5	YUN4305	CCH	95.9	32.2	3.1	44	68
6	YUN4306	CCH	92.5	18.7	3.1	30	68
7	YUN4307	CCH	102.5	22.7	7.1	30	60

TILT CORR

(Wulf)

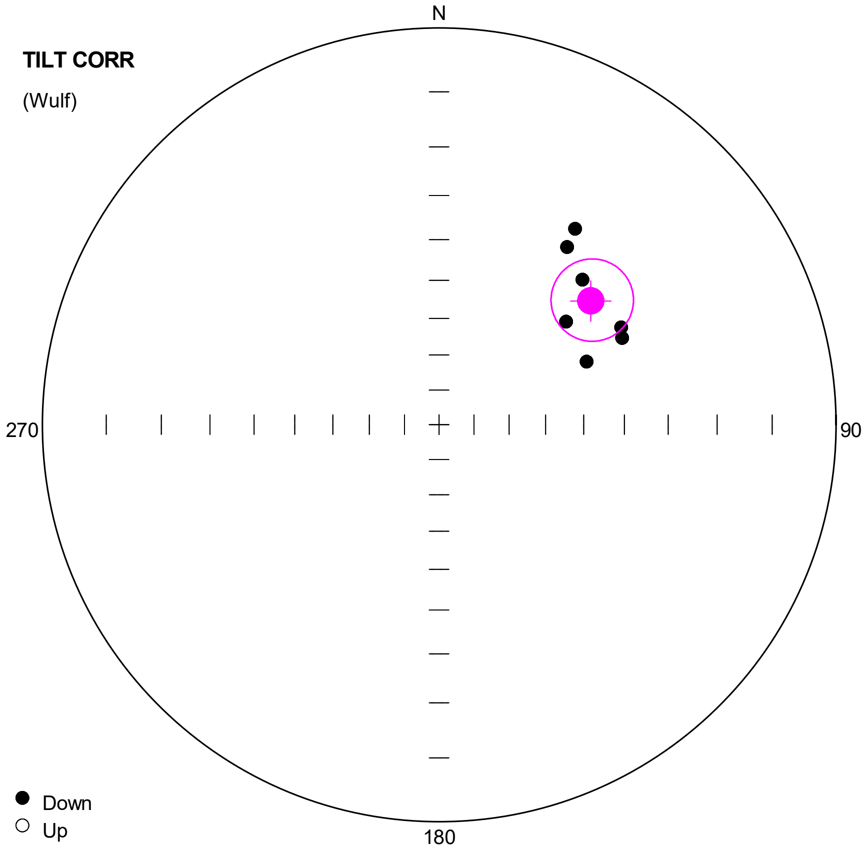

Number of data points: 7

Fisher statistics

Mean vector: 50.79 / 37.51

Resultant vector: 6.85

(X= 3.44, Y= 4.21, Z= 4.17)

Estimated precision, k: 41.06

95% Confidence limit: 9.53

95% Confidence limit, approximation: 8.26

Orientation matrix

1st eigenvalue: 0.96

1st eigenvector: 50.83 / 37.53

2nd eigenvalue: 0.04

2nd eigenvector: 155.97 / 18.78

3rd eigenvalue: 0.01

3rd eigenvector: 266.93 / 46.45

VGP

Site latitude: 65

Site longitude: 14.04

Pole latitude: 35.04 (-35.04)

Pole longitude: 131.97 (-48.03)

Paleolatitude: 21 (-21)

dp: 6.6

dm: 11.22

#	Name	State	Dec	Inc	MAD	Limit1	Limit2
1	YUN4301	CCH	34.8	28.0	2.3	40	68
2	YUN4302	CCH	44.7	35.6	2.9	44	68
3	YUN4303	CCH	61.9	35.0	4.2	40	68
4	YUN4304	CCH	35.8	32.2	6.0	40	68
5	YUN4305	CCH	51.0	45.2	3.1	44	68
6	YUN4306	CCH	64.7	35.9	3.1	30	68
7	YUN4307	CCH	66.9	46.0	7.1	30	60

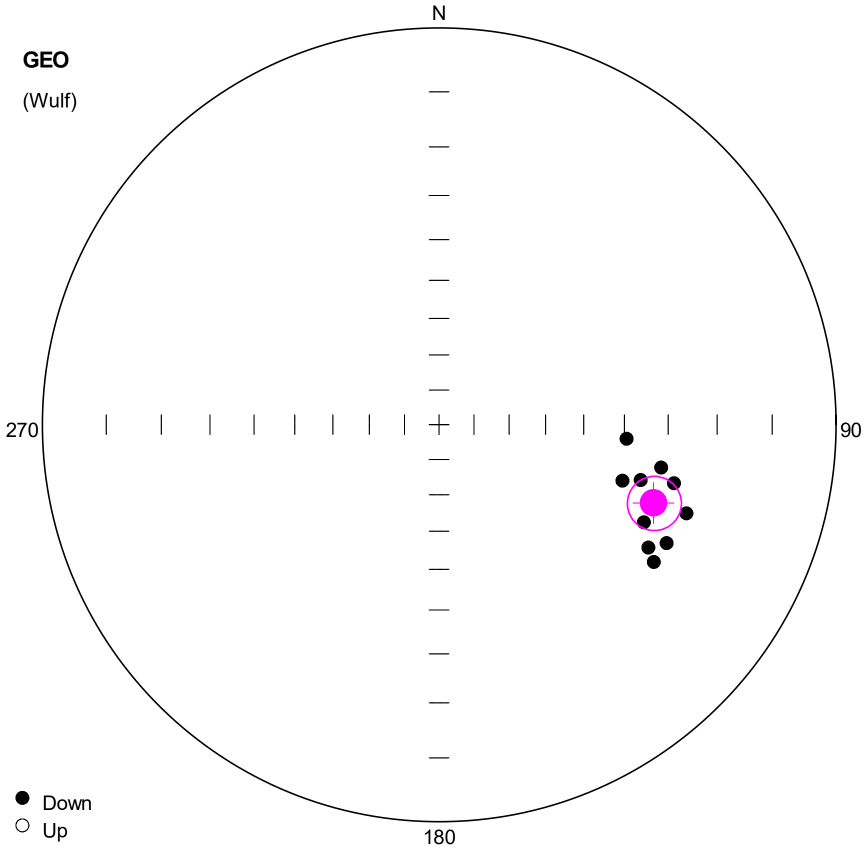

Number of data points: 10

Fisher statistics

Mean vector: 110.07 / 30.21
Resultant vector: 9.87
(X= -2.93, Y= 8.01, Z= 4.97)
Estimated precision, k: 69.23
95% Confidence limit: 5.85
95% Confidence limit, approximation: 5.32

Orientation matrix

1st eigenvalue: 0.97
1st eigenvector: 110.08 / 30.19
2nd eigenvalue: 0.02
2nd eigenvector: 1.82 / 28.32
3rd eigenvalue: 0
3rd eigenvector: 237.53 / 46.27

VGP

Site latitude: 65
Site longitude: 14.04
Pole latitude: 6.55 (-6.55)
Pole longitude: 79.24 (-100.76)
Paleolatitude: 16.23 (-16.23)
dp: 3.61
dm: 6.5

#	Name	State	Dec	Inc	MAD	Limit1	Limit2
1	YUN4401	CCH	117.5	24.2	5.9	30	52
2	YUN4402	CCH	105.4	34.4	5.4	30	60
3	YUN4403	CCH	100.9	30.6	5.9	35	60
4	YUN4404	CCH	120.4	27.1	5.8	30	56
5	YUN4405	CCH	122.6	24.6	5.7	35	60
6	YUN4406	CCH	115.5	30.5	2.9	30	60
7	YUN4407	CCH	94.3	39.3	5.5	35	64
8	YUN4408	CCH	104.0	27.2	4.9	35	60
9	YUN4409	CCH	107.0	38.4	8.2	40	64
10	YUN4410	CCH	109.7	23.0	5.6	35	60

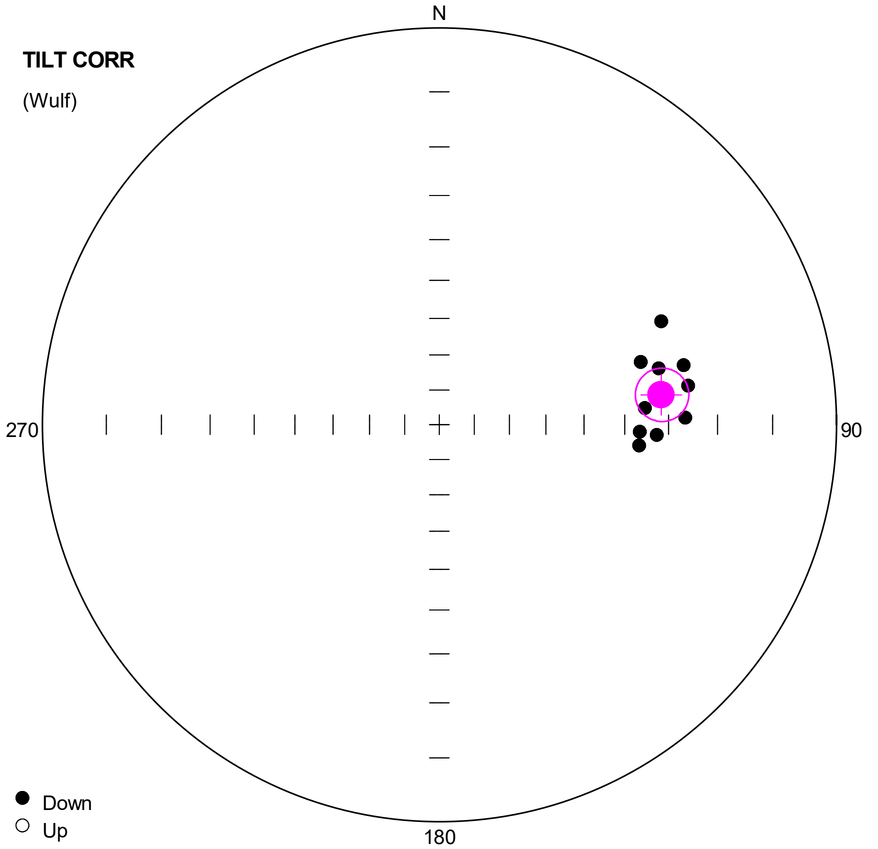

Number of data points: 10

Fisher statistics

Mean vector: 82.3 / 31.2

Resultant vector: 9.87

(X= 1.13, Y= 8.37, Z= 5.11)

Estimated precision, k: 69.3

95% Confidence limit: 5.84

95% Confidence limit, approximation: 5.32

Orientation matrix

1st eigenvalue: 0.97

1st eigenvector: 82.33 / 31.2

2nd eigenvalue: 0.02

2nd eigenvector: 182.11 / 15.67

3rd eigenvalue: 0

3rd eigenvector: 295.04 / 54.26

VGP

Site latitude: 65

Site longitude: 14.04

Pole latitude: 18.47 (-18.47)

Pole longitude: 103.66 (-76.34)

Paleolatitude: 16.85 (-16.85)

dp: 3.66

dm: 6.54

#	Name	State	Dec	Inc	MAD	Limit1	Limit2
1	YUN4401	CCH	92.7	32.5	5.9	30	52
2	YUN4402	CCH	75.6	30.6	5.4	30	60
3	YUN4403	CCH	76.3	25.3	5.9	35	60
4	YUN4404	CCH	92.0	36.4	5.8	30	56
5	YUN4405	CCH	96.0	36.3	5.7	35	60
6	YUN4406	CCH	85.4	35.1	2.9	30	60
7	YUN4407	CCH	65.0	26.7	5.5	35	64
8	YUN4408	CCH	81.1	25.2	4.9	35	60
9	YUN4409	CCH	72.7	34.0	8.2	40	64
10	YUN4410	CCH	88.4	26.4	5.6	35	60

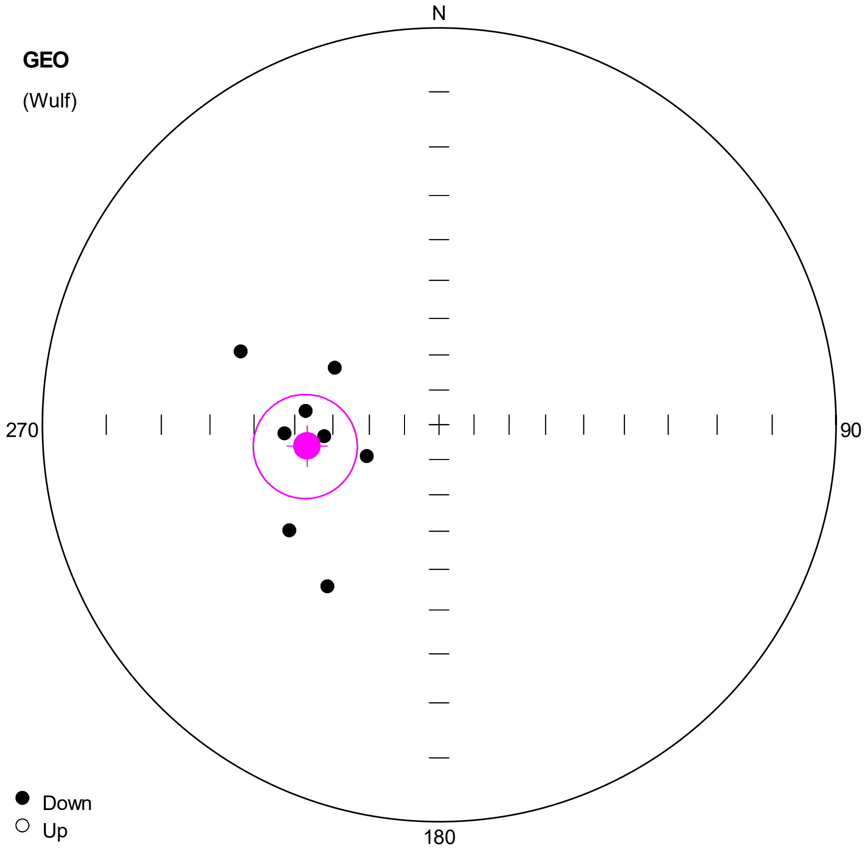

Number of data points: 9

Fisher statistics

Mean vector: 260.82 / 52.75
Resultant vector: 8.49
(X= -0.82, Y= -5.07, Z= 6.76)
Estimated precision, k: 15.72
95% Confidence limit: 13.4
95% Confidence limit, approximation: 11.77

Orientation matrix

1st eigenvalue: 0.89
1st eigenvector: 261.58 / 52.96
2nd eigenvalue: 0.08
2nd eigenvector: 352.91 / 1.01
3rd eigenvalue: 0.02
3rd eigenvector: 83.67 / 37.02

VGP

Site latitude: 65
Site longitude: 14.04
Pole latitude: 26.2 (-26.2)
Pole longitude: -52.8 (127.2)
Paleolatitude: 33.32 (-33.32)
dp: 12.77
dm: 18.5

#	Name	State	Dec	Inc	MAD	Limit1	Limit2	
1	YUN4501	CCH	264.3	57.6	6.3	30	64	
2	YUN4502	CCH	246.5	67.5	5.7	35	64	
3	YUN4503	CCH	298.6	56.7	12.7	35	60	
4	YUN4505	CCH	290.3	33.9	9.3	44	64	
5	YUN4506	CCH	214.6	37.3	19.5	35	60	O
6	YUN4507	CCH	275.9	52.7	10.1	30	64	
7	YUN4508	CCH	234.8	40.4	8.6	35	64	
8	YUN4509	CCH	260.6	54.2	5.4	30	64	
9	YUN4510	CCH	266.8	47.4	5.3	40	64	

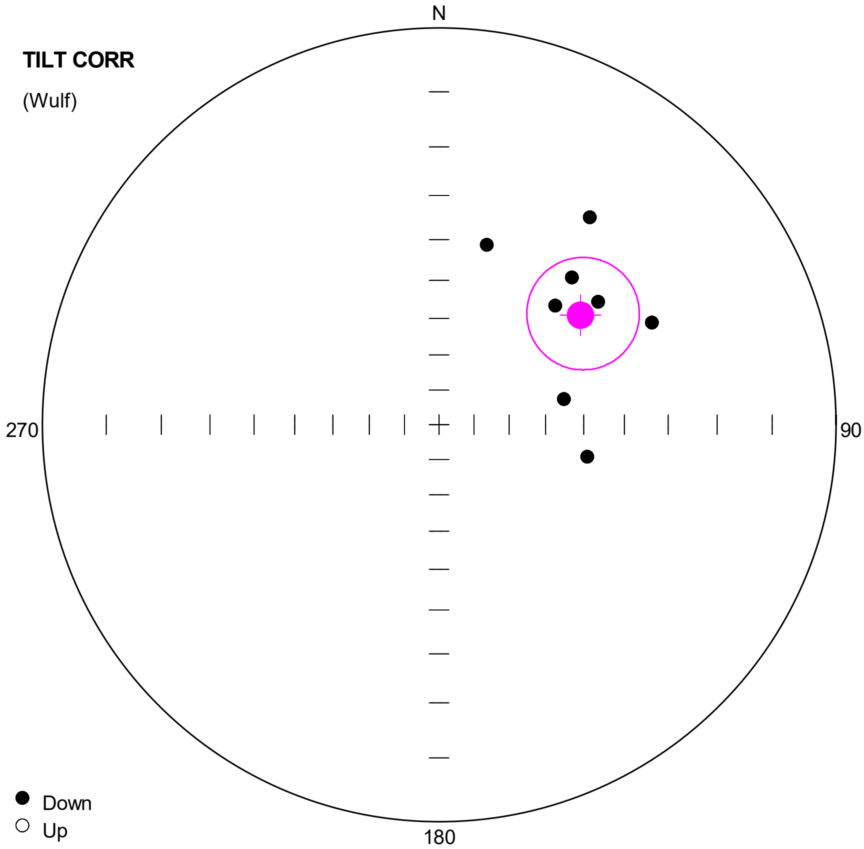

Number of data points: 9

Fisher statistics

Mean vector: 52.28 / 41.5
Resultant vector: 8.49
(X= 3.89, Y= 5.03, Z= 5.63)
Estimated precision, k: 15.72
95% Confidence limit: 13.4
95% Confidence limit, approximation: 11.77

Orientation matrix

1st eigenvalue: 0.89
1st eigenvector: 51.82 / 41.13
2nd eigenvalue: 0.08
2nd eigenvector: 157.93 / 17.64
3rd eigenvalue: 0.02
3rd eigenvector: 265.56 / 43.6

VGP

Site latitude: 65
Site longitude: 14.04
Pole latitude: 37.09 (-37.09)
Pole longitude: 128.96 (-51.04)
Paleolatitude: 23.86 (-23.86)
dp: 9.99
dm: 16.36

#	Name	State	Dec	Inc	MAD	Limit1	Limit2	
1	YUN4501	CCH	52.3	36.3	6.3	30	64	
2	YUN4502	CCH	64.4	28.5	5.7	35	64	
3	YUN4503	CCH	36.0	24.3	12.7	35	60	
4	YUN4505	CCH	14.9	39.8	9.3	44	64	
5	YUN4506	CCH	102.2	48.2	19.5	35	60	O
6	YUN4507	CCH	42.1	36.9	10.1	30	64	
7	YUN4508	CCH	78.4	54.4	8.6	35	64	
8	YUN4509	CCH	53.1	40.2	5.4	30	64	
9	YUN4510	CCH	44.3	44.5	5.3	40	64	

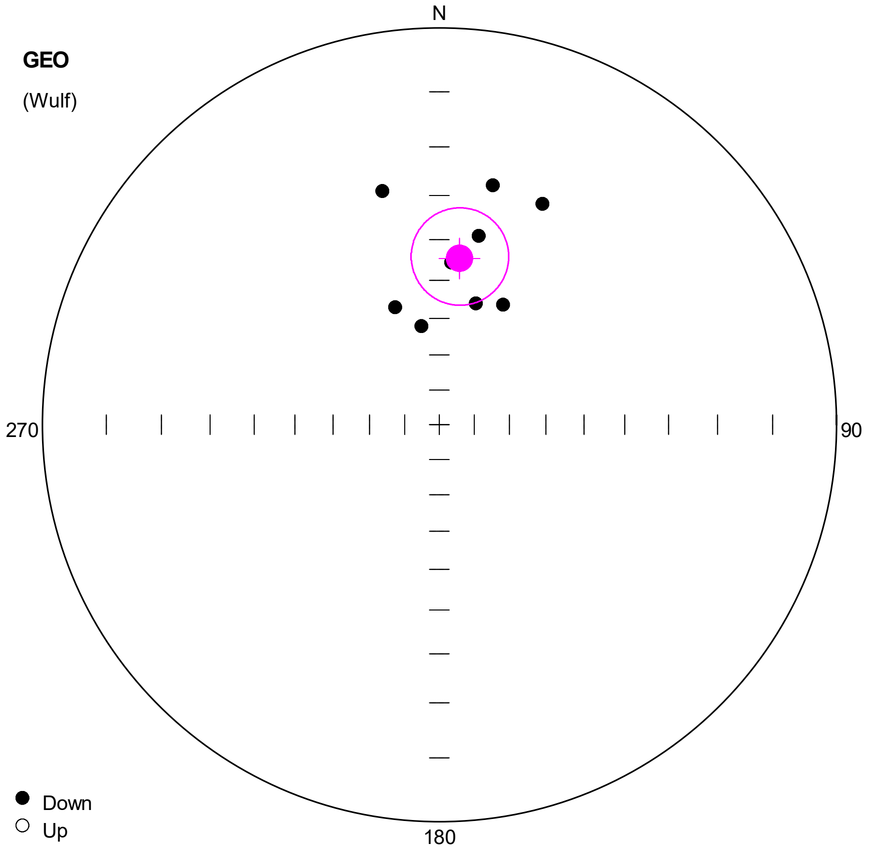

Number of data points: 9

Fisher statistics

Mean vector: 6.92 / 44.25
Resultant vector: 8.6
(X= 6.11, Y= 0.74, Z= 6)
Estimated precision, k: 19.78
95% Confidence limit: 11.87
95% Confidence limit, approximation: 10.49

Orientation matrix

1st eigenvalue: 0.91
1st eigenvector: 7.06 / 44.34
2nd eigenvalue: 0.05
2nd eigenvector: 223.88 / 39.33
3rd eigenvalue: 0.03
3rd eigenvector: 117.14 / 19.36

VGP

Site latitude: 65
Site longitude: 14.04
Pole latitude: 50.72 (-50.72)
Pole longitude: -175.8 (4.2)
Paleolatitude: 25.97 (-25.97)
dp: 9.35
dm: 14.89

#	Name	State	Dec	Inc	MAD	Limit1	Limit2	
1	YUN4601	CCH	25.0	26.9	8.6	48	64	
2	YUN4602	CCH	346.3	27.6	10.3	35	60	
3	YUN4603	CCH	11.8	38.2	5.3	35	60	
4	YUN4604	CCH	12.6	26.6	9.2	40	52	
5	YUN4605	CCH	4.2	45.4	12.2	35	60	
6	YUN4606	CCH	27.9	52.2	11.3	35	56	
7	YUN4607	CCH	349.7	61.7	10.1	35	56	O
8	YUN4608	CCH	339.4	54.9	8.4	44	60	
9	YUN4609	CCH	16.8	54.6	7.3	40	68	

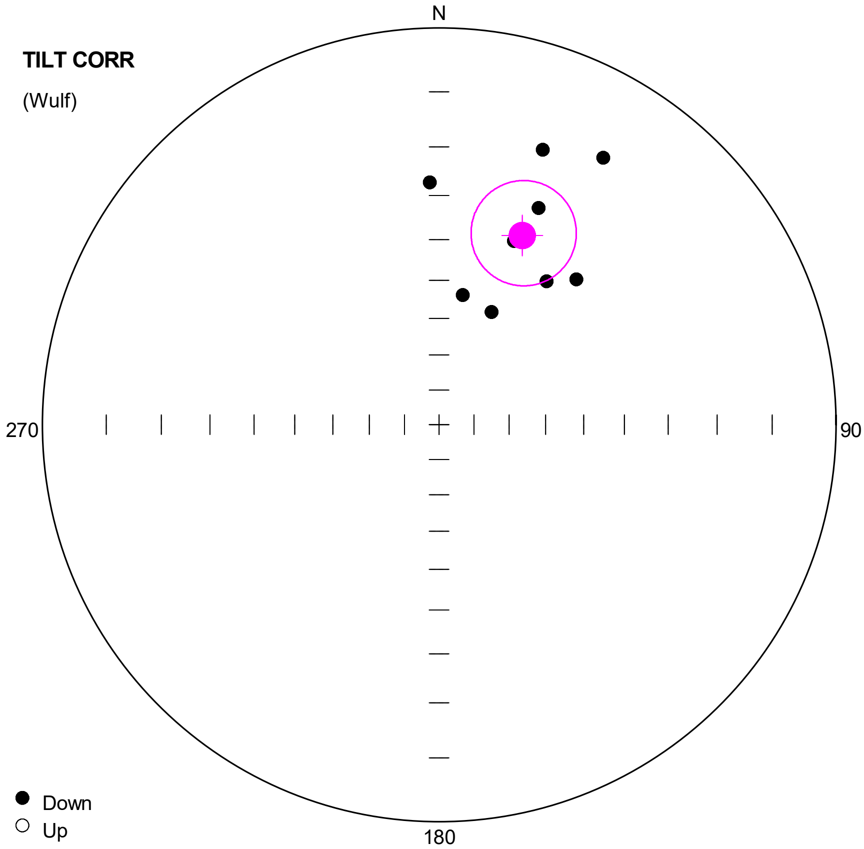

Number of data points: 9

Fisher statistics

Mean vector: 23.76 / 35
Resultant vector: 8.59
(X= 6.44, Y= 2.84, Z= 4.93)
Estimated precision, k: 19.74
95% Confidence limit: 11.88
95% Confidence limit, approximation: 10.5

Orientation matrix

1st eigenvalue: 0.91
1st eigenvector: 23.92 / 35.04
2nd eigenvalue: 0.05
2nd eigenvector: 207.41 / 54.91
3rd eigenvalue: 0.03
3rd eigenvector: 115.07 / 1.64

VGP

Site latitude: 65
Site longitude: 14.04
Pole latitude: 41.65 (-41.65)
Pole longitude: 163.45 (-16.55)
Paleolatitude: 19.3 (-19.3)
dp: 7.89
dm: 13.69

#	Name	State	Dec	Inc	MAD	Limit1	Limit2	
1	YUN4601	CCH	31.6	13.4	8.6	48	64	
2	YUN4602	CCH	357.8	27.2	10.3	35	60	
3	YUN4603	CCH	24.7	28.0	5.3	35	60	
4	YUN4604	CCH	20.7	17.0	9.2	40	52	
5	YUN4605	CCH	22.2	36.9	12.2	35	60	
6	YUN4606	CCH	43.4	36.5	11.3	35	56	
7	YUN4607	CCH	25.0	55.2	10.1	35	56	O
8	YUN4608	CCH	10.4	53.3	8.4	44	60	
9	YUN4609	CCH	36.9	41.4	7.3	40	68	

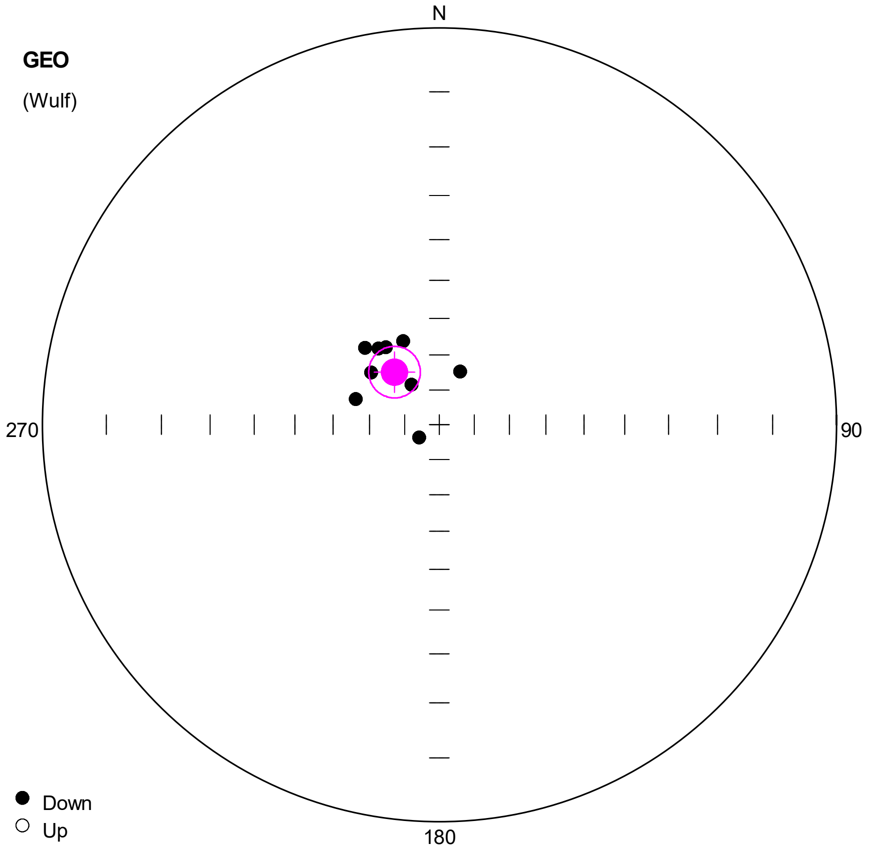

Number of data points: 10

Fisher statistics

Mean vector: 319.54 / 70.27
Resultant vector: 9.8
(X= 2.52, Y= -2.15, Z= 9.23)
Estimated precision, k: 45.76
95% Confidence limit: 7.22
95% Confidence limit, approximation: 6.54

Orientation matrix

1st eigenvalue: 0.96
1st eigenvector: 319.52 / 70.13
2nd eigenvalue: 0.02
2nd eigenvector: 129.56 / 19.59
3rd eigenvalue: 0.02
3rd eigenvector: 220.69 / 3.17

VGP

Site latitude: 65
Site longitude: 14.04
Pole latitude: 67.5 (-67.5)
Pole longitude: -84.75 (95.25)
Paleolatitude: 54.35 (-54.35)
dp: 10.76
dm: 12.46

#	Name	State	Dec	Inc	MAD	Limit1	Limit2	
1	YUN4701	CCH	321.4	62.4	6.9	35	64	
2	YUN4702	CCH	325.4	63.3	8.6	35	60	
3	YUN4703	CCH	325.3	76.0	7.8	40	64	
4	YUN4704	CCH	319.3	70.4	4.5	40	64	
5	YUN4705	CCH	307.5	65.6	3.5	40	64	
6	YUN4706	CHT	287.1	65.2	1.7	56	68	
7	YUN4707	CHT	237.1	83.1	6.7	44	68	
8	YUN4708	CCH	316.0	59.9	5.7	40	60	O
9	YUN4709	CCH	336.7	64.2	5.3	40	60	
10	YUN4710	CCH	21.5	73.6	5.4	40	60	

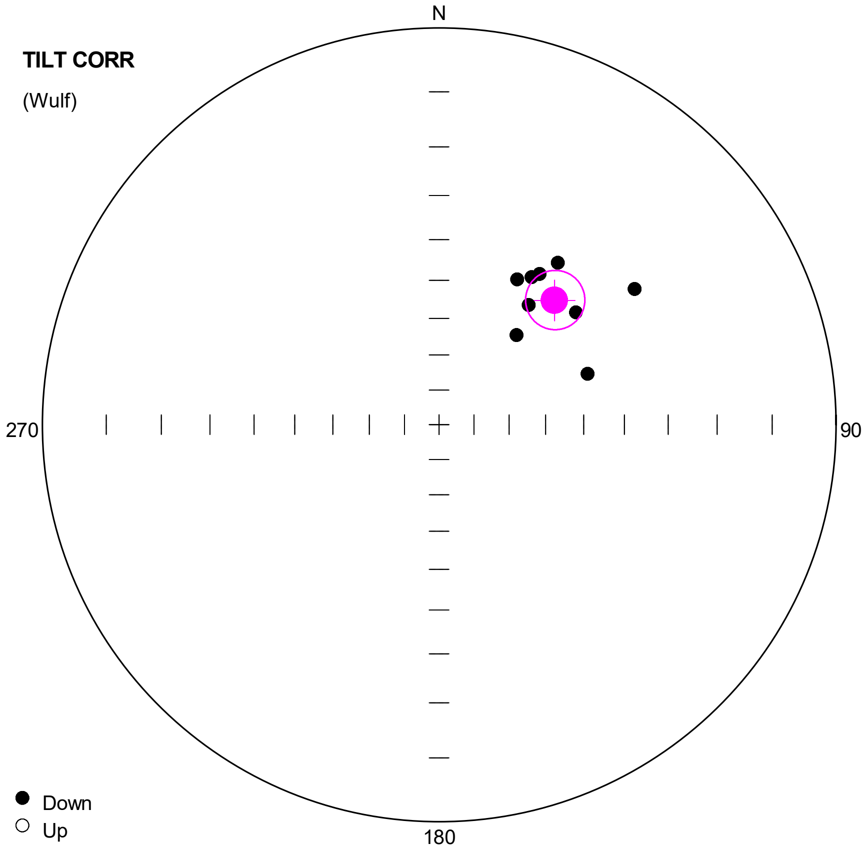

Number of data points: 10

Fisher statistics

Mean vector: 42.87 / 43.74
Resultant vector: 9.8
(X= 5.19, Y= 4.82, Z= 6.78)
Estimated precision, k: 45.75
95% Confidence limit: 7.22
95% Confidence limit, approximation: 6.55

Orientation matrix

1st eigenvalue: 0.96
1st eigenvector: 42.68 / 43.75
2nd eigenvalue: 0.02
2nd eigenvector: 305.42 / 7.52
3rd eigenvalue: 0.02
3rd eigenvector: 207.76 / 45.27

VGP

Site latitude: 65
Site longitude: 14.04
Pole latitude: 42.11 (-42.11)
Pole longitude: 138.23 (-41.77)
Paleolatitude: 25.57 (-25.57)
dp: 5.63
dm: 9.01

#	Name	State	Dec	Inc	MAD	Limit1	Limit2	
1	YUN4701	CCH	32.1	42.6	6.9	35	64	
2	YUN4702	CCH	33.7	40.9	8.6	35	60	
3	YUN4703	CCH	50.6	41.9	7.8	40	64	
4	YUN4704	CCH	43.0	43.8	4.5	40	64	
5	YUN4705	CCH	36.9	48.7	3.5	40	64	
6	YUN4706	CHT	40.9	56.8	1.7	56	68	
7	YUN4707	CHT	71.1	46.8	6.7	44	68	
8	YUN4708	CCH	28.3	44.9	5.7	40	60	O
9	YUN4709	CCH	36.3	36.3	5.3	40	60	
10	YUN4710	CCH	55.3	28.1	5.4	40	60	

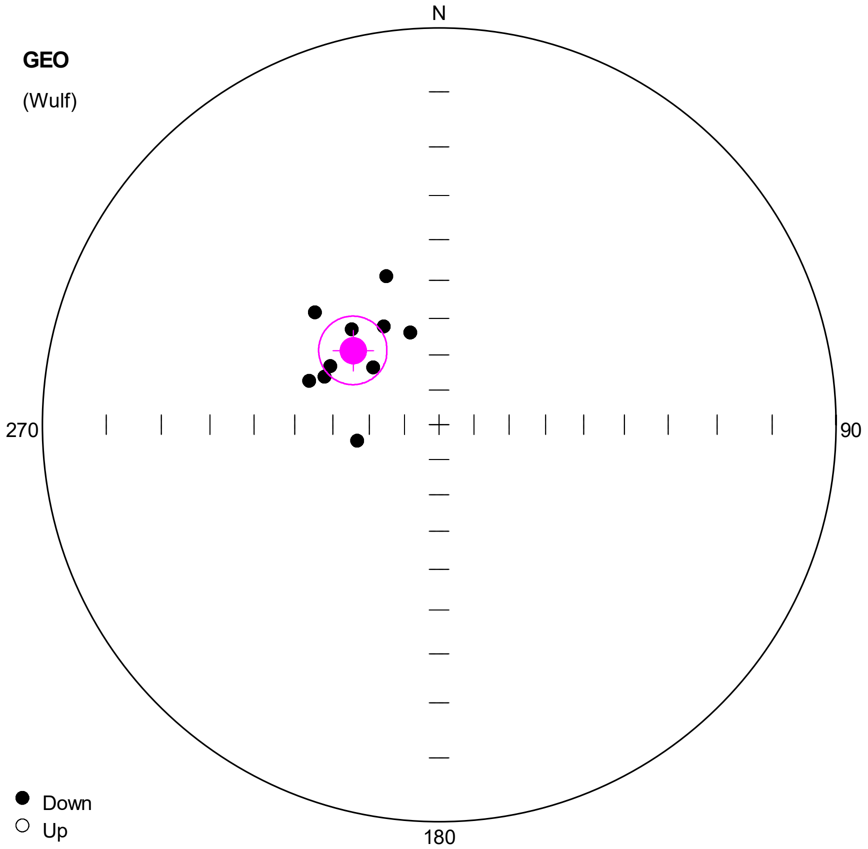

Number of data points: 10

Fisher statistics

Mean vector: 310.78 / 58.14
Resultant vector: 9.69
(X= 3.34, Y= -3.87, Z= 8.23)
Estimated precision, k: 28.98
95% Confidence limit: 9.13
95% Confidence limit, approximation: 8.22

Orientation matrix

1st eigenvalue: 0.94
1st eigenvector: 310.82 / 58.05
2nd eigenvalue: 0.04
2nd eigenvector: 206.45 / 8.8
3rd eigenvalue: 0.02
3rd eigenvector: 111.23 / 30.43

VGP

Site latitude: 65
Site longitude: 14.04
Pole latitude: 51.55 (-51.55)
Pole longitude: -94.37 (85.63)
Paleolatitude: 38.81 (-38.81)
dp: 9.94
dm: 13.47

#	Name	State	Dec	Inc	MAD	Limit1	Limit2
1	YUN4901	CCH	258.9	66.3	10.4	35	64
2	YUN4902	CCH	292.7	55.3	14.3	30	64
3	YUN4903	CCH	288.7	51.9	14.5	40	64
4	YUN4904	CCH	298.3	55.4	8.1	35	64
5	YUN4905	CCH	312.1	44.3	5.3	40	64
6	YUN4906	CCH	340.4	46.7	6.6	35	60
7	YUN4907	CCH	342.7	62.7	4.8	40	64
8	YUN4908	CCH	330.7	58.3	4.0	35	64
9	YUN4909	CCH	317.5	53.9	3.0	44	64
10	YUN4910	CCH	311.0	65.2	12.9	40	64

TILT CORR

(Wulf)

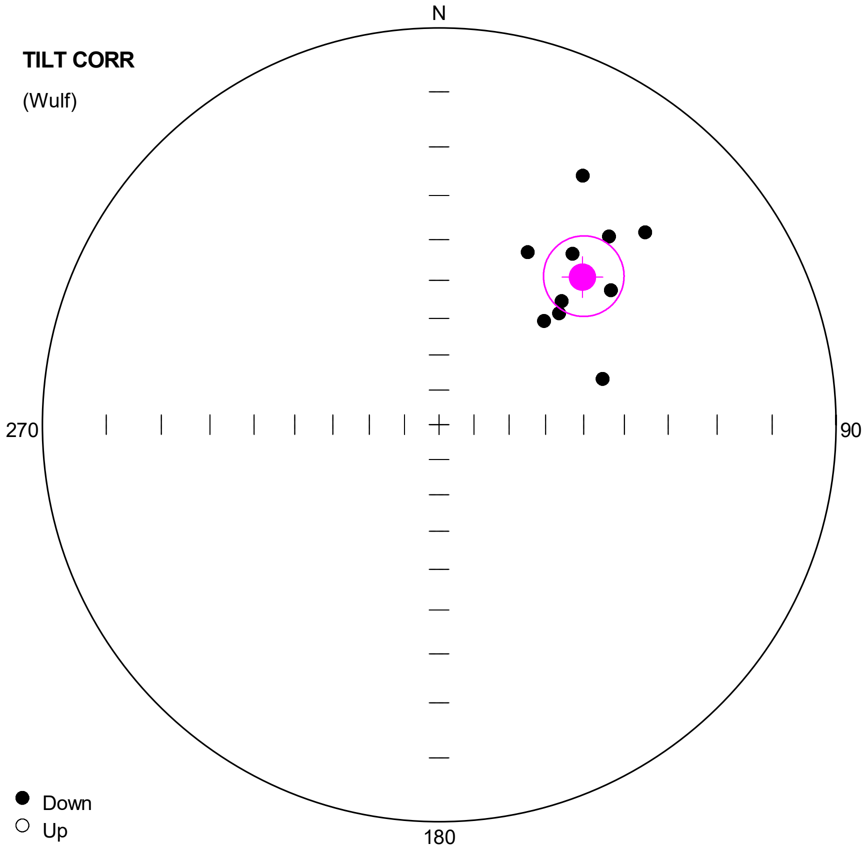

Number of data points: 10

Fisher statistics

Mean vector: 44.16 / 35.21
Resultant vector: 9.69
(X= 5.68, Y= 5.52, Z= 5.59)
Estimated precision, k: 28.95
95% Confidence limit: 9.13
95% Confidence limit, approximation: 8.23

Orientation matrix

1st eigenvalue: 0.94
1st eigenvector: 44.06 / 35.22
2nd eigenvalue: 0.04
2nd eigenvector: 171.65 / 40.83
3rd eigenvalue: 0.02
3rd eigenvector: 290.69 / 29.33

VGP

Site latitude: 65
Site longitude: 14.04
Pole latitude: 35.98 (-35.98)
Pole longitude: 139.76 (-40.24)
Paleolatitude: 19.44 (-19.44)
dp: 6.08
dm: 10.54

#	Name	State	Dec	Inc	MAD	Limit1	Limit2
1	YUN4901	CCH	74.4	43.7	10.4	35	64
2	YUN4902	CCH	47.2	45.2	14.3	30	64
3	YUN4903	CCH	45.4	49.2	14.5	40	64
4	YUN4904	CCH	44.8	42.6	8.1	35	64
5	YUN4905	CCH	27.2	37.9	5.3	40	64
6	YUN4906	CCH	30.0	18.2	6.6	35	60
7	YUN4907	CCH	47.0	19.2	4.8	40	64
8	YUN4908	CCH	42.1	24.9	4.0	35	64
9	YUN4909	CCH	38.0	32.7	3.0	44	64
10	YUN4910	CCH	52.0	32.4	12.9	40	64

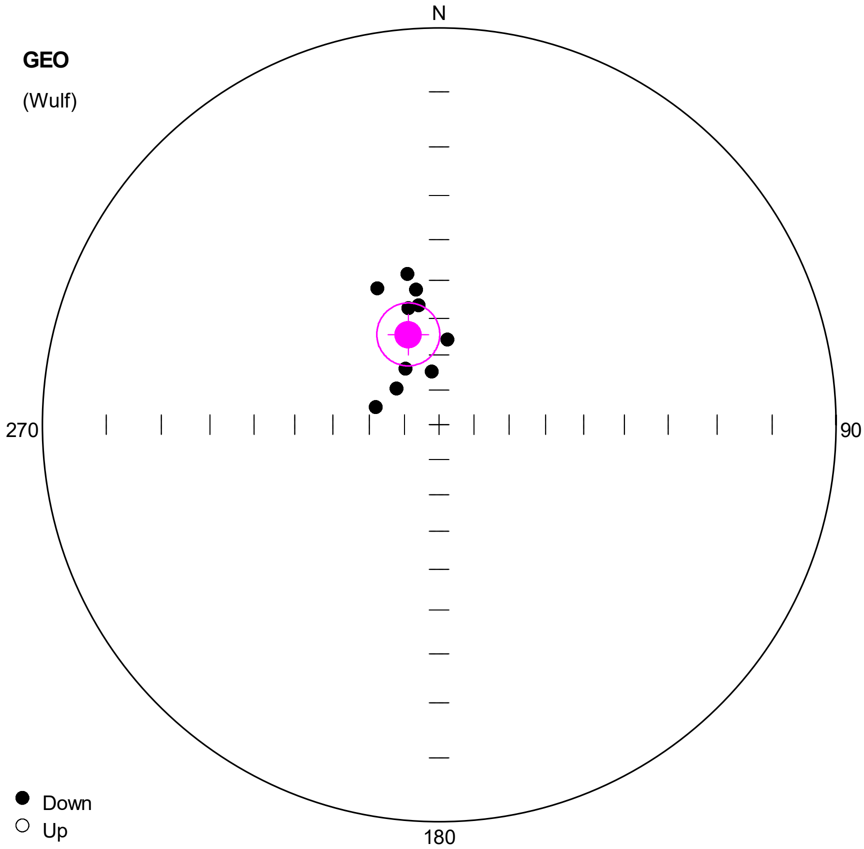

Number of data points: 10

Fisher statistics
Mean vector: 341.08 / 63.06
Resultant vector: 9.72
(X= 4.17, Y= -1.43, Z= 8.67)
Estimated precision, k: 32.72
95% Confidence limit: 8.57
95% Confidence limit, approximation: 7.74

Orientation matrix
1st eigenvalue: 0.95
1st eigenvector: 341.31 / 62.98
2nd eigenvalue: 0.04
2nd eigenvector: 188.13 / 24.47
3rd eigenvalue: 0.01
3rd eigenvector: 93.17 / 10.75

VGP
Site latitude: 65
Site longitude: 14.04
Pole latitude: 67.01 (-67.01)
Pole longitude: -129.67 (50.33)
Paleolatitude: 44.53 (-44.53)
dp: 10.61
dm: 13.49

#	Name	State	Dec	Inc	MAD	Limit1	Limit2	
1	YUN5001	CCH	310.3	74.0	8.7	48	60	
2	YUN5002	CCH	285.5	71.2	4.2	44	60	O
3	YUN5003	CCH	348.2	47.6	5.3	40	64	O
4	YUN5004	CCH	329.1	71.3	12.9	48	64	O
5	YUN5005	CCH	352.1	74.6	8.7	35	60	
6	YUN5006	CCH	335.7	48.7	4.4	30	60	
7	YUN5007	CCH	350.4	51.9	3.7	35	60	
8	YUN5008	CCH	350.3	56.1	5.8	35	64	
9	YUN5009	CCH	345.3	56.3	5.8	35	64	
10	YUN5010	CCH	5.6	65.7	8.2	35	64	

TILT CORR

(Wulf)

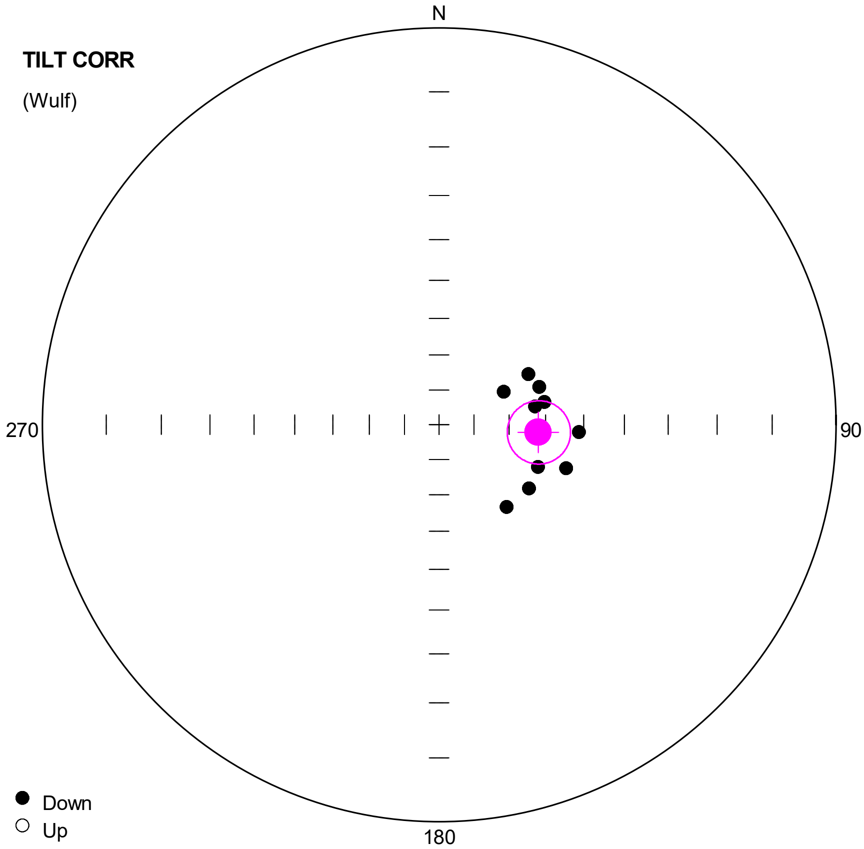

Number of data points: 10

Fisher statistics

Mean vector: 94.32 / 61.92
Resultant vector: 9.72
(X= -0.35, Y= 4.56, Z= 8.58)
Estimated precision, k: 32.67
95% Confidence limit: 8.58
95% Confidence limit, approximation: 7.75

Orientation matrix

1st eigenvalue: 0.95
1st eigenvector: 94.08 / 61.86
2nd eigenvalue: 0.04
2nd eigenvector: 359.92 / 2.22
3rd eigenvalue: 0.01
3rd eigenvector: 268.74 / 28.03

VGP

Site latitude: 65
Site longitude: 14.04
Pole latitude: 36.62 (-36.62)
Pole longitude: 79.07 (-100.93)
Paleolatitude: 43.14 (-43.14)
dp: 10.31
dm: 13.3

#	Name	State	Dec	Inc	MAD	Limit1	Limit2	
1	YUN5001	CCH	125.3	58.9	8.7	48	60	
2	YUN5002	CCH	140.6	59.9	4.2	44	60	O
3	YUN5003	CCH	60.5	61.0	5.3	40	64	O
4	YUN5004	CCH	113.1	59.7	12.9	48	64	O
5	YUN5005	CCH	109.0	52.6	8.7	35	60	
6	YUN5006	CCH	63.0	69.3	4.4	30	60	
7	YUN5007	CCH	69.4	59.8	3.7	35	60	
8	YUN5008	CCH	77.9	59.6	5.8	35	64	
9	YUN5009	CCH	79.2	62.3	5.8	35	64	
10	YUN5010	CCH	93.0	51.1	8.2	35	64	

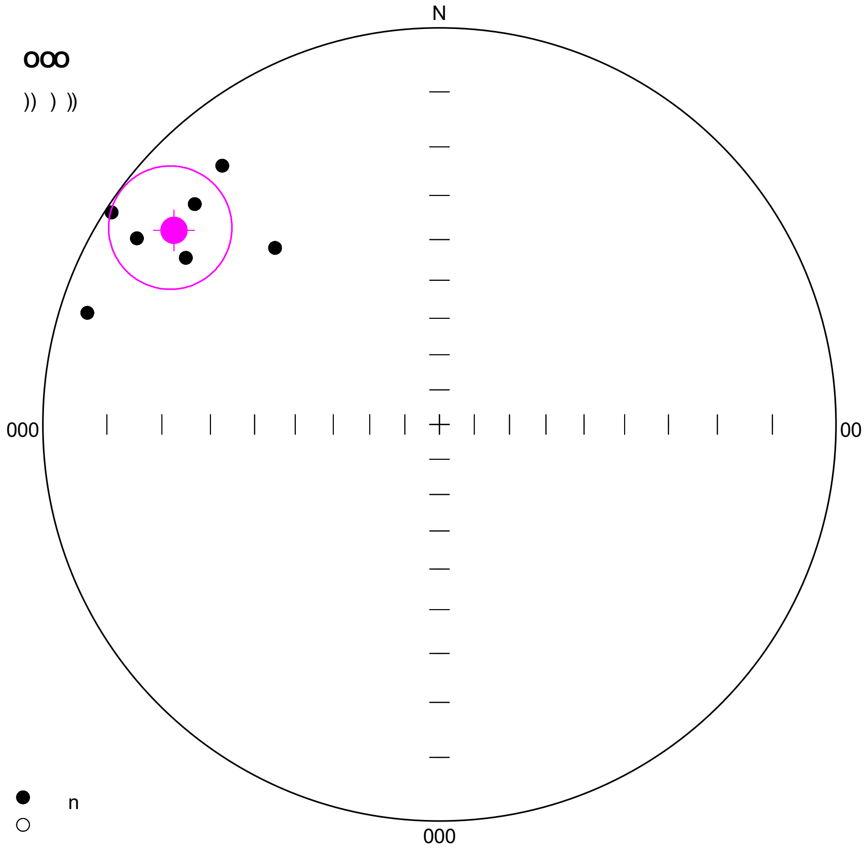

7 77 7777777777777777777

s7s77777777s7

7 7 77 0 7700 700770

) 7 7 7 77 7700

))) 707))))7)0))) 0707)

722 7 72 2) 2)700

0)7)2 7 2227 00)70

0)7)2 7 2227) 22 72 070)

O777777777 777x

0 7 25 7) 070)

0 7 25 7 77 0 7707 007

0 25 7) 07 0)

0 25 7 77) 7) 7 77

25 7) 0700

25 7 77 000707))7

POP

27 727) 7)

27 5 27) 0)7 0)

727) 007) 0) 007)0)

527) 0007)0)007)0)

727)) 7 0))7 0)

) 7 0

2 0077

77	7 77 777777	7777777	777 7s	7777s	777	77 77 7777	77 77 7777
0	) NN) 000		0070	0077	0 70	0	70
0	) NN) 000	7	00077	) 70	) 70	))	70
	) NN) 00	7	0 7	0) 70	77	) 0	70
)	) NN) 00)		0070	070	0070	0	70
)	) NN) 00)	7	0070	007)	070	) 0	) 7
7	) NN) 007		0070	070	007)	0	) 7
0	) NN) 000		0077	77	070	))	) 7

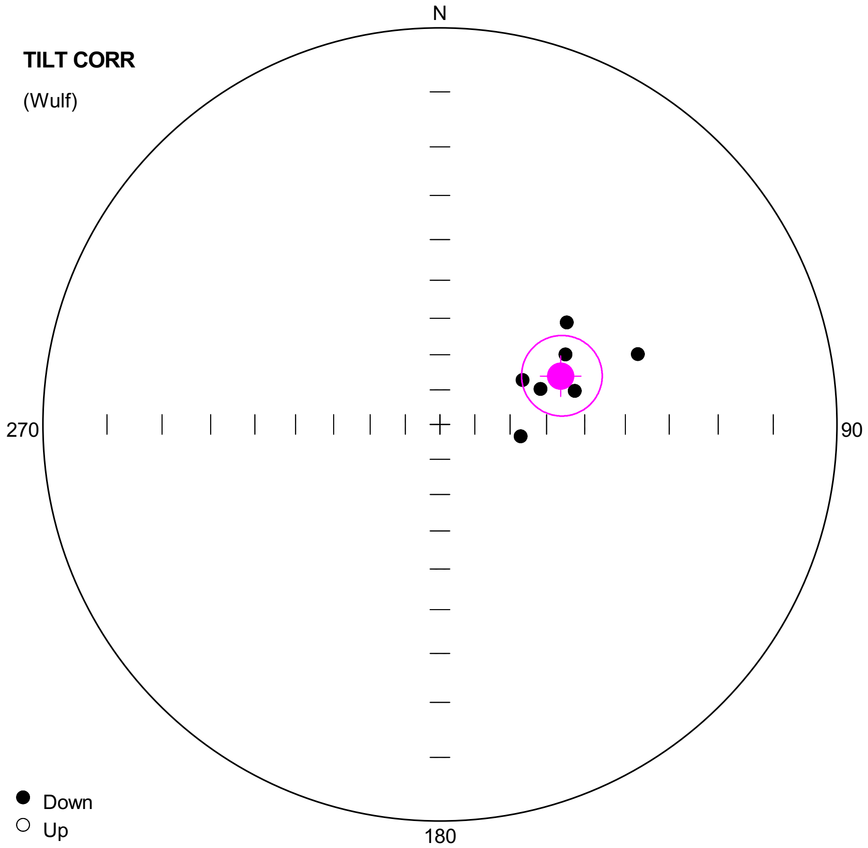

Number of data points: 7

Fisher statistics

Mean vector: 68.16 / 53.73

Resultant vector: 6.82

(X= 1.5, Y= 3.75, Z= 5.5)

Estimated precision, k: 34.21

95% Confidence limit: 10.47

95% Confidence limit, approximation: 9.05

Orientation matrix

1st eigenvalue: 0.95

1st eigenvector: 68.06 / 53.77

2nd eigenvalue: 0.04

2nd eigenvector: 223.31 / 33.64

3rd eigenvalue: 0.01

3rd eigenvector: 321.36 / 11.89

VGP

Site latitude: 65

Site longitude: 14.04

Pole latitude: 39.81 (-39.81)

Pole longitude: 107.07 (-72.93)

Paleolatitude: 34.27 (-34.27)

dp: 10.21

dm: 14.62

#	Name	State	Dec	Inc	MAD	Limit1	Limit2
1	YUNN5101	Ch	60.8	50.2	13.8	30	60
2	YUNN5102	Cht	98.4	66.8	5.9	44	60
3	YUNN5103	Cht	76.0	51.4	3.6	48	60
4	YUNN5104	Ch	61.7	63.4	12.8	30	60
5	YUNN5105	Cht	70.4	34.2	8.2	40	56
6	YUNN5106	Ch	51.2	45.4	17.4	30	56
7	YUNN5108	Ch	70.6	59.9	8.9	44	56

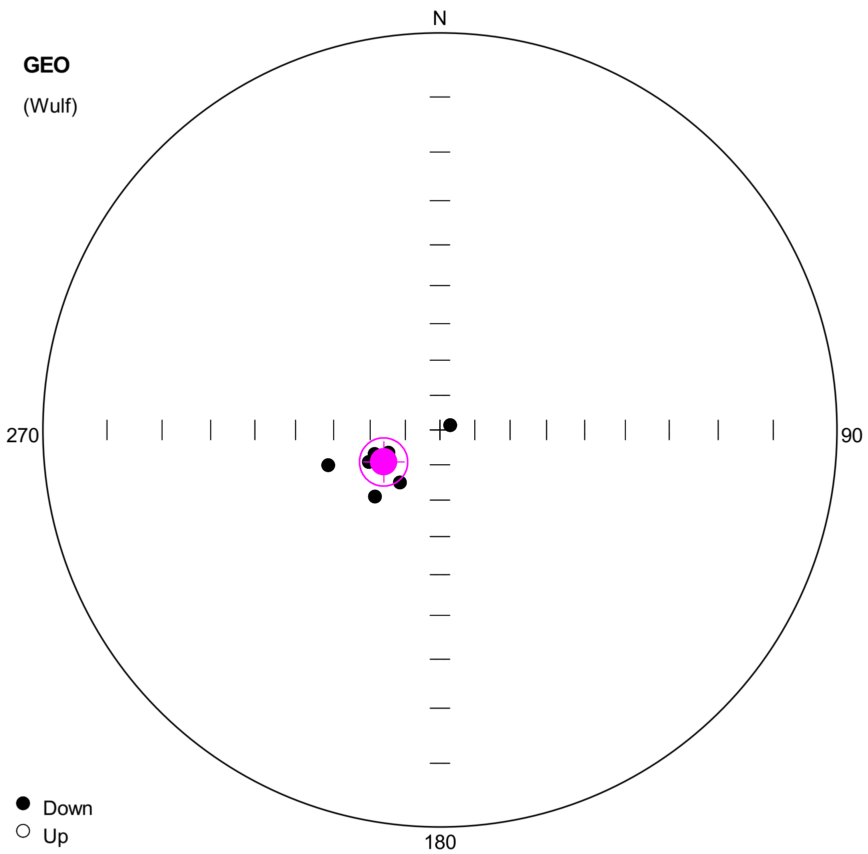

Number of data points: 9

Fisher statistics

Mean vector: 240.51 / 71.51
Resultant vector: 8.86
(X= -1.38, Y= -2.45, Z= 8.41)
Estimated precision, k: 58.83
95% Confidence limit: 6.77
95% Confidence limit, approximation: 6.08

Orientation matrix

1st eigenvalue: 0.97
1st eigenvector: 240.49 / 71.4
2nd eigenvalue: 0.02
2nd eigenvector: 66.96 / 18.49
3rd eigenvalue: 0.01
3rd eigenvector: 336.31 / 1.95

VGP

Site latitude: 65
Site longitude: 14.04
Pole latitude: 39.63 (-39.63)
Pole longitude: -24.87 (155.13)
Paleolatitude: 56.23 (-56.23)
dp: 10.4
dm: 11.86

#	Name	State	Dec	Inc	MAD	Limit1	Limit2
1	YUNN5201	Clt	249.7	70.1	7.9	35	48
2	YUNN5202	Ch	244.4	72.0	3.8	30	60
3	YUNN5204	Ch	65.7	86.7	4.5	35	60
4	YUNN5205	Cht	224.3	63.6	3.6	44	60
5	YUNN5206	Cht	217.2	71.1	4.8	40	60
6	YUNN5207	Cht	245.7	67.8	3.8	35	60
7	YUNN5208	Ch	252.5	57.1	7.7	30	60
8	YUNN5209	Ch	241.9	71.6	3.9	30	60
9	YUNN5210	Ch	246.2	73.9	6.4	35	60

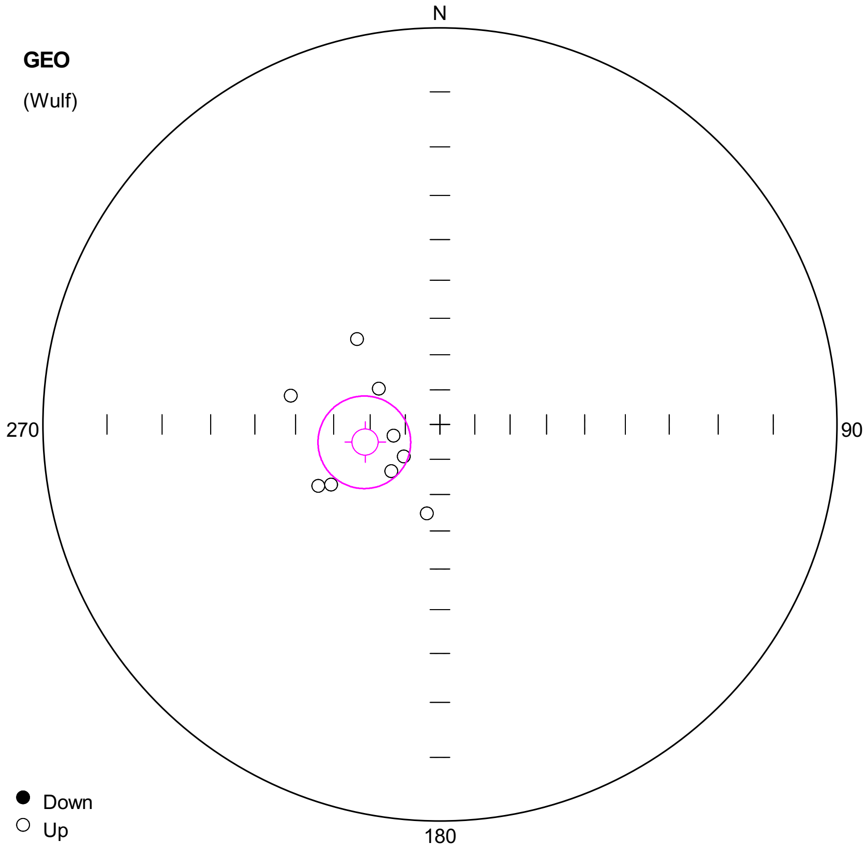

Number of data points: 9

Fisher statistics

Mean vector: 256.79 / -68.12
Resultant vector: 8.53
(X= -0.73, Y= -3.1, Z= -7.92)
Estimated precision, k: 17.06
95% Confidence limit: 12.83
95% Confidence limit, approximation: 11.3

Orientation matrix

1st eigenvalue: 0.9
1st eigenvector: 76.19 / 68.16
2nd eigenvalue: 0.07
2nd eigenvector: 335.3 / 4.33
3rd eigenvalue: 0.03
3rd eigenvector: 243.6 / 21.36

VGP

Site latitude: 65
Site longitude: 14.04
Pole latitude: -50.09 (50.09)
Pole longitude: -94.1 (85.9)
Paleolatitude: -51.23 (51.23)
dp: 18.11
dm: 21.56

#	Name	State	Dec	Inc	MAD	Limit1	Limit2	
1	YUNN5201	CHT	228.3	-76.1	1.0	64	64	OA
2	YUNN5202	CHT	226.2	-70.7	1.0	64	64	OA
3	YUNN5204	CHT	243.2	-52.1	1.0	64	64	OA
4	YUNN5205	CHT	300.3	-69.8	1.0	64	64	OA
5	YUNN5206	CHT	241.1	-55.2	1.0	64	64	OA
6	YUNN5207	CHT	280.9	-48.1	1.0	64	64	OA
7	YUNN5208	CHT	188.3	-64.5	1.0	64	64	OA
8	YUNN5209	CHT	256.5	-76.3	1.0	64	64	OA
9	YUNN5210	CHT	315.9	-56.6	1.0	64	64	OA

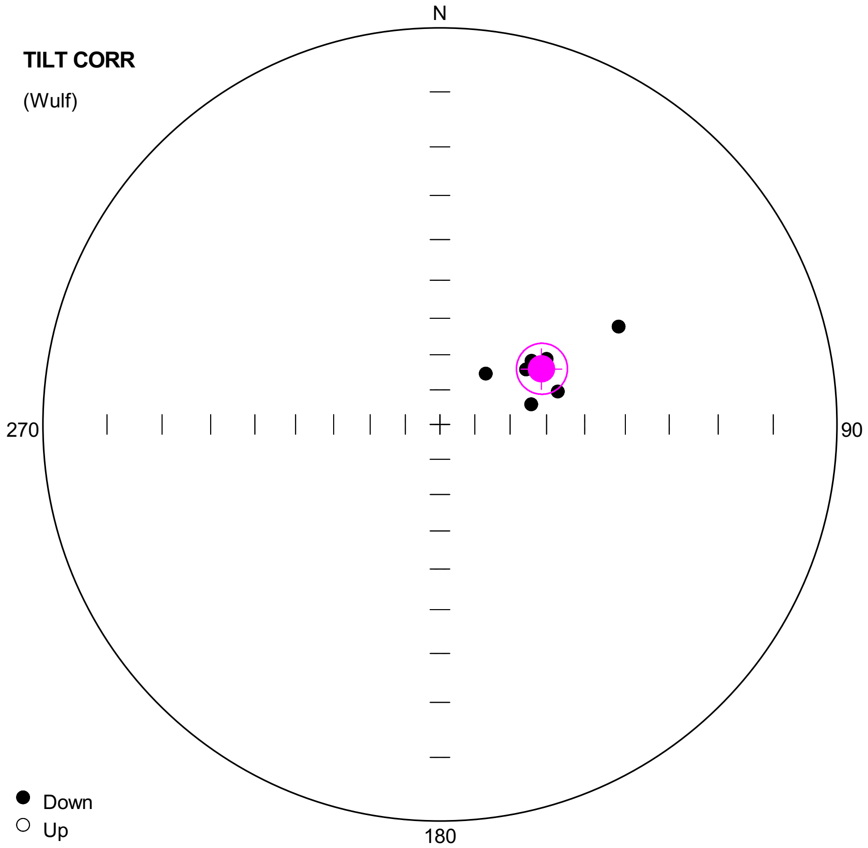

Number of data points: 9

Fisher statistics

Mean vector: 61.29 / 57.49
Resultant vector: 8.86
(X= 2.29, Y= 4.18, Z= 7.47)
Estimated precision, k: 58.75
95% Confidence limit: 6.77
95% Confidence limit, approximation: 6.09

Orientation matrix

1st eigenvalue: 0.97
1st eigenvector: 61.3 / 57.6
2nd eigenvalue: 0.02
2nd eigenvector: 247.59 / 32.24
3rd eigenvalue: 0.01
3rd eigenvector: 155.79 / 2.85

VGP

Site latitude: 65
Site longitude: 14.04
Pole latitude: 45.99 (-45.99)
Pole longitude: 110.79 (-69.21)
Paleolatitude: 38.12 (-38.12)
dp: 7.26
dm: 9.91

#	Name	State	Dec	Inc	MAD	Limit1	Limit2
1	YUNN5201	Clt	55.3	58.6	7.9	35	48
2	YUNN5202	Ch	59.1	56.9	3.8	30	60
3	YUNN5204	Ch	61.3	35.7	4.5	35	60
4	YUNN5205	Cht	77.6	63.5	3.6	44	60
5	YUNN5206	Cht	74.4	55.7	4.8	40	60
6	YUNN5207	Cht	57.4	61.1	3.8	35	60
7	YUNN5208	Ch	42.1	70.4	7.7	30	60
8	YUNN5209	Ch	60.5	57.4	3.9	30	60
9	YUNN5210	Ch	58.5	55.0	6.4	35	60

TILT CORR

(Wulf)

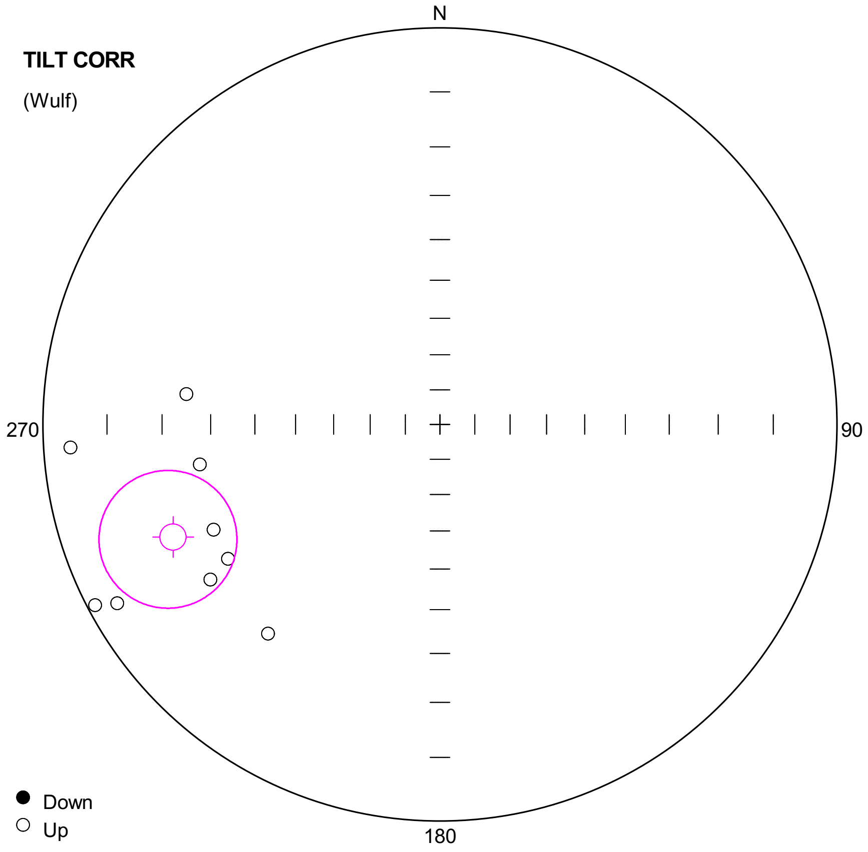

Number of data points: 9

Fisher statistics

Mean vector: 247.1 / -17.77
Resultant vector: 8.53
(X= -3.16, Y= -7.48, Z= -2.6)
Estimated precision, k: 17.03
95% Confidence limit: 12.84
95% Confidence limit, approximation: 11.31

Orientation matrix

1st eigenvalue: 0.9
1st eigenvector: 66.86 / 17.77
2nd eigenvalue: 0.07
2nd eigenvector: 157.12 / 0.82
3rd eigenvalue: 0.03
3rd eigenvector: 249.68 / 72.21

VGP

Site latitude: 65
Site longitude: 14.04
Pole latitude: -17.81 (17.81)
Pole longitude: -58.77 (121.23)
Paleolatitude: -9.1 (9.1)
dp: 6.9
dm: 13.32

#	Name	State	Dec	Inc	MAD	Limit1	Limit2	
1	YUNN5201	CHT	237.6	-25.4	1.0	64	64	OA
2	YUNN5202	CHT	235.9	-20.2	1.0	64	64	OA
3	YUNN5204	CHT	242.3	-1.1	1.0	64	64	OA
4	YUNN5205	CHT	260.5	-27.0	1.0	64	64	OA
5	YUNN5206	CHT	241.0	-4.2	1.0	64	64	OA
6	YUNN5207	CHT	266.4	-4.0	1.0	64	64	OA
7	YUNN5208	CHT	219.4	-21.4	1.0	64	64	OA
8	YUNN5209	CHT	245.0	-25.7	1.0	64	64	OA
9	YUNN5210	CHT	276.8	-24.5	1.0	64	64	OA

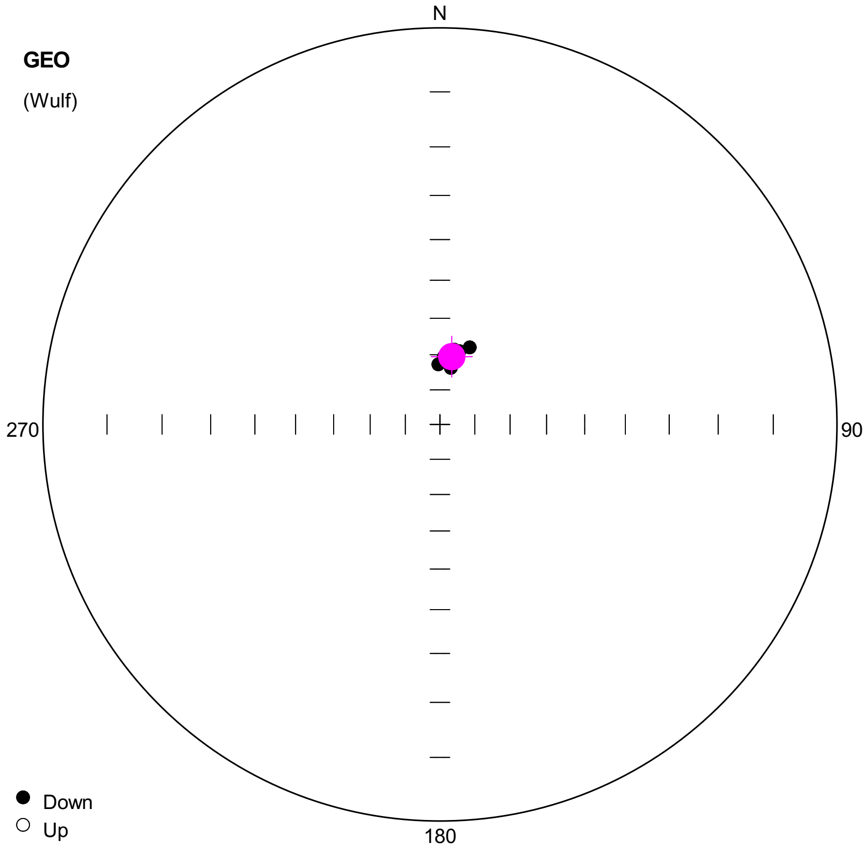

Number of data points: 10

Fisher statistics

Mean vector: 9.95 / 70.33
Resultant vector: 9.99
(X= 3.31, Y= 0.58, Z= 9.4)
Estimated precision, k: 715.32
95% Confidence limit: 1.81
95% Confidence limit, approximation: 1.66

Orientation matrix

1st eigenvalue: 1
1st eigenvector: 9.94 / 70.33
2nd eigenvalue: 0
2nd eigenvector: 239.7 / 13.01
3rd eigenvalue: 0
3rd eigenvector: 146.28 / 14.5

VGP

Site latitude: 65
Site longitude: 14.04
Pole latitude: 78.33 (-78.33)
Pole longitude: 164.25 (-15.75)
Paleolatitude: 54.43 (-54.43)
dp: 2.7
dm: 3.12

#	Name	State	Dec	Inc	MAD	Limit1	Limit2
1	YUNN5301	Ch	10.6	68.3	5.1	35	60
2	YUNN5302	Ch	21.1	66.5	5.6	20	68
3	YUNN5303	Ch	11.1	73.5	5.0	20	68
4	YUNN5304	Ch	5.9	70.2	3.1	20	68
5	YUNN5305	Ch	5.3	71.1	2.6	20	68
6	YUNN5306	Ch	14.9	68.4	2.5	35	68
7	YUNN5307	Ch	13.3	70.1	5.0	40	68
8	YUNN5308	Ch	3.4	70.7	4.4	35	68
9	YUNN5309	Ch	11.2	70.6	3.7	30	68
10	YUNN5310	Ch	358.6	72.8	4.2	20	68

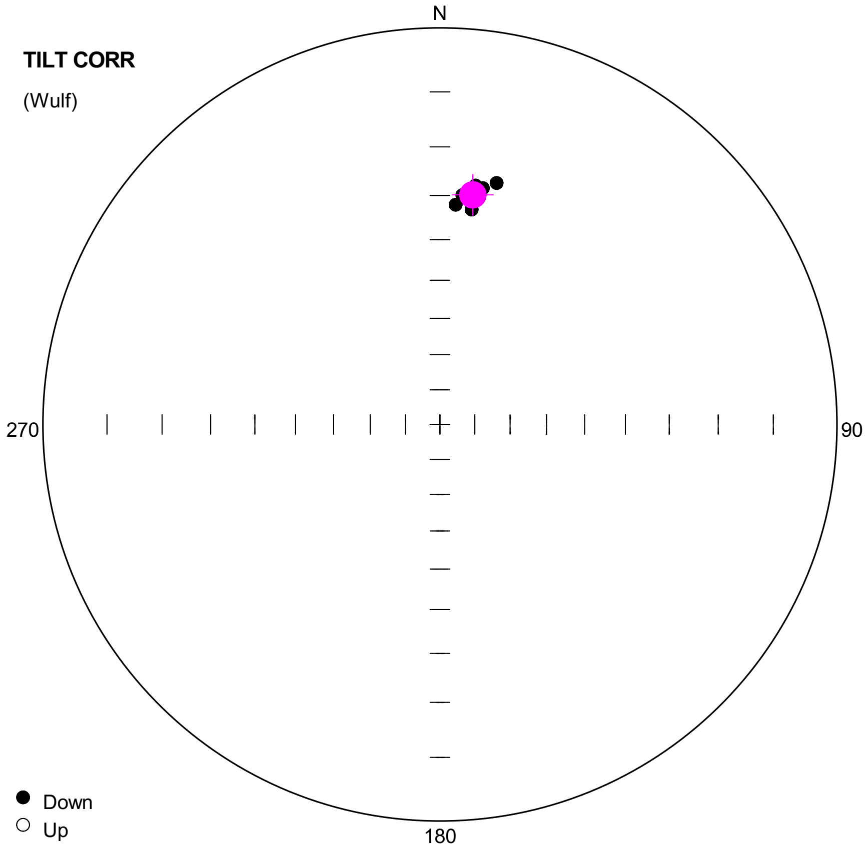

Number of data points: 10

Fisher statistics

Mean vector: 8.15 / 29.34
Resultant vector: 9.99
(X= 8.62, Y= 1.23, Z= 4.89)
Estimated precision, k: 713.21
95% Confidence limit: 1.81
95% Confidence limit, approximation: 1.66

Orientation matrix

1st eigenvalue: 1
1st eigenvector: 8.15 / 29.34
2nd eigenvalue: 0
2nd eigenvector: 255.96 / 33.9
3rd eigenvalue: 0
3rd eigenvector: 128.63 / 42.06

VGP

Site latitude: 65
Site longitude: 14.04
Pole latitude: 40.39 (-40.39)
Pole longitude: -176.28 (3.72)
Paleolatitude: 15.7 (-15.7)
dp: 1.1
dm: 2

#	Name	State	Dec	Inc	MAD	Limit1	Limit2
1	YUNN5301	Ch	8.5	27.3	5.1	35	60
2	YUNN5302	Ch	13.2	26.0	5.6	20	68
3	YUNN5303	Ch	8.4	32.6	5.0	20	68
4	YUNN5304	Ch	6.6	29.2	3.1	20	68
5	YUNN5305	Ch	6.4	30.1	2.6	20	68
6	YUNN5306	Ch	10.3	27.6	2.5	35	68
7	YUNN5307	Ch	9.5	29.1	5.0	40	68
8	YUNN5308	Ch	5.6	29.7	4.4	35	68
9	YUNN5309	Ch	8.6	29.7	3.7	30	68
10	YUNN5310	Ch	4.1	31.9	4.2	20	68

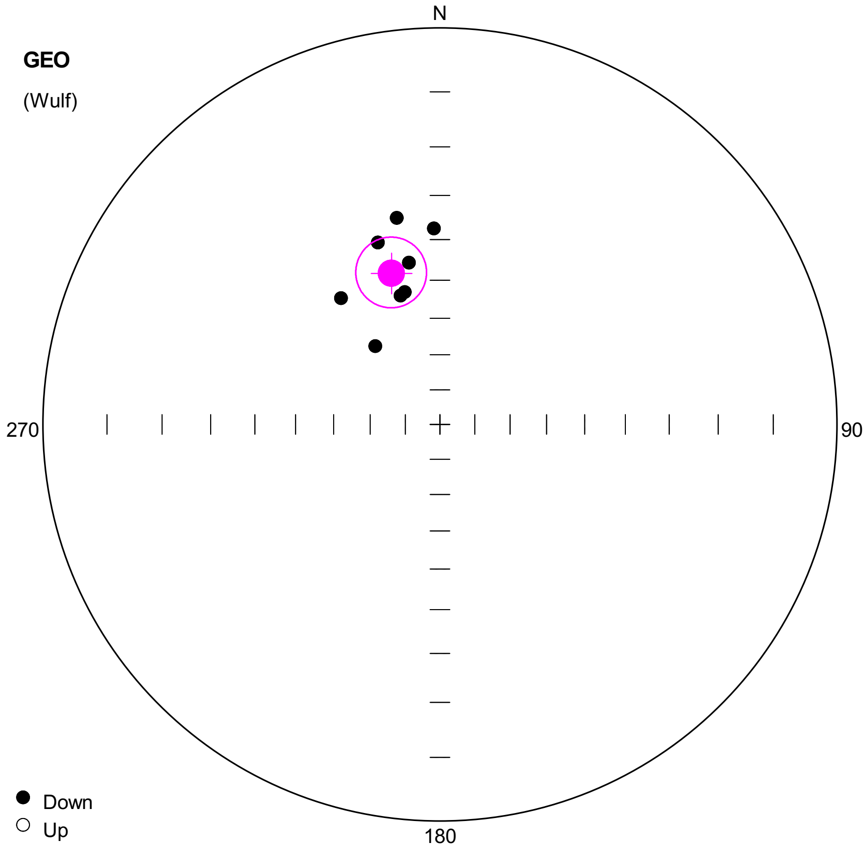

Number of data points: 8

Fisher statistics

Mean vector: 342.2 / 46.4

Resultant vector: 7.83

(X= 5.14, Y= -1.65, Z= 5.67)

Estimated precision, k: 40.81

95% Confidence limit: 8.77

95% Confidence limit, approximation: 7.75

Orientation matrix

1st eigenvalue: 0.96

1st eigenvector: 342.28 / 46.35

2nd eigenvalue: 0.03

2nd eigenvector: 212.16 / 31.58

3rd eigenvalue: 0.01

3rd eigenvector: 104.13 / 26.72

VGP

Site latitude: 65

Site longitude: 14.04

Pole latitude: 51.04 (-51.04)

Pole longitude: -140.47 (39.53)

Paleolatitude: 27.7 (-27.7)

dp: 7.23

dm: 11.27

#	Name	State	Dec	Inc	MAD	Limit1	Limit2
1	YUNN5401	Ch	341.2	38.3	12.1	20	52
2	YUNN5402	Ch	345.1	51.9	7.9	20	60
3	YUNN5403	Ch	349.2	44.9	3.7	20	60
4	YUNN5404	Ch	358.2	37.4	8.0	35	68
5	YUNN5405	Ch	348.2	34.0	5.4	30	68
6	YUNN5406	Ch	343.0	52.5	5.5	30	64
7	YUNN5409	Clt	321.9	46.0	20.0	20	48
8	YUNN5410	Ch	320.6	61.3	3.8	40	64

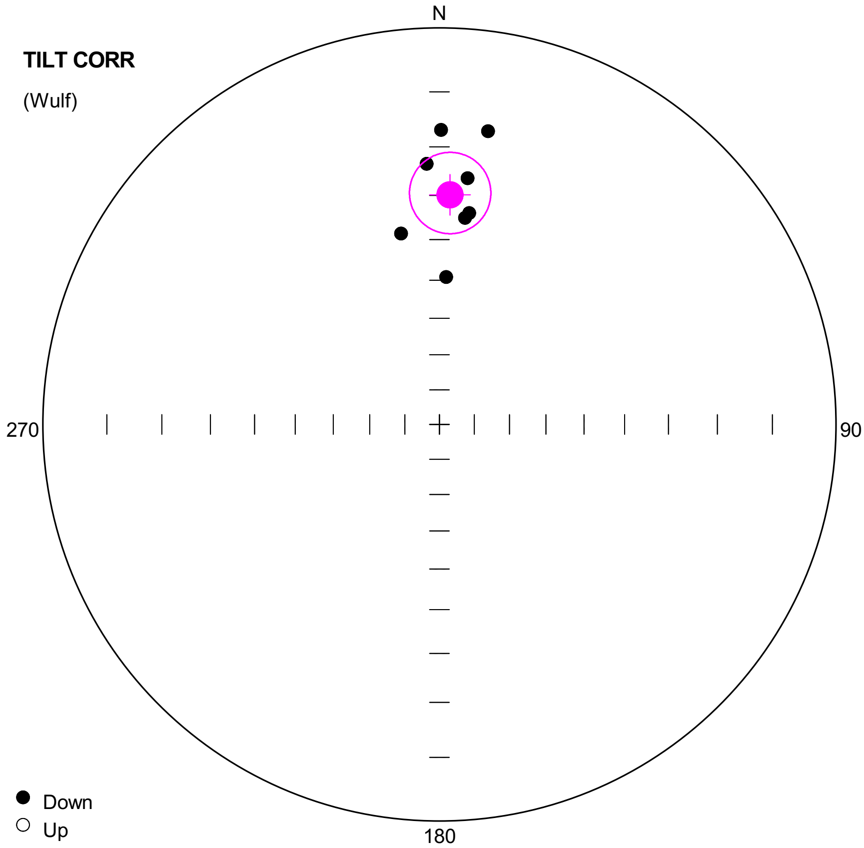

Number of data points: 8

Fisher statistics

Mean vector: 2.63 / 29.8
Resultant vector: 7.83
(X= 6.79, Y= 0.31, Z= 3.89)
Estimated precision, k: 40.93
95% Confidence limit: 8.76
95% Confidence limit, approximation: 7.74

Orientation matrix

1st eigenvalue: 0.96
1st eigenvector: 2.65 / 29.73
2nd eigenvalue: 0.03
2nd eigenvector: 199.54 / 59.17
3rd eigenvalue: 0.01
3rd eigenvector: 96.92 / 7.43

VGP

Site latitude: 65
Site longitude: 14.04
Pole latitude: 40.95 (-40.95)
Pole longitude: -169.3 (10.7)
Paleolatitude: 15.98 (-15.98)
dp: 5.38
dm: 9.71

#	**Name**	**State**	**Dec**	**Inc**	**MAD**	**Limit1**	**Limit2**
1	YUNN5401	Ch	357.2	23.3	12.1	20	52
2	YUNN5402	Ch	8.0	33.4	7.9	20	60
3	YUNN5403	Ch	6.5	26.0	3.7	20	60
4	YUNN5404	Ch	9.4	16.3	8.0	35	68
5	YUNN5405	Ch	0.3	16.8	5.4	30	68
6	YUNN5406	Ch	7.1	34.6	5.5	30	64
7	YUNN5409	Clt	348.7	37.7	20.0	20	48
8	YUNN5410	Ch	2.6	49.2	3.8	40	64

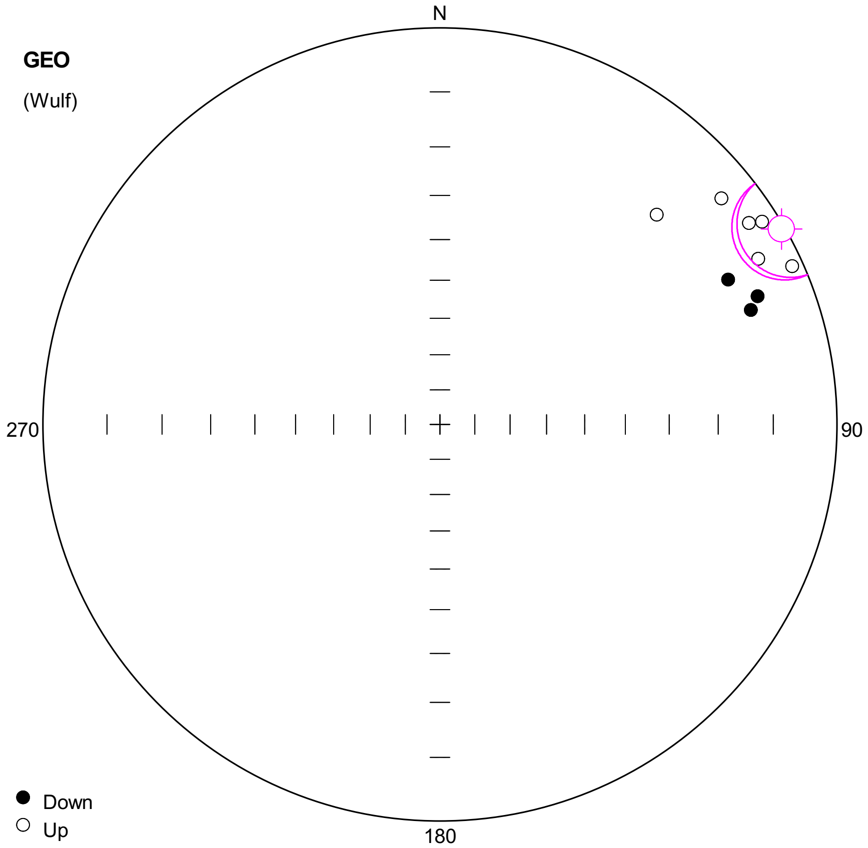

Number of data points: 9

Fisher statistics

Mean vector: 60.17 / -0.49
Resultant vector: 8.83
(X= 4.39, Y= 7.66, Z= -0.08)
Estimated precision, k: 46.48
95% Confidence limit: 7.63
95% Confidence limit, approximation: 6.84

Orientation matrix

1st eigenvalue: 0.96
1st eigenvector: 240.23 / 0.46
2nd eigenvalue: 0.03
2nd eigenvector: 149.67 / 49.97
3rd eigenvalue: 0
3rd eigenvector: 330.61 / 40.02

VGP

Site latitude: 65
Site longitude: 14.04
Pole latitude: 11.91 (-11.91)
Pole longitude: 131.59 (-48.41)
Paleolatitude: -0.25 (0.25)
dp: 3.82
dm: 7.63

#	Name	State	Dec	Inc	MAD	Limit1	Limit2
1	YUNN5502	Ch	45.9	-15.5	7.2	30	68
2	YUNN5503	Ch	69.8	10.3	4.5	35	68
3	YUNN5504	Ch	63.3	11.8	14.0	20	68
4	YUNN5505	Ch	57.8	-2.4	10.2	30	68
5	YUNN5506	Ch	62.5	-5.8	6.6	30	68
6	YUNN5507	Cht	65.8	-1.6	5.7	48	68
7	YUNN5508	Ch	56.9	-4.2	8.5	30	68
8	YUNN5509	Ch	68.0	8.4	10.0	30	68
9	YUNN5510	Ch	51.2	-5.4	16.8	30	64

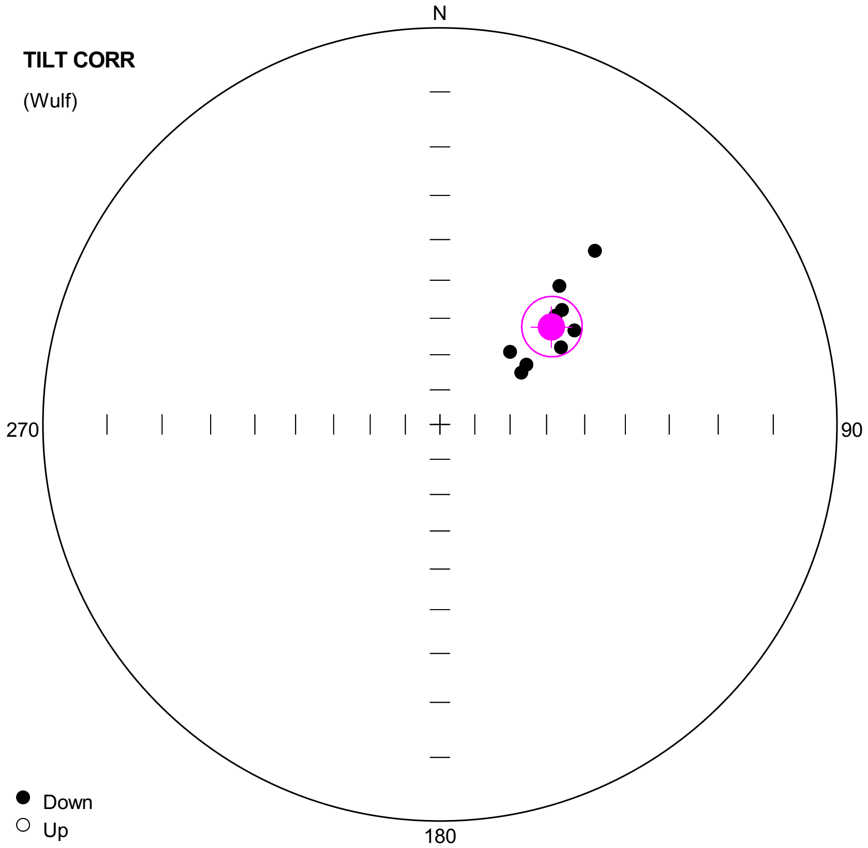

Number of data points: 9

Fisher statistics
Mean vector: 48.77 / 49.1
Resultant vector: 8.83
(X= 3.81, Y= 4.35, Z= 6.67)
Estimated precision, k: 46.32
95% Confidence limit: 7.64
95% Confidence limit, approximation: 6.86

Orientation matrix
1st eigenvalue: 0.96
1st eigenvector: 48.83 / 49.16
2nd eigenvalue: 0.03
2nd eigenvector: 208.91 / 39.1
3rd eigenvalue: 0
3rd eigenvector: 307.11 / 9.96

VGP
Site latitude: 65
Site longitude: 14.04
Pole latitude: 43.97 (-43.97)
Pole longitude: 129.2 (-50.8)
Paleolatitude: 30 (-30)
dp: 6.69
dm: 10.11

#	Name	State	Dec	Inc	MAD	Limit1	Limit2
1	YUNN5502	Ch	41.7	29.2	7.2	30	68
2	YUNN5503	Ch	57.6	62.7	4.5	35	68
3	YUNN5504	Ch	44.0	61.5	14.0	20	68
4	YUNN5505	Ch	46.8	46.4	10.2	30	68
5	YUNN5506	Ch	55.0	45.1	6.6	30	68
6	YUNN5507	Cht	57.5	50.2	5.7	48	68
7	YUNN5508	Ch	46.8	44.3	8.5	30	68
8	YUNN5509	Ch	55.4	60.3	10.0	30	68
9	YUNN5510	Ch	40.8	40.5	16.8	30	64

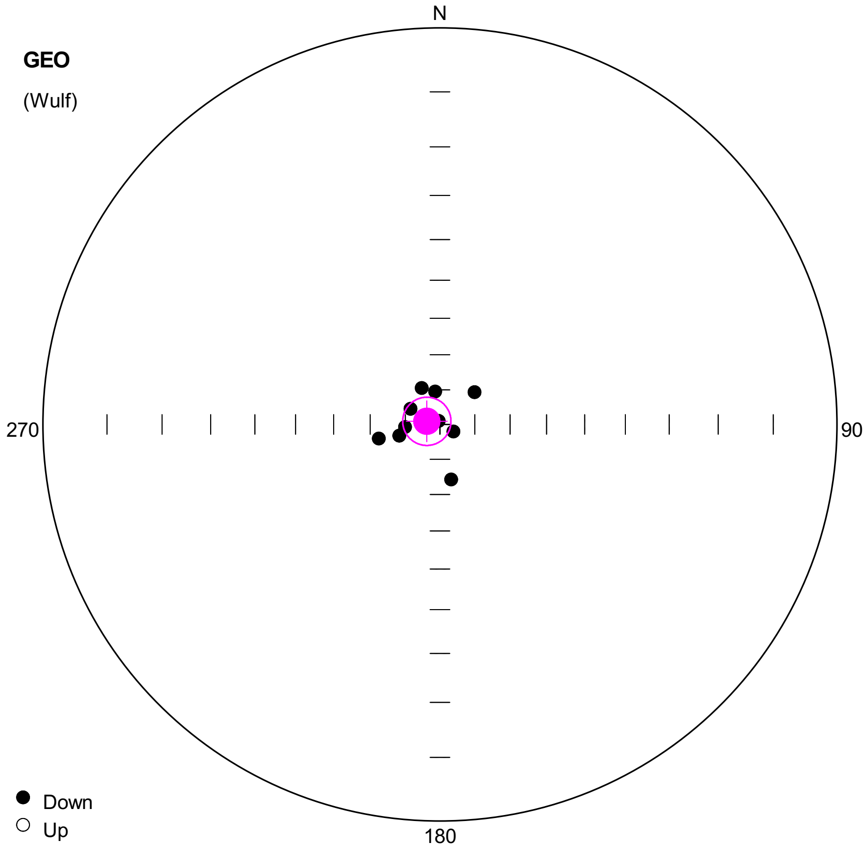

Number of data points: 10

Fisher statistics
Mean vector: 283.7 / 86.1
Resultant vector: 9.82
(X= 0.16, Y= -0.65, Z= 9.79)
Estimated precision, k: 49.3
95% Confidence limit: 6.95
95% Confidence limit, approximation: 6.31

Orientation matrix
1st eigenvalue: 0.96
1st eigenvector: 284.28 / 86.05
2nd eigenvalue: 0.02
2nd eigenvector: 52.99 / 2.47
3rd eigenvalue: 0.02
3rd eigenvector: 143.12 / 3.08

VGP
Site latitude: 65
Site longitude: 14.04
Pole latitude: 65.72 (-65.72)
Pole longitude: -4.58 (175.42)
Paleolatitude: 82.23 (-82.23)
dp: 13.71
dm: 13.8

#	Name	State	Dec	Inc	MAD	Limit1	Limit2
1	YUNN5601	Ch	254.5	77.9	3.3	30	68
2	YUNN5602	Ch	265.7	79.9	1.0	44	64
3	YUNN5603	Ch	168.5	73.9	5.2	30	64
4	YUNN5604	Ch	117.3	85.6	3.4	20	64
5	YUNN5605	Ch	333.5	78.3	2.6	40	68
6	YUNN5606	Ch	352.1	80.4	3.0	30	64
7	YUNN5607	Ch	46.8	76.4	2.4	35	60
8	YUNN5608	Ch	339.8	88.9	4.4	35	68
9	YUNN5609	Ch	257.0	72.1	5.6	20	68
10	YUNN5610	Ch	297.8	80.4	4.6	20	64

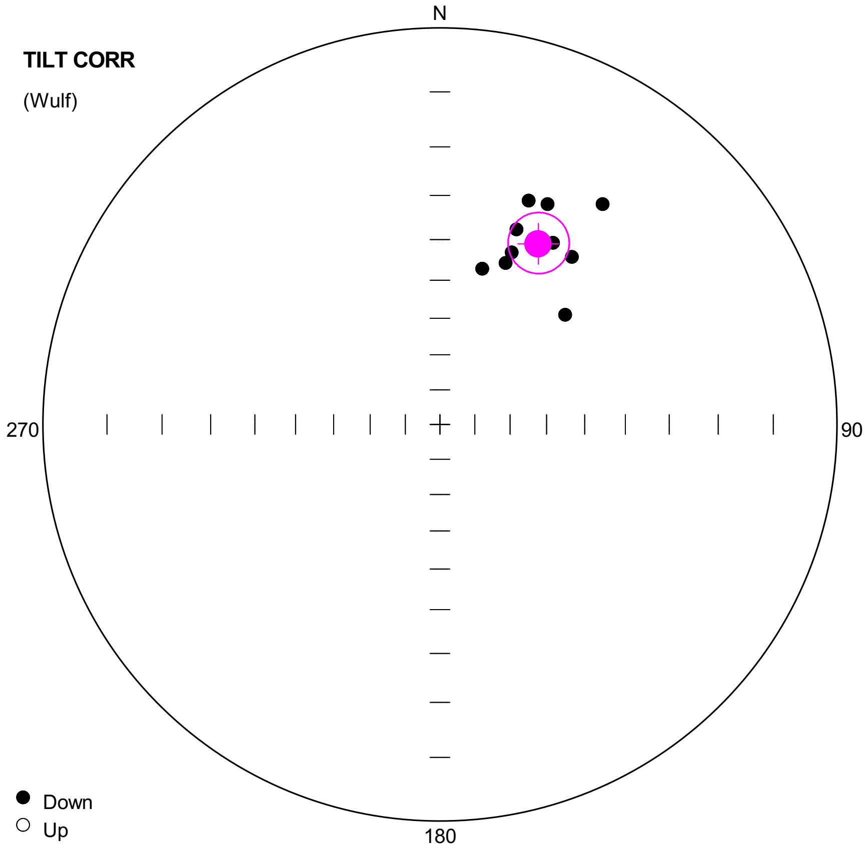

Number of data points: 10

Fisher statistics

Mean vector: 28.48 / 35.21
Resultant vector: 9.82
(X= 7.05, Y= 3.82, Z= 5.66)
Estimated precision, k: 49.45
95% Confidence limit: 6.94
95% Confidence limit, approximation: 6.3

Orientation matrix

1st eigenvalue: 0.96
1st eigenvector: 28.4 / 35.19
2nd eigenvalue: 0.02
2nd eigenvector: 244.09 / 49.04
3rd eigenvalue: 0.02
3rd eigenvector: 131.82 / 18.21

VGP

Site latitude: 65
Site longitude: 14.04
Pole latitude: 40.69 (-40.69)
Pole longitude: 157.68 (-22.32)
Paleolatitude: 19.44 (-19.44)
dp: 4.62
dm: 8.01

#	Name	State	Dec	Inc	MAD	Limit1	Limit2
1	YUNN5601	Ch	22.1	42.6	3.3	30	68
2	YUNN5602	Ch	22.6	39.7	1.0	44	64
3	YUNN5603	Ch	48.8	44.5	5.2	30	64
4	YUNN5604	Ch	38.2	33.5	3.4	20	64
5	YUNN5605	Ch	21.6	27.5	2.6	40	68
6	YUNN5606	Ch	26.0	26.6	3.0	30	64
7	YUNN5607	Ch	36.4	20.8	2.4	35	60
8	YUNN5608	Ch	31.9	33.3	4.4	35	68
9	YUNN5609	Ch	15.2	45.7	5.6	20	68
10	YUNN5610	Ch	21.4	34.3	4.6	20	64

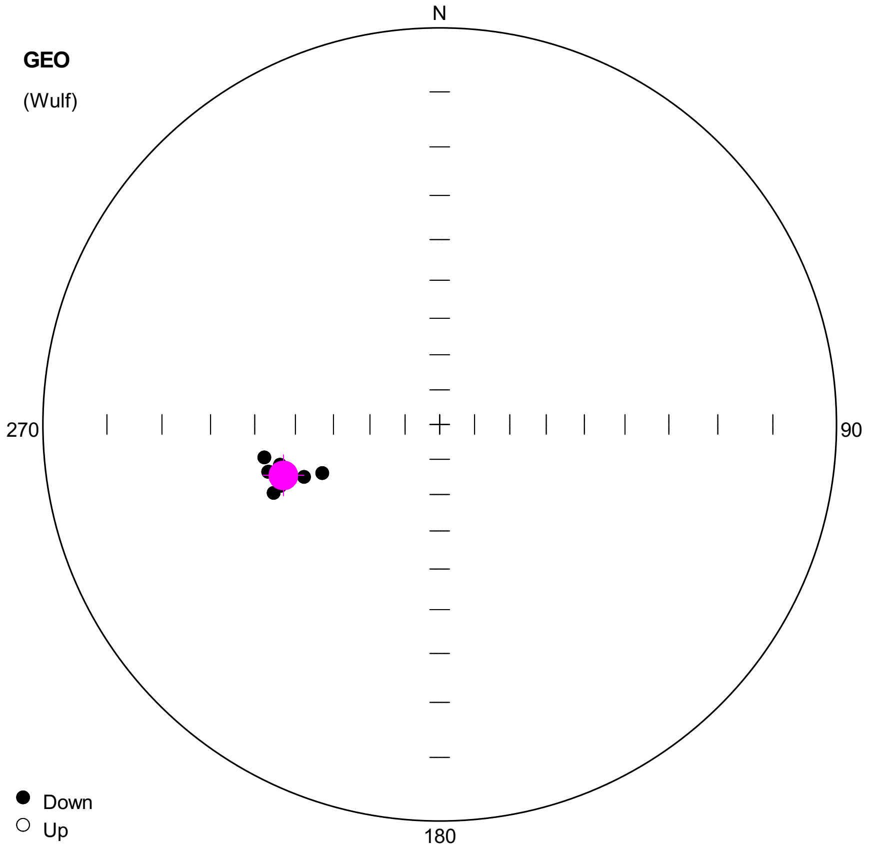

Number of data points: 9

Fisher statistics

Mean vector: 251.96 / 45.01
Resultant vector: 8.96
(X= -1.96, Y= -6.03, Z= 6.34)
Estimated precision, k: 224.04
95% Confidence limit: 3.45
95% Confidence limit, approximation: 3.12

Orientation matrix

1st eigenvalue: 0.99
1st eigenvector: 251.96 / 45
2nd eigenvalue: 0.01
2nd eigenvector: 105.04 / 39.96
3rd eigenvalue: 0
3rd eigenvector: 0 / 17.21

VGP

Site latitude: 65
Site longitude: 14.04
Pole latitude: 16.76 (-16.76)
Pole longitude: -48.6 (131.4)
Paleolatitude: 26.57 (-26.57)
dp: 2.76
dm: 4.36

#	Name	State	Dec	Inc	MAD	Limit1	Limit2	
1	YUNN5701	Ch	248.8	49.7	14.6	20	60	
2	YUNN5702	Ch	259.3	41.6	2.2	35	64	OA
3	YUNN5703	Ch	254.5	41.9	7.8	30	60	
4	YUNN5704	Ch	254.5	41.7	5.6	20	64	
5	YUNN5705	Ch	247.6	41.3	2.9	30	68	
6	YUNN5706	Ch	247.5	54.5	6.1	35	68	
7	YUNN5708	Ch	249.3	45.5	5.0	44	64	
8	YUNN5709	Ch	255.8	44.9	6.3	30	60	
9	YUNN5710	Ch	248.9	43.4	4.6	35	64	

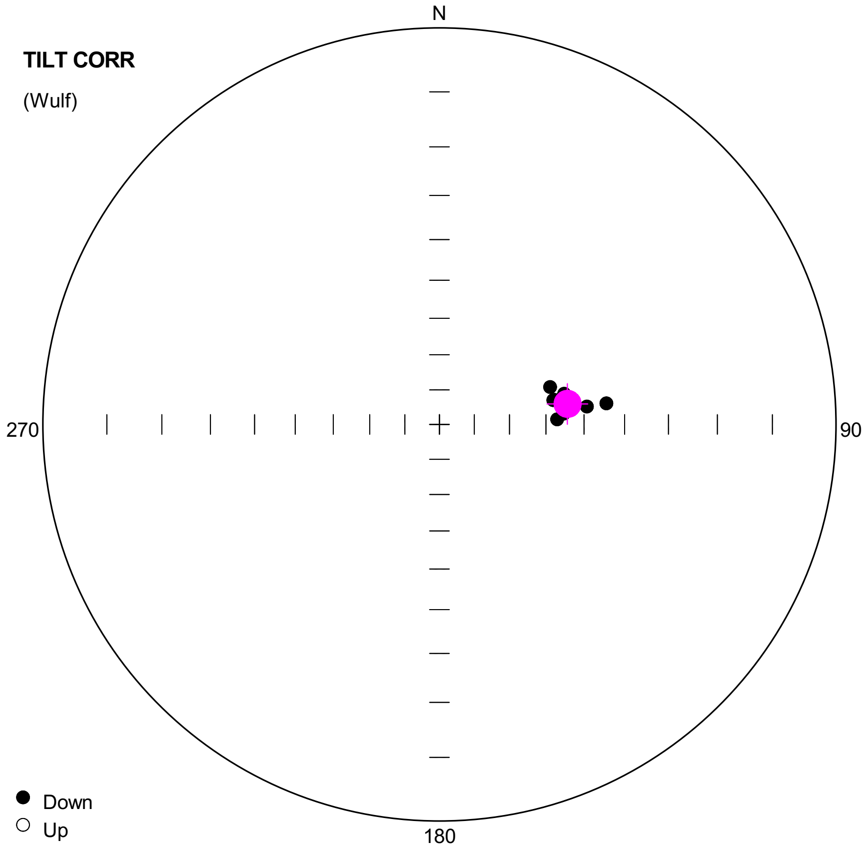

Number of data points: 9

Fisher statistics

Mean vector: 80.81 / 53.82
Resultant vector: 8.96
(X= 0.85, Y= 5.22, Z= 7.24)
Estimated precision, k: 224.62
95% Confidence limit: 3.44
95% Confidence limit, approximation: 3.11

Orientation matrix

1st eigenvalue: 0.99
1st eigenvector: 80.81 / 53.83
2nd eigenvalue: 0.01
2nd eigenvector: 282.72 / 34.15
3rd eigenvalue: 0
3rd eigenvector: 185.5 / 10.5

VGP

Site latitude: 65
Site longitude: 14.04
Pole latitude: 34.55 (-34.55)
Pole longitude: 95.73 (-84.27)
Paleolatitude: 34.36 (-34.36)
dp: 3.37
dm: 4.81

#	Name	State	Dec	Inc	MAD	Limit1	Limit2	
1	YUNN5701	Ch	83.1	48.9	14.6	20	60	
2	YUNN5702	Ch	71.4	57.2	2.2	35	64	OA
3	YUNN5703	Ch	78.0	57.0	7.8	30	60	
4	YUNN5704	Ch	78.0	57.3	5.6	20	64	
5	YUNN5705	Ch	87.6	56.9	2.9	30	68	
6	YUNN5706	Ch	82.8	44.0	6.1	35	68	
7	YUNN5708	Ch	83.8	53.1	5.0	44	64	
8	YUNN5709	Ch	76.2	54.1	6.3	30	60	
9	YUNN5710	Ch	85.0	55.0	4.6	35	64	

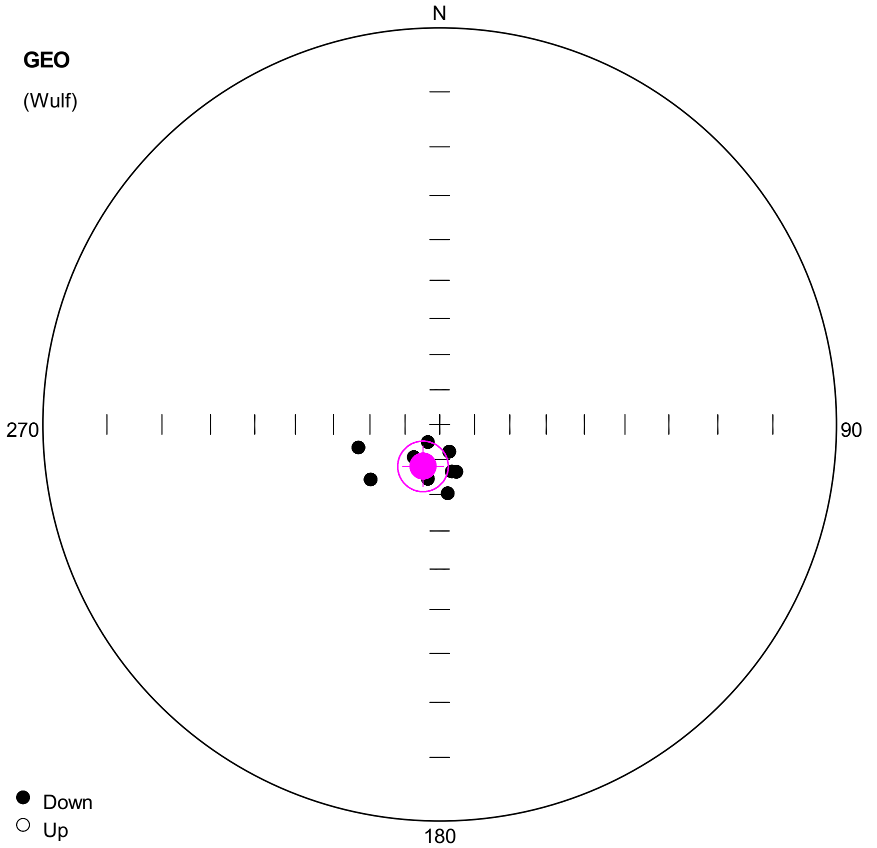

Number of data points: 9

Fisher statistics

Mean vector: 201.85 / 77.07
Resultant vector: 8.85
(X= -1.84, Y= -0.74, Z= 8.62)
Estimated precision, k: 52.11
95% Confidence limit: 7.2
95% Confidence limit, approximation: 6.46

Orientation matrix

1st eigenvalue: 0.97
1st eigenvector: 201.33 / 77.11
2nd eigenvalue: 0.03
2nd eigenvector: 97.9 / 3.04
3rd eigenvalue: 0.01
3rd eigenvector: 7.23 / 12.52

VGP

Site latitude: 65
Site longitude: 14.04
Pole latitude: 41.3 (-41.3)
Pole longitude: 2.11 (-177.89)
Paleolatitude: 65.34 (-65.34)
dp: 12.52
dm: 13.42

#	Name	State	Dec	Inc	MAD	Limit1	Limit2
1	YUNN5801	Ch	173.3	70.2	4.6	20	68
2	YUNN5802	Ch	160.3	81.7	7.1	35	68
3	YUNN5803	Ch	213.9	83.9	10.7	30	68
4	YUNN5804	Ch	165.3	76.0	6.0	35	64
5	YUNN5805	Ch	231.4	64.9	10.5	30	64
6	YUNN5806	Cht	254.2	66.0	5.8	40	68
7	YUNN5807	Ch	218.2	78.0	7.9	30	68
8	YUNN5808	Ch	160.6	75.6	7.6	35	64
9	YUNN5809	Ch	192.2	74.0	9.5	20	68

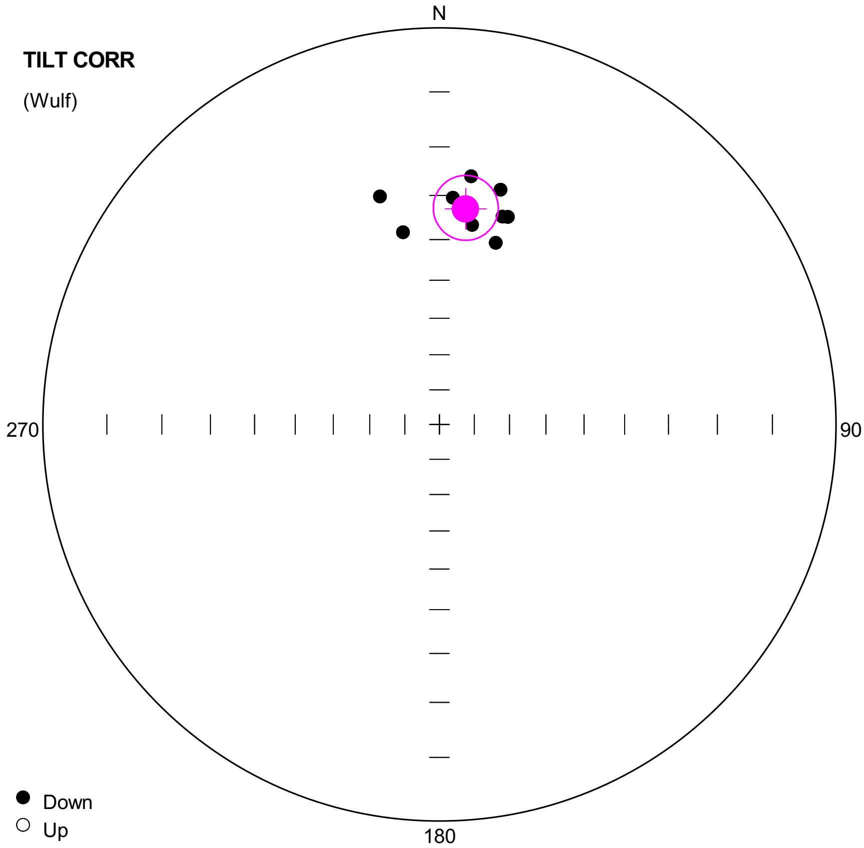

Number of data points: 9

Fisher statistics

Mean vector: 6.88 / 32.61
Resultant vector: 8.85
(X= 7.4, Y= 0.89, Z= 4.77)
Estimated precision, k: 52.08
95% Confidence limit: 7.2
95% Confidence limit, approximation: 6.47

Orientation matrix

1st eigenvalue: 0.97
1st eigenvector: 7.03 / 32.6
2nd eigenvalue: 0.03
2nd eigenvector: 276.43 / 0.93
3rd eigenvalue: 0.01
3rd eigenvector: 184.98 / 57.39

VGP

Site latitude: 65
Site longitude: 14.04
Pole latitude: 42.51 (-42.51)
Pole longitude: -174.87 (5.13)
Paleolatitude: 17.74 (-17.74)
dp: 4.6
dm: 8.14

#	Name	State	Dec	Inc	MAD	Limit1	Limit2
1	YUNN5801	Ch	17.2	38.8	4.6	20	68
2	YUNN5802	Ch	14.6	27.1	7.1	35	68
3	YUNN5803	Ch	7.3	25.5	10.7	30	68
4	YUNN5804	Ch	16.9	32.6	6.0	35	64
5	YUNN5805	Ch	349.3	37.5	10.5	30	64
6	YUNN5806	Cht	345.4	28.6	5.8	40	68
7	YUNN5807	Ch	3.4	30.4	7.9	30	68
8	YUNN5808	Ch	18.3	32.3	7.6	35	64
9	YUNN5809	Ch	9.3	36.0	9.5	20	68

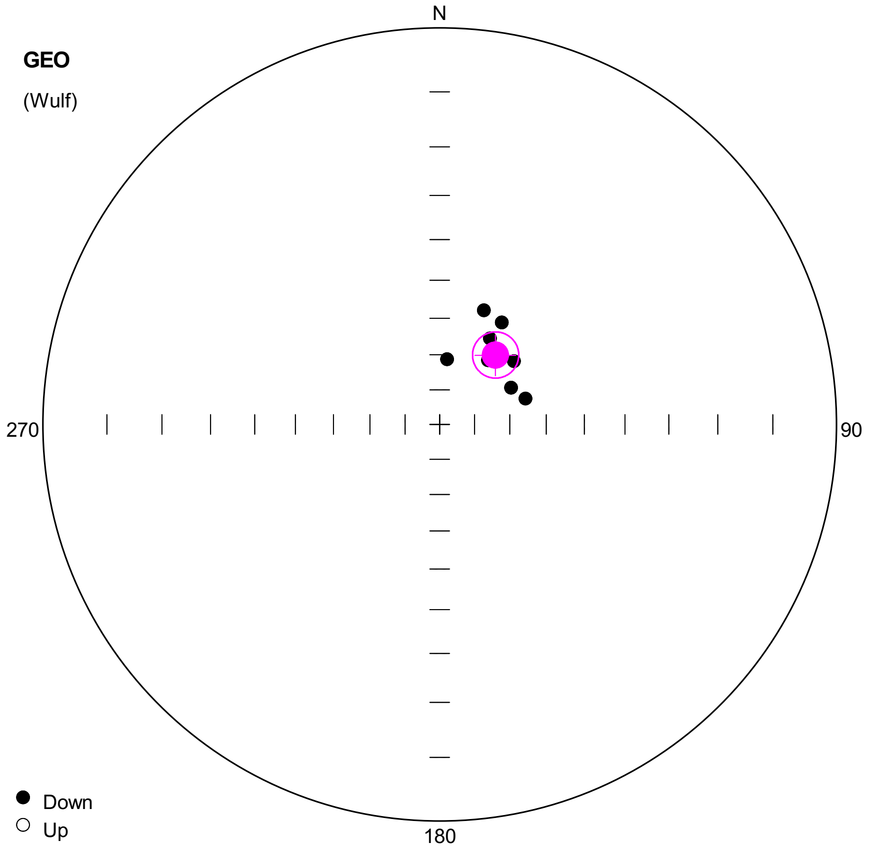

Number of data points: 9

Fisher statistics

Mean vector: 38.75 / 64.74
Resultant vector: 8.88
(X= 2.95, Y= 2.37, Z= 8.03)
Estimated precision, k: 66.7
95% Confidence limit: 6.35
95% Confidence limit, approximation: 5.71

Orientation matrix

1st eigenvalue: 0.97
1st eigenvector: 38.74 / 64.73
2nd eigenvalue: 0.02
2nd eigenvector: 146.06 / 8
3rd eigenvalue: 0.01
3rd eigenvector: 239.62 / 23.8

VGP

Site latitude: 65
Site longitude: 14.04
Pole latitude: 62.3 (-62.3)
Pole longitude: 126.51 (-53.49)
Paleolatitude: 46.67 (-46.67)
dp: 8.21
dm: 10.21

#	Name	State	Dec	Inc	MAD	Limit1	Limit2
1	YUNN5901	Cht	49.6	62.4	4.1	52	68
2	YUNN5902	Cht	73.3	64.6	7.7	52	68
3	YUNN5903	Cht	31.3	56.5	4.1	60	68
4	YUNN5904	Cht	39.5	65.7	2.6	60	68
5	YUNN5905	Cht	37.1	67.1	2.8	60	68
6	YUNN5906	Cht	6.4	71.2	5.2	60	68
7	YUNN5907	Cht	30.4	61.8	2.4	60	68
8	YUNN5908	Cht	21.2	55.7	7.1	60	68
9	YUNN5910	Cht	62.7	67.1	13.0	48	68

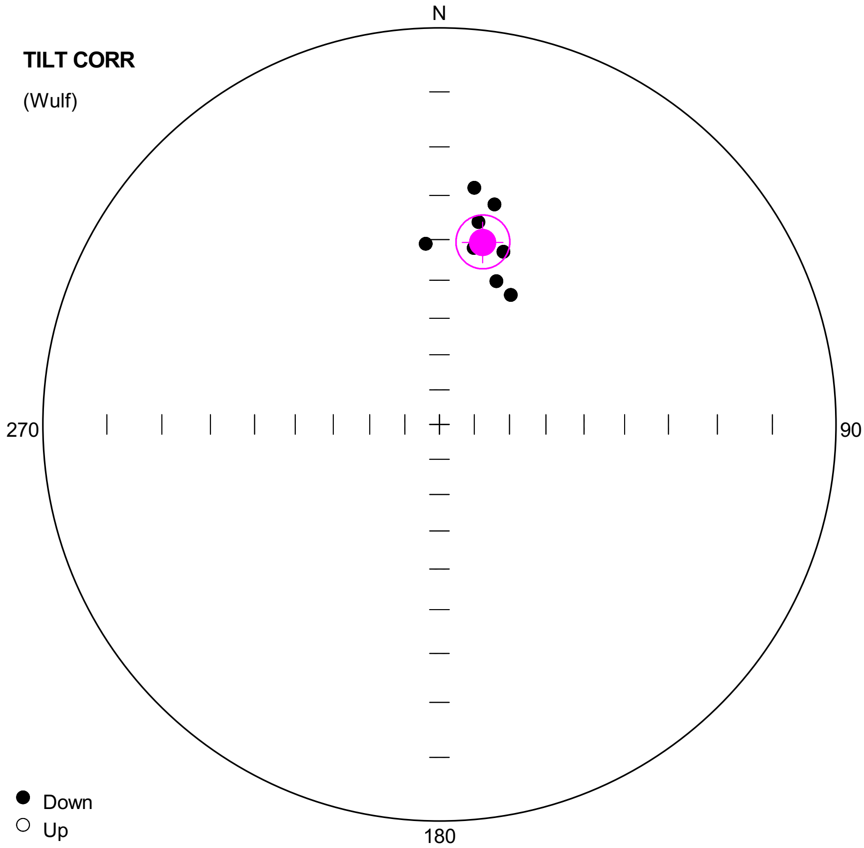

Number of data points: 9

Fisher statistics

Mean vector: 13.35 / 39.52
Resultant vector: 8.88
(X= 6.67, Y= 1.58, Z= 5.65)
Estimated precision, k: 66.68
95% Confidence limit: 6.35
95% Confidence limit, approximation: 5.72

Orientation matrix

1st eigenvalue: 0.97
1st eigenvector: 13.36 / 39.5
2nd eigenvalue: 0.02
2nd eigenvector: 140.63 / 36.3
3rd eigenvalue: 0.01
3rd eigenvector: 255.36 / 29.66

VGP

Site latitude: 65
Site longitude: 14.04
Pole latitude: 46.53 (-46.53)
Pole longitude: 175.96 (-4.04)
Paleolatitude: 22.41 (-22.41)
dp: 4.56
dm: 7.61

#	Name	State	Dec	Inc	MAD	Limit1	Limit2
1	YUNN5901	Cht	20.3	40.2	4.1	52	68
2	YUNN5902	Cht	28.8	49.1	7.7	52	68
3	YUNN5903	Cht	14.1	30.5	4.1	60	68
4	YUNN5904	Cht	13.0	40.5	2.6	60	68
5	YUNN5905	Cht	11.0	41.2	2.8	60	68
6	YUNN5906	Cht	355.7	40.9	5.2	60	68
7	YUNN5907	Cht	10.9	35.1	2.4	60	68
8	YUNN5908	Cht	8.4	27.8	7.1	60	68
9	YUNN5910	Cht	21.7	47.5	13.0	48	68

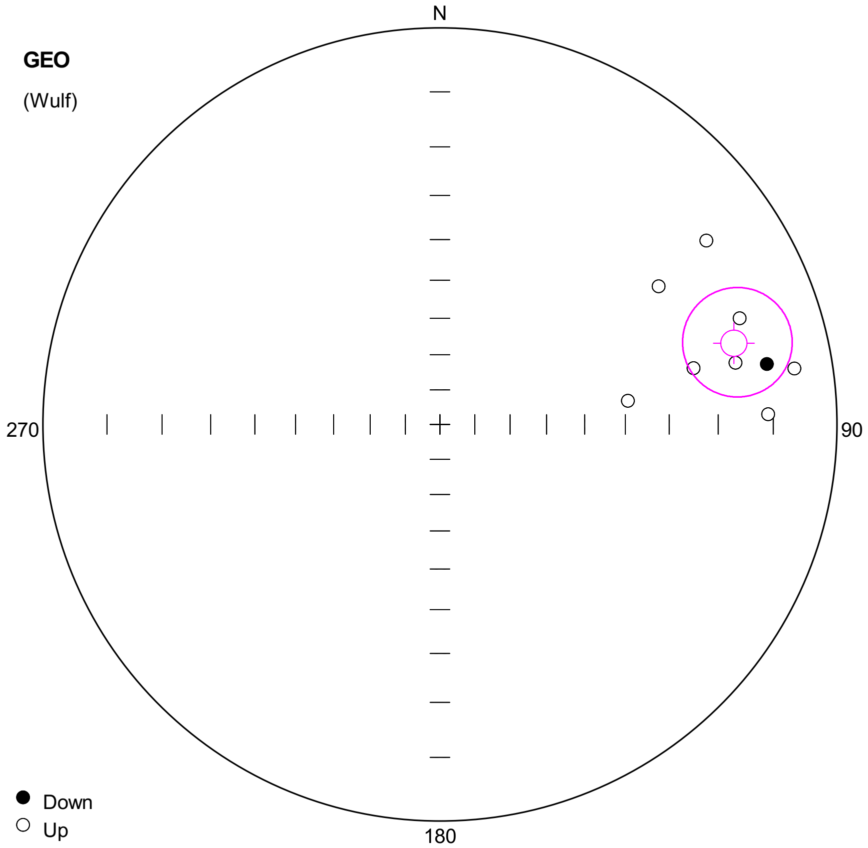

Number of data points: 10

Fisher statistics

Mean vector: 74.51 / -14.96
Resultant vector: 9.64
(X= 2.49, Y= 8.97, Z= -2.49)
Estimated precision, k: 24.86
95% Confidence limit: 9.88
95% Confidence limit, approximation: 8.88

Orientation matrix

1st eigenvalue: 0.93
1st eigenvector: 254.53 / 14.96
2nd eigenvalue: 0.04
2nd eigenvector: 118.24 / 69.71
3rd eigenvalue: 0.03
3rd eigenvector: 348.17 / 13.39

VGP

Site latitude: 65
Site longitude: 14.04
Pole latitude: -0.47 (0.47)
Pole longitude: 121.25 (-58.75)
Paleolatitude: -7.61 (7.61)
dp: 5.2
dm: 10.14

#	Name	State	Dec	Inc	MAD	Limit1	Limit2	
1	YUNN6001	Ch	55.4	-11.6	18.5	30	64	
2	YUNN6002	Clt	57.7	-23.8	9.3	20	52	
3	YUNN6003	Cht	70.5	-12.6	17.7	48	68	
4	YUNN6004	Ch	78.2	-15.5	14.2	20	64	
5	YUNN6005	Cht	74.6	-14.8	23.0	40	64	
6	YUNN6006	Cht	77.5	-23.6	24.6	44	64	
7	YUNN6007	Cht	79.5	10.1	9.2	56	64	
8	YUNN6008	Cht	82.8	-39.0	29.8	56	68	
9	YUNN6009	Ch	81.0	-5.8	9.0	35	60	
10	YUNN6010	Cht	88.2	-10.8	8.3	44	60	OA

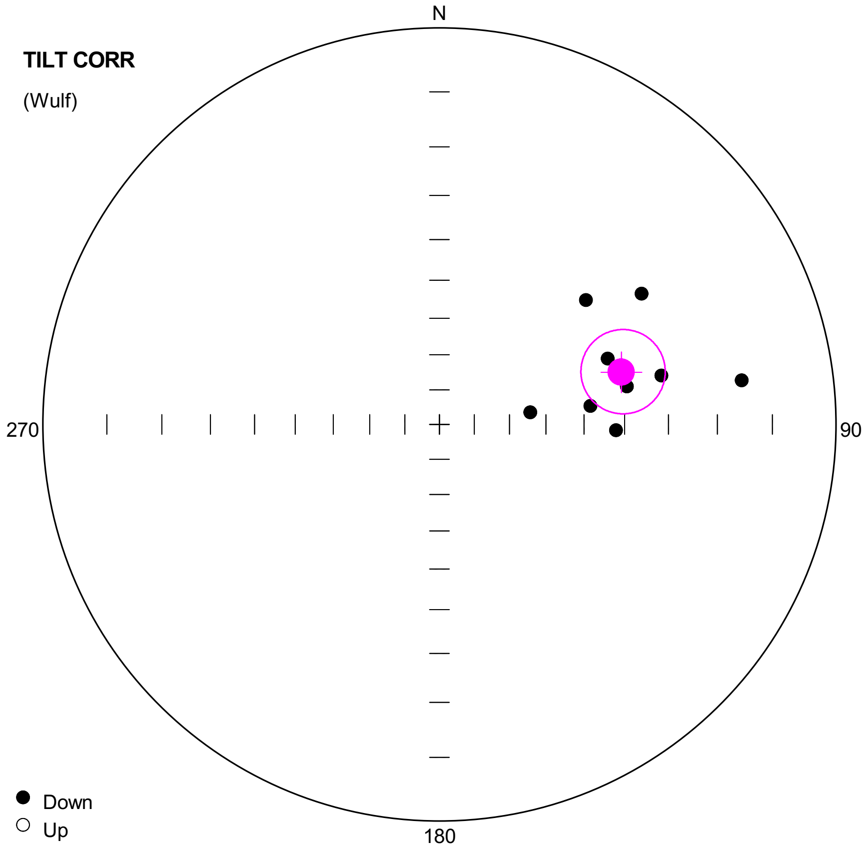

Number of data points: 10

Fisher statistics

Mean vector: 73.93 / 38.98
Resultant vector: 9.64
(X= 2.07, Y= 7.2, Z= 6.06)
Estimated precision, k: 24.88
95% Confidence limit: 9.88
95% Confidence limit, approximation: 8.88

Orientation matrix

1st eigenvalue: 0.93
1st eigenvector: 73.95 / 38.98
2nd eigenvalue: 0.04
2nd eigenvector: 236.92 / 49.76
3rd eigenvalue: 0.03
3rd eigenvector: 337.04 / 8.46

VGP

Site latitude: 65
Site longitude: 14.04
Pole latitude: 26.64 (-26.64)
Pole longitude: 108.79 (-71.21)
Paleolatitude: 22.03 (-22.03)
dp: 7.02
dm: 11.78

#	Name	State	Dec	Inc	MAD	Limit1	Limit2	
1	YUNN6001	Ch	49.7	38.3	18.5	30	64	
2	YUNN6002	Clt	57.1	27.5	9.3	20	52	
3	YUNN6003	Cht	68.6	41.0	17.7	48	68	
4	YUNN6004	Ch	78.5	38.5	14.2	20	64	
5	YUNN6005	Cht	74.0	39.1	23.0	40	64	
6	YUNN6006	Cht	77.6	30.4	24.6	44	64	
7	YUNN6007	Cht	82.5	64.0	9.2	56	64	
8	YUNN6008	Cht	81.7	14.8	29.8	56	68	
9	YUNN6009	Ch	83.0	48.0	9.0	35	60	
10	YUNN6010	Cht	91.9	42.0	8.3	44	60	OA

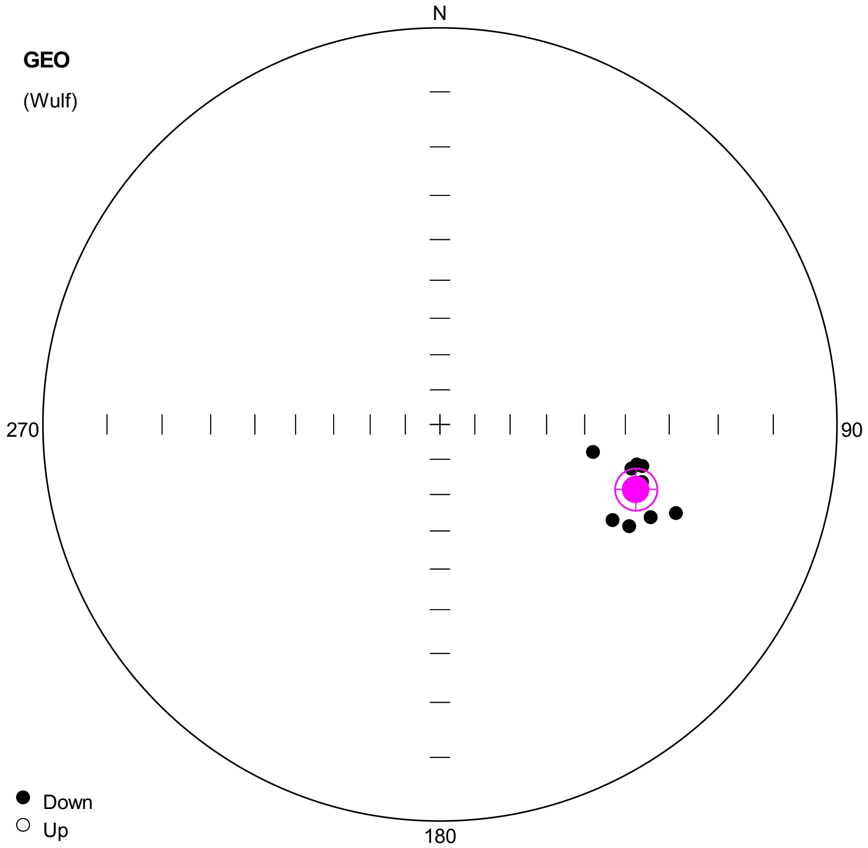

Number of data points: 10

Fisher statistics

Mean vector: 108.35 / 35.11
Resultant vector: 9.91
(X= -2.55, Y= 7.7, Z= 5.7)
Estimated precision, k: 102.71
95% Confidence limit: 4.79
95% Confidence limit, approximation: 4.37

Orientation matrix

1st eigenvalue: 0.98
1st eigenvector: 108.34 / 35.1
2nd eigenvalue: 0.01
2nd eigenvector: 347.41 / 36.18
3rd eigenvalue: 0.01
3rd eigenvector: 227.23 / 34.51

VGP

Site latitude: 65
Site longitude: 14.04
Pole latitude: 10.08 (-10.08)
Pole longitude: 79.47 (-100.53)
Paleolatitude: 19.37 (-19.37)
dp: 3.18
dm: 5.52

#	Name	State	Dec	Inc	MAD	Limit1	Limit2
1	YUNN6101	Ch	110.6	25.2	4.8	40	52
2	YUNN6102	Ch	105.9	34.2	3.5	35	56
3	YUNN6103	Ch	103.0	37.3	4.6	40	56
4	YUNN6104	Ch	119.0	37.1	8.0	35	56
5	YUNN6105	Ch	101.6	35.0	7.1	35	56
6	YUNN6106	Ch	107.5	34.2	10.5	40	56
7	YUNN6107	Ch	113.8	29.8	6.4	40	56
8	YUNN6108	Ch	101.5	36.3	3.6	35	56
9	YUNN6109	Ch	118.3	33.1	8.5	40	56
10	YUNN6110	Ch	100.2	47.2	2.5	40	56

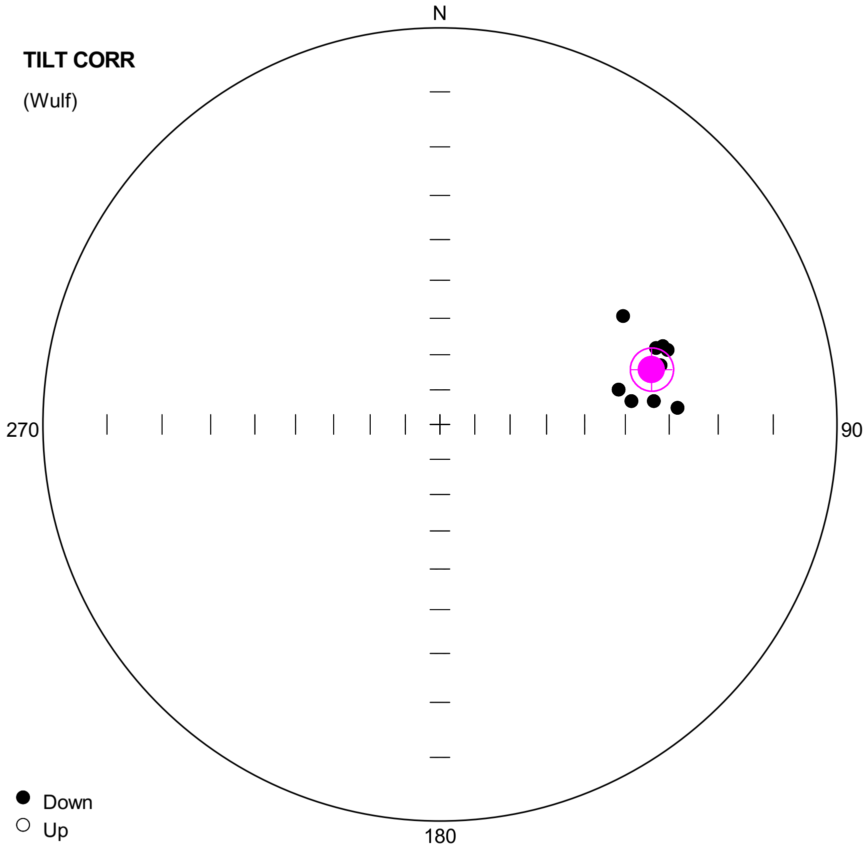

Number of data points: 10

Fisher statistics
Mean vector: 75.45 / 32.37
Resultant vector: 9.91
(X= 2.1, Y= 8.1, Z= 5.31)
Estimated precision, k: 102.82
95% Confidence limit: 4.79
95% Confidence limit, approximation: 4.37

Orientation matrix
1st eigenvalue: 0.98
1st eigenvector: 75.47 / 32.36
2nd eigenvalue: 0.01
2nd eigenvector: 170.88 / 8.47
3rd eigenvalue: 0.01
3rd eigenvector: 273.78 / 56.28

VGP
Site latitude: 65
Site longitude: 14.04
Pole latitude: 22.03 (-22.03)
Pole longitude: 109.57 (-70.43)
Paleolatitude: 17.59 (-17.59)
dp: 3.05
dm: 5.4

#	Name	State	Dec	Inc	MAD	Limit1	Limit2
1	YUNN6101	Ch	86.0	28.1	4.8	40	52
2	YUNN6102	Ch	75.0	30.2	3.5	35	56
3	YUNN6103	Ch	70.5	30.0	4.6	40	56
4	YUNN6104	Ch	79.0	40.7	8.0	35	56
5	YUNN6105	Ch	71.9	27.8	7.1	35	56
6	YUNN6106	Ch	75.9	31.3	10.5	40	56
7	YUNN6107	Ch	83.8	33.1	6.4	40	56
8	YUNN6108	Ch	70.6	28.5	3.6	35	56
9	YUNN6109	Ch	83.1	38.2	8.5	40	56
10	YUNN6110	Ch	59.4	33.6	2.5	40	56

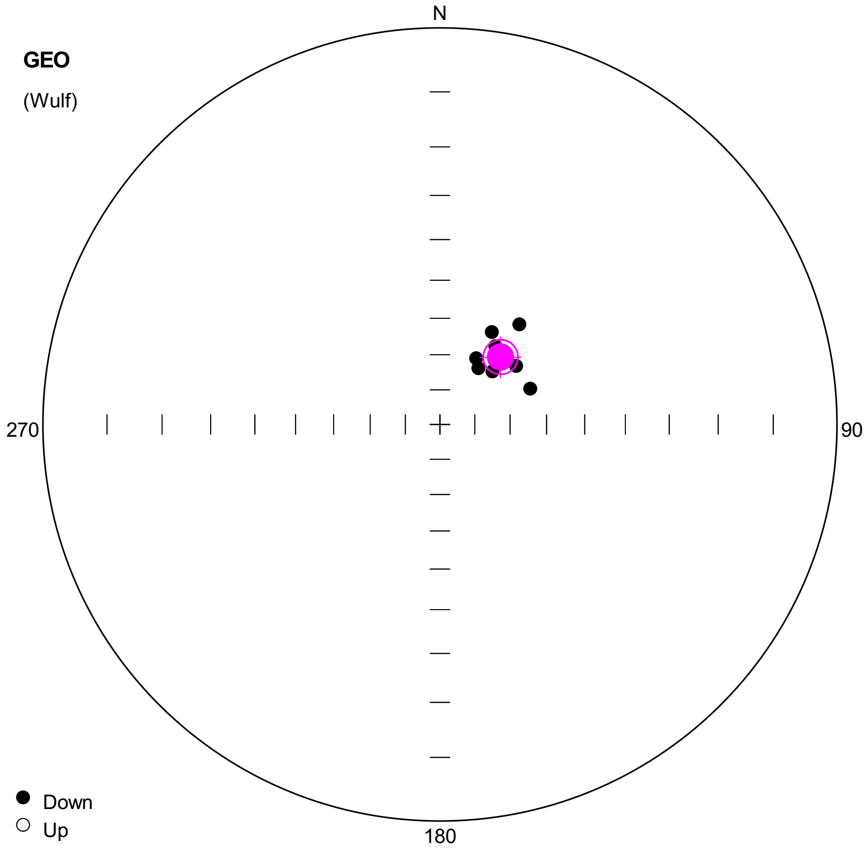

Number of data points: 9

Fisher statistics

Mean vector: 41.85 / 64.31
Resultant vector: 8.93
(X= 2.88, Y= 2.58, Z= 8.05)
Estimated precision, k: 118.19
95% Confidence limit: 4.76
95% Confidence limit, approximation: 4.29

Orientation matrix

1st eigenvalue: 0.99
1st eigenvector: 41.81 / 64.32
2nd eigenvalue: 0.01
2nd eigenvector: 145.58 / 6.53
3rd eigenvalue: 0.01
3rd eigenvector: 238.6 / 24.72

VGP

Site latitude: 65
Site longitude: 14.04
Pole latitude: 60.61 (-60.61)
Pole longitude: 123.51 (-56.49)
Paleolatitude: 46.1 (-46.1)
dp: 6.08
dm: 7.6

#	Name	State	Dec	Inc	MAD	Limit1	Limit2
1	YUNN6201	Ch	43.8	64.1	3.0	40	64
2	YUNN6202	Ch	38.5	54.3	1.9	40	64
3	YUNN6203	Ch	34.2	70.5	6.0	30	60
4	YUNN6204	Ch	52.4	62.8	3.5	40	64
5	YUNN6206	Ch	28.6	68.5	4.2	35	68
6	YUNN6207	Ch	35.2	62.8	3.7	35	68
7	YUNN6208	Ch	68.4	62.5	3.0	30	56
8	YUNN6209	Ch	29.4	60.1	3.4	30	68
9	YUNN6210	Ch	44.7	68.7	5.0	30	56

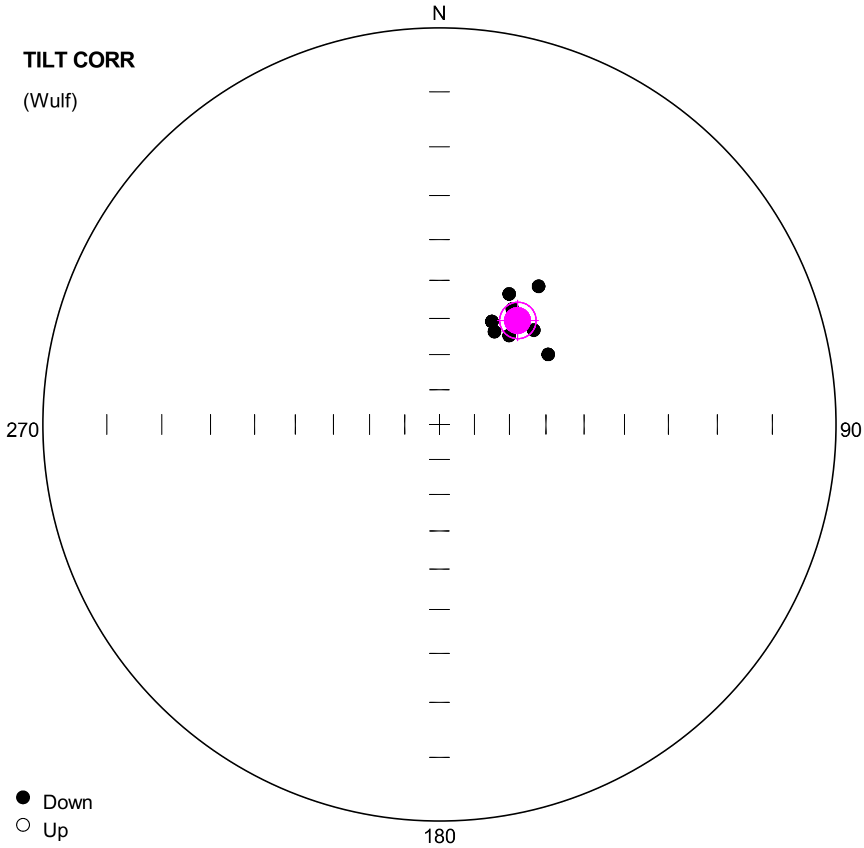

Number of data points: 9

Fisher statistics

Mean vector: 36.97 / 53.7

Resultant vector: 8.93

(X= 4.23, Y= 3.18, Z= 7.2)

Estimated precision, k: 118.34

95% Confidence limit: 4.75

95% Confidence limit, approximation: 4.29

Orientation matrix

1st eigenvalue: 0.99

1st eigenvector: 36.94 / 53.71

2nd eigenvalue: 0.01

2nd eigenvector: 143.88 / 12.08

3rd eigenvalue: 0.01

3rd eigenvector: 242.07 / 33.62

VGP

Site latitude: 65

Site longitude: 14.04

Pole latitude: 52.1 (-52.1)

Pole longitude: 140.01 (-39.99)

Paleolatitude: 34.24 (-34.24)

dp: 4.63

dm: 6.64

#	Name	State	Dec	Inc	MAD	Limit1	Limit2
1	YUNN6201	Ch	38.4	53.6	3.0	40	64
2	YUNN6202	Ch	35.7	43.6	1.9	40	64
3	YUNN6203	Ch	30.7	59.6	6.0	30	60
4	YUNN6204	Ch	45.1	52.8	3.5	40	64
5	YUNN6206	Ch	27.1	57.5	4.2	35	68
6	YUNN6207	Ch	32.3	52.0	3.7	35	68
7	YUNN6208	Ch	57.2	53.9	3.0	30	56
8	YUNN6209	Ch	28.1	49.1	3.4	30	68
9	YUNN6210	Ch	38.1	58.2	5.0	30	56

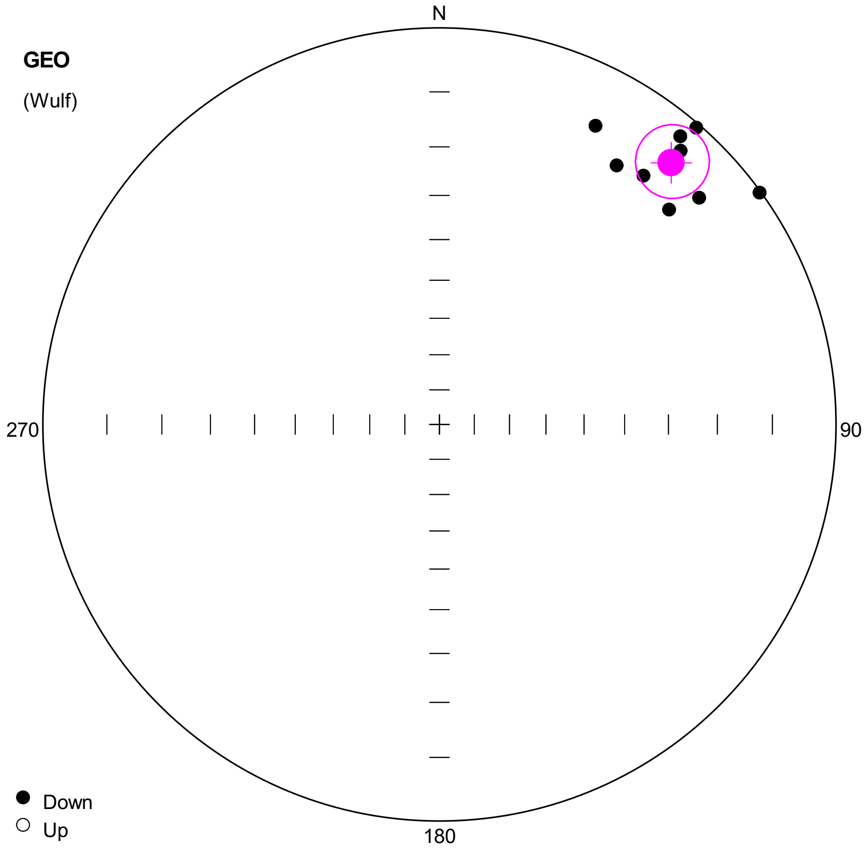

Number of data points: 9

Fisher statistics

Mean vector: 41.53 / 7.22

Resultant vector: 8.89

(X= 6.61, Y= 5.85, Z= 1.12)

Estimated precision, k: 75.24

95% Confidence limit: 5.97

95% Confidence limit, approximation: 5.38

Orientation matrix

1st eigenvalue: 0.98

1st eigenvector: 41.53 / 7.22

2nd eigenvalue: 0.02

2nd eigenvector: 308.73 / 21.05

3rd eigenvalue: 0.01

3rd eigenvector: 149.45 / 67.63

VGP

Site latitude: 65

Site longitude: 14.04

Pole latitude: 21.9 (-21.9)

Pole longitude: 148.55 (-31.45)

Paleolatitude: 3.62 (-3.62)

dp: 3.02

dm: 6.01

#	Name	State	Dec	Inc	MAD	Limit1	Limit2
1	YUNN6301	Ch	40.9	0.6	6.3	40	64
2	YUNN6303	Ch	48.9	8.0	5.1	35	56
3	YUNN6304	Ch	39.4	11.9	6.3	40	60
4	YUNN6305	Ch	41.4	4.8	5.7	35	64
5	YUNN6306	Ch	39.9	3.1	5.8	35	56
6	YUNN6307	Ch	34.4	13.3	7.4	40	64
7	YUNN6308	Ch	46.9	13.2	12.8	40	68
8	YUNN6309	Ch	54.1	0.2	7.5	35	68
9	YUNN6310	Ch	27.6	9.3	8.8	35	68

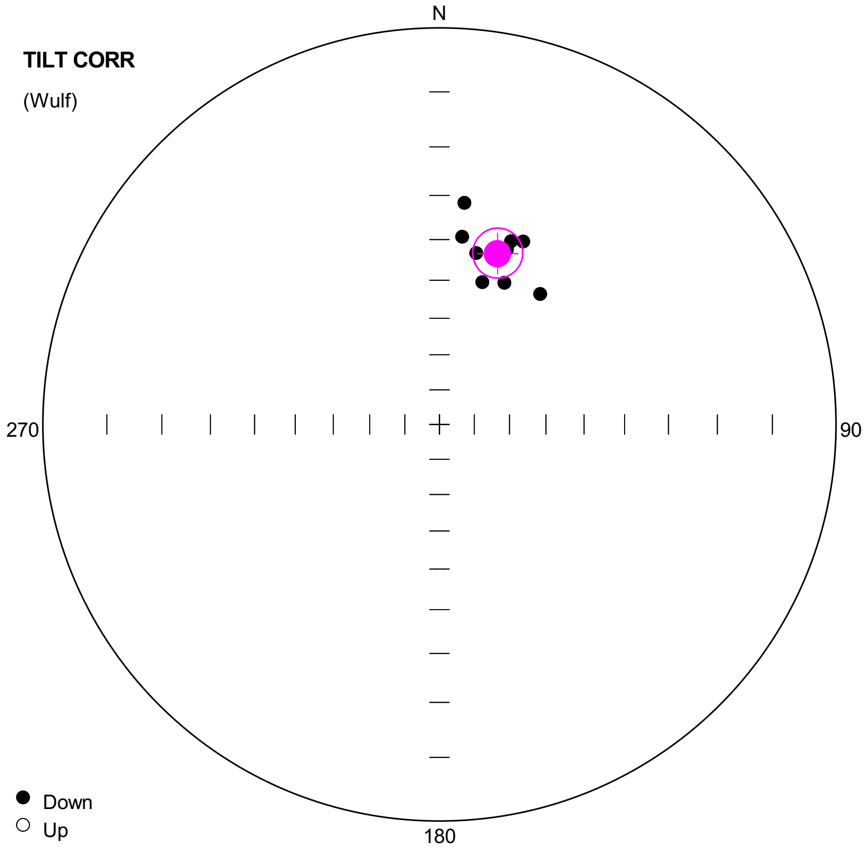

Number of data points: 9

Fisher statistics

Mean vector: 18.76 / 41.08
Resultant vector: 8.89
(X= 6.35, Y= 2.16, Z= 5.84)
Estimated precision, k: 75.31
95% Confidence limit: 5.97
95% Confidence limit, approximation: 5.38

Orientation matrix

1st eigenvalue: 0.98
1st eigenvector: 18.76 / 41.08
2nd eigenvalue: 0.02
2nd eigenvector: 128.84 / 21.5
3rd eigenvalue: 0.01
3rd eigenvector: 239.01 / 41.2

VGP

Site latitude: 65
Site longitude: 14.04
Pole latitude: 46.8 (-46.8)
Pole longitude: 168.53 (-11.47)
Paleolatitude: 23.55 (-23.55)
dp: 4.42
dm: 7.26

#	Name	State	Dec	Inc	MAD	Limit1	Limit2
1	YUNN6301	Ch	24.6	36.2	6.3	40	64
2	YUNN6303	Ch	24.7	47.1	5.1	35	56
3	YUNN6304	Ch	12.1	42.3	6.3	40	60
4	YUNN6305	Ch	21.1	39.4	5.7	35	64
5	YUNN6306	Ch	21.4	37.2	5.8	35	56
6	YUNN6307	Ch	6.9	39.0	7.4	40	64
7	YUNN6308	Ch	16.8	48.9	12.8	40	68
8	YUNN6309	Ch	37.7	44.9	7.5	35	68
9	YUNN6310	Ch	6.4	31.3	8.8	35	68

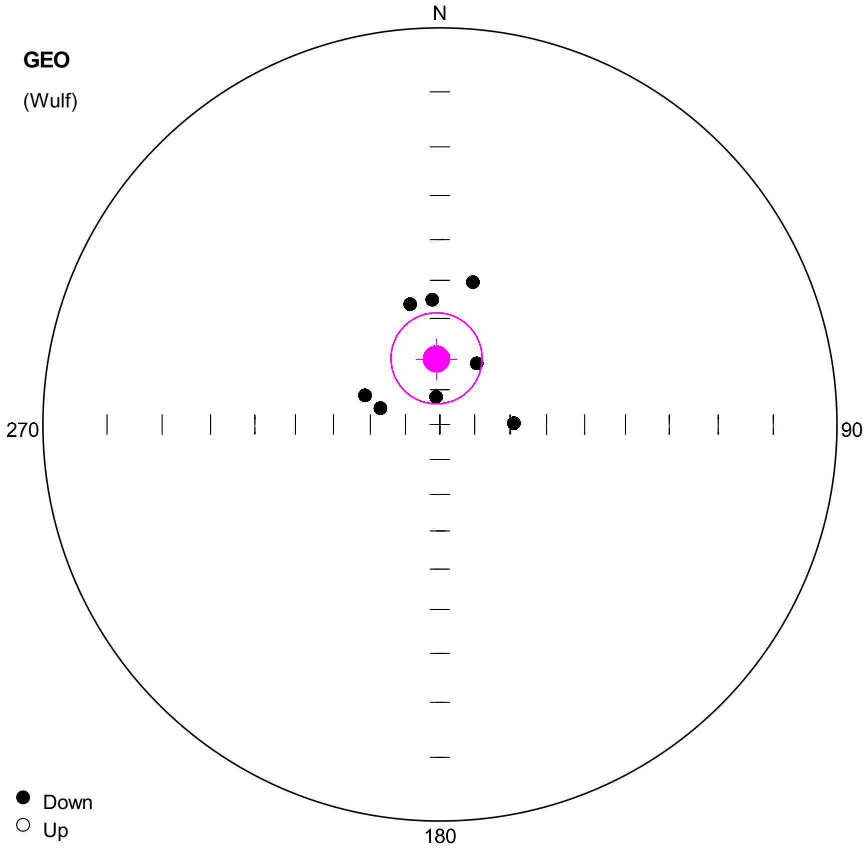

Number of data points: 9

Fisher statistics

Mean vector: 356.97 / 71.24

Resultant vector: 8.54

(X= 2.74, Y= -0.15, Z= 8.08)

Estimated precision, k: 17.3

95% Confidence limit: 12.74

95% Confidence limit, approximation: 11.22

Orientation matrix

1st eigenvalue: 0.9

1st eigenvector: 356.74 / 71.1

2nd eigenvalue: 0.05

2nd eigenvector: 204.37 / 16.87

3rd eigenvalue: 0.05

3rd eigenvector: 111.84 / 8.26

VGP

Site latitude: 65

Site longitude: 14.04

Pole latitude: 80.69 (-80.69)

Pole longitude: -155.38 (24.62)

Paleolatitude: 55.81 (-55.81)

dp: 19.44

dm: 22.25

#	Name	State	Dec	Inc	MAD	Limit1	Limit2	
1	YUNN6401	Cht	2.7	71.2	5.0	56	68	
2	YUNN6402	Cht	31.0	69.6	8.0	48	68	
3	YUNN6403	Cht	356.5	55.0	0.0	64	68	
4	YUNN6404	Cht	346.1	55.3	8.4	56	68	
5	YUNN6405	Cht	291.3	67.1	6.5	56	68	
6	YUNN6406	Cht	352.1	82.0	7.1	60	68	OA
7	YUNN6407	Cht	13.1	49.6	18.7	60	68	
8	YUNN6408	Cht	89.1	68.9	4.0	52	68	
9	YUNN6410	Cht	285.3	72.3	13.0	60	68	

TILT CORR

(Wulf)

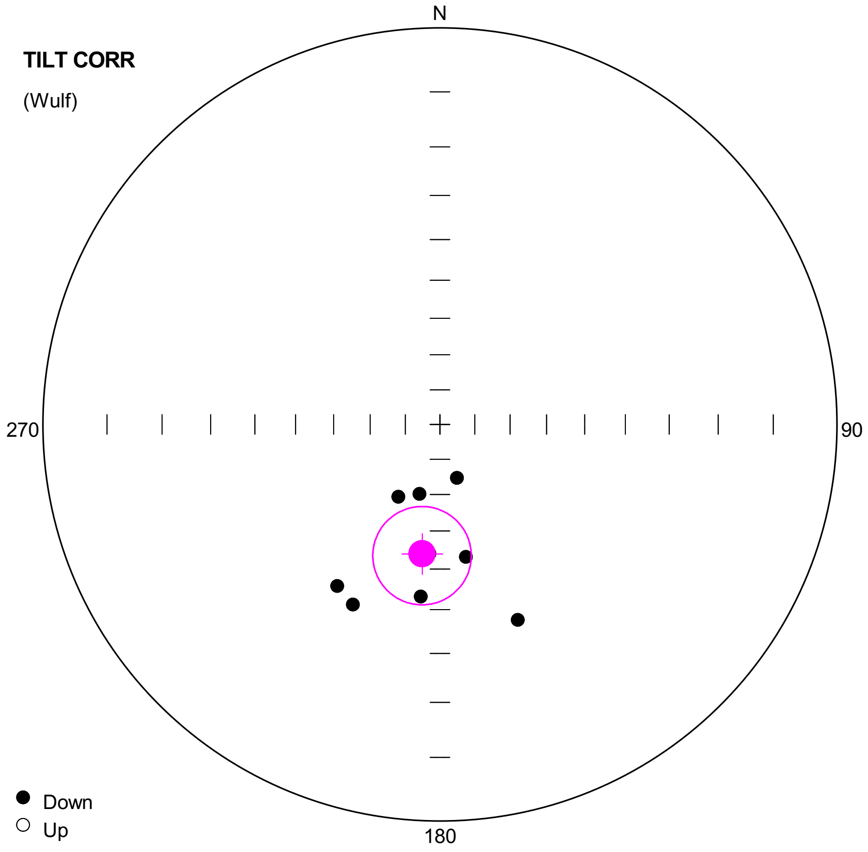

Number of data points: 9

Fisher statistics

Mean vector: 187.81 / 53.57
Resultant vector: 8.54
(X= -5.02, Y= -0.69, Z= 6.87)
Estimated precision, k: 17.27
95% Confidence limit: 12.75
95% Confidence limit, approximation: 11.23

Orientation matrix

1st eigenvalue: 0.9
1st eigenvector: 187.97 / 53.69
2nd eigenvalue: 0.05
2nd eigenvector: 28.88 / 34.47
3rd eigenvalue: 0.05
3rd eigenvector: 291.9 / 10.04

VGP

Site latitude: 65
Site longitude: 14.04
Pole latitude: 9.3 (-9.3)
Pole longitude: 7.5 (-172.5)
Paleolatitude: 34.11 (-34.11)
dp: 12.39
dm: 17.77

#	Name	State	Dec	Inc	MAD	Limit1	Limit2	
1	YUNN6401	Cht	184.7	53.8	5.0	56	68	
2	YUNN6402	Cht	168.9	52.4	8.0	48	68	
3	YUNN6403	Cht	196.3	69.3	0.0	64	68	
4	YUNN6404	Cht	209.8	66.3	8.4	56	68	
5	YUNN6405	Cht	212.4	38.5	6.5	56	68	
6	YUNN6406	Cht	186.3	42.8	7.1	60	68	OA
7	YUNN6407	Cht	162.2	73.9	18.7	60	68	
8	YUNN6408	Cht	158.3	34.1	4.0	52	68	
9	YUNN6410	Cht	205.8	36.5	13.0	60	68	

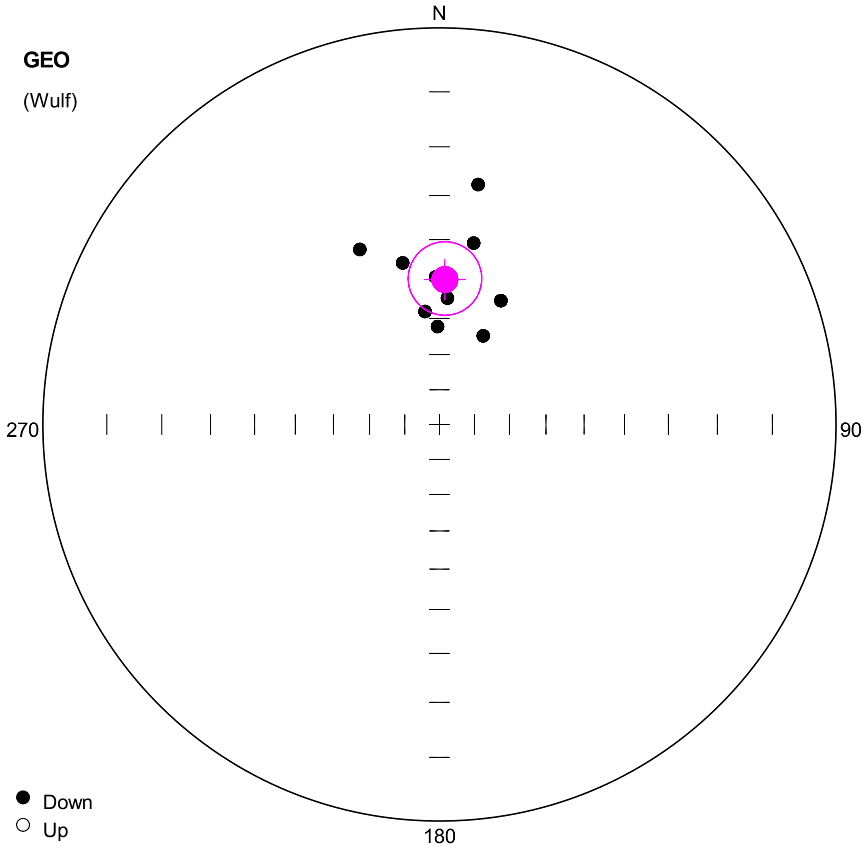

Number of data points: 10

Fisher statistics

Mean vector: 2.12 / 49.83

Resultant vector: 9.68

(X= 6.24, Y= 0.23, Z= 7.39)

Estimated precision, k: 27.74

95% Confidence limit: 9.33

95% Confidence limit, approximation: 8.41

Orientation matrix

1st eigenvalue: 0.94

1st eigenvector: 2.14 / 49.98

2nd eigenvalue: 0.04

2nd eigenvector: 141.2 / 32.38

3rd eigenvalue: 0.03

3rd eigenvector: 245.17 / 20.84

VGP

Site latitude: 65

Site longitude: 14.04

Pole latitude: 55.61 (-55.61)

Pole longitude: -169.2 (10.8)

Paleolatitude: 30.64 (-30.64)

dp: 8.3

dm: 12.45

#	Name	State	Dec	Inc	MAD	Limit1	Limit2
1	YUNN6501	Cht	359.0	62.3	0.0	64	68
2	YUNN6502	Cht	352.7	58.0	0.0	64	68
3	YUNN6503	Cht	347.2	44.7	0.0	64	68
4	YUNN6504	Cht	358.5	49.2	0.0	64	68
5	YUNN6505	Cht	335.5	38.3	0.0	64	68
6	YUNN6506	Cht	3.7	54.6	0.0	64	68
7	YUNN6507	Cht	9.2	27.0	0.0	64	68
8	YUNN6508	Cht	26.4	62.0	0.0	64	68
9	YUNN6509	Cht	10.7	40.1	0.0	64	68
10	YUNN6510	Cht	26.4	51.6	8.8	60	68

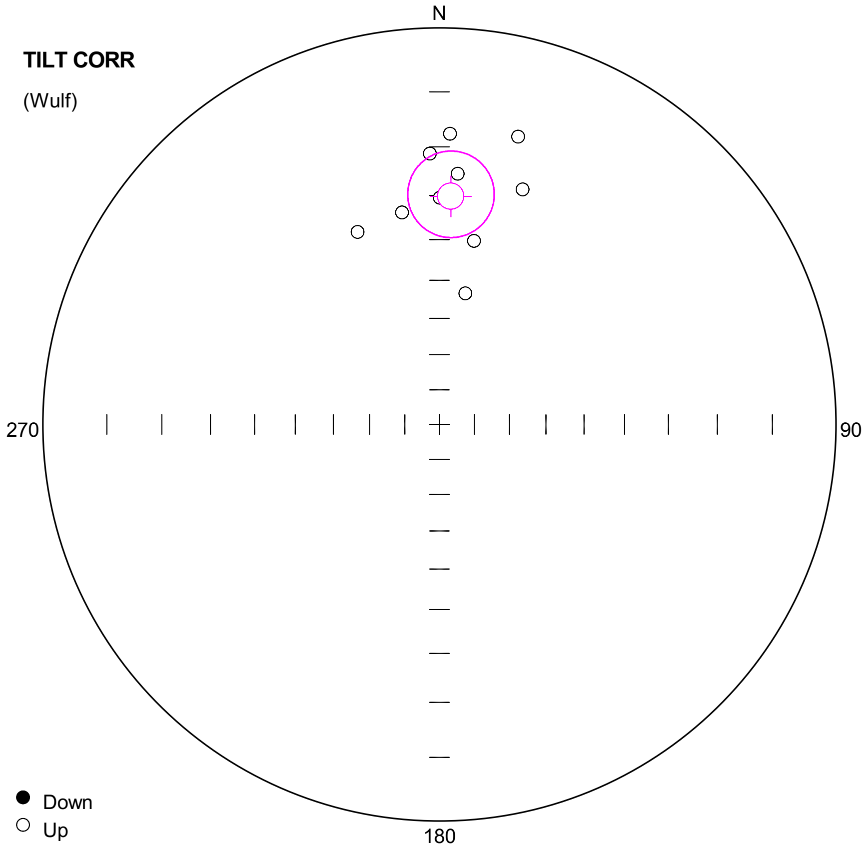

Number of data points: 10

Fisher statistics

Mean vector: 2.86 / -30.11

Resultant vector: 9.68

(X= 8.36, Y= 0.42, Z= -4.85)

Estimated precision, k: 27.7

95% Confidence limit: 9.34

95% Confidence limit, approximation: 8.41

Orientation matrix

1st eigenvalue: 0.94

1st eigenvector: 182.88 / 29.96

2nd eigenvalue: 0.04

2nd eigenvector: 59.21 / 43.89

3rd eigenvalue: 0.03

3rd eigenvector: 293.4 / 31.31

VGP

Site latitude: 65

Site longitude: 14.04

Pole latitude: 8.8 (-8.8)

Pole longitude: -168.73 (11.27)

Paleolatitude: -16.17 (16.17)

dp: 5.76

dm: 10.37

#	Name	State	Dec	Inc	MAD	Limit1	Limit2
1	YUNN6501	Cht	2.1	-17.5	0.0	64	68
2	YUNN6502	Cht	358.0	-21.3	0.0	64	68
3	YUNN6503	Cht	350.0	-33.0	0.0	64	68
4	YUNN6504	Cht	0.1	-30.5	0.0	64	68
5	YUNN6505	Cht	337.0	-34.4	0.0	64	68
6	YUNN6506	Cht	4.2	-25.3	0.0	64	68
7	YUNN6507	Cht	11.2	-52.8	0.0	64	68
8	YUNN6508	Cht	15.3	-16.1	0.0	64	68
9	YUNN6509	Cht	10.7	-39.6	0.0	64	68
10	YUNN6510	Cht	19.5	-25.7	8.8	60	68

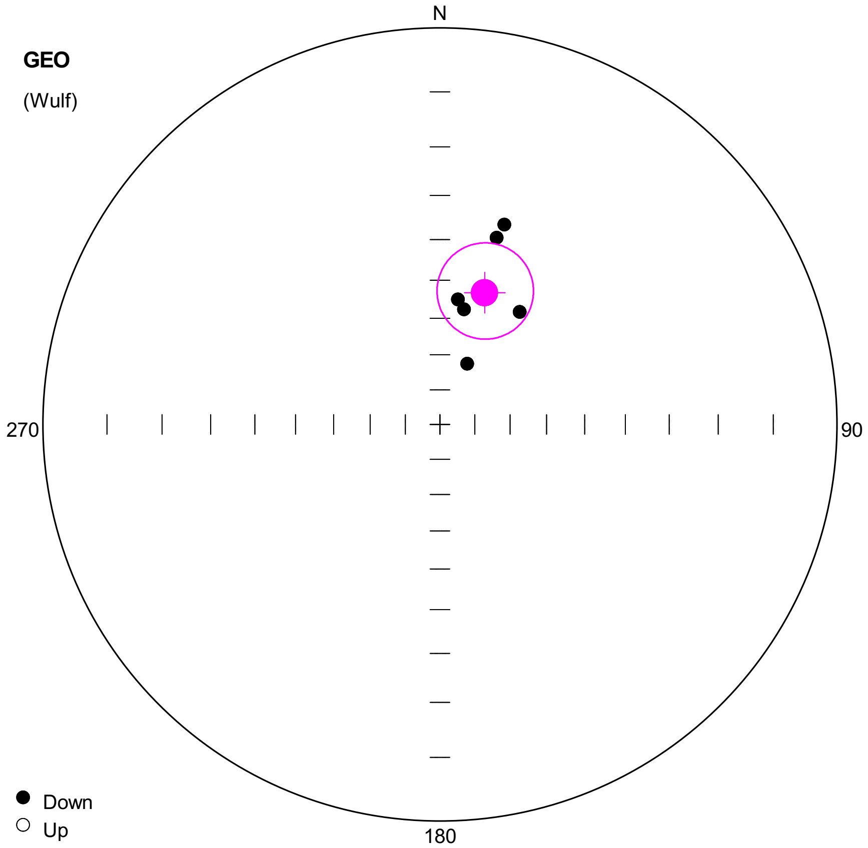

Number of data points: 6

Fisher statistics

Mean vector: 18.69 / 51.34

Resultant vector: 5.84

(X= 3.45, Y= 1.17, Z= 4.56)

Estimated precision, k: 30.53

95% Confidence limit: 12.32

95% Confidence limit, approximation: 10.34

Orientation matrix

1st eigenvalue: 0.95

1st eigenvector: 18.65 / 51.32

2nd eigenvalue: 0.05

2nd eigenvector: 195.07 / 38.62

3rd eigenvalue: 0.01

3rd eigenvector: 286.46 / 1.75

VGP

Site latitude: 65

Site longitude: 14.04

Pole latitude: 55.07 (-55.07)

Pole longitude: 165.72 (-14.28)

Paleolatitude: 32.01 (-32.01)

dp: 11.35

dm: 16.72

#	Name	State	Dec	Inc	MAD	Limit1	Limit2
1	YUNN6601	Ch	8.2	54.7	4.6	35	68
2	YUNN6602	Ch	11.8	57.0	4.5	40	68
3	YUNN6603	Ch	24.1	71.0	12.8	48	68
4	YUNN6604	Ch	17.8	34.2	8.6	20	56
5	YUNN6605	Ch	35.3	51.7	12.5	30	56
6	YUNN6606	Ch	16.9	37.6	7.9	30	56

TILT CORR

(Wulf)

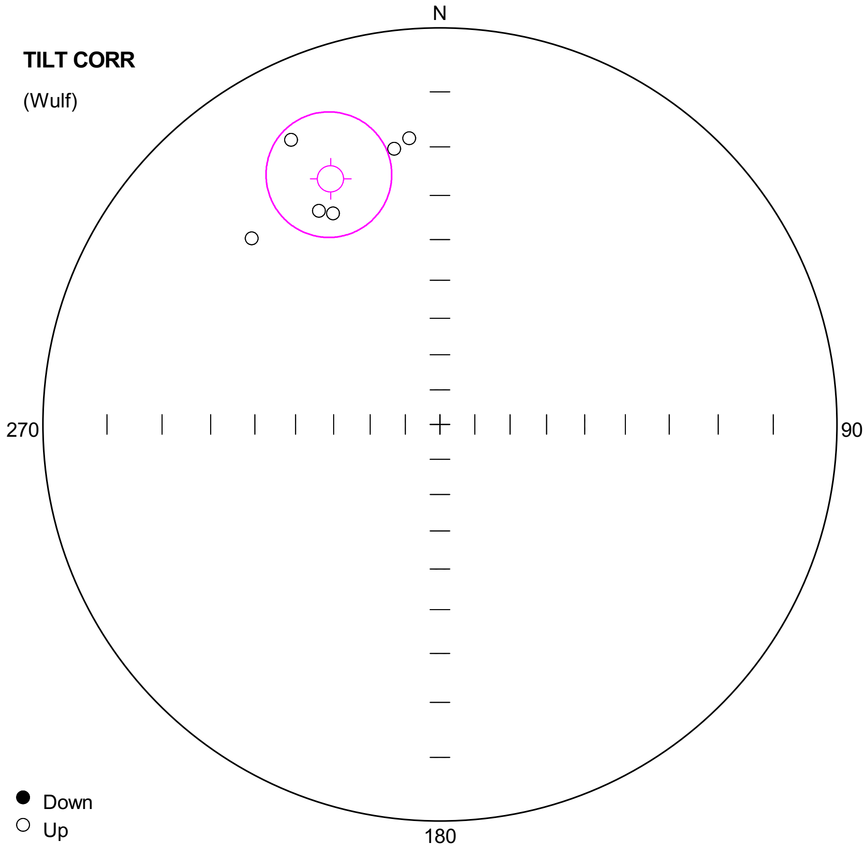

Number of data points: 6

Fisher statistics

Mean vector: 336.04 / -21.74
Resultant vector: 5.84
(X= 4.95, Y= -2.2, Z= -2.16)
Estimated precision, k: 30.58
95% Confidence limit: 12.31
95% Confidence limit, approximation: 10.34

Orientation matrix

1st eigenvalue: 0.95
1st eigenvector: 156.06 / 21.76
2nd eigenvalue: 0.05
2nd eigenvector: 62.75 / 8.24
3rd eigenvalue: 0.01
3rd eigenvector: 313.23 / 66.58

VGP

Site latitude: 65
Site longitude: 14.04
Pole latitude: 11.63 (-11.63)
Pole longitude: -141.97 (38.03)
Paleolatitude: -11.28 (11.28)
dp: 6.86
dm: 13

#	Name	State	Dec	Inc	MAD	Limit1	Limit2
1	YUNN6601	Ch	333.2	-28.4	4.6	35	68
2	YUNN6602	Ch	330.5	-26.5	4.5	40	68
3	YUNN6603	Ch	314.7	-22.6	12.8	48	68
4	YUNN6604	Ch	353.9	-18.1	8.6	20	56
5	YUNN6605	Ch	332.4	-12.0	12.5	30	56
6	YUNN6606	Ch	350.6	-19.7	7.9	30	56

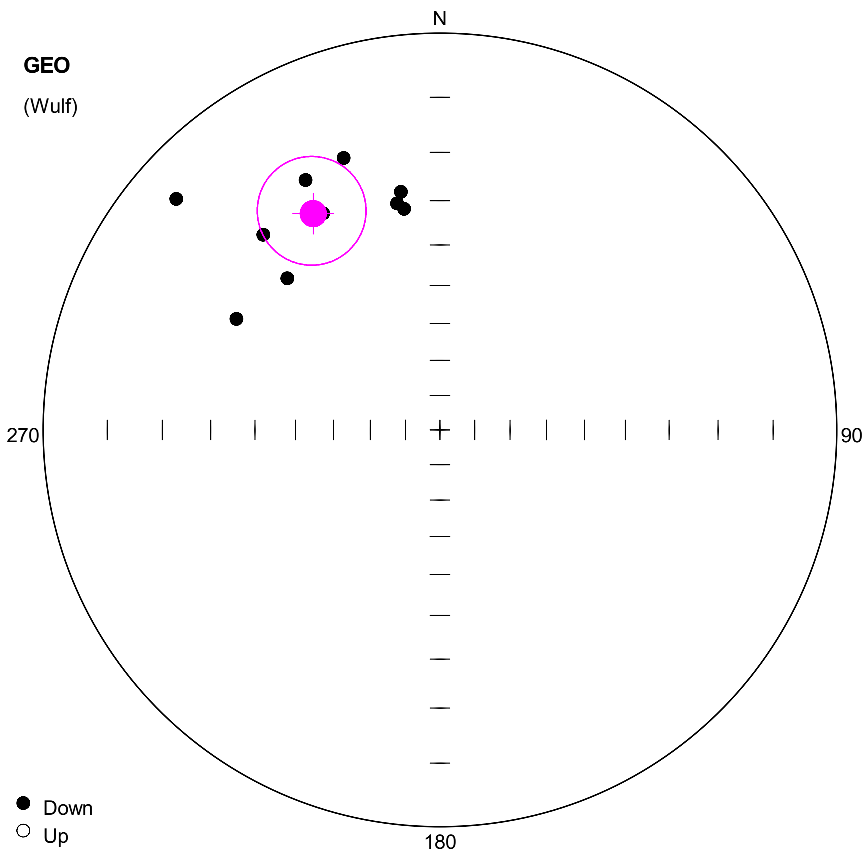

Number of data points: 10

Fisher statistics

Mean vector: 329.64 / 25.44
Resultant vector: 9.54
(X= 7.44, Y= -4.36, Z= 4.1)
Estimated precision, k: 19.76
95% Confidence limit: 11.14
95% Confidence limit, approximation: 9.96

Orientation matrix

1st eigenvalue: 0.91
1st eigenvector: 329.94 / 25.43
2nd eigenvalue: 0.07
2nd eigenvector: 63.25 / 6.92
3rd eigenvalue: 0.02
3rd eigenvector: 167.35 / 63.51

VGP

Site latitude: 65
Site longitude: 14.04
Pole latitude: 34.37 (-34.37)
Pole longitude: -129.4 (50.6)
Paleolatitude: 13.38 (-13.38)
dp: 6.47
dm: 12

#	Name	State	Dec	Inc	MAD	Limit1	Limit2	
1	YUNN6701	Ch	349.3	29.7	3.0	30	64	OA
2	YUNN6702	Ch	311.2	7.1	5.7	30	64	OA
3	YUNN6703	Ch	350.7	27.4	5.1	20	64	OA
4	YUNN6704	Ch	298.6	29.4	6.7	20	64	OA
5	YUNN6705	Ch	317.9	22.9	3.9	20	56	OA
6	YUNN6706	Ch	350.8	31.1	4.0	20	64	OA
7	YUNN6708	Ch	331.7	26.4	3.4	30	64	
8	YUNN6709	Ch	340.5	18.0	5.3	35	64	OA
9	YUNN6710	Ch	331.7	18.9	4.3	20	64	OA
10	YUNN6711	Ch	314.8	33.1	5.3	20	68	OA

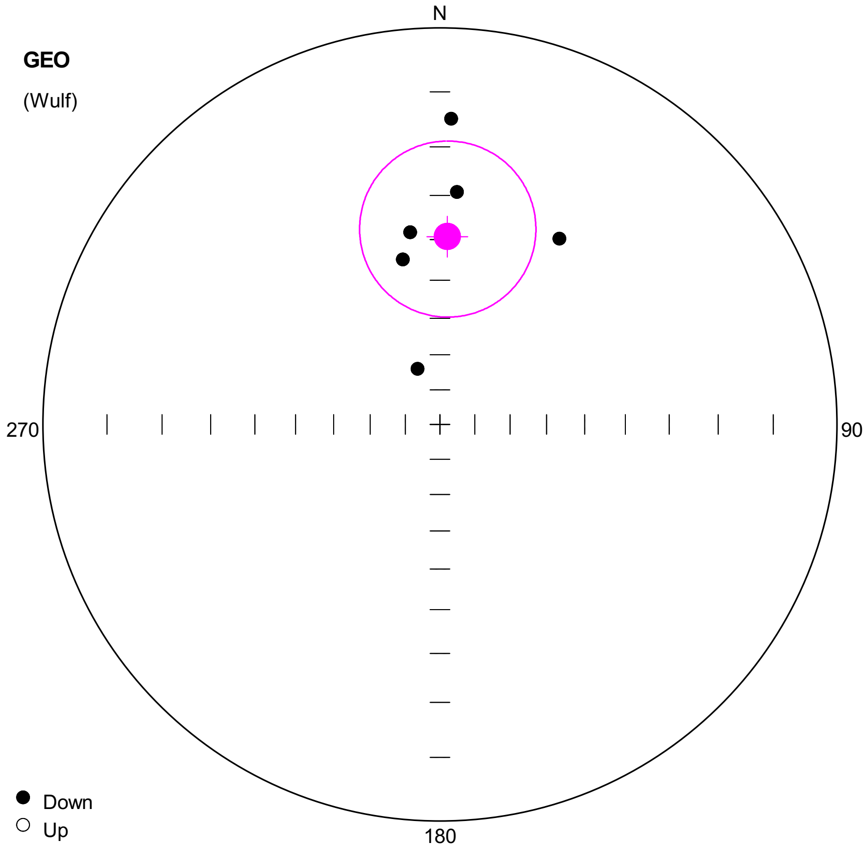

Number of data points: 6

Fisher statistics

Mean vector: 2.26 / 39.26

Resultant vector: 5.57

(X= 4.31, Y= 0.17, Z= 3.53)

Estimated precision, k: 11.74

95% Confidence limit: 20.39

95% Confidence limit, approximation: 16.68

Orientation matrix

1st eigenvalue: 0.87

1st eigenvector: 2.06 / 38.5

2nd eigenvalue: 0.1

2nd eigenvector: 211.61 / 47.57

3rd eigenvalue: 0.04

3rd eigenvector: 104.45 / 15.09

VGP

Site latitude: 65

Site longitude: 14.04

Pole latitude: 47.2 (-47.2)

Pole longitude: -169.04 (10.96)

Paleolatitude: 22.23 (-22.23)

dp: 14.57

dm: 24.38

#	Name	State	Dec	Inc	MAD	Limit1	Limit2	
1	YUNN6801	Ch	2.1	14.7	8.2	20	68	OA
2	YUNN6803	Ch	351.2	37.8	2.2	20	52	OA
3	YUNN6804	Ch	4.2	29.1	5.1	20	64	OA
4	YUNN6805	Ch	347.4	43.8	6.2	20	64	OA
5	YUNN6806	Ch	338.1	72.8	7.3	40	64	OA
6	YUNN6808	Ch	32.7	31.8	10.1	48	64	OA

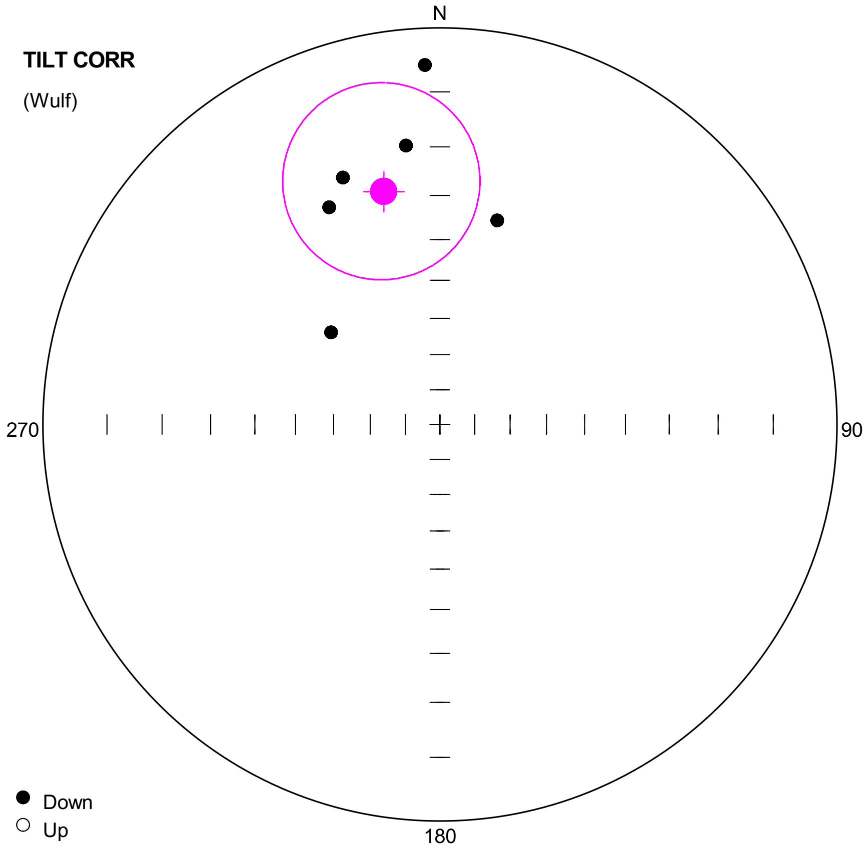

Number of data points: 6

Fisher statistics

Mean vector: 346.44 / 27.72

Resultant vector: 5.57

(X= 4.8, Y= -1.16, Z= 2.59)

Estimated precision, k: 11.74

95% Confidence limit: 20.39

95% Confidence limit, approximation: 16.68

Orientation matrix

1st eigenvalue: 0.87

1st eigenvector: 346.69 / 26.98

2nd eigenvalue: 0.1

2nd eigenvector: 233.97 / 37.18

3rd eigenvalue: 0.04

3rd eigenvector: 102.87 / 40.91

VGP

Site latitude: 65

Site longitude: 14.04

Pole latitude: 38.88 (-38.88)

Pole longitude: -149.02 (30.98)

Paleolatitude: 14.72 (-14.72)

dp: 12.17

dm: 22.28

#	Name	State	Dec	Inc	MAD	Limit1	Limit2	
1	YUNN6801	Ch	357.6	5.6	8.2	20	68	OA
2	YUNN6803	Ch	338.6	22.5	2.2	20	52	OA
3	YUNN6804	Ch	353.1	19.4	5.1	20	64	OA
4	YUNN6805	Ch	333.0	26.9	6.2	20	64	OA
5	YUNN6806	Ch	310.3	50.5	7.3	40	64	OA
6	YUNN6808	Ch	15.7	33.8	10.1	48	64	OA

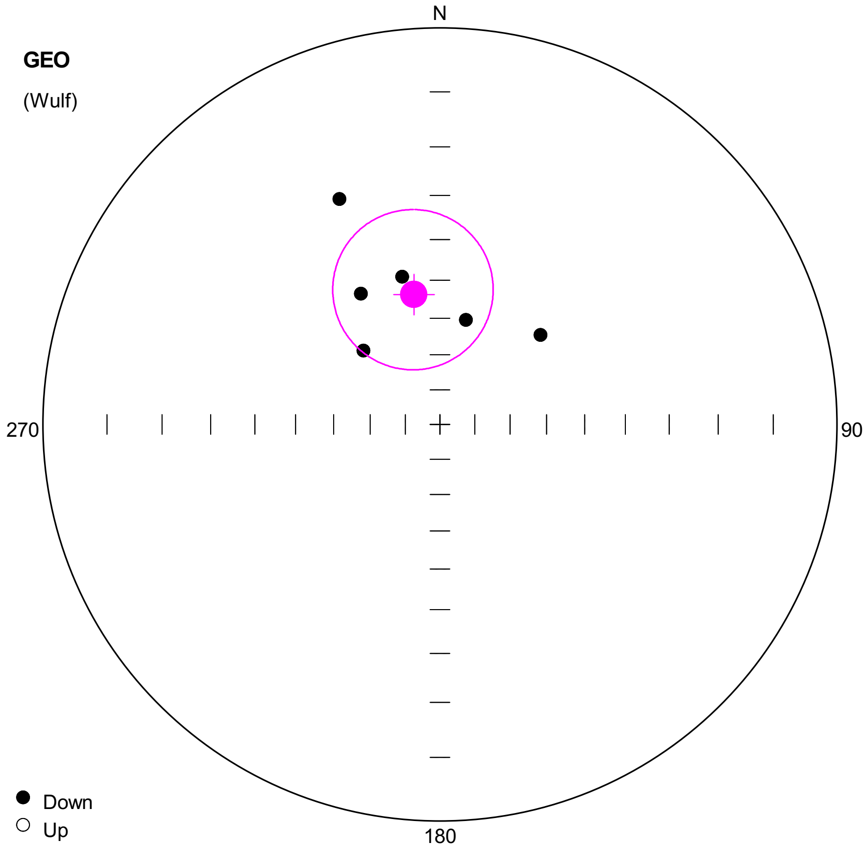

Number of data points: 6

Fisher statistics

Mean vector: 348.65 / 53.01
Resultant vector: 5.57
(X= 3.29, Y= -0.66, Z= 4.45)
Estimated precision, k: 11.61
95% Confidence limit: 20.52
95% Confidence limit, approximation: 16.77

Orientation matrix

1st eigenvalue: 0.87
1st eigenvector: 347.52 / 52.92
2nd eigenvalue: 0.1
2nd eigenvector: 105.63 / 19.6
3rd eigenvalue: 0.03
3rd eigenvector: 207.53 / 30.07

VGP

Site latitude: 65
Site longitude: 14.04
Pole latitude: 57.83 (-57.83)
Pole longitude: -148.03 (31.97)
Paleolatitude: 33.58 (-33.58)
dp: 19.67
dm: 28.41

#	Name	State	Dec	Inc	MAD	Limit1	Limit2	
1	YUNN6901	Cmt	336.0	26.2	6.1	40	60	
2	YUNN6902	Ch	314.0	60.0	7.4	20	68	OA
3	YUNN6903	Ch	14.0	59.6	8.8	20	64	OA
4	YUNN6904	Ch	48.3	52.5	15.8	40	64	
5	YUNN6907	Ch	328.9	47.9	4.4	30	64	OA
6	YUNN6908	Ch	345.7	48.0	3.4	20	56	OA

TILT CORR

(Wulf)

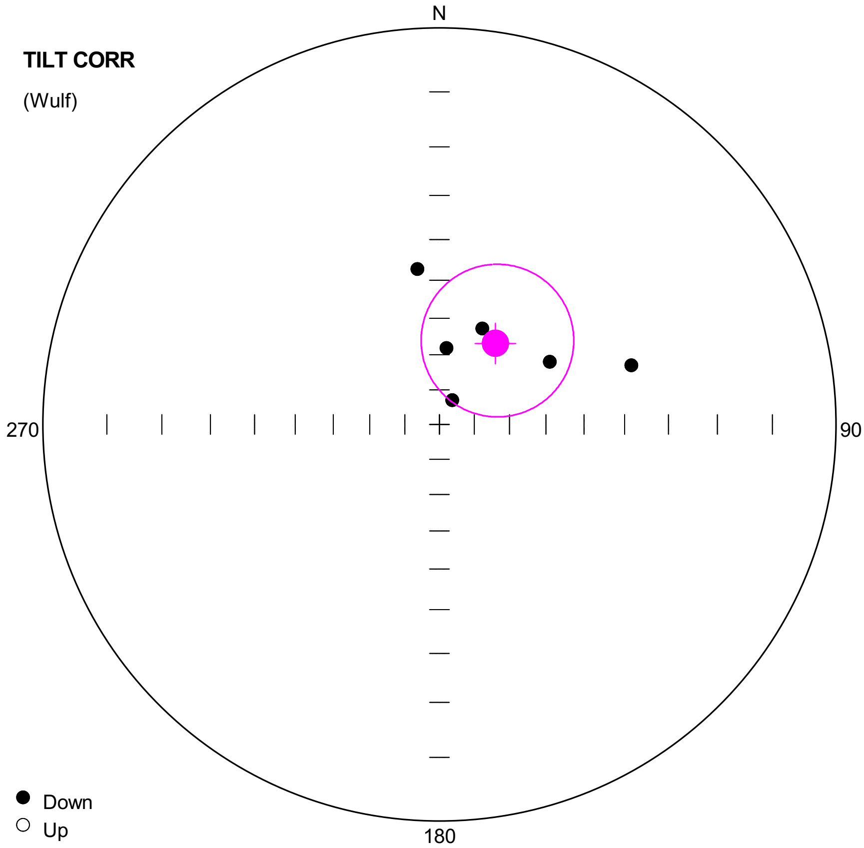

Number of data points: 6

Fisher statistics

Mean vector: 34.58 / 62.09

Resultant vector: 5.57

(X= 2.15, Y= 1.48, Z= 4.92)

Estimated precision, k: 11.63

95% Confidence limit: 20.5

95% Confidence limit, approximation: 16.76

Orientation matrix

1st eigenvalue: 0.87

1st eigenvector: 33.55 / 62.58

2nd eigenvalue: 0.1

2nd eigenvector: 286.23 / 8.78

3rd eigenvalue: 0.03

3rd eigenvector: 191.95 / 25.76

VGP

Site latitude: 65

Site longitude: 14.04

Pole latitude: 61.06 (-61.06)

Pole longitude: 135.5 (-44.5)

Paleolatitude: 43.34 (-43.34)

dp: 24.74

dm: 31.85

#	Name	State	Dec	Inc	MAD	Limit1	Limit2	
1	YUNN6901	Cmt	351.9	46.8	6.1	40	60	
2	YUNN6902	Ch	27.7	82.1	7.4	20	68	OA
3	YUNN6903	Ch	60.4	54.5	8.8	20	64	OA
4	YUNN6904	Ch	72.9	36.3	15.8	40	64	
5	YUNN6907	Ch	5.4	68.1	4.4	30	64	OA
6	YUNN6908	Ch	24.1	60.3	3.4	20	56	OA

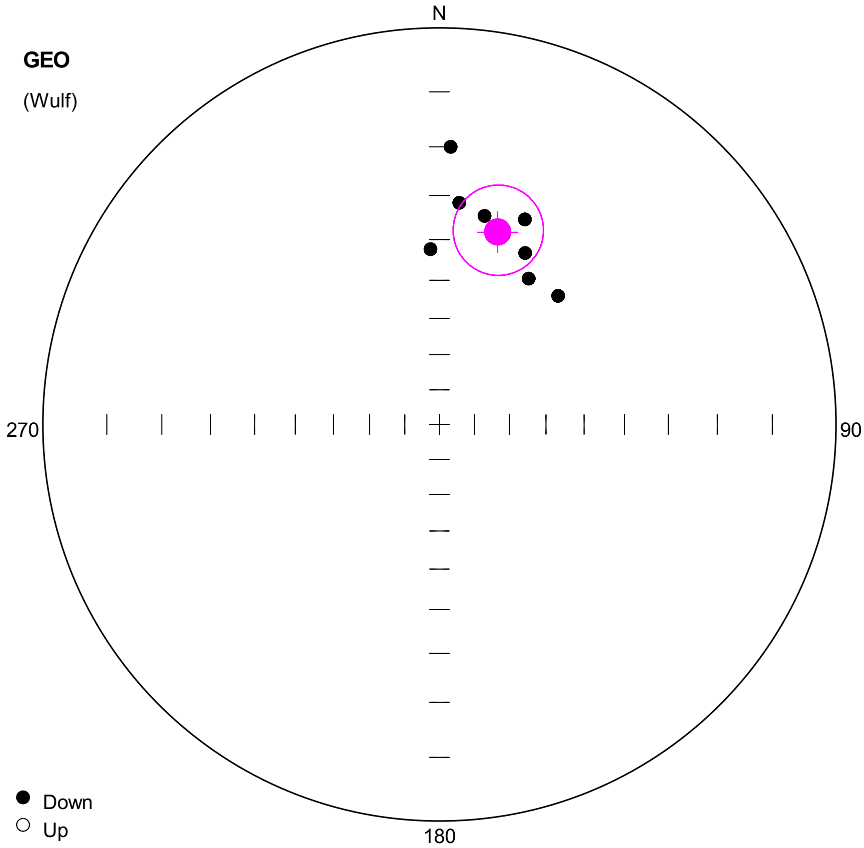

Number of data points: 8

Fisher statistics

Mean vector: 16.83 / 36.27
Resultant vector: 7.76
(X= 5.99, Y= 1.81, Z= 4.59)
Estimated precision, k: 29.71
95% Confidence limit: 10.33
95% Confidence limit, approximation: 9.08

Orientation matrix

1st eigenvalue: 0.94
1st eigenvector: 16.83 / 36.26
2nd eigenvalue: 0.05
2nd eigenvector: 123.6 / 21.47
3rd eigenvalue: 0.01
3rd eigenvector: 237.57 / 45.93

VGP

Site latitude: 65
Site longitude: 14.04
Pole latitude: 43.78 (-43.78)
Pole longitude: 171.93 (-8.07)
Paleolatitude: 20.15 (-20.15)
dp: 7
dm: 12.03

#	Name	State	Dec	Inc	MAD	Limit1	Limit2	
1	YUNN7001	Ch	5.1	31.4	6.8	20	68	
2	YUNN7002	Ch	22.6	31.5	4.5	30	64	
3	YUNN7003	Ch	26.6	38.4	5.0	35	60	
4	YUNN7004	Ch	2.3	20.0	6.9	30	64	OA
5	YUNN7005	Ch	12.2	33.5	5.4	30	64	
6	YUNN7006	Ch	42.8	42.4	5.1	40	60	
7	YUNN7007	Ch	31.5	43.4	6.7	35	64	
8	YUNN7008	Ch	357.1	42.3	12.2	30	64	

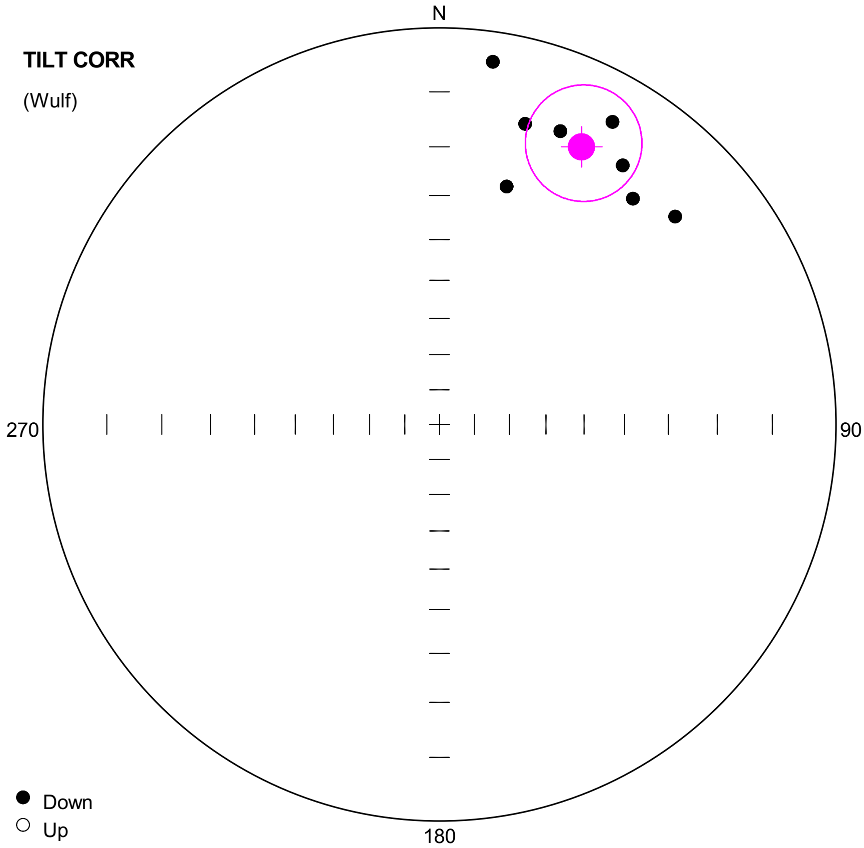

Number of data points: 8

Fisher statistics

Mean vector: 27.12 / 13.63
Resultant vector: 7.76
(X= 6.72, Y= 3.44, Z= 1.83)
Estimated precision, k: 29.77
95% Confidence limit: 10.32
95% Confidence limit, approximation: 9.07

Orientation matrix

1st eigenvalue: 0.94
1st eigenvector: 27.12 / 13.62
2nd eigenvalue: 0.05
2nd eigenvector: 117.9 / 3.2
3rd eigenvalue: 0.01
3rd eigenvector: 220.86 / 75.99

VGP

Site latitude: 65
Site longitude: 14.04
Pole latitude: 28.85 (-28.85)
Pole longitude: 162.93 (-17.07)
Paleolatitude: 6.91 (-6.91)
dp: 5.38
dm: 10.54

#	Name	State	Dec	Inc	MAD	Limit1	Limit2	
1	YUNN7001	Ch	15.9	13.5	6.8	20	68	
2	YUNN7002	Ch	29.8	7.4	4.5	30	64	
3	YUNN7003	Ch	35.3	12.7	5.0	35	60	
4	YUNN7004	Ch	8.4	4.5	6.9	30	64	OA
5	YUNN7005	Ch	22.4	12.7	5.4	30	64	
6	YUNN7006	Ch	48.6	13.2	5.1	40	60	
7	YUNN7007	Ch	40.6	16.3	6.7	35	64	
8	YUNN7008	Ch	15.8	26.1	12.2	30	64	

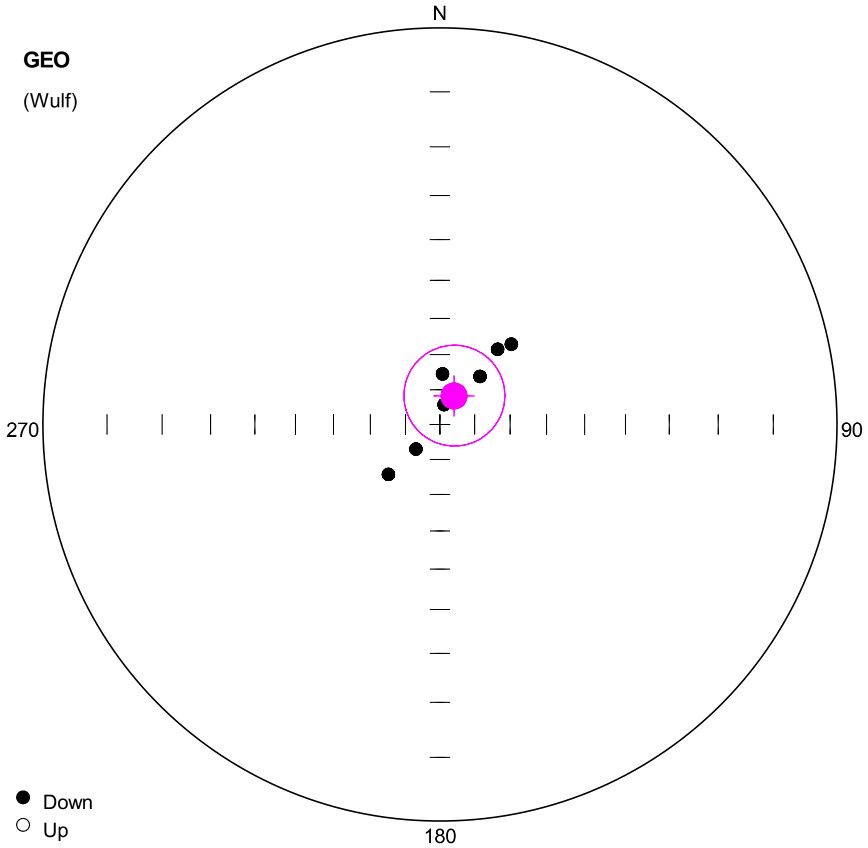

Number of data points: 7

Fisher statistics

Mean vector: 26.34 / 80.84
Resultant vector: 6.68
(X= 0.95, Y= 0.47, Z= 6.59)
Estimated precision, k: 18.56
95% Confidence limit: 14.39
95% Confidence limit, approximation: 12.28

Orientation matrix

1st eigenvalue: 0.91
1st eigenvector: 26.61 / 80.48
2nd eigenvalue: 0.09
2nd eigenvector: 221.79 / 9.2
3rd eigenvalue: 0
3rd eigenvector: 131.4 / 2.45

VGP

Site latitude: 65
Site longitude: 14.04
Pole latitude: 78.18 (-78.18)
Pole longitude: 55.72 (-124.28)
Paleolatitude: 72.13 (-72.13)
dp: 26.74
dm: 27.74

#	Name	State	Dec	Inc	MAD	Limit1	Limit2	
1	YUNN7101	Ch	2.9	75.5	22.0	20	56	
2	YUNN7102	Ch	37.5	63.1	12.3	20	64	
3	YUNN7104	Ch	223.8	80.1	3.6	20	60	OA
4	YUNN7105	Ch	225.9	69.5	7.6	20	68	OA
5	YUNN7106	Ch	12.1	84.2	21.2	56	68	OA
6	YUNN7108	Ch	41.7	59.7	3.2	48	56	OA
7	YUNN7109	Ch	39.9	72.1	4.4	30	56	OA

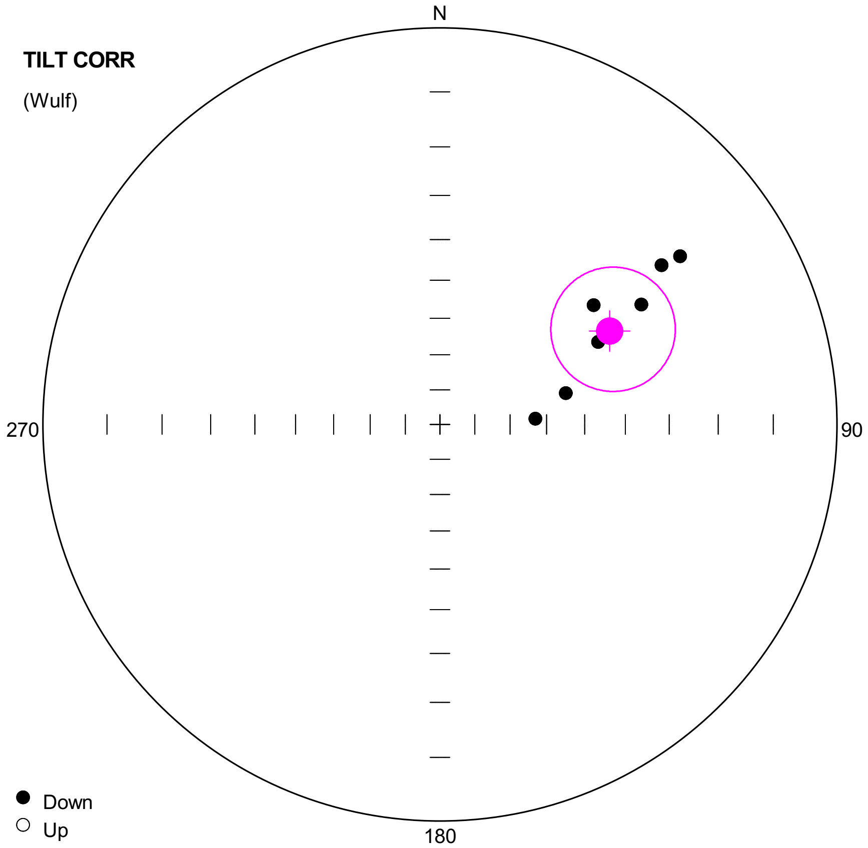

Number of data points: 7

Fisher statistics

Mean vector: 61.13 / 37.99

Resultant vector: 6.68

(X= 2.54, Y= 4.61, Z= 4.11)

Estimated precision, k: 18.58

95% Confidence limit: 14.38

95% Confidence limit, approximation: 12.27

Orientation matrix

1st eigenvalue: 0.91

1st eigenvector: 60.9 / 37.67

2nd eigenvalue: 0.09

2nd eigenvector: 207.39 / 47.2

3rd eigenvalue: 0

3rd eigenvector: 317.01 / 17.27

VGP

Site latitude: 65

Site longitude: 14.04

Pole latitude: 31.31 (-31.31)

Pole longitude: 121.32 (-58.68)

Paleolatitude: 21.33 (-21.33)

dp: 10.04

dm: 16.99

#	Name	State	Dec	Inc	MAD	Limit1	Limit2	
1	YUNN7101	Ch	52.2	37.8	22.0	20	56	
2	YUNN7102	Ch	54.3	21.0	12.3	20	64	
3	YUNN7104	Ch	76.1	53.8	3.6	20	60	OA
4	YUNN7105	Ch	86.5	62.9	7.6	20	68	OA
5	YUNN7106	Ch	62.5	41.6	21.2	56	68	OA
6	YUNN7108	Ch	55.0	17.1	3.2	48	56	OA
7	YUNN7109	Ch	59.2	28.9	4.4	30	56	OA

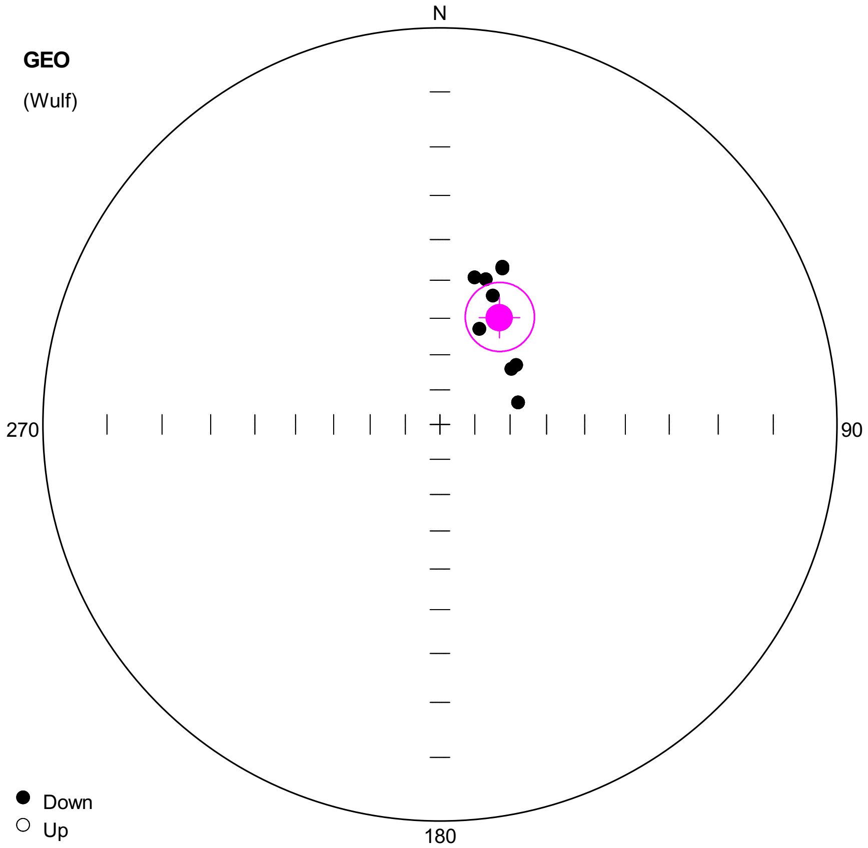

Number of data points: 9

Fisher statistics

Mean vector: 29.04 / 55.74

Resultant vector: 8.76

(X= 4.31, Y= 2.39, Z= 7.24)

Estimated precision, k: 33.06

95% Confidence limit: 9.09

95% Confidence limit, approximation: 8.12

Orientation matrix

1st eigenvalue: 0.95

1st eigenvector: 28.76 / 55.6

2nd eigenvalue: 0.05

2nd eigenvector: 161.49 / 24.92

3rd eigenvalue: 0

3rd eigenvector: 262.37 / 22.11

VGP

Site latitude: 65

Site longitude: 14.04

Pole latitude: 56.53 (-56.53)

Pole longitude: 148.84 (-31.16)

Paleolatitude: 36.28 (-36.28)

dp: 9.32

dm: 13.01

#	Name	State	Dec	Inc	MAD	Limit1	Limit2
1	YUNN7202	Ch	21.8	44.1	7.9	35	64
2	YUNN7203	Ch	21.6	43.7	5.8	30	60
3	YUNN7204	Ch	17.5	48.0	7.4	30	64
4	YUNN7205	Ch	13.3	48.3	4.1	20	64
5	YUNN7206	Ch	74.3	66.9	5.3	35	64
6	YUNN7207	Ch	22.5	60.8	4.4	30	64
7	YUNN7208	Cht	22.3	51.3	3.6	48	64
8	YUNN7209	Ch	52.0	62.6	6.3	30	60
9	YUNN7210	Ch	52.0	64.3	4.3	35	64

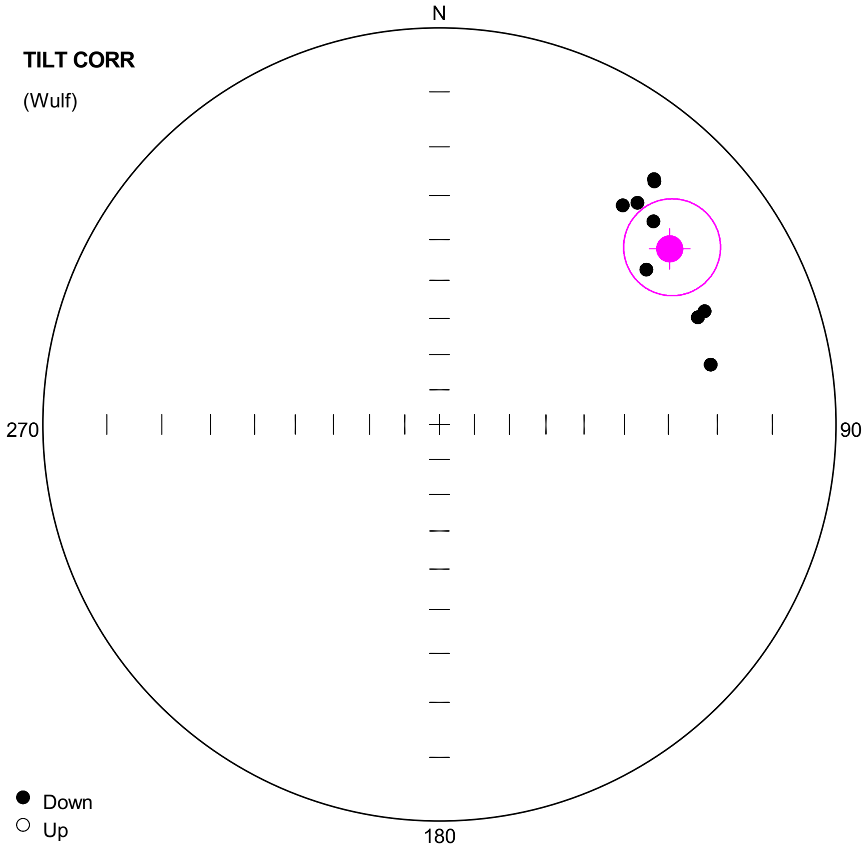

Number of data points: 9

Fisher statistics

Mean vector: 52.68 / 17.73

Resultant vector: 8.76

(X= 5.06, Y= 6.63, Z= 2.67)

Estimated precision, k: 33.12

95% Confidence limit: 9.08

95% Confidence limit, approximation: 8.11

Orientation matrix

1st eigenvalue: 0.95

1st eigenvector: 52.46 / 17.71

2nd eigenvalue: 0.05

2nd eigenvector: 146 / 10.96

3rd eigenvalue: 0

3rd eigenvector: 266.25 / 68.98

VGP

Site latitude: 65

Site longitude: 14.04

Pole latitude: 23.33 (-23.33)

Pole longitude: 135.26 (-44.74)

Paleolatitude: 9.08 (-9.08)

dp: 4.88

dm: 9.41

#	Name	State	Dec	Inc	MAD	Limit1	Limit2
1	YUNN7202	Ch	41.5	11.4	7.9	35	64
2	YUNN7203	Ch	41.2	11.2	5.8	30	60
3	YUNN7204	Ch	41.8	16.3	7.4	30	64
4	YUNN7205	Ch	39.9	18.5	4.1	20	64
5	YUNN7206	Ch	77.6	20.0	5.3	35	64
6	YUNN7207	Ch	53.2	23.8	4.4	30	64
7	YUNN7208	Cht	46.5	16.7	3.6	48	64
8	YUNN7209	Ch	66.9	18.0	6.3	30	60
9	YUNN7210	Ch	67.5	19.6	4.3	35	64

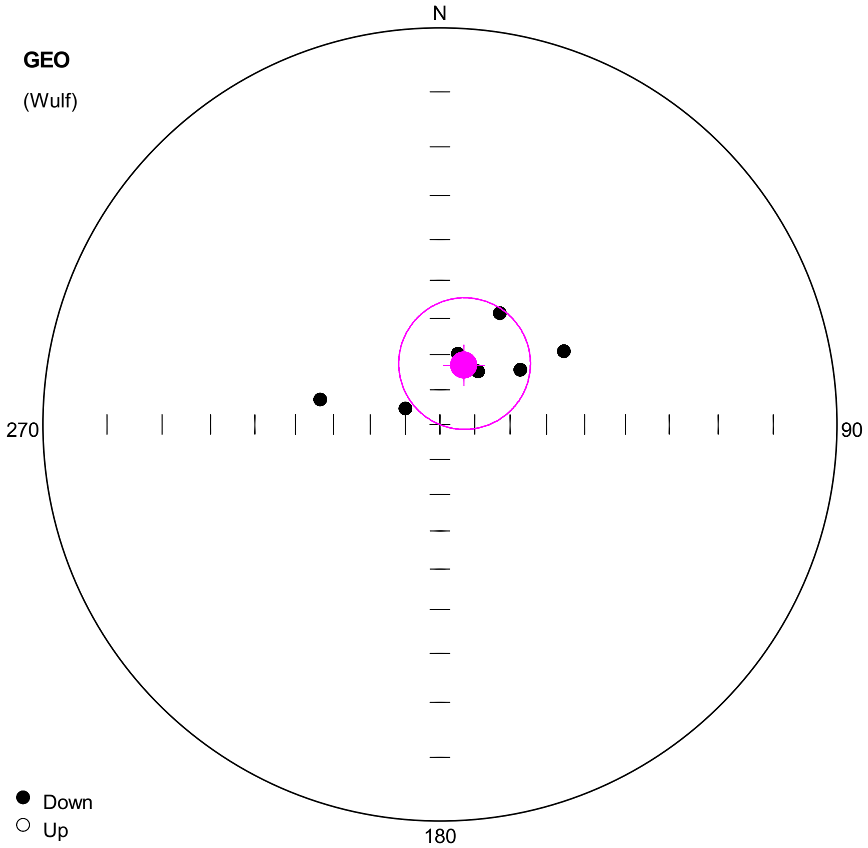

Number of data points: 7

Fisher statistics

Mean vector: 21.9 / 71.68
Resultant vector: 6.49
(X= 1.89, Y= 0.76, Z= 6.16)
Estimated precision, k: 11.77
95% Confidence limit: 18.35
95% Confidence limit, approximation: 15.42

Orientation matrix

1st eigenvalue: 0.87
1st eigenvector: 24.99 / 70.95
2nd eigenvalue: 0.12
2nd eigenvector: 256.15 / 12.22
3rd eigenvalue: 0.01
3rd eigenvector: 162.96 / 14.39

VGP

Site latitude: 65
Site longitude: 14.04
Pole latitude: 76.45 (-76.45)
Pole longitude: 132.57 (-47.43)
Paleolatitude: 56.49 (-56.49)
dp: 28.31
dm: 32.23

#	Name	State	Dec	Inc	MAD	Limit1	Limit2
1	YUNN7301	Ch	294.9	79.1	11.1	30	64
2	YUNN7303	Ch	281.7	55.8	20.4	30	64
3	YUNN7304	Ch	14.3	69.2	9.2	30	60
4	YUNN7305	Ch	35.7	71.3	4.5	44	60
5	YUNN7306	Ch	59.4	50.1	5.9	44	64
6	YUNN7307	Ch	55.8	62.5	7.2	30	56
7	YUNN7309	Ch	28.3	54.7	8.6	40	60

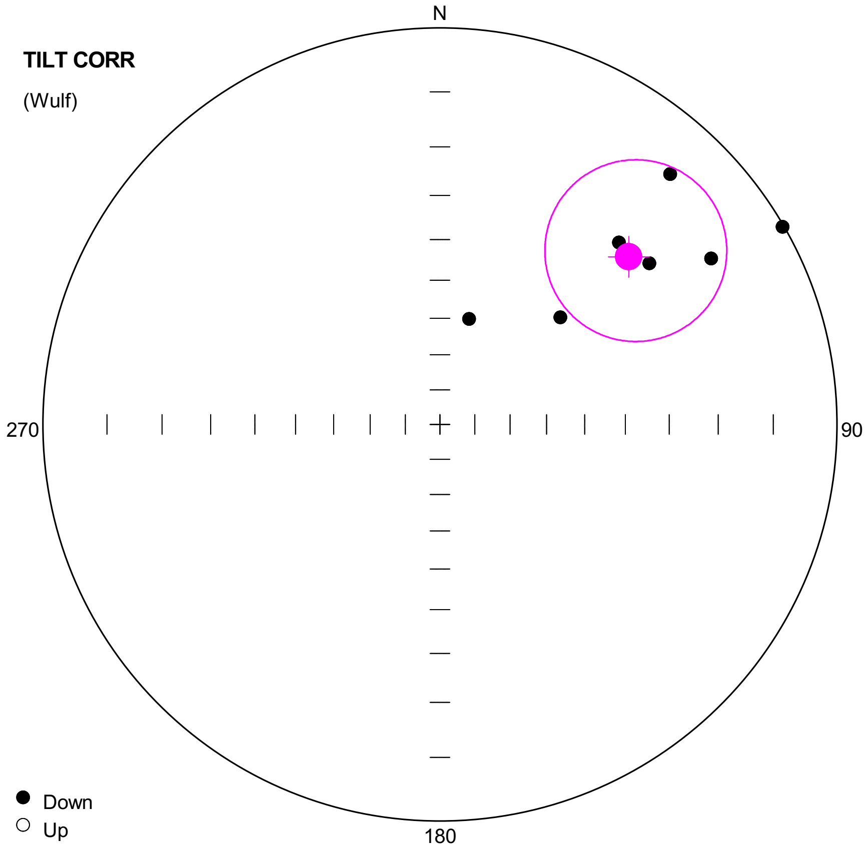

Number of data points: 7

Fisher statistics

Mean vector: 48.35 / 25.07
Resultant vector: 6.49
(X= 3.91, Y= 4.39, Z= 2.75)
Estimated precision, k: 11.8
95% Confidence limit: 18.33
95% Confidence limit, approximation: 15.41

Orientation matrix

1st eigenvalue: 0.87
1st eigenvector: 48.87 / 23.93
2nd eigenvalue: 0.12
2nd eigenvector: 270.9 / 59.14
3rd eigenvalue: 0.01
3rd eigenvector: 147.3 / 18.29

VGP

Site latitude: 65
Site longitude: 14.04
Pole latitude: 28.68 (-28.68)
Pole longitude: 138.01 (-41.99)
Paleolatitude: 13.16 (-13.16)
dp: 10.59
dm: 19.7

#	Name	State	Dec	Inc	MAD	Limit1	Limit2
1	YUNN7301	Ch	48.3	45.8	11.1	30	64
2	YUNN7303	Ch	15.5	59.1	20.4	30	64
3	YUNN7304	Ch	44.5	24.5	9.2	30	60
4	YUNN7305	Ch	52.4	22.7	4.5	44	60
5	YUNN7306	Ch	60.0	0.2	5.9	44	64
6	YUNN7307	Ch	58.5	12.6	7.2	30	56
7	YUNN7309	Ch	42.6	8.8	8.6	40	60

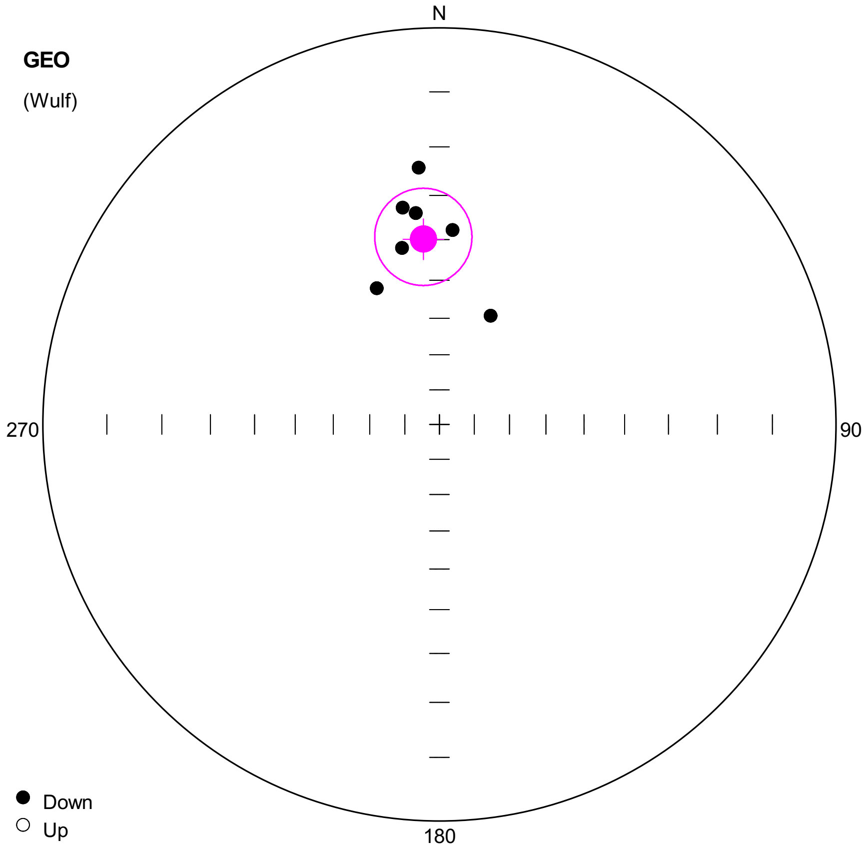

Number of data points: 7

Fisher statistics

Mean vector: 355.06 / 39.73

Resultant vector: 6.79

(X= 5.2, Y= -0.45, Z= 4.34)

Estimated precision, k: 28.75

95% Confidence limit: 11.45

95% Confidence limit, approximation: 9.87

Orientation matrix

1st eigenvalue: 0.94

1st eigenvector: 354.85 / 39.47

2nd eigenvalue: 0.04

2nd eigenvector: 137.86 / 44.12

3rd eigenvalue: 0.02

3rd eigenvector: 247.91 / 19.48

VGP

Site latitude: 65

Site longitude: 14.04

Pole latitude: 47.44 (-47.44)

Pole longitude: -159.21 (20.79)

Paleolatitude: 22.57 (-22.57)

dp: 8.25

dm: 13.75

#	Name	State	Dec	Inc	MAD	Limit1	Limit2
1	YUNN7404	Ch	348.0	41.1	3.6	30	64
2	YUNN7405	Ch	335.3	48.6	6.7	44	64
3	YUNN7406	Ch	3.9	37.7	5.1	56	64
4	YUNN7407	Cht	350.4	32.0	8.2	52	64
5	YUNN7408	Ch	355.4	24.0	5.2	40	68
6	YUNN7409	Ch	353.6	33.6	7.0	30	64
7	YUNN7410	Ch	25.3	56.3	4.4	44	64

TILT CORR

(Wulf)

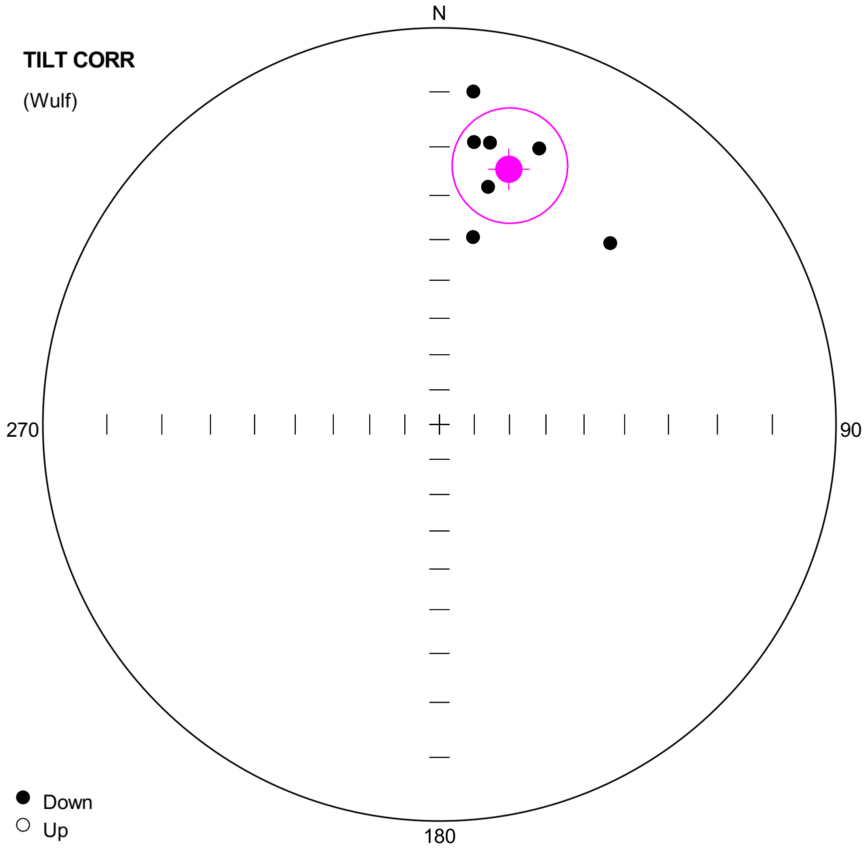

Number of data points: 7

Fisher statistics

Mean vector: 15.2 / 22.62
Resultant vector: 6.79
(X= 6.05, Y= 1.64, Z= 2.61)
Estimated precision, k: 28.75
95% Confidence limit: 11.45
95% Confidence limit, approximation: 9.87

Orientation matrix

1st eigenvalue: 0.94
1st eigenvector: 14.89 / 22.51
2nd eigenvalue: 0.04
2nd eigenvector: 115.98 / 24.89
3rd eigenvalue: 0.02
3rd eigenvector: 248.09 / 55.32

VGP

Site latitude: 65
Site longitude: 14.04
Pole latitude: 35.74 (-35.74)
Pole longitude: 175.6 (-4.4)
Paleolatitude: 11.77 (-11.77)
dp: 6.44
dm: 12.14

#	Name	State	Dec	Inc	MAD	Limit1	Limit2
1	YUNN7404	Ch	11.6	27.1	3.6	30	64
2	YUNN7405	Ch	10.2	38.7	6.7	44	64
3	YUNN7406	Ch	19.9	17.0	5.1	56	64
4	YUNN7407	Cht	7.0	18.7	8.2	52	64
5	YUNN7408	Ch	5.8	9.7	5.2	40	68
6	YUNN7409	Ch	10.2	18.4	7.0	30	64
7	YUNN7410	Ch	43.3	25.7	4.4	44	64

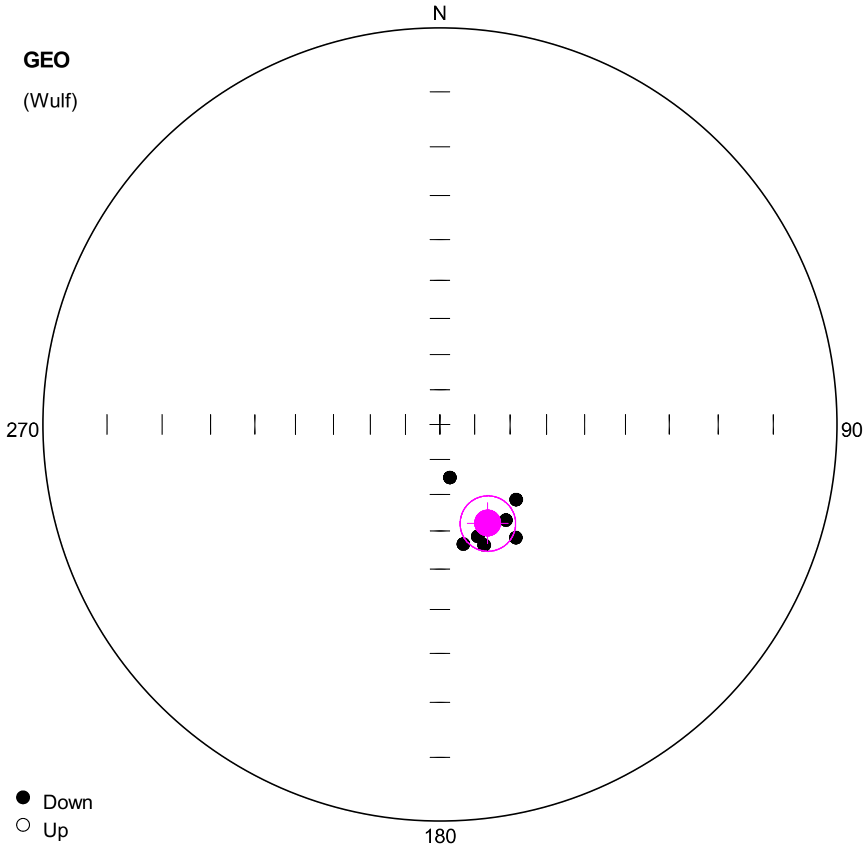

Number of data points: 7

Fisher statistics

Mean vector: 154.24 / 59.14
Resultant vector: 6.91
(X= -3.19, Y= 1.54, Z= 5.93)
Estimated precision, k: 67.07
95% Confidence limit: 7.42
95% Confidence limit, approximation: 6.46

Orientation matrix

1st eigenvalue: 0.97
1st eigenvector: 154.22 / 59.07
2nd eigenvalue: 0.02
2nd eigenvector: 309.51 / 28.57
3rd eigenvalue: 0.01
3rd eigenvector: 45.52 / 10.88

VGP

Site latitude: 65
Site longitude: 14.04
Pole latitude: 16.84 (-16.84)
Pole longitude: 34.42 (-145.58)
Paleolatitude: 39.93 (-39.93)
dp: 8.3
dm: 11.1

#	Name	State	Dec	Inc	MAD	Limit1	Limit2
1	YUNN7501	Ch	134.6	59.8	12.6	30	56
2	YUNN7502	Clt	146.2	52.1	10.9	20	52
3	YUNN7503	Cmt	161.3	56.8	6.5	48	56
4	YUNN7505	Ch	145.4	57.3	9.5	35	60
5	YUNN7506	Ch	169.3	74.5	8.3	30	60
6	YUNN7507	Cmt	169.0	55.8	5.1	44	56
7	YUNN7508	Cmt	159.9	54.1	20.0	35	52

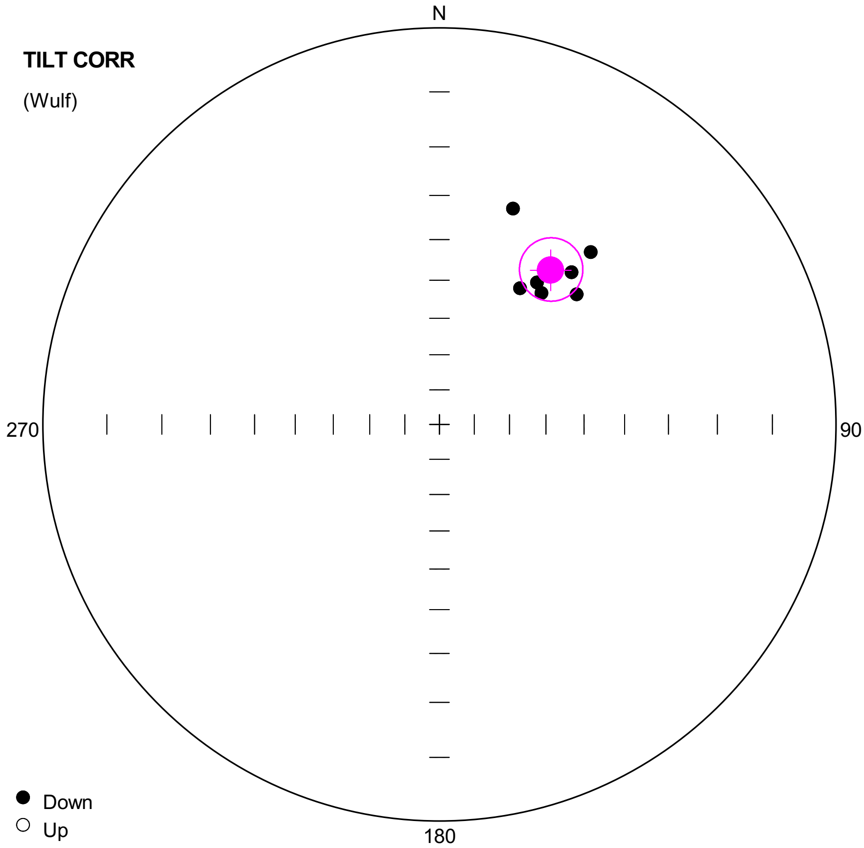

Number of data points: 7

Fisher statistics

Mean vector: 35.75 / 38.79
Resultant vector: 6.91
(X= 4.37, Y= 3.15, Z= 4.33)
Estimated precision, k: 66.99
95% Confidence limit: 7.43
95% Confidence limit, approximation: 6.47

Orientation matrix

1st eigenvalue: 0.97
1st eigenvector: 35.83 / 38.84
2nd eigenvalue: 0.02
2nd eigenvector: 138.08 / 14.76
3rd eigenvalue: 0.01
3rd eigenvector: 244.72 / 47.4

VGP

Site latitude: 65
Site longitude: 14.04
Pole latitude: 41.01 (-41.01)
Pole longitude: 148.12 (-31.88)
Paleolatitude: 21.9 (-21.9)
dp: 5.26
dm: 8.84

#	Name	State	Dec	Inc	MAD	Limit1	Limit2
1	YUNN7501	Ch	41.3	29.9	12.6	30	56
2	YUNN7502	Clt	46.5	39.0	10.9	20	52
3	YUNN7503	Cmt	34.5	43.1	6.5	48	56
4	YUNN7505	Ch	41.0	36.1	9.5	35	60
5	YUNN7506	Ch	18.8	30.2	8.3	30	60
6	YUNN7507	Cmt	30.6	46.5	5.1	44	56
7	YUNN7508	Cmt	37.9	44.5	20.0	35	52

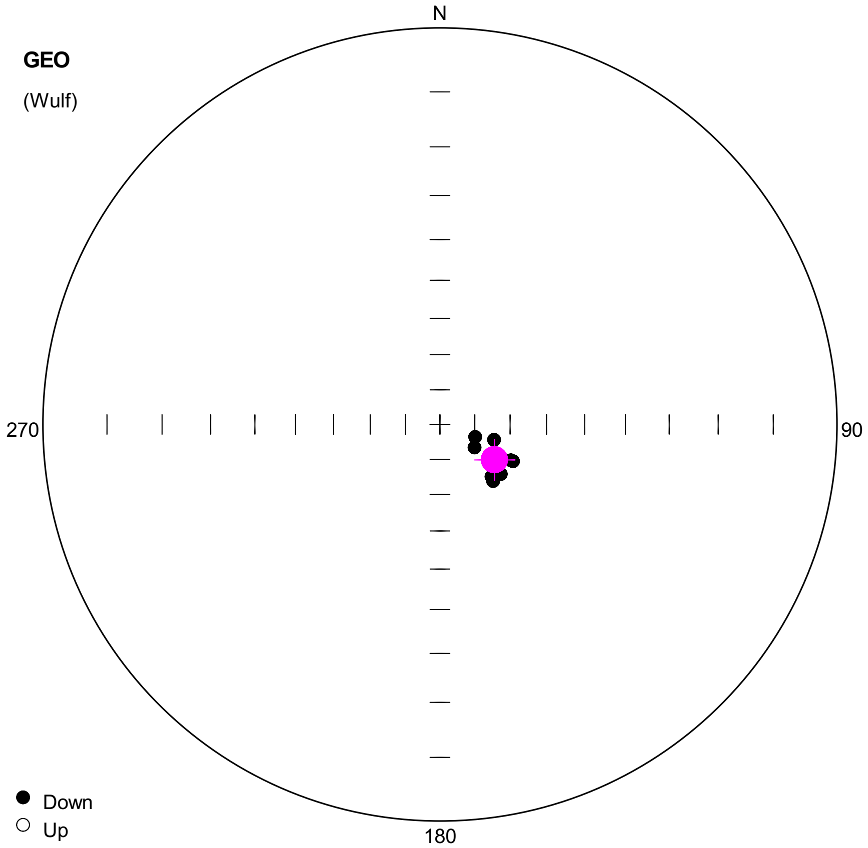

Number of data points: 10

Fisher statistics

Mean vector: 123.01 / 71.39
Resultant vector: 9.96
(X= -1.73, Y= 2.66, Z= 9.44)
Estimated precision, k: 211.76
95% Confidence limit: 3.33
95% Confidence limit, approximation: 3.04

Orientation matrix

1st eigenvalue: 0.99
1st eigenvector: 123.01 / 71.38
2nd eigenvalue: 0.01
2nd eigenvector: 328.36 / 16.93
3rd eigenvalue: 0
3rd eigenvector: 236.06 / 7.51

VGP

Site latitude: 65
Site longitude: 14.04
Pole latitude: 38.55 (-38.55)
Pole longitude: 50.83 (-129.17)
Paleolatitude: 56.05 (-56.05)
dp: 5.1
dm: 5.82

#	Name	State	Dec	Inc	MAD	Limit1	Limit2
1	YUNN7601	Ch	129.2	67.6	1.5	40	64
2	YUNN7602	Ch	109.7	79.2	8.3	30	64
3	YUNN7603	Ch	123.7	78.0	5.7	20	64
4	YUNN7604	Ch	136.8	67.8	3.1	40	64
5	YUNN7605	Ch	135.3	69.0	4.1	30	68
6	YUNN7606	Ch	105.9	73.9	3.5	48	68
7	YUNN7607	Ch	117.9	72.0	5.0	30	64
8	YUNN7608	Ch	117.0	67.4	9.7	40	64
9	YUNN7609	Ch	116.8	66.7	5.1	30	68
10	YUNN7610	Ch	127.2	69.9	5.1	30	68

TILT CORR

(Wulf)

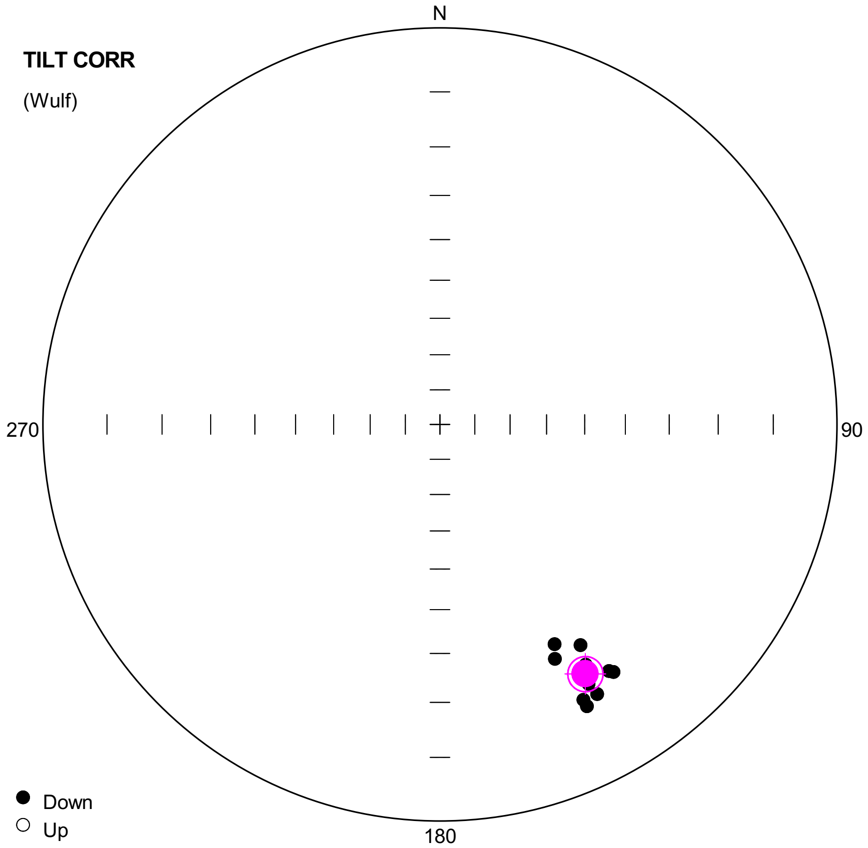

Number of data points: 10

Fisher statistics

Mean vector: 149.81 / 17.96

Resultant vector: 9.96

(X= -8.19, Y= 4.76, Z= 3.07)

Estimated precision, k: 212.34

95% Confidence limit: 3.32

95% Confidence limit, approximation: 3.04

Orientation matrix

1st eigenvalue: 0.99

1st eigenvector: 149.81 / 17.95

2nd eigenvalue: 0.01

2nd eigenvector: 301.42 / 69.78

3rd eigenvalue: 0

3rd eigenvector: 56.87 / 8.99

VGP

Site latitude: 65

Site longitude: 14.04

Pole latitude: -12.45 (12.45)

Pole longitude: 44.59 (-135.41)

Paleolatitude: 9.21 (-9.21)

dp: 1.79

dm: 3.45

#	Name	State	Dec	Inc	MAD	Limit1	Limit2
1	YUNN7601	Ch	149.8	13.6	1.5	40	64
2	YUNN7602	Ch	152.5	26.0	8.3	30	64
3	YUNN7603	Ch	153.9	23.3	5.7	20	64
4	YUNN7604	Ch	152.5	12.6	3.1	40	64
5	YUNN7605	Ch	152.5	13.9	4.1	30	68
6	YUNN7606	Ch	147.5	23.2	3.5	48	68
7	YUNN7607	Ch	148.8	19.4	5.0	30	64
8	YUNN7608	Ch	145.6	16.0	9.7	40	64
9	YUNN7609	Ch	145.0	15.4	5.1	30	68
10	YUNN7610	Ch	150.2	16.0	5.1	30	68

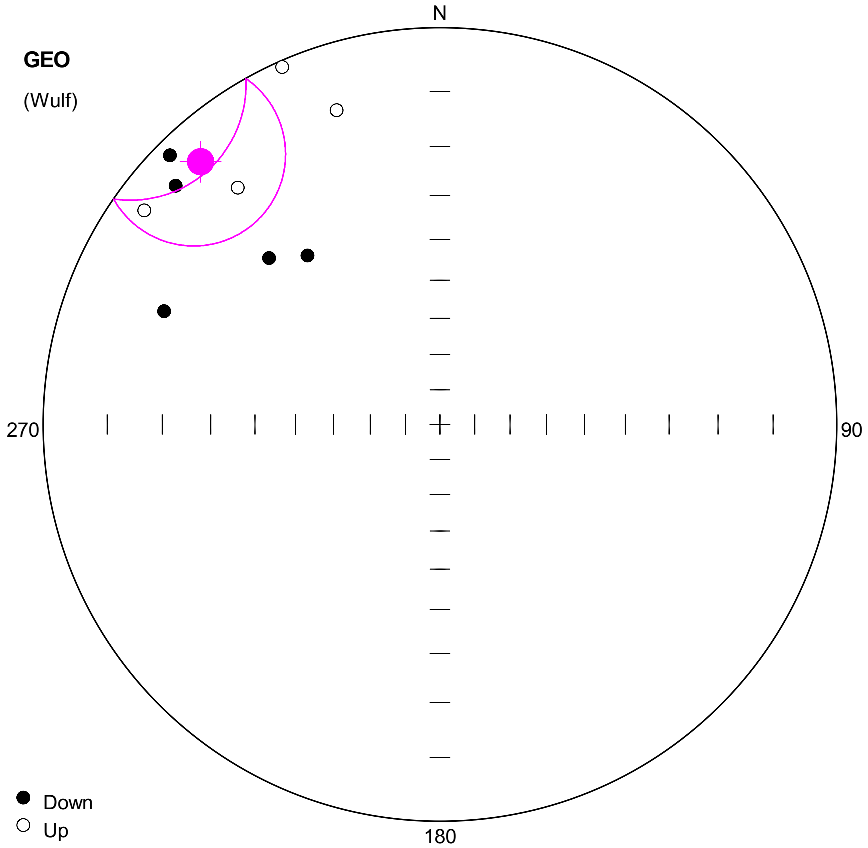

Number of data points: 9

Fisher statistics

Mean vector: 317.67 / 6.32
Resultant vector: 8.41
(X= 6.18, Y= -5.63, Z= 0.93)
Estimated precision, k: 13.65
95% Confidence limit: 14.45
95% Confidence limit, approximation: 12.63

Orientation matrix

1st eigenvalue: 0.88
1st eigenvector: 317.5 / 6.13
2nd eigenvalue: 0.08
2nd eigenvector: 218.87 / 54.4
3rd eigenvalue: 0.04
3rd eigenvector: 51.79 / 34.9

VGP

Site latitude: 65
Site longitude: 14.04
Pole latitude: 21.22 (-21.22)
Pole longitude: -119.8 (60.2)
Paleolatitude: 3.17 (-3.17)
dp: 7.29
dm: 14.52

#	Name	State	Dec	Inc	MAD	Limit1	Limit2	
1	YUNN7701	Ch	319.5	-13.8	6.1	44	60	
2	YUNN7702	Cmt	336.2	-0.9	2.3	40	56	OA
3	YUNN7703	Ch	305.9	-4.8	17.4	40	60	
4	YUNN7704	Ch	321.9	33.2	9.3	35	64	
5	YUNN7705	Ch	314.9	2.3	9.0	35	56	
6	YUNN7706	Ch	292.3	16.2	7.9	35	56	
7	YUNN7707	Ch	341.8	-10.4	19.1	30	64	
8	YUNN7708	Ch	312.1	6.2	11.4	35	60	
9	YUNN7709	Ch	314.2	28.0	17.7	35	60	

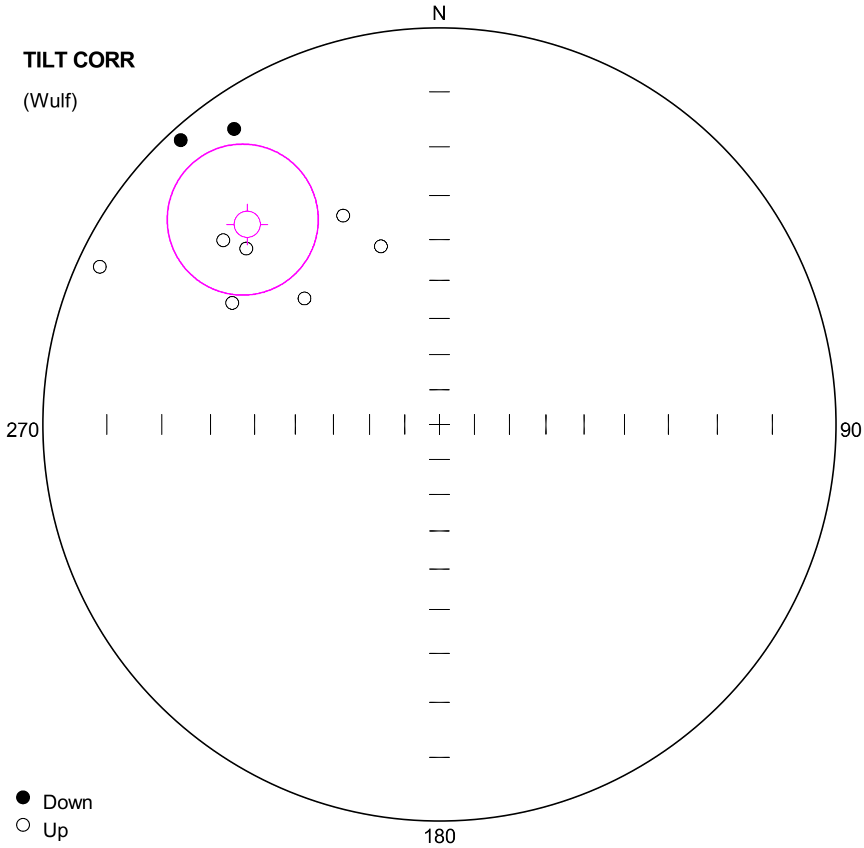

Number of data points: 9

Fisher statistics

Mean vector: 316.16 / -20.06
Resultant vector: 8.41
(X= 5.7, Y= -5.47, Z= -2.89)
Estimated precision, k: 13.65
95% Confidence limit: 14.45
95% Confidence limit, approximation: 12.63

Orientation matrix

1st eigenvalue: 0.88
1st eigenvector: 135.94 / 20.2
2nd eigenvalue: 0.08
2nd eigenvector: 265.39 / 59.92
3rd eigenvalue: 0.04
3rd eigenvector: 37.7 / 21.3

VGP

Site latitude: 65
Site longitude: 14.04
Pole latitude: 7.88 (-7.88)
Pole longitude: -122.5 (57.5)
Paleolatitude: -10.34 (10.34)
dp: 7.92
dm: 15.13

#	Name	State	Dec	Inc	MAD	Limit1	Limit2	
1	YUNN7701	Ch	313.0	-40.1	6.1	44	60	
2	YUNN7702	Cmt	335.3	-29.8	2.3	40	56	OA
3	YUNN7703	Ch	300.4	-27.6	17.4	40	60	
4	YUNN7704	Ch	325.2	5.6	9.3	35	64	
5	YUNN7705	Ch	312.3	-23.3	9.0	35	56	
6	YUNN7706	Ch	294.9	-3.3	7.9	35	56	
7	YUNN7707	Ch	341.8	-39.4	19.1	30	64	
8	YUNN7708	Ch	310.4	-18.8	11.4	35	60	
9	YUNN7709	Ch	317.7	1.8	17.7	35	60	

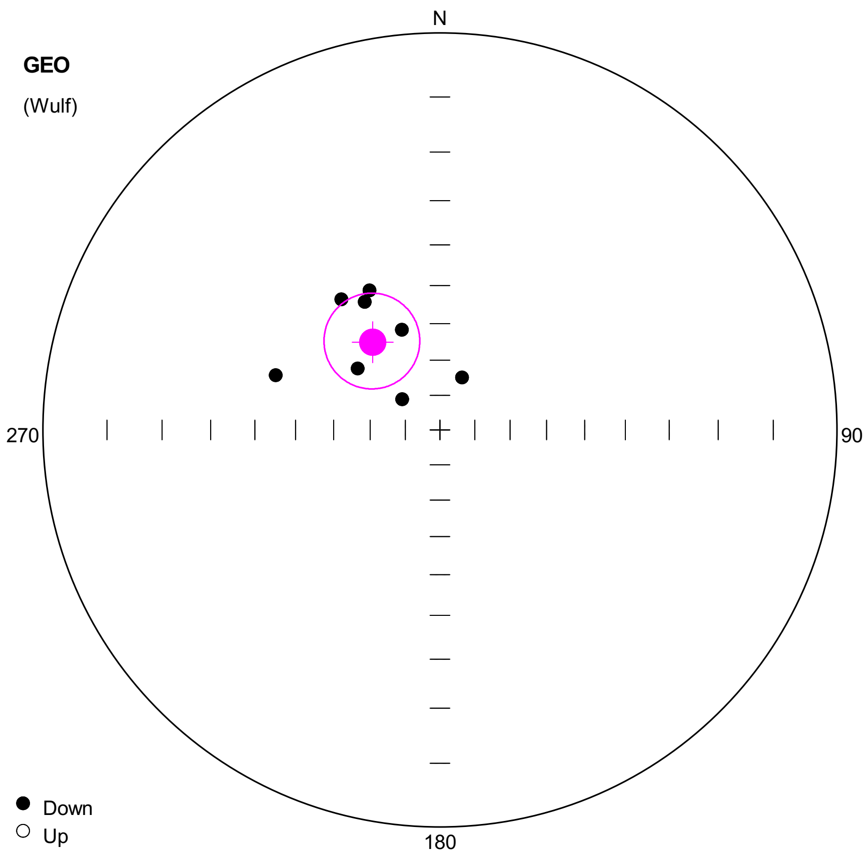

Number of data points: 8

Fisher statistics

Mean vector: 322.56 / 58.87
Resultant vector: 7.65
(X= 3.14, Y= -2.4, Z= 6.55)
Estimated precision, k: 19.82
95% Confidence limit: 12.75
95% Confidence limit, approximation: 11.12

Orientation matrix

1st eigenvalue: 0.92
1st eigenvector: 322.78 / 58.68
2nd eigenvalue: 0.06
2nd eigenvector: 105.79 / 25.92
3rd eigenvalue: 0.03
3rd eigenvector: 203.98 / 16.33

VGP

Site latitude: 65
Site longitude: 14.04
Pole latitude: 56.77 (-56.77)
Pole longitude: -107.26 (72.74)
Paleolatitude: 39.62 (-39.62)
dp: 14.16
dm: 19

#	Name	State	Dec	Inc	MAD	Limit1	Limit2
1	YUNN7801	Ch	306.7	61.0	11.9	30	56
2	YUNN7802	Ch	333.2	47.0	14.1	30	64
3	YUNN7803	Ch	339.2	59.8	16.4	20	64
4	YUNN7804	Ch	288.4	42.9	25.7	20	60
5	YUNN7805	Clt	329.6	49.0	9.6	20	56
6	YUNN7808	Ch	323.0	45.2	16.5	30	60
7	YUNN7809	Ch	22.9	73.7	25.9	30	56
8	YUNN7810	Ch	309.1	76.1	24.8	20	64

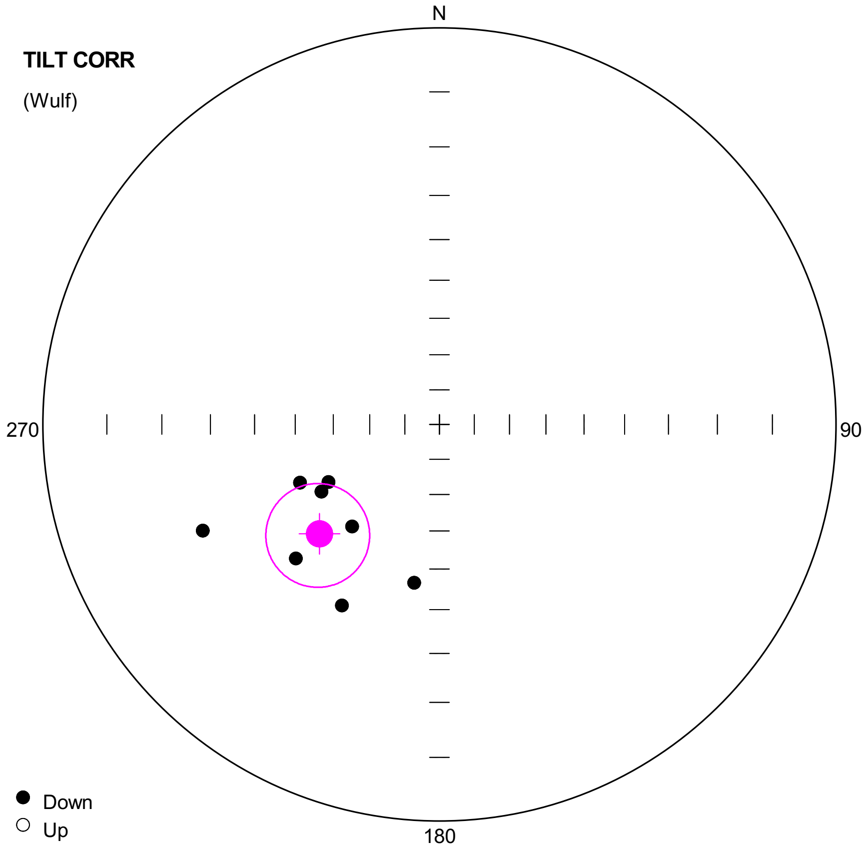

Number of data points: 8

Fisher statistics

Mean vector: 227.68 / 45.49

Resultant vector: 7.65

(X= -3.61, Y= -3.96, Z= 5.45)

Estimated precision, k: 19.8

95% Confidence limit: 12.76

95% Confidence limit, approximation: 11.12

Orientation matrix

1st eigenvalue: 0.91

1st eigenvector: 227.9 / 45.65

2nd eigenvalue: 0.06

2nd eigenvector: 127.07 / 10.41

3rd eigenvalue: 0.03

3rd eigenvector: 27.39 / 42.48

VGP

Site latitude: 65

Site longitude: 14.04

Pole latitude: 9.05 (-9.05)

Pole longitude: -27.83 (152.17)

Paleolatitude: 26.96 (-26.96)

dp: 10.31

dm: 16.22

#	Name	State	Dec	Inc	MAD	Limit1	Limit2
1	YUNN7801	Ch	227.0	37.3	11.9	30	56
2	YUNN7802	Ch	242.6	55.0	14.1	30	64
3	YUNN7803	Ch	220.5	52.6	16.4	20	64
4	YUNN7804	Ch	245.8	23.6	25.7	20	60
5	YUNN7805	Clt	240.4	52.2	9.6	20	56
6	YUNN7808	Ch	247.3	48.3	16.5	30	60
7	YUNN7809	Ch	189.0	46.0	25.9	30	56
8	YUNN7810	Ch	208.3	35.2	24.8	20	64

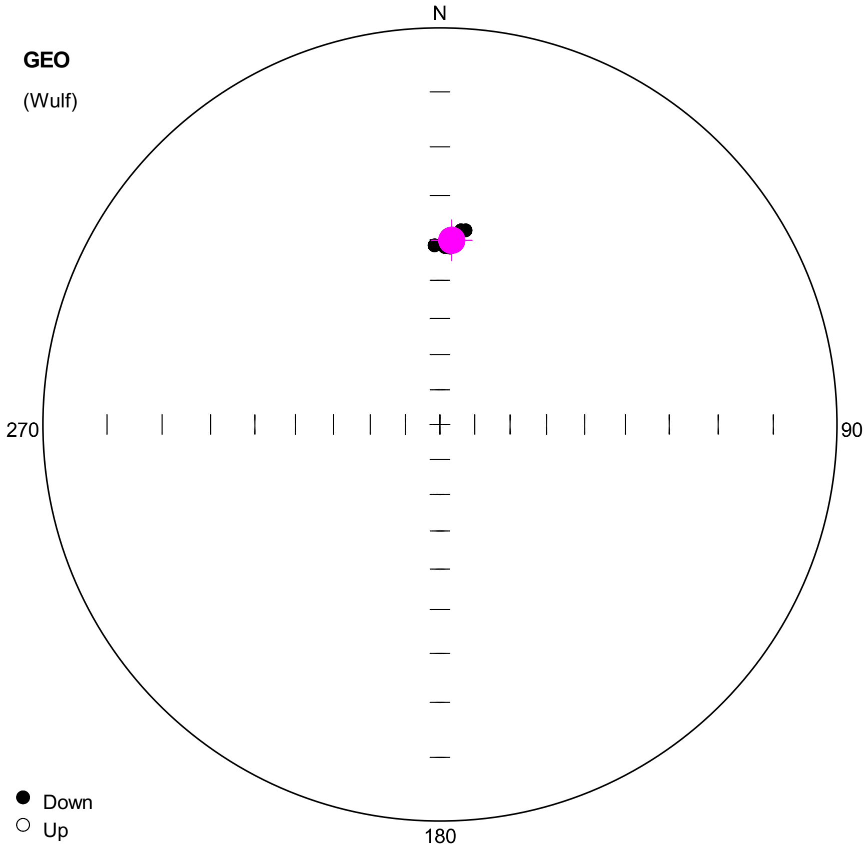

Number of data points: 8

Fisher statistics

Mean vector: 3.68 / 40.07

Resultant vector: 7.99

(X= 6.1, Y= 0.39, Z= 5.14)

Estimated precision, k: 814.74

95% Confidence limit: 1.94

95% Confidence limit, approximation: 1.73

Orientation matrix

1st eigenvalue: 1

1st eigenvector: 3.69 / 40.07

2nd eigenvalue: 0

2nd eigenvector: 247.81 / 27.42

3rd eigenvalue: 0

3rd eigenvector: 134.19 / 37.68

VGP

Site latitude: 65

Site longitude: 14.04

Pole latitude: 47.74 (-47.74)

Pole longitude: -171.01 (8.99)

Paleolatitude: 22.81 (-22.81)

dp: 1.41

dm: 2.34

#	Name	State	Dec	Inc	MAD	Limit1	Limit2
1	YUNN7901	Ch	358.3	41.4	2.5	35	68
2	YUNN7904	Ch	5.5	40.9	4.0	30	64
3	YUNN7905	Ch	6.2	37.6	8.6	35	60
4	YUNN7906	Ch	3.6	40.1	5.3	20	64
5	YUNN7907	Ch	1.6	41.8	4.9	35	68
6	YUNN7908	Ch	3.2	41.9	4.1	20	68
7	YUNN7909	Ch	7.5	37.5	3.1	20	68
8	YUNN7910	Ch	3.2	39.1	4.9	20	68

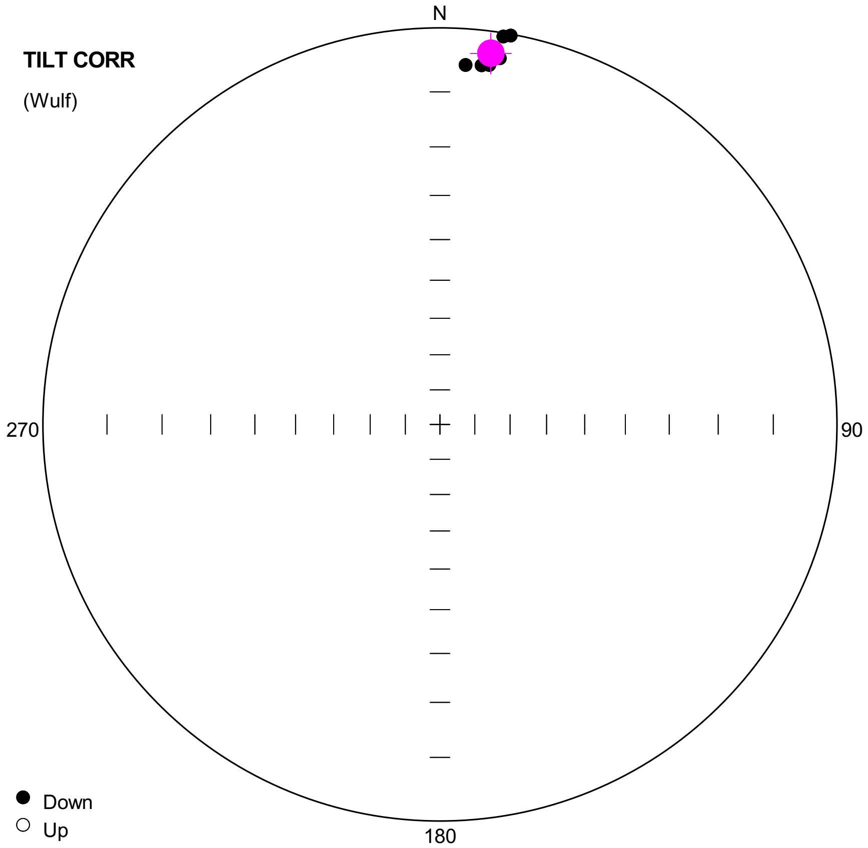

Number of data points: 8

Fisher statistics

Mean vector: 7.8 / 3.28
Resultant vector: 7.99
(X= 7.9, Y= 1.08, Z= 0.46)
Estimated precision, k: 811.91
95% Confidence limit: 1.95
95% Confidence limit, approximation: 1.74

Orientation matrix

1st eigenvalue: 1
1st eigenvector: 7.8 / 3.28
2nd eigenvalue: 0
2nd eigenvector: 274.16 / 47.99
3rd eigenvalue: 0
3rd eigenvector: 100.74 / 41.82

VGP

Site latitude: 65
Site longitude: 14.04
Pole latitude: 26.39 (-26.39)
Pole longitude: -174.67 (5.33)
Paleolatitude: 1.64 (-1.64)
dp: 0.97
dm: 1.95

#	Name	State	Dec	Inc	MAD	Limit1	Limit2
1	YUNN7901	Ch	4.1	5.5	2.5	35	68
2	YUNN7904	Ch	9.3	3.8	4.0	30	64
3	YUNN7905	Ch	9.3	0.5	8.6	35	60
4	YUNN7906	Ch	7.7	3.4	5.3	20	64
5	YUNN7907	Ch	6.6	5.3	4.9	35	68
6	YUNN7908	Ch	7.8	5.1	4.1	20	68
7	YUNN7909	Ch	10.3	0.2	3.1	20	68
8	YUNN7910	Ch	7.3	2.4	4.9	20	68

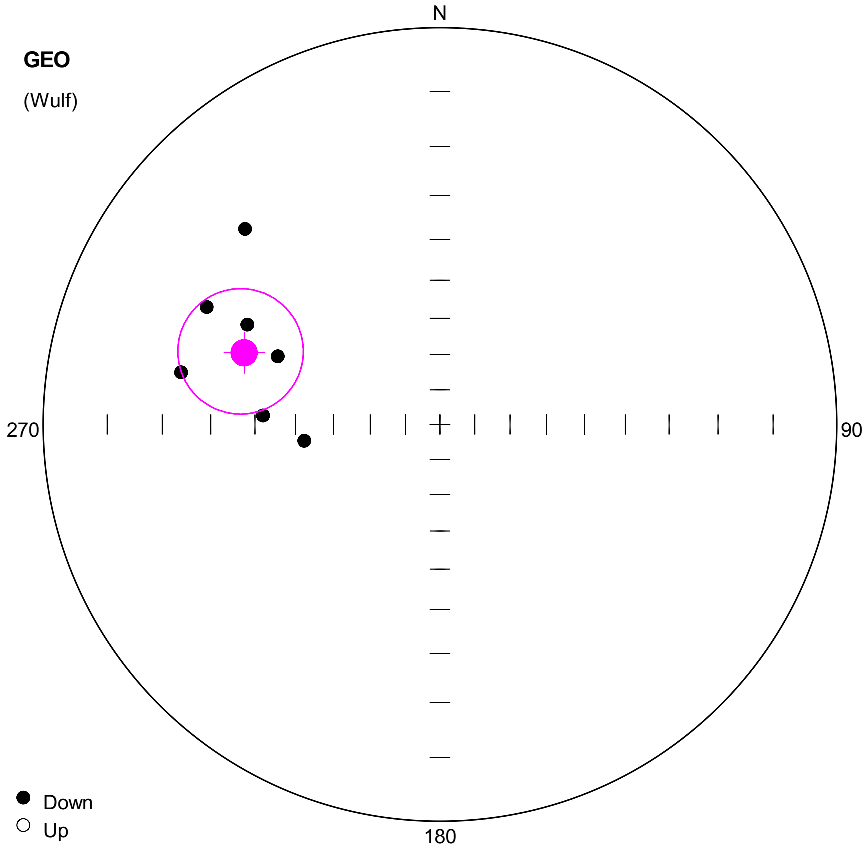

Number of data points: 7

Fisher statistics

Mean vector: 290.15 / 34.59
Resultant vector: 6.69
(X= 1.9, Y= -5.17, Z= 3.8)
Estimated precision, k: 19.38
95% Confidence limit: 14.06
95% Confidence limit, approximation: 12.02

Orientation matrix

1st eigenvalue: 0.91
1st eigenvector: 290.11 / 34.5
2nd eigenvalue: 0.07
2nd eigenvector: 174.08 / 32.56
3rd eigenvalue: 0.01
3rd eigenvector: 53.41 / 38.62

VGP

Site latitude: 65
Site longitude: 14.04
Pole latitude: 25.66 (-25.66)
Pole longitude: -86.01 (93.99)
Paleolatitude: 19.02 (-19.02)
dp: 9.27
dm: 16.15

#	Name	State	Dec	Inc	MAD	Limit1	Limit2
1	YUNN8001	Ch	296.7	23.3	6.3	20	64
2	YUNN8002	Ch	272.9	41.9	4.5	20	64
3	YUNN8003	Ch	297.4	32.7	18.2	20	60
4	YUNN8005	Ch	263.1	52.0	9.2	20	64
5	YUNN8006	Ch	315.1	20.4	9.6	20	60
6	YUNN8008	Ch	292.8	42.2	30.9	20	64
7	YUNN8009	Ch	281.4	22.7	7.9	20	60

TILT CORR

(Wulf)

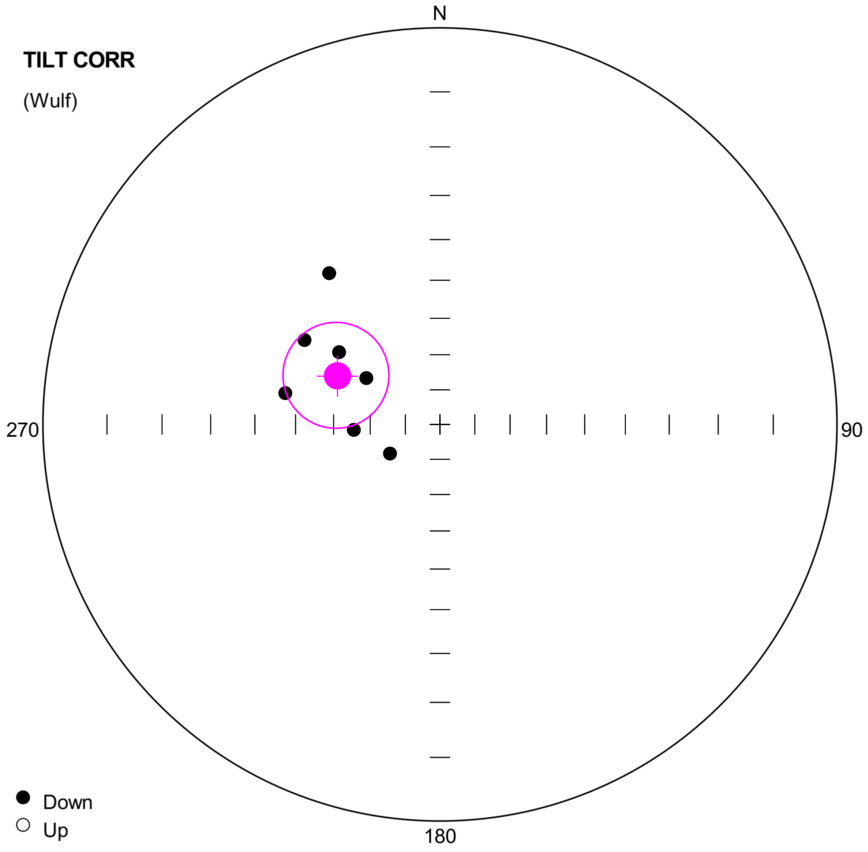

Number of data points: 7

Fisher statistics

Mean vector: 295.34 / 58.14
Resultant vector: 6.69
(X= 1.51, Y= -3.19, Z= 5.68)
Estimated precision, k: 19.42
95% Confidence limit: 14.05
95% Confidence limit, approximation: 12.01

Orientation matrix

1st eigenvalue: 0.92
1st eigenvector: 295.26 / 58.06
2nd eigenvalue: 0.07
2nd eigenvector: 162.19 / 23.06
3rd eigenvalue: 0.01
3rd eigenvector: 62.87 / 20.83

VGP

Site latitude: 65
Site longitude: 14.04
Pole latitude: 45.16 (-45.16)
Pole longitude: -78.98 (101.02)
Paleolatitude: 38.82 (-38.82)
dp: 15.3
dm: 20.74

#	Name	State	Dec	Inc	MAD	Limit1	Limit2
1	YUNN8001	Ch	302.0	46.2	6.3	20	64
2	YUNN8002	Ch	266.4	65.5	4.5	20	64
3	YUNN8003	Ch	305.6	55.3	18.2	20	60
4	YUNN8005	Ch	239.6	73.4	9.2	20	64
5	YUNN8006	Ch	323.8	39.4	9.6	20	60
6	YUNN8008	Ch	302.3	65.3	30.9	20	64
7	YUNN8009	Ch	281.5	46.7	7.9	20	60

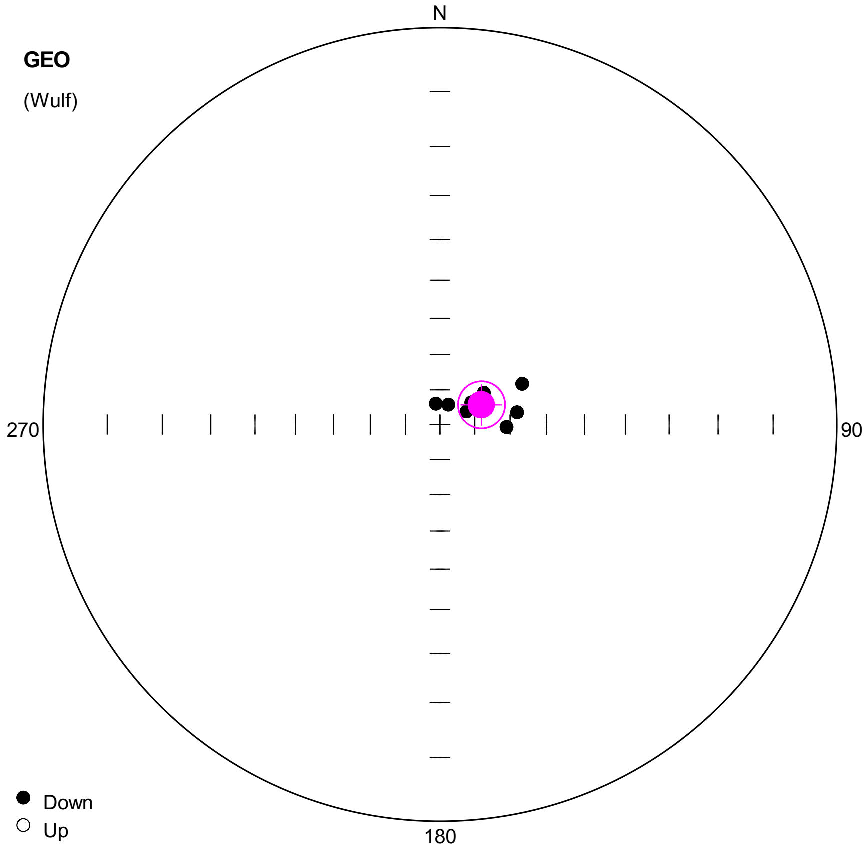

Number of data points: 8

Fisher statistics

Mean vector: 64.51 / 76.84
Resultant vector: 7.9
(X= 0.77, Y= 1.62, Z= 7.69)
Estimated precision, k: 69.45
95% Confidence limit: 6.69
95% Confidence limit, approximation: 5.94

Orientation matrix

1st eigenvalue: 0.98
1st eigenvector: 64.51 / 76.85
2nd eigenvalue: 0.02
2nd eigenvector: 270.2 / 11.89
3rd eigenvalue: 0
3rd eigenvector: 179.03 / 5.54

VGP

Site latitude: 65
Site longitude: 14.04
Pole latitude: 63.9 (-63.9)
Pole longitude: 74.4 (-105.6)
Paleolatitude: 64.94 (-64.94)
dp: 11.58
dm: 12.45

#	Name	State	Dec	Inc	MAD	Limit1	Limit2
1	YUNN8101	Ch	55.0	79.0	6.8	40	64
2	YUNN8102	Ch	81.1	67.7	6.0	35	64
3	YUNN8103	Ch	63.8	64.0	7.0	40	64
4	YUNN8104	Ch	63.9	81.5	6.5	30	64
5	YUNN8105	Ch	349.0	83.9	12.2	44	64
6	YUNN8106	Ch	54.2	74.5	13.2	30	64
7	YUNN8107	Ch	92.2	70.9	7.8	20	64
8	YUNN8109	Ch	23.4	83.8	4.5	44	64

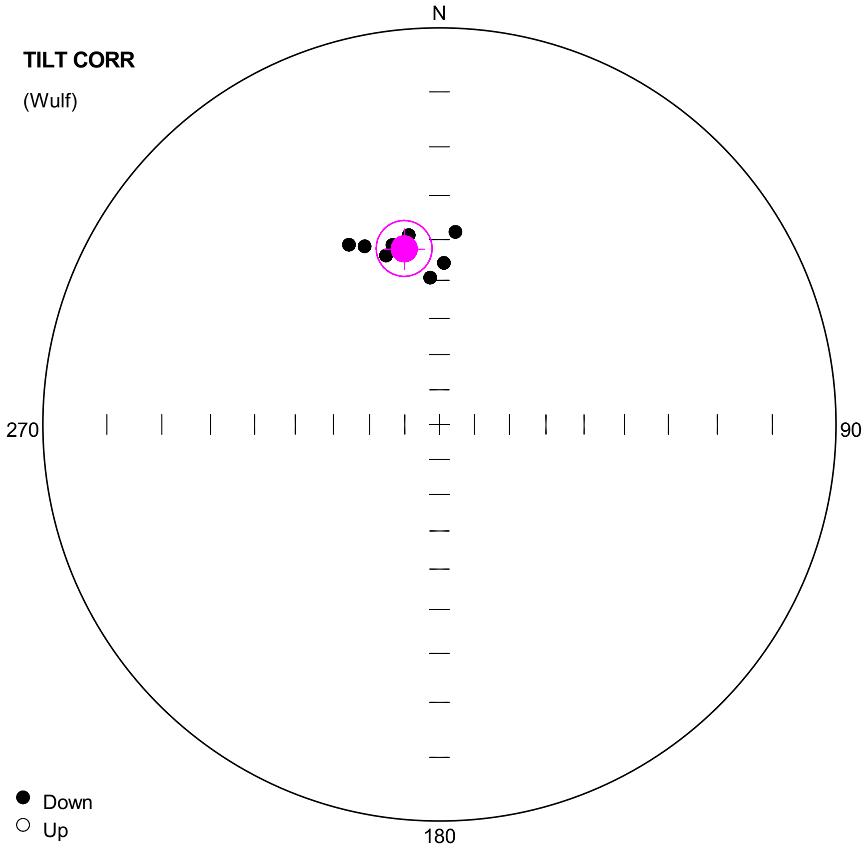

Number of data points: 8

Fisher statistics

Mean vector: 348.63 / 41.45

Resultant vector: 7.9

(X= 5.81, Y= -1.17, Z= 5.23)

Estimated precision, k: 69.64

95% Confidence limit: 6.68

95% Confidence limit, approximation: 5.93

Orientation matrix

1st eigenvalue: 0.98

1st eigenvector: 348.62 / 41.45

2nd eigenvalue: 0.02

2nd eigenvector: 89.82 / 12.4

3rd eigenvalue: 0

3rd eigenvector: 192.93 / 45.9

VGP

Site latitude: 65

Site longitude: 14.04

Pole latitude: 48.17 (-48.17)

Pole longitude: -150.28 (29.72)

Paleolatitude: 23.82 (-23.82)

dp: 4.98

dm: 8.16

#	Name	State	Dec	Inc	MAD	Limit1	Limit2
1	YUNN8101	Ch	345.3	39.9	6.8	40	64
2	YUNN8102	Ch	1.6	45.7	6.0	35	64
3	YUNN8103	Ch	4.8	38.1	7.0	40	64
4	YUNN8104	Ch	342.5	41.9	6.5	30	64
5	YUNN8105	Ch	333.3	36.2	12.2	44	64
6	YUNN8106	Ch	350.8	38.4	13.2	30	64
7	YUNN8107	Ch	356.4	49.3	7.8	20	64
8	YUNN8109	Ch	337.2	38.1	4.5	44	64

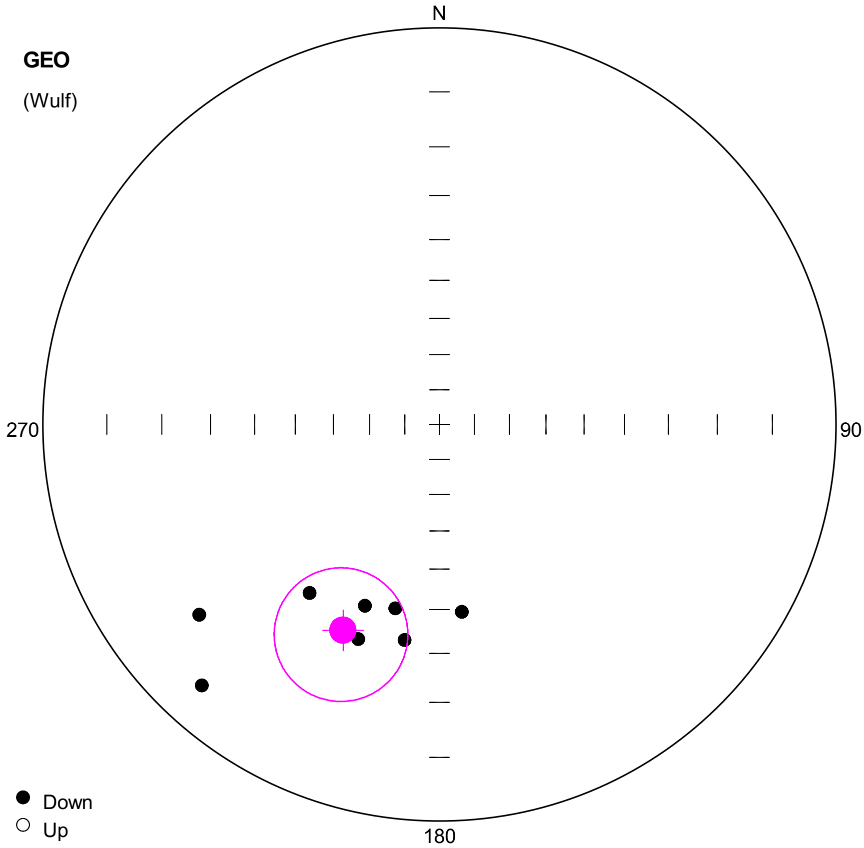

Number of data points: 8

Fisher statistics

Mean vector: 205.12 / 30.39
Resultant vector: 7.56
(X= -5.9, Y= -2.77, Z= 3.82)
Estimated precision, k: 15.79
95% Confidence limit: 14.38
95% Confidence limit, approximation: 12.45

Orientation matrix

1st eigenvalue: 0.89
1st eigenvector: 204.74 / 30.76
2nd eigenvalue: 0.1
2nd eigenvector: 96.18 / 28.14
3rd eigenvalue: 0.01
3rd eigenvector: 332.65 / 45.92

VGP

Site latitude: 65
Site longitude: 14.04
Pole latitude: -6.44 (6.44)
Pole longitude: -10.16 (169.84)
Paleolatitude: 16.34 (-16.34)
dp: 8.9
dm: 16

#	Name	State	Dec	Inc	MAD	Limit1	Limit2
1	YUNN8201	Ch	189.2	32.3	6.8	44	56
2	YUNN8202	Ch	217.6	33.6	5.1	30	64
3	YUNN8203	Ch	231.6	14.6	8.0	20	64
4	YUNN8204	Ch	202.3	37.4	9.7	40	64
5	YUNN8205	Ch	200.7	29.9	7.8	40	64
6	YUNN8206	Ch	222.3	6.7	5.4	35	64
7	YUNN8207	Ch	173.2	39.1	7.6	35	64
8	YUNN8208	Ch	193.5	39.0	20.8	20	60

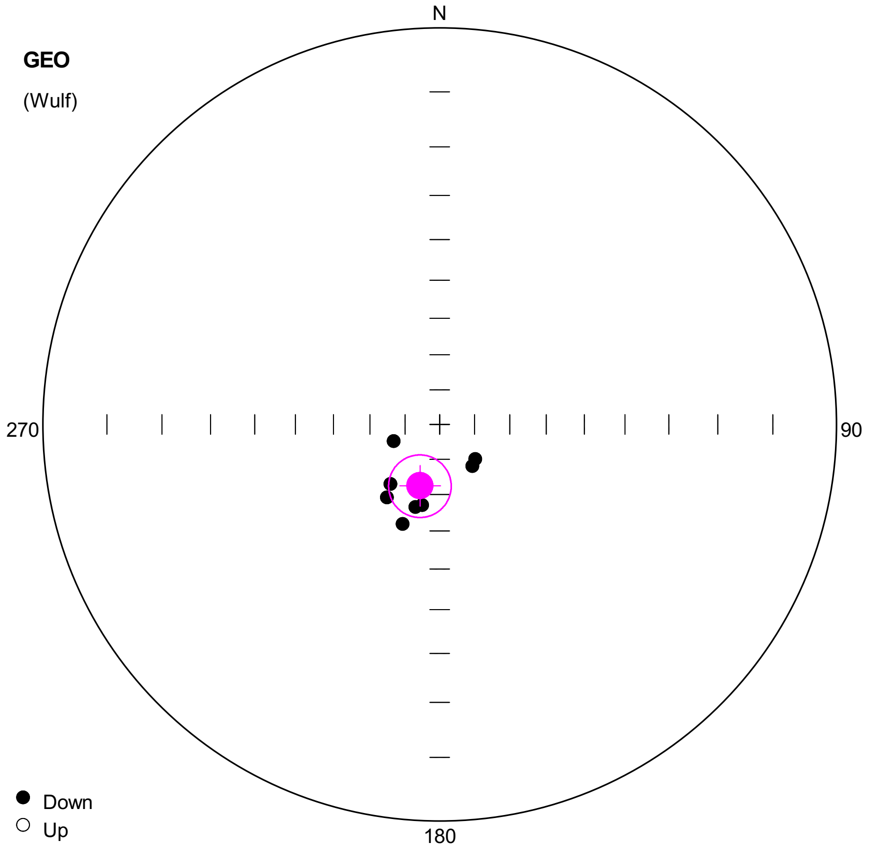

Number of data points: 8

Fisher statistics

Mean vector: 197.85 / 71.56
Resultant vector: 7.83
(X= -2.36, Y= -0.76, Z= 7.43)
Estimated precision, k: 40.7
95% Confidence limit: 8.79
95% Confidence limit, approximation: 7.76

Orientation matrix

1st eigenvalue: 0.96
1st eigenvector: 198.06 / 71.45
2nd eigenvalue: 0.03
2nd eigenvector: 65.64 / 12.75
3rd eigenvalue: 0.01
3rd eigenvector: 332.59 / 13.24

VGP

Site latitude: 65
Site longitude: 14.04
Pole latitude: 32.06 (-32.06)
Pole longitude: 2.46 (-177.54)
Paleolatitude: 56.3 (-56.3)
dp: 13.52
dm: 15.41

#	Name	State	Dec	Inc	MAD	Limit1	Limit2	
1	YUNN8201	CHT	192.3	66.5	1.0	64	64	OA
2	YUNN8202	CHT	196.4	65.5	1.0	64	64	OA
3	YUNN8203	CHT	219.6	68.0	1.0	64	64	OA
4	YUNN8204	CHT	200.4	60.0	1.0	64	64	OA
5	YUNN8205	CHT	250.0	75.9	1.0	64	64	OA
6	YUNN8206	CHT	215.9	64.4	1.0	64	64	OA
7	YUNN8207	CHT	134.3	75.7	1.0	64	64	OA
8	YUNN8208	CHT	142.0	74.8	1.0	64	64	OA

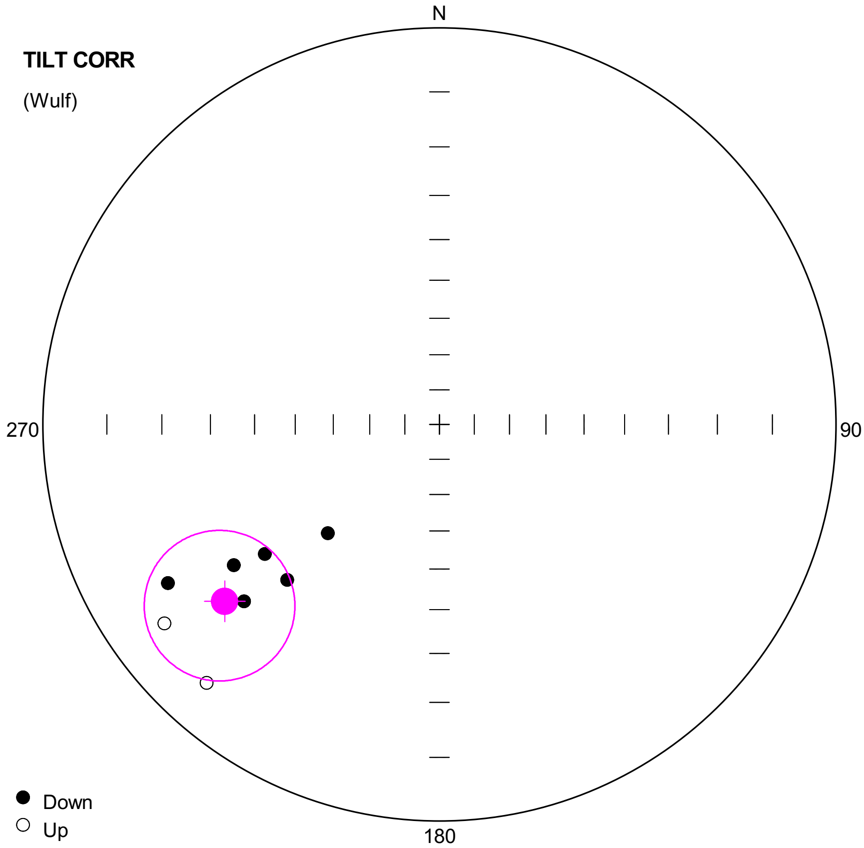

Number of data points: 8

Fisher statistics

Mean vector: 230.53 / 19.9
Resultant vector: 7.56
(X= -4.52, Y= -5.49, Z= 2.57)
Estimated precision, k: 15.77
95% Confidence limit: 14.39
95% Confidence limit, approximation: 12.46

Orientation matrix

1st eigenvalue: 0.89
1st eigenvector: 230.66 / 20.38
2nd eigenvalue: 0.1
2nd eigenvector: 53.1 / 69.6
3rd eigenvalue: 0.01
3rd eigenvector: 320.96 / 0.8

VGP

Site latitude: 65
Site longitude: 14.04
Pole latitude: -5.91 (5.91)
Pole longitude: -35.75 (144.25)
Paleolatitude: 10.26 (-10.26)
dp: 7.88
dm: 15.06

#	Name	State	Dec	Inc	MAD	Limit1	Limit2
1	YUNN8201	Ch	224.4	32.5	6.8	44	56
2	YUNN8202	Ch	239.7	13.2	5.1	30	64
3	YUNN8203	Ch	234.1	-8.9	8.0	20	64
4	YUNN8204	Ch	235.6	25.7	9.7	40	64
5	YUNN8205	Ch	227.8	22.8	7.8	40	64
6	YUNN8206	Ch	222.0	-7.5	5.4	35	64
7	YUNN8207	Ch	225.7	47.1	7.6	35	64
8	YUNN8208	Ch	233.4	32.5	20.8	20	60

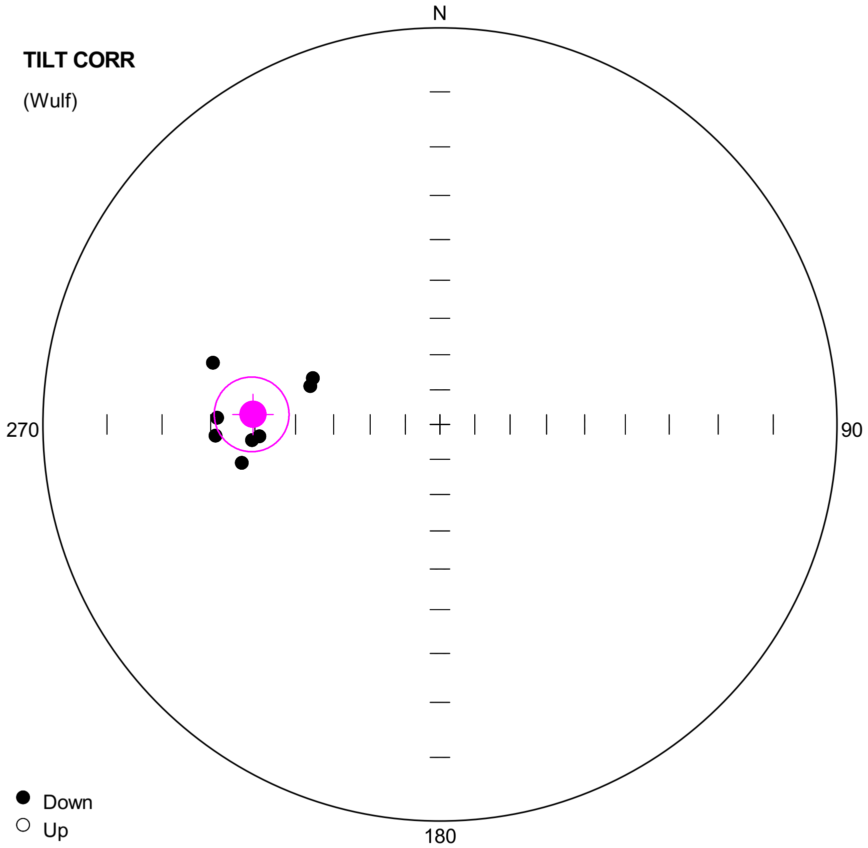

Number of data points: 8

Fisher statistics

Mean vector: 273.09 / 39.49
Resultant vector: 7.83
(X= 0.33, Y= -6.03, Z= 4.98)
Estimated precision, k: 40.65
95% Confidence limit: 8.79
95% Confidence limit, approximation: 7.76

Orientation matrix

1st eigenvalue: 0.96
1st eigenvector: 272.96 / 39.41
2nd eigenvalue: 0.03
2nd eigenvector: 42.45 / 37.73
3rd eigenvalue: 0.01
3rd eigenvector: 156.89 / 28.13

VGP

Site latitude: 65
Site longitude: 14.04
Pole latitude: 21.49 (-21.49)
Pole longitude: -68.81 (111.19)
Paleolatitude: 22.39 (-22.39)
dp: 6.31
dm: 10.53

#	Name	State	Dec	Inc	MAD	Limit1	Limit2	
1	YUNN8201	CHT	266.2	41.0	1.0	64	64	OA
2	YUNN8202	CHT	265.2	39.2	1.0	64	64	OA
3	YUNN8203	CHT	271.7	31.4	1.0	64	64	OA
4	YUNN8204	CHT	259.0	36.1	1.0	64	64	OA
5	YUNN8205	CHT	285.2	28.7	1.0	64	64	OA
6	YUNN8206	CHT	267.1	31.0	1.0	64	64	OA
7	YUNN8207	CHT	290.1	52.4	1.0	64	64	OA
8	YUNN8208	CHT	286.5	52.4	1.0	64	64	OA

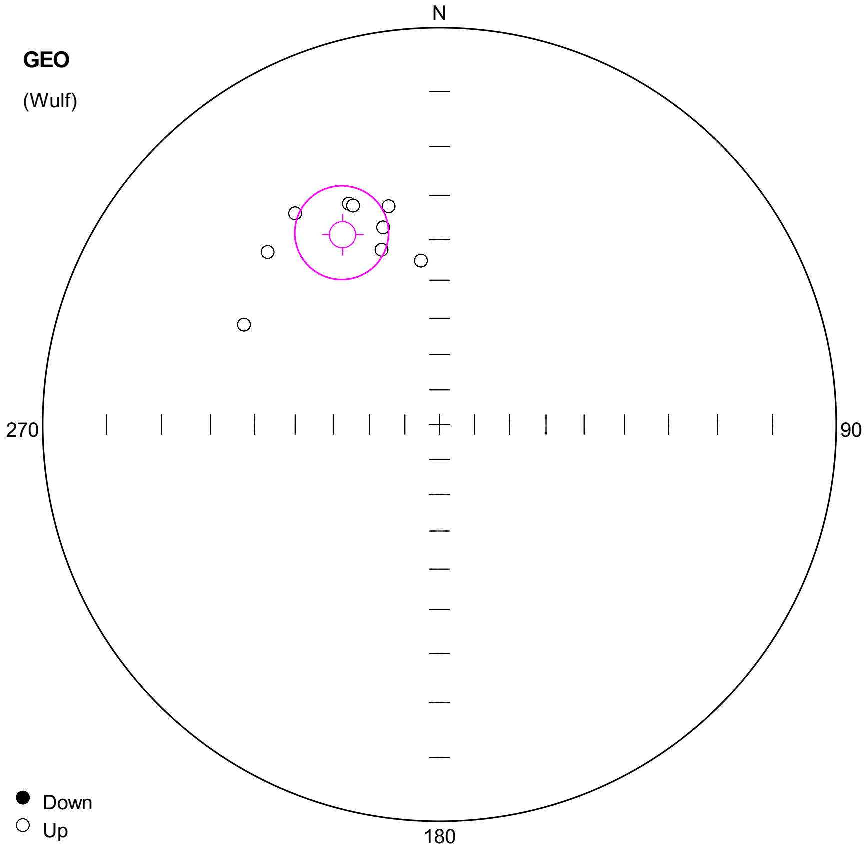

Number of data points: 9

Fisher statistics

Mean vector: 332.97 / -33.53
Resultant vector: 8.68
(X= 6.45, Y= -3.29, Z= -4.8)
Estimated precision, k: 25.22
95% Confidence limit: 10.45
95% Confidence limit, approximation: 9.29

Orientation matrix

1st eigenvalue: 0.93
1st eigenvector: 153.47 / 33.43
2nd eigenvalue: 0.06
2nd eigenvector: 248.81 / 8.03
3rd eigenvalue: 0.01
3rd eigenvector: 350.59 / 55.36

VGP

Site latitude: 65
Site longitude: 14.04
Pole latitude: 4.14 (-4.14)
Pole longitude: -140.33 (39.67)
Paleolatitude: -18.33 (18.33)
dp: 6.78
dm: 11.9

#	Name	State	Dec	Inc	MAD	Limit1	Limit2
1	YUNN8301	Cht	341.7	-40.3	2.1	60	68
2	YUNN8302	Cht	346.9	-31.1	8.1	60	68
3	YUNN8303	Cht	337.7	-28.0	4.0	60	68
4	YUNN8305	Cht	315.1	-27.0	2.0	60	68
5	YUNN8306	Cht	353.6	-44.9	0.0	64	68
6	YUNN8307	Cht	344.1	-35.4	9.5	60	68
7	YUNN8308	Cht	297.0	-32.1	1.3	60	68
8	YUNN8309	Cht	338.5	-28.7	6.7	60	68
9	YUNN8310	Cht	325.7	-24.4	0.0	64	68

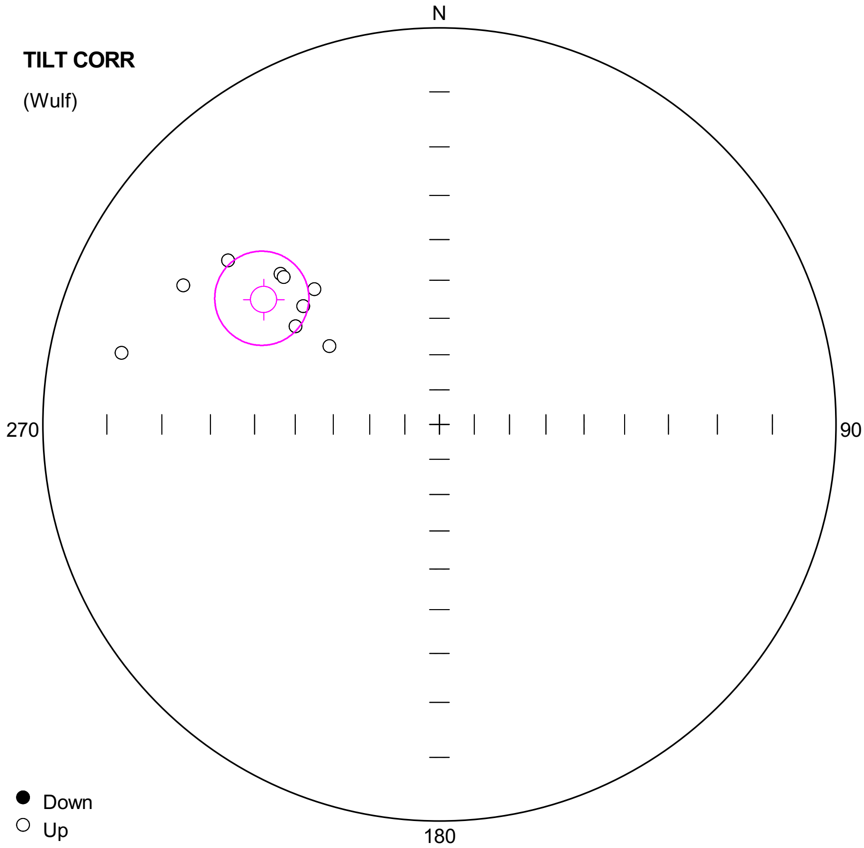

Number of data points: 9

Fisher statistics

Mean vector: 305.39 / -32.93
Resultant vector: 8.68
(X= 4.22, Y= -5.94, Z= -4.72)
Estimated precision, k: 25.28
95% Confidence limit: 10.44
95% Confidence limit, approximation: 9.28

Orientation matrix

1st eigenvalue: 0.93
1st eigenvector: 125.81 / 33.17
2nd eigenvalue: 0.06
2nd eigenvector: 257.01 / 45.22
3rd eigenvalue: 0.01
3rd eigenvector: 16.93 / 26.34

VGP

Site latitude: 65
Site longitude: 14.04
Pole latitude: -2.66 (2.66)
Pole longitude: -115.03 (64.97)
Paleolatitude: -17.94 (17.94)
dp: 6.71
dm: 11.83

#	Name	State	Dec	Inc	MAD	Limit1	Limit2
1	YUNN8301	Cht	304.3	-42.6	2.1	60	68
2	YUNN8302	Cht	317.3	-40.2	8.1	60	68
3	YUNN8303	Cht	313.5	-32.2	4.0	60	68
4	YUNN8305	Cht	298.5	-17.4	2.0	60	68
5	YUNN8306	Cht	305.5	-52.4	0.0	64	68
6	YUNN8307	Cht	311.0	-41.1	9.5	60	68
7	YUNN8308	Cht	282.7	-11.2	1.3	60	68
8	YUNN8309	Cht	313.4	-33.2	6.7	60	68
9	YUNN8310	Cht	307.8	-22.0	0.0	64	68

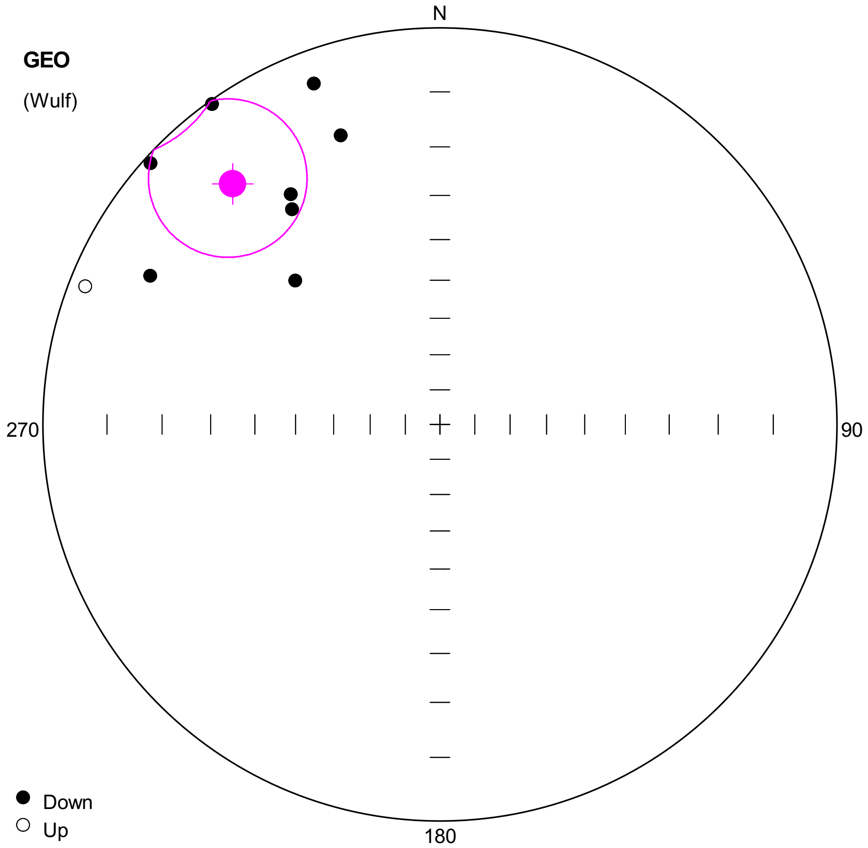

Number of data points: 9

Fisher statistics

Mean vector: 319.29 / 12.65

Resultant vector: 8.47

(X= 6.26, Y= -5.39, Z= 1.85)

Estimated precision, k: 14.98

95% Confidence limit: 13.75

95% Confidence limit, approximation: 12.06

Orientation matrix

1st eigenvalue: 0.89

1st eigenvector: 319.68 / 12.75

2nd eigenvalue: 0.08

2nd eigenvector: 53.77 / 17.48

3rd eigenvalue: 0.04

3rd eigenvector: 195.4 / 68.11

VGP

Site latitude: 65

Site longitude: 14.04

Pole latitude: 24.8 (-24.8)

Pole longitude: -120.4 (59.6)

Paleolatitude: 6.4 (-6.4)

dp: 7.13

dm: 14

#	Name	State	Dec	Inc	MAD	Limit1	Limit2
1	YUNN8401	Cmt	339.7	5.0	6.9	30	64
2	YUNN8402	Cmt	324.6	0.5	7.0	20	64
3	YUNN8403	Cmt	314.9	35.6	8.3	40	64
4	YUNN8405	Cmt	341.1	14.8	6.3	20	64
5	YUNN8406	Cmt	327.1	20.7	8.0	35	64
6	YUNN8407	Cmt	325.5	23.3	12.3	40	60
7	YUNN8408	Cmt	297.2	11.3	8.3	44	64
8	YUNN8409	Cmt	291.3	-2.4	18.6	35	64
9	YUNN8410	Cmt	312.1	1.0	13.9	20	64

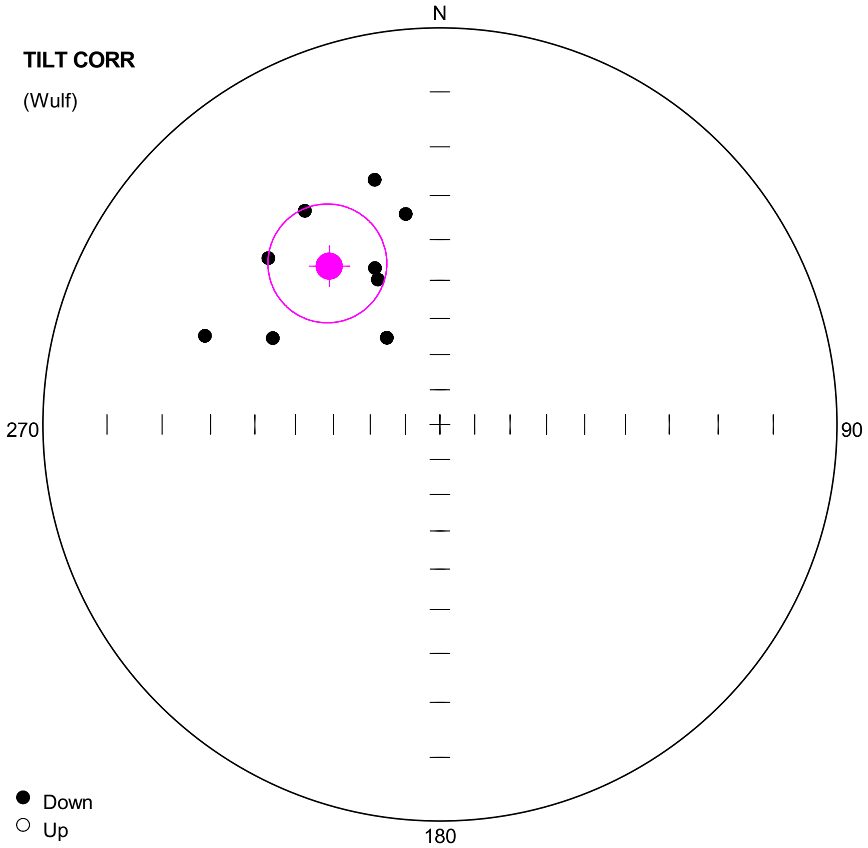

Number of data points: 9

Fisher statistics

Mean vector: 325.06 / 38.09

Resultant vector: 8.47

(X= 5.46, Y= -3.82, Z= 5.22)

Estimated precision, k: 14.97

95% Confidence limit: 13.75

95% Confidence limit, approximation: 12.06

Orientation matrix

1st eigenvalue: 0.89

1st eigenvector: 325.56 / 38.11

2nd eigenvalue: 0.08

2nd eigenvector: 58.61 / 3.88

3rd eigenvalue: 0.04

3rd eigenvector: 153.52 / 51.63

VGP

Site latitude: 65

Site longitude: 14.04

Pole latitude: 40.79 (-40.79)

Pole longitude: -121.19 (58.81)

Paleolatitude: 21.4 (-21.4)

dp: 9.62

dm: 16.27

#	Name	State	Dec	Inc	MAD	Limit1	Limit2
1	YUNN8401	Cmt	345.1	24.9	6.9	30	64
2	YUNN8402	Cmt	327.7	25.0	7.0	20	64
3	YUNN8403	Cmt	328.5	61.3	8.3	40	64
4	YUNN8405	Cmt	350.8	33.5	6.3	20	64
5	YUNN8406	Cmt	337.5	43.8	8.0	35	64
6	YUNN8407	Cmt	336.8	46.7	12.3	40	60
7	YUNN8408	Cmt	297.3	39.3	8.3	44	64
8	YUNN8409	Cmt	290.7	25.4	18.6	35	64
9	YUNN8410	Cmt	314.1	27.9	13.9	20	64

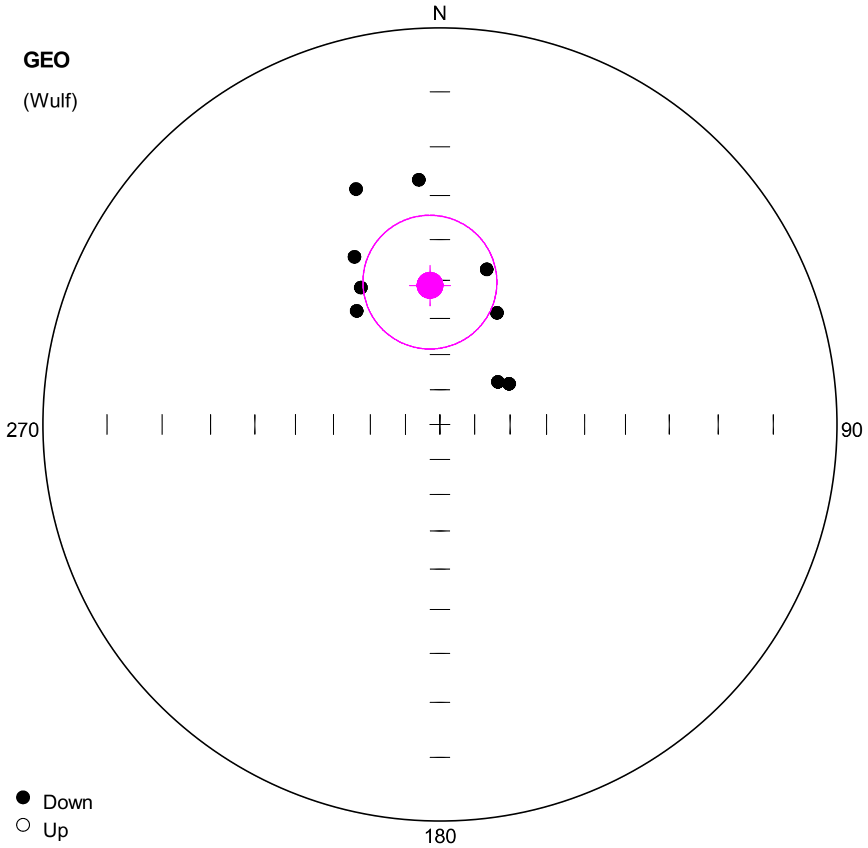

Number of data points: 9

Fisher statistics

Mean vector: 355.93 / 51.31
Resultant vector: 8.21
(X= 5.12, Y= -0.36, Z= 6.41)
Estimated precision, k: 10.1
95% Confidence limit: 17.02
95% Confidence limit, approximation: 14.68

Orientation matrix

1st eigenvalue: 0.83
1st eigenvector: 355.24 / 50.82
2nd eigenvalue: 0.13
2nd eigenvector: 125.84 / 27.94
3rd eigenvalue: 0.03
3rd eigenvector: 230.21 / 25.08

VGP

Site latitude: 65
Site longitude: 14.04
Pole latitude: 56.88 (-56.88)
Pole longitude: -159.63 (20.37)
Paleolatitude: 31.98 (-31.98)
dp: 15.67
dm: 23.1

#	Name	State	Dec	Inc	MAD	Limit1	Limit2
1	YUNN8502	Cmt	53.8	69.5	5.8	30	64
2	YUNN8503	Cmt	16.8	45.6	6.1	30	64
3	YUNN8504	Cmt	323.8	51.0	7.9	40	64
4	YUNN8505	Cmt	27.1	54.9	14.0	40	56
5	YUNN8506	Cmt	330.0	46.6	15.8	30	64
6	YUNN8507	Cmt	355.1	26.5	6.4	20	64
7	YUNN8508	Cmt	59.6	67.2	8.1	35	52
8	YUNN8509	Cmt	340.4	25.6	13.8	30	60
9	YUNN8510	Cmt	333.0	39.3	14.4	30	60

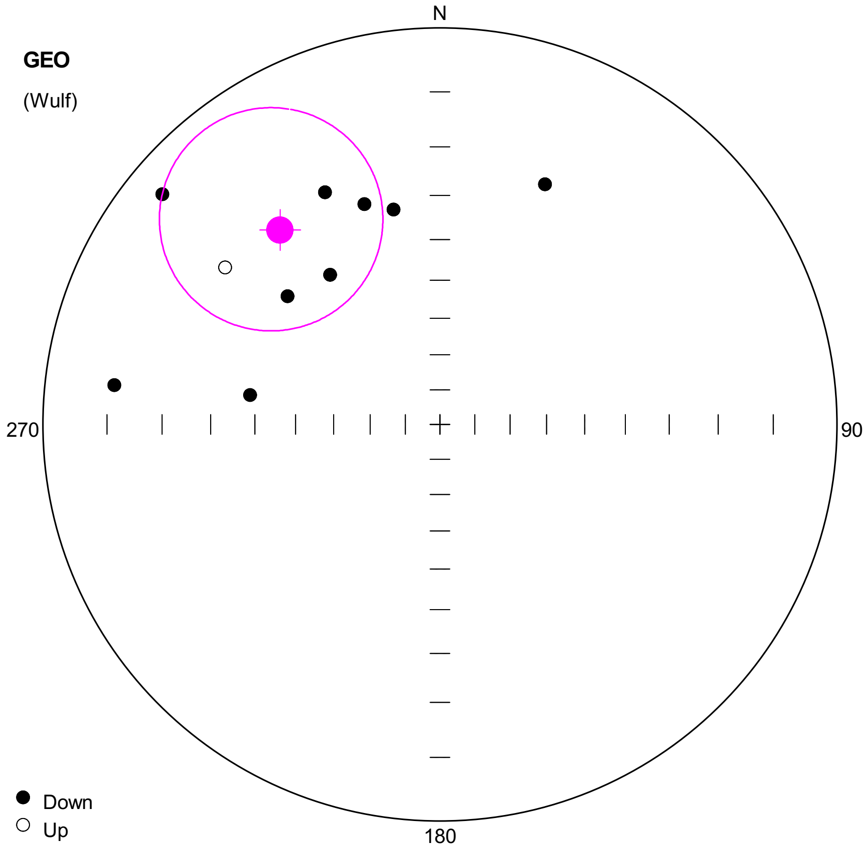

Number of data points: 10

Fisher statistics

Mean vector: 320.59 / 25.2
Resultant vector: 8.4
(X= 5.87, Y= -4.83, Z= 3.58)
Estimated precision, k: 5.64
95% Confidence limit: 22.34
95% Confidence limit, approximation: 18.65

Orientation matrix

1st eigenvalue: 0.73
1st eigenvector: 320.26 / 26.4
2nd eigenvalue: 0.19
2nd eigenvector: 59.46 / 17.86
3rd eigenvalue: 0.08
3rd eigenvector: 179.59 / 57.31

VGP

Site latitude: 65
Site longitude: 14.04
Pole latitude: 31.69 (-31.69)
Pole longitude: -119.38 (60.62)
Paleolatitude: 13.24 (-13.24)
dp: 12.93
dm: 24.03

#	Name	State	Dec	Inc	MAD	Limit1	Limit2	
1	YUNN8501	CHT	333.7	23.7	1.0	64	64	OA
2	YUNN8502	CHT	347.8	32.0	1.0	64	64	OA
3	YUNN8503	CHT	341.1	29.2	1.0	64	64	OA
4	YUNN8504	CHT	310.1	36.7	1.0	64	64	OA
5	YUNN8505	CHT	278.8	38.4	1.0	64	64	OA
6	YUNN8506	CHT	323.8	39.9	1.0	64	64	OA
7	YUNN8507	CHT	276.9	10.9	1.0	64	64	OA
8	YUNN8508	CHT	23.6	23.1	1.0	64	64	OA
9	YUNN8509	CHT	309.7	5.5	1.0	64	64	OA
10	YUNN8510	CHT	306.2	-22.3	1.0	64	64	OA

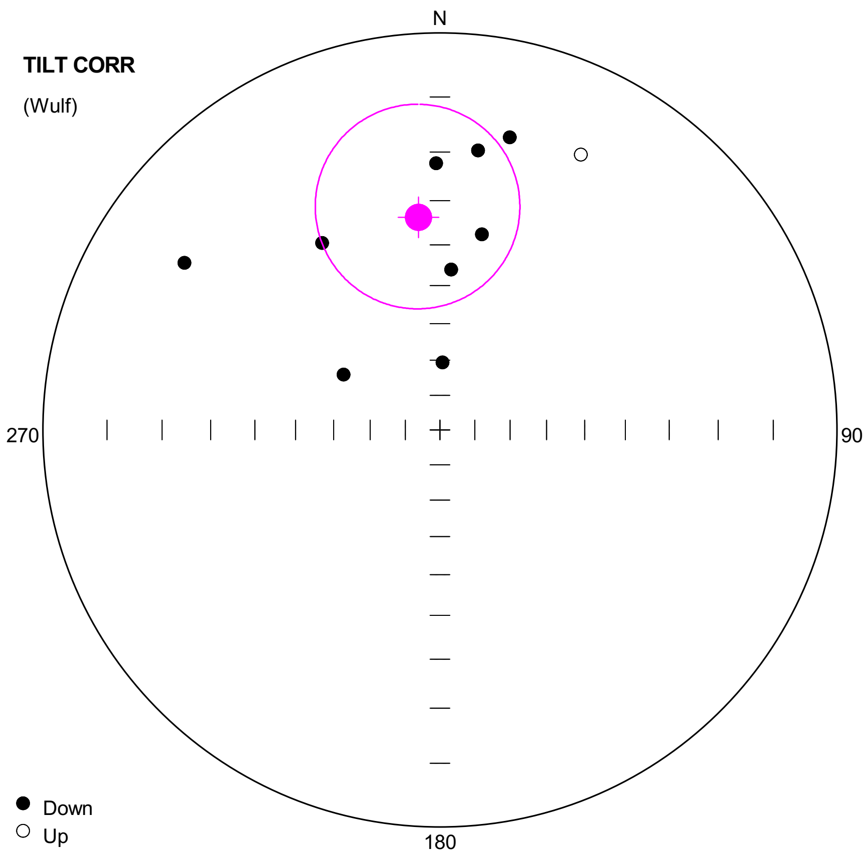

Number of data points: 10

Fisher statistics

Mean vector: 354.25 / 33.41
Resultant vector: 8.4
(X= 6.98, Y= -0.7, Z= 4.63)
Estimated precision, k: 5.63
95% Confidence limit: 22.34
95% Confidence limit, approximation: 18.65

Orientation matrix

1st eigenvalue: 0.73
1st eigenvector: 355.41 / 34.21
2nd eigenvalue: 0.19
2nd eigenvector: 236.86 / 35.1
3rd eigenvalue: 0.08
3rd eigenvector: 115.57 / 36.47

VGP

Site latitude: 65
Site longitude: 14.04
Pole latitude: 43.1 (-43.1)
Pole longitude: -158.48 (21.52)
Paleolatitude: 18.26 (-18.26)
dp: 14.46
dm: 25.42

#	Name	State	Dec	Inc	MAD	Limit1	Limit2	
1	YUNN8501	CHT	359.2	22.2	1.0	64	64	OA
2	YUNN8502	CHT	13.4	15.7	1.0	64	64	OA
3	YUNN8503	CHT	7.8	19.2	1.0	64	64	OA
4	YUNN8504	CHT	4.0	45.9	1.0	64	64	OA
5	YUNN8505	CHT	2.2	70.7	1.0	64	64	OA
6	YUNN8506	CHT	12.1	36.5	1.0	64	64	OA
7	YUNN8507	CHT	299.9	58.7	1.0	64	64	OA
8	YUNN8508	CHT	27.1	-14.2	1.0	64	64	OA
9	YUNN8509	CHT	327.8	31.8	1.0	64	64	OA
10	YUNN8510	CHT	303.2	14.9	1.0	64	64	OA

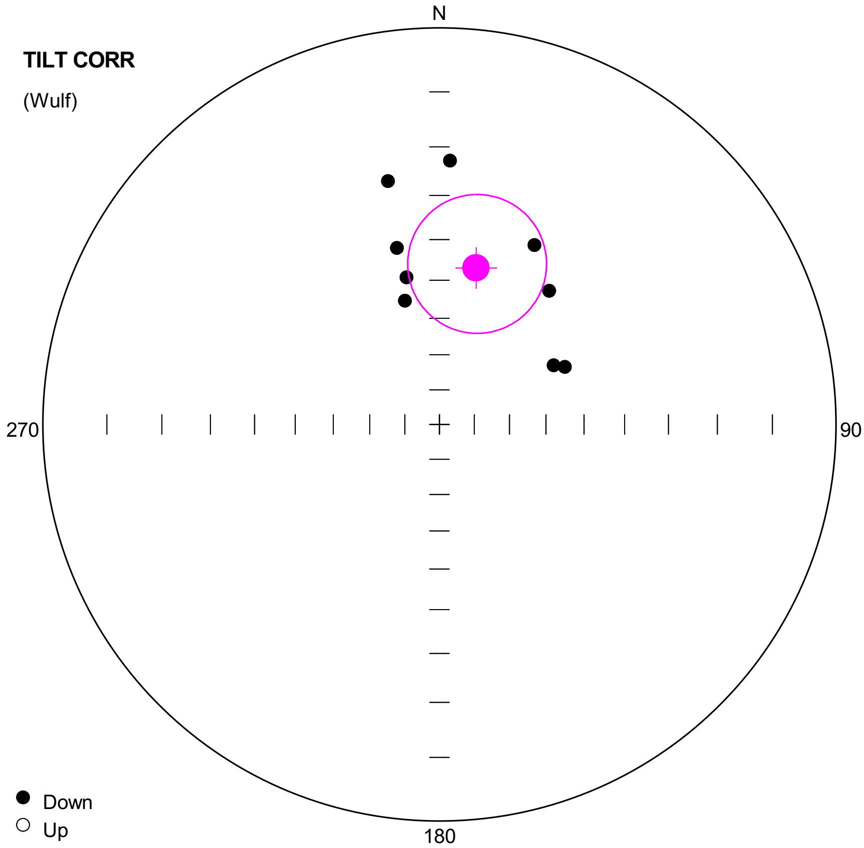

Number of data points: 9

Fisher statistics

Mean vector: 13.18 / 45.88
Resultant vector: 8.21
(X= 5.56, Y= 1.3, Z= 5.89)
Estimated precision, k: 10.09
95% Confidence limit: 17.03
95% Confidence limit, approximation: 14.69

Orientation matrix

1st eigenvalue: 0.83
1st eigenvector: 12.35 / 45.59
2nd eigenvalue: 0.13
2nd eigenvector: 120.79 / 17.22
3rd eigenvalue: 0.03
3rd eigenvector: 225.51 / 39.35

VGP

Site latitude: 65
Site longitude: 14.04
Pole latitude: 51.36 (-51.36)
Pole longitude: 175.1 (-4.9)
Paleolatitude: 27.28 (-27.28)
dp: 13.88
dm: 21.75

#	Name	State	Dec	Inc	MAD	Limit1	Limit2
1	YUNN8502	Cmt	62.6	54.1	5.8	30	64
2	YUNN8503	Cmt	27.9	35.8	6.1	30	64
3	YUNN8504	Cmt	344.5	54.1	7.9	40	64
4	YUNN8505	Cmt	39.4	42.9	14.0	40	56
5	YUNN8506	Cmt	347.4	48.4	15.8	30	64
6	YUNN8507	Cmt	2.3	22.7	6.4	20	64
7	YUNN8508	Cmt	65.4	51.6	8.1	35	52
8	YUNN8509	Cmt	348.1	25.8	13.8	30	60
9	YUNN8510	Cmt	346.5	40.8	14.4	30	60

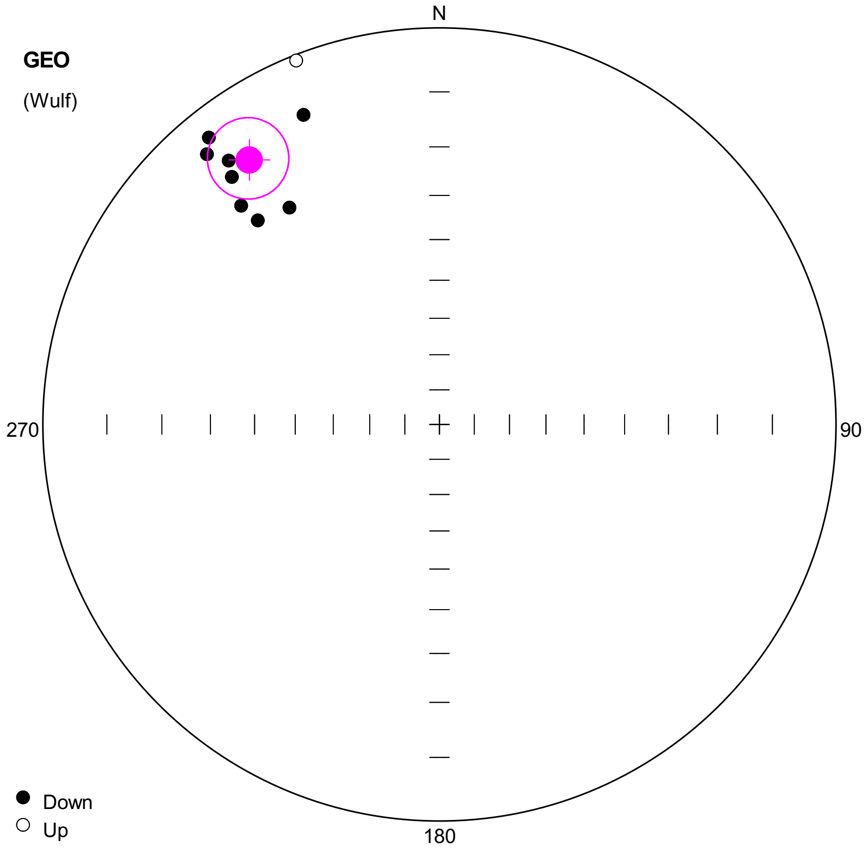

Number of data points: 9

Fisher statistics

Mean vector: 324.28 / 11.2
Resultant vector: 8.85
(X= 7.05, Y= -5.07, Z= 1.72)
Estimated precision, k: 55.13
95% Confidence limit: 7
95% Confidence limit, approximation: 6.29

Orientation matrix

1st eigenvalue: 0.97
1st eigenvector: 324.19 / 11.23
2nd eigenvalue: 0.02
2nd eigenvector: 223.03 / 44.26
3rd eigenvalue: 0.01
3rd eigenvector: 65.07 / 43.57

VGP

Site latitude: 65
Site longitude: 14.04
Pole latitude: 25.51 (-25.51)
Pole longitude: -125.88 (54.12)
Paleolatitude: 5.65 (-5.65)
dp: 3.6
dm: 7.1

#	Name	State	Dec	Inc	MAD	Limit1	Limit2	
1	YUNN8601	Cmt	319.3	6.1	2.2	30	56	OA
2	YUNN8602	Cmt	320.0	11.7	4.6	30	56	OA
3	YUNN8603	Cmt	336.3	9.1	3.5	20	56	OA
4	YUNN8604	Cmt	325.3	22.8	27.2	20	64	
5	YUNN8605	Cmt	321.2	4.3	3.0	20	56	OA
6	YUNN8606	Cmt	317.8	16.7	4.2	30	60	OA
7	YUNN8607	Cmt	321.4	9.2	4.0	20	60	OA
8	YUNN8608	Cmt	318.3	20.9	6.9	20	64	OA
9	YUNN8609	Cmt	338.5	-0.8	3.6	20	52	OA

TILT CORR

(Wulf)

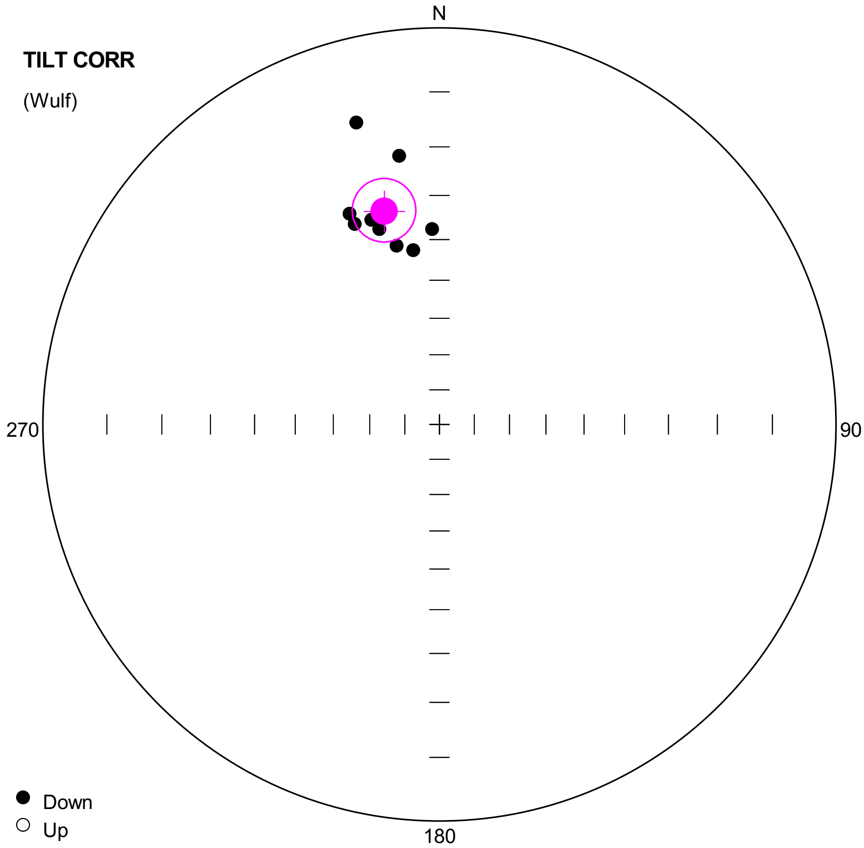

Number of data points: 9

Fisher statistics

Mean vector: 345.47 / 31.91
Resultant vector: 8.85
(X= 7.28, Y= -1.89, Z= 4.68)
Estimated precision, k: 55.13
95% Confidence limit: 7
95% Confidence limit, approximation: 6.28

Orientation matrix

1st eigenvalue: 0.97
1st eigenvector: 345.44 / 32
2nd eigenvalue: 0.02
2nd eigenvector: 149.19 / 56.94
3rd eigenvalue: 0.01
3rd eigenvector: 250.76 / 7.44

VGP

Site latitude: 65
Site longitude: 14.04
Pole latitude: 41.3 (-41.3)
Pole longitude: -147.37 (32.63)
Paleolatitude: 17.29 (-17.29)
dp: 4.42
dm: 7.87

#	Name	State	Dec	Inc	MAD	Limit1	Limit2	
1	YUNN8601	Cmt	337.1	32.5	2.2	30	56	OA
2	YUNN8602	Cmt	342.9	35.5	4.6	30	56	OA
3	YUNN8603	Cmt	351.5	21.2	3.5	20	56	OA
4	YUNN8604	Cmt	357.9	37.5	27.2	20	64	
5	YUNN8605	Cmt	336.9	30.0	3.0	20	56	OA
6	YUNN8606	Cmt	346.5	40.3	4.2	30	60	OA
7	YUNN8607	Cmt	341.6	32.9	4.0	20	60	OA
8	YUNN8608	Cmt	351.5	42.1	6.9	20	64	OA
9	YUNN8609	Cmt	344.6	13.4	3.6	20	52	OA

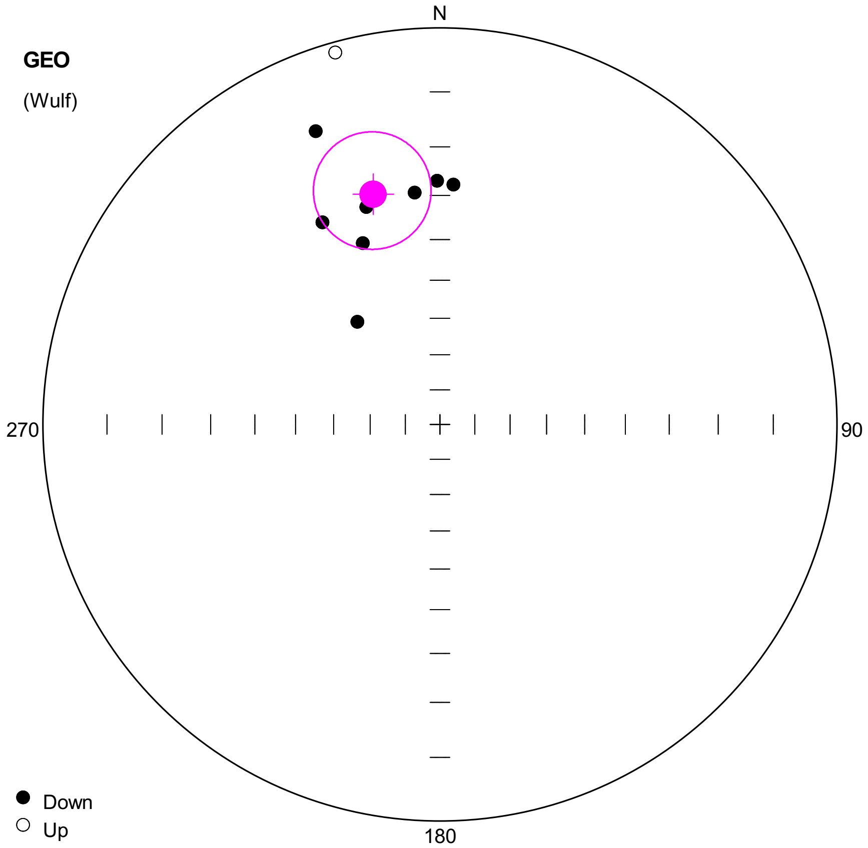

Number of data points: 9

Fisher statistics

Mean vector: 343.86 / 27.71
Resultant vector: 8.56
(X= 7.28, Y= -2.11, Z= 3.98)
Estimated precision, k: 18.38
95% Confidence limit: 12.34
95% Confidence limit, approximation: 10.89

Orientation matrix

1st eigenvalue: 0.91
1st eigenvector: 344.03 / 27.74
2nd eigenvalue: 0.06
2nd eigenvector: 198.56 / 57.45
3rd eigenvalue: 0.03
3rd eigenvector: 82.5 / 15.66

VGP

Site latitude: 65
Site longitude: 14.04
Pole latitude: 38.52 (-38.52)
Pole longitude: -145.85 (34.15)
Paleolatitude: 14.71 (-14.71)
dp: 7.36
dm: 13.48

#	Name	State	Dec	Inc	MAD	Limit1	Limit2
1	YUNN8701	Cmt	329.9	29.0	8.2	30	56
2	YUNN8702	Cmt	337.0	37.2	12.5	20	52
3	YUNN8703	Cmt	321.2	53.3	9.8	30	56
4	YUNN8704	Cmt	344.3	-1.5	11.3	35	60
5	YUNN8705	Cmt	359.3	26.9	17.7	30	60
6	YUNN8706	Cmt	337.1	12.5	23.7	30	60
7	YUNN8707	Cmt	341.3	29.9	6.2	35	56
8	YUNN8708	Cmt	3.2	27.6	14.6	44	60
9	YUNN8709	Cmt	353.8	29.1	6.6	44	60

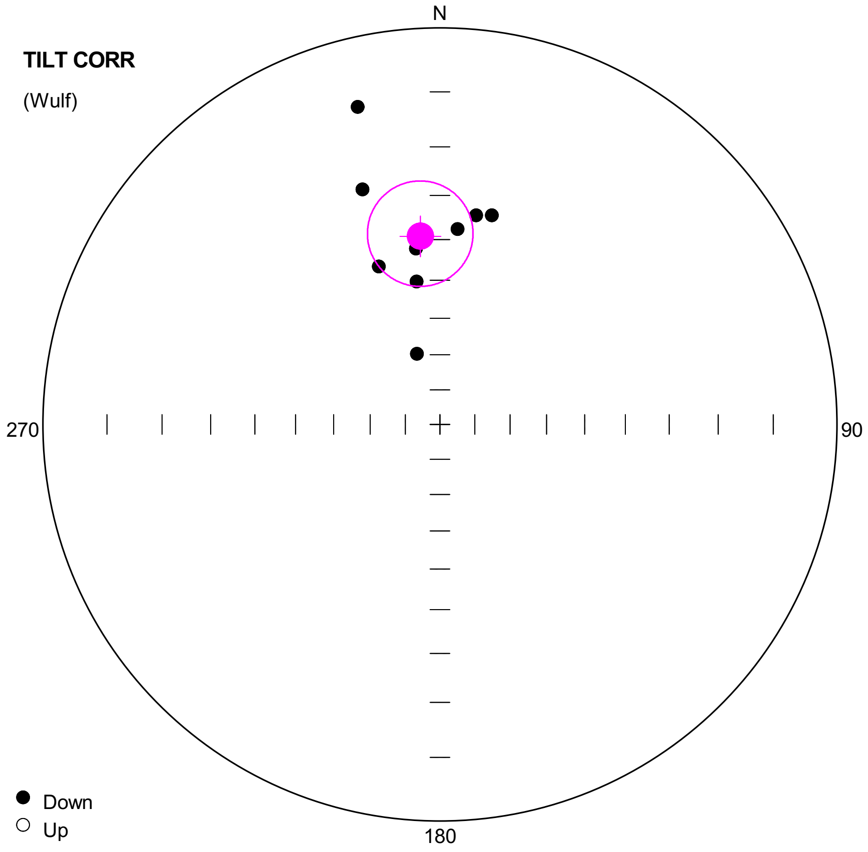

Number of data points: 9

Fisher statistics

Mean vector: 354.08 / 39
Resultant vector: 8.57
(X= 6.62, Y= -0.69, Z= 5.39)
Estimated precision, k: 18.4
95% Confidence limit: 12.33
95% Confidence limit, approximation: 10.88

Orientation matrix

1st eigenvalue: 0.91
1st eigenvector: 354.27 / 38.98
2nd eigenvalue: 0.06
2nd eigenvector: 173.12 / 51.01
3rd eigenvalue: 0.03
3rd eigenvector: 263.82 / 0.56

VGP

Site latitude: 65
Site longitude: 14.04
Pole latitude: 46.87 (-46.87)
Pole longitude: -157.92 (22.08)
Paleolatitude: 22.04 (-22.04)
dp: 8.77
dm: 14.7

#	Name	State	Dec	Inc	MAD	Limit1	Limit2
1	YUNN8701	Cmt	338.9	43.8	8.2	30	56
2	YUNN8702	Cmt	350.8	49.9	12.5	20	52
3	YUNN8703	Cmt	342.0	68.8	9.8	30	56
4	YUNN8704	Cmt	345.5	10.8	11.3	35	60
5	YUNN8705	Cmt	9.8	33.7	17.7	30	60
6	YUNN8706	Cmt	341.8	26.1	23.7	30	60
7	YUNN8707	Cmt	352.2	41.8	6.2	35	56
8	YUNN8708	Cmt	13.9	33.0	14.6	44	60
9	YUNN8709	Cmt	5.2	37.4	6.6	44	60

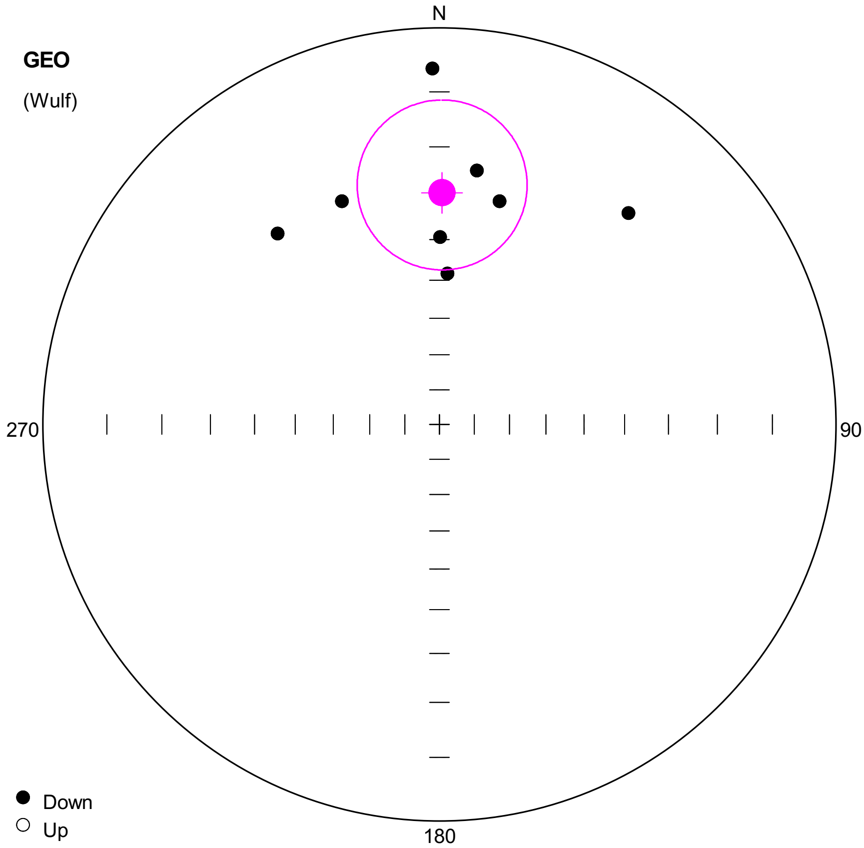

Number of data points: 8

Fisher statistics

Mean vector: 0.62 / 29.41
Resultant vector: 7.33
(X= 6.38, Y= 0.07, Z= 3.6)
Estimated precision, k: 10.43
95% Confidence limit: 17.99
95% Confidence limit, approximation: 15.32

Orientation matrix

1st eigenvalue: 0.85
1st eigenvector: 0.59 / 29.58
2nd eigenvalue: 0.12
2nd eigenvector: 268.32 / 3.99
3rd eigenvalue: 0.04
3rd eigenvector: 171.36 / 60.1

VGP

Site latitude: 65
Site longitude: 14.04
Pole latitude: 40.74 (-40.74)
Pole longitude: -166.75 (13.25)
Paleolatitude: 15.74 (-15.74)
dp: 10.98
dm: 19.88

#	Name	State	Dec	Inc	MAD	Limit1	Limit2
1	YUNN8801	Cmt	0.2	39.4	8.8	44	64
2	YUNN8802	Cmt	8.4	24.2	7.9	40	64
3	YUNN8803	Cmt	336.4	26.9	11.5	35	60
4	YUNN8805	Cmt	358.9	6.2	12.2	35	60
5	YUNN8806	Cmt	319.7	25.5	10.9	30	60
6	YUNN8807	Cmt	15.1	29.5	11.6	30	64
7	YUNN8808	Cmt	3.1	48.3	13.5	20	48
8	YUNN8809	Cmt	41.8	18.9	5.4	40	64

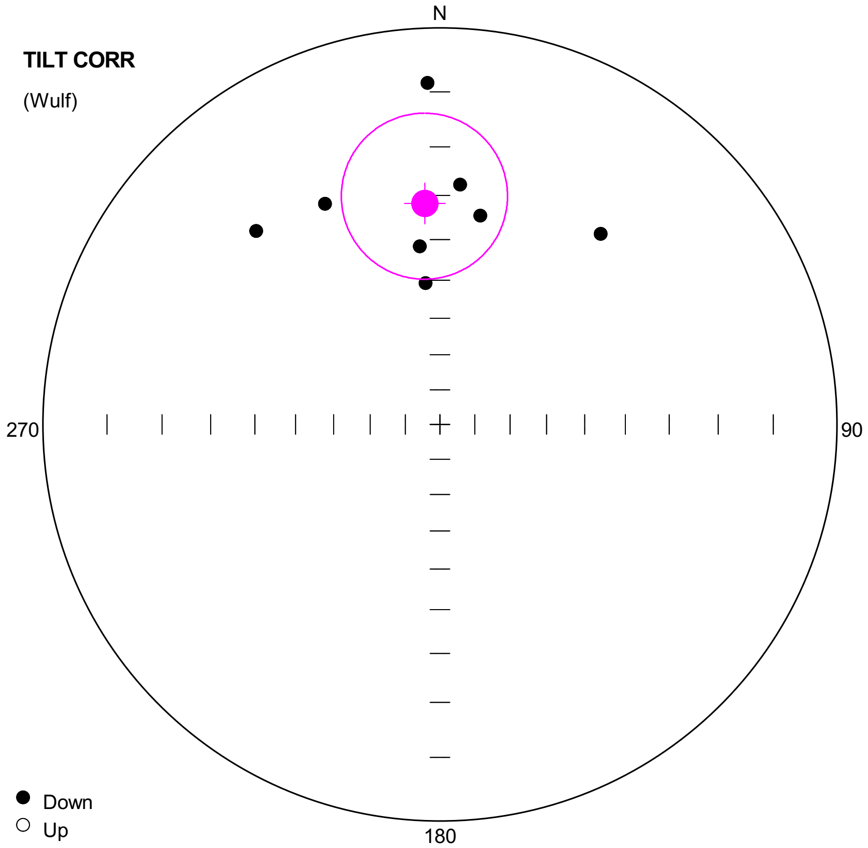

Number of data points: 8

Fisher statistics

Mean vector: 356.1 / 31.63
Resultant vector: 7.33
(X= 6.23, Y= -0.42, Z= 3.84)
Estimated precision, k: 10.44
95% Confidence limit: 17.98
95% Confidence limit, approximation: 15.32

Orientation matrix

1st eigenvalue: 0.85
1st eigenvector: 356.03 / 31.8
2nd eigenvalue: 0.12
2nd eigenvector: 88.35 / 3.74
3rd eigenvalue: 0.04
3rd eigenvector: 184.33 / 57.93

VGP

Site latitude: 65
Site longitude: 14.04
Pole latitude: 42.04 (-42.04)
Pole longitude: -160.93 (19.07)
Paleolatitude: 17.12 (-17.12)
dp: 11.33
dm: 20.18

#	Name	State	Dec	Inc	MAD	Limit1	Limit2
1	YUNN8801	Cmt	353.6	41.4	8.8	44	64
2	YUNN8802	Cmt	4.8	27.5	7.9	40	64
3	YUNN8803	Cmt	332.5	25.8	11.5	35	60
4	YUNN8805	Cmt	357.9	8.5	12.2	35	60
5	YUNN8806	Cmt	316.5	22.2	10.9	30	60
6	YUNN8807	Cmt	10.9	33.6	11.6	30	64
7	YUNN8808	Cmt	354.2	50.6	13.5	20	48
8	YUNN8809	Cmt	40.1	25.7	5.4	40	64

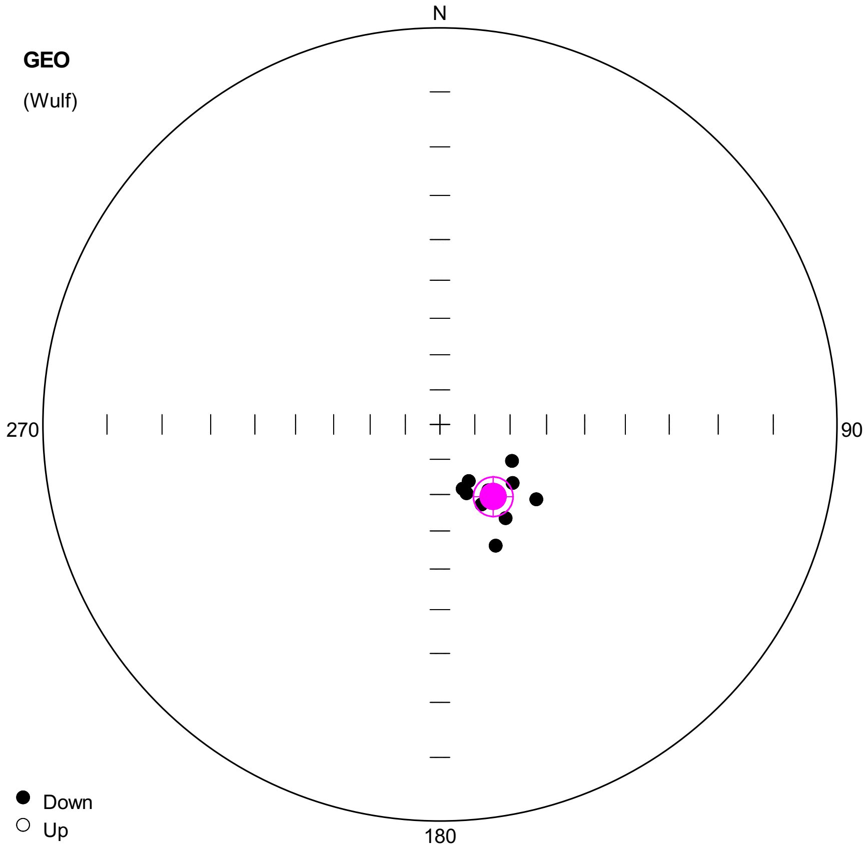

Number of data points: 10

Fisher statistics

Mean vector: 143.65 / 64.59
Resultant vector: 9.89
(X= -3.42, Y= 2.52, Z= 8.93)
Estimated precision, k: 80.27
95% Confidence limit: 5.42
95% Confidence limit, approximation: 4.94

Orientation matrix

1st eigenvalue: 0.98
1st eigenvector: 143.67 / 64.61
2nd eigenvalue: 0.01
2nd eigenvector: 287.48 / 20.96
3rd eigenvalue: 0.01
3rd eigenvector: 22.83 / 13.68

VGP

Site latitude: 65
Site longitude: 14.04
Pole latitude: 24.99 (-24.99)
Pole longitude: 40.82 (-139.18)
Paleolatitude: 46.46 (-46.46)
dp: 6.99
dm: 8.71

#	Name	State	Dec	Inc	MAD	Limit1	Limit2
1	YUNN8901	Cht	159.0	68.9	0.0	64	68
2	YUNN8902	Cht	152.5	64.4	0.0	64	68
3	YUNN8903	Cht	128.8	63.5	0.0	64	68
4	YUNN8904	Cht	116.8	67.0	0.0	64	68
5	YUNN8905	Cht	145.0	57.8	0.0	64	68
6	YUNN8906	Cht	127.9	55.8	0.0	64	68
7	YUNN8907	Cht	155.3	52.8	0.0	64	68
8	YUNN8908	Cht	152.9	71.8	0.0	64	68
9	YUNN8909	Cht	160.4	70.5	0.0	64	68
10	YUNN8910	Cht	143.7	66.7	0.0	64	68

TILT CORR

(Wulf)

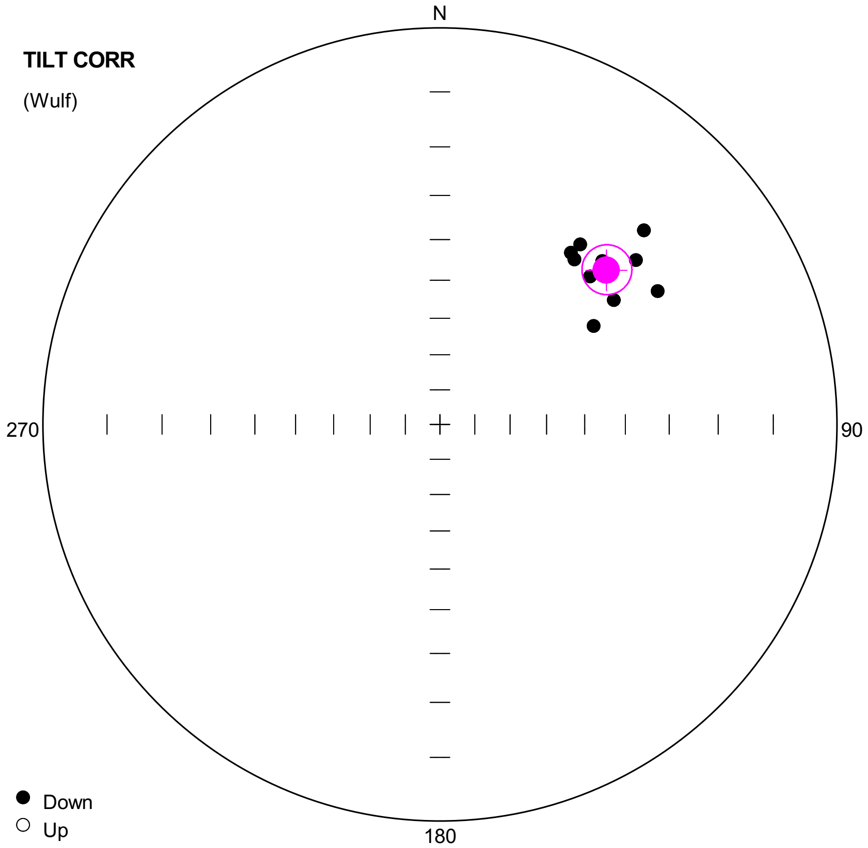

Number of data points: 10

Fisher statistics

Mean vector: 47.11 / 30.47
Resultant vector: 9.89
(X= 5.8, Y= 6.24, Z= 5.01)
Estimated precision, k: 80.32
95% Confidence limit: 5.42
95% Confidence limit, approximation: 4.94

Orientation matrix

1st eigenvalue: 0.98
1st eigenvector: 47.08 / 30.47
2nd eigenvalue: 0.01
2nd eigenvector: 309.93 / 11.95
3rd eigenvalue: 0.01
3rd eigenvector: 201.06 / 56.79

VGP

Site latitude: 65
Site longitude: 14.04
Pole latitude: 32.12 (-32.12)
Pole longitude: 137.95 (-42.05)
Paleolatitude: 16.39 (-16.39)
dp: 3.36
dm: 6.04

#	Name	State	Dec	Inc	MAD	Limit1	Limit2
1	YUNN8901	Cht	39.2	33.6	0.0	64	68
2	YUNN8902	Cht	45.4	34.0	0.0	64	68
3	YUNN8903	Cht	50.0	24.4	0.0	64	68
4	YUNN8904	Cht	46.4	19.3	0.0	64	68
5	YUNN8905	Cht	54.4	33.4	0.0	64	68
6	YUNN8906	Cht	58.5	24.5	0.0	64	68
7	YUNN8907	Cht	57.4	40.6	0.0	64	68
8	YUNN8908	Cht	37.9	30.2	0.0	64	68
9	YUNN8909	Cht	37.3	32.9	0.0	64	68
10	YUNN8910	Cht	44.8	29.7	0.0	64	68

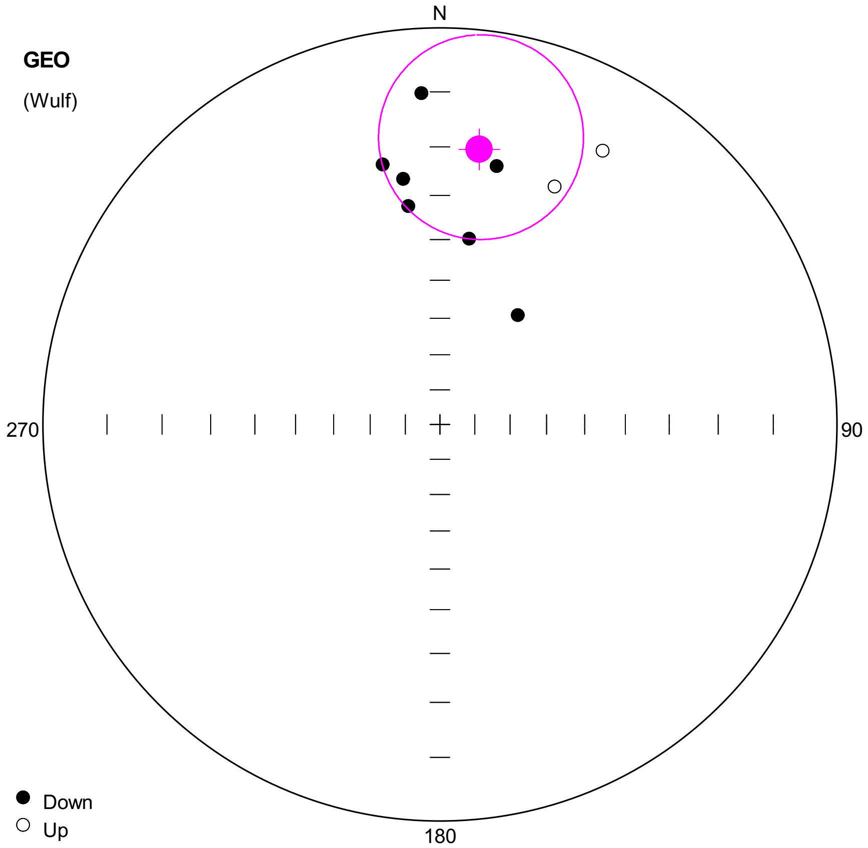

Number of data points: 9

Fisher statistics

Mean vector: 8.1 / 19.94
Resultant vector: 8
(X= 7.45, Y= 1.06, Z= 2.73)
Estimated precision, k: 8.03
95% Confidence limit: 19.35
95% Confidence limit, approximation: 16.46

Orientation matrix

1st eigenvalue: 0.8
1st eigenvector: 6.32 / 21.53
2nd eigenvalue: 0.15
2nd eigenvector: 232.32 / 60.4
3rd eigenvalue: 0.05
3rd eigenvector: 104.26 / 19.3

VGP

Site latitude: 65
Site longitude: 14.04
Pole latitude: 34.99 (-34.99)
Pole longitude: -175.71 (4.29)
Paleolatitude: 10.28 (-10.28)
dp: 10.6
dm: 20.26

#	Name	State	Dec	Inc	MAD	Limit1	Limit2
1	YUNN9101	Cmt	12.4	22.6	9.9	30	52
2	YUNN9102	Cmt	25.7	-22.7	4.1	30	48
3	YUNN9103	Cmt	351.8	31.8	7.8	44	56
4	YUNN9104	Cmt	8.9	39.3	6.8	40	60
5	YUNN9105	Cmt	30.7	-12.5	5.6	35	52
6	YUNN9106	Cmt	35.4	52.6	11.6	20	60
7	YUNN9109	Cmt	356.8	10.2	9.2	35	60
8	YUNN9110	Cmt	351.5	25.9	3.2	35	64
9	YUNN9111	Cmt	347.6	22.3	7.9	40	56

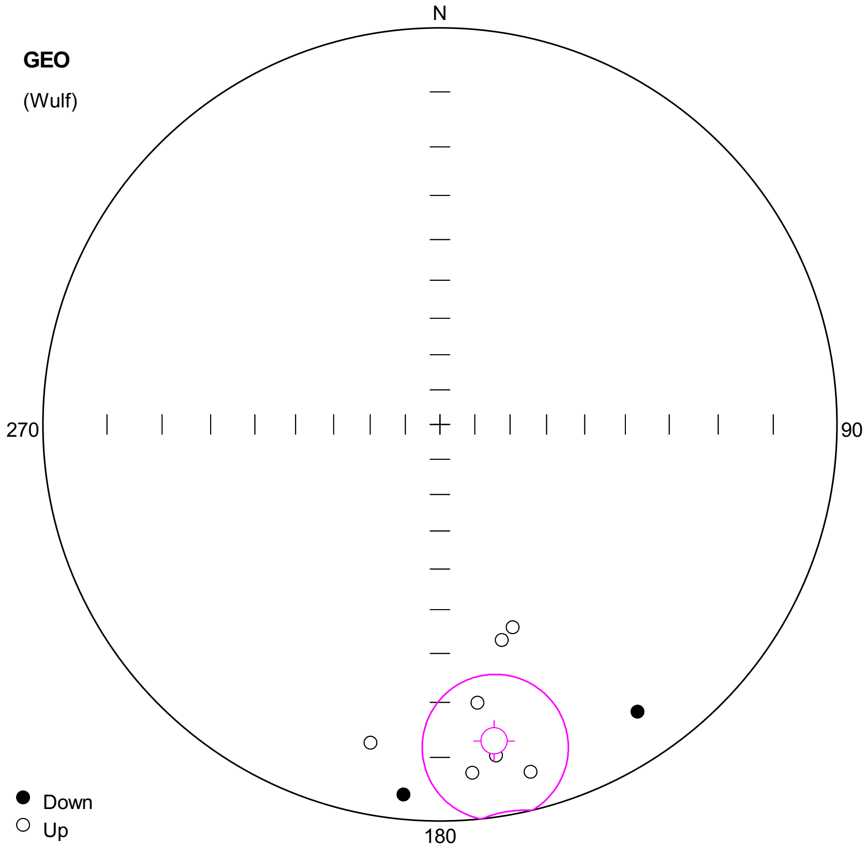

Number of data points: 9

Fisher statistics

Mean vector: 170.31 / -12.04
Resultant vector: 8.55
(X= -8.24, Y= 1.41, Z= -1.78)
Estimated precision, k: 17.69
95% Confidence limit: 12.59
95% Confidence limit, approximation: 11.1

Orientation matrix

1st eigenvalue: 0.9
1st eigenvector: 350.56 / 12.17
2nd eigenvalue: 0.05
2nd eigenvector: 238.92 / 59.68
3rd eigenvalue: 0.05
3rd eigenvector: 86.95 / 27.3

VGP

Site latitude: 65
Site longitude: 14.04
Pole latitude: -30.68 (30.68)
Pole longitude: 25.27 (-154.73)
Paleolatitude: -6.09 (6.09)
dp: 6.51
dm: 12.8

#	Name	State	Dec	Inc	MAD	Limit1	Limit2	
1	YUNN9101	Cht	165.4	-5.7	6.1	56	64	OA
2	YUNN9102	Cht	164.0	-31.0	7.0	52	60	OA
3	YUNN9103	Cht	174.7	-7.2	10.9	52	60	OA
4	YUNN9104	Cht	192.3	-11.2	9.7	60	64	OA
5	YUNN9105	Cht	160.3	-33.0	2.0	56	60	OA
6	YUNN9106	Cht	172.3	-19.4	4.5	60	64	OA
7	YUNN9109	Cht	145.5	7.4	1.7	60	64	OA
8	YUNN9110	Cht	170.4	-9.5	1.4	60	64	OA
9	YUNN9111	Cht	185.6	3.7	19.2	60	64	OA

TILT CORR

(Wulf)

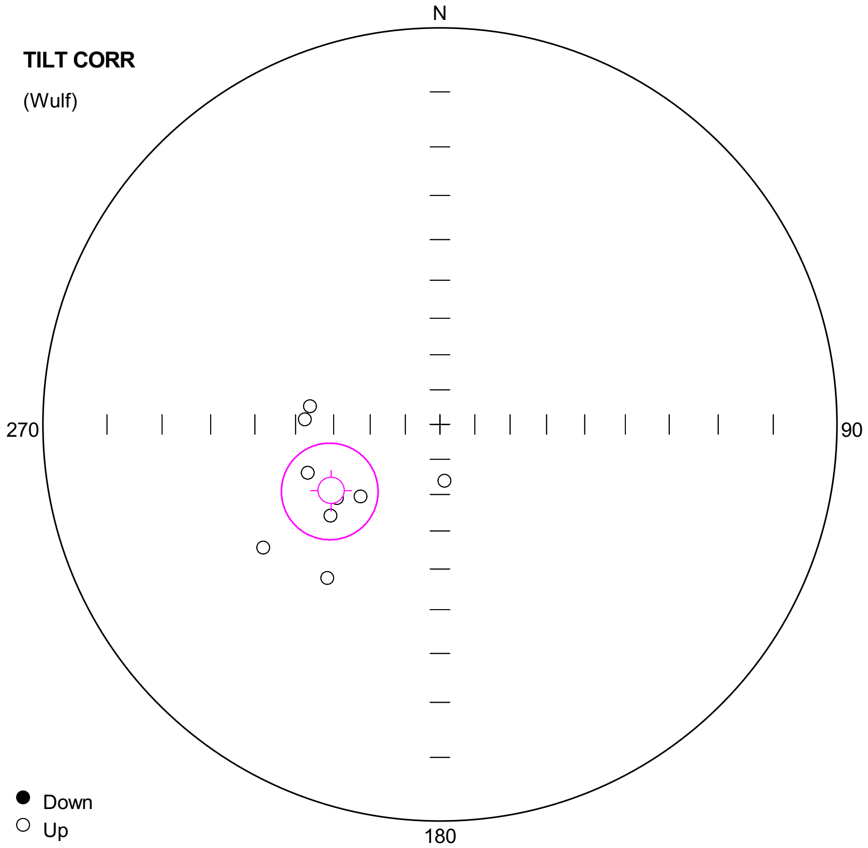

Number of data points: 9

Fisher statistics

Mean vector: 238.73 / -54.44
Resultant vector: 8.55
(X= -2.58, Y= -4.25, Z= -6.95)
Estimated precision, k: 17.7
95% Confidence limit: 12.58
95% Confidence limit, approximation: 11.09

Orientation matrix

1st eigenvalue: 0.9
1st eigenvector: 58.89 / 54.17
2nd eigenvalue: 0.05
2nd eigenvector: 166.27 / 12.17
3rd eigenvalue: 0.05
3rd eigenvector: 264.35 / 33.1

VGP

Site latitude: 65
Site longitude: 14.04
Pole latitude: -44.36 (44.36)
Pole longitude: -64.39 (115.61)
Paleolatitude: -34.96 (34.96)
dp: 12.49
dm: 17.73

#	Name	State	Dec	Inc	MAD	Limit1	Limit2	
1	YUNN9101	Cht	227.8	-59.8	6.1	56	64	OA
2	YUNN9102	Cht	272.1	-52.4	7.0	52	60	OA
3	YUNN9103	Cht	230.2	-50.5	10.9	52	60	OA
4	YUNN9104	Cht	235.1	-33.0	9.7	60	64	OA
5	YUNN9105	Cht	278.0	-53.4	2.0	56	60	OA
6	YUNN9106	Cht	249.9	-51.0	4.5	60	64	OA
7	YUNN9109	Cht	175.3	-73.8	1.7	60	64	OA
8	YUNN9110	Cht	234.4	-54.6	1.4	60	64	OA
9	YUNN9111	Cht	216.2	-38.7	19.2	60	64	OA

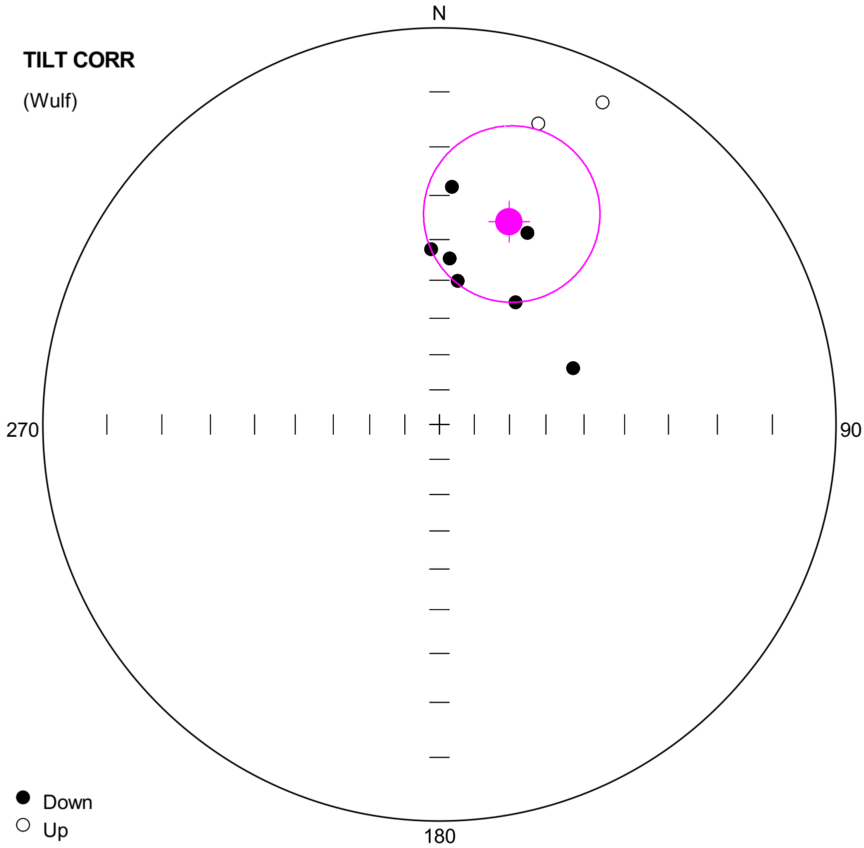

Number of data points: 9

Fisher statistics

Mean vector: 18.94 / 33.22

Resultant vector: 8

(X= 6.33, Y= 2.17, Z= 4.38)

Estimated precision, k: 8.02

95% Confidence limit: 19.37

95% Confidence limit, approximation: 16.47

Orientation matrix

1st eigenvalue: 0.8

1st eigenvector: 17.87 / 35.35

2nd eigenvalue: 0.15

2nd eigenvector: 192.61 / 54.53

3rd eigenvalue: 0.05

3rd eigenvector: 286.11 / 2.49

VGP

Site latitude: 65

Site longitude: 14.04

Pole latitude: 41.45 (-41.45)

Pole longitude: 169.74 (-10.26)

Paleolatitude: 18.13 (-18.13)

dp: 12.5

dm: 22

#	Name	State	Dec	Inc	MAD	Limit1	Limit2
1	YUNN9101	Cmt	24.7	34.0	9.9	30	52
2	YUNN9102	Cmt	18.2	-12.8	4.1	30	48
3	YUNN9103	Cmt	7.3	49.9	7.8	44	56
4	YUNN9104	Cmt	31.9	50.1	6.8	40	60
5	YUNN9105	Cmt	26.9	-5.4	5.6	35	52
6	YUNN9106	Cmt	67.2	49.8	11.6	20	60
7	YUNN9109	Cmt	3.0	28.1	9.2	35	60
8	YUNN9110	Cmt	3.6	44.5	3.2	35	64
9	YUNN9111	Cmt	357.3	42.3	7.9	40	56

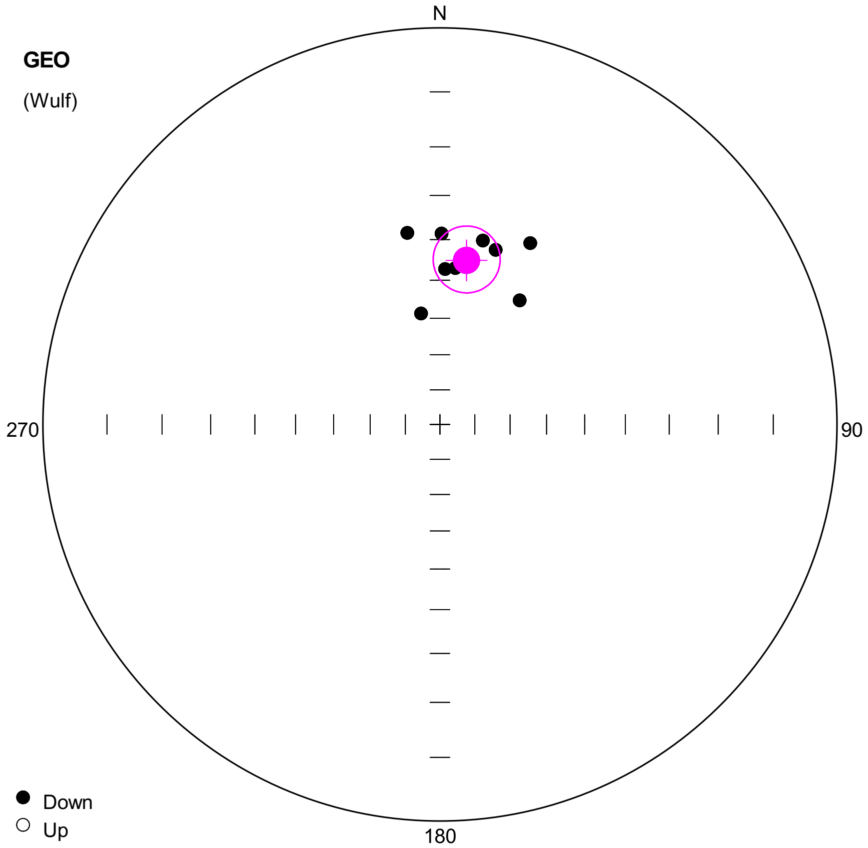

Number of data points: 9

Fisher statistics

Mean vector: 9.16 / 44.53

Resultant vector: 8.8

(X= 6.2, Y= 1, Z= 6.17)

Estimated precision, k: 40.42

95% Confidence limit: 8.2

95% Confidence limit, approximation: 7.34

Orientation matrix

1st eigenvalue: 0.96

1st eigenvector: 9.14 / 44.48

2nd eigenvalue: 0.03

2nd eigenvector: 271.04 / 8.17

3rd eigenvalue: 0.01

3rd eigenvector: 172.96 / 44.37

VGP

Site latitude: 65

Site longitude: 14.04

Pole latitude: 50.75 (-50.75)

Pole longitude: -179 (1)

Paleolatitude: 26.19 (-26.19)

dp: 6.49

dm: 10.32

#	Name	State	Dec	Inc	MAD	Limit1	Limit2
1	YUNN9201	Cmt	17.7	40.4	12.6	20	64
2	YUNN9202	Cmt	13.1	39.1	10.0	20	64
3	YUNN9204	Cmt	5.6	46.8	5.6	20	64
4	YUNN9205	Cmt	350.4	58.3	5.8	20	64
5	YUNN9206	Cmt	26.5	35.9	6.0	20	64
6	YUNN9207	Cmt	0.5	38.6	7.4	30	60
7	YUNN9208	Ch	350.4	37.8	3.7	30	68
8	YUNN9209	Ch	1.9	47.2	7.0	30	68
9	YUNN9210	Cmt	32.7	49.2	19.1	30	60

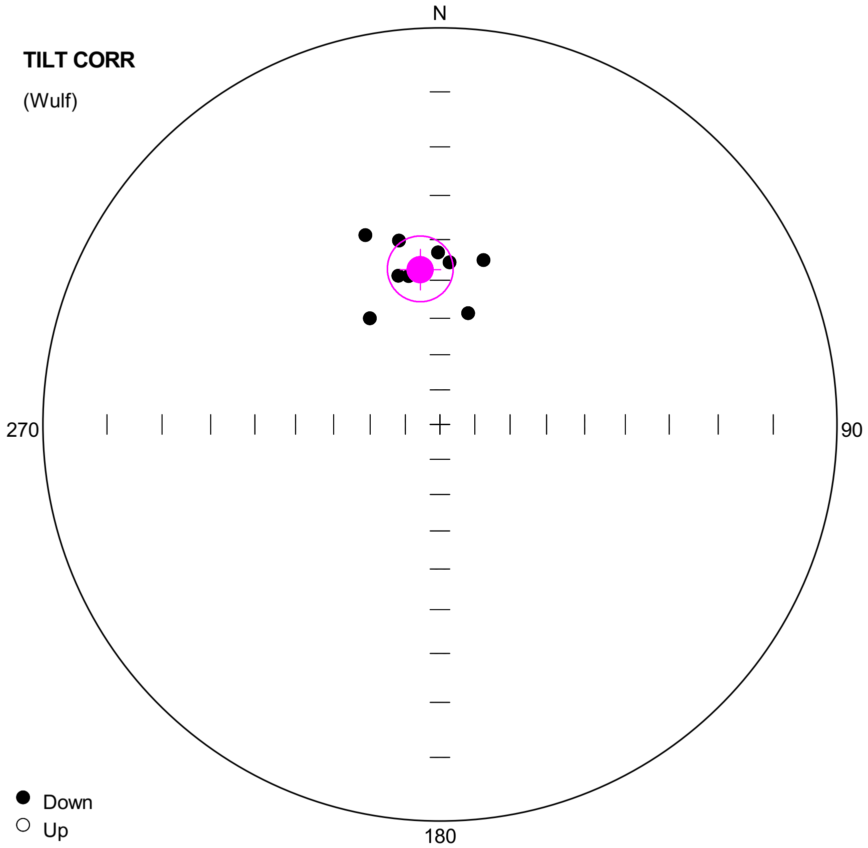

Number of data points: 9

Fisher statistics

Mean vector: 352.77 / 47.06
Resultant vector: 8.8
(X= 5.95, Y= -0.75, Z= 6.44)
Estimated precision, k: 40.33
95% Confidence limit: 8.21
95% Confidence limit, approximation: 7.35

Orientation matrix

1st eigenvalue: 0.96
1st eigenvector: 352.79 / 47.01
2nd eigenvalue: 0.03
2nd eigenvector: 90.9 / 7.5
3rd eigenvalue: 0.01
3rd eigenvector: 187.71 / 42.01

VGP

Site latitude: 65
Site longitude: 14.04
Pole latitude: 52.97 (-52.97)
Pole longitude: -155.36 (24.64)
Paleolatitude: 28.25 (-28.25)
dp: 6.86
dm: 10.61

#	Name	State	Dec	Inc	MAD	Limit1	Limit2
1	YUNN9201	Cmt	3.4	45.5	12.6	20	64
2	YUNN9202	Cmt	359.4	43.1	10.0	20	64
3	YUNN9204	Cmt	348.1	48.2	5.6	20	64
4	YUNN9205	Cmt	326.6	54.5	5.8	20	64
5	YUNN9206	Cmt	14.8	43.6	6.0	20	64
6	YUNN9207	Cmt	347.5	39.2	7.4	30	60
7	YUNN9208	Ch	338.5	35.7	3.7	30	68
8	YUNN9209	Ch	344.4	47.5	7.0	30	68
9	YUNN9210	Cmt	14.2	57.7	19.1	30	60

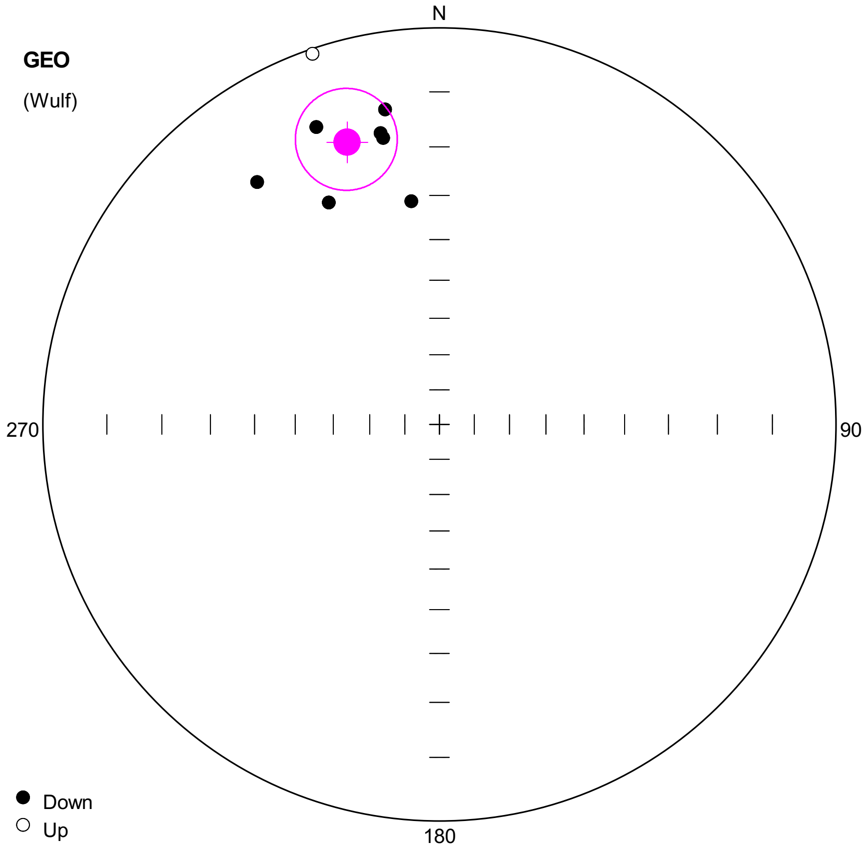

Number of data points: 8

Fisher statistics

Mean vector: 341.9 / 16.37
Resultant vector: 7.8
(X= 7.12, Y= -2.33, Z= 2.2)
Estimated precision, k: 35.84
95% Confidence limit: 9.38
95% Confidence limit, approximation: 8.27

Orientation matrix

1st eigenvalue: 0.95
1st eigenvector: 341.97 / 16.35
2nd eigenvalue: 0.03
2nd eigenvector: 87.4 / 42.19
3rd eigenvalue: 0.02
3rd eigenvector: 235.94 / 43.26

VGP

Site latitude: 65
Site longitude: 14.04
Pole latitude: 31.95 (-31.95)
Pole longitude: -144.72 (35.28)
Paleolatitude: 8.35 (-8.35)
dp: 4.99
dm: 9.67

#	Name	State	Dec	Inc	MAD	Limit1	Limit2
1	YUNN9301	Cmt	337.5	11.9	12.5	30	60
2	YUNN9302	Cmt	352.8	30.9	8.3	20	64
3	YUNN9304	Ch	323.1	15.2	10.3	30	64
4	YUNN9305	Ch	333.5	26.0	6.0	30	64
5	YUNN9306	Ch	341.1	-0.7	5.1	30	60
6	YUNN9308	Ch	350.2	12.3	8.7	30	60
7	YUNN9309	Cmt	348.6	16.3	8.2	44	68
8	YUNN9310	Cmt	348.9	17.3	9.0	30	64

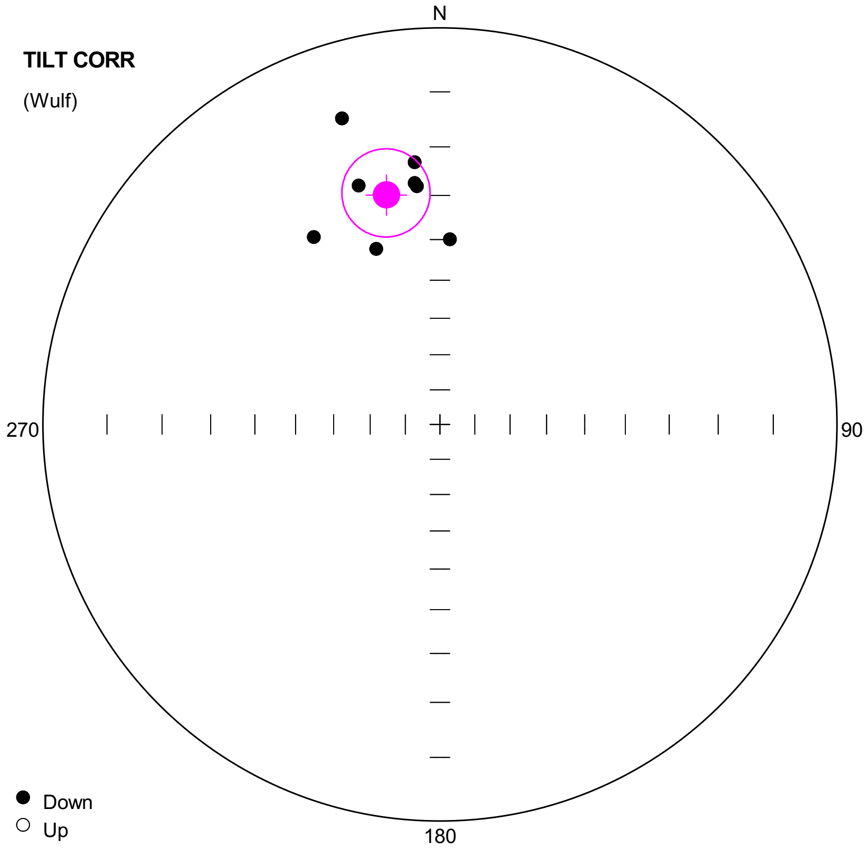

Number of data points: 8

Fisher statistics

Mean vector: 346.88 / 28.56

Resultant vector: 7.81

(X= 6.68, Y= -1.56, Z= 3.73)

Estimated precision, k: 35.92

95% Confidence limit: 9.37

95% Confidence limit, approximation: 8.26

Orientation matrix

1st eigenvalue: 0.95

1st eigenvector: 346.96 / 28.53

2nd eigenvalue: 0.03

2nd eigenvector: 92.66 / 26.47

3rd eigenvalue: 0.02

3rd eigenvector: 217.91 / 49.21

VGP

Site latitude: 65

Site longitude: 14.04

Pole latitude: 39.43 (-39.43)

Pole longitude: -149.49 (30.51)

Paleolatitude: 15.22 (-15.22)

dp: 5.65

dm: 10.29

#	Name	State	Dec	Inc	MAD	Limit1	Limit2
1	YUNN9301	Cmt	341.2	25.1	12.5	30	60
2	YUNN9302	Cmt	3.1	39.9	8.3	20	64
3	YUNN9304	Ch	326.1	30.7	10.3	30	64
4	YUNN9305	Ch	340.1	39.6	6.0	30	64
5	YUNN9306	Ch	342.3	12.0	5.1	30	60
6	YUNN9308	Ch	354.5	22.8	8.7	30	60
7	YUNN9309	Cmt	354.0	27.1	8.2	44	68
8	YUNN9310	Cmt	354.5	27.8	9.0	30	64

GEO

(Wulf)

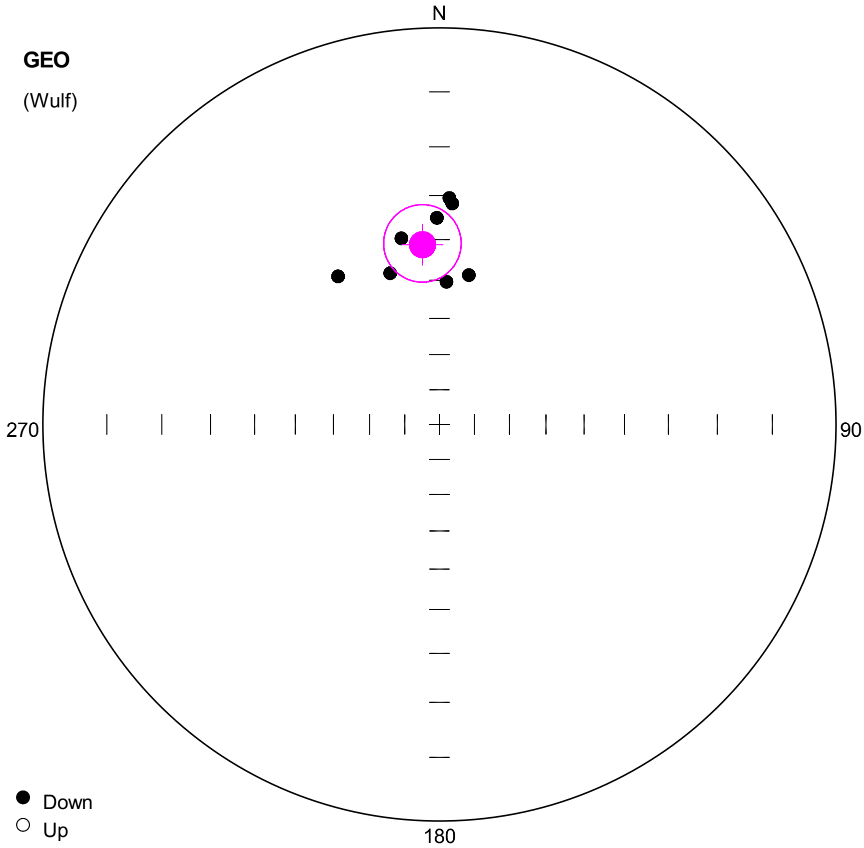

Number of data points: 8

Fisher statistics

Mean vector: 354.6 / 41.06
Resultant vector: 7.81
(X= 5.86, Y= -0.55, Z= 5.13)
Estimated precision, k: 36.85
95% Confidence limit: 9.25
95% Confidence limit, approximation: 8.15

Orientation matrix

1st eigenvalue: 0.95
1st eigenvector: 354.76 / 41.02
2nd eigenvalue: 0.03
2nd eigenvector: 252.22 / 14.01
3rd eigenvalue: 0.01
3rd eigenvector: 147.45 / 45.61

VGP

Site latitude: 65
Site longitude: 14.04
Pole latitude: 48.39 (-48.39)
Pole longitude: -158.49 (21.51)
Paleolatitude: 23.53 (-23.53)
dp: 6.83
dm: 11.24

#	Name	State	Dec	Inc	MAD	Limit1	Limit2	
1	YUNN9401	Ch	325.6	41.3	5.9	30	64	
2	YUNN9402	Ch	359.3	35.0	19.5	30	64	
3	YUNN9403	Ch	342.0	46.3	3.5	20	60	OA
4	YUNN9404	Ch	348.5	38.8	5.7	20	64	OA
5	YUNN9405	Ch	2.9	50.4	14.7	20	64	
6	YUNN9407	Ch	2.5	30.5	16.3	20	60	
7	YUNN9408	Ch	3.3	31.7	11.4	20	68	OA
8	YUNN9409	Ch	11.2	48.0	9.0	20	52	

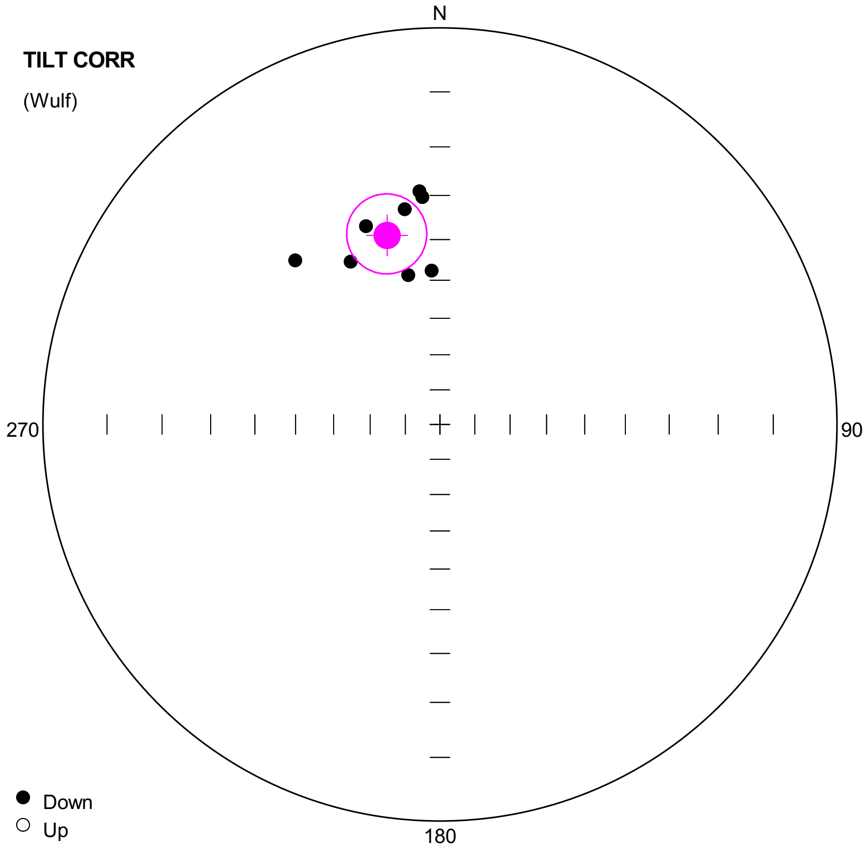

Number of data points: 8

Fisher statistics

Mean vector: 344.39 / 37.33
Resultant vector: 7.81
(X= 5.98, Y= -1.67, Z= 4.74)
Estimated precision, k: 36.87
95% Confidence limit: 9.24
95% Confidence limit, approximation: 8.15

Orientation matrix

1st eigenvalue: 0.95
1st eigenvector: 344.55 / 37.32
2nd eigenvalue: 0.03
2nd eigenvector: 252.96 / 2.08
3rd eigenvalue: 0.01
3rd eigenvector: 160.23 / 52.6

VGP

Site latitude: 65
Site longitude: 14.04
Pole latitude: 44.69 (-44.69)
Pole longitude: -145.24 (34.76)
Paleolatitude: 20.87 (-20.87)
dp: 6.38
dm: 10.86

#	Name	State	Dec	Inc	MAD	Limit1	Limit2	
1	YUNN9401	Ch	318.6	32.3	5.9	30	64	
2	YUNN9402	Ch	350.7	32.4	19.5	30	64	
3	YUNN9403	Ch	331.3	39.9	3.5	20	60	OA
4	YUNN9404	Ch	339.6	33.9	5.7	20	64	OA
5	YUNN9405	Ch	348.0	47.9	14.7	20	64	
6	YUNN9407	Ch	355.0	28.9	16.3	20	60	
7	YUNN9408	Ch	355.6	30.2	11.4	20	68	OA
8	YUNN9409	Ch	356.9	47.6	9.0	20	52	

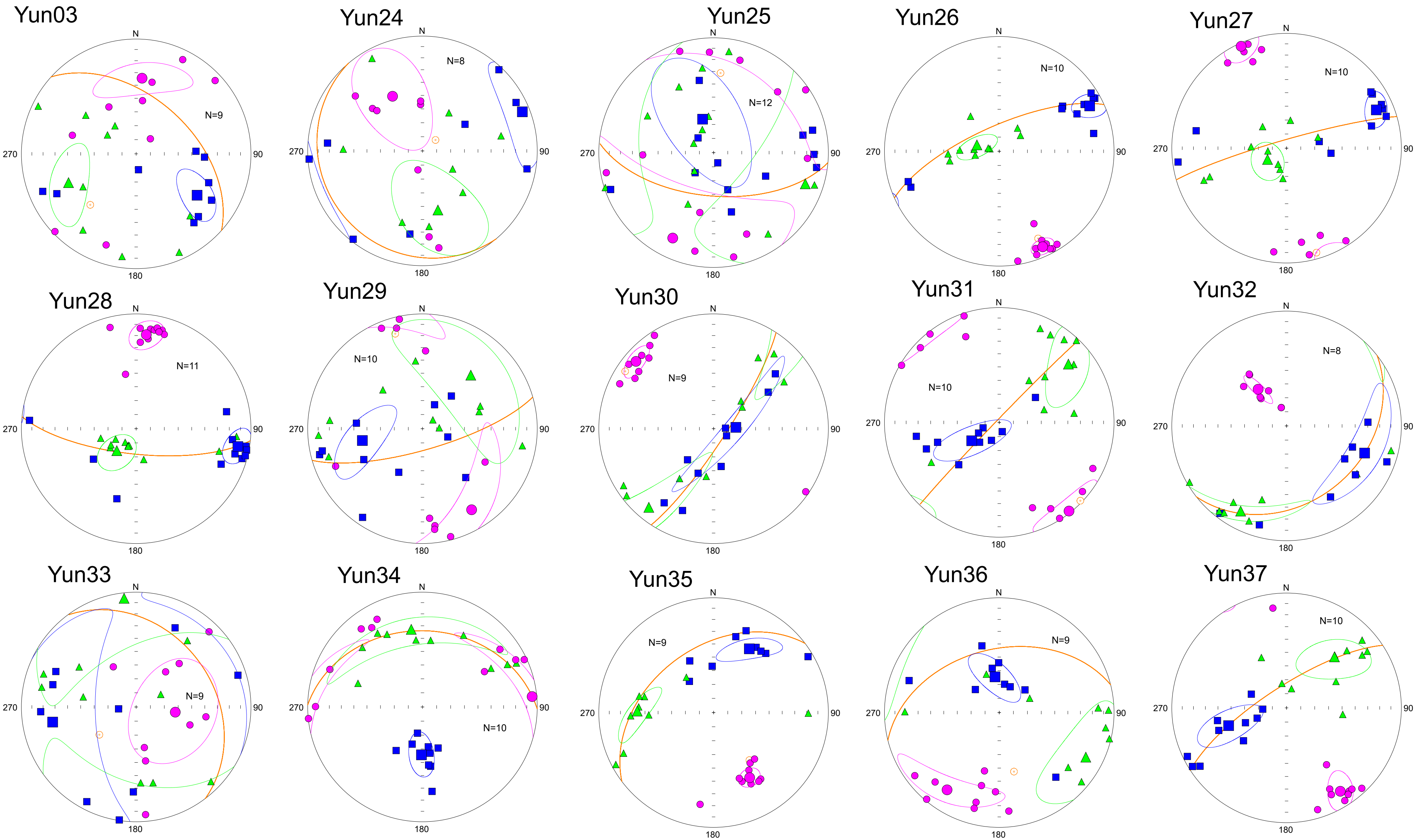
Yun03
N
270
90
180
N=9
Yun24
N=8
Yun25
N=12
Yun26
N=10
Yun27
N=10
Yun28
N=11
Yun29
N=10
Yun30
N=9
Yun31
N=10
Yun32
N=8
Yun33
N=9
Yun34
N=10
Yun35
N=9
Yun36
N=9
Yun37
N=10

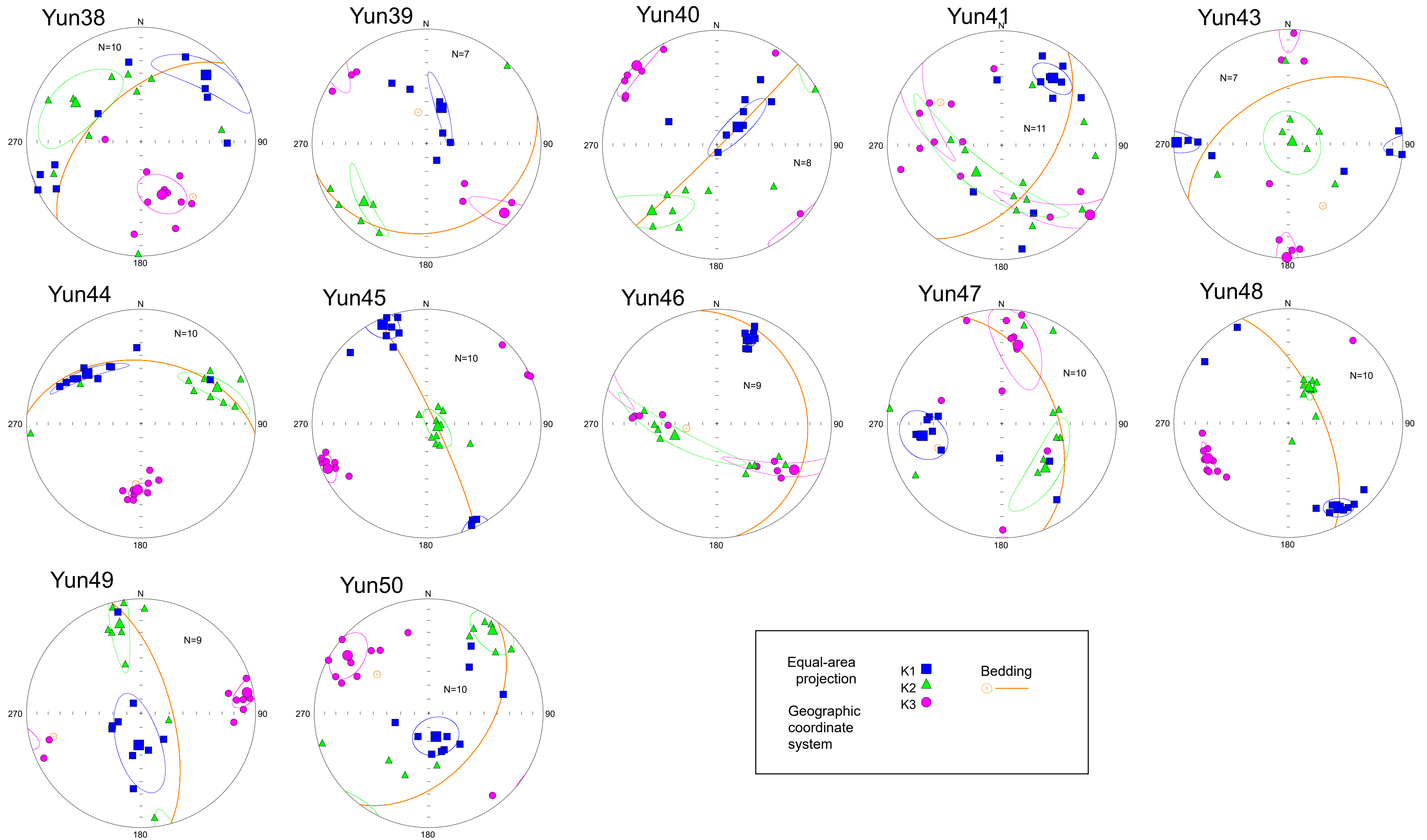
Yun38
N=10
Yun39
N=7
Yun40
N=8
Yun41
N=11
Yun43
N=7
Yun44
N=10
Yun45
N=10
Yun46
N=9
Yun47
N=10
Yun48
N=10
Yun49
N=9
Yun50
N=10
N
90
180
270
Equal-area projection
Geographic coordinate system
K1
K2
K3
Bedding

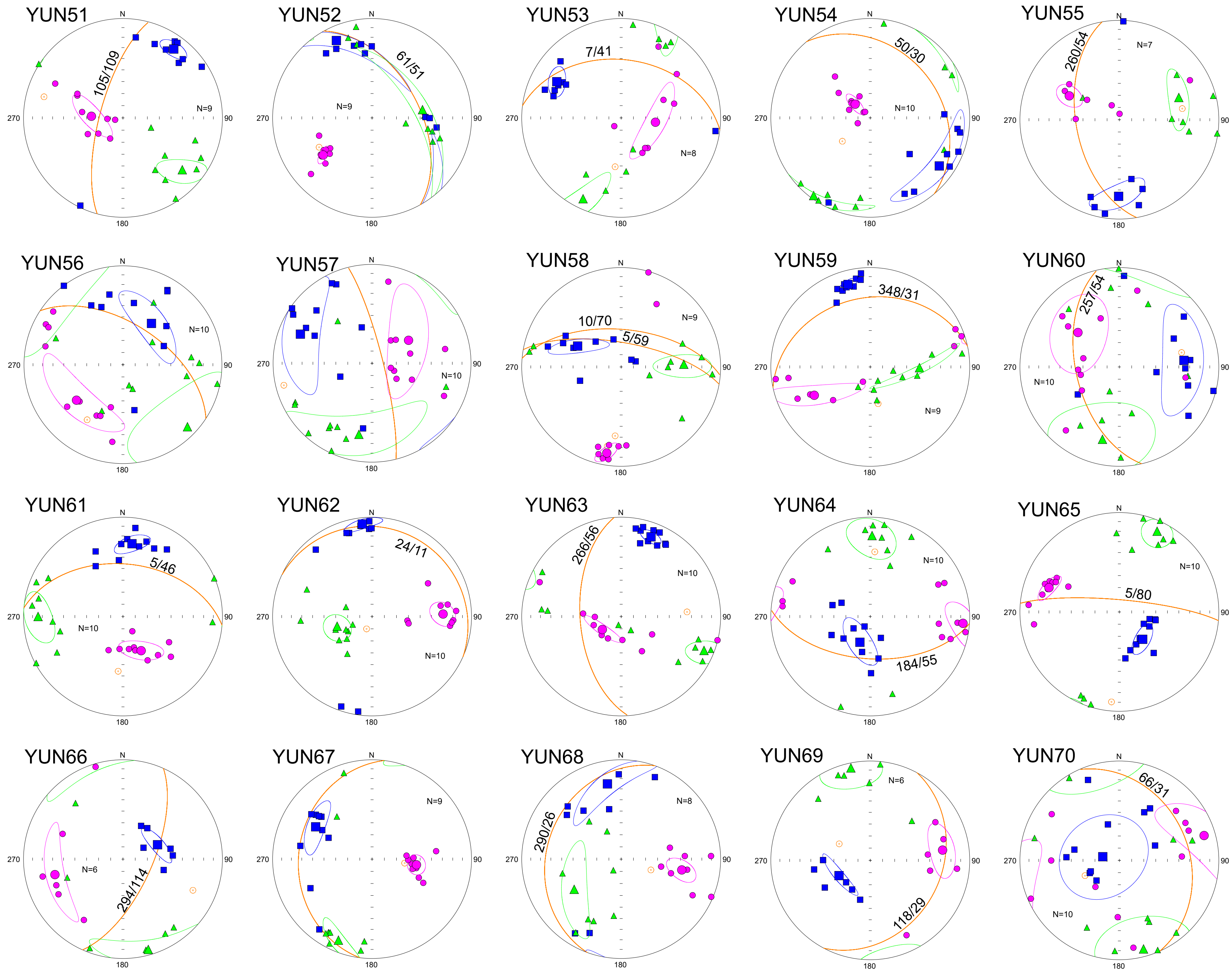

YUN51
105/109
N=9
YUN52
61/51
N=9
YUN53
7/41
N=8
YUN54
50/30
N=10
YUN55
260/54
N=7
YUN56
N=10
YUN57
N=10
YUN58
10/70
5/59
N=9
YUN59
348/31
N=9
YUN60
257/54
N=10
YUN61
5/46
N=10
YUN62
24/11
N=10
YUN63
266/56
N=10
YUN64
184/55
N=10
YUN65
5/80
N=10
YUN66
294/114
N=6
YUN67
N=9
YUN68
290/26
N=8
YUN69
118/29
N=6
YUN70
66/31
N=10
N
90
180
270

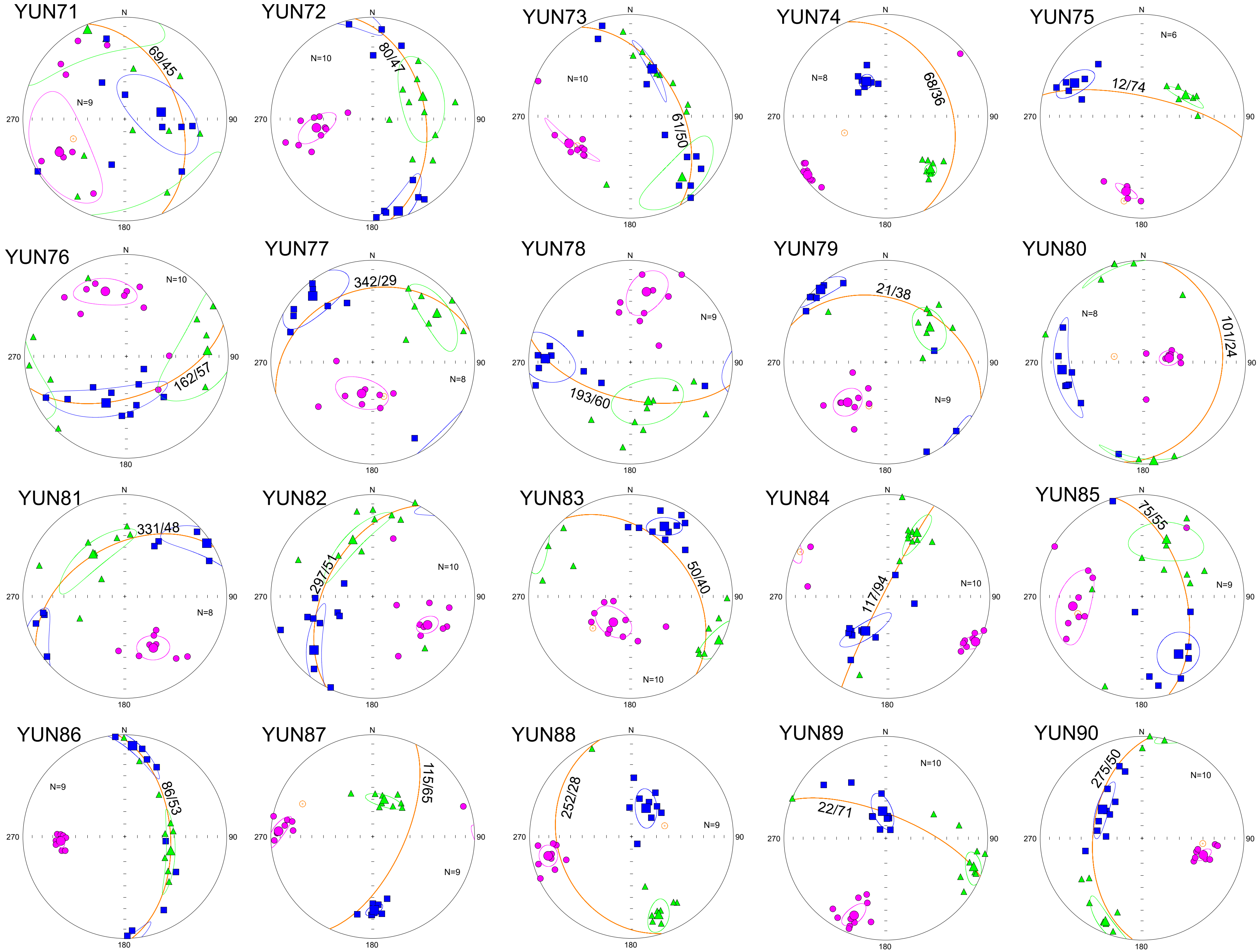

YUN71
N=9
69/45
YUN72
N=10
80/47
YUN73
N=10
61/50
YUN74
N=8
68/36
YUN75
N=6
12/74
YUN76
N=10
162/57
YUN77
N=8
342/29
YUN78
N=9
193/60
YUN79
N=9
21/38
YUN80
N=8
101/24
YUN81
N=8
331/48
YUN82
N=10
297/51
YUN83
N=10
50/40
YUN84
N=10
117/94
YUN85
N=9
75/55
YUN86
N=9
86/53
YUN87
N=9
115/65
YUN88
N=9
252/28
YUN89
N=10
22/71
YUN90
N=10
275/50
N
90
180
270

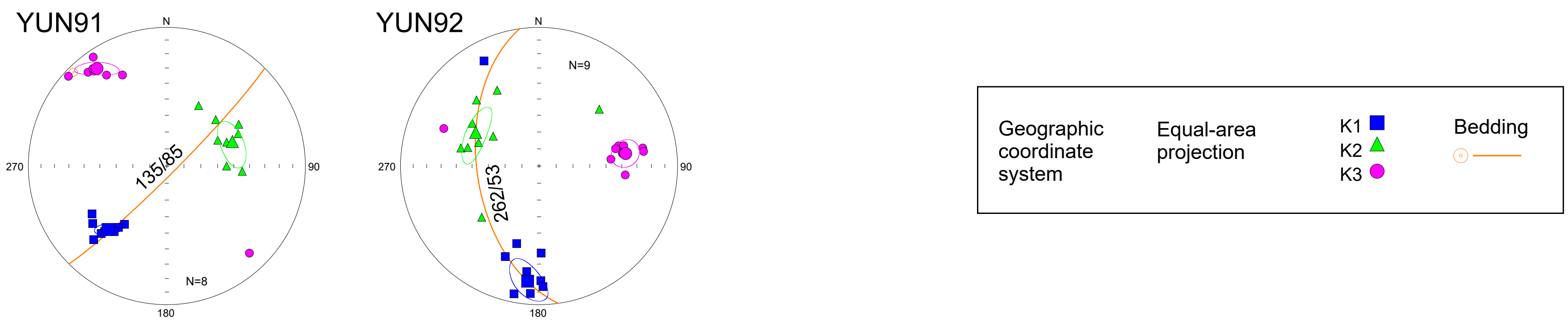
YUN91
N
270
90
180
135/85
N=8
YUN92
N
270
90
180
262/53
N=9
Geographic coordinate system
Equal-area projection
K1
K2
K3
Bedding

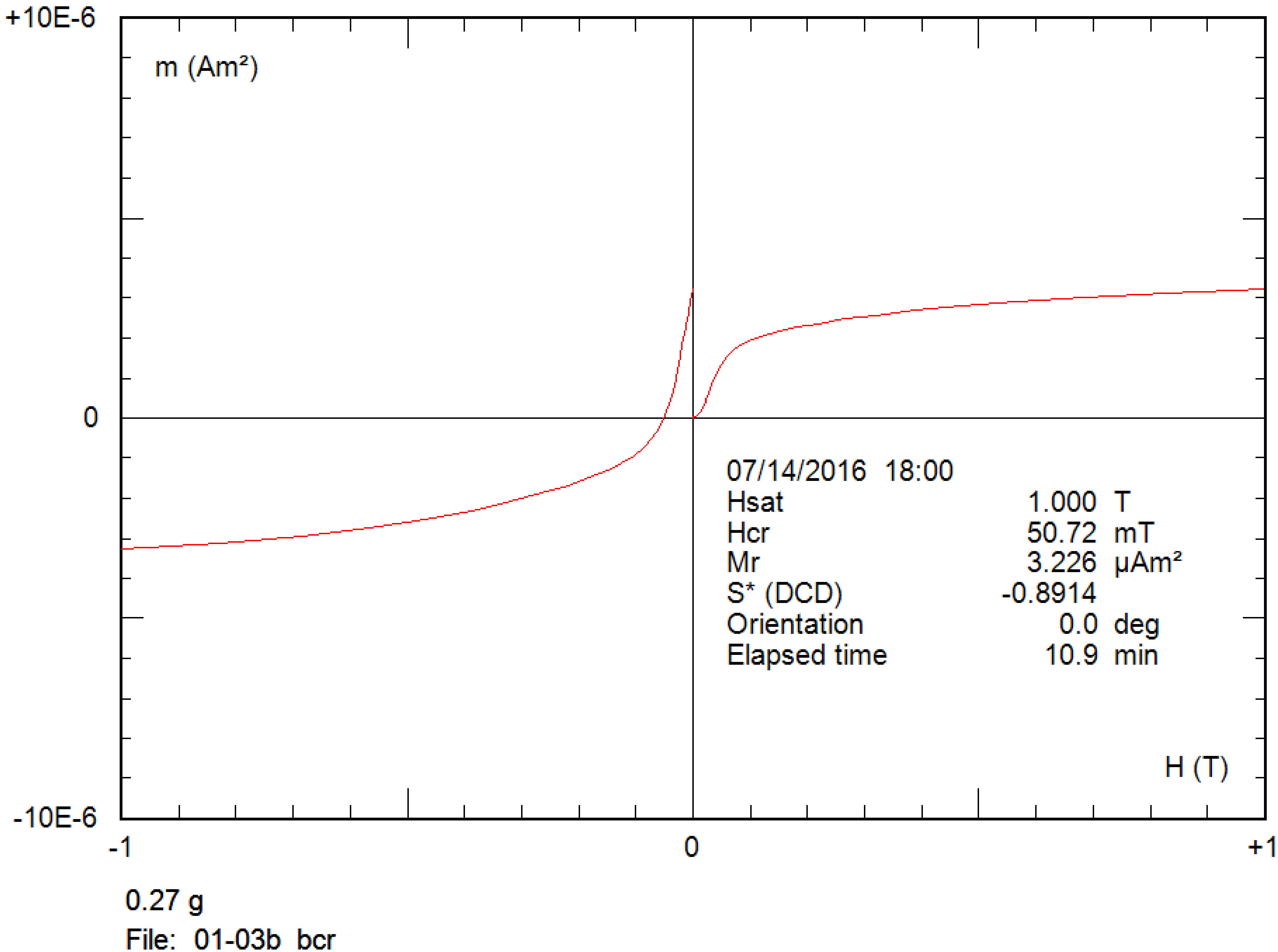

+10E-6
m (Am²)
0
-10E-6
-1
0
+1
H (T)
07/14/2016 18:00
Hsat 1.000 T
Hcr 50.72 mT
Mr 3.226 µAm²
S* (DCD) -0.8914
Orientation 0.0 deg
Elapsed time 10.9 min
0.27 g
File: 01-03b_bcr

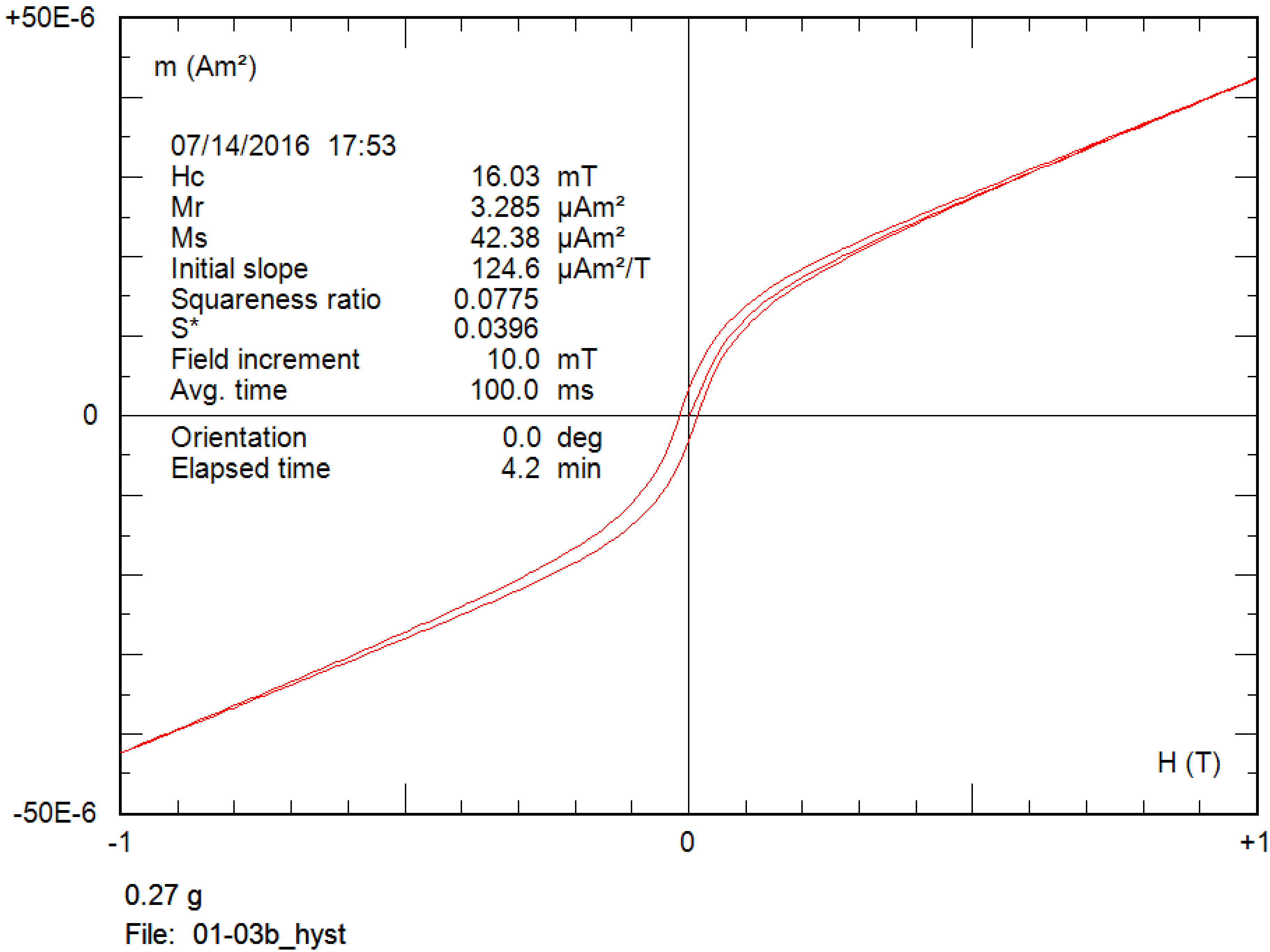
+50E-6
m (Am²)
07/14/2016 17:53
Hc 16.03 mT
Mr 3.285 μAm²
Ms 42.38 μAm²
Initial slope 124.6 μAm²/T
Squareness ratio 0.0775
S* 0.0396
Field increment 10.0 mT
Avg. time 100.0 ms
0
Orientation 0.0 deg
Elapsed time 4.2 min
H (T)
-50E-6
-1
0
+1
0.27 g
File: 01-03b_hyst

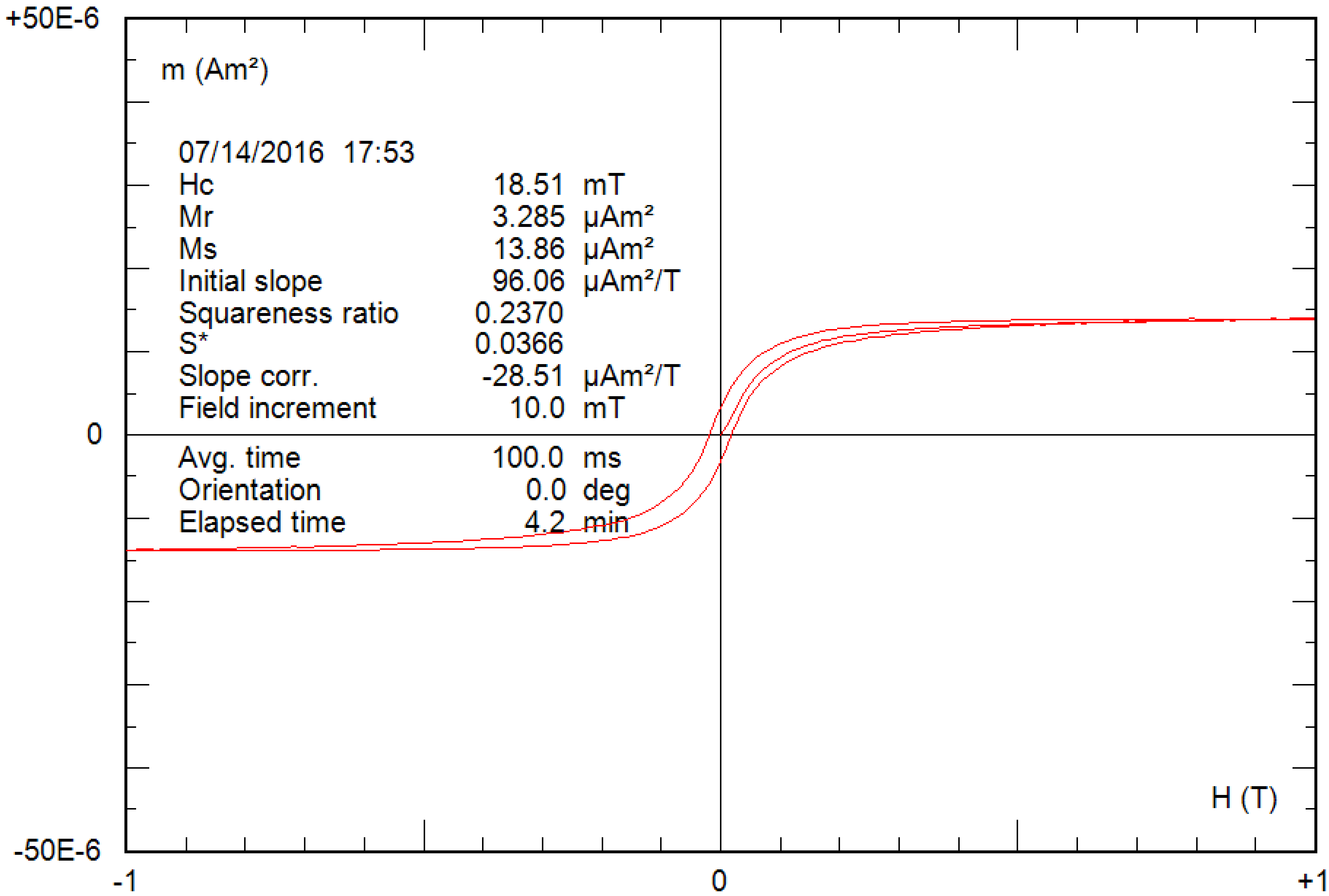

0.27 g

File: 01-03b_hyst_corr

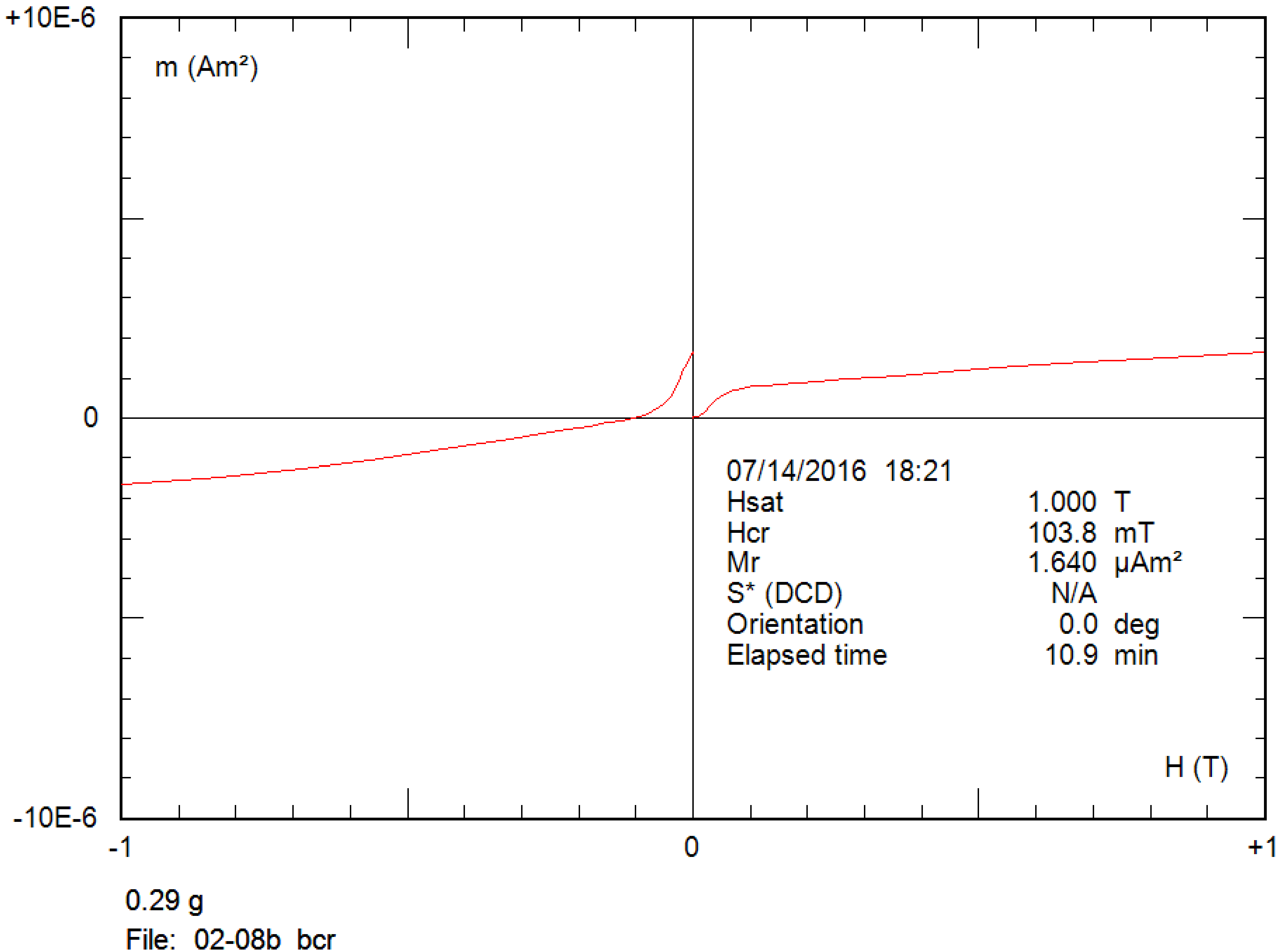

+10E-6
m (Am²)
0
-10E-6
07/14/2016 18:21
Hsat 1.000 T
Hcr 103.8 mT
Mr 1.640 μAm²
S* (DCD) N/A
Orientation 0.0 deg
Elapsed time 10.9 min
H (T)
-1
0
+1
0.29 g
File: 02-08b_bcr

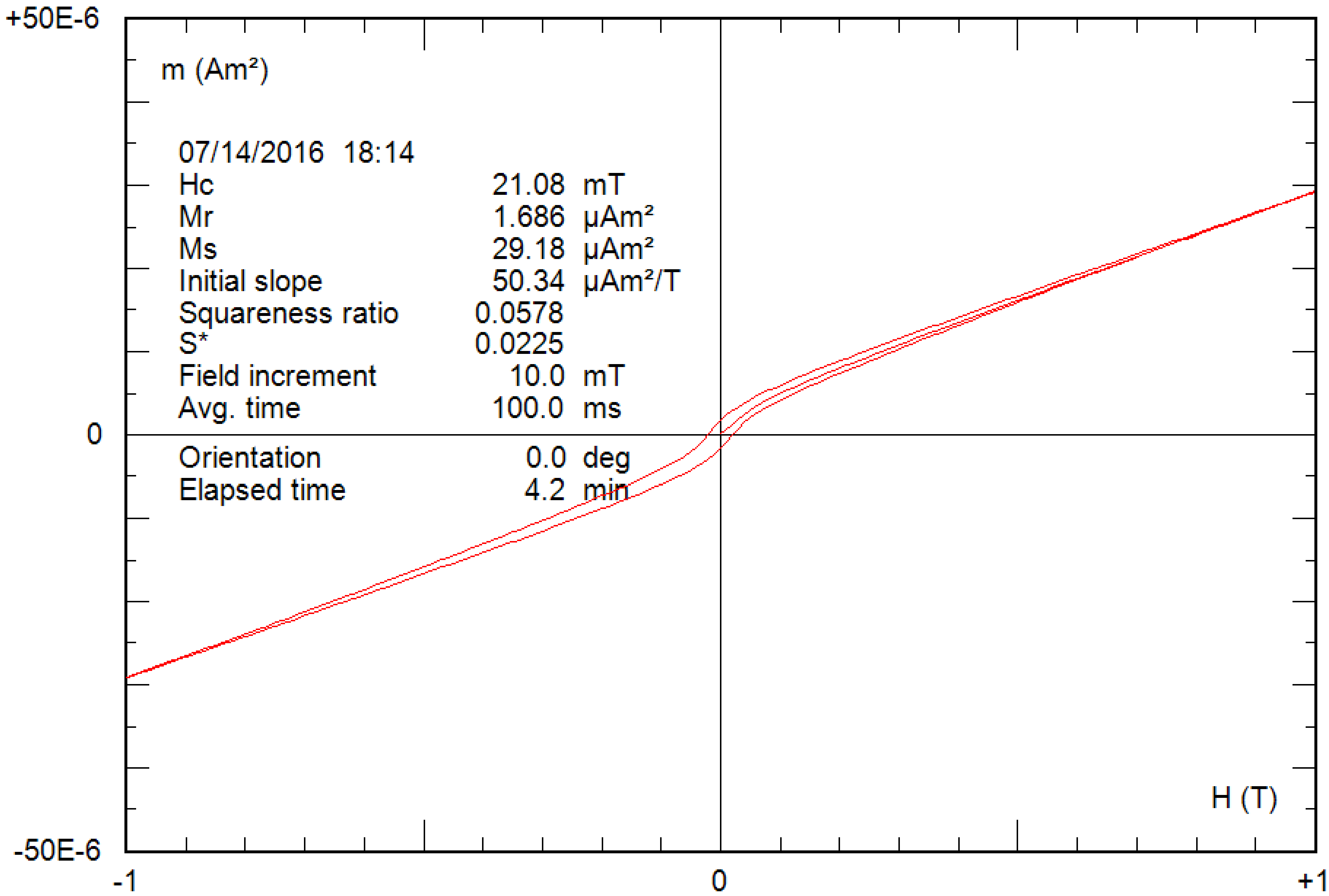

0.29 g

File: 02-08b_hyst

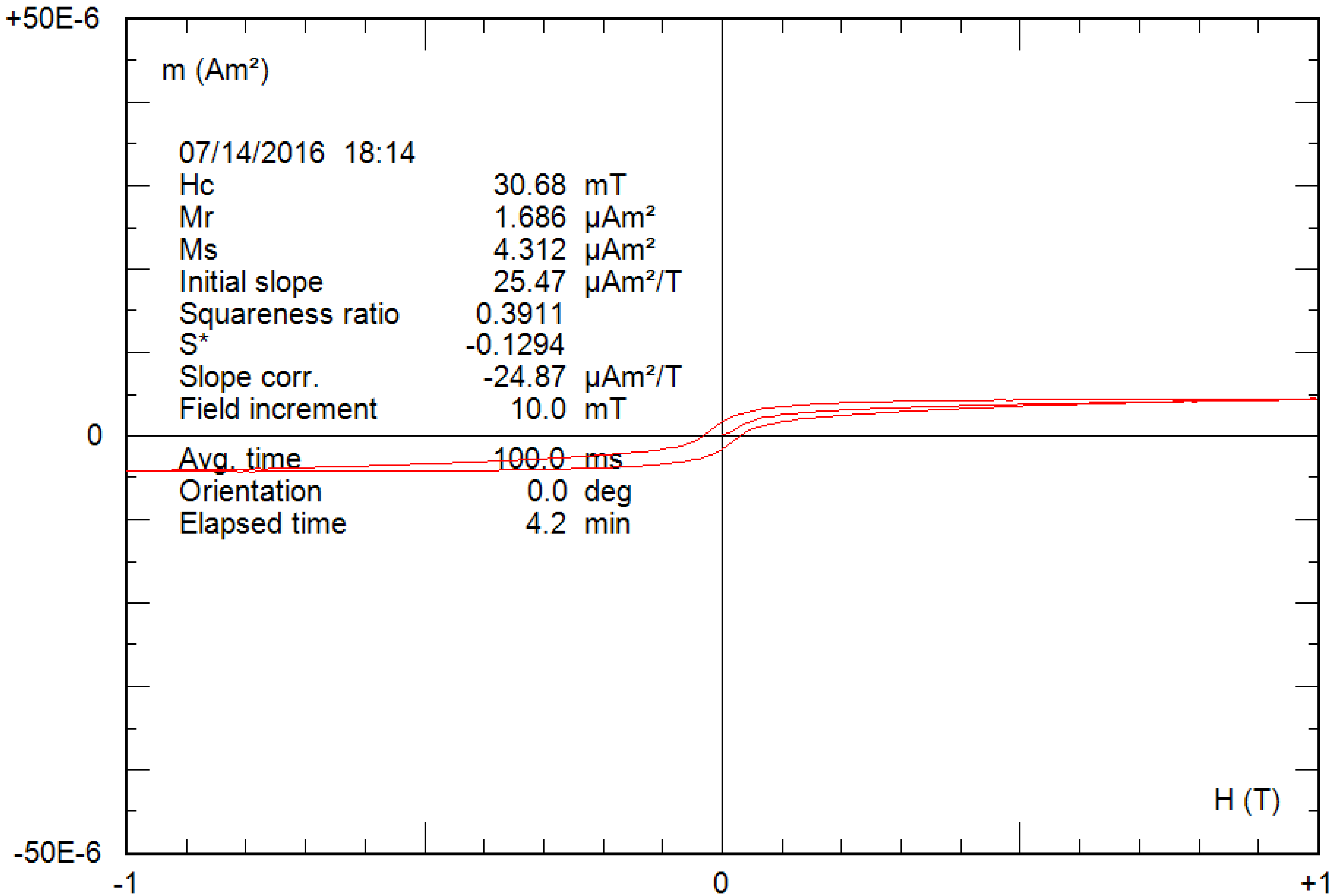

0.29 g

File: 02-08b_hyst_corr

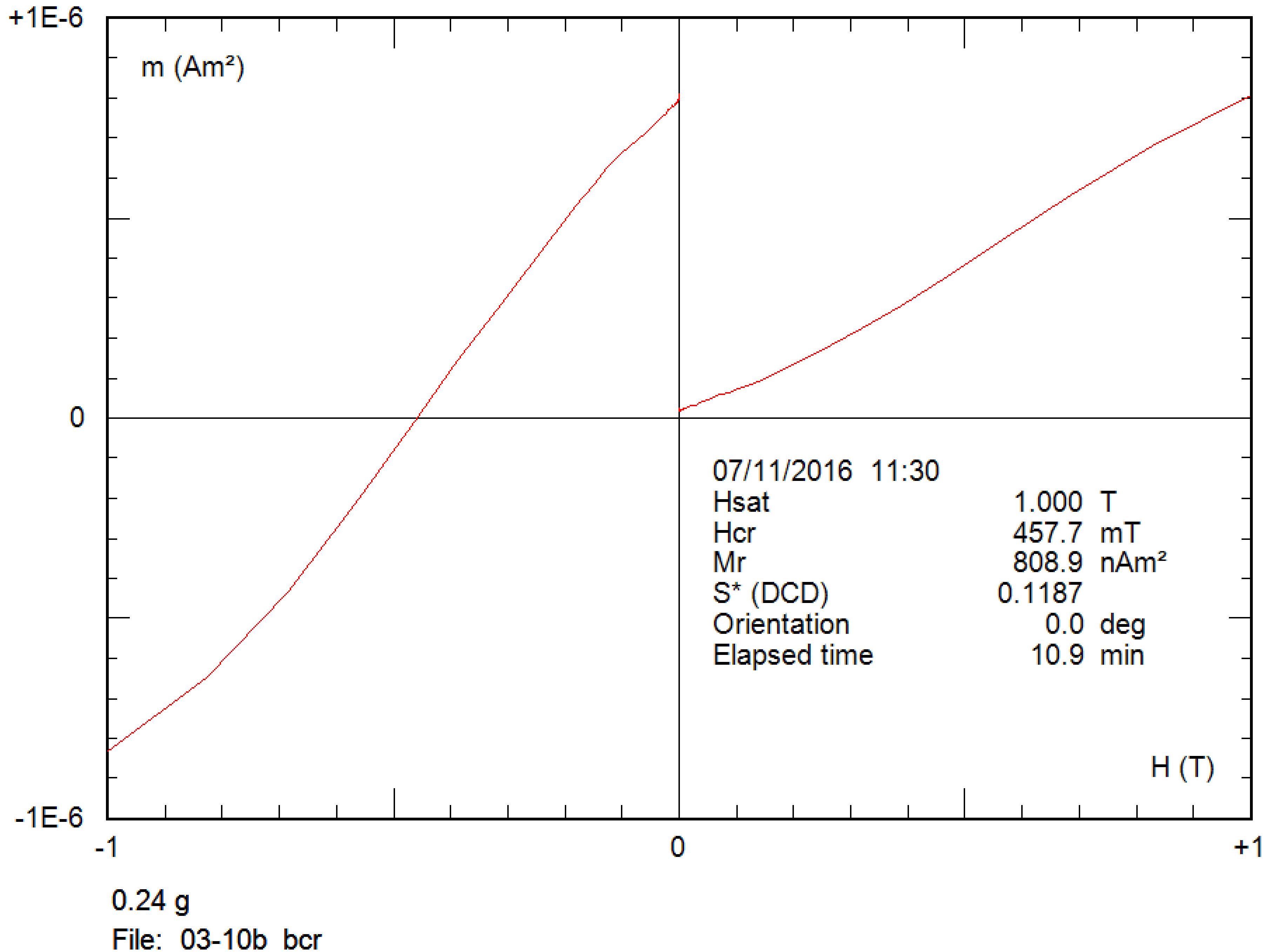
+1E-6
m (Am²)
0
-1E-6
-1
0
+1
H (T)
07/11/2016 11:30
Hsat 1.000 T
Hcr 457.7 mT
Mr 808.9 nAm²
S* (DCD) 0.1187
Orientation 0.0 deg
Elapsed time 10.9 min
0.24 g
File: 03-10b_bcr

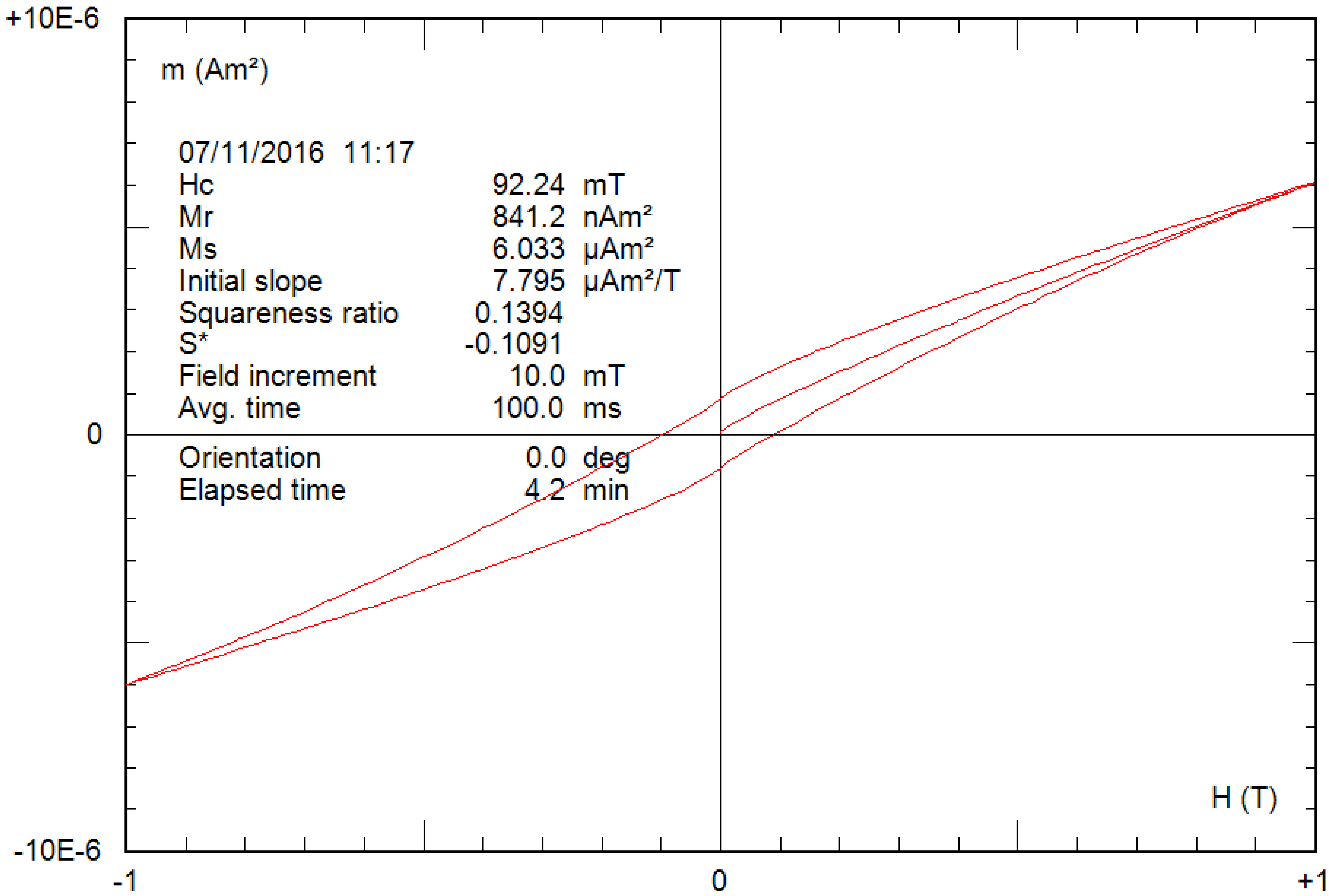

0.24 g

File: 03-10b_hyst

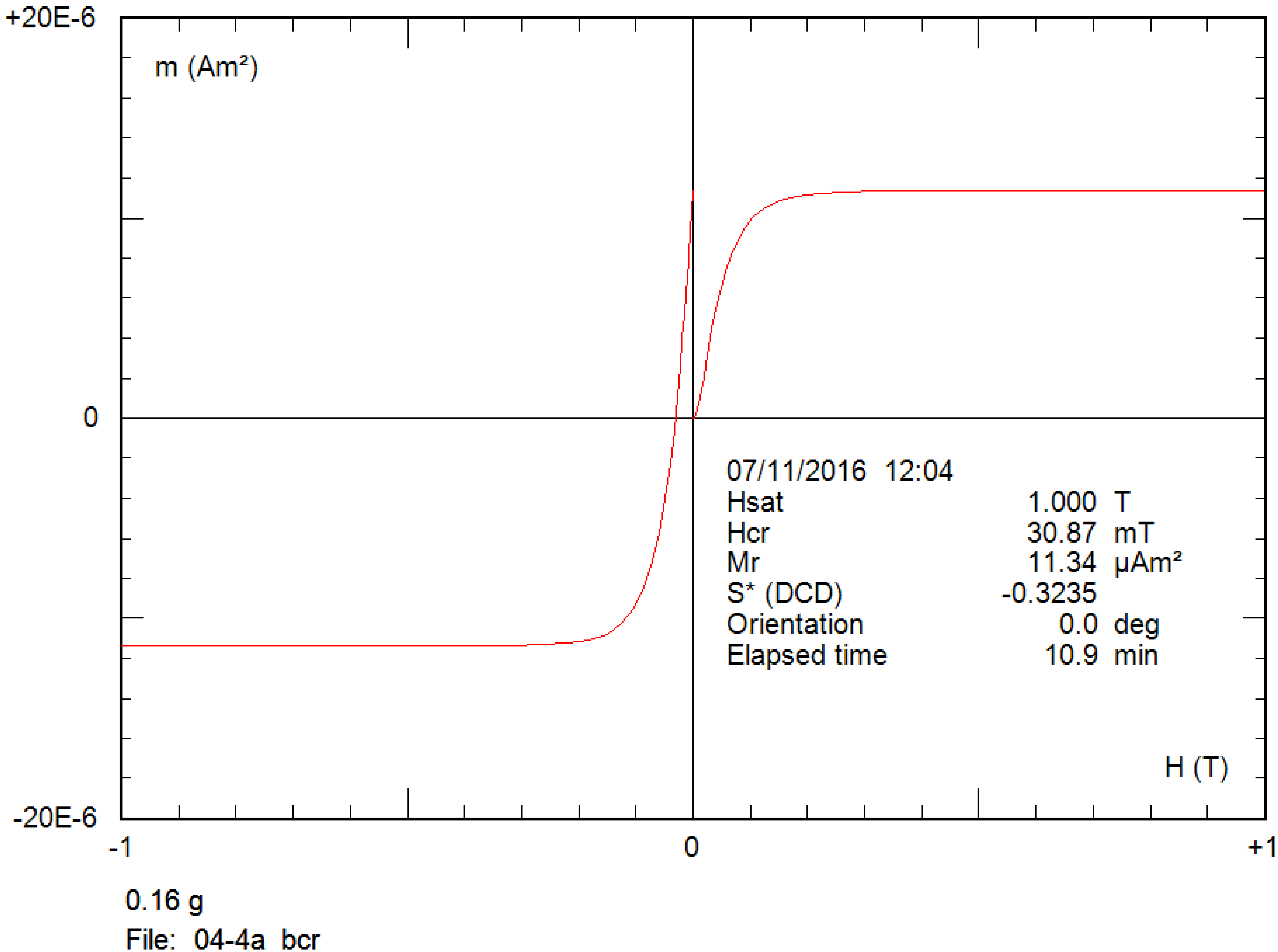
+20E-6
m (Am²)
0
-20E-6
-1
0
+1
H (T)
07/11/2016 12:04
Hsat 1.000 T
Hcr 30.87 mT
Mr 11.34 μAm²
S* (DCD) -0.3235
Orientation 0.0 deg
Elapsed time 10.9 min
0.16 g
File: 04-4a_bcr

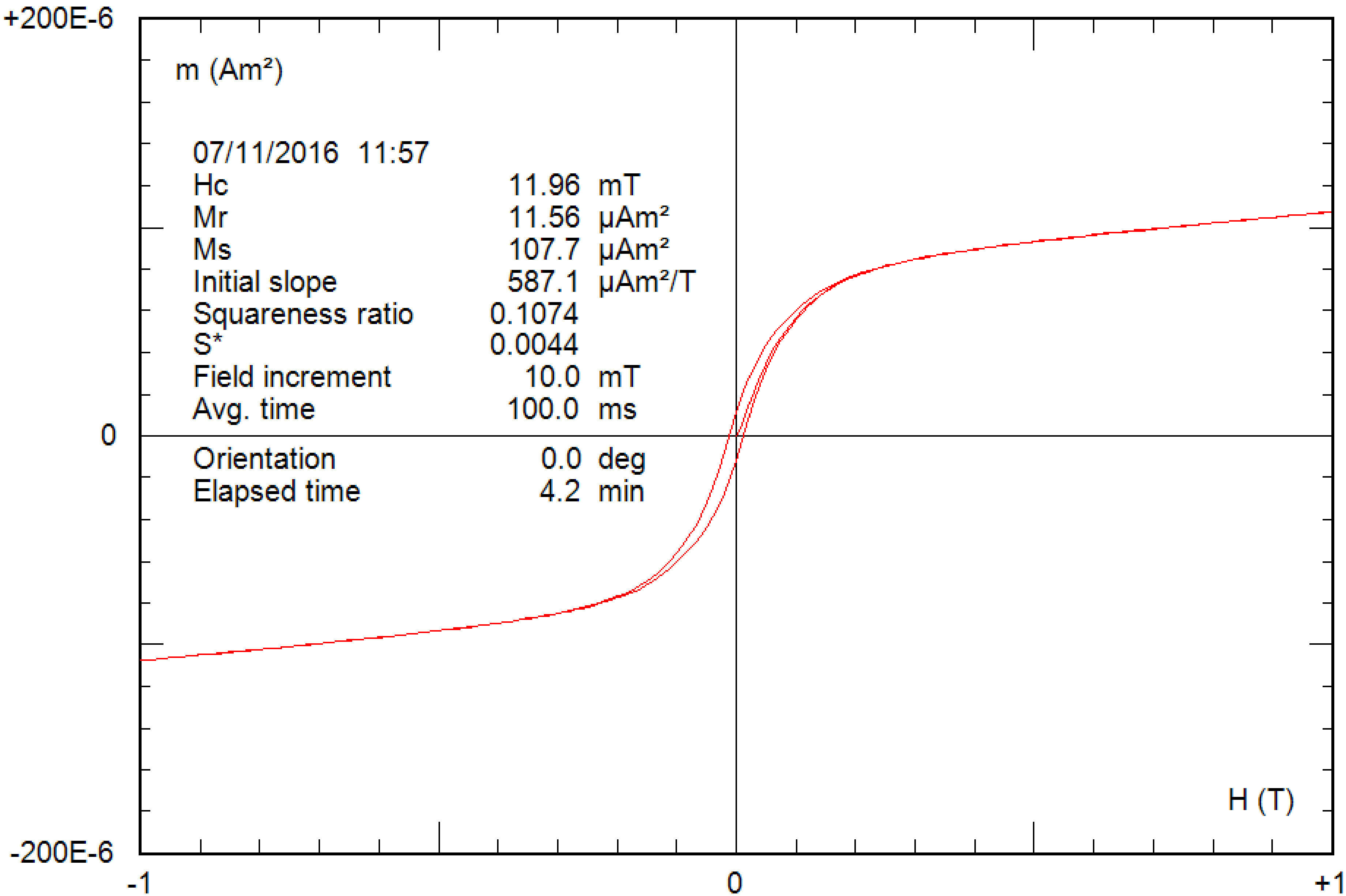

0.16 g
File: 04-4a_hyst

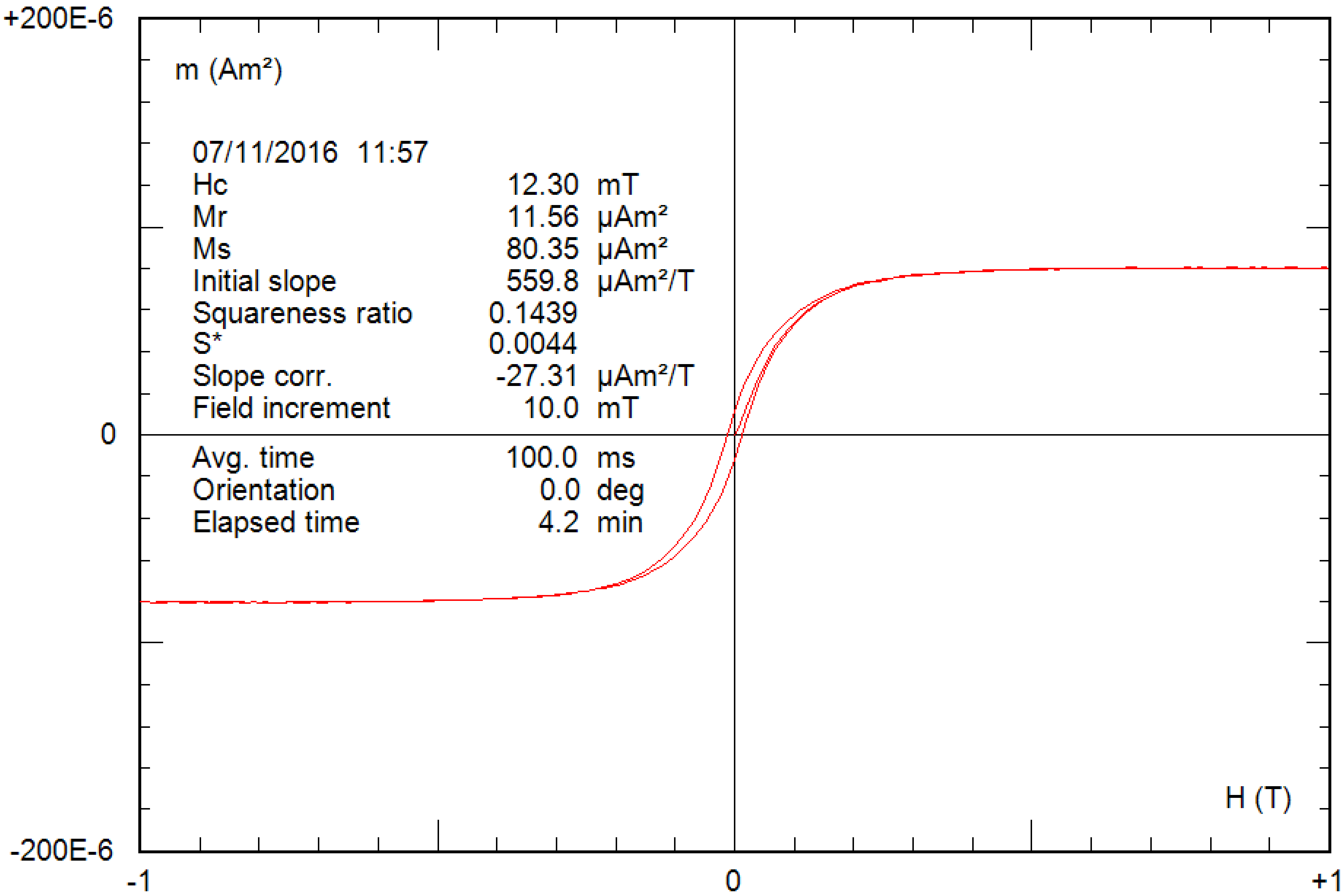

0.16 g

File: 04-4a_hyst_corr

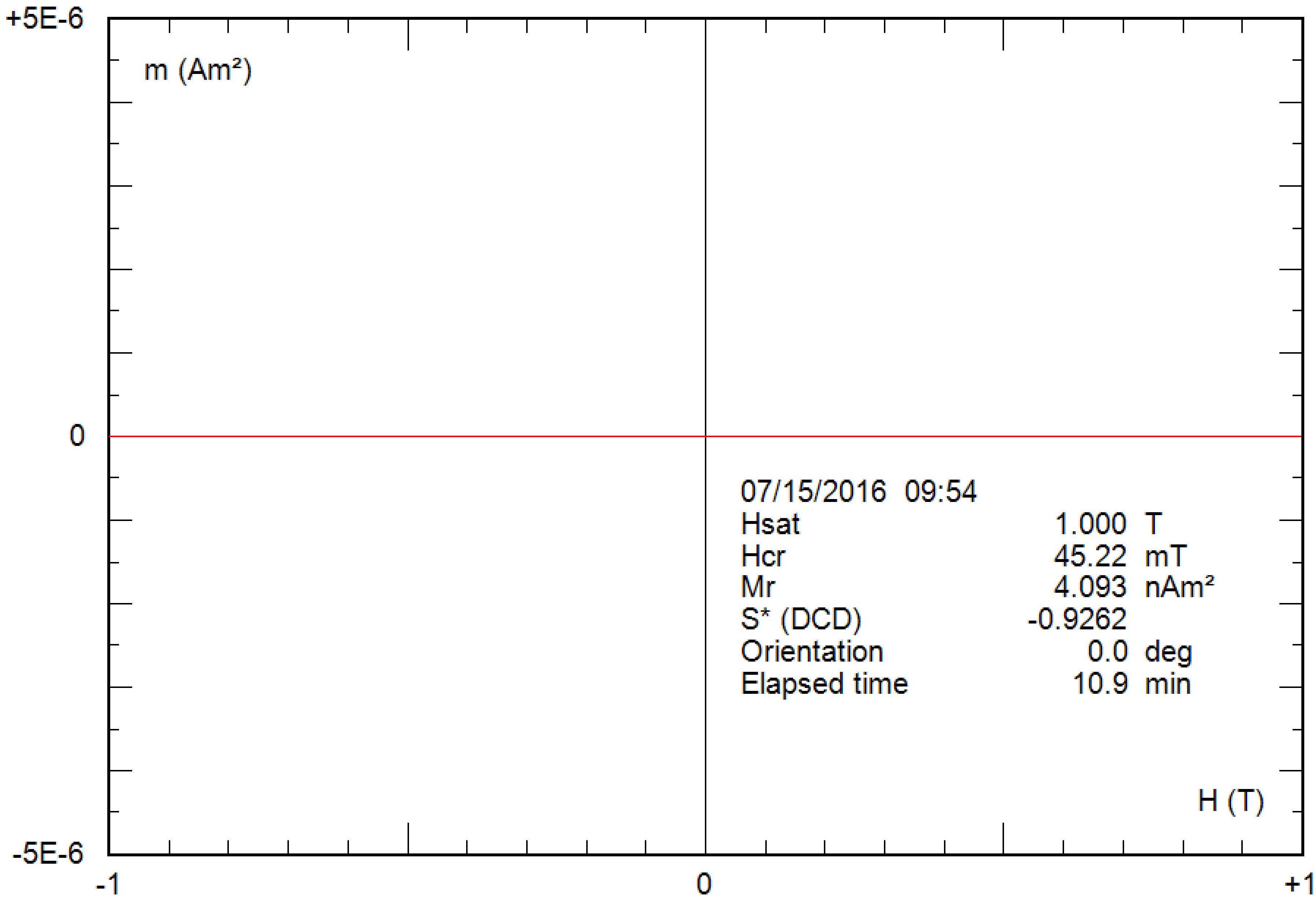

0.21 g
File: 05-01a_bcr

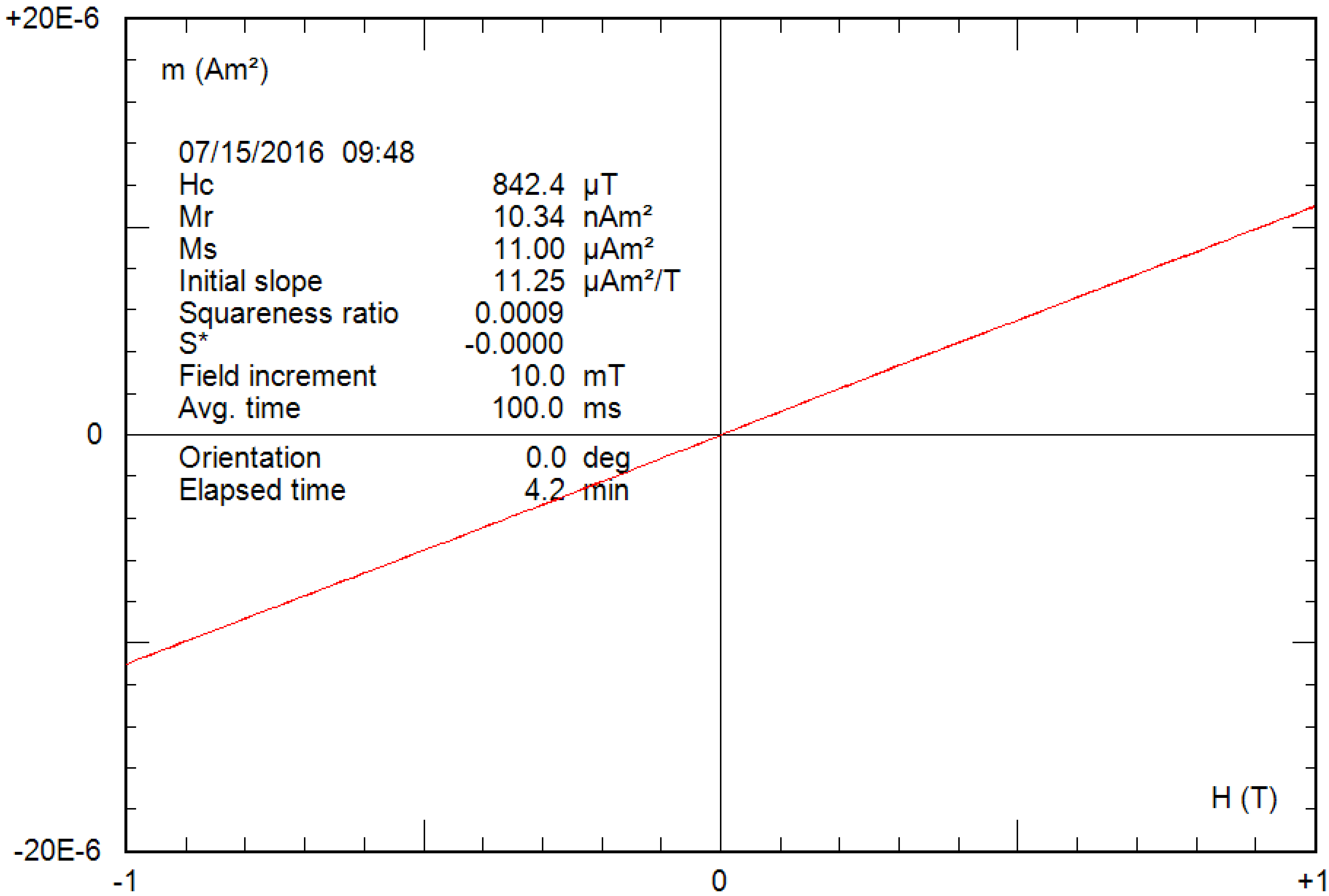

0.21 g

File: 05-01a_hyst

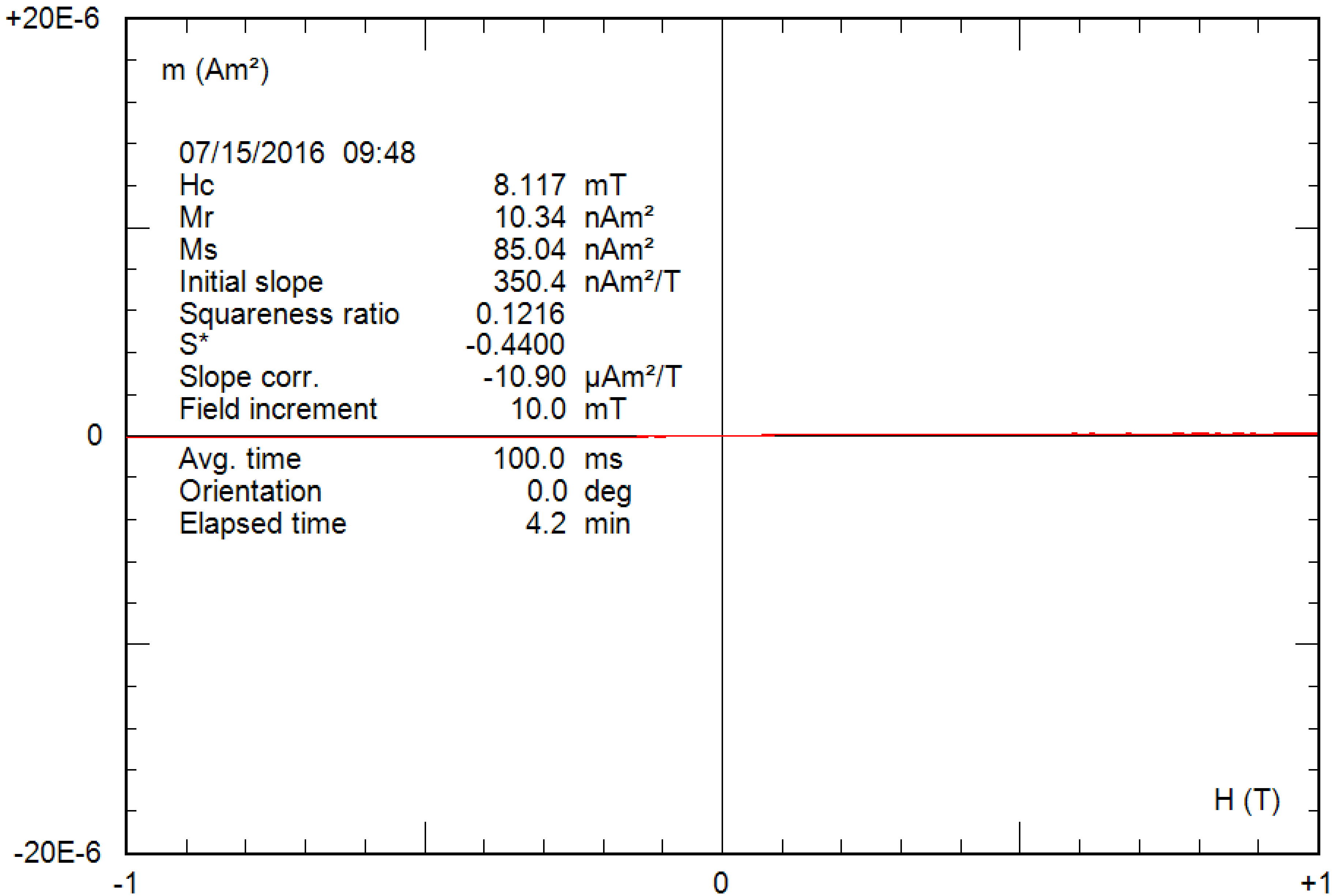

0.21 g

File: 05-01a_hyst_corr

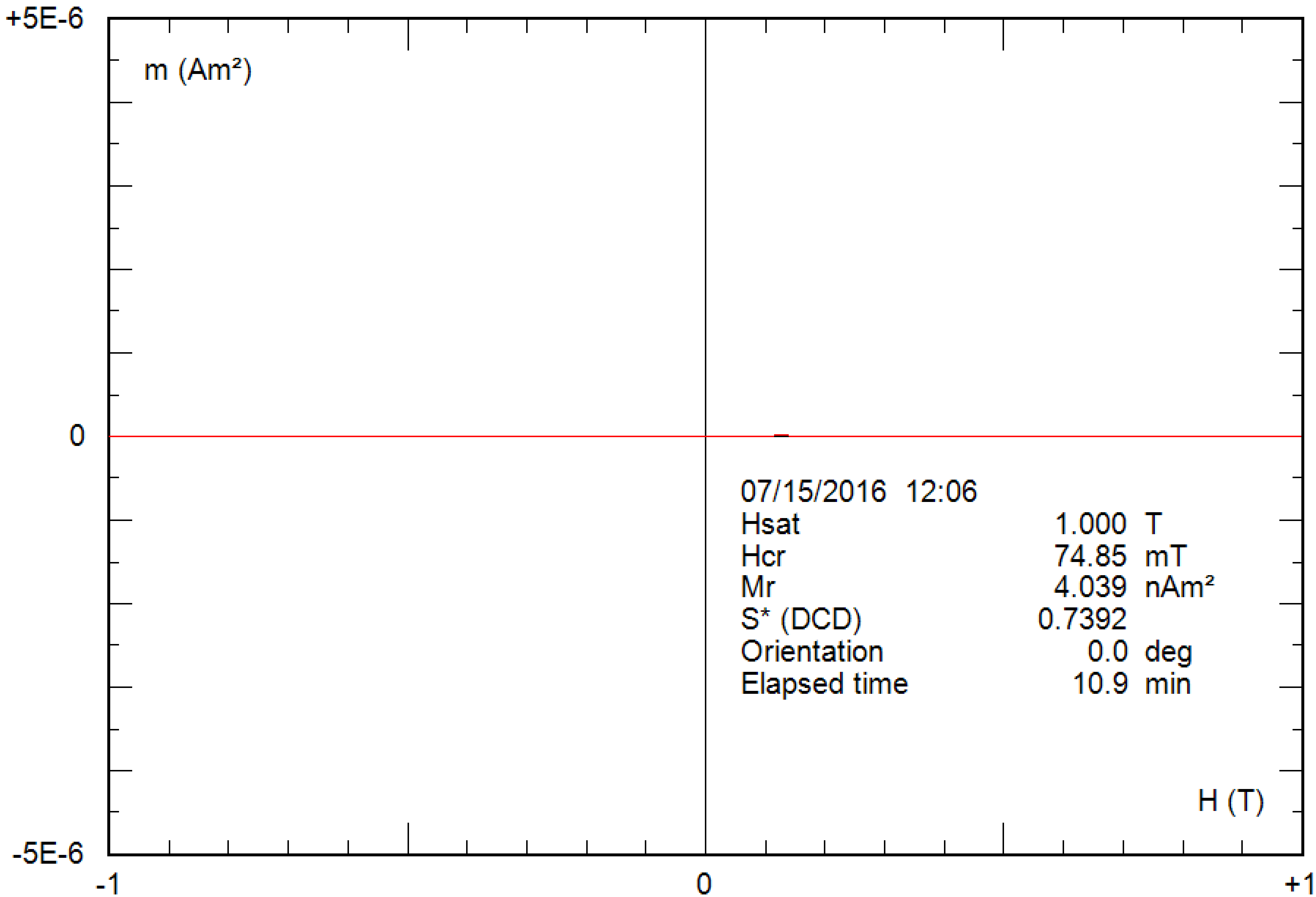

0.19 g

File: 06-07a_bcr

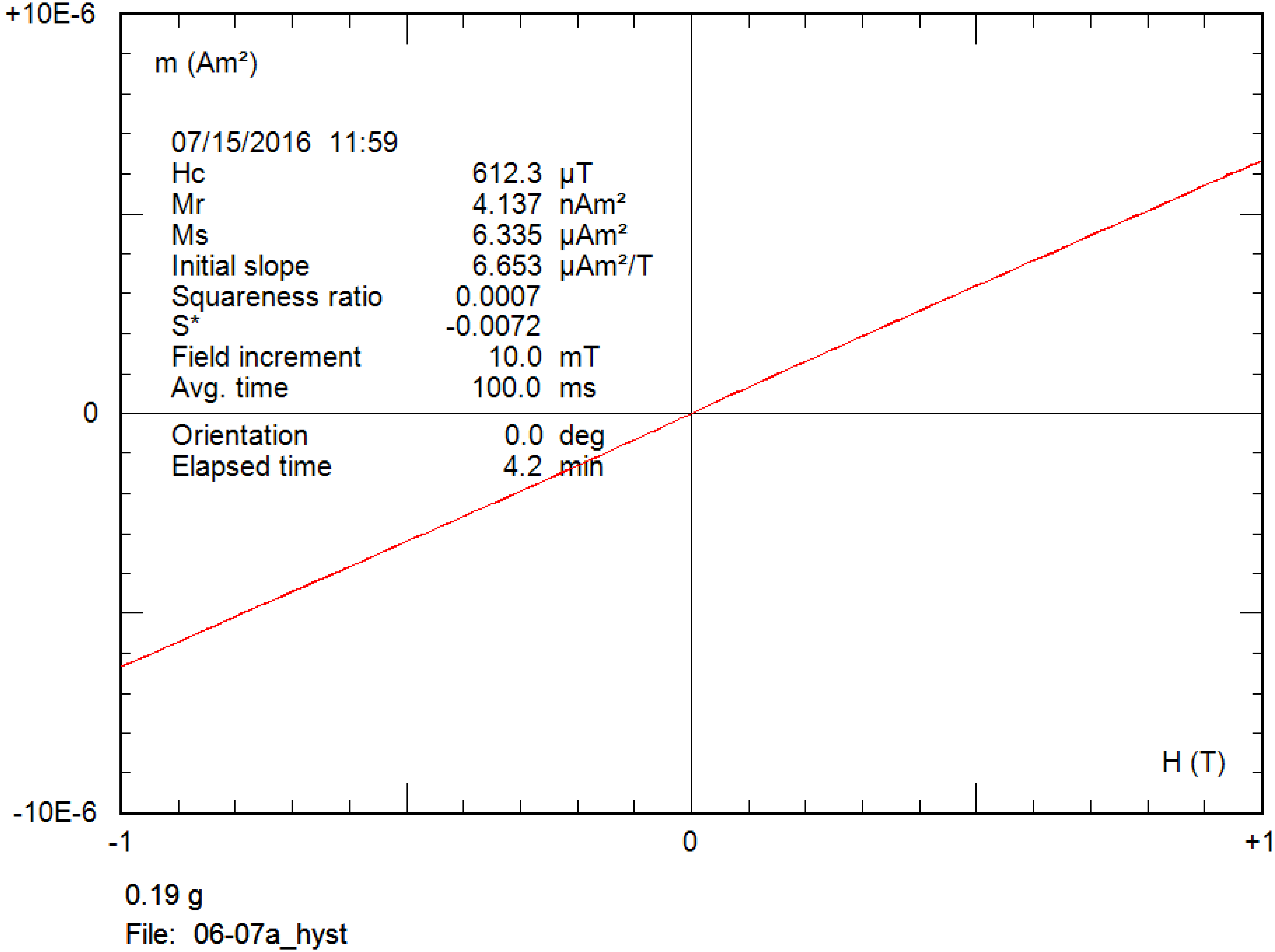
+10E-6
m (Am²)
07/15/2016 11:59
Hc 612.3 µT
Mr 4.137 nAm²
Ms 6.335 µAm²
Initial slope 6.653 µAm²/T
Squareness ratio 0.0007
S* -0.0072
Field increment 10.0 mT
Avg. time 100.0 ms
0
Orientation 0.0 deg
Elapsed time 4.2 min
H (T)
-10E-6
-1
0
+1
0.19 g
File: 06-07a_hyst

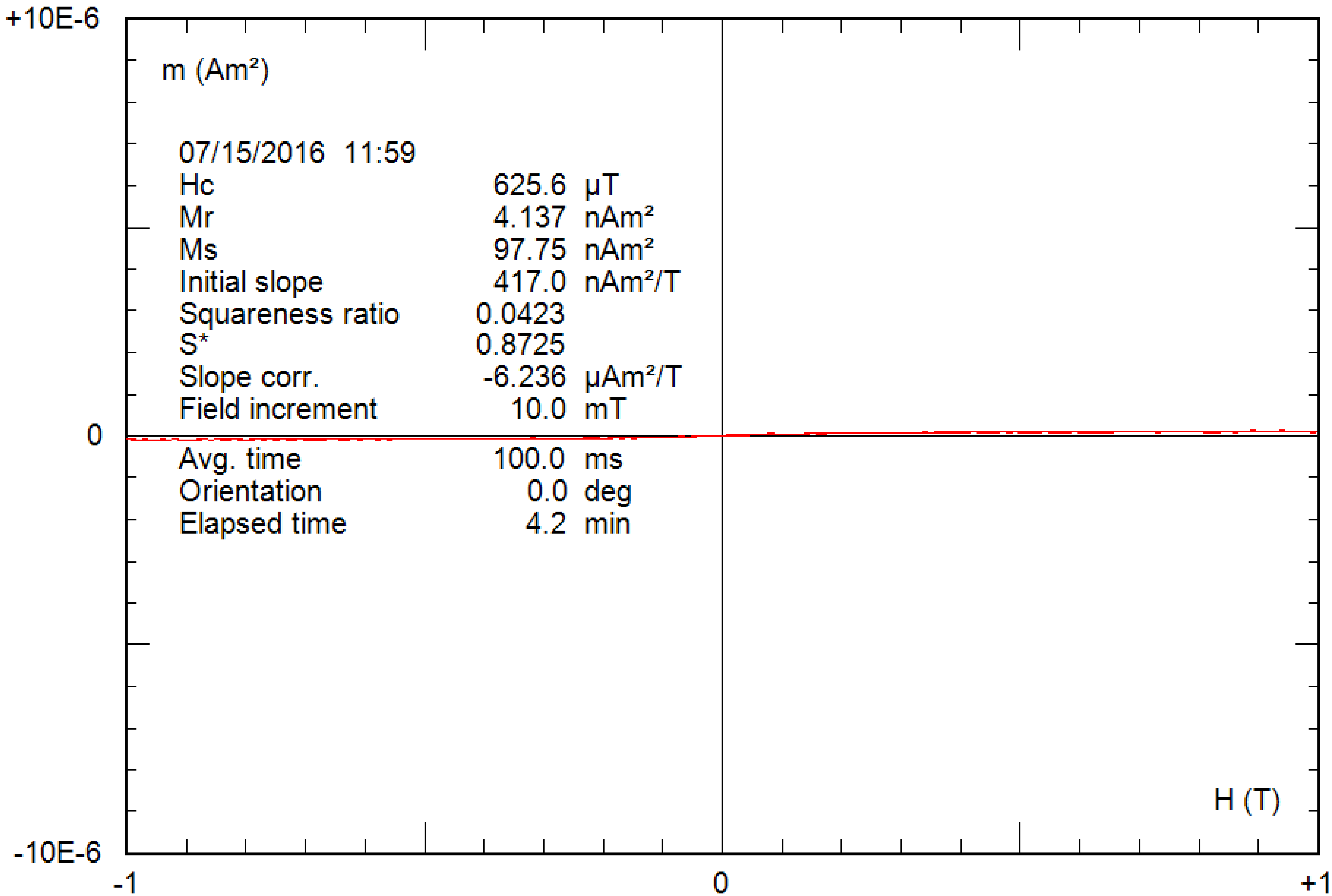

0.19 g

File: 06-07a_hyst_corr

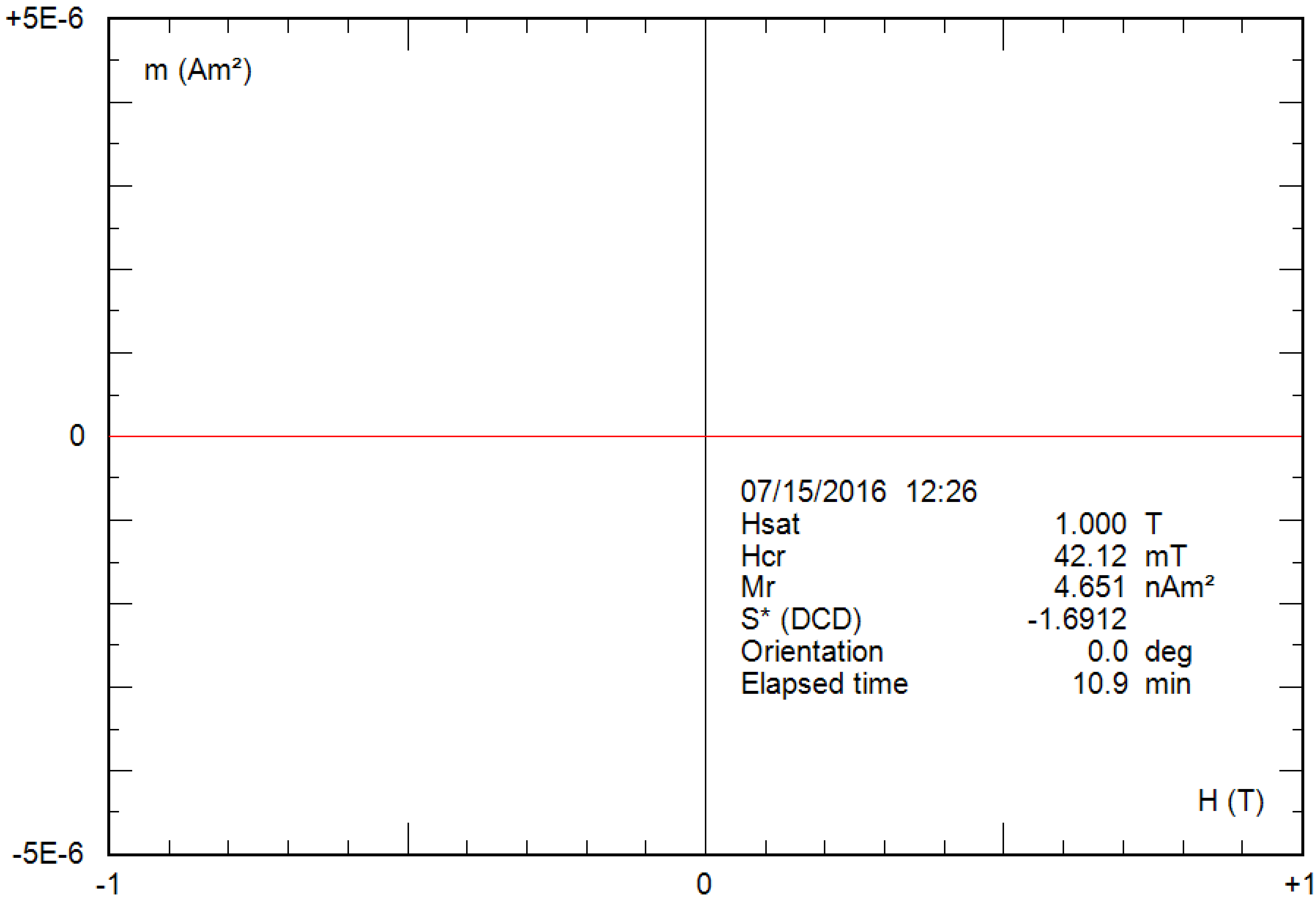

0.22 g

File: 07-01a_bcr

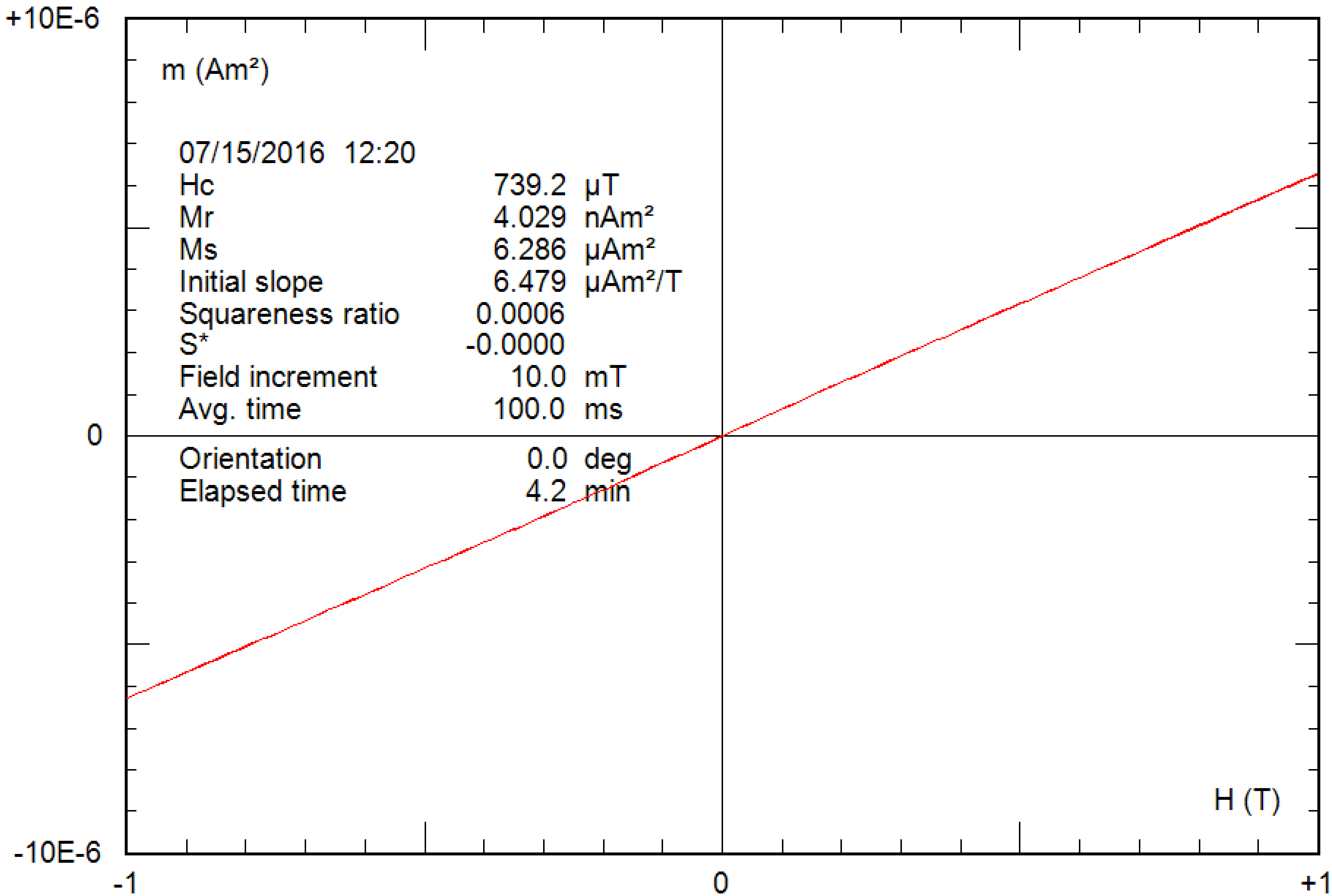

0.22 g

File: 07-01a_hyst

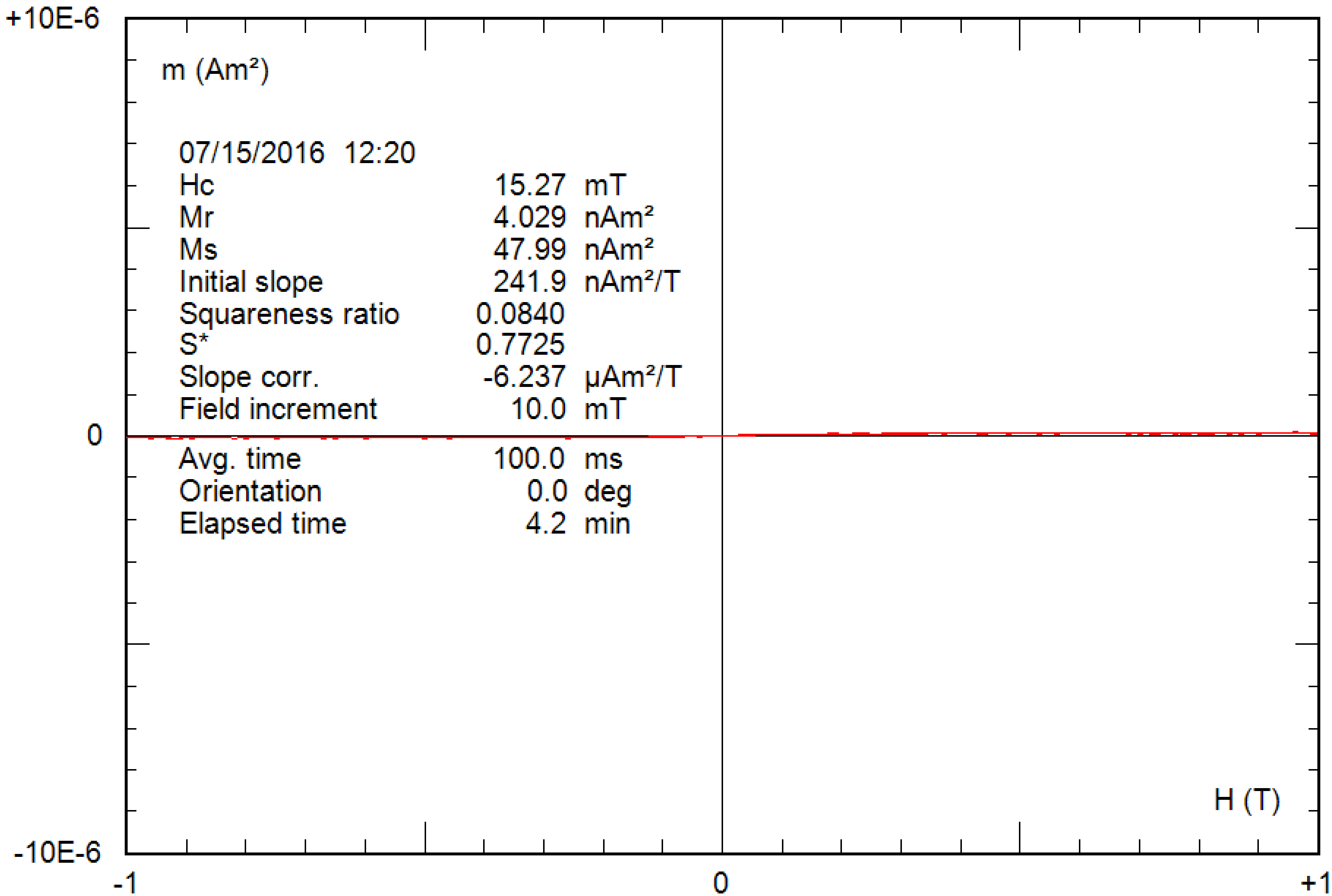

0.22 g

File: 07-01a_hyst_corr

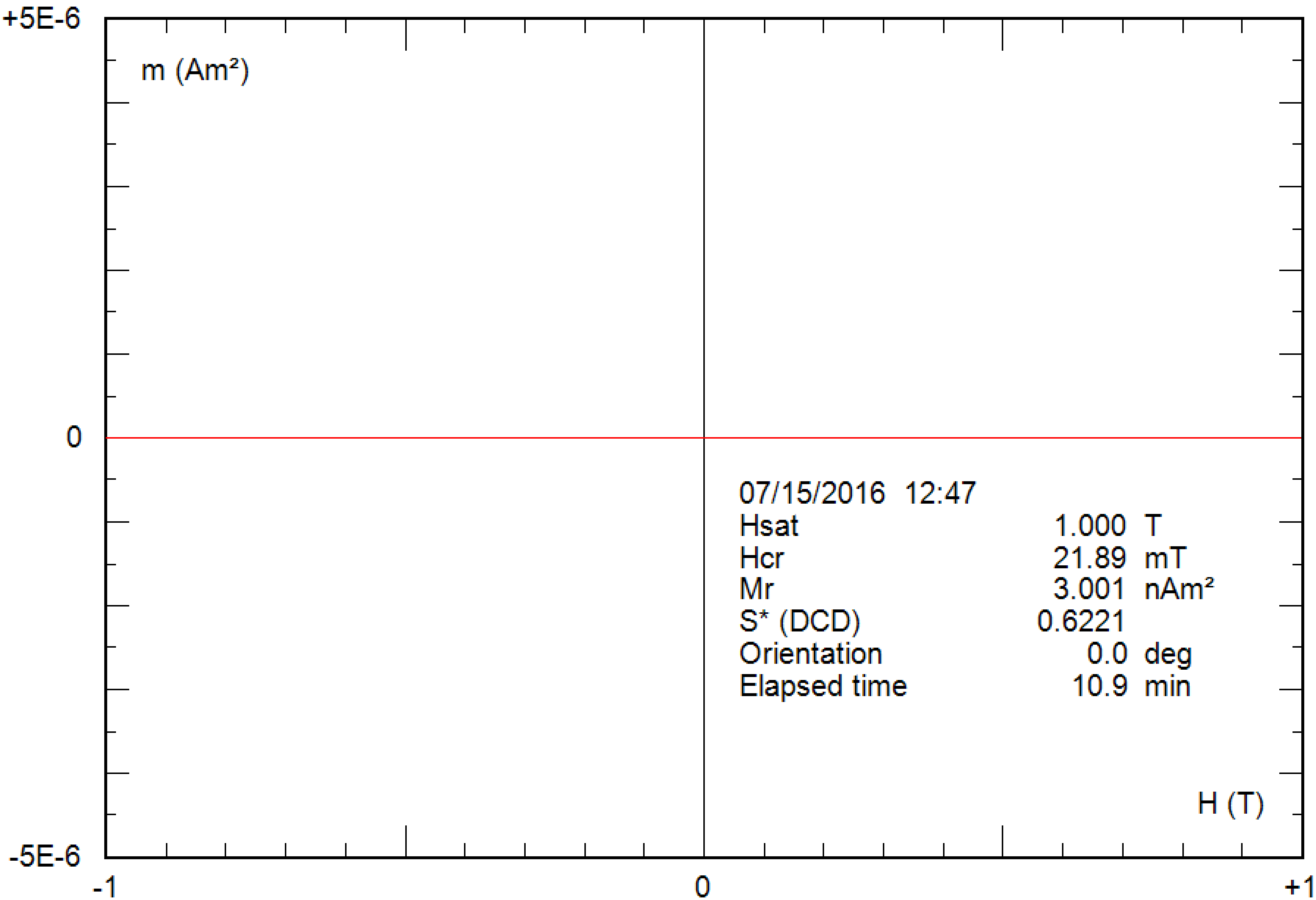

0.20 g

File: 08-04a_bcr

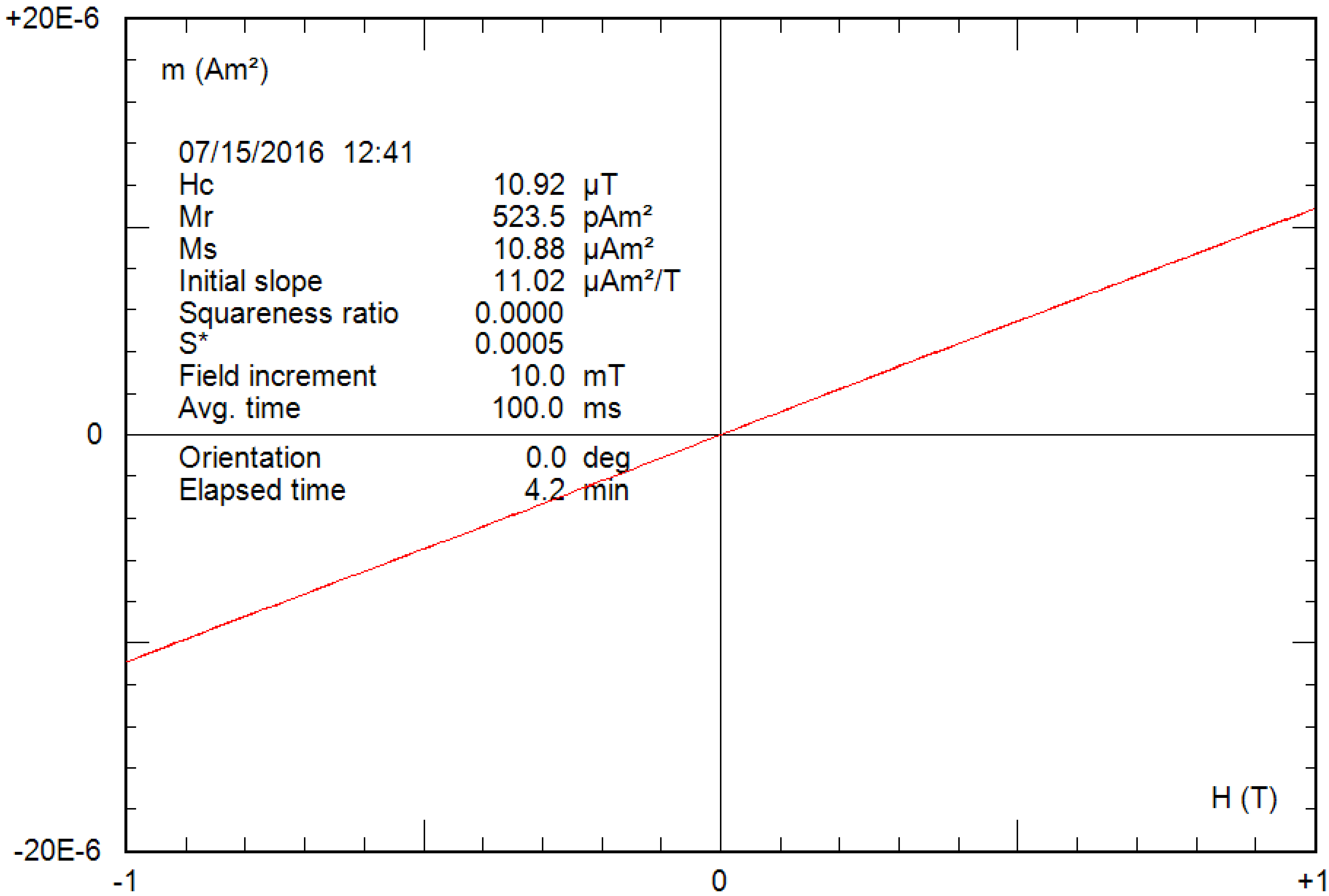

0.20 g

File: 08-04a_hyst

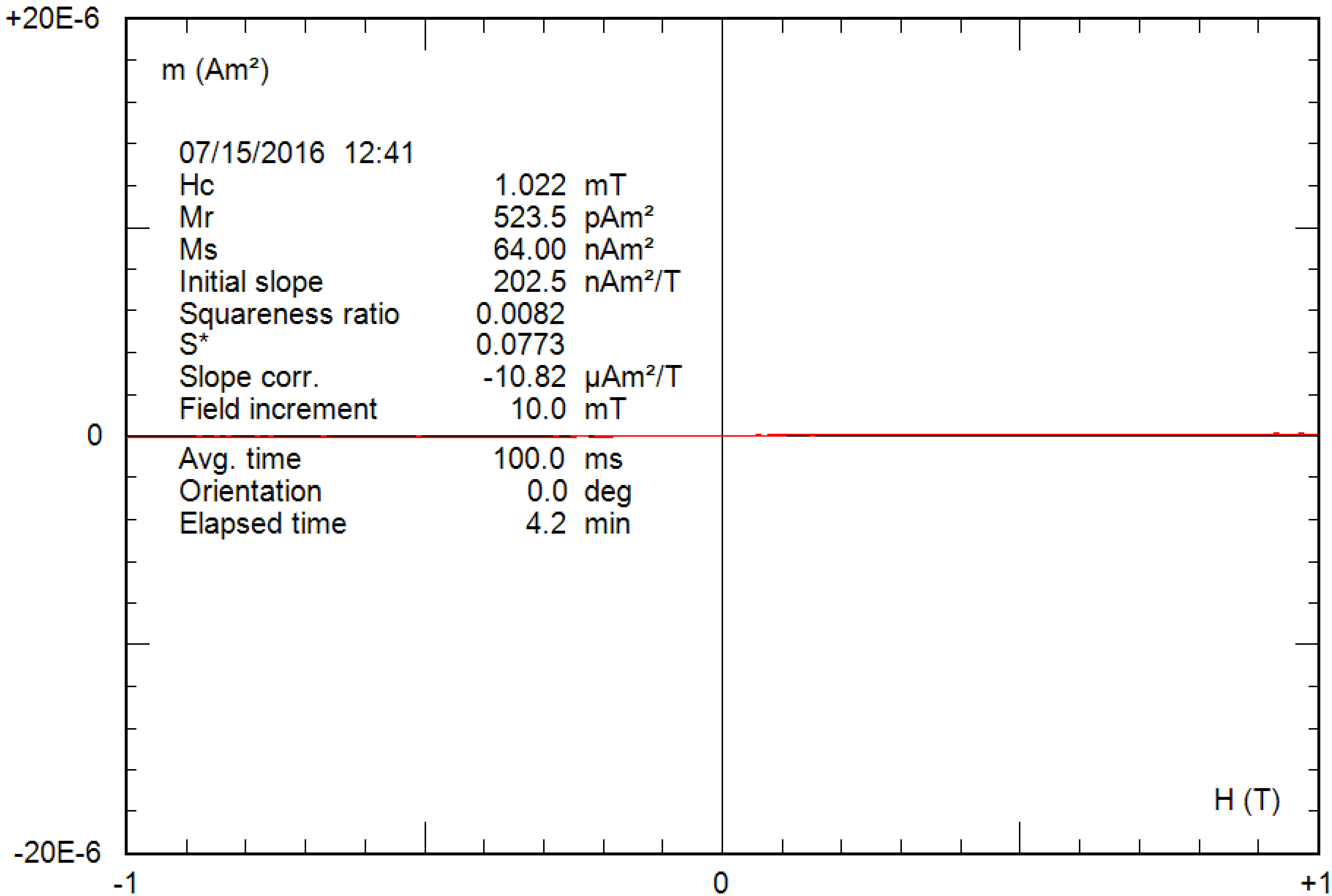

0.20 g

File: 08-04a_hyst_corr

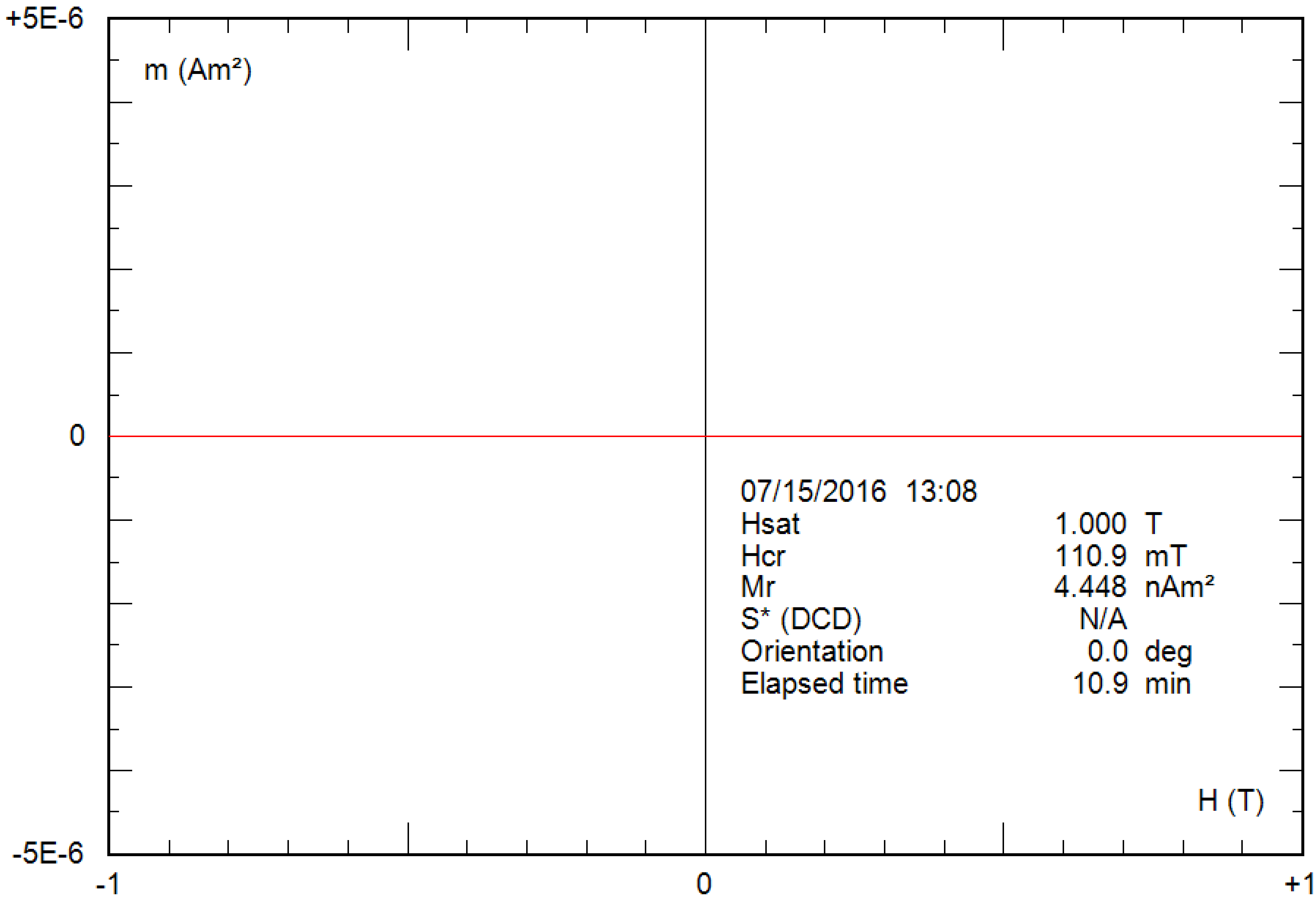

0.19 g

File: 09-04a_bcr

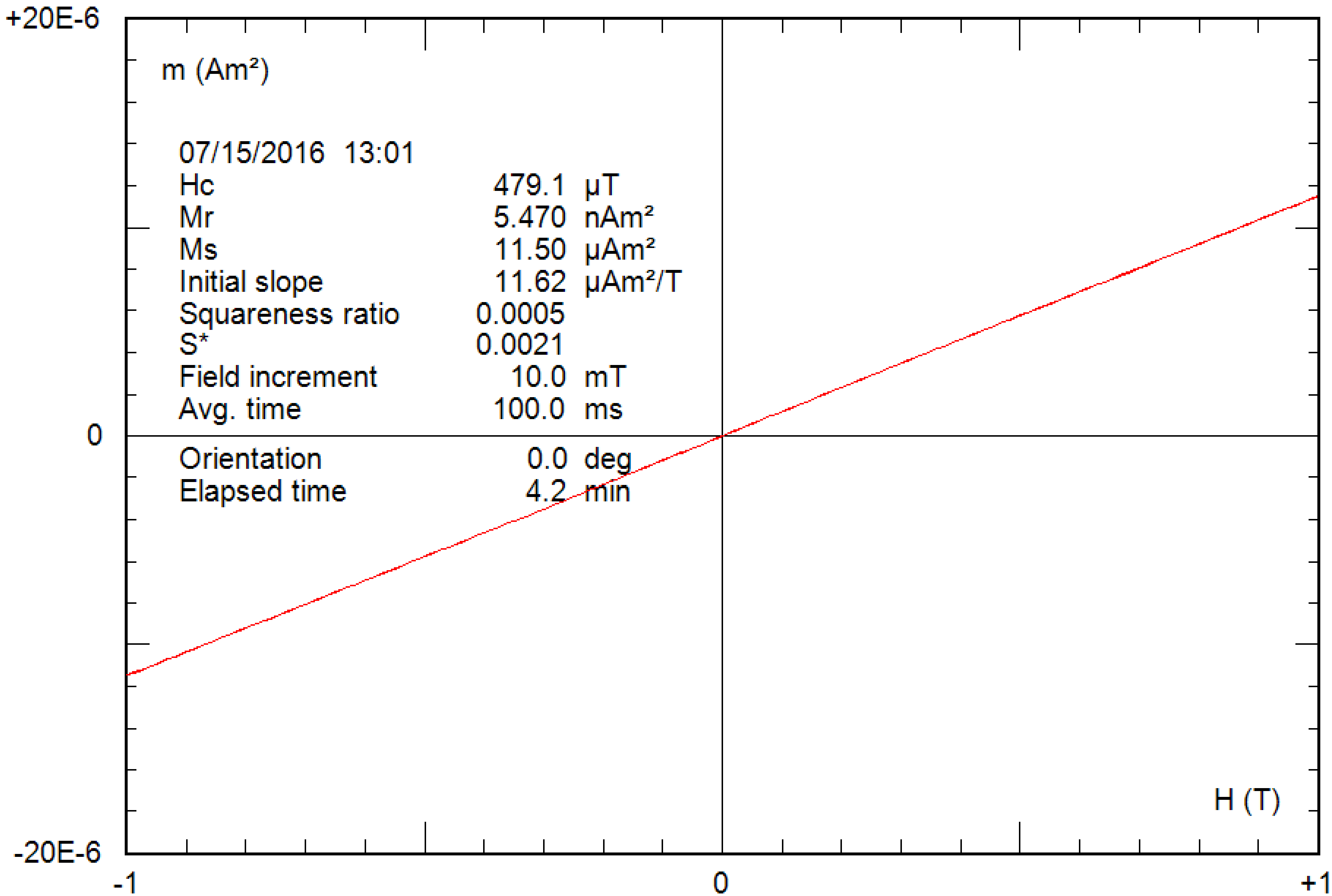

0.19 g

File: 09-04a_hyst

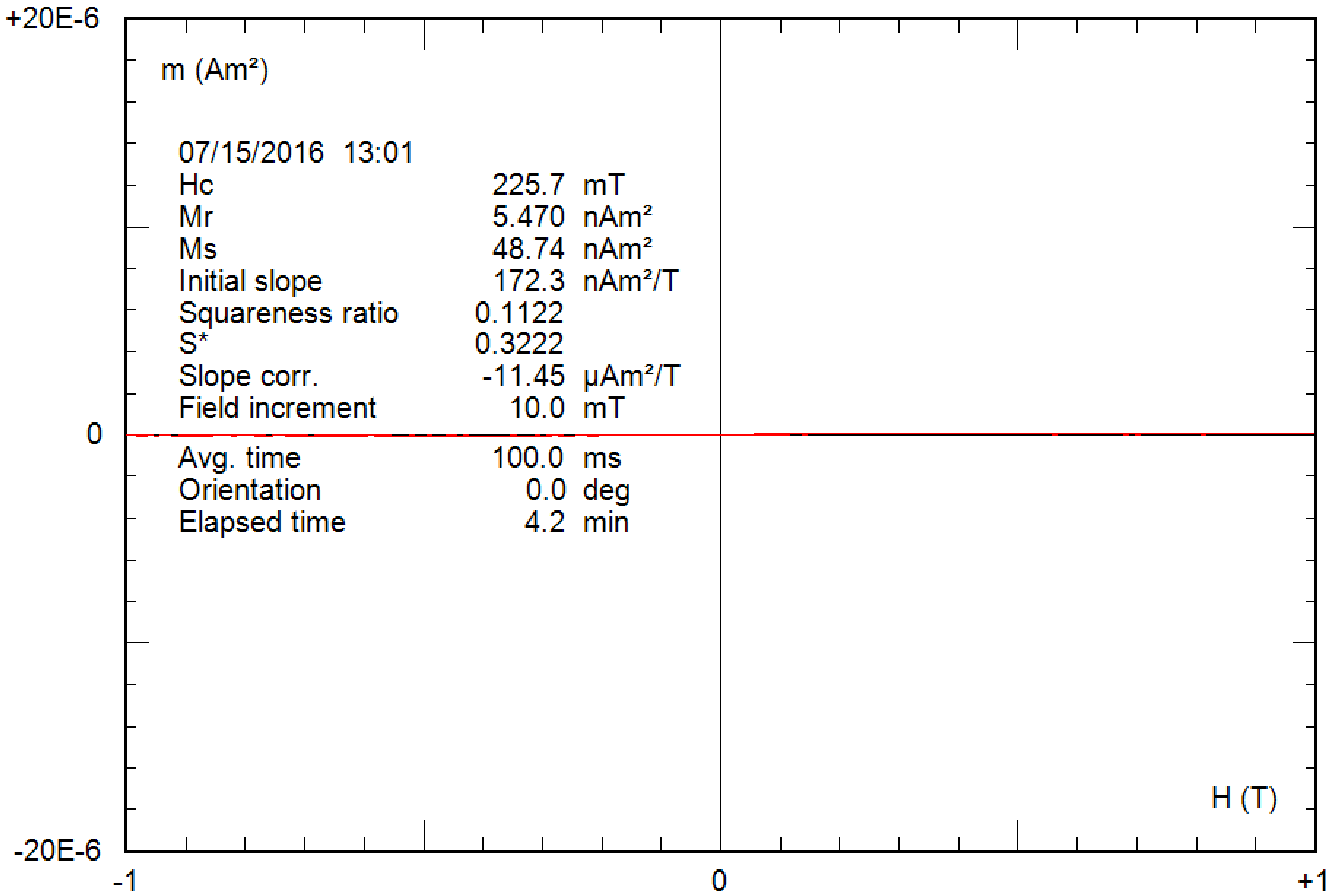

0.19 g

File: 09-04a_hyst_corr

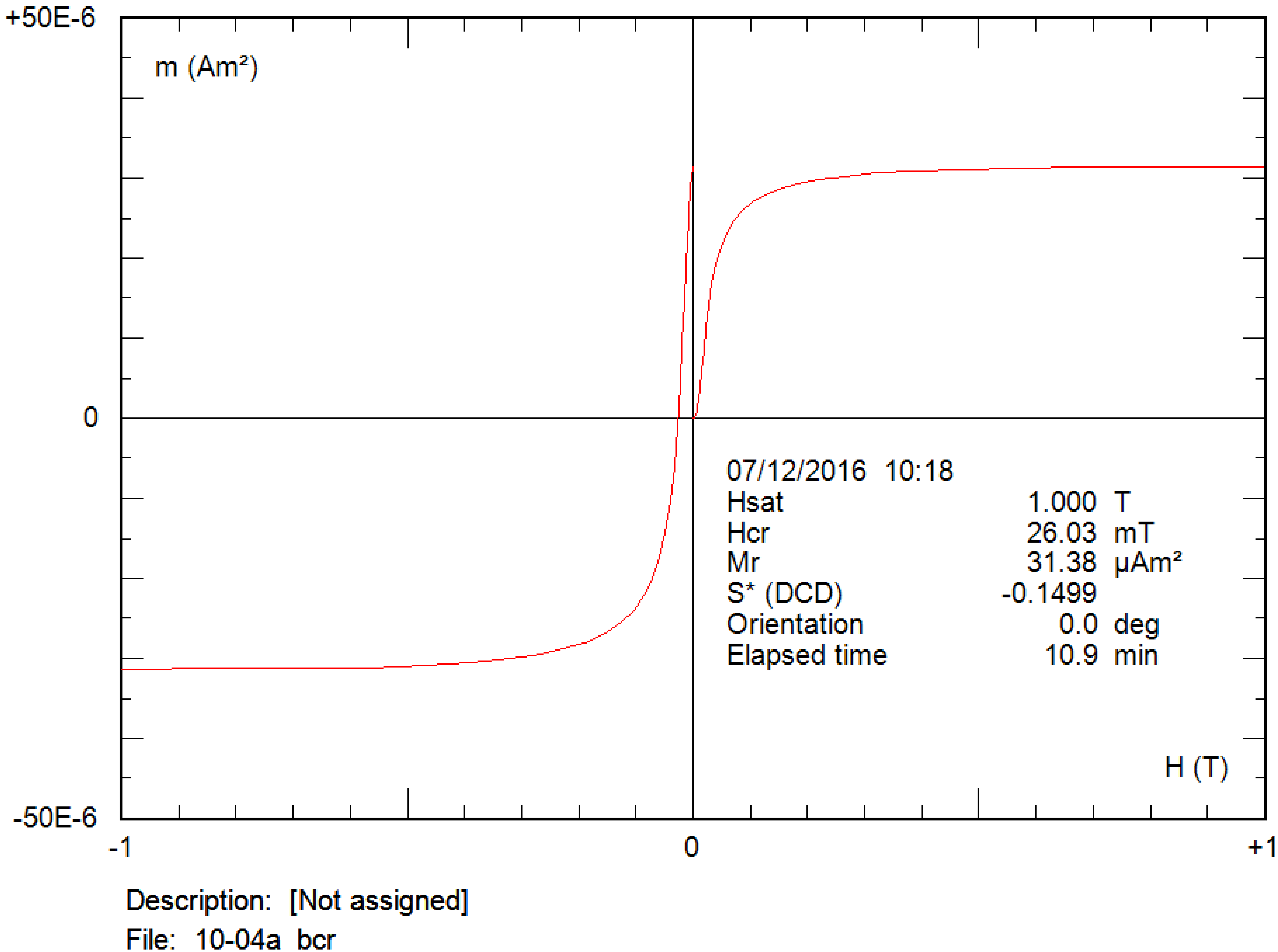
+50E-6
m (Am²)
0
-50E-6
-1
0
+1
H (T)
07/12/2016 10:18
Hsat 1.000 T
Hcr 26.03 mT
Mr 31.38 µAm²
S* (DCD) -0.1499
Orientation 0.0 deg
Elapsed time 10.9 min
Description: [Not assigned]
File: 10-04a_bcr

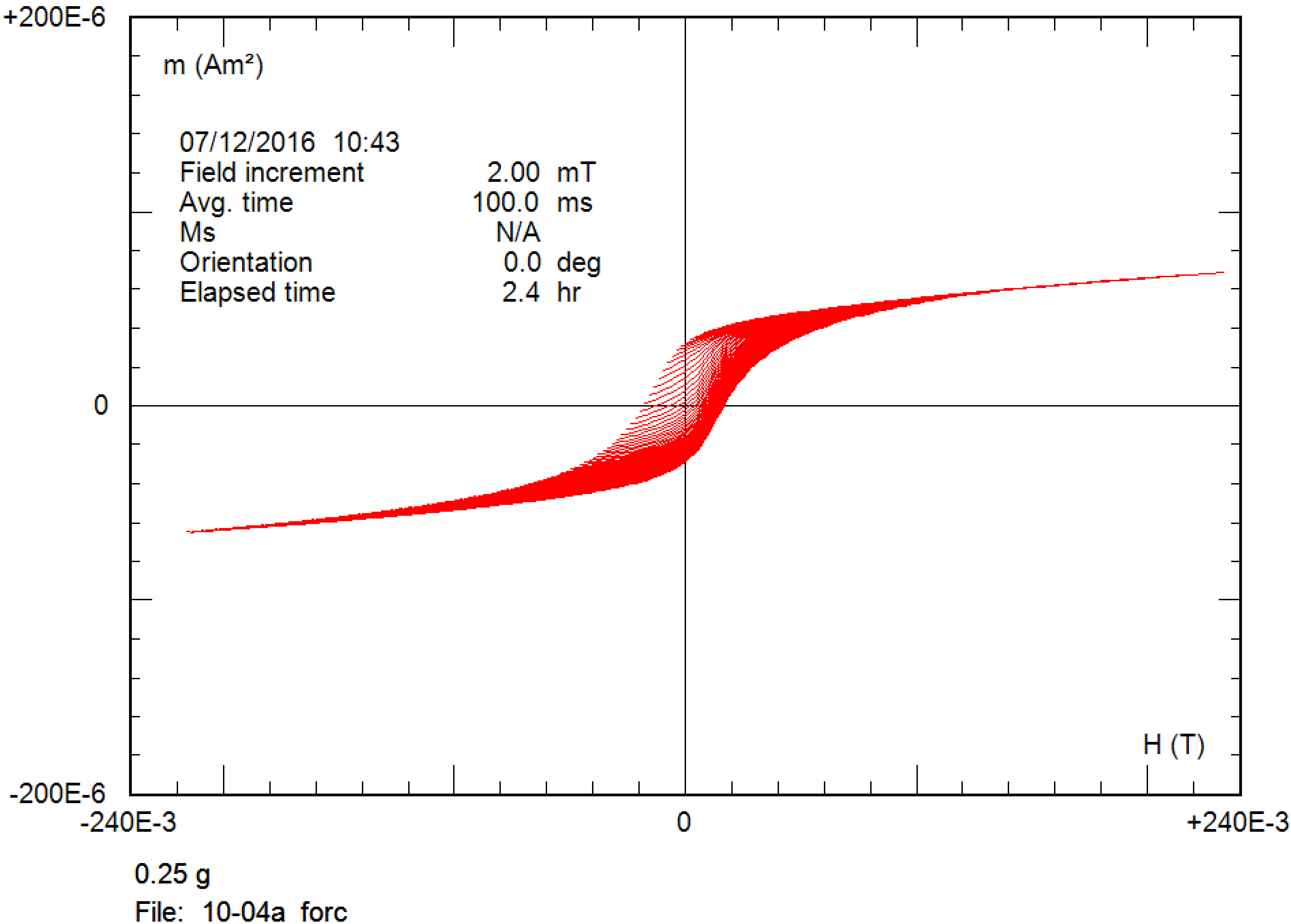

+200E-6
m (Am²)
07/12/2016 10:43
Field increment 2.00 mT
Avg. time 100.0 ms
Ms N/A
Orientation 0.0 deg
Elapsed time 2.4 hr
0
H (T)
-200E-6
-240E-3
0
+240E-3
0.25 g
File: 10-04a_forc

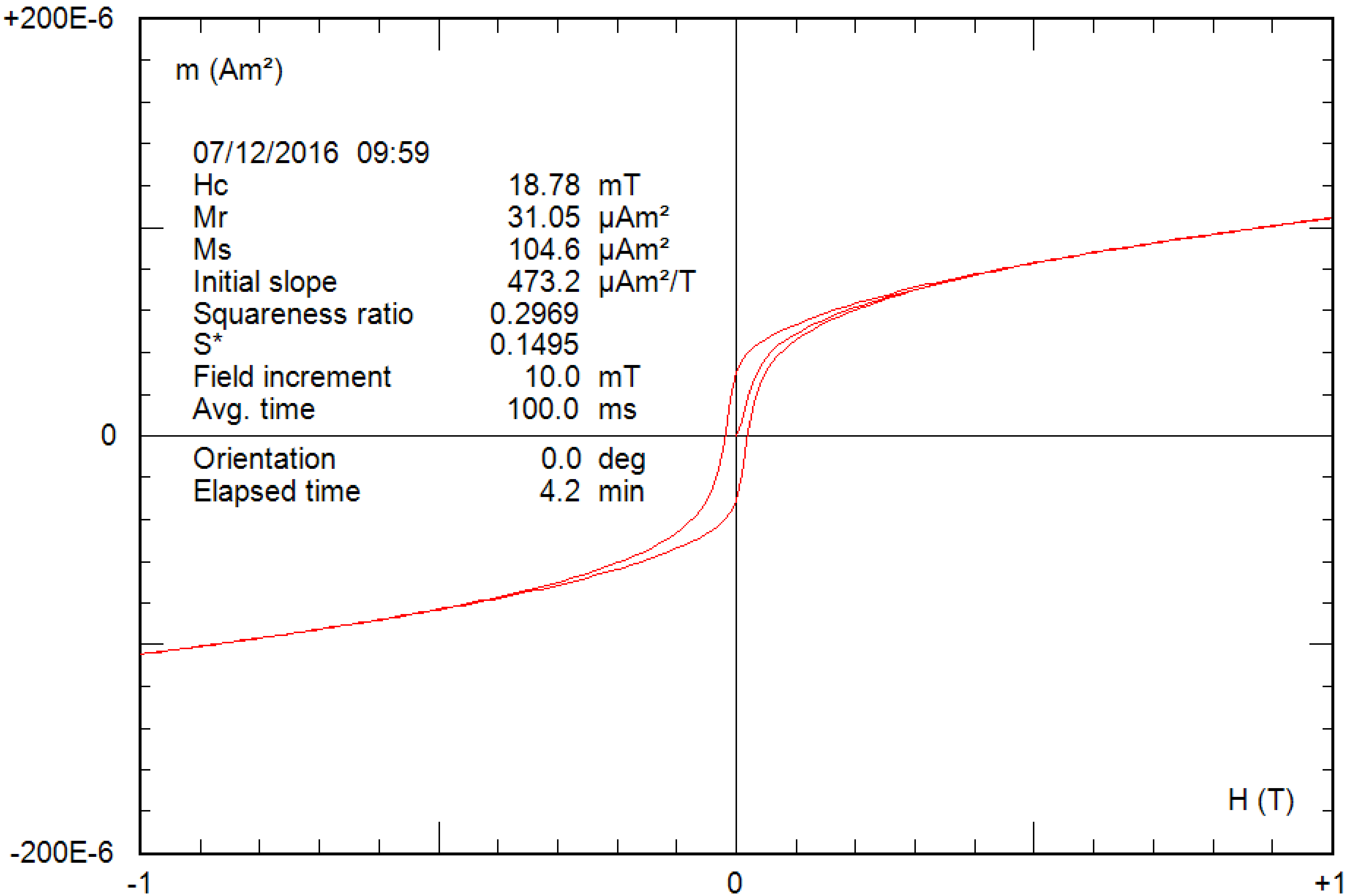

0.25 g

File: 10-04a_hyst

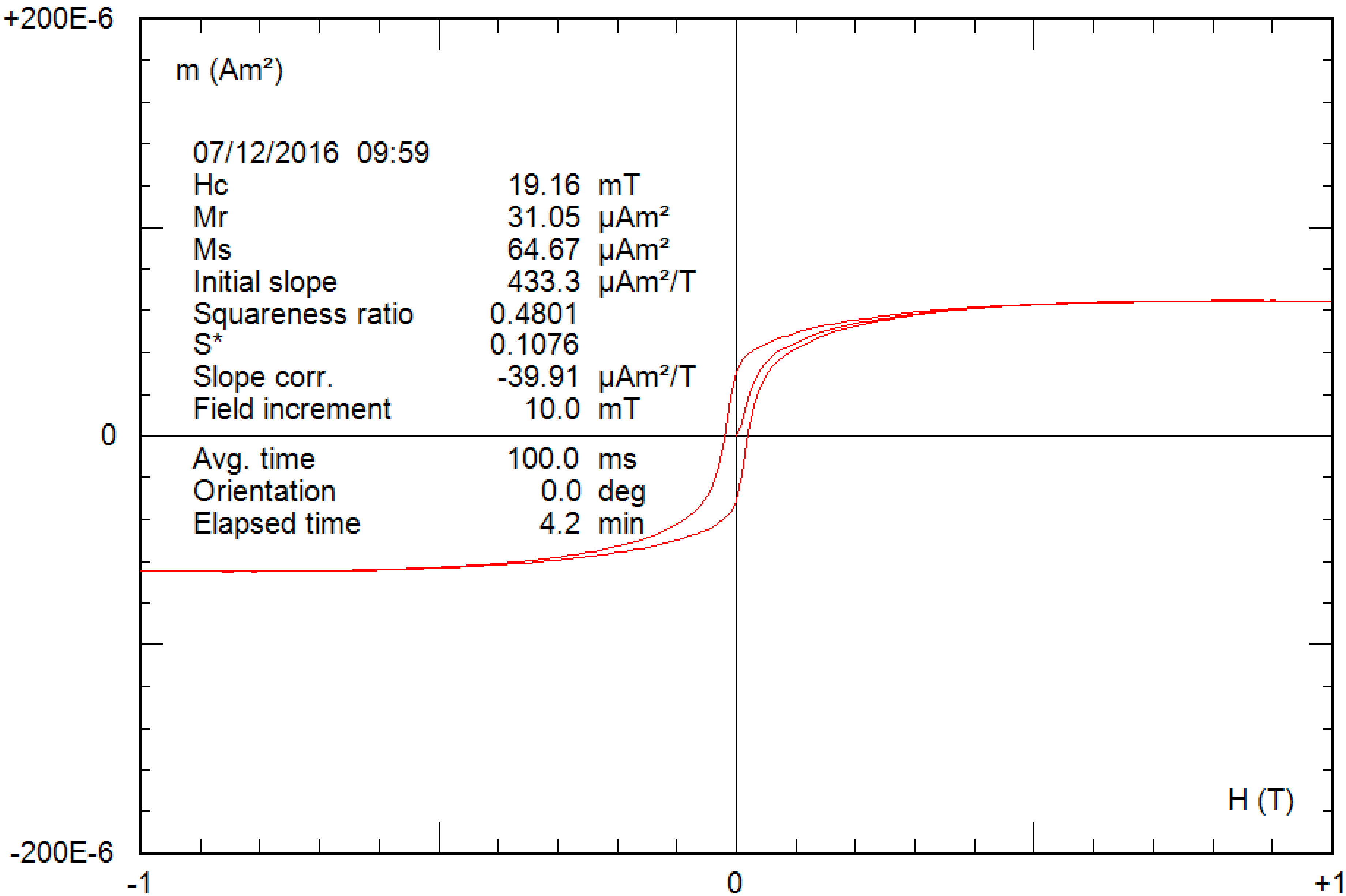

0.25 g

File: 10-04a_hyst_corr

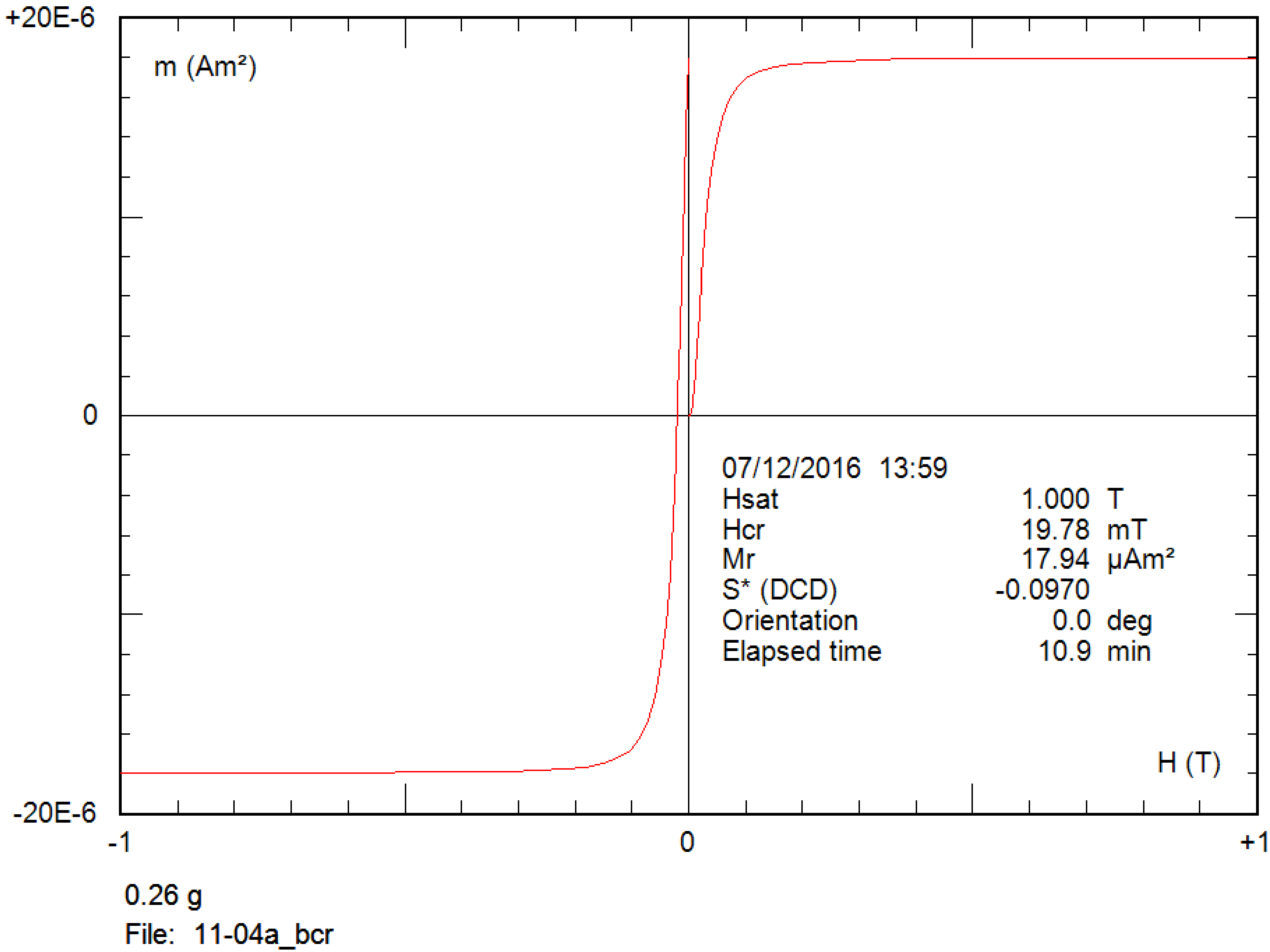
+20E-6
m (Am²)
0
-20E-6
-1
0
+1
H (T)
07/12/2016 13:59
Hsat 1.000 T
Hcr 19.78 mT
Mr 17.94 µAm²
S* (DCD) -0.0970
Orientation 0.0 deg
Elapsed time 10.9 min
0.26 g
File: 11-04a_bcr

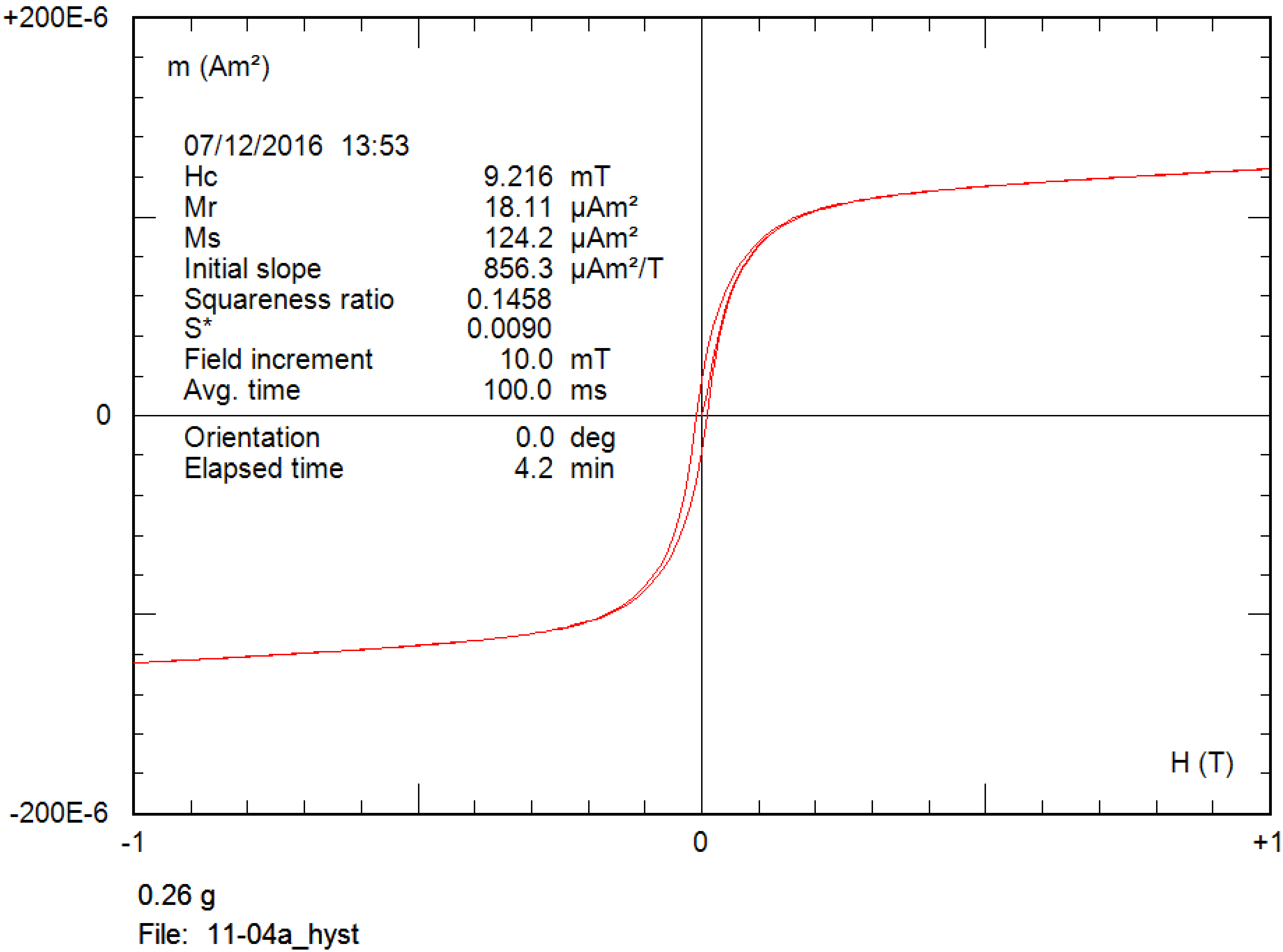
+200E-6
m (Am²)
07/12/2016 13:53
Hc 9.216 mT
Mr 18.11 µAm²
Ms 124.2 µAm²
Initial slope 856.3 µAm²/T
Squareness ratio 0.1458
S* 0.0090
Field increment 10.0 mT
Avg. time 100.0 ms
0
Orientation 0.0 deg
Elapsed time 4.2 min
H (T)
-200E-6
-1
0
+1
0.26 g
File: 11-04a_hyst

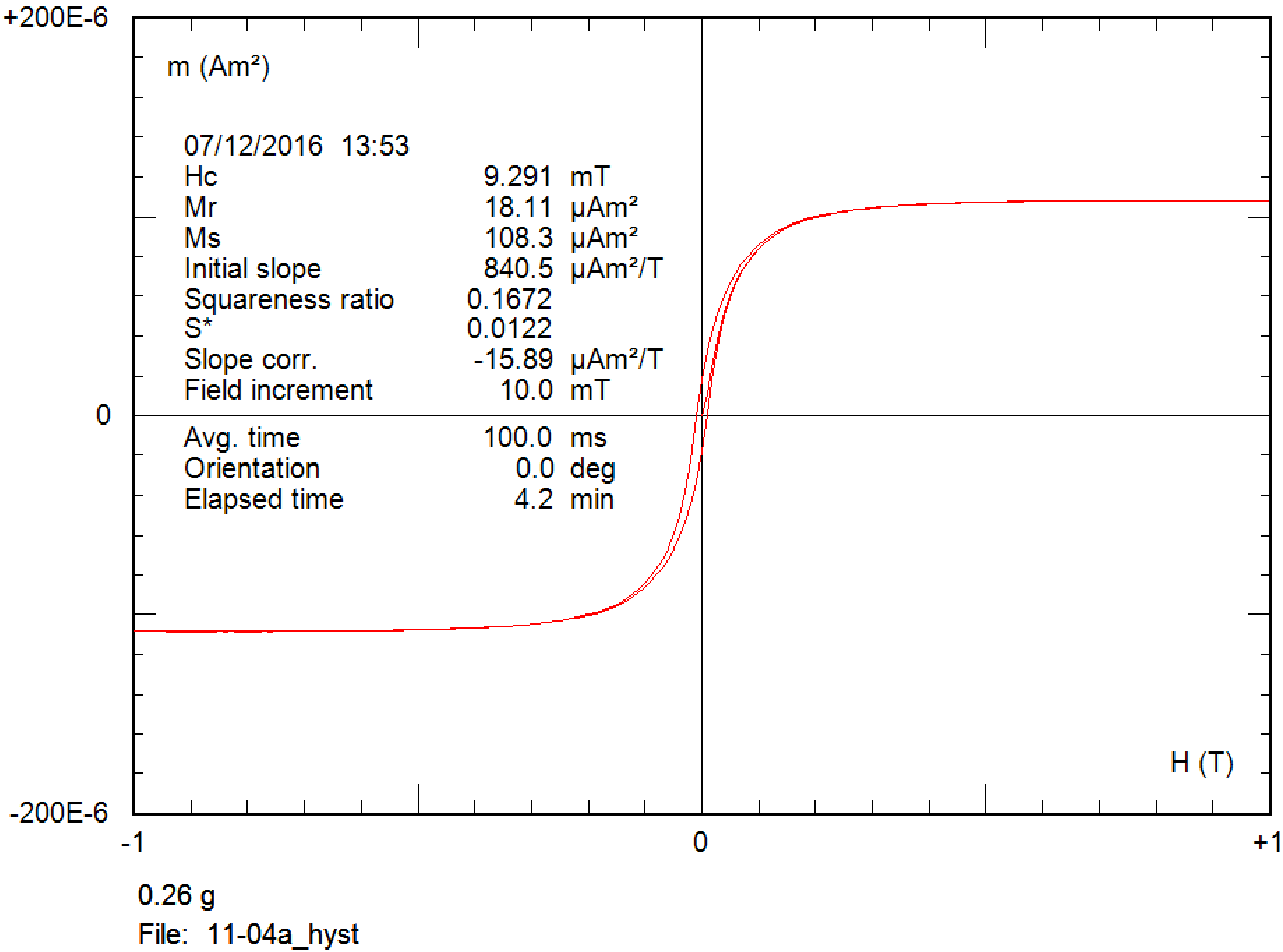
+200E-6
m (Am²)
07/12/2016 13:53
Hc 9.291 mT
Mr 18.11 µAm²
Ms 108.3 µAm²
Initial slope 840.5 µAm²/T
Squareness ratio 0.1672
S* 0.0122
Slope corr. -15.89 µAm²/T
Field increment 10.0 mT
0
Avg. time 100.0 ms
Orientation 0.0 deg
Elapsed time 4.2 min
H (T)
-200E-6
-1
0
+1
0.26 g
File: 11-04a_hyst

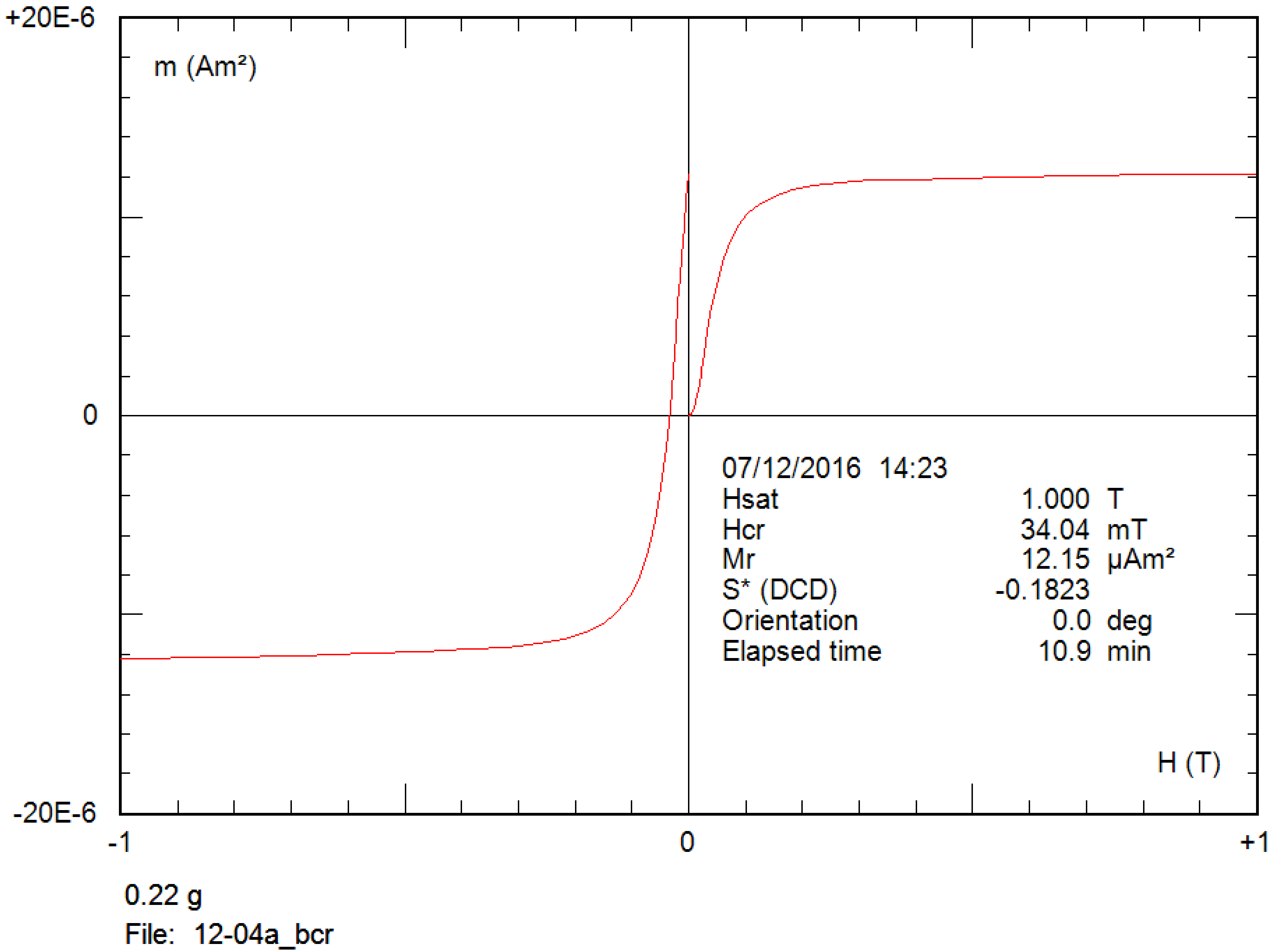
+20E-6
m (Am²)
0
-20E-6
-1
0
+1
H (T)
07/12/2016 14:23
Hsat 1.000 T
Hcr 34.04 mT
Mr 12.15 µAm²
S* (DCD) -0.1823
Orientation 0.0 deg
Elapsed time 10.9 min
0.22 g
File: 12-04a_bcr

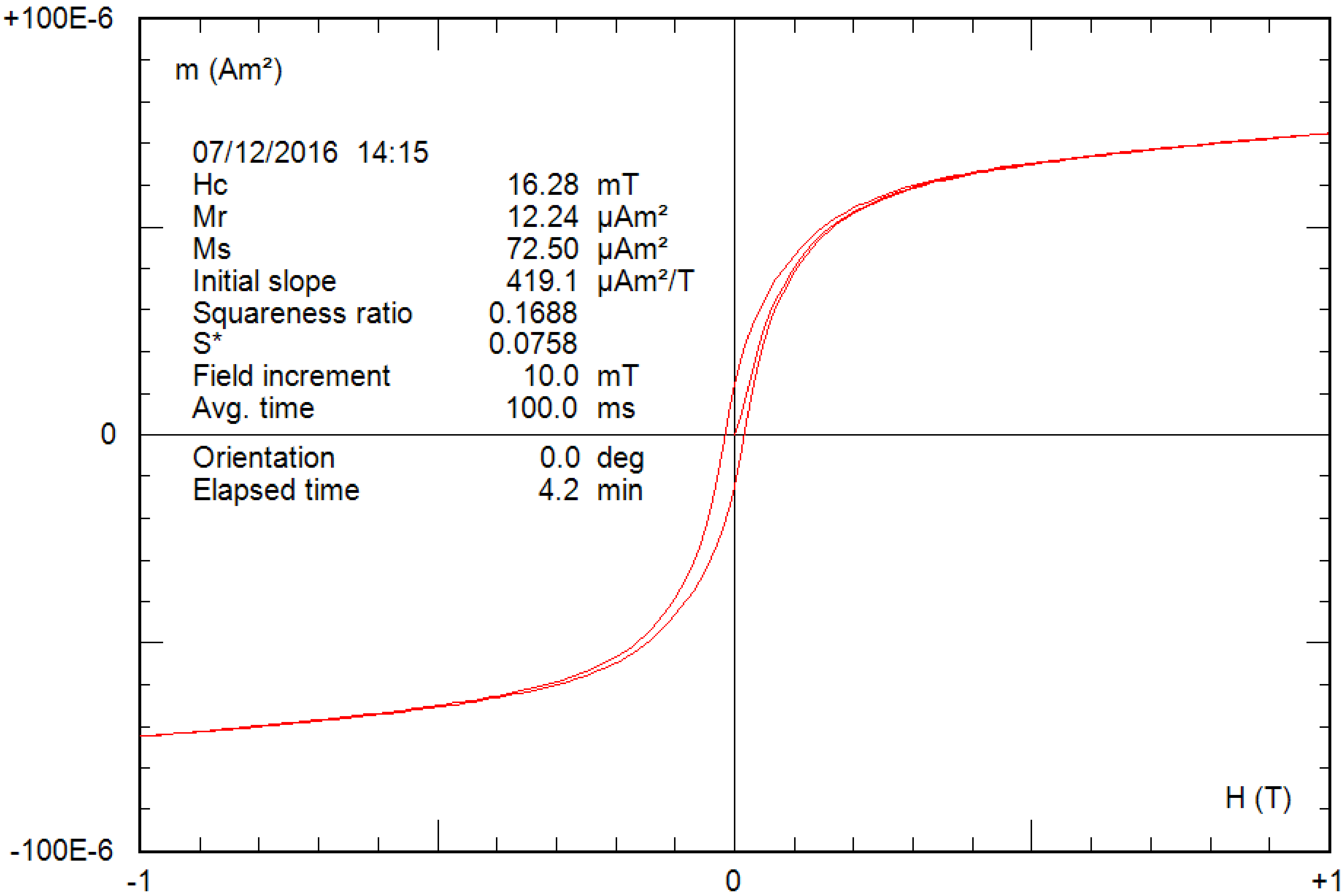

0.22 g

File: 12-04a_hyst

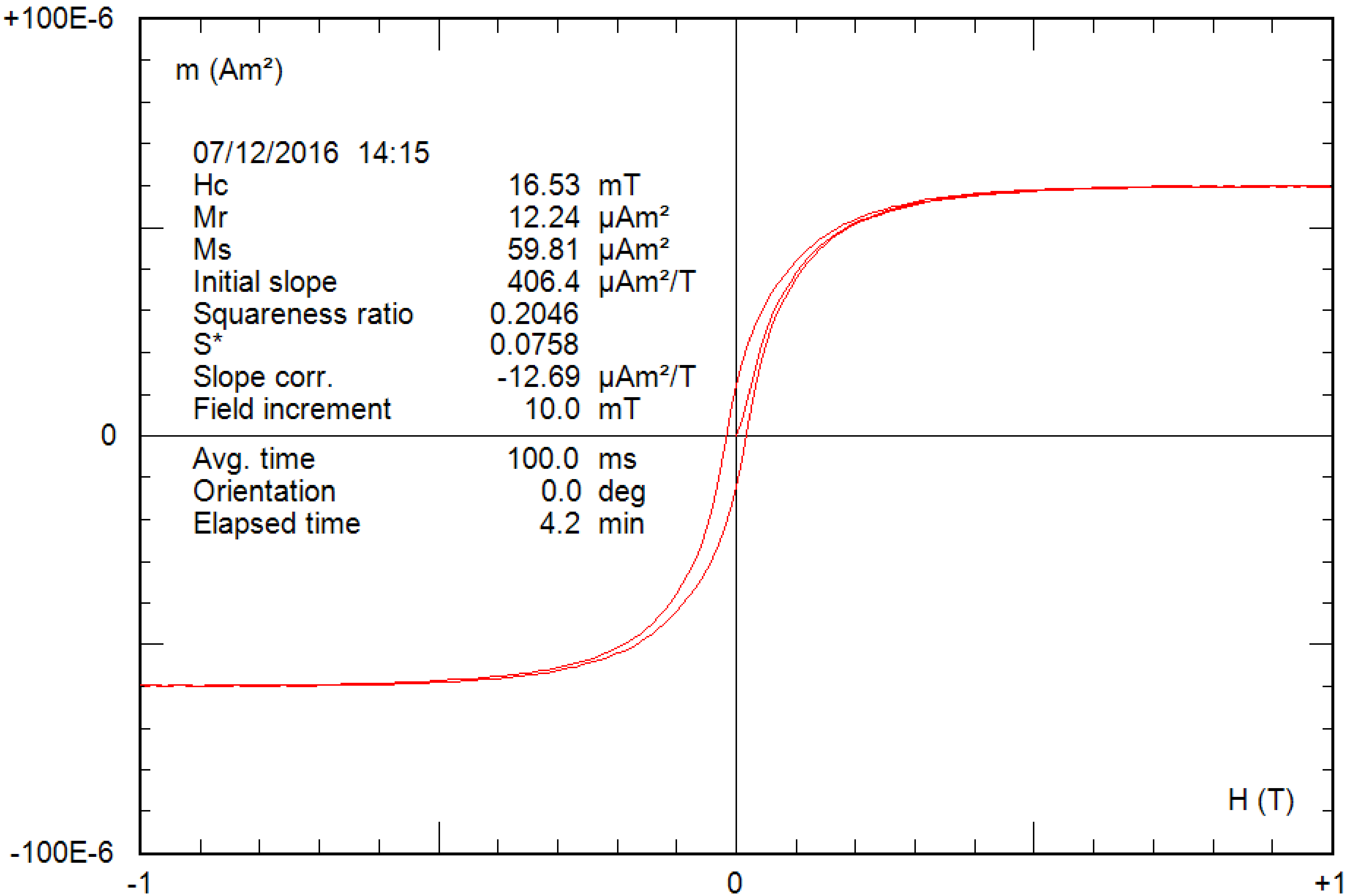

0.22 g

File: 12-04a_hyst_corr

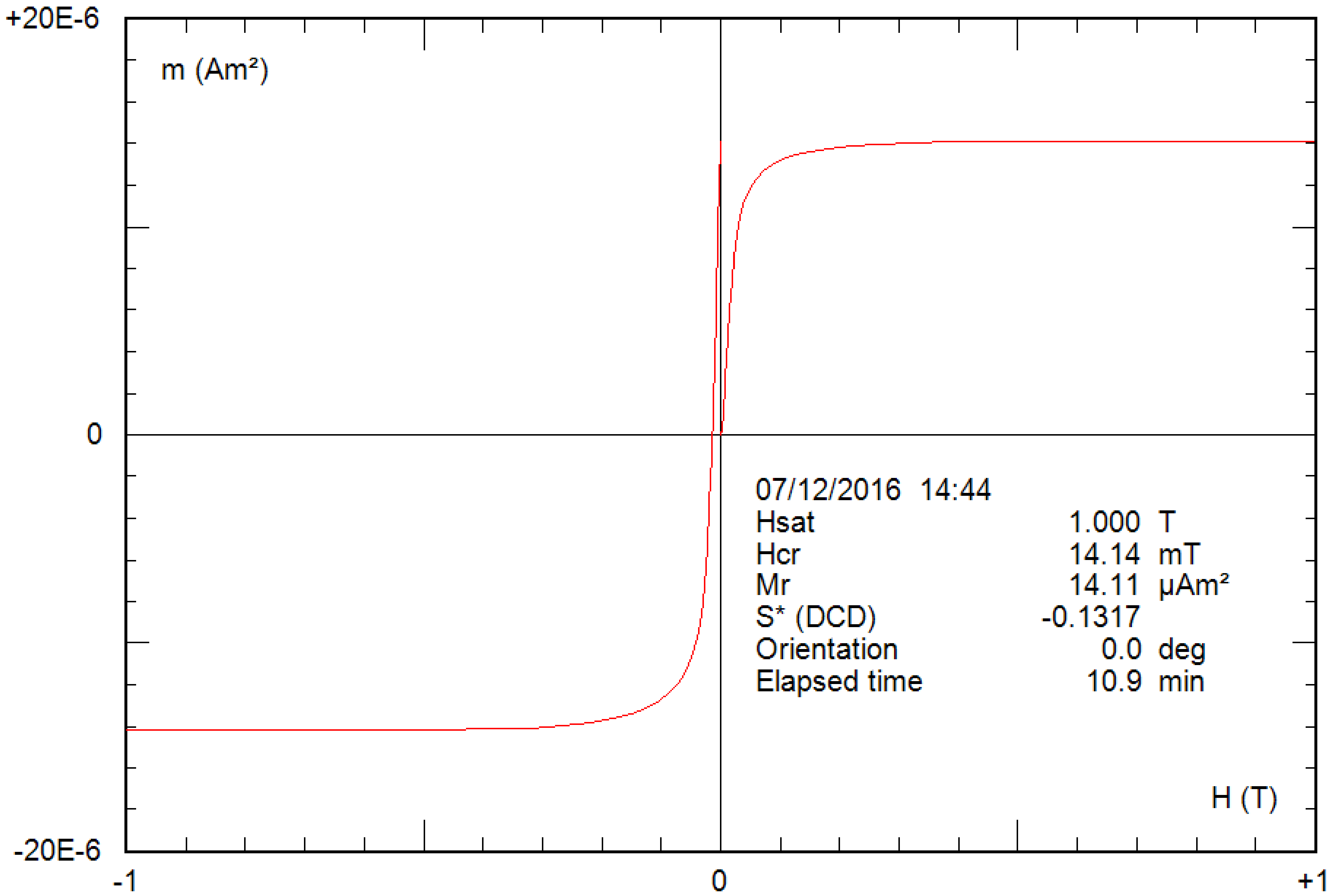

0.25 g

File: 13-04a_bcr

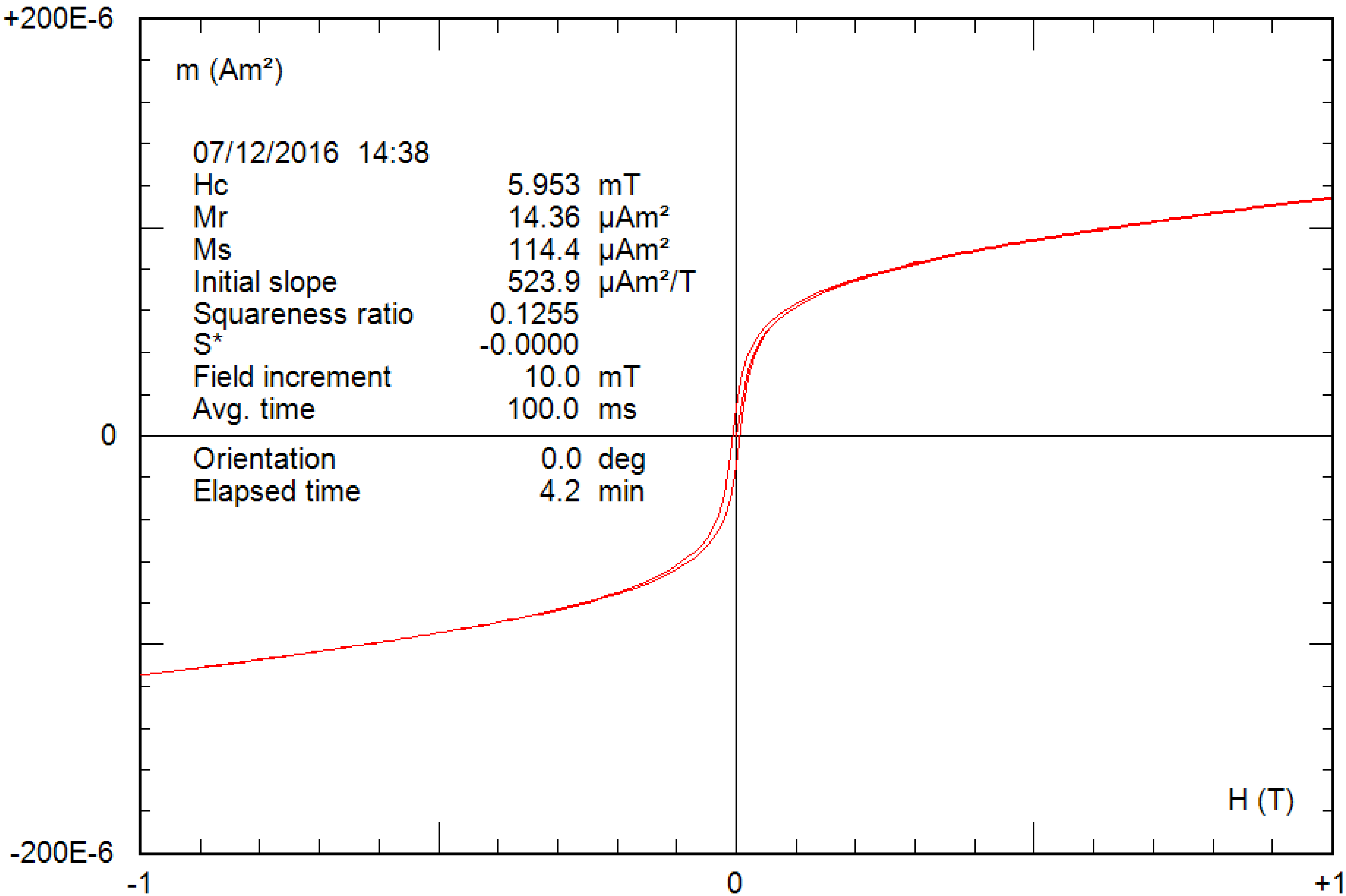

0.25 g

File: 13-04a_hyst

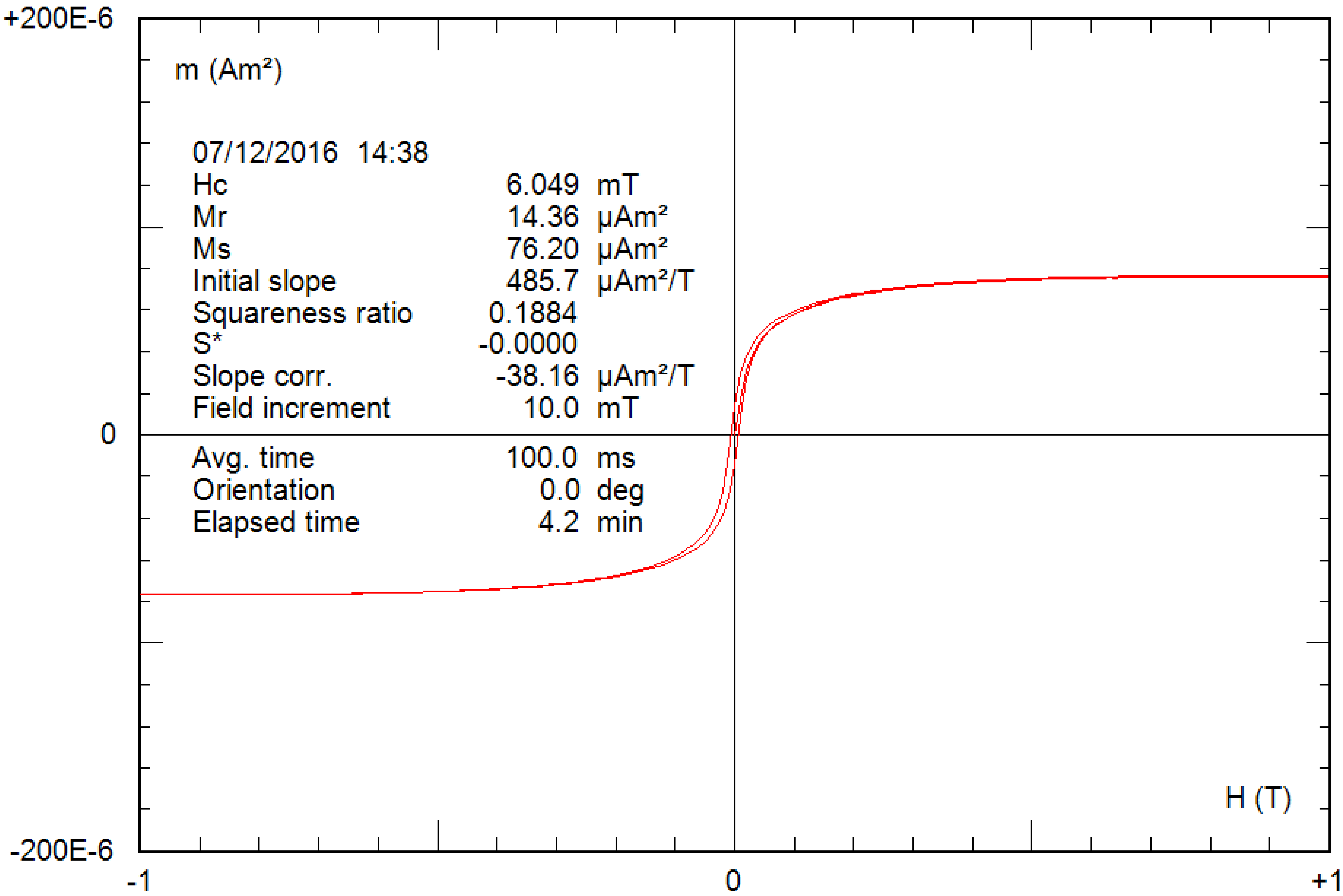

0.25 g

File: 13-04a_hyst_corr

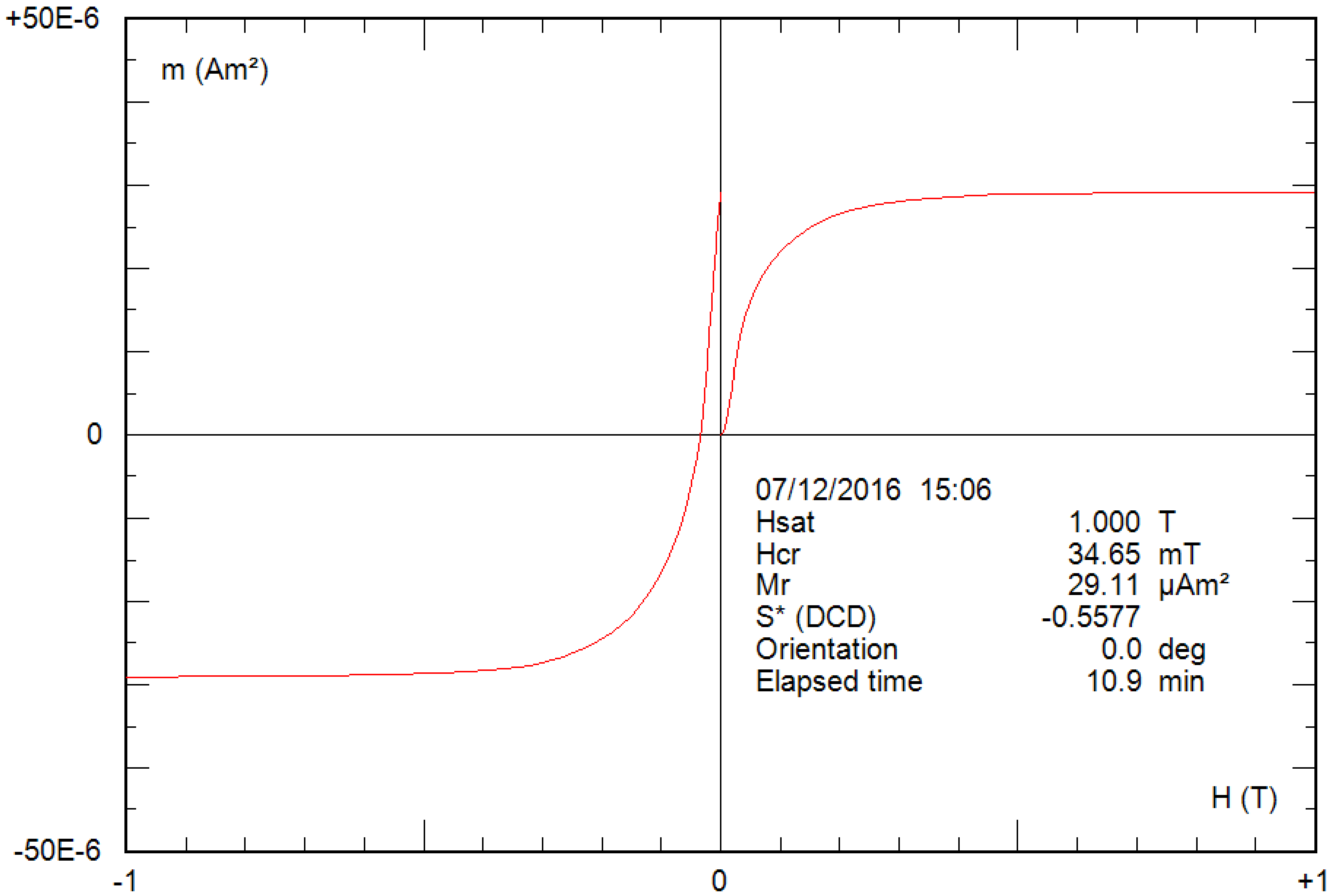

0.21 g

File: 14-04a_bcr

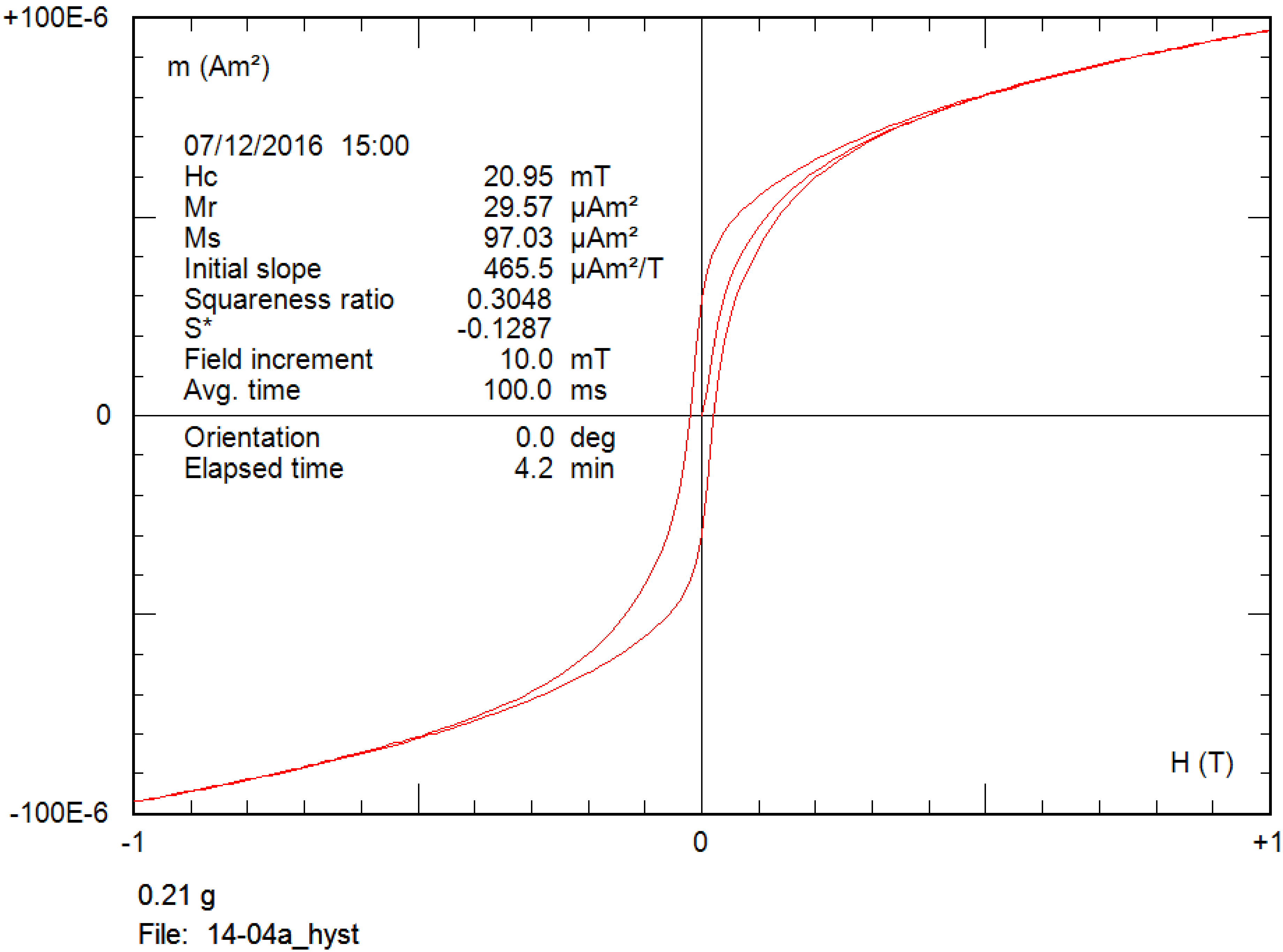
+100E-6
m (Am²)
07/12/2016 15:00
Hc 20.95 mT
Mr 29.57 µAm²
Ms 97.03 µAm²
Initial slope 465.5 µAm²/T
Squareness ratio 0.3048
S* -0.1287
Field increment 10.0 mT
Avg. time 100.0 ms
0
Orientation 0.0 deg
Elapsed time 4.2 min
H (T)
-100E-6
-1
0
+1
0.21 g
File: 14-04a_hyst

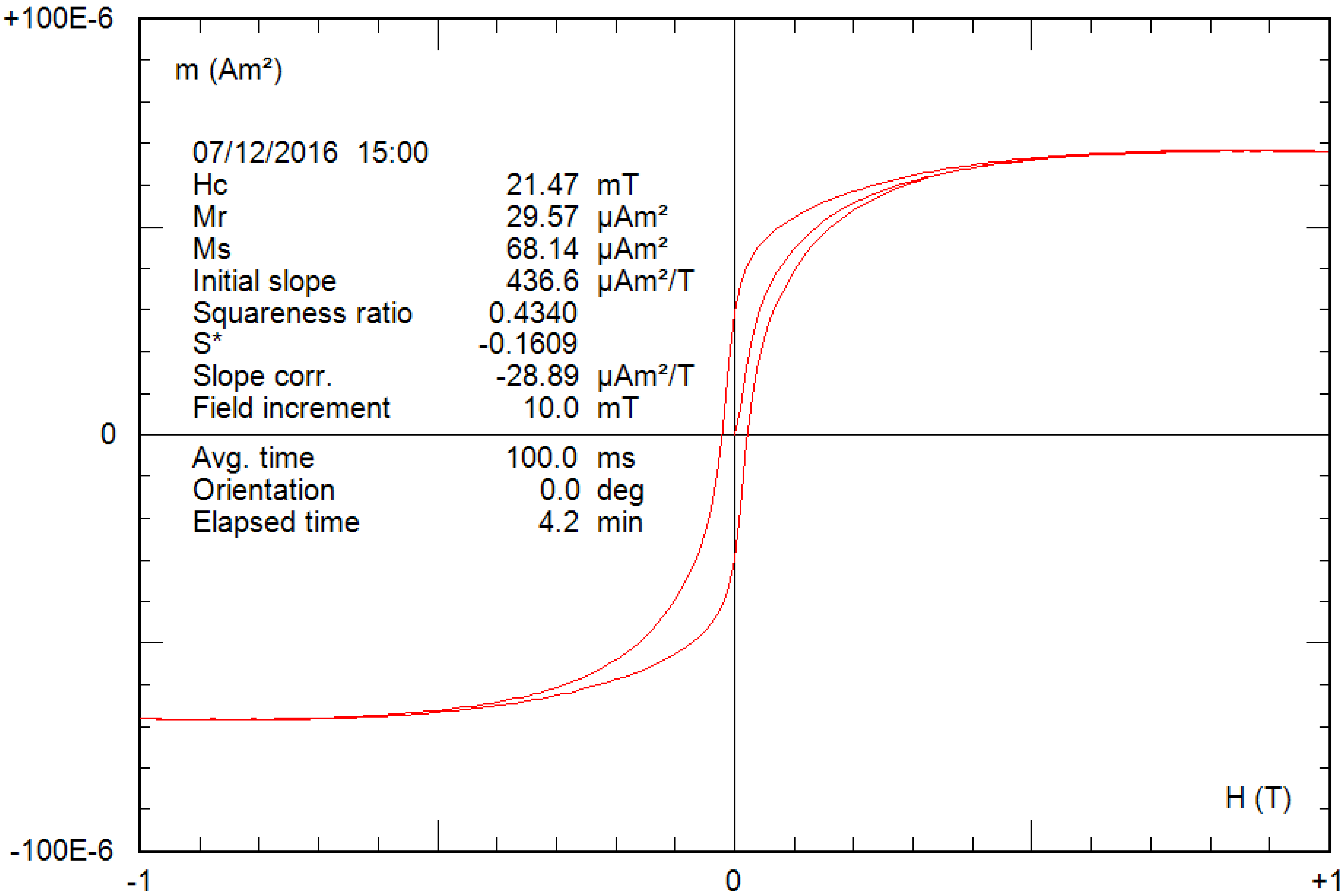

0.21 g

File: 14-04a_hyst_corr

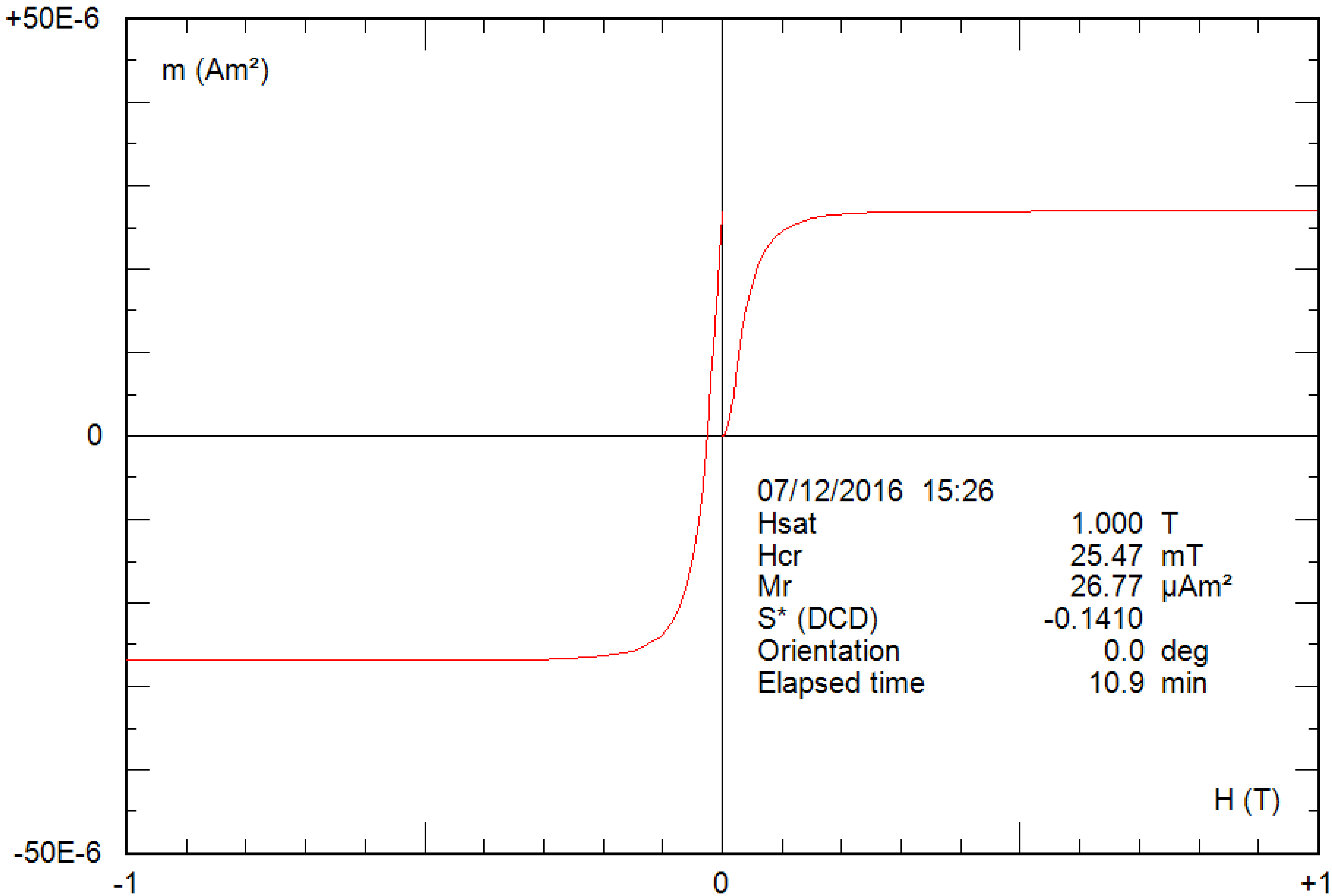

0.25 g

File: 15-04a_bcr

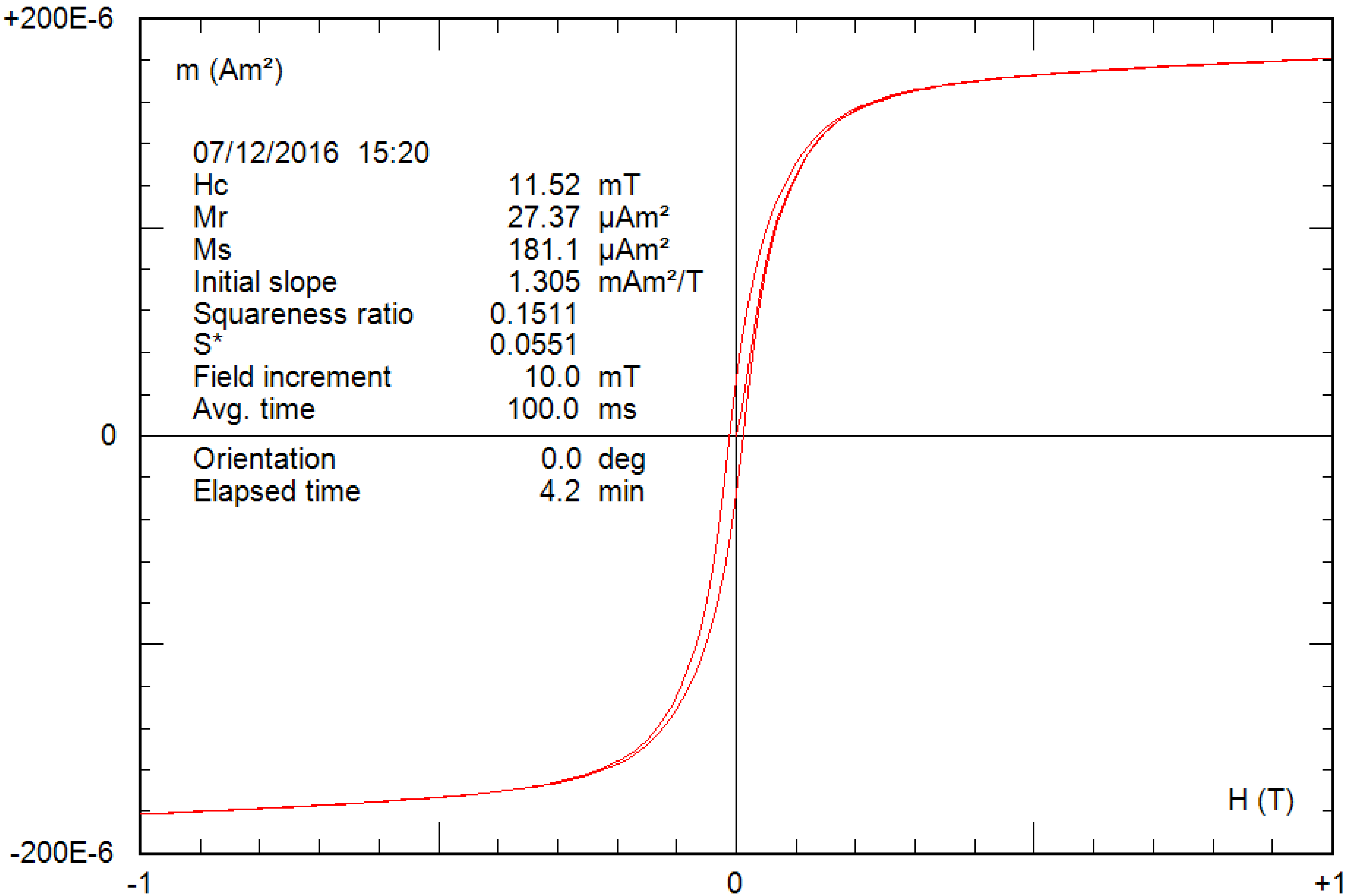

0.25 g

File: 15-04a_hyst

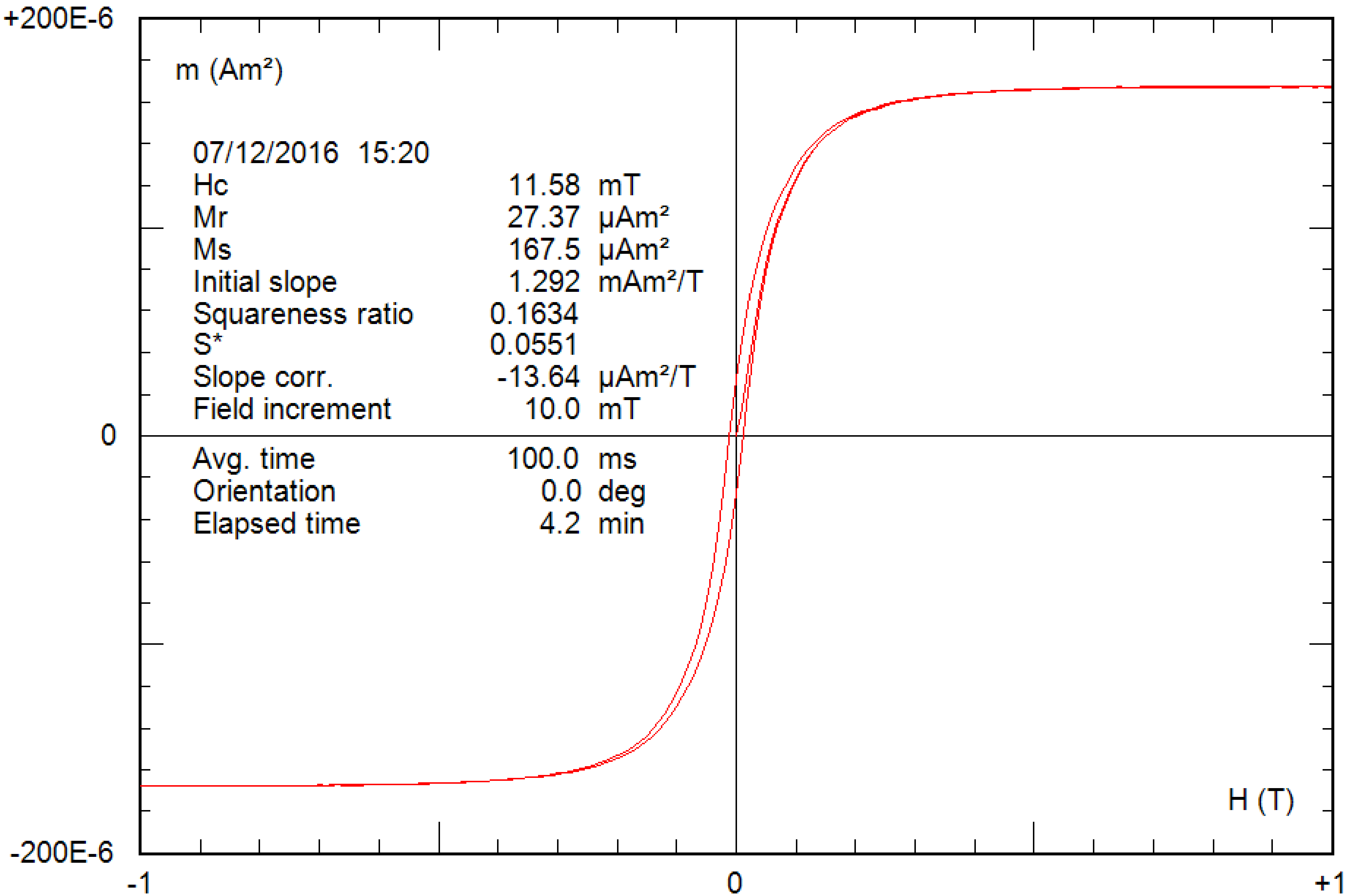

0.25 g

File: 15-04a_hyst_corr

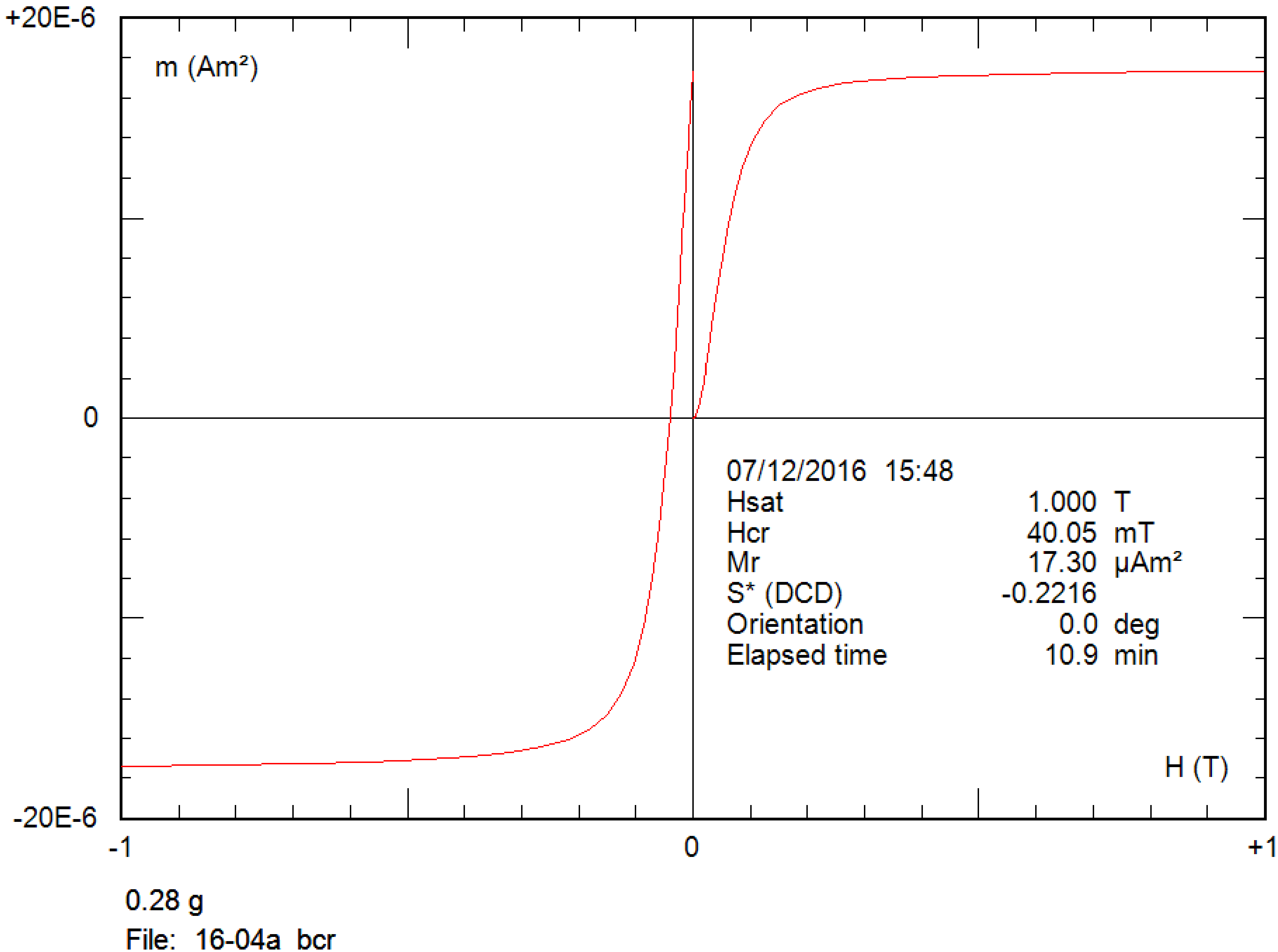

+20E-6
m (Am²)
0
-20E-6
-1
0
+1
H (T)
07/12/2016 15:48
Hsat 1.000 T
Hcr 40.05 mT
Mr 17.30 µAm²
S* (DCD) -0.2216
Orientation 0.0 deg
Elapsed time 10.9 min
0.28 g
File: 16-04a_bcr

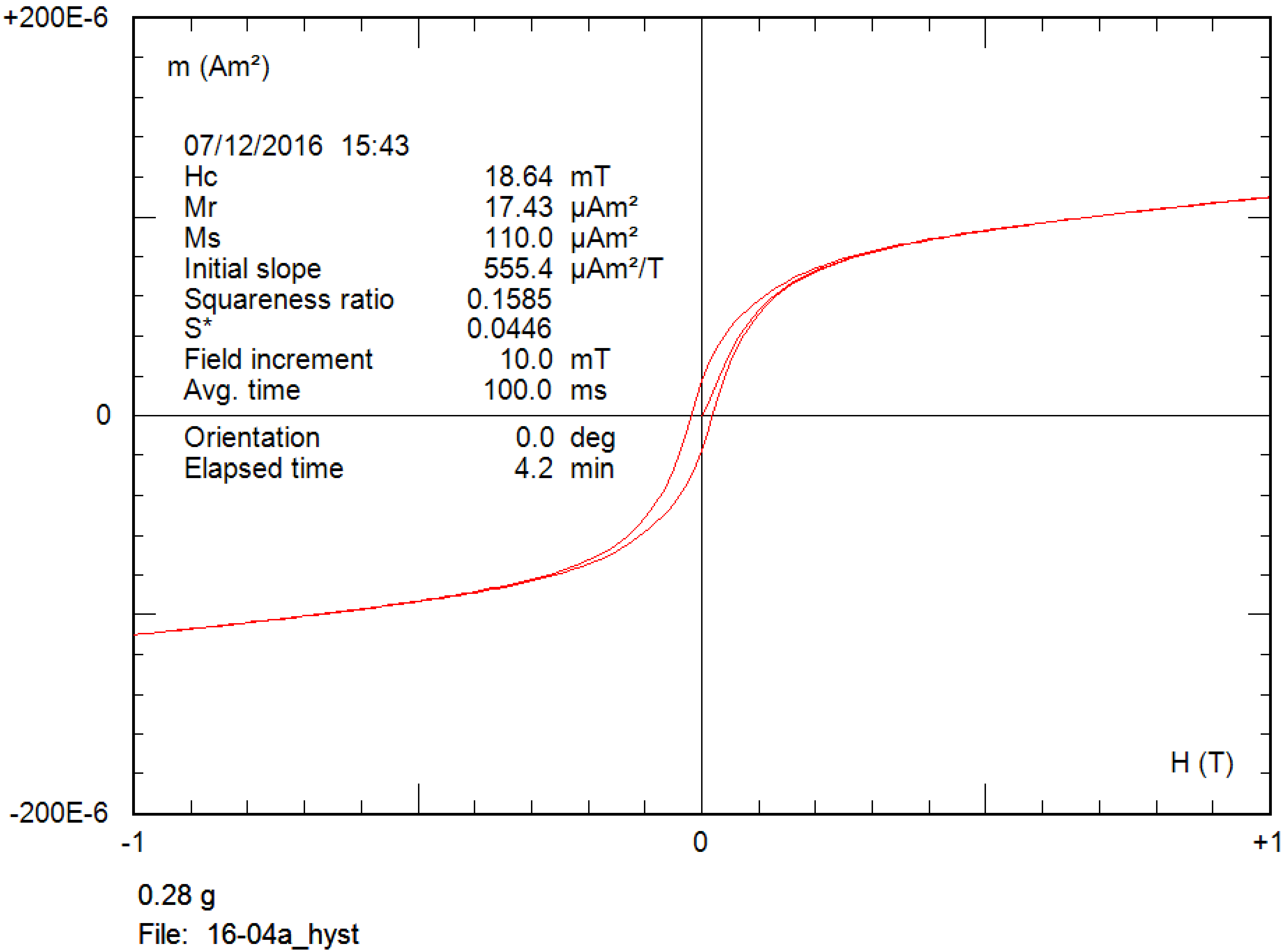
+200E-6
m (Am²)
07/12/2016 15:43
Hc 18.64 mT
Mr 17.43 µAm²
Ms 110.0 µAm²
Initial slope 555.4 µAm²/T
Squareness ratio 0.1585
S* 0.0446
Field increment 10.0 mT
Avg. time 100.0 ms
0
Orientation 0.0 deg
Elapsed time 4.2 min
H (T)
-200E-6
-1
0
+1
0.28 g
File: 16-04a_hyst

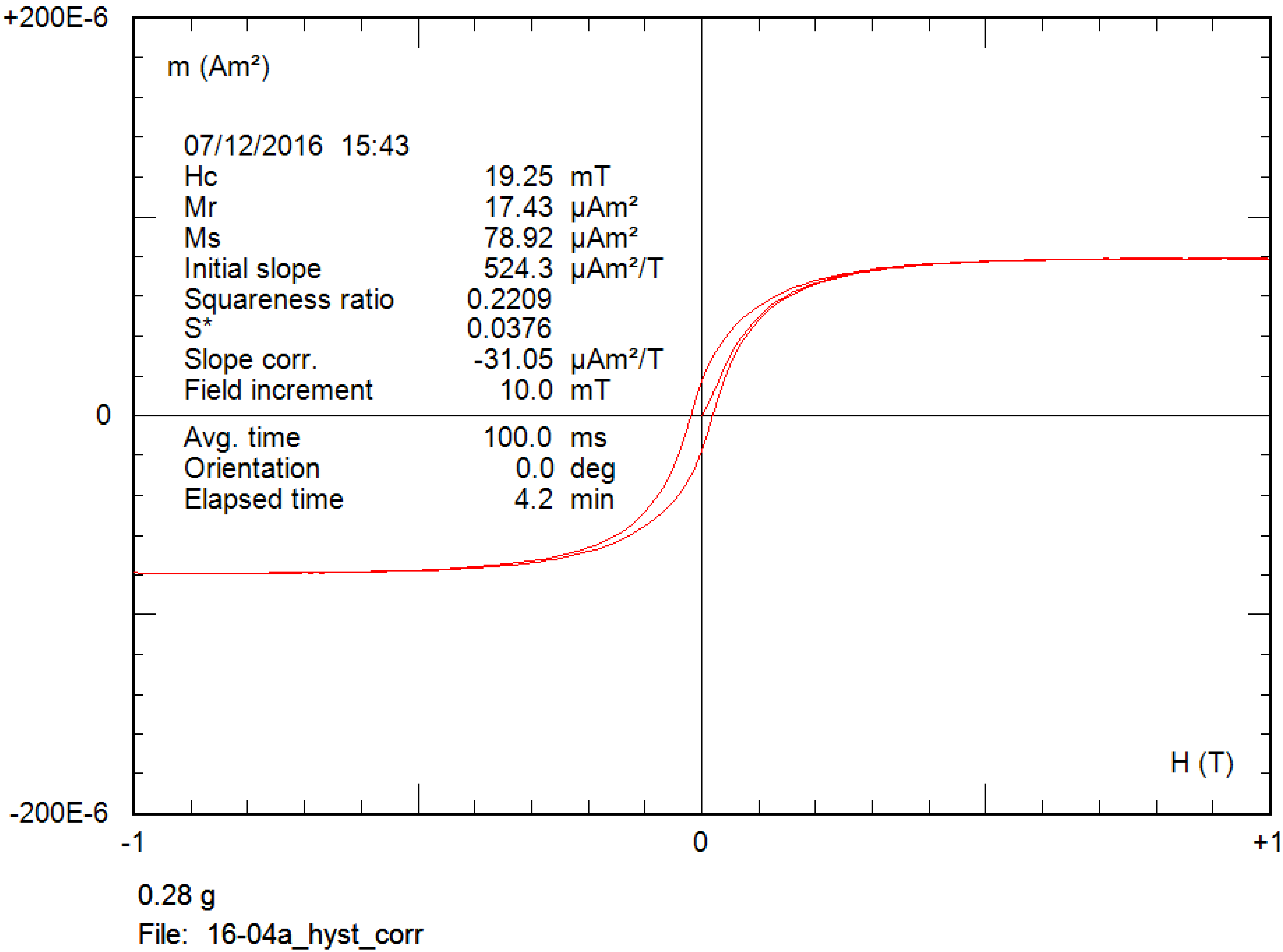

+200E-6
m (Am²)
07/12/2016 15:43
Hc 19.25 mT
Mr 17.43 µAm²
Ms 78.92 µAm²
Initial slope 524.3 µAm²/T
Squareness ratio 0.2209
S* 0.0376
Slope corr. -31.05 µAm²/T
Field increment 10.0 mT
0
Avg. time 100.0 ms
Orientation 0.0 deg
Elapsed time 4.2 min
H (T)
-200E-6
-1
0
+1
0.28 g
File: 16-04a_hyst_corr

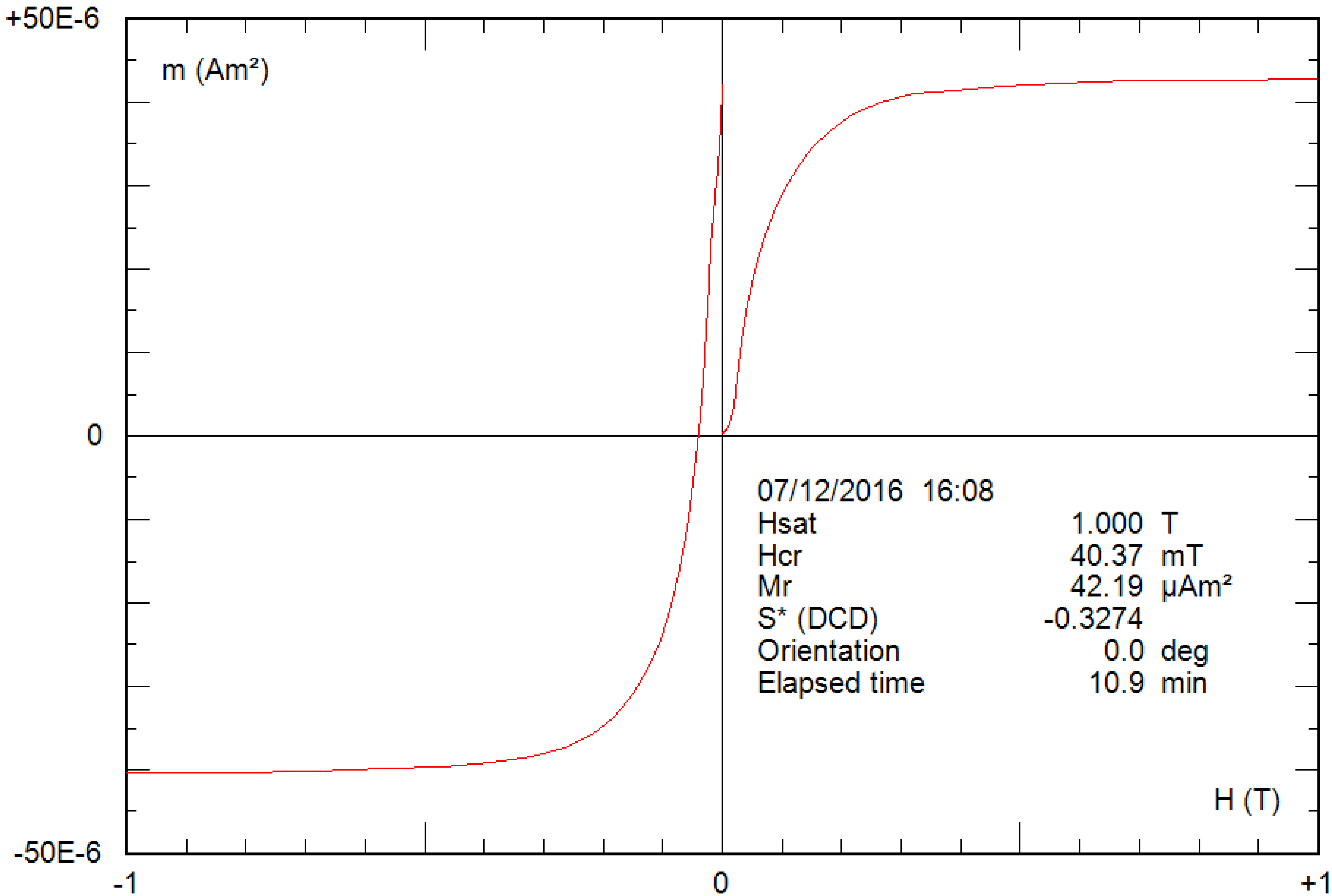

0.25 g
File: 17-04a_bcr

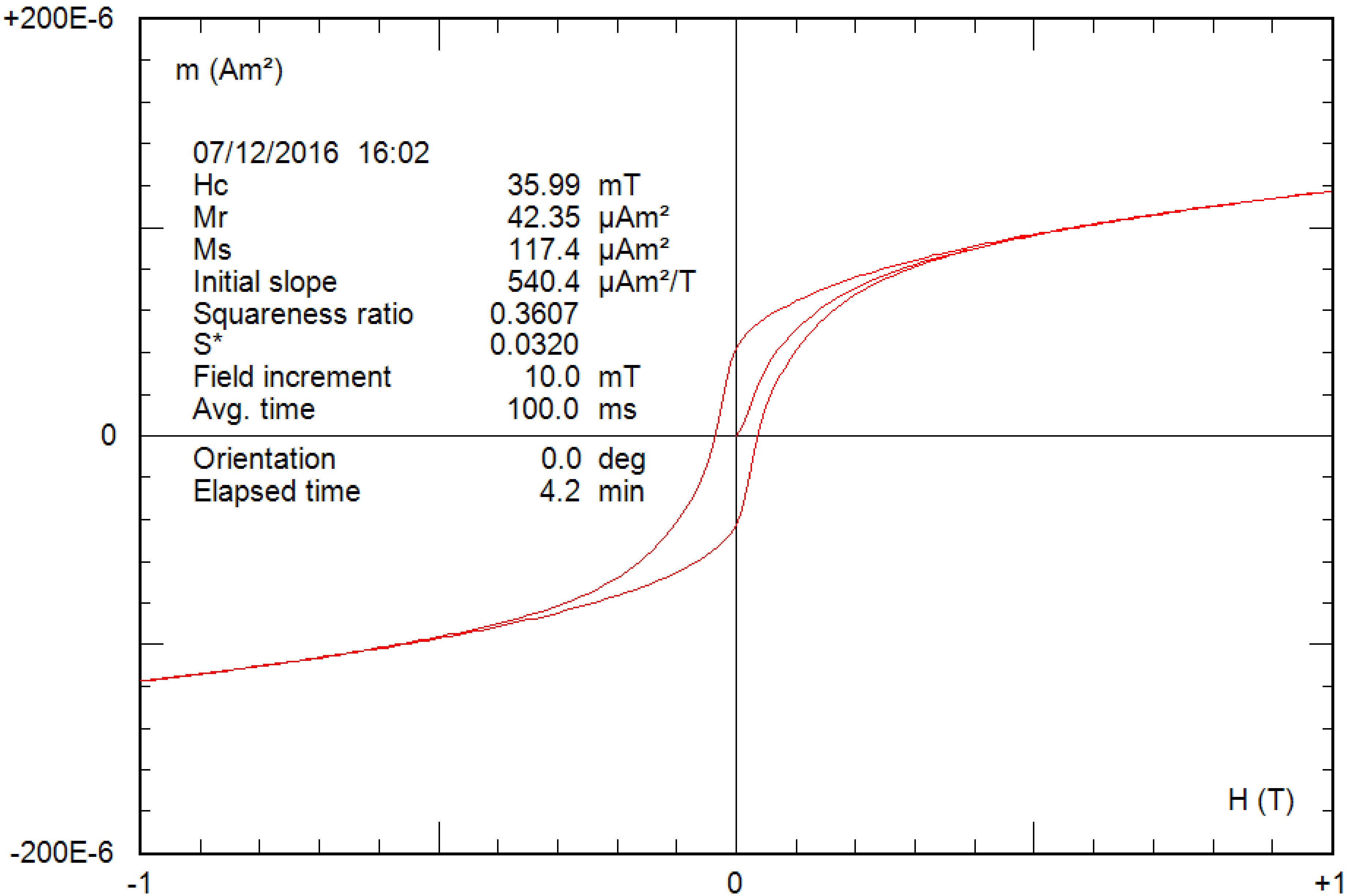

0.25 g

File: 17-04a_hyst

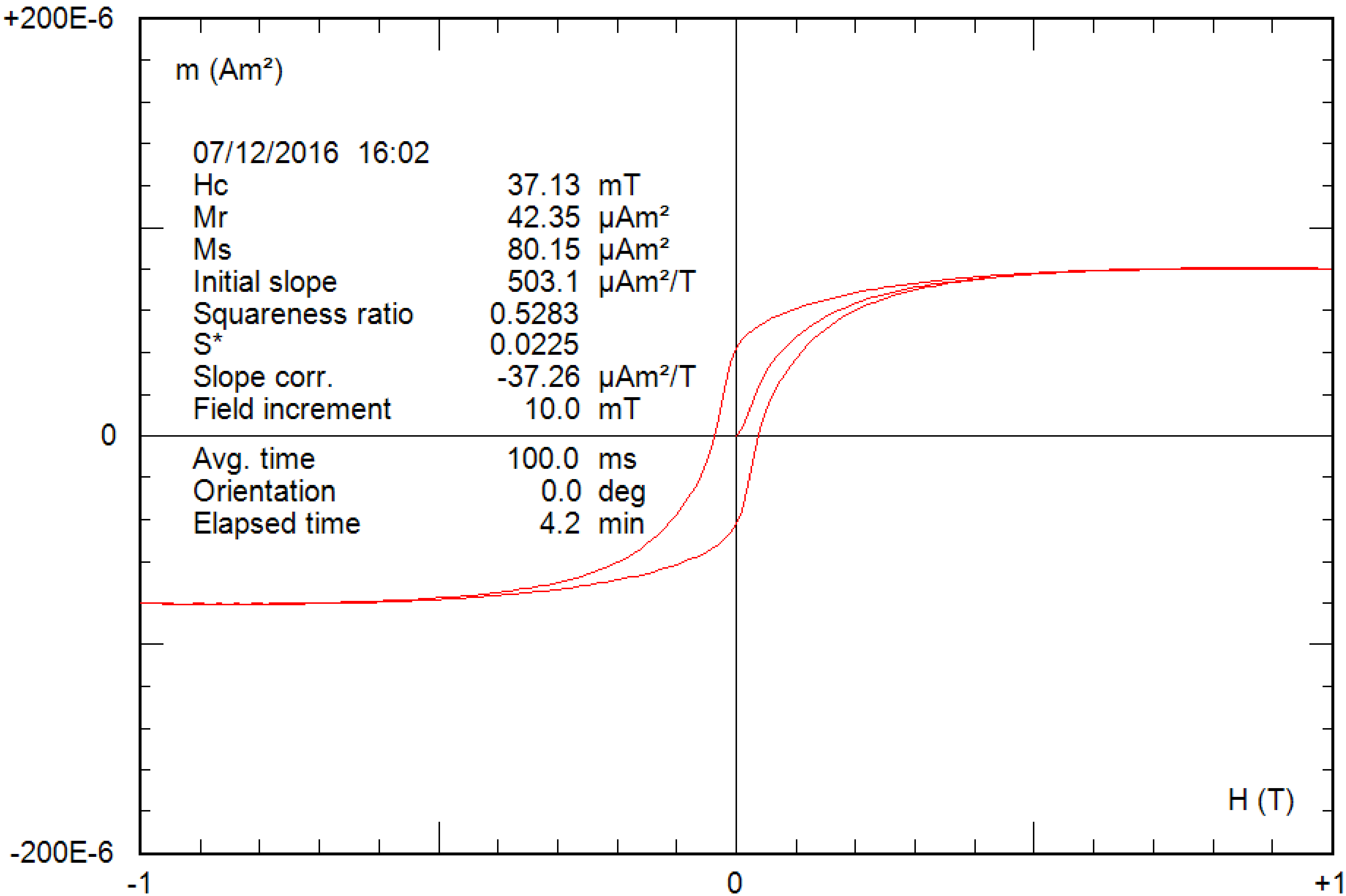

0.25 g

File: 17-04a_hyst_corr

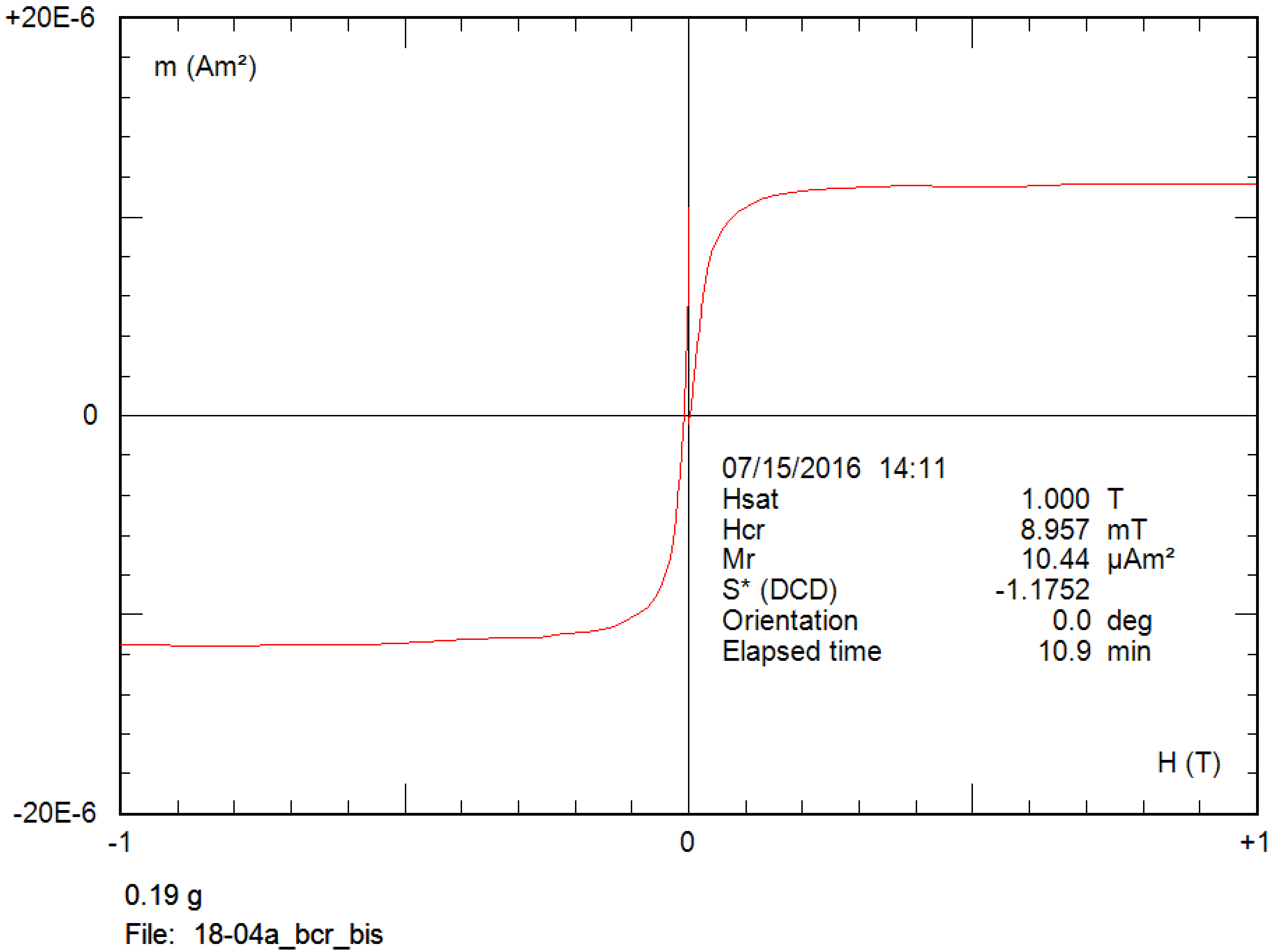
+20E-6
m (Am²)
0
-20E-6
-1
0
+1
H (T)
07/15/2016 14:11
Hsat 1.000 T
Hcr 8.957 mT
Mr 10.44 µAm²
S* (DCD) -1.1752
Orientation 0.0 deg
Elapsed time 10.9 min
0.19 g
File: 18-04a_bcr_bis

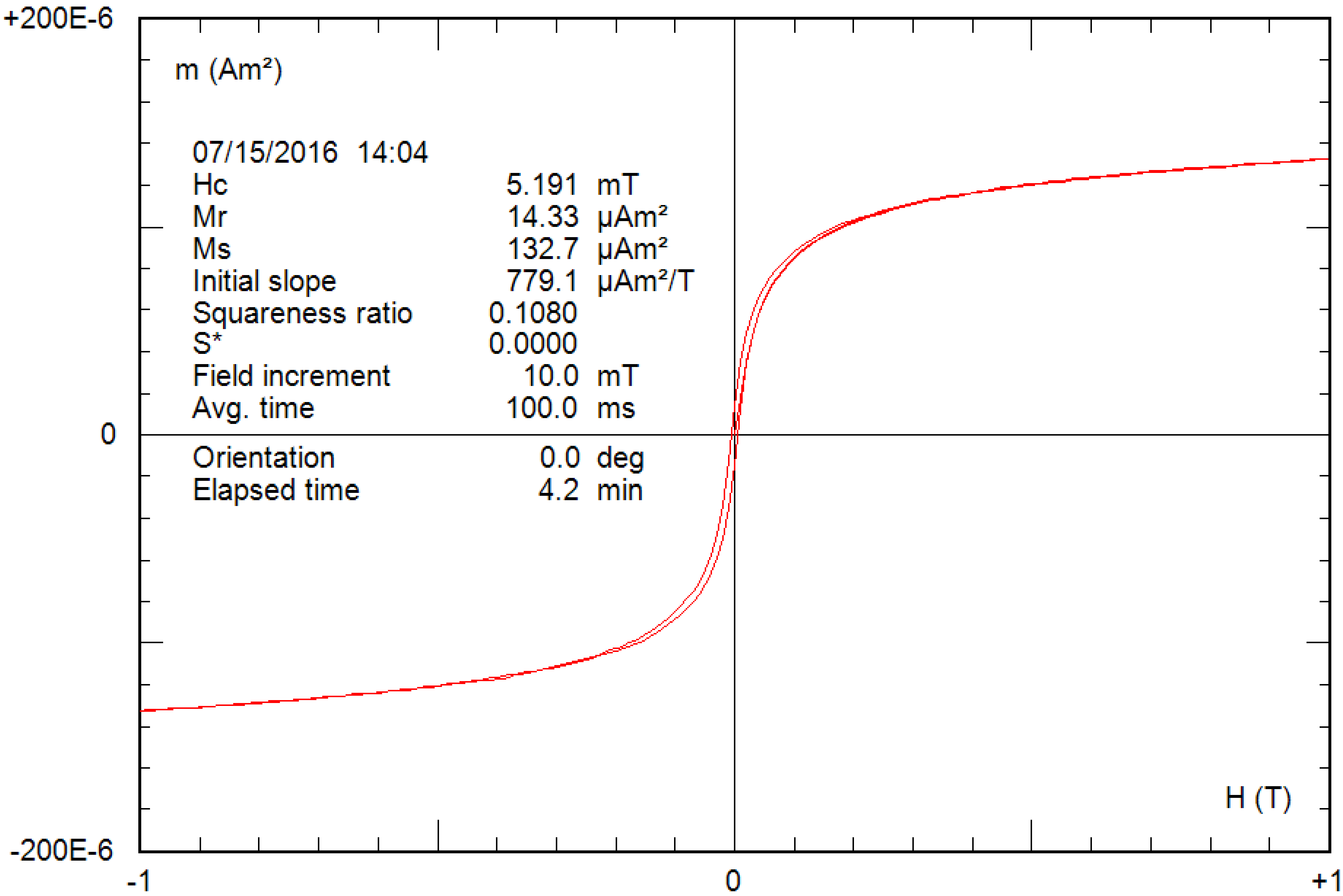

0.19 g

File: 18-04a_hyst_bis

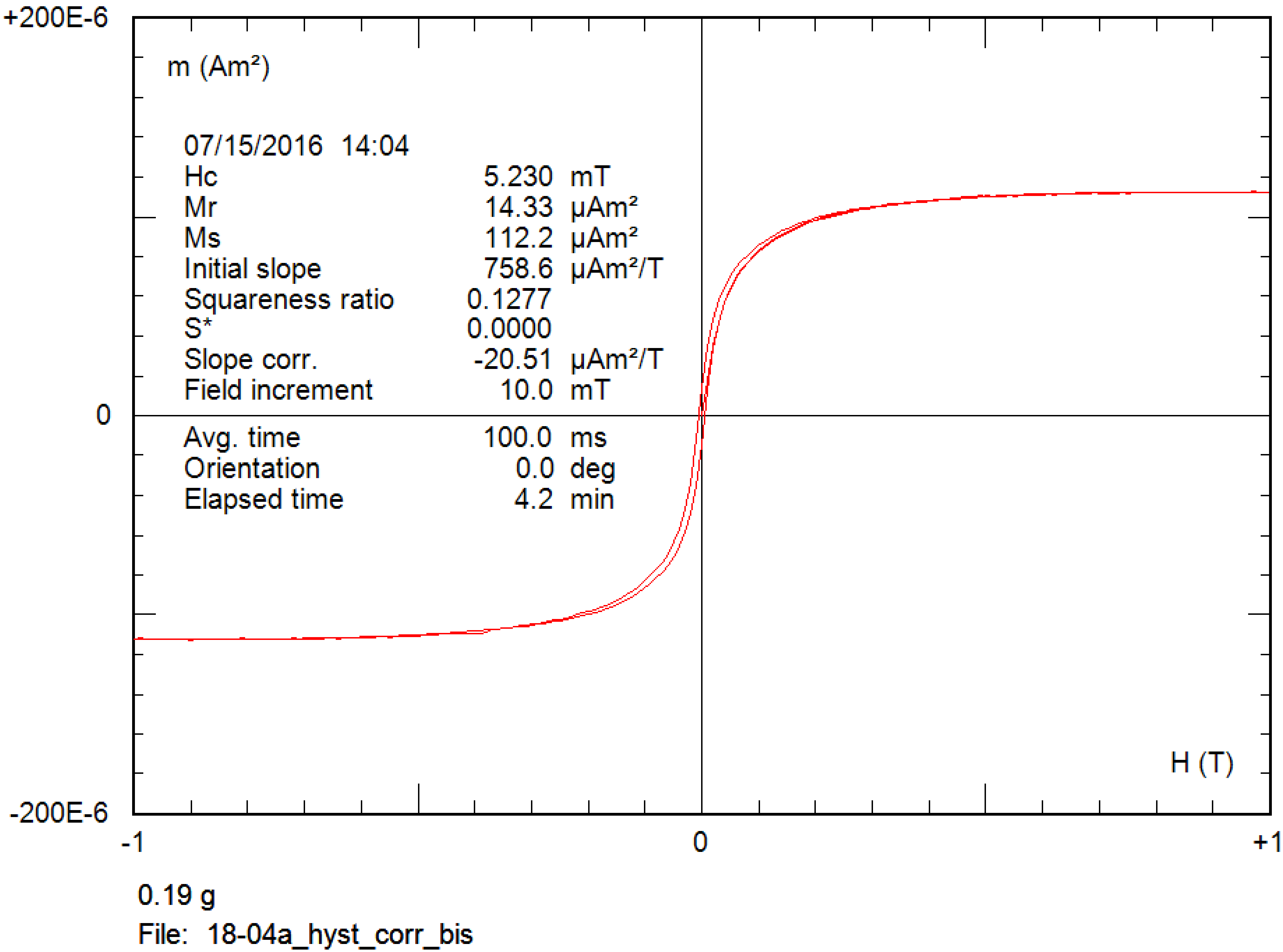

+200E-6
m (Am²)
07/15/2016 14:04
Hc 5.230 mT
Mr 14.33 µAm²
Ms 112.2 µAm²
Initial slope 758.6 µAm²/T
Squareness ratio 0.1277
S* 0.0000
Slope corr. -20.51 µAm²/T
Field increment 10.0 mT
0
Avg. time 100.0 ms
Orientation 0.0 deg
Elapsed time 4.2 min
H (T)
-200E-6
-1
0
+1
0.19 g
File: 18-04a_hyst_corr_bis

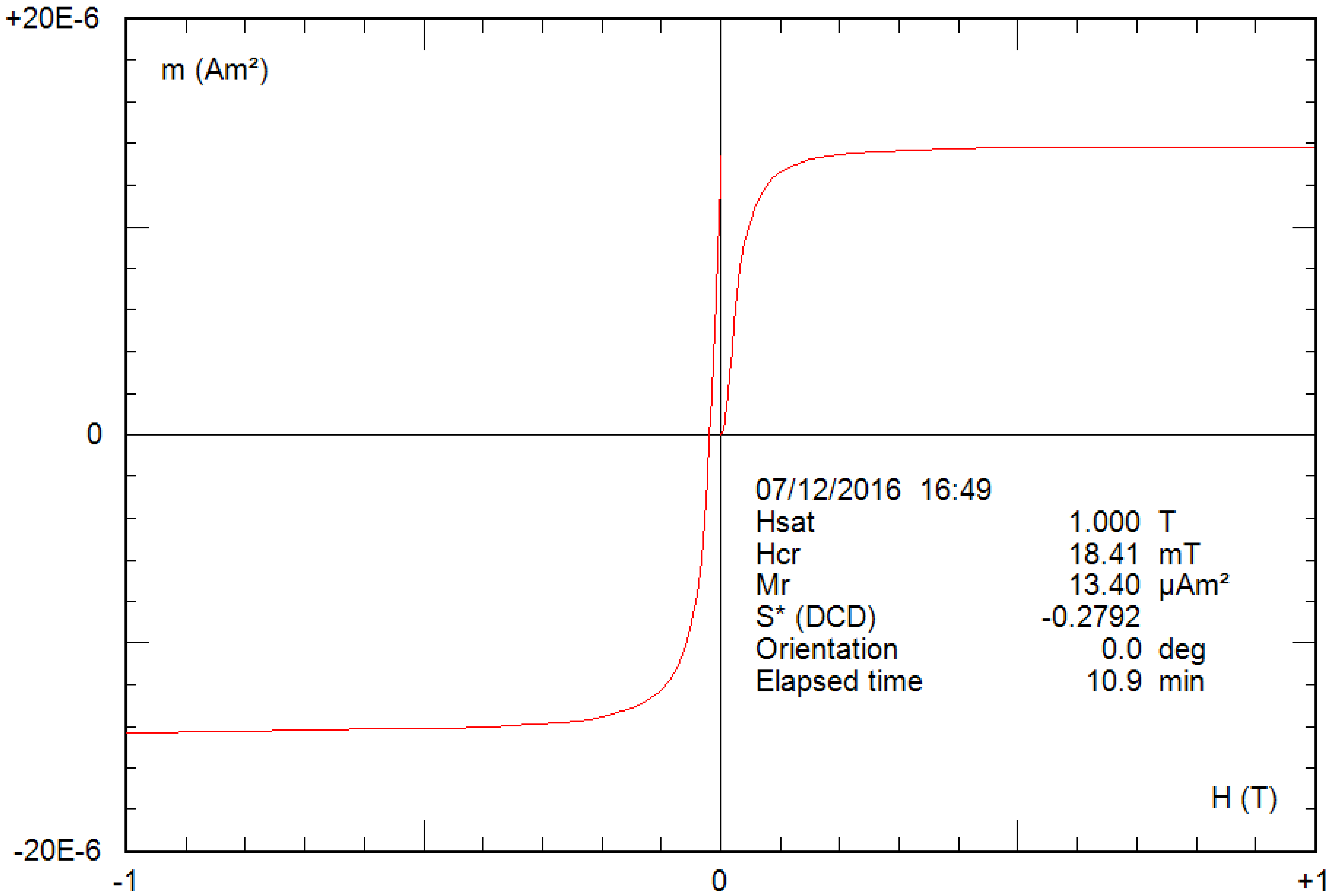

0.25 g

File: 19-04a_bcr

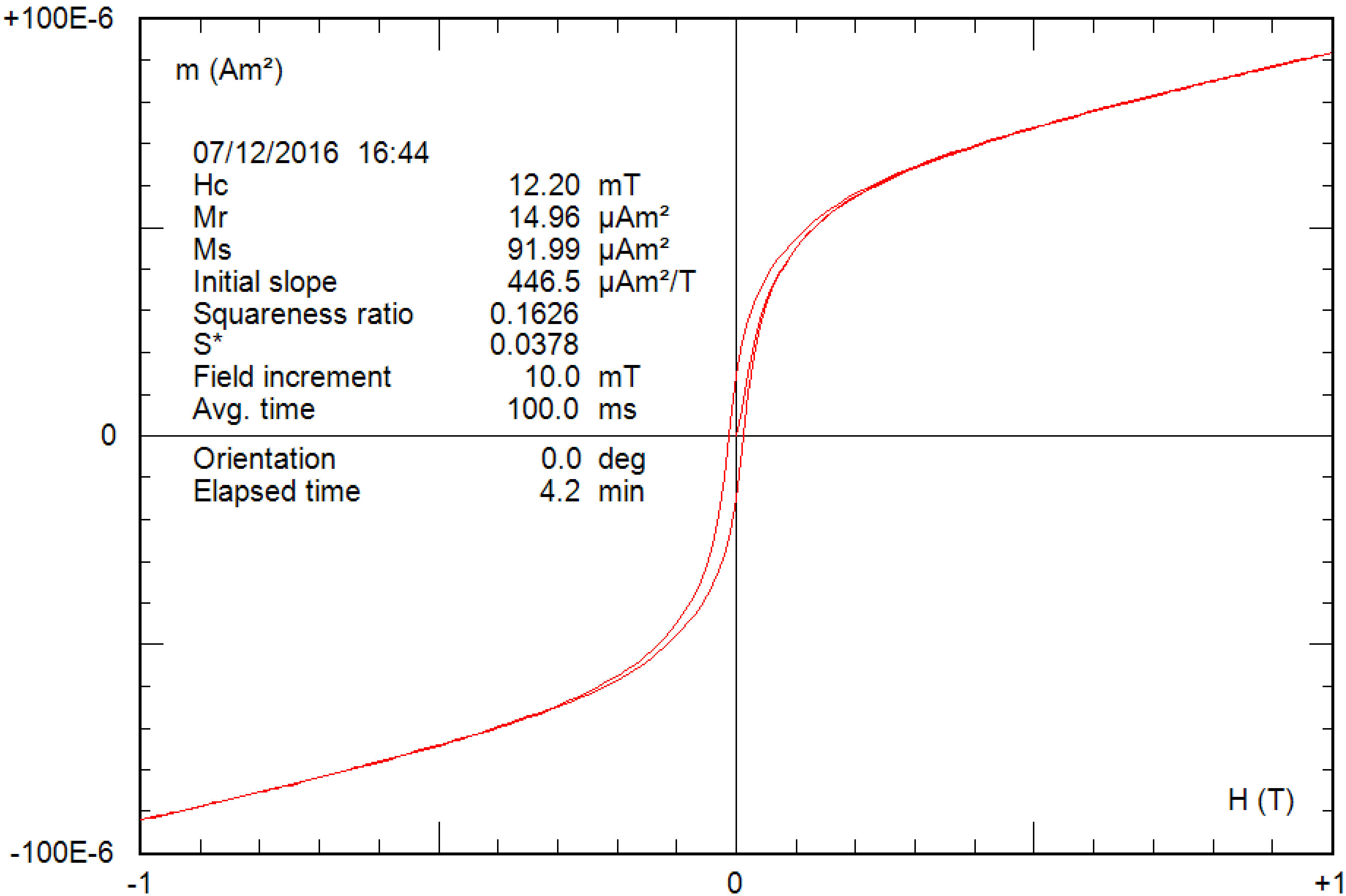

0.25 g

File: 19-04a_hyst

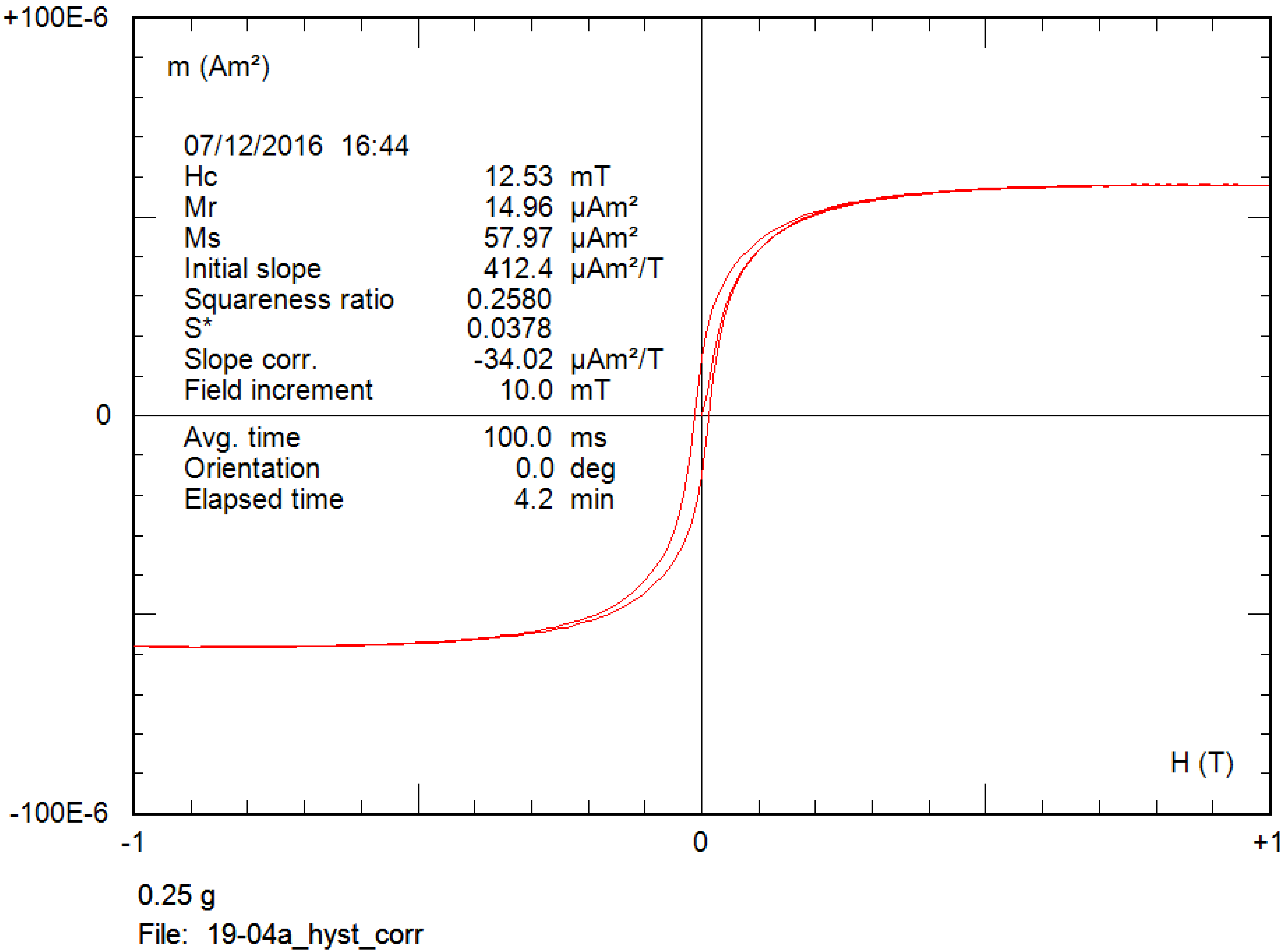
+100E-6
m (Am²)
07/12/2016 16:44
Hc 12.53 mT
Mr 14.96 µAm²
Ms 57.97 µAm²
Initial slope 412.4 µAm²/T
Squareness ratio 0.2580
S* 0.0378
Slope corr. -34.02 µAm²/T
Field increment 10.0 mT
0
Avg. time 100.0 ms
Orientation 0.0 deg
Elapsed time 4.2 min
H (T)
-100E-6
-1
0
+1
0.25 g
File: 19-04a_hyst_corr

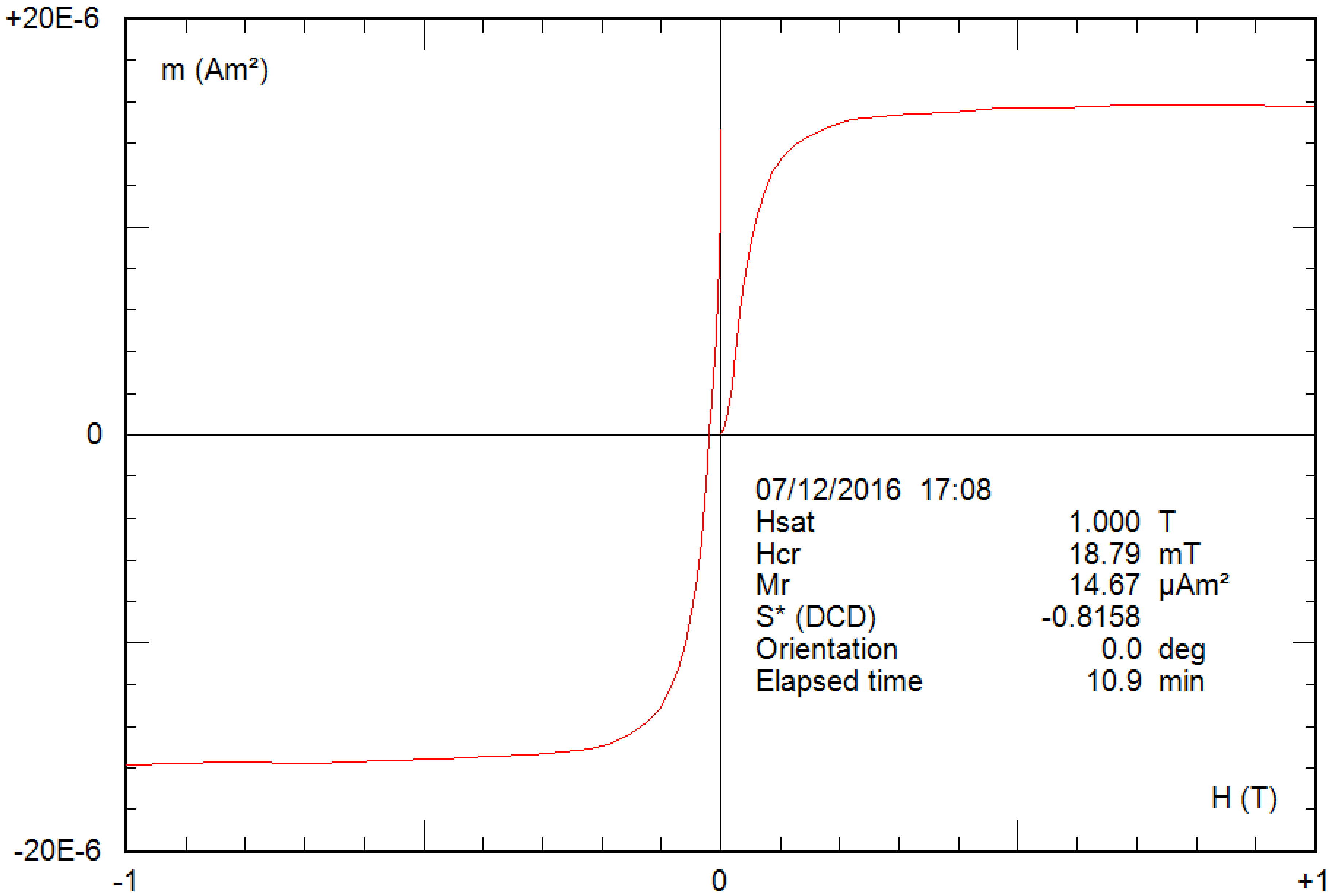

0.25 g

File: 20-04a_bcr

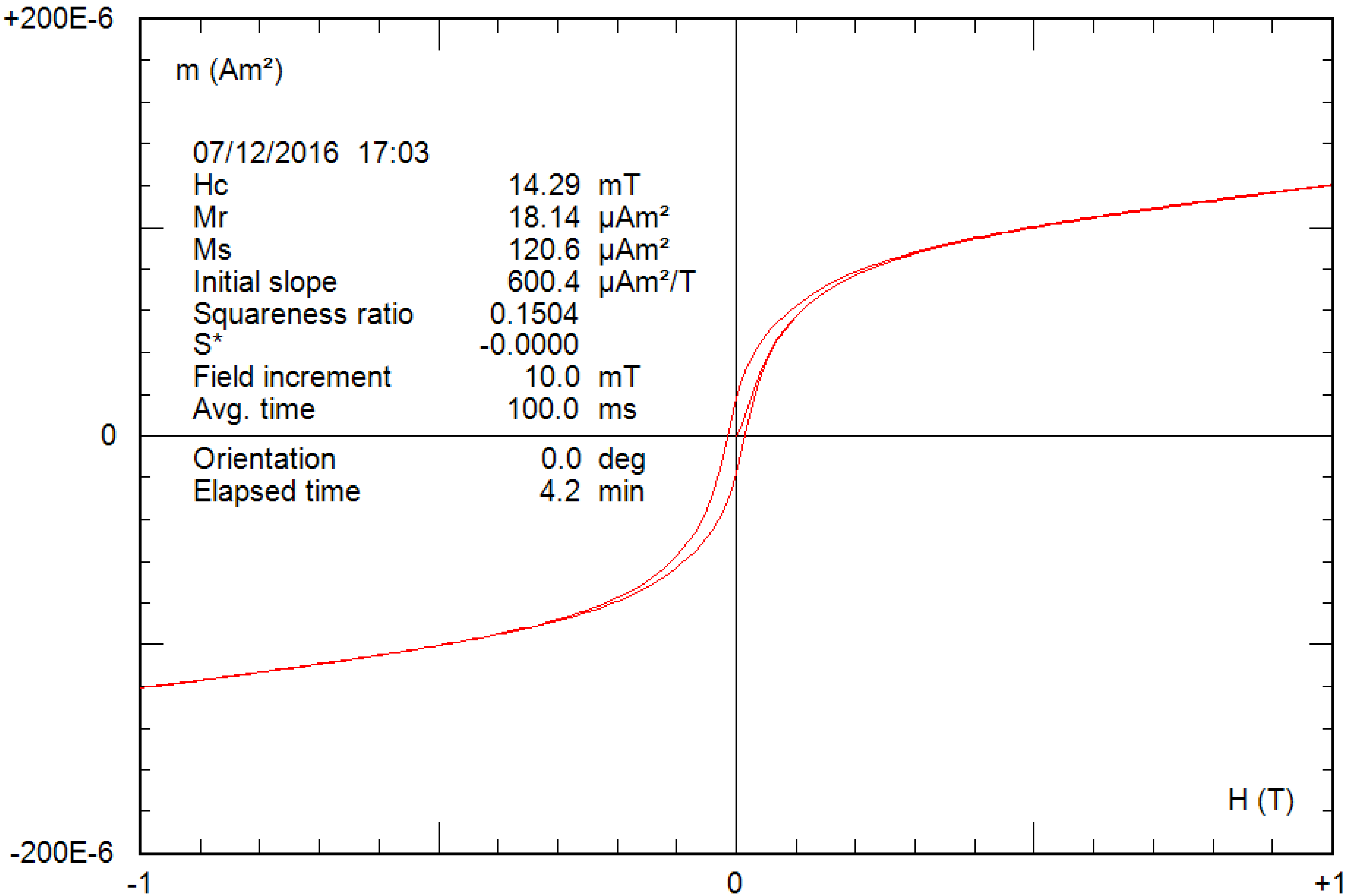

0.25 g

File: 20-04a_hyst

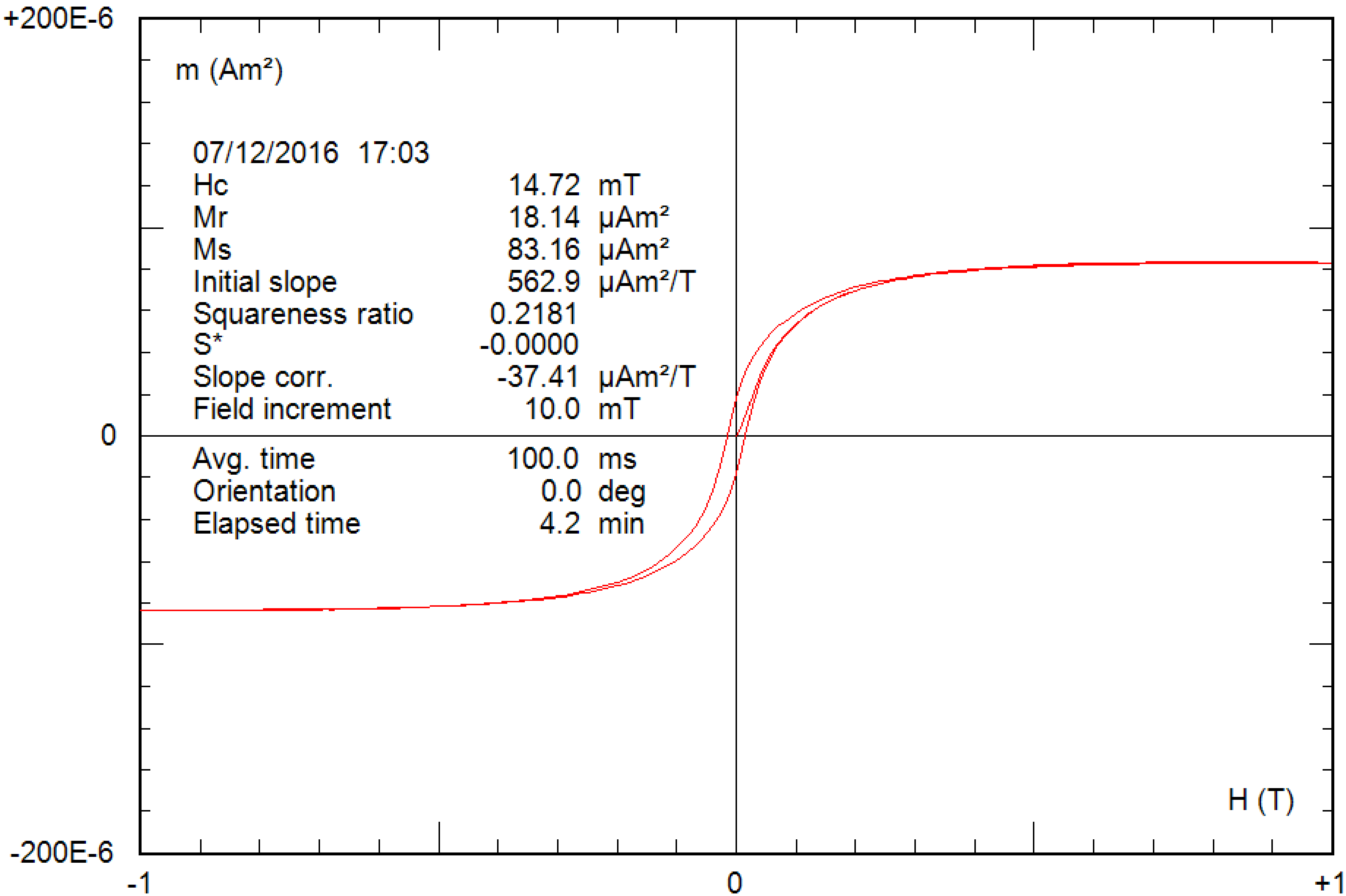

0.25 g

File: 20-04a_hyst_corr

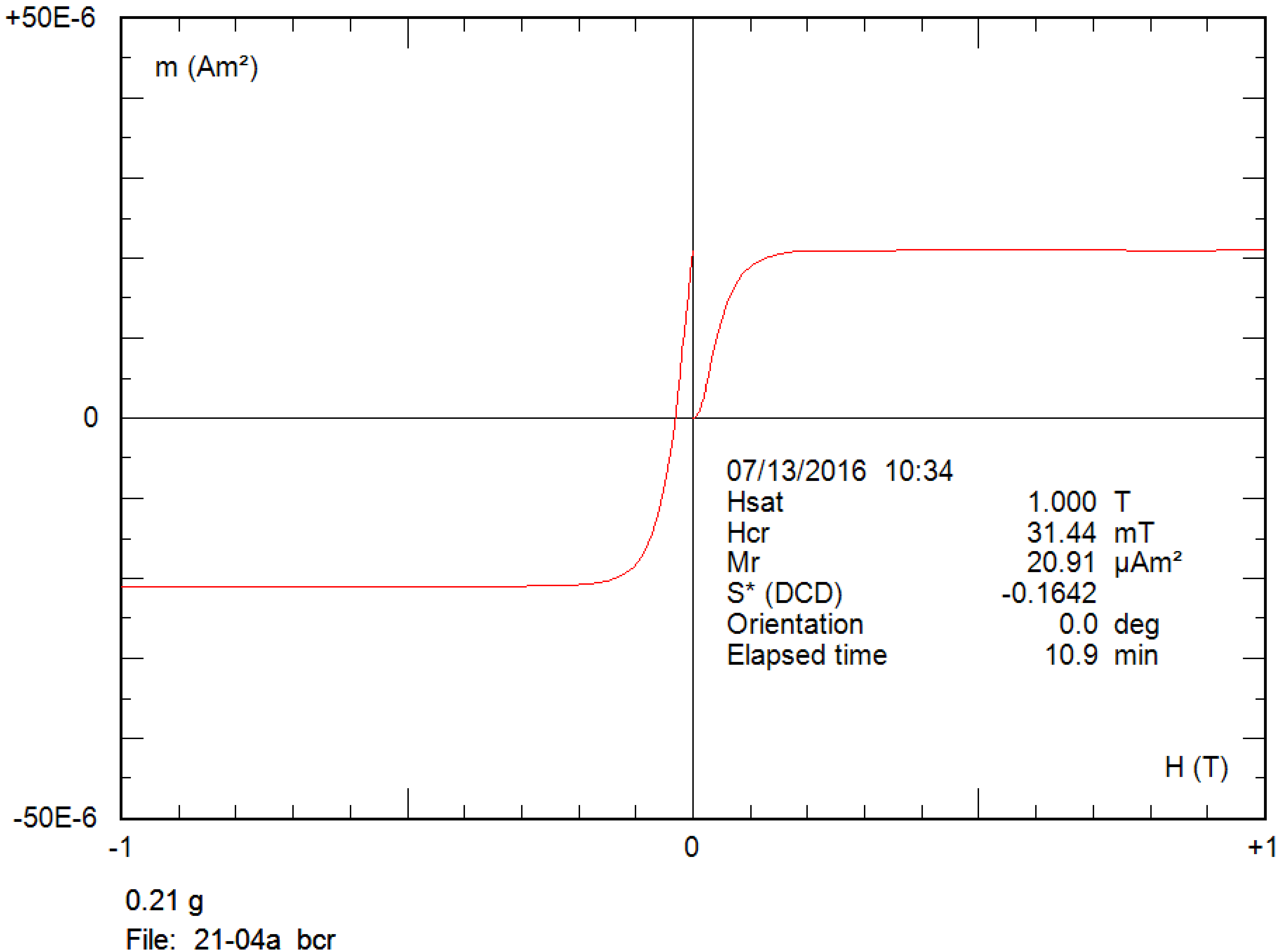
+50E-6
m (Am²)
0
-50E-6
-1
0
+1
H (T)
07/13/2016 10:34
Hsat 1.000 T
Hcr 31.44 mT
Mr 20.91 µAm²
S* (DCD) -0.1642
Orientation 0.0 deg
Elapsed time 10.9 min
0.21 g
File: 21-04a_bcr

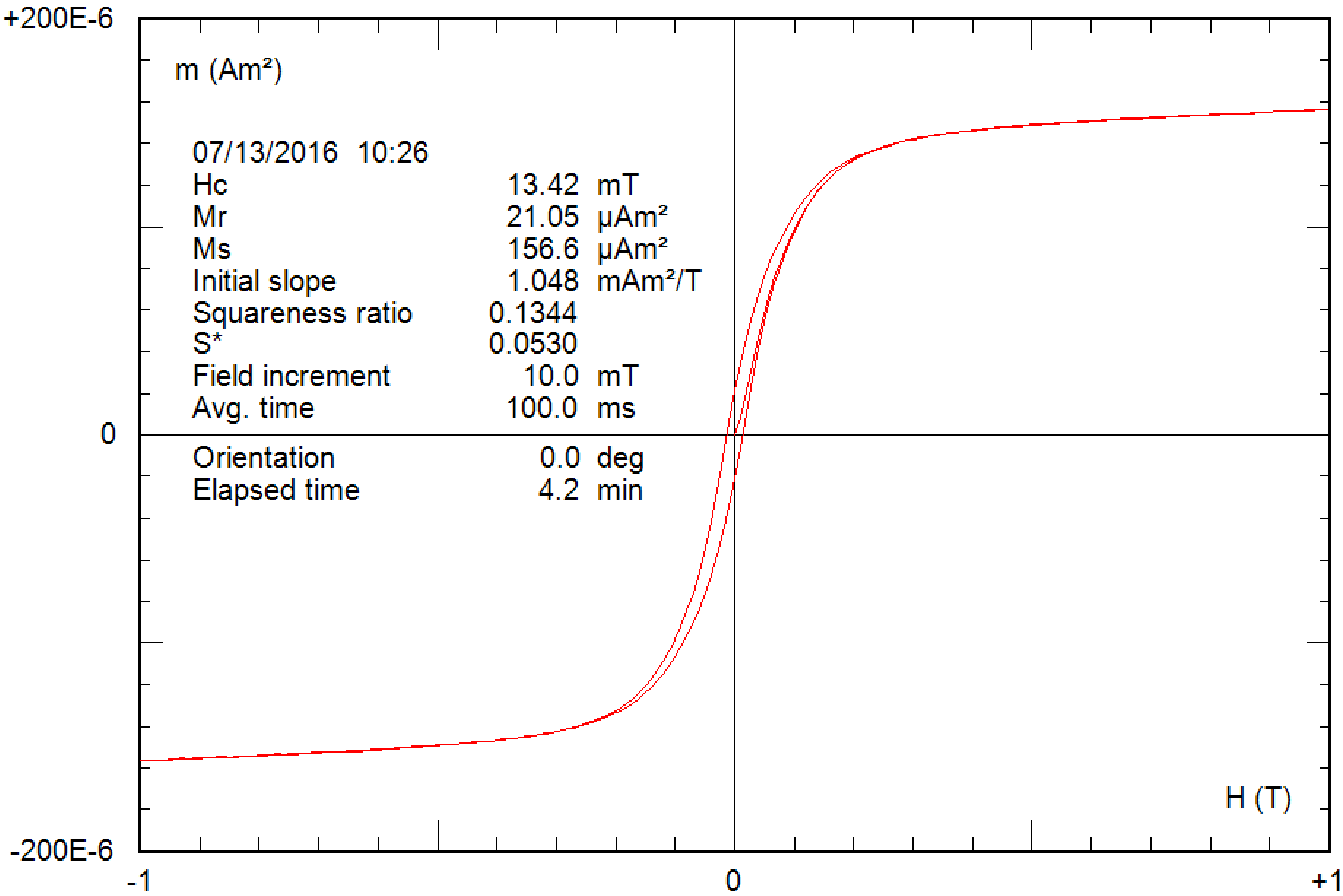

0.21 g

File: 21-04a_hyst

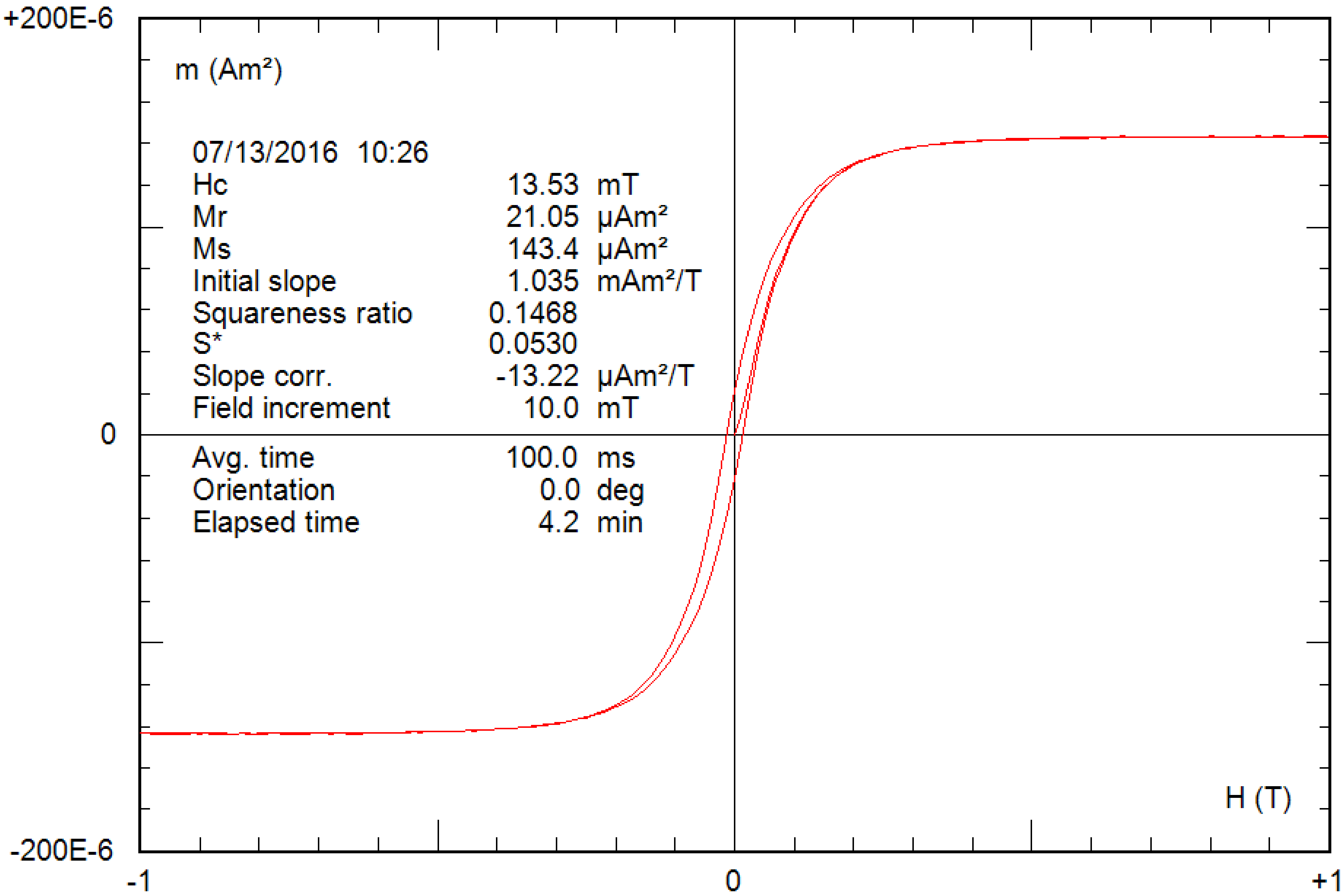

0.21 g

File: 21-04a_hyst_corr

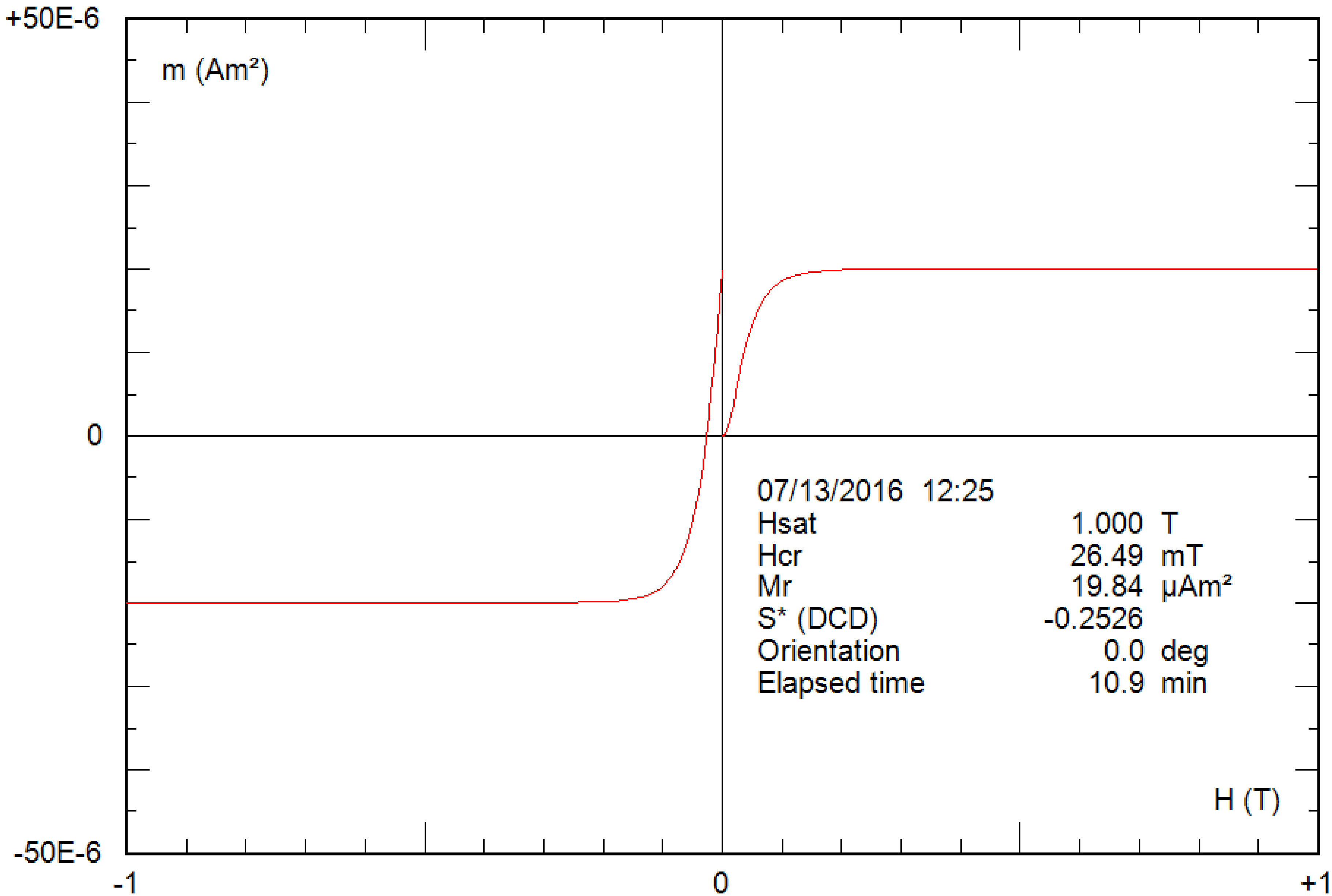

0.24 g

File: 22-04a_bis bcr

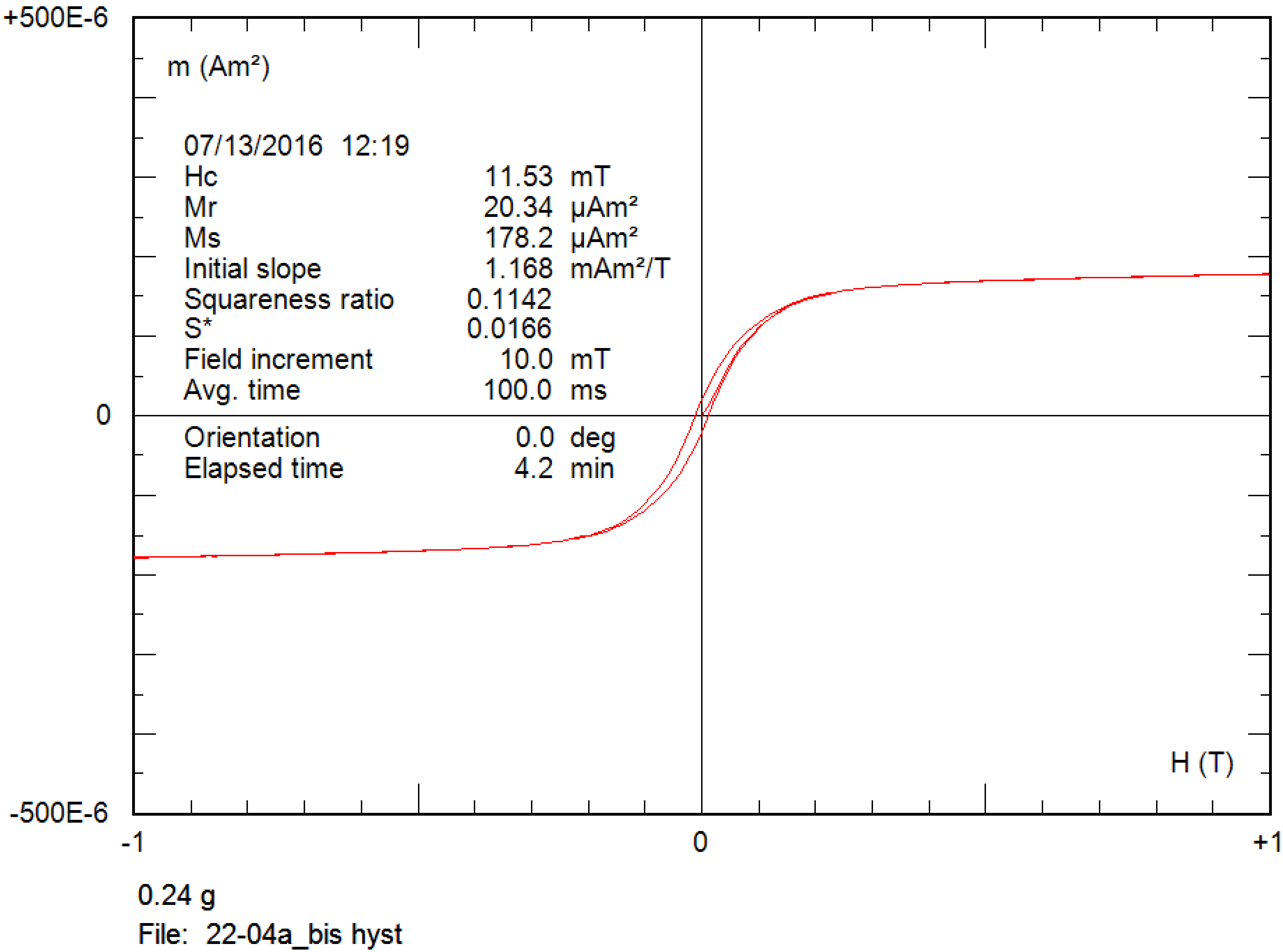
+500E-6
m (Am²)
07/13/2016 12:19
Hc 11.53 mT
Mr 20.34 µAm²
Ms 178.2 µAm²
Initial slope 1.168 mAm²/T
Squareness ratio 0.1142
S* 0.0166
Field increment 10.0 mT
Avg. time 100.0 ms
0
Orientation 0.0 deg
Elapsed time 4.2 min
H (T)
-500E-6
-1
0
+1
0.24 g
File: 22-04a_bis hyst

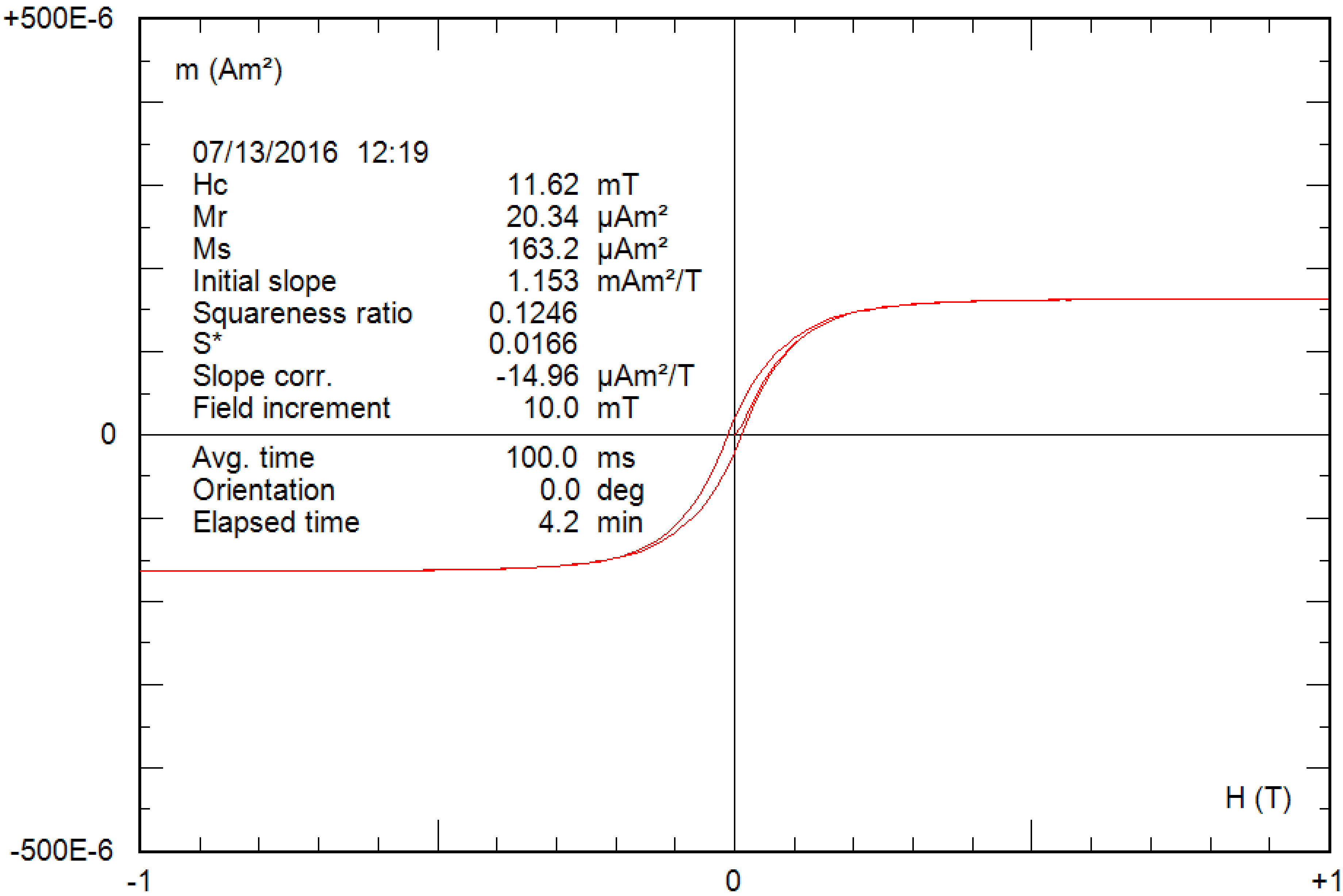

0.24 g

File: 22-04a_bis hyst_corr

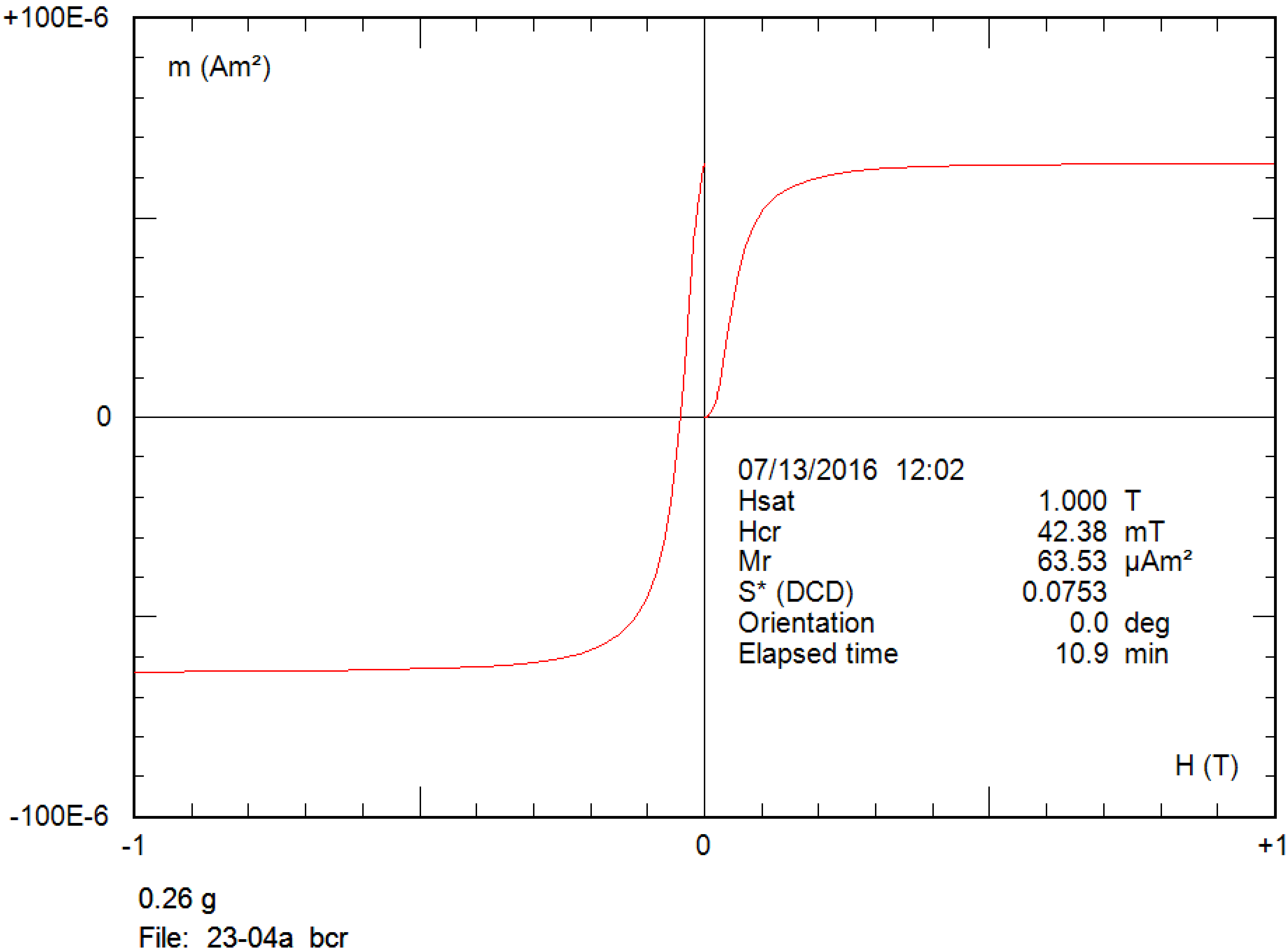
+100E-6
m (Am²)
0
-100E-6
07/13/2016 12:02
Hsat 1.000 T
Hcr 42.38 mT
Mr 63.53 µAm²
S* (DCD) 0.0753
Orientation 0.0 deg
Elapsed time 10.9 min
H (T)
-1
0
+1
0.26 g
File: 23-04a_bcr

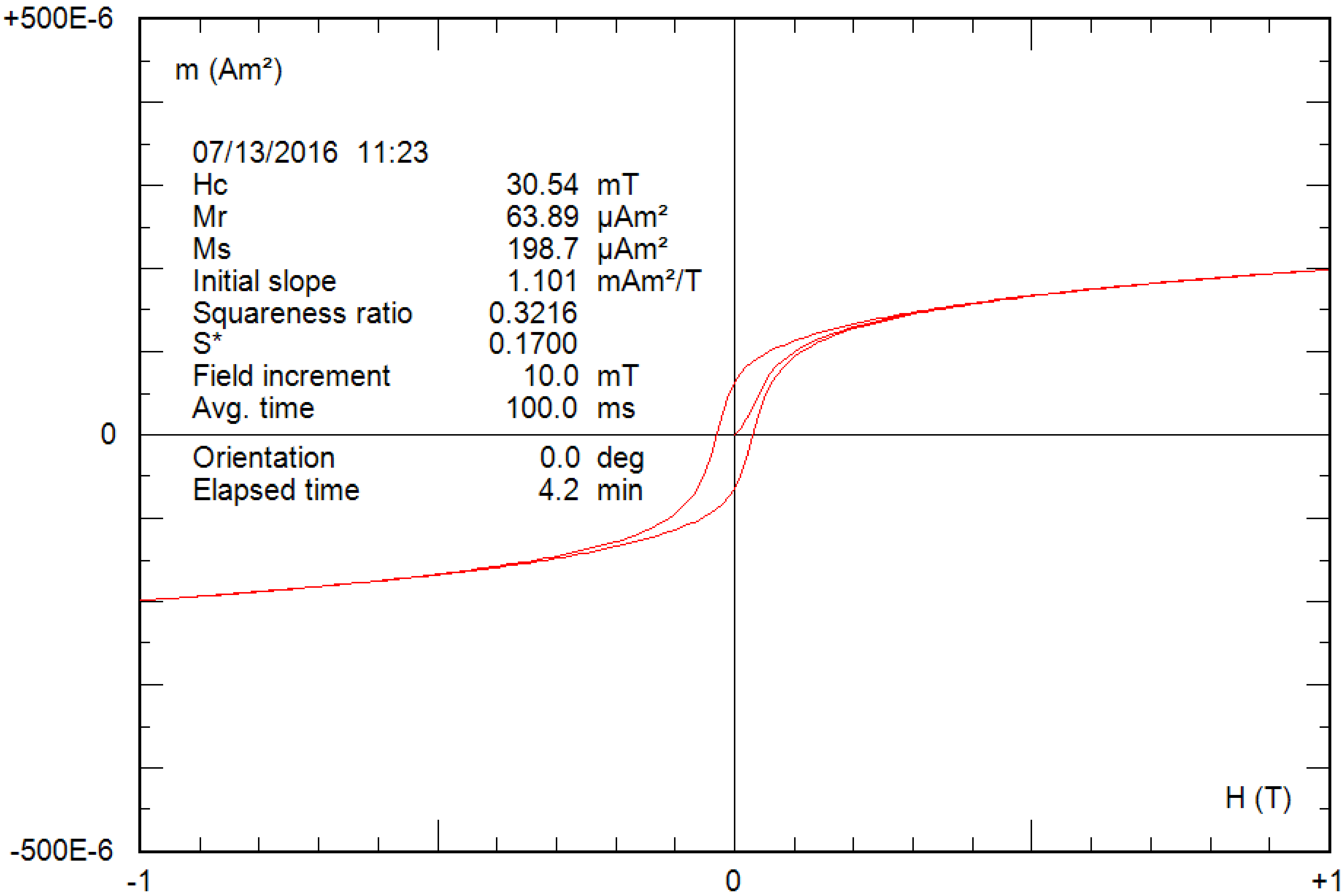

0.26 g

File: 23-04a_hyst

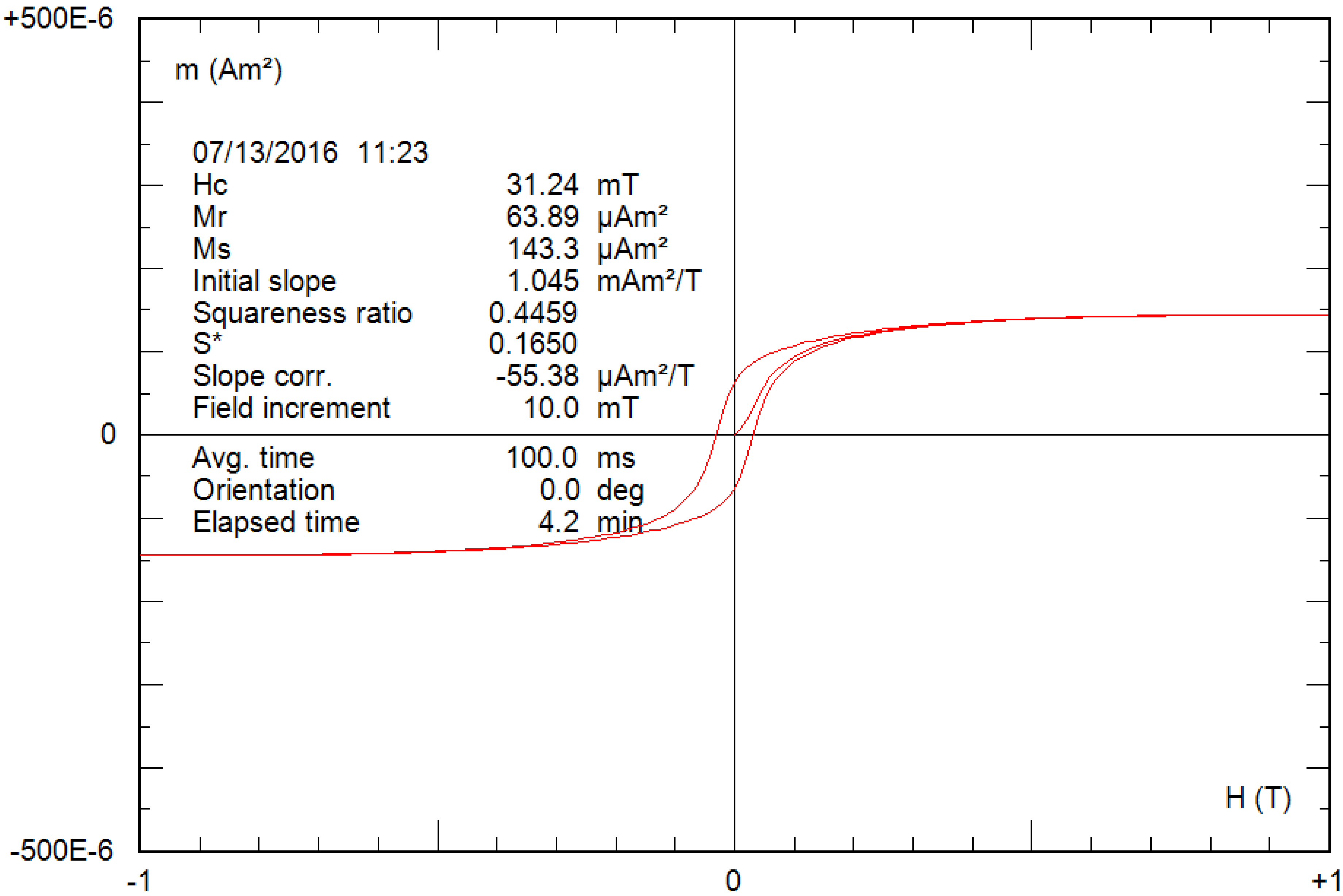

0.26 g

File: 23-04a_hyst_corr

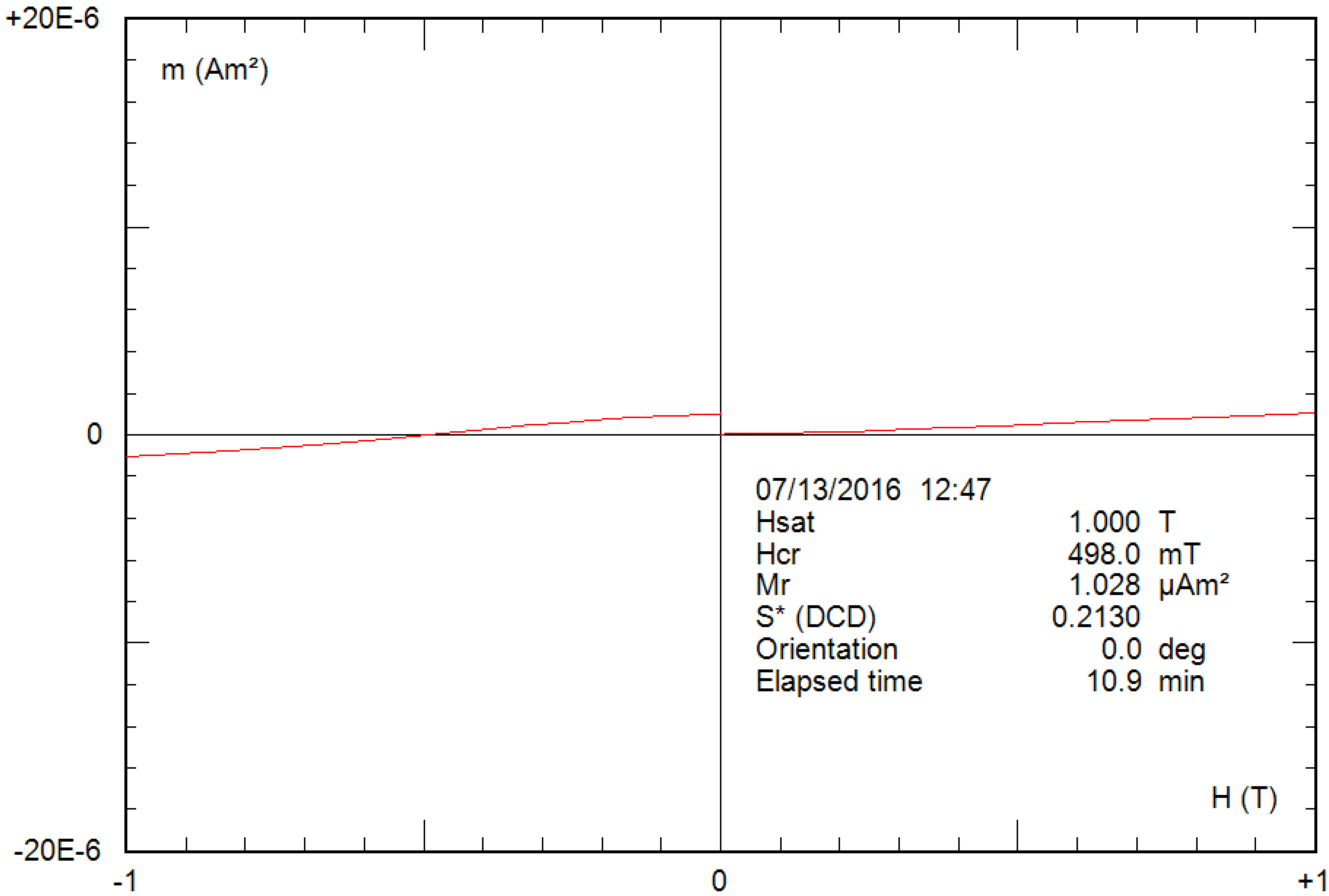

0.24 g

File: 24-08b_bcr

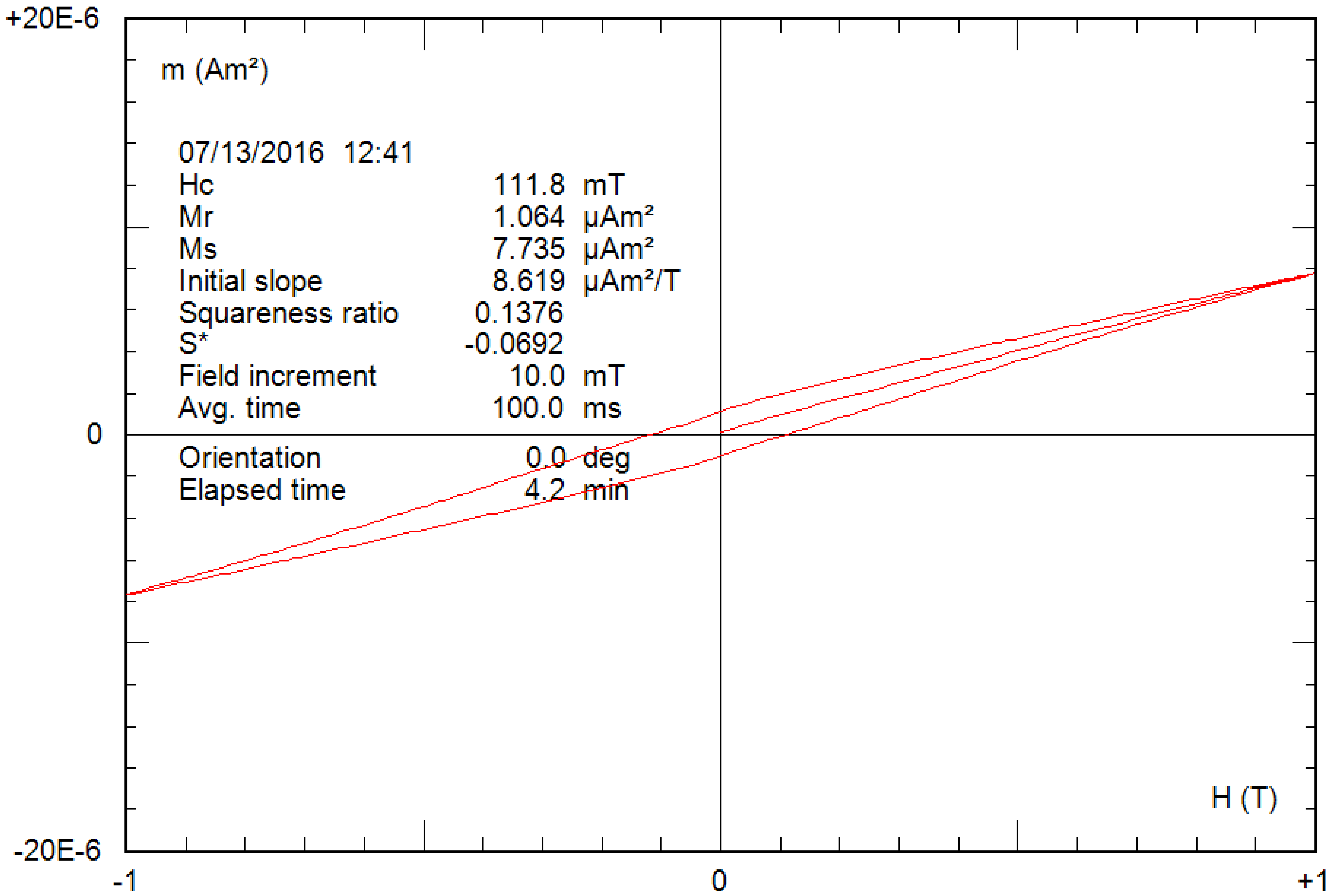

0.24 g

File: 24-08b_hyst

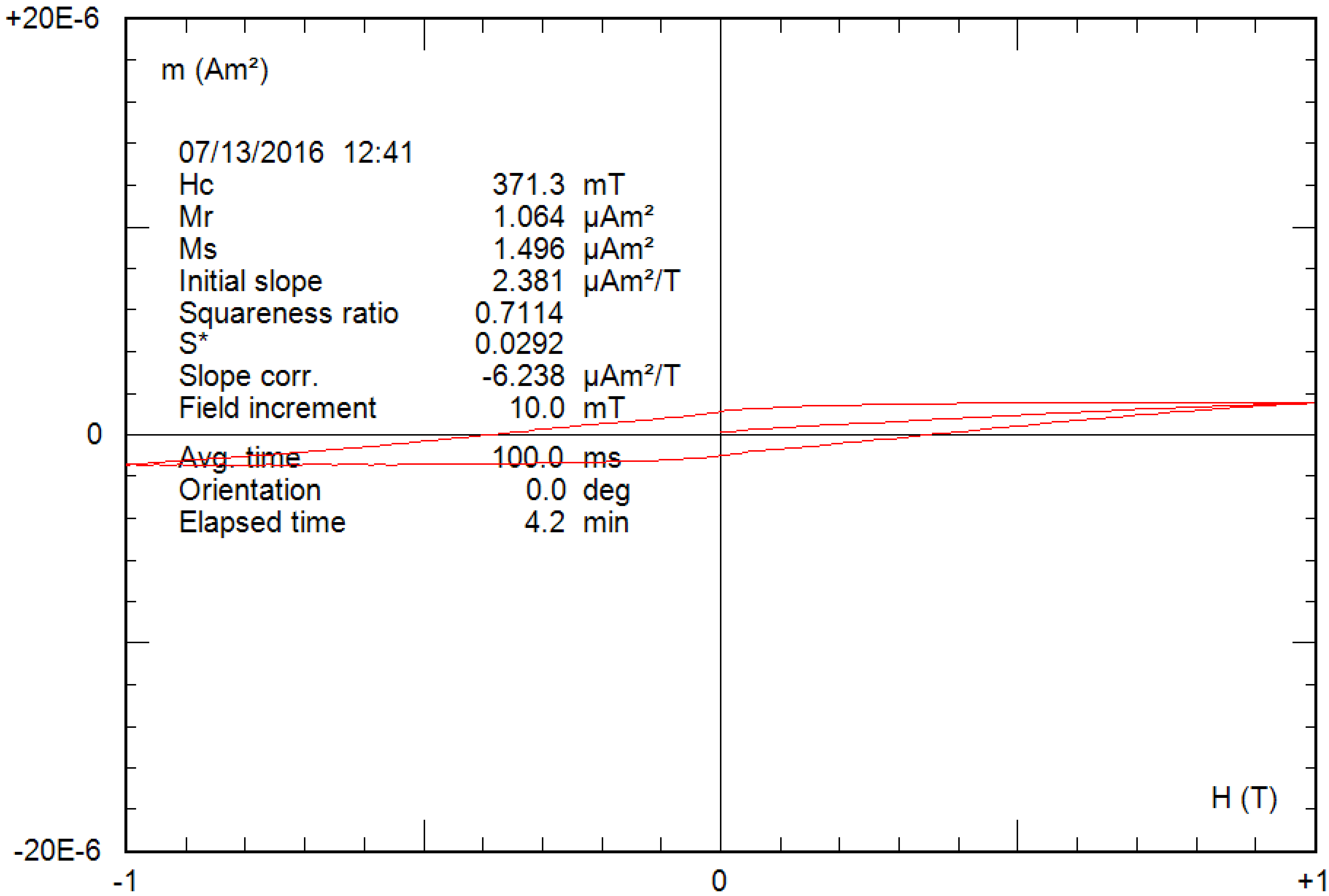

0.24 g

File: 24-08b_hyst_corr

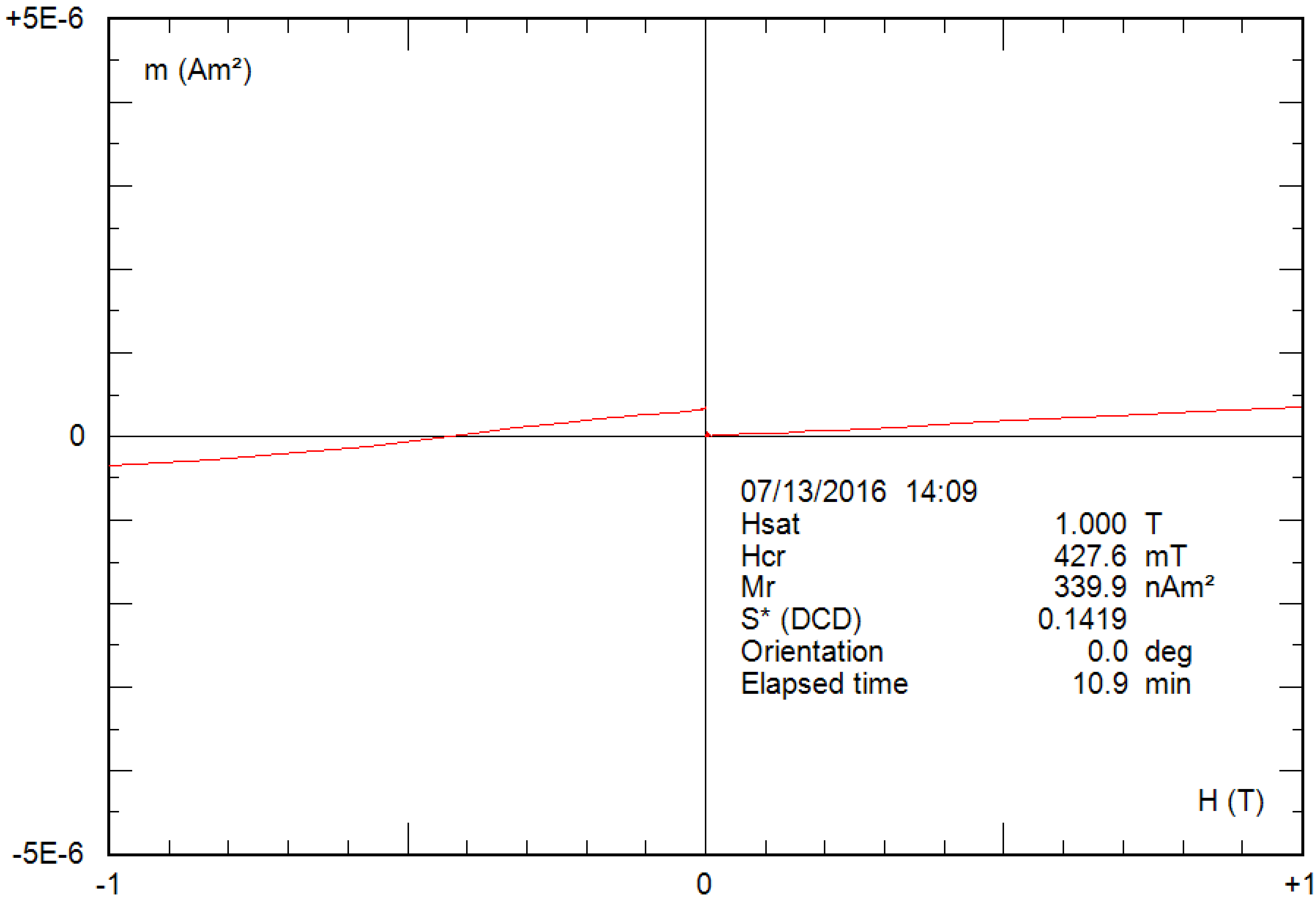

0.26 g

File: 25-04c_bcr

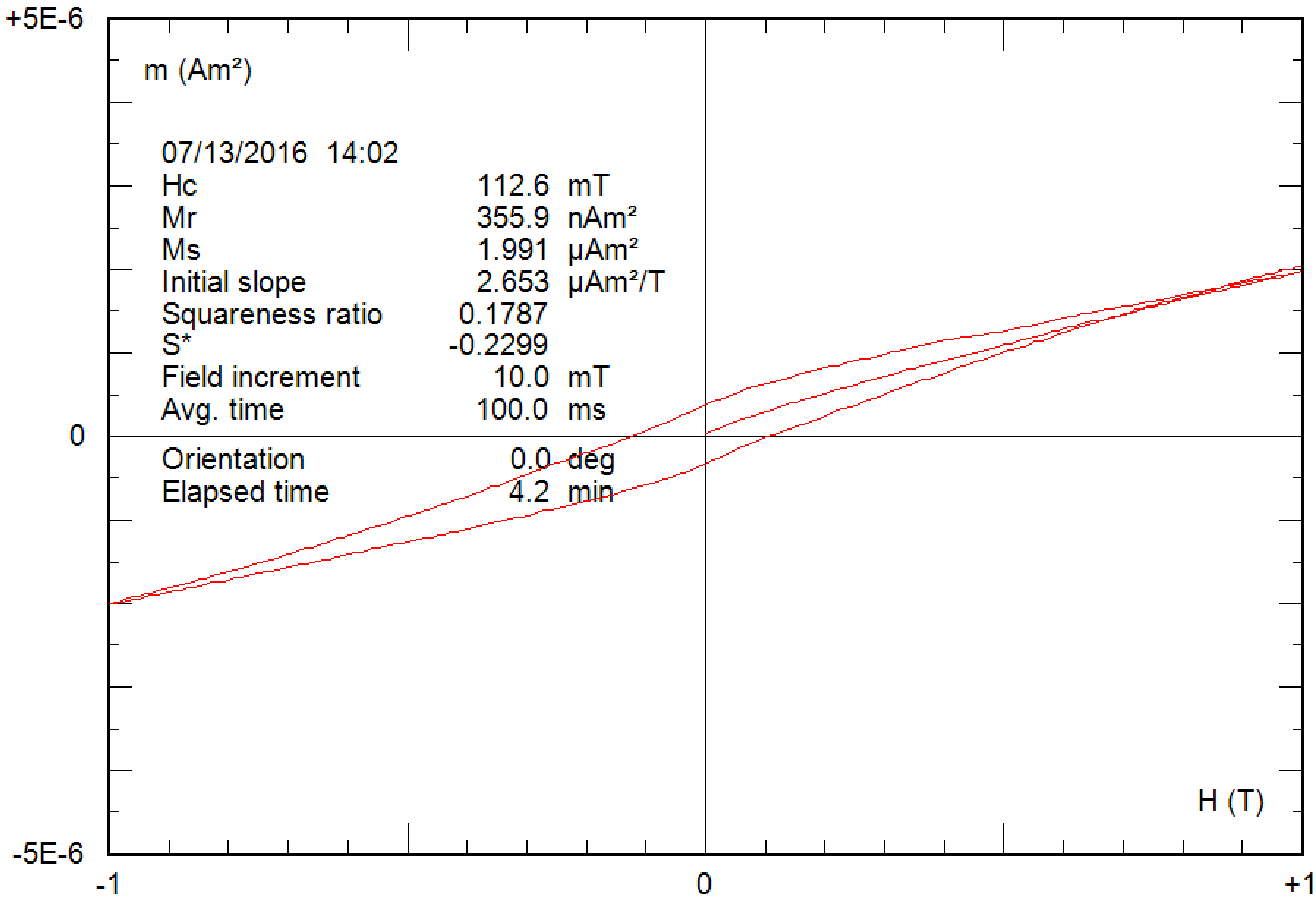

0.26 g

File: 25-04c_hyst

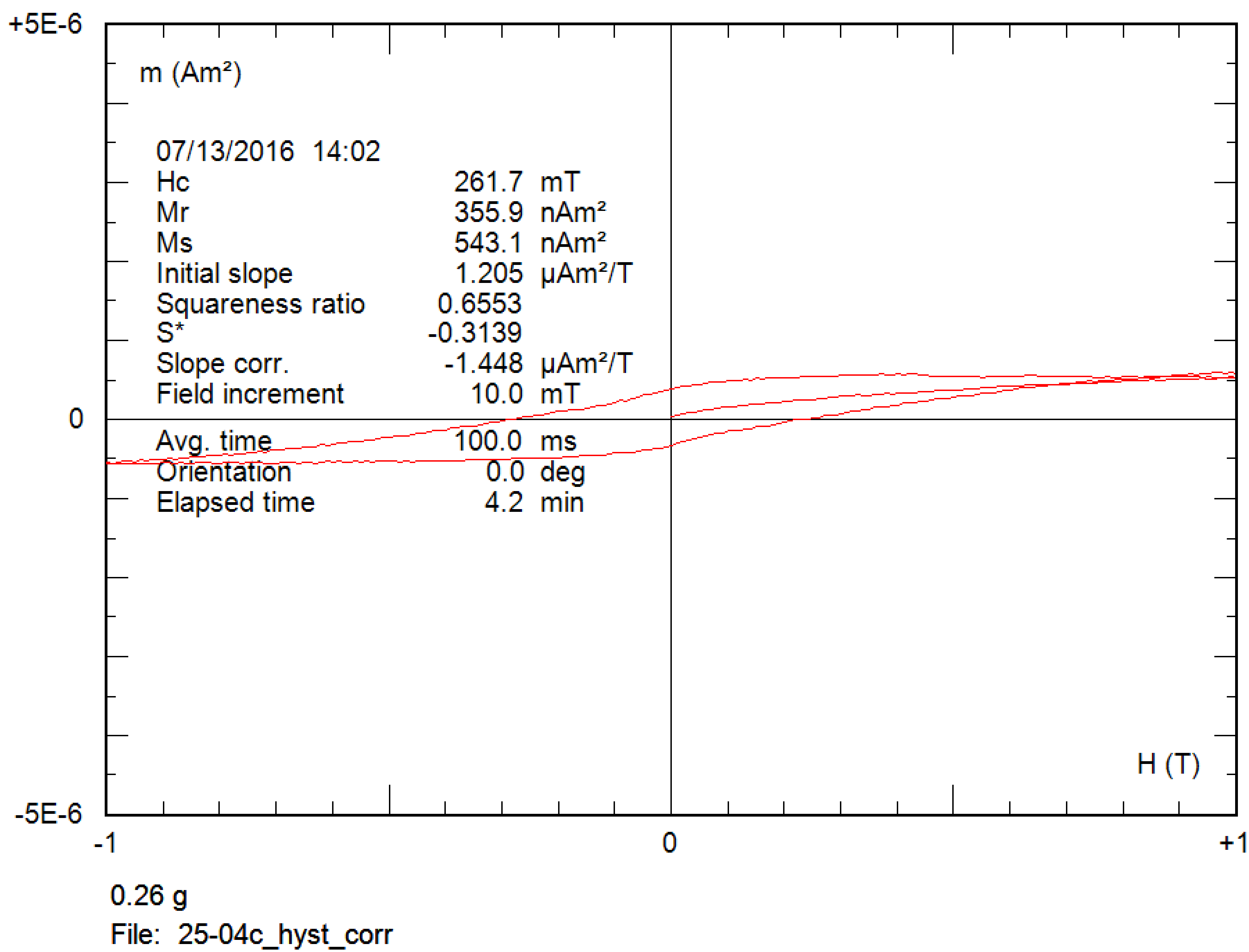
+5E-6
m (Am²)
07/13/2016 14:02
Hc 261.7 mT
Mr 355.9 nAm²
Ms 543.1 nAm²
Initial slope 1.205 µAm²/T
Squareness ratio 0.6553
S* -0.3139
Slope corr. -1.448 µAm²/T
Field increment 10.0 mT
0
Avg. time 100.0 ms
Orientation 0.0 deg
Elapsed time 4.2 min
H (T)
-5E-6
-1
0
+1
0.26 g
File: 25-04c_hyst_corr

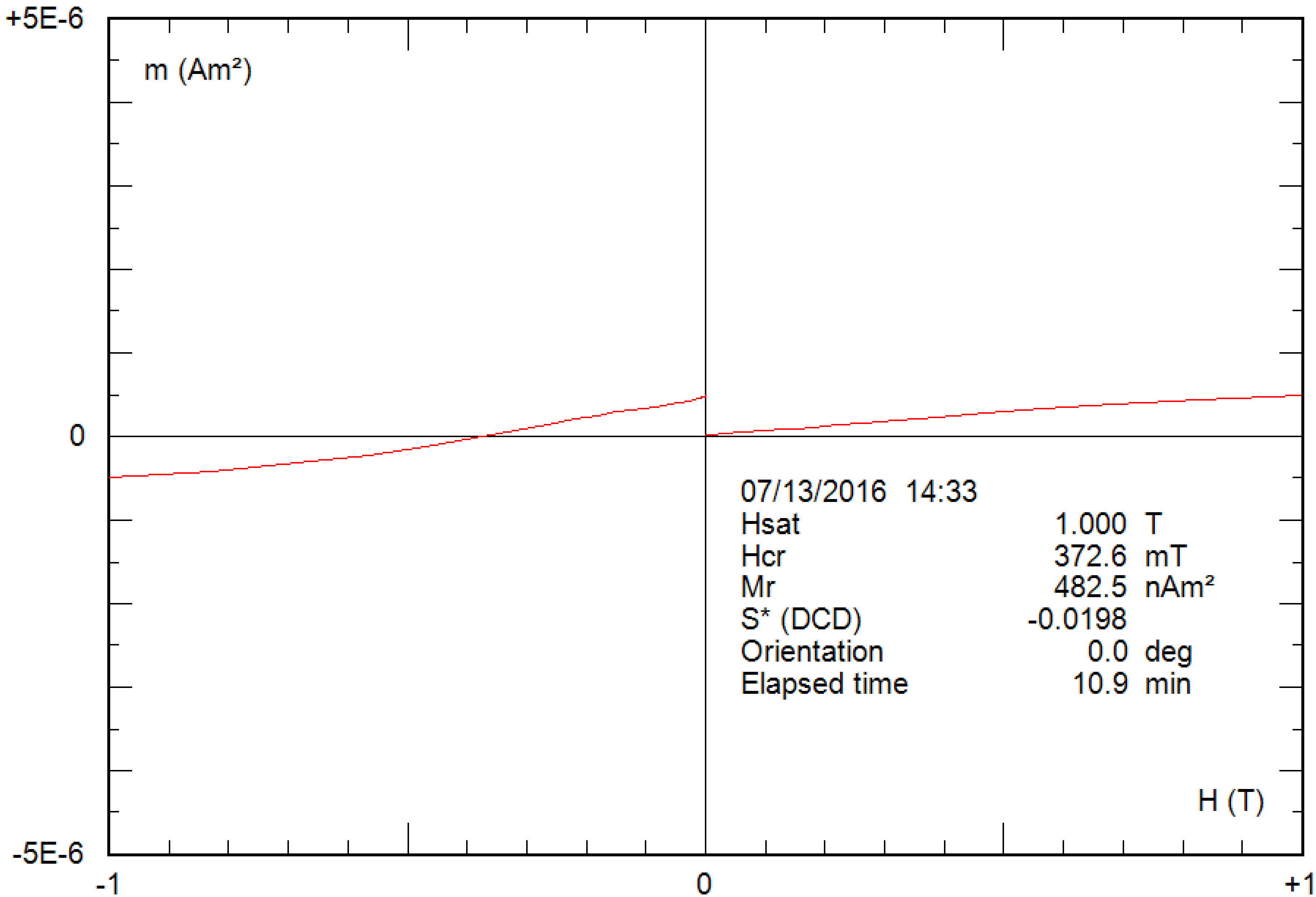

0.25 g

File: 26-04c_bcr

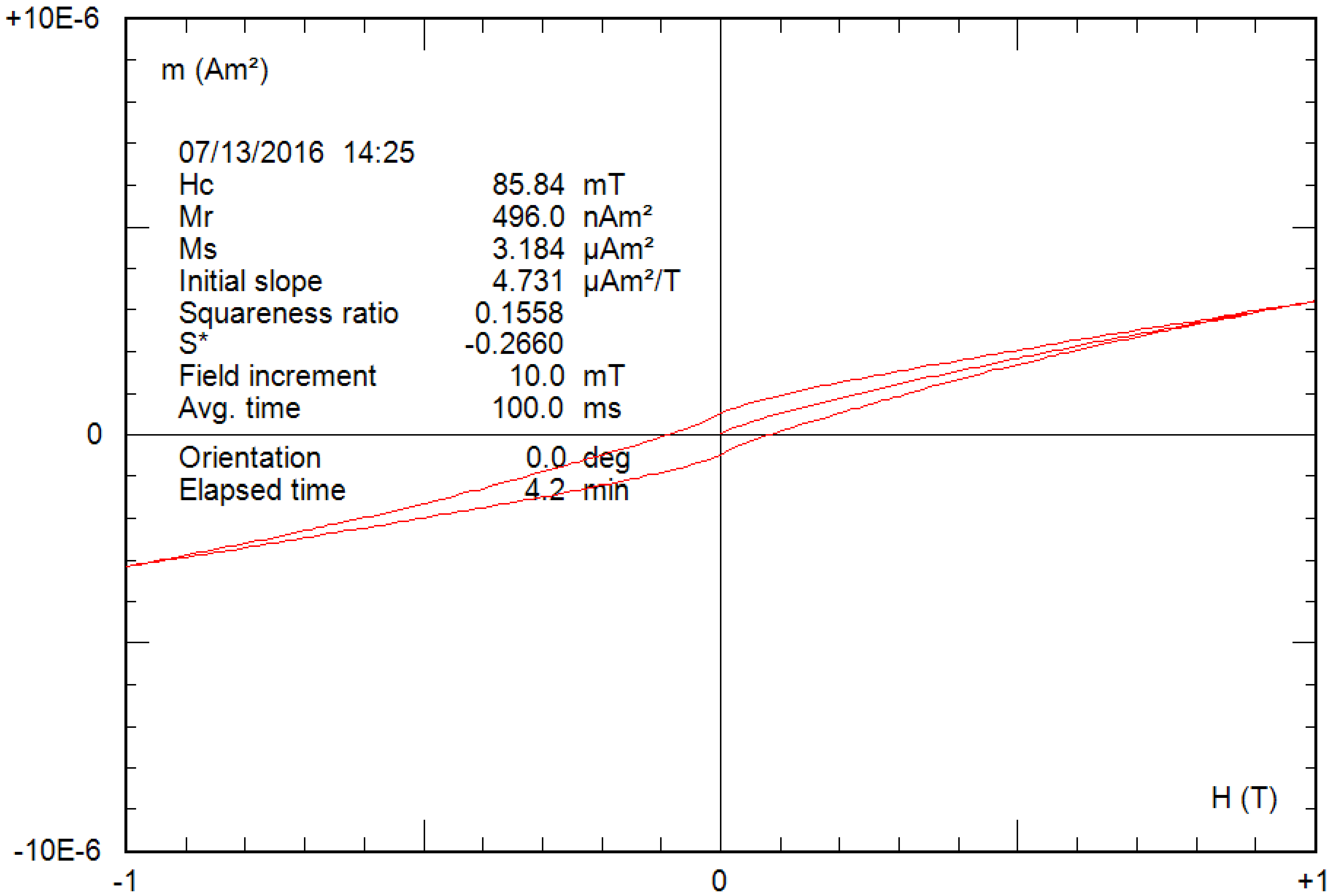

0.25 g

File: 26-04c_hyst

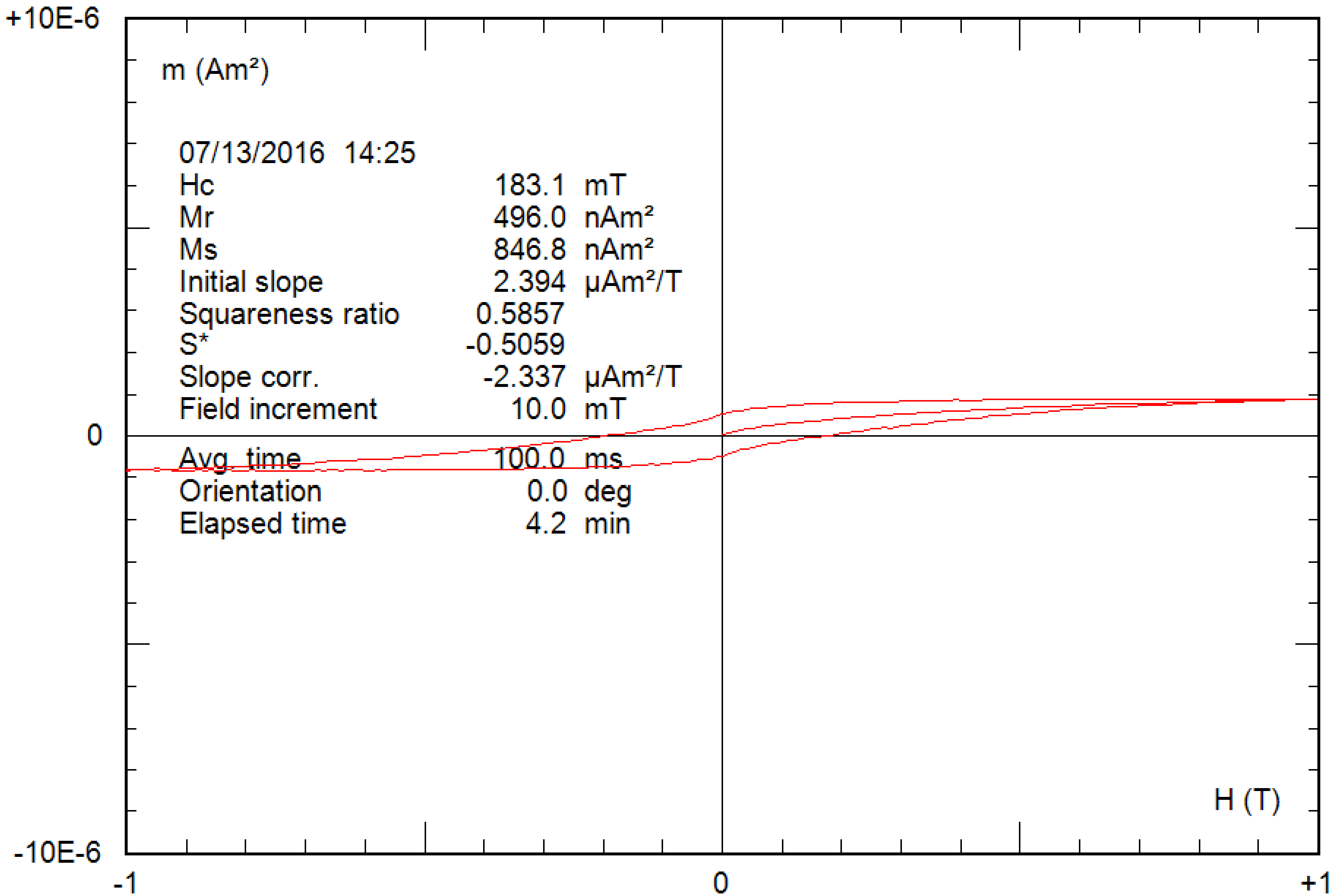

0.25 g

File: 26-04c_hyst_corr

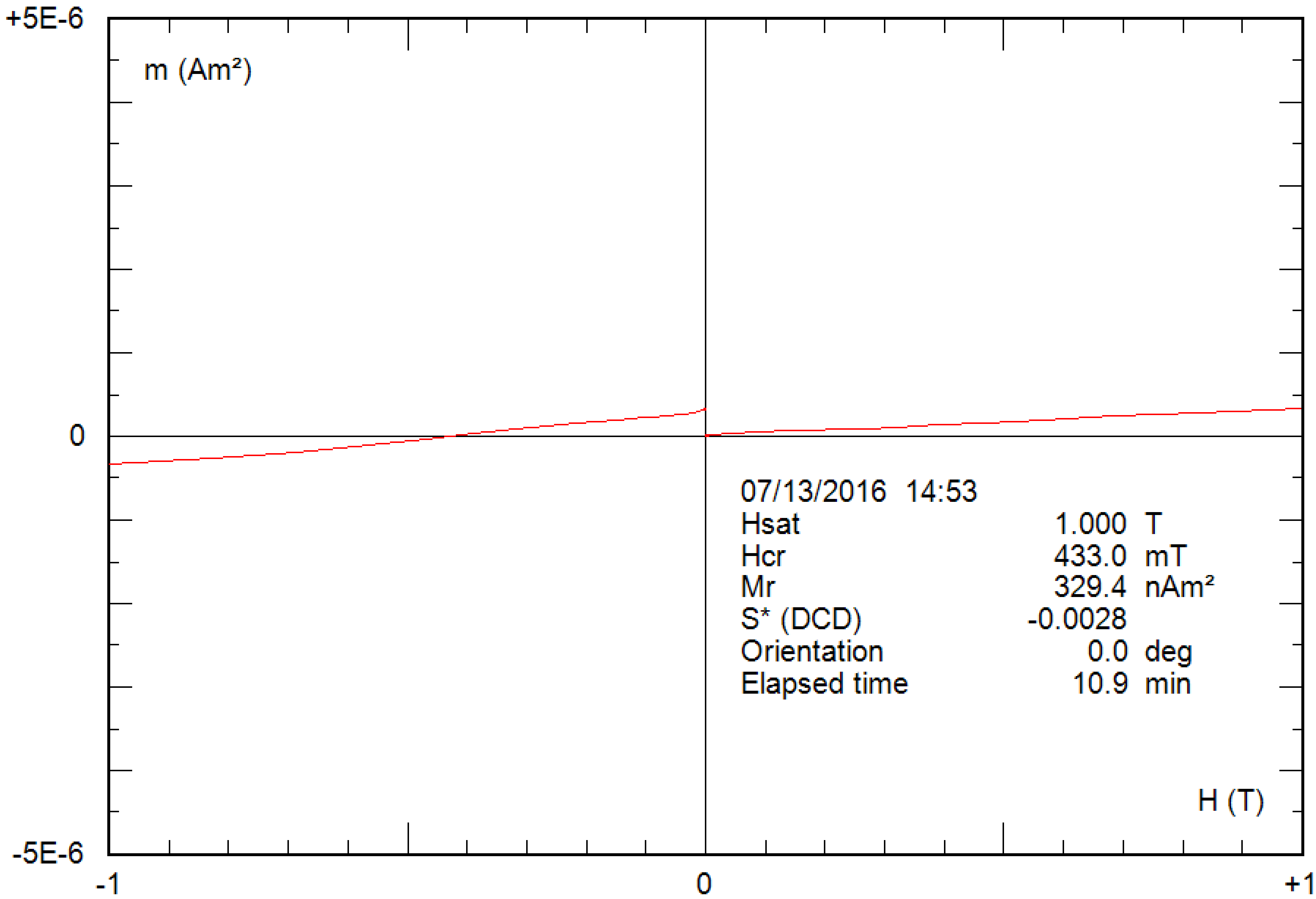

0.25 g

File: 27-08b_bcr

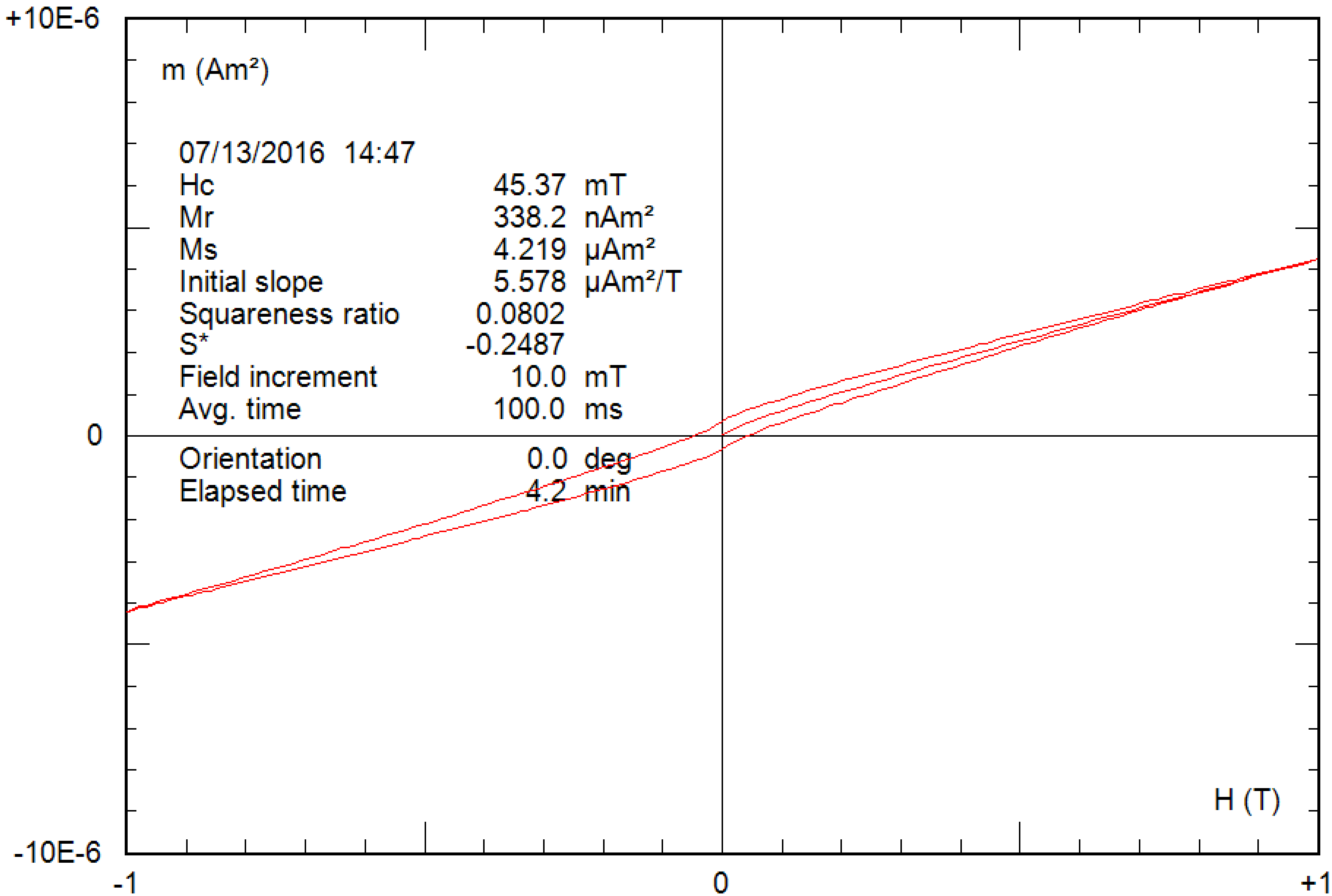

0.25 g

File: 27-08b_hyst

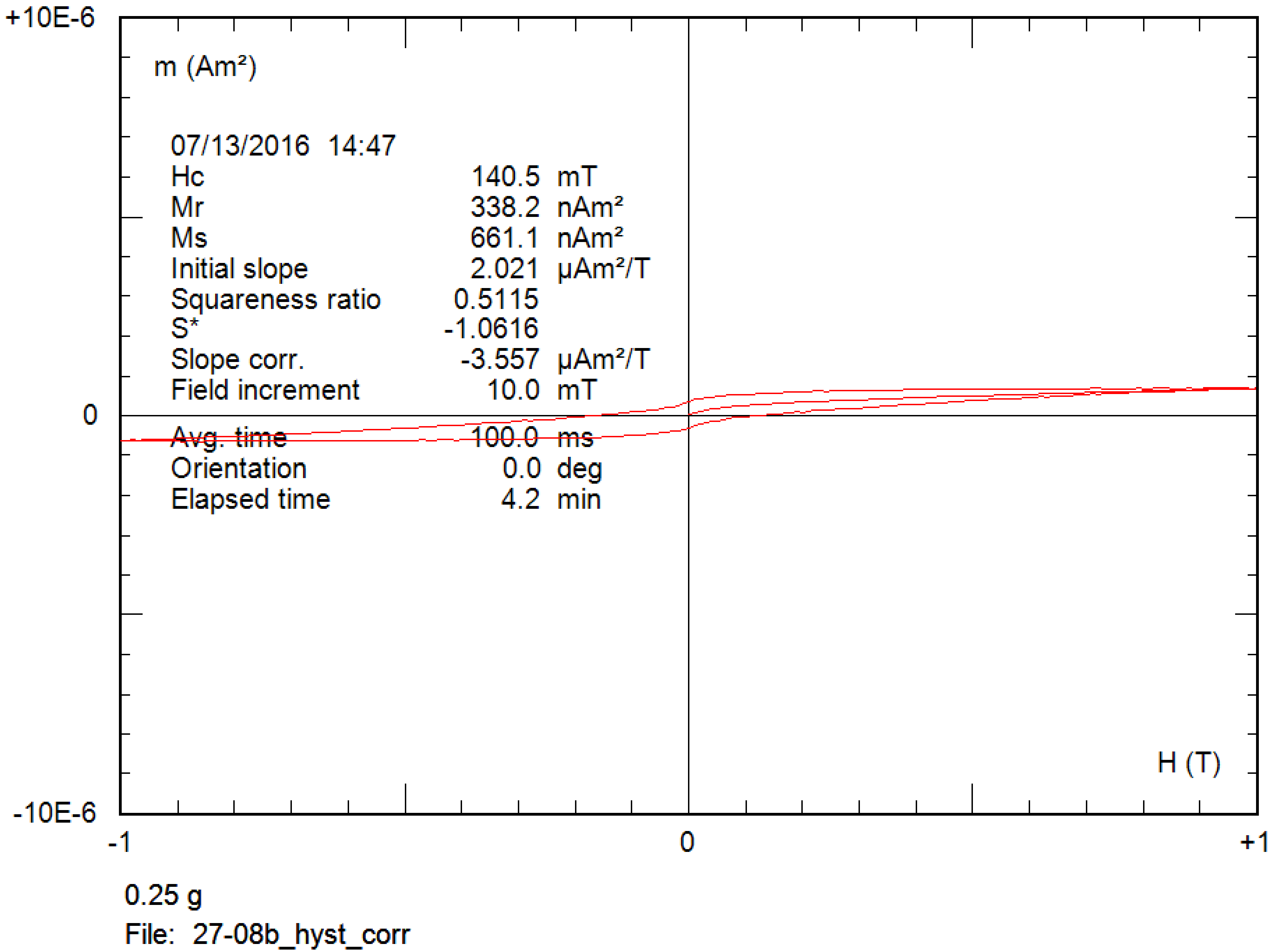
+10E-6
m (Am²)
07/13/2016 14:47
Hc 140.5 mT
Mr 338.2 nAm²
Ms 661.1 nAm²
Initial slope 2.021 µAm²/T
Squareness ratio 0.5115
S* -1.0616
Slope corr. -3.557 µAm²/T
Field increment 10.0 mT
0
Avg. time 100.0 ms
Orientation 0.0 deg
Elapsed time 4.2 min
H (T)
-10E-6
-1
0
+1
0.25 g
File: 27-08b_hyst_corr

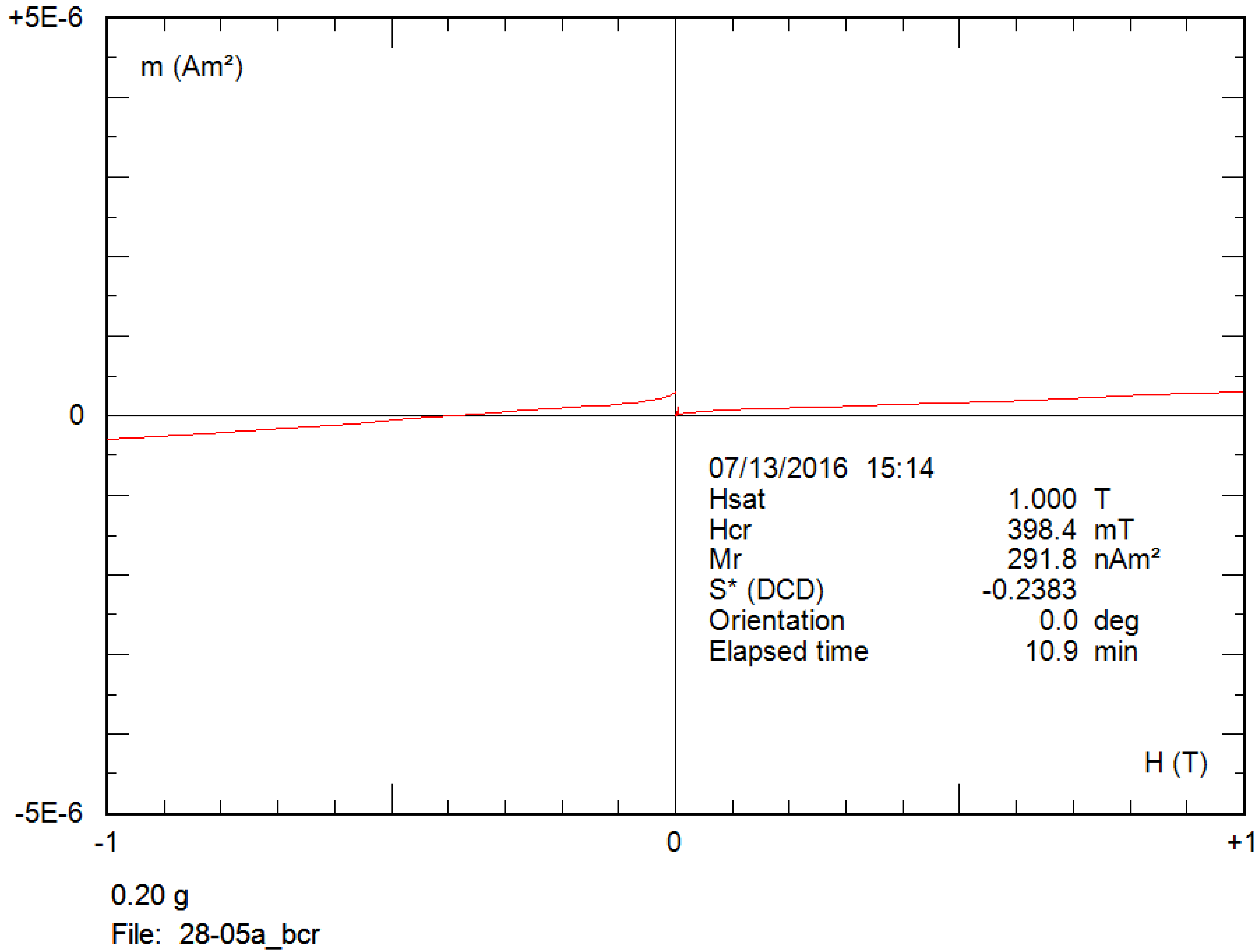
+5E-6
m (Am²)
0
-5E-6
-1
0
+1
H (T)
07/13/2016 15:14
Hsat 1.000 T
Hcr 398.4 mT
Mr 291.8 nAm²
S* (DCD) -0.2383
Orientation 0.0 deg
Elapsed time 10.9 min
0.20 g
File: 28-05a_bcr

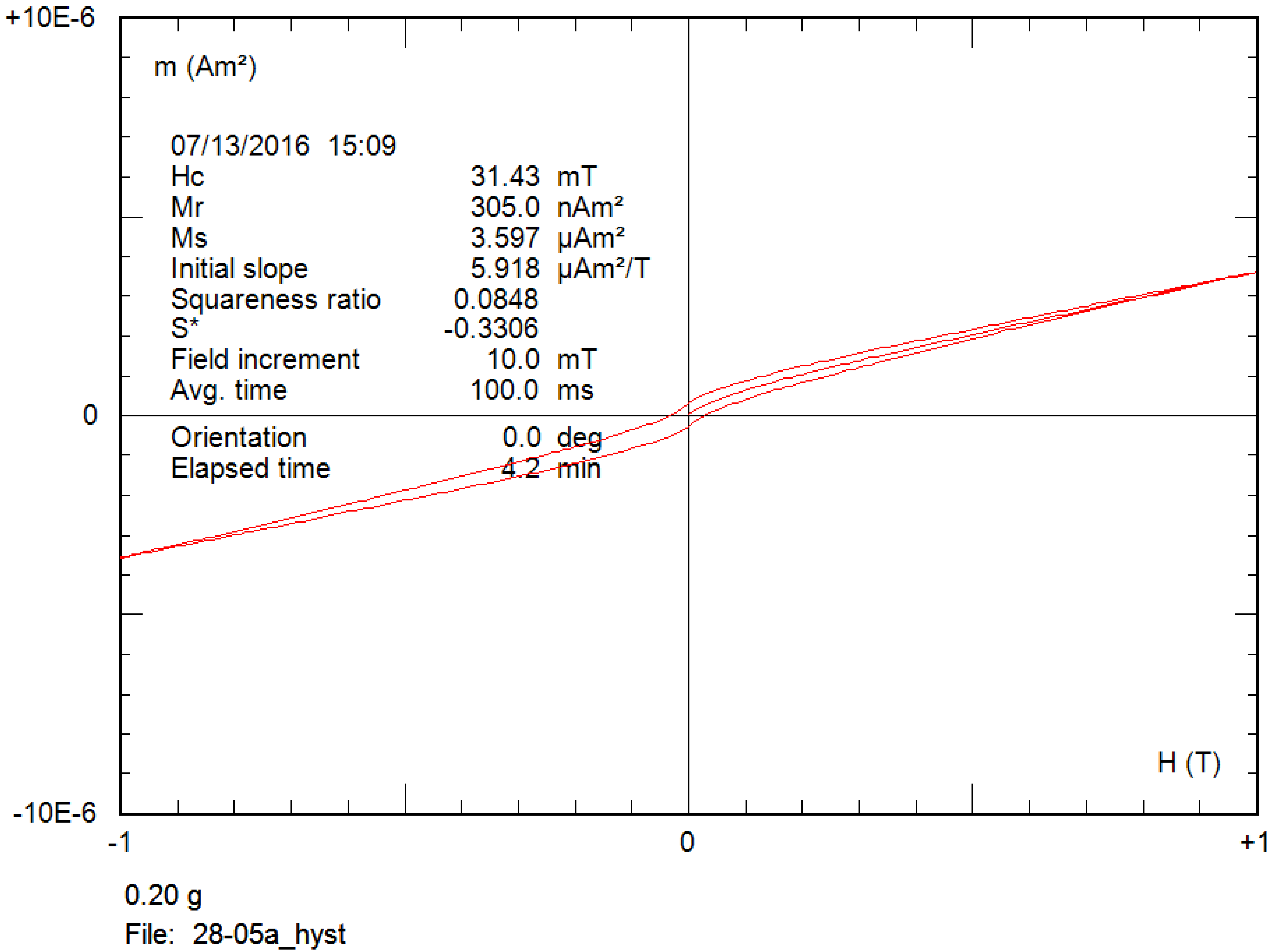
+10E-6
m (Am²)
07/13/2016 15:09
Hc 31.43 mT
Mr 305.0 nAm²
Ms 3.597 µAm²
Initial slope 5.918 µAm²/T
Squareness ratio 0.0848
S* -0.3306
Field increment 10.0 mT
Avg. time 100.0 ms
0
Orientation 0.0 deg
Elapsed time 4.2 min
H (T)
-10E-6
-1
0
+1
0.20 g
File: 28-05a_hyst

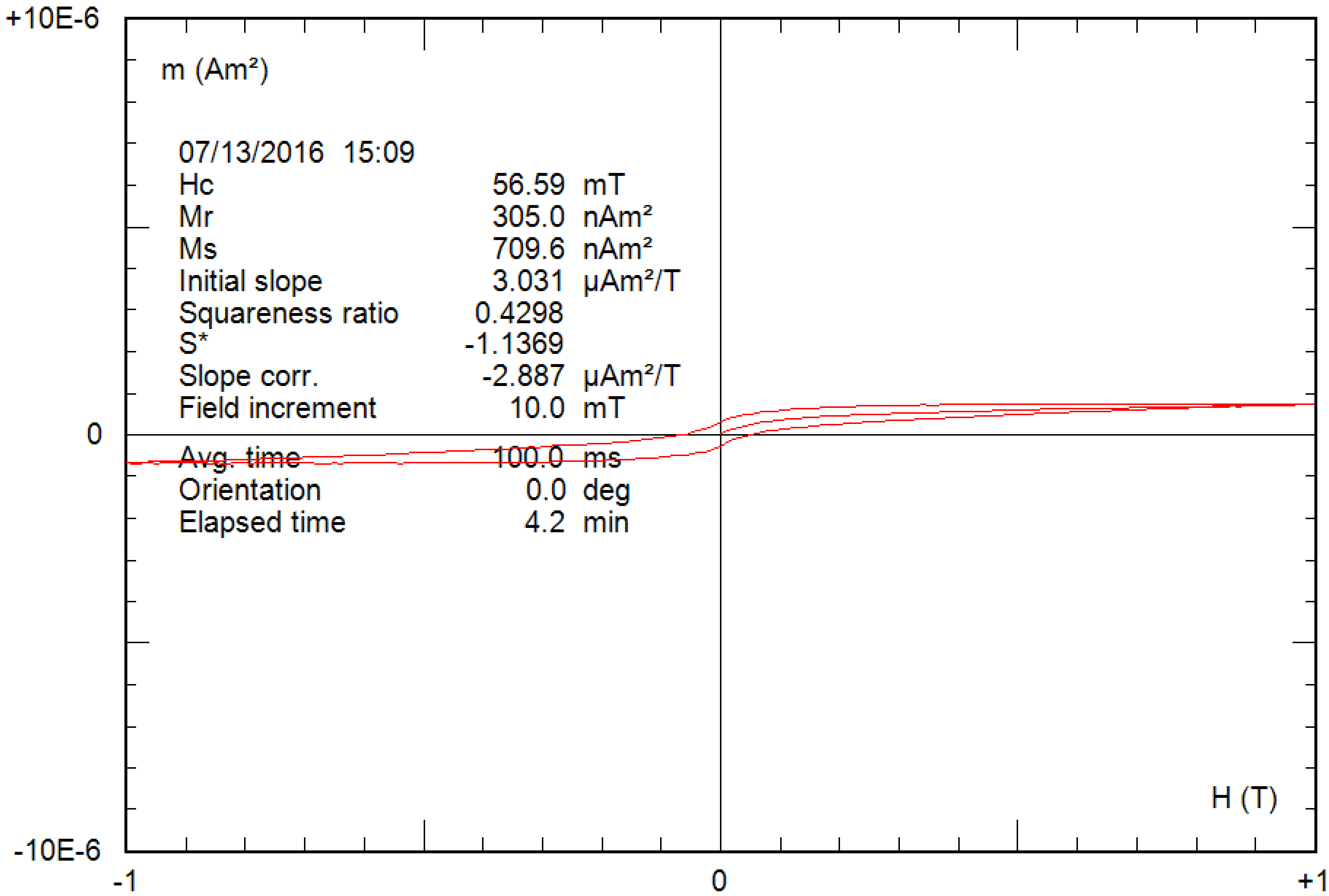

0.20 g

File: 28-05a_hyst_corr

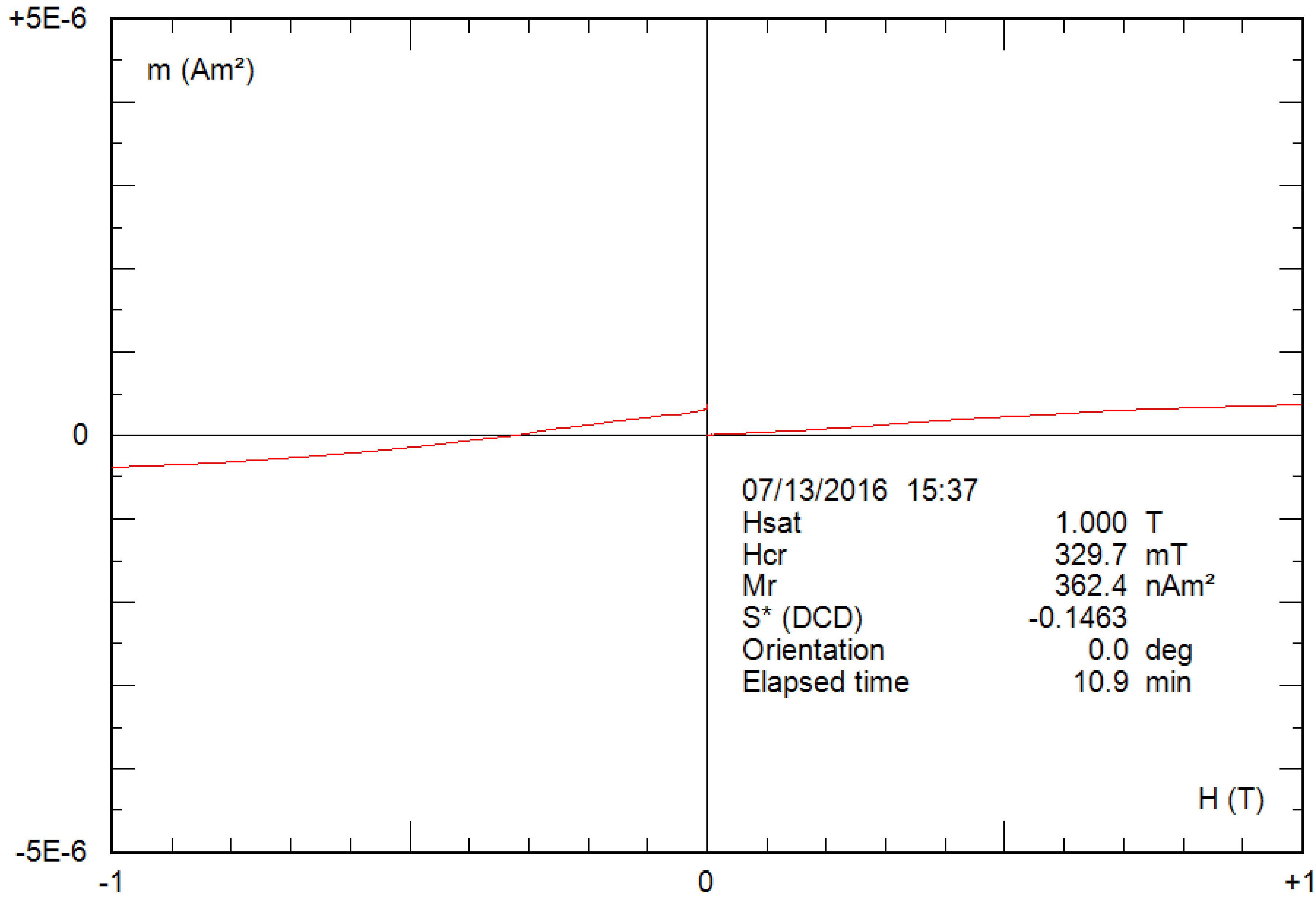

0.27 g

File: 29-02c_bcr

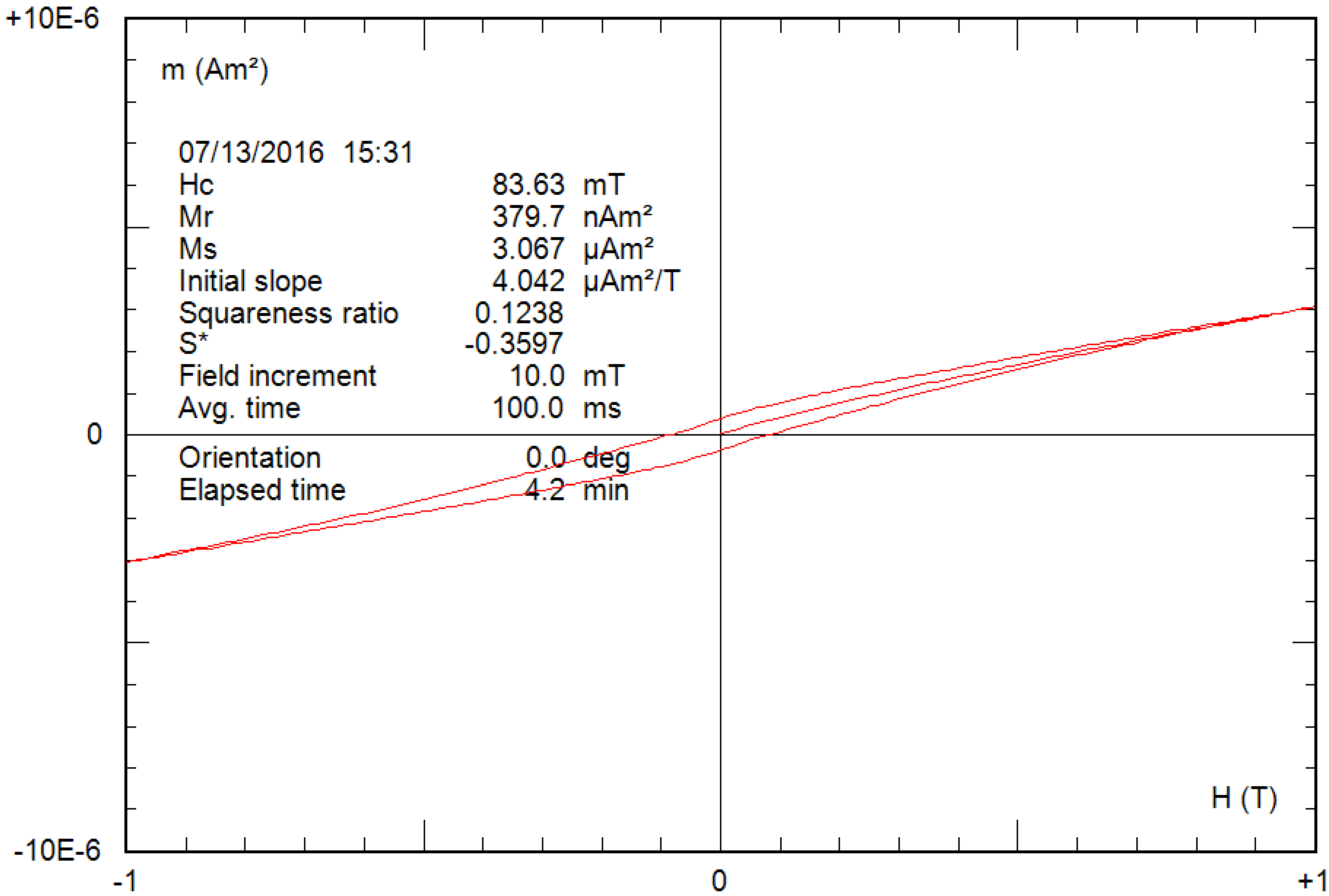

0.27 g

File: 29-02c_hyst

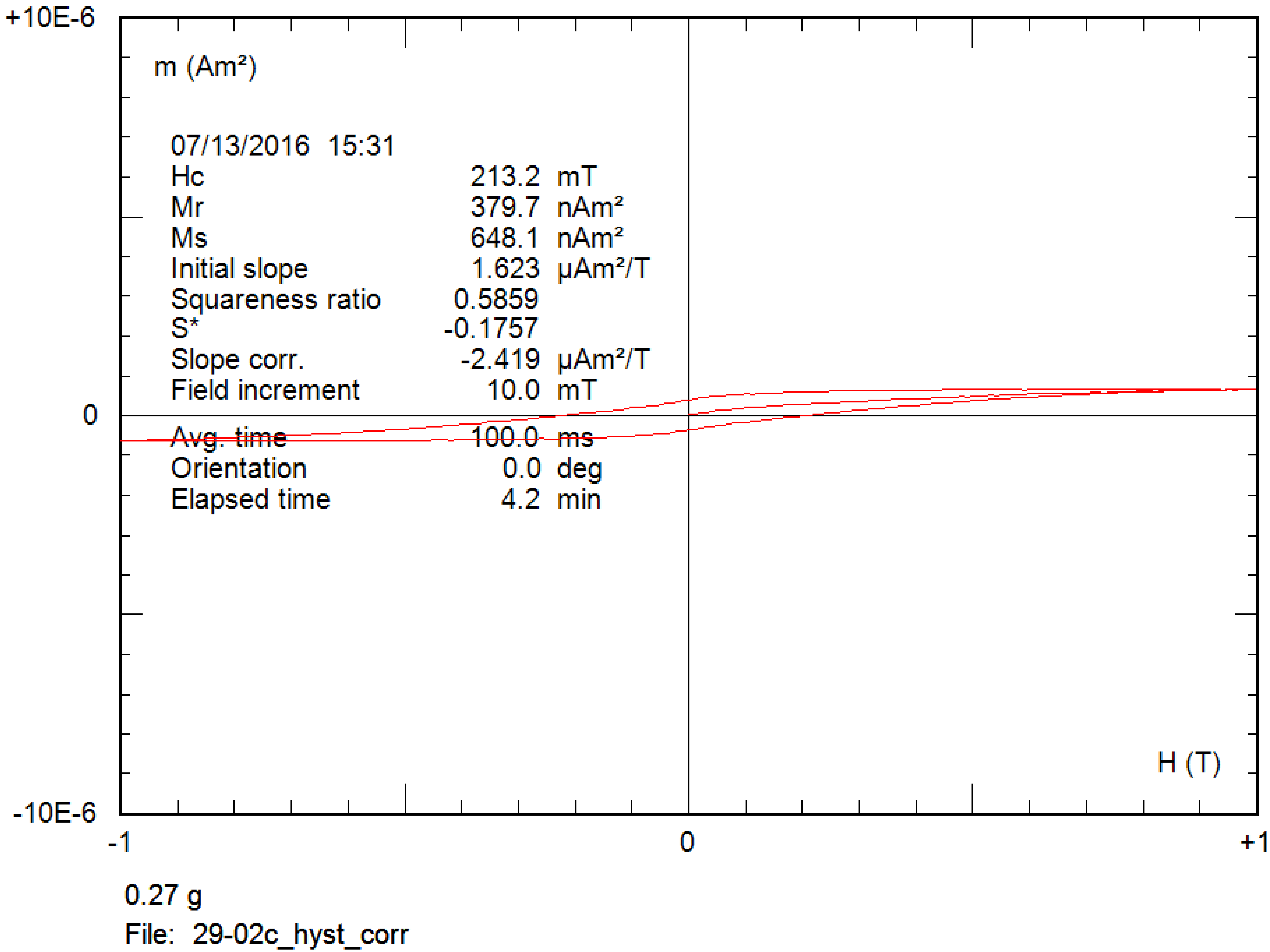
+10E-6
m (Am²)
07/13/2016 15:31
Hc 213.2 mT
Mr 379.7 nAm²
Ms 648.1 nAm²
Initial slope 1.623 µAm²/T
Squareness ratio 0.5859
S* -0.1757
Slope corr. -2.419 µAm²/T
Field increment 10.0 mT
0
Avg. time 100.0 ms
Orientation 0.0 deg
Elapsed time 4.2 min
H (T)
-10E-6
-1
0
+1
0.27 g
File: 29-02c_hyst_corr

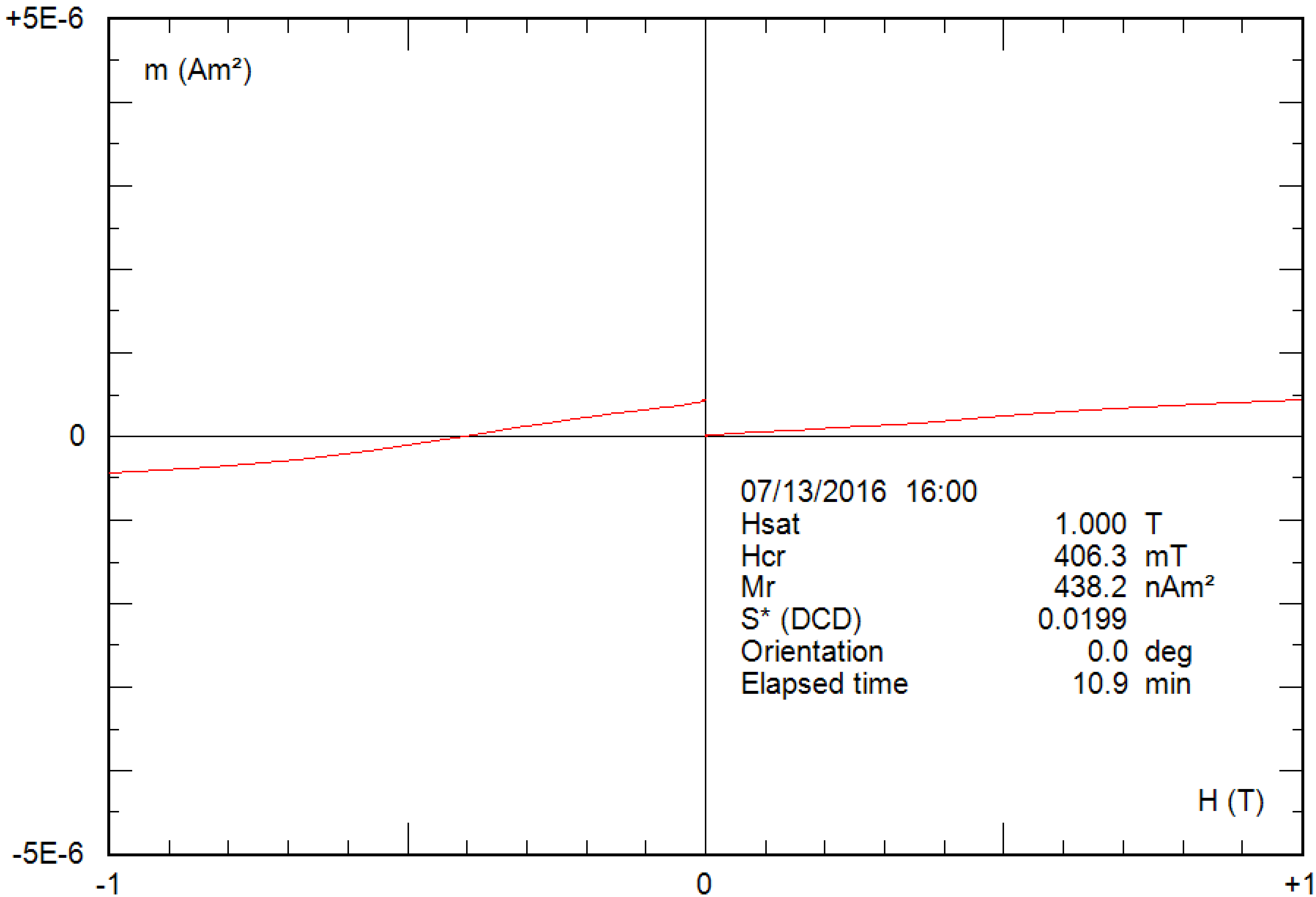

0.25 g

File: 30-10b_bcr

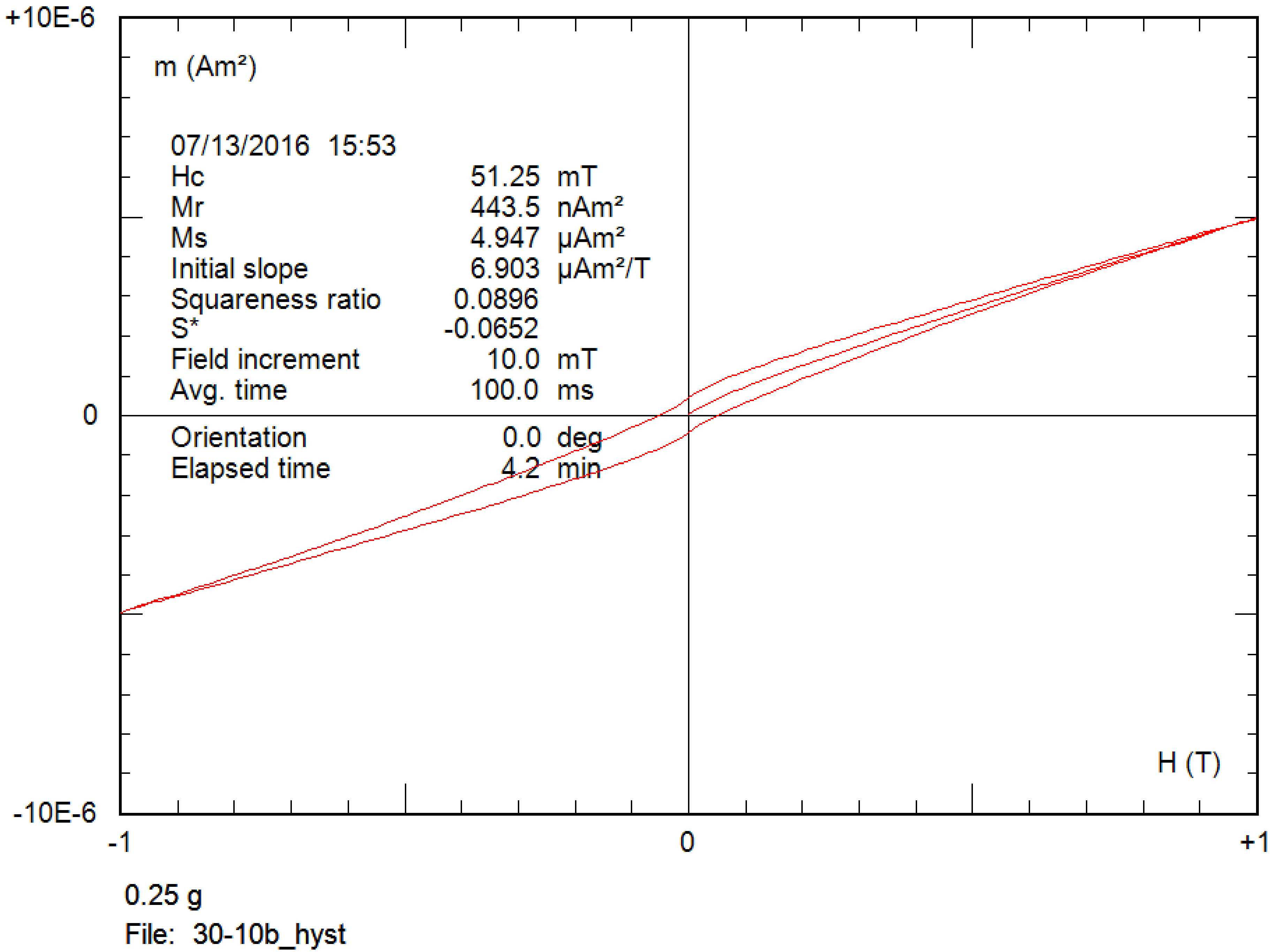
+10E-6
m (Am²)
07/13/2016 15:53
Hc 51.25 mT
Mr 443.5 nAm²
Ms 4.947 µAm²
Initial slope 6.903 µAm²/T
Squareness ratio 0.0896
S* -0.0652
Field increment 10.0 mT
Avg. time 100.0 ms
0
Orientation 0.0 deg
Elapsed time 4.2 min
H (T)
-10E-6
-1
0
+1
0.25 g
File: 30-10b_hyst

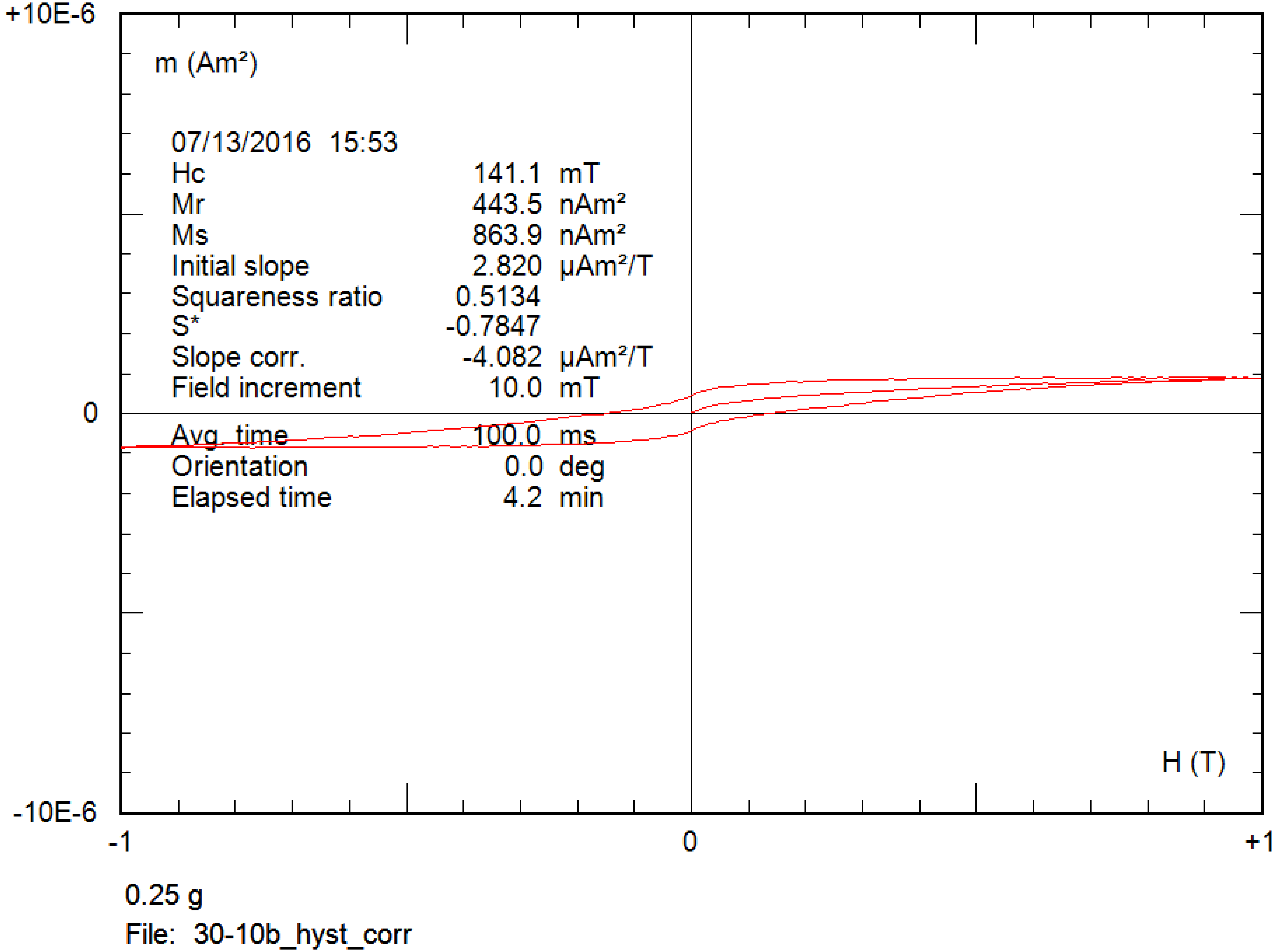

+10E-6
m (Am²)
07/13/2016 15:53
Hc 141.1 mT
Mr 443.5 nAm²
Ms 863.9 nAm²
Initial slope 2.820 µAm²/T
Squareness ratio 0.5134
S* -0.7847
Slope corr. -4.082 µAm²/T
Field increment 10.0 mT
0
Avg. time 100.0 ms
Orientation 0.0 deg
Elapsed time 4.2 min
H (T)
-10E-6
-1
0
+1
0.25 g
File: 30-10b_hyst_corr

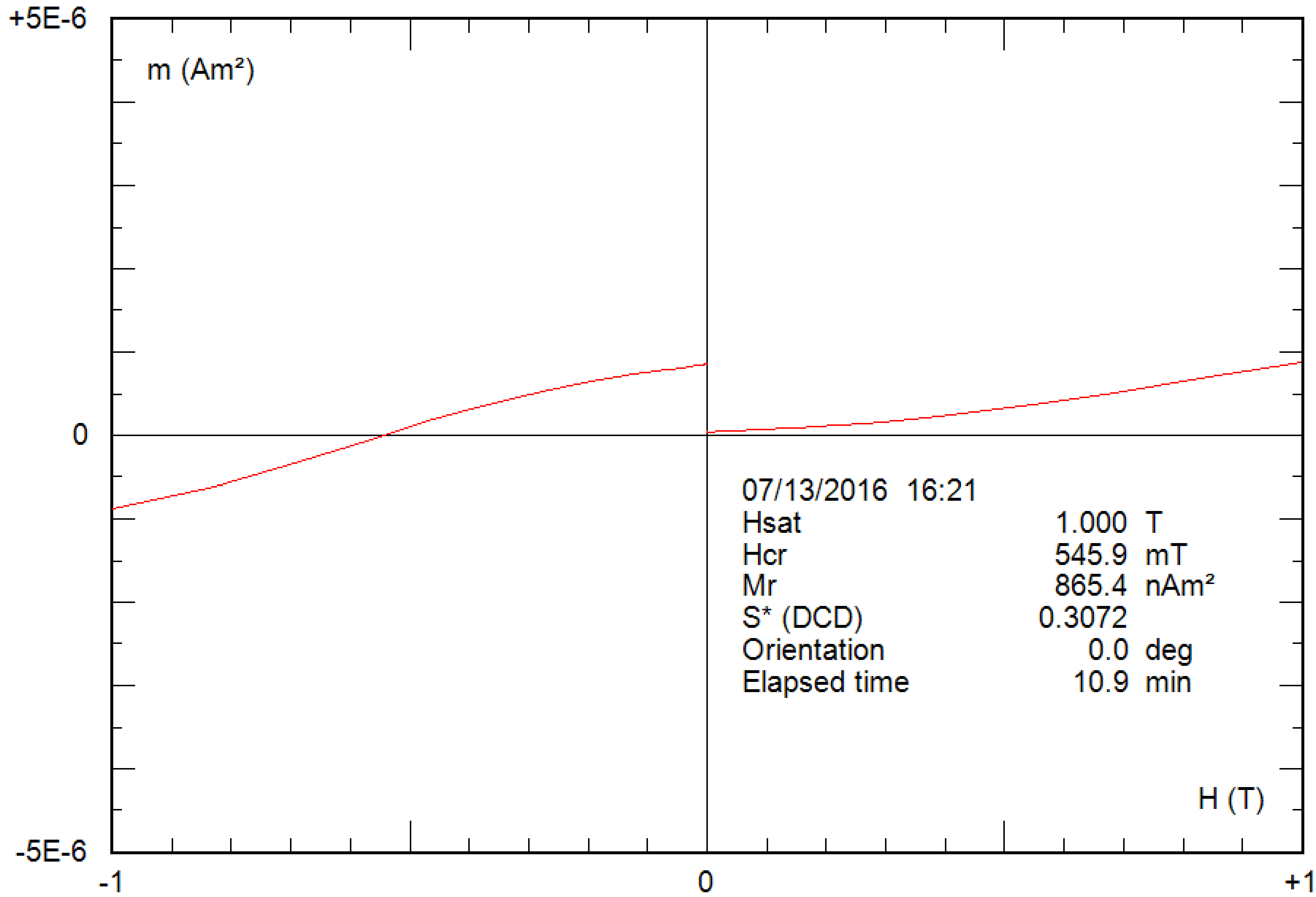

0.19 g

File: 31-06c_bcr

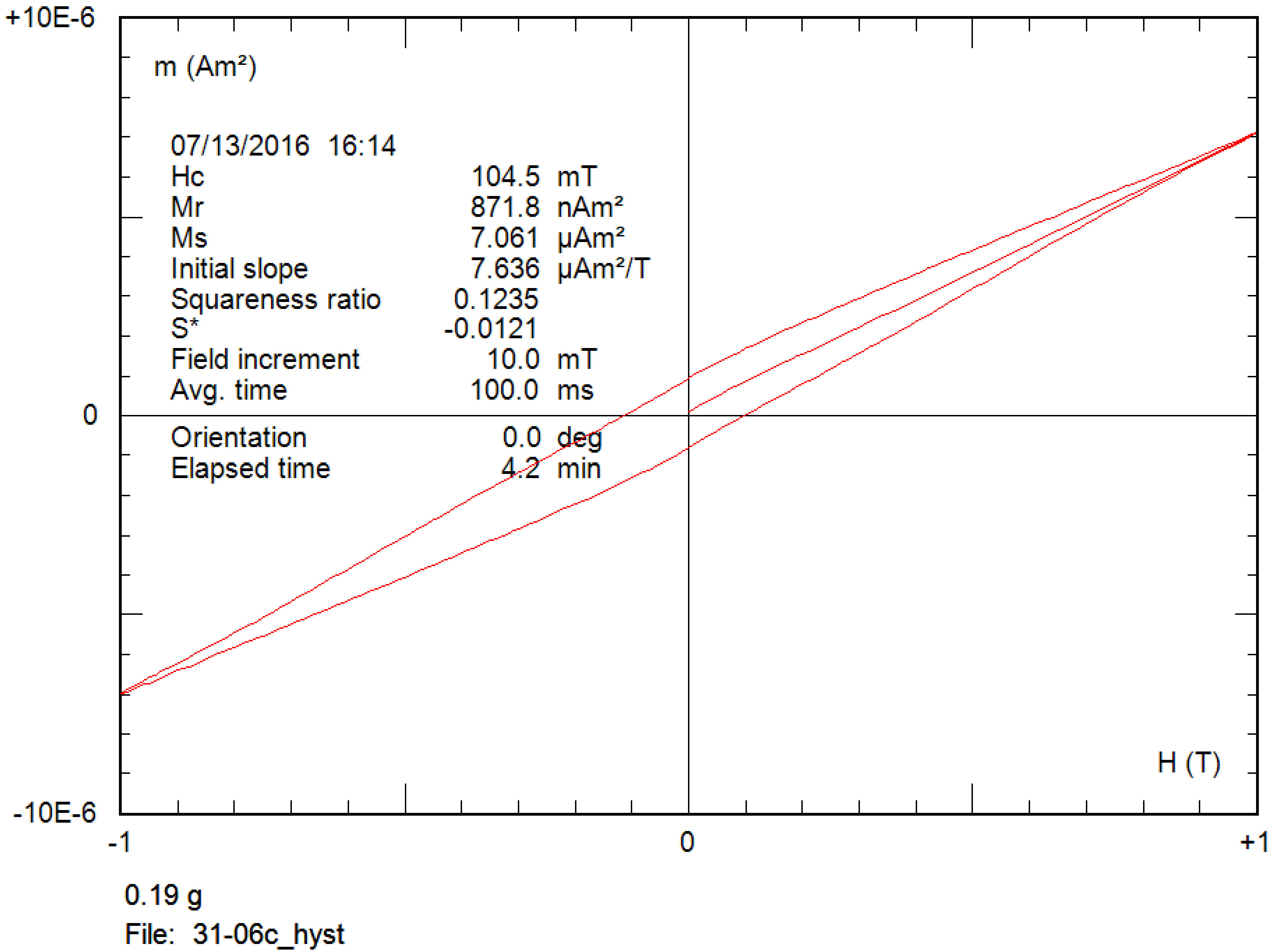
+10E-6
m (Am²)
07/13/2016 16:14
Hc 104.5 mT
Mr 871.8 nAm²
Ms 7.061 µAm²
Initial slope 7.636 µAm²/T
Squareness ratio 0.1235
S* -0.0121
Field increment 10.0 mT
Avg. time 100.0 ms
0
Orientation 0.0 deg
Elapsed time 4.2 min
H (T)
-10E-6
-1
0
+1
0.19 g
File: 31-06c_hyst

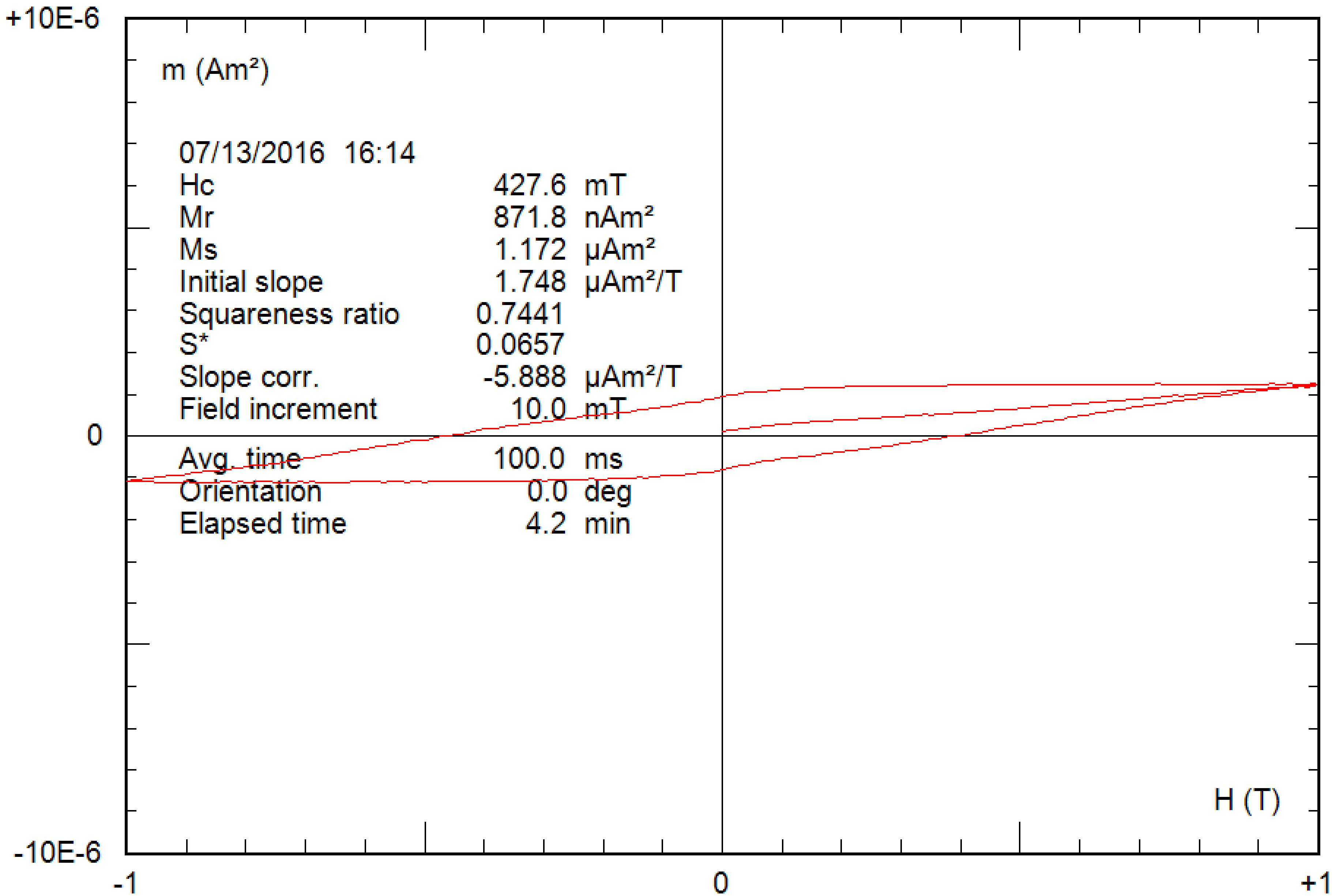

0.19 g

File: 31-06c_hyst_corr

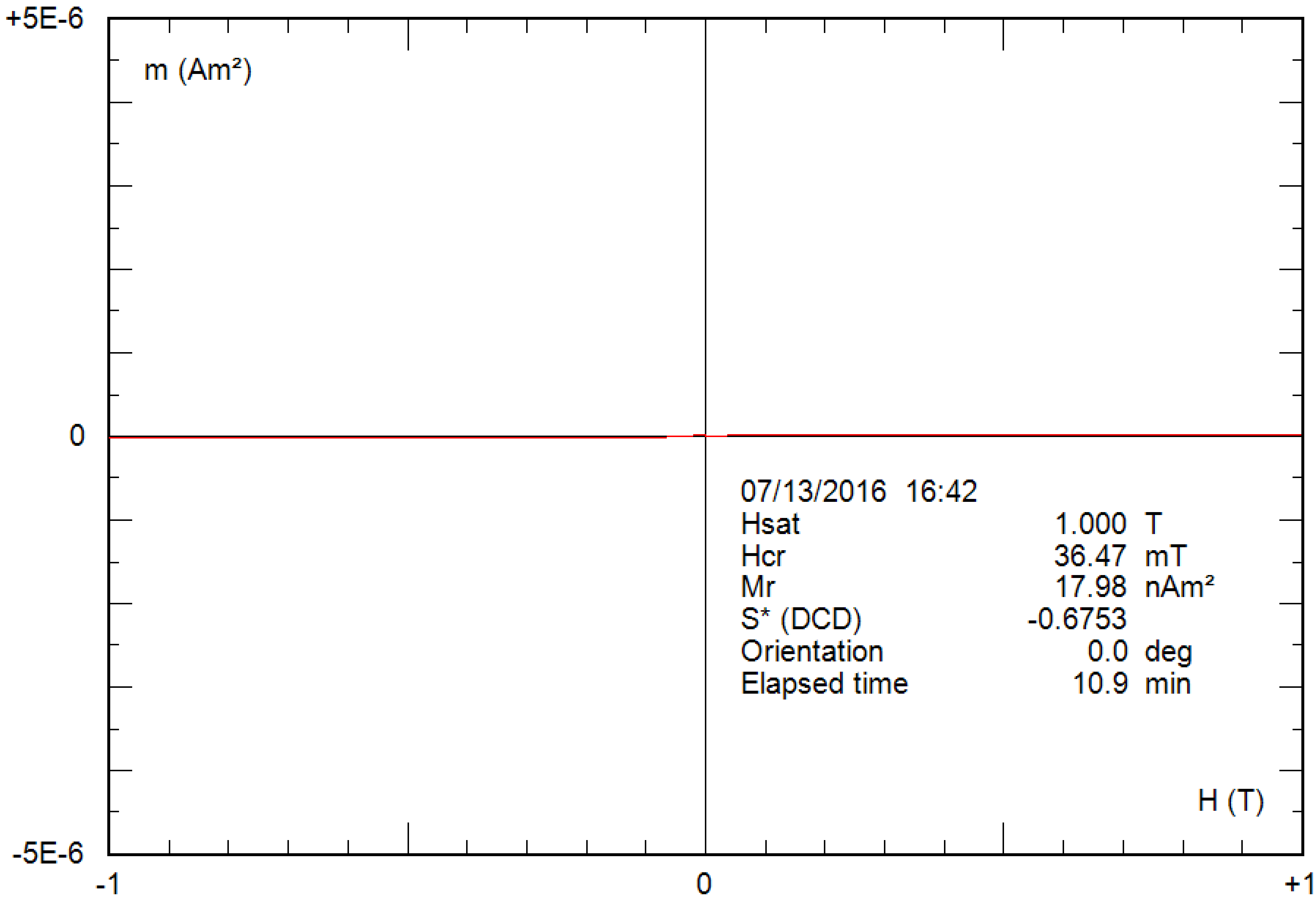

0.22 g

File: 32-01c_bcr

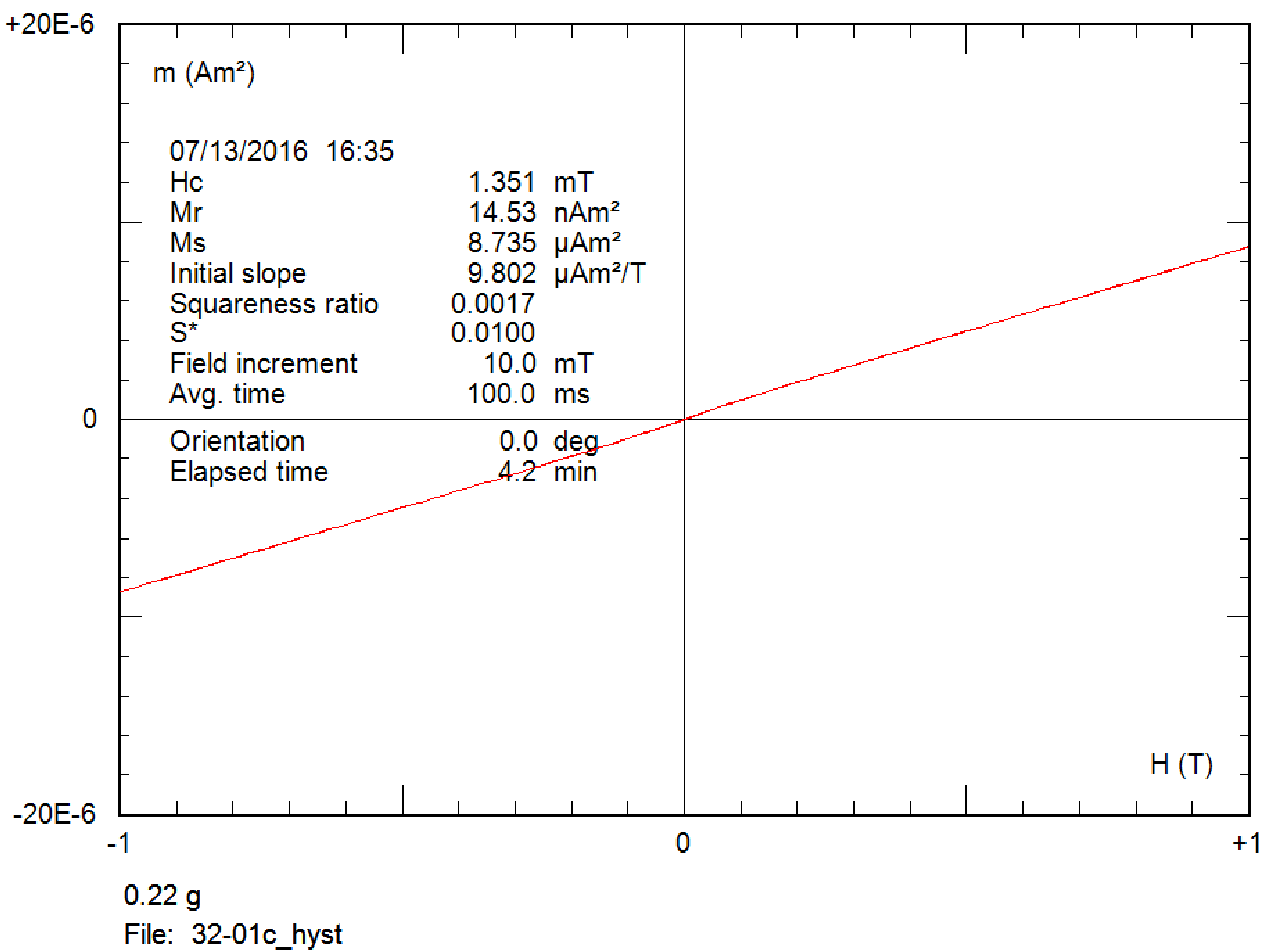
+20E-6
m (Am²)
07/13/2016 16:35
Hc 1.351 mT
Mr 14.53 nAm²
Ms 8.735 µAm²
Initial slope 9.802 µAm²/T
Squareness ratio 0.0017
S* 0.0100
Field increment 10.0 mT
Avg. time 100.0 ms
0
Orientation 0.0 deg
Elapsed time 4.2 min
H (T)
-20E-6
-1
0
+1
0.22 g
File: 32-01c_hyst

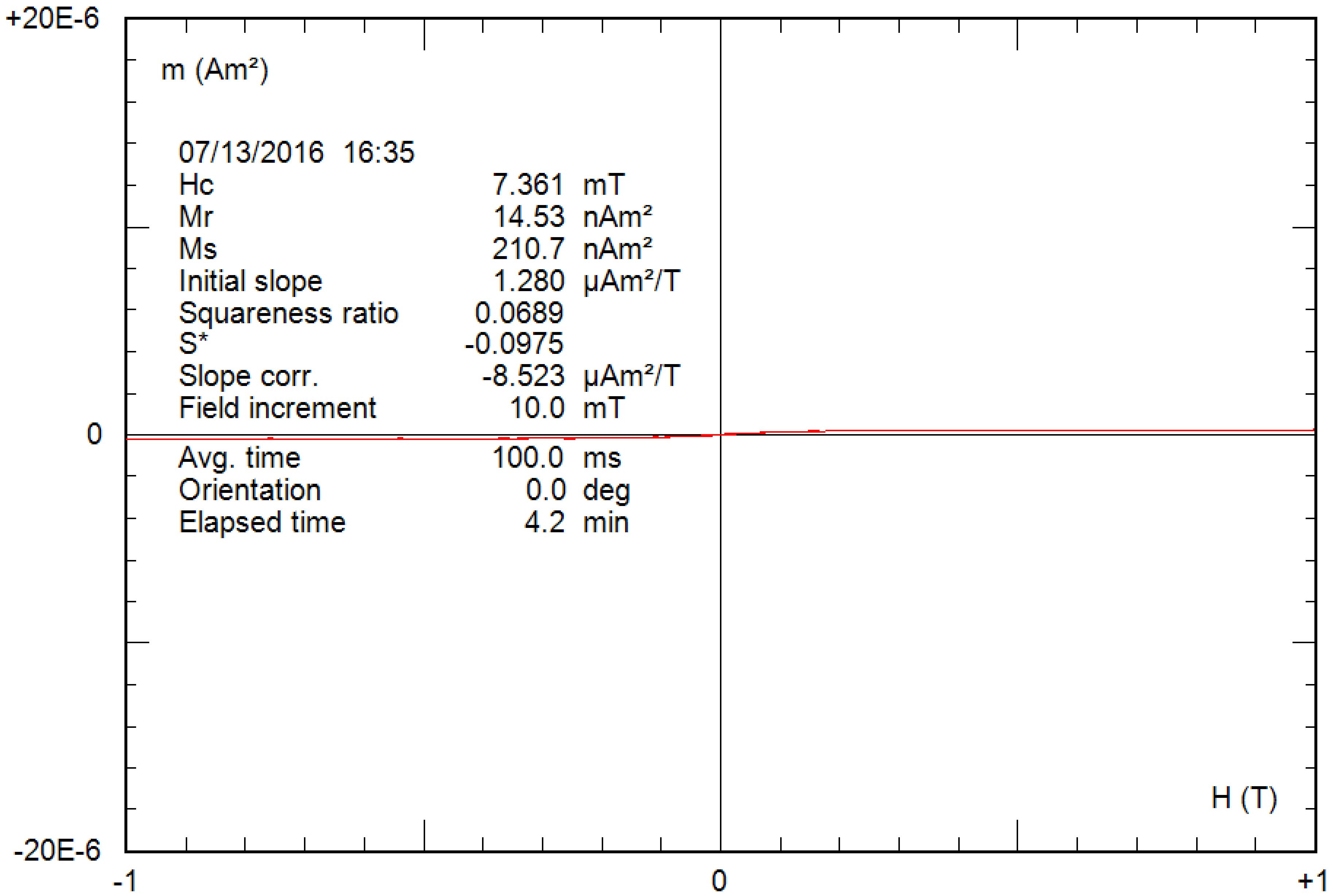

0.22 g

File: 32-01c_hyst_corr

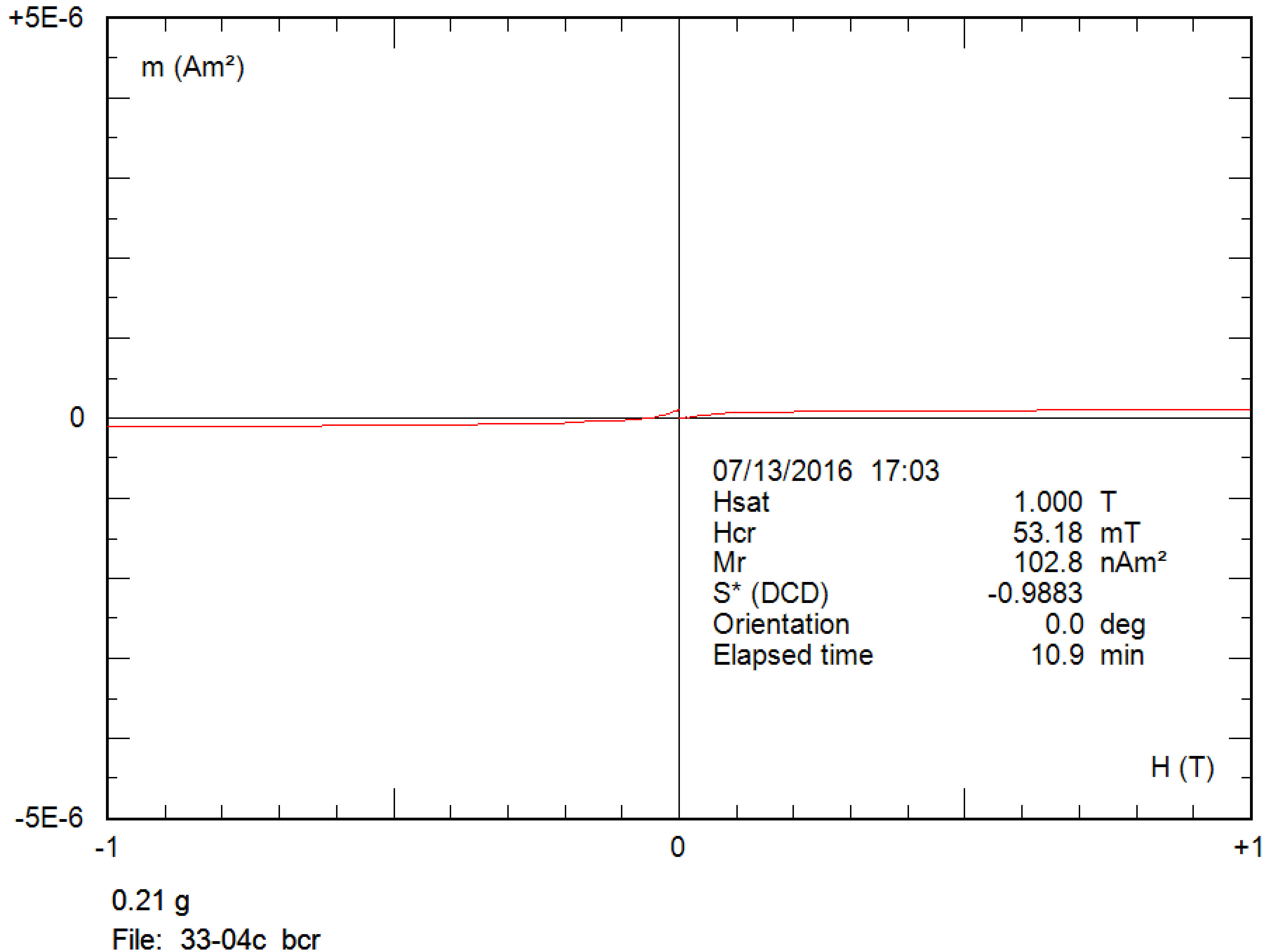
+5E-6
m (Am²)
0
-5E-6
-1
0
+1
H (T)
07/13/2016 17:03
Hsat 1.000 T
Hcr 53.18 mT
Mr 102.8 nAm²
S* (DCD) -0.9883
Orientation 0.0 deg
Elapsed time 10.9 min
0.21 g
File: 33-04c_bcr

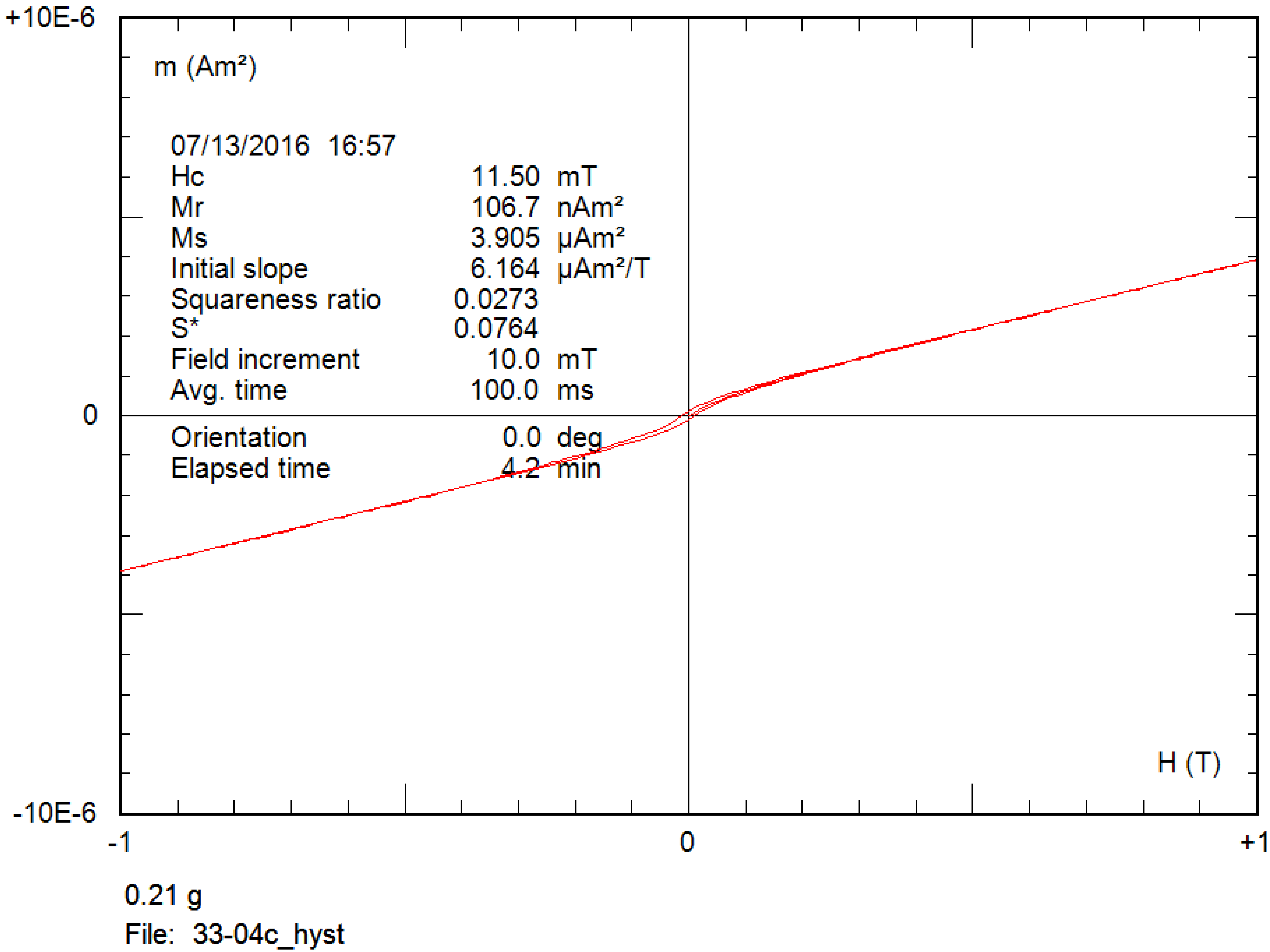
+10E-6
m (Am²)
07/13/2016 16:57
Hc 11.50 mT
Mr 106.7 nAm²
Ms 3.905 µAm²
Initial slope 6.164 µAm²/T
Squareness ratio 0.0273
S* 0.0764
Field increment 10.0 mT
Avg. time 100.0 ms
0
Orientation 0.0 deg
Elapsed time 4.2 min
H (T)
-10E-6
-1
0
+1
0.21 g
File: 33-04c_hyst

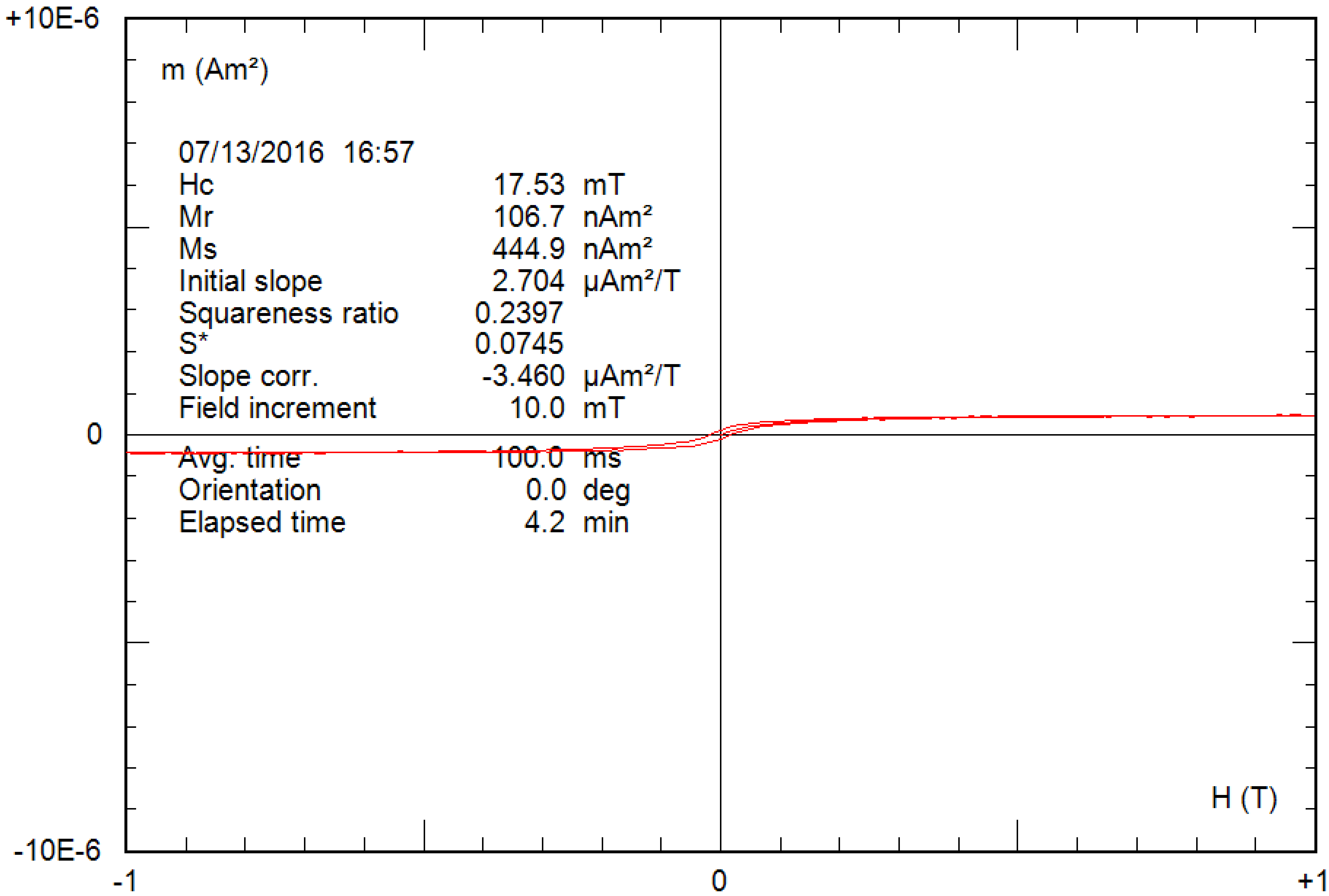

0.21 g

File: 33-04c_hyst_corr

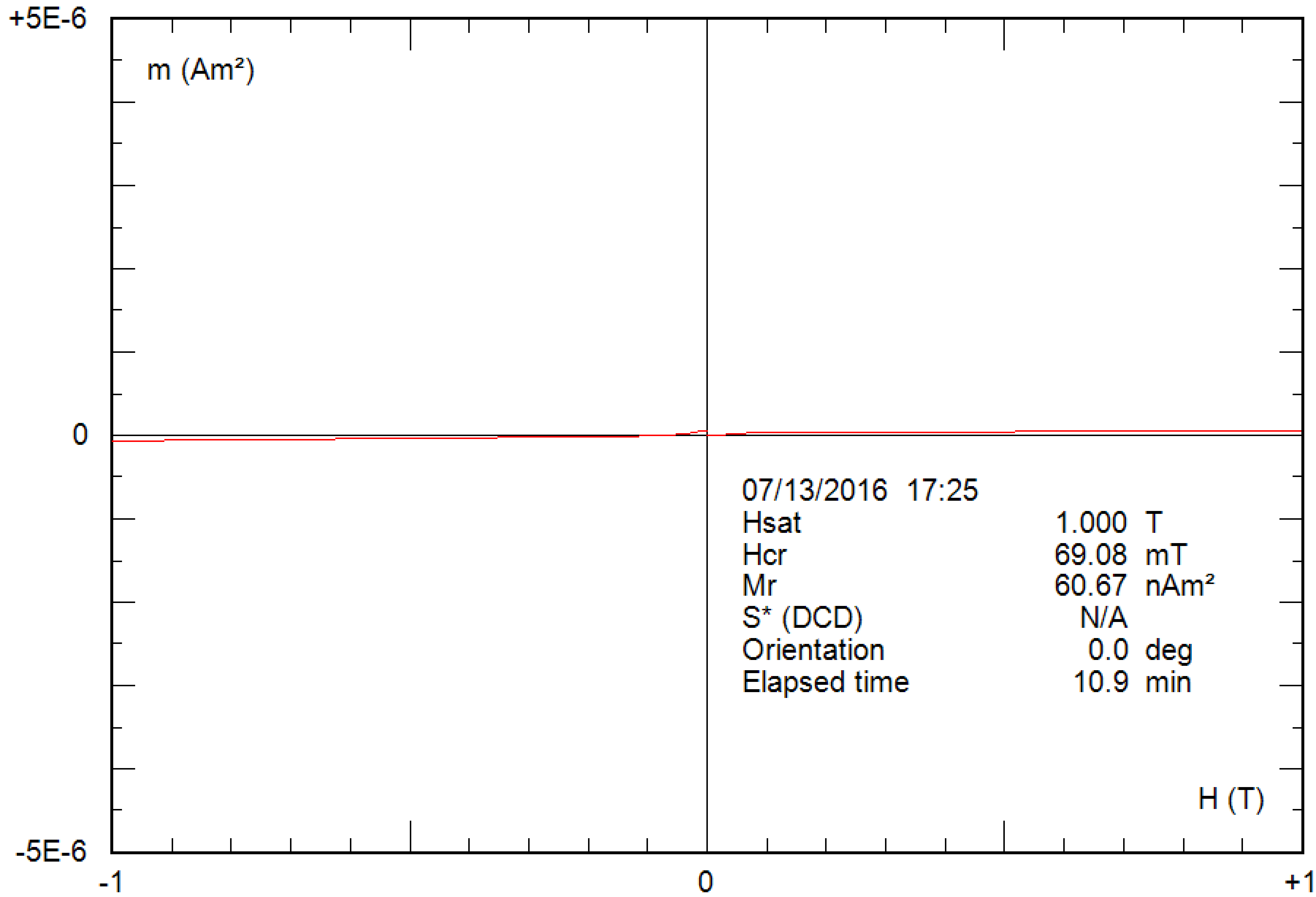

0.23 g

File: 34-03b_bcr

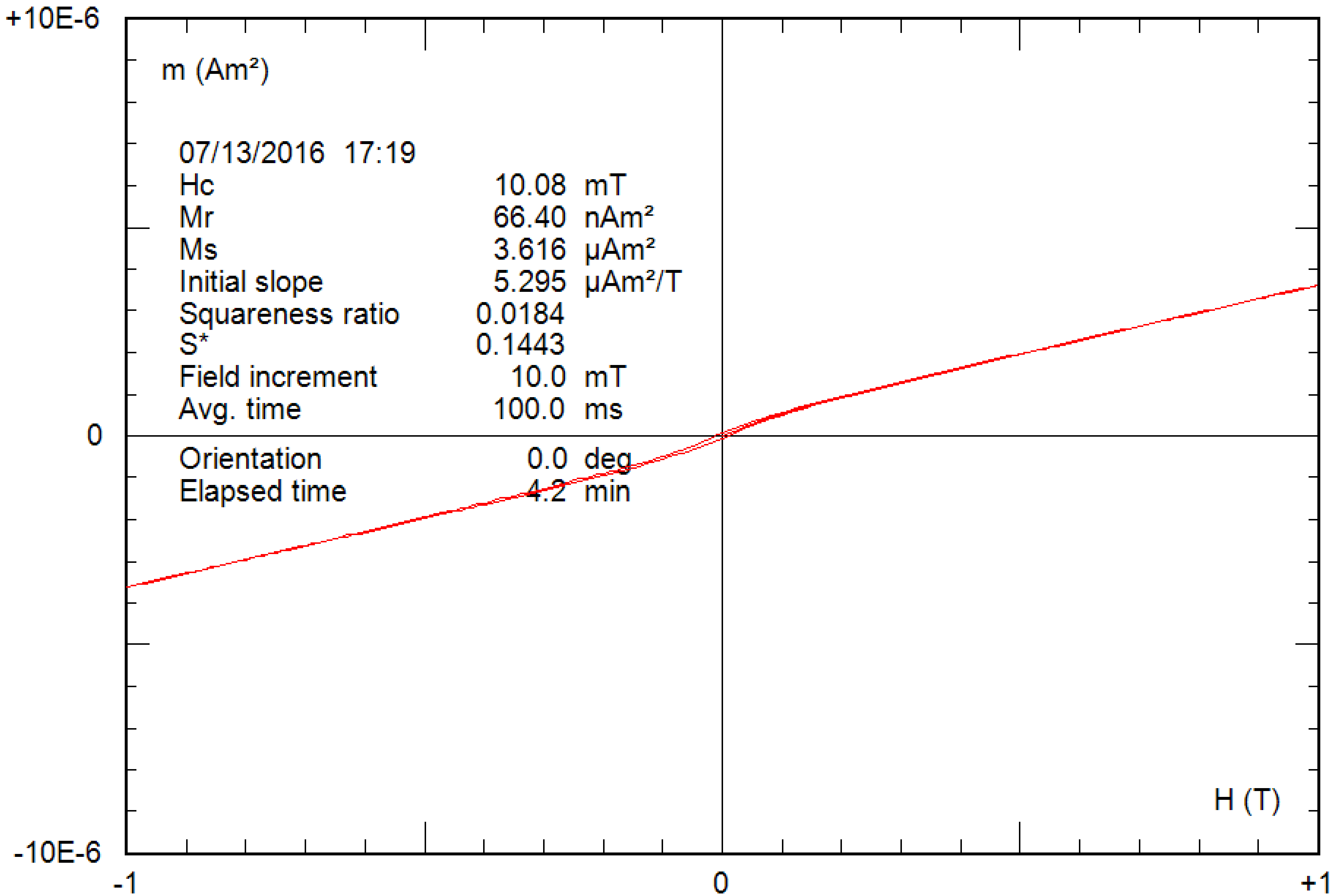

0.23 g

File: 34-03b_hyst

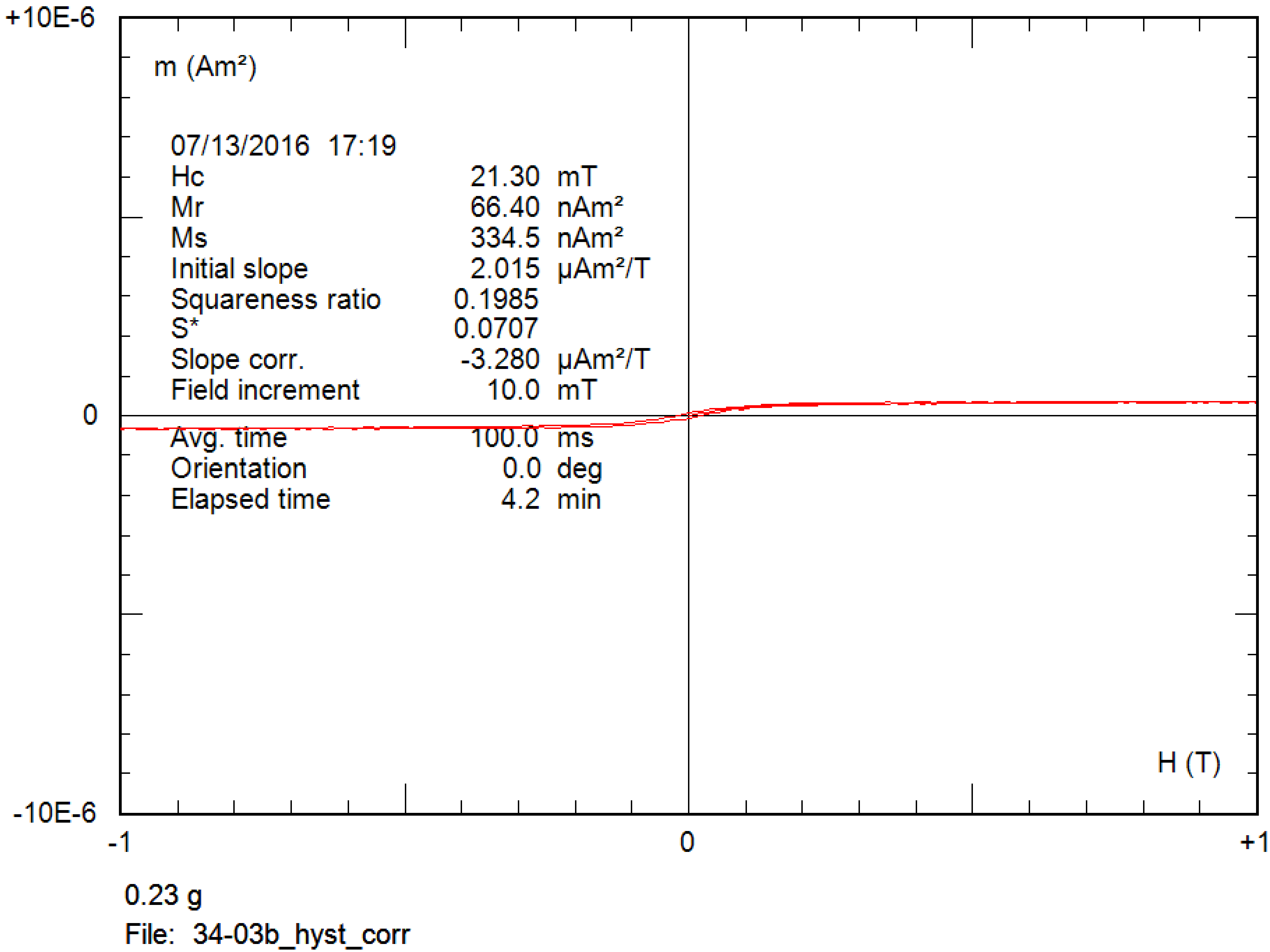
+10E-6
m (Am²)
07/13/2016 17:19
Hc 21.30 mT
Mr 66.40 nAm²
Ms 334.5 nAm²
Initial slope 2.015 µAm²/T
Squareness ratio 0.1985
S* 0.0707
Slope corr. -3.280 µAm²/T
Field increment 10.0 mT
0
Avg. time 100.0 ms
Orientation 0.0 deg
Elapsed time 4.2 min
H (T)
-10E-6
-1
0
+1
0.23 g
File: 34-03b_hyst_corr

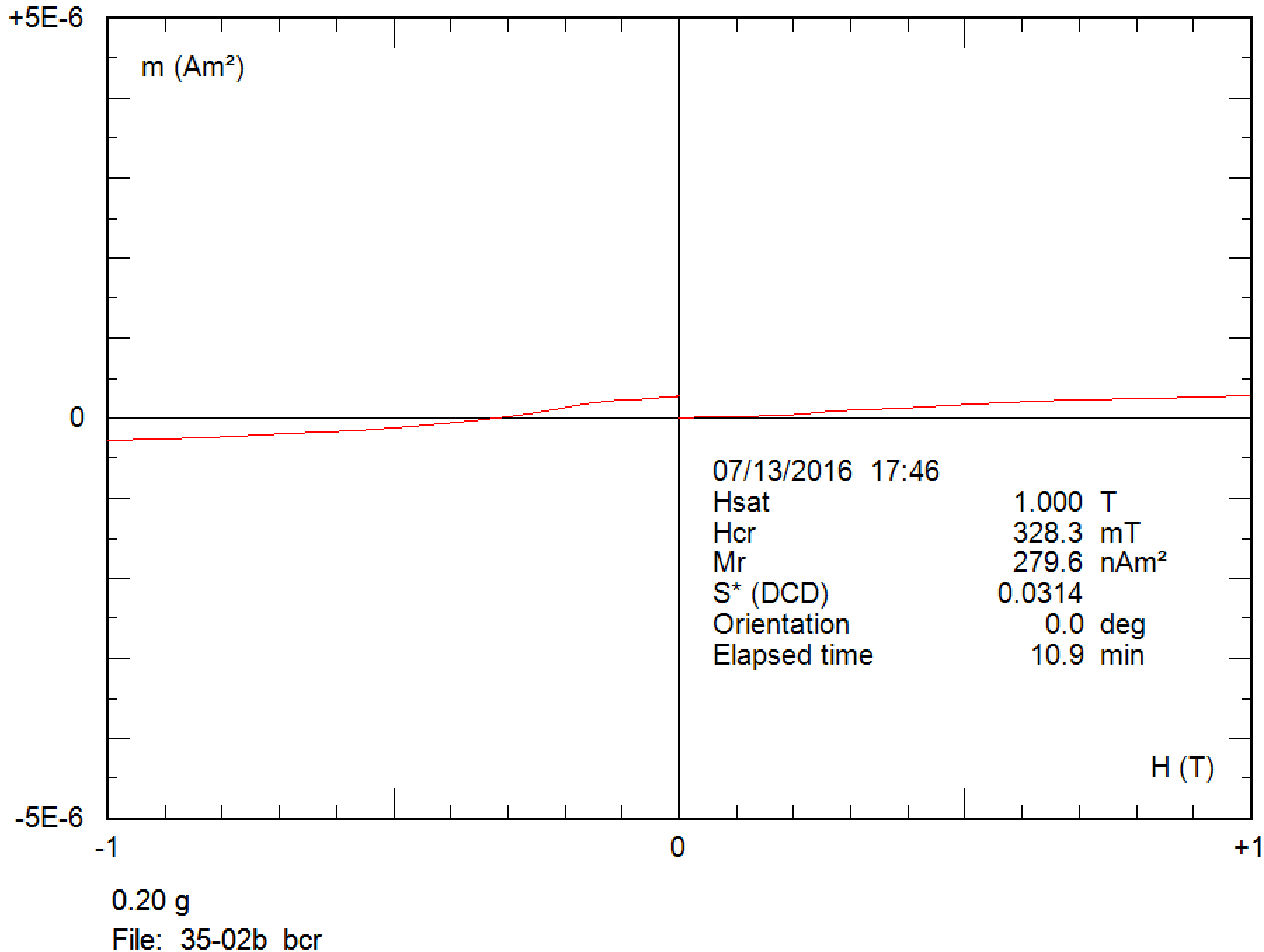
+5E-6
m (Am²)
0
-5E-6
-1
0
+1
H (T)
07/13/2016 17:46
Hsat 1.000 T
Hcr 328.3 mT
Mr 279.6 nAm²
S* (DCD) 0.0314
Orientation 0.0 deg
Elapsed time 10.9 min
0.20 g
File: 35-02b_bcr

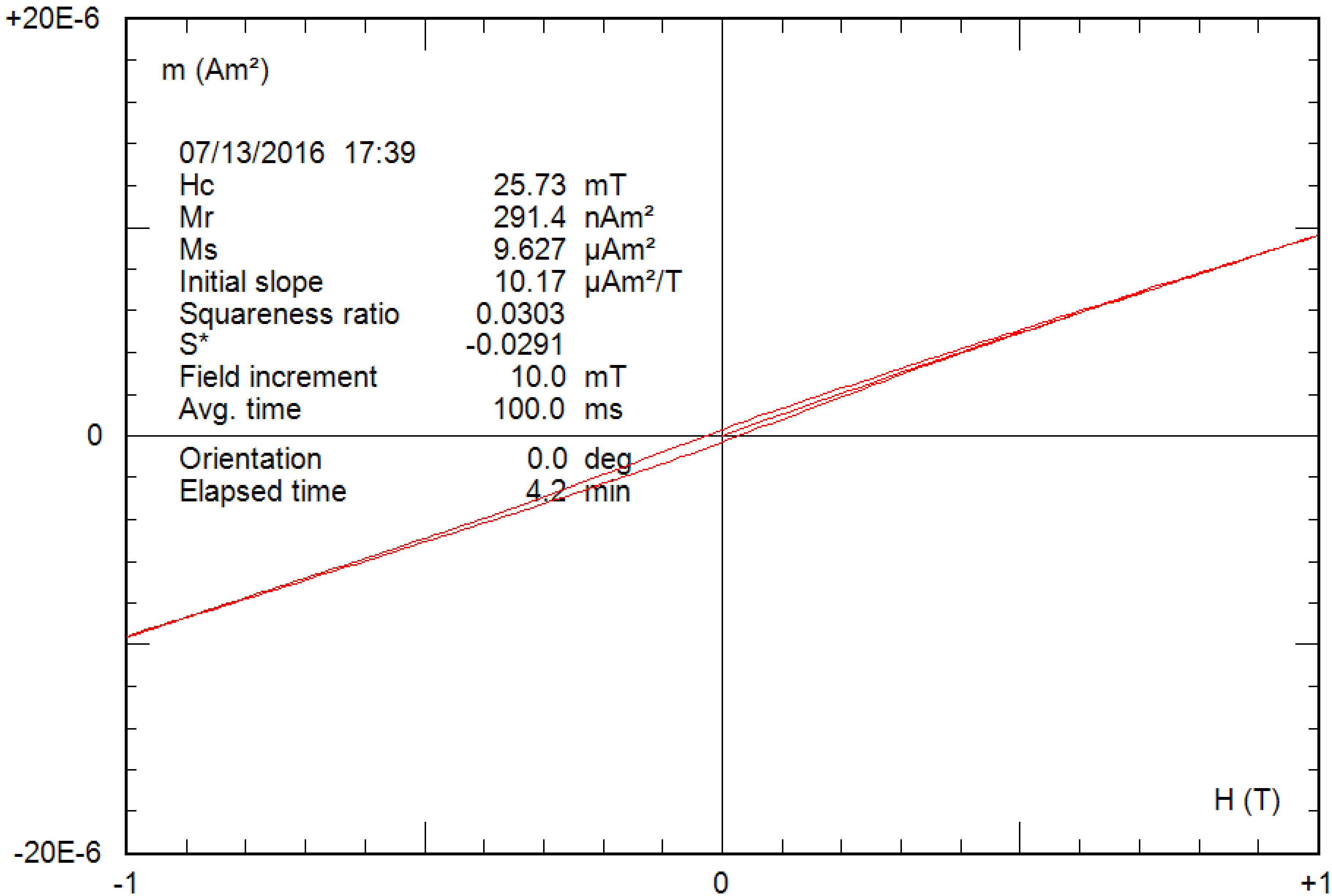

0.20 g

File: 35-02b_hyst

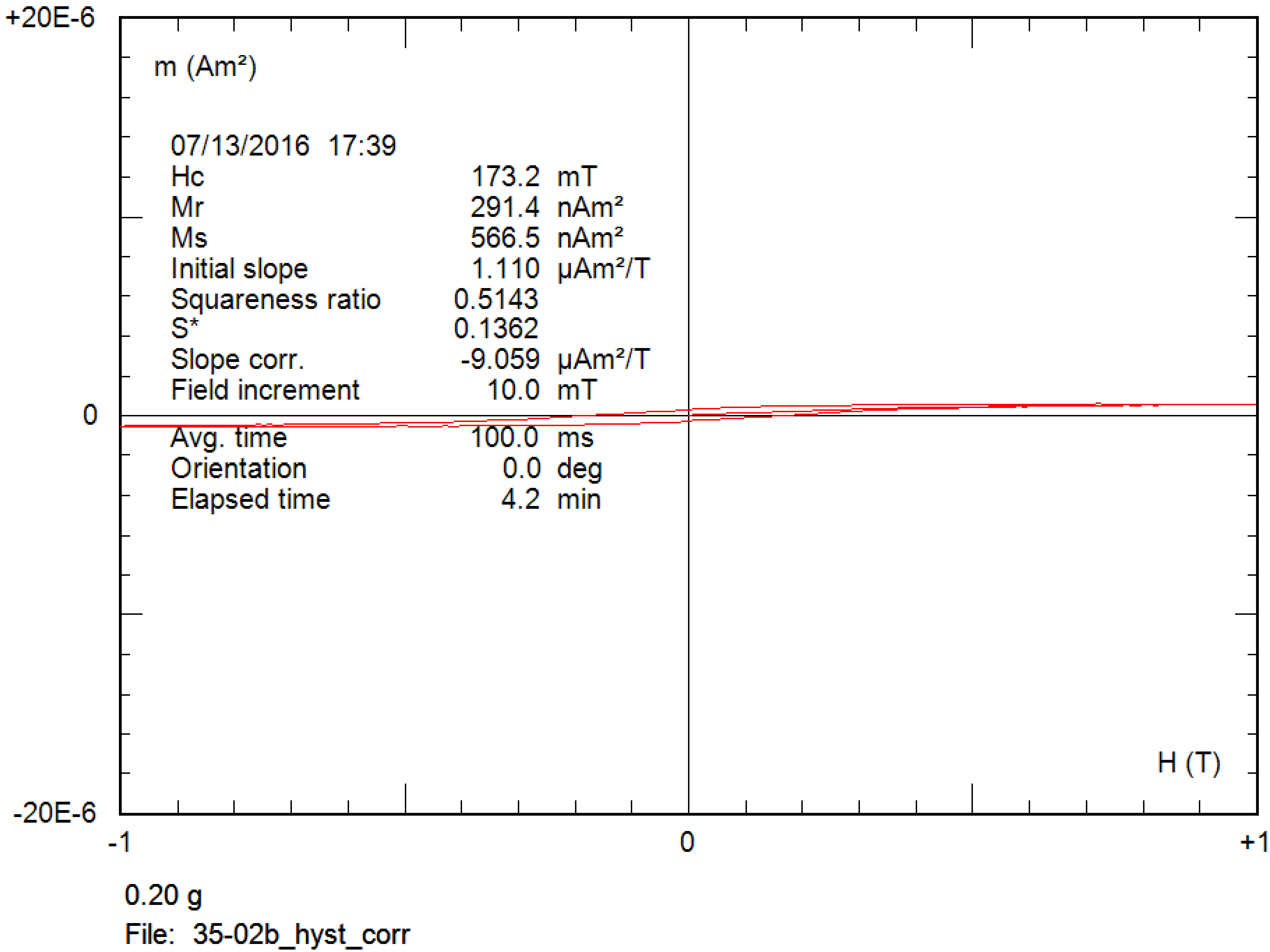

+20E-6
m (Am²)
07/13/2016 17:39
Hc 173.2 mT
Mr 291.4 nAm²
Ms 566.5 nAm²
Initial slope 1.110 µAm²/T
Squareness ratio 0.5143
S* 0.1362
Slope corr. -9.059 µAm²/T
Field increment 10.0 mT
0
Avg. time 100.0 ms
Orientation 0.0 deg
Elapsed time 4.2 min
H (T)
-20E-6
-1
0
+1
0.20 g
File: 35-02b_hyst_corr

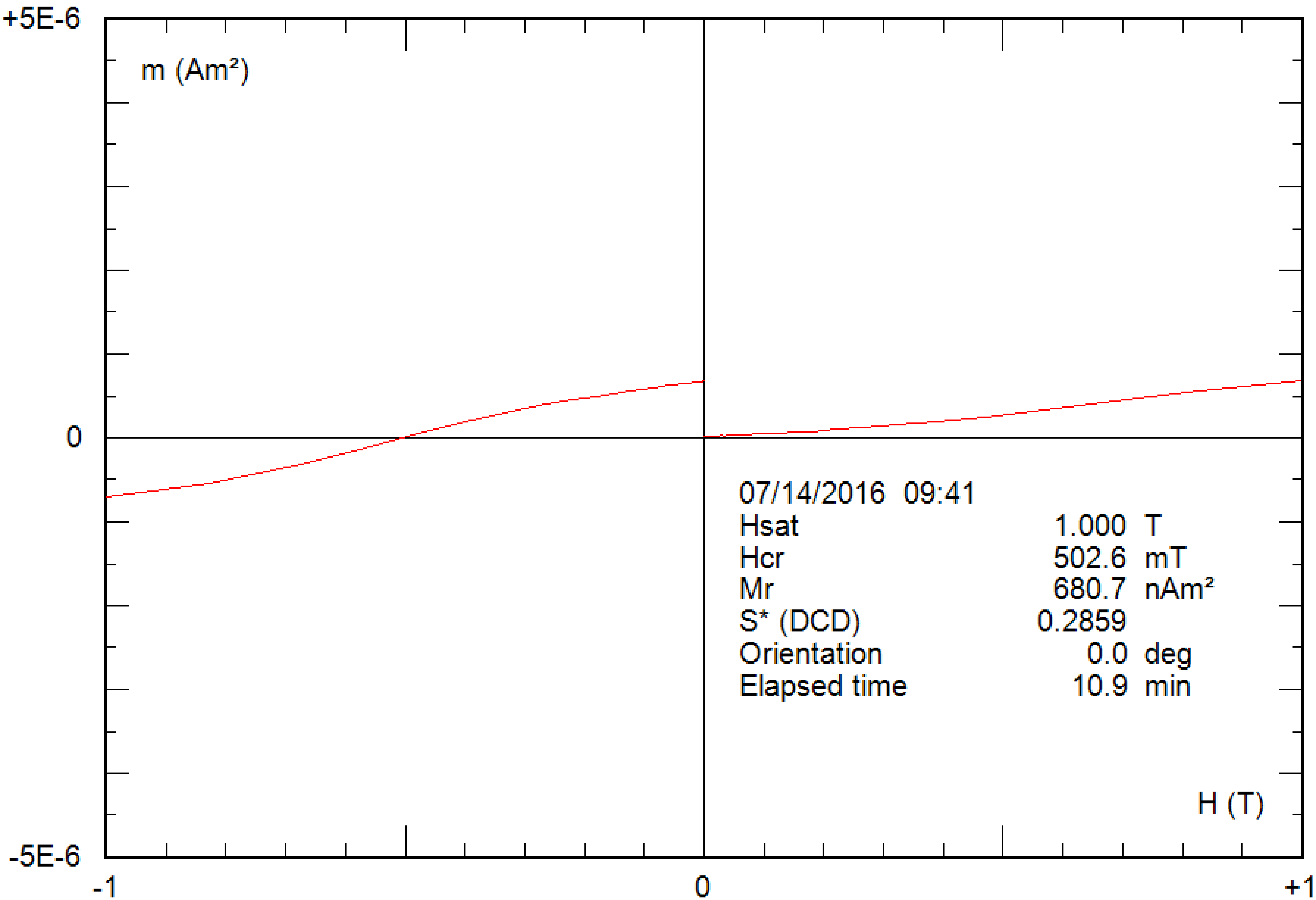

0.27 g
File: 36-07c_bcr

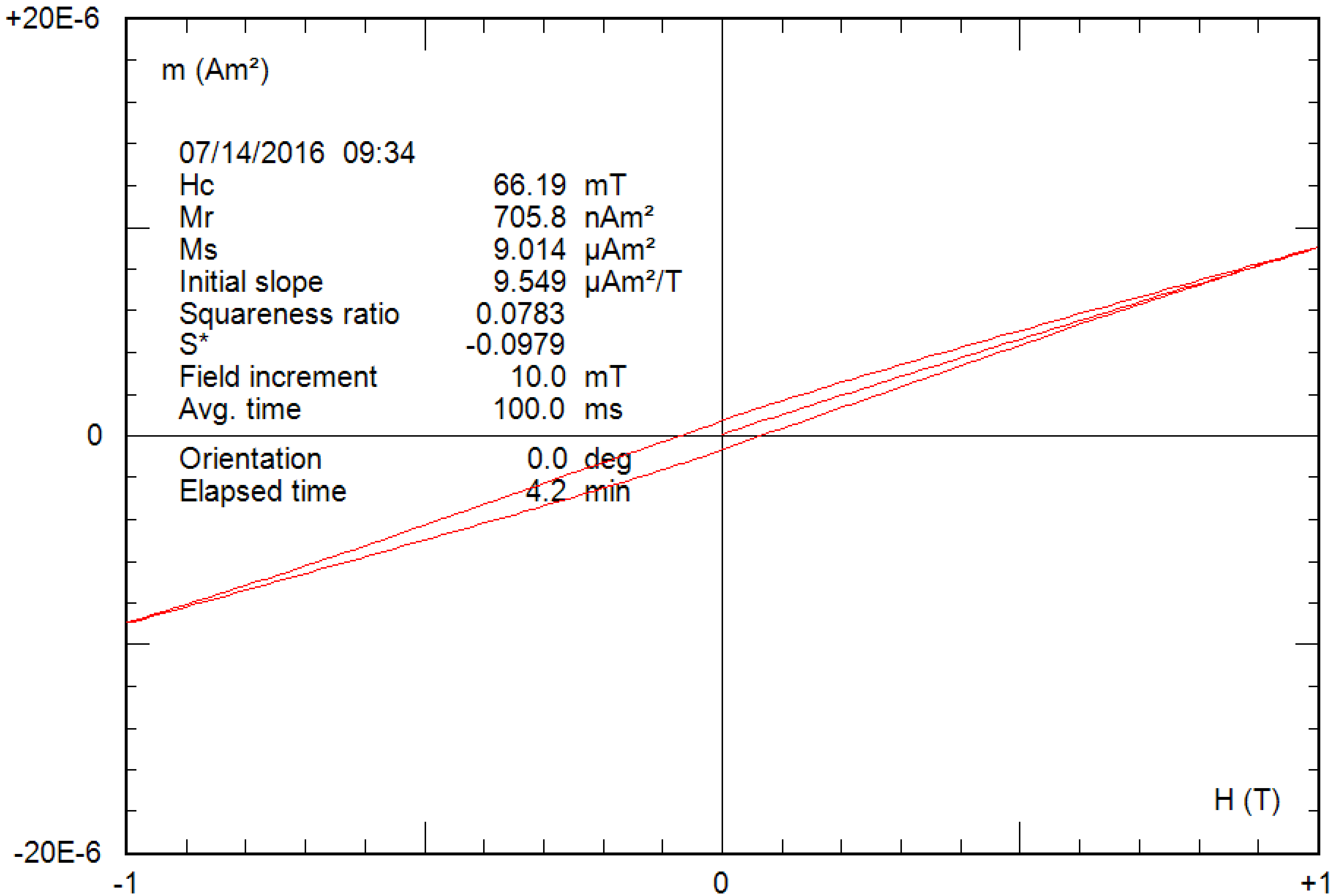

0.27 g

File: 36-07c_hyst

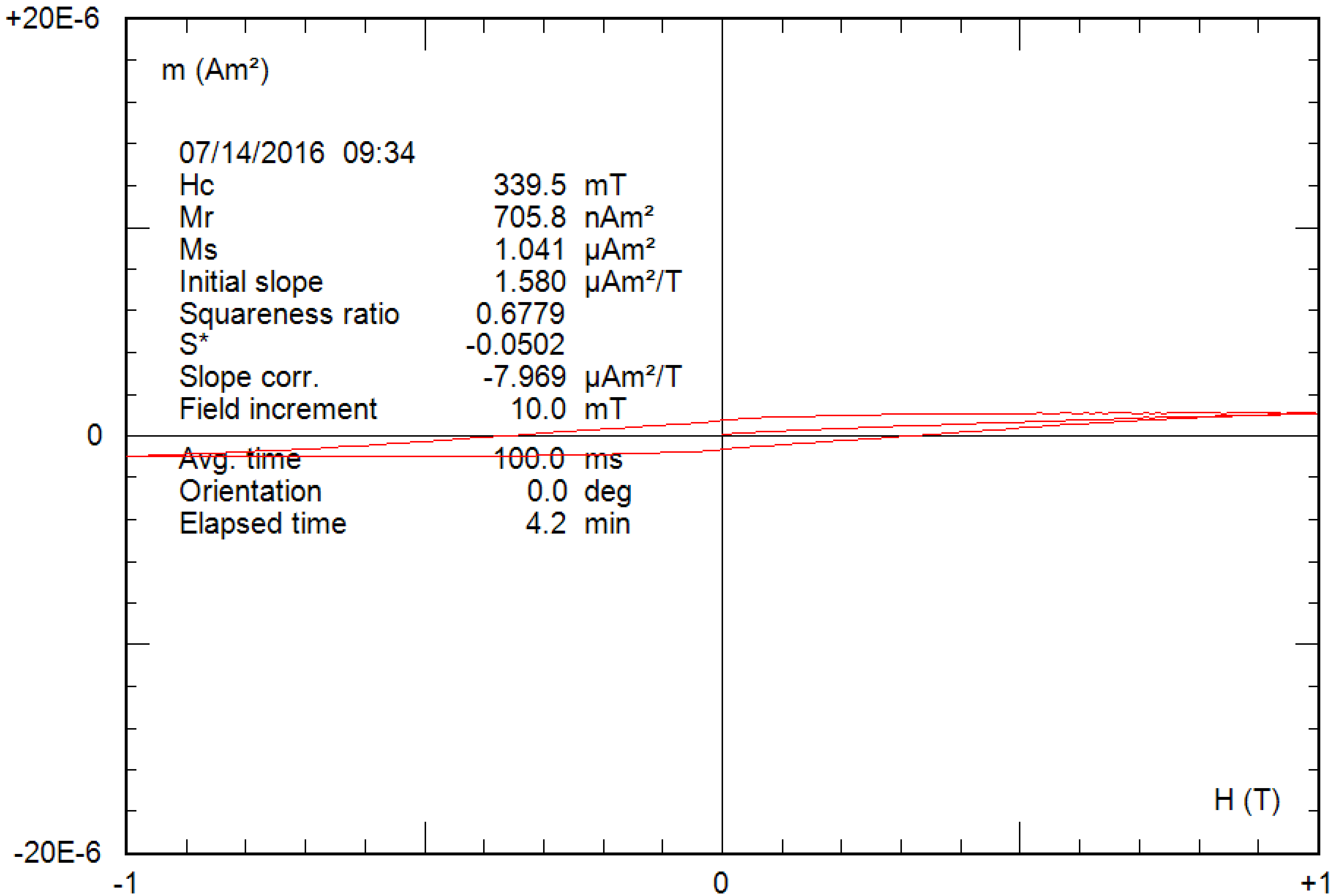

0.27 g

File: 36-07c_hyst_corr

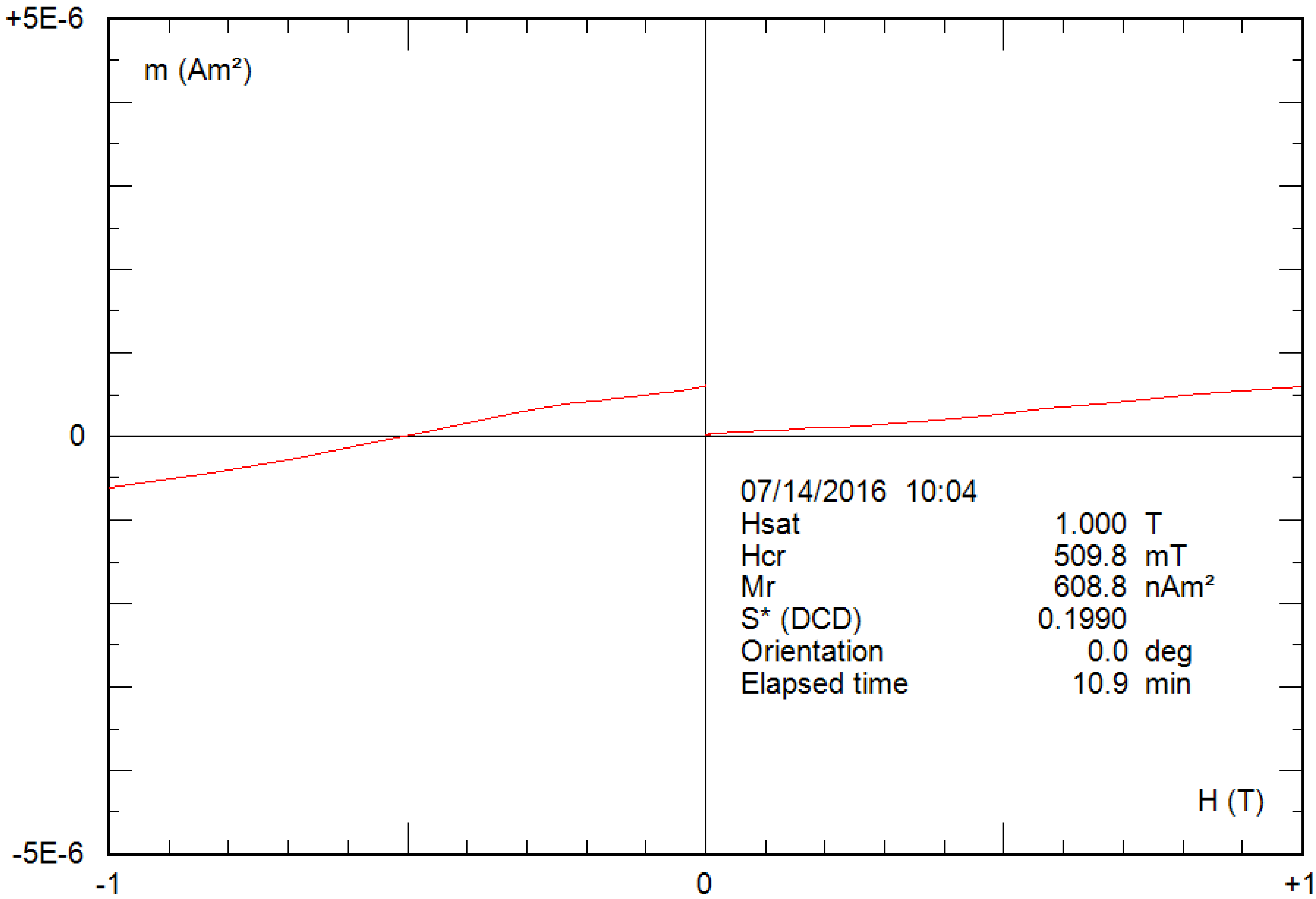

0.29 g

File: 37-03c_bcr

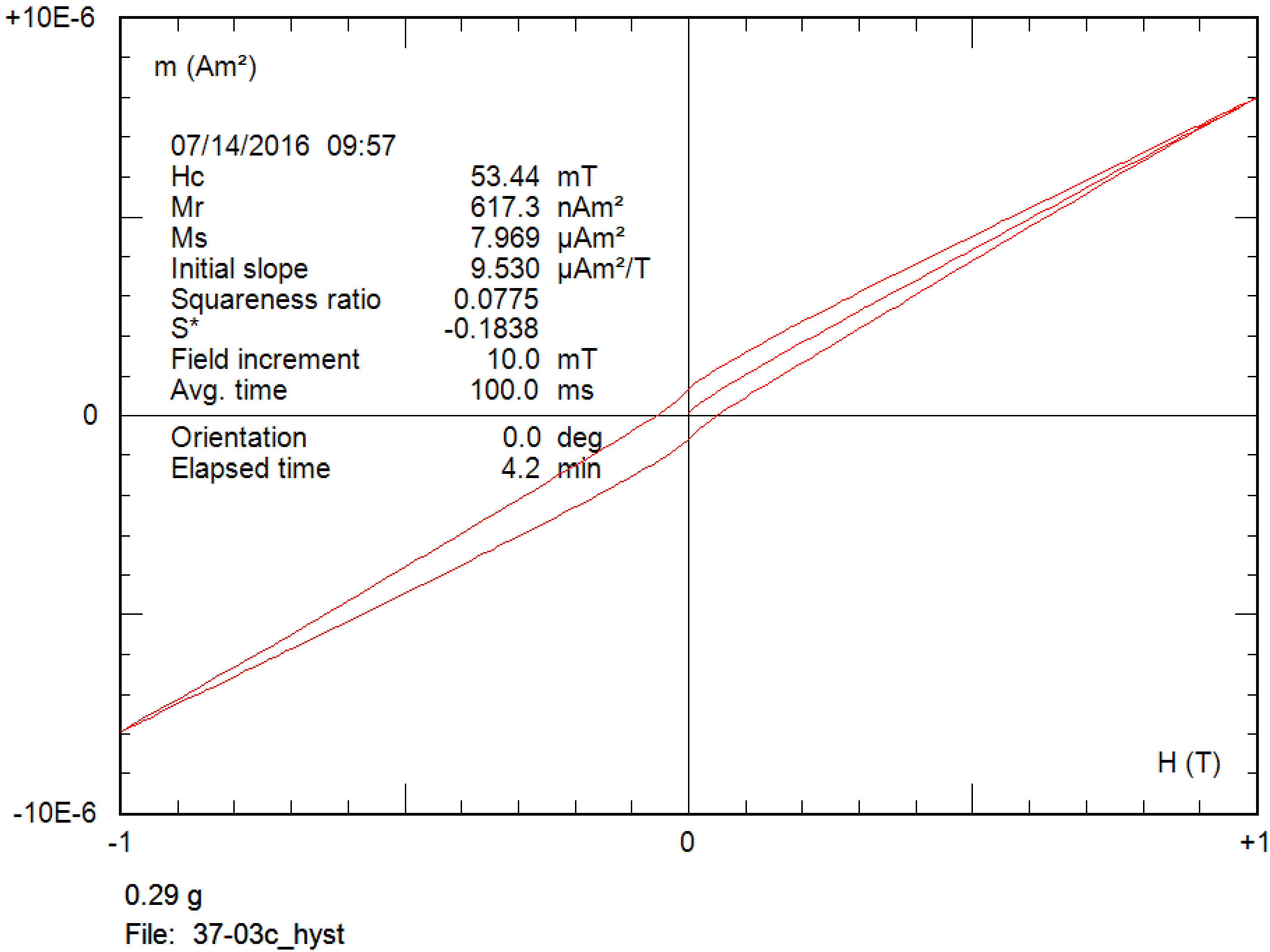
+10E-6
m (Am²)
07/14/2016 09:57
Hc 53.44 mT
Mr 617.3 nAm²
Ms 7.969 µAm²
Initial slope 9.530 µAm²/T
Squareness ratio 0.0775
S* -0.1838
Field increment 10.0 mT
Avg. time 100.0 ms
0
Orientation 0.0 deg
Elapsed time 4.2 min
H (T)
-10E-6
-1
0
+1
0.29 g
File: 37-03c_hyst

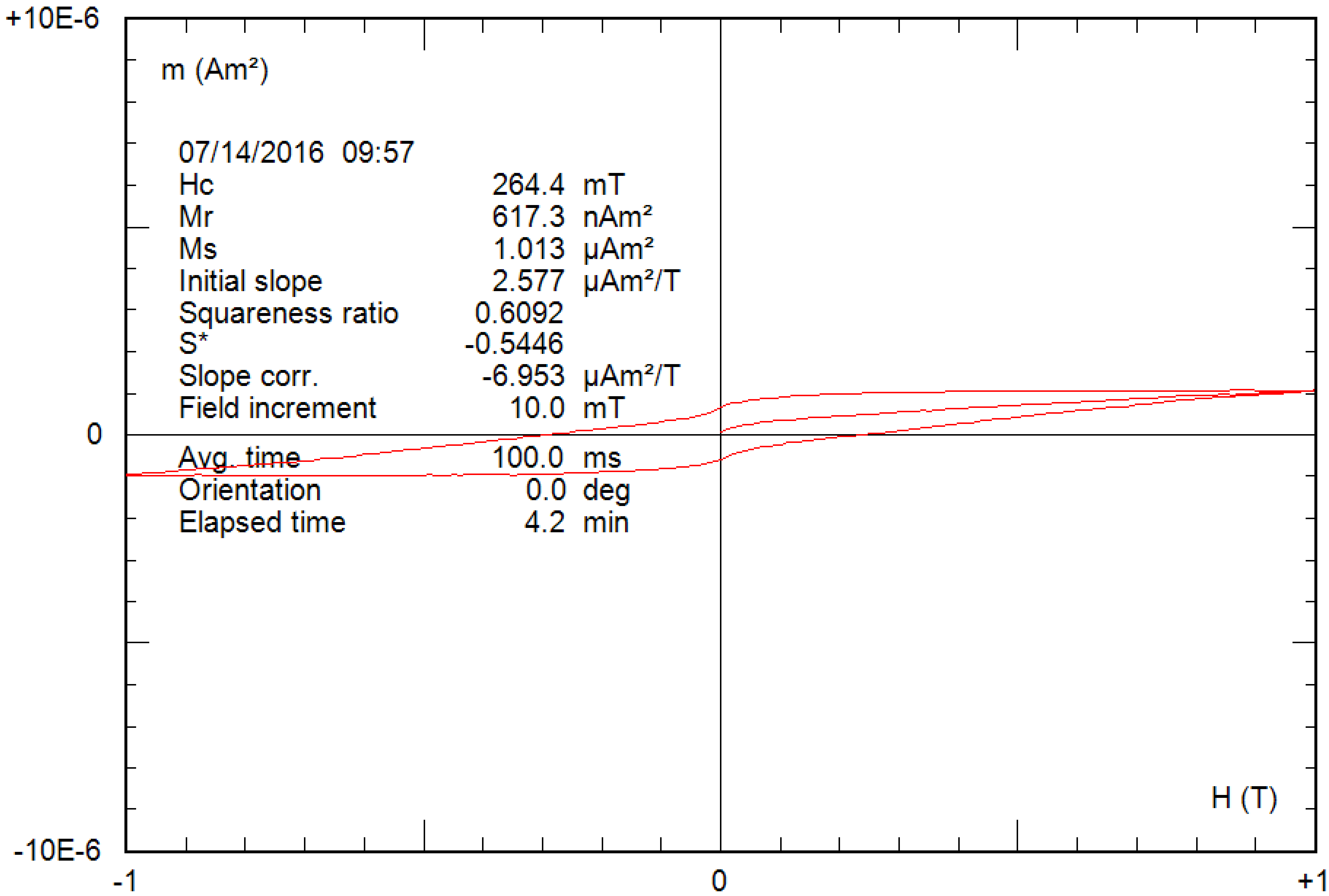

0.29 g

File: 37-03c_hyst_corr

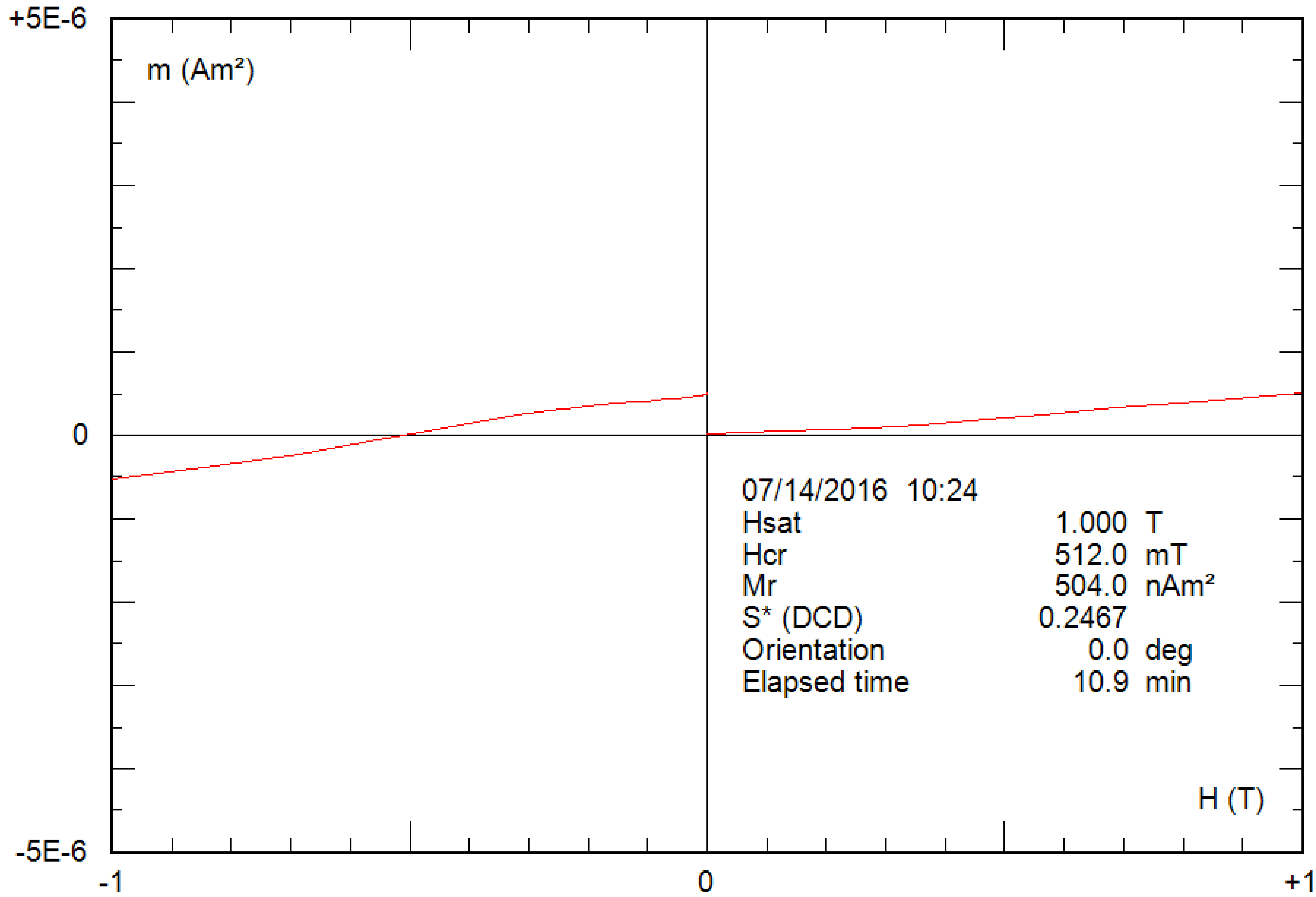

0.26 g

File: 38-04c_bcr

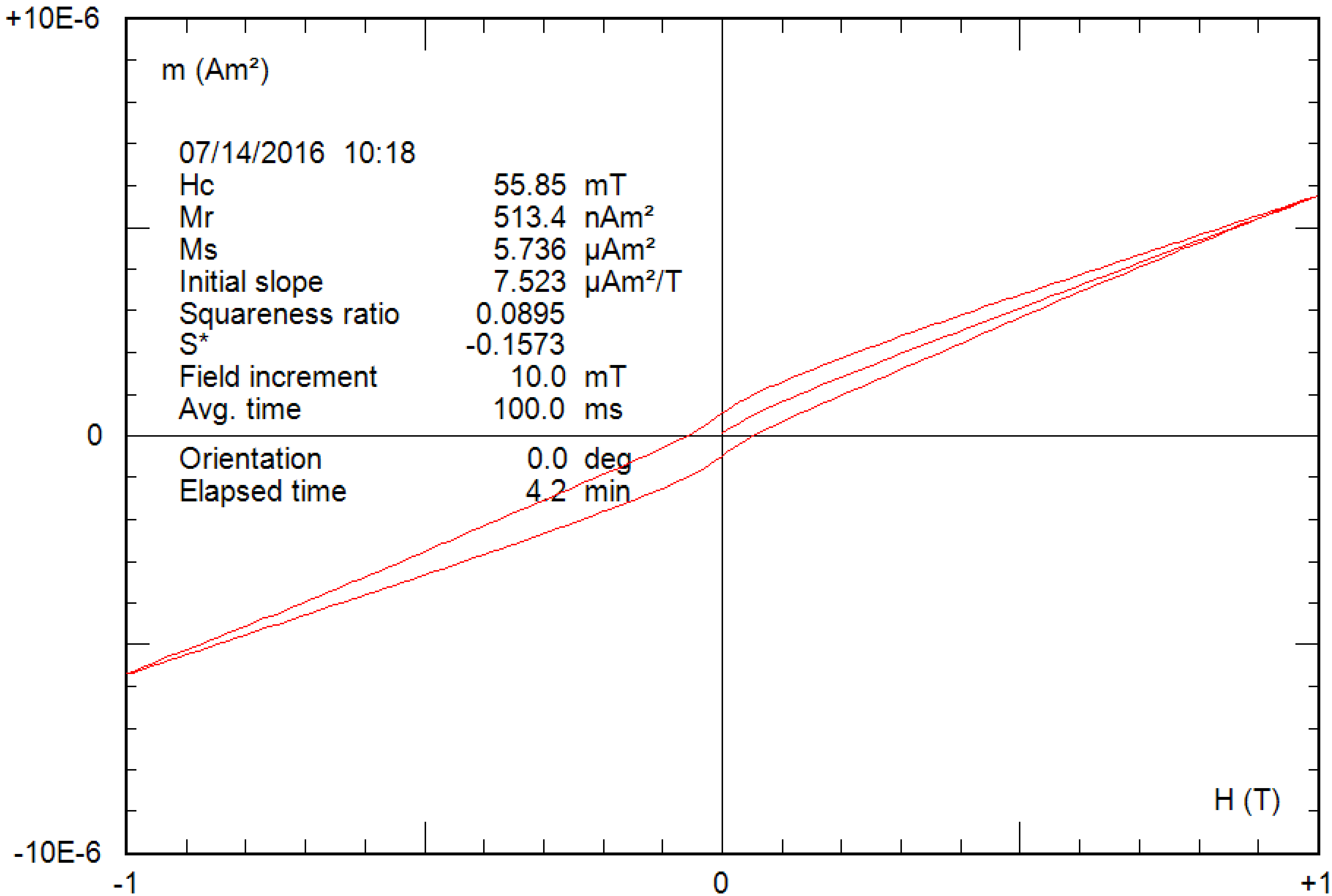

0.26 g

File: 38-04c_hyst

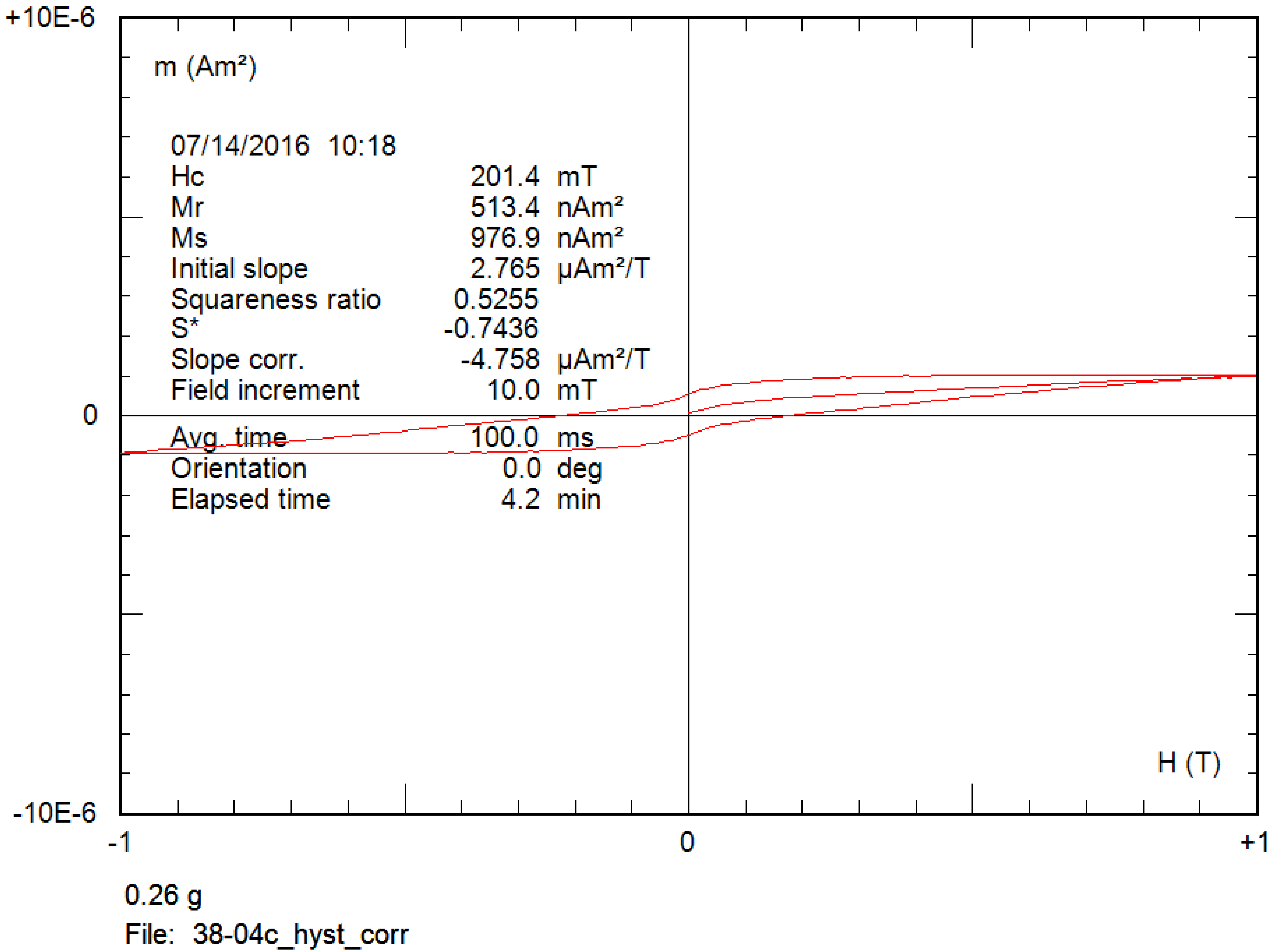
+10E-6
m (Am²)
07/14/2016 10:18
Hc 201.4 mT
Mr 513.4 nAm²
Ms 976.9 nAm²
Initial slope 2.765 µAm²/T
Squareness ratio 0.5255
S* -0.7436
Slope corr. -4.758 µAm²/T
Field increment 10.0 mT
0
Avg. time 100.0 ms
Orientation 0.0 deg
Elapsed time 4.2 min
H (T)
-10E-6
-1
0
+1
0.26 g
File: 38-04c_hyst_corr

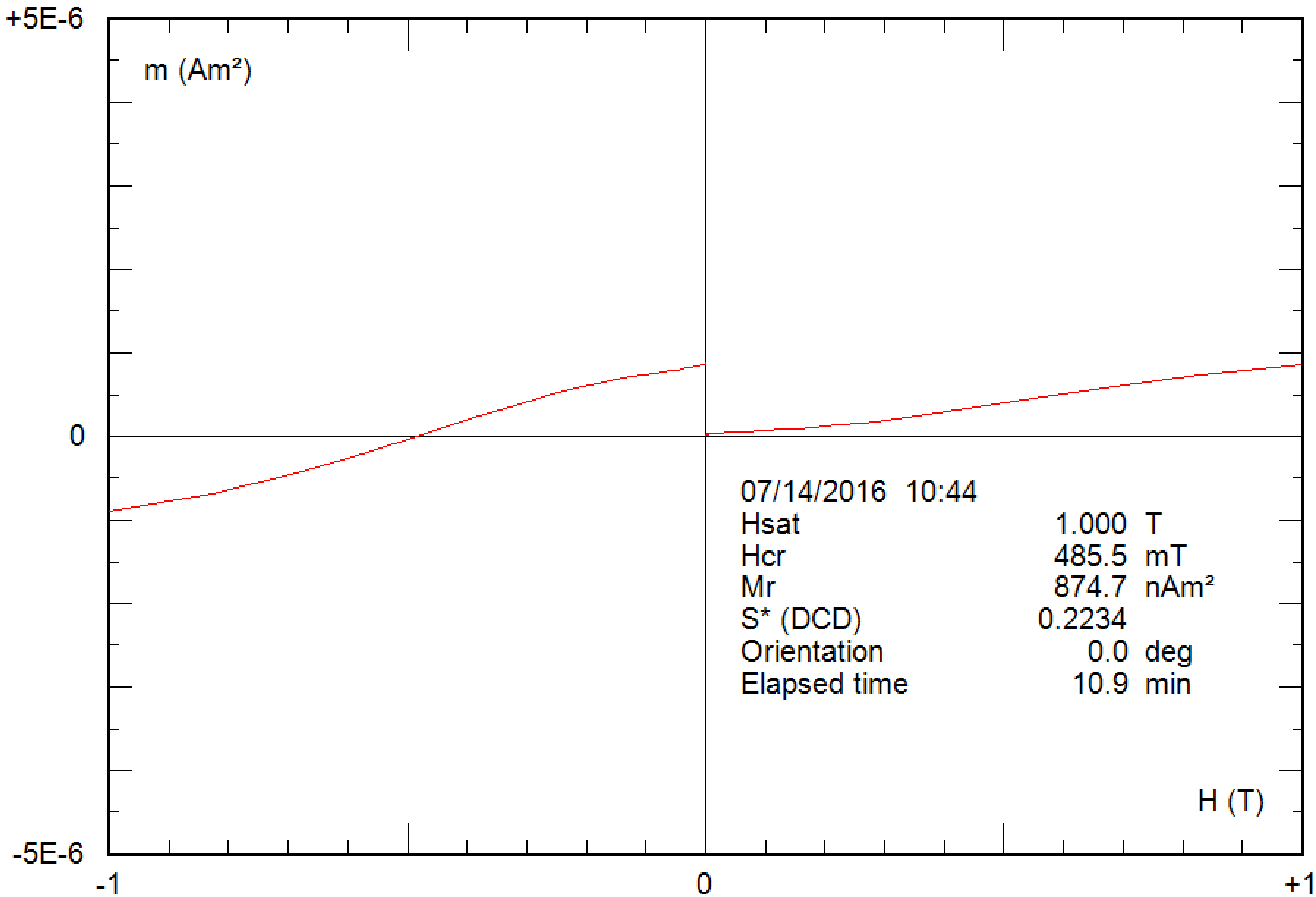

0.24 g

File: 39-04b_bcr

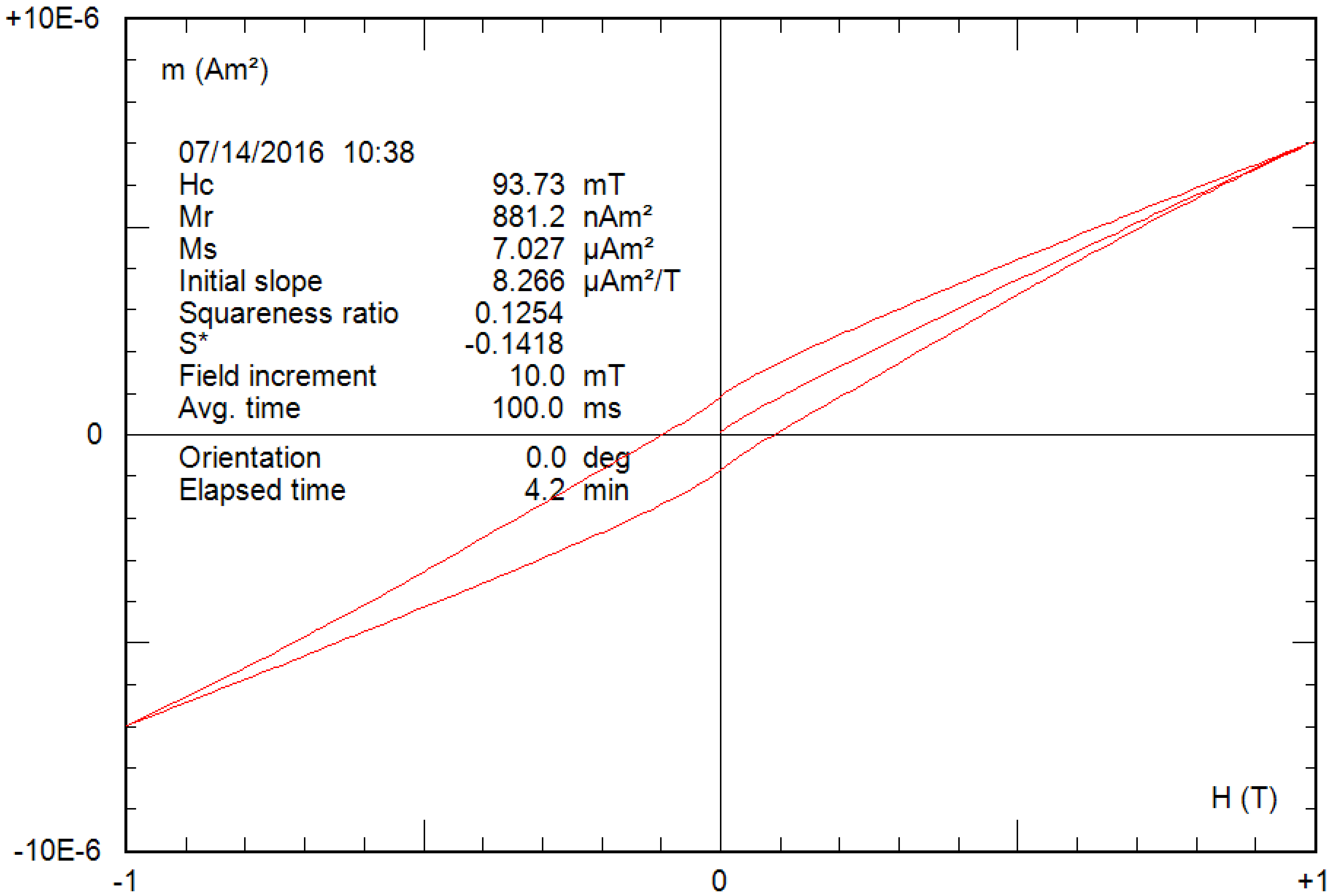

0.24 g

File: 39-04b_hyst

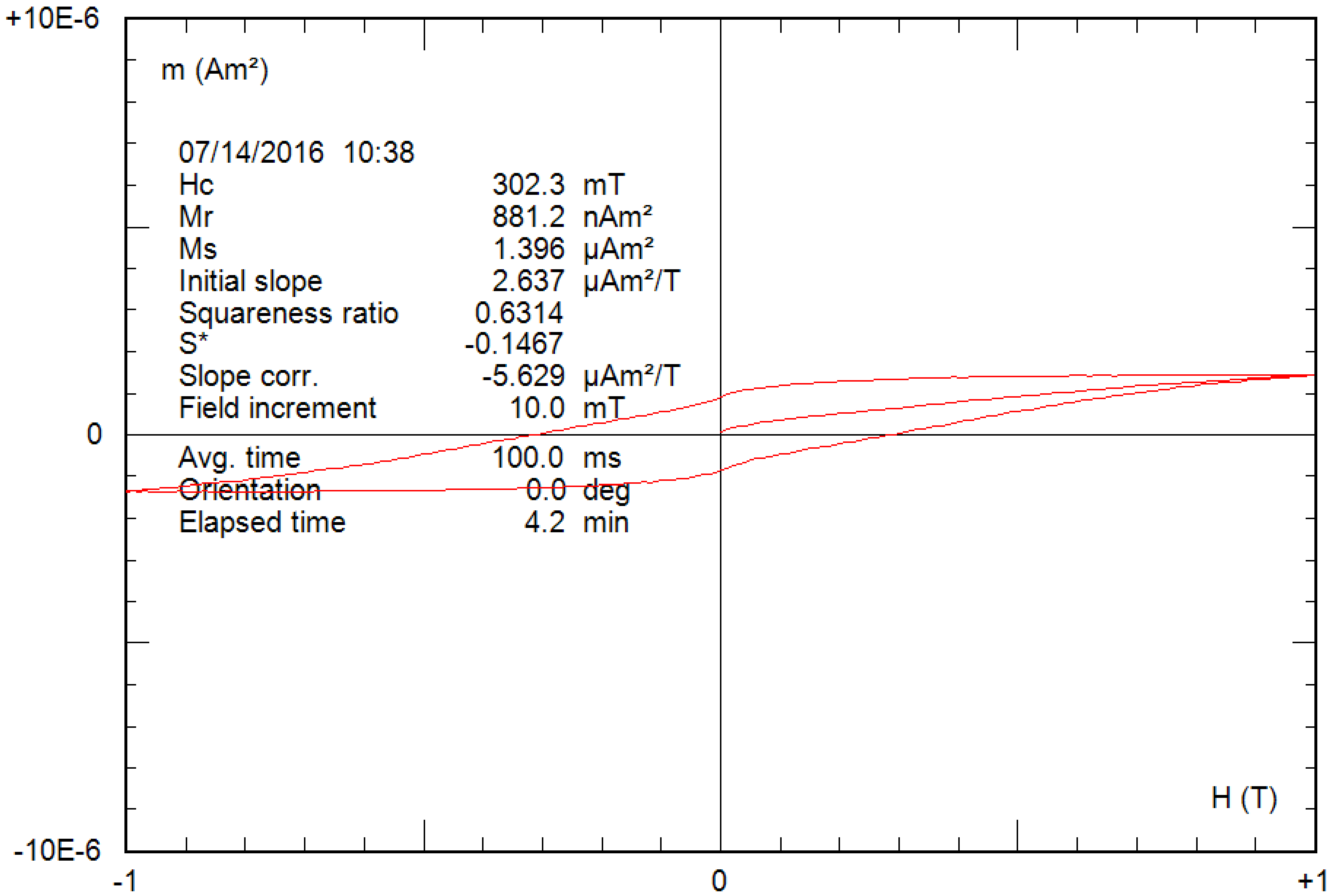

0.24 g

File: 39-04b_hyst_corr

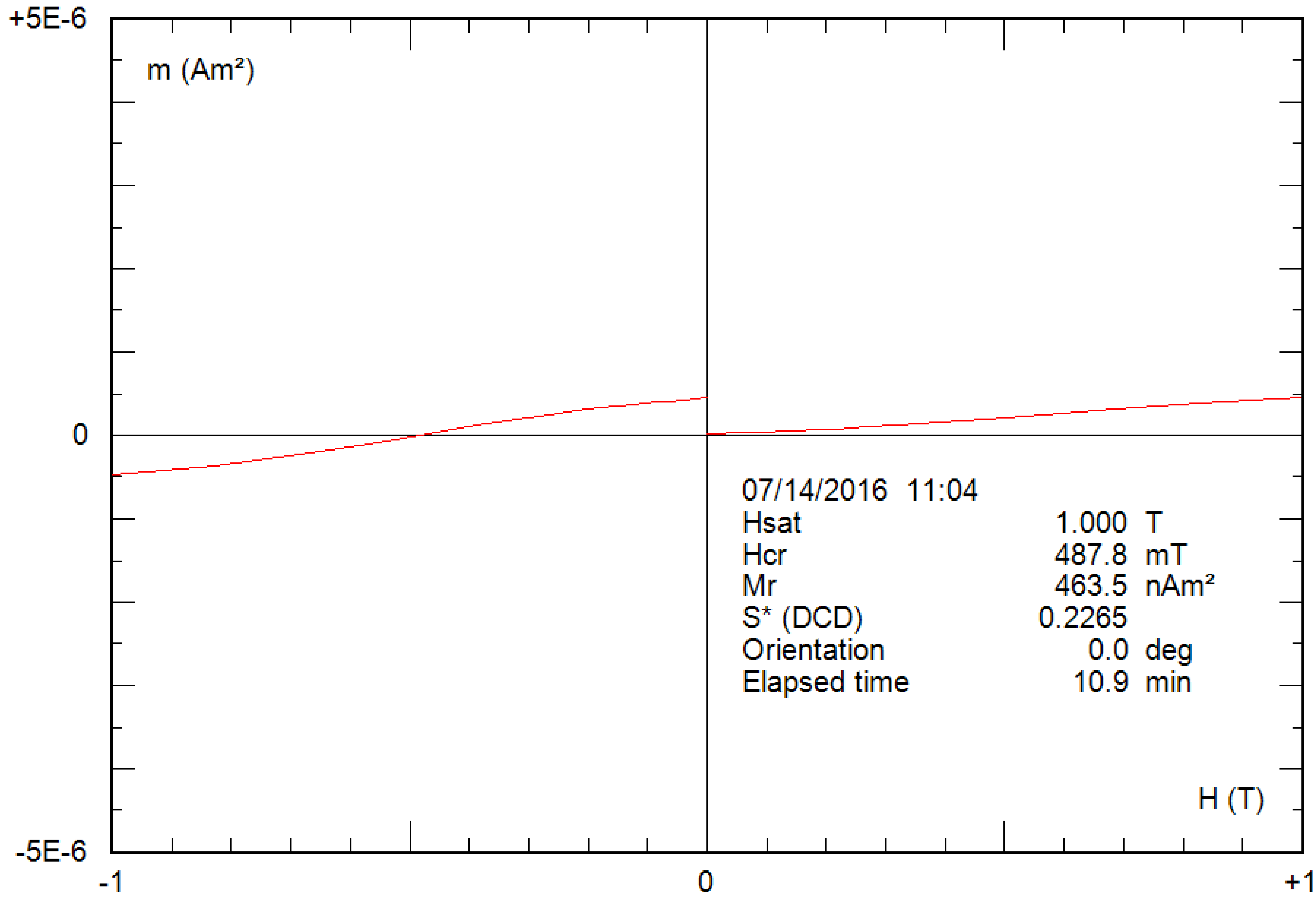

0.22 g

File: 40-05c_bcr

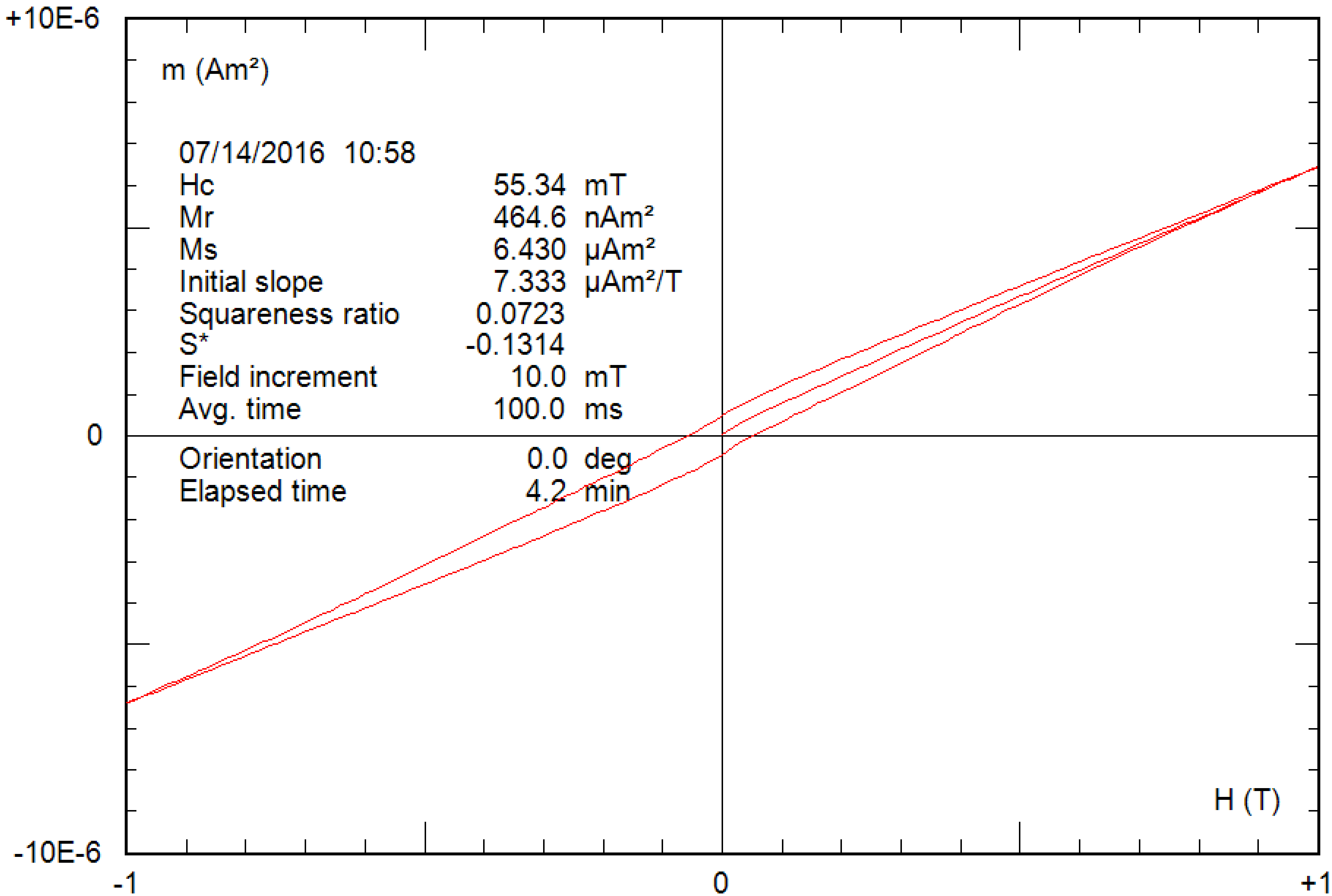

0.22 g

File: 40-05c_hyst

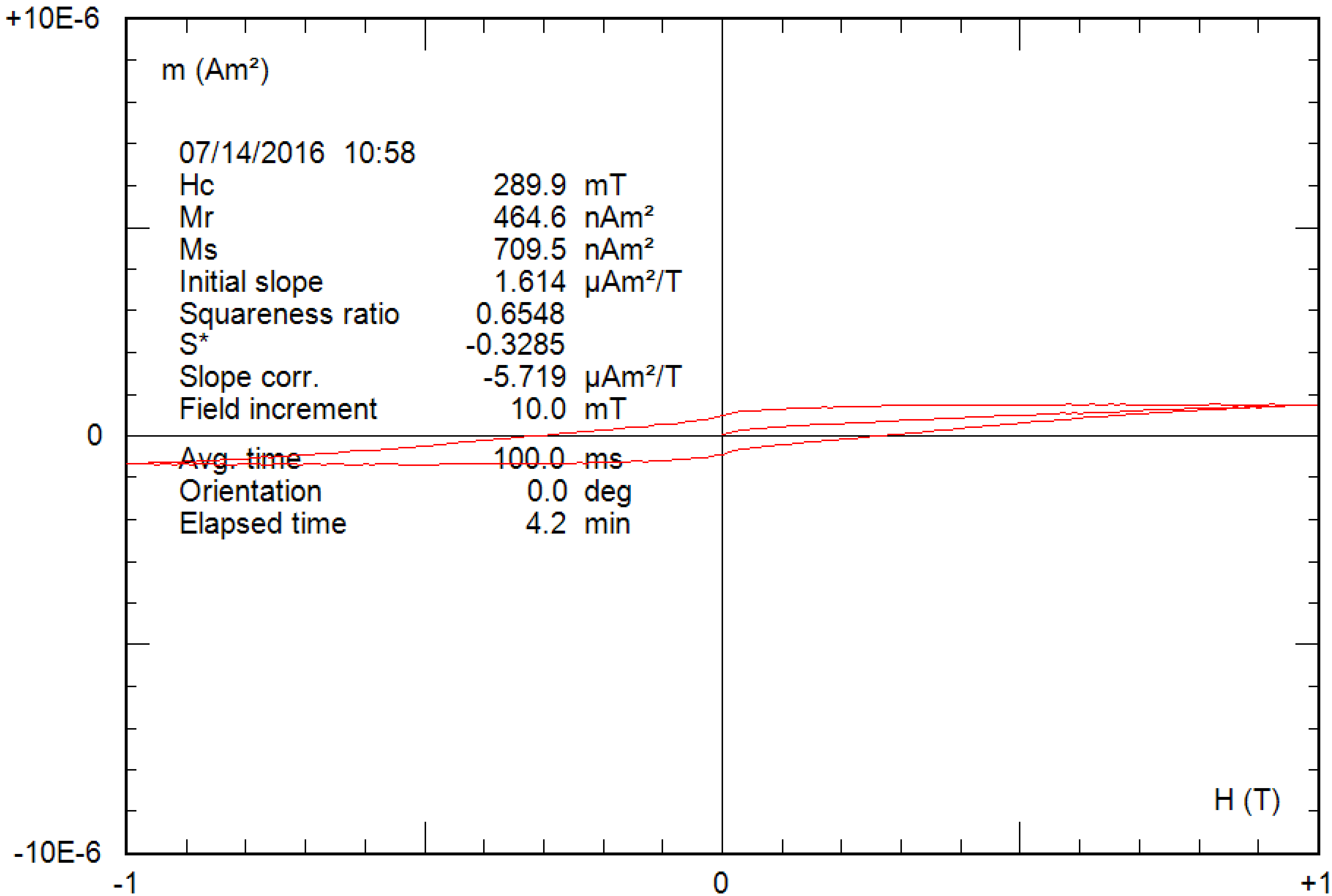

0.22 g

File: 40-05c_hyst_corr

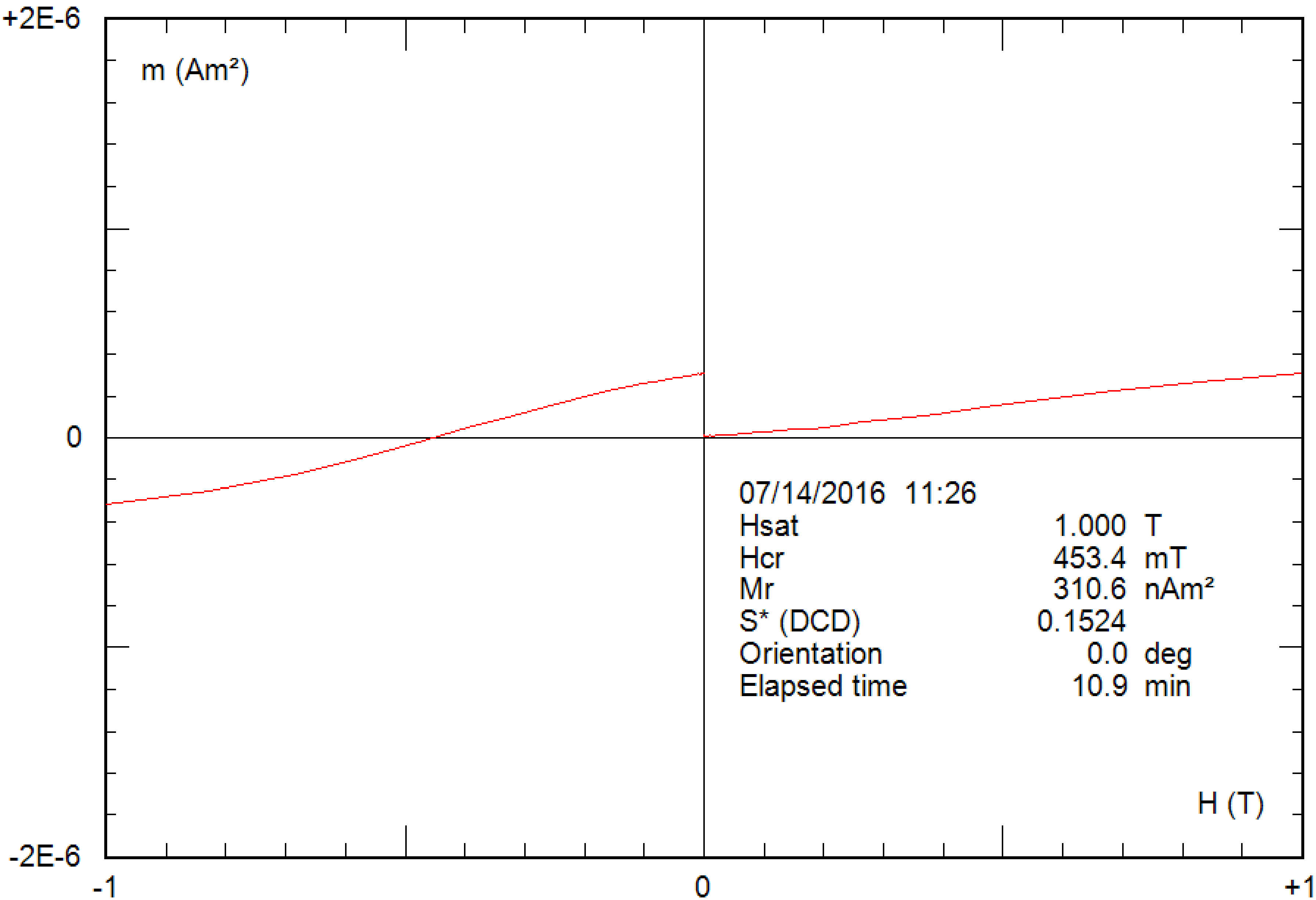

0.26 g

File: 41-04c_bcr

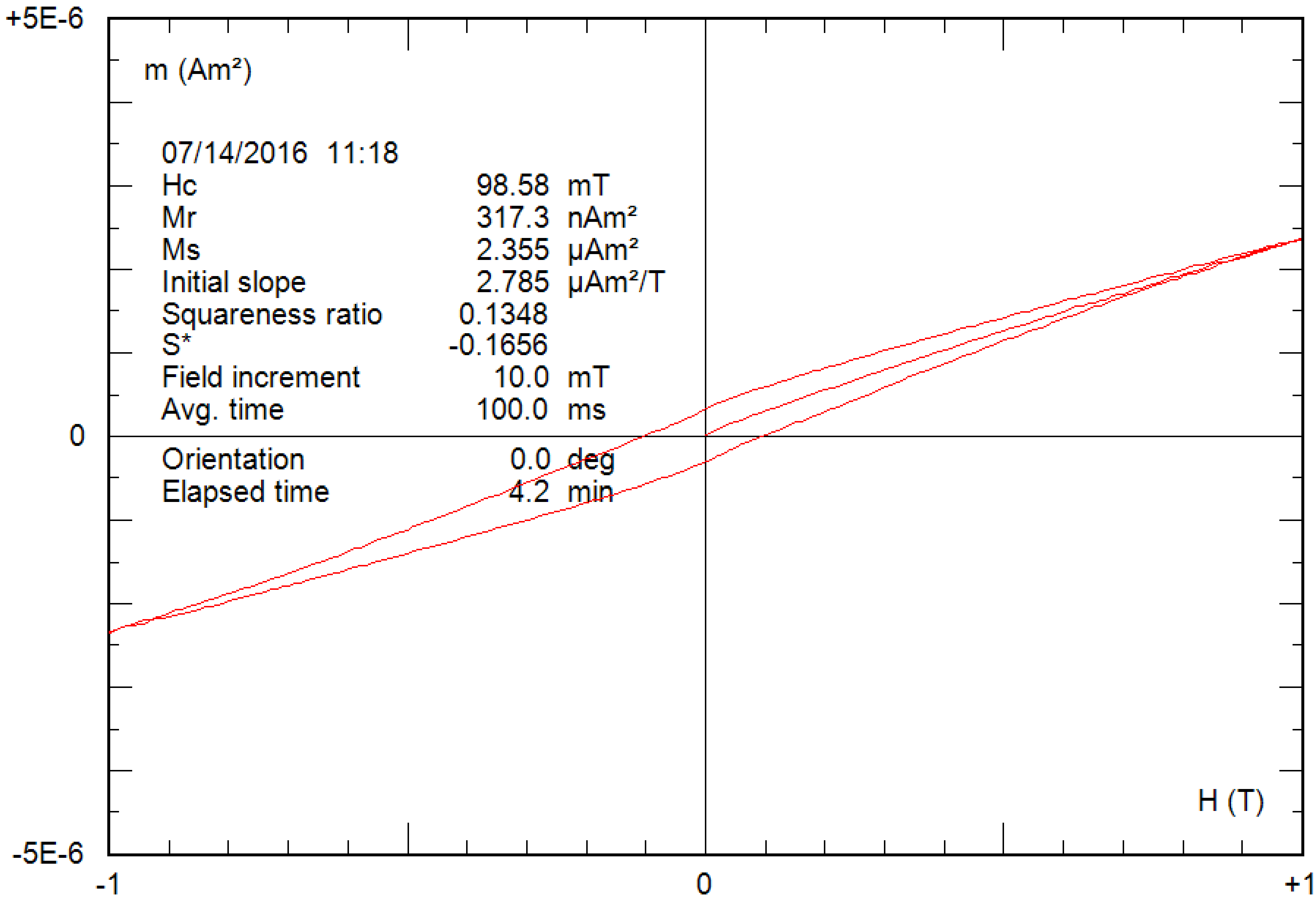

0.26 g

File: 41-04c_hyst

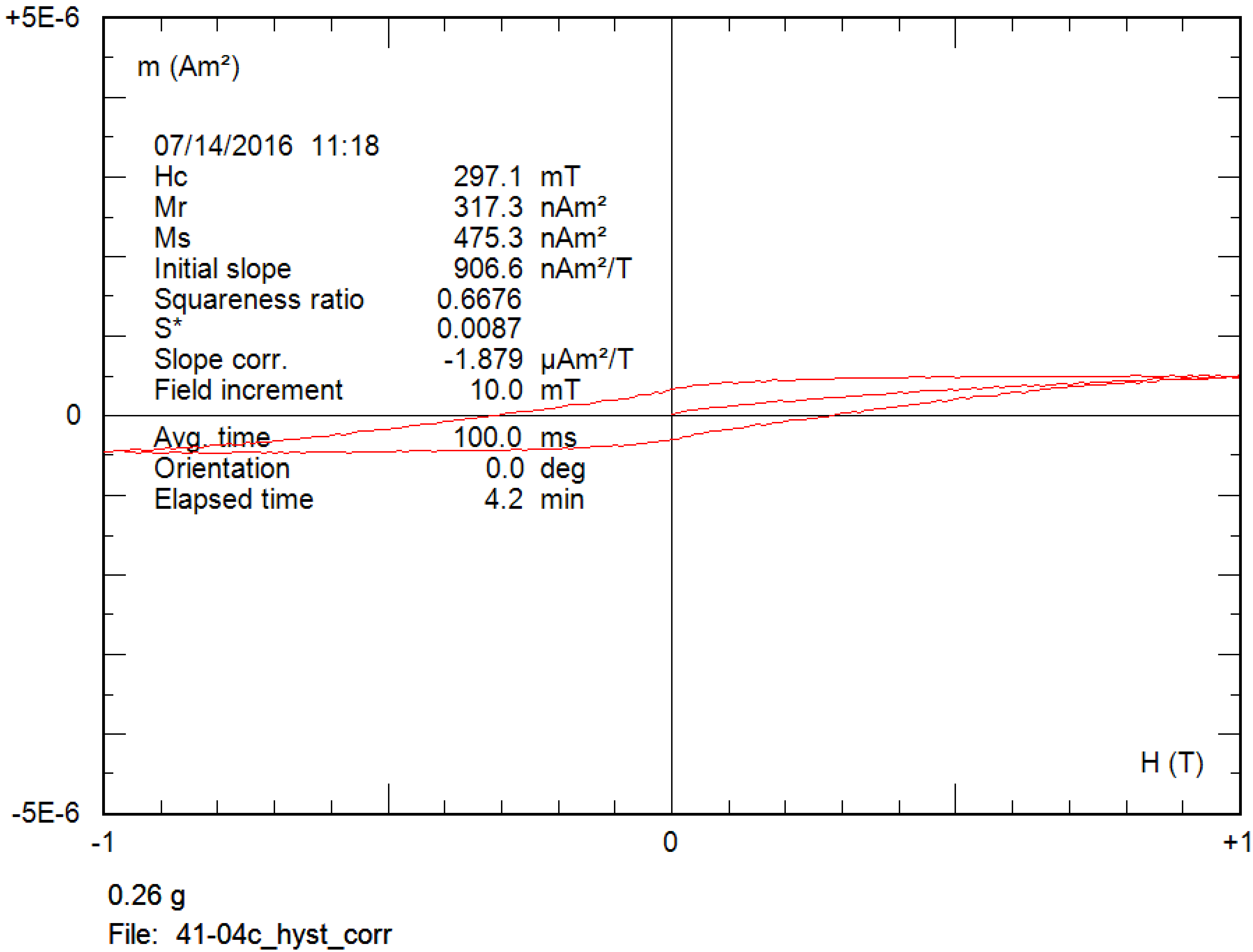
+5E-6
m (Am²)
07/14/2016 11:18
Hc 297.1 mT
Mr 317.3 nAm²
Ms 475.3 nAm²
Initial slope 906.6 nAm²/T
Squareness ratio 0.6676
S* 0.0087
Slope corr. -1.879 µAm²/T
Field increment 10.0 mT
0
Avg. time 100.0 ms
Orientation 0.0 deg
Elapsed time 4.2 min
H (T)
-5E-6
-1
0
+1
0.26 g
File: 41-04c_hyst_corr

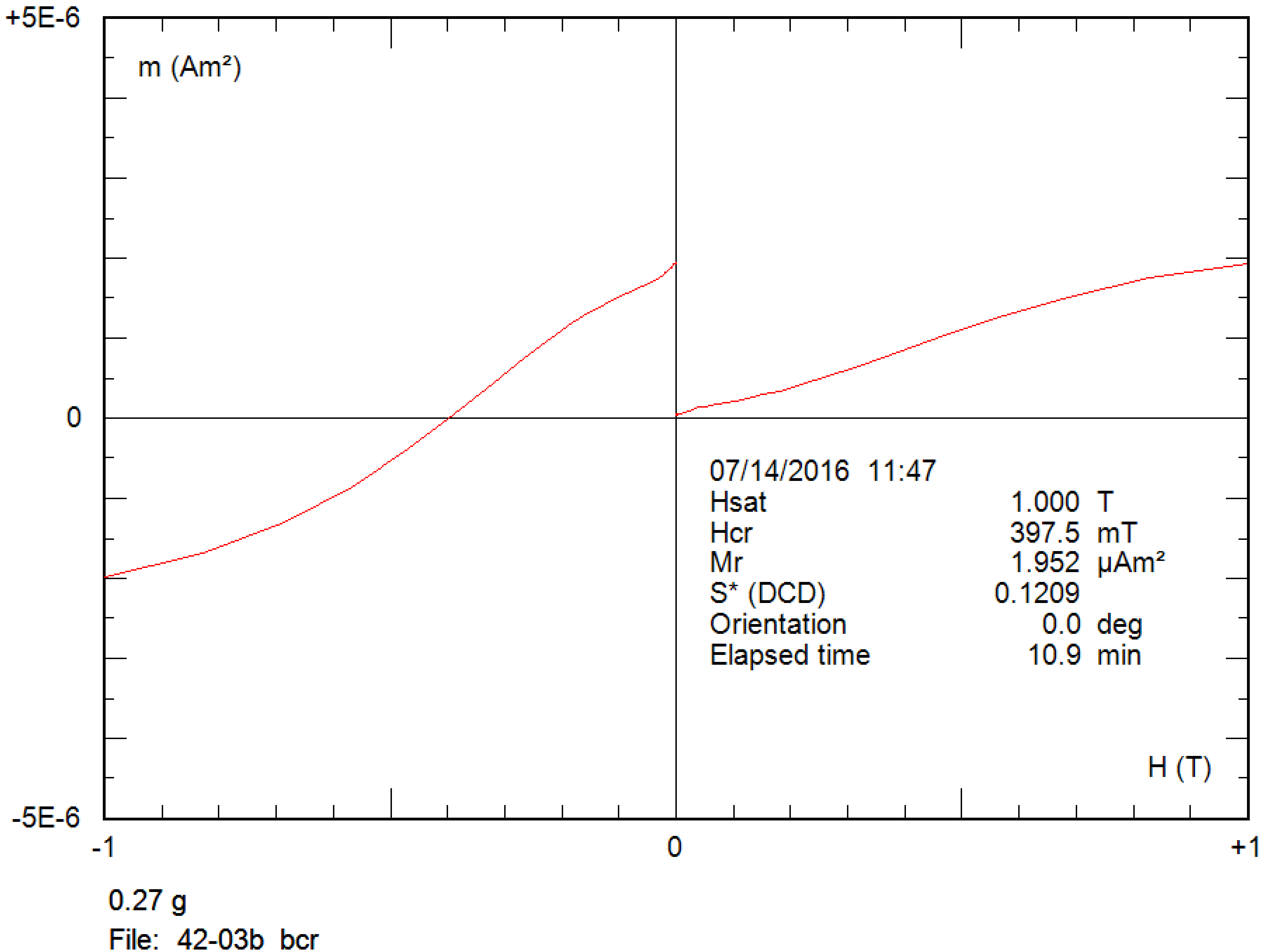
+5E-6
m (Am²)
0
-5E-6
-1
0
+1
H (T)
07/14/2016 11:47
Hsat 1.000 T
Hcr 397.5 mT
Mr 1.952 µAm²
S* (DCD) 0.1209
Orientation 0.0 deg
Elapsed time 10.9 min
0.27 g
File: 42-03b_bcr

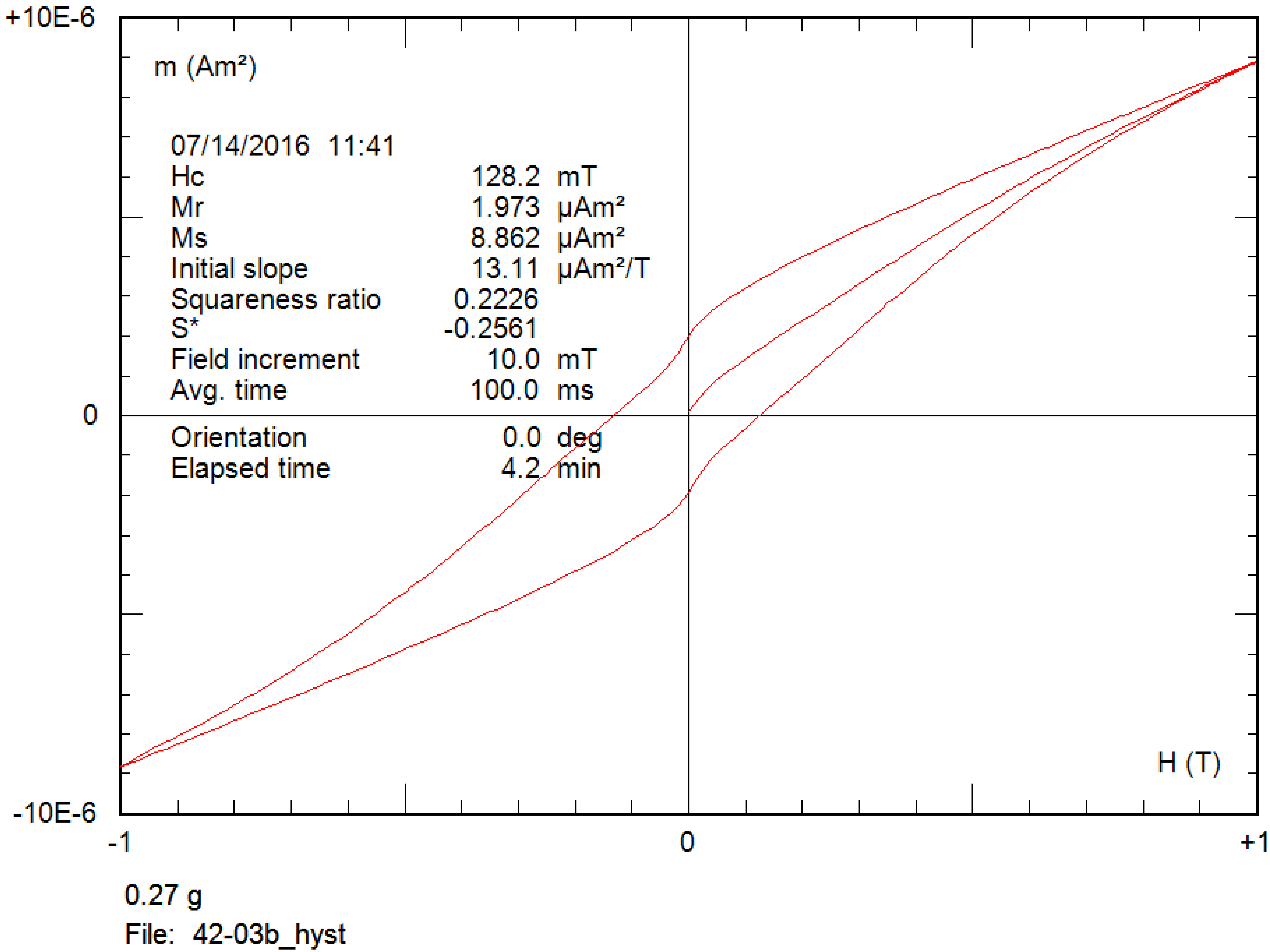

+10E-6
m (Am²)
07/14/2016 11:41
Hc 128.2 mT
Mr 1.973 µAm²
Ms 8.862 µAm²
Initial slope 13.11 µAm²/T
Squareness ratio 0.2226
S* -0.2561
Field increment 10.0 mT
Avg. time 100.0 ms
0
Orientation 0.0 deg
Elapsed time 4.2 min
H (T)
-10E-6
-1
0
+1
0.27 g
File: 42-03b_hyst

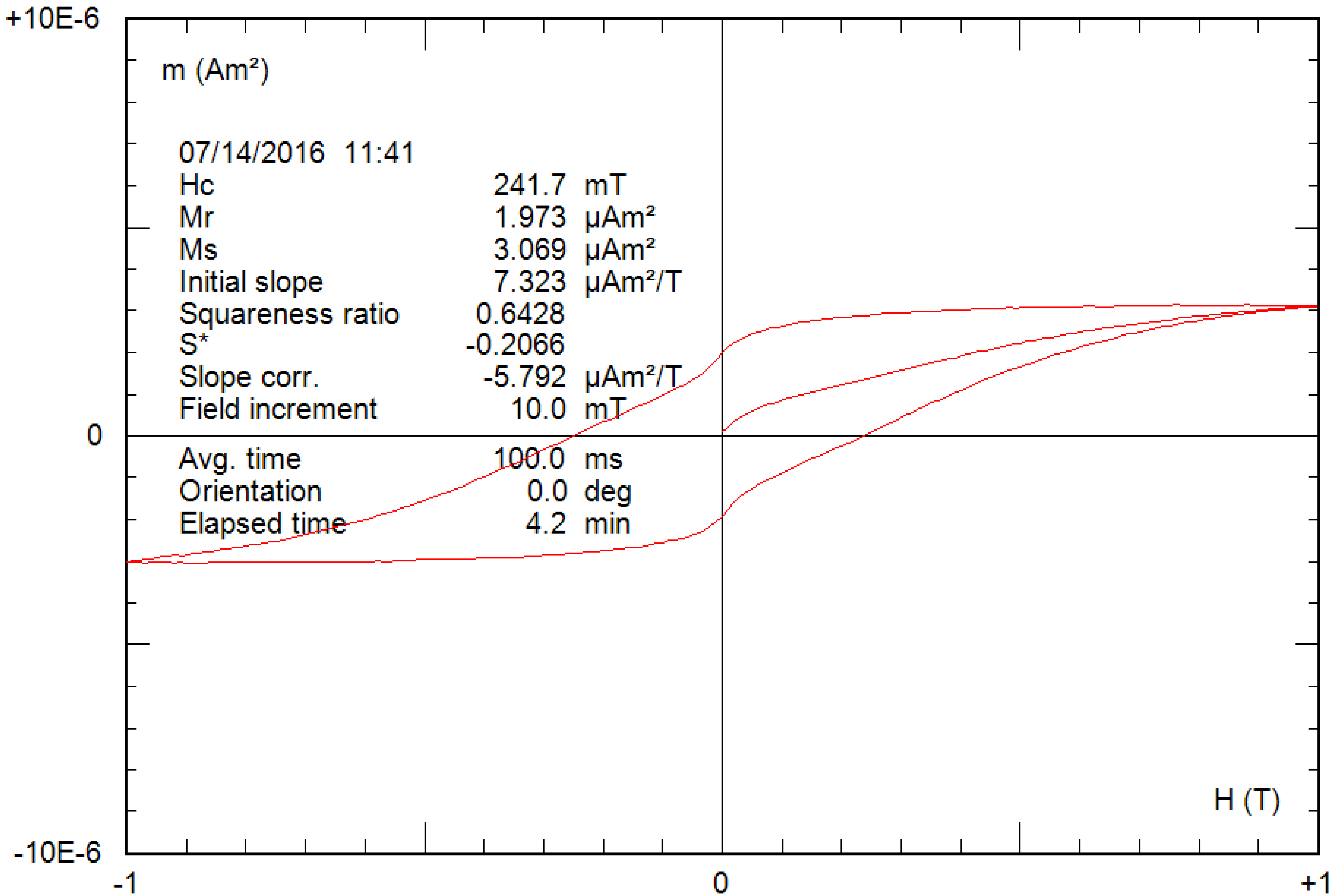

0.27 g

File: 42-03b_hyst_corr

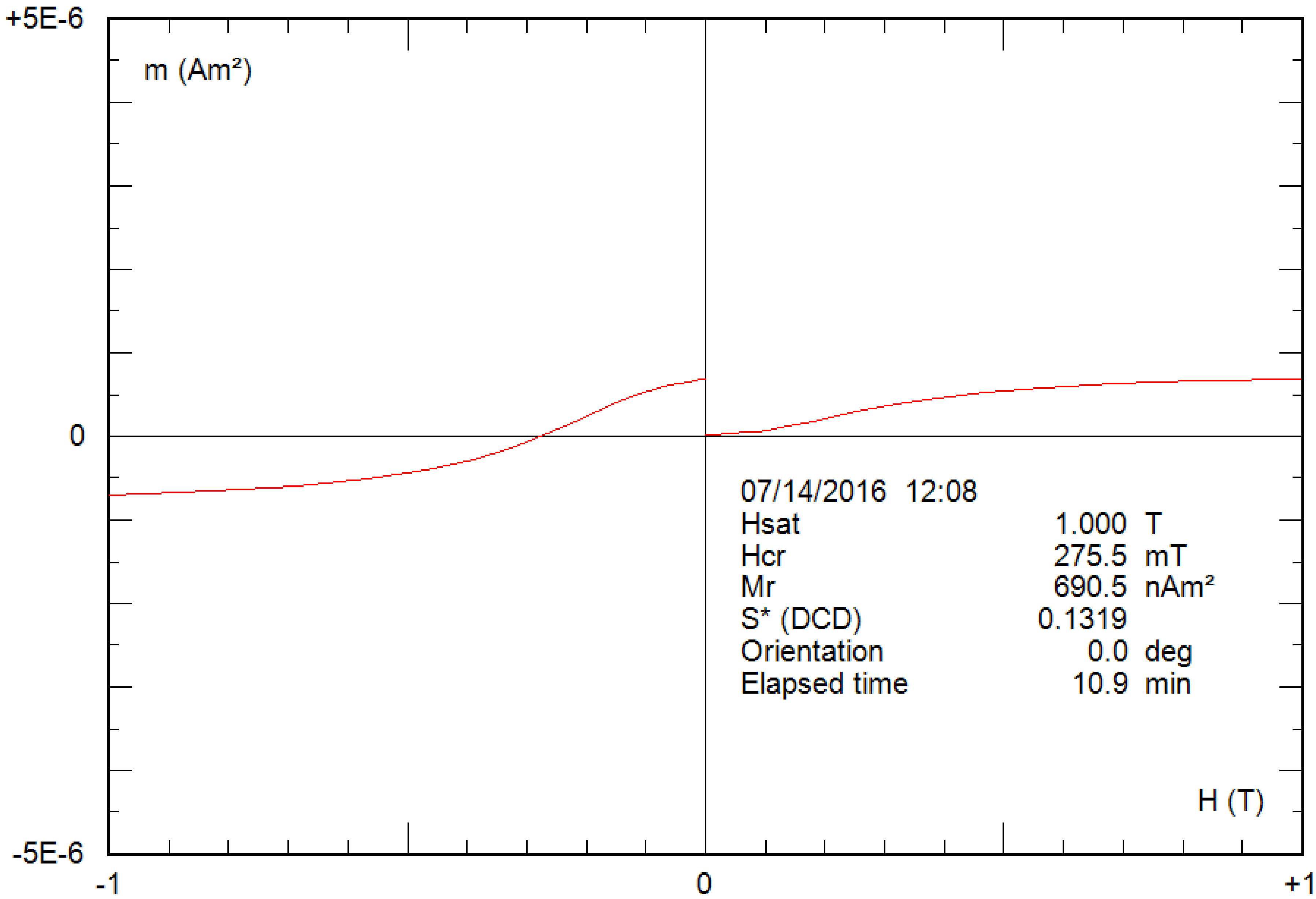

0.24 g

File: 43-05c_bcr

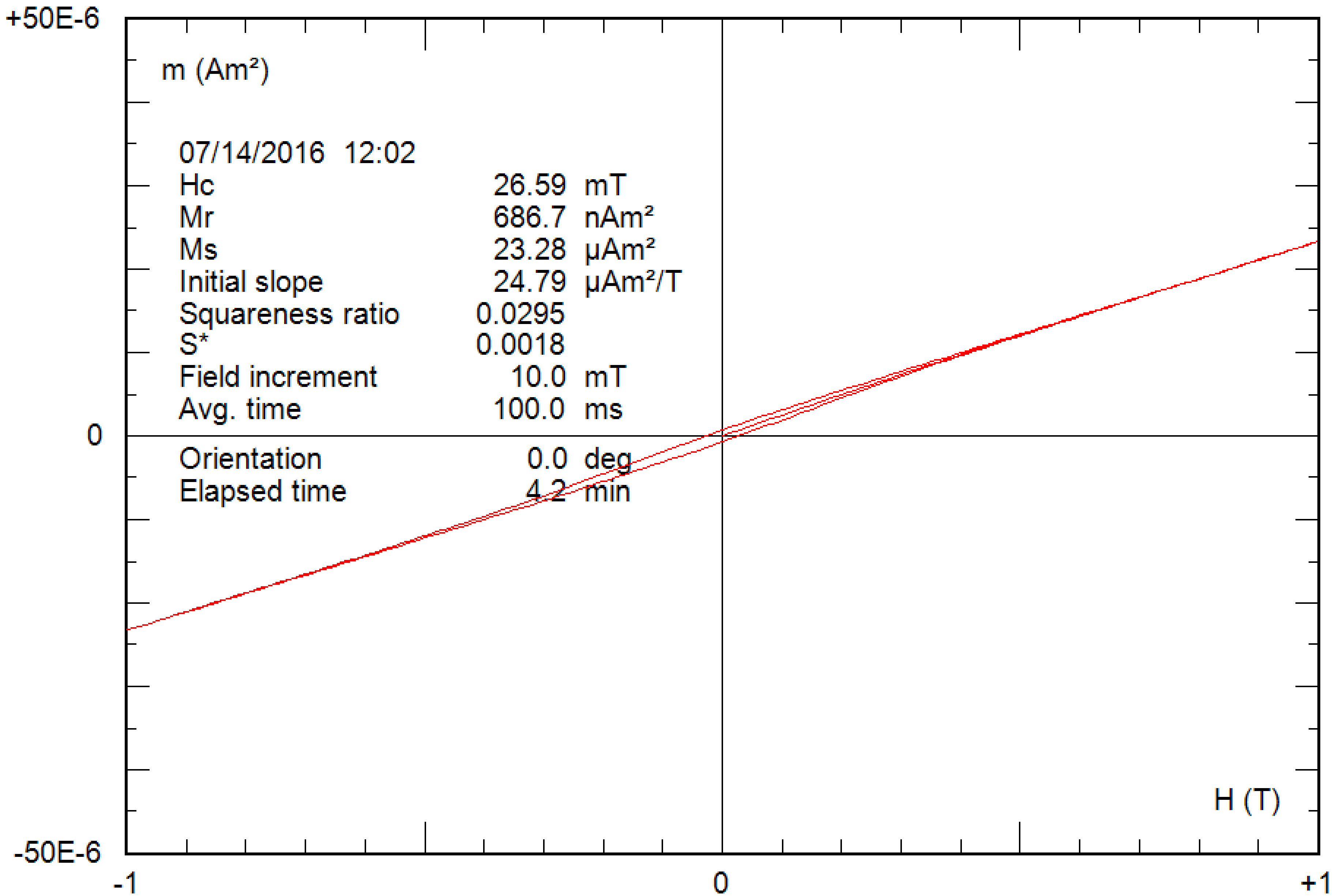

0.24 g

File: 43-05c_hyst

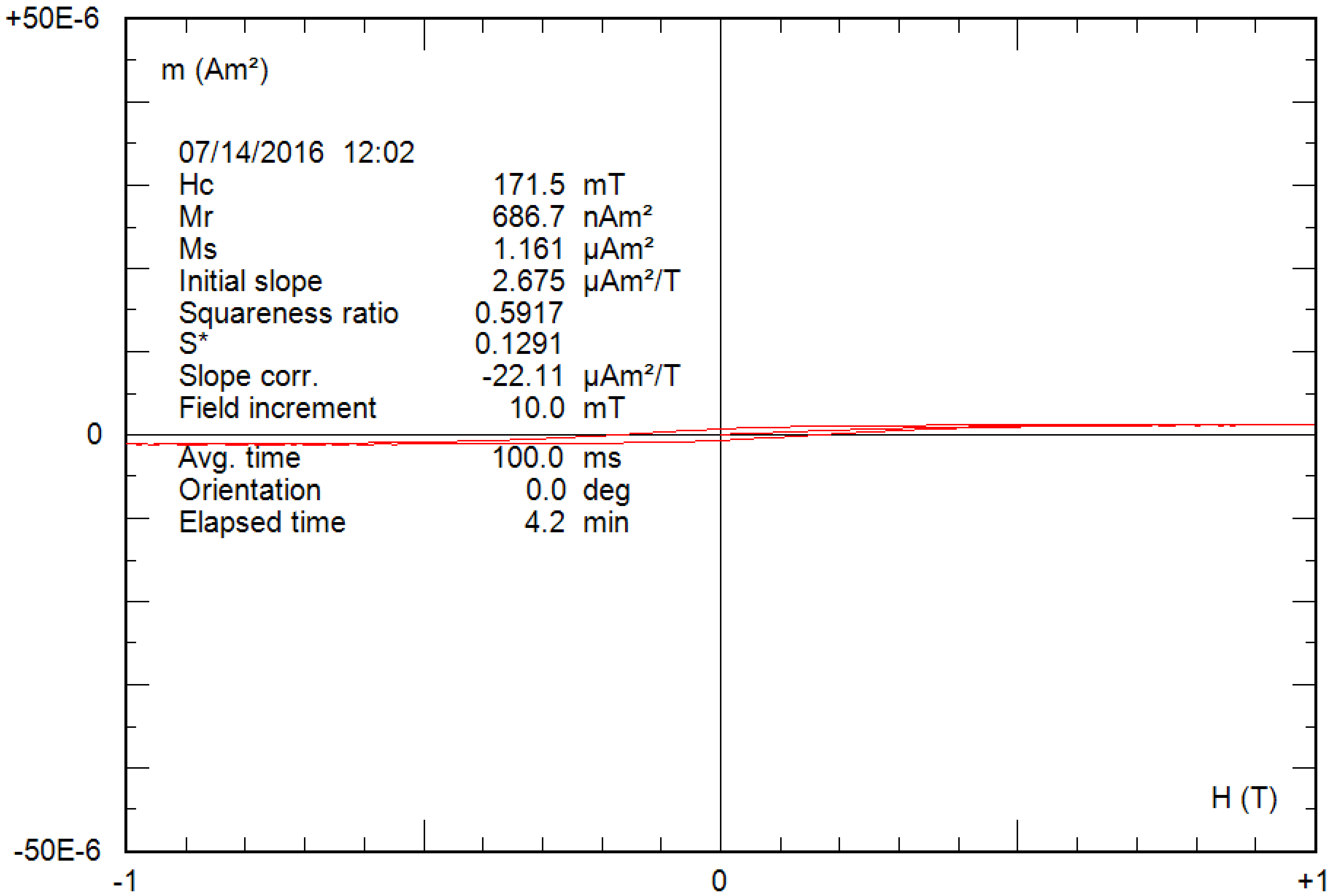

0.24 g

File: 43-05c_hyst_corr

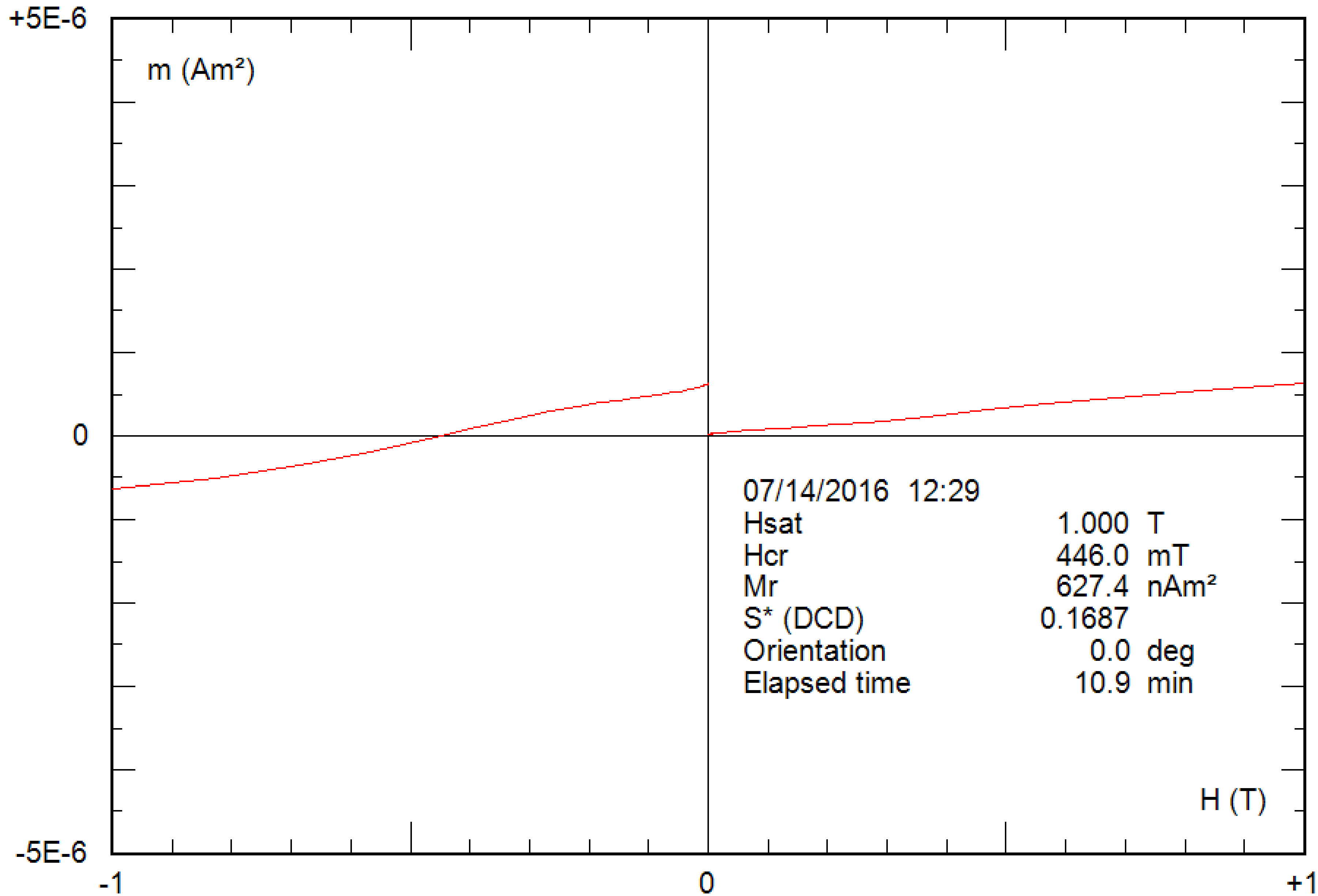

0.24 g

File: 44-10c_bcr

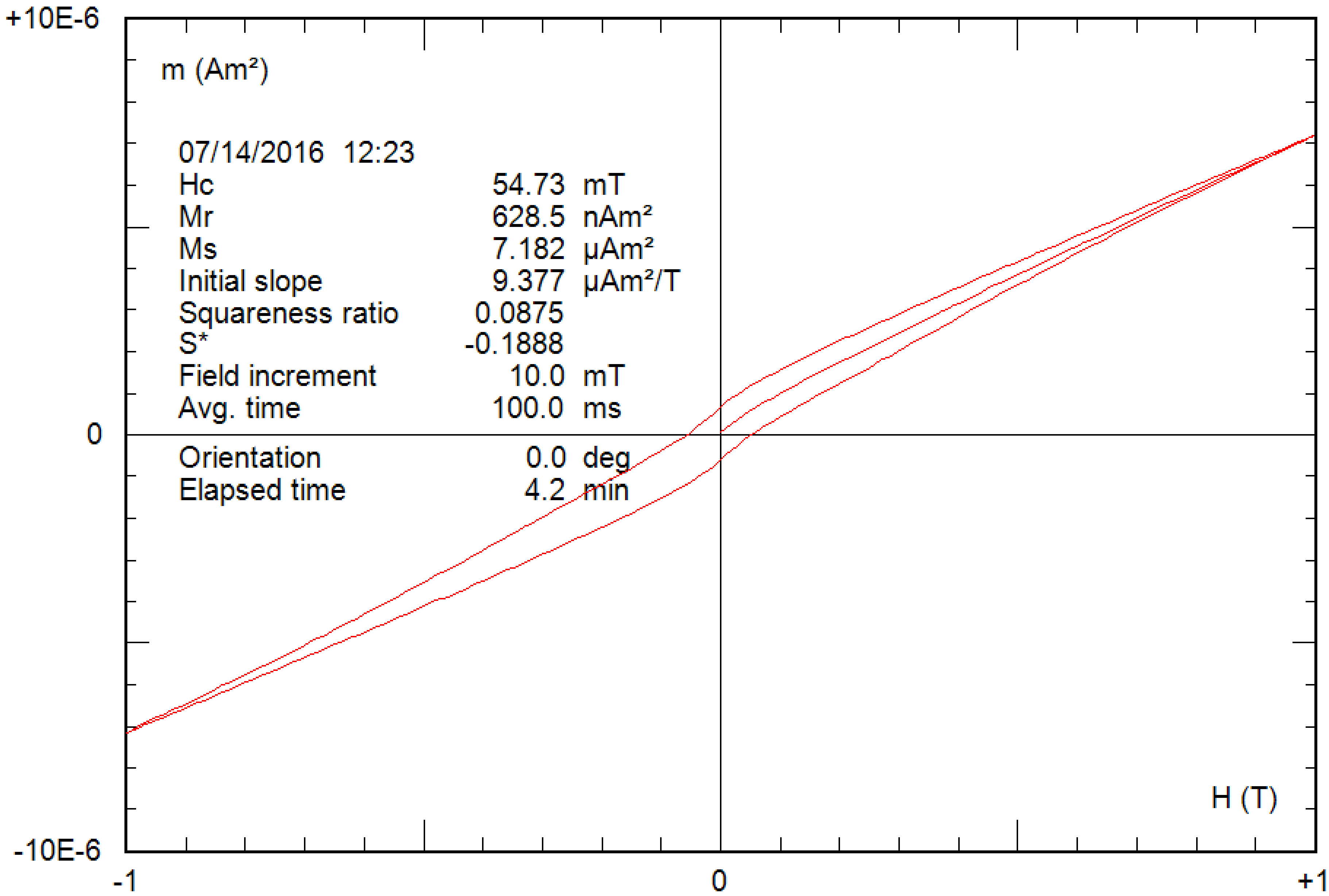

0.24 g

File: 44-10c_hyst

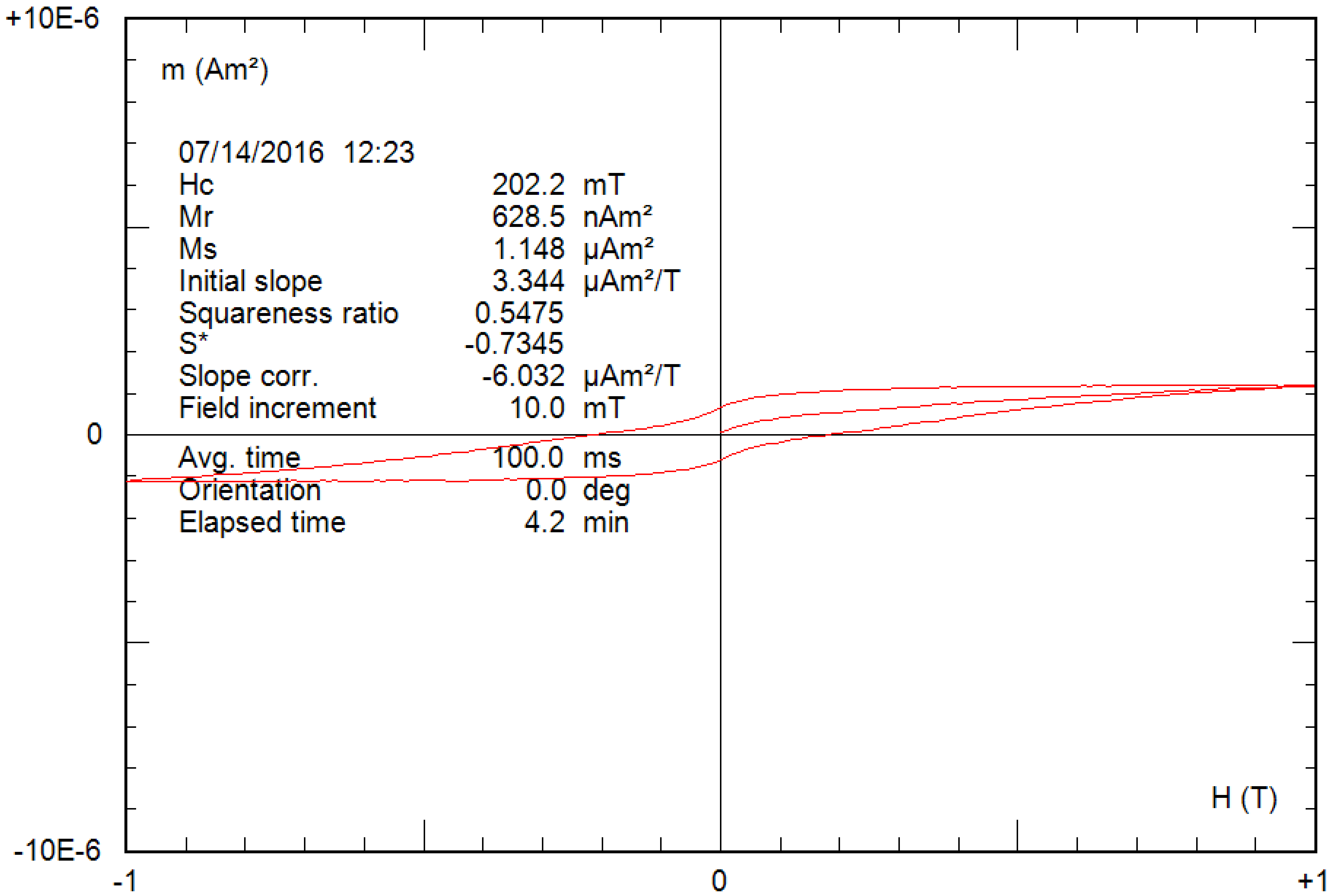

0.24 g

File: 44-10c_hyst_corr

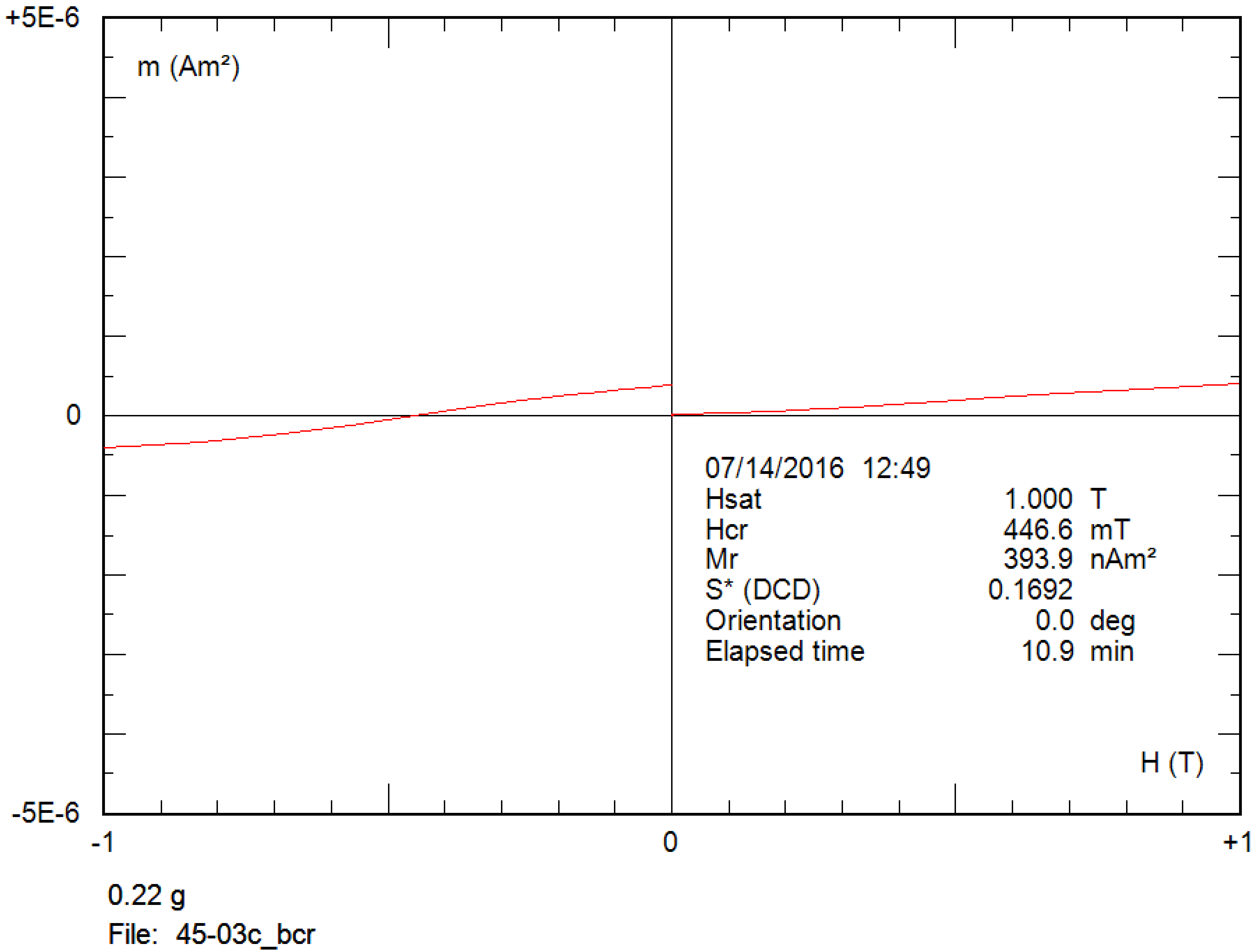

+5E-6
m (Am²)
0
-5E-6
-1
0
+1
H (T)
07/14/2016 12:49
Hsat 1.000 T
Hcr 446.6 mT
Mr 393.9 nAm²
S* (DCD) 0.1692
Orientation 0.0 deg
Elapsed time 10.9 min
0.22 g
File: 45-03c_bcr

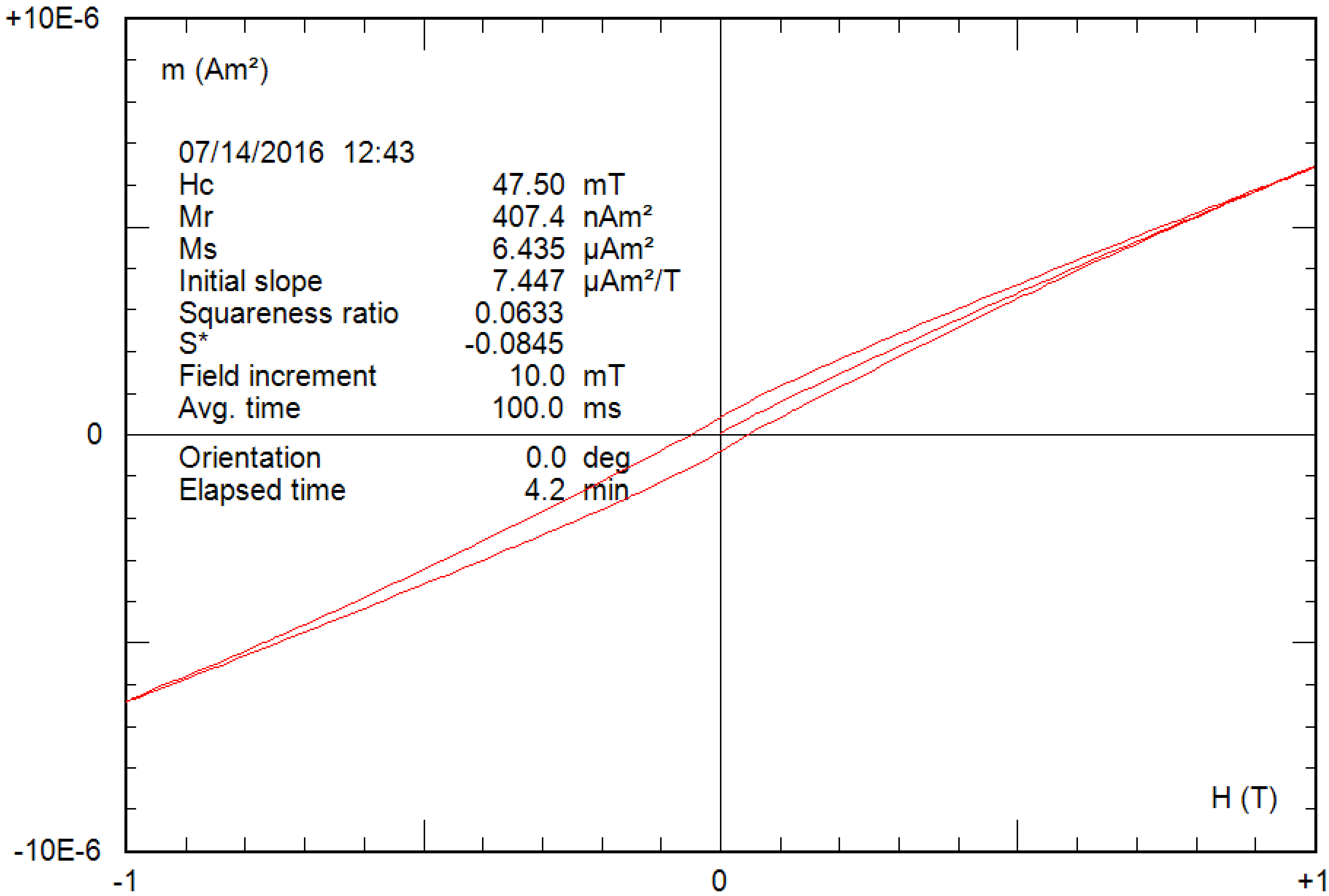

0.22 g

File: 45-03c_hyst

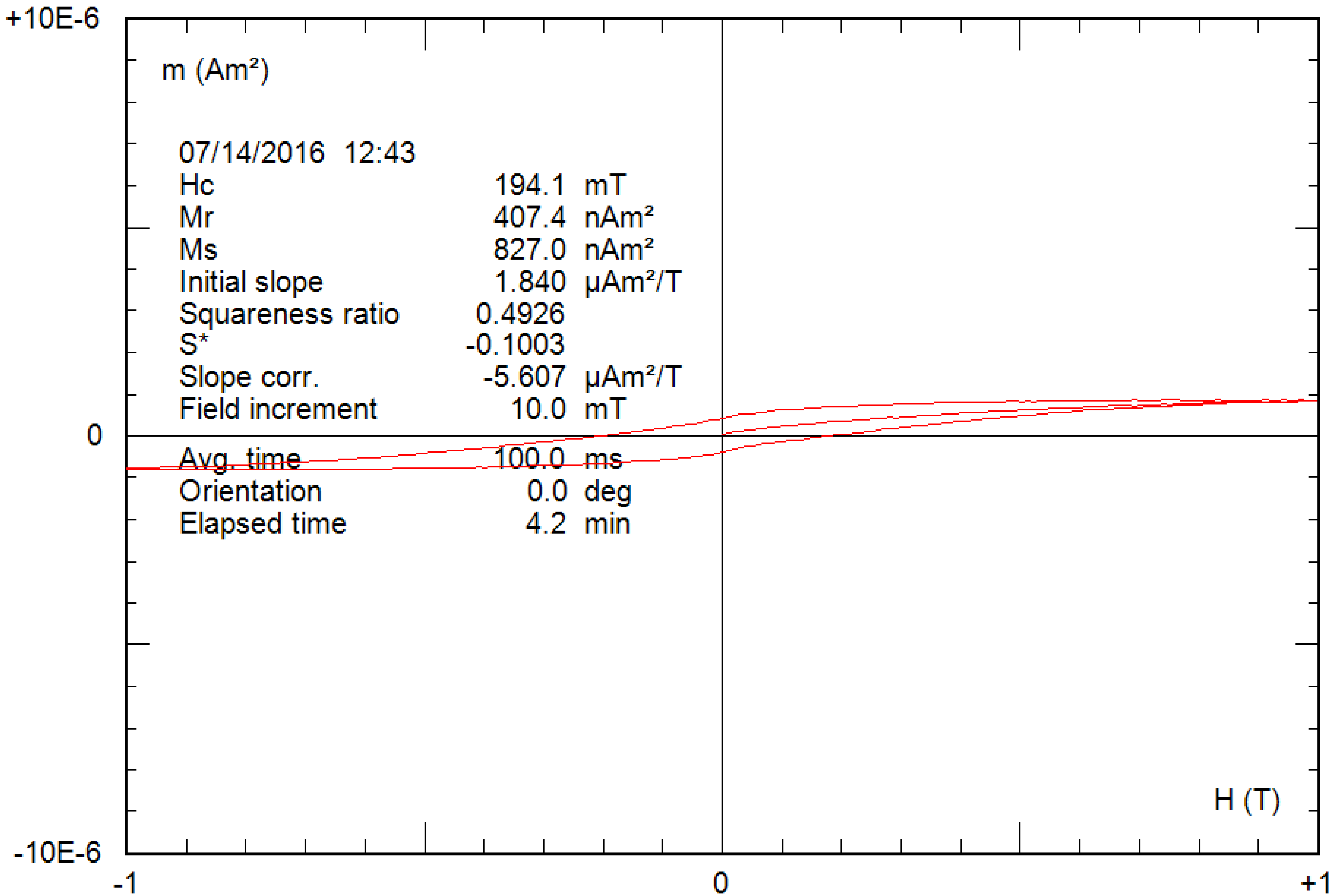

0.22 g

File: 45-03c_hyst_corr

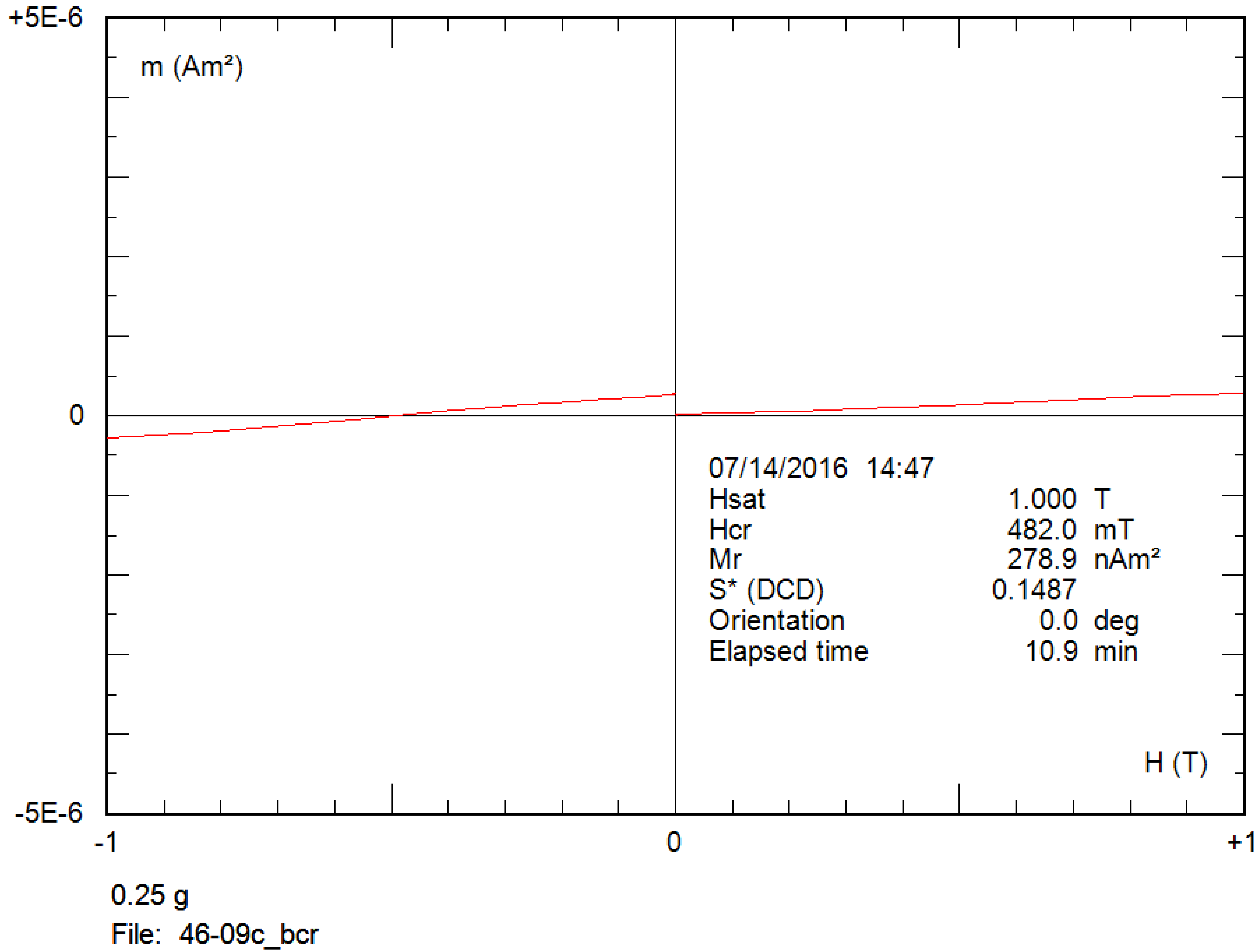
+5E-6
m (Am²)
0
-5E-6
-1
0
+1
H (T)
07/14/2016 14:47
Hsat 1.000 T
Hcr 482.0 mT
Mr 278.9 nAm²
S* (DCD) 0.1487
Orientation 0.0 deg
Elapsed time 10.9 min
0.25 g
File: 46-09c_bcr

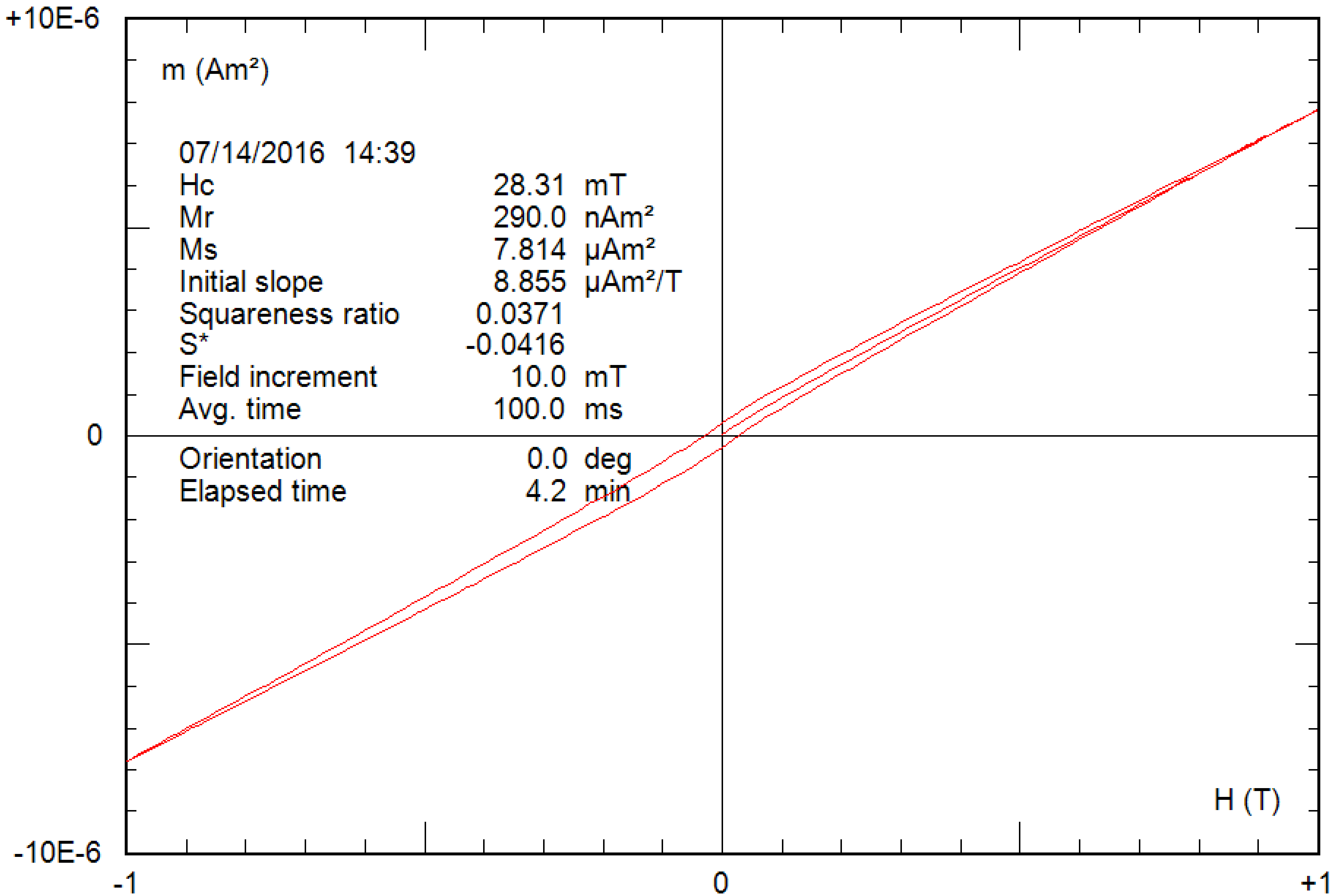

0.25 g

File: 46-09c_hyst

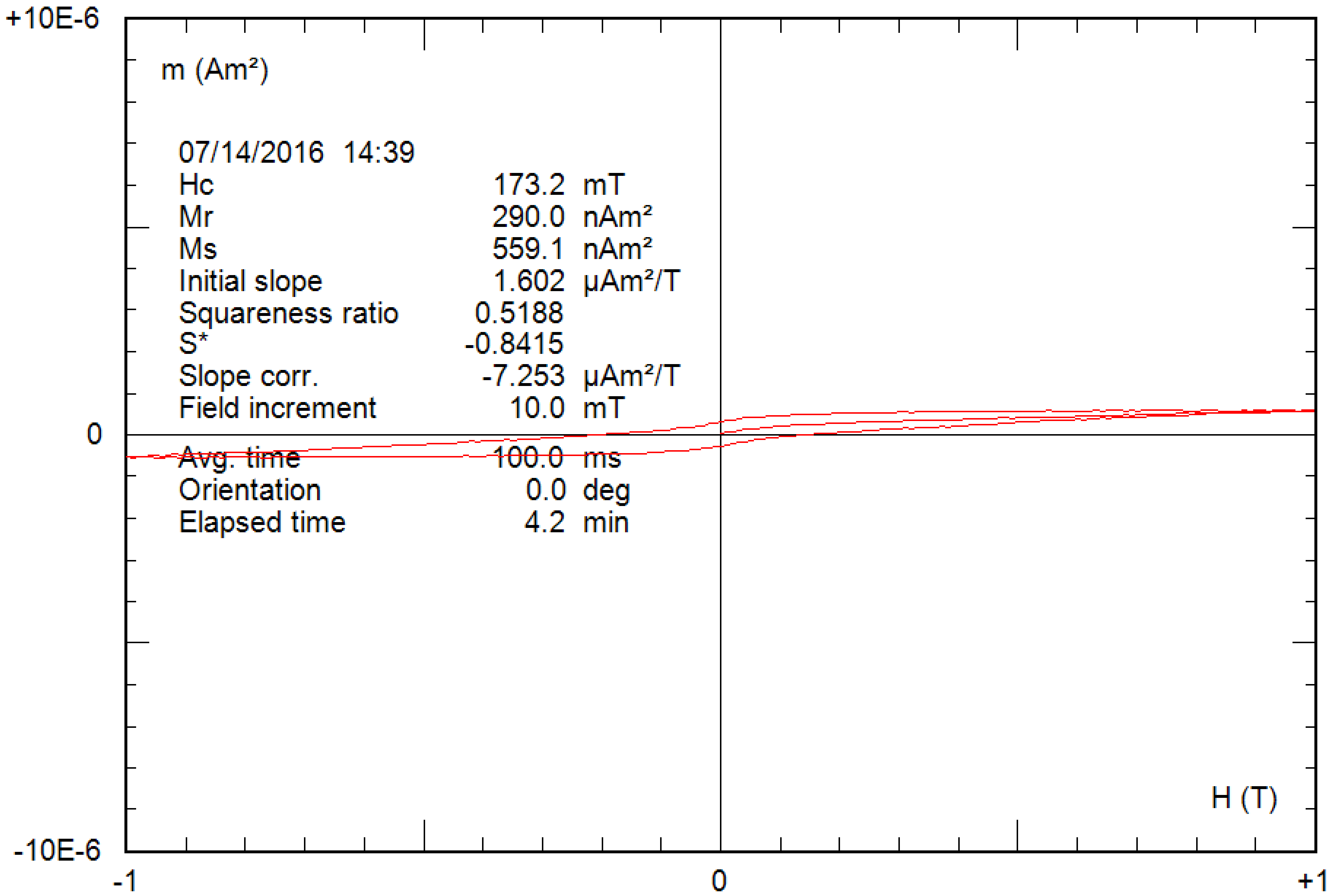

0.25 g

File: 46-09c_hyst_corr

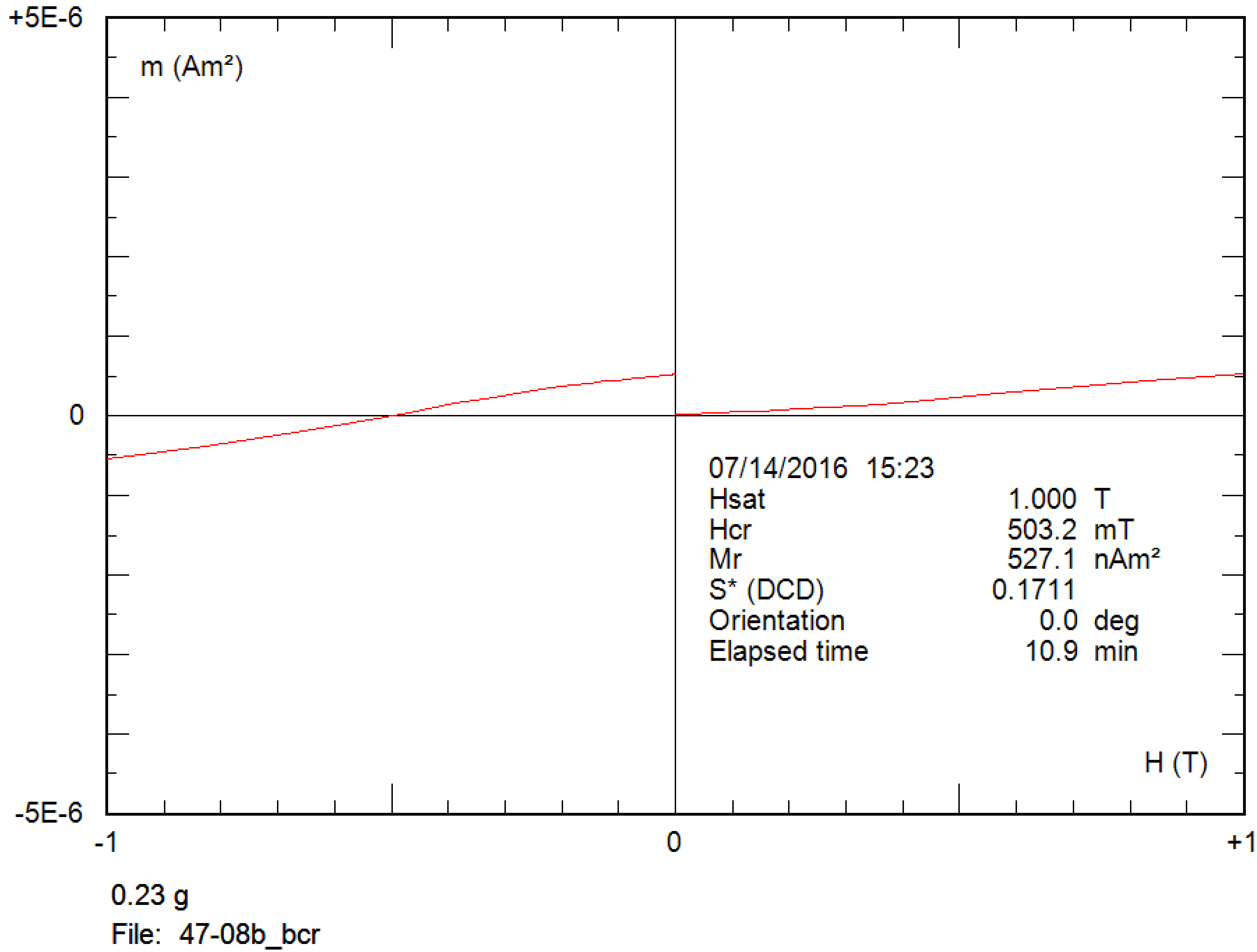
+5E-6
m (Am²)
0
-5E-6
-1
0
+1
H (T)
07/14/2016 15:23
Hsat 1.000 T
Hcr 503.2 mT
Mr 527.1 nAm²
S* (DCD) 0.1711
Orientation 0.0 deg
Elapsed time 10.9 min
0.23 g
File: 47-08b_bcr

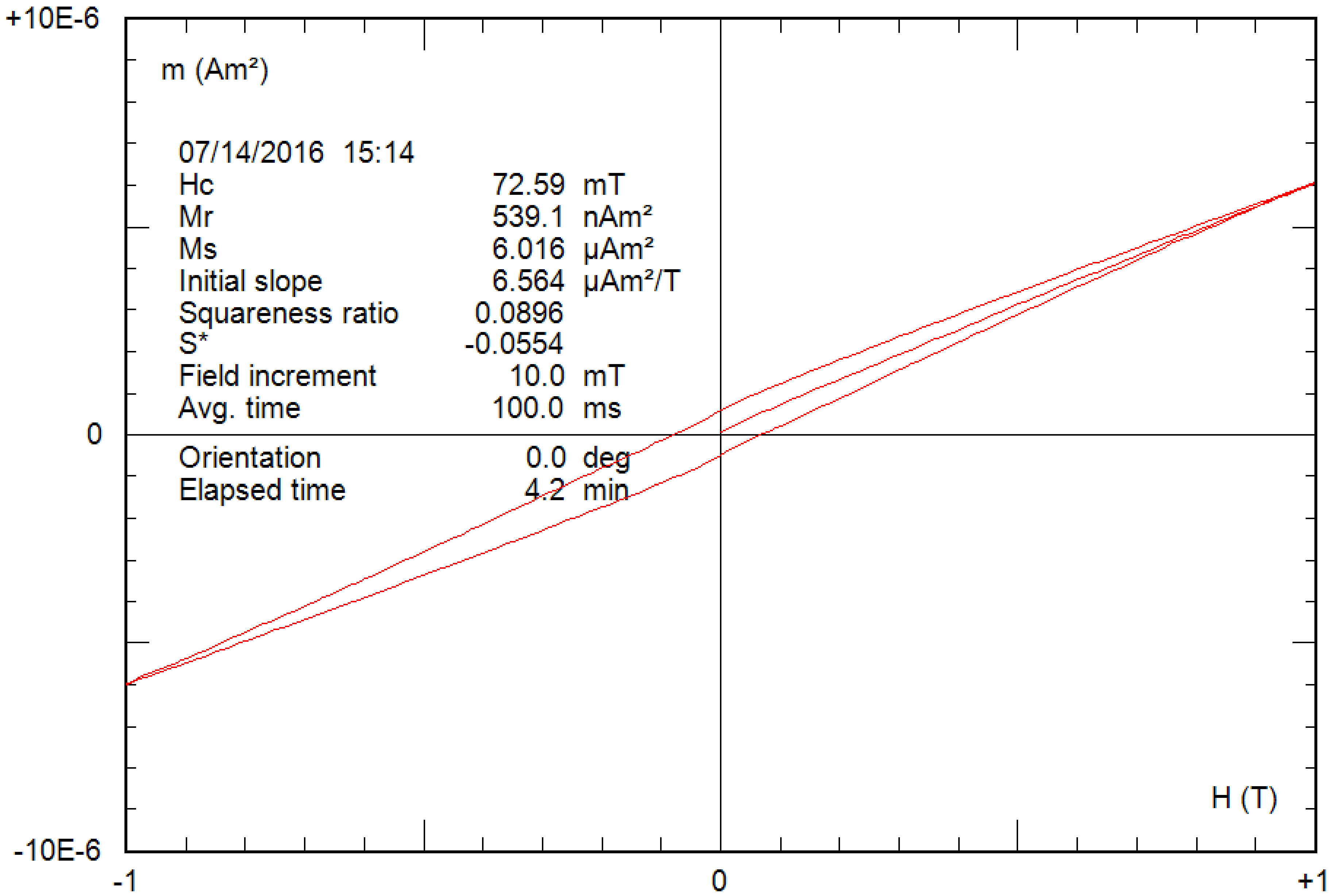

0.23 g

File: 47-08b_hyst

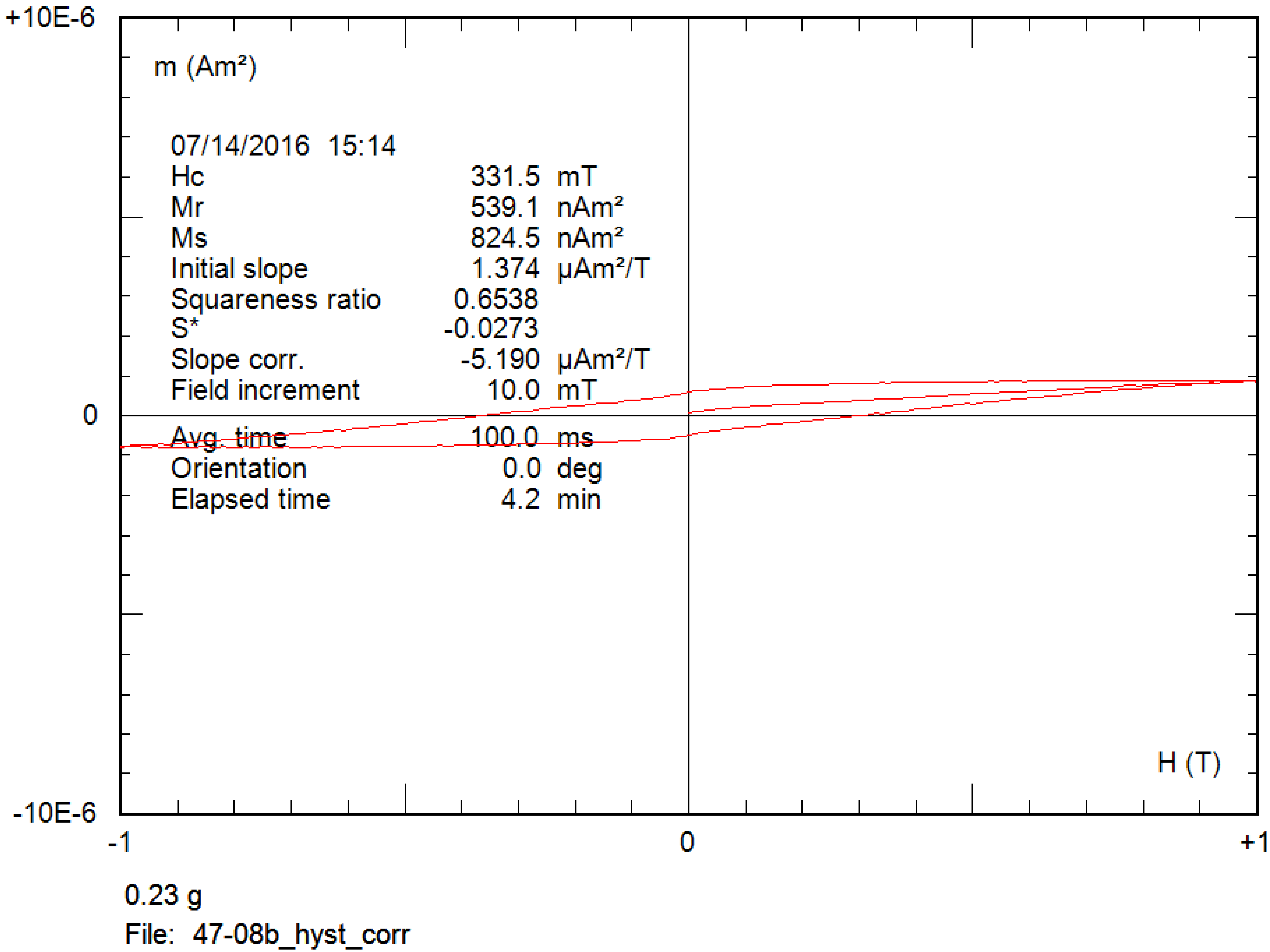
+10E-6
m (Am²)
07/14/2016 15:14
Hc 331.5 mT
Mr 539.1 nAm²
Ms 824.5 nAm²
Initial slope 1.374 µAm²/T
Squareness ratio 0.6538
S* -0.0273
Slope corr. -5.190 µAm²/T
Field increment 10.0 mT
0
Avg. time 100.0 ms
Orientation 0.0 deg
Elapsed time 4.2 min
H (T)
-10E-6
-1
0
+1
0.23 g
File: 47-08b_hyst_corr

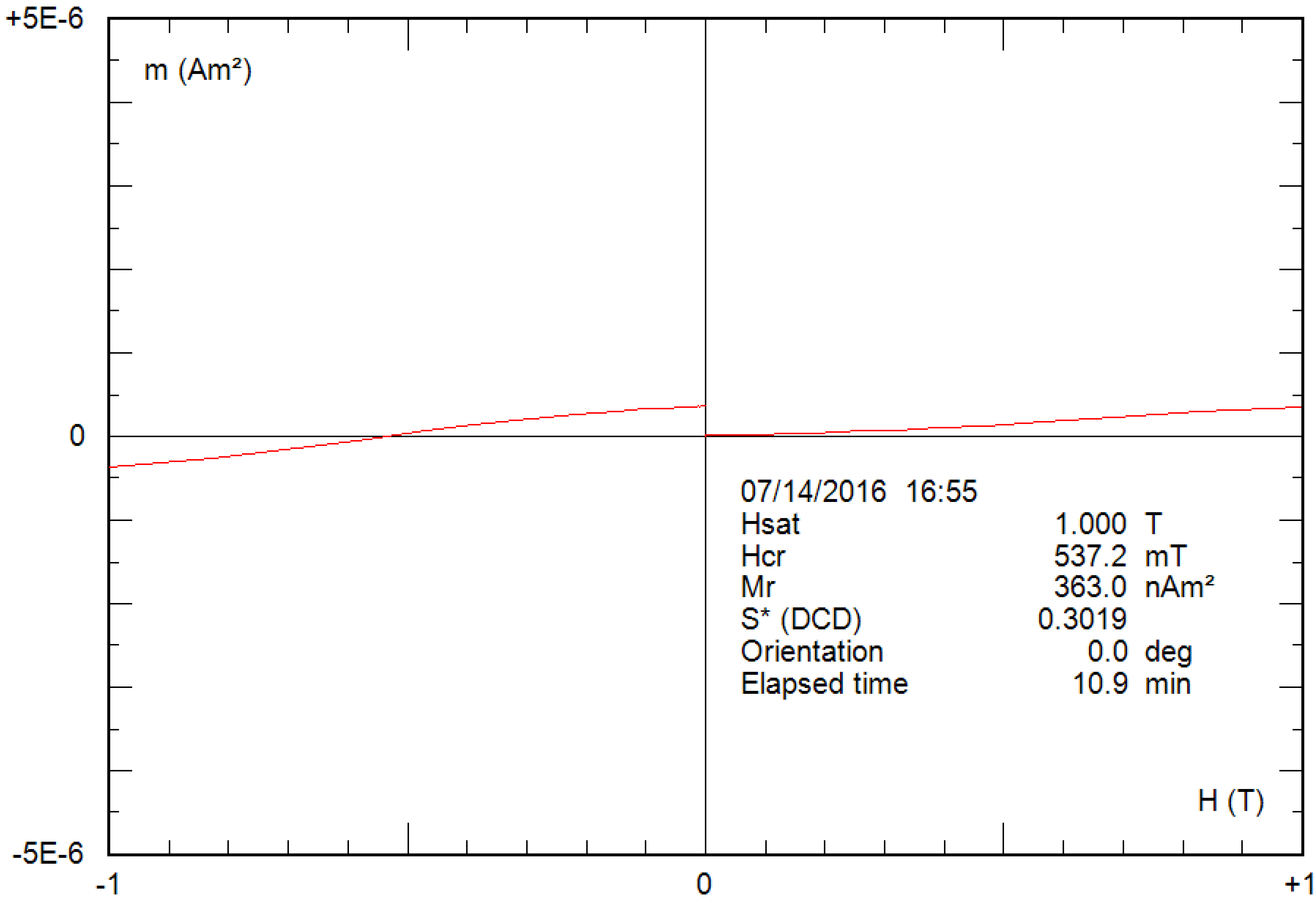

0.25 g

File: 48-05c_bcr

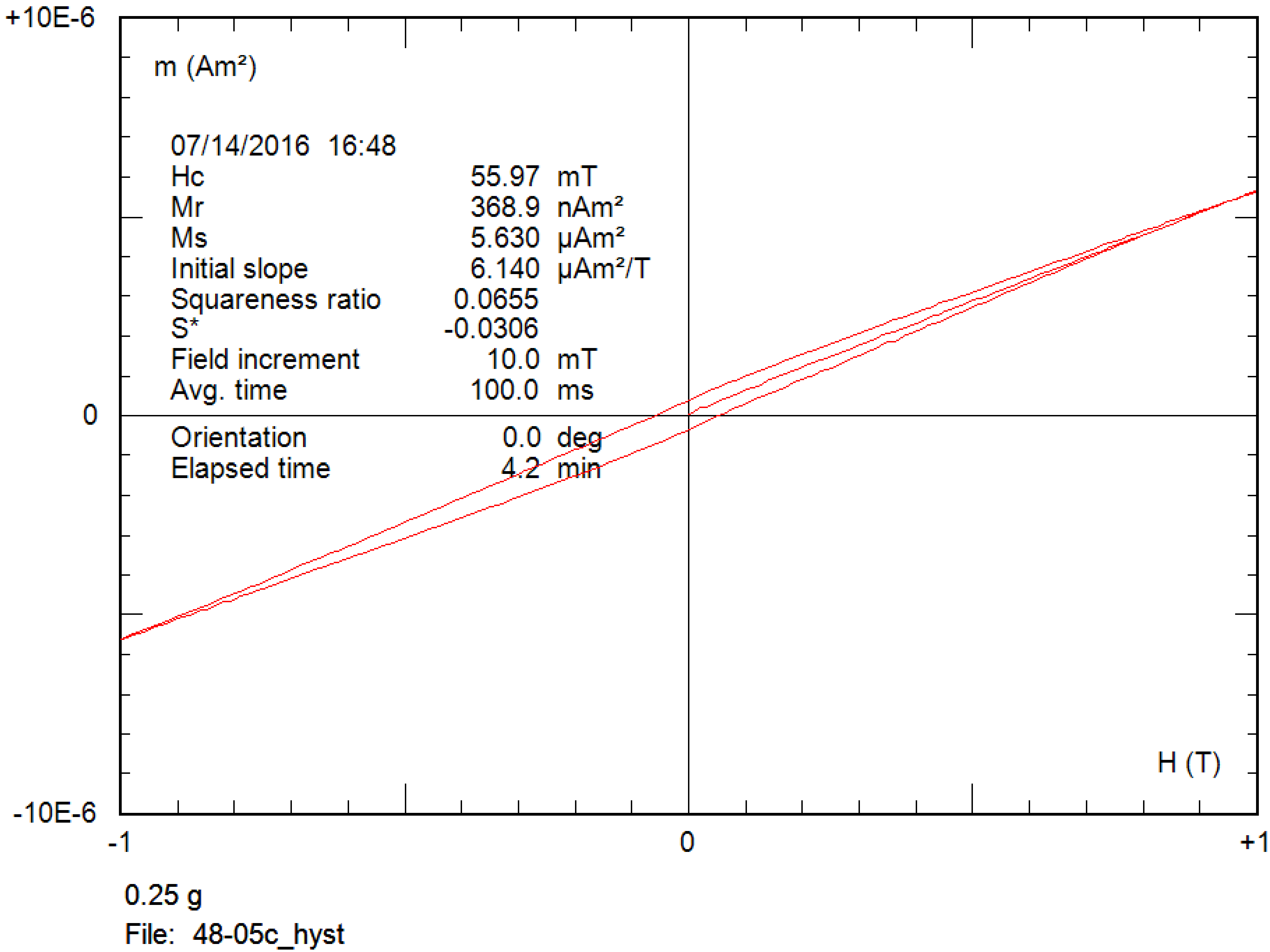

+10E-6
m (Am²)
07/14/2016 16:48
Hc 55.97 mT
Mr 368.9 nAm²
Ms 5.630 µAm²
Initial slope 6.140 µAm²/T
Squareness ratio 0.0655
S* -0.0306
Field increment 10.0 mT
Avg. time 100.0 ms
0
Orientation 0.0 deg
Elapsed time 4.2 min
H (T)
-10E-6
-1
0
+1
0.25 g
File: 48-05c_hyst

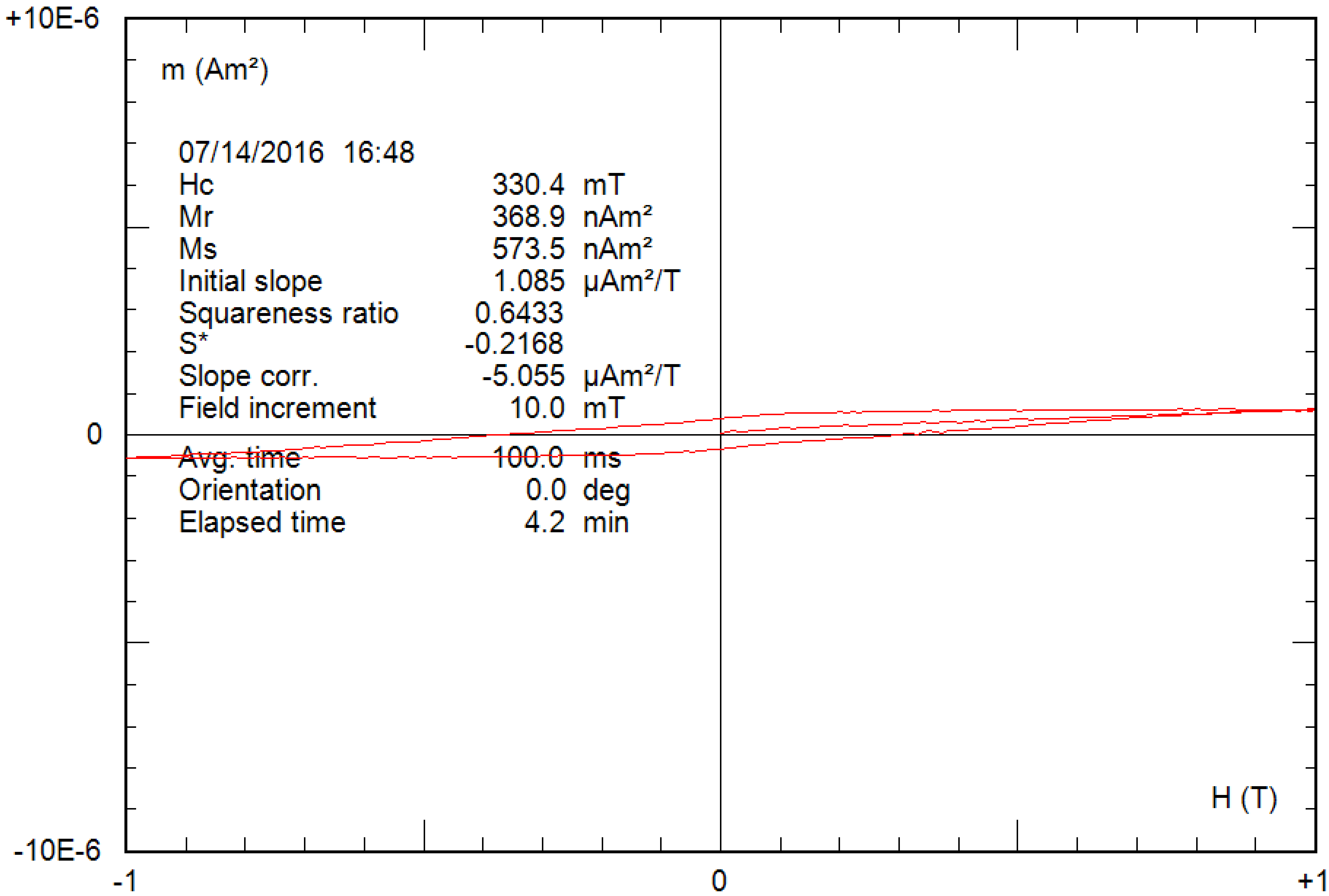

0.25 g

File: 48-05c_hyst_corr

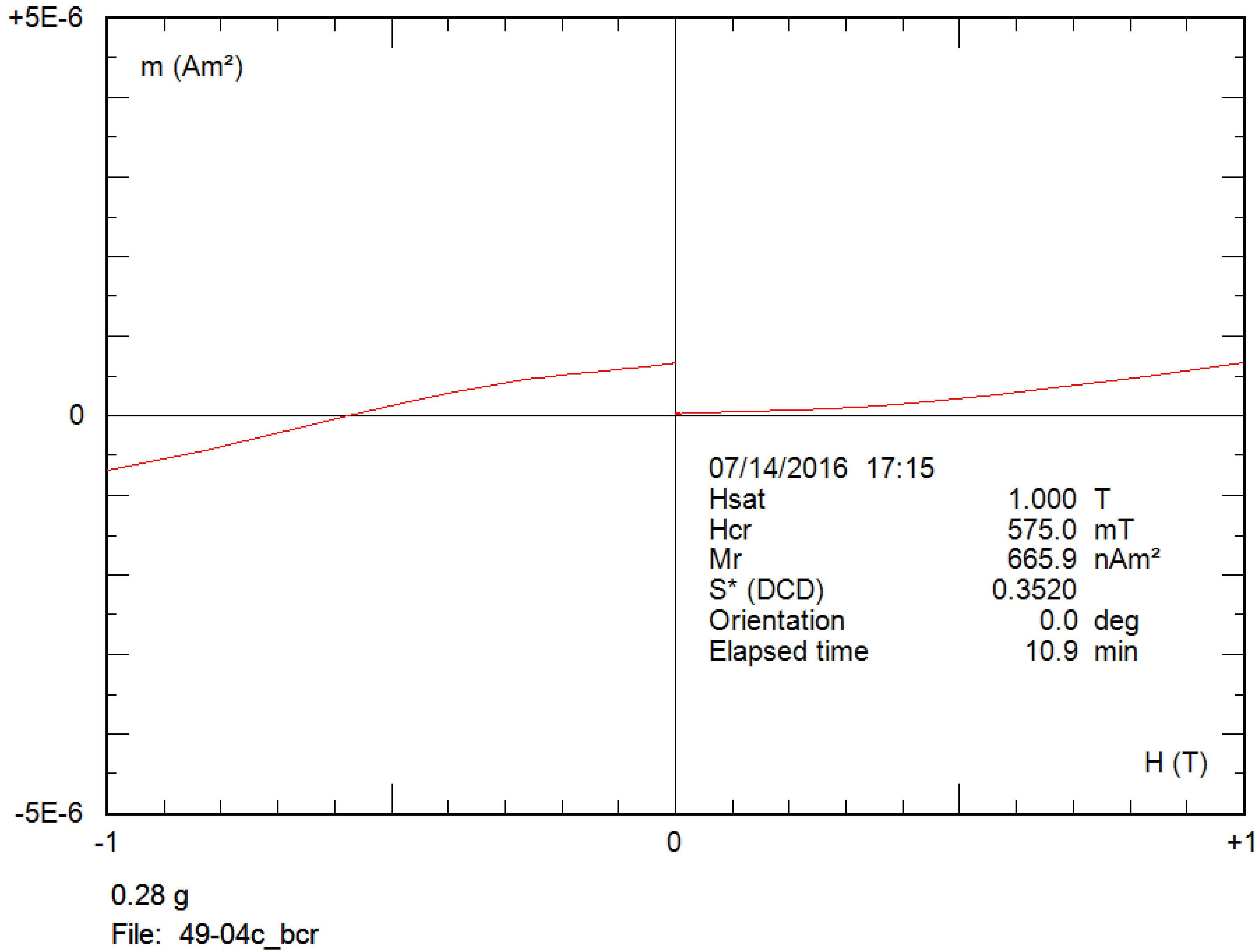
+5E-6
m (Am²)
0
-5E-6
-1
0
+1
H (T)
07/14/2016 17:15
Hsat 1.000 T
Hcr 575.0 mT
Mr 665.9 nAm²
S* (DCD) 0.3520
Orientation 0.0 deg
Elapsed time 10.9 min
0.28 g
File: 49-04c_bcr

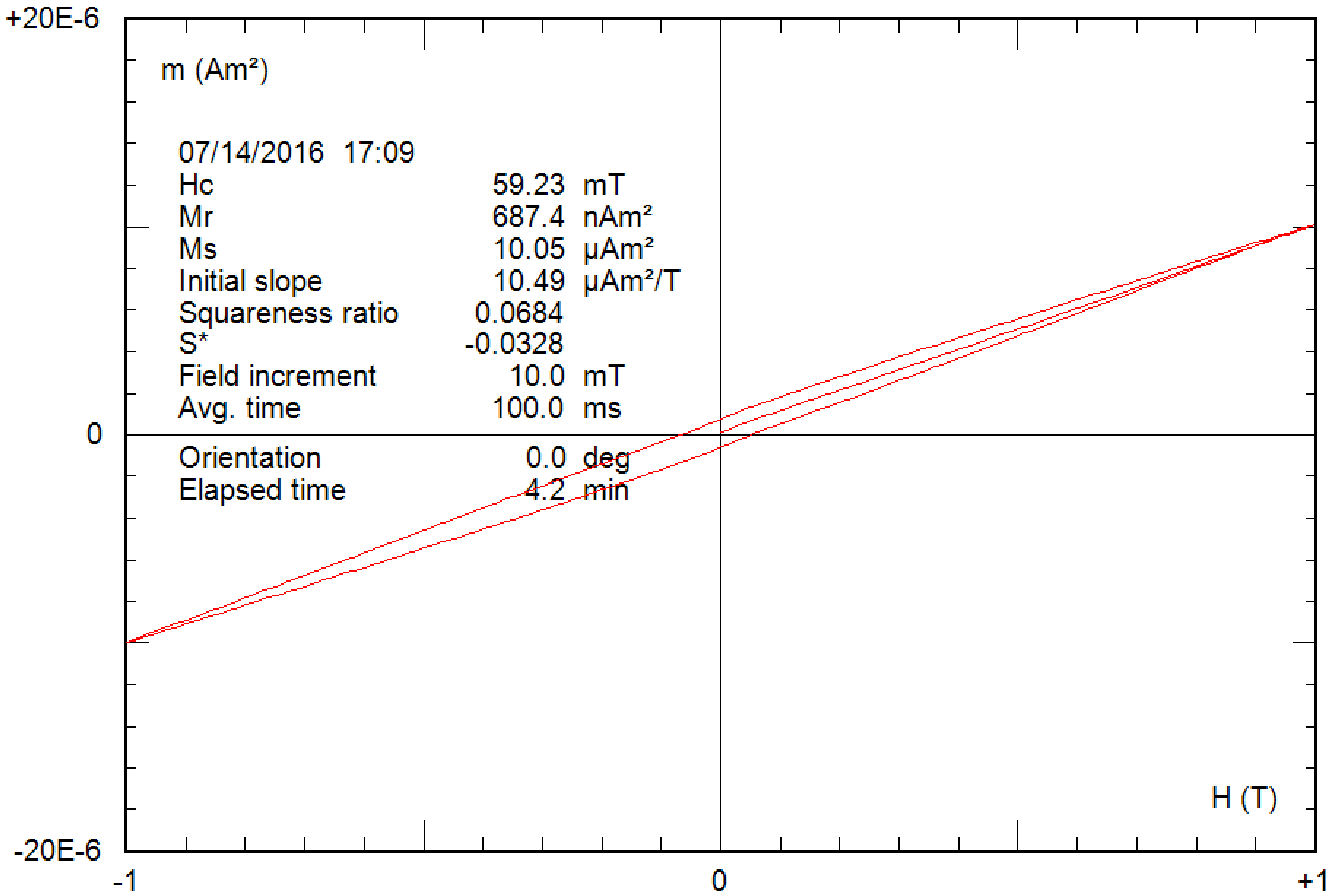

0.28 g

File: 49-04c_hyst

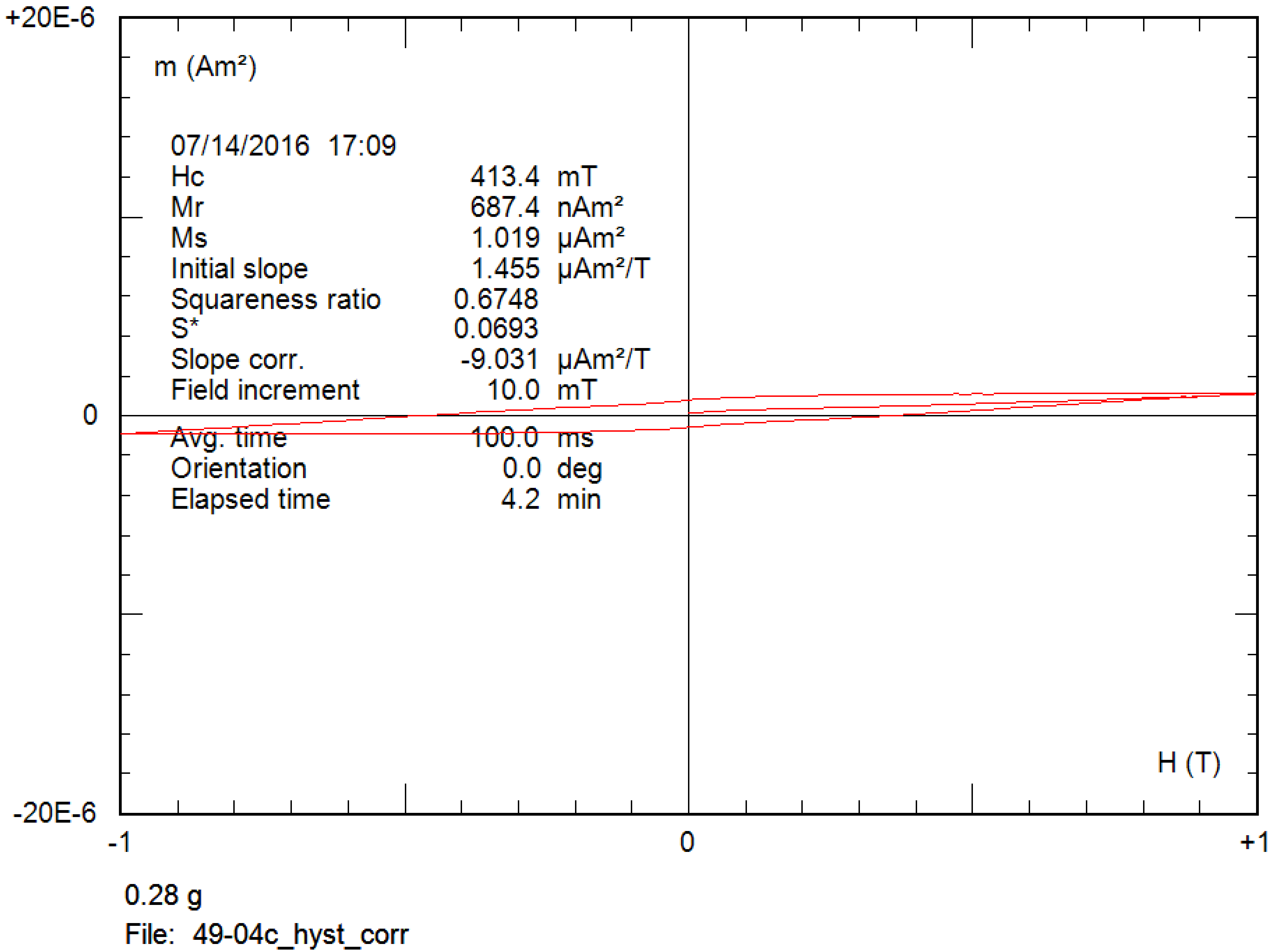
+20E-6
m (Am²)
07/14/2016 17:09
Hc 413.4 mT
Mr 687.4 nAm²
Ms 1.019 µAm²
Initial slope 1.455 µAm²/T
Squareness ratio 0.6748
S* 0.0693
Slope corr. -9.031 µAm²/T
Field increment 10.0 mT
0
Avg. time 100.0 ms
Orientation 0.0 deg
Elapsed time 4.2 min
H (T)
-20E-6
-1
0
+1
0.28 g
File: 49-04c_hyst_corr

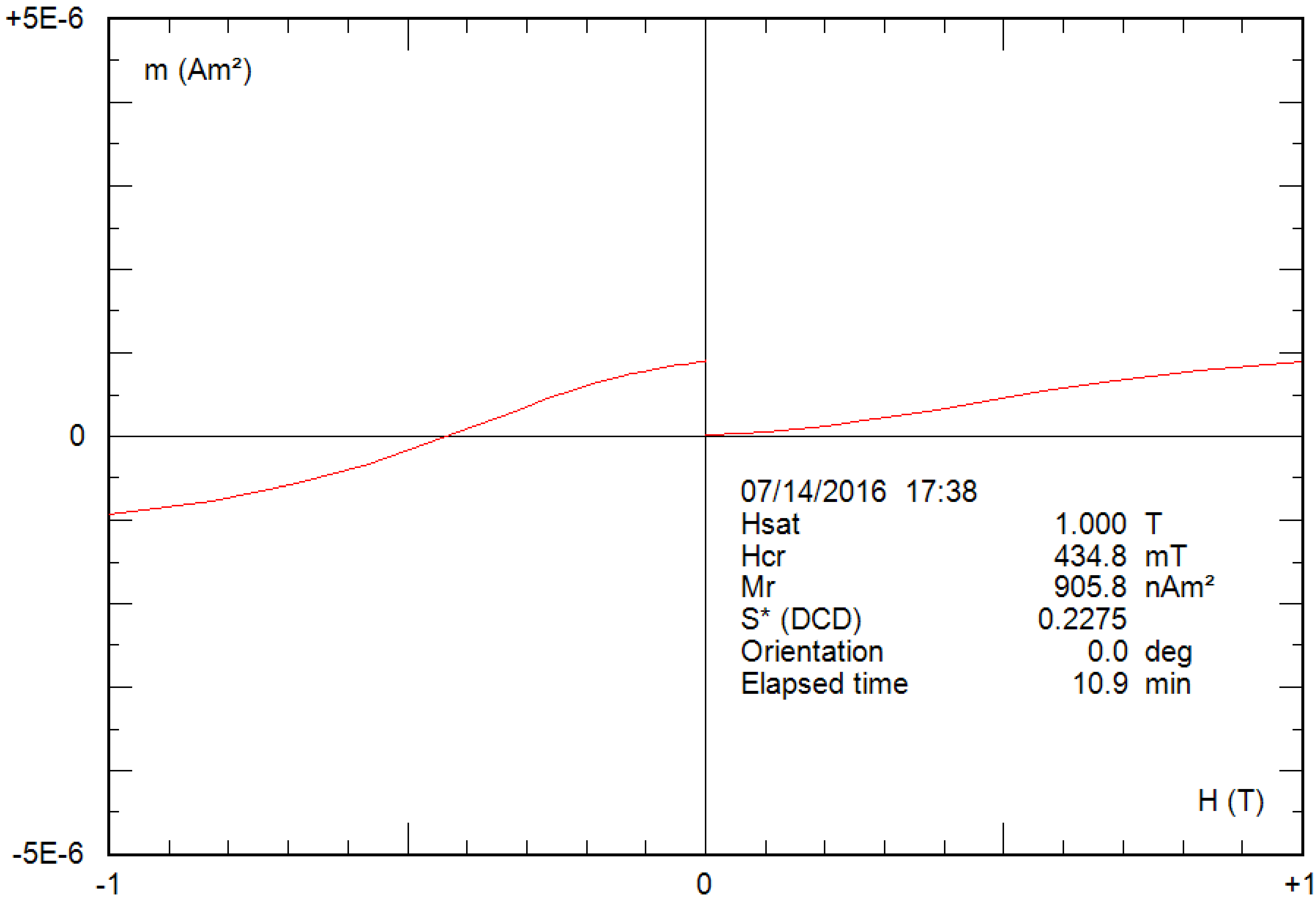

0.22 g

File: 50-10c_bcr

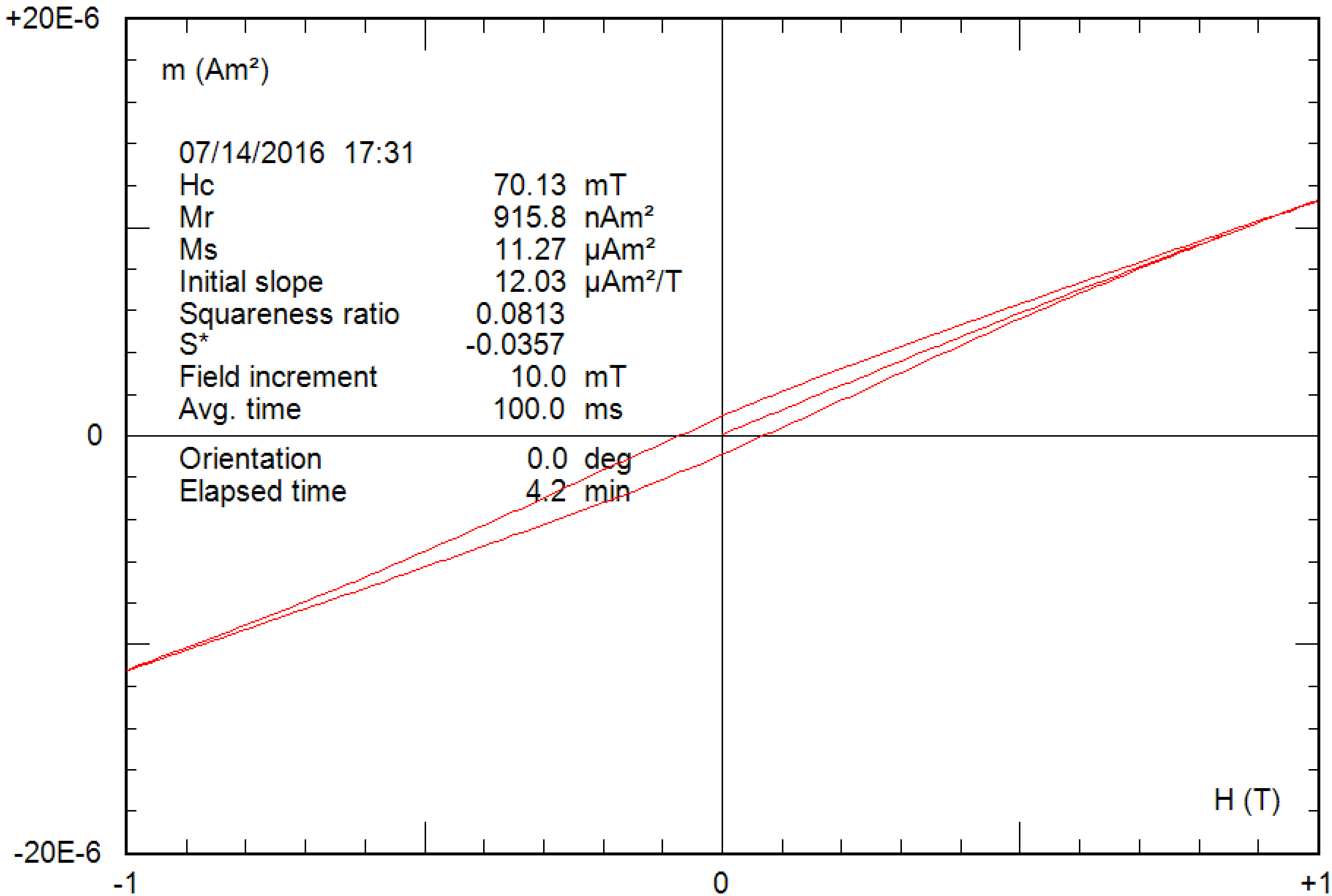

0.22 g

File: 50-10c_hyst

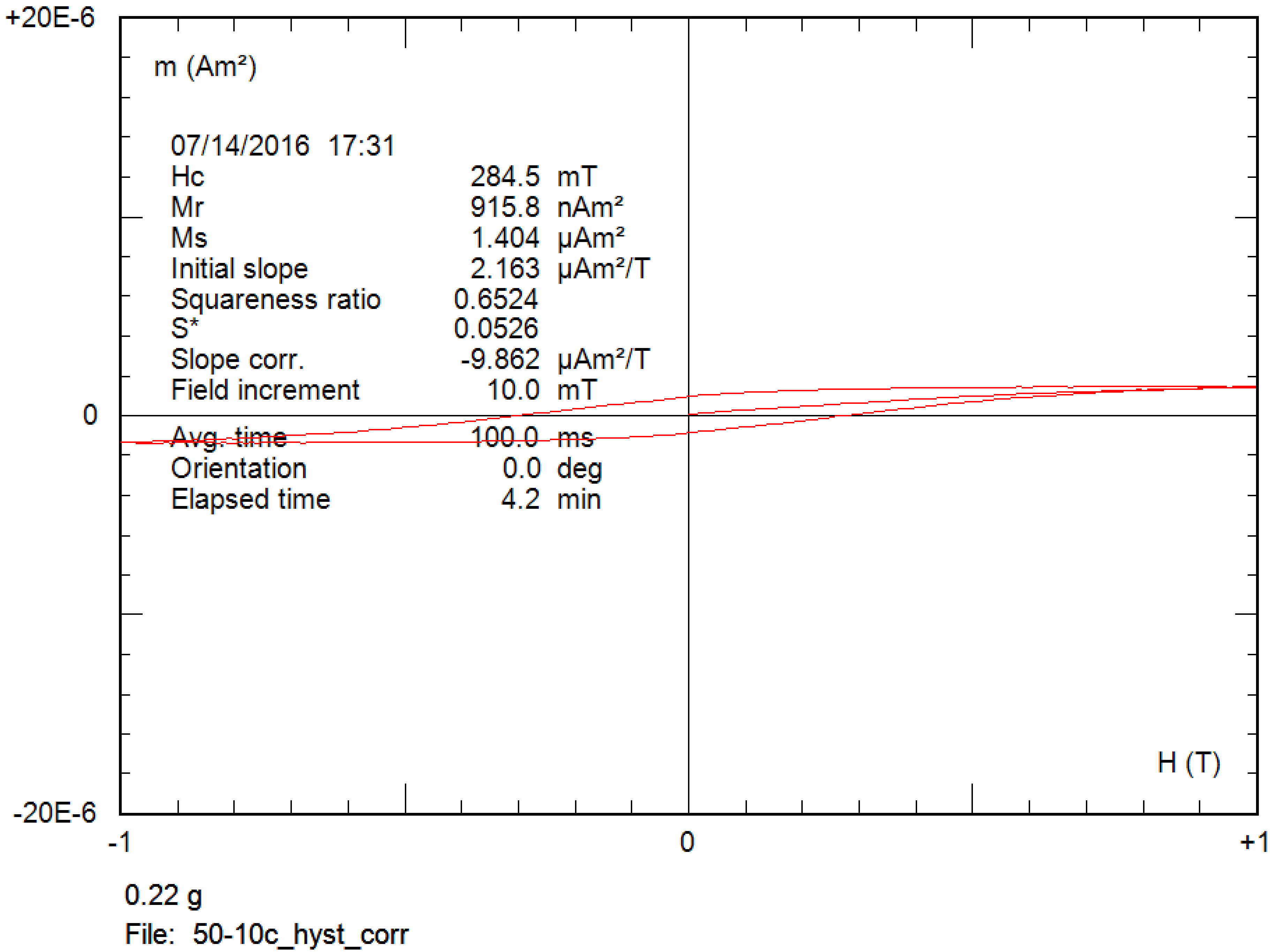
+20E-6
m (Am²)
07/14/2016 17:31
Hc 284.5 mT
Mr 915.8 nAm²
Ms 1.404 µAm²
Initial slope 2.163 µAm²/T
Squareness ratio 0.6524
S* 0.0526
Slope corr. -9.862 µAm²/T
Field increment 10.0 mT
0
Avg. time 100.0 ms
Orientation 0.0 deg
Elapsed time 4.2 min
H (T)
-20E-6
-1
0
+1
0.22 g
File: 50-10c_hyst_corr